PTB

OTTO VON GUERICKE
UNIVERSITÄT
MAGDEBURG

HELMHOLTZ
FONDS e.V.

14th International Symposium on Hazards, Prevention and Mitigation of Industrial Explosions

Braunschweig, Germany | July 11 – 15, 2022

Proceedings

ISHPMIE2022
Braunschweig, Germany

Physikalisch-Technische Bundesanstalt

Otto von Guericke Universität Magdeburg

Proceedings

of the

14th International Symposium on Hazards, Prevention and Mitigation of Industrial Explosions

DOI: 10.7795/810.20221124

Citation Template:

Author 1, Author 2, ... : "Title of article", pp. n1 - n2 . In: "Proceedings of the 14th International Symposium on Hazards, Prevention and Mitigation of Industrial Explosions (ISHPMIE 2022)", Braunschweig, Germany, 2022. DOI: 10.7795/810.20221154

Herausgeber:
Physikalisch-Technische Bundesanstalt
Bundesallee 100
38116 Braunschweig, Germany
Dr. Michael Beyer
Dr. Arnas Lucassen
3.7 | Fundamentals of Explosion Protection
phone: +49 531 592-3700
e-mail: michael.beyer@ptb.de
ishpmie2022.ptb.de
ishpmie2022@ptb.de

DOI: 10.7795/810.20221124

DOI: 10.7795/810.20221124

Contents

Message from the Local Organizing Committee *(Michael Beyer)* **9**
Message from the Program Committee *(Holger Großhans)* **10**
List of Symposium Committees **11**

Plenary and Review (*Holger Großhans*)

Hybrid mixture explosions – A brief review **12**

Peng Zhao, Dejian Wu, Stefan H. Spitzer, Arne Krietsch, Paul Amyotte, Ulrich Krause (#8)

Session 01: Advances in explosion protection: Strategies, measures, and protective equipment I *(Dieter Gabel)*

Flameproof enclosure and pressure relief: Status quo **55**

Sabrina Herbst, Johanna Gerlach; Leo Siegle, Frank Engelmann, Thorsten Arnhold (#8)

Influence of vent distribution on the violence of a gas explosion **65**

Jérôme Daubech, Emmanuel Leprette, Christophe Proust (#66)

Gas phase explosions in oxygen enriched atmospheres **79**

Simon Egan (#69)

Session 02: Explosion modelling and simulation I *(Josué Melguizo-Gavilanes)*

Investigation on flame propagation and particle decomposition behavior of dust explosion in MIKE 3 apparatus **89**

Yangyue Pan, Christoph Spijker, Harald Raupenstrauch (#19)

TGA-FTIR for kinetic and evolved gas analysis of the coal particles in dust deflagration **98**

Yangyue Pan, Christoph Spijker, Harald Raupenstrauch (#20)

A Numerical Model for the Minimum Ignition Temperature of Dust Clouds **115**

Tengfei Chen, Jo van Caneghem, Jan Degrève, Jan Berghmans, Filip Verplaetsen, Maarten Vanierschot (#53)

Session 03: Explosion testing I *(Regis Bauwens)*

Acceleration sensitivity of piezoelectric pressure sensors and the influence on the measurement of explosion pressures **128**

Tim Krause, Jens Brunzendorf, Detlev Markus, Harun Kanbur, Niels Springer, Otto Walch, Christian Herr (#29)

A comparative study between two ignition sources: electric igniter versus pyrotechnic igniter **148**

Stephane Bernard, Chayma El Gadha, Mame William Louis (#30)

Measurement of dust flame propagation and temperature with low wall influence **158**

Christoph Spijker, Stefan Puttinger, Simon Schneiderbauer, Stefan Pirker, Georg Meyer, Christoph Buchner, Tino Lindner-Silwester (#37)

Session 04: Hydrogen safety I *(Chunkan Yu)*

Large-scale tests to investigate the consequences of exposing cryogenic storage vessels containing liquid hydrogen to a fire load **168**

Martin Kluge, Abdel Karim Habib, Kees van Wingerden (#49)

Experimental investigation into the consequences of release of liquified hydrogen onto and under water **182**

Martin Kluge, Abdel Karim Habib, Kees van Wingerden (#50)

Minimum diameters for CH4/H2-air mixtures: implications for natural gas cooktop burners **197**

Paola Cristian Mejía-Botero, Josué Melguizo-Gavilanes, Fernando Veiga-López (#57)

Session 05: Explosion prevention I *(Ritsu Dobashi)*

Experimental study of humidity influence on triboelectric charging of particle-laden duct flows **210**

Holger Grosshans, Wenchao Xu (#15)

Assessment of explosion risks caused by cone discharges when filling silos and containers with pellets **220**

Martin Glor, Ute Hesener (#46)

Review on CFD modeling of electrostatic powder charging during pneumatic conveying **231**

Holger Grosshans, Simon Jantac (#84)

Session 06: Dust explosions I *(Maria Portarapillo)*

Classification of Dispersibility for Combustible Dust based on Hausner Ratio **244**

Yajie Bu, Albert Addo, Paul Amyotte, Yuan Chunmiao (#11)

Moderation of Fe dust explosion by nano-sized Fe2O3 and Fe3O4 powders **256**

Yongzheng Guo, Kaiyue Ren, Peng Zhao, Weixing Huang, Aizhu Wei, Dejian Wu (#60)

Dust cloud behaviour in the modified Hartmann tube **268**

Enrico Danzi, Olivier Dufaud, Fausto Franchini, Luca Marmo, Matteo Pietraccini (#88)

Session 07: Explosion modelling and simulation II *(Holger Großhans)*

A CFD Based Methodology to Design an Explosion Prevention System For Li-Ion Based Battery Energy Storage System **281**

Anil Kapahi Kapahi, Sunil Lakshmipathy, Stefan Kraft, Jens Conzen, Alberto Alvarez-Rodriguez (#71)

Modelling Methodology for Deflagration Vent Design of Battery Energy Storage Systems **299**

Sunil Lakshmipathy, Anil Kapahi Kapahi, Jerome Taveau, Stefan Kraft, Jens Conzen (#73)

Probabilistic Risk Assessment for domino effect due to Vapor Cloud Explosions using an integrated Petri-Bayesian network approach **311**

Julio Ariel Dueñas Santana, Orelvis González Gómez, Jesus Luis Orozco (#93)

Session 08: Explosion prevention II *(Hannes Kern)*

Inert gas influence on limiting experimental safe gap of fuel-air mixtures at various initial pressures **322**
Maria Mitu, Sabine Zakel, Thomas Stolz (#9)

The capabilities of flame arresters on explosive mixtures with increased inert gas content **332**
Frank Stolpe, Samah Bendada (#43)

Session 09: Explosion-protected devices I *(Jérôme Taveau)*

Thermal evaluation of junction and connection boxes in explosion protection **340**
Florian Koch, Detlev Markus, Ulrich Krause, Peter Thurnherr (#7)

Analysis of flanged joints for flameproof enclosed devices of gas group IIC according to the standard IEC 60079-1 **348**
Victor Hugo Padron Herrera (#24)

An experimental and a numerical study of a vented dust explosion in an 11.5 m3 vessel **360**
Chen Huang Huang (#38)

Session 10: Explosion modelling and simulation III *(Lorenz Boeck)*

Dust Particle Sedimentation in the 20 L Standard Vessel for Dust Explosion Tests **371**
Maria Portarapillo, Almerinda Di Benedetto, Marco Trofa, Roberto Sanchirico (#25)

Improved modelling of hydrogen explosions – representing effects of varying concentration and reduced oxygen atmospheres **381**
Melodía Lucas, Helene Hisken, Trygve Skjold, Bjørn Arntzen (#64)

Characterizing the Reactivity of Large-Scale Explosions Using a Dimensionless Two-Parameter Combustion Model **393**
Regis Bauwens, Lorenz Boeck, Sergey Dorofeev (#70)

Session 11: Hybrid mixture explosions I *(Sabine Zakel)*

The role of vapor fraction in hydrocarbon mist explosion **404**
Stéphanie El-Zahlanieh, Amelie Jean, Alexis Vignes, Olivier Dufaud (#68)

Where one plus one equals three: the MIT of hybrid mixtures **417**
Paul Geoerg, Stefan Spitzer, Dieter Gabel, Ulrich Krause (#17)

Session 13: Dust Explosions II *(Chris Cloney)*

Dust Explosions in Vessel-Pipe Systems at Large Scale **429**
Lorenz Boeck, Regis Bauwens, Sergey Dorofeev (#16)

Thermal Structure of Aluminum Dust Explosion with Additional Carbon Dioxide **440**
Pojul Chang, Toshio Mogi, Ritsu Dobashi (#26)

Ageing Effect on Ignition Sensitivity of Lignocellulosic Dusts **452**
Maria Portarapillo, Almerinda Di Benedetto, Roberto Sanchirico, Enrico Danzi, Luca Marmo (#59)

Recycling of plastics: dust explosion risk evaluation **465**
Enrico Danzi, Luca Marmo, Maria Portarapillo, Roberto Sanchirico, Almerinda Di Benedetto (#61)

Session 14: Hydrogen Safety III *(Stefan Essmann)*

Schlieren imaging investigations of hot gas kernel expansion caused by slow contact-break discharges **477**
Carsten Uber, Steffen Franke, Michael Hilbert, Dirk Uhrland, Niklas Schüler (#3)

Investigating the influence of additional inductivity in electrical circuits during ignition caused by contact break discharges **488**
Bogdan Barbu, Carsten Uber, Frank Berger, Michael Hilbert (#4)

Investigation of the safety related ignition processes of laminar strained premixed NH3-H2-air flames **498**
Chunkan Yu, Detlev Markus, Robert Schießl, Ulrich Maas, Bo Shu, Sven Eckart, Harmut Krause, Stefan Essmann, Agustin Valera-Medina (#67)

Experimental and numerical modelling of igniting hydrogen/air mixtures in inter-connected vessels **508**
Bisham McCarthy-Singh, Tim Krause, Detlev Markus, Holger Grosshans, Manideep Manchikatla, Alberto Gambaruto (#74)

Session 15: Flame propagation and acceleration I *(Arnas Lucassen)*

Research on the flame stability of biodiesel/diesel blends in small-scale combustion based on data fusion **525**
Gongping Mao, Huan Mao, Zhijian Xu, Chunkan Yu (#21)

Influence of the flammable cloud geometry on the gas explosion effects **537**
Jérôme Daubech, Jérôme Hébrard, Emmanuel Leprette (#65)

Session 16: Explosion prevention III *(Paul Amyotte)*

Explosive properties of selected aerosols determined in the spherical 5 l test chamber **549**
Adrian Toman, Wojciech Adamus (#45)

Holi powder potential dust explosions **560**
Blanca Castells, Isabel Amez, Javier Garcia-Torrent, David León (#33)

Session 17: Dust Explosions III *(Dejian Wu)*

Investigation of Marginally Explosible Dusts **575**
Albert Addo, Maria Portarapillo, Almerinda Di Benedetto, Yajie Bu, Paul Amyotte, Yuan Chunmiao, Ashok Dastidar, Faisal Khan (#10)

Turbulence generated by dust dispersion in the standard 1 m3 vessel **592**
Zdzisław Dyduch (#72)

Session 18: Case studies I *(Oswald Losert)*

Qualification in explosion protection - use of an adaptive learning platform **600**
Patrick Dyrba (#28)

Learning From the Past: The Importance of Risk Assessment in Aluminium Dust Processes **607**
Marco Barozzi, Marco Derudi, Martina Silvia Scotton, Sabrina Copelli (#41)

Session 19: Hybrid mixture explosions II *(Enrico Danzi)*

The maximum rate of pressure rise of hybrid mixtures **626**

Stefan Spitzer, Enis Askar, Paul Geoerg, Dieter Gabel, Arne Krietsch, Ulrich Krause (#5)

1st International Round Robin Test on Safety Characteristics of Hybrid Mixtures **639**

Stefan Spitzer, Arne Krietsch (#18)

Making hybrid mixtures explosion a common case **650**

Matteo Pietraccini, Pierre-Alexandre Glaude, Anthony Dufour, Olivier Dufaud (#77)

Session 20: Ignition phenomena I *(Michael Hilbert)*

Experimental study on inert products, moisture, and particle size effect on the minimum ignition energy of combustible dusts **662**

Isabel Amez, Blanca Castells, David León, Javier Garcia-Torrent, Ljiljana Medic (#32)

Thermal Ignition: Effects of Fuel, Ambient Pressure and Nitrogen Dilution **678**

Conor Martin, Joseph Shepherd (#48)

Ignition energy and flame propagation in ethylene oxide- air mixtures **693**

Christophe Proust (#85)

Session 23: Explosion modelling and experiments I *(Bo Shu)*

Experimental study of Unconfined Lean Hydrogen-Oxygen Explosions **701**

Tomoyuki Johzaki, Takuma Endo, Wookyung Kim, Keita Tanaka, Akihiro Ueda, Yangkyun Kim (#54)

CFD modelling of vented explosions for chambers of two different scales **713**

Guillaume Lecocq, Jérôme Daubech, Emmanuel Leprette (#51)

Experimental and numerical study of the fuel effect on flame propagation in long open tubes **724**

Guillaume Lecocq, Jérôme Daubech, Emmanuel Leprette (#52)

DOI: 10.7795/810.20221124

Greetings from the Local Organizing Committee Chair

On behalf of the Local Organizing Committee, I welcome you to the 14th international Symposium on Hazards, Prevention and Mitigation of Industrial Explosions in the week from July 11 to 15, 2022. The host is the Physikalisch-Technische Bundesanstalt in Braunschweig together with the Otto von Guericke University Magdeburg.

The series of International Symposia on Hazards, Prevention and Mitigation of Industrial Explosions has a long tradition. After 12 undisturbed symposia, the past ISHPMIE 2020 had to take place as an online forum due to the corona pandemic. Despite the short-term organization of the ISHPMIE 2020 Forum, we had 575 registered participants. That could be regarded as a very good success for these circumstances.

Now we are very pleased to host the ISHPMIE 2022 as well. I would like to thank the International Organizing Committee for giving us the opportunity to meet at the 14th Symposium in Braunschweig. Unfortunately, we are not yet free from the obstructive circumstances of the Corona Pandemic. As a result, many scientists especially from Asia cannot come and present their contributions in person. The political situation related to the Russian war in Ukraine led to further restrictions. However, we did not let this discourage us and we hope to experience a motivating face-to-face conference again.

We have used the opportunity for stimulating additions. We will try out the "Industry meets science" forum for the first time. Here we invited representatives from industry and associations to discuss their view on the needs and future challenges in research with the participants. Another new element is the "Young researcher's night" where the young scientists are brought together to expand their network. As with previous symposia, Best Paper Awards will be presented, and selected articles will be proposed for publication in a special volume of the Journal of Loss Prevention in the Process Industries.

Finally, I would like to thank all colleagues for their support. Without them, the preparation and implementation of such a symposium would not be possible: First and foremost the ISHPMIE 2022 organization team and the many helping hands of the PTB and the Otto von Guericke University Magdeburg, my co-chairs Ulrich Kraus and Detlev Markus, the program chair Holger Großhans together with the authors, reviewers and moderators, the supporting organizations of the symposium mentioned on the website as well as Trygve Skjold and the International Organizing Committee. Thanks very much!

I wish all participants an interesting conference week with many contacts and fruitful discussions.

Michael Beyer
Local Organizing Committee Chair

Foreword of the Proceeding Editors

It is our pleasure to present the proceedings of the 14th International Symposium on Hazards, Prevention, and Mitigation of Industrial Explosions (ISHPMIE). After the pandemic forced us to hold the previous Symposium online, the 14th ISHPMIE finally offered the opportunity to meet in person in Braunschweig. Despite the invaluable experience of offline interaction, these proceedings are still affected by the global situation. Some authors faced travel restrictions and could not present their work on-site, which reduced the number of contributions from certain regions of the world.

Nevertheless, we are happy to compile proceedings consisting of 60 high-quality papers that reflect the scientific state-of-the-art. All articles in this volume have been subject to a peer-review process administered by the Proceeding Editors. We are thankful to the 70 expert referees who guaranteed the professional and scientific standards expected of ISHPMIE. After the conference, Elsevier will publish selected papers from the 14th ISHPMIE in a special issue of the Journal of Loss Prevention in the Process Industries.

We strongly believe this year's ISHPMIE was a successful restart for the tradition of the Symposium series, stimulating the scientific exchange between all participants.

Dr. Holger Grosshans
Dr. Wenchao Xu
Simon Jantac

Physikalisch-Technische Bundesanstalt

Symposium Committees

International Organizing Committee

T. Skjold (Norway, Chair), P. Amyotte (Canada), R. Dobashi (Japan), R. K. Eckhoff (Norway), S. Frolov (Russia), W. Gao (P. R. China), M. Nifuku (Japan), M. Pegg (Canada), I. Sochet (France), J. R. Taveau (USA), M. Beyer (Germany), U. Krause (Germany)

Honorary Members

R. Klemens (Poland), K. Lebecki (Poland), P. Wolanski (Poland)

Local Organizing Committee

Michael Beyer (PTB, Chair), Ulrich Krause (OvGU, Co-Chair), Detlev Markus (PTB, Co-Chair), Maria Brodel, Dieter Gabel, Holger Großhans, Michael Hilbert, Tim Krause, Christian Lehrmann, Carola Lotz-Foerster, Arnas Lucassen, Irina Mulyasch, Carola Schierding, Christine Werner, Sabine Zakel

Program Committee

Ulrich Krause, Holger Großhans, Simon Jantac, Wenchao Xu

DOI: 10.7795/810.20221124

Hybrid mixture explosions – A brief review

Peng Zhao [a], Dejian Wu [a, b, *], Stefan H. Spitzer [c], Arne Krietsch [b], Paul Amyotte [d], Ulrich Krause [a]

[a] *Otto von Guericke University, Universitätsplatz 2, D-39106 Magdeburg, Germany*
[b] *Division 2.1 "Explosion Protection Gases and Dusts", Bundesanstalt für Materialforschung und -prüfung (BAM), Unter den Eichen 87, D-12205 Berlin, Germany*
[c] *Physikalisch Technise Bundesanstalt (PTB), Bundesallee 100, 38116 Braunschweig, Germany*
[d] *Department of Process Engineering & Applied Science, Dalhousie University, Halifax, NS, B3H 4R2, Canada*
E-mail*:* *dejian.wu@bam.de*

Abstract: The hybrid mixture of combustible dusts and flammable gases/vapours widely exist in various industries, including mining, petrochemical, metallurgical, textile and pharmaceutical. It may pose a higher explosion risk than gas or dust explosions since the hybrid explosions can still be initiated even though both the gas and the dust concentration are lower than their lower explosion limit (LEL) values. Understanding the explosion threat of hybrid mixtures not only contributes to the inherent safety and sustainability of industrial process design, but promotes the efficiency of loss prevention and mitigation. To date, however, there is no test standard available to determine the safety parameters of hybrid mixture explosions, nor the flame propagation and quenching mechanism or theoretical explanation behind these parameters. This review presents a state-of-the-art overview of the comprehensive understanding of hybrid mixture explosions in an experimental study level; thereby, the main limitations and challenges to be faced are explored. The discussed main contents include explosion regime and classification of hybrid mixtures, the experimental measurement for the safety parameters of hybrid mixtures (i.e., explosion sensitivity and severity parameters) via typical test apparatuses, the detailed flame propagation/quenching characteristics behind the explosion severities/sensitivities of hybrid mixtures. This work aims to summarize the essential basics of experimental studies, and to provide the perspectives based on the current research gaps to understand the explosion hazards of hybrid mixtures in-depth.

Keywords: *hybrid mixture; explosion regime; safety parameter; flame characteristic; test standard.*

Nomenclature:

A: The front flame surface (m^2).
A_f: The surface of the cross section of the tube (m^2).
C: The gas volume concentration (vol.%).
C_0: The gas concentration (vol.%).
$\overline{C}_{p,A}$: The molar specific heat of air at constant pressure (kJ/kmol.K).
$\overline{C}_{p,g}$: The molar specific heat of gas at constant pressure (kJ/kmol.K).
C_d: The initial dust concentration (g/cm^3).
C_g: The concentration of oxygen (g/cm^3).
c: The dust concentration in the flammable hybrid

m_d: The mass of dust (g).
m_g: The mass of gas (g).
P_{max}: Maximum explosion pressure (Kpa).
P_{max}^{G}: The maximum explosion pressure of the combustible gas (Kpa).
P_{max}^{St}: The maximum explosion pressure of dust (Kpa).
r_b: The radii of the initial prefilled balloon (m).
r_{b0}: The radii of the following inflated balloon (m).
r_f: The radii of the dust flame (m).
S_u: The burning velocity (m/s).

DOI: 10.7795/810.20221124

mixture (g/m^3).

$(dP/dt)_{max}$: The maximum rate of pressure rate (Kpa/s).

ΔH_g: The completed combustion heat of flammable (kJ/kg).

ΔH_d: The completed combustion heat of dust (kJ/kg).

$-\Delta h_{R,d}$: The reaction heat of combustible dust (kJ/kmol).

I[E_2]: The number of tests with successful ignition at E2.

(NI + I) × [E2] : The total number of tests at the energy level of E2.

K_{St} : The dust explosion index.

K_G: The gas explosion index.

LEL: Lower explosion limit.

LOC: Lower oxygen concentration.

LEL_H : Lower explosion limit of hybrid mixture (kmol/kmol).

MEC: Minimum explosible concentration

$MIE_{mixture}$: The minimum ignition energy of the mixture (J).

MIE_i: The minimum ignition energy of each ingredient (J).

MIE_{hybrid}: MIE of hybrid mixtures (J).

MIE_{dust}: MIE of dust in the mixtures (J).

MIE_{gas}: MIE of dust in the mixtures (J).

S_g: The mean unburnt gas velocity averaged over the tube cross-section area A_f (m/s).

T_f: Refers to the flame temperature (K).

T_i: Refers to the temperature of ambient or initial (K).

$T_{i,hybrid}$: The minimum ignition temperature of hybrid mixtures.

$T_{i.d}$: The minimum ignition temperature of particles (K).

$T_{i.g}$: The minimum ignition temperature of gas (K).

x_d: The mole fraction of dust (kmol/kmol).

x_g: The mole fraction of gas (kmol/kmol).

X_g: The mole fraction of flammable gas in the hybrid mixture system.

$X_{g,stoic.}$: The theoretical stoichiometric coefficient of complete combustion of the flammable.

y_d: The mass fraction of dust in dust–gas mixture.

y_g: The mass fraction of gas in dust–gas mixture.

y: The volume concentration of the flammable gas in the hybrid mixture (vol %).

$\%Vol_i$: The volume percentage of each flammable compound.

$\alpha \approx \frac{E_{a,h}}{RT_p}$: The empirical power index.

ρ_u: The density of unburnt fuel ahead of the flame front (g/m^3).

1. Introduction

Hybrid mixtures are defined in NFPA 69 as mixtures of combustible dusts and flammable gases, where the dust concentration is above 10% of the minimum explosible concentration (MEC) and the gas is above 10% of the lower flammability limit (LFL) (NFPA-69, 2014). Since the development of the industry, significant hybrid mixture accidents have been reported. In 1902, a worst coal mine explosion occurred in Australia, which killed 96 people at Mount Kembla Mine (Radford, 2015), only in 2013, the reported death toll due to coal mine explosions, in China alone, was 1089 (Kundu et al., 2018).

The hybrid mixtures of combustible dusts and flammable gases are widely existing in coal mining, petrochemical, metallurgical, textile and pharmaceutical industries (Britton, 1999; Eckhoff, 2016). One of the most notable susceptible industrial activity zones for hybrid mixture explosion is in underground coal mine, where methane and coal dust coexist. In addition, the explosion risk of combustible dusts in non-atmospheric condition has been studied in recent years, such as self-ignition and smouldering behaviours (Wu et al., 2015, 2016b, 2017a, 2017b, 2018 & 2019) explosion severity and flame speed (Hosseinzadeh et al., 2016) and the minimum ignition temperature of dust cloud (MITC) (Wu et al., 2016). The results from these studies mentioned above show that O_2 mole fraction plays a crucial role in explosion risk of coal dusts, with increasing O_2 mole fraction in the system, the explosion/ignition risk increase correspondingly. Furthermore, the presence of flammable gases (e.g., CH_4, CO, H_2) releasing from the self-ignition or smouldering of coal dusts may pose a higher explosion risk when they are mixed with coal dust (Eckhoff, 2005b; Dufaud et al., 2012; Yu et al., 2019). Meanwhile, the releasing of CO_2 due to the smouldering could change or diluent the gas ambient from air condition to $O_2/N_2/CO_2$ atmospheres.

Although the explosion characteristics of hybrid mixtures have been widely studied for hundreds of years the knowledge is still insufficient.

It is worthy to note that the explosion risk still exists even when the concentration of flammable gas and combustible dust are lower than their lower explosion limitation or minimum explosion concentration respectively (Sanchirico et al. 2015a; Addai et al., 2015b; Zhao et al., 2020). Therefore, many researchers have performed extensive work experimentally and theoretically on this topic. Two empirical models were developed for predicting the LEL of hybrid mixtures based on the experimental data, i.e., Bartknecht’s curve and Le Chatelier’s line (Bartknecht, 1981; Glassman, 1996). The experimental results from Zhao et al. (2009) show that the lower flammability limits of binary hydrocarbon mixtures can be fit by Le Chatelier’s Law very well. However, either Bartknecht’s law or Le Chatelier’s law is conditional dependence according to the research results obtained from lots of researchers (Khalili et al., 2012; Addai et al., 2015b; Zhao et al., 2020). The reason is that for a certain kind of hybrid mixtures, the explosion will happen under the condition of the fuel concentration even beyond those two empirical formulae. Thus, there is still a lot of work to be done. To develop more reliable and universal models, some researchers have several attempts on it. Jiang et al. and & Ji et al. further developed the new equations based on the Bartknecht’s curve and Le Chatelier’s line by identifying the different exponent of the power function, and the experimental data show accepted agreement with the results predicted by the proposed formula (Jiang et al., 2014 & 2015; Ji et al., 2022).

Based on the experimental data, the evaluating explosion regime was developed creatively and originally, divided into five different areas based on the different reaction regimes of hybrid mixtures, i.e., dust driven explosion, dual-fuel explosion, gas driven explosion, synergic explosion and no explosion (Garcia-Agreda et al., 2011). It provided a clear and systematic research approach and attracted extensive attention. According to this kind of diagram, the explosion characteristics including the severity of hybrid mixture explosions and comparison to pure dust/air and vapour/air explosions were investigated (Sanchirico et al., 2011). After that, the theoretical study on the deflagration index K_{St} for a model hybrid mixture (methane-nicotinic acid) at changing the gas and dust concentration was performed (Russo et al., 2012), therefore the evaluating regime diagram got further refined. According to the research results obtained from (Denkevits, 2007; Denkevits and Hoess, 2015), which studied the effects of dust reactivity and flammable concentration on the explosion severity of hybrid mixtures, an additional evaluating regime for subdividing the gas-driven, dual-fuel regimes and dust driven regimes was proposed (Cloney et al., 2013 & 2017), indicating that the gas-driven and dual fuel regimes are in reality a continuum based on the relative combustion time-scales of the dust and gas.

One of the effective research ways to extend evaluating regime diagram is to combine the research of flame propagation behaviour which usually studied in transparent tube, as known, dust explosions are time-dependent flame propagation process. The description with "lumped parameter models" like the K_{St} value are of limited validity only, especially for the explosions of hybrid mixtures. Therefore, compared with the explosion parameters, e.g., K_G or K_{St}, it has the advantage of visualization of combustion and to emphasize the influence of flow velocities on the flame propagation process. Indeed, there are extensive research works focusing on the flame propagation of hybrid mixtures and in general, these works can be divided roughly into two categories:

1. Investigation on the flame propagation behaviour of hybrid mixtures with the concentration of each composition is far higher than their LEL/MEC, including the influential factors on the flame propagation of hybrid mixtures, i.e., fuel concentration (Cassel et al., 1953; Sun et al., 2003), thermal radiation (Christophe et al., 2017), particle size (Yuzuriha et al., 2017; Zhang et al., 2017b), turbulence level (Cloney et al., 2018a; Zhang et al., 2018) etc., the research of flame structure and temperature profile (Sun et al., 1998a, 2001a & 2006).

2. Investigation on the quenching characteristics of flame propagation by means of equipping some obstacles or other block devices (Goroshin et al., 1996a; Tang et al., 2009; Palecka et al., 2015) and the ignition and flame propagation in hybrid mixtures of lycopodium (Abbas et al., 2022).

However, the near-LEL flame characteristics and the quenching condition have not been well studied. Indeed, from the viewpoint of protection and mitigation associated with fire safety during hybrid mixture explosions, the research on near-LEL flame characteristics is quite important, especially for the research of explosion sensitivity such as LEL and LOC which have not been well elucidated from the viewpoint of flame propagation. This work aims to summarize the essential basics of experimental studies, and to provide the perspectives based on the current research gaps to understand the explosion hazards of hybrid mixtures in-depth.

2. Explosion regimes and classifications of hybrid mixtures

The most extensive work on hybrid mixtures has involved the measurements of the lean flammability limits of coal dust with methane addition (Foniok, 1985; Cashdollar et al., 1987). And accordingly, the empirical models which originally derived based on the Bartknecht's curve and Le Chatelier's line, were constantly being perfected. The explosion characteristics of hybrid mixtures, therefore, can be understood more comprehensively and systematically.

2.1 Classification of hybrid explosions

The evaluating regime diagram were divided into five areas based on the two predictive models (seen in equation 1 & 2) which are Le-Chatelier's line and Bartknecht's curve (Bartknecht, 1981; Glassman, 1996), i.e., dust driven explosion, dual-fuel explosion, gas driven explosion, synergic explosion and no explosion, it was used to evaluate the interaction between dust and flammable according to the explosion regimes (Garcia-Agreda et al., 2011), shown in Fig. 1, where the x-axis is expressed by the ratio of flammable gas concentration in the hybrid mixture to the lower explosion limit (LEL) of the gas in the air and the y-axis is expressed by the ratio of dust concentration in the hybrid mixture to minimum explosion concentration of the dust in the air.

Le-Chatelier's model:

$$\frac{c}{MEC}+\frac{y}{LEL}=1 \tag{1}$$

Bartknecht's model:

$$\frac{c}{MEC}=\left(\frac{y}{LEL}-1\right)^2 \tag{2}$$

where c and y mean refer to the dust concentration in the flammable hybrid mixture (g/m^3) and the volume concentration of the flammable gas in the hybrid mixture (vol %) respectively. MEC is the minimum dust explosion concentration (g/m^3), LEL is the lower explosion limit of the flammable gas (vol %).

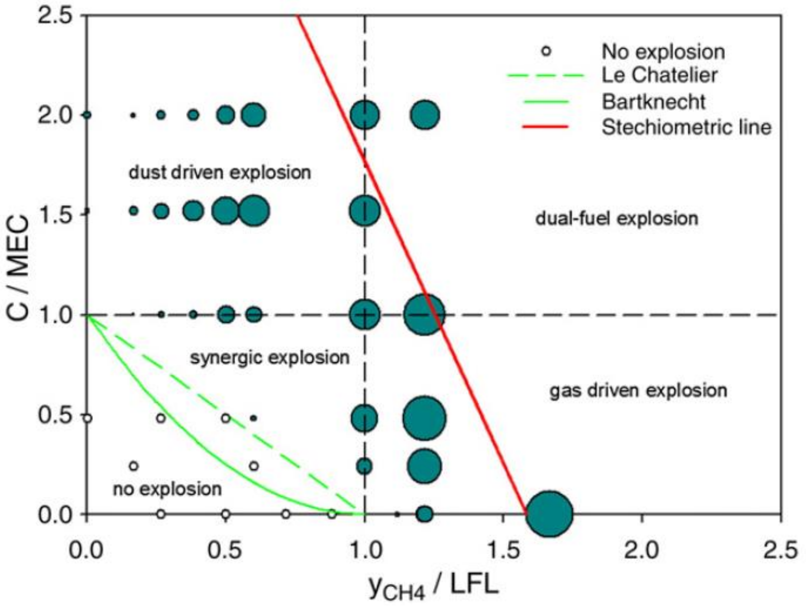

Fig. 1 *Explosion regimes in the plane methane content/nicotinic acid concentration (Garcia-Agreda et al., 2011).*

Based on this evaluating explosion regime, a lot of researchers conducted more studies on hybrid mixtures. The explosion characteristics of different types of hybrid mixtures were further investigated (Addai et al., 2015b; Zhao et al., 2020 & 2021). For further developing this evaluating explosion regime diagram, the stoichiometric line was introduced into the diagram by Sanchirico et al. (2011) to study the severity of hybrid mixture explosions and comparison to pure dust/air and vapour/air explosions, the area of dust driven explosion, dual-fuel explosion and gas driven explosion were studied (Fig. 2). But according to the intensive experimental data associated with hybrid mixtures, the predictive ability of those two empirical models are quite condition-dependence (Khalili et al., 2012). The results showed that the classical models developed by Bartknecht or Le Chatelier are not always conservative from a safety point of view, and the similar experimental phenomenon was also found in other literatures (Addai et al., 2015b; Zhao et al., 2020), indicating that these classical models have a strong conditional dependence. Therefore, focusing on the exponent of the power function, more comprehensive and systematically predictive models were developed and proposed. Jiang et al. (2014 & 2015) developed a new formula based on the classical models developed by Bartknecht or Le Chatelier by introducing two indexes: K_{St} and K_G, and the experimental data showed that the proposed formula accurately predicts the explosion and non-explosion boundary.

Jiang's model (2014 & 2015):

$$\frac{c}{MEC}=\left(1-\frac{y}{LEL}\right)^{(1.12\pm0.03)\frac{K_{St}}{K_G}} \tag{3}$$

where the K_{St} is the dust explosion index and K_G is the gas explosion index.

By comparing those predictive models, it was found that they all predict the LEL of a hybrid mixture by constructing a functional relationship between the flammable gas concentration (y), and the dust concentration (c). These models are all consistent in the structural form of the function, which is a power function relationship between the flammable gas concentration, and the dust concentration, so a more comprehensive model was proposed (Ji et al., 2022).

Ji's model (2022):

$$\frac{c}{\mathrm{MEC}}=\left(1-\frac{y}{\mathrm{LEL}}\right)^{\lambda} \tag{4}$$

$$\lambda=5.12\times10^{-7}\times e^{\frac{\left(P_{max}^{G}+P_{max}^{St}\right)^{2}\cdot \lg(K_G+K_{St})}{0.34}}+1.1 \tag{5}$$

where P_{max}^{G} is the maximum explosion pressure of the combustible gas, P_{max}^{St} is the maximum explosion pressure of dust.

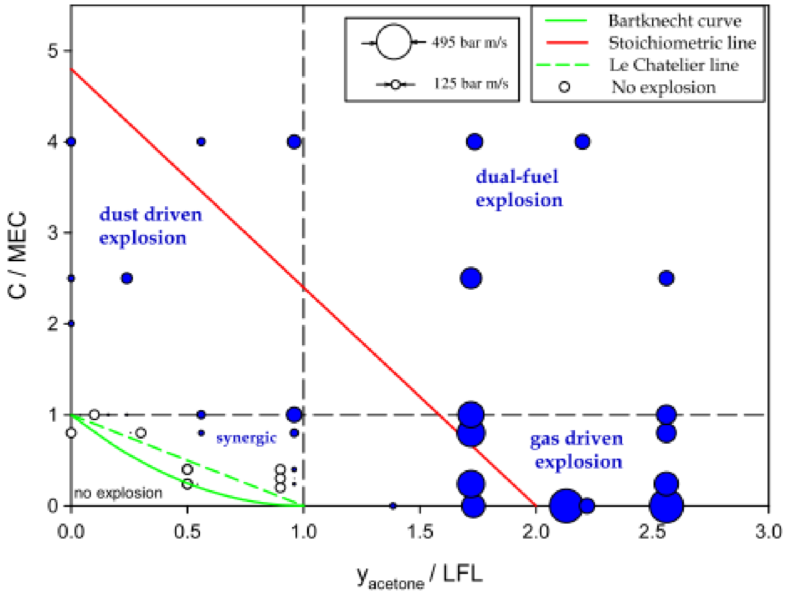

Fig. 2 *Explosion regimes at t_v ¼ 60 ms (Circles dimensions are proportional to K_{st}) (Sanchirico et al., 2011).*

Besides, a simple mathematical model has been derived from the enthalpy balance of the whole system assuming that the combustion kinetics of pure species are independent and unchanged by the presence of other combustible species, complete conversion of the reactants and no heat losses was proposed (Abbas et al., 2019).

$$LEL_H=\frac{\overline{C}_{p,A}\Delta T}{x_d\left((-\Delta h_{R,d})-\overline{C}_{p,A}\Delta T\right)+x_g\left((-\Delta h_{R,d})-\overline{C}_{p,g}\Delta T\right)+\overline{C}_{p,A}\Delta T}.100 \tag{6}$$

where LEL_H is lower explosion limit of hybrid mixture (kmol/kmol), x_d and x_g are the mole fraction of dust and gas (kmol/kmol) respectively, $\overline{C}_{p,A}$ and $\overline{C}_{p,g}$ are the molar specific heat of air and gas at constant pressure (kJ/kmol.K) respectively, $-\Delta h_{R,d}$ is the reaction heat of combustible dust (kJ/kmol) and $\Delta \mathrm{T}=\left(T_f-T_i\right)$ refers to the rise in temperature from ambient or initial to the flame temperature.

By collecting, comparing and summarizing the experimental data associated with hybrid mixtures available in literatures (Denkevits, 2007; Denkevits and Hoess, 2015), an approach for evaluating the explosion regime was proposed based on the different ignition energy (Cloney et al., 2013 & 2017). The diagram can be re-divided according to the different of amount of ignition energy (high ignition pyrotechnic igniter) and low ignition energy (electric spark ignitor) and combustion mechanism, gas-driven, dual-fuel regimes and dust driven regimes were refined. As shown in Fig. 3.

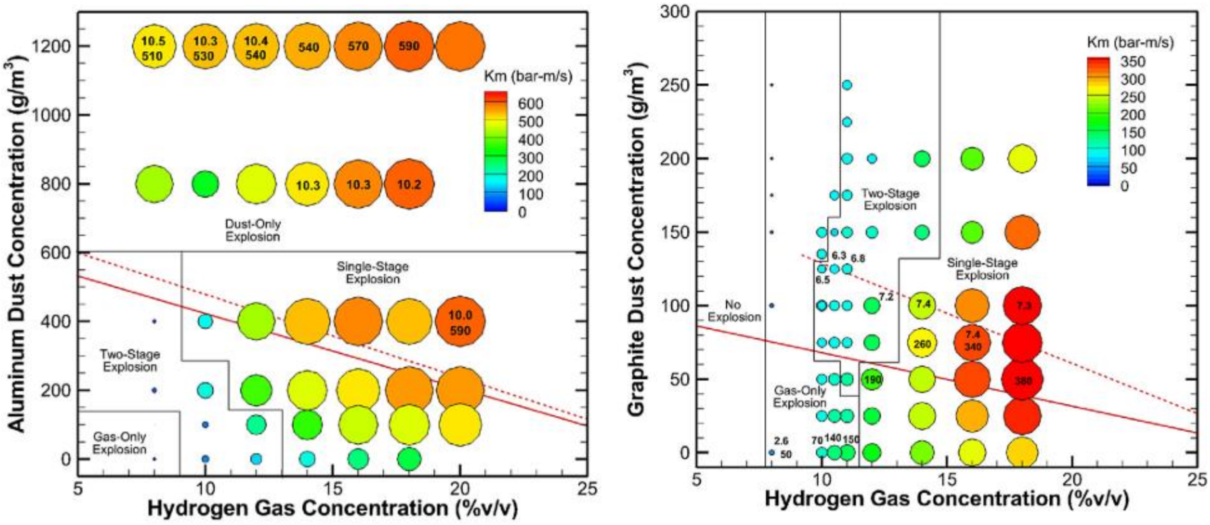

Fig. 3. *Hybrid explosion regime diagram for high-reactivity (left), low-reactivity (right) dust reproduced from the experimental data of for spark ignition and 60 ms delay. The largest values of P_m (bar) and K_m (bar-m/s) are indicated for each recorded gas concentration as text (Cloney et al., 2017).*

The deviations of the mathematical models may arise from the fact, that in none of the previous works the gas amount was verified and small deviations of it have an impact on the characteristics.

2.2 Chemical kinetics and combustion mechanism of hybrid mixtures

More than one century ago, in 1885, the experimental phenomenon that mixing coal dusts with methane at a concentration lower than the methane lower flammability limit (i.e., 4.1% in air) would allow the explosion of the dust/gas mixture was observed (Engler, 1885). From then on, the studies on the explosion characteristics and combustion mechanism of hybrid mixtures have been ongoing.

In general, the combustion behaviour through hybrid mixtures depends on a number of steps of the oxidation process of the combustible fraction. 1. The devolatilization of the volatile fraction of the solid fuel (not for dust with non-volatile), 2. Mixing of the volatiles with oxygen in the gas phase, 3. Combustion of the flammable gas in the gas phase, 4. Combustion of the remaining solid fraction (mostly char) (Krause and Kasch, 2000). For combustible dust with or without volatiles, the chemical kinetics and combustion mechanisms of them during combustion can be very different.

For organic dusts, a two-phase combustion model was developed by (Slezak et al., 1985) to investigate the flame propagation in rich mixtures of coal dust in air environment, which including heterogeneous combustion, pyrolysis of the coal, and homogeneous combustion of volatile matter and the optically thick limit for radiative heat transfer. After that, many researchers conducted experiments to investigate the combustion mechanisms of dust explosions, their research mainly started with the particle size, flame propagation and temperature profile (Ju et al., 1998; Han et al., 2000; Dobashi and Senda, 2002 & 2006). Moreover, the inerting effect on the combustion of hybrid mixtures by introducing some inert substances like carbon dioxide, nitrogen and other components was also studied to investigate the influence on the combustion mechanism (Wang et al., 2020b). Based on the experimental data available in the literature, the combustion mechanisms of hybrid mixtures including the effect of inert gas was concluded in Fig. 4.

For most of the metal dust, like iron powder, copper powder, silicon powder etc. the combustion behaviour will occur in the surface of the particle with the help of high enough ignition energy (Sun et al., 1998a, 2001a & 2003). In particular, iron is a suitable candidate as it burns purely heterogeneously by surface reactions. The iron–air adiabatic flame temperature is similar with the methane flame temperature, which allows the observation of both flames simultaneously. It has also been shown that iron can burn in either a diffusion-controlled or a kinetically-controlled regime depending on, among other things, the oxidizing environment (Julien et al., 2015a). But, with the addition of methane, the ignition energy will decrease and the combustion will occur more easily (Julien et al., 2014 & 2015a), and correspondingly, the flame structure will change.

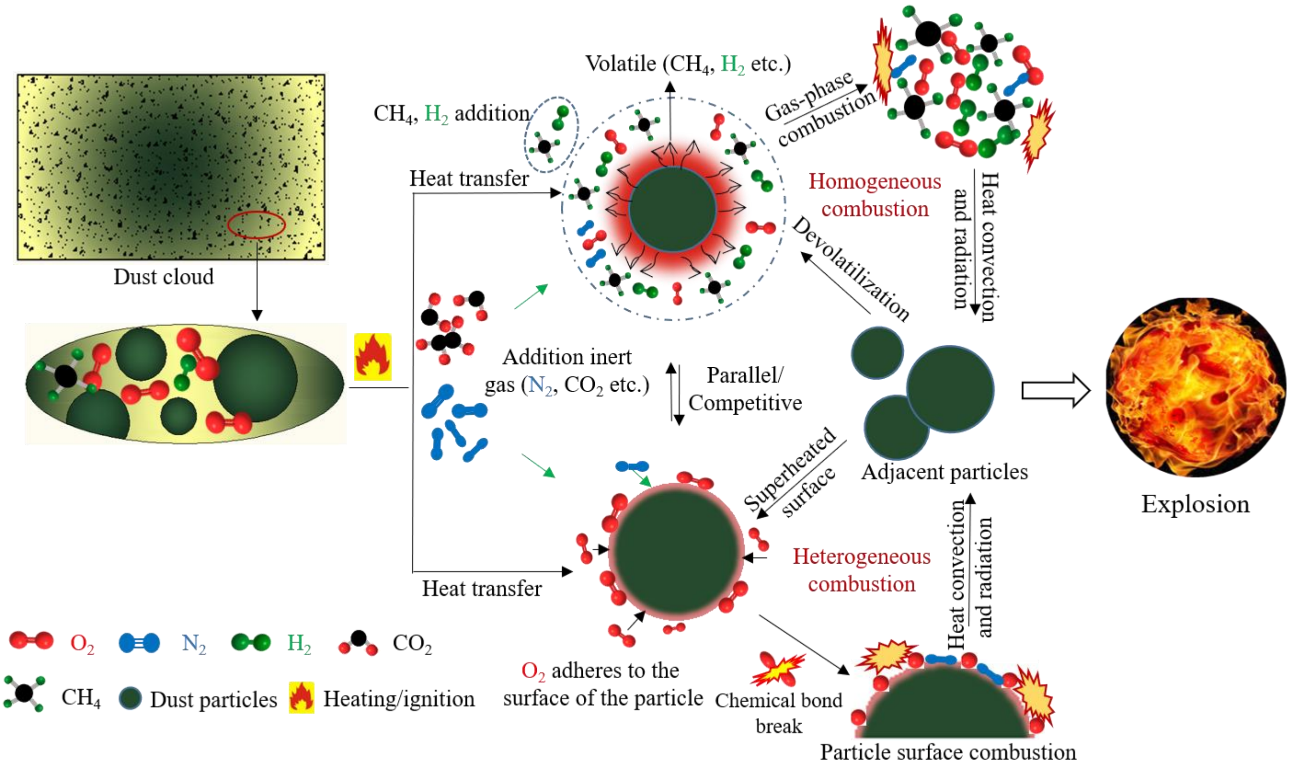

***Fig 4.** Schematics of combustion mechanism of hybrid mixtures including inerting effect (Wu et al., 2021b & Wu et al., 2022).*

As the promising candidate of clean combustion energy, aluminium was also studied intensively either using the pure dust or with addition of flammable gases, like methane or hydrogen. Unlike the combustion of iron, the combustion of aluminium suspension has two characteristics: 1. The devolatilization will occur. 2. The formation of Alania coat which cover the aluminium core, which makes the combustion mechanism more complex than that of iron powder. Therefore, understanding the combustion mechanism of aluminium particles in details is the basement for understanding the flame propagation of aluminium dust suspension and aluminium-based hybrid mixtures in depth. For decades, lots of researchers dedicated their contribution to research the combustion of not only the isolated individual aluminium particles but the aluminium suspension (Bucher et al., 1996; Goroshin et al., 1996b; Dufaud et al., 2010). With the addition of flammable gases like hydrogen, the combustion mechanism of aluminium powder will change and the combustion mechanism was concluded (Fig. 5 (Yu et al., 2020)). The combustion mechanism of aluminium particles was revealed by (Bucher et al., 1996; Jing et al., 2021 & 2022), which is shown in Fig. 6.

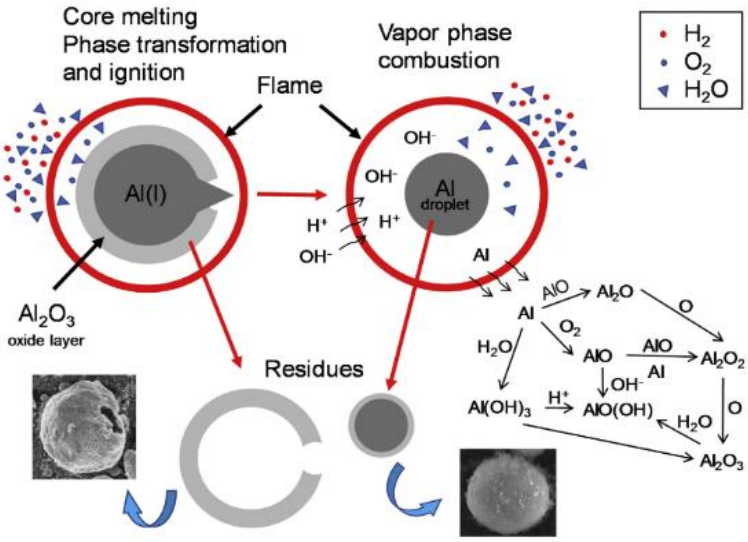

Fig. 5. *Reaction mechanism of aluminium dust explosion in hydrogen/air environment (Yu et al., 2020).*

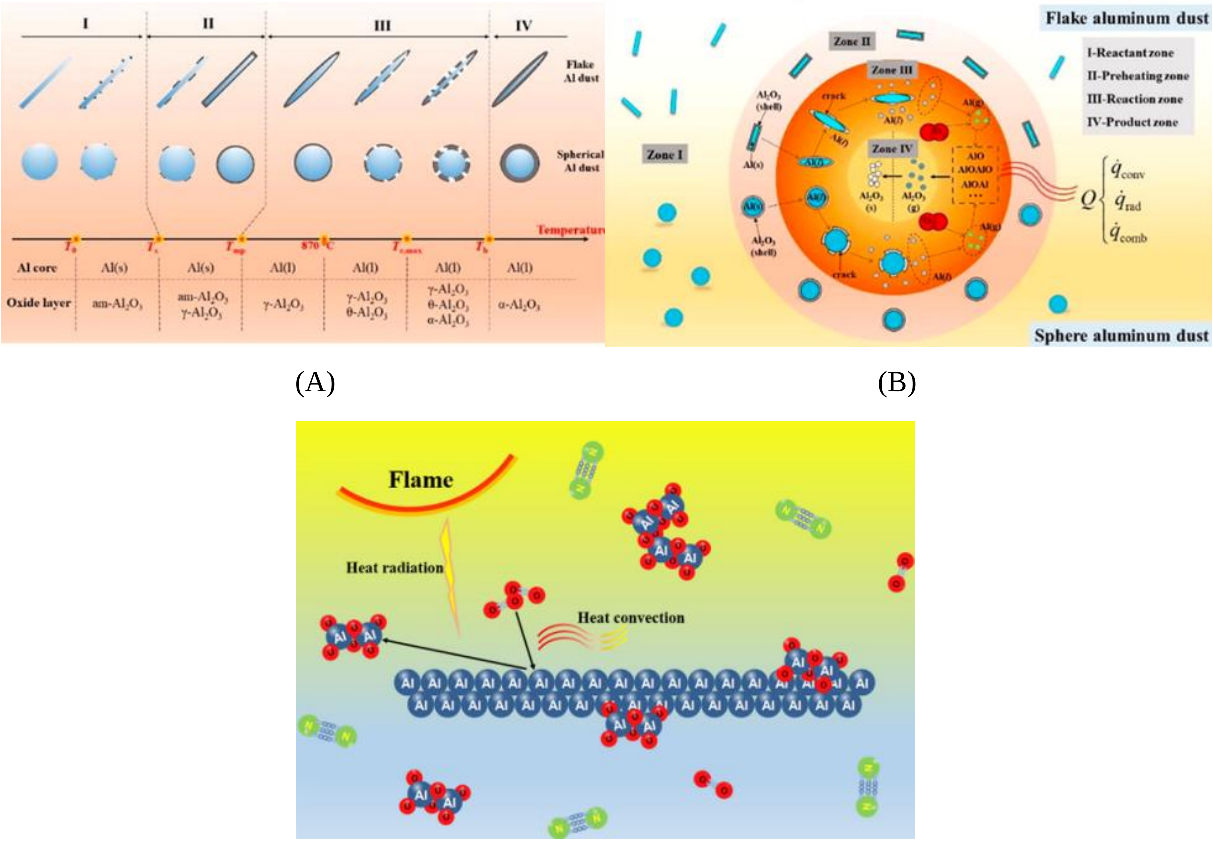

(A)

(B)

(C)

Fig. 6. *(A) Melting-oxidation mechanism, (B) Growth mechanism of oxide layer, (C) transient reaction mechanism of flake aluminium dust (Jing et al., 2021 & 2022).*

In particular, heat transfer plays an important role during the combustion of dust suspension and flame propagation including conductive heat transfer and thermal radiation (Badiola and Dreizin, 2013; Thimothée et al., 2016). The role of thermal radiation was investigated by Christophe et al. (2017) who studied the thermal radiation in dust flame propagation and proposed a new experimental measurement of thermal radiation in dust flames together with a physical interpretation, shown in Fig.

7. By generating and analysing the pyrolysis gases of some carbohydrates such as starch, Dufaud et al. (2011) demonstrated that the pyrolysis phase could not be systematically neglected when considering the dust explosion kinetics.

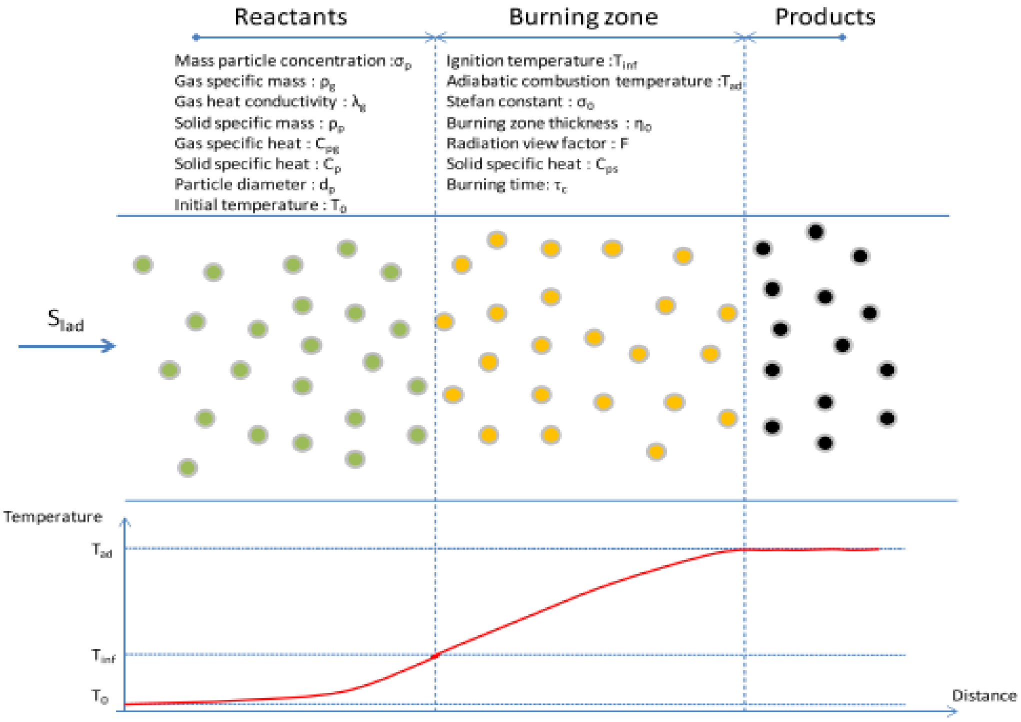

Fig. 7. *Cassel's problem and definitions (Christophe et al., 2017).*

3 Experimental measurements for different explosion safety characteristics

3.1 Experimental apparatus

For now, there is still no standard apparatus and procedure available especially for the study of explosion behaviour of hybrid mixtures. So, to better experimental study on the hybrid mixture explosion, a variety of standardized and modified experimental apparatus were adopted for experiment tests, including ISO 1 m^3 explosion chamber, 20L-sphere, Godbert- Greenwald (G-G) furnace or BAM furnace, Hartman tube or MIKE 3, which originally used in the experiment of combustible dust explosion.

At the very beginning, Hartmann tube was widely used in the research of dust cloud explosion due to its characteristics of low cost, simple structure and easy maintenance (Sweis, 2006; Nifuku et al., 2007). However, the accuracy of the results measured by Hartmann tubes is poor because of the small volume, the use of electrostatic ignition and the poor flame propagation path. Since the experimental results measured by ISO 1 m^3 device were close to practical industries (Going et al., 2000; Dastidar et al., 2001), therefore, it has long been used as the only standard device to test the explosion characteristics of dust (Zhen and Leuckel, 1997; Garcia-Torrent et al., 1998; La´zaro and Torrent, 2000). Numerous researchers have attempted to reduce the volume of the 1 m^3 device and have found that to achieve a balance between ease of testing and realistic data, the volume of the vessel must not be less than 20 L (Eckhoff, 2003). On this basis, the 20L-sphere was developed (Siwek, 1996), shown in Fig. 8, and the experimental results were confirmed to be in good agreement with the ISO 1 m^3 device (Cashdollar and Chatrathi, 1993; Proust et al., 2007). A USBM 20 L laboratory explosibility chamber was used to conduct experiments and the results indicated, that the results from experiments show relatively good agreement with those from full-scale experimental mine tests (Cashdollar, 1996). The 20L-sphere has the advantages of small size, easy operation, low experimental costs, high accuracy and gradually replaced ISO 1 m3 as the main apparatus of laboratory research dust explosion equipment. In addition, G-G furnace has also been widely used for determining the minimum ignition temperature (MIT) (Addai et al., 2016b), and the modified Hartman tube was also often used for the measurement of the minimum ignition energy (MIE) (Norman et al., 2015). Fig. 8 & Fig. 9 give the pictures of those apparatus mentioned above. **Table 1** lists the apparatus used popularly for measuring the flame propagation behaviour.


a. ISO 1 m^3 explosion chamber b. 20L-sphere

***Fig. 8**. Apparatus used for the experimental research of dust cloud*


a. MIKE III apparatus b. G-G furnace

***Fig. 9**. Apparatus used for the measurement of MIE and MIT*

***Table 1**: Apparatus used for the research of flame propagation.*

Source	Main apparatus	Supplementary apparatus	Remark
		Vertical tube	
Liu et al. (2007) Yin et al. (2009)	Rectangular tube, 8 × 8 × 50 cm.	A high-speed video camera. A thermocouple. A Schlieren optical part. A time controller.	The upper end of the tube is open
Gao et al. (2014a, 2014b)	Cyl. vertical tube, d = 68 mm.	A high-speed video camera. A thermal infrared imaging device.	The tube has different lengths including 300 mm, 600 mm, 900 mm. The upper end of the tube is open.

Chen et al. (1996)	Cyl. vertical tube, $d_{upper} = 64$ mm, $d_{lower} = 44$ mm	A high-speed video camera. A band-pass filter. A light attenuator. A laser-scattering optical instrument. A two-dimensional particle images. Velocimetry system.	At the end of spray, the middle part of the duct was moved down to its bottom position such that the combustible particle cloud was provided in an open space.
Ju et al. (1998a, 1998b)	$d_{upper} = 60$ mm, $d_{central} = 96$ mm, $d_{lower} = 84$ mm		
Dobashi et al. (2006)	$d_{upper} = 94$ mm		
Sun et al. (2000,2001a, 2001b, 2005)	$V_{tube} = 1$ L, $d = 76$ mm		
Gao et al. (2015, 2017)	$d_{upper} = 95$ mm		
Zhang et al. (2016, 2017, 2020) Yu et al. (2016, 2020)	$V_{com.\ chamber} = 1$ L, $d_{central} = 96$ mm		
Yuzuriha et al. (2017)	Rectangular tube, 7 × 7 × 30 cm	A high-speed video camera.	A mesh was attached to the top of the duct, which prevented the particles out of the duct.
Zhang et al. (2017)	Rectangular tube, 8 × 8 × 50 cm	A high-speed video camera. A fine thermocouple and an ion current probe.	The top of the duct is open and the bottom is closed.
Chang et al. (2020)	A modified Hartmann tube, 7 × 7 × 29 cm	A 25 µm R-type thermocouple.	-
Yu et al. (2021)	Rectangular tube, 10 × 10 × 50 cm	A high-speed video camera. A light attenuator. A fast response pressure sensor with. an acquisition frequency of 100 kHz.	A closed chamber.
	Transparent latex balloons		
Skjold et al. (2013)	A transparent latex balloon. A balloon holder. A dispersion nozzle. A downward-facing spark gap.	A high-speed video camera.	Using chemical igniter.
Cheng et al. (2018)	A transparent latex balloon. A balloon holder. A dispersion nozzle.	A high-speed video camera.	Using chemical igniter.
Julien et al. (2015b, 2015c) Vickery et al. (2017)		A high-speed video camera. A neutral density filters. A photodiode and a microphone.	Spark ignition.
	"Bunsen burner"		
Goroshin et al. (1996a, 1996b)	Burner	An Ocean Optics USB 4000 spectrometer coupled with a	-

Soo et al. (2013) Julien et al. (2015a)		100-micro optical fiber. A high-resolution digital camera A high-speed video camera A variable neutral-density filter	
	Other apparatus		
Chen et al. (2005)	Cyl. horizontal tube, $d = 14$ cm, $L = 12$ m	20 sets of specially designed dispersion systems. Six piezoelectric transducers.	One end of the combustion tube is joined to a 10 m^3 damp-tank. The other end is sealed with a flange mounted evenly with six ignitors.
Krause et al. (2006)	Cyl. vertical tube, $d = 30$ cm, $L = 1.45$ m	A high-speed video camera	-
Kern et al. (.2015)	Cyl. vertical tube, $d = 14$ cm	Five silicon photodiodes An optical system with photodiodes A high-speed video camera	The dust feeding device was located at the top of the tube.
Wang et al. (2016)	Rectangular tube, 8 × 8 × 50 cm.	A gas supply unit. Two thermocouples. An ignition system. A high-speed video camera. A synchronization controller	The bottom end of the chamber was closed and the top end was open.
Xia et al. (2021)	A constant volume spherical chamber: $d = 200$ mm, $H = 280$ mm. $V = 6.19 \times 10^{-3}$ m^3	Three types of photography were used to capture the flame propagation: direct imaging, OH radical photography, and schlieren photography.	Capacitor discharge ignition.
Arne et al. (2021)	Cyl. vertical tube, $d = 7$ cm, $L = 1$ m	A high-speed video camera A dust concentration measurement system	-

3.2 Determination of explosion severities parameters

The determination of explosion severities parameters of hybrid mixtures is significantly important for better understanding of the explosion behaviour of hybrid mixtures and the rationalization safety design of industrial process involving the combustible dust materials (Cashdollar, 2000), especially for the hybrid mixtures. Therefore, many researchers paid their attention to the research of severity parameters, including the maximum explosion pressure (P_{max}), the maximum rate of explosion pressure rise ($(dp/dt)_{max}$) and the explosion index (K_{st}) (Denkevits, 2007; Li et al., 2012; Ji et al., 2018). It is important to know, that the addition of flammable gases into the dust suspension system will increase the explosion severity compared with pure dust suspension (Dufaud et al. 2008; Addai et al., 2015a; Kundu et al., 2018; Song et al., 2019). The effect of the addition of flammable gas on the explosion severity was shown in Fig. 10.

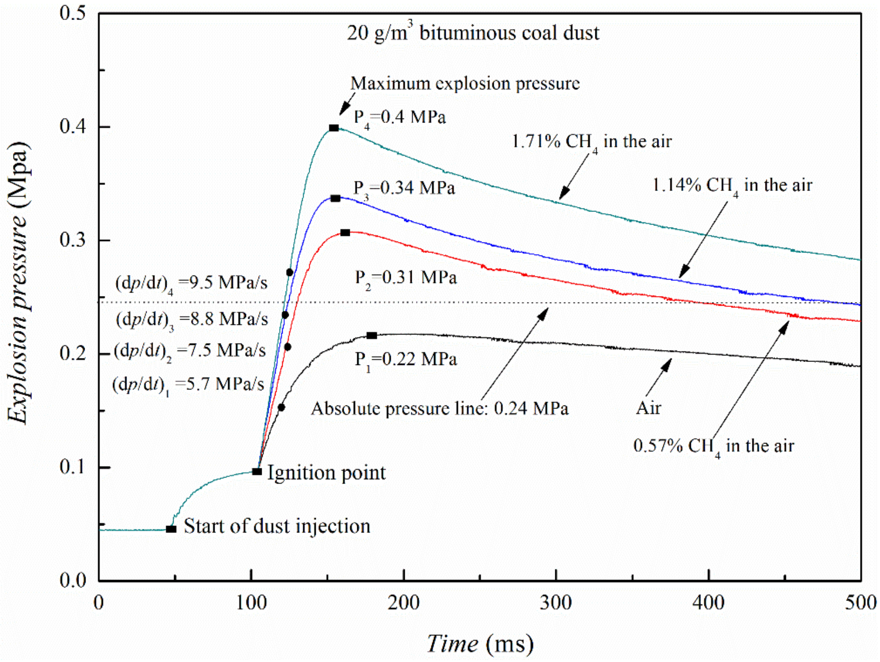

Fig. 10. *The effect of small amount of CH_4 on the explosion process of 20 g/m^3 bituminous coal dust (Zhao et al., 2020)*.

But the explosion severity cannot be promoted all the time with addition of flammable within the confined explosion chamber due to the oxygen consumption caused deeply by flammable gas presence and increased the oxygen diffusion resistance in the hybrid mixtures, which reduced the reaction intensity of oxygen in dust particle surfaces. The decrease of dust particle burning ratio reduced hybrid mixture's explosive property (Li et al., 2012), and this phenomenon can be seen in Fig. 11.

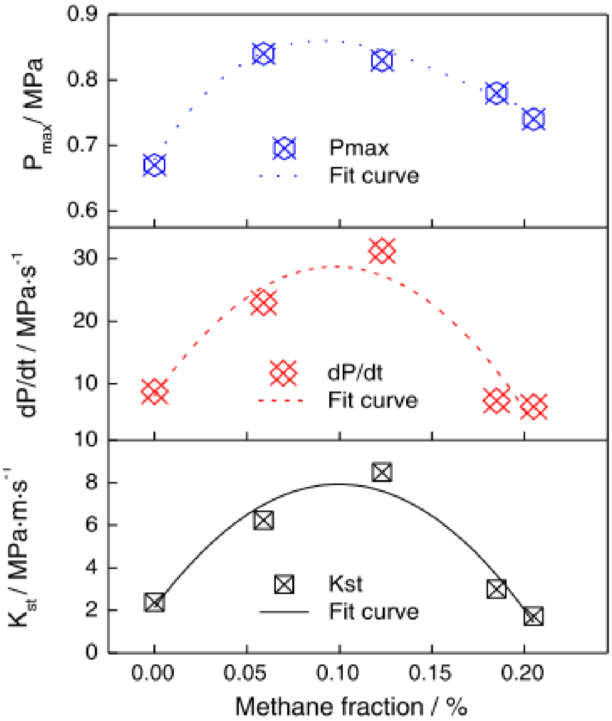

Fig. 11. *Effect of methane fraction on coal dust explosion parameters (Li et al., 2012)*.

Besides, at the same concentration of coal dusts, the addition of CH_4 poses a higher explosion risk and higher explosion severity than the hydrogen and carbon monoxide due to the highest heat of combustion (Zhao et al., 2020). The volatile content also plays an important role on the investigation of the influence of flammable gases on the explosion severity of hybrid mixtures, that is the influence of methane on the explosion severity is more pronounced for coal dust with lower volatile content, but on ignition sensitivity it is more pronounced for a coal dust with a higher volatile content (Wang et al., 2020b).

3.3 Determination of explosion sensitivity parameters

It is well known that explosion sensitivity parameters are crucial for the prevention of explosions. At the same time, better understanding them before conducting the industrial manufacture in the industrial sites involving the combustible dust is beneficial to the industrial manager. So, explosion sensitivity parameters, including the minimum explosion concentration (MEC for pure dust) or lower explosion limit (LEL for flammable gas or hybrid mixtures), minimum ignition temperature (MIT), minimum ignition energy (MIE), lower oxygen concentration (LOC) etc. has attracted the attentions of many researchers to study experimentally and theoretically. Unfortunately, for testing of explosion sensitivity parameters of hybrid mixtures, MEC for instance, no standard device or protocol has been developed so far.

3.3.1 MEC/LEL

Minimum explosible concentration (MEC), as a crucial sensitivity parameter in dust explosion evaluation and prevention, is the concentration boundary above which a dust-oxidant mixture will propagate a flame in the presence of adequate ignition source. MEC has been found to be influenced by particle size, ignition energy, fuel properties and gas conditions, as well as explosion criterion (Chawla et al., 1996; Yuan et al., 2012b; Addai et al., 2015b). Knowledge of the MEC is therefore of practical concern in the safe handling of flammable materials (Chawla et al., 1996).

It is interesting to know that for hybrid mixture testing, no standard device or protocol has been defined so far, most common experimental apparatus used for this purpose is 20L-sphere, following same protocol as for the MEC determination with an addition of introduction of flammable gas in the system. This is usually done by partial pressure method (Abbas et al., 2022). Using the 20L-sphere, many researchers studied the MEC of hybrid mixtures and found that the addition of flammable gases, the LEL or explosion sensitivity will decrease correspondingly (Amyotte et al., 1993; Sweis, 2006; Garcia-Agreda et al., 2011; Khalili et al., 2012; Yuan et al., 2012a & 2012b; Addai et al., 2015b; Kim et al., 2019; Zhao et al., 2020). The difference of MEC value between two kinds of 20L-spheres and 1 m^3 also were investigated by Cashdollar and Chatrathi (1993) and found that the values of MEC measured in the 20L-sphere with 2.5 kJ ignitors were comparable to those measured in the 1 m^3 chamber with 10 kJ ignitors, at higher ignition energies in the 20L-sphere, there was evidence of overdriving, suggesting a scale-effect of the measurement associated with the value of MEC.

Based on the determination method of MEC for flammable gas, tube method was also introduced into the measurement of MEC value of hybrid mixtures (Khalili et al., 2012; Addai et al., 2017b; Abbas et al., 2022). Because of the different configuration of testing apparatus, the LEL value of hybrid mixtures were different. As shown in Table 2.

Table 2: *Comparison of MEC of lycopodium (Abbas et al., 2022).*

	Median particle size (μm)	

Source		Elemental analysis (% wt.)					Ignition source	Apparatus	MEC (g/m^3)
		C	H	O	N	S			
Addai (2016)	32	69	9.6	19.6	1.3	-	10 J permanent spark	20L-sphere	125
Addai et al., (2017b)	32	69	9.6	19.6	1.3	-	Hot surface at 420 °C	G-G furnace	108
Sanchirico et al., (2015b)	32	59	8.1	21.9	2.4	-	10 J permanent spark	20-L sphere	125
Abbas et al., (2019)	31.7	68	9.6	20.7	1	0.3	10 J permanent spark	20-L sphere	93
GESTIS-DUST-EX	30	-	-	-	-	-	2 kJ/10 kJ chem. Ignitor	20-L/1 m3 sphere	＜15
Abbas et al., (2022)	31.7	68	9.6	20.7	1	0.3	10 J permanent spark	Open tube apparatus	49.6

Assuming that the combustion kinetics of pure species are independent and unchanged by the presence of other combustible species, complete conversion of the reactants and no heat losses, a simple mathematical model has been derived from the enthalpy balance of the whole system (Abbas et al., 2019), and the predictive formula was shown in table 1, and the assumptions required to arrive at this equation include:

1. Complete combustion of the total fuel present in the system;
2. No heat losses occur from the system;
3. Combustion kinetics of the pure species are independent and unchanged by the presence of other combustible species;
4. The adiabatic temperature rise at the flammability limit is the same for all the species. As for the numerical simulation for predicting LEL of hybrid mixtures. Cloney et al. (2018) studied the lower explosion limits of hybrid mixtures containing 10 μm coal dust particles and methane gas by using computational fluid dynamics and found that Le Chatelier's Law is applicable for the small particles studied, and Bartknecht's curve appeared to be conservative.

3.3.2 MIE

Nearly 130 years ago, Holtzwart and von Meyer demonstrated experimentally that explosible dust clouds could be ignited by electric sparks (Eckhoff, 2019). As an essential sensitivity parameter of dust cloud explosion, determining the minimum ignition energy (MIE) of flammable mixtures is critical for identifying possibility of accidental hazard in industry. The MIE is usually stated as a range of values rather than a single value. But in order to compare the MIE of the different combustible powders more clearly, we use only a single value. This value can be estimated using the probability of ignition as stated below (Pang et al., 2021):

$$\log MIE = \log E_2 - I[E_2] \times \frac{(\log E_2 - \log E_1)}{(NI+I)\times[E_2]+1} \tag{7}$$

where $I[E_2]$ is the number of tests with successful ignition at E2 and (NI + I) × [E2] stands for the total number of tests at the energy level of E2. The values obtained using the above formula will have a maximum uncertainty of 1 mJ.

By using the MIKE III usually, the MIE values for hybrid mixtures will be determined. Just like the measurement of the MEC adopting the testing protocol for testing pure dust cloud, so does the MIE. Therefore, many researchers have investigated the values of different dust substances and studied the effect of ignition energy on the dust explosion (Eckhoff, 1975; Eckhoff and Enstad, 1976; Van Laar, 1983; Au et al., 1992; Bartknecht, 1993; Beck et al., 1997; Kuai et al., 2013; Kim et al., 2019). A predictive model was proposed to predictive the dust mixtures consisting of different kinds of dust based on the mixing rule for Le Chatelier (1891) for the estimation of the flammability limits for mixtures of gases (Hosseinzadeh et al., 2015).

$$\frac{1}{MIE_{mixture}} = \sum \frac{(\%Vol_i)}{MIE_i} \tag{8}$$

where $MIE_{mixture}$ and MIE_i are the minimum ignition energy of the mixture and minimum ignition energy of each ingredient, respectively. Also $\%Vol_i$ represents the volume percentage of each flammable compound.

As for the determination of MIE value of hybrid mixtures, the ignition sensitivity of combustible dust can be strongly increased by an addition of a few percentages of combustible gases or vapours, even with contents lower than the LEL. It has notably been shown that hybrid mixtures can also be explosible when both the concentrations of the dust and the vapor are below their respective explosible limits (Pilao et al., 2006; Dufaud et al., 2009; Addai et al., 2016a). An empirical model was developed to predict the MIE value of hybrid mixtures (Addai et al., 2016a), seen in the follow:

$$MIE_{hybrid} = \frac{(MIE_{dust})}{(MIE_{dust}/MIE_{gas})^{C/C_0}} \tag{9}$$

where MIE_{hybrid}, MIE_{dust} and MIE_{gas} are MIE of hybrid mixtures, dust and flammable gas in the mixtures, respectively, C is the gas volume concentration (vol.%), C_0 is the gas concentration (vol.%) leading to the lowest MIE, MIE_{dust} and MIE_{gas} are minimum ignition energy of dust and gas, respectively. Bedises, it has been noticed that the minimum explosion energy (MIE) of dust clouds could decrease as soon as a few percentages of combustible gases or solvents were added (Khalili et al., 2012). Influences of adding a small amount of combustible gases (e.g., methane or propane) on the minimum ignition energy of coal, cellulose or PVC dusts were investigated for about three decades (Franke, 1978; Pellmont, 1979; Pellmont, 1980). In addition, the effect of oxygen concentration, inert gas and CH_4/H_2 addition on minimum ignition energy of coal dusts was also investigated (Wu et al., 2022).

3.3.3 MIT

The minimum ignition temperature (MIT) is a critical sensitivity parameter when conducting hazard assessment posed by a hot surface in industries that either process or handle hybrid mixtures. For the determination of the MIT of hybrid mixtures the G-G furnace which has to be modified in such a way that besides the generation of a dust–air mixture also a flammable gas or vapour can be added to the mixture was used. Based on this modified apparatus, the MIT of hybrid mixtures of dusts and gases or solvents was investigated (Addai et al., 2016a; Addai et al., 2017a), and the results showed that a significant decrease of the MIT of gas, solvent or dust and an increase in the likelihood of explosion when a small amount of dust, which was either below the minimum explosion concentration or not ignitable by itself, was mixed with gas and vice versa. After that, a predictive model that can be used to estimate the minimum ignition temperature of dusts and hybrid mixtures was developed (Addai et al., 2016), and the two models proposed to predict the MIT of hybrid-mixtures are in satisfactory agreement with the experimental results.

Model A:

$$T_{i,hybrid} = T_{i,g}\left(\frac{T_{i.d}}{T_{i.g}}\right)^{C_d/C_g} \tag{10}$$

Model B：

$$T_{i,hybrid} = \frac{1}{\frac{y_d}{T_{i.d}}+\frac{y_g}{T_{i.g}}} \tag{11}$$

$$y_g = \frac{m_g}{m_g+m_d} \qquad y_d = \frac{m_d}{m_g+m_d} \tag{12}$$

where $T_{i,hybrid}$ refers to the minimum ignition temperature of hybrid mixtures, $T_{i.d}$, $T_{i.g}$, C_d and C_g stand for the minimum ignition temperature of particles (K), minimum ignition temperature of gas (K), initial dust concentration (g/cm^3) and concentration of oxygen (g/cm^3) respectively, obtained from the experimental results, y_d, y_g, m_d and m_g represent the mass fraction of dust in dust–gas mixture, mass fraction of gas in dust–gas mixture, mass of dust (g) and mass of gas (g), respectively.

The MIT of carbonaceous dust clouds in air with CH_4/ H_2/CO below the gas lower explosion limit was also investigated (Tan et al., 2020), and the results showed that all flammable gases have distinct effects on the MITC of the dust samples and volatile matter content of dust plays an important role during the ignition process, at the same time, a theoretical model was developed to predictive the MIT of hybrid mixtures, seen as follows:

$$\ln T_{mci} = \frac{1}{\alpha-2}\ln(constant) + \frac{1}{\alpha-2}\ln\left[f(X_g)\right] \tag{13}$$

$$f(X_g) = 1-\left(\frac{X_g}{X_{g,stoic.}}\right)\left(\frac{\Delta H_g}{\Delta H_d}\right) \tag{14}$$

where X_g is the mole fraction of flammable gas in the hybrid mixture system, $X_{g,stoic.}$ is the theoretical stoichiometric coefficient of complete combustion of the flammable, ΔH_g and ΔH_d are the completed combustion heat (kJ/kg) of flammable and dust, respectively. And $\alpha \approx \frac{E_{a,h}}{RT_p}$ is the empirical power index, 'constant' is a lumped parameter only depending on the physical-chemical properties of the given dust cloud. The minimum ignition temperature of coal dust clouds in oxy-fuel combustion atmospheres was studied by Wu et al. (2016), and the results showed that the dust explosion risk increases significantly with increasing O_2 mole fraction by reducing the minimum ignition temperature for the three tested coal dust clouds dramatically (even by 100 ◦C). Based on the theoretical model, further research was conducted and studied the ignition temperature and mechanism of carbonaceous dust clouds by means of experiment and theoretical method, the results showed that the global heterogeneous ignition model suits well for the hybrid mixtures of anthracite or bituminous coal dusts (Wu et al., 2021).

3.3.4 LOC

As an essential sensitivity parameter of dust cloud explosion also, LOC have been researching by many researchers for many years. Much research has been performed on the determination of LOC values for single fuel air diluent mixtures (Cashdollar, 1996; Eckhoff, 2005; Man and Gibbins, 2011; Norman et al., 2015). The experiment under oxy-fuel condition was conducted (Li et al., 2020e), and found that when the dust explosion occurred under the condition of oxy-fuel atmospheres comparing with N_2, CO_2 performed a stronger impact on the limiting oxygen concentration (LOC). For the light metal dust (e.g., magnesium) explosions experiment conducted (Li et al., 2009), and found that under the condition of low dust concentration, the inerting performance of CO_2 was also found to be higher than that of N_2. The effect of oxygen concentration on oxy-fuel combustion characteristic and interactions of coal gangue and pine sawdust was researched (Zhang et al., 2019), the results indicated that the increase of oxygen concentration from 20% to 40% could improve interactions between coal gangue and pine sawdust obviously. However, relatively small improvement of interactions was detected between coal gangue and pine sawdust when oxygen concentration was further increased from 60% to 80%. The LOC at different initial pressures for polyester resin was studied (Tsai et al., 2018), and the results show that the explosion pressure can be significantly lessened with lower LOC.

The explosion characteristics of different ranks coal dust in oxy-fuel atmosphere was studied and found that the impact of the oxy-fuel atmosphere onto increased explosion risks is lower than it could be concluded from an increase in oxygen concentration in the system (Moroń et al., 2016).

The limiting oxygen concentration of hybrid mixtures consisting of fifteen combustible dusts and methane, ethanol and isopropanol hybrid mixtures was studied (Addai et al., 2019), and found that the limiting oxygen concentrations of the hybrid mixtures was lower than those of dust air mixtures when the relatively weaker spark igniter was used.

In addition, the present paper also summarized some representative research work and their research conclusions, giving more comprehensive understanding about the research of hybrid mixtures. Table 3 shows the summarization of the research results related to the dust explosion.

Table 3. Summarization of some research results related to the dust explosion.

References	Materials		Testing parameters	Ignition energy	Main conclusions
	Substances	Properties			
Xia et al., (2021)		D_{dust} : 3, 10, 20, and 30 µm C_{dust} : 0.6 to 2.3 kg/m^3.	Turbulent flame propagation velocities	Spark ignitior	The turbulent flame propagation velocity slightly increased with low mass ratio of small particles, while it sharply increased with high mass ratio of small particles.
Zhang et al., (2017)	Polymethyl methacrylate (PMMA) particle	Dv(90) (µm) (MZ-30H, SX-500H, MX-80H3wT, MP-300): 43.2, 7.4, 1.4, 46.8. C_{dust}: 450 g/m^3.	1. Flame propagation velocities. 2. Flame temperatures.		The faster the flame propagated, the higher maximum flame temperature was.

Zhang et al., (2016)		Dv (90) (mm) (MZ-30H, MP-300): 43.2, 46.8. C_{dust} : 105 g/m^3 - 217 g/m^3 for 100nm, 72 to 170 g/m^3 for 30 mm.	1. Flame structures 2. Flame propagation velocities.		Smaller particles maintained the leading part of the propagating flame and governed the combustion process of PMMA dust clouds.
Gao et al., (2015)	Hexadecanol dust.	Dv (90) (mm): 30.44 µm. C_{dust}: 188.70 g/m^3	1. Flame configurations. 2. Motion behaviors of the unburned particles ahead of flame front.	Spark ignitior	The flame propagate towards from small particles firstly to larger particles
Cao et al., (2014)		D_{50}: 32 µm for coal dust #1 and 34 µm for coal dust #2.	1. Flame-propagation velocities. 2. The thermal-radiation effects	Spark ignitior: 5 J	The flame propagated more quickly and with a higher temperature in the more volatile coal-dust cloud
Li et al., (2018)	coal-dust	C_{dust}: 60-500 g/m^3	(Flame propagation speed)	Chemical ignitor: 5 kJ	During coal dust explosion, much more solid fragments are produced by the thermal stress and blast shock impacts.
Wang et al., (2020)		D_{90} (A1, A2, B1, B2): 71.9, 56.8, 143 and 107. C_{dust}: 500g/m^3. C_{gas}: 0-10 vol%.	1. MEC. 2. P_{max}. 3. $(dP/dt)_{max}$. 4. (K_{st} or K_G)		The influence of methane on the explosion severity is more pronounced for

					coal dust with lower volatile content
Song et al., (2019)	Coal-dust/methane	D_{50}: 28 µm for coal dust #1 and 76 µm for coal dust #2, 133 µm for coal dust #3. C_{dust}: 50 - 400 g/m^3, C_{gas}: 5, 8, 10 vol%.		Chemical ignitor: 10 kJ	The maximum explosion pressure and maximum rate of pressure rise keep rising with the increasing initial pressure.
Addai et al., (2015)	Starch/methane/acetone	C_{dust}: 5-1000 g/m^3, C_{gas}: 1-4 vol%	1. MEC. 2. P_{max}. 3. $(dP/dt)_{max}$.	Spark ignitior: 10 J	A hybrid mixture explosion is possible even when dust, gas and vapor concentrations are respectively lower than their minimum explosion concentration (MEC) of dust and lower explosion limit (LEL) of gas and vapor.
Kosinski et al., (2013)	Carbon black/propane	C_{dust}: 0-500 g/m^3, C_{gas}: 0-5 vol%	1. P_{max}. 2. $(dP/dt)_{max}$.	Chemical ignitor: 1 kJ.	Addition of some quantities of combustible gases (here: propane) may sustain combustion processes.
					The addition of

Yu et al., (2021)	Aluminum dust/ hydrogen	D_{50}: 56.18 μm C_{dust}: 1000, 1500 and 2000 g/m^3, C_{gas}: 0-30 vol%	1. Flame morphology. 2. Flame propagation velocity.	Spark ignitior	hydrogen can significantly affect the ignition delay time and the flame propagation velocity of the hybrid mixtures
Yu et al., (2020)		D_{50}: 56.18 μm C_{dust}: 1000, 1500 and 2000 g/m^3, C_{gas}: 0, 5, 10 vol%	1. Flame morphology and microstructures. 2. Flame propagation velocities		Attributable to a variety of intermediate products competing for oxygen and absorbing heat, the hybrid explosion residues cooled faster, porous oxide layers and incompletely oxidized aluminum spheres with small particle sizes were formed

In summary, dust explosions are time-dependent flame propagation process, therefore, safety characteristics are the critical parameters, including ignition temperature, ignition energy, lower explosion limitation and oxygen concentration, etc. to maintain the sustainable flame propagation. Knowing these characteristic parameters in depth will have significantly beneficial to understand the flame propagation behaviour and the prevention and mitigation of potential explosion risk in industrial scenario.

4 Flame characteristics and propagation

4.1 Flame propagation behaviours during the dust explosion process

As early as 1968, the flame propagation of combustible dust and flammable gases mixtures was already studied (Singer and Liebman, 1968), and a comparison was made between the combustion flames of aluminium powder and coal powder in a methane/air environment. To better understand the flame propagation of dust cloud combustion, the combustion mechanism of isolated particle is essential. A theoretical study on the combustion of dust clouds from the scale of dust particles was performed (Nomura and Tanaka, 1992), they established the combustion model of particles based on some assumption. The picture of combustion model was shown in Fig. 12.

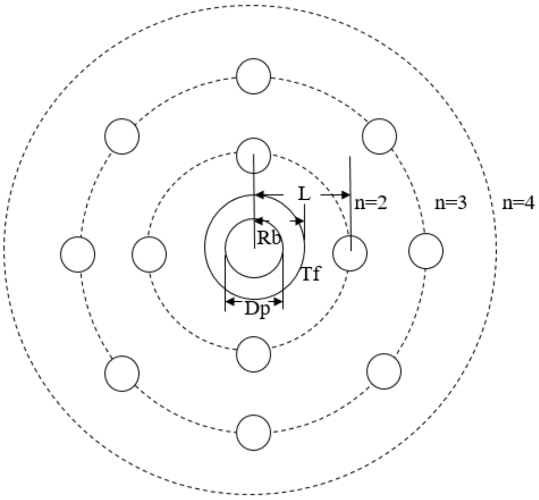

Fig. 12. *Dust cloud model (Nomura and Tanaka, 1992).*

Dahoe et al. (1996) studied the role of flame thickness in the validity of the “cube-root” law about the dust explosion in the spherical vessels and developed a model (the three-zone model) for the pressure evolution of confined dust explosions in spherical vessels which takes the flame thickness into account, the pressure-time curves that are generated with this model show a good resemblance with those measured in practice. The model was shown in Table 4.

Table 4. *An overview of the different phases that the flame front goes through during an explosion (Dahoe et al., 1996).*

Case 1	$\delta \le R_{vessel}$	Case 2	$\delta > R_{vessel}$
Phase 1a:	$r_{rear} = 0.0$	Phase 2a:	$r_{rear} = 0.0$
	$r_{front} < \delta$		$r_{front} < R_{vessel}$
Phase 1b:	$r_{rear} = r_{front} - \delta$	Phase 2b:	$r_{rear} = 0.0$
	$\delta \le r_{front} \le R_{vessel}$		$r_{front} = R_{vessel}$
Phase 1c:	$\delta \le r_{rear} \le R_{vessel}$	Phase 2c:	$0.0 < r_{rear} \le R_{vessel}$
	$r_{front} = R_{vessel}$		$r_{front} = R_{vessel}$

As we all know, for better understand the flame propagation behaviour of hybrid mixtures, the research on the pure dust is essential and basement. The structure of flames propagating through metal particle clouds and the behaviour of metal particles near the flames have been examined experimentally (Sun et al., 1998 & 2006a), and the result show that the combustion zone consists of luminous particles without gas-phase flame and the velocity of particles at the leading edge of combustion zone is nearly proportional to the flame velocity. After that, the temperature profile across the combustion zone propagating through an iron particle cloud and the concentration profile of particles across a flame propagating through an iron particle cloud were also investigated (Sun et al., 2001 & 2003). Julien et al. (2015a) studied the flame structures and particle combustion regimes are studied in hybrid fuel mixtures of methane and iron using a modified Bunsen burner with two different oxidizing environments: stoichiometric methane–air mixture and lean methane–oxygen–nitrogen mixture, making the content of oxygen different in those two cases, and the result showed that existing a critical concentration of iron powder that a coupled flame front in the combustion products of the methane flame can be formed. Furthermore, after the metal-powder flame formation, a double front structure separated by a dark zone is observed in the kinetic regime, whereas the two flames overlap and form a single Bunsen cone in the case of the diffusion regime, as shown in Fig. 13 & 14.

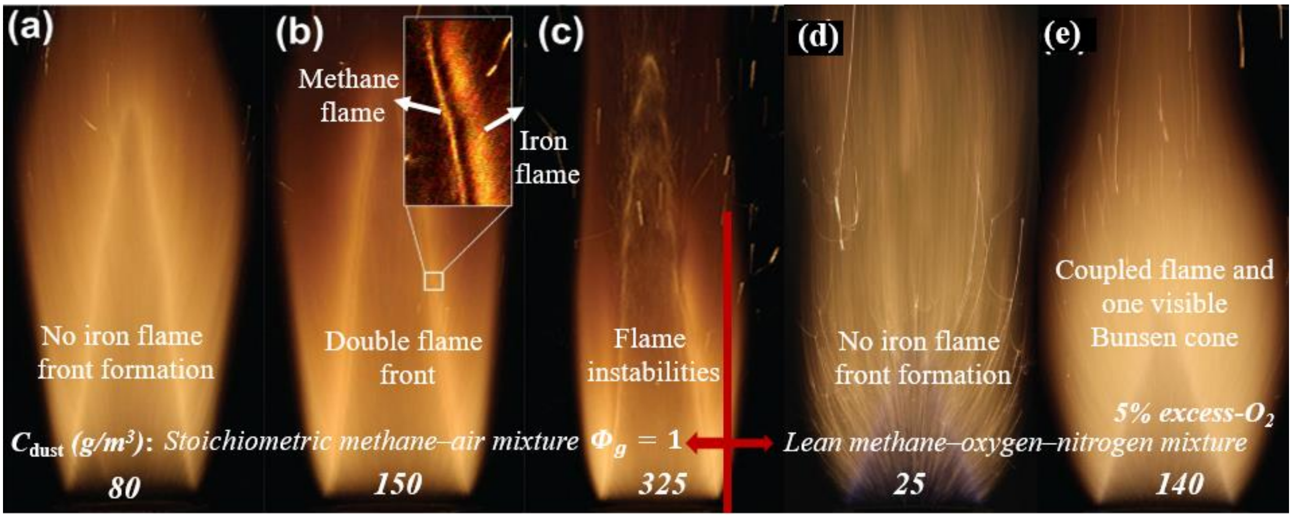

Fig. 13. *Iron–methane hybrid flames (Julien et al., 2015a).*

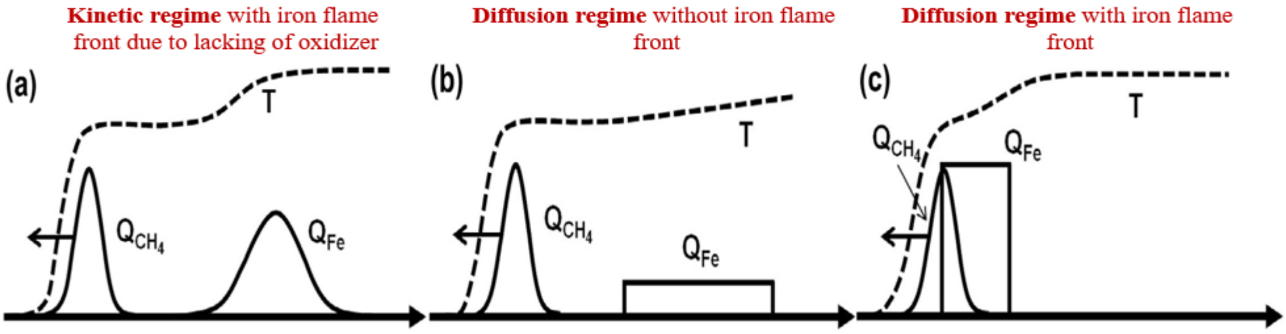

Fig. 14. *Different combustion regimes observed in the work of Julien et al. (2015a).*

Besides, the motion behaviour of particles ahead of the flame front were investigation by combining the particle image velocimetry (PIV) techniques, the combustion mechanism was revealed by Gao et al. (2015a) and Haghiri and Bidabadi (2011) and shown in Fig. 15.

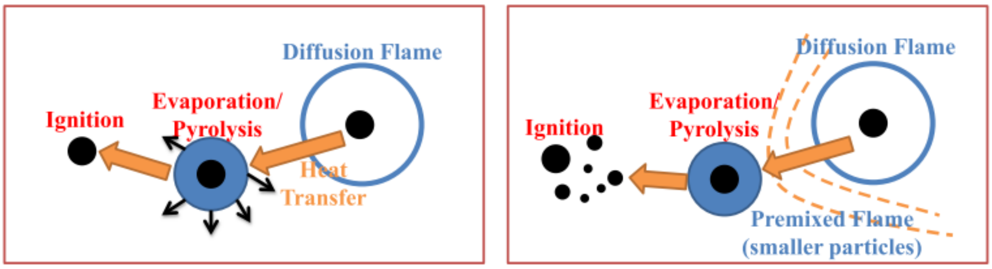

(a) Relay ignition mechanism **(b) Actual flame propagation model**

Fig. 15*. Flame propagation mechanism (Gao et al., 2015a).*

There are lot of influential factors that can affect the flame propagation behaviours, including the particle size distribution, particles concentration (Gan et al. 2018a; Zhang et al., 2018), radiation (Cao et al., 2014a; Bidabadi and Azad, 2015; Christophe et al., 2017), turbulence and material thermal characteristics (Gao et al., 2012 & 2013), etc. Besides, the volatile content involved in the dust also have effect on the combustion of dust and flame propagation, i.e., coal dusts with higher volatile matter contents (V_{daf}), lower vitrinite reflectance ($R_{o,max}$) and less ash contents (A_{ad}) show stronger explosion severity (Li et al., 2018a). Based on the analysis on the post-explosion residues, experimental results from Li et al. (2018) indicated that there is a linear relationship between explosion flame propagation speed and dust concentration and quantitatively analysed by standard method the emission properties of gaseous products during coal dust explosion, explained the structure evolution during coal particle explosion process.

4.2 Effect of particle size and its distribution on the flame propagation

According to the research results obtained from the literatures (Dufaud et al., 2010; Kuai et al., 2011; Zhang et al., 2017b; Zhang et al., 2017a; Liu et al., 2018; Ichinose et al., 2020). The flame propagation behaviour varied with the particle size distributions, even if Sauter mean diameter (D_{32}) was same, and flame can propagate very fast in small and monodispersed particles which didn't contain large particles (Yuzuriha et al., 2017). Gan et al. (2018b) studied the effects of polyethylene particle size distributions on flame propagations of hybrid mixtures of ethylene/polyethylene, the results showed that flame propagation velocities and maximum flame temperatures increased with the decrease of particle size distribution as a whole. On the other hand, particles with nano-size and micro-size will display quite different flame propagation characteristics during the combustion of its suspension. In general, compared with micro-size combustible particles, particles with nano-size have some unique properties (Yetter et al., 2009; Krietsch et al., 2015):

1. The increased specific surface area may lead to an increase in ignition sensitivity and reaction severity.
2. Some powders may show pyrophoric behaviour when sized down to nano-scale.
3. Oxygen adsorption at reactive surfaces of individual particles may result in a passivation of the powder.
4. Powders may tend to form agglomerates which are of microscale.

Experimental results have shown that, in the one hand, for nano-particles, flame was characterized by a regular spherical shape and spatially continuous combustion structure combined with a number of luminous spot flames. The flame propagation mechanism was similar to that of a premixed gas flame coupled with solid surface combustion of the agglomerates. On the other hand, smaller particles maintained the leading part of the propagating flame and governed the combustion process of PMMA dust clouds (Zhang et al., 2016). Similar experimental phenomenon was also observed from other relevant literatures (Bouillard et al., 2010; Escot Bocanegra et al., 2011; Li et al., 2016; Yu et al., 2016; Gao et al., 2017; Chang et al., 2020; Danzi et al., 2021;). And the flame propagation mechanism of nano-size and micro-size particle suspension was concluded as shown in Fig. 16.

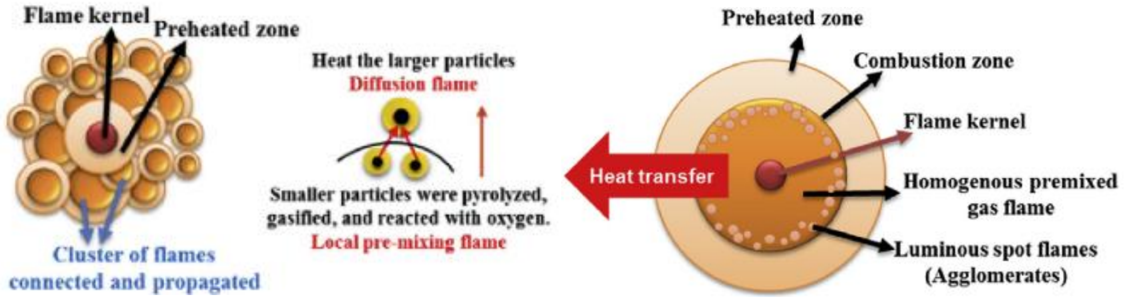

(A) (B)

Fig. 16. *Flame propagation and structure through 100 nm (A)/30 mm (B) PMMA dust cloud (Zhang et al., 2016).*

4.3 Flame quenching distance

One of the important fundamental parameters in laminar flame theory is the flame quenching distance, as it is closely related to the characteristic laminar flame thickness and structure. Together with burning velocity, the quenching distance is a fundamental flame characteristic that reflects both the flame propagation mode and its structure (Palecka et al., 2015). The quenching distance and flame speed under aluminium-oxygen-nitrogen and aluminium-oxygen-helium environment was investigated by Goroshin et al. (1996a) and found that the quenching distance and flame speed are very weak functions of dust concentration in rich mixtures and the substitution of nitrogen for helium in air increases the minimum quenching distance from 5 to 7 mm, as shown in Fig. 17.

Under the experimental conditions of reduced-gravity environment, Tang et al. (2009) studied flame quenching distance using iron particles, the results showed that the flame quenching distance increases linearly with particle size from less than 2 mm quenching distance for the 3 µm-sized dust to 10 mm quenching distance for the 27µm -sized dust, which is agreement with the numerical results from Bidabadi et al. (2016) and Bozorg et al. (2019), who found that flame propagation through iron powders composed of smaller particles is faster, and the quenching distance is lower. And the reason can be explained that increasing particle size increases the flame thickness and decreases the burning velocity (i.e., increases the quenching distance (Jarosinski et al., 1988). Palecka et al. (2015) investigated quenching distance of flames in hybrid methane–aluminium mixtures, and found that Coupled aluminium–methane flame fronts only appear above a threshold aluminium concentration around 300 g/m3. Below this concentration, the appearance and quenching behaviours of the methane flame seeded with reactive aluminium and inert SiC dusts are similar, as shown in Fig. 18.

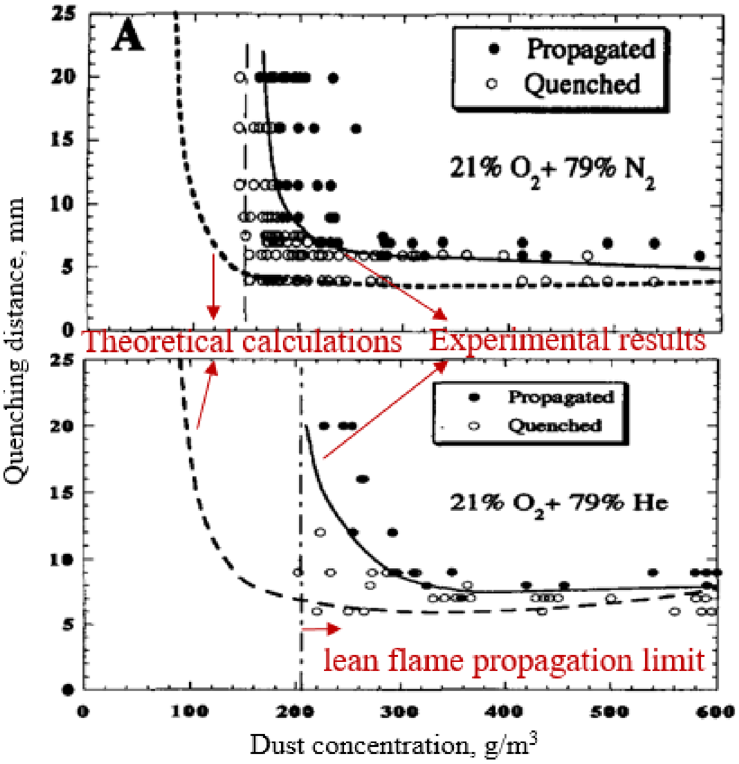

Fig. 17. *Quenching distance as a function of dust concentration (Goroshin et al., 1996a).*

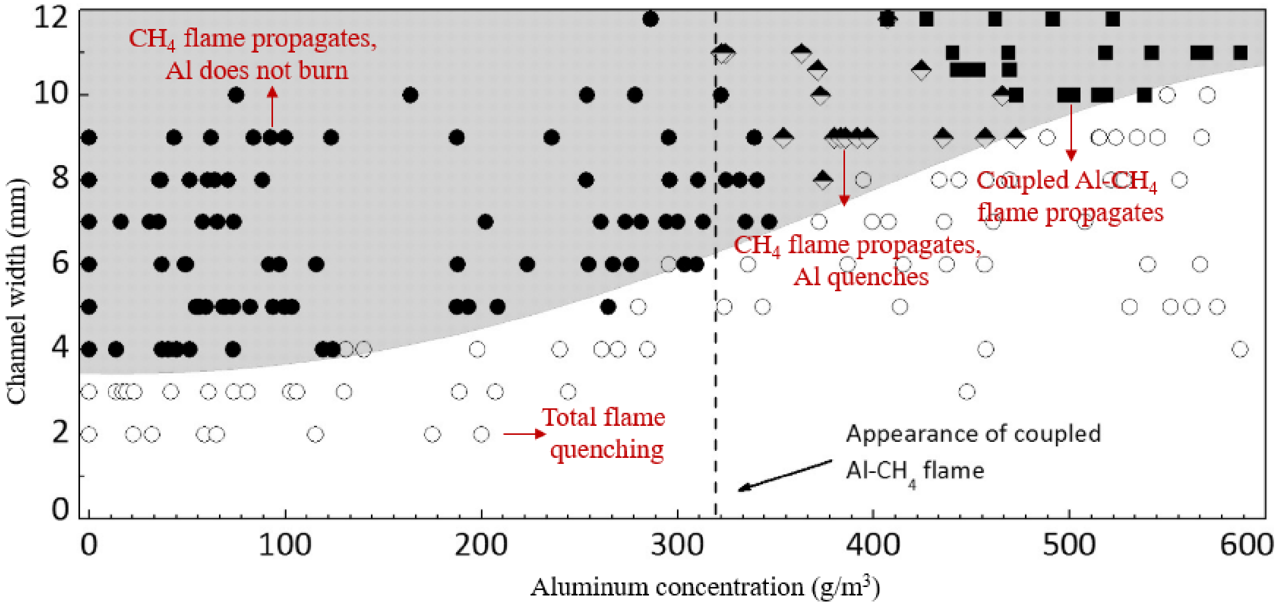

Fig. 18. *Results of flame quenching experiments at different concentrations of aluminium dust in 16.3% O_2/8.1% CH_4/ 75.6% N_2/Al mixtures* (Palecka et al., 2015).

4.4 Burning velocity

Burning velocity of fuel-air mixtures are always used to characterize the reactivity of fuel-air mixtures. In distinction to other explosion parameters, e.g., K_G or K_{st}, burning velocity show the advantage to emphasize the influence of flow velocities on the flame propagation (Krause and Kasch, 2000). As mentioned above, there is a lack of the standard protocol associated with the measurement of burning for dust-air suspension, the methods available in the literatures for measuring the burning velocity of dust-air suspension are derived from that of flammable gas, including tube method and burner method, soap bubble, explosion vessel. In particular, the tube method is best for burning velocity up to 80 cm/s, and that the constant volume bomb method is best for the higher burning velocity (Andrews and Bradley, 1972). Some empirical models were introduced to calculate the value of burning velocity with some assumptions.

$$S_u = \frac{A}{A_f} S_s \tag{15}$$

where S_u is the burning velocity, A is the front flame surface and A_f is the surface of the cross section of the tube. This model will valid under the assumptions of S_u is constant value over the entire cross section of the tube, the density of unburnt fuel ahead of the flame front ρ_u is constant and the flame speed is uniform over the tube cross section.

In another case, because the flame aerodynamics changes as the flame propagates along the tube and invalidate the assumption of a constant S_u over the cross section, the flame area A_f is also variable, therefore, the following model was proposed:

$$S_u = \frac{A}{A_f} \left(S_s - S_g\right) \tag{16}$$

where S_g is the mean unburnt gas velocity averaged over the tube cross-section area A_f.

Based on those models, the burning velocity of metal particles with nano-sized were investigated experimentally (Krietsch et al., 2021). At the same, considering the stretched of the flame due to the turbulence during the propagation and the partial confinement of the tube method, the thermal expansion factor α and flame's stretching factor K called Karlovitz's factor were introduced into the Equetion-1, and the un-stretched flame burning velocity was investigated (Cuervo et al., 2017;

Torrado et al., 2017), and the results show that he stretching of a gas flame is strongly influenced by the addition of dusts. Nevertheless, for lower gas concentrations and larger dust concentrations called ‘dust-driven regime’, the presence of powders tends to limit the flame velocity to that of the less reactive compound.

$$\mathrm{K} = \frac{1}{A_f}\frac{dA_f}{dt} \tag{17}$$

$$S_u = -LK + S_u^0 \tag{18}$$

Burner method were also used for investigating the burning velocity of hybrid mixtures by many researchers (Goroshin et al., 1996b; Soo et al., 2013; Julien et al., 2014). Goroshin et al. (996b) studied the burning velocity in fuel-rich aluminium dusts cloud, and found that burning velocity was a strong function of the molecular transport properties of the carrier gas, and the weak dependence of the flame speed on dust concentration is a direct result of the weak dependence of the particle burning rate in the diffusive regime on the flame temperature. In addition, a simplified, time-dependent numerical model that considers the influence of both diffusional and kinetic rates on the particle combustion process was proposed to study the thermal structure and burning velocity of flames in non-volatile fuel suspensions (Soo et al., 2016).

Over the years, McGill University has been developing alternative experimental techniques based on direct observation of dust flames, yielding reliable fundamental parameters such as flame burning velocity, temperature and structure, a new apparatus for investigating flame propagation in turbulent dust clouds at near constant pressure conditions was designed by Skjold et al. (2013). After that, an extensive series of balloon experiments were performed (Julien et al., 2015b & 2015c), and found that the flame speed of stable flames is found to be a strong function of the heat conductivity of the gas mixture, and pulsating and spiral-like flames are discovered in fuel-lean mixtures, and flames with cellular patterns occur in very-fuel-rich suspensions. By using the same balloon setup, Vickery et al. (2017) studied the propagation of isobaric spherical flames in hybrid aluminium-methane fuel mixtures and indicated that the difference in behaviour at low concentrations in mixtures with and without excess oxygen is explained by the ability of aluminium particles reacting with free oxygen to ignite and burn in the diffusion-limited combustion mode. The maximum effective burning velocity was proposed to be used as the substitute of the K_{St} but shows less apparatus dependent than the corresponding K_{St} values (Pu et al., 2007). For metal hydride suspension, the flame propagation behaviours and influential factors of TiH_2 dust explosions at a constant pressure were also studied (Cheng et al., 2018), and the results indicated that the burning mechanism of TiH_2 dust is thought to be mainly controlled by diffusion regime, the appearance of hydrogen gas accelerates the combustion rate of TiH_2 particles and also makes the TiH_2 dust changed from a discrete media to a continuum, which may account for the phenomenon that the flame speed in dust cloud of TiH_2 is larger than that of Ti at the same concentrations no matter in air or oxygen atmosphere. The burning velocity of this kind of apparatus, i.e., isobaric condition created by the transparent balloon, was calculated from the following equation:

$$S_L = S_f\left[1 - \frac{(r_b^3 - r_{b0}^3)}{r_f^3}\right] \tag{19}$$

where r_b, r_{b0}, r_f are radii of the initial prefilled balloon, the following inflated balloon and the dust flame respectively, which can be obtained from measuring the still frames of flame front, and the S_f represents the flame speed propagated in dust cloud (Skjold et al., 2013).

4.5 Flame propagation mechanism

Understanding the flame propagation mechanism in depth is essential for designing the protective measurements in industrial scenario. According to the different combustion steps between particles with low-volatile and particle with high-volatile, the research on the flame propagation mechanism should be start with two categories roughly: heterogeneous combustion (the combustion occurs in the surface of the particles) and homogeneous combustion (the combustion occurs in the gas phase), in fact, in some cases, the combustion process can be combined with heterogeneous combustion and homogeneous combustion (Tan et al., 2020). In spite of intensive contribution associated with hybrid mixtures explosion have been done (Chen and Fan, 2005; Jinhua et al., 2006; Wang et al., 2006; Liu et al., 2007; Kern et al., 2015; Gao et al., 2015; Ajrash et al., 2017), the flame propagation mechanism of hybrid mixtures still cannot be clarified, especially on the interaction between the gas phase and solid phase, including the heat transfer (conductive and thermal radiation), mass transfer and flow state.

Similar with the gas flames, flames in particulate suspensions at the laboratory scale are primarily driven by molecular heat diffusion and have comparable burning velocities (Bergthorson et al., 2015). However, they exhibit several significant differences in their structure and behaviour from homogeneous flames due to their multiphase nature. The flame propagation behaviours of aluminium suspension were studied intensively (Marmo et al., 2004; Chen and Fan, 2005; Dufaud et al., 2010; Julien et al., 2015b; Julien et al., 2015c; Li et al., 2016; Sun et al., 2006b; Yu et al., 2016). Furthermore, the main distinctive feature of a flame in a solid suspension is the ability of particles to ignite. Namely, to transition from a combustion regime limited by reaction kinetics to a regime limited by diffusion of the oxidizing gas towards the particle surface, or in the case of evaporating particles, towards the micro-flame enveloping each individual particle. After ignition, the temperature of the particle or micro-flame can exceed the gas temperature by several hundred degrees, often surpassing the adiabatic flame temperature for fuel-lean mixtures. The particle combustion rate in the diffusion combustion regime is a weak, non-Arrhenius, function of gas temperature (Soo et al., 2016). Unlike gas flames, the width of the flame reaction zone in particle suspensions can span a large temperature range and can be comparable to, or even exceed, that of the preheat zone (Goroshin et al., 1996a). The existence of diffusion micro-flames within a global flame-front (in effect, flames within the flame), which are insensitive to the bulk gas temperature, makes dust flames resistant to heat loss (Frank-Kamenetskii, 1969; Tang et al., 201; Bergthorson et al., 2015;) and also serves to maintain a constant burning velocity with increasing fuel concentration in fuel-rich mixtures (Goroshin et al., 1996). The addition of flammable gas into the particulate suspension can have significant effect on the flame propagation characteristics, including the flame velocity (Yu et al., 2020), flame structure (Soo et al., 2013), burning velocity (Soo et al., 2013; Julien et al., 2015c) and the flame propagation stability (Yu et al., 2020), etc.

The most popular hybrid mixtures used in the laboratory is the combination of coal dust and flammable gases, like methane, hydrogen and carbon monoxide, etc. According to the intensive experimental data available in the literatures (Liu et al., 2007; Li et al., 2012; Addai et al., 2015a, 2015b & 2017; Song et al., 2019; Zhao et al., 2020 & 2021), the synergetic effect between in the hybrid mixtures play a significant role in promoting the combustion and decreasing the sensitivity of combustion of hybrid mixtures. For investigating the synergetic effect of flammable gas and organic dust at the condition of LEL concentration, lycopodium and methane were selected (Abbas et al., 2022), and the result indicated that for hybrid mixtures of carbonaceous dusts (like lycopodium) at their LEL, ignition occurs in the gas phase, however, flame propagation is only possible through a two-way interaction of dust and gas during the course of combustion. Gao et al. (2015) studied the flame propagation mechanism in dust explosions, there were two different combustion regimes: kinetics-controlled regime and devolatilization controlled regime, which observed during the experiment, seen in Fig. 19.

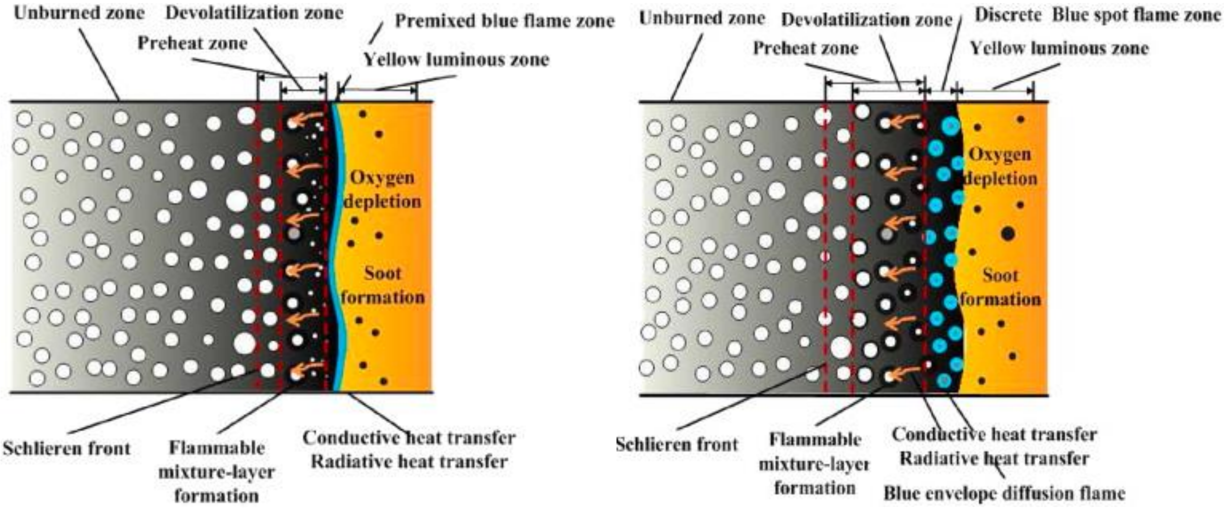

(a) Kinetics controlled regime (b) Devolatilization-controlled regime.

Fig. 19*. Schematics of flame propagation mechanisms in dust explosions. (a). Kinetics controlled regime, (b). Devolatilization-controlled regime (Gao et al., 2015).*

Based on the simulation results and the research results from Garcia-Agreda et al (2011), Cloney (2018) further investigated the explosion evaluating regime by taking the equivalence ratio analysis and timescale analysis into account and explained the flame propagation mechanism in details, as shown in Figs. 20 & 21. The results demonstrated that maximum burning velocity for hybrid mixtures may occur along lines of constant Φ_h^v (volatile component equivalence ratio) for small particle sizes and that a kinetic-limited combustion regime may be present for Φ_h^t (total equivalence ratio) and an impeded gas flame regime where the dust could not react fast enough to contribute to energy release in the flame front.

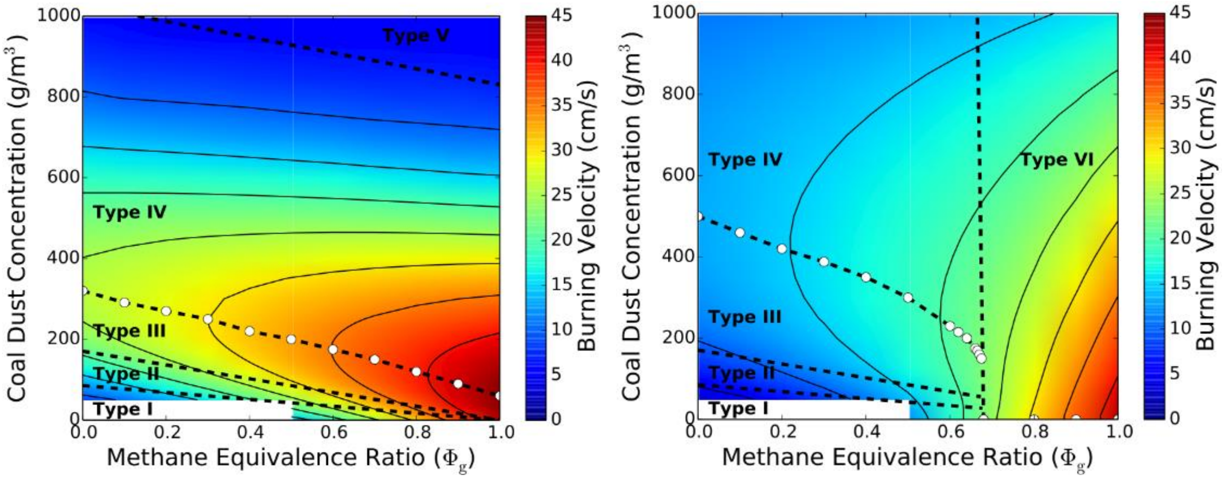

(a) (b)

Fig. 20. *Burning velocity and combustion regime diagram for hybrid mixtures of (a) 10μm, (b) 33 μm coal dust particles and methane gas (Cloney, 2018).*

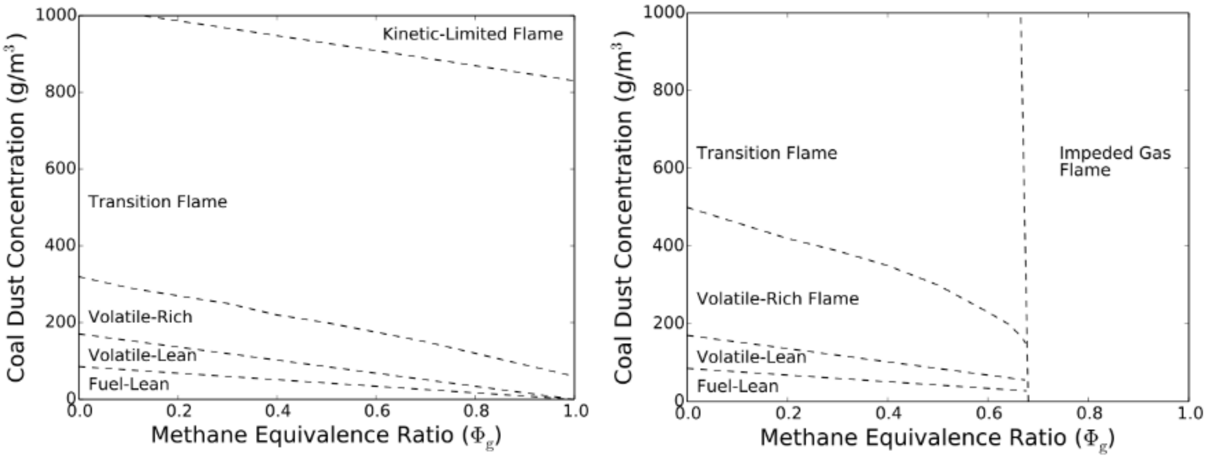

(a) (b)

Fig. 21. *Combustion regime diagram of hybrid mixtures of (a) 10μm, (b) 33 μm coal dust particles and methane gas (Cloney, 2018).*

Metals can react with the products of hydrocarbon flames (i.e., steam and carbon dioxide), and the addition of metals to hydrocarbon fuels significantly increases the energy density of the hybrid fuel mixture. As we know from the literatures, for hybrid mixtures of metal dust and flammable gas (Soo et al., 2013; Julien et al., 2015a), at low concentrations, the metal in suspension behaves as an inert additive which only acts to increase the heat capacity of the mixture, resulting in lower flame temperatures and reduced burning velocities. Above a critical concentration of metal fuel, the metal particles reacting with the hydrocarbon combustion products form a flame front which thermally couples to the methane flame, resulting in the stabilization of burning velocity with increasing metal-fuel concentration. Therefore, the flame propagation mechanism of aluminium and methane hybrid mixtures was investigated and shown in Fig. 22 (Vickery et al., 2017). According to the experimental results (Yu et al., 2021), with the increase of the hydrogen concentration in the hybrid mixture, the relation of the maximum flame propagation velocity $v_{\max}$ with the hydrogen concentration will experienced three stages: first stage, the $v_{\max}$ is almost equivalent to that of pure aluminium dust. Second stage, the $v_{\max}$ increases slightly. Third stage, the $v_{\max}$ increases significantly, which can exceed more than 50 times the $v_{\max}$ of pure aluminium dust, and the flame propagation mechanism was revealed as shown in Fig. 23.

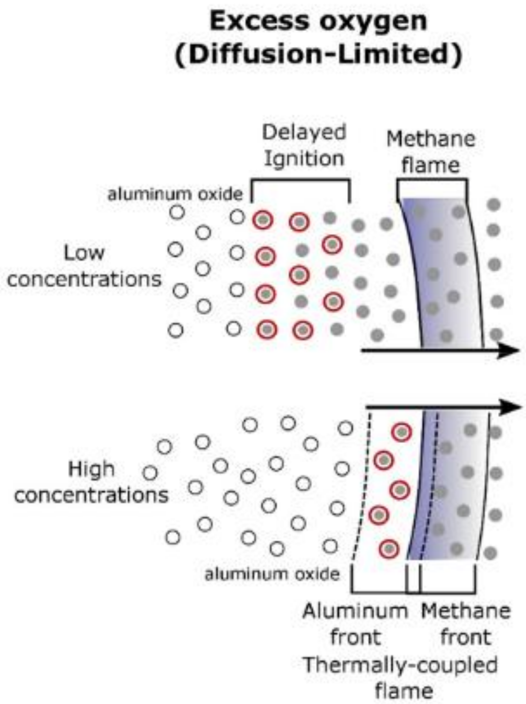

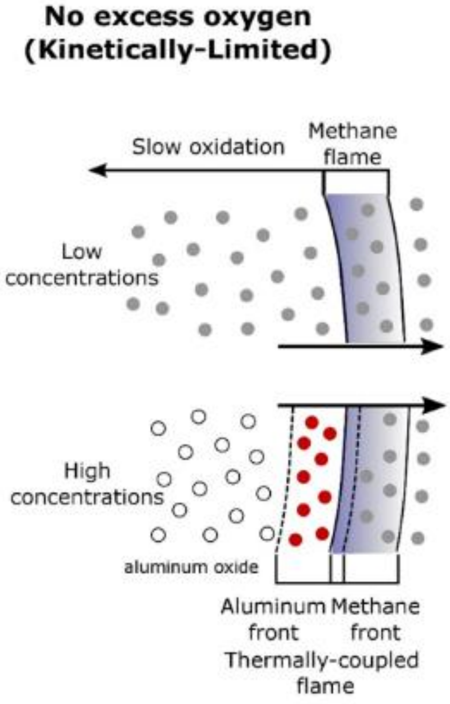

Fig. 22. Particle mode of combustion and aluminium-methane flame interactions are shown. In mixtures with excess oxygen, the particles burn in the diffusion-limited regime with micro-diffusion flames around each particle. In mixtures without excess oxygen, burning aluminium particles are depicted simply as red without a diffusion-flame present around the particle (Vickery et al., 2017).

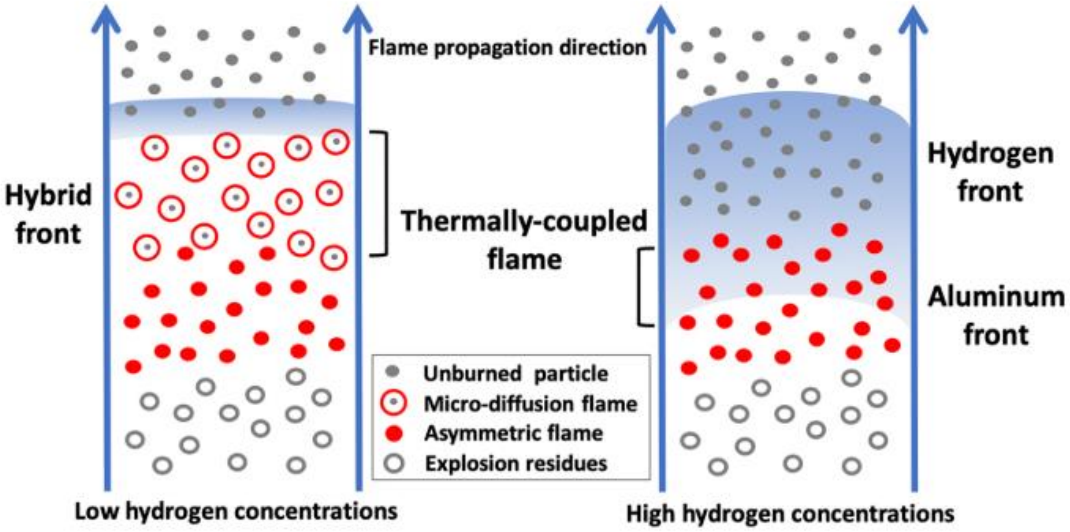

Fig. 23. Particle combustion mode and hydrogen–aluminium flame interactions (Yu et al., 2021).

Numerical simulations as a promising approach have been developed to gain insight into the dust explosion behaviour (Murillo et al., 2013; Cao et al., 2014). In order to compensate for the deficiency of dust explosion experiments, the simplified geometry of the 20-L spherical chamber was established and the dust dispersion process (Di Benedetto et al., 2013), explosion process was simulated, and then the dust velocity and temperature field were obtained (Salamonowicz et al., 2015). In addition, by establishing and using 3D numerical simulation associated with 20L-sphere, the effect of oxygen level, particle size, and dust concentration (Li et al., 2020a), ignition delay (refers to the turbulence level inside the chamber) (Li et al., 2020a & 2020b) on the flame evolution characteristics and explosion severity of corn-starch dust cloud deflagration were investigated and developed an approach to estimating the safety degree for underground coal mines. Furthermore, the transient temperature evolution of pulverized coal cloud deflagration in a methane–oxygen atmosphere was also be studied (Li et al., 2020), and the results pointed out that turbulence in the conveying process is responsible for dust agglomeration during the explosion. Numerical simulation of hybrid mixtures were also conducted by researchers (Redlinger, 2015; Cloney, 2018), the dynamics of wheat starch powder/pyrolysis gases hybrid mixtures in the 20-L explosion chamber was studied by performed the CFD numerical simulation and experiment (Pico et al., 2020a & 2020b), and the results suggest that the combined effect of the dust-phase and gas-phase reactions have a distinctive dissipative effect on the turbulence levels and that higher turbulence decay levels during the explosion step of the test are related to higher explosion severities and the explosion regimes proposed in the literature are not universally-applicable to all types of hybrid mixtures. The effect of environment temperature and the fluid flow state on the explosion of hybrid mixtures were also simulated in 20L-sphere (Di Benedetto et al., 2013; Wang et al., 2020).

Compared with the results of study (Cao et al., 2014), the further simulation results show that the airflow velocity in the closed vessel is higher than that in the half closed one, which causes secondary entrainment and the Domino effect. This effect will promote more serious consistent explosion (Cao et al., 2017). Inside the combustion tube, the particle motion and distribution before ignition were studied numerically (Cheng et al., 2020), and the results show that there were no flames near the wall of the tube due to particles gathering and attaching to the wall, and during the explosion venting, particles flew out of the tube before the flame, the venting flame exhibited a “mushroom cloud” shape due to interactions with the vortex, and the flame maintained this shape as it was driven upward by the vortex.

5. Conclusions and suggestions for future research

This review presents a state-of-the-art overview of the comprehensive understanding of hybrid mixture explosion in experimental study level; thereby, the main limitations and challenges to be faced are explored. The discussed main contents include, explosion regime and classification of hybrid mixtures, the experimental measurement for the safety parameters of hybrid mixtures (i.e., explosion sensitivity and severity parameters) via typical test apparatuses, the detailed flame propagation/quenching characteristics behind the explosion severities/sensitivities of hybrid mixtures. In spite of the extensive work on the explosion characteristics of hybrid mixtures have been done by many researchers, there are still some scientific questions need to be answered:

1. According to the experimental results from Denkevits et al. (2007&2015), the ignition energy and dust reactivity will also have a significant influence on the division of the diagram, especially for the gas-driven regime. While based on the experimental results from (Khalil, 2013; Hossain et al., 2014; Ajrash et al., 2016), dust-driven regime can be further divided based on the different combustion propagation mechanisms of dust (diffusion-controlled or kinetically controlled propagation). Primarily, what the key roles of the reaction kinetics play during the hybrid mixture explosions is required to explain. The simple arithmetic addition could not explain how the synergic explosion of the interaction between different phases fuels when neither the gas/vapor fuel concentration reaches its LEL nor the particle fuel, especially for the hybrid mixtures of gas fuel and non-volatile particle fuel. As a result, study on the fundamental chemical kinetics of hybrid mixtures is of significance to explain the hybrid mixture explosion regimes.

2. Moreover, hybrid mixture tends to have higher values of explosion severity parameters and lower values of explosion sensitivity parameters compared with pure gas/vapor or dust/mist explosions. Therefore, the hybrid flame behaviours and interplay with overpressure, including

acceleration and quenching are of interest. On the one hand, the overpressure and its rise are attribute to the flame front acceleration with combustion product expansions. Study on hybrid flame acceleration, thus, not only helps us to understand the lumped explosion severity parameters, namely $P_{\max}$ and $(dp/dt)_{\max}$ or deflagration index (K_{St}), but also the explosion suppression and the deflagration to detonation transition (DDT) mechanism at the worst scenarios. On the other hand, the flame quenching in the deflagration resulting in the extinguishment or unsuccessful of explosion. This suggests that understanding the hybrid flame quenching would explain the explosion sensitivity parameters such as LEL, LOC, MIT and MIE, and also provide the fundamentals for explosion inerting and venting.

3. The other direction might go to the study on the hybrid or multiphase DDT process. The key role of the reactivity and transport phenomena of hybrid mixtures in the forming of DDT is of significant interest for both industrial safety and detonation engine applications. For instance, the critical conditions of the initiation of shock wave, the interplay between the flame front and shock wave, and the forming and instability of detonation wave. For better understand the explosion and detonation process of hybrid mixtures, the multi-physics numerical model with high precision is needed and applied to the research of explosion characteristics of hybrid mixtures.

The last but not the least is that more type and multiphase of hybrid mixture or hazardous materials are required to be studied in future works, including phase of fuels (gas/vapor, liquid/solid particle), type of oxidants (air/oxygen/gaseous oxides, solid oxidants, water/hydrogen peroxide/organic peroxide), since most of the studies to date mainly focused on two-phase fuels. Non-atmospheric ambient and process conditions are also of interest, such as micro-gravity, elevated/reduced temperature or pressure, boundary condition and configuration, size-effect, turbulence intensity and obstacle etc. This work aims to summarize the essential basics of experimental studies and to provide the perspectives based on the current research gaps to understand the explosion hazards of hybrid mixtures in-depth.

Since the safety characteristics are dependent on experimental parameters like the ignition energy, ignition source or the particle size distribution of the dust, the need for a new standard method is obvious to be able to compare the data from different laboratories.

References

Abbas, Z., Gabel, D., Krietsch, A., Krause, U., 2022. Qusi-static dispersion of dusts for the determination of lower explosion limits of hybrid mixtures. J. Loss Prev. Process. Ind. 74, 104640.

Abbas, Z., Zinke, R., Gabel, D., Addai, E.K., Darbanan, A.F., Krause, U., 2019. Theoretical evaluation of lower explosion limit of hybrid mixtures. J. Loss Prev. Process. Ind. 60, 296-302.

Addai, E.K., 2016. Investigation of Explosion Characteristics of Multiphase Fuel Mixtures with Air. phD thesis.

Addai, E.K., Addo, A., Abbas, Z., Krause, U., 2017a. Investigation of the minimum ignition temperature and lower explosion limit of multi-components hybrid mixtures in the Godbert-Greenwald furnace. Process Saf. Environ. Protect. 111, 785-794.

Addai, E.K., Clouthier, M., Amyotte, P., Safdar, M., Krause, U., 2019. Experimental investigation of limiting oxygen concentration of hybrid mixtures. J. Loss Prev. Process. Ind. 57, 120-130.

Addai, E.K., Gabel, D., Kamal, M., Krause, U., 2016a. Minimum ignition energy of hybrid mixtures of combustible dusts and gases. Process Saf. Environ. Protect. 102, 503-512.

Addai, E.K., Gabel, D., Krause, U., 2015a. Explosion characteristics of three component hybrid mixtures. Process Saf. Environ. Protect. 98, 72-81.

Addai, E.K., Gabel, D., Krause, U., 2015b. Lower explosion limit of hybrid mixtures of burnable gas and dust. J. Loss Prev. Process. Ind. 36, 497-504.

Addai, E.K., Gabel, D., Krause, U., 2016b. Experimental investigation on the minimum ignition temperature of hybrid mixtures of dusts and gases or solvents. J Hazard Mater 301, 314-326.

Addai, E.K., Gabel, D., Krause, U., 2016c. Models to estimate the minimum ignition temperature of dusts and hybrid mixtures. J Hazard Mater 304, 73-83.

Addai, E.K., Gabel, D., Krause, U., 2017b. Lower explosion limit/minimum explosible concentration testing for hybrid mixtures in the Godbert-Greenwald furnace. Process Saf. Prog. 36, 81-94.

Ajrash, M.J., Zanganeh, J., Moghtaderi, B., 2016. Effects of ignition energy on fire and explosion characteristics of dilute hybrid fuel in ventilation air methane. J. Loss Prev. Process. Ind. 40, 207-216.

Ajrash, M.J., Zanganeh, J., Moghtaderi, B., 2017. The flame deflagration of hybrid methane coal dusts in a large-scale detonation tube (LSDT). Fuel 194, 491-502.

Amyotte, P.R., Mintz, K.J., Pegg, M.J., Sun, Y.H., 1993. The ignitability of coal dust-air and methane-coal dust-air mixtures. Fuel 72, 671-679.

Andrews, G.E., Bradley, D., 1972. Determination of Burning Velocities: A Critical Review. Combust. and Flame 18, 133-153.

Au, S., Haley, R., Smy, P.R., 1992. The Influence of the Igniter-Induced Blast Wave Upon the Initial Volume and Expansion of the Flame Kernel. Combust. and flame. 88, 50-60.

Badiola, C., Dreizin, E.L., 2013. Combustion of micron-sized particles of titanium and zirconium. Proc. Combust. Inst. 34, 2237-2243.

Bartknecht, W., 1981. Explosions Course Prevention Protection. Springer Verlag, Berlin.

Bartknecht, W., 1993. Vorbeugender Explosionsschutz, Explosionsschutz. Springer, pp. 297-418.

Beck, H., Glienke, N., Möhlmann, C., 1997. Combustion and explosion characteristics of dusts. HVBG.

Bergthorson, J.M., Goroshin, S., Soo, M.J., Julien, P., Palecka, J., Frost, D.L., Jarvis, D.J., 2015. Direct combustion of recyclable metal fuels for zero-carbon heat and power. Applied Energy 160, 368-382.

Bidabadi, M., Azad, A.V., 2015. Effects of radiation on propagating spherical flames of dust–air mixtures. Powder Technol. 276, 45-59.

Bidabadi, M., Mohebbi, M., Poorfar, A. K., Hochgreb, S., Lin, C, Biouki, S. A., Hajilou, M., 2016. Modeling quenching distance and flame propagation speed through an iron dust cloud with spatially random distribution of particles. J. Loss Prev. Process. Ind. 43, 138-146.

Bouillard, J., Vignes, A., Dufaud, O., Perrin, L., Thomas, D., 2010. Ignition and explosion risks of nanopowders. J Hazard Mater 181, 873-880.

Bozorg, M. V., Bidabadi, M., Bordbar, V., 2019. Numerical investigation of flame behavior and quenching distance in randomly distributed poly-dispersed iron dust cloud combustion within a narrow channel. J. Hazard. Mater. 367, 482-491.

Britton, L.G., 1999. Avoiding Static Ignition Hazards in Chemical Operations. New York, USA: Centre for Chemical Process Safety/AICh E 172.

Bucher, P., Yetter, R.A., Dryer, F.L., 1996. Flmame structure measurement of single, isolated aluminum particles burning in air. Twenty-Sixth Symposium (International) on Combustion, 1899-1908.

Cao, W., Gao, W., Liang, J., Xu, S., Pan, F., 2014a. Flame-propagation behavior and a dynamic model for the thermal-radiation effects in coal-dust explosions. J. Loss Prev. Process. Ind. 29, 65-71.

Cao, W., Gao, W., Peng, Y., Liang, J., Pan, F., Xu, S., 2014b. Experimental and numerical study on flame propagation behaviors in coal dust explosions. Powder Technol. 266, 456-462.

Cao, W., Qin, Q., Cao, W., Lan, Y., Chen, T., Xu, S., Cao, X., 2017. Experimental and numerical studies on the explosion severities of coal dust/air mixtures in a 20-L spherical vessel. Powder Technol. 310, 17-23.

Cashdollar, K.L., 1996. Coal dust explosibility. J. Loss Prev. Process. Ind. 9, 65-76.

Cashdollar, K.L., 2000. Overview of dust explosibility characteristics. J. Loss Prev. Process. Ind. 13, 183-199.

Cashdollar, K.L., Chatrathi, K., 1993. Minimum Explosible Dust Concentrations Measured in 20-L and 1-M3 Chambers.

Combust. Sci. Technol. 87, 157-171.

Cashdollar, K.L., Sapko, M.J., Weiss, E.S., M. Hertzberg, 1987. Laboratory and mine dust explosion research at the Bureau of Mines, Industrial dust explosions.

Materials, West Conshohocken, PA. ASTM Special Technical Publication (STP), American Society for Testing 958, 107-123.

Cassel, H.M., Gupta, A.K.D., Guruswamy, S., 1953. Factors affecting flame propagetion through dust clouds. Flame propagation in explosive gas mixtures.

Chang, P.-J., Mogi, T., Dobashi, R., 2020. Flame propagation through dust clouds of nano and micron scale aluminum particles. J. Loss Prev. Process. Ind. 68, 104266.

Chawla, N., Amyotte, P.R., Pegg, M.J., 1996. A comparison of experimental methods to determine the minimum explosible concentration of dusts. Fuel 75, 654-658.

Chen, Z., Fan, B., 2005. Flame propagation through aluminum particle cloud in a combustion tube. J. Loss Prev. Process. Ind.18, 13-19.

Cheng, F., Chang, Z., Luo, Z., Liu, C., Li, H., Wang, T., 2020. Numerical study on premixing characteristics and explosion process of starch in a vertical pipe under turbulent flow. J. Loss Prev. Process. Ind. 68, 104303.

Cheng, Y., Meng, X., Ma, H., Liu, S., Wang, Q., Shu, C., Shen, Z., Liu, W., Song, S., Hua, F., 2018. Flame propagation behaviors and influential factors of TiH2 dust explosions at a constant pressure. Int. J. Hydrogen Energ. 43, 16355-16363.

Christophe, P., Rim, B.M., Mohamed, G., Khashayar, S., Jérôme, F., 2017. Thermal radiation in dust flame propagation. J. Loss Prev. Process. Ind. 49, 896-904.

Cloney, C.T., 2018. Burning velocity and lower flammability limits of hybrid mixtures containing combustible dust and flammable gas, PhD thesis.

Cloney, C.T., Amyotte, P.R., Khan, F.I., Ripley, R.C., 2013. Development of an organizational framework for studying dust explosion phenomena. J. Loss Prev. Process. Ind. xxx, 1-8.

Cloney, C.T., Ripley, R.C., Pegg, M.J., Amyotte, P.R., 2017. Evaluating regime diagrams for closed volume hybrid explosions. J. Loss Prev. Process. Ind. 49, 912-918.

Cloney, C.T., Ripley, R.C., Pegg, M.J., Amyotte, P.R., 2018a. Laminar burning velocity and structure of coal dust flames using a unity Lewis number CFD model. Combust. and Flame 190, 87-102.

Cloney, C.T., Ripley, R.C., Pegg, M.J., Khan, F., Amyotte, P.R., 2018b. Lower flammability limits of hybrid mixtures containing 10 micron coal dust particles and methane gas. Process Saf. Environ. Protect. 120, 215-226.

Cuervo, N., Dufaud, O., Perrin, L., 2017. Determination of the burning velocity of gas/dust hybrid mixtures. Process Saf. Environ. Protect. 109, 704-715.

Dahoe, A.E., Zevenbergen, J.F., Lemkowitz, S.M., Scarlett, B., 1996. Dust explosions in spherical vessels_ The role of flame thickness in the validity of the ‘tube-root law’. J. Loss Prev. Process. Ind. 9, 33-44.

Danzi, E., Pio, G., Marmo, L., Salzano, E., 2021. The explosion of non-nano iron dust suspension in the 20-l spherical bomb. J. Loss Prev. Process. Ind. 71, 104447.

Dastidar, A., Amyotte, P., Going, J., Chatrathi, K., 2001. Inerting of coal dust explosions in laboratory and intermediate-scale chambers. Fuel 80, 1593-1602.

Denkevits, A., 2007. Explosibility of hydrogen–graphite dust hybrid mixtures. J. Loss Prev. Process. Ind.20, 698-707.

Denkevits, A., Hoess, B., 2015. Hybrid H_2/Al dust explosions in Siwek sphere. J. Loss Prev. Process. Ind. 36, 509-521.

Di Benedetto, A., Russo, P., Sanchirico, R., Di Sarli, V., 2013. CFD simulations of turbulent fluid flow and dust dispersion in the 20 liter explosion vessel. AIChE Journal 59, 2485-2496.

Dobashi, R., Senda, K., 2002. Mechanisms of flame propagation through suspended combustible particles. Journal de Physique IV 12.

Dobashi, R., Senda, K., 2006. Detailed analysis of flame propagation during dust explosions by UV band observations. J. Loss Prev. Process. Ind. 19, 149-153.

DOI: 10.7795/810.20221124

Dufaud, O., Pettin, L., Traoré, M., 2008. Dust/vapour explosion: Hybrid behaviours? J. Loss Prev. Process. Ind. 21(4), 481-484.

Dufaud, O., Perrin, L., Traoré, M., Chazelet, S., Thomas, D., 2009. Explosions of vapour/dust hybrid mixtures: A particular class. Powder Technol. 190, 269-273.

Dufaud, O., Poupeau, M., Khalili, I., Cuervo, N., Christodoulou, M., Olcese, R., Dufour, A., Perrin, L., 2011. Comparing Pyrolysis Gases and Dusts Explosivities: A Clue to Understanding Hybrid Mixtures Explosions? Ind. Eng. Chem. Res. 51, 7656-7662.

Dufaud, O., Traoré, M., Perrin, L., Chazelet, S., Thomas, D., 2010. Experimental investigation and modelling of aluminum dusts explosions in the 20 L sphere. J. Loss Prev. Process. Ind. 23, 226-236.

Eckhoff, R.K., 1975. Towards Absolute Minimum Ignition Energies For Dust Clouds? Combust. and Flame 24, 53-64.

Eckhoff, R.K., 2003. Dust explosions in the process industries, in: Publishing, A.G.P. (Ed.).

Eckhoff, R.K., 2005a. Current status and expected future trends in dust explosion research. J. Loss Prev. Process. Ind. 18, 225-237.

Eckhoff, R.K., 2005b. Gas and dust explosions caused by smoldering combustion in powder layers and deposits. Explosion Hazards in the Process Industries.

Eckhoff, R.K., 2016. Gas and Dust Explosions Caused by Smouldering Combustion in Powder Layers and Deposits. Explosion Hazards in the Process Industries, 2nd Edition.

Eckhoff, R.K., 2019. Measurement of minimum ignition energies (MIEs) of dust clouds – History, present, future. J. Loss Prev. Process. Ind. 61, 147-159.

Eckhoff, R.K., Enstad, G., 1976. Why Are "Long" Electric Sparks More Effective Dust Explosion Initiators Than "Short" Ones? 27, 129-131.

Engler, C., 1885. Beitrage zur Kenntniss der Staubexplosionen Chemische Industrie, 171-173.

Escot Bocanegra, P., Sarou-Kanian, V., Davidenko, D., Chauveau, C., Gökalp, I., 2011. Studies on the burning of micro- and nanoaluminum particle clouds in air. 47-62.

Foniok, R., 1985. Hybrid dispersive mixtures and inertized mixtures of coal dust. explosiveness and ignitability. Staub Reinhalt. Luft 45, 151-154.

Frank-Kamenetskii, D.A., 1969. Diffusion and Heat Exchange in Chemical Kinetics. Plenum press, New York.

Franke, H., 1978. Bestimmung der Minderstzudenergie von Kohlenstaub/Methan/Luft Gemisches (hybride Gemische). VDI-Berichte 304, 69-72.

Gan B., Li B., Jiang H., Zhang D., Bi M., Gao W. 2018a. Ethylene/polyethylene hybrid explosions: Part 1. Effects of ethylene concentrations on flame propagations. J. Loss Prev. Process. Ind. 54, 93-102.

Gan B., Li B., Jiang H., Zhang D., Bi M., Gao W. 2018b. Ethylene/polyethylene hybrid explosions: Part 2. Effects of polyethylene particle size distributions on flame propagations. J. Loss Prev. Process. Ind. 55, 134-143.

Gao, W., Dobashi, R., Mogi, T., Sun, J., Shen, X., 2012. Effects of particle characteristics on flame propagation behavior during organic dust explosions in a half-closed chamber. J. Loss Prev. Process. Ind. 25, 993-999.

Gao, W., Mogi, T., Rong, J., Yu, J., Yan, X., Dobashi, R., 2015a. Motion behaviors of the unburned particles ahead of flame front in hexadecanol dust explosion. Powder Technol. 271, 125-133.

Gao, W., Mogi, T., Yu, J., Yan, X., Sun, J., Dobashi, R., 2015b. Flame propagation mechanisms in dust explosions. J. Loss Prev. Process. Ind. 36, 186-194.

Gao, W., Zhang, X., Zhang, D., Peng, Q., Zhang, Q., Dobashi, R., 2017. Flame propagation behaviours in nano-metal dust explosions. Powder Technol. 321, 154-162.

Gao, W., Zhong, S., Mogi, T., Liu, H., Rong, J., Dobashi, R., 2013. Study on the influence of material thermal characteristics on dust explosion parameters of three long-chain monobasic alcohols. J. Loss Prev. Process. Ind. 26, 186-196.

Garcia-Agreda, A., Di Benedetto, A., Russo, P., Salzano, E., Sanchirico, R., 2011. Dust/gas mixtures explosion regimes. Powder Technol. 205, 81-86.

Garcia-Torrent, J., Conde-Lazaro, E., Wiien, C., Rautalin, A., 1998. Biomass dust explosibility at elevated initial pressures. Fuel 77, 1093-1097.

Glassman, I., 1996. Combustion, 3rd ed, Academic Press, San Diego, USA.

Going, J.E., Chatrathi, K., Cashdollar, K.L., 2000. Flammability limit measurements for dusts in 20-L and 1-m3 vessels. J. Loss Prev. Process. Ind. 13, 209-219.

Goroshin, S., Bidabadi, M., Lee, J.H.S., 1996a. Quenching Distance of Laminar Flame in Aluminum Dust Clouds. Combust. and Flame 105, 147-160.

Goroshin, S., Fomenko, I., Lee, J.H.S., 1996b. Burning velocities in fuel-rich aluminum dust clouds. Twenty-Sixth Symposium (International) on Combustion 1966, 1961-1967.

Haghiri, A., Bidabadi, M., 2011. Dynamic behavior of particles across flame propagation through micro-iron dust cloud with thermal radiation effect. Fuel 90, 2413-2421.

Han, O.-S., Yashima, M., Matsuda, T., Matsui, H., Miyake, A., Ogawa, T., 2000. Behavior of flames propagating through lycopodium dust clouds in a vertical duct. J. Loss Prev. Process. Ind. 13, 449–457.

Hossain, M.N., Amyotte, P., Abuswer, M., Dastidar, A., Khan, F., Eckhoff, R., Chunmiao, Y., 2014. Influence of liquid and vapourized solvents on explosibility of pharmaceutical excipient dusts. Process Saf. Prog. 33, 374-379.

Hosseinzadeh, S., Norman, F., Verplaetsen, F., Berghmans, J., Van den Bulck, E., 2015. Minimum ignition energy of mixtures of combustible dusts. J. Loss Prev. Process. Ind. 36, 92-97.

Hosseinzadeh, S., Norman, F., Verplaetsen, F., Berghmans, J., Van den Bulck, E., 2016. A study on the effects of using different ignition sources on explosion severity characteristics of coals in oxy-fuel atmospheres. J. Loss Prev. Process. Ind. 43, 53-60.

Ichinose, K., Mogi, T., Dobashi, R., 2020. Effects of the Particle Size and Agglomeration on the Minimum Explosible Concentration and Flame Propagation Velocity in Dust Clouds. Combust. Explo. Shock+. 56, 421-426.

Ji, W., Wang, Y., Yang, J., He, J., Wen, X., Wang, Y., 2022. Methods to predict variations of lower explosion limit associated with hybrid mixtures of flammable gas and dust. Fuel 310, 122138.

Ji, W., Yu, J., Yu, X., Yan, X., 2018. Experimental investigation into the vented hybrid mixture explosions of lycopodium dust and methane. J. Loss Prev. Process. Ind. 51, 102-111.

Jiang, J., Liu, Y., Mannan, M.S., 2014. A correlation of the lower flammability limit for hybrid mixtures. J. Loss Prev. Process. Ind. 32, 120-126.

Jiang, J., Liu, Y., Mashuga, C.V., Mannan, M.S., 2015. Validation of a new formula for predicting the lower flammability limit of hybrid mixtures. J. Loss Prev. Process. Ind. 35, 52-58.

Jing, Q., Wang, D., Liu, Q., Ren, L., Wang, Y., Liu, C., Shen, Y., Wang, Z., 2021. Study on transient reaction mechanism and explosion intensity parameters of micron-sized flake aluminum dust in air. Chem. Eng. Sci. 246, 116884.

Jing, Q., Wang, D., Liu, Q., Shi, C., Liu, J., 2022. Ignition sensitivity and explosion behaviors of micron-sized aluminum powder: Comparison between flake aluminum powder and spherical aluminum powder. Chem. Engi. Sci. 252.

Jarosinski, J., Lee, J. H., Knystautas, R., Crowley, J.D., 1988. Quenching of dust-air flames. Symposium (International) on Combusiton. 21 (1), 1917-1924.

Ju, W. Dobashi, R., Hirano, T., 1998. Reaction zone structures and propagation mechanisms of flames in stearic acid particle clouds. J. Loss Prev. Process. Ind. 11, 423-430.

Julien, P., Soo, M., Goroshin, S., Frost, D.L., Bergthorson, J.M., Glumac, N., Zhang, F., 2014. Combustion of Aluminum Suspensions in Hydrocarbon Flame Products. J. Propul. Poweer. 30, 1047-1054.

Julien, P., Whiteley, S., Goroshin, S., Soo, M.J., Frost, D.L., Bergthorson, J.M., 2015a. Flame structure and particle-combustion regimes in premixed methane–iron–air suspensions. Proc. Combust. Inst. 35, 2431-2438.

Julien, P., Vickery, J., Goroshin, S., Frost, D.L., Bergthorson, J.M., 2015b. Freely-propagating flames in aluminum dust clouds. Combust. and Flame 162, 4241-4253.

Julien, P., Vickery, J., Whiteley, S., Wright, A., Goroshin, S., Bergthorson, J.M., Frost, D.L., 2015c. Effect of scale on freely propagating flames in aluminum dust clouds. J. Loss Prev. Process. Ind. 36, 230-236.

Kern, H., Wieser, G.J., Raupenstrauch, H., 2015. Flame propagation in lycopodium/air mixtures below atmospheric pressure. J. Loss Prev. Process. Ind. 36, 281-286.

Khalil, Y.F., 2013. Experimental investigation of the complex deflagration phenomena of hybrid mixtures of activated carbon dust/hydrogen/air. J. Loss Prev. Process. Ind. 26, 1027-1038.

Khalili, I., Dufaud, O., Poupeau, M., Cuervo-Rodriguez, N., Perrin, L., 2012. Ignition sensitivity of gas–vapor/dust hybrid mixtures. Powder Technol. 217, 199-206.

Kim, W., Soga, T., Johzaki, T., Endo, T., Kato, T., Choi, K., 2019. Minimum ignition energy and minimum explosible concentration of L-isoleucine and glycine powder. Powder Technol. 347, 207-214.

Krause, U., Kasch, T., 2000. The influence of flow and turbulence on flame propagation through dust-air mixtures. J. Loss Prev. Process. Ind. 13, 291-298.

Krietsch, A., Reyes Rodriguez, M., Kristen, A., Kadoke, D., Abbas, Z., Krause, U., 2021. Ignition temperatures and flame velocities of metallic nanomaterials. J. Loss Prev. Process. Ind. 71, 104482.

Krietsch, A., Scheid, M., Schmidt, M., Krause, U., 2015. Explosion behaviour of metallic nano powders. J. Loss Prev. Process. Ind. 36, 237-243.

Kuai, N., Huang, W., Du, B., Yuan, J., Li, Z., Gan, Y., Tan, J., 2013. Experiment-based investigations on the effect of ignition energy on dust explosion behaviors. J. Loss Prev. Process. Ind. 26, 869-877.

Kuai, N., Li, J., Chen, Z., Huang, W., Yuan, J., Xu, W., 2011. Experiment-based investigations of magnesium dust explosion characteristics. J. Loss Prev. Process. Ind. 24, 302-313.

Kundu, S.K., Zanganeh, J., Eschebach, D., Moghtaderi, B., 2018. Explosion severity of methane–coal dust hybrid mixtures in a ducted spherical vessel. Powder Technol. 323, 95-102.

La´zaro, E.C., Torrent, J.G.a., 2000. Experimental research on explosibility at high initial pressures of combustible dusts. J. Loss Prev. Process. Ind. 13, 221-228.

Li, G., Yuan, C., Fu, Y., Zhong, Y., Chen, B., 2009. Inerting of magnesium dust cloud with Ar, N_2 and CO_2. J Hazard Mater 170, 180-183.

Li, H., Chen, X., Deng, J., Shu, C., Kuo, C., Yu, Y., Hu, X., 2020a. CFD analysis and experimental study on the effect of oxygen level, particle size, and dust concentration on the flame evolution characteristics and explosion severity of cornstarch dust cloud deflagration in a spherical chamber. Powder Technol. 372, 585-599.

Li, H., Deng, J., Chen, X., Shu, C., Kuo, C., Hu, X., 2020b. Influence of ignition delay on explosion severities of the methane–coal particle hybrid mixture at elevated injection pressures. Powder Technol. 367, 860-876.

Li, H., Deng, J., Chen, X., Shu, C., Kuo, C., Zhai, X., Wang, Q., Hu, X., 2020c. Qualitative and quantitative characterisation for explosion severity and gaseous–solid residues during methane–coal particle hybrid explosions: An approach to estimating the safety degree for underground coal mines. Process Saf. Environ. Protect. 141, 150-166.

Li, H., Deng, J., Chen, X., Shu, C., Kuo, C., Zhai, X., Wang, Q., Hu, X., 2020d. Transient temperature evolution of pulverized coal cloud deflagration in a methane–oxygen atmosphere. Powder Technol. 366, 294-304.

Li, H., Deng, J., Shu, C., Kuo, C., Yu, Y., Hu, X., 2020e. Flame behaviours and deflagration severities of aluminium powder–air mixture in a 20-L sphere: Computational fluid dynamics modelling and experimental validation. Fuel 276, 118028.

Li, Q., Lin, B., Dai, H., Zhao, S., 2012. Explosion characteristics of H_2/CH_4/air and CH4/coal dust/air mixtures. Powder Technol. 229, 222-228.

Li, Q., Tao, Q., Yuan, C., Zheng, Y., Zhang, G., Liu, J., 2018a. Investigation on the structure evolution of pre and post explosion of coal dust using X-ray diffraction. Int. J. Heat Mass Tran. 120, 1162-1172.

Li, Q., Wang, K., Zheng, Y., Mei, X., Lin, B., 2016. Explosion severity of micro-sized aluminum dust and its flame propagation properties in 20 L spherical vessel. Powder Technol. 301, 1299-1308.

Li, Q., Yuan, C., Tao, Q., Zheng, Y., Zhao, Y., 2018b. Experimental analysis on post-explosion residues for evaluating coal dust explosion severity and flame propagation behaviors. Fuel 215, 417-428.

Liu, S., Cheng, Y., Meng, X., Ma, H., Song, S., Liu, W., Shen, Z., 2018. Influence of particle size polydispersity on coal dust explosibility. J. Loss Prev. Process. Ind. 56, 444-450.

Liu, Y., Sun, J., Chen, D., 2007. Flame propagation in hybrid mixture of coal dust and methane. J. Loss Prev. Process. Ind. 20, 691-697.

Man, C.K., Gibbins, J.R., 2011. Factors affecting coal particle ignition under oxyfuel combustion atmospheres. Fuel 90, 294-304.

Marmo, L., Cavallero, D., Debernardi, M.L., 2004. Aluminium dust explosion risk analysis in metal workings. J. Loss Prev. Process. Ind. 17, 449-465.

Moroń, W., Ferens, W., Czajka, K.M., 2016. Explosion of different ranks coal dust in oxy-fuel atmosphere. Fuel Processing Technol. 148, 388-394.

Murillo, C., Dufaud, O., Bardin-Monnier, N., López, O., Munoz, F., Perrin, L., 2013. Dust explosions: CFD modeling as a tool to characterize the relevant parameters of the dust dispersion. Chem. Eng. Sci. 104, 103-116.

NFPA-69, 2014. Standard on Explosion Preventiion Systems. National Fire Protection Agency, Quincy, MA.

Nifuku, M., Koyanaka, S., Ohya, H., Barre, C., Hatori, M., Fujiwara, S., Horiguchi, S., Sochet, I., 2007. Ignitability characteristics of aluminium and magnesium dusts that are generated during the shredding of post-consumer wastes. J. Loss Prev. Process. Ind. 20, 322-329.

Nomura, S., Tanaka, T., 1992. Theoretical analysis of dust explosions Powder Technol. 71, 189-196.

Norman, F., Hosseinzadeh, S., Bulck, E.V., Berghmans, J., Verplaetsen, F., 2015. Dust explosion severity characteristics of Indonesian Sebuku coal in oxy-fuel atmospheres. 7th European Combustion Meeting (ECM 2015).

Palecka, J., Julien, P., Goroshin, S., Bergthorson, J.M., Frost, D.L., Higgins, A.J., 2015. Quenching distance of flames in hybrid methane–aluminum mixtures. Proc. Combust. Inst. 35, 2463-2470.

Pang L., Cao J., Zhao Y., Yuan C. Yang K., Zhang Z., 2021. Minimum ignition energy of LDPE dust/ethylene hybrid mixture. J. Loss Prev. Process. Ind. 72, 104546.

Pellmont, G., 1979. Explosions-und Zündverhalten von hybriden Gemischen aus brennbaren Stäuben und Brenngasen. ETH Zurich.

Pellmont, G., 1980. Minimum ignition energy of combustible dusts and explosion behaviour of hybrid mixtures, 3rd International Symposium on Loss Prevention and Safety Promotion in the Process Industries, pp. 851-862.

Pico, P., Ratkovich, N., Muñoz, F., Dufaud, O., 2020a. Analysis of the explosion behaviour of wheat starch/pyrolysis gases hybrid mixtures through experimentation and CFD-DPM simulations. Powder Technol. 374, 330-347.

Pico, P., Ratkovich, N., Muñoz, F., Dufaud, O., 2020b. CFD-DPM and experimental study of the dynamics of wheat starch powder/pyrolysis gases hybrid mixtures in the 20-L Sphere. Powder Technol. 372, 638-658.

Pilao, R., Ramalho, E., Pinho, C., 2006. Overall characterization of cork dust explosion. J Hazard Mater 133, 183-195.

Proust, C., Accorsi, A., Dupont, L., 2007. Measuring the violence of dust explosions with the “20l sphere” and with the standard “ISO 1m3 vessel”. J. Loss Prev. Process. Ind. 20, 599-606.

Pu, Y.K., Jia, F., Wang, S., Skjold, T., 2007. Determination of the maximum effective burning velocity of dust–air mixtures in constant volume combustion. J. Loss Prev. Process. Ind. 20, 462-469.

Radford, J., 2015. "What happened tragic day of Mt Kembla Mine disaater" (Illawarra Mercury website,). http://www.illawarramecury.com.au/story/2441786/what-happened-tragic-day-of-mt-kembla-mine-disaster/) (Accessed: 14 August 2015).

Redlinger, R., 2015. Numerical simulation of hybrid dust/gas explosion experiments in the standard 20-L sphere. Fusion Eng. Des. 100, 419-424.

Russo, P., Benedettob, A.D., Sanchirico, R., 2012. Theoretical Evaluation of the Explosion Regimes of Hybrid Mixtures. Chemical Engineering Transactions 26, 51-56.

Salamonowicz, Z., Kotowski, M., Półka, M., Barnat, W., 2015. Numerical simulation of dust explosion in the spherical 20l vessel. Bulletin of the Polish Academy of Sciences Technical Sciences 63, 289-293.

Sanchirico, R., Di Benedetto, A., Garcia-Agreda, A., Russo, P., 2011. Study of the severity of hybrid mixture explosions and comparison to pure dust–air and vapour–air explosions. J. Loss Prev. Process. Ind. 24, 648-655.

Sanchirico, R., Russo, P., Saliva A., Doussot, A., Di Sarli D, V., Di Benedetto, A., 2015a. Explosion of lycopodium-nicotinic acid methane complex hybrid mixtures. J. Loss Prev. Process. Ind. 36, 505-508.

Sanchirico, R., Russo, P., Di Sarli, V., Di Benedetto, A., 2015b. On the explosion and flammability behavior of mixtures of combustible dusts. Process Saf. Environ. Protect. 94, 410-419.

Singer, J.M., Liebman, I., 1968. Spherical Flames of Spark-ignited Dust Clouds. Central Electricity Generating Board 12.

Siwek, R., 1996. Determination of technical safety indices and factors influencing hazard evaluation of dusts. J. Loss Prev. Process. Ind. 9, 21-31.

Skjold, T., Olsen, K.L., Castellanos, D., 2013. A constant pressure dust explosion experiment. J. Loss Prev. Process. Ind. 26, 562-570.

Slezak, S.E., Buckius, R.O., Krier, H., 1985. A Model of Flame Propagation in Rich Mixtures of Coal Dust in Air. Combust. and Flame 59, 251-265.

Song, S., Cheng, Y., Meng, X., Ma, H., Dai, H., Kan, J., Shen, Z., 2019. Hybrid CH4/coal dust explosions in a 20-L spherical vessel. Process Saf. Environ. Protect. 122, 281-287.

Soo, M., Julien, P., Goroshin, S., Bergthorson, J.M., Frost, D.L., 2013. Stabilized flames in hybrid aluminum-methane-air mixtures. Proc. Combust. Inst. 34, 2213-2220.

Soo, M., Kumashiro, K., Goroshin, S., Frost, D.L., Bergthorson, J.M., 2016. Thermal structure and burning velocity of flames in non-volatile fuel suspensions. Proc. Combust. Inst. 36, 2351-2358.

Sun, J., Dobashi, R., Hirano, T., 1998a. Structure of flames propagating through metal particle clouds and behavior of particles. Twenty-Seventh Symposium (International) on Combustion/The Combustion Institute, 2405-2411.

Sun, J., Dobashi, R., Hirano, T., 2001a. Temperature profile across the combustion zone propagating through an iron particle cloud. J. Loss Prev. Process. Ind. 14, 463-467.

Sun, J., Dobashi, R., Hirano, T., 2006a. Velocity and number density profiles of particles across upward and downward flame propagating through iron particle clouds. J. Loss Prev. Process. Ind. 19, 135-141.

Sun, J., Dobashi, R., Hirano, T., 2006b. Structure of flames propagating through aluminum particles cloud and combustion process of particles. J. Loss Prev. Process. Ind. 19, 769-773.

Sun, J., Dobashi, R., Hirano, T., 1998b. Structure of flames propagating through metal particle clouds and behavior of particles. Twenty-Seventh Symposium (International) on Combustion/The Combustion Institute, 2405–2411.

Sun, J., Dobashi, R., Hirano, T., 2001b. Temperature profile across the combustion zone propagating an iron particle cloud. J. Loss Prev. Process. Ind. 14, 463–467.

Sun, J., Dobashi, R., Hirano, T., 2003. Concentration profile of particles across a flame propagating through an iron particle cloud. Combust. and Flame 134, 381-387.

Sweis, F.K., 2006. The effect of admixed material on the minimum explosible concentration of oil shale. J. Loss Prev. Process. Ind. 19, 701-704.

Tan, X., Schmidt, M., Zhao, P., Wei, A., Huang, W., Qian, X., Wu, D., 2020. Minimum ignition temperature of carbonaceous dust clouds in air with $CH_4/H_2/CO$ below the gas lower explosion limit. Fuel 264, 116811.

Tang, F.-D., Goroshin, S., Higgins, A., Lee, J., 2009. Flame propagation and quenching in iron dust clouds. Proc. Combust. Inst. 32, 1905-1912.

Tang, F.-D., Goroshin, S., Higgins, A.J., 2011. Modes of particle combustion in iron dust flames. Proc. Combust. Inst. 33, 1975-1982.

Thimothée, R., Chauveau, C., Halter, F., Gökalp, I., 2016. Experimental Investigation of the Mechanisms of Cellular Instabilities Developing on Spherical Two-Phase Flames. Combust. Sci. Technol. 188, 2026-2043.

Torrado, D., Cuervo, N., Pacault, S., Glaude, P.-A., Dufaud, O., 2017. Influence of carbon black nanoparticles on the front flame velocity of methane/air explosions. J. Loss Prev. Process. Ind. 49, 919-928.

Tsai, Y., Ho, S., Huang, A., Shu, C., 2018. Potential explosion hazard of polyester resin dust formed from a granulation process: Limiting oxygen concentration with different pressures. Appl. Therm. Eng. 135, 74-82.

Van Laar, G., 1983. Influence of Moisture Content on the Minimum Ignition Energy (MIE) of Dust/Air Mixtures. Report on the Working Group Minimum Ignition Energy. TNO Prins Mautits Laboratorium.

Vickery, J., Julien, P., Goroshin, S., Bergthorson, J.M., Frost, D.L., 2017. Propagation of isobaric spherical flames in hybrid aluminum-methane fuel mixtures. J. Loss Prev. Process. Ind. 49, 472-480.

Wang, D., Qian, X., Wu, D., Ji, T., Zhang, Q., Huang, P., 2020a. Numerical study on hydrodynamics and explosion hazards of corn starch at high-temperature environments. Powder Technol. 360, 1067-1078.

Wang, Q., Sun, Y., Jiang, J., Deng, J., Shu, C., Luo, Z., Wang, Q., 2020b. Inhibiting effects of gas–particle mixtures containing CO2, Mg(OH)2 particles, and NH4H2PO4 particles on methane explosion in a 20-L closed vessel. J. Loss Prev. Process. Ind. 64.

Wang, S., Pu, Y., Jia, F., Gutkowski, A., Jarosinski, J., 2006. An Experimental Study on Flame Propagation in Cornstarch Dust Clouds. Combust. Sci. Technol. 178, 1957-1975.

Wang, Y., Qi, Y., Gan, X., Pei, B., Wen, X., Ji, W., 2020c. Influences of coal dust components on the explosibility of hybrid mixtures of methane and coal dust. J. Loss Prev. Process. Ind. 67, 104222.

Wu, D., Huang, X., Norman, F., Verplaetsen, F., Berghmans, J., Van den Bulck, E., 2015. Experimental investigation on the self-ignition behaviour of coal dust accumulations in oxy-fuel combustion system. Fuel 160, 245-254.

Wu, D., Krietsch, A., Schmidt, M., Krause, U., 2022. Effect of oxygen concentration, inert gas and CH_4/H_2 addition on minimum ignition energy of coal dusts. J. Loss Prev. Process. Ind. 77, 104772.

Wu, D., Norman, F., Vanierschot, M., Verplaetsen, F., Berghmans, J., 2018. Self-heating characteristics of coal dust deposits by a hot gas flow in oxy-fuel atmospheres. Appl. Therm. Eng. 131, 947-957.

Wu, D., Norman, F., Verplaetsen, F., Van den Bulck, E., 2016a. Experimental study on the minimum ignition temperature of coal dust clouds in oxy-fuel combustion atmospheres. J Hazard Mater 307, 274-280.

Wu, D., Vanierschot, M., Verplaetsen, F., Berghmans, J., Van den Bulck, E., 2016b. Numerical study on the ignition behavior of coal dust layers in air and O2/CO2 atmospheres. Appl. Them. Eng. 109, 709-717.

Wu, D., Norman, F., Schmidt, M., Vanierschot, M., Verplaetsen, F., Berghmans, J., Van den Bulck, E., 2017a. Numerical investigation on the self-ignition behaviour of coal dust accumulations: The roles of oxygen, diluent gas and dust volume. Fuel 188, 500-510.

Wu, D., Schmidt, M., Huang, X., Verplaetsen, F., 2017b. Self-ignition and smoldering characteristics of coal dust accumulations in O2/N2 and O2/CO2 atmospheres. Proc. Combust. Inst. 36, 3195-3202.

Wu, D., Song, Z., Schmidt, M., Zhang, Q., Qian, X., 2019. Theoretical and numerical study on ignition behaviour of coal dust layers on a hot surface with corrected kinetic parameters. J Hazard Mater 368, 156-162.

Wu, D., Tan, X., Wei, A., Duan, Q., Huang, W., Schmidt, M., 2021a. Ignition temperature and mechanism of carbonaceous dust clouds: The roles of volatile matter, CH4 addition, O2 mole fraction and diluent gas. J Hazard Mater 405, 124189.

Wu, W., Wei, A., Huang, W., Zhao, P., Schmidt, M., Krause, U., Wu, D., 2021b. Experimental and theoretical study on the inhibition effect of CO2/N2 blends on the ignition behavior of carbonaceous dust clouds. Process Saf. Environ. Protect. 153, 1-10.

Yetter, R.A., Risha, G.A., Son, S.F., 2009. Metal particle combustion and nanotechnology. Proc. Combust. Inst. 32, 1819-1838.

Yu, J., Zhang, X., Zhang, Q., Wang, L., Ji, K., Peng, L., Gao, W., 2016. Combustion behaviors and flame microstructures of micro- and nano-titanium dust explosions. Fuel 181, 785-792.

Yu, X., Yu, J., Wang, C., Lv, X., Wang, Y., Hou, Y., Yan, X., 2021. Experimental study on the overpressure and flame propagation of hybrid hydrogen/aluminum dust explosions in a square closed vessel. Fuel 285, 119222.

Yu, X., Yu, J., Zhang, X., Ji, W., Lv, X., Hou, Y., Li, Z., Yan, X., 2020. Combustion behaviors and residues characteristics in hydrogen/aluminum dust hybrid explosions. Process Saf. Environ. Protect. 134, 343-352.

Yu, X., Yu, J., Zhang, X., Ji, W., Yan, X., 2019. Combustion behaviors and residues characteristics in hydrogen/aluminum dust hybrid eplosions. Process Saf. Environ. Protect. 134, 343-352.

Yuan, J., Huang, W., Du, B., Kuai, N., Li, Z., Tan, J., 2012a. An Extensive Discussion on Experimental Test of Dust Minimum Explosible Concentration. Procedia Eng. 43, 343-347.

Yuan, J., Huang, W., Ji, H., Kuai, N., Wu, Y., 2012b. Experimental investigation of dust MEC measurement. Powder Technol. 217, 245-251.

Yuzuriha, Y., Gao, W., Mogi, T., Dobashi, R., 2017. Effects of particle size distributions on flame propagation behavior through dust clouds of PMMA. J. Loss Prev. Process. Ind. 49, 852-858.

Zhang, H., Chen, X., Zhang, Y., Niu, Y., Yuan, B., Dai, H., He, S., 2017a. Effects of particle size on flame structures through corn starch dust explosions. J. Loss Prev. Process. Ind. 50, 7-14.

Zhang, Q., Liu, L., Shen, S., 2018. Effect of turbulence on explosion of aluminum dust at various concentrations in air. Powder Technol. 325, 467-475.

Zhang, X., Yu, J., Gao, W., Zhang, D., Sun, J., Guo, S., Dobashi, R., 2017b. Effects of particle size distributions on PMMA dust flame propagation behaviors. Powder Technol. 317, 197-208.

Zhang, X., Yu, J., Yan, X., Xie, Q., Gao, W., 2016. Flame propagation behaviors of nano- and micro-scale PMMA dust explosions. J. Loss Prev. Process. Ind. 40, 101-111.

Zhang, Y., Zhao, J., Ma, Z., Yang, F., Cheng, F., 2019. Effect of oxygen concentration on oxy-fuel combustion characteristic and interactions of coal gangue and pine sawdust. Waste Manage. 87, 288-294.

Zhao, F., Rogers, W.J., Sam Mannan, M., 2009. Experimental measurement and numerical analysis of binary hydrocarbon mixture flammability limits. Process Saf. Environ. Protect. 87, 94-104.

Zhao, P., Schmidt, M., Krause, U., Duan, Q., Krietsch, A., Wu, D., 2021. Experimental study on the minimum explosion concentration of anthracite dust: The roles of O2 mole fraction, inert gas and CH_4 addition. J. Loss Prev. Process. Ind. 71, 104490.

Zhao, P., Tan, X., Schmidt, M., Wei, A., Huang, W., Qian, X., Wu, D., 2020. Minimum explosion concentration of coal dusts in air with small amount of $CH_4/H_2/CO$ under 10-kJ ignition energy conditions. Fuel 260, 116401.

Zhen, G., Leuckel, W., 1997. Effects of ignitors and turbulence on dust. J. Loss Prev. Process. Ind. 10, 317-324.

DOI: 10.7795/810.20221124

Flameproof enclosure and pressure relief: Status quo

S. Herbst [a], J. Gerlach [a]; L. Siegle [a]; F. Engelmann [a] & T. Arnhold [b]

[a] Ernst Abbe University Jena (INNOK Research Group, Jena, Germany)
[b] R. STAHL Aktiengesellschaft (VP Technology, Waldenburg, Germany)

E-mail: sabrina.herbst@eah-jena.de

Abstract

The purpose of the ignition protection type *flameproof enclosure* is to contain the permissible explosion inside and prevent its transfer to the surrounding explosive atmosphere. The exothermic reaction requires that chemical energy can be converted into thermal and mechanical energy. Consequently, the *flameproof enclosure* must be designed for the possible increase in temperature and pressure that may result from this sudden oxidation/degradation reaction. This is realised by designing the housing in accordance with the stresses that may arise, taking into account a max. 4-fold safety factor and flameproof joints.

This principle of action is questioned by the Ernst-Abbe-University of Applied Sciences Jena and the company R. Stahl Schaltgeräte GmbH. Pressure relief is intended to minimise the thermal and mechanical energy inside the *flameproof enclosure* caused by the explosion. Pressure relief, therefore, has the function of an energy store, among other things. Consequently, the load acting on the housing is reduced and the temperature of the gas flowing out of the pressure relief is lowered to a permissible value. Accordingly, the overall requirements for *flameproof enclosures* change and an enclosure for this ignition protection type can be designed in a more material-saving way.

This approach has been studied extensively as part of several research projects. After successful completion of these basic tests, the determination of influencing parameters and their effect on small enclosures followed with the help of different test series. The knowledge gained was transferred to larger enclosures and the effect investigated through further test series, in order to develop a marketable product based on this knowledge.

Keywords: *flameproof enclosure, pressure relief, product innovation*

1. Introduction

Companies are constantly required to adapt their products and business models to future developments, in order to maintain their competitiveness. The megatrends currently influencing tomorrow's world and the environment include digitalisation, globalisation, resource scarcity and climate protection, including decarbonisation, EY (2020). In the area of unit goods production, the megatrends of globalisation, a lack of resources and climate protection have already been having an increasing impact for years through a wide variety of influences. This industry is characterised by high material, production and transport costs.

In the field of explosion protection, a sub-area of safety technology, a very high profile of requirements must be fulfilled by the products. For example, the products are used in a wide range of industries, from harsh industrial and maritime environments on drilling platforms, to cleanrooms in the pharmaceutical industry. This leads to a very wide range of environmental conditions – from the Arctic cold in Siberia to sandstorms in the Middle East. Likewise, requirements of restrictive legislation and standardisation must be taken into account, which may have national and regional differences.

A globally proven technical solution principle for enabling equipment for use in potentially explosive atmospheres is the *flameproof enclosure* type of protection, Wittler, M. (2005). This type of ignition protection has existed in its basic operating principle since the beginning of the 20th century until today. In order to adapt to today's megatrend requirements, this principle can be challenged, in order to develop a resource-saving *flameproof enclosure* with reduced material use and a low weight. Within the framework of several research projects, this active principle was questioned by the Ernst-Abbe-University of Applied Sciences Jena and the company R. Stahl Schaltgeräte GmbH

2. Flameproof enclosure

The task of the ignition protection type *flameproof enclosure* is to contain a permissible explosion inside and prevent its transfer to the surrounding explosive atmosphere. This enables non-explosion-proof equipment to be qualified for use in a potentially explosive atmosphere. The non-explosion-proof equipment is inserted into the *flameproof enclosure* and installed with it in the hazardous area. If, for example, a hot surface – caused by a malfunction in the non-explosion-protected equipment – ignites the explosive gas atmosphere, the explosion is contained by the *flameproof enclosure* and transmission to the outside is prevented. The exothermic reaction of the explosion means that chemical energy can be converted into thermal and mechanical energy. Consequently, the *flameproof enclosure* must be designed for the possible increase in temperature and pressure that may result from this sudden oxidation/degradation reaction. This is realised by the following functional elements, the design of which is recommended in accordance with the specifications of the IEC 60079-1 standard (DIN 2015):

- Appropriate design of the enclosure according to the stresses that may arise, taking into account a max. 4-fold safety factor
- Flameproof joints
- Appropriately designed accessories such as fasteners, connectors, etc.

In the field of electrical explosion protection, this ignition protection type is often used for switchgears, control and display devices, controls, motors, transformers, heaters and luminaires. In non-electrical explosion protection, the use of this ignition protection type enables the use of friction clutches, brakes, catalytic converters and cartridge heaters in potentially explosive atmospheres.

The requirements for the ignition protection type *flameproof enclosure* necessitate a very material-intensive construction of the enclosures in which the equipment, which has a potential ignition source, is used. The consequences are high material and manufacturing costs, which lead to price-intensive products. Currently commercially available aluminium flameproof enclosures with a volume of about two litres have a weight of about four kilograms, such as the enclosure of the 8265 series, size 2 from R. Stahl AG, Stahl (2022) or the enclosure of type 07-4C, GUB0A0A0 from Bartec Top Holding GmbH, Bartex (2022). The development of the flameproof enclosures is also characterised by the elaborate testing and certification processes. Combined, these factors lead to extensive challenges in the development of new innovative products.

3. Pressure relief

3.1 Pressure relief in technology

Pressure is a force acting on a surface. The result is mechanical tension in the body. Relief occurs when the reduction in pressure takes place. According to the physical principles, this can be realised by minimising the force, as well as increasing the surface area. As a result, the mechanical tensions created in the body are minimised. This relationship forms the physical basis of the general function of *pressure relief*.

DOI: 10.7795/810.20221124

From a technical disciplinary perspective, there are a large number of applications of the *pressure relief* function, which are, however, based on different types of function and operating principles. On the one hand, a distinction must be made between active and passive function fulfilment. An activating and active mechanism represents active function fulfilment. If the function carrier can generate the required function through its geometry and the materials used, the function is fulfilled passively. On the other hand, the active principles used to realise the *pressure relief* function differ. Most pressure relief systems achieve the function by increasing the available volume and surface area. Another option is the conversion of the acting energy, as the example of flameless pressure relief demonstrates. The existing mechanical and thermal energy is transferred and absorbed by a flame filter. This results in a minimisation of the pressure-causing force.

Table 1: *Operating principles of the pressure relief function in technical systems*

Technical system with the pressure relief function	**Active (A)/ Passive (P) function carrier**	**Principle of action: Volume enlargement**		**Principle of action: □ Enlargement of the loaded surface**	**Principle of action: □ Heat transfer/ conversion of existing energy**
		Unlimited volume	**Limited volume**		
Ball valve with pressure relief	A		●		
Safety valves	A	●	●		
Rupture discs/Bursting plugs	A	●	●		
Pressure relief flaps	A	●	●		
Explosion flap	A	●	●		
Pressure relief dome	A	●	●		
Pressure relief louvre	A	●	●		
Flameless pressure relief	A/P	●	●	●	●

Table 1 shows that the function of pressure relief is primarily realised by integrating additional components actively into machines and systems. A possible integration of the pressure relief function as a passive function in existing elements of the machines and systems minimises the originally required effort and can maintain the existing installation space as well as reduce it if necessary

3.2 Flameproof enclosure: Integration pressure relief

The pressure relief function offers many innovative approaches in the field of explosion protection. In particular, the ignition protection type *flameproof enclosure* harbours extensive optimisation potential, which can, for example, induce a reduction in the necessary use of materials. In order to withstand the pressure caused by an explosion, massive wall thicknesses are required, among other things. If the causative parameters of an explosion and its consequences can be influenced at the site of explosion generation by relieving the pressure, it might be possible to effectively minimise the forces and heat that occur. As a result, a *flameproof enclosure* would have to meet lower requirements and can be designed in a material-saving way.

This approach has already been looked at in more detail with different ideas and approaches. Among other things, patents describing different ways of relieving pressure should be highlighted. Hornig (2013) provides the first design guidelines for the design of flameproof enclosures with pressure relief openings caused by porous materials. In the context of this investigation, materials made of tape winding, sintered particle bulk and sintered short fibres were available.

The overall objective of the research projects presented here is to gain knowledge on the design of passive pressure relief elements for the ignition protection type *flameproof enclosure*. The passive pressure relief system is intended to minimise the maximum explosion pressure that occurs, in order to create the possibility of dimensioning a material-reduced enclosure. The combustion process in the casing, therefore, determines the functions of the pressure relief system. On the one hand, gas must be able to flow out of the enclosure, and on the other hand, the energy generated by the exothermic reaction must be absorbed. The high temperatures in the burnt gas and the resulting pressure must be reduced. Figure 1 illustrates the relationships.

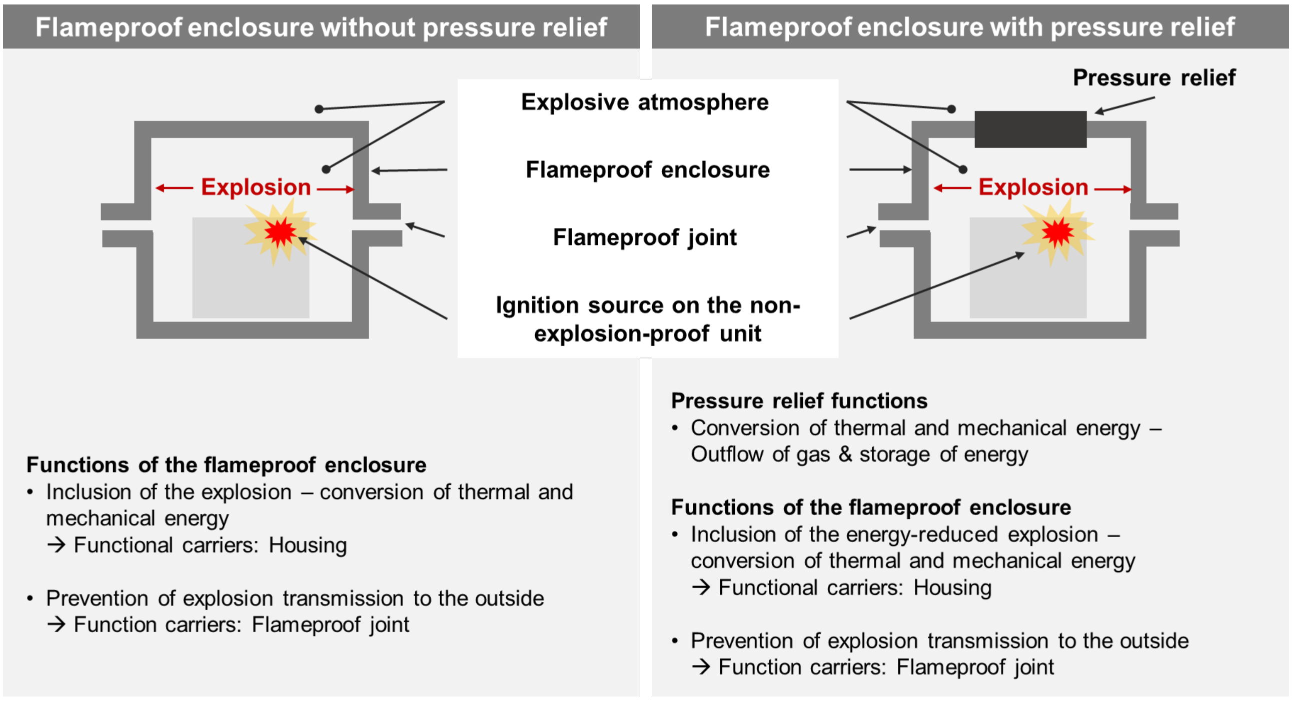

Fig. 1. *Flameproof enclosure and pressure relief functions*

For reasons of efficiency, the different functions of pressure relief should be realised by one functional support. This allows the use of an integral design in the flameproof enclosure. Ideally, the pressure relief element fulfils its function passively. The potential for this has already been demonstrated in the studies by Hornig (2013), among others. Therefore, the pressure relief element should consist of a porous material and with a defined, reproducible structure. The basic requirement ensures that the relief of pressure through a defined channel in the material is clearly determinable and reproducible, and that the tolerances caused by the manufacturing process can be contained. A comprehensive list of requirements also defines further demands and wishes that the pressure relief element should fulfil.

4. Experimental determination of basic parameters

4.1 Procedure

Within the framework of several research projects, the detailed investigation of the research approach is carried out. In the first step, basic insights into the functioning of the principle of action must be developed. Among other things, questions regarding material selection, geometry and material configuration must be analysed, in order to be able to define the parameters of an applicable pressure relief element. The starting point for these basic experiments is small flameproof enclosures with volumes of up to approx. 20 litres. The Ernst-Abbe-University of Applied Sciences Jena is primarily conducting this fundamental research project (Herbst et al., 2017, Herbst, 2018). These investigations comprise extensive series of dynamic explosion tests with test gases of gas group IIC in various test laboratories, including those of notified bodies. Basic findings of this sub-step will be presented in the following chapters.

4.2 Material selection

As a result of detailed research efforts to pre-select a defined and reproducible material, it can be stated that these requirements can be met by using wire cloth or spherical particles. Both materials make it possible to generate a structure or texture porosity. With the aid of a flameproof enclosed housing, which was supplemented by a cover modified with a pressure relief element, dynamic explosion tests were carried out as preliminary tests for the final determination of the basic material selection. The results of the tests show that both materials relieve pressure with their textural porosity. A reduction of the reference pressure by 50 % can be achieved. However, ignition breakdowns could not be avoided when using the ball particles as bulk material. Furthermore, the handling of the ball particles requires significantly more effort. Accordingly, the use of wire mesh is established as the basic material for the development of the pressure relief elements.

4.3 Dimensioning parameters

4.3.1. Connections

The pressure relief element is to be integrated in a flameproof enclosure by integral construction. The aim of the entire system is to reduce pressure and surface temperature. It must be taken into account that no ignition source may be created by the pressure relief element and that the normative requirements of the temperature classes also apply to this element.

The pressure relief element is influenced by parameters of the housing and itself. In addition, the bond between the flameproof enclosure and passive pressure relief elements can also significantly affect the pressure relief capability. Consequently, the possible parameters of all objects must be taken into account to define the dimensioning, see Figure 2.

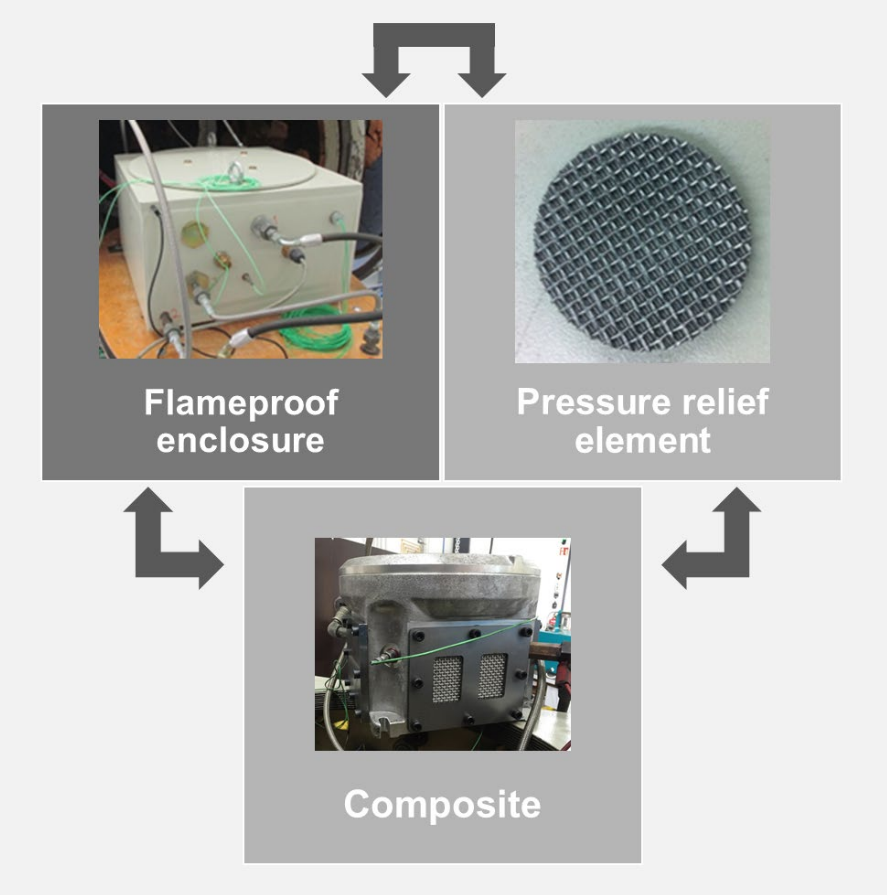

Fig. 2. *Interacting objects in the dimensioning of the pressure relief element*

The flameproof enclosure has a defined, unchanging volume. When these components are installed inside the enclosure, there is a change in volume, which can be very individual and specific. Furthermore, most applications require feedthroughs on the enclosure to operate the components protected by the enclosure and to integrate them into the system. Consequently, the internal volume available for the enrichment of explosive atmospheres, the arrangement of feedthroughs and the equipment of the enclosure can have an influence on the design of the pressure relief elements.

As the pre-selection of the material has shown, the pressure relief element consists of wire mesh layers. The configuration of these laminate layers can significantly influence the function of pressure relief. In addition, the size, shape and number of surfaces can also be important parameters for the optimal generation of pressure relief.

In the composite, it can be assumed that the ratio of the volume and the inner surface to the pressure relief surface exerts an important influence on the function of the pressure relief. Furthermore, due to the possible heat transfer, the connection between the pressure relief element and the housing could also be of importance.

4.3.2 Parameters for influencing the pressure

Several tests showed that increasing the pressure relief area can reduce the maximum explosion pressure. The pressure reduction curves of selected enclosures with a volume of approximately 1.7 litres and 3.8 litres show that the integration of pressure relief areas up to a certain ratio of the absolute pressure relief area to the inner surface of the enclosure effectively reduces the maximum explosion pressure. Beyond this point, a further reduction of the maximum explosion pressure is only possible through a greatly increased introduction of pressure relief surfaces. Thus, the statement of the degressive course of the pressure relief as a function of the relative pressure relief area by Hornig (2013) can be confirmed. The inflection point, which designates the area of the most effective relief of the maximum explosion pressure, lies at approx. 9 % relative pressure relief area for the empty enclosures considered. This is a key finding of these studies. Furthermore, it can be seen that the integration of a relative pressure relief area of around 1 % for an enclosure with a volume of around 21 litres requires significantly higher values of the reduced maximum explosion pressure than for smaller enclosures with volumes of around 1.7 litres and 3.8 litres. In addition, the results show that the maximum explosion pressure in the largest enclosure (volume of around 21 litres) can be reduced with increments in the relative pressure relief area whose distance is smaller. Thus, the relative area of most effective relief of maximum blast pressure could occur at a smaller percentage value. Consequently, the pressure relief function, which is realised by pressure relief elements made of wire mesh, has a dependency on the housing volume.

Furthermore, the test results show that the specific configuration of the wire cloth does not have a significant influence on the pressure relief in the context of these investigations. The configurations have porosity in the range of 56 % to 64 %. Consequently, the variance of this parameter is minimal.

4.3.3 Parameters influencing the maximum surface temperature

The results of the temperatures measured at the outer surface of the pressure relief elements of all test series show that differences can occur between the temperature development in the centre and at the edge of the pressure relief element. The closer the distance between these two temperature values, the more effectively the entire surface of the pressure relief element is used for heat transfer. The temperature values at the centre of the pressure relief element primarily achieve the higher values.

The overview of the results of the maximum generated temperatures shows differences in comparison to the dependence between the relative relief area and the reduced maximum explosion pressures. With an increase in the relative pressure relief area, the maximum temperatures generated decrease, but only with minimal distances. In contrast, the temperatures with the smallest relative relief areas take on very high values. Due to this, it can be assumed that a pressure relief area that is too small leads to gas flows that have a very high amount of energy. If the surface of a pressure relief element heats up to the temperature corresponding to the ignition temperature of the gas used due to the energy conversion, ignitions of the explosive gas mixture are possible.

In addition to the relative pressure relief area, the temperature is also significantly influenced by the distribution of this. This is confirmed by all test series. With an increase in the pressure relief area or the number of pressure relief areas (openings), the maximum temperatures at the centre of the pressure relief element surface decrease the centre of the pressure relief element surface.

Furthermore, the development of the temperature is also significantly determined by the wire mesh configuration. Across the board, the lowest temperature values were achieved when using the wire mesh configuration with the highest values for pressure loss (325 Pa at 1 m/s) and the pressure loss coefficient (540 at 1 m/s). In this respect, the ability of the pressure relief elements to transfer heat can be estimated with the help of these characteristic values.

4.4 Insights into the selection of manufacturing processes

The integration of the pressure relief elements is the basis for the development of a flameproof enclosure with passive pressure relief elements. The main component of the pressure relief element is the wire mesh. The composite or the required connecting elements serve to integrate the wire mesh, but could also have a possible influence on the functional realisation.

The connection can be realised by a form, force or material closure. Depending on the requirements, the conditions of these individual variants must also be taken into account. In the first series of tests, friction-locked connections were used. The connection between the wire mesh and the housing was made indirectly or directly. An indirect connection is the use of adapters, and the use of drilled wire mesh laminates positioned on bolts attached to the enclosure is equivalent to a direct connection. With both variants, the realisation of material sample changes and modification of the pressure relief area is possible without increased effort. This flexibility is not required for a later product, which means that other joining techniques should be favoured. Another significant aspect is the number of pressure relief elements. Especially from a production point of view, the integration of one element would be the most optimal variant. The more production steps involved in inserting and aligning the elements, for example, the higher the production costs. For this reason, the possibility of incorporating several pressure relief elements simultaneously should also be considered. Accordingly, two possible starting positions result: on the one hand, the use of individual wire mesh elements and, on the other hand, the integration of large-area wire mesh panels. As a result, different requirements and functions have to be taken into account when selecting connection techniques. If the integration of individual wire mesh elements is considered, a solution must be generated that enables the simultaneous integration of several wire mesh elements. On the other hand, when integrating wire mesh panels, a potentially necessary separation of the pressure relief area must also be taken into consideration.

The use of detachable or non-detachable connections depends on the application. For the test series, detachable connections are the most optimal solution due to their adaptability. Here, the screw and clamp joining techniques are the most effective methods, as a change in configuration can be made possible with little effort and commercially available tools. The wire mesh can be processed using a wide variety of manufacturing methods such as sawing, drilling and lasering. Nevertheless, these solutions are characterised by a high degree of assembly time. For the application in future products, the non-detachable connections are, therefore, of great interest, as the additional manufacturing steps can be implemented without considerable additional effort. Furthermore, it can be assumed that material- and form-fitting connections produce more favourable conditions for heat transfer, which would enable the thermal energy absorbed by the material of the wire mesh to be transferred to the housing. According to the manufacturer, the wire mesh can be welded. However, the final implementation will depend on the thickness of the wire mesh. A highly efficient realisation of the composite could be the pouring. In order to test the realisation in a first preliminary test, two wire mesh elements with a size of 100 x 100 millimetres are cast around with a frame. The results show that the melt does not fill the wire cloth, but only slightly penetrates the wire cloth at the edges, see Figure 3.

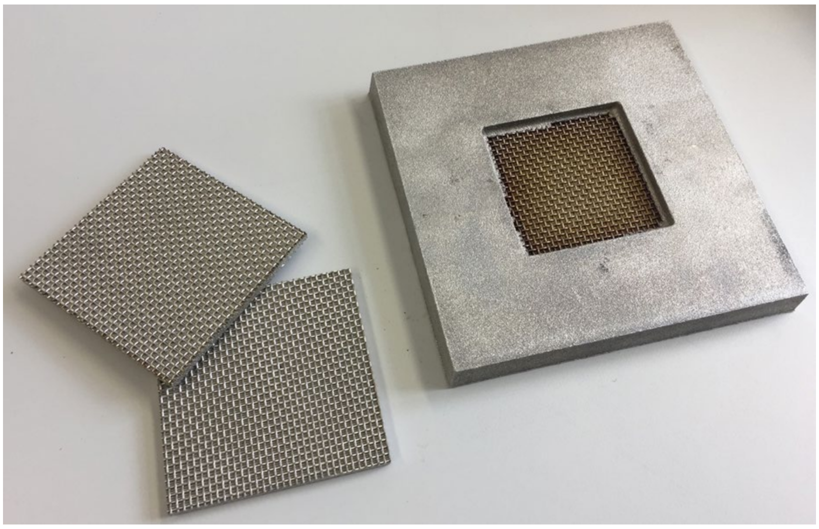

Fig. 3. *Cast-in pressure relief elements*

4.5 Notes on the design

Based on the findings, a housing with pressure relief was developed for a circuit breaker. The requirements for this development are very practical and require the consideration of manufacturing, economic and application-oriented aspects. Among other things, this sub-project is also intended to determine findings for the approach to product development and design.

A standardised size 6 GUBox enclosure from R. Stahl is often used for the circuit-breaker in use. This housing has a mass of around 30 kilograms according to Stahl (2015). The aim is that a specific housing with passive pressure relief elements can reduce the weight by at least 50%.

This target has been exceeded, as the weight saving achieved through the use of the pressure relief elements corresponds to around 72.5 %. It is also possible to save installation space. Table 2 shows the comparison.

Table 2: *Comparison of the circuit-breaker enclosures*

Criterion	Conventionally used pressure-resistant cast iron enclosures	Pressure-resistant cast housing with passive pressure relief elements
Weight	27.8 kg	7.65 kg
Installation space	L: 410mm x W: 410 mm x H: 281 mm	L: 342mm x W: 220 mm x H: 218 mm

Design guidelines were derived across the board. The content of these design guidelines includes procedures for dimensioning pressure relief elements, measures for increasing the pressure relief capacity, as well as design and production-related information on integration.

5. Further development to a marketable product

Based on this extensive knowledge, the goal of R. Stahl Schaltgeräte GmbH was to develop a market-ready pressure-relieved enclosure. The pressure relief element allows the ignition protection type *flameproof enclosure* to be made more efficient and versatile. By reducing the pressure, it may be possible to design larger enclosures. Reduced mechanical stress requirements open up the option of aiming for enclosure sizes that were previously technically and economically unfeasible due to the materials required. However, larger enclosures offer extensive advantages, among other things from the point of view of maintenance and servicing. This approach, the realisation of new large enclosure sizes from a volume of 20 litres through pressure relief, is being investigated by R. Stahl Schaltgeräte GmbH on the basis of the principles developed by the Ernst-Abbe-University of Applied Sciences Jena. Based on the design guidelines, the development of different test enclosures takes place.

Subsequently, a large number of test series are carried out in laboratories of selected test centres. The experiments are being carried out by an interdisciplinary team from R. Stahl Schaltgeräte GmbH and the Ernst-Abbe-University of Applied Sciences Jena. The results can confirm large extents of the knowledge already gained.

Then, the development of a series product will start by an interdisciplinary team at R. Stahl Schaltgeräte GmbH. At the beginning of the development project, regular project meetings support the transfer of knowledge between the individual project participants of the different phases. Further test series expand the state of knowledge and develop the technology further. Likewise, questions of production technology for the realisation of series production are answered with different cooperation partners.

The result is the EXpressure product range, which is approved for use in zones 2 and 1 as *flameproof enclosure "d"* and equipment protection by special protection "s". This approval required the cooperation of two notified bodies. This product range already resembles control cabinets from the safe industrial sector. Currently, the volume of this enclosure series ranges from 24 litres to 980 litres. Instead of dividing the overall electrical function among several enclosures, a single large flameproof installation space is now sufficient for the entire control or distribution system. For this reason, flexibility is increased in the event of changes.

6. Conclusions

The research work of the last few years transferred the idea of pressure relief through the development of fundamental correlations and findings into a technology that is now being used in the first market-ready products. This has been made possible by the close cooperation between science and business.

However, the use of pressure relief opens up even more ways of use. Enclosure sizes with a volume of over 1,000 litres are conceivable. Initial test series with an enclosure that has a volume of around 1,300 litres confirm this. Furthermore, the use of the pressure relief elements is also possible in other ignition protection types. In addition to casting with metallic materials, integration in the injection moulding process of plastics is also conceivable. Therefore, pressure relief will continue to be an important topic in the field of explosion protection in the coming years.

In summary, this project shows that through industry-oriented research, the results can be profitably implemented in industry in a timely manner. Therefore, this industry-oriented research at universities is absolutely necessary and an important pillar of Germany as a high-tech location.

Acknowledgements

The authors would like to express their sincere thanks to all project participants and cooperating suppliers for their excellent cooperation.

References

Bartec (2022). Druckfeste Gehäuse GUB Ex d IIC, Aluminium & Edelstahl. https://www.bartec.de/ProdCatalogue/Assets/Datasheets/lng_1/413607_GUB_d.pdf

Bund (2022). BUNDESREPUBLIK DEUTSCHLAND, VERTRETEN DURCH DAS BUNDESMINISTERIUM FÜR WIRTSCHAFT, DIESES WIEDERUM VERTRETEN DURCH DEN PRÄSIDENTEN DER PHYSIKALISCH-TECHNISCHEN BUNDESANSTALT BRAUNSCHWEIG UND BERLIN, 38116 BRAUNSCHWEIG, DE. Verfahren zur Führung von im lnnern eines Gehäuses gebildeten Explosionsgasen durch zünddurchschlagsicher ausgebildete Spalte und explosionsgeschütztes Gehäuse. Erfinder: U. KLAUSMEYER. Anmeldung: 17. Juni 1998. Deutschland. DE 198 26 911 A1

EY (2020). Are you reframing your future or is the future reframing you?: Understanding megatrends will help you see opportunities where others don’t. EYGM Limited. https://assets.ey.com/content/dam/ey-sites/ey-com/en_gl/topics/megatrends/ey-megatrends-2020.pdf

DIN (2015). DIN Deutsches Institut für Normung e. V. DIN EN 60079-1, Explosionsgefährdete Bereiche – Teil 1: Geräteschutz durch druckfeste Kapselung „d“ (IEC 60079-1:2014); Deutsche Fassung EN 60079-1:2014, April 2015.

Herbst, S., Engelmann, F., Grote, K.-H. (2017): Der Einsatz von Druckentlastung im Explosionsschutz – eine innovative Basis für den Leichtbau. Vortrag und Beitrag beim 15. Gemeinsames Kolloquium Konstruktionstechnik 2017. Universität Duisburg-Essen vom 05. bis 06. Oktober 2017 in Duisburg

Herbst, S. (2018). Druckentlastung im Explosionsschutz, Magdeburg: Otto-von-Guericke-Universität Magdeburg, Diss.,

Hornig, J. (2013). Permeable Werkstoffe zur zünddurchschlagsicheren Explosionsdruckentlastung. Gestaltung und Anwendungsmöglichkeiten. Zugl.: Magdeburg, Univ., Fak. für Maschinenbau, Diss., 2012. Aachen: Shaker, *Fortschritte in der Maschinenkonstruktion*. ISBN 978-3-8440-1835-6.

Stahl (2015) Ex d Gehäuse aus Leichtmetall, „Druckfeste Kapselung“. Reihe 8265, https://r-stahl.com/uploads/tx_aimeos/Files/i_/de/8265_EmptyEnclosures_EK00_III_de.pdf

Stahl (2022). Ex d Gehäuse aus Leichtmetall reihe 8265 Art. Nr. 165781 . https://r-stahl.com/de/global/produkte/kabel-und-leitungseinfuehrungen-komponenten-und-gehaeuse/leergehaeuse/ex-d-aluminium/ex-d-gehaeuse-aus-leichtmetall-reihe-8265-46888/165781-46925/

Wittler, M. (2005). EXAM Neuer Name, große Tradition. *EXZeitschrift,* 37/2005: 58-62.

DOI: 10.7795/810.20221124

Influence of vent distribution on the violence of a gas explosion

Daubech J.[1],*, Leprette E.[1], Proust C. [1,2]

[1] Institut National de l'Environnement Industriel et des Risques, Parc Technologique ALATA, BP 2, 60550 Verneuil-en-Halatte, France.

[2] Sorbonne Universités, UTC-TIMR, 1 rue Dr Schweitzer, 60200 Compiègne, France.
*Corresponding author's email: jerome.daubech@ineris.fr

Abstract

The development of new energies (battery, fuel cell, electrolyser, storage, etc.) leads to the implementation of these applications in ISO shipping containers. Depending on the technology, such containment can lead to a risk of accumulation of flammable gas and therefore explosion. Indeed, the explosion of an ISO container can have major effects, as in the case of the accident that occurred in British Columbia (Canada) in 2013. This accident destroyed completely the container. The adjacent containers were deformed, and houses' and vehicles' windows were blown out within 150 m. One door of the container was projected to 100 meters. To avoid such future disasters, an efficient strategy of mitigation should be implemented. The use of vent panels is one of the most popular protection techniques to mitigate the confined explosion risk. The role of explosion vents is to discharge the excess gas produced by the combustion to limit the explosion overpressure to an acceptable value compatible with the mechanical strength of the enclosure to be protected. The calculation of the vent area can be difficult due to the multiplicity of parameters that will influence the venting process. In most cases, the widely studied situation is that of an enclosure filled with a flammable mixture with explosion discharge orifices generally concentrated in one single area. There is little research into the influence of the distribution of the explosion venting area on the surface of the enclosure to be protected. This paper presents the results of an experimental study where 1.2 m^2 of vent area was spread over the surface of a 37 m^3 explosion chamber. Four configurations of vent areas distribution are studied. Two flammable mixtures are used respectively 15.5% and 17.4 % hydrogen-air with two locations of the ignition source.

Keywords: *Vented gas explosion, vent, secondary explosion*

1. Introduction

The development of new energies (battery, fuel cell, electrolyser, storage, etc.) leads to the implementation of these applications in ISO shipping containers. Depending on the technology, such containment can lead to a risk of accumulation of flammable gas and therefore explosion. Indeed, the explosion of an ISO container can have major effects, as in the case of the accident (WorkSafeBC, 2013) that occurred on April 13th, 2013 in Saanich in British Columbia (Canada). At around 6:30 AM, an explosion occurred in a shipping container used for various storage, resulting in the destruction of the container and damage to the surroundings. Adjacent containers were deformed, and houses and vehicles' windows were blown out. The container was torn off, the walls were flattened, and some parts of the container were landed up to 275 meters away. The explosion blew out both ends of the container, hurtled the roof 15 meters, and shot one of the doors about 100 meters across the site (Fig 1.). The blast also damaged windows in the surroundings "as far about a half a block away" i.e., glasses were broken around 150 meters. The cause of the explosion (WorkSafeBC, 2013) is a leak from the 20lb propane tank of a barbecue, stored inside a large steel shipping container. The leak resulting from the open valves created an explosive atmosphere inside the shipping container. A soft drink cooling circuit that cycled and sparked ignited the flammable mixture and triggered the explosion. Damage analyses allow to estimate the maximum overpressure involved in the explosion. The level of overpressure inside the container is around 2.5 bar. So, to avoid this kind of disaster, it's necessary to define some strategy of mitigation.

a. Container after the explosion
b. Container's door projected at 100 m

c. Container after the explosion
d. Broken windows on the apartment block

Fig. 1. *Damage of explosion in ISO container (from WorkSafeBC, 2013)*

The use of vent panels is one of the most popular protection techniques to mitigate the confined explosion risk. The role of vents is to discharge the excess gas produced by combustion outside a volume to limit the explosion overpressure to an acceptable value compatible with the mechanical strength of the enclosure to be protected.

The physics of vented deflagration has been studied for a long time (Cooper et al, 1986, Bimson et al, 1993, Catlin et al, 1996, Proust et al, 2010, Bauwens et al, 2011, Daubech et al, 2011). The widely studied situation is that of an enclosure filled with a flammable mixture with explosion discharge orifices generally concentrated in one single area.

After the ignition of the flammable mixture, the initial flame growth leads to the production of hot combustion products. Due to the thermal expansion of the burnt gases, the internal pressure in the enclosure increases. When the pressure in the enclosure reaches the opening pressure of the explosion vents, the reactive mixture can be expelled to the outside forming a swirling cloud. When the flame reaches the openings, it can ignite this reactive cloud, producing a secondary explosion in front of the vent.

Catlin (1991) accurately studied the evolution of the flame front contour from ignition to flame exit through the vent. He noticed 3 different stages during flame propagation. Immediately after ignition, the flame front grows spherically around the ignition source. It then elongates into an ellipsoid of revolution and evolves into an ellipsoid truncated from its base as the flame approaches the vent. As a result of the pressure increase in the enclosure, part of the flammable cloud is expelled from the enclosure and takes the shape of a mushroom (Cooper et al, 1986). Other authors agree that it is shaped like a ball with a radius of the same order of magnitude as the hydraulic diameter of the vent (Harrison et al, 1987). The physics of the combustion of the outer cloud in the secondary explosion is poorly understood. But it is possible to describe the combustion process (Catlin, 1991) of this flammable cloud in 3 phases:

- Phase I: The flame velocity does not vary significantly from the flame velocity inside the enclosure, while the mushroom shape of the vortex continues to develop. During this phase, there are no high levels of overpressure associated with the secondary explosion.
- Phase II: The flame arrives at the head of the mushroom and suffers from an abrupt increase in the surface area. It is at this point that the pressure effects of this explosion occur.
- Phase III: This last phase is characterized by a spherical flame propagation through the remaining reactive volume

Some authors (Bauwens, 2010, 2012, Daubech, 2013, Sommersel, 2017, Skjold, 2019) show experimentally the influence of different parameters such as the initial concentration of the flammable mixture, the initial turbulence, and the presence of obstacles or the position of ignition source the explosion chamber. But the major problem with vent installation is that vent panels are generally located in the same area. This situation can create a very huge external explosion (Daubech et al, 2011) with a high level of overpressure. The distribution of vents on the surface of the enclosure to be protected has been little studied.

This paper proposes to study the influence of vent distribution on the violence of a gas explosion. The vent holes are distributed on the walls of the 37 m^3 explosion chamber. The total surface of vents is 1.2 m^2. Several configurations of vent surface installation are proposed. Two hydrogen flammable mixtures are used with two positions of an ignition source.

2. Experimental set-up

The explosion chamber is a 37.5 m^3 parallelepipedal volume (internal dimensions: 6 m long, 2.5 m wide, and 2.5 m high) designed to withstand an explosion overpressure of 2 bar (Fig 2.). It is a metal structure made of H-irons and modular side frames which can be fitted with solid walls to completely block the surface or can be customized to accommodate the vent panels or viewing windows.

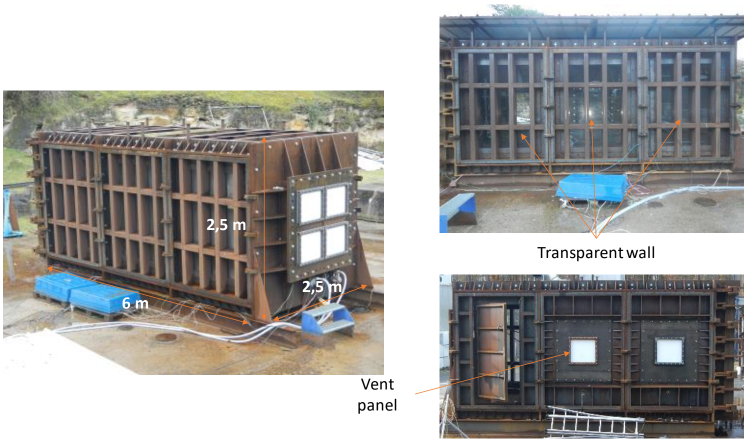

Fig. 2. *37.5 m^3 explosion chamber*

The injection of flammable gas into the explosion chamber is carried out from a 5 m^3 tank. The gas injection pressure is monitored by a pressure sensor located upstream of the injection pilot valve. It is set to 5 bar. The injection is carried out through a 20 mm diameter circular orifice. The leakage rate is about 50 g/s. The H2 concentrations are monitored by 6 oxygen analysers located at different heights in the explosion chamber. The turbulence generated by the leak is sufficient to completely homogenize the flammable atmosphere. The turbulence generated by the leak is sufficient to completely homogenize the flammable atmosphere. To ensure that the flammable atmosphere is completely quiescent, a time of 30 s is allowed between the end of the hydrogen injection and ignition.

The instrumentation includes 2 internal pressure sensors P1 and P2 (Kistler 0-2 bar piezoresistive sensors) and 2 external pressure sensors settled in lens supports Lent 1 and lent 2 (Kistler 0-2 bar piezoresistive sensors). To visualize the explosion and opening of the vents, a high-speed camera (Phantom MIRO – 2000 i/s) and an HD camera are used. The flammable mixture is ignited with a pyrotechnical match of 60 J.

A total vent area of 1.2 m^2 divided into 4 unit areas of 0.3 m^2 (0.6 m x 0.5 m) is used to study the influence of vent distribution on the explosion dynamics. Four vent distribution configurations were studied (Fig. 3). The first configuration is the reference for which the 4 unit vents are in the same area. For the following configurations, the unit vents are distributed on two sides of the explosion chamber. The external pressure sensors are always located on the vent axes so that their location changes from one configuration to another. Fig 3. also presents an overview of the instrumentation location for each configuration.

Two ignition source locations are studied:

- at the centre of the wall opposite the 4 unit vents of configuration 1,
- at the centre of the explosion chamber.

Two quiescent flammable mixtures are used:

- 15.5 % vol. hydrogen-air mixture,
- 17.4 % vol. hydrogen-air mixture.

For each vent panel distribution, one experimental configuration is conducted twice to test the reproducibility with a good level of success.

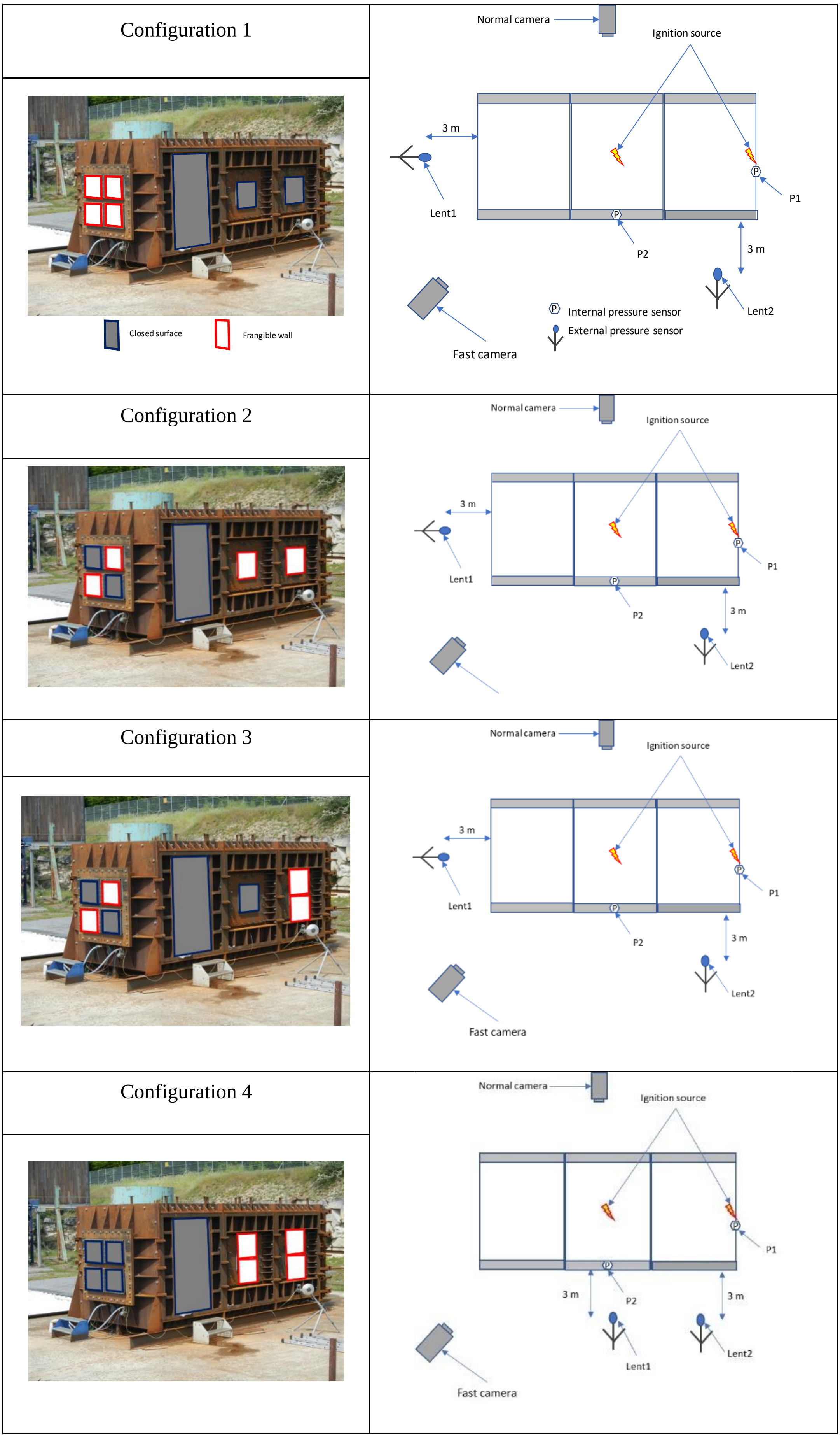

Fig. 3. *Four vent distribution configurations and instrumentation positions*

The unit safety vents have an area of 0.3 m^2. Vents are made of a PE plastic sheet held in place by a 5 cm square or flat iron frame screwed to the support plate (Fig. 4) depending on the chosen configuration. The opening overpressure of this plastic sheet is about 80 mbar when held by the square iron frame, and 50 mbar when held by the flat iron frame. The values of opening overpressure are experimentally determined. The surface density of the plastic sheet is 0.150 kg/m^2.

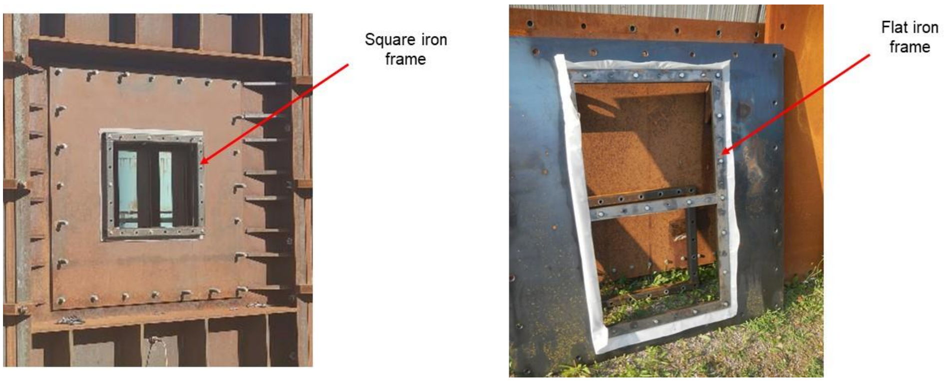

Fig. 4. *Fixing iron frame*

16 tests were carried out crossing:

- the 4 frangible wall distributions (Configuration 1 to 4)
- the 2 explosive atmospheres
- the 2 ignition positions

3. Results and discussion

Typical results

Fig 5. presents the characteristic internal and external overpressures for the first configuration with the ignition on the side opposite the 4 unit vents located on the same flange for the 15.5 % and 17.4 % hydrogen-air quiescent mixtures. The phenomenology observed was already presented by Daubech et al (2013) and can be divided into the following steps:

1. Ignition
2. Flame propagation and pressure increase in the explosion chamber,
3. Opening of the vent as soon as the internal pressure reaches its opening pressure,
4. Discharge of part of the flammable cloud to the outside,
5. Formation of the external vortex,
6. Competition between the production of burnt gases by the flame and the discharge of the gases through the vent,
7. Ignition of the external cloud by the flame reaching the vent and explosion
8. Internal combustion in progress
9. Discharge of combustion products through the vent and pressure drop in the enclosure
10. End of internal combustion

For the 15.5 % H_2-air mixture, the maximum inside overpressure reaches 250 mbar and the external overpressure reaches 50 mbar.

For the 17.4 % H_2-air mixture, the maximum inside overpressure reaches 400 mbar and the external overpressure reaches 165 mbar.

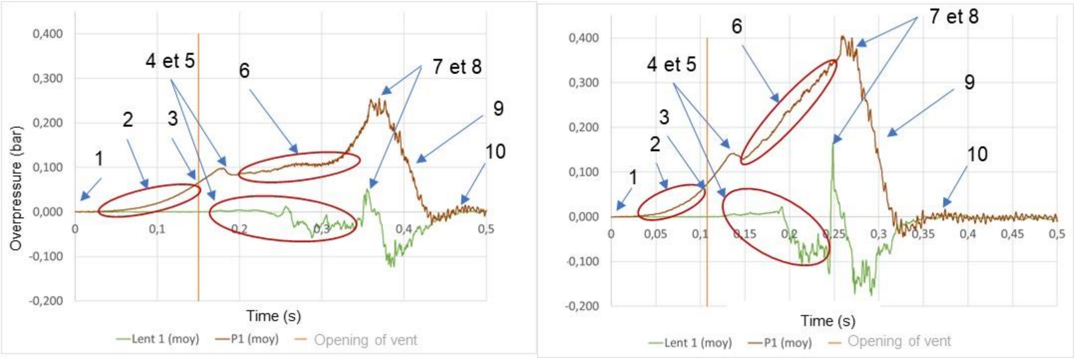

a b

Fig. 5. *Internal and external overpressures for configuration 1 - Ignition on the side opposite the 4 unit vent surface located on the same flange – 15.5 % (a) and 17.4 % (b) hydrogen-air quiescent mixtures.*

Influence of ignition location

Fig 6. presents the internal and external overpressures for the first configuration with the backwall and the central ignition for the 15.5 % hydrogen-air quiescent mixtures.

For an identical venting configuration, the internal overpressure is greater when the ignition takes place as far as possible from the vents (250 mbar for the backwall ignition vs. 160 mbar for the central ignition). With the backwall ignition, the flame takes longer to reach the discharge surfaces of the explosion than for the central ignition. The amount of burnt gas produced by the flame when it runs every 6 m of the explosion chamber is greater than the amount of burnt gas produced for a central ignition.

The external overpressure related to the secondary explosion is greater when the ignition is central compared to the backwall ignition (90 mbar vs. 50 mbar). It can be explained by the fact that the flame reaches the vent earlier in the central ignition The external cloud is still in the form of a vortex at the time of ignition. In the case of backwall ignition, the external vortex can degenerate in a form of a fresh gas jet during the internal flame developments already as observed by Daubech et al (2017). The flame propagation in a compact external cloud as a vortex leads to a more powerful secondary explosion.

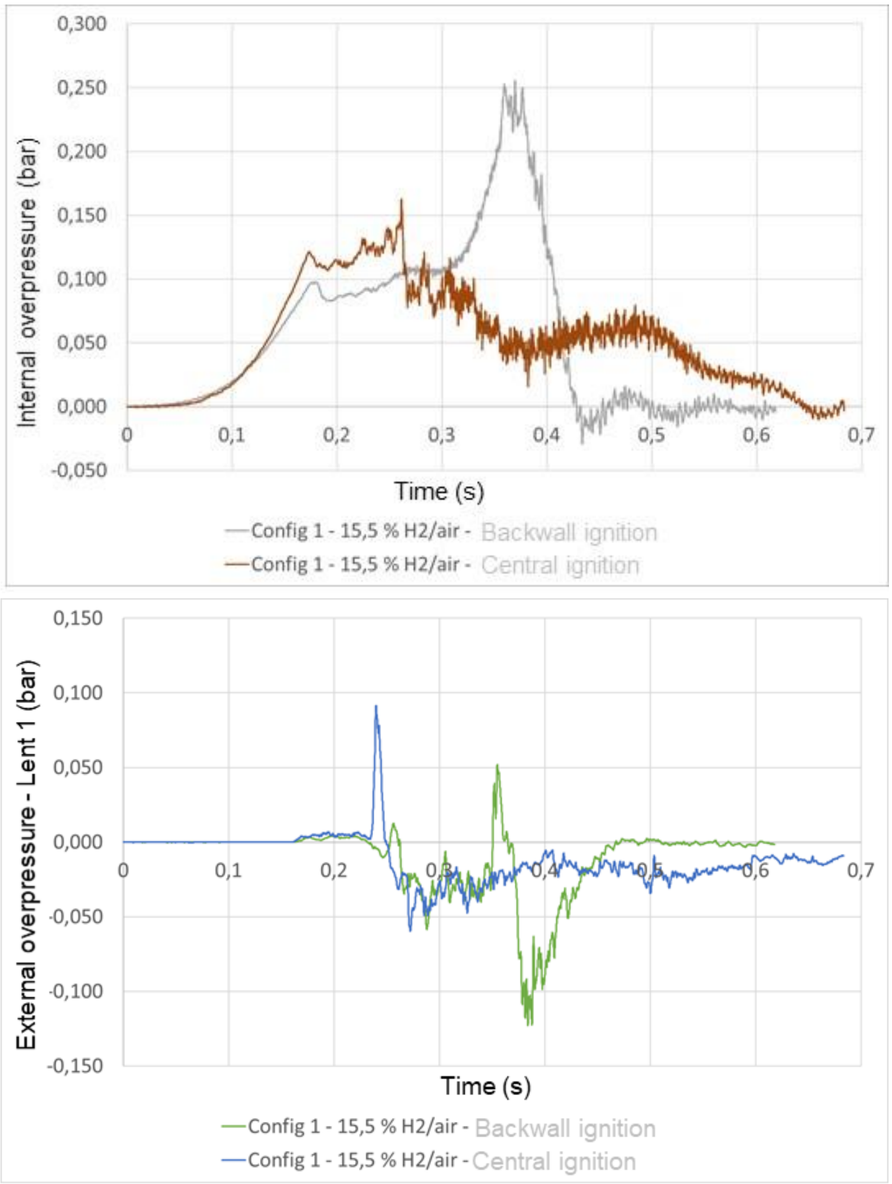

Fig. 6. *Internal and external overpressures for configuration 1 - Backwall and central ignition – 15.5 % hydrogen-air quiescent mixtures*

Influence of the distribution of vent areas on the explosion violence

Fig 7. presents the internal and external overpressures for configurations 1 to 4 with the backwall ignition for the 15.5 % hydrogen-air quiescent mixtures. Table 1 sums up the values of overpressures.

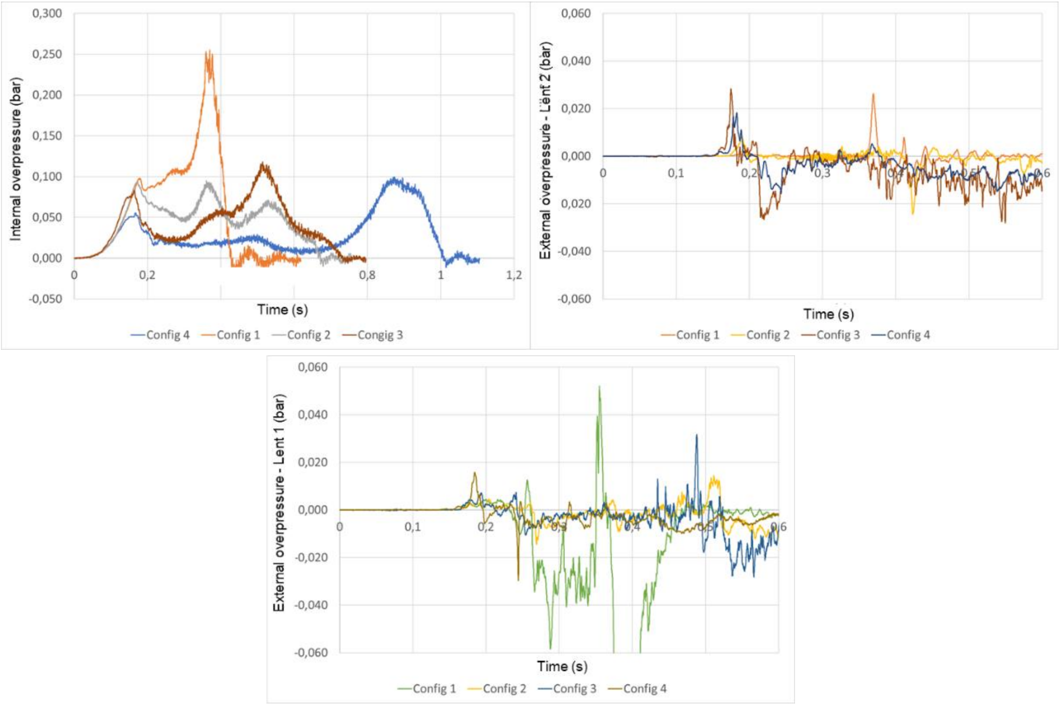

Fig. 7. *Internal and external overpressures for configurations 1 to 4 - Backwall ignition – 15.5 % hydrogen-air quiescent mixtures*

Table 1. *Internal and external overpressure for configurations 1 to 4 - Backwall ignition – 15.5 % hydrogen-air quiescent mixtures*

n° Configuration	Internal overpressure (mbar)	External overpressure – Lent 1 (mbar) [b]	External overpressure – Lent 2 (mbar)
Config 1	250	50	25
Config 2	90	16	7
Config 3	110	30	28
Config 4	95	18	16

We notice that higher internal and external overpressures are reached for configuration 1. The internal overpressures for configurations 2, 3, and 4 have the same order of magnitude around 100 mbar. Configurations 2 and 4 give the same order of magnitude for internal and external overpressures. In comparison, the overpressures of configuration 3 are higher.

Fig 8. presents the internal and external overpressures for configurations 1 to 4 with the backwall ignition for the 17.4 % hydrogen-air quiescent mixtures. Table 2 sums up the values of overpressures.

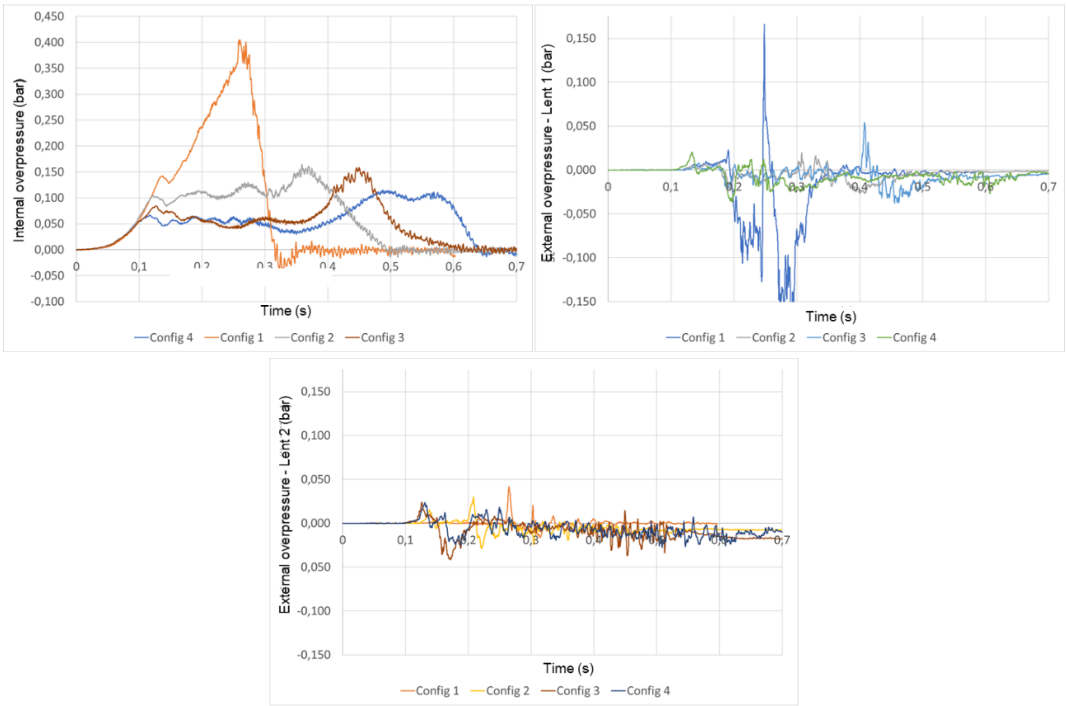

Fig. 8. *Internal and external overpressures for configurations 1 to 4 - Backwall ignition – 17.4 % hydrogen-air quiescent mixtures*

Table 2. *Internal and external overpressure for configurations 1 to 4 - Backwall ignition – 17.4 % hydrogen-air quiescent mixtures*

n° Configuration	Internal overpressure (mbar)	External overpressure – Lent 1 (mbar) [b]	External overpressure – Lent 2 (mbar)
Config 1	400	165	40
Config 2	150	17	30
Config 3	150	55	21
Config 4	110	20	22

We notice that higher internal and external overpressures are reached for configuration 1. The internal overpressures for configurations 2, 3, and 4 have the same order of magnitude around 135 mbar. But the internal overpressure for configuration 4 is lower than for configurations 2 and 3. Configurations 2 and 4 give the same order of magnitude for external overpressures.

In the above-mentioned experiments for backwall ignition, a strong decrease in internal overpressure of at least a factor of 2 and a decrease in external overpressures of at least a factor of 3 is observed. If we try to understand the behavior of the flame in the case of configuration 1 (Fig. 9.a), the discharge of the explosion is performed at a single point. This maximizes the flame path between the ignition source and the vents. It also results in the formation of a single large cloud outside the explosion chamber which explodes violently. In the case of vents distributed over the surface of the explosion chamber (Fig. 9.b), the discharge of the explosion takes place at several points. This results in a significant reduction of the flame path between the ignition source and the venting surfaces. Several external clouds are generated but with smaller volumes, which results in potentially less powerful explosions because the explosion energy is lower. After the explosion of these external clouds in front of the venting surfaces, the combustion products inside the test chamber are discharged. Thus, the flame is no longer subject to the volume expansion of the combustion products, which leads to a decrease in the flame propagation velocity.

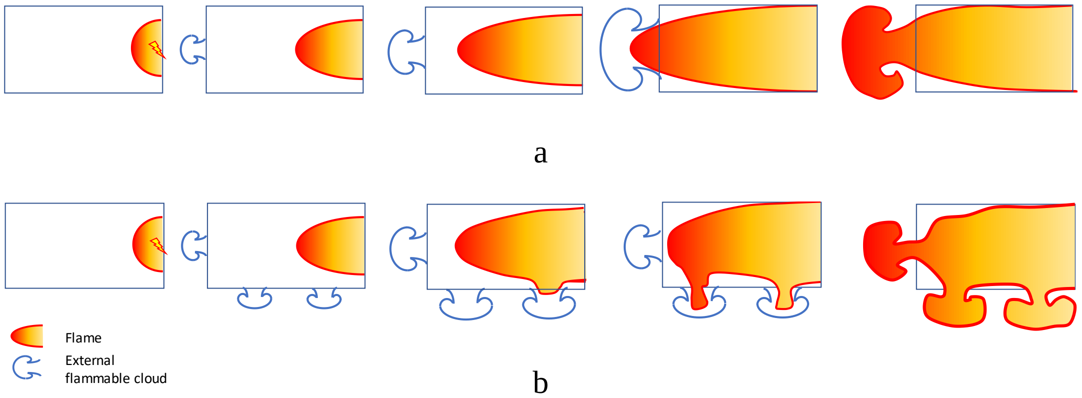

Fig. 9. *Flame behavior in case of vent surfaces in the same location (a) and in case of distributed vent surfaces for backwall ignition*

In general, configuration 2 leads to the lowest external overpressure levels if we combine the measurements of Lent 1 and Lent 2 for both concentrations. Even if the internal overpressures for configurations 2, 3, and 4 have the same order of magnitude for both concentrations, there are some differences. Specific work should be done to explain these differences. Several causes could be put forward: the influence of external explosion on the internal overpressure or the interaction of flame with the Rayleigh Taylor instability whose intensity could be modified by the vent distribution.

Fig 10. presents the internal and external overpressures for configurations 1 to 4 with the central ignition for the 15.5 % hydrogen-air quiescent mixtures. Table 3 sums up the values of overpressures.

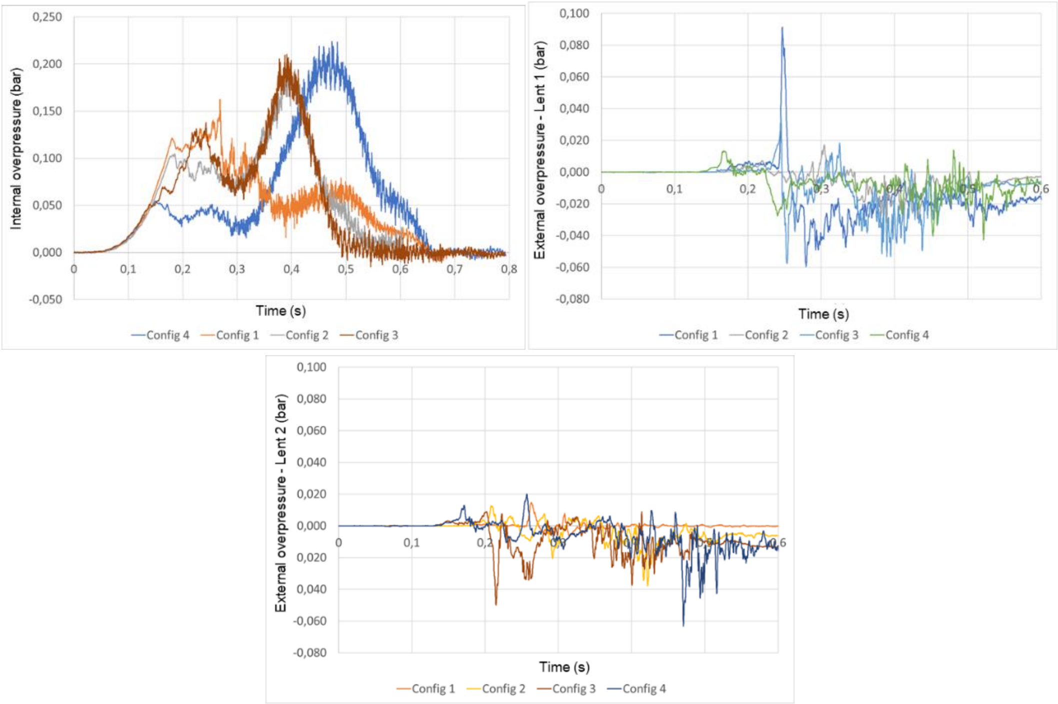

Fig. 10. *Internal and external overpressures for configurations 1 to 4 - Central ignition – 15.5 % hydrogen-air quiescent mixtures*

For a central ignition, the tests are only performed for 15.5 % hydrogen-air quiescent mixtures. We see that the internal overpressures are of the same order of magnitude with or without distributed surfaces. On the other hand, there is a strong attenuation of the external explosion overpressures by a factor of about 3.

Table 3. *Internal and external overpressure for configurations 1 to 4 - Central ignition – 15.5 % hydrogen-air quiescent mixtures*

n° Configuration	Internal overpressure (mbar)	External overpressure – Lent 1 (mbar) [b]	External overpressure – Lent 2 (mbar)
Config 1	200	90	14
Config 2	160	16	11
Config 3	200	33	8
Config 4	210	20	20

If we try to understand the behavior of the flame in the case of configuration 1 (Fig. 11.a), the discharge of the explosion occurs at a single point. The flame path from the ignition source to the vent surfaces is shorter compared to the backwall ignition. But this results in the formation of a single large cloud outside the explosion chamber that explodes violently. But, after the explosion of this large outer cloud, the combustion products inside the test chamber are discharged while the internal combustion is not yet finished. Thus, the flame is no longer subject to the volume expansion of the combustion products, resulting in a decrease in the flame propagation velocity. This explains the significant increase in combustion time between tests with backwall and centre ignition. In the case of vents distributed over the surface of the explosion chamber (Fig. 11.b), the explosion discharge takes place at several points. As with the backwall ignition, several external clouds are generated but with smaller volumes, resulting in potentially less powerful explosions because the explosion energy is lower. But it is found that the inside overpressure peak occurred approximatively at the same time from one configuration to the other. This could be explained by the fact that, in the case of the central ignition for all the studied configurations, the vent surfaces are approximately equidistant from the ignition source. Thus, the flame would reach the vent surfaces at approximately the same time.

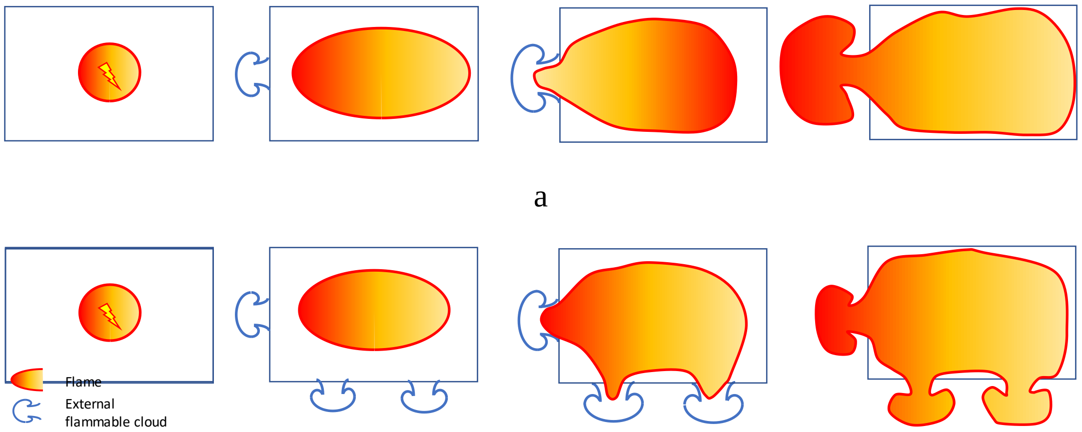

a

b

Fig. 11. *Flame behavior in case of vent surfaces in the same location (a) and in case of distributed vent surfaces for central ignition*

4. Conclusion

The influence of the distribution of venting surfaces depends strongly on the location of the ignition source. If the ignition point is located close to a wall, the distribution of vents on several sides is very favorable. In the case of a central ignition point, however, the distribution of vents has little influence on the reduced pressure.

On the other hand, the distribution of venting surfaces over the surface of a building or a confined space leads to a significant reduction in external explosion overpressures compared to the situation with a single venting surface. This greatly reduces the risk of a secondary explosion.

The secondary explosion phenomenon is often responsible for significant damage and large overpressure effect distances around hazardous installations. There could be a significant advantage in distributing venting or explosion discharge surfaces on the surface of new energy installations to facilitate their installation in highly constrained environments such as urban environments.

In general, distributing the venting panels across the entire surface of the enclosure seems to be the best option: this leads to the lowest external overpressures in experiments, and it enables to have at least one vent not too far from any hypothetical ignition source.

References

WorkSafeBC report on the shipping container accident in Saanich on April 23, 2013. Notice of incident number: 2013161290130

COOPER M.MG., FAIRWEATHER M., TITE P. (1986), On the mechanisms of pressure generation in vented explosions, Comb. and Flame, vol. 65, pp. 1-14

BIMSON S.J. , BULL D.C., CRESSWELL T.M., MARKS P.R., MASTERS A.P., PROTHERO A., PUTTOCK J.S., ROWON J.J., SAMUELS B. (1993), An experimental study of the physics of gaseous deflagration in a very large vented enclosure, Proceedings of the 14th International Colloquium on the Dynamics of Explosions and Reactive Systems, Coimbra, Portugal, August 1st-6th, 1993

CHOW S.K., CLEAVER R.P., FAIRWEATHER M., WALKER D.G. (2000), An experimental study of vented explosions in a 3:1 aspect ratio cylindrical vessel, TransIChemE, vol. 78, part B, pp425-433

HARRISON A.J., EYRE J.A. (1987), "External Explosions" as a result of explosion venting, Combustion Sci. and Tech. n°52, pp 91-106

CATLIN C.A. (1991), Scale effects on the external combustion caused by venting of a confined explosion, Comb. and Flame, vol. 83, pp. 399-411

PROUST C., LEPRETTE E. (2010), The dynamics of vented gas explosions., Process Safety Progress, vol. 29, pp. 231-235

BAUWENS C.R., CHAFFEE J., DOROFEEV S.B. (2011), Vented explosion overpressures from combustion of hydrogen and hydrocarbon mixtures, Int. J. of Hydrogen Energy, vol. 36, pp. 2329-2336

DAUBECH J., PROUST C., JAMOIS D., LEPRETTE E. (2011), Dynamics of vented hydrogen-air deflagrations, ICHS

SOMMERSEL, O. K., VAAGSAETHER K., BJERKETVEDT, D. (2017), “Hydrogen explosions in 20′ ISO container, International Journal of Hydrogen Energy, 16 March 2017, Volume 42, Issue 11, Pages 7740-7748

SKJOLD, T., HISKEN, H., LAKSHMIPATHY, S., ATANGA, G., BERNARD, L., VAN WINGERDEN, M., OLSEN, K.L., HOLME, M.N., TURØY, N.M., MYKLEBY, M., VAN WINGERDEN, K., (2019). Vented hydrogen deflagrations in containers: Effect of congestion for homogeneous and inhomogeneous mixtures. International Journal of Hydrogen Energy 44, 8819–8832

Bauwens, C.R., Chaffee, J. and Dorofeev, S. (2010), “Effect of Ignition Location, Vent Size and Obstacles on Vented Explosion Overpressure in Propane-Air Mixtures”, Combustion Science and Technology,182:11-12, 1915-1932.

Bauwens C.R., Chao J., Dorofeev S.B., « Effect of hydrogen concentration on vented explosion overpressures from lean hydrogen-air deflagrations » International J. of Hydrogen Energy, 17599-17605 (2012)

Daubech, J., Proust, C., Gentilhomme, O., Jamois, C., Mathieu, L. Hydrogen-air vented explosions: new experimental data; ICHS5; Brussels September 2013 Paper 165

Daubech J, Proust C, Lecocq G (2017), « Propagation of a confined explosion to an external cloud », Journal of Loss Prevention in the Process Industries, Volume 49, Part B, September 2017, Pages 805-813

DOI: 10.7795/810.20221124

Gas phase explosions in oxygen enriched atmospheres

EGAN Simon Mark [a],

[a] Solvay HSE, Lyon, France

E-mail: simon-mark.egan@solvay.com

Abstract

In the last seven years in the Solvay group of chemical companies, we have experienced three incidents involving gas phase explosions in oxygen enriched atmospheres, one in a laboratory facility and two in full scale manufacturing plants. This article gives a summary of each incident, suggests ways in which the hazards of oxygen-enriched atmospheres can be anticipated and shows how to evaluate the risk of such explosions.

Table 1: *Summary of incidents*

Year	Fuel present in gas phase mixture	Consequences
2015	Dichloromethane	Explosion of pipe
2016	Hydrocarbon + polar solvent	Explosion of flexible steel hose
2021	Isopropanol	Blown gaskets on reactor

Keywords: *case studies, explosion prevention.*

1. Introduction

The Solvay group of chemical companies was founded by the Belgian researcher Ernst Solvay in 1863. Today Solvay operates over one hundred chemical factories worldwide. We manufacture a very wide range of different chemical products, including speciality plastics such as polyvinylidene difluoride (PVDF), rare earth metals and sodium bicarbonate. PVDF is used as a binder in lithium ion batteries. Rare earth metals are used in electronics and in the catalytic treatment units fitted to reduce exhaust emissions from cars. Sodium bicarbonate is now finding a use to treat the emissions of sulphur dioxide from the diesel engines of ships.

We try to operate all of our chemical plants without harming our operators, our neighbours or the environment. When an incident occurs, we analyse it carefully. We share the lessons which can be learnt inside our group and, whenever possible, outside. In this article, we describe three incidents involving gas phase explosions of oxygen-enriched atmospheres, one that occurred in a laboratory facility and two that occurred in full scale manufacturing plants.

2. Explosion of a gaseous mixture of dichloromethane and oxygen

2.1 Description

An explosion occurred in a vent pipe. A piece of glass equipment and a length of polypropylene pipe shattered in several pieces. One person suffered temporary hearing loss but no harm was caused to the environment. Fragments of glass and polypropylene were ejected several tens of meters away.

2.2 The facts

The installation is complex with several reactors and other pieces of equipment. The vent lines from each equipment item are connected to a vent header network. Gases produced in each equipment item pass through the vent header network and are treated before release to the atmosphere. The treatment takes place either in a scrubber to remove toxic gases or in a thermal treatment unit to remove Volatile Organic Compounds (VOC). On the day of the explosion, a chemical operation was carried out in a reactor in three successive phases:

1. A mixture of various chemicals was heated to distill off the dichloromethane that it contained,
2. Hydrogen peroxide 35% was fed in over 10 hours to carry out an oxidation reaction,
3. Potassium hydroxide 45% was added to decompose the excess of hydrogen peroxide.

During the first and second phases, the gases produced were sent to the scrubber, because the thermal treatment unit was stopped for maintenance. During the third phase, the gases produced were sent to the thermal treatment unit. The explosion occurred during this last phase.

2.3 The explanation

During the first phase, the dichloromethane, which had been distilled off, cooled and condensed in the lowest points of the vent network. During the third phase, the reaction between hydrogen peroxide and potassium hydroxide produced pure oxygen. This gas also went through the vent network. Vapors of dichloromethane mixed with oxygen gas. This mixture was inside explosive limits and it ignited in the thermal treatment unit. A flame front blew back along the vent line. The overpressure shattered a piece of glass equipment and ruptured a length of polypropylene pipe.

2.4 The lessons

2.1.1 Flammability of dichloromethane

Dichloromethane has no flash point and is not classified as a flammable liquid under international regulations. However mixtures of dichloromethane vapour and air are explosive. The following data are given by the GESTIS database (https://gestis-database.dguv.de/search)

- Melting point = -97 °C
- Boiling point under atmospheric pressure = 40 °C
- Saturated vapour pressure at 20 °C = 470 hPa
- Upper Explosive Limit (UEL) = 22% v/v
- Lower Explosive Limit (LEL) = 13% v/v
- Autoignition temperature (AIT) = 605 °C
- IEC/ATEX explosion group = IIA
- Maximum Explosion Pressure = 5.9 bar
- Minimum Ignition Energy (MIE) = 9300 mJ

The last piece of data shows why dichloromethane shows no flash point. Its Minimum Ignition Energy is higher than the energy of sparks used in flash point measurements. According to Britton (1999), the Minimum Ignition Energy of dichlormethane is five orders of magnitude lower in pure oxygen than in air and the explosive limits are wider:

- Upper Explosive Limit (UEL) = 68% v/v
- Lower Explosive Limit (LEL) = 11.7% v/v
- Minimum Ignition Energy (MIE) = 0.137 mJ

DOI: 10.7795/810.20221124

2.1.2 Decomposition of hydrogen peroxide to give oxygen

Hydrogen peroxide is sold as a solution in water with a mass concentration of 20 % to 70 %. It is slightly acidic, with a pH of about 3. It decomposes to give water and gaseous oxygen, as shown below:

$$H_2O_2\,(l) \;\rightarrow\; H_2O\,(l) \;+\; \tfrac{1}{2}O_2\,(g)$$

The decomposition of hydrogen peroxide is slow at ambient temperature and mildly acidic pH. It is catalysed by strong acids and bases as well as by very many metal ions and indeed other substances.

2.1.3 Blow-back of flame from thermal oxidizers

In order to reduce emissions of Volatile Organic Compounds, it is usual to treat waste gas streams using a thermal oxidizer. This usually consists of a hot ceramic bed. The waste gas is passed over the bed and heated to temperatures in excess of 700 °C. At such temperatures the organic compounds are burnt, giving water, carbon dioxide etc. However, it is important to note that the waste gas fed to the thermal oxidizer must be outside of explosive limits. If waste gas inside explosive limits is fed to a thermal oxidizer, ignition will occur and a flame front will blow back along the vent line to the source of the waste gas. The flame front will accelerate as it travels back down the vent line. It may well reach the speed of sound in the gas mixture and so change from a deflagration to a detonation regime.

2.5 Where did we go wrong?

A risk analysis had been carried for the process. But the working group was not aware that dichloromethane was flammable. They knew that oxygen was produced in the third phase of this operation but they did not realise that the flammability limits of dichloromethane are much wider in oxygen than in air. Nor did they imagine that dichloromethane, which was boiled off in the first phase of the process, would condense in the vent network and then mix with the oxygen gas produced in the third phase.

3. Explosion of a gaseous mixture of hydrocarbon, polar solvent, oxygen and nitrogen

3.1 Description

An explosion occurred inside a bunker used for research purposes. A flexible stainless steel hose ruptured in several places and one person suffered a slight ear injury (tinnitus). The building structure was not affected and there was no release of material to the environment.

Fig. 1. *The flexible hose after the incident*

3.2 The facts

The accident occurred during the last of approximately 250 experiments designed to optimise a new process for manufacture of a commercial product by oxidation of a common hydrocarbon. The experiments were all carried out in a 250 ml pressure vessel (design pressure 200 bar), situated inside a bunker. The reaction involved the following steps.

1. Charge the reactor with 75 g of the hydrocarbon, a polar solvent and a catalyst.
2. Close the reactor and pressurize with nitrogen to (10 to 30 bar gauge).
3. Start the stirrer and heat to the desired temperature (60 to 90 °C).
4. Inject the following simultaneously to the liquid phase:
   a. a mixture of nitrogen and oxygen
   b. aqueous hydrogen peroxide.

We had assessed the safety of this process in our Process Safety Laboratories before the experimental work started. We had shown that, at the desired temperature range and at pressures up to 10 bar gauge, the concentration of flammable gases (i.e. hydrocarbon plus solvent) in the gas phase of the reactor would always be between the Lower Explosive Limit (LEL) and the Upper Explosive Limit (UEL). For this reason, it was recommended to keep the ratio of oxygen to nitrogen below the Limiting Oxygen Concentration (LOC) of 7 % (see figure 2 below).

However, with a ratio [O2]/([O2]+[N2]) below the LOC of 7 %, the reaction yield and process throughput were found to be rather poor. The working temperature was raised from 60 °C to 90 °C and the working pressure from 10 to 30 bar gauge. Progressively higher levels of oxygen were then tried, generally in the range of 41 % to 45 %, instead of the value of less than 7 % which had been advised. In the final experiment, the working pressure was 30 bar and the level of oxygen measured in the gas phase was at a record high level of 52 %.

An explosion occurred, causing the rupture of a flexible line, certified for 206 bar. The reactor itself was not damaged, but its rupture disc had blown. A person was present in the bunker at this point and he suffered an ear injury (tinnitus).

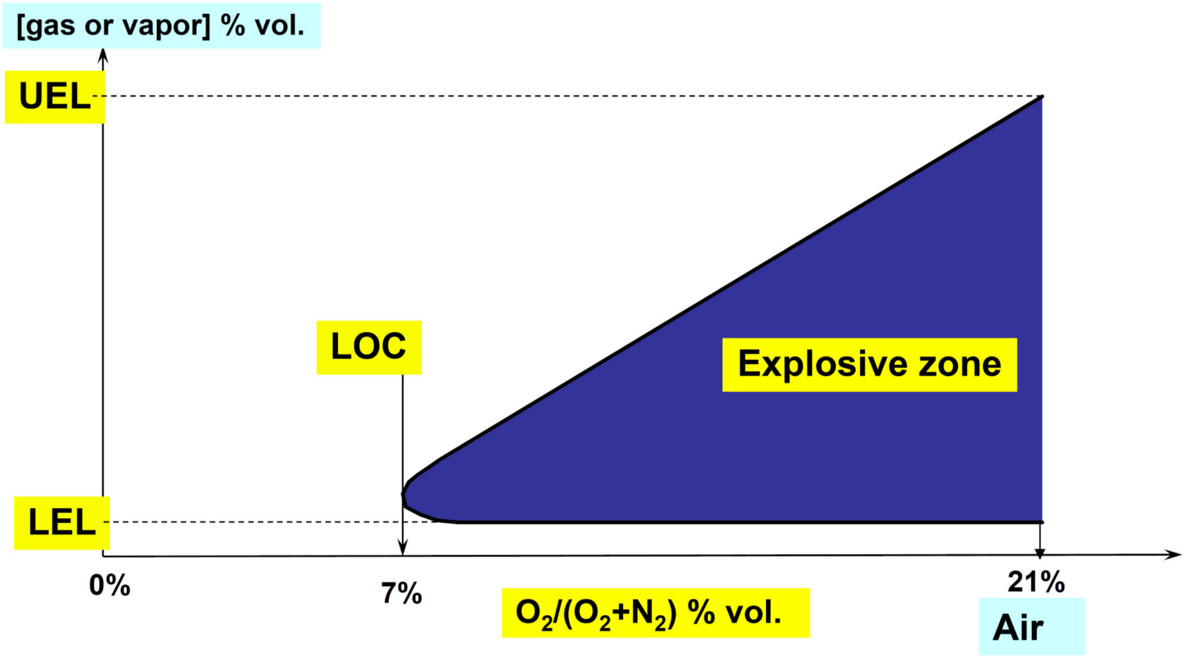

Fig. 2. *Illustrative flammability diagram for a hydrocarbon in air*

3.3 The explanation

After the incident we established that the gas phase of the reactor had been inside explosive limits for most if not all of the 250 experiments carried out. It seems that an ignition source was only found on the last experiment, where the level of oxygen was highest. In general, it is well established that the energy required for ignition of a given fuel is much reduced at high levels of oxygen, as we saw in the case of dichloromethane.

3.4 The lessons

The pattern of damage to the flexible hose, which was ruptured in several places, suggests that the explosion propagated as a detonation. A gas phase detonation propagates at a speed which is at least equal to the speed of sound in the gas mixture. That means that rupture at one point, releasing gas and reducing the pressure at that point, does not stop the propagation of the flame front.

3.5 Where did we go wrong?

This incident demonstrates that recipients of process safety information must be able to understand, interpret and apply that information. Despite the availability of a thorough report detailing the hazards and safety limits of the chemical system in question, the group operating the equipment did not understand how to apply its recommendations. For the same reason they were not in a position to correctly interpret the effect of changed operating conditions. In this case, they believed an increase in operating pressure would compensate for a rise in operating temperature and place the system below the LEL; but this was not the case.

This type of reaction is carried out in a bunker, because it is recognised that the reactions are experimental, using materials which are dangerous. There are two separate reactors in the same bunker, each controlled from outside the bunker by a technician. According to the Standard Operating Procedure, no person shall be present when a reaction is being carried out in one or other reactor. In this case, a technician was in the bunker whilst the reaction was being carried out. If the Standard Operating Procedure had been followed, there would have been no human consequences.

4. Explosion of a gaseous mixture of isopropanol and oxygen

4.1 Description

A chemical process was scaled up and transferred from one location to another. On the first batch in the new location, the gaskets on the uppermost part of the reactor were blown out and a fire started. The fire was extinguished. Nobody was injured and there was no damage to the environment.

Fig. 3. *Top of the reactor after the incident*

4.2 The facts

We were developing a process for a new product grade. The process involved mixing water, isopropanol, guar (a naturally occurring polymer of sugar), hydrogen peroxide and aqueous sodium hydroxide solution. It was operated at atmospheric pressure at temperatures up to 55 °C. As part of the development, it was tried out at various locations, increasing the scale. The incident occurred on the first batch carried out in a 5 m^3 glass lined mild steel reactor. The process was carried out as intended. But, during the operation, the operators suddenly heard the sound of a loud explosion and saw that the reactor was on fire. The site fire brigade extinguished the fire.

Nobody was injured. The damage to the equipment included blown gaskets on the lid of the reactor (see figure 4 above) and one broken glass seal pot on a breather line. We estimate that the pressure inside the reactor reached 12 to 13 bar gauge, i.e. at least twice the design pressure of 6 bar gauge.

4.3 The explanation

After the incident, we showed that the reaction generates oxygen under normal conditions. That is to say, the mixture is alkaline, so the hydrogen peroxide solution which is fed in is converted to water and oxygen. The reactor was initially under nitrogen, but the rate of generation of oxygen would have been enough to create an oxygen enriched atmosphere in the headspace of the reactor in four minutes. This would have formed a mixture of oxygen and isopropanol vapor inside explosive limits.

4.4 The lessons

Mixtures of flammable gas with pure oxygen or air enriched with oxygen are very easy to ignite compared to mixtures of the same gas with air. The MIE is commonly reduced by a factor of 100 or more (see table 2 below). NFPA 53 cites several incidents involving the spontaneous ignition of deposits of grease etc. in oxygen rich atmospheres at ambient temperature. Also, an explosion of a mixture of flammable gas with oxygen gives a much higher pressure than a mixture of the same gas with air, so this one deviation increases both the probability and severity of the scenario.

4.5 Where did we go wrong?

In the previous trials of the process, some or all of the oxygen formed had been displaced by a continuous purge with nitrogen. In the new location we did not realize that this was necessary. We thought that it was sufficient to ensure that the vessel was under a nitrogen atmosphere at the start of the batch.

5. Comparison of gas phase explosions in air and in oxygen

Table 2 lists the main flammability characteristics of some typical fuels in air and in pure oxygen. Some trends are obvious:

1. Minimum Ignition Energy (MIE) is reduced, in most cases by two orders of magnitude.
2. Autoignition temperature (AIT) is reduced in some cases.
3. Flammability Limits are wider i.e. the LEL is slightly reduced whilst the UEL is much higher.

According to NFPA 53, the pressure ratio, i.e. the final absolute pressure divided by the initial absolute pressure, is about 7 for typical hydrocarbons in air but 33 in oxygen. In elongated geometries, such as pipes, flame acceleration leading to detonation is more likely.

Table 2: *Characteristics of different fuels in air and pure oxygen*

Fuel gas	**Air**				**Oxygen**			
	MIE mJ	**AIT °C**	**LEL %v/v**	**UEL %v/v**	**MIE mJ**	**AIT °C**	**LEL %v/v**	**UEL %v/v**
Acetone	1.15	465	2.6	12.8	0.0024		2.5	60
Acetylene	0.017	305	2.5	100	0.0002	296	2.5	100
n-butane	0.25	288	1.6	8.4	0.009	278	1.6	49
Dichloromethane	9300	615	13	22	0.137	606	11.7	68
Diethyl ether	0.19	193	1.9	36	0.0012	182	2.0	82
Ethane	0.24	515	3.0	12.5	0.0019	506	3.0	66
Ethylene	0.084	490	2.7	36	0.00094	485	3.0	80
n-hexane	0.24	225	1.1	7.5	0.006	218	1.2	52*
Hydrogen	0.016	520	4.0	75	0.0012	400	4.0	95
Methane	0.21	630	5.0	15	0.0027		5.1	61
Propane	0.25		2.1	9.5	0.0021			

The values are taken from BRITTON (1999), NFPA 53 and the GESTIS database

* determined at 93 °C

6. Risk analysis

Everybody knows you should do a Process Risk Analysis on a chemical process. But anybody who has ever tried knows that it is difficult to do so thoroughly. Chemical installations are complex. Chemical processes are difficult to understand. Chemicals often react in ways we do not anticipate or with consequences that we did not imagine, as was the case in the three incidents described above.

The main hazards of the chemical industry are as follows:

- Physical explosion or implosion
- Gas phase explosion
- Dust explosion
- Fire
- Runaway reaction
- Condensed phase detonation
- Loss of containment leading to acute effects on human health and the ecosystem.

To assess the risk of a gas phase explosion for a process involving a chemical reaction, it is vital to ask three questions:

1. Is an oxidant gas used or generated by the primary (wanted) reaction or by a secondary (unwanted) reaction? Oxidant gases include oxygen (O_2), ozone (O_3), nitric oxide (NO), nitrogen dioxide (NO_2,), nitrous oxide (N_2O), fluorine (F_2,) and chlorine (Cl_2). For example, EGAN (2015) describes a gas phase explosion in a diazotisation reactor. In this case the oxidant gas was nitric oxide.

2. Is a fuel, such as a hydrocarbon present in the form of a gas or vapor? At least 99% of chemical processes I have dealt with have some kind of fuel, either as a solvent or as a reagent or as a product.

3. Does the reaction involve materials that could act as ignition sources? An example would be activated Raney Nickel. “Raney nickel” is an alloy of nickel and aluminium, usually supplied in the form of granules. Activation means treating it with aqueous sodium hydroxide, which dissolves most of the aluminium, leaving granules containing nickel in finely divided form, which can be used as a hydrogenation catalyst. Activated Raney nickel must always be kept under water or in an inert atmosphere. If it comes into contact with air, the spontaneous oxidation of the fine particles of nickel make it glow red hot and it becomes a powerful ignition source.

If a danger of gas phase explosion does exist for a given chemical process, the next step is to acquire all of the data need to carry out a risk assessment, such as:

- Explosion limits of the fuel in the oxidant gas which are usually expressed by:
    - LEL (Lower Explosive Limit),
    - UEL (Upper Explosive Limit)
    - LOC (Limiting Oxygen Concentration)
- Parameters linked to its ignition, such as:
    - Gas group (A to D under the NFPA system and IIA, IIB or IIC under the IEC/ATEX system)
    - MIE (Minimum Ignition Energy)
    - AIT (Autoigniton Temperature)
- Parameters linked to explosion violence, such as:
    - P_{Max} (Maximum Explosion Pressure)
    - K_G (Normalised rate of pressure rise)
    - Fundamental burning velocity

All of this data must be acquired under conditions comparable with those of the process. For example, if a process operates under a pressure of 10 bar gauge and 200 °C, the explosive limits determined at atmospheric pressure and ambient temperature will not be representative. Indeed, in general, the explosive range (i.e. the gap between LEL and UEL) increases with increasing pressure and temperature.

With such data, determined under representative conditions, we can then evaluate possible scenarios of gas phase explosion where all three of the following causes are present in the same place at the same time:

1. Oxidant gas in sufficient concentration (≥ LOC)
2. Fuel gas within explosive limits (LEL to UEL)
3. Effective ignition source (i.e. energy > MIE or temperature > AIT).

In the case of a gas phase explosion inside a vessel, a fourth cause is sometimes added, for example when the maximum explosion pressure is above the vessel design pressure but below the pressure expected to cause rupture (typically 3 times the design pressure):

4. Rupture frequency based on a comparison of the maximum explosion pressure, the vessel design pressure and the estimated rupture pressure of the vessel.

Each cause is given a frequency of occurrence which may be:

- **Given** (occurring more than ten times per year)
- **Very frequent** (occurring between one and ten times per year)
- **Frequent** (occurring between once every ten years and once per year)
- **Possible** (occurring between once every thousand years and once every ten years)
- **Improbable** (occurring between once every hundred thousand years and once every thousand years)

EGAN (2016-A) describes the method used to estimate ignition frequency, which depends on:

- The characteristics (MIE, AIT, etc. of the explosive mixture)
- The volume within explosive limits (for example many more ignition sources are to be found outside a vessel then inside)
- The various ignition sources, such as electrical equipment, which may be present and their suitability for explosive atmospheres.

We assess all ignition sources (electrical equipment, static electrical discharges, friction, electromagnetic radiation, heat, etc.) and for a given scenario, we base the overall ignition frequency on the ignition source which we consider to be the most frequent for the gaseous mixture concerned. The following assessments of ignition frequency are typical:

• Given	=1/1	Hydrogen released to an area not rated for that gas,
• Very Frequent	≈1/10	Methane released to an area with unrated electrical equipment,
• Frequent	≈1/100	Methane released to an area with equipment rated for zone 2,
• Possible	≈1/1000	Methane released to an area with equipment rated for zone 1.

Our estimation of ignition frequency is based on feedback from everyday experience handling hydrocarbons, such as gasoline, under air containing 21 % volume of oxygen. For example, we know from experience that mixtures of gasoline vapor and air within explosive limits will often be present when handling this material but control of ignition sources is an effective way to prevent explosions and fires.

The same thing cannot be said for gaseous mixtures of hydrocarbons and air enriched in oxygen or in other gases such as chlorine. For such mixtures, experience indicates that ignition nearly always occurs by both thermal and electrostatic mechanisms. Therefore, the ignition frequency is “Given”, or, if there is sufficient practical experience and data on the mixture, at best “Very Frequent”.

EGAN (2016-B) describes the method we use to assess scenarios in a Process Risk Analysis. From the frequency of the necessary, sufficient and independent causes of each scenario, we estimate its Probability of occurrence, over a period of one year, on a scale ranging from 1 to 10^{-6}. We assess the Severity level of the scenario in terms of human and environment consequences on a scale from Low (any human or environmental consequences are clearly reversible) to Disastrous (exposure of 100 people to a risk of dying or very long term pollution).

We then assess the Risk level of the scenario from its Probability and its Severity. We define three levels of Risk:

- Risk 1 (Unacceptable) – it is mandatory to reduce the Probability or Severity of such scenarios by suitable means such as adding preventive or protective safeguards.
- Risk 2 (Intermediate) – the Probability or Severity of such scenarios should be reduced by suitable means such as adding preventive or protective safeguards.
- Risk 3 (Acceptable) – the existing safeguards must be maintained in good working order.

The higher the level of the Severity of Consequences the lower needs to be the Probability to get an "Acceptable" level of Risk. In the case of a gas phase explosion, preventive safeguards might include:

- On line analysis of the level of oxygen in the gas phase of a reactor, such as one used for oxidation of a hydrocarbon, with automatic shutdown of the system if the level of oxygen is too high,
- Explosion venting,
- Explosion suppression.

Protective safeguards might include placing a reactor in a bunker.

7. Conclusions

Three incidents involving gas phase explosions occurred in the Solvay group of chemical companies over a period of seven years. In each case, the oxygen was derived from the decomposition of hydrogen peroxide used in the process. The incidents show how important it is to identify chemical reactions which release oxygen and to take this into account when assessing the risk. A gas phase explosion of a given fuel gas or vapor in oxygen may be compared with an explosion of the same fuel in air as follows:

1. Minimum Ignition Energy is reduced, in most cases by two orders of magnitude.
2. Autoignition temperature is reduced in some cases.
3. Flammability Limits are wider i.e. the LEL is slightly reduced whilst the UEL is much higher.
4. Explosion pressure ratio is higher : ≈7 in air and ≈33 in oxygen.
5. In elongated geometries, such as pipes, flame acceleration leading to detonation is more likely.

References

Britton (1999). Avoiding Static Ignition Hazards in Chemical Operations (CCPS).

Egan, S. M. (2015). Learning lessons from eight gas explosions, Loss Prevention Bulletin, 243: 18-27.

Egan, S. M. (2016-A). Ignition Frequency in Process Risk Analysis at Solvay, Chemical Engineering Transactions, 48: 289-295.

Egan, S. M. (2016-B). Process Risk Analysis within Solvay, Chemical Engineering Transactions, 48: 823-828.

NFPA 53 (2016) Recommended Practice on Materials, Equipment, and Systems Used in Oxygen-EnrichedAtmospheres

DOI: 10.7795/810.20221124

Investigation on flame propagation and particle decomposition behavior of dust explosion in MIKE 3 apparatus

Yangyue Pan[a], Christoph Spijker[a] & Harald Raupenstrauch[a]
[a] Montanuniversitaet Leoben, Austria
E-mail: *yangyue.pan@unileoben.ac.at*

Abstract

Due to high turbulence and high particle load in the MIKE 3 apparatus, the flame behavior is hard to be observed. The previous study showed that particle clusters are the reason for the irregular flame front (Pan et al., 2022b). In this study, we investigate the influence of dust suspension conditions of different particle sizes as well as the particle decomposition behavior during the explosion in experimental and simulation methods. The experiment of coal dust explosion was conducted in the MIKE 3 apparatus. Five size ranges: 32 - 45 μm, 45 - 63 μm, 63 - 71 μm, 71 - 125 μm, 125 - 250 μm were tested and the flame propagation process was recorded by a high-speed camera. The flame front over time was detected using the MATLAB image post-processing code. In the simulation, the default solver coalChemistryFoam in OpenFOAM was used. Three mono-sized particles were simulated: 25 μm, 125 μm and 250 μm. The particle positions of each case were extracted from the simulation of dust dispersions in MIKE 3 (Pan et al., 2020). The particle volatile content was modified to match the coal dust characters. The flame propagates towards the particle clusters and the intense radiation shows a luminous flame. Due to the high turbulence and unevenly distributed coal clouds, the flame shape is asymmetrical. The simulation result shows that the uneven distribution of particles has little influence on the flame propagation in the MIKE 3 apparatus.

Keywords: *dust explosion, MIKE 3, OpenFOAM, Eulerian-Lagrangian*

1 Introduction

The simulation of dust explosion still faces challenges due to the complexity of multiphase flow and chemical reactions. To investigate the process, proper simulation models should be used accordingly. The simulation methods for multiphase phase flow are the Eulerian and Lagrangian approaches. For the Eulerian method, particles and air are described as continuum phases, where the solid particle is implemented with a pseudo fluid model. The percentage of each phase in a cell is described with a coefficient. This method is able to determine the flow field properties such as flame propagation profile out of the embedded chemical reaction model. However, the particle trajectories are not predicted due to the assumption of the pseudo-fluid model. The Lagrangian method provides the possibility of detailed investigation of particle effects. The particles are seen as individuals and data such as components and reaction rate is available. At the same time, the biggest drawback of this method is the high requirement of computation time. The experimental instruments are able to provide repeatable results but also many stays unknown to us. For example, in the previous study, the dust concentration along the MIKE 3 tube prior to ignition varies due to different particle sizes. Moreover, the rapid explosion makes it hard to observe the chemical reactions and transport phenomena. In this study, continuous work is carried out to study the explosion process of dust explosion in the MIKE 3 apparatus in experimental and simulation methods. The open-source toolkit OpenFOAM version 5x was used in the simulation work.

2 Experiment setup

The experimental apparatus used in the study is shown in Fig. 1. MIKE 3 is a modified Hartmann tube that is widely used in laboratories to test the minimum ignition energy of powders. The apparatus consists of the dispersion tube, dispersion system, pneumatic system, high-voltage electrodes, measurement and detection system. An additional high-speed video camera was set to record the experiment process. For each dust class, tests were repeated five times to assure consistency of the measurement results. All the tests are carried out under ambient pressure and temperature condition.

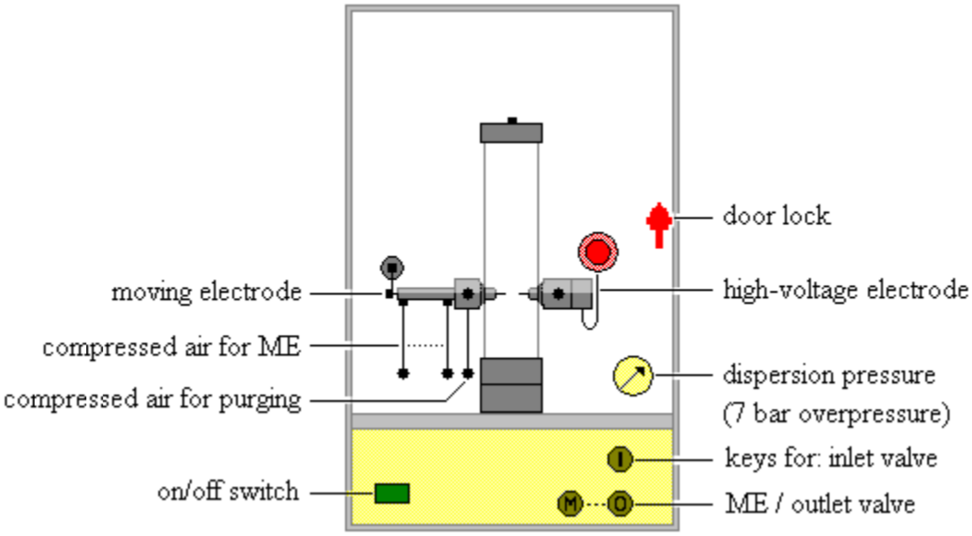

***Fig. 1**: Experimental instrument: MIKE 3 apparatus from Kuehner AG (Cesana and Siwek, 2010).*

The sample used in the experiment is coal with a density of 1007 kg/m^3 measured in acetone liquid using a pycnometer. The coal sample was firstly milled and dried and then sieved into five different sizes: 32 - 45 μm, 45 - 63 μm, 63 - 71 μm, 71 - 125 μm, 125 - 250 μm. In the experiment, 900 mg of dust sample was put on the curved bottom under the nozzle. When the experiment started, an air blast was released from a high-pressure container into the dispersion tube. The dust is lifted with the high turbulence flow and forms a cloud in the dispersion tube. According to the test standard in dust explosion, the spark discharge is drawn from the electrodes at the height of 100 mm above the tube bottom after a certain time from the dust dispersion. The delay of the discharge time from the onset of air blast is the ignition delay time, which is 60 ms in the tests. The ignition delay time decides the turbulence level and dust cloud concentration in the flow domain at the instant of spark ignition. The ignition energy is set at 1000 mJ to ensure dust ignition. The detailed introduction and result analysis of the dust explosion experiment can be found in documents (CEN EN 13821, 2003, Hosseinzadeh et al., 2018).

2.1 Model description

The current study is based on OpenFOAM 5.x version, in which the solver coalChemistryFoam was employed. The coalChemistryFoam is a transient, compressible solver with the utility of chemical reaction and multiphase flow. The solver uses RANS (Reynolds-Averaged Navier Stokes) model as the turbulence model and closes up with k-epsilon model. The evaporation and devolatilization of the particles were also modeled. The Lagrangian particles was used to couple with the gas, which the trajectories are tracked in the combustion process.

To track the particle movement, the Newton's second law was used by considering all the forces exerting on each particle.

$$m_p \frac{\partial^2 x_p}{\partial t^2} = m_p [F_D(u - u_p) + \frac{g(\rho_p - \rho)}{\rho_p}] \tag{1}$$

where m_p , u_p, ρ_p are the particle mass, velocity, and density, respectively. The terms on the right side of the Eq. 1 are the drag force and the gravity. The drag force $m_p F_D(u - u_p)$ is calculated depending on the particle Reynolds number (Re_p) and drag coefficient (C_D) (Morsi and Alexander, 1972).

$$F_D = \frac{0.75 \mu C_D Re_p}{\rho_p d_p^2} \tag{2}$$

$$Re_p = \frac{\rho_p d_p |u - u_p|}{\mu} \tag{3}$$

d_p represents the particle diameter, and μ is the dynamic viscosity of the fluid. Due to the interaction of the two phases, more forces are taking part in the dispersion. In this study, the forces in the two-phase system, such as the pressure difference on particles owing to the velocity difference (lift force), are not considered. This is because the lift force has negligible influence on the trajectories of particles Morsi and Alexander (1972) and the pressure difference is low. Therefore, considering the micro size of particles, the buoyancy force and drag forces significantly influence the dispersed phase.

Due to the coal samples being dried prior to the experiment, there exists no adsorbed water. Therefore, the liquid evaporation models are deactivated. According to the Thermogravimetric analysis, the coal particles have 34.77% volatile gas component until 1200 K, including 52.71% CH4, 47.29% CO2. The solid part of the coal at 1200 K consists of 16% incombustible ash and 84% carbon molecules. The constantRateDevolatilization model was used to calculate the coal decomposition with a constant rate in the form of a single-step Arrhenius expression:

$$\dot{m}^p_{Yi} = m^p_{Yi} A_v \, exp(\frac{E_{a,v}}{RT_p}) \tag{4}$$

A_v and $E_{a,v}$ are the pre-exponential coefficient (kg/s) and activation energy $(J/kg \cdot K)$. Yi represents the gas components in the coal particles. The surface reaction considers the direct reaction of carbon and oxygen on the surface of the particle:

$$C(s) \quad + \quad O_2 \quad \longrightarrow \quad CO_2 \tag{5}$$

where the oxygen from the gas phase is consumed and carbon dioxide is produced from the heterogeneous reaction. The diffusion-limited surface reaction model is used to specify the surface reaction rate, which is limited by the oxygen diffused to the particle surface (Field, 1969, Cloney et al., 2018).

$$\frac{m_p}{dt} = -4\pi \, d_p \, D_{i,m} \frac{Y_{O_2} T_\infty \rho}{T_p + T_\infty} \tag{6}$$

where $D_{i,m}$ represents the diffusion coefficient for oxygen (m^2/s). Y_{O_2} is the local mass fraction of oxygen in the gas at the surface of the particle. The devolatilization process is followed by a series of chemical reactions due to the release of combustible gases. The evolved gases participate in the computational cell in the gas phase and participate in the homogeneous reaction. One chemical reaction mechanism for CH4 was considered in the simulation.

$$CH_4 \quad + \quad 2O_2 \quad \longrightarrow \quad CO_2 \quad + \quad H_2O \tag{7}$$

The reaction rate is represented by an irreversible Ahrrenius equation, where only CH4 is combusted in the gas phase:

$$\dot{m}^{g}_{CH_4} = m_{CH_4} A_v \, exp(-\frac{E_{a,v}}{RT_\infty}) \tag{8}$$

The reaction model in the gas phase used the Partially Stirred Perfect Reactor (PaSR) model. In each simulation cell, the reactants are perfectly mixed only in part of the cell. This model considered the chemical and time scales to prevent overpredicting the chemical reaction process. A robust chemical reaction solver Seulex was used.

According to the movement momentum, chemical reaction, heat transfer from the particles, the momentum, chemical component and energy level in each computation cell is affected by the particle sources. The sources are registered as source terms in the conservation equations in the gas phase transportation.

$$\frac{\partial \rho}{\partial t} + \nabla \cdot \phi = S^{\rho}_{p} \tag{9}$$

where ρ is the density of the fluid (kg/m^3). u is the fluid velocity (m/s). ϕ is mass flux ($kg/m^2 \cdot s$).

2.1.1 Numeriacl Domain

A two-dimensional numerical domain was used, shown in Fig. 2. The geometry simplified the domain of the MIKE 3 apparatus into a rectangular plane. It has a dimension of 300 mm in height and 68 mm in diameter. The spark ignition source is located at the center of the tube at the height of 100 m, which is marked with a red sphere in the figure. The diameter of the ignition source is 6 mm. The geometry is discretized into 22 000 hexahedra cells. The grid size is 1 mm and is enough to capture the intensive heat transport phenomenon. The top of the geometry is the outlet and others are walls as boundary conditions. The initial temperature in the internal field is 300 K. Figure. 2 b indicates the particle positions at the instant of spark ignition. The positions are obtained from previous simulation results in the particle propagation simulation (Pan et al., 2020, 2022a). Contrast cases with evenly distributed particles are also simulated to explore the influence of particle concentration. The temperature in the ignition source is 2000 K. It starts from 0.001 s and lasts for 0.1 s in order to ignite the particles. The particles are set as fixed in three cases: 25 μm, 125 μm and 250 μm. The total particle mass is 900 mg and the mass parcel basis is used in the simulation. The solid particles are two-way coupled with the flow domain. A summary of the simulation parameters used in the present study is shown in Table 1.

***Table 1**: Simulation parameters used in the model.*

Parameter	Value
Fluid	Air
Solid	Coal dust
Particle size (μm)	25, 125, 250
Dust concentration (g/m^3)	750
Particle density (g/m^3)	1 007
Ambient pressure (Pa)	100 000
Temperature (fluid) (K)	300
Temperature (solid) (K)	300
Ignition temperature (K)	2 000
Cell size (m)	0.001 - 0.002
Simulation time (ms)	500
Ignition period (ms)	0 - 100

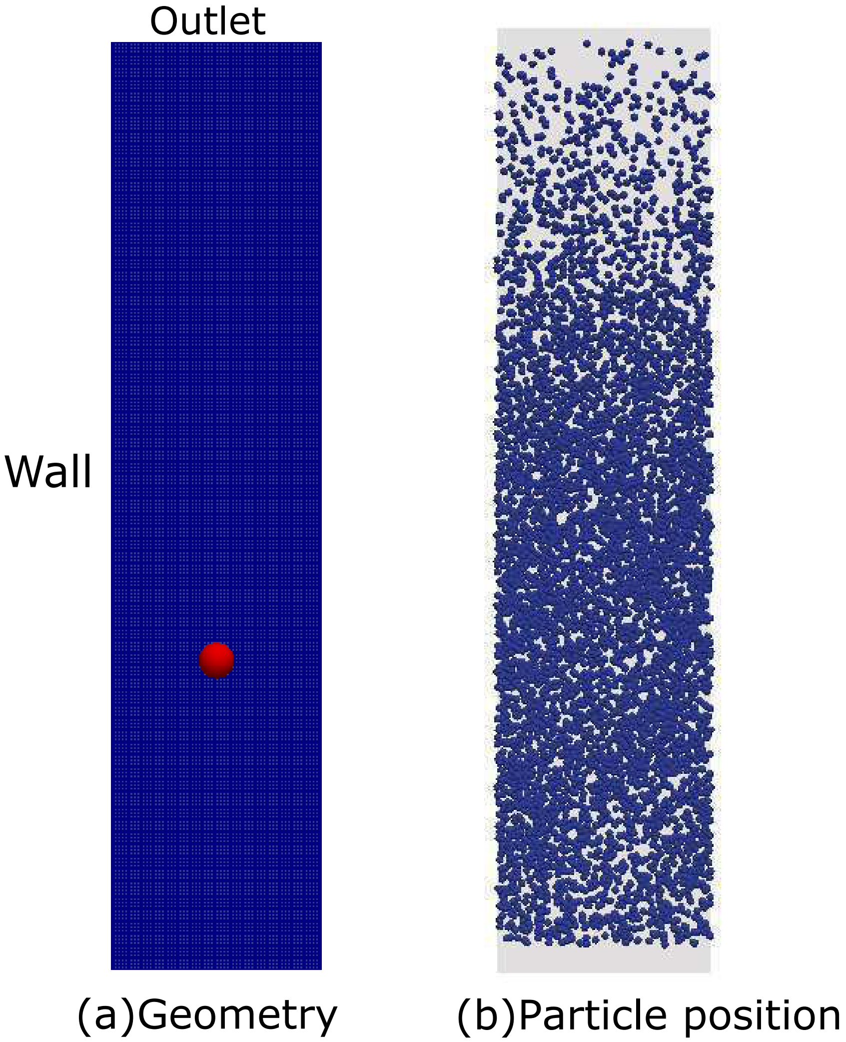

***Fig. 2**: The numerical domain of simulation.(a) The two-dimensional geometry represented with meshes. Outlet is on the top. The red sphere (D = 6 mm) marks the position of the ignition position. (b) The initial particle positions of 125 μm particles at the instance of ignition (Pan et al., 2020).*

3 RESULT AND DISCUSSION

3.1 Flame propagation behavior

Fig. 3 shows a series of recorded images of the flame propagation of coal dust at a concentration of 750 $g/m3$ and particle diameter of 71 - 125 μm. At 0.001 s, a faint flame shows after the spark ignition which propagates slowly for several milliseconds. It is the burning of small particles and the particle volatile is quickly released due to the high specific surface area. The particles are separated by the volatile released from the heated particles. When the oxygen diffused to the surrounding of the particle, the combustible volatile gases react. The heat from combustion continues to heat up the separated particles. The flame starts to be luminous which is a diffusion-controlled reaction. The flame shape is irregular due to the particle suspension conditions at the instance of ignition. As seen in 0.03 s, the flame has a direction towards the left wall because of more particle accumulation and more reactant. The flame propagates along the wall and continues to heat particles nearby. Therefore, the particles on the right side of the tube are ignited. The flame has a very luminous part in the active reaction center due to the high volatile content released from particles. This also explains the irregular flame front. The flame top front is hard to capture as a result of scattering burning particles, which can be observed in 0.07 s. Similar irregular flames were also observed by Kern et al. (2015), who did flame propagation experiments using lycopodium particles in a 2-meter long cylindrical tube.

DOI: 10.7795/810.20221124

Unlike his result, the flame in the MIKE 3 does not propagate intensely to the bottom of the tube due to the lack of oxygen. Only part of the dust is combusted which can be identified from 0.04 s to 0.08 s. Similarly, the particle concentration towards the right bottom of the tube is higher and more combustion heat is produced indicating a lower temperature gradient in the neighborhood of the particle. The high particle concentration part is named particle clusters in the study of Hosseinzadeh et al. (2018). The flame reached the top of the tube at 0.08 s. After that, the flame still burns as the flame extinct and more oxygen is diffused to the tube bottom.

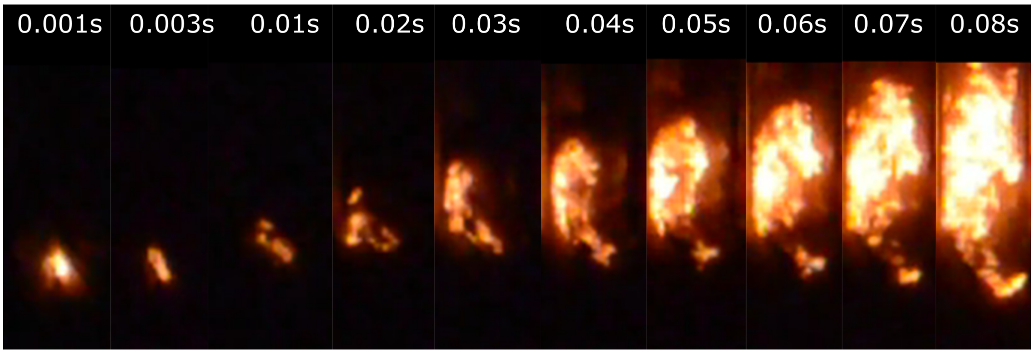

***Fig. 3**: High-speed direct images of dust explosion flame evolvement over time (coal cloud size: 71-125 μm, dust concentration: 750 g/m^3).*

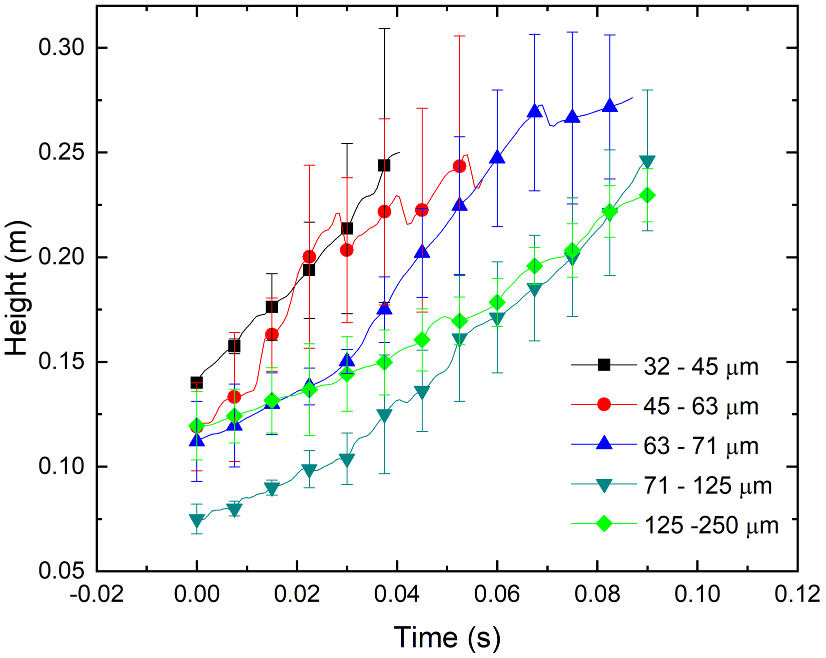

***Fig. 4**: Variation of flame front positions in experiment over time (dust concentration: 750 g/m^3).*

The variation of flame front positions with different particle size ranges is shown in Fig. 4. The flame front in each video frame is captured using RGB filters in MATLAB™. One example of the image process is shown in Fig. 5. Firstly, the resolution of each frame in the video is obtained. In this example, the pixel count is 650” × 240”. In each frame, the colored image is filtered by red, green and blue color. In the presented example, the green tunnel filter is used because it gives the best edge capture. The threshold in the green tunnel filter is defined and at last the Fig.5c returns the edge of the flame shape. The treatment was applied to all the frames and the flame front position was obtained by the pixel value. Finally, the flame front positions were defined and corresponding times are counted by the frame number.

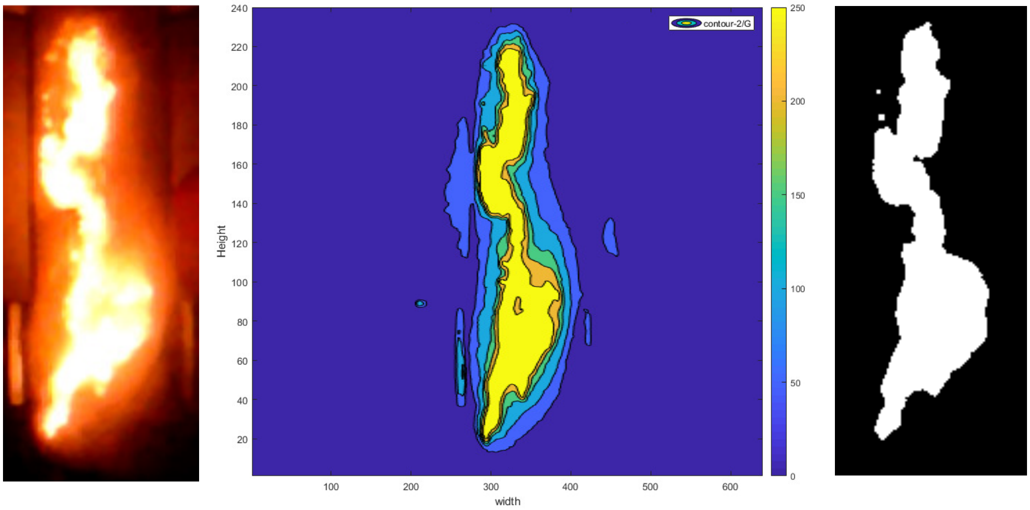

(a) Original (b) Green tunnel level (c) Flame edge

***Fig. 5**: Flame image treatment process by RGB filters.(a) The original snapshot of the dust flame; (b) The green tunnel image; (c) Flame shape filtered by the threshold value of the green tunnel.*

The flame propagation velocity increases after a while. It means that the flame reaches the tube wall and due to the confinement, the pressure increase and the velocity of flame increases. For example, in 71 - 125 μm case, the time when it reaches the tube wall is around 0.05 s, which corresponds to the Fig. 3. As the particle size decreases, there is an overall pattern that the lateral flame propagation becomes faster due to the lower critical time. The flame velocity also increases as the particle size decreases. However, the flame propagation is strongly influenced by the initial flame position generated during the spark. The starting positions of the flames increase as well as the particle decreases. This can be explained by the cloud clusters in the domain. The smaller particles tend to concentrate at a higher position at the same ignition delay time, leading the initial flame to a higher position.

3.2 Flame propagation in simulation

Because the particle cluster affected the flame propagations during the explosion, different particle distributions were used in the simulation. Fig. 6 summarised the flame propagation in the simulations. The letter 'e' marks the cases with evenly distributed particles. The flame propagates over time until it reaches the outlet. The 250 μm case finishes the propagation at 0.16 s, much slower than the other two cases. However, the flame speed of the smallest particles 25 μm is not higher than the 125 μm particles because the 25 μm particle escape from the outlet and less fuel exists. The initial particle positions do not seem to influence the flame propagation. The thermal expansion and the evolved gases push away the particles at the flame front.

3.3 Particle propagation characteristics

Comparative simulations whose initial particle positions are evenly distributed over the tube were carried out in order to discover the particle behaviors.The results of particle concentration and gas content over time from particle size 250 μm case are shown in Fig. 7. The x-axis is the position over the tube axis, and the y-axis is the concentration of the particles.

Starting form different concentration distributions, a 'U' shape gradually forms when the ignition starts in both cases(Fig.7a,7b). The particle concentration decrease remarkably near the ignition

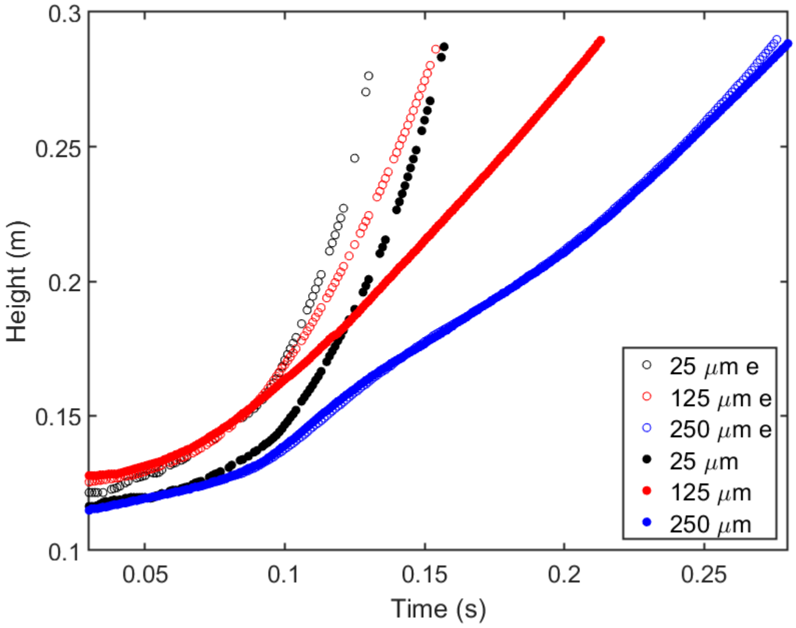

***Fig. 6**: Flame front propagation with different initial particle positions in the simulations.*

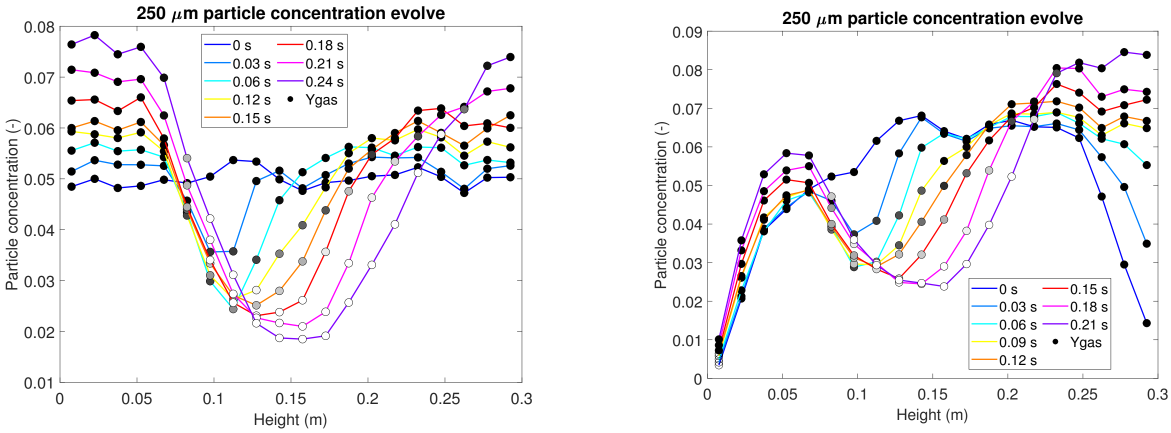

(a) Evenly distributed initial positions. *(b) Unevenly distributed initial positions.*

***Fig. 7**: 250 µm particle concentration and volatile content evolve over the axis of the tube.*

source over time. Particles that are lower than the ignition point descend to the bottom of the tube. The shape ’U’ becomes wider over time as a result of the flame propagation. In Fig. 7b, the initial position of particles are distributed in the domain with different concentrations. There are more particles between 0.1 m and 0.25 m and less particles near the bottom of the tube.The particle concentration at the bottom of the tube does not increase remarkably and resulting in a higher particle concentration at the top of the tube comparing to the Fig.7a.

The particle volatile content is marked as circles and the shade of the filling represents the remained volatile, where black means that all of the volatiles are present, and blank means that all of the volatiles have been released.On the other hand, they can be representative of the flame front position.The lowest particle concentration can be found near the center of the flame due to the gas expansion. The particles near the ignition source start to decompose as the flame forms. Then, more particles are burnt when the flame propagates.

4 Conclusions

The flame propagation behavior in the MIKE 3 apparatus was studied in this paper with experiments and CFD simulations. The dust explosion of 32 - 45 μm, 45 - 63 μm, 63 - 71 μm, 71 - 125 μm, 125 - 250 μm particles were carried out with concentration of 750 g/m^3. The flame in the experiment tends to propagate in the direction of the particle clusters. As a result, the flame shape is asymmetrical over the axis. The flame cluster indicates the uneven distribution of particles at the instance of ignition. When the particle size increases, the flame speed decrease. It is also found in the simulation result.A comparative simulation with evenly distributed particle concentration was carried out.

Acknowledgements

PY acknowledges the financial support of the China Scholarship Council (CSC, No. 201808420277). The authors are grateful for the computing time granted by the Chair of Thermal Processing Technology (TPT), University of Leoben.

References

CEN EN 13821 (2003). *Potentially explosive atmospheres - Explosion prevention and protection - Determination of minimum ignition energy of dust/air mixtures.* European standard, Brussels.

Cesana, C., Siwek, R. (2010). *Manual MIKE 3 apparatus.* Kuehner AG.

Cloney, C. T., Ripley, R. C., Pegg, M. J., Amyotte, P. R. (2018). *Laminar burning velocity and structure of coal dust flames using a unity Lewis number CFD model.* Combustion and Flame, 190:87–102. ISSN 00102180. doi:10.1016/j.combustflame.2017.11.010.

Field, M. A. (1969). *Rate of combustion of size-graded fractions of char from a low-rank coal between 1 200°k and 2 000°k.* Combustion and Flame, 13:237–252.

Hosseinzadeh, S., Vanierschot, M., Norman, F., Verplaetsen, F., Berghmans, J. (2018). *Flame propagation and flow field measurements in a Hartmann dust explosion tube.* Powder Technology. ISSN 1873328X. doi:10.1016/j.powtec.2017.10.001.

Kern, H., Wieser, G. J., Raupenstrauch, H. (2015). *Flame propagation in lycopodium/air mixtures below atmospheric pressure.* Journal of Loss Prevention in the Process Industries, 36:281–286.

Morsi, S., Alexander, A. (1972). *An investigation of particle trajectories in two-phase flow systems.* Journal of Fluid mechanics, 55(2):193–208.

Pan, Y., Spijker, C., Raupenstrauch, H. (2020). *Investigations on the effect of particle size on dust dispersion in mike 3 apparatus.* In *13th International Symposium on Hazards, Prevention, and Mitigation of Industrial Explosions (ISHPMIE).*

Pan, Y., Spijker, C., Raupenstrauch, H. (2022a). *CFD modeling of particle dispersion behavior in the MIKE 3 apparatus.* Alexandria Engineering Journal, 61(12):9305–9313. ISSN 11100168. doi:10.1016/j.aej.2022.03.039.

Pan, Y., Spijker, C., Raupenstrauch, H. (2022b). *Numerical investigations on dust explosion process in MIKE 3 apparatus.* In *Proceedings of the Tenth International Seminar on Fire and Explosion Hazards*, pages 56–64. Oslo,Norway.

DOI: 10.7795/810.20221124

TGA-FTIR for kinetic and evolved gas analysis of the coal particles in dust deflagration

Yangyue Pan[a], Christoph Spijker[a] & Harald Raupenstrauch[a]
[a] Montanuniversitaet Leoben, Austria
E-mail: *yangyue.pan@unileoben.ac.at*

Abstract

The common approach in the dust deflagration simulations ignores the temperature gradient inside of the particles. Therefore, the reaction rate of the particle at one temperature remains constant. In order to explore the mass loss and evolve gas characters during the coal particle decomposition procedures, a single-particle model was created using OpenFOAM tool kit. In this study, the pyrolysis characteristics and gas properties of the coal sample were determined by TGA-FTIR. The evolution of gases in real-time was investigated and implemented as kinetic models in the dust deflagration. To solve the heat and mass transfer of the single-particle, a two-phase solver based on the eulerian method was developed based on reactingFoam.The porosity of the coal particle was included with respect to the coal mass. The result of the heat and mass transfer of the single-particle model agrees well with the experiment. In order to simulate the particle behavior in the dust explosion, new boundary conditions extracted from dust explosion simulations will be implemented. The final goal of the single-particle model is to implement the new particle decomposition behavior into the full scale of dust explosion simulations.

Keywords: *dust deflagration, coal, single-particle model, TGA-FTIR, kinetics, OpenFOAM*

1 Introduction

A dust explosion is fundamentally a phenomenon from solid fuel combustion. In the safety science field, dust explosion is unknown due to its complexity. The level of severity is highly dependent on the particle species, the humidity and the particle agglomeration. The combustion mechanisms of the single-particle is an intrinsic view to understand the dust explosion itself and to provide reliable disaster control parameters. The dust explosion is a rapid chemical reaction process where useful data from the explosion studies are hard to get. The numerical methods and hardware development make the computational fluid dynamics (CFD) applicable in more research fields by using reliable sub-models (Skjold, 2007). The details of chemistry and physical processes will be revealed and adopted by industries in system designs. The chemical and physical sub-models in CFD simulation are critical in dust explosion to have a reproduction of the process in dust deflagration. The open-source CFD tool OpenFOAM, which has existing functions and is flexible for new models, is used in the study.

Thermogravimetric analysis aided with Fourier transform infrared spectroscopy (TGA-FTIR) has been used in coal particle analysis. The temperature-programmed system records the mass loss in coal particles and evolved gas from the pyrolysis. In the particle combustion stages, the pyrolysis of particles will have an impact on the temperature and the gas composition of the surrounding fluid phase due to heat and mass transfer. On the other hand, due to the combustion and interaction between the two phases, the TGA-FTIR results are not sufficient in predicting the particle behavior for dust deflagration. The complex physical transition and chemical reaction require proper boundary conditions in order to model physical phenomenons in the dust explosion. A new solver loaded with new particle models is created to solve the mass, heat and momentum transport in the particle. The single particle is resolved and Eulerian approach is used in order to present details of the gas production and transport. A porosity variable ξ is introduced in the model.

2 Experiment method

To build up the single-particle model, a coal sample was used. In order to minimize the effect of inner particle reactions, the bulk coal was processed into a small particle size. A ball mill was used firstly to grind the bulk coal and then the coal dust was sieved into a particle size range of 20-32 μm. The coal was dried in an oven at 100 °C for 12 hours. The element analysis result of the coal sample is shown in Table. 1. Fig. 1 shows the scanning electron microscopy (SEM) images of the coal sample. Fig. 1a shows a non-consistent shape and rough surfaces of the particle. In Fig. 1b, a porous structure was found.

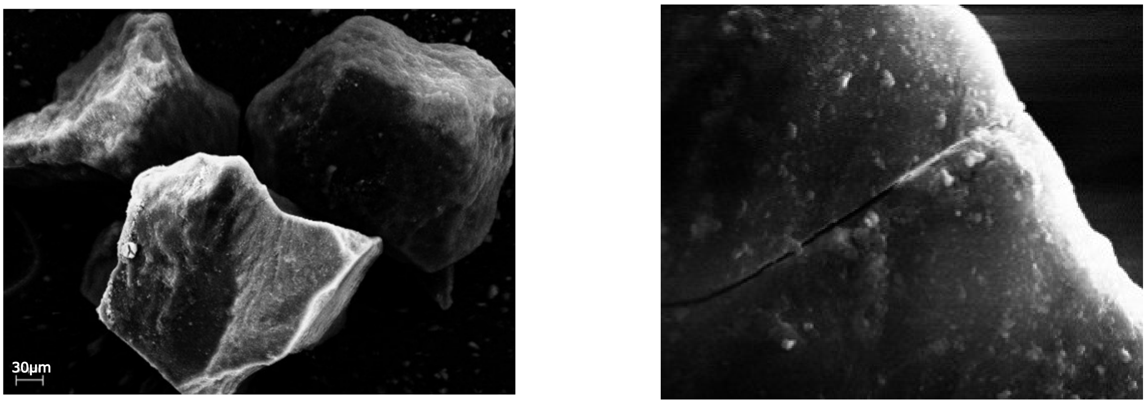

(a) Overall view of particle shape. *(b) Porous structure of the coal particle.*

Fig. 1: *Surface structure of the coal sample.*

Table 1: *Element analysis of the coal sample, air-dry basis.*

	Element analysis (wt. %)				
	C	H	O	N	S
Coal	73.9	4.87	4.81	1.47	-

The thermogravimetric analysis was carried out in the chair of Process Engineering of Industrial Environmental Protection, University of Leoben. In each heating rate, 10 mg of sample was heated up from 30 °C to 1100 °C at heating rates of 30 °C/min. The inert purging gas N_2 was used to displace air in the pyrolysis zone with a flow rate of 100 ml/min. By this means, the sample was not oxidized by Oxygen. The evolved gas was measured using the complementary FTIR spectrometer.

3 Kinetic analysis

3.1 TGA experiment result

The TGA result is shown in Fig. 2.The mass of coal samples was normalized by their initial value. The first derivative of mass change on time (dm/dt, DTG curve) is also plotted into the figure. The highest peak occurs at between 700 - 800 K. It corresponds to the main decomposition stage. In this stage, the coal mass decreases remarkably due to active pyrolysis. In the meantime, volatile gases, CO, CO_2, CH_4 and light hydrocarbons are released and measured in the FTIR analyzer. The mass of coal decreased around 30% of the total weight in this stage. The second reaction rate is not able to shape a "step" in the TG curve and can only be observed in the DTG curve. The second peak in the DTG occurs between 900 - 1100 K. In this stage, the reaction rate value of the peak is distinctly lower than the first peak. The mass loss of the coal in this stage is from the second pyrolysis of the gaseous tar. The total mass loss of the coal during the experiment is 34.98% ($\beta = 30K/min$). The reaction rate of the first and second peaks are $10.66 \times 10^{-4}\ s^{-1}$ at 749.7 K and $1.411 \times 10^{-4}\ s^{-1}$ at 1050 K.

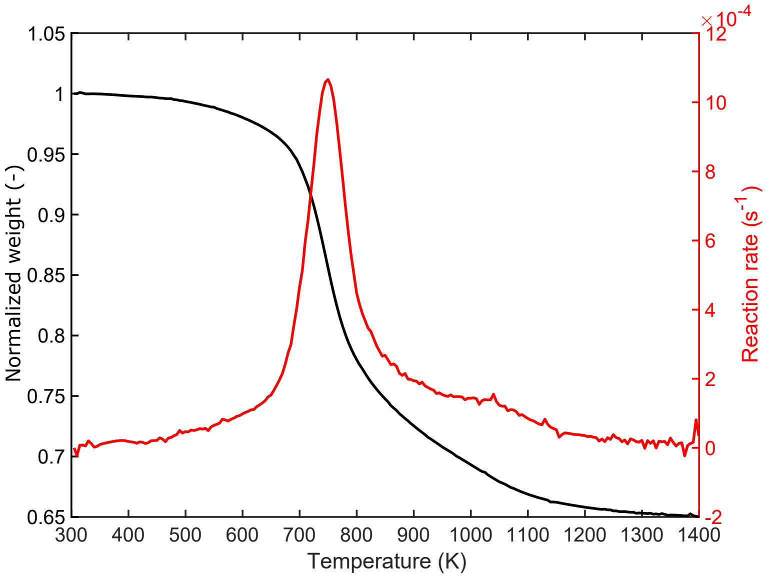

***Fig. 2**: TG and DTG data of coal sample at 30 K/min.*

Due to the complex reaction of the coal, the kinetics of the coal decomposition can not be described by one reaction. Instead of describing the kinetics of coal decomposition, one approach is to use the production of evolved gases. By studying the reaction of each gas species individually, the kinetic parameters are obtained. This method gives the opportunity to divide the total kinetics of the coal into several reactions of the pyrolysis gases. The sum of the produced gases is equal to the total mass loss of the coal.

3.2 Evolved gas analysis

FTIR examined the gaseous products of TGA in order to investigate the kinetics further. In the test, mid-infrared light was used to detect the gas molecules. Molecules and functional groups can be identified at specific bands. Furthermore, a real-time measurement was applied to obtain the spectrogram in a three-dimensional way. Fig. 3 is the spectrum of the evolved gases at 30 K/min.

The three dimensions are absorbance, temperature and wavenumber, respectively. The absorbance varies from 0 to 1, indicating the intensity of infrared light absorbed by the gases at a specific wavenumber. If the absorbance is 0, the infrared light is not absorbed. According to Beer Lambert's law (Euqation. (1)), the gas concentration is proportional to the absorbance.

$$A = \varepsilon\, c\, l \tag{1}$$

where A is absorbance. ε is molar absorption coefficient, $L/(mol \cdot cm)$. c is molar concentration, mol/m^3. l is the path length, cm. The coefficient is a characteristic constant when the temperature and wavenumber is fixed. It describes the ability of the species to absorb light in a specific wavelength (King et al., 2002).

Therefore, the absorbance can reflect the concentration of each gaseous products. Gaseous products can be identified with their wavenumber. The pyrolysis product of the coal that are detected are CO (2190 cm^{-1}),CO_2 (2345 cm^{-1}),CH_4 (1295 cm^{-1} and 2810 cm^{-1}), and light carbohydrates (1450 cm^{-1}). We assume the light carbohydrates as C_2H_4. Molecules such as CH_4 absorbs both bands at 1295 cm^{-1} and 2810 cm^{-1}, showing two peaks in the spectrum. The absorbance peak of each evolved gas is marked in the spectrum graphic.

In Fig. 3, the gas release at the beginning of the experiment is very low. It can be observed that the coal starts to release CO_2 at the beginning, which is slightly earlier than the other gases. Then the CO_2 gradually rises as the temperature increases. The H_2O is not observed because the coal was pre-processed in the drying oven. The intensive gas release is between 800 K and 1100 K, which is in correspondence with the active mass loss period of the coal. For CH_4 and C_2H_4, they have relatively small ranges. The concentration of CO_2 reduces after the intensive gas release period and then increases remarkably as a result of tar pyrolysis. At the end of the measurement, the continuous temperature rise enables char decomposition and gas production. However, in the study of dust explosion, the coal dust is not fully combusted, which means that we only need to consider the pyrolysis stage of the coal.

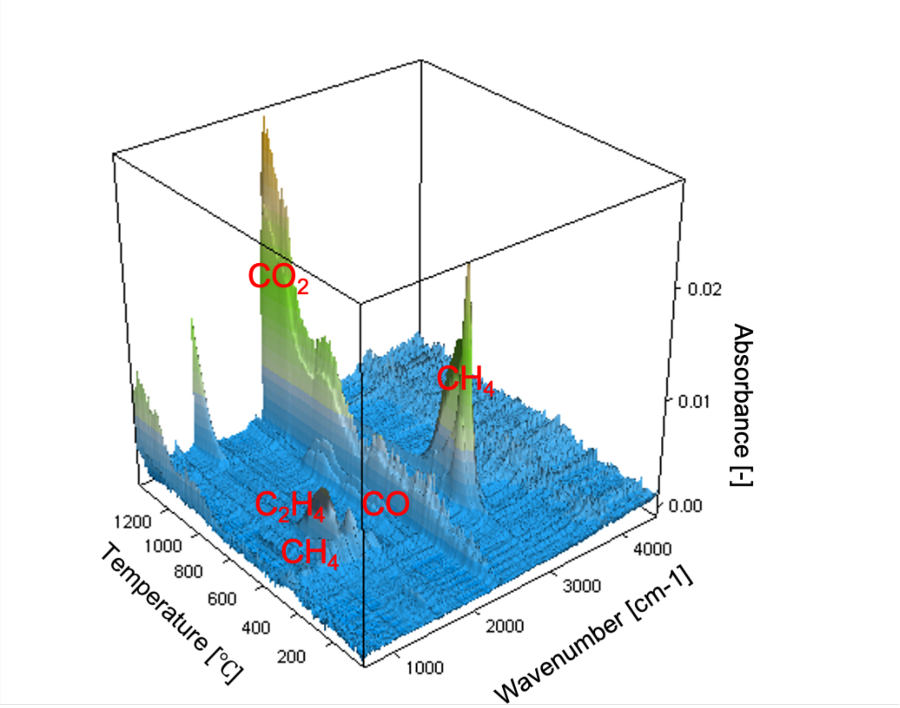

Fig. 3: *FTIR three-dimensional spectrum of evolved gas at 30 K/min (Kittinger, 2019).*

The molar absorption coefficients of evolved gases (Table. 2) are used to calculate their concentration. The concentration of each gas is calculated and plotted in Fig. 4. It can be observed that the C_2H_4 and the CO_2 gases have higher concentrations. There is a high release amount of CO and CO_2 after 1200 K due to the decomposition of the char, which will not be discussed in this study. The production of C_2H_4 and CH_4 are located at the active decomposition temperature range. In this range, the concentration of CO_2 is on the same level as C_2H_4, thus leading to the fast mass loss of the coal. Around 1050 K, the high concentrations of CO_2 and C_2H_4 are the results of the second reaction due to the tar decomposition.

Table 2: *Molar abosrption coefficient of evolved gases (Dong et al., 2017).*

CO $L/mol \cdot cm$	CO_2 $L/mol \cdot cm$	CH_4 $L/mol \cdot cm$	C_2H_4 $L/mol \cdot cm$
1146	945	784	612

By rearranging the concentration, the mass loss due to each evolved gas is plotted in a sequence to compare with the coal mass loss, as shown in Fig. 5. For example, the final value of CO at 1400 K is the start value of CO_2 at 400 K. Therefore, the final value of the last gas, C_2H_4, shows the residual coal mass. CO_2 takes the highest mass fraction among the gas products. The start point of production of CO and CO_2 are earlier, which is around 650 K. Each gas will be analyzed to obtain its kinetic data in the following section.

DOI: 10.7795/810.20221124

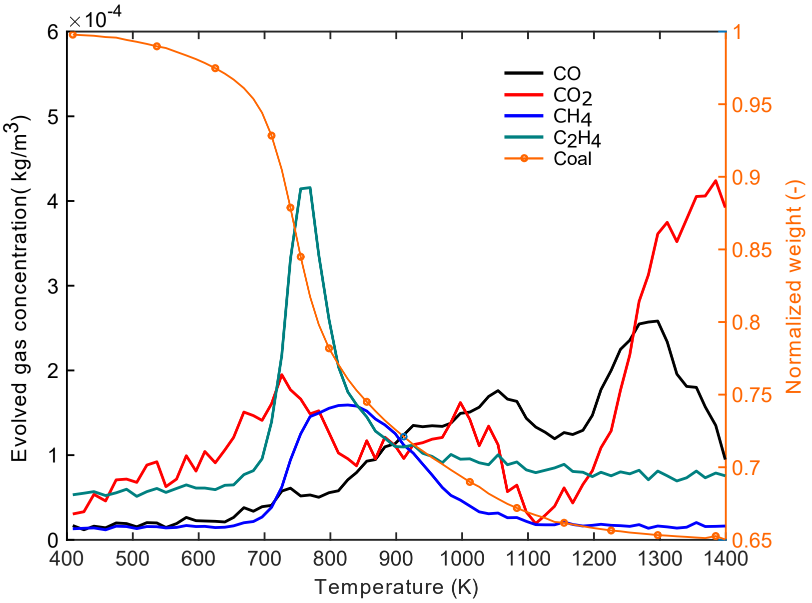

***Fig. 4**: Evolved gas concentration compares with normalized coal mass loss.*

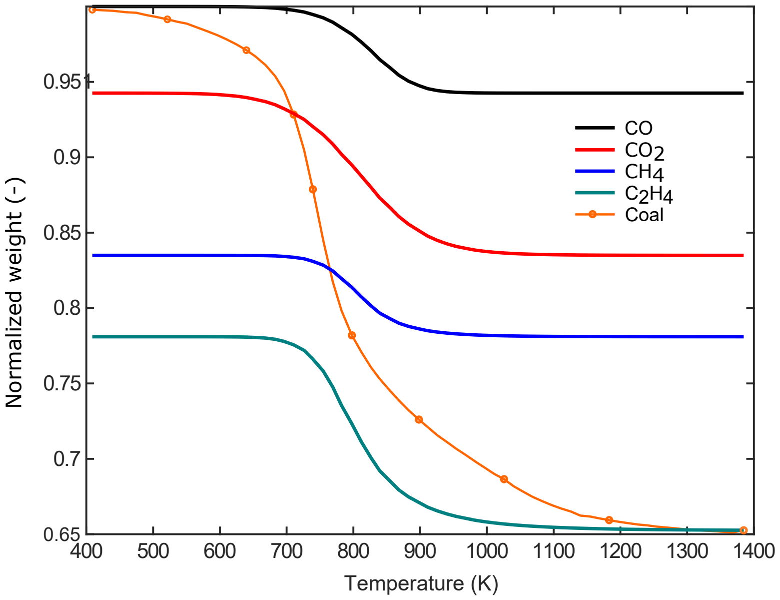

***Fig. 5**: Total coal mass loss and the mass loss due to evolved gases.*

3.3 Evolved gas kinetics

For a mass-related pyrolysis speed $r_j^{pyro}(kg/m^3 \cdot s)$ of a gas component i from a single, independent parallel reaction j applies:

$$r_j^{pyro} = A_j exp(-\frac{E_j}{RT})(V_{max,j} - V_j)^{n_j} \qquad j = 1, ..., n_{pyro} \tag{2}$$

where $V_{max,j}$ is the mass fraction determined experimentally. For the calculation of the formation rates r_j^{pyro} of the individual independent, parallel pyrolysis reactions (n_{pyro}) were considered at a certain point in time t. A mass fraction of V_j from solid is already volatilized to this point in time. These solid fractions that are released by the decomposition reactions of the solid will be represented by the evolved-gas mass fractions. The total formation rate of one gas component i results from the sum of the individual independent parallel reactions:

$$r_i^{pyro} = \sum_{j=1} r_j^{pyro} \qquad i = 1, ..., n_{gas} \tag{3}$$

In order to implement the kinetic data into simulation models, the kinetics of each gas evolution is fitted by using parallel gas reaction kinetic equations. Take the gas specie CH_4 as an example, the reaction rate is calculated out of the gas concentration:

$$r_{CH_4} = A_1 exp(-\frac{E_1}{RT})(V_{max,1} - V_1)^{n_1} \tag{4}$$

Take logarithmic on both sides of the Equation (4) for CH_4:

$$ln(r_{CH_4}) = lnA_1 + (-\frac{E_1}{RT}) + n_1 * (V_{max,1} - V_1) \tag{5}$$

The kinetic parameters can be fitted out of Logarithmic-linear method.

Due to two reaction peaks being observed in the reaction rate of CO_2 (Fig. 4), two parallel reaction models were used in MATLAB© to calculate its kinetics. The fitting curves are shown in Fig. 6, compared with the experiment result. Compared to the first peak, the second one is not distinct but essential for describing the tar decomposing stage. The reaction stages are not separated into primary and secondary pyrolysis stages in this method. This simplification will reduce the computation time when considering high solid loading combustions. The total mass over the temperature range is plotted in Fig. 6b. The difference between the model and experiment result is about 2%. The models of other gas species are in Fig. 7-9.The gas release over time is in good agreement with the experimental data. Therefore, the model can predict the gas evolve profile. The kinetic data of the coal profiled using evolved gases determined experimentally is shown in Table. 3, where $T_b = E_j/R$.

***Table 3**: Pyrolysis kinetic data of coal (30 K/min).*

Gas	A(1/s)	T_b (K)	$V_{max}(kg/kg)$	Order, n (-)
CO	1.60E+08 7.00E+03	14000 10500	0.9778 0.9426	2 2
CO_2	9.00E+08 8.00E+03	15000 10000	0.86 0.8353	2.4 2
CH_4	1.00E+04	9000	0.781	2
C_2H_4	1.00E+06	13000	0.6523	1.6

In the modeling of the formation of a single gas component (e.g., CO, CO_2), up to two independent parallel reactions j were used in the calculations for coal pyrolysis. However, if necessary, more independent parallel reactions can be used to describe the formation of a single pyrolysis gas component.

4 Model implementation

In this part, the single-particle model will be set up using the TGA data for the coal particles. The SEM picture of one coal particle shows the porous channel on the surface with a width of around 1 μm. Therefore, the steps for setting up the single-particle model start from implementing the physical property of a single coal particle and then applying the kinetic of particle decomposition into the simulation. The modification of the solver is based on reactingFoam. It is a transient solver for the turbulent flow of compressible fluids, including the chemical reactions used for dust combustion. The already existing solver rhoPorousSimpleFoam is not used because the diameter of the pores is fixed in the solver and does not include chemical properties for further reaction modeling.

DOI: 10.7795/810.20221124

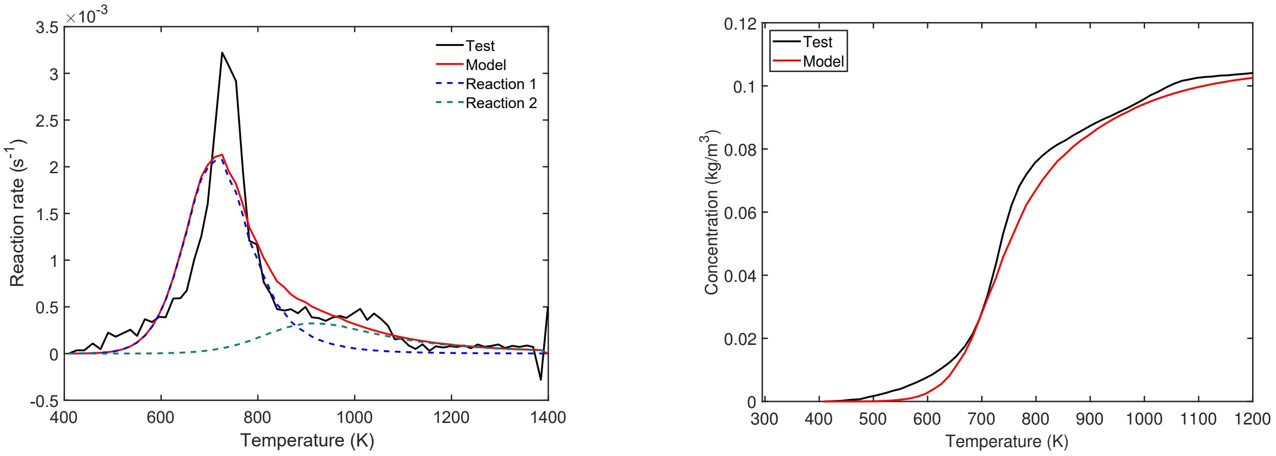

(a) CO_2 total reaction rate and sub reaction rates over temperature.

(b) CO_2 mass increase over temperature.

***Fig. 6**: Comparison of evolved gas reaction model with the experimental result: CO_2.*

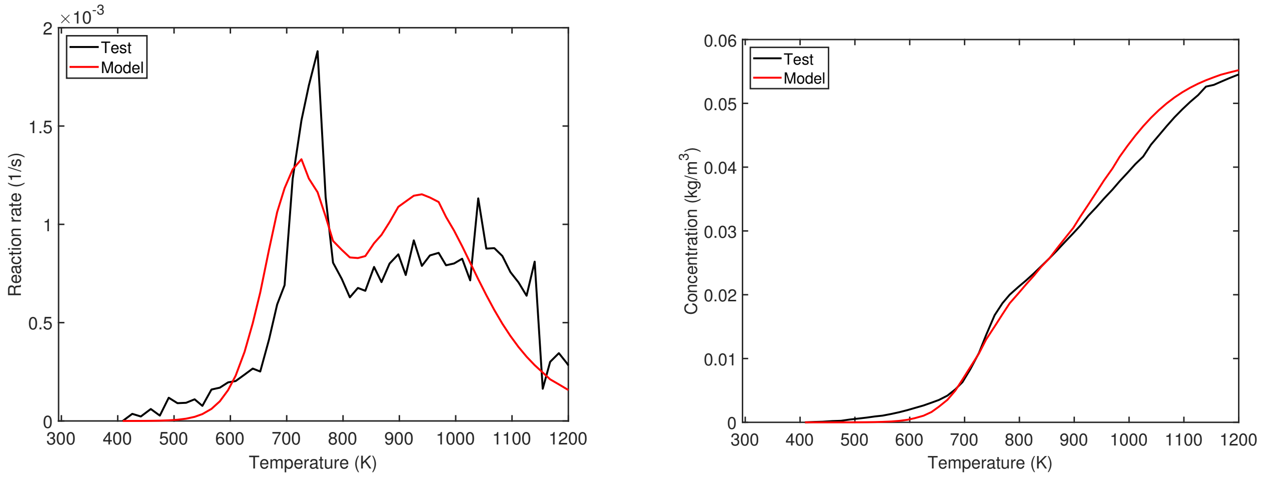

(a) CO total reaction rate over temperature.

(b) CO mass increase over temperature.

***Fig. 7**: Comparison of evolved gas reaction model with the experimental result: CO.*

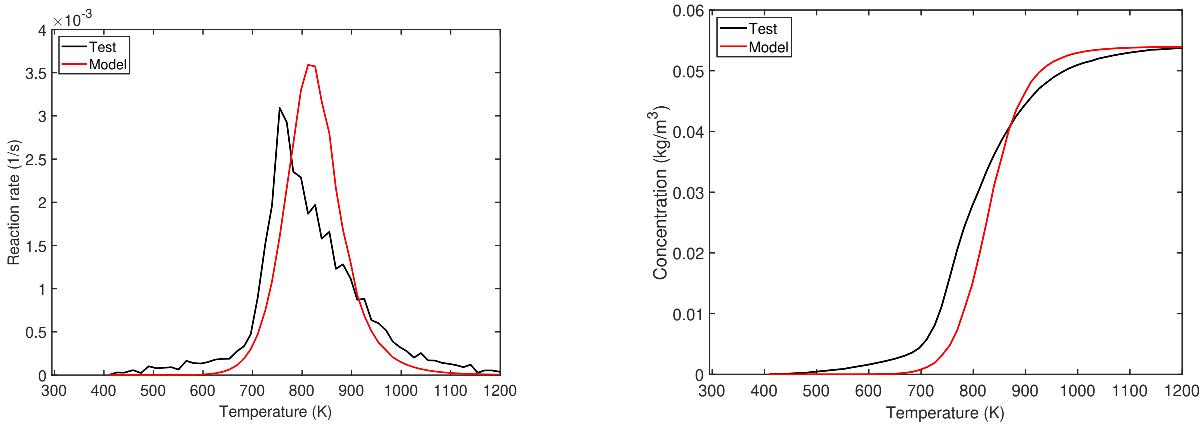

(a) CH_4 total reaction rate over temperature.

(b) CH_4 mass increase over temperature.

***Fig. 8**: Comparison of evolved gas reaction model with the experimental result: CH_4.*

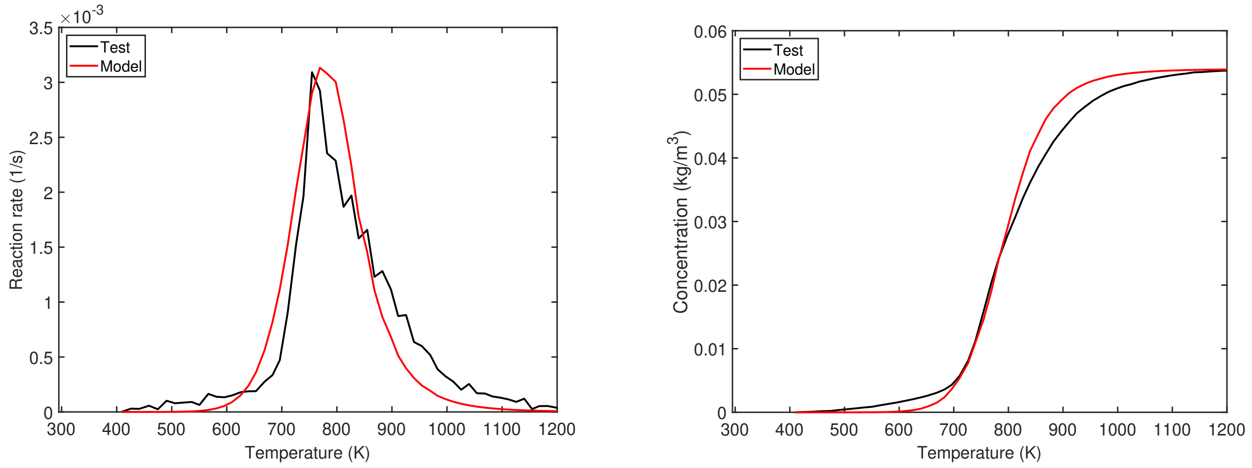

(a) C_2H_4 total reaction rate over temperature. *(b) C_2H_4 mass increase over temperature.*

***Fig. 9**: Comparison of evolved gas reaction model with the experimental result:C_2H_4.*

4.1 Transport effect

The heterogeneous reactions and phase transitions in coal particles will lead to a mass fraction change in species. Furthermore, due to the combustion, the enthalpy in the gas phase is increased. Therefore the temperature increases. The temperature increase results in pressure increase or decrease in the flow, thus creating a convective flow in the gas phase inside the particle. To model this flow, an Euler-Euler approach was used for the gas phase. The pressure drop is then derived by considering the pore diameter and the void volume.

The porous structure of the coal particle is assumed as a parallel channel (see in Fig. 1b). The Navier-Stokes equation for a 2D flow in the channel can be written in the cartesian coordinates on x direction as,

$$u\frac{\partial U}{\partial x} + v\frac{\partial U}{\partial y} - \nu\nabla^2 U = -\frac{1}{\rho}\frac{\partial p}{\partial x} \tag{6}$$

where, u,v are the velocities on x, y coordinates, m/s, ν is the kinematic viscosity of the fluid, m^2/s, ρ is the density of the fluid, kg/m^3.

The flow is assumed on x direction, so $v = 0$ (see in Fig. 10). For a fully developed flow in the steady state, u only changes along the y coordinate,and it keeps constant over the x coordinates at any y position.Therefore,$dU/dx = 0$. First two terms in Equation. (6) will be eliminated. The third term of Equation. (6) can be written as,

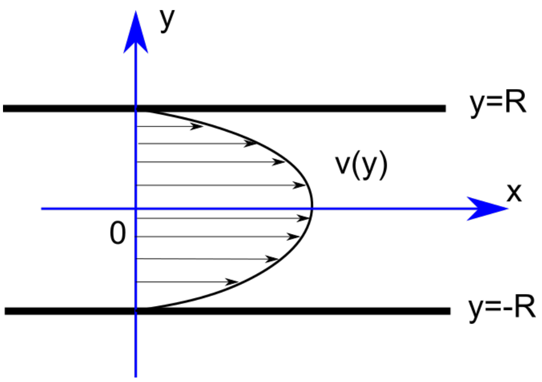

***Fig. 10**: Schematic of the fully developed fluid flow in a 2D channel.*

$$\nu\nabla^2 U = \nu(\frac{d^2U}{dx^2} + \frac{d^2U}{dy^2}) \tag{7}$$

Similarily, $d^2U/dx^2 = 0$, and Equation. (6) will finally be formed in,

$$\mu\frac{d^2U}{dy^2} = \frac{\partial p}{\partial x} \tag{8}$$

where μ is dynamic viscosity, $\mu = \rho\nu, N \cdot s/m^2$.

On the channel walls, the fluid velocity is zero ($U(top) = 0$, $U(bottom) = 0$). In the middle of the flow channel, there is $dU/dy = 0$. Using these values, the equation can be integrated and result as,

$$-\frac{\partial p}{\partial x} = \mu\overline{U} \cdot \frac{12}{D^2_{pore}} \tag{9}$$

This equation gives the relationship of the pressure drop on x direction, the diameter of the channel,D, and the average velocity, $\overline{U}$ on the direction of the channel.

To include the porous structure of the particle, the porosity coefficient ξ is introduced into the conservative equations. $\xi = 1$ represents a void domain where only gas exists. $\xi = 0$ represents a solid domain. The conservative momentum equation is three-dimensional in order to perform spatial observations within the model as well. The gas volume and the hydraulic pore diameter are stored in as "volScalarFields" because their value change comes from chemical reactions.

$$\frac{\xi\rho_g U}{\partial t} + \nabla\cdot(\xi\rho_g UU) - \nabla\cdot(\xi\tau_g) + \xi\mu\frac{12U}{D^2_{pore}} = -\xi\nabla p + \xi\rho_g g + S_U \tag{10}$$

The continuity equation of the gas phase is relatively simple. In addition to the transient term and convective transportation term, it contains source terms from the heterogeneous reactions.

$$\frac{\partial\xi\rho_g U}{\partial t} + \nabla\cdot(\xi\rho_g U) = S_m \tag{11}$$

Besides the transient and convective terms, the S_m are the interphase mass transfer terms from the solid phase due to heterogeneous reactions at the gas-solid interface or from physical processes such as evaporation. For our kinetic model, $\sum_{n=1}^{N} S_{gn} = 1$. In which N is the total number of species. In the solid phase, no convective transport takes place, and there is only a transient term from the pyrolysis for each species. Thereby, X is the mass concentration of the substance i in the computation cell. This will be implemented in the next steps.

$$\frac{\partial X_i}{\partial t} = -S_m \tag{12}$$

4.2 Conservation of energy

The energy equation for the gas phase in terms of the gas phase temperature is:

$$\xi C_{pg}(\frac{\partial T_g}{\partial t} + U\cdot\nabla T_g) = \nabla\cdot q_g - H_{gs} - \Delta H_{rg} \tag{13}$$

where C_{pg} is the heat capacity of gas mixture;q_g is the gas-phase conductive heat flux;H_{gs} describes fluid-solid interphase heat transfer, and H_{rg} is the heat of reaction in the gas phase.

The energy transport in the solid phase is implemented as an implicit function coupled with the gas phase using the heat transfer between two phases. The energy conservation of the particle phase includes the temporal dissipation of the volume-specific heat, the convective transport and the energy exchange to the gas phase.

$$\frac{(1-\xi)\rho_s C_{ps} T_s}{\partial t} - \nabla \cdot ((1-\xi)\lambda_s \nabla T_s) = S_g + \xi S_h \tag{14}$$

$$S_g = \xi A_V h(T_g - T_s) \tag{15}$$

The volume-specific heat flow between the two phases is determined by the volume-specific particle surface A_V and the average heat transfer coefficient h. The heat transfer coefficient is calculated using the particle Reynolds number through the similarity relationship described by Ranz-Marshall Ranz and Marshall (1952).

The energy conservation equation of the gas phase includes the time derivation of the volume-specific heat, the convective transport, the diffusive transport, the energy transfer to the gas phase and the source term for the energy from the particle combustion. This source term is derived from the combustion model via the source term Q and the enthalpy of combustion H.

$$\frac{(\xi \rho_g h)}{t} + \nabla(\xi \rho_g U h) - \nabla \cdot (\xi \alpha_{eff} \nabla h) = S_s + (1-\xi) S_h \tag{16}$$

4.3 Conservation of species

To fulfil heterogeneous reactions, the volatile from coal is created as volume scalars in the *createFields.H* file. Four evolved gases are assumed according to the coal kinetics data: CO, CO_2, CH_4, and C_2H_4. The species equation in the solid phase only considers the source terms in the heterogeneous reactions from chapter 3.2. In Equation. 17, X_i is the mass concentration of the substance i in the entire calculation cell.

$$\frac{\partial(X_i)}{\partial t} = -S_{het} \tag{17}$$

The conservation equation for the substances of the gas phase considers the porous volume, the source term of the heterogeneous reaction.

$$\frac{\partial(\xi \rho_g Y_i)}{\partial t} + \nabla(\xi \rho_g U Y_i) - \nabla \cdot (\xi D_{eff} \nabla \rho_g Y_i) = S_{het} + S_i \tag{18}$$

where Y_i is the mass fraction of the substance i from the gas phase. D_{eff} is the diffusivity, S_{het} and S_i are the source terms from the heterogeneous and homogeneous reactions respectively.

In the context of this work, the heterogeneous reaction after pyrolysis is not considered because the Oxygen is exhausted in the gas phase reaction during the dust deflagration.

5 Numerical approach

The coal particle is assumed to be in a sphere shape. To evaluate the models, a 1D geometry was created. As shown in Fig. 11, the geometry is a 6° x 6° section of a sphere in 100 equidistant cells along the axis. On the axis, the positive z-direction is pointing to the surface of the particle and the end of the other direction is the coal core. In this geometry, only two boundary conditions are needed. The first one is the particle surface, which is the outlet. The other surfaces on the geometry are "wedges", which represent the rotational symmetry of the geometry. The desired particle size can be defined by scaling the finished computational grid.

5.1 Thermophysical properties

In OpenFOAM, the temperature dependence of the fluid viscosity is determined through the Sutherland relationship with fixed valued for the Sutherland temperature T_{su} and the Sutherland coefficient

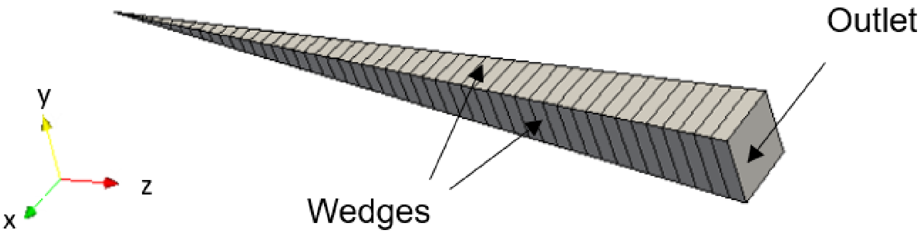

***Fig. 11**: Illustration of the computational grid of the 1D coal particle geometry.*

A_{su} implemented.

$$\mu = \frac{A_{su}\sqrt{T}}{1+T_{su}/T} \tag{19}$$

From the experiment result of Tomeczek (Tomeczek and Palugniok, 1996), the specific heat capacity c_s $(kJ/kg \cdot K)$ of coal during pyrolysis is correlated by the polynomial:

$$C_{ps}(T) = A1 + B1T + C1T^2 + D1T^3 + E1T^4 \tag{20}$$

where T is in °C, $A1 = 1.13 kJkg^{-1}K^{-1}$, $B1 = 3.58 \times 10^{-3} kJkg^{-1}K^{-2}$, $C1 = 2.28 \times 10^{-6} kJkg^{-1}K^{-3}$, $D1 = -9.81 \times 10^{-9} kJkg^{-1}K^{-4}$, $E1 = 4.63 \times 10^{-12} kJkg^{-1}K^{-5}$. The coefficients of Rydultowy coal from the paper are chosen for this study due to the similarity of the components between Rydultowy coal and the coal from this study.

The thermal conductivity for coal λ_s $(W/m \cdot K)$ is assumed to be a linear function of the temperature (Badzioch S, Field MA, 1964).

$$\lambda_s(T) = 0.23 \times (1 + 0.0033T) \tag{21}$$

5.2 Boundary condition

The heat and mass transfer coefficient on the particle surface should be employed by considering the dust deflagration boundary condition to the particle. The boundary condition is applied to the outlet in Fig. 11, where the pressure is 100 kPa and the velocity gradient is zero.

The description of heat transfer is based on the formulation according to Wittig et al. (2012), where the particle porosity effect in the surface heat transfer was considered. The Nusselt number on such surface is correlated with porosity ξ, Reynolds number and Prandtl number:

$$Nu = (4.31 - 12.71\xi + 9.81\xi^2) \cdot (1 + 0.8Re^{0.6}Pr^{\frac{1}{3}}) \tag{22}$$

The particle Reynolds number is calculated using the relative velocity between the particle and the environment fluid flow (Skjold, 2003). It is the ratio between inertial force and the viscous force on the particle and characterizes the flow around the particle.

$$Re = \frac{\rho_g |U_g - U_s| d_p}{\mu_g} \tag{23}$$

where U_g and U_s are the fluid velocity and particle velocity, ρ_g is the fluid density, d_p is the diameter of the particle, μ_g is the fluid dynamic viscosity. The particle velocity and fluid velocity used in dust deflagration is from (Pan et al., 2020).

The temperature dependent heat transfer coefficient of coal particle surface is obtained by inserting the variables into the function:

$$h_c(T) = Nu \cdot \frac{\lambda_g}{d_p} \tag{24}$$

In the implementation of the heat transfer coefficient into OpenFOAM boundary conditions, the temperature of the solid part and fluid part of one coal particle were considered separately.

The mass transfer of each species on the boundary is based on the formulation according to Ranz and Marshall (1952), where the particle Reynolds number has a range of validity from 0 to 200. The empirical functions were used because the occurring particle Reynolds numbers in the simulation of flame acceleration ranges between 0 and 36.2 (Spijker and Raupenstrauch, 2017). The Sherwood number is in correlation with the Reynolds number and Schmidt number.

$$Sh_i = 2 + 0.6Re^{1/2}Sc_i^{1/3} \tag{25}$$

The convective mass transfer rate of the coal particle surface is

$$h_{mix,i} = \frac{Sh_i D_{mix,i}}{d_p} \tag{26}$$

The temperature gradient and the individual substances gradient on the surface boundary are defined in the 0 folders of each OpenFOAM simulation case.

$$grad(T) = -\frac{h_c}{\lambda_s} \cdot (T_s - T_{inf}) \tag{27}$$

$$grad(Y_{mix,i}) = -\frac{h_{mix,i}(T)}{D_{mix,i}(T)} \cdot (Y_{b,i} - Y_{inf,i}) \tag{28}$$

where h_s , λ_s and T_s, T_{inf} are heat transfer coefficient between the particle and its surrounding air, thermal conductivity and temperature of the particle, and surrounding air temperature. The $Y_{mix,i}$ is the mass fraction of each specie from gas mixture;$Y_{b,i}$ and $Y_{inf,i}$ are the mass concentration of species i on the boundary and surrounding air.

6 Results and discussion

6.1 Model validation

6.1.1 Temperature profile

To validate the single-particle model, the boundary condition with temperature ramp 30 K/min was adapted to the simulation model. The particle is heated from room temperature to 1400 K over time. The temperature curves of solid and fluid phases on both of the particle surface and core positions are plotted in 12. Due to the low heating rate, the particle undergoes a long heat exchange time and reaches the boundary temperature. Except for the earlier stage, there is a temperature difference between the core and surface of the particle in both surface and core positions. There is a lower temperature profile in the core of the particle in fluid and solid phases. This is because of the low porosity inside of the particle in the early devolatilization stage, where the heat transfer takes time to reach the core of the particle.

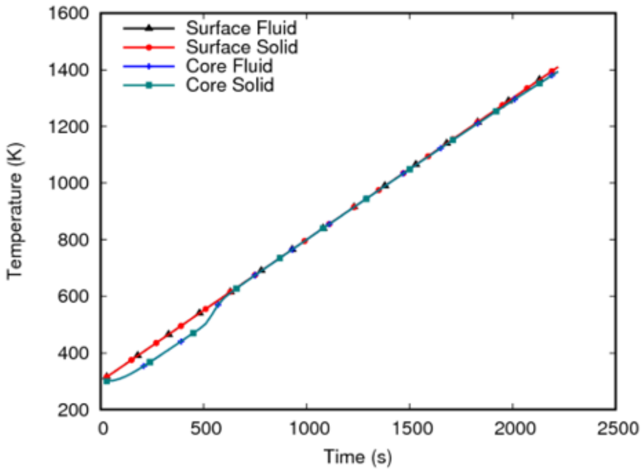

***Fig. 12**: Temperature profile of particle over time ($T_{bc}: 30K/min$).*

6.1.2 Heterogeneous reactions

The simulation result of the total mass decrease of coal is plotted and compared with the experiment result in Fig. 13a. In the simulation, the coal starts to decompose from 580 K, which is a little slower than the experiment. The lower prediction continues until 900 K.

The mass of the gas species that are evolved out of the solid particle is compared with the FTIR tests in Fig. 13b-13d. The prediction of the C_2H_4 has some differences with the experiments. It has a lower prediction at the beginning, which leads to the delayed reaction in Fig.13. The prediction of the CO and CO_2 mass increase are very well. The difference in 900 - 1000 K of CO and 750 - 1000 K comes from the model. The difference can be eliminated by more prediction functions but this would result in less applicability of the model. The variation is acceptable from the implemented model. Therefore, the single-particle model is able to predict particle behavior in high temperatures and can be used for further studies.

6.2 Shock tests and temperature profile

In order to explore the temperature profile and reactions of coal particles under sudden heat up conditions (Equation. (27 - 28)), the shock test with groovyBC(Gschaider, 2009) was carried out in the single-particle model. Constant temperature 1000 K was used as the boundary condition and four particle sizes: 25 μm, 50 μm, 125 μm, 250 μm were simulated. The temperature increase in the shock tests are in Fig. 14. The positions of particle core and surface are examined both in the fluid and solid phase of the particle. The T_c and T_s represent core temperature and surface temperature, respectively.

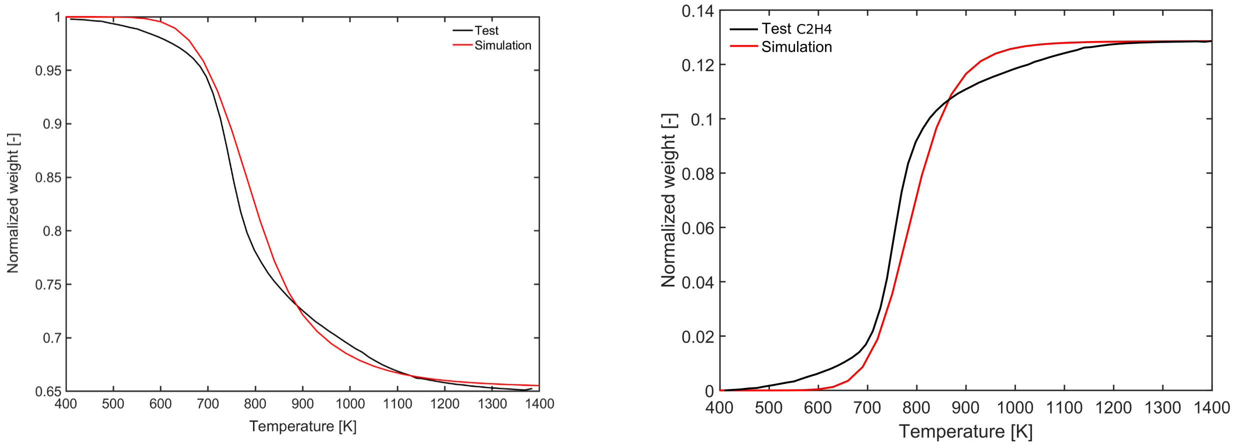

(a) Coal total mass decrease. *(b) C_2H_4 mass increase.*

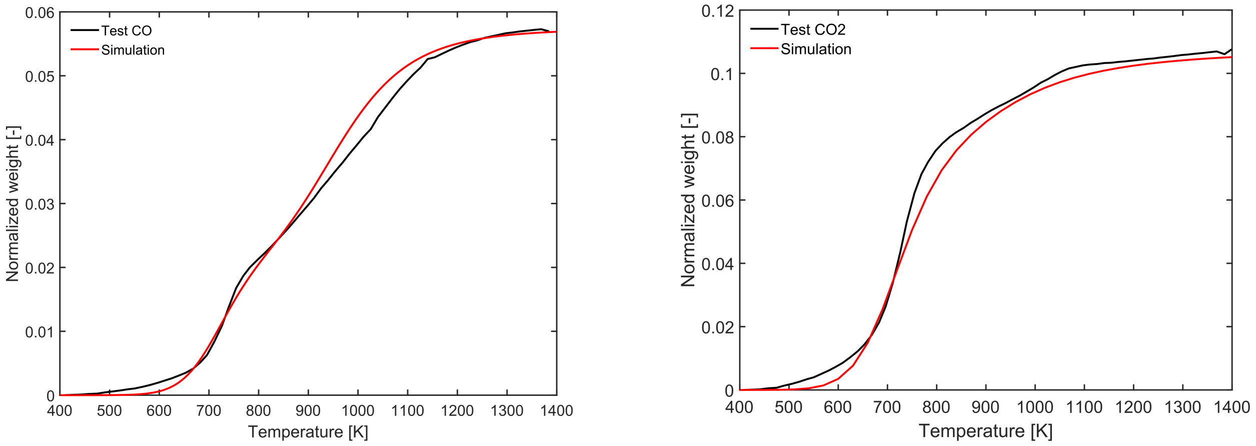

(c) CO mass increase *(d) CO_2 mass increase*

Fig. 13*: Comparision of simulation and experimental results: (a) Total coal mass loss over time; (b) C_2H_4; (c) CO; (d) CO_2.*

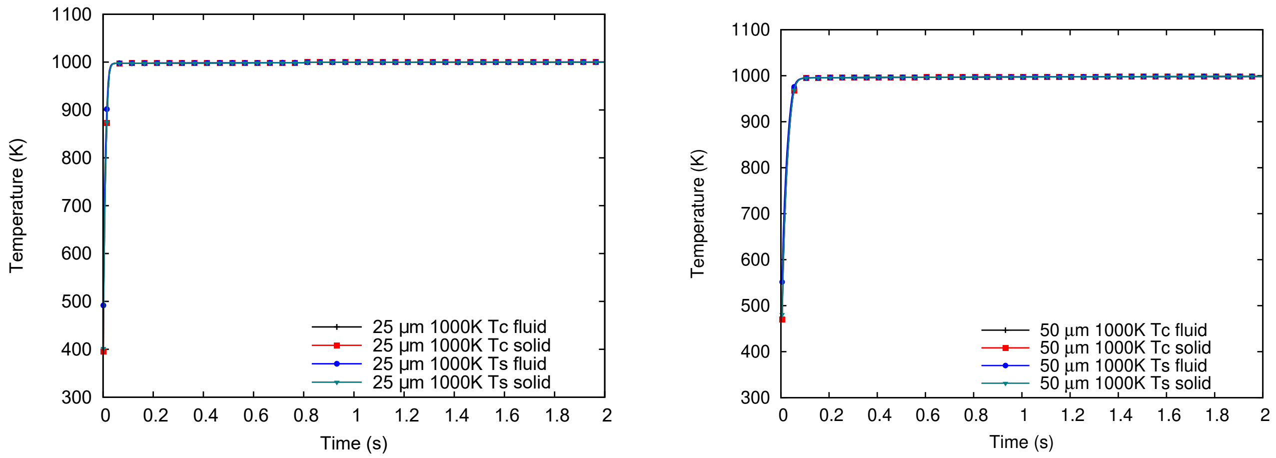

(a) 25µm *(b) 50µm*

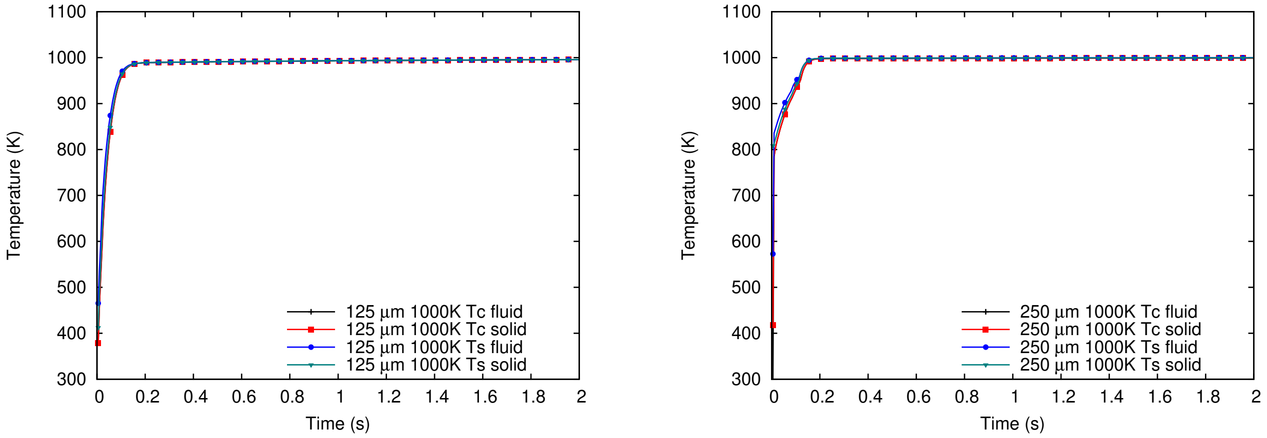

(c) 125µm *(d) 250µm*

Fig. 14: *The temperature increase over time of four particle sizes: (a)25 µm;(b)50 µm;(c)125 µm;(d)250 µm.* ($T_{bc} = -\frac{h_{mix}}{\lambda_s}(T_s - 1000K)$).

Due to the intensive heat exchange, the temperature of the particle increases to 1000 K within a very short time range. The particle also undergoes rapid heterogeneous reactions and produces pyrolysis gases. The difference between the particle core and solid is less remarkable than in Fig. 12. The temperature gradient in the particle will be further studied in the next steps by using different heating temperature. When the particle size increases, the time to heat up the particle increase. In Fig. 14d, the temperature increase rate decreases significantly. This is due to the increase of the coal pore size and a lower heat transfer between the boundary and the particle.

6.3 0D comparative model

In order to explore the inner particle temperature gradient effect on the prediction of particle reactions. A 0D model using MATLAB was created to model the reaction rate without the temperature gradient. The surface temperature increased to 2000 K in the comparison work, which is a more extreme situation than the 1000 K in the previous part.

The volume averaged temperature from the 1D model was used in the model. The kinetic models of the evolve gases as well as the particle size, the simulation time keep the same as the 1D OpenFOAM model. The reaction rates of the evolve gases from the 0D and 1D models are compared in Fig. 15. The dots represent the 0D model results.The 0D results are almost the same as the 1D model.Each gas specie reaction rate from different particle size is compared. When the particle size becomes larger, the maximum reaction rate of particles becomes lower. It takes more time for larger particles to heat up

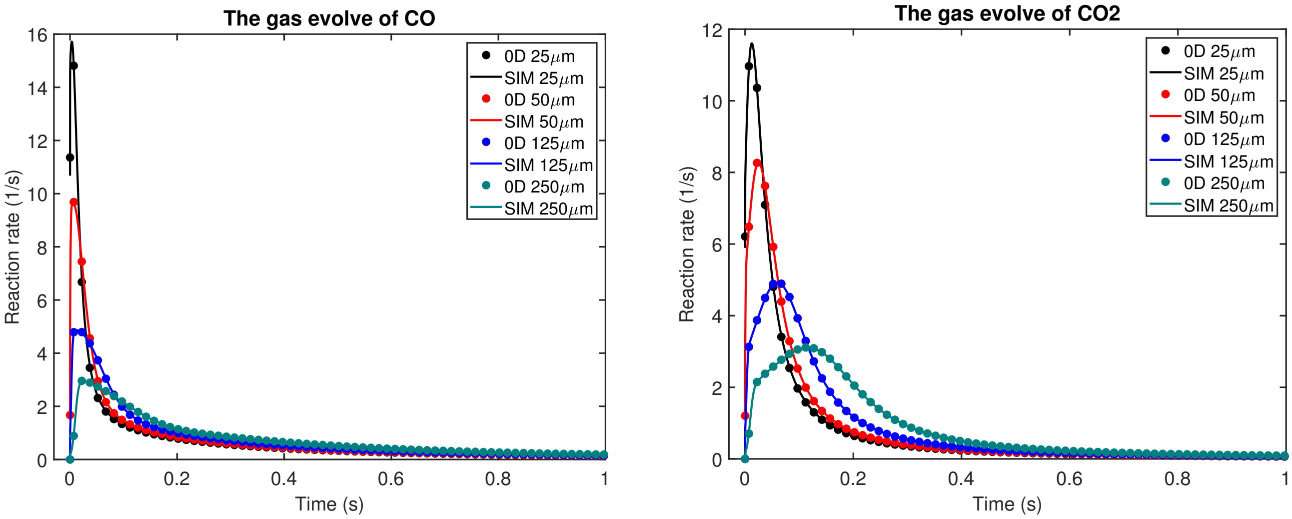

(a) CO *(b) CO_2*

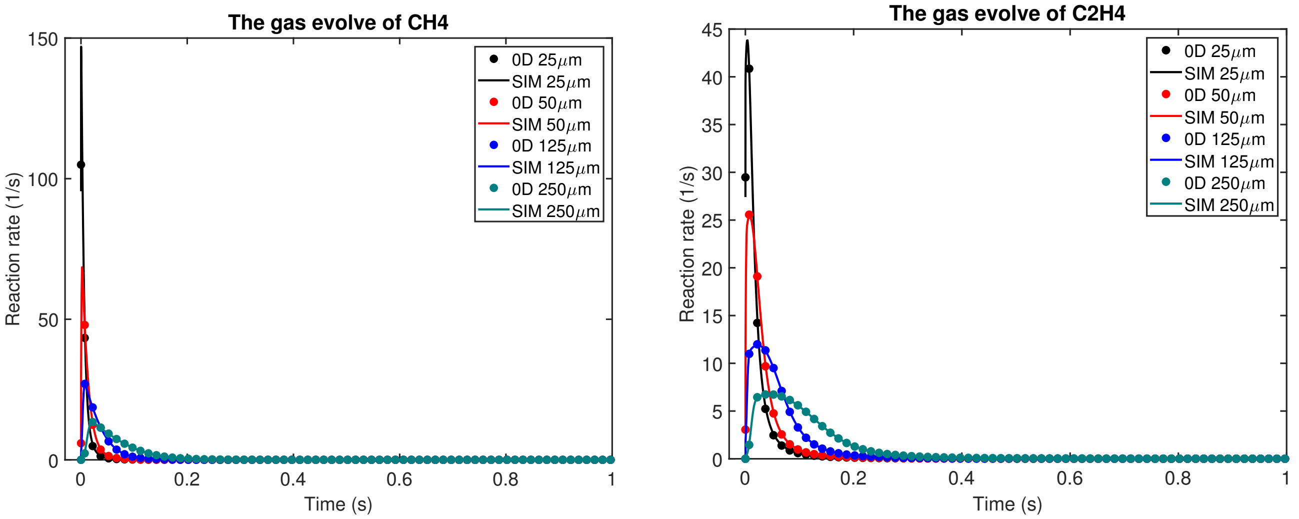

(c) CH_4 *(d) C_2H_4*

Fig. 15*: 2000 K shock test results:comparison of the evolve gas reaction rate between 0-D and 1-D models.Each gas evolve is compared between different particle sizes.(a)CO; (b)CO_2; (c)CH_4; (d)C_2H_4.*

and therefore the particles releases gases slower. In the deflagration, the CO_2 has the widest reaction peak. And the CH_4 is the least one but with very high maximum reaction rate values. However, the dots from 0D cases fall on the simulation results exactly. They do not make a remarkable difference. Therefore, the temperature gradient inside of the particles which are not larger than 250 μm can be ignored in the dust deflagration.

7 Conclusions

In this paper, a single-particle model was developed for the deflagration of coal dust. The TGA experiments were conducted to obtain the kinetic data of the coal sample. Two active pyrolysis phases were identified in the TG curve: at 700 - 800 K and 900 - 1000 K. The second reaction rate peak is due to the gases tar reaction when the temperature increase to a higher range. In the dust deflagration simulations, the second pyrolysis should not be ignored because it would lead to a lower reaction rate and not promising predictions. Therefore, an alternative approach by counting the evolved gases was used. The evolved gases during the pyrolysis of coal are analyzed by the FTIR instrument. In order to implement the kinetic data and evolved gas content into the dust deflagration simulations, submodels of the gas evolvement are applied. The kinetic data of the gases were obtained, some of which are two-function models. The models were implemented into the CFD simulations, which is a two-phase Eulerian model including the particle porosity, heat transport of conduction and convection, the pyrolysis of particle and species transport in the porous structure.Finally, a 0D model was created in order to explore the inner particle temperature gradient effect.

The single-particle model shows promising results in the prediction of dust decomposition, including the heterogeneous reaction and mass and heat transport phenomenon. From the 0D and 1D simulation results, the temperature gradient does not effect strongly on the evolution of the volatile content of the particle if the particle size is under $250\mu m$. The further steps would be using the single-particle model to predict the dust explosion process. By using a simplified model, the computation time would be reduced remarkably and a new method in predicting the dust explosion process is proposed.

Acknowledgements

PY acknowledges the financial support of the China Scholarship Council (CSC, No. 201808420277). The authors are grateful for the computing time granted by the Chair of Thermal Processing Technology (TPT), University of Leoben.

References

Badzioch S, Field MA, G. D. (1964). *Investigation of temperature variation of thermal conductivity and thermal diffusivity of coal.* Fuel, 43(4):267–272.

Dong, M., Zheng, C., Miao, S., Zhang, Y., Du, Q., Wang, Y., Tittel, F. K. (2017). *Development and measurements of a mid-infrared multi-gas sensor system for CO, CO2 and CH4 detection.* Sensors (Switzerland), 17(10). ISSN 14248220. doi:10.3390/s17102221.

Gschaider, B. F. (2009). *groovybc.*

King, P. L., Vennemann, T. W., Holloway, J. R., Hervig, R. L., Lowenstern, J. B., Forneris, J. F. (2002). *Analytical techniques for volatiles: A case study using intermediate (andesitic) glasses.* American Mineralogist, 87(8-9):1077–1089. ISSN 0003004X. doi:10.2138/am-2002-8-904.

Kittinger, F. (2019). *Simultaneous thermal analysis with ftir gas analysis.* Technical report, Montanuniveristaet Leoben.

Pan, Y., Spijker, C., Raupenstrauch, H. (2020). *Investigations on the effect of particle size on dust dispersion in mike 3 apparatus.* In *13th International Symposium on Hazards, Prevention, and Mitigation of Industrial Explosions (ISHPMIE).*

Ranz, W., Marshall (1952). *Evaporation from drops.* Chemical Engineering Progress, 48:141–146.

Skjold, T. (2003). *Selected aspects of turbulence and combustion in 20-Litre explosion vessels: Development of Experimental Apparatus and Experimental Investigation.* (June):324.

Skjold, T. (2007). *Review of the DESC project.* Journal of Loss Prevention in the Process Industries, 20(4-6):291–302. ISSN 09504230. doi:10.1016/j.jlp.2007.04.017.

Spijker, C., Raupenstrauch, H. (2017). *Numerical investigation on inner particle effects in lycopodium/air dust deflagrations.* Journal of Loss Prevention in the Process Industries, 49:870–879.

Tomeczek, J., Palugniok, H. (1996). *Specific heat capacity and enthalpy of coal pyrolysis at elevated temperatures.* Fuel, 75(9):1089–1093. ISSN 00162361. doi:10.1016/0016-2361(96)00067-1.

Wittig, K., Golia, A., Nikrityuk, P. A. (2012). *3D numerical study on the influence of particle porosity on heat and fluid flow.* Progress in Computational Fluid Dynamics, An International Journal, 12(2/3):207. ISSN 1468-4349. doi:10.1504/PCFD.2012.047463.

DOI: 10.7795/810.20221124

A Numerical Model for the Minimum Ignition Temperature of Dust Clouds

Tengfei Chen [a], Jo Van Caneghem [b], Jan Degrève [c], Jan Berghmans [d], Filip Verplaetsen [c,e], &
Maarten Vanierschot [a]

[a] KU Leuven, Department of Mechanical Engineering, Group T Leuven Campus, A. Vesaliusstraat 13, B-3000 Leuven, Belgium
[b] KU Leuven, Department of Materials Engineering, Group T Leuven Campus, A. Vesaliusstraat 13, B-3000 Leuven, Belgium
[c] KU Leuven, Department of Chemical Engineering, Celestijnenlaan 200F, B-3001 Leuven, Belgium
[d] KU Leuven, Department of Mechanical Engineering, Celestijnenlaan 300A, B-3001 Leuven, Belgium
[e] Adinex NV, Brouwerijstraat 11, B-2200 Herentals, Belgium

E-mail: tengfei.chen@kuleuven.be & chentf19946@163.com

Abstract

This paper presents a numerical model for the calculation of the minimum ignition temperature (MIT) of dust clouds based on the Godbert-Greenwald furnace. The model considers heat transfer between the air and dust particles, the dust particle reaction kinetics, and the residence times of dust clouds in the furnace. For all the 13 dust samples studied, deviations between the calculated and the experimental MIT values are within 20% (6.57% on average). There is also good agreement between the experimental and the numerical MIT variation trends against dust concentration and particle size. Two different ignition modes are discovered. The first one consists in ignition near the furnace wall for bigger particles characterized by rather short residence times. In the second mode, the ignition starts from the center of the furnace by self-heating of the dust cloud for smaller particles with longer residence times. For magnesium, as dust concentration increases, the lowest ignition temperature of the dust cloud *IT(conc)* decreases first, then transits to increase at a certain point. The transition happens at different dust concentrations for different particle sizes. Moreover, the MIT of the magnesium dust cloud generally increases as particle size increases, but the increasing trend stagnates within a certain medium particle size range.

Keywords: *minimum ignition temperature, dust clouds, numerical model*

1. Introduction

The minimum ignition temperature (MIT) of a dust cloud is an important parameter for the assessment of the dust cloud explosion risks with hot surface ignition sources in related process industries. Numerous experimental studies on the MIT of dust clouds have been undertaken in recent years (Nifuku et al. (2007), Cao et al. (2012), Boilard et al. (2013), Mittal (2014), Janès et al.(2014), Miao et al.(2016), Addai et al. (2016a, 2016b, 2017), Mishra et al. (2018), Cao et al. (2019), Deng et al. (2019), Tan et al. (2020), Wang et al. (2020), Sun et al. (2020), Gabel et al. (2021) and Krietsch et al. (2021)). The most popular apparatus to measure the MIT is the Godbert-Greenwald furnace (G-G furnace) (Eckhoff, 2019). With the G-G furnace, the MIT is defined as the "the lowest temperature of a hot surface on which the most ignitable mixture of the dust with air is ignited under specified test conditions" (ISO/IEC 80079-20-2, 2016). The tests have to be performed under variation of both dispersion pressure and dust concentration until the MIT is found. Although there are theoretical models developed for the MIT calculation (Yuan et al. (2012), Addai et al. (2016c) and Arshad et al.

(2021)), these models ignore the temperature gradient and evolution inside a dust cloud during the ignition process.

In this study, a numerical model is established for the MIT calculation of dust clouds based on the G-G furnace, with consideration of the heat transfer between the air and dust particles, the dust particle reaction kinetics, and the residence time of dust particles in the furnace. As mentioned above, G-G furnace is the most popular MIT testing equipment, thus most of the available experimental MIT data are also generated with the G-G furnace. Therefore, numerical data with the model developed based on the G-G furnace expected to be more comparable with the experimental results. Temperature gradient and evolution in the dust cloud is studied in detail for different dusts and different furnace temperatures, then the calculated MIT data are compared with the experimental results. Finally, the influence of dust concentration and particle size on the MIT is discussed.

2. Methods and materials

2.1 Physical model

The physical model for the MIT calculation of dust clouds in Fig. 1 is based on the G-G furnace MIT testing equipment illustrated in Fig. 2. In such a furnace, the dust particles are not pre-mixed with the hot gas initially present in the furnace chamber, but are blown into the chamber with the cold pressurized gas forming an initial cold dust cloud with ambient temperature. The initially cold dust cloud is then gradually heated up during its downwards movement. Therefore, the ignition of a dust cloud not only depends on the furnace temperature, but also on the dust cloud residence time in the furnace chamber before the dust cloud falls out from bottom of the furnace. If the dust particles cannot absorb enough heat for their ignition during their residence time, then it is likely that the ignition fails.

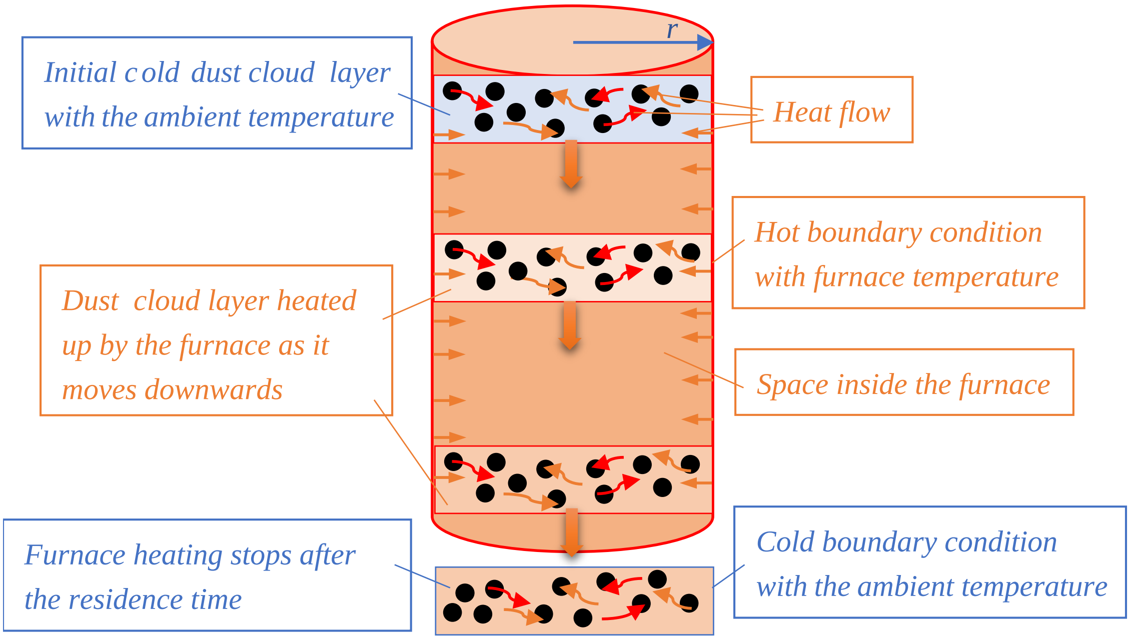

Fig. 1. *Physical model for the MIT calculation*

DOI: 10.7795/810.20221124

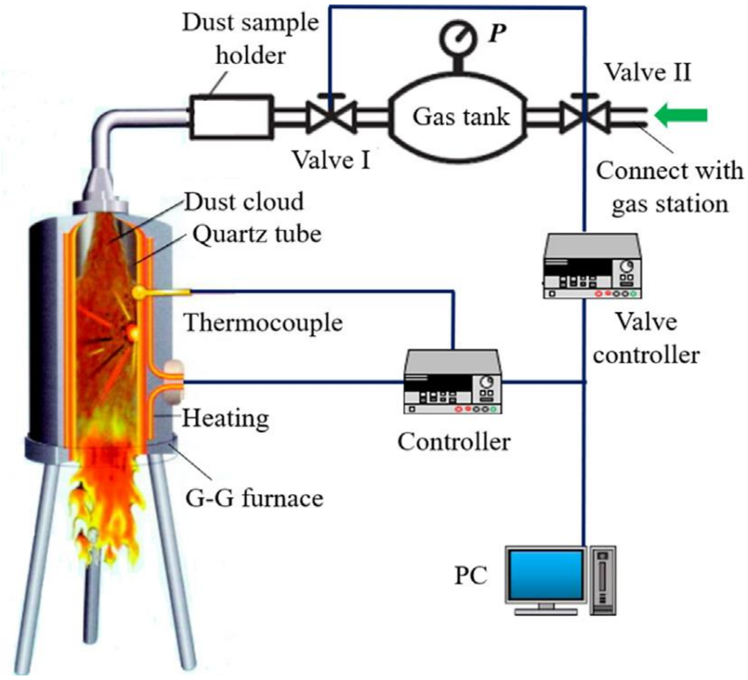

Fig. 2. *Schematic diagram for G-G furnace set up (Tan et al., 2020)*

In Fig. 1, an initially cold dust cloud layer in a cylindrical space with the size of the furnace heating chamber is used to simulate the dust cloud ignition process in the G-G furnace MIT test. Ideally, the dust particles are assumed to be distributed uniformly in the dust cloud layer. Since dust clouds in the test are not pre-heated before entering the heating chamber, the initial dust cloud layer temperature in Fig. 1 is set as the ambient temperature. During the dust cloud residence time in the furnace, the cylindrical dust cloud layer boundary temperature is set as the furnace heating surface temperature. Afterwards, the boundary temperature is set to be the ambient temperature to simulate the scenario after the dust cloud layer drops out of the furnace heating chamber. It must be noted that the numerical model for the MIT calculation is a one-dimensional model, so in Fig. 1 the axial direction is assumed to be adiabatic. In the G-G furnace tests, successful ignition of the dust cloud requires a visual observation of the flame. Therefore, in this numerical study the criterion for successful ignition of the dust cloud is also the occurrence of ignition in the dust cloud and the propagation of ignition through the dust cloud.

2.2 Governing equations

The dust cloud residence time in the furnace heating chamber can be estimated based on the settling velocity of the dust particles obtained by the Stokes law (Hosseinzadeh, 2018):

$$v_s = \frac{(\rho_s - \rho_g) d_p^2 g}{18\mu} \tag{1}$$

$$t_{res} = \frac{H_{fur}}{v_s} \tag{2}$$

where

ρ_s — particle density, kg/m^3;

ρ_g — gas density, kg/m^3;

d_p— particle size, m;

g — gravity acceleration, 9.81 m/s^2;

μ — dynamic viscosity, N·s/m^2, calculated with Sutherland's formula as a function of the furnace inner surface temperature (White, F.M., 2006);

v_s — dust particle settling velocity, m/s;

t_{res} — dust cloud residence time in the G-G furnace, s;

H_{fur} — height of the G-G furnace, m.

It must be noted that in a real dust cloud in the G-G furnace, the residence time can be different among the dust particles and between the particles and the gas phase. The residence time is also subject to the dust blowing pressure. Therefore, Eq. (1) and Eq. (2) can be viewed as an ideal mathematical expectation of the dust cloud residence time in the furnace. Moreover, the sudden drop of the boundary temperature after the residence time is also not a realistic setting. It must be admitted that the physical model in Fig. 1 is after all a highly simplified model, focusing on the very basic characteristics of the dust cloud ignition process in the G-G furnace.

Similar to the governing equations of the dust cloud minimum ignition energy (MIE) calculation (Chen et al., 2020; Chen et al., 2021), the MIT calculation in this study is also based upon the heat transfer in the gas phase and from the gas to the dust particles. Considering the cylindrical shape of the furnace, it is assumed here that the heat transfer is mainly in the radial direction. This leads to the following energy balance equation (Taler and Duba, 2006)):

$$\varepsilon_g \rho_g C_{p\_g} \frac{\partial T_g(r,t)}{\partial t} = \frac{1}{r}\frac{\partial}{\partial r}\left(\varepsilon_g\, k_g r \frac{\partial T_g(r,t)}{\partial r}\right) - \left(1-\varepsilon_g\right) h_s a_p \left(T_g(r,t) - T_s(r,t)\right) + \left(1-\varepsilon_g\right)\omega_{org} Q_{org} \quad (3)$$

with initial conditions: $T_g(r\ ,0) = T_a$ and

boundary conditions: $T_g\left(r_{fur}, t \le t_{res}\right) = T_{fur}$, $T_g\left(r_{fur}, t > t_{res}\right) = T_a$ and

$$\frac{\partial T_g(0,t)}{\partial r} = 0$$

where

ε_g— volume fraction of the gas phase (in this study it is the air) in the dust cloud;

C_{p_g}— gas specific heat, J·(kg·K)$^{-1}$;

k_g— gas thermal conductivity, W·(m·K)$^{-1}$;

a_p —$\frac{S}{V_s} = \frac{6}{d_p}$, specific external surface area of particle, 1/m;

V_s —volume of a single particle, $V_s = \frac{4}{3}\pi\left(\frac{d_p}{2}\right)^3$;

h_s— convective heat transfer coefficient, $h_s = \frac{N_u k_g}{d_p}$, W·(m^2·K)$^{-1}$, N_u— Nusselt number, assumed constant for dust particles (Nu = 2) (Yarin and Hetsroni, 2004);

S — surface area of a single particle, $S = 4\pi\left(\frac{d_p}{2}\right)^2$, m^2;

$T_g(r,t)$ — air temperature, K;

$T_s(r,t)$ — particle temperature, K;

T_a — ambient air temperature, 300 K;

T_{fur} — furnace inner surface temperature, K;

r_{fur} — furnace inner radius, m;

ω_{org}— volume reaction rate of organic dust particles, kg·(m^3·s)$^{-1}$;

Q_{org} — heat of combustion per mass of the organic material, J/kg.

The evolution of the particle temperature is governed by the following equation (Yarin and Hetsroni (2004)):

$$\rho_s C_{p\_s} \frac{dT_s(r,t)}{dt} = h_s a_p \left(T_g(r,t) - T_s(r,t)\right) + \omega_{met} Q_{met} \tag{4}$$

With initial condition: $T_s(r,0) = T_a$

where:

C_{p_s}— particle specific heat, J·(kg·K)$^{-1}$;

ω_{met}— volume reaction rate of metal dust particles, kg·(m^3·s)$^{-1}$;

Q_{met} — heat of combustion per mass of the metal material, J/kg.

It must be noted that it is assumed that for organic dust particles, their combustion happens mainly in the gas phase (Wu et al., 2022), and for metal particles their combustion happens usually on the particle surface (Yuan et al., 2012). Therefore, in this study the heat generation from organic dust particles $\omega_{org} Q_{org}$ is put in Eq. (3) and from metal dust particles $\omega_{met} Q_{met}$ is put in Eq. (4). With the discrete particle distribution in space, the above equations can only be solved numerically. In this study, the same numerical approach for the MIE calculation in Chen et al. (2020, 2021) is applied for the MIT calculation using the finite difference and energy balance method.

2.3 Materials

The dust materials used for the MIT calculation in this study are listed in Table 1, along with the corresponding G-G furnace parameters of r_{fur} and H_{fur}. Basic properties such as particle density, heat of combustion and heat capacity can all be found in Chen et al. (2021). Table 1 also includes the forms of Arrhenius equations for the volumetric reaction rate ω from literature for all the studied dust materials.

***Table 1:** Material properties and furnace parameters*

Material	r_{fur}/m	H_{fur}/m	ω/ kg·(m^3·s)$^{-1}$
Magnesium (Nifuku et al., 2007)	0.03	0.526	$\omega_{Mg} = A_{Mg}\rho_g Y_{O_2,S} a_p e^{\frac{-E_{Mg}}{RT_s}}$, A_{Mg} — 8.6·10^8 m/s, ρ_g —1.205 kg/m^3, $Y_{O_2,S}$ —0.232, E_{Mg} — 188780 J/mol. (Gurevich et al., 1968)
Aluminum (Nifuku et al., 2007)	0.03	0.526	$\omega_{Al} = A_{Al} a_p e^{\frac{-E_{Al}}{RT_s}}$, A_{Al} — 1.6·10^7 kg·(m^2·s)$^{-1}$, E_{Al} — 57600lgd$_p$+562600 J/mol. (Zhang et al., 2020)
Zirconium (Cao et al., 2019)	0.0195	0.23	$\omega_{Zr} = A_{Zr}\rho_s \frac{6(d_p-2\varepsilon_0)^2}{{d_p}^2(d_p-2\varepsilon_0)\varepsilon_0} e^{\frac{-E_{Zr}}{RT_s}}$, A_{Zr} — 4.361·10^{-5} m^2·s^{-1}, E_{Zr} — 36400lgd$_p$+266200 J/mol, ε_0 — 1.45 nm. (Zhang et al., 2020; Bakradze, 2011)
Lycopodium (Addai et al., 2016a)	0.0175	0.42	$\omega_{Lyco} = A_{Lyco}\rho_s e^{\frac{-E_{Lyco}}{RTa}}$, A_{Lyco} —10$^{7.04}$ s^{-1}, E_{Lyco} — 121102 J/mol. (Zhou, 2013)
Corn starch (Addai et al., 2016a)	0.0175	0.42	$\omega_{Corn} = A_{Corn}\rho_s e^{\frac{-E_{Corn}}{RTa}}$, A_{Corn} —10$^{12.2}$ s^{-1}, E_{Corn} — 218650 J/mol. (Zhou, 2013)
Mahogany wood (Chen et al., 2016)	0.0195	0.23	$\omega_{Wood} = A_{Wood}\rho_s e^{\frac{-E_{Wood}}{RTa}}$, A_{Wood} —3.04·10^6 s^{-1}, E_{Wood} — 104800 J/mol. (Wen et al., 2004)

A — pre-exponential factor; E — activation energy; $Y_{O_2,S}$ — mass fraction of the oxygen on metal surface; R — universal gas constant, 8.314 J/(mol·K); ε_0 — initial oxide thickness of metal particles.

It must be noted that in Cao et al. (2019) and Chen et al. (2016), r_{fur} and H_{fur} of the furnace used for their tests are not clearly stated. However, the commonly used G-G furnace has r_{fur} of around

0.0195 m, and H_{fur} of approximately 0.23 m with a volume of around 0.27 L (Mittal, 2014). Therefore, in this study, these common values for r_{fur} and H_{fur} are assumed for the calculation of the zirconium powder (Cao et al., 2019) and mahogany wood powder (Chen et al., 2016).

3. Results and discussion

3.1 Temperature profiles

Figure 3 and 4 show gas temperature profiles of a 29 µm and a 90 µm magnesium dust cloud at critical furnace temperatures, respectively. During the ignition process, the gas phase acts as heat carrier from the furnace to the particles and the heat exchanger between particles, so here the gas temperature profiles are used to help in understanding the ignition process. Clearly, the 250 g/m^3 29 µm magnesium dust cloud can be successfully ignited with T_{fur} of 762 K which gives rise to a sudden temperature jump. While with T_{fur} of 761 K, such sudden temperature jump cannot be observed in the dust cloud so the ignition fails at this temperature. Therefore, the MIT of 250 g/m^3 29 µm magnesium dust cloud is 762 K. Similarly, based on Fig. 4, the MIT of 1000 g/m^3 90 µm magnesium dust cloud is 829 K.

Comparison between Fig. 3(a) and Fig. 4(a) also reveals some interesting aspects regarding the ignition process. Figure. 3(a) refers to smaller particles of 29 µm characterized by a rather longer residence time of 23.2 s (Eq. (1) and (2)) with T_{fur} = 762 K. It shows that by the time of 23.2 s, gas temperature profiles across the dust cloud already rise to the same level of the furnace temperature. Then even after 23.2 s when the dust cloud layer falls out from the furnace, the self-heating from the chemical reaction of dust particles still enables a thermal runaway at the center of the dust cloud. Afterwards, the ignition propagates from the center outwards throughout the dust cloud. On the other hand, Fig. 4(a) refers to the bigger particles of 90 µm with shorter residence time of 2.54 s with T_{fur} = 829 K. As a result, by the time of 2.54 s, Fig. 4(a) shows that at radial positions with r < 0.02 m the gas temperature profiles still stay near the ambient level. Therefore, the self-heating of the dust cloud is rather insignificant with such a short residence time, and the ignition starts from particles near the hot furnace boundary and then propagates inwards to the center of the dust cloud. In conclusion, for dust clouds with shorter residence times in the furnace, successful ignition depends on the thermal ignition of dust particles near the hot furnace boundary within the residence time. For dust clouds with longer residence times in the furnace, successful ignition relies more on whether the self-heating of the dust cloud during (and even after) the residence time can trigger a thermal explosion inside the dust cloud.

It must be noted that in this numerical model there is a sudden drop of the boundary temperature of the dust cloud from the furnace temperature to the ambient temperature. This is a very ideal assumption. In reality, the drop of the boundary temperature takes time, so the assumption of sudden drop of the boundary temperature can result in rather high MIT predictions. However, on the other hand, after the dust cloud drops out of the furnace, in reality the dust cloud will potentially expand since the physical restriction of the furnace wall is lifted. This expansion factor is a disadvantage for the heat accumulation in the dust cloud, but it is also not considered in the numerical model, so this will lead to potential lower MIT predictions. It must be admitted that the physical behaviors of the dust cloud during the MIT test is rather complex, with the current simple numerical model some influencing factors cannot be revealed.

DOI: 10.7795/810.20221124

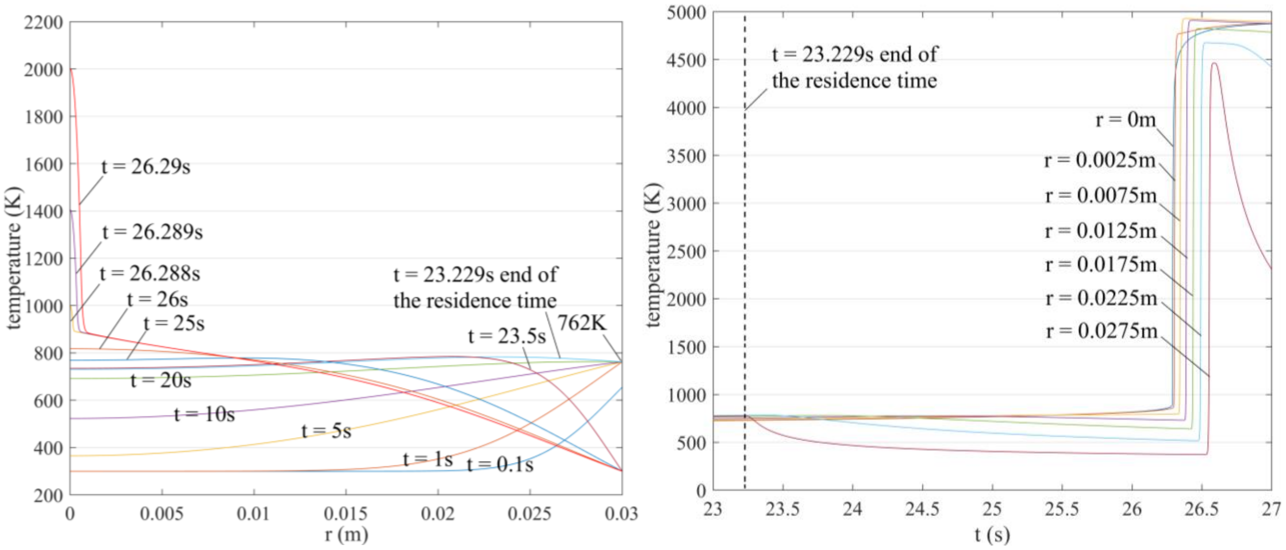

a. T_{fur} = 762 K

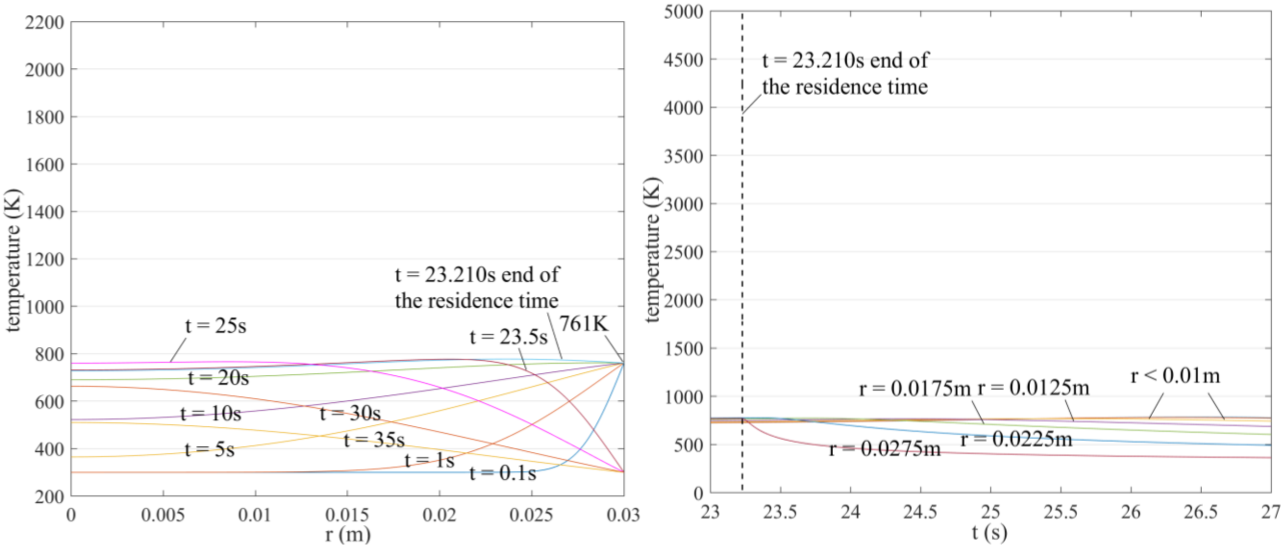

b. T_{fur} = 761 K

Fig. 3. *Gas phase temperature profiles of 250 g/m^3 29 µm magnesium dust cloud with T_{fur} of 762 K and 761 K*

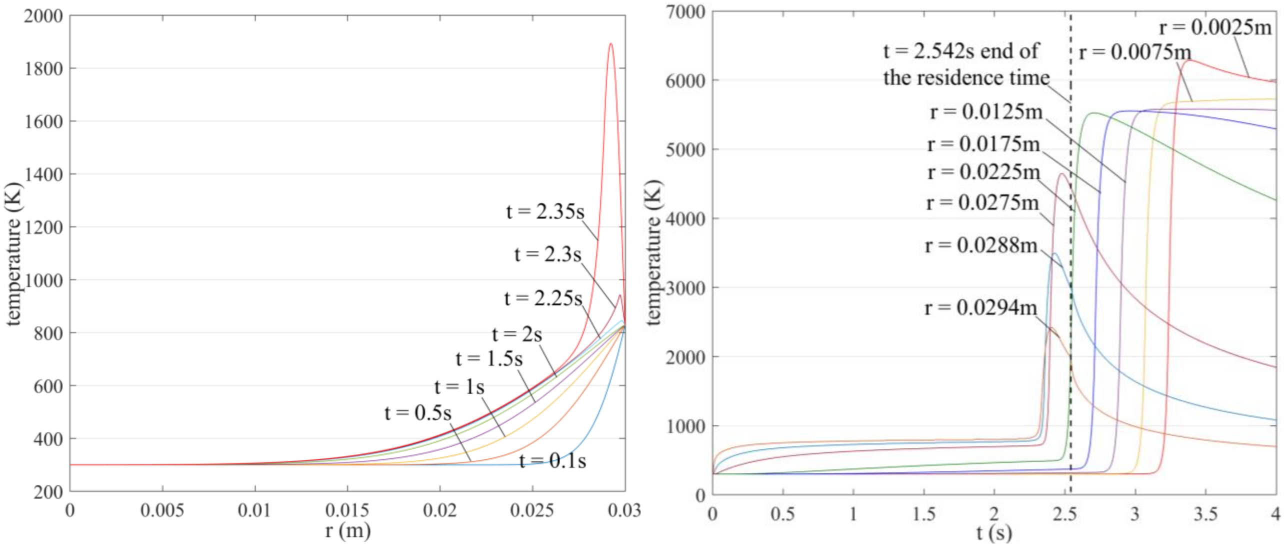

a. T_{fur} = 829 K

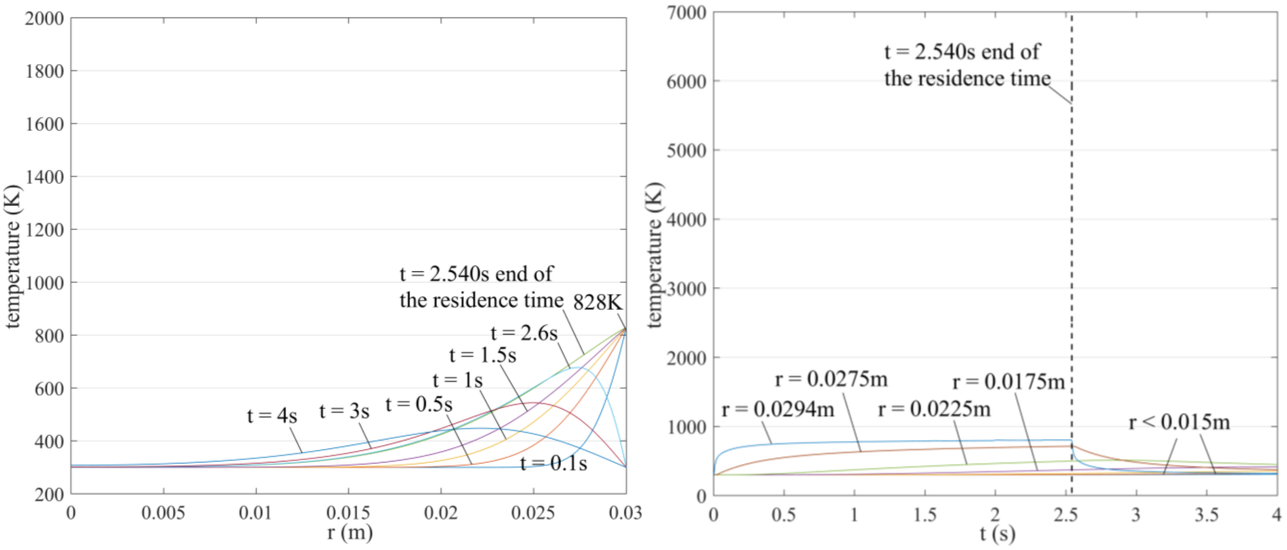

b. T_{fur} *= 828 K*

Fig. 4. *Gas phase temperature profiles of 1000 g/m*^{3} *90 μm magnesium dust cloud with* T_{fur} *of 829 K and 828*

3.2 Comparison between experimental and numerical MIT data

Table 2: *Comparison between the experimental and calculated MIT for the studied dusts (calculated data within the dust concentration range: 10 ~ 5000 g/m3)*

Dust	**Particle size /μm**	**MIT experimental /K**	**MIT numerical /K**	**Absolute error (MIT numerical−MIT experimental)/K**	**Relative error $(\frac{MIT\ numerical}{MIT\ experimental} -$ 1)/%**
Magnesium (Nifuku et al., 2007)	10	786	634	-152	-19.3
	29	803	757	-46	-5.73
	41	803	792	-11	-1.37
	60	836	825	-11	-1.32
	90	848	828	-20	-2.36
	115	851	827	-24	-2.82
	137	858	837	-21	-2.45
	163	898	879	-19	-2.12
Aluminum (Nifuku et al., 2007)	15	1023	1126	103	10.1
Zirconium (Cao et al., 2019)	33.5	503	464	-39	-7.75
Lycopodium (Addai et al., 2016)	31	680	609	-71	-10.4
Corn starch (Addai et al., 2016)	29	645	757	112	17.4
Mahogany wood (Chen et al., 2016)	85.5	733	750	17	2.32

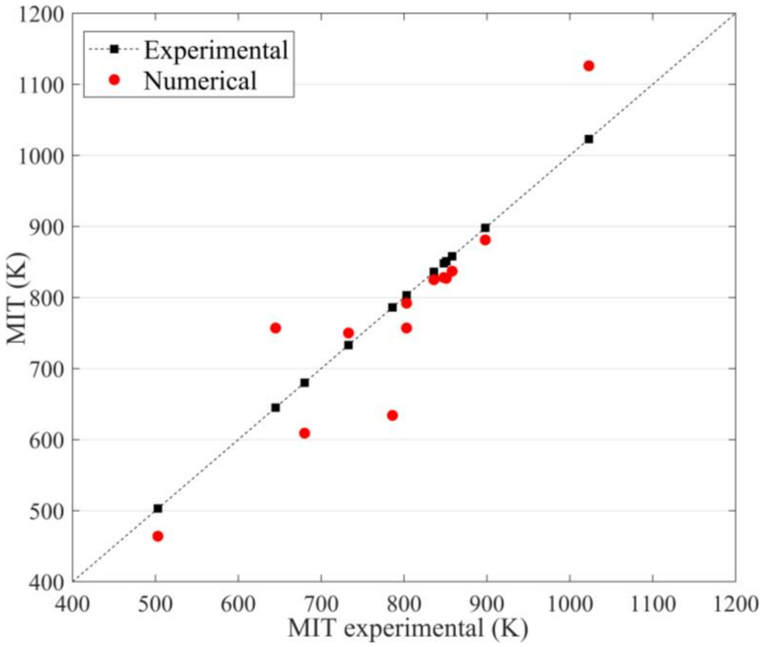

Fig. 5. *Comparison between the experimental and calculated MIT for the studied dusts (calculated data within the dust concentration range: 10 ~ 5000 g/m^3) (data from Table 2)*

Table 2 and Fig. 5 compare the experimental and calculated MIT results. In general, the numerical model in this study is proven to agree with the experimental data. However, there are still deviations between the absolute experimental and numerical MIT values. From the perspective of the relative error, deviations between the experimental and calculated MIT values are within 20% with an average deviation of 6.57%. When it comes to the absolute error, among the 13 dusts studied, 7 dusts are with the absolute error lower than 25 K, 2 dusts with 25 ~ 50 K, but there are 3 dusts with absolute errors higher than 100 K. Deviations mainly come from the simplification and idealization of the physical model, uncertainty in the Arrhenius forms of the volumetric reaction rate ω, inaccuracy of the experimental tests and possible agglomeration of certain materials or sizes of dust particles. Moreover, comparing with the experimental tests, the estimated dust cloud residence time with Eq. (1) and Eq. (2) is also expected to be longer, because Eq. (1) and (2) only considers particle settling without the influence of the injection of dust particles by the compressed air blast. This can explain why the MIT predictions for the majority of the studied dusts are rather conservative. For 10 μm magnesium and 15 μm aluminum dusts, the overly high error can come from the agglomeration of dust particles which is often observed for smaller dust particles. For the 31 μm lycopodium and 29 μm corn starch dust, the most likely cause for the deviation is the uncertainty of ω: in Table 1, the ω forms of these two dust materials come from the same literature (Zhou, 2013). The chemical reaction processes of organic dusts are generally more complex than metal dusts, so the uncertainties in the ω forms can potentially leads to bigger deviations for organic dusts. In order to generate more accurate MIT predictions, more precise mathematical forms of the chemical reaction rates of the dust particles are required.

3.3 *Influence of particle size and dust concentration on the MIT*

Fig. 6 illustrates the experimental and numerical variation trends of the *IT(conc)* (lowest dust cloud ignition temperature as a function of the dust concentration) of the magnesium dusts with different particle sizes. Fig. 7 compares the MIT against particle size for magnesium dusts. In Fig. 7, the numerical MIT data are minimum values of the function *IT(conc)* within the dust concentration range of 10 ~ 5000 g/m^3. These 2 figures also show that the experimental and the numerical data are in good agreement. The rather big deviations for smaller particle sizes can be due to particle agglomeration in the experiments as mentioned above.

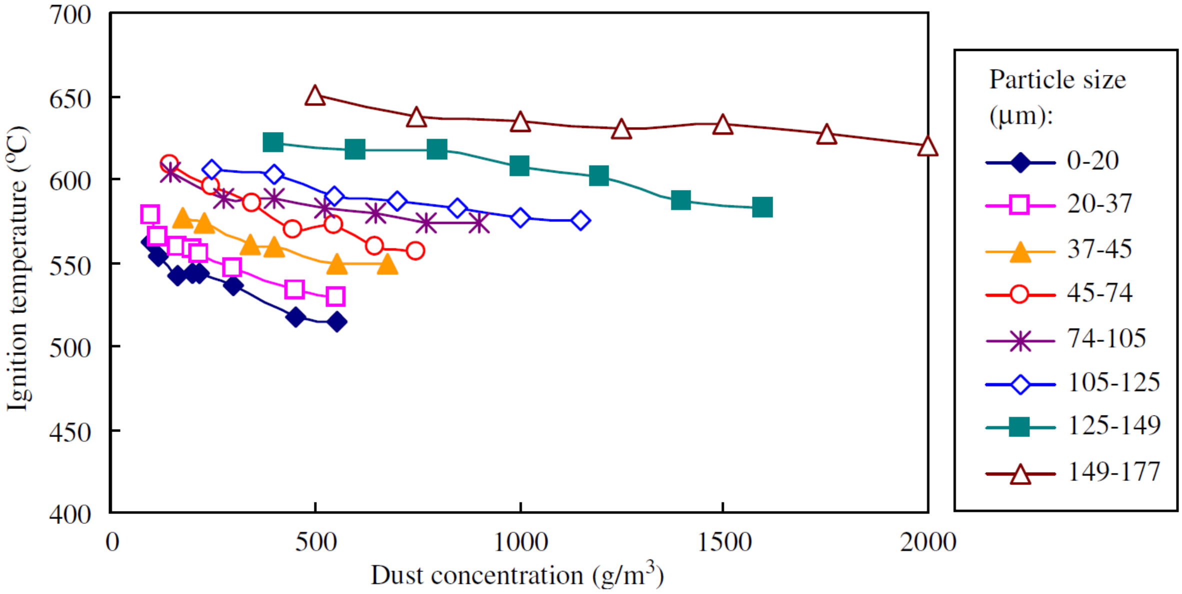

a. Experimental (Nifuku et al., 2007)

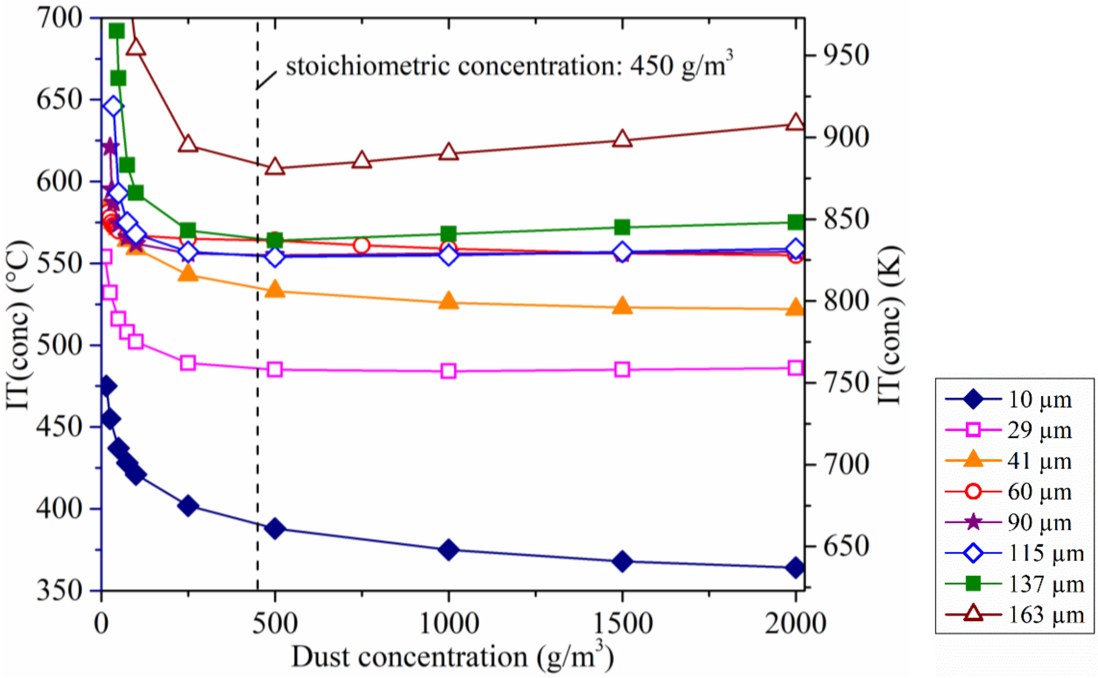

b. Calculated

Fig. 6. *The experimental and numerical IT(conc) (lowest dust cloud ignition temperature as a function of the dust concentration) for magnesium dusts*

As the concentration increases, due to the increase in dust particles participating in the dust cloud ignition process, the *IT(conc)* generally decreases first. However, after the concentration increases beyond a certain value, the *IT(conc)* starts to increase due to the increasing heat sink effect from the further added number of dust particles. According to the calculated results, for dust clouds with bigger particles (90, 115, 137 and 163 μm), the transition from decrease to increase generally happens at approximately the stoichiometric concentration. For dust clouds with smaller particles (10, 29, 41 and 60 μm), the transition happens usually at concentration levels higher than the stoichiometric concentration. This can be because of the two different ignition modes of the dust clouds as discovered in Fig. 4. For bigger particles with rather short residence times, the ignition is more of local thermal ignition, so they are more sensitive to the rise of heat sink effect under higher concentrations. However, for smaller particles with rather longer residence times in the furnace, the ignition is more of general thermal explosion of the whole dust cloud, which relies more on the self-heating of the magnesium particles. Under this circumstance, the rise of heat sink effect of dust particles is no longer necessarily a negative factor under higher dust concentrations.

On the other hand, the variation of the magnesium MIT against particle size shows a more complex trend: as particle size increases from 10 μm to 60 μm, the MIT increases along with the increase of the particle size. Then, as particle size increases from 60 μm to 137 μm, the increase of the MIT seems to be stagnant, the variation trend reaches a plateau. Finally, as the particle size increases further from 90 μm to 163 μm, the MIT increase continues again. This complex variation trend is likely to result from the combined influence of the shifting ignition modes and the decrease of dust cloud residence time in the furnace as the particle size increases. However, more thorough explanation of this unique variation trend awaits further study.

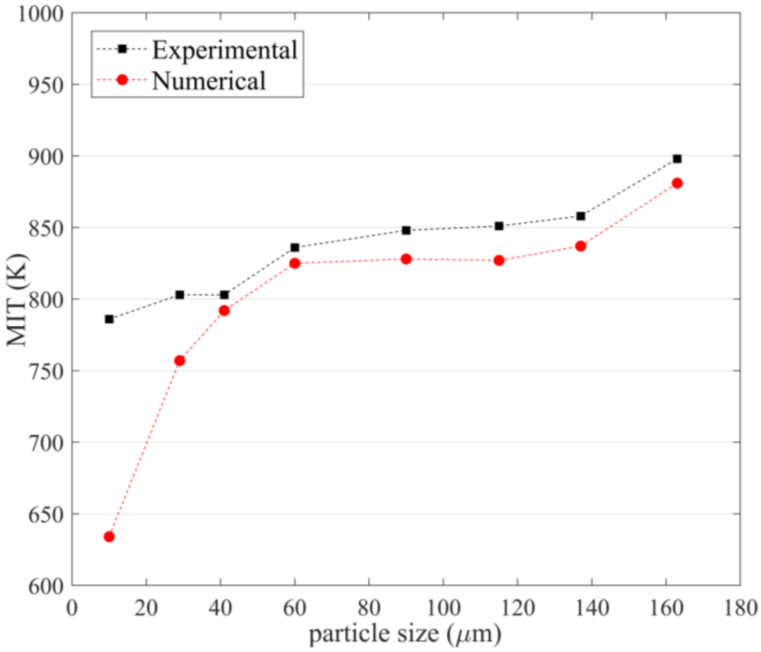

Fig. 7. *The experimental (Nifuku et al., 2007) and numerical MIT data (minimum IT(conc) value within the dust concentration range: 10 ~ 5000 g/m^3) against particle size for magnesium dusts*

4. Conclusions

In this study, a numerical model is established for the calculation of the minimum ignition temperature (MIT) of dust clouds based on the Godbert-Greenwald (G-G) furnace, considering heat transfer between the air and dust particles, the dust particle reaction kinetics, and the residence times of dust clouds in the furnace. From the analysis of the temperature profiles and comparison of the obtained numerical MIT data and the experimental results, the following conclusions can be drawn:

(1) For all the 13 dusts studied, deviations between the calculated and the experimental MIT data are within 20% (6.57% on average). There is also great accordance between the experimental and numerical MIT variation trends against dust concentration and particle size.

(2) Gas temperature profiles reveal two different ignition modes for dust clouds: one is a wall side ignition of bigger particles with rather short residence times, the other one is central thermal explosion by self-heating of the dust cloud for smaller particles with longer residence times.

(3) As dust concentration increases, the lowest ignition temperature of the dust cloud *IT(conc)* decreases first, then transits to increase at a certain point. The transition happens at different concentrations for different particle sizes. Moreover, the MIT (minimum *IT(conc)* value within 10 ~ 5000 g/m^3 dust concentration range) generally increases as the particle size increases, but the increasing trend stagnates within a certain medium particle size range, afterwards the increase continues.

Acknowledgements

The authors gratefully acknowledge the financial contribution from China Scholarship Council (201806030181)

References

Addai, E.K., Gabel, D. & Krause, U. (2016a). Experimental investigations of the minimum ignition energy and the minimum ignition temperature of inert and combustible dust cloud mixtures. *Journal of Hazardous Materials*, 307: 302-311.

Addai, E.K., Gabel, D. & Krause, U. (2016b). Experimental investigation on the minimum ignition temperature of hybrid mixtures of dusts and gases or solvents. *Journal of Hazardous Materials*, 301: 314-326.

Addai, E.K., Gabel, D. & Krause, U. (2016c). Models to estimate the minimum ignition temperature of dusts and hybrid mixtures. *Journal of Hazardous Materials*, 304: 73-83.

Addai, E.K., Addo, A., Abbas, Z. & Krause, U. (2017). Investigation of the minimum ignition temperature and lower explosion limit of multi-components hybrid mixtures in the Godbert-Greenwald furnace. *Process Safety and Environmental Protection*, 111: 785-794.

Arshad, U., Ammar Taqvi, S.A. & Buang, A. (2021). Modelling of the minimum ignition temperature (MIT) of corn dust using statistical analysis and artificial neural networks based on the synergistic effect of concentration and dispersion pressure. *Process Safety and Environmental Protection*, 147: 742-755.

Bakradze, G. (2011). Initial oxidation of zirconium: oxide-film growth kinetics and mechanisms. *Max-Planck-Institut für Intelligente Systeme (ehemals Max-Planck-Institut für Metallforschung) Stuttgart.*

Boilard, S.P., Amyotte, P.R., Khan, F.I., Dastidar, A.G. & Eckhoff, R.K. (2013). Explosibility of micron- and nano- size Titanium powders. *Journal of Loss Prevention in the Process Industries*, 26(6): 1646-1654.

Cao, W., Huang, L., Zhang, J., Xu, S., Qiu, S. & Pan, F. (2012). Research on characteristic parameters of coal-dust explosion. *Procedia Engineering*, 45: 442-447.

Cao, Y., Su, H., Ge, L.F., Li, Y.Y., Wang, Y.X., Xie, L.F. & Li, B. (2019). Ignition sensitivity and flame propagation of zirconium powder clouds. *Journal of Hazardous Materials*, 365: 413-420.

Chen, G.H., Jiang, H.Y.J. and Wang, X.H. (2016). Study on characteristic of mahogany wood dust explosion. *Fire Science and Technology*, 35(9): 1200-1203.

Chen, T.F., Berghmans, J., Degrève, J., Verplaetsen, F., Van Caneghem, J.& Vanierschot, M. (2020a). A Thermal Model for the Minimum Ignition Energy of Dusts. *Proceedings of the 13th International Symposium on Hazards, Prevention and Mitigation of Industrial Explosions (ISHPMIE 2020)*, 494-505. Braunschweig, Germany, 2020.

Chen, T.F., Berghmans, J., Degrève, J., Verplaetsen, F., Van Caneghem, J.& Vanierschot, M. (2021). A theoretical model for the prediction of the minimum ignition energy of dust clouds. *Journal of Loss Prevention in the Process Industries*, 73: 104594.

Deng, J., Qu, J., Wang, Q., Zhai, X., Xiao, Y., Cheng, Y. & Shu, C.M. (2019). Minimum ignition temperature of aluminum dust clouds via the Godbert–Greenwald furnace. *Process Safety and Environmental Protection*, 129: 176-183.

Eckhoff, R.K. (2019). Measuring hot-surface minimum ignition temperatures of dust clouds – History, present, future. *Journal of Loss Prevention in the Process Industries*, 59: 63-76.

Gabel, D., Geoerg, P., Franken, F. & Krause, U. (2021). Nex-Hys: minimum ignition temperature of hybrid mixtures. *Journal of Loss Prevention in the Process Industries*, 72: 104502.

Gurevich, M.A., & Stepanov, A.M. (1968). Ignition Limits of a Metal Particle. *Fizika Goreniyai Vzryva*, 4(2):189-195.

Hosseinzadeh, S. (2018). Study of Dust Explosion Characteristics and their Determination. *KU Leuven*.

ISO/IEC 80079-20-2, 2016. International Standard: Explosive Atmospheres- Part 20-2: Material Characteristics - Combustible Dusts Test Methods. *International Electrotechnical Commission, Geneva*.

Janès, A., Vignes, A., Dufaud, O., & Carson, D. (2014). Experimental investigation of the influence of inertsolids on ignition sensitivity of organic powders. *Process Safety and Environmental Protection*, 92: 311-323.

Krietsch, A., Reyes Rodriguez, M., Kristen, A., Kadoke, D., Abbas, Z. & Krause, U. (2021). Ignition temperatures and flame velocities of metallic nanomaterials. *Journal of Loss Prevention in the Process Industries,* 71: 104482.

Miao, N., Zhong, S. & Yu, Q. (2016). Ignition characteristics of metal dusts generated during machining operations in the presence of calcium carbonate. *Journal of Loss Prevention in the Process Industries,* 40: 174-179.

Mishra, D.V. & Azam, S. (2018). Experimental investigation on effects of particle size, dust concentration and dust-dispersion-air pressure on minimum ignition temperature and combustion process of coal dust clouds in a G-G furnace. *Fuel*, 227: 424-433.

Mittal, M. (2014). Explosion characteristics of micron- and nano- size Magnesium powders. *Journal of Loss Prevention in the Process Industries*, 27(1): 55-64.

Nifuku, M., Koyanaka, S., Ohya, H., Barre, C., Hatori, M., Fujiwara, S., Horiguchi, S. & Sochet, I. (2007). Ignitability characteristics of aluminium and magnesium dusts that are generated during the shredding of post-consumer wastes. *Journal of Loss Prevention in the Process Industries*, 20: 322-329.

Sun, H., Wang, Z. & Zhang, Q. (2020). Effect of pressure for dust dispersion on minimum ignition temperature. *Journal of Loss Prevention in the Process Industries*, 68: 104305.

Taler, J. & Duba, P. (2006). Approximate analytical methods for solving transient heat conduction problems. In: Solving Direct and Inverse Heat Conduction Problems. Springer Berlin Heidelberg, Berlin, Heidelberg. pp. 587–604.

Tan, X., Schmidt, M., Zhao, P. Wei, A., Huang, W., Qian, X. & Wu, D. (2020). Minimum ignition temperature of carbonaceous dust clouds in air with $CH_4/H_2/CO$ below the gas lower explosion limit. *Fuel*, 264: 116811.

Wang, Q., Fang, X., Shu, C.M., Wang, Q., Sheng, Y., Jiang, J., Sun, Y. & Sheng, Z. (2020). Minimum ignition temperatures and explosion characteristics of micron-sized aluminium powder. *Journal of Loss Prevention in the Process Industries*, 64: 104076.

Wen, L., Wang, S., Shi, H., Fang, M., Luo, Z. & Cen, K. (2004). Kinetic study on the pyrolysis of wood. *Fire Science and Technology*, 23(1): 1-5.

White, F.M. (2006). Viscous Fluid Flow, 3rd ed., McGraw-Hill.

Wu, D., Krietsch, A., Schmidt, M. & Krause, U. (2022), Effect of oxygen concentration, inert gas and CH4/H2 addition on the minimum ignition energy of coal dusts. *Journal of Loss Prevention in the Process Industries*, 72: 104546.

Yarin, L.P. & Hetsroni, G., (2004). Dynamics of a Single Particle. In Combustion of Two-Phase Reactive Media. Springer Berlin Heidelberg, Berlin, Heidelberg.

Yuan, C., Li, C., Li, G. & Zhang, P. (2012). Ignition temperature of magnesium powder clouds: A theoretical model. *Journal of Hazardous Materials*, 239-240: 294-301.

Zhang, Y., Luo, X., Li, C., Shi, D. & Zhang, H. (2020). Analytical Model for Size Effect of Activation Energy of Zirconium and Aluminum Particles. *Rare Metal Materials and Engineering*, 49(12): 4097-4102.

Zhou, L.G. (2013). The Study of Pyrolysis Kinetics and Smouldering Propagation Model of Combustible Powders. Northeastern University, Shenyang.

DOI: 10.7795/810.20221124

Acceleration sensitivity of piezoelectric pressure sensors and the influence on the measurement of explosion pressures

Tim Krause [a], Harun Kanbur [a], Niels Springer [a], Jens Brunzendorf [a], Detlev Markus [a], Otto Walch [b]
& Christian Heer [c]

[a] Physikalisch-Technische Bundesanstalt (PTB), Braunschweig, Germany
[b] R. STAHL Schaltgeräte GmbH, Waldenburg, Germany
[c] Kistler Instrumente AG, Winterthur, Switzerland

E-mail: *tim.krause@ptb.de*

Abstract

To measure the explosion pressure inside an enclosure, it is common to install a piezoelectric pressure sensor in the enclosure wall. The pressure wave of the internal explosion inevitably leads to vibrations of the enclosure walls. This unwanted but naturally occurring motion is also transmitted to the pressure sensor mounted in the enclosure wall and results in inertial forces affecting the piezoelectric element. During the measurement of the explosion pressure, this affects the output signal of the pressure sensor since an undesired signal due to the acceleration of the pressure sensor is superimposed on the desired pressure signal. This behaviour of the sensor is described as acceleration sensitivity. The level of acceleration sensitivity depends on the type and construction design of the pressure sensor. Even though this sensor behaviour is basically not a new phenomenon, the evaluation of an international comparison between Ex testing laboratories in the field of flameproof enclosures has shown that the consideration of this issue is a major challenge in daily practice concerning the measurement of explosion pressures and is even often completely neglected.

This work evaluates the behaviour of various piezoelectric pressure sensors with respect to the influence of acceleration and investigates the specific impact on the explosion pressure measurement in the field of flameproof enclosures. For this purpose, explosions from typically used explosive mixtures such as hydrogen, propane and ethyne in air are examined. These investigations involve simple model enclosures with various specifications as well as a commercially available equipment for hazardous areas. By using blind holes and specially designed adapters, a practical method is applied to be able to detect the effect of acceleration on the sensor signal separately from the pressure signal. For this purpose, both the discrete-time pressure curves and the frequency components are analysed using Fast Fourier Transform. The use of signal filters as a practical and fast approach to address these unwanted signal components is discussed and evaluated.

This paper provides guidelines for typical end-users in the field of flameproof enclosures how to handle acceleration of piezoelectric pressure sensors and the influence on the measurement of explosion pressures correctly.

Keywords: *flameproof enclosures, explosion pressure, piezoelectric pressure sensor, acceleration sensitivity*

1. Introduction

Equipment intended for use in potentially explosive atmospheres (Ex equipment) may only be placed on the market if it is certified to meet the special technical requirements of the corresponding type of protection as defined by e.g., IEC standards of the IEC 60079 series. Ex testing laboratories conduct various tests according to these standards on test samples provided by the manufacturer. For Ex equipment of the type of protection flameproof enclosures, the ability of the enclosure to withstand the pressure of an internal explosion in accordance with IEC 60079-1 (IEC, 2014) is one of the main properties to be tested. Here the basis of these tests is the determination of the explosion pressure, which acts as a reference pressure for further overpressure tests. These overpressure tests are executed with 1.5 to 4 times of the reference pressure, depending on the certification procedure. The correct measurement of the explosion pressure as reference pressure is therefore important, as any measurement deviation is multiplied subsequently. The analysis of an international comparison between Ex testing laboratories on this subject as well as current discussions from the field of certification show that the influence of acceleration respectively the acceleration sensitivity of the pressure sensors used is an insufficiently considered influencing factor when determining the explosion pressure.

The explosion pressure inside a flameproof enclosure inevitably leads to a vibration of the enclosure walls (Krause, 2017). The deflection of this vibration depends on the material and wall thickness, as well as on the level of the explosion pressure (Spörhase, 2021). The movement of the enclosure wall is also transmitted to the pressure sensor mounted in it and leads to inertial forces acting on the piezoelectric element. This can influence the output signal of the pressure sensor during the explosion pressure measurement since an undesired signal due to the acceleration of the pressure sensor is superimposed on the desired pressure signal (Tichý, 1980). This behaviour of piezoelectric pressure sensors is called acceleration sensitivity and is usually differentiated according to the directions of action "axial" and "radial". The respective level of acceleration sensitivity depends on the construction design of the pressure sensor. The influence of acceleration for specific applications and the compensation of acceleration-related effects are addressed in several scientific studies (Ren, 2013). In addition to methods for changing the sensor design with regard to the piezoelectric element (Wang, 2021), there are also approaches to compensate acceleration-related influences with digital filters based on suitable mathematical models (Xu, 2019). However, these partially promising approaches are not universally applicable, as they often refer to specific applications, might produce incorrect results due to incomplete discrimination between the acceleration-induced and the pressure-induced signals, may involve very complex mathematical calculations or are limited e.g., mechanical adjustments to improve a certain property cause another property to deteriorate.

The reason for the insufficient attention to this issue is often the lack of awareness and thus of recognising the problem in the first place. The fact that in practice there are many different pressure curves in the field of flameproof enclosure due to changing test parameters such as enclosure geometry, combustible-air mixture, sensor position, sensor type, etc., intensifies the challenge of detecting an influence of acceleration on the pressure sensor that causes an altered pressure signal. The aim of this work is therefore to discuss practical methods to detect acceleration influences on the explosion pressure measurement in general and to minimise or eliminate these unwanted influences accordingly.

2. Experimental setup

The experiments performed are based on the IEC 60079-1 standard regarding the test requirements for determining explosion pressure for flameproof enclosures. The experiments are initially performed with all the combustible-air mixtures and pressure sensors described in the following subsections. Later, the consideration of the combustible is reduced to hydrogen-air mixtures since the influence of acceleration is most significant here. Also, the focus regarding the pressure sensors is laid on those types with the highest and lowest acceleration sensitivity.

2.1 Test setup and test samples

The schematic representation of the experimental setup can be seen in Figure 1. Two different test samples are considered. The first one (included in Figure 1) is a simple model sample of a flameproof enclosure consisting of a combination of two cylindrical chambers. The chambers are made of stainless steel of the same inner diameter (Ø 161.5 mm) with different lengths (short chamber l = 250 mm; long chamber l = 500 mm) connected by an orifice plate with a 15 mm hole in the centre. The long chamber is closed with a stainless steel flange of 22 mm thickness and represents the ignition side, with a centrally located spark plug on the flange. The short chamber represents the pressure measurement side, which is also closed by a flange. To vary the effect of acceleration forces both a 22 mm thick stainless steel flange and a 16 mm thick aluminium flange are examined. As shown in Figure 2 for pressure measurement a centrally located threaded hole for the pressure sensor is used on each of the two varying flanges. In addition, a blind hole with the same depth is applied slightly offset for both flanges (without connection to the explosion volume). Another pressure sensor of the same type is installed in this blind hole to provide the output signal without the actual pressure signal, but only the influence of the acceleration on the pressure sensor.

As a second test sample, a real Ex equipment consisting of a MCCB (Molded Case Circuit Breaker) in the design of a flameproof enclosure is used (see Figure 3). The enclosure is made of glass fibre reinforced polyamide (PA 66) with external dimensions of 254 mm x 149 mm x 189 mm (length x width x height). The spark plug as ignition source is located in the lower area of the length side. The pressure sensor for pressure measurement is installed by means of a threaded hole on the front side. Due to the thin wall thickness of the enclosure, a blind hole for the use of a second pressure sensor to measure the influence of acceleration is not practical. Furthermore, due to the complex geometry without many straight surfaces, it is also not possible to use a second measuring point in a comparable position to the pressure sensor. For this reason, instead of a blind hole, a specially designed adapter with a closed front is used for the determination of the acceleration influence directly with the threaded hole of the actual pressure measurement. The combustibles used for the experiments are hydrogen (31 ± 1 vol. % H_2), propane (4.6 ± 0.3 vol. % C_3H_8) and ethyne (14 ± 1 vol. % C_2H_2) in air. The respective combustible-air mixture is purged into the test sample by using mass flow controllers and the concentration ratio is verified by an oxygen analyser. After the ignition of the combustible-air mixture within the test sample by the spark plug, the pressure curve of the explosion is recorded by piezoelectric pressure sensors. The pressure sensors generate a charge in linear

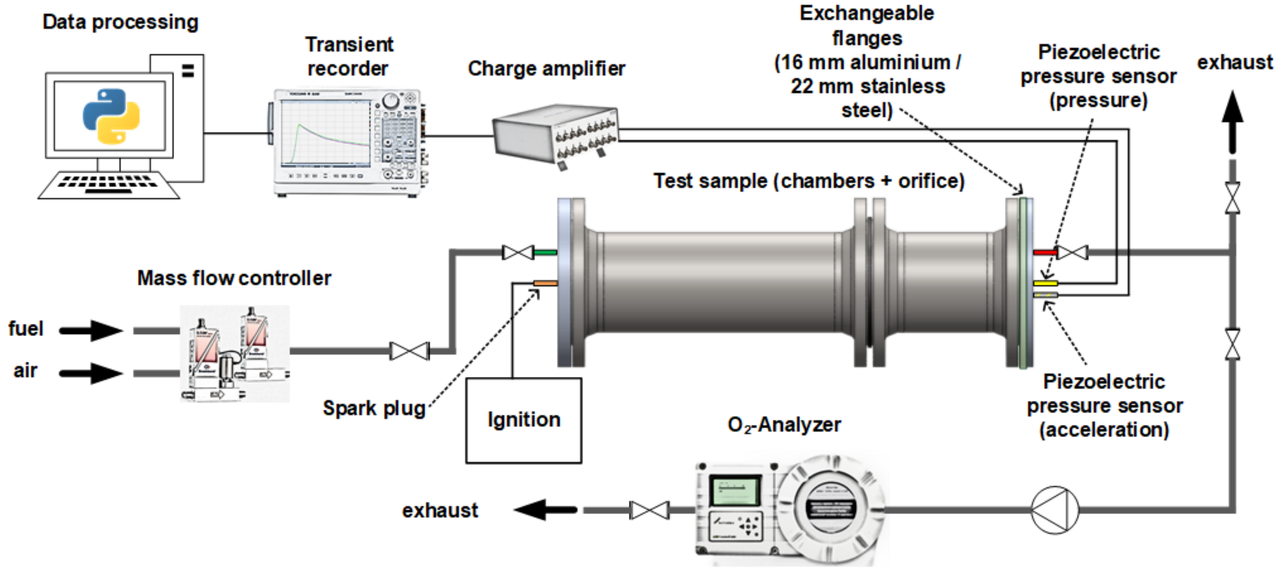

Fig. 1. *Schematic representation of the experimental setup including the test sample consisting of cylindrical chambers, orifice plate and exchangeable flanges (16 mm aluminium flange / 22 mm stainless steel flange)*

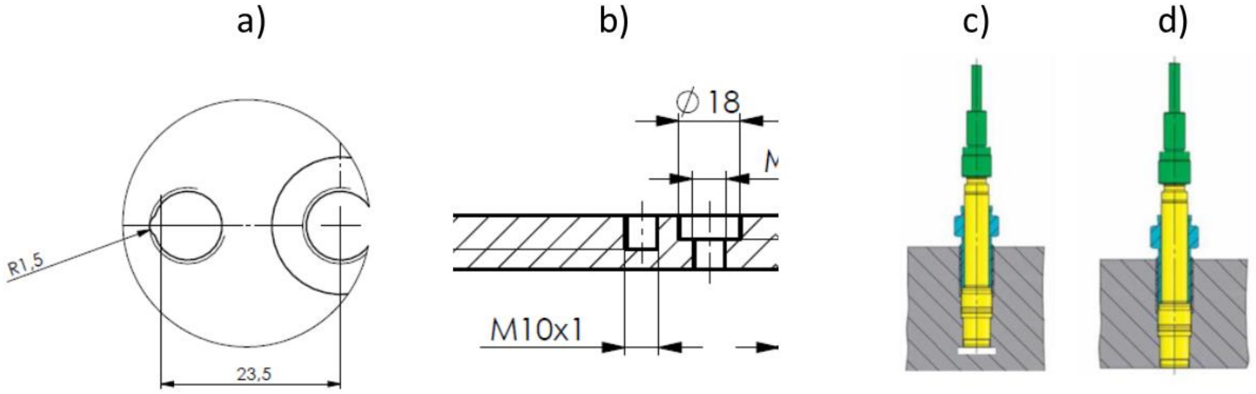

Fig. 2. *Details of the constructional implementation of pressure measurement and the use of a pressure sensor to investigate acceleration influences: a) Section of through hole and blind hole (top view), b) Section of cross-sectional view for through hole and blind hole, c) Pressure sensor installed in blind hole, d) Pressure sensor installed in through hole.*

correlation to the pressure which is converted into a voltage by a charge amplifier (Type: Kistler LabAmp 5167). This voltage signal is recorded with a transient recorder before it is processed further using Python software. The pressure sensors used for determining the acceleration influences in the blind hole or when using the closed adapters work with the same measuring chain. During signal acquisition, the sensor signals are filtered with a low-pass filter with a cut-off frequency of 20 kHz (Butterworth, 2nd order) in the charge amplifier to prevent aliasing effects (Grünigen, 2004). Further filters such as the low-pass filter with a 3 dB point of 5 kHz ±0.5 kHz, which is standard according to standard IEC 60079-1, or the band-stop filters that are used in these investigations are realised in the post-processing via Python. The sampling rate for all measurements is 10 MS/s. To protect the pressure sensors from thermal shock effects caused by the explosion heat, the sensor membranes are prepared with a 1 mm layer of RTV silicone (Krause, 2021). To exclude the influence of variations in temperature on the explosion pressure and the vibrations of the enclosure walls, the tests were conducted within the range of 25 °C to 28 °C with temperature monitoring.

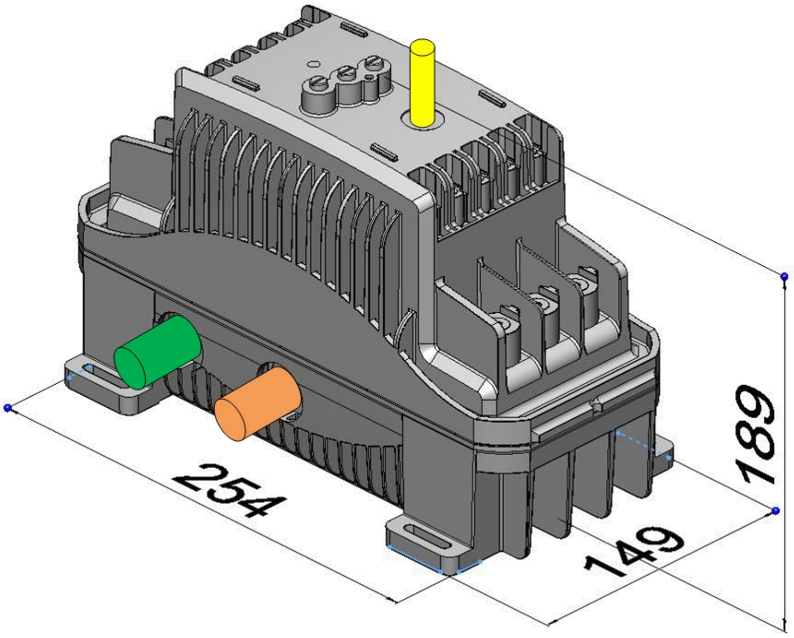

Fig. 3. *Second test sample: "Real Ex equipment" consisting of an MCCB (Molded Case Circuit Breaker) designed as a flameproof enclosure with gas inlet (green marking), ignition source (orange marking) and pressure sensor (yellow marking). (Gas outlet not visible on the back). All units in mm.*

2.2 *Piezoelectric pressure sensors*

The pressure sensors considered in this work are all piezoelectric pressure sensors since piezoelectric pressure measurement technology is widespread in the determination of explosion pressures according to IEC 60097-1 and represents the current state of the technology. Piezoresistive pressure sensors are of minor relevance for the target group considered in these investigations, as they have further practical disadvantages in addition to the lower flexibility regarding measurement ranges (Krause, 2021). This is also clearly reflected in the feedback from the Ex testing laboratories participating in the international comparison regarding the pressure measurement technology used. All participants exclusively used piezoelectric pressure sensors. The types of pressure sensors considered in this work are listed in Table 1 together with relevant technical specifications. The design and principle of piezoelectric pressure sensors are comparable across manufacturers. To exclude possible influences due to different manufacturing quality, sensors from one manufacturer are used. For these pressure sensors measurements to determine the acceleration sensitivity were conducted prior to the actual experimental explosion tests to measure the explosion pressures. For this purpose, two pressure sensors of each type were measured in axial direction three times by a shaker (Type: Tira S5220) for six frequency ranges (100 Hz, 1 kHz, 2 kHz, 3 kHz, 4 kHz, 5 kHz). The experimental setup is shown in Figure 4 and the averaged results in Figure 5.

Table 1: *Pressure sensors to be investigated with relevant technical specifications (Kistler, 2021)*

Type of sensor	Pressure range in bar	Natural frequency in kHz	Sensitivity (typ.) in pC/bar
Kistler 601CAA	0 … 250	>215	-37
Kistler 601H	0 … 1000	≈150	-16
Kistler 603CAA	0 … 1000	>500	-5
Kistler 6031	0 … 250	≈160	-14

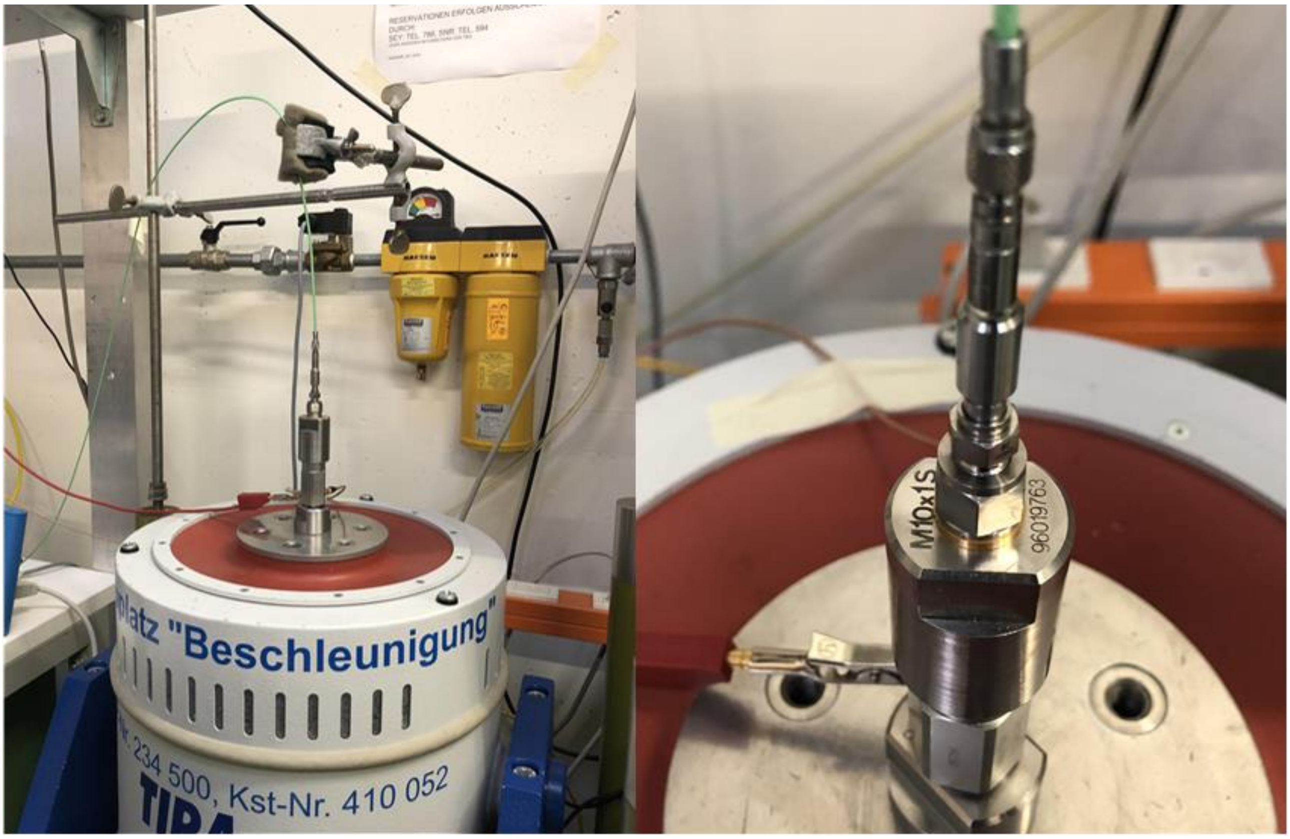

Fig. 4. *Pressure sensors during the determination of acceleration sensitivity by using a shaker*

DOI: 10.7795/810.20221124

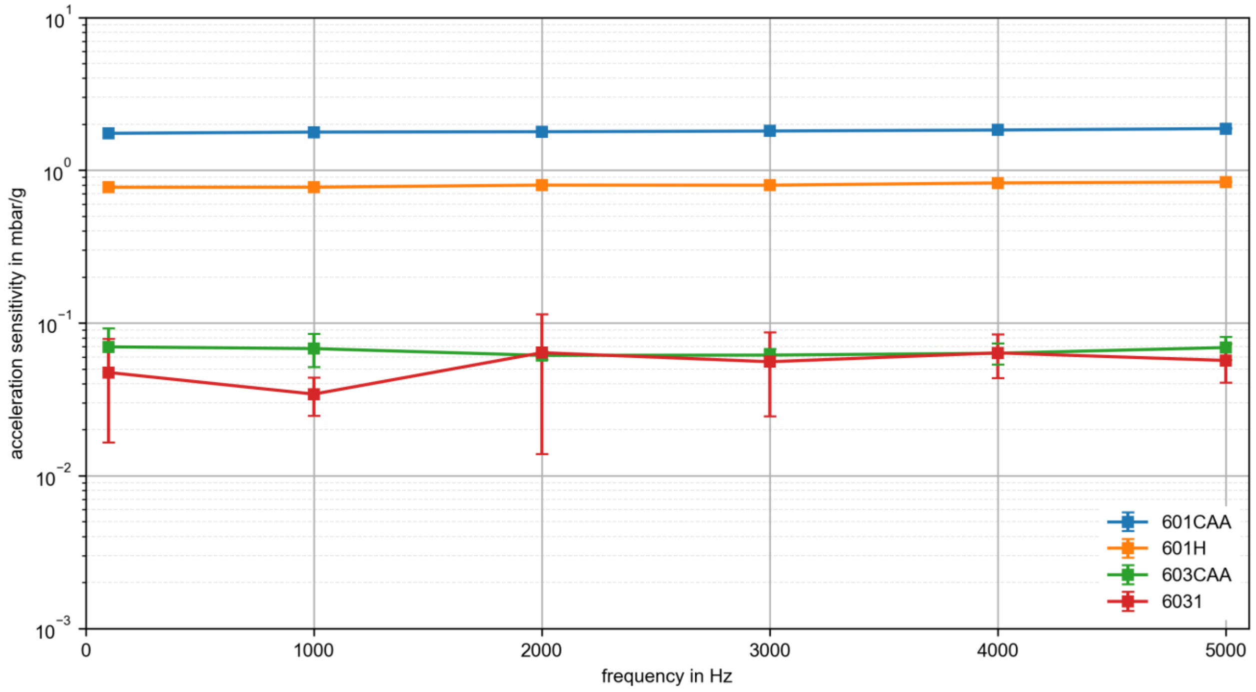

Fig. 5. *Acceleration sensitivity for different pressure sensors and different frequencies in mbar per unit of the free fall acceleration g = 9.81 m/s*^{2}.

In the results for the acceleration sensitivity for the pressure sensors considered in Figure 5, the 601CAA sensor with $\bar{a}_{\text{acc. sen, 601CAA}} = 1.8$ mbar/g has the highest averaged acceleration sensitivity for the frequencies considered followed by sensor 601H with $\bar{a}_{\text{acc, sen, 601H}} = 0.8$ mbar/g. The sensors 603CAA with $\bar{a}_{\text{acc., sen, 603CAA}} = 0.07$ mbar/g and 6031 with $\bar{a}_{\text{acc., sen, 6031}} = 0.05$ mbar/g have an acceleration compensated design with lower acceleration sensitivity in a comparable range.

3. Acceleration sensitivity on piezoelectric pressure sensors

The behaviour of the pressure sensor types under consideration is investigated with varying acceleration. Figure 6 shows the results of the explosion pressure measurement of the pressure sensors for the two different flange types and three different combustible-air mixtures. The explosion pressures result in each case from the mean values of five individual measurements. The results for a hydrogen-air mixture using the 22 mm stainless steel flange show comparable explosion pressures with $p_{\text{ex, 601CAA}} = 12.37$ bar, $p_{\text{ex, 601H}} = 13.06$ bar, $p_{\text{ex, 603CAA}} = 12.51$ bar and $p_{\text{ex, 6031}} = 11.79$ bar within the expected scatter for all four pressure sensor types and are all within the expected order of magnitude. The standard deviations are also in a comparable range with $\sigma_{\text{601H}} = 0.45$ bar, $\sigma_{\text{603CAA}} = 0.40$ bar, $\sigma_{\text{6031}} = 0.43$ bar. The standard deviation of the 601CAA is slightly smaller with $\sigma_{\text{601CAA}} = 0.27$ bar. Changing the flange to the 16 mm aluminium flange while keeping all other specifications when performing the experiments should produce comparable explosion pressures as expected, since none of the parameters influencing the explosion pressure change. While this expectation is fulfilled for the pressure sensor types 601H, 603CAA and 6031 (with $p_{\text{ex, 601H}} = 12.57$ bar, $p_{\text{ex, 603CAA}} = 12.74$ bar and $p_{\text{ex, 6031}} = 11.88$ bar), it can be observed for the pressure sensor type 601CAA that the result for the explosion pressure is about 32 % higher with $p_{\text{ex, 601CAA}} = 16.31$ bar. In addition to this, the standard deviation has more than doubled, which is also not observed for the other pressure sensors in this scale. A similar but less pronounced picture also arises for the results of the propane-air mixture and the ethyne-air mixture when considering the two pressure sensors 601CAA (with the highest acceleration sensitivity) and the 6031 (with the lowest acceleration sensitivity). While the explosion pressures for the 6031 sensors are in a comparable range within the scatter for both flange types (for C_3H_8: $p_{\text{ex, 6031, 22 mm}} = 15.81$ bar, $p_{\text{ex, 6031, 16 mm}} = 15.80$ bar;

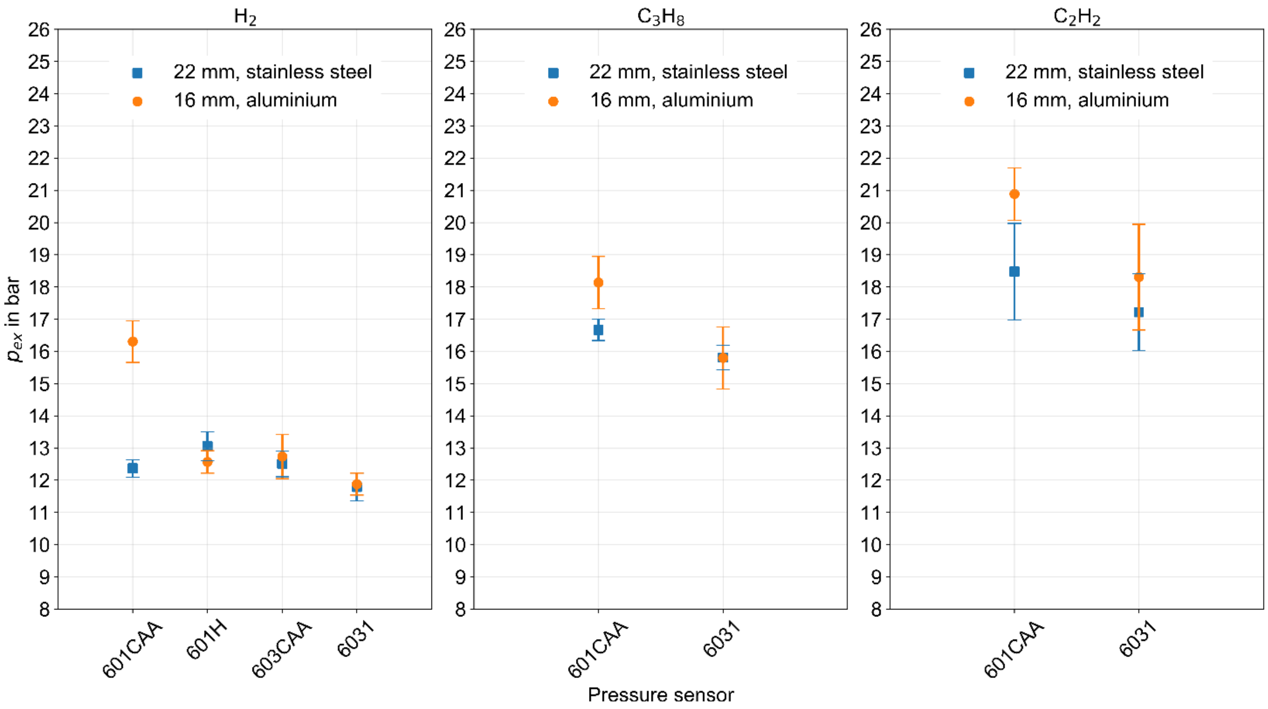

Fig. 6. *Explosion pressures of different pressure sensor types for two flange types and three different combustible-air mixtures.*

for C_2H_2: $p_{\text{ex, 6031, 22 mm}}$ = 17.22 bar, $p_{\text{ex, 6031, 16 mm}}$ = 18.31 bar), a more significant increase occurs for the sensors 601CAA when changing to the 16 mm flange (for C_3H_8: $p_{\text{ex, 601CAA, 22 mm}}$ = 16.67 bar, $p_{\text{ex, 601CAA, 16 mm}}$ = 18.14 bar; for C_2H_2: $p_{\text{ex, 601CAA, 22 mm}}$ = 18.48 bar, $p_{\text{ex, 601CAA,16 mm}}$ = 20.89 bar). To investigate the reason for this behaviour, it is useful to analyse the pressure curves for the configurations considered. For this purpose, Figure 7 shows the pressure curves for the pressure sensors of all four pressure sensor types for a hydrogen-air mixture for both flanges. Since the averaging of the pressure curves from the five individual measurements of each pressure sensor type is not meaningful due to time shifts, the pressure curve of an individual experiment is used as an example for the respective pressure sensor. Diagram a) shows the output signals of the pressure sensors installed in the centre through hole and in direct contact with the explosion volume using the 22 mm stainless steel flange. Diagram b) shows the output signals of the pressure sensors assigned to the same experiment, which are installed in the blind hole and where there is no contact to the explosion volume - thus the sensor is exposed to the same mechanical vibrations, but not to the explosion pressure. It can be seen that, corresponding to the comparable explosion pressures, the pressure curves of all four pressure sensors also show almost identical characteristics. For the pressure sensors in the blind holes, there are also signal curves that do not reflect the explosion pressure curve but result from the effect of acceleration on the pressure sensors. The relatively low output signals vary depending on the sensor between approx. ± 1 bar for sensor 601CAA and approx. + 0.34 bar/- 0.02 bar for sensor 6031. The sensor signal of 603CAA is in a similarly low range as the signal of sensor 6031. The sensor signal of 601H is with + 0.6 bar/- 0.32 bar between the values of sensors 6031 and 601CAA. The level of the output signals here reflects the acceleration sensitivities of the respective sensors (see Figure 5). The higher the acceleration sensitivity of the pressure sensor in the blind hole, the higher the corresponding output signal. However, the direct influence on the explosion pressures as well as the pressure curves is small, which is shown by the comparable results. The analysis of the pressure curves and the output signals of the pressure sensors mounted in the blind holes using the 16 mm aluminium flange comes to a different result. In accordance with the previous discussion of diagrams a) and b), the pressure curves of the pressure sensors in the through hole (diagram c)) and the output signals of the pressure sensors in the blind holes (diagram d)) are also shown in the diagrams of Figure 7. As discussed for Figure 6, comparable values result for the explo-

DOI: 10.7795/810.20221124

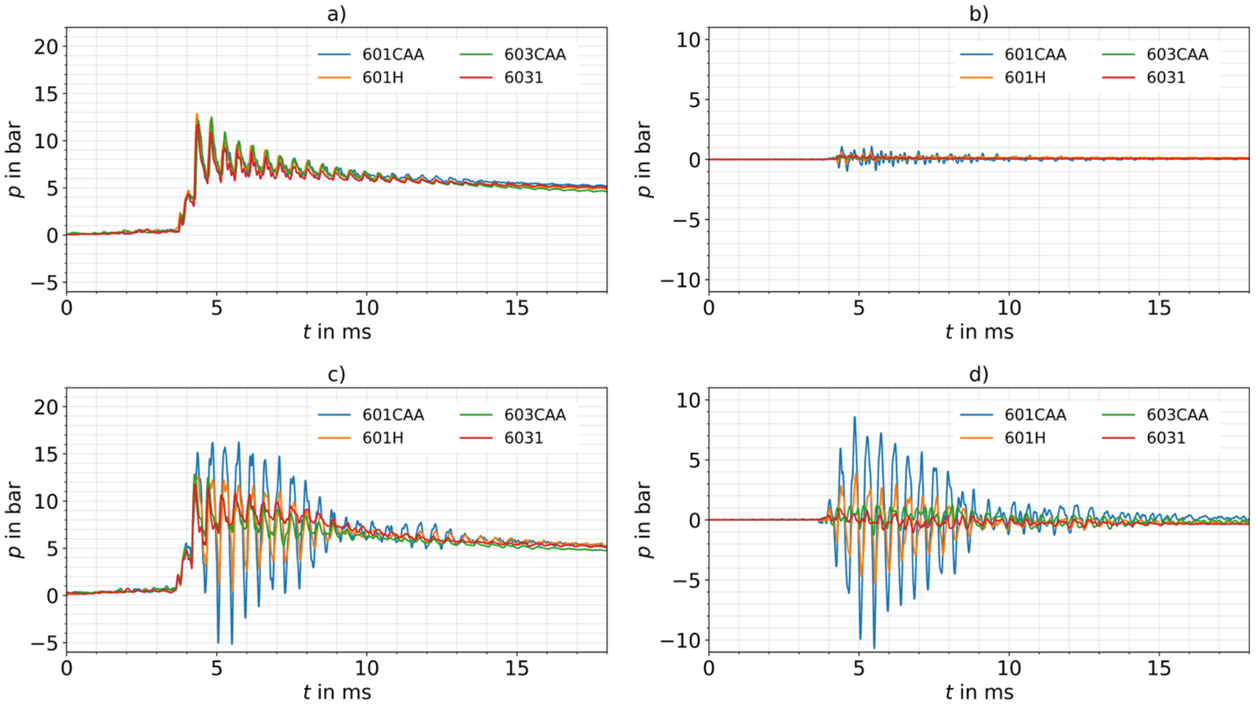

00

Fig. 7. Pressure curves (diagram a): 22 mm stainless steel flange and diagram c): 16 mm aluminium flange) and output signals of the pressure sensors mounted in the blind hole (diagram b): 22 mm stainless steel flange and diagram d): 16 mm aluminium flange) of different pressure sensor types for a hydrogen-air mixture (31 ± 1 vol. % H_2) on the test sample consisting of cylinders and orifice.

sion pressures of the pressure sensors 601H, 603CAA and 6031. This is also shown in the pressure curves considered in diagram c). The signal curves of the pressure sensors 603CAA and 6031 show an almost identical behaviour as with the 22 mm stainless steel flange. The signal curves of the 601H and 601CAA sensors, in contrast, deviate significantly. While this deviation does not have a noticeable effect on the measured value for the explosion pressure in the case of the 601H pressure sensor, but is rather characterised by an increased undershoot, the sensor signal of the 601CAA is superimposed by a strongly oscillating signal, both in the positive and in the negative direction. An increased explosion pressure erroneously follows from this overshooting. The reason for the oscillations in the pressure sensors 601H and 601CAA superimposed on the pressure signal becomes obvious when looking at the output signals of the pressure sensors in the blind holes, shown in diagram d). Here it can be seen that the acceleration in the case of the pressure sensor 601H and even more in the case of the pressure sensor 601CAA leads to an oscillation behaviour in the output signal, which is superimposed on the corresponding pressure signals in diagram c) in an almost identical curve form. The maximum amplitudes of the output signals of the pressure sensors 6031 and 603CAA installed in the blind hole have approximately tripled compared to the output signals of the 22 mm stainless steel flange and are in a range of approx. ± 1 bar. With the 601H sensor, the maximum amplitude of the output signal has increased by a factor of approx. 9 with + 3.82 bar/- 5.35 bar, with a change of the maximum amplitude into the negative range. With the pressure sensor 601CAA, the largest increase of the output signal with + 8.57 bar/- 10.7 bar occurs in negative amplitude by a factor of approx. 11 and in positive amplitude by approx. 8.6. These results also reflect the ranking of the acceleration sensitivity of the pressure sensors. Furthermore, it can be seen for the configurations considered that accelerations that lead to output signals of $\leq \pm 1$ bar for the pressure sensors installed in the blind hole do not cause any significant changes in the output signals of the pressure sensors installed in the centre through hole that reflect the pressure curve.

In the following, the pressure curves of the experimental results for the propane-air mixture (see Figure 8) and the ethyne-air mixture (see Figure 9) are presented in the same way as in the previously

DOI: 10.7795/810.20221124

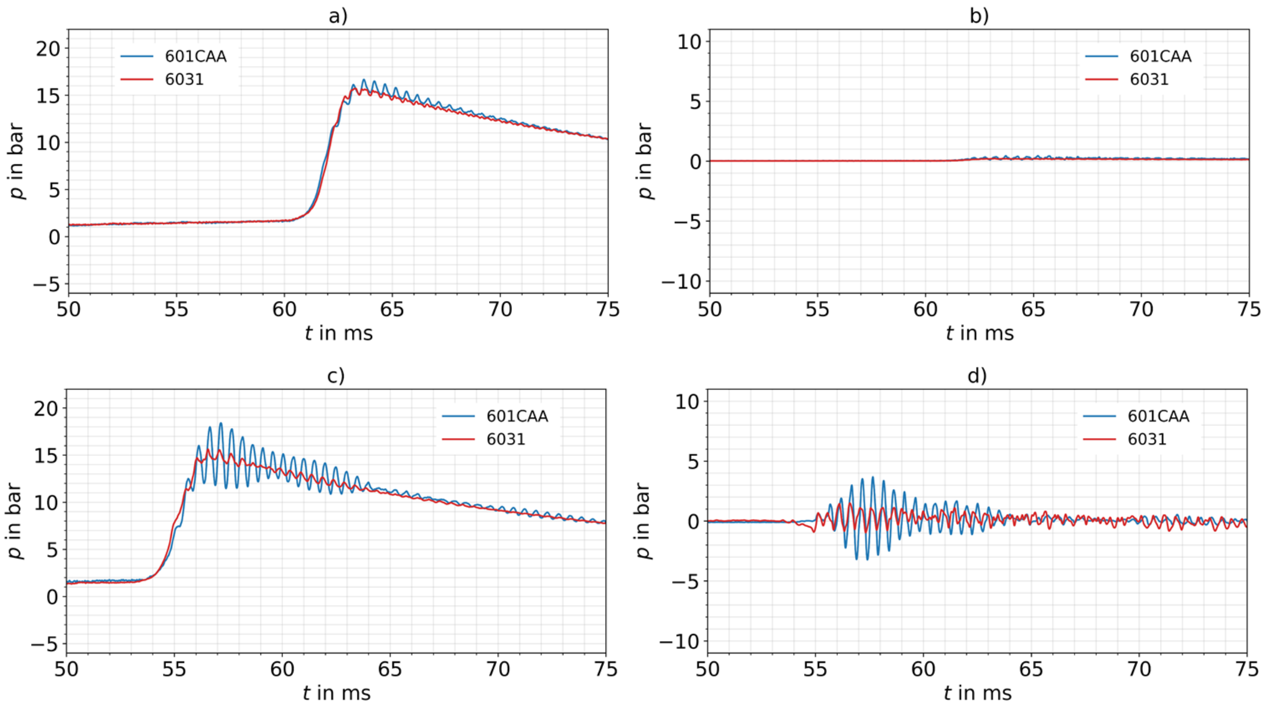

Fig. 8. *Pressure curves (diagram a): 22 mm stainless steel flange and diagram c): 16 mm aluminium flange) and output signals of the pressure sensors mounted in the blind hole (diagram b): 22 mm stainless steel flange and diagram d): 16 mm aluminium flange) of different pressure sensor types for a propane-air mixture (4.6 ± 0.3 vol. %* C_3H_8*) on the test sample consisting of cylinders and orifice.*

performed analysis of the hydrogen-air mixtures but reduced to the sensors 601CAA (high acceleration sensitivity) and 6031 (low acceleration sensitivity). For the propane-air mixture in Figure 8, it can be seen in general that the pressure curve differs from a pressure curve after ignition

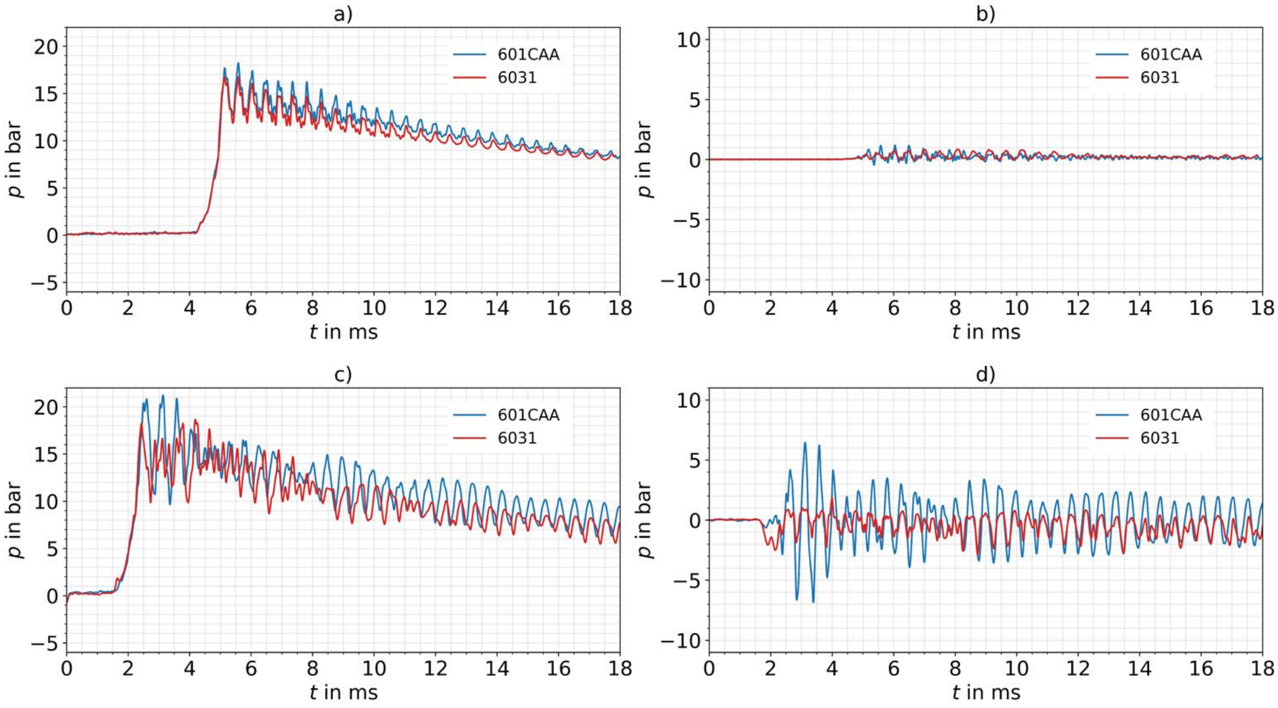

Fig. 9. *Pressure curves (diagram a): 22 mm stainless steel flange and diagram c): 16 mm aluminium flange) and output signals of the pressure sensors mounted in the blind hole (diagram b): 22 mm stainless steel flange and diagram d): 16 mm aluminium flange) of different pressure sensor types for an ethyne-air mixture (14 ± 1 vol. %* C_2H_2*) on the test sample consisting of cylinders and orifice.*

of a hydrogen-air mixture. Both the pressure rise time and the decay of the pressure are significantly slower, which is due to the lower laminar combustion speed of propane. While the overall explosion pressure is higher, the reflective pressure wave superimposed on the global pressure waveform is visible but significantly reduced. The explosion pressures of the two pressure sensors 601CAA and 6031 shown in diagram a) are of a comparable order of magnitude with $p_{\text{ex, 601CAA, 22 mm}}$ = 16.67 bar and $p_{\text{ex, 6031, 22 mm}}$ = 15.71 bar within the scatter. The maximum amplitudes of the output signals of the pressure sensors installed in the blind holes (diagram b)) are small with + 0.46 bar for the sensor 601CAA and with + 0.14 bar for the sensor 6031 and about half as large compared to the hydrogen-air mixture. Also, here the situation changes with the transition to a 16 mm aluminium flange. Diagram c) shows that the explosion pressure increases by approx. 11 % to $p_{\text{ex, 601CAA, 16 mm}}$ = 18.51 bar when using the pressure sensor 601CAA, while a comparable value is achieved with the pressure sensor 6031 with a change of approx. - 0.5 % to $p_{\text{ex, 6031, 16 mm}}$ = 15.63 bar. With the 601CAA pressure sensor, an oscillating signal of higher frequency is superimposed on the actual pressure signal, which leads to the increased amplitude. The signal curve of the 6031 is almost unchanged, only a slightly increased oscillation on the pressure curve can be seen. In diagram d) the output signals of the pressure sensors installed in the blind hole also show the cause of the signal superimposition. Due to an oscillation of the flange and a resulting acceleration of the pressure sensor, an amplitude of + 3.68 bar/- 3.22 bar results for the sensor 601CAA and a value range of + 1.50 bar/- 0.96 bar for the sensor 6031. For the sensor 601CAA this results in an increase of the output signal by a factor of approx. 8 for the positive range as well as a deflection into the negative range for the first time. The factorial increase for sensor 6031 is of an order of 10.

When analysing the data of an ethyne-air mixture in Figure 9, a similar behaviour can be seen as with the two combustible-air mixtures investigated previously. Using the 22 mm stainless steel flange (see diagram a)), the two pressure sensor types 601CAA with $p_{\text{ex, 601CAA, 22 mm}}$ = 18.84 bar and 6031 with $p_{\text{ex, 6031, 22 mm}}$ = 17.22 bar give comparable explosion pressures and curve characteristics. The reflective pressure wave superimposed on the global pressure is clearly visible, an imposed signal due to acceleration is not immediately recognisable here. The maximum amplitudes of the output signals of the pressure sensors when using the blind hole (see diagram b)) are in the range of ± 1 bar. Both the pressure curves and the maximum amplitudes of the output signals of the sensors in the blind hole are similar to the results of the hydrogen-air mixture. Diagrams c) and d) show the signal curves when using a 16 mm aluminium flange. Here, partly clear changes in the signal characteristics are recognisable. According to diagram c) the explosion pressures for the sensor 601CAA with $p_{\text{ex, 601CAA, 16 mm}}$ = 20.89 bar have increased by approx. 13 % compared to the result with the 22 mm stainless steel flange. For the sensor 6031, with $p_{\text{ex, 6031, 16 mm}}$ = 18.31 bar, there is also an increase, albeit smaller, of about 6 % in comparison. The pressure curves show clear signal overlays, especially for the 601CAA sensor, which is the reason for the increase in explosion pressure. The cause of these signal overlays also results here from the observation of the output signals of the pressure sensors in the blind hole, shown in diagram d). Due to the acceleration of the pressure sensors, the amplitudes of the sensor signal for the 601CAA sensor are in the range of + 6.45 bar/- 6.85 bar, i.e., about 6 to 7 times higher than for the 22 mm stainless steel flange. The amplitudes of the sensor signal of the 6031 are in the range of + 1.83 bar/- 2.89 bar, i.e., increased by a factor of 2-3. It can be clearly seen that the signal curves of the output signals of the sensors in the blind hole are also reflected in the pressure curves of the sensors. According to the level of the acceleration sensitivities of the pressure sensors, the signal overlay is stronger for sensor 601CAA than for sensor 6031.

It can be stated that all pressure sensors examined in this section are affected by acceleration due to the vibration of the enclosure wall. The level of this acceleration influence depends on the one hand on the real acceleration level due to the explosion effect (the higher the explosion pressure increase over time $(dp/dt)_{\text{ex}}$ the higher the acceleration) and the vibration behaviour of the enclosure wall (flange material and thickness). On the other hand, the acceleration sensitivity due to the respective sensor design plays a decisive role. This acceleration influence can be represented very well by using the pressure sensor with a blind hole without connection to the explosion volume. Even though there is an amplitude in the output signal for all pressure sensors considered, no significant influence on the pressure signal can be detected as long as the output signal is within a range of about ± 1 bar for the configurations being investigated.

4. Signal components of the pressure sensor signal for explosion pressure measurement

To analyse the sensor signals in more depth, it is helpful to apply the method of frequency analysis. Here, the discrete-time sensor signal is separated into its frequency components by means of a Fast Fourier Transform (FFT) and depicted on a discrete frequency spectrum. This procedure allows individual components of the sensor signal to be analysed in isolation and thus assigned to a specific cause. The FFT is applied to both output signals, the one of the pressure sensor in the central through hole with contact to the explosion volume and the one of the pressure sensor in the blind hole without direct connection to the explosion volume. The method of parallel observation of both signals supports the analysis and allocation of the signal components of the actual pressure signal. Since the influence of acceleration is greatest when using the hydrogen-air mixture, only this frequency analysis is presented in Figure 10 and discussed below. However, the results and findings can also be transferred to the configurations with the propane-air mixture and the ethyne-air mixture. The upper two diagrams show the frequency spectra when using the 22 mm stainless steel flange for diagram a) the pressure sensor installed in the through hole and for diagram b) the pressure sensor installed in the blind hole. In the lower two diagrams c) and d) of the same figure, the frequency spectra for the 16 mm aluminium flange are shown correspondingly. The amplitudes are normalised to the maximum value for the respective flange type. In diagram a), in analogy to the pressure curves in Figure 7, there are also corresponding signal curves for the frequency range for all four pressure sensor types. The pressure signal in the range around 0 kHz is the dominant component in the frequency spectrum. Furthermore, a signal component in the range around 2.2 kHz can be identified, as well as its associated second and third harmonic oscillation. This is an oscillation superimposed on the pressure signal with a period of about 0.45 ms, as can be seen in Figure 7. The fact that this is not an

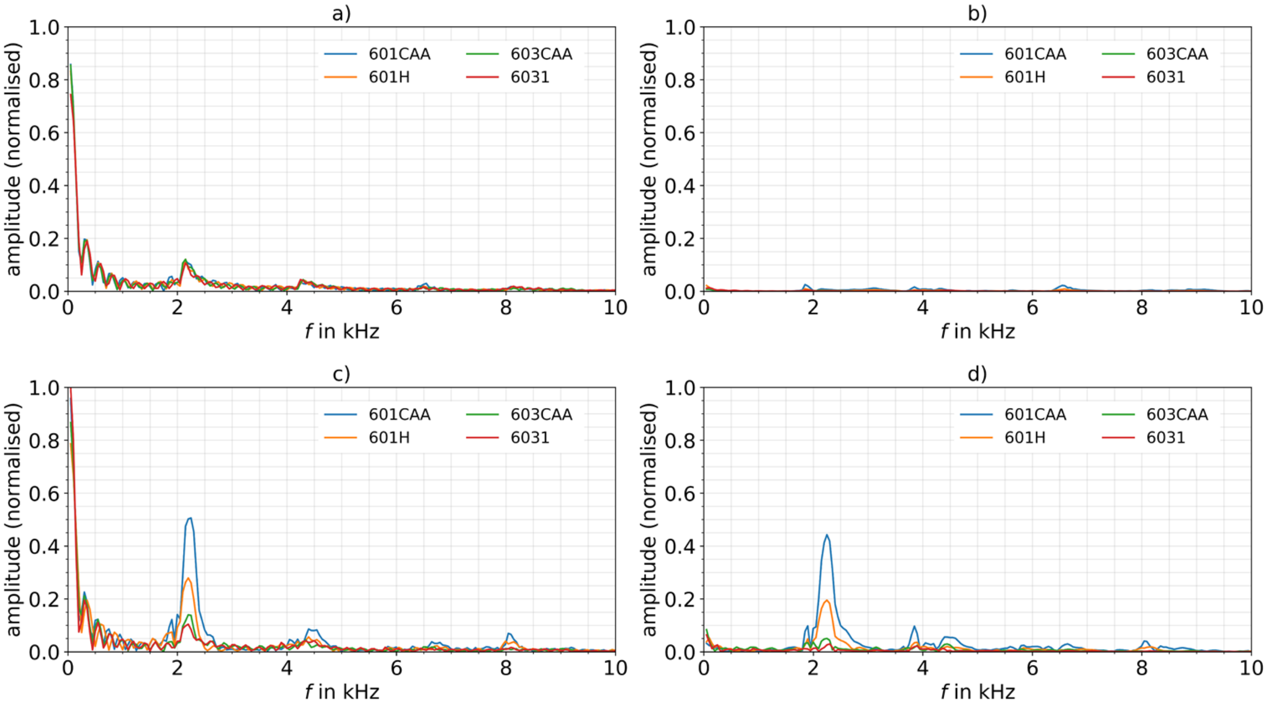

Fig. 10. *Frequency spectra normalised to the highest amplitude for sensor signals of different pressure sensor types for a hydrogen-air mixture (31 ± 1 vol. %* H_2*) on the test sample consisting of cylinders and orifice for pressure sensors in through hole with: a) 22 mm stainless steel flange, c): 16 mm aluminium flange and for pressure sensors in blind hole with: b) 22 mm stainless steel flange, d) 16 mm aluminium flange.*

acceleration effect on the pressure sensors can be explained by two aspects. First, the signal amplitudes for all four pressure sensors are of the same order of magnitude despite different acceleration sensitivities and second, this would be reflected in the frequency spectra of the pressure sensors in the blind hole in diagram b). Here, however, no significant frequency components are visible in relation to the frequency spectrum of the pressure signal. Rather, the signal component is the pressure wave travelling back and forth within the test sample (in the part of the 250 mm long cylindrical stainless steel chamber), which will be explained in more detail later in this section (see Figure 11). For the frequency spectrum of the pressure measurement when using the 16 mm aluminium flange in diagram c), however, there are significantly different characteristics compared to the 22 mm stainless steel flange. In the low-frequency range, the actual pressure signals are also visible for all four pressure sensor types, with comparable characteristics. However, for the range immediately above 2 kHz, frequency components of increased amplitude can be seen, beginning in decreasing order with the greatest amplitude for pressure sensor 601CAA followed by 601H, 603CAA and 6031. While the frequency signal of pressure sensors 6031 and 603CAA is essentially the previously mentioned running pressure wave in the test sample, the observation of the signal curve of the pressure sensors in the blind hole in diagram d) shows that another signal in the comparable frequency range is superimposed on this signal. This is the influence of acceleration on the pressure sensors, which is also reflected in the different signal curves for the pressure sensors in the time domain (see diagram c) in Figure 7). In summary, it can be stated that the signals of the pressure sensors are essentially composed of three components: the pressure as a result of the explosion, the running pressure wave in the test sample and the acceleration effect of the pressure sensor. The level of the first two components is independent of the type of pressure sensor, but the level of the third component is not. To illustrate that a signal component superimposed on the pressure signal occurs due to a running pressure wave when using the hydrogen-air mixture, a further experiment is conducted with a slightly modified test sample. Here, in the test sample used, the 250 mm long stainless steel chamber is exchanged for a chamber of double length with otherwise identical characteristics. In this case, the explosion test for a hydrogen-air mixture is carried out with the 22 mm stainless steel flange and the pressure sensor type 601CAA. This combination results in the most significant running wave in the test sample with a simultaneous low influence of the acceleration.

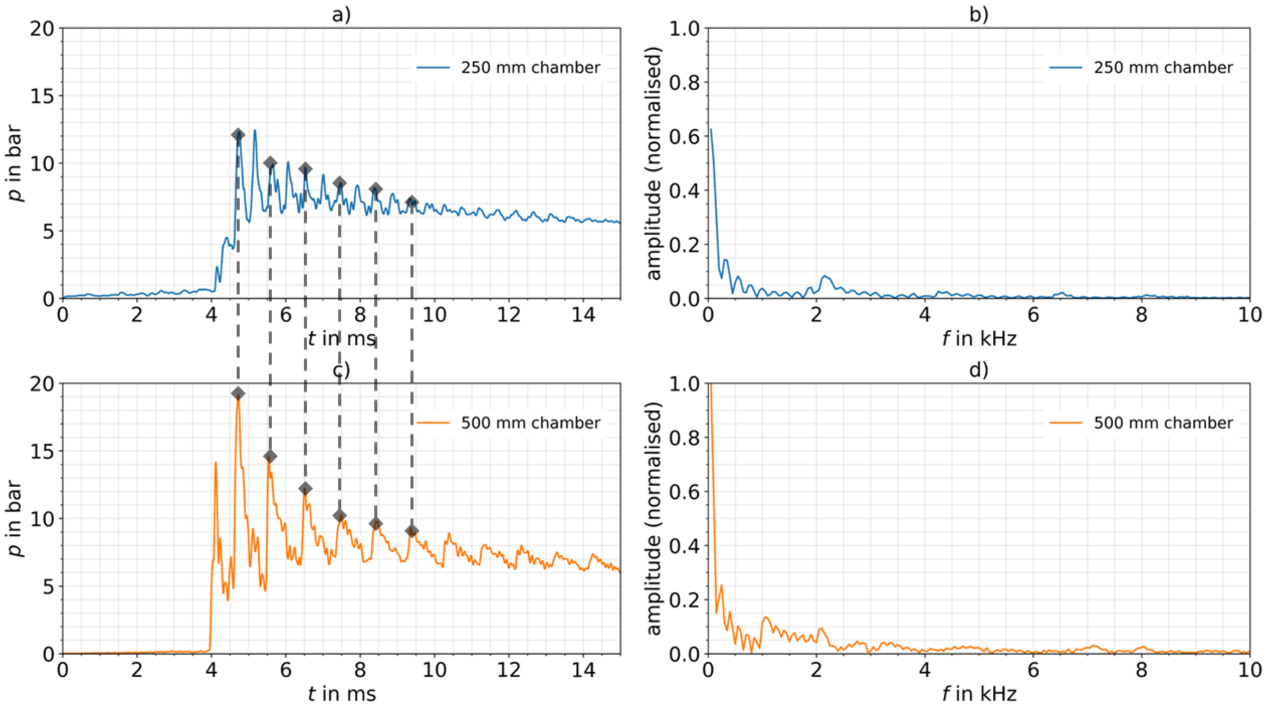

Fig. 11. *Pressure curves with frequency spectra for two length combinations of the test sample for a hydrogen-air mixture (31 ± 1 vol. % H_2) with 22 mm stainless steel flange and sensor 601CAA.*

The pressure curve resulting from the experiment is shown in Figure 11 in comparison to the already known pressure curve of the original test sample. Diagram a) shows the pressure curve for the combination with the 250 mm chamber (from Figure 7). Diagram c) shows the pressure curve for the combination with the 500 mm chamber. Comparable pressure curve characteristics can be seen. Furthermore, the period of the oscillation superimposed on the pressure signals due to the running wave is doubled for the combination with 500 mm chamber with approx. 0.9 ms compared to the combination with 250 mm chamber with approx. 0.45 ms. Also, when comparing the corresponding frequency spectra shown in diagrams b) and d), it can be seen that the corresponding frequency component of the signal of the running wave occurs in the range around 2 kHz for the combination with 250 mm chamber and in the range around 1 kHz for the combination with 500 mm chamber, as well as the corresponding harmonic oscillations. This shows that the signal component in question must be the reciprocating pressure wave in the test sample, since the other possible signal components discussed do not change their period or frequency with the change in length of the test sample. In the combination with a 500 mm chamber, the pressure wave travels twice the distance, which leads to a corresponding doubling of the period and halving of the frequency.

The second signal component, which in our considerations can be superimposed on the actual pressure signal in addition to the running wave in the test sample, results from the acceleration effect of the pressure sensor. As discussed in the previous investigations, the magnitude of this signal component is essentially dependent on the pressure rise time of the explosion as well as the acceleration sensitivity of the pressure sensor. The frequency of the signal component results from the vibration frequency of the test sample enclosure due to the explosion of the combustible-air mixture, which is transmitted to the pressure sensor installed in the test sample enclosure wall. From the frequency analyses for the pressure sensors installed in the blind holes, signal components in the range above 2 kHz, with varying intensity, are obtained for all combustible-air mixtures considered. To show that this signal component can be causally attributed to the acceleration, the use of an impulse hammer is suitable. With the impulse hammer test, the dynamic behaviour of the mechanical structure of the test sample can be investigated (see Figure 12). For this purpose, the enclosure of the test sample is excited to vibrate by a hammer blow, which is also transmitted to the pressure sensors installed in the through hole and blind hole. The sensor signal of the pressure sensors is then recorded as in a usual signal acquisition for the determination of an explosion pressure and thus exclusively

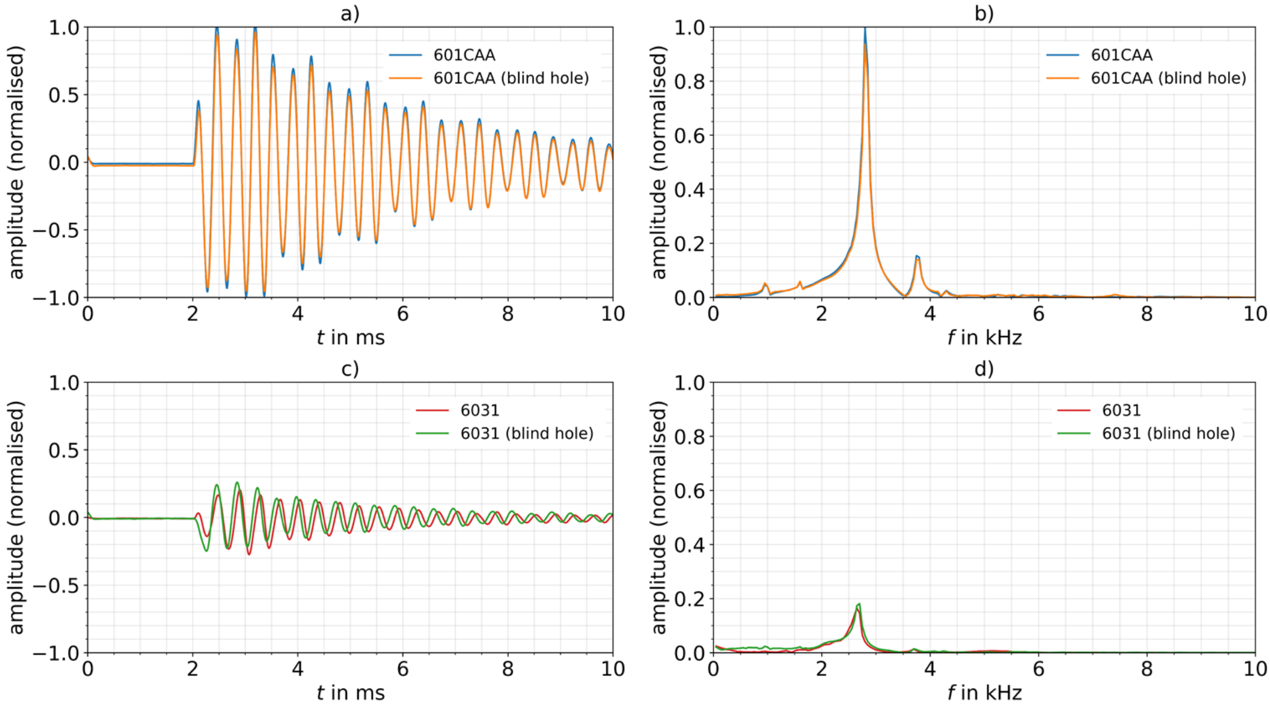

Fig. 12. *Signal curves with frequency spectra for impulse hammer test for test sample with 22 mm stainless steel flange and sensors 601CAA and 6031.*

represents the acceleration effect. The applied impact force is recorded by a quartz force sensor located in the hammer head. Figure 12 shows the signal responses normalised to the impact force for the pressure sensors 601CAA (diagram a)) and 6031(diagram c)), each installed in the through hole and in the blind hole. The test sample with the 16 mm aluminium flange is used here. For both sensor types in both installation variants, an oscillation with a period duration of approx. 0.37 ms can be detected. The signal amplitude of the pressure sensors 601CAA is higher compared to the pressure sensors 6031, which is due to the higher acceleration sensitivity. Diagrams b) and d) show the associated frequency spectra. For both pressure sensor types and installation types, there is a dominant signal component in the range of 2.7 kHz. This corresponds approximately to the signal component that occurs in the sensor signals during the explosion tests. The small deviation can be explained by the different excitation forms and effective locations of the explosion and the impulse hammer. This result shows that the dynamic behaviour of the test samples leads to an acceleration effect of the pressure sensors, which can influence the actual pressure signal.

5. Consideration of the acceleration influence on the pressure sensor signal

While the signal components *pressure as a result of the explosion of the combustible-air mixture* and *running wave in the test sample* are desired quantities to be recorded in the measurement of explosion pressures, the signal component *acceleration effect of the pressure sensors* is a quantity that falsifies the pressure curve signal and thus negatively influences the measurement. In the following, two approaches are discussed to consider the unwanted signal component of the acceleration effect and to separate it from the desired signal components. In detail, the test sample configuration using a hydrogen-air mixture (31 ± 1 vol % H_2) and the 16 mm aluminium flange for the 601CAA pressure sensor is considered, since a correspondingly high acceleration effect occurs. Both approaches are compared with the results of the 601CAA for the 22 mm stainless steel flange (see Figure 7) as the target curve, as there is no significant acceleration effect here. The approach of the first method is to eliminate the frequency components of the acceleration determined by means of frequency analysis from the frequency components of the pressure using the respective frequency spectra. To do this, the frequency spectrum of the pressure sensor installed in the blind hole is subtracted from the frequency spectrum of the pressure sensor in contact with the explosion volume, i.e., the actual pressure measurement. The resulting new frequency spectrum is then transformed back into a discrete time signal using the inverse function of the Fast Fourier Transform (IFFT). Figure 13 illustrates the individual steps. Diagram a) shows the problem and thus the starting point of the consideration with the pressure curve of the 601CAA as the quantity to be corrected with clearly visible acceleration influences. In addition, this diagram shows the pressure curve of the 601CAA for the 22 mm stainless steel flange with the same configuration as the desired signal without significant acceleration influences. Both signal curves are significantly different. Diagram b) shows the new frequency spectrum, which results from the subtraction of the frequency spectra as already described (see Figure 10: diagram c) and d)). For comparison, the target frequency spectrum of the 601CAA with 22 mm stainless steel flange is also plotted (see Figure 10: Diagram a)). It can be indicated that the frequency component of the acceleration above 2 kHz is significantly reduced and the new frequency spectrum shows an overall improved match with the target spectrum. Diagram c) shows the resulting pressure curve for the 601CAA from the subtraction procedure compared again with the pressure curve of the 601CAA for the 22 mm stainless steel flange. The comparability of the two signal curves is significantly improved. Furthermore, the newly formed (adjusted) pressure curve with $p_{\text{ex, adj., 601CAA}}$ = 13.25 bar results in a 20.2 % lower explosion pressure than the original value for the 16 mm aluminium flange of $p_{\text{ex, 601CAA, 16 mm}}$ = 16.23 bar. Compared to the own value of $p_{\text{ex, 601CAA, 22 mm}}$ = 12.45 bar for the explosion pressure when using the 22 mm stainless steel flange, the difference is now less than 1 bar. These results show that the applied subtraction method of the frequency spectra is applicable for the considered configuration and that a compensation of the acceleration influences could be achieved without suppressing the signal component of the running pressure wave. The results after applying the described procedure to the configurations with propane-

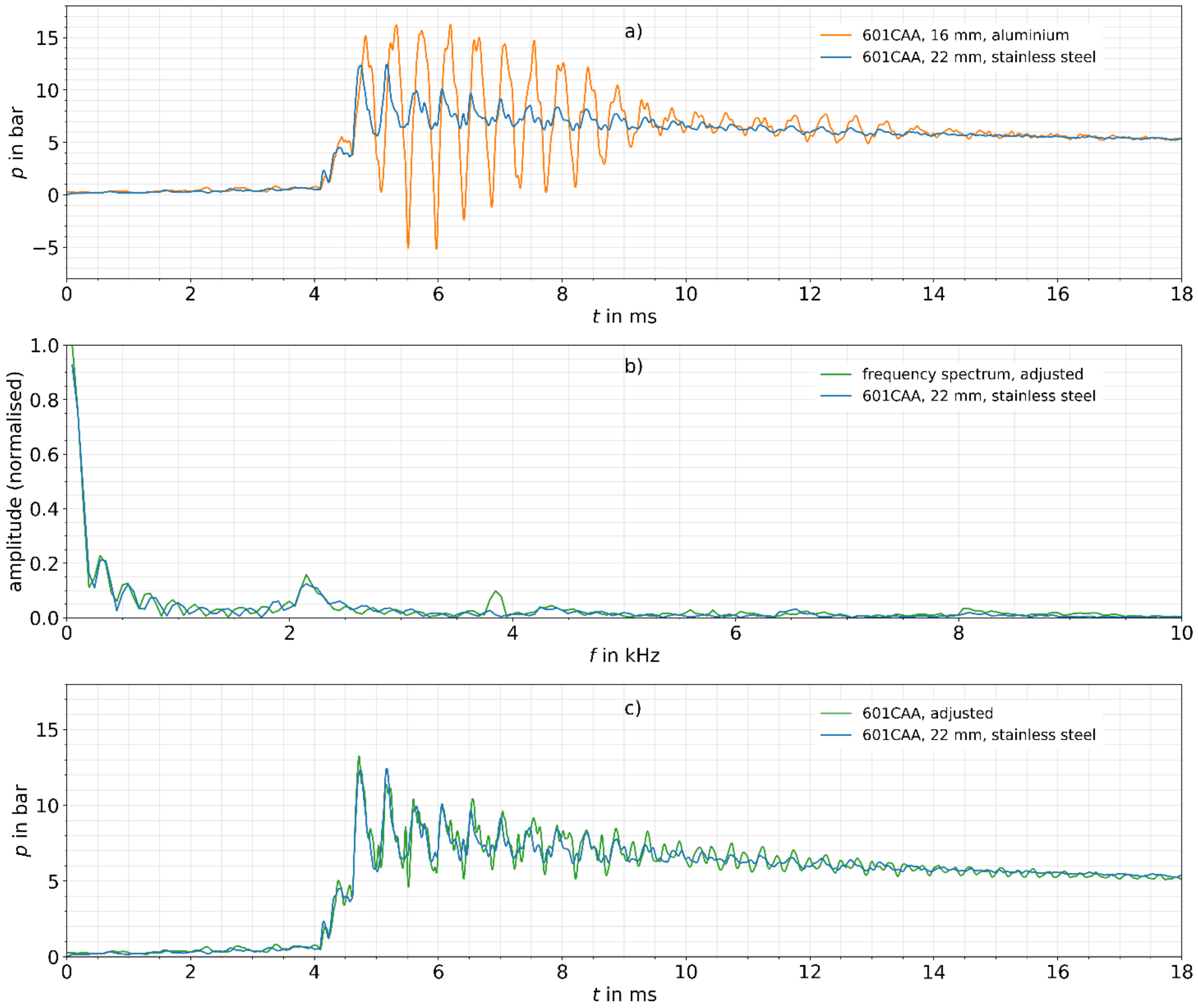

Fig. 13. *Pressure curves and frequency spectra for the pressure sensor 601CAA using the 16 mm aluminium flange in comparison to the 22 mm stainless steel flange for a hydrogen-air mixture (31 ± 1 vol. % H_2) using the subtraction method: a) original signal with acceleration component for the 601CAA, b) frequency spectrum for the 601CAA after application of the subtraction method, c) corrected pressure curve of the 601CAA.*

air mixture and ethyne-air mixture are summarised in Figure 14 (without showing the intermediate step of the frequency spectra). Diagrams a) and c) show the initial situation for both the propane-air mixture (diagram a)) and the ethyne-air mixture (diagram c)) with the pressure curves for the two flanges under consideration, 16 mm aluminium and 22 mm stainless steel. The pressure curve for the 16 mm aluminium flange is the signal to be corrected, while the pressure curve for the 22 mm stainless steel flange represents the target curve. The diagrams b) and d) show the resulting new pressure curves after application of the subtraction method of the frequency spectra in comparison to the target curves for propane (diagram b)) and ethyne (diagram d)). Also, for these cases, an improved comparability in the explosion pressure levels and in the characteristics of the signal curves can be demonstrated.

Overall, the investigations for the three different combustible-air mixtures show that the acceleration influences can be compensated with the discussed method without significantly influencing a running pressure wave. However, this method requires considerable effort in post-processing the signal curves and is therefore not always fully applicable in practical use.

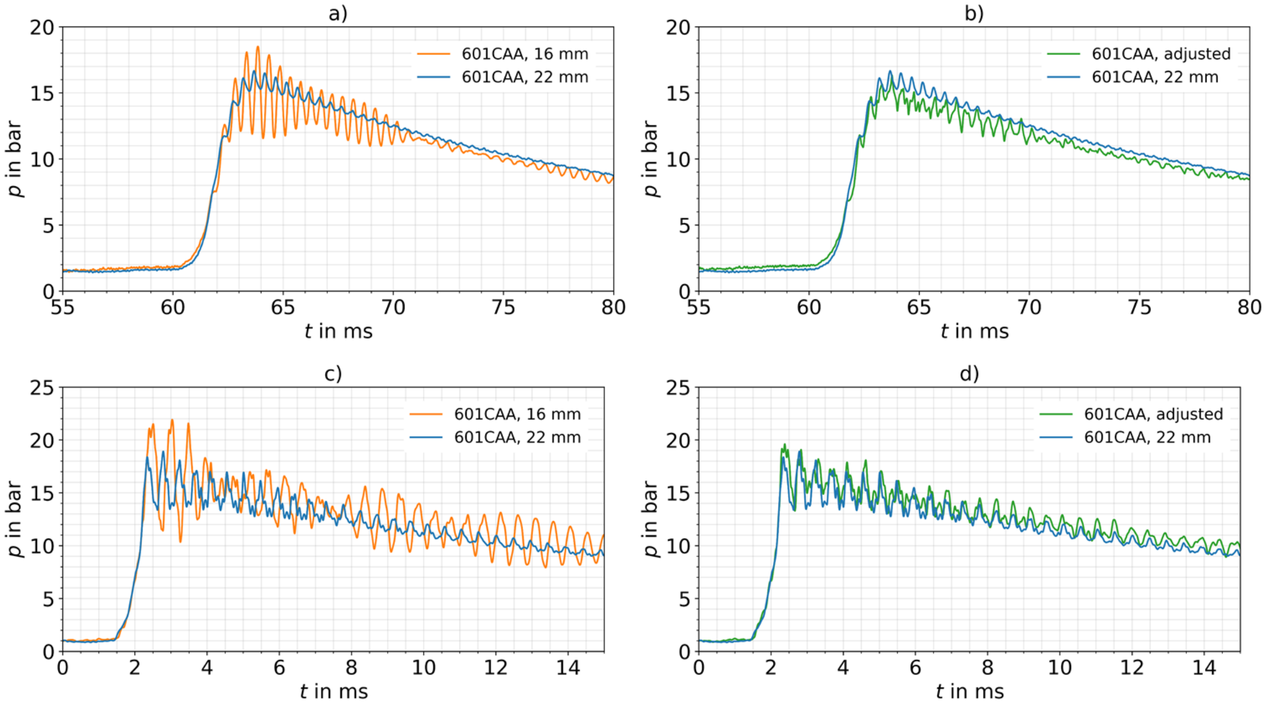

Fig. 14. *Pressure curves for the pressure sensor 601CAA for the 16 mm aluminium flange in comparison to the 22 mm stainless steel flange using the subtraction method for a propane-air mixture (4.6 ± 0.3 vol. % C_3H_8) (diagrams a) and b)) and an ethyne-air mixture (14 ± 1 vol. % C_2H_2) (diagrams c) and d)) with a) and c): original signal with acceleration component for the 601CAA; and b) and d): corrected pressure curve of the 601CAA.*

The second method for considering the influence of acceleration on the pressure sensor signal focuses on the application or adaptation of filter functions. In the following, the same cases are considered as with the previously examined subtraction procedure of the frequency spectra. The procedure for this approach is that a "tailored" filter adjustment is made individually for the corresponding pressure curve. The signal curves and frequency spectra of the pressure sensors from the blind holes (without connection to the explosion volume) are also used as a basis here. The filter functions are then specifically selected during the data post-processing so that the corresponding frequency components due to acceleration effects in the frequency spectrum of the pressure sensor in the blind hole are filtered out. This resulting filter function is then subsequently applied to the actual pressure signal. For this purpose, Figure 15 shows the frequency spectra of the pressure sensors from the blind holes of the 16 mm aluminium flange resulting from the filter adaptation in comparison to the frequency spectra of the 22 mm stainless steel flange as a target spectrum for the three combustible-air mixtures considered. In addition, the new pressure curves resulting from the filter adjustment are also shown in the same figure. While a low-pass filter with a 3 dB point at 5 kHz (Butterworth, 2nd order) is used as standard for the sensor signals when using the 22 mm stainless steel flange, a combination of several filter functions is used for the sensor signals to be corrected with the 16 mm aluminium flange, depending on the combustible-air mixture used. For the hydrogen-air mixture, the combination of a low-pass filter (Bessel, 3rd order) with a cut-off frequency of 3.7 kHz and a bandstop filter for the frequency range 1.9 kHz to 3.2 kHz (Butterworth, 2nd order) is applied. The result in diagram a) shows a frequency spectrum that clearly approximates the target spectrum (compared to the original frequency spectrum without filter adjustment from Figure 10, diagram d)). The frequency components due to the influence of the acceleration from the original signal in the range above 2 kHz and 4 kHz are clearly reduced. Diagram b) shows the pressure signal after applying the adjusted filter functions. Also here, an improved match of the pressure signals can be seen in the comparison. The original pressure signal with acceleration influences of $p_{\text{ex, 601CAA, 16 mm}}$ = 16.23 bar is $p_{\text{ex, adj., 601CAA}}$ = 11.44 bar after application of the new filter functions and is thus closer to the target value $p_{\text{ex, 601CAA, 22 mm}}$ = 12.45 bar, although slightly lower. Furthermore, a slight phase shift can be

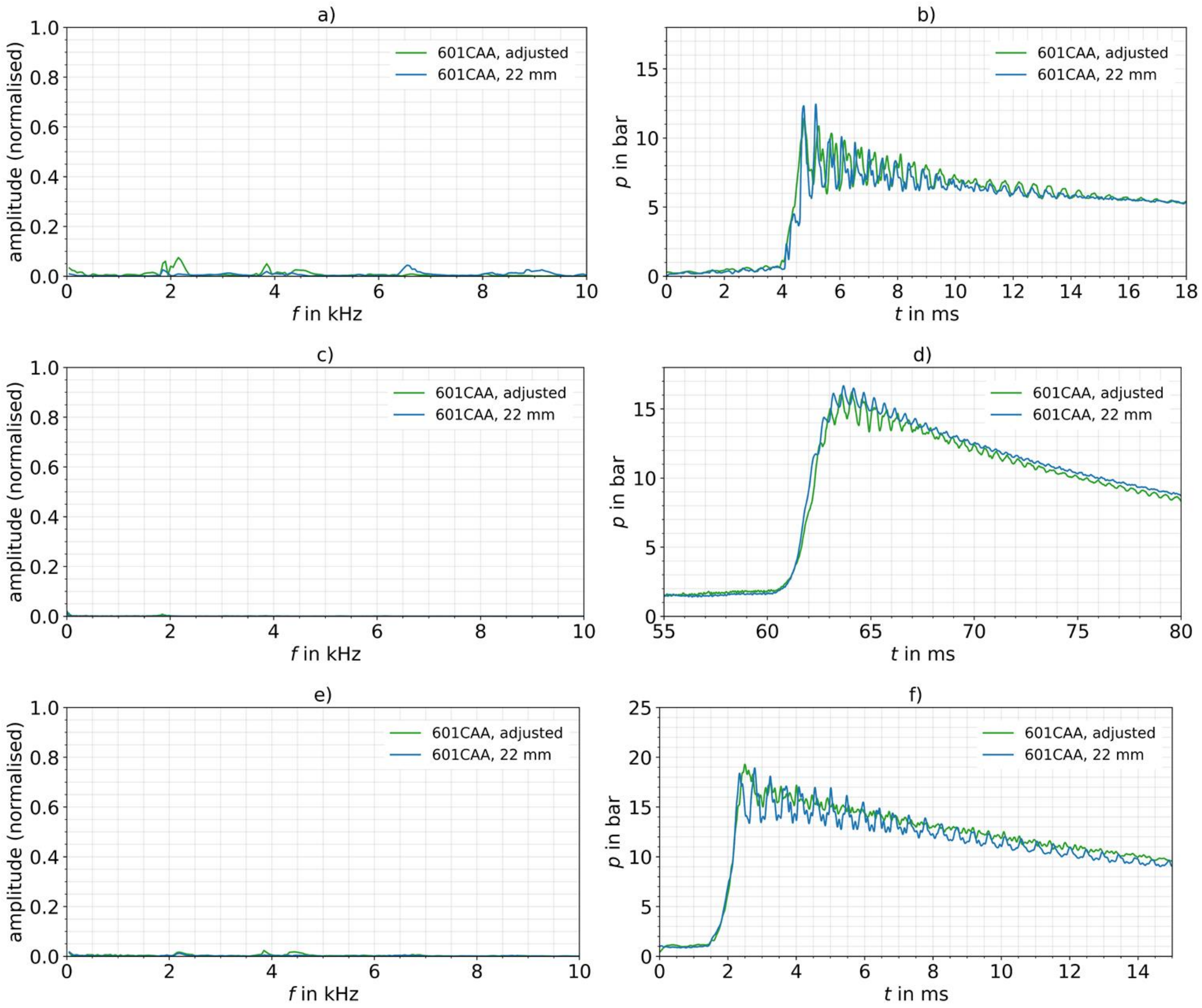

Fig. 15. *Frequency spectra and pressure curves for the pressure sensor 601CAA for the 16 mm aluminium flange in comparison to the 22 mm stainless steel flange using the filter adapting method for a hydrogen-air mixture (31 ± 1 vol. %* H_2*) (diagrams a) and b), propane-air mixture (4.6 ± 0.3 vol. %* C_3H_8*) (diagrams c) and d)) and an ethyne-air mixture (14 ± 1 vol. %* C_2H_2*) (diagrams e) and f)) with a),c) and e): frequency spectra of the pressure sensors from the blind holes after filter adapting; and b),d) an f): filtered pressure curve of the 601CAA.*

detected between the signal curves, which is a characteristic property of the applied filter functions. In analogy, improved matches of the frequency spectra and signal characteristics can also be achieved for the propane-air mixtures using a band-stop filter for the frequency range 1.8 kHz to 2.5 kHz (Butterworth, 2nd order) in addition to the standard filter (see diagrams c) and d)) as well as for the ethyne-air-mixture applying two filter applications consisting of a band-stop filter (frequency range: 1.9 kHz to 3.2 kHz; Butterworth, 2nd order) and a low-pass filter (cut-off frequency: 4 kHz, Bessel, 2nd order) (see diagrams e) and f)). In summary, it can be stated that for the configurations considered, when varying three combustible-air mixtures, it is possible by adapting the filter functions used to reduce the acceleration components influencing the pressure signal to such an extent that they no longer significantly alter the pressure signal. For this method, it is also necessary to record the signal curve of a pressure sensor in parallel, which has no direct connection to the explosion volume (blind hole) and thus only represents the effect of the acceleration of the sensor in the sensor signal. Due to the large number of possible pressure curves resulting from the almost infinite variations in the boundary conditions of the test with regard to different geometries, combustible-air mixtures, pressure sensors, filter options, etc., it is not possible to specify a particular filter for this procedure in advance. It is always necessary to analyze to what extent the acceleration sensitivity of the pressure sensor affects the pressure signal and subsequently apply an appropriate filter function.

6. Influence of acceleration on the pressure signal using the example of a real Ex equipment

In this part of the work, the knowledge gained from the previous investigations is applied to determine the explosion pressure on a real Ex equipment with substantial acceleration of the enclosure walls. For this purpose, the second test sample (see Figure 3) and the experimental setup specified in section 2.1 are used. In this case, as described, instead of using a second pressure sensor of the same type for determining the influence of acceleration in the blind hole, a second measurement is conducted with the identical sensor, but using an adapter with a closed front. Figure 16 shows the sensor signals for sensor types 601CAA and 6031 for the use of a hydrogen-air mixture, both for the through hole for measuring the pressure and for the closed adapter to determine the acceleration effects. Diagram a) shows that the explosion of the hydrogen-air mixture inside the test sample leads to different pressure curves and explosion pressures depending on the type of pressure sensor used. A clear oscillation signal is superimposed on the pressure curve of the 601CAA, which with $p_{\text{ex, 601CAA}}$ = 7.67 bar leads to an explosion pressure increased by approx. 38% compared to the 6031 with $p_{\text{ex, 6031}}$ = 5.56 bar. The frequency spectra assigned to the pressure curves in diagram c) also cause of this superimposed oscillation becomes evident when looking at the sensor signals of the pressure sensors using the closed adapter (see diagram b)). For the 601CAA sensor, the acceleration influences lead to higher signal oscillations due to the higher acceleration sensitivity than for the acceleration compensated 6031 sensor. The corresponding frequency spectrum in diagram d) also shows the frequency component with increased amplitude of the 601CAA in the range around 1 kHz. In order to consider the identified acceleration influences on the pressure signal of the sensor 601CAA, the second method of adapting the filter function is applied. In this case, the use of the first method discussed for subtracting the frequency spectra does not lead to a sufficient reduction in the influence of acceleration on the sensor signal. The reason for this is that the pressure measurement

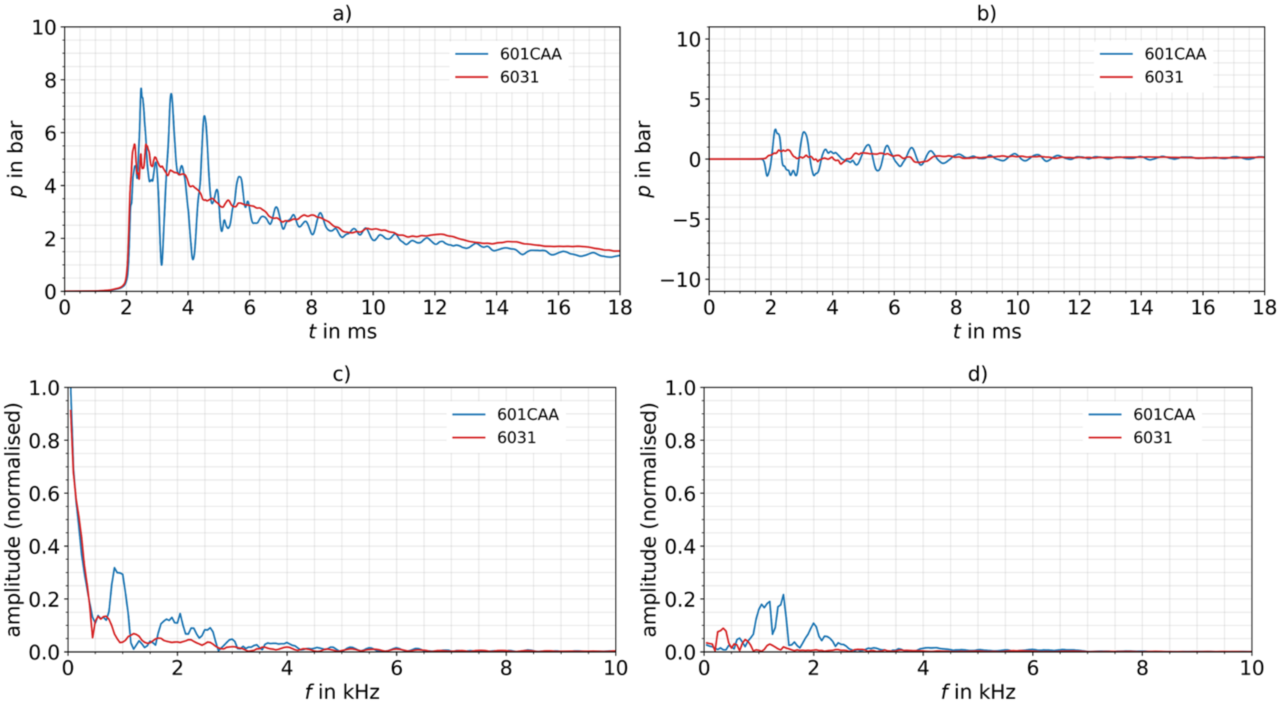

__Fig. 16.__ Pressure curves and frequency spectra for the pressure sensors 601CAA and 6031 for the second test sample “real Ex equipment” for a hydrogen-air mixture (31 ± 1 vol. % H_2); diagram a): Pressure curves of the pressure sensors; diagram b): Signal curves of the pressure sensors with closed adapter; diagram c): Frequency spectra of the pressure curves of the pressure sensors; diagram d): Frequency spectra of the signal curves of the pressure sensors with closed adapter.

using the through hole is not measured in parallel with the sensor signal using the closed adapter, due to the enclosure geometry. This always leads to slightly different signal curves due to different explosions. The filter function adapted using the signal curve from the sensor in the closed adapter and its frequency spectrum is applied to the pressure signal measured by the 601CAA. In addition to the standard low-pass filter with a 3 dB point at 5 kHz (Butterworth, 2nd order), a band-stop filter is used in the frequency range from 0.6 kHz to 3 kHz (Bessel, 2nd order). The resulting new signal curves for the pressure sensor (diagram a)) and the sensor for determining the acceleration (diagram b)) are shown in Figure 17. The influence of the acceleration on the sensor signal is significantly reduced by adapting the filter function. The explosion pressure with $p_{\text{ex, 601CAA, adj.}} = 5.58$ bar is now in the comparable range to the explosion pressure of $p_{\text{ex, 6031}} = 5.56$ bar measured by the sensor 6031. In addition, the consistency of the characteristics of the signal curves are improved compared to the original ones (see Figure 16). Also, for real Ex equipment without idealized housing geometry, it is shown that with the help of a procedure for determining the acceleration influences on the sensor type used (here by using the closed adapter) and a corresponding adaptation of the filter functions, the acceleration influences affecting the pressure signal can be reduced.

7. Conclusions

When measuring explosion pressures, vibrations of the enclosure walls occurring as a result of the explosion can be transmitted to the pressure sensors used and, depending on the acceleration sensitivity of the sensor, alter the measurement result. This can lead to an unwanted signal being superimposed on the desired pressure signal. In this paper it is demonstrated that this unwanted additional signal can be of the order of several bar. If this parasitic signal component remains undetected, this can lead to incorrect test results and hence to higher requirements, e.g., for testing and certification of Ex equipment. Thus, it is first important to be able to determine that there is an unwanted influence on the sensor signal due to acceleration effects. To determine this influence, a

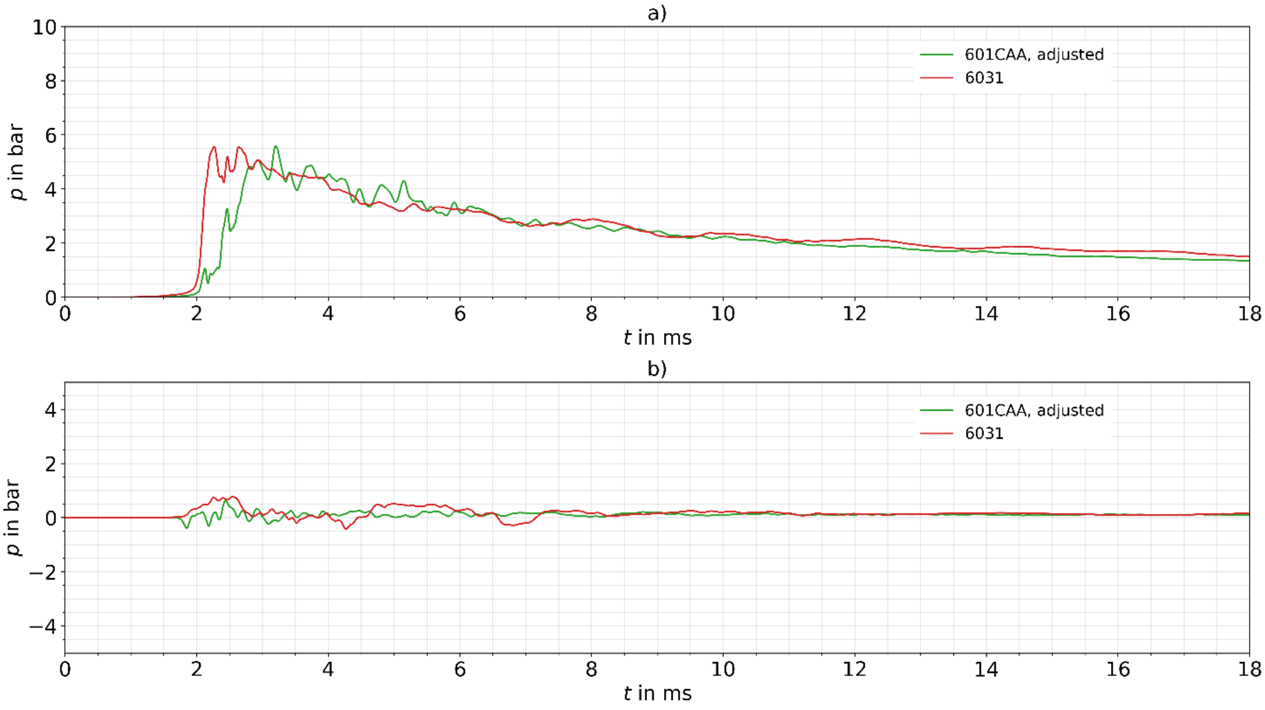

Fig. 17. *Pressure curves for the pressure sensor 601CAA for the test sample “real Ex equipment” in comparison to sensor 6031 using the filter adapting method for a hydrogen-air mixture (31 ± 1 vol. %* H_2*) in diagram a) and the associated sensor signals of the identical sensors using closed adapters in diagram b)*

simple and practical procedure is to install a pressure sensor of the same type close to the actual measuring location, but without contact to the explosion volume. This can be in the form of a blind hole or a closed adapter, depending on the test sample characteristics. With this information, measures can be taken to reduce the influence of the acceleration sensitivity of pressure sensors on the measurement of explosion pressures. The simplest, but rarely practicable option is to use appropriate pressure sensors with which the problem does not occur (low acceleration sensitivity). However, this depends on the level of acceleration and is therefore not a general solution. Especially since acceleration sensitivity is not the only decisive technical specification of relevance for pressure sensors. The other more universal and thus more practical possibility is to eliminate the acceleration contributions via the subtraction of the frequency spectra or to apply individual filter functions that specifically filter out the acceleration components. Which method is more appropriate depends on the test parameters and must be decided individually. The difficulty regarding the determination of explosion pressures in the context of flameproof enclosures according to IEC 60079-1 is that only a low-pass filter with a 3 dB point of 5 kHz ±0.5 kHz shall be used to smooth the signal. However, this filter specification does not solve the problem; on the contrary, it severely limits the possibilities for meeting the challenge with the methods presented in this work. The authors therefore recommend that the acceleration sensitivity of pressure sensors be considered when determining explosion pressures by a) using pressure sensors that are insensitive to acceleration or b) adapting the strict specification of the filter in the IEC 60079-1 standard. When adjusting the filter specifications, care must be taken to ensure that this does not lead to a significant underestimation of the actual explosion pressure.

References

International Electrotechnical Commission (2014), *IEC 60079-1, Explosive Atmospheres - Part 1: Equipment Protection by Flameproof Enclosures “d”*, Edition 7.0

Krause, T., Bewersdorff, J., Markus, D. (2017), *Investigations of static and dynamic stresses of flameproof enclosures*, Journal of Loss Prevention in the Process Industries, Volume 49, Part B, pp. 775-784, Elsevier; doi: https://doi.org/10.1016/j.jlp.2017.04.015

Spörhase, S., Brombach, F., Eckhardt, F., Krause, T., Markus, D., Küstner, B., Walch, O. (2021), *Untersuchungen zur Vergleichbarkeit der statischen und dynamischen Überdruckprüfung von druckfesten Kapselungen*, Paper submitted to Forschung im Ingenieurwesen in September 2021, Springer; ISSN (electronic): 1434-086

Tichý, J., Gautschi, G. (1980), *Piezoelektrische Meßtechnik*, Springer-Verlag; ISBN 3-540-09448

Ren, Z., Jia, Z., Zhang, J., Shang, Y., Gao, S. (2013), *Research on the Dynamic Error and Acceleration Compensation for the Piezoelectric Sensor*, Sensors & Transducers, Vol. 153, Issue 6, pp. 118-123; ISSN: 1726-5479 (Online)

Wang, G., Li, Y., Cui, H., Yang, X., Yang, C., Chen, N. (2021), *Acceleration self-compensation mechanism and experimental research on shock wave piezoelectric pressure sensor*, Mechanical Systems and Signal Processing, Volume 150, Elsevier;
doi: https://doi.org/10.1016/j.ymssp.2020.107303

Xu, F., Ma, T. (2019), *Modeling and Studying Acceleration-Induced Effects of Piezoelectric Pressure Sensors Using System Identification Theory*, Sensors (Basel), 19(5): 1052;
doi: 10.3390/s19051052

Grüningen, D. (2004), *Digitale Signalverarbeitung*, 3. Auflage, Fachbuchverlag Leipzig;
ISBN: 3-446-22861-6

Krause, T., Meier, M., Brunzendorf, J. (2021), *Influence of thermal shock of piezoelectric pressure sensors on the measurement of explosion pressures*, Journal of Loss Prevention in the Process Industries, Volume 71, Elsevier; doi: https://doi.org/10.1016/j.jlp.2021.104523

Kistler (2021), *Data sheets piezoelectric presser sensors type 601CAA, 601H, 603CAA, 6031*, Kistler Group, Switzerland

DOI: 10.7795/810.20221124

A comparative study between two ignition sources: electric igniter versus pyrotechnic igniter

Chayma EL GADHA, Stéphane BERNARD and Mame WILLIAM-LOUIS
Laboratoire PRISME EA 4229, IUT de Bourges, University of Orleans, INSA-CVL, France

E-mail: stephane.bernard@univ-orleans.fr
chayma.el-gadha@univ-orleans.fr

Abstract

The risk assessment of combustible explosive dust is based on the determination of the probability of dust dispersion, the identification of potential ignition sources and the evaluation of explosion severity. It is achieved in most of cases with the two main experimental normalized devices such as the Hartmann tube (spark ignition) and the 20L spherical bomb (with the 5 kJ pyrotechnic ignitors).

Ignition energy of the 5kJ ignitor is well calibrated and generates a reproducible ignition. But on the other hand this ignition is not punctual and the over pressure produced is nearly 2 bars. Moreover, the pyrotechnic igniter accelerates the combustion with multi ignition points in a large volume and that disturbs the kinetics. In this way, this ignition source does not allow to analyse the combustion products because the composition of the pyrotechnic igniter was found in the combustion products.

This article deals with the comparison of two ignition sources in the 20 L spherical bomb. A large panel of classical explosive dusts is studied with electrical and pyrotechnic ignitors, in order to evaluate the possibility to establish a correspondence between parameters obtained with these two ignition technics.

Severity parameters of Aluminium powder, titanium alloy and nicotinic acid CaRo 11 were measured by using the two types of ignition system in our 20 L spherical bomb equipped with the Kühner dihedral injector. The maximum explosion overpressure P_{max} and dust deflagration index K_{st} were measured in a large range of concentration allowing to propose correlations between electrical and pyrotechnic ignition for each parameter and each type of powder. The relevance of these correlations will be discussed.

Keywords: Dust explosions, Pyrotechnic ignitor, Electric spark ignitor, Aluminium, Titanium, Nicotinic acid.

1. Introduction

Safety features are essential for determining the risks of explosion when handling combustible dust and for designing safety measures. This dust safety-related properties are often inspected without considering the influence of the ignition source as mentioned by (Askar & Schröder, 2019).

The explosion characteristics severity maximum explosion pressure P_{max} and maximum rate of explosion pressure rise $(dp/dt)_{max}$ are determined in closed vessels such as the 20-L-sphere.

Tests are preformed according to the international standards, for example the EN 14034 series (2004-2006).

For explosion tests on dusts, chemical igniters are primarily used (DIN EN 14034; ASTM1226). There are standardized chemical igniters with defined energies ranging from 1000J to 10000J. The igniters generate a large spherical flame with a volume over the 20 L bomb, as described by (Proust, et al., 2007), and the ignition is not punctual but multipoint. This last point contradicts one of the original objectives of the sphere which was to have a central point ignition. Moreover, the pyrotechnic igniter accelerates the combustion and disturbs the kinetics. In this way, this ignition source does not allow to analyze the combustion products because the composition of the pyrotechnic igniter was found in the combustion products.

The need for alternative ignition sources arises due to several drawbacks of pyrotechnic igniters, in addition to their high cost and high energy input compared to most ignition sources used in practice. This type of ignition source should be less expensive, generally available, and allow the operator to use it without a certificate of competency. Another ignition source that fulfils these requirements is the "spark ignition".

A previous paper from (Scheid, et al., 2013) reports the test results of a comparative study between two ignition sources: pyrotechnical igniter and exploding wire. P_{max} and $(dp/dt)_{max}$ values from 5 different dusts were determined with both ignition sources in the range of 100 J to 1 kJ. The P_{max} values determined with exploding wire were less than 10% lower than values determined according to the test standard. The influence of the ignition energy of the igniter on the maximum explosion pressure seems to be almost negligible. In contrast to that $(dp/dt)_{max}$ values determined according to the test standard led to 30% higher values.

(Spitzer, et al., 2021) present results of a comparative calorimetric and visual study between four different types of ignition sources (Exploding wire, Chemical igniter, Induction spark and Surface-gap spark). The influence of the electrode-orientation, distance as well as ignition energy on the reproducibility of the exploding wire igniter was tested.

For the study maximum explosion pressure and maximum explosion pressure rise values from CaRo11, aluminium and titanium dusts were determined with both ignition sources. Dust explosions are generally characterized by complex reaction mechanisms, which depend on the chemical composition of the dust, dust concentrations and flow conditions. (Van der Wel, 1993) distinguishes between different reactions mechanisms depending on whether the reaction takes place in the gas phase by evaporation or at solid surface in form of gaseous products or solid or liquid material.

This paper concerns the comparison of two ignition sources in the 20 L spherical: electric igniter versus pyrotechnic igniter. A large panel of classical explosive dusts is studied with these ignitors, in order to evaluate the possibility to establish a correspondence between parameters obtained with these two ignition technics. The dusts were selected such that different combustion mechanisms were considered: Aluminium powder, titanium alloy and nicotinic acid CaRo 11.

DOI: 10.7795/810.20221124

2. Materials and Equipement

2.1 Materials

Aluminium powder used in the present work is a commercial micron sized aluminium powder (purity>99.7%) supplied by the company M&C "Métaux & Chimie" and referenced F3915. For titanium, Ti6Al4V powders were manufactured by TLS Technik spezialpulver. The size distribution of these powders was determined with a laser diffraction technique (Malvern).The result is presented in **Table 1**. This measure provides a statistical analysis via $D_v(10)$, $D_v(50)$ and $D_v(90)$.

Table 1: *Particles size*

	AlF3915	Ti6Al4V
D_{10}, µm	8	11.88
D_{50}, µm	35	26.42
D_{90} ,µm	80	44.3

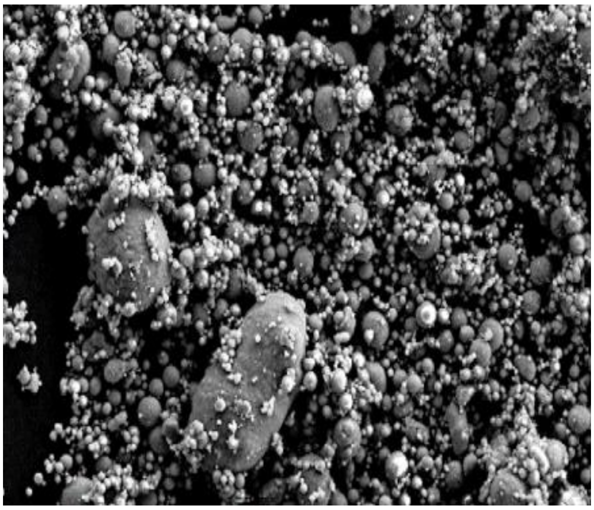

Fig. 1. *SEM photography of pure aluminium*

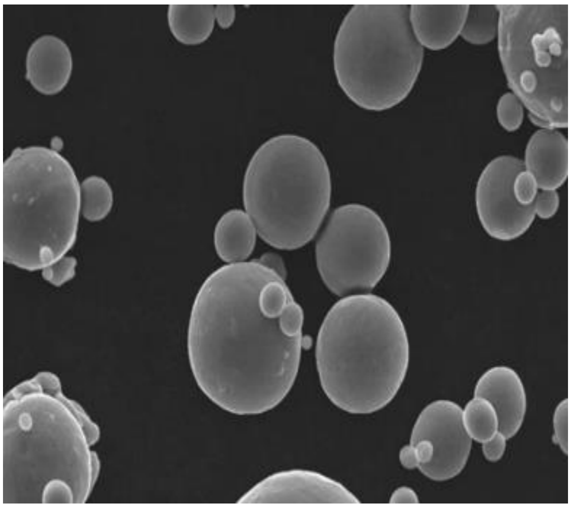

Fig. 2. *SEM photography of Ti6Al4V 26 µm*

The SEM photography ***Fig. 1*** and ***Fig. 2*** showed that AlF3915 and Ti6Al4V particles are spherical. (Millogo, et al., 2018) and (Millogo, et al., 2020)

2.2 20L sphere

The explosions were carried out in a spherical 20 L explosion vessel designed at the PRISME Laboratory (**Fig. 3**) in accordance with the international standard EN 14034-3 (British Standards Institution, 2006) in order to characterize the ability of powders to explode. The parameters measured are the maximum explosion overpressure P_{max} and the maximum rate of pressure rise in the sphere, $(\frac{dP}{dt})_{max}$ over the explosive range for a given dust.

This experimental setup consists of a hollow sphere made of alloyed steel, a dust storage container connected with the chamber through a dust outlet electro valve (Kühner AG). The dust was injected at the bottom of the tank with the standard compliant dihedral injector. A rebound nozzle (Kühner AG) (**Fig. 4**) disperses the particles with the air in the chamber generating a turbulent flow in order to reach homogeneous dust dispersion. At the end of the injection period, the atmospheric pressure is reached. The explosion signal is measured by a

Kistler 701A sensor and the acquisition is performed by a Keysight digital oscilloscope and recorded on a computer.

The tests with the pyrotechnical igniters (5kJ) as an ignition source were performed using the standard control unit of the 20L sphere. For tests with electric spark, a spark generator device is made by the laboratory itself according to the standard requirements, was used. Its design was detailed in (Bernard, et al., 2010)

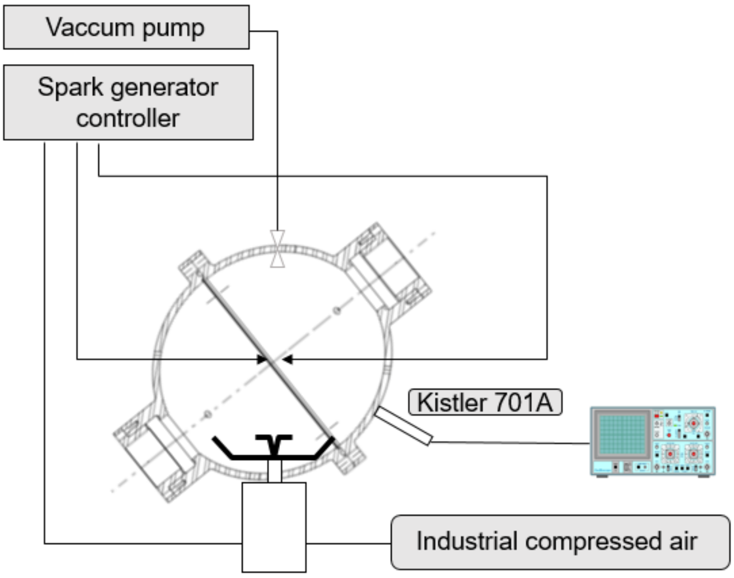

Fig. 3. *Design of spherical chamber of 20 litters volume*

Fig. 4*. The rebound nozzle*

2.3 Ignition source

2.3.1 Ignition processes

Ignition of combustible dust clouds occurs only in the presence of a flame source or a sufficient heat source. In general, ignition is triggered in a variety of ways from low-energy to high-energy ignition sources (Amyotte & Eckhoff, 2010). However, the ignition source differs in terms of power and energy. The ignition source can significantly influence the dynamics and course of the scattered dust explosion (Yuan, et al., 2015). In the industry, there can be several types of significant ignition sources that can cause dust to explode. These are typically a spark, a hot surface, overheating, direct fire, etc. These ignition sources are characterized by the fundamental parameter of "ignition energy"(the energy of the ignition source that ignites a cloud of dust) and the dynamics of the ignition process (spark is punctual source, fire/combustion is a "slow" source, in terms of dust burning rate), (Amyotte, 2014, Eckhoff, 2002, Kuracina, et al., 2021).

One of the fundamental differences of these ignitors is the ignition mechanism. While for the ignition spark an electric arc is generated the pyrotechnical igniter emits flames and burning solids.

2.3.2 Electrical ignition system

The electric arc ignition system consists of a high voltage generator, whose discharge initiates an arc between the electrodes. A generator provides the ignition energy by capacitor discharge, and whose delivered voltage and current, as well as the arc holding time, are adjustable. The system produces spark at nearly constant power and controls the spark energy by controlling the duration of the spark. The spark current is adjustable between 2 and 8 A and was set to 4 A in this study. The arc voltage is 82.5 V. As the voltage and current intensity are constant, energy is inly proportional to the spark duration:$\mathrm{E} = \mathrm{U_{arc}}.\mathrm{I_{arc}} \mathrm{x}\, \tau_{\mathrm{arc}}$, this time could be changed over the range of 1µs-100ms. The arc energy value achieved with such an arrangement is in the range from 10 mJ to 500 J, making possible to measure the ignition energy of the less ignitable dusts as detailed by (Bernard, et al., 2010).The energy deposited in the discharge reaches 66 J. In this paper we only recall the electric scheme (**Fig. 5**). The spark generator has, in addition, a "trigger" output (synchronized on the beginning of the cycle at cycle at time t_0) which allows to trigger an external device. Pointed electrodes made of tungsten were used with a 2.4 mm diameter. The electrodes' extremities are shaped at an angle of 40°. This configuration allows minimal erosion of the electrodes and provides a conical shape to generate the spark.

The experimental ignition conditions for the electrical ignition system are summarized in **Table 2** (Bernard, et al., 2017)

Table 2 : *Ignition condition in the 20 L spherical bomb*

Parameter	Value
Spark current intensity,A	4
Spark power,W	330
Spark energy,J	66
Electrodes gap,mm	4
Electrode shape	Conical (40°)

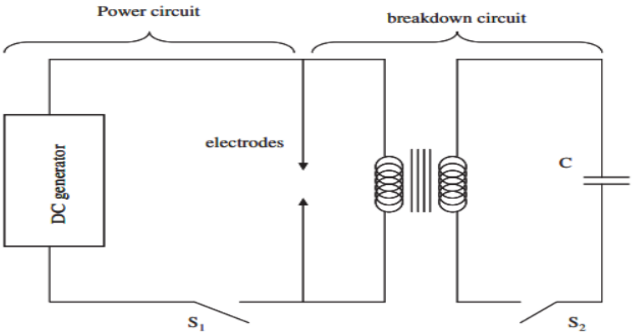

Fig. 5. *Electric scheme of the spark generator (Bernard, et al., 2012)*

2.3.3 Pyrotechnic Igniter

The ASTM E1226-12a standard specifies the exact composition and quantity of the mixture in a chemical igniter. The chemical igniters consist of small plastic or aluminium buckets filled with a firing charge of 40% zirconium, 30% barium nitrate and 30% barium peroxide. A sealing cap keeps the firing charge inside An electrical fuse head is connected to two wires for a precise electrically controlled ignition from the outside of the apparatus (see DIN EN 14034). The ignition source was placed in the middle of the sphere and connected to the electrodes of the lid of the chamber, such as it is described in the test standards.

3. Results and discussion

3.1 Severity parameter results: K_{st} and P_{max}

3.1.1 CaRo11

The calibration of our 20 L sphere was performed by using Caro 11 powder and compared to “round robin results”. The K_{st} max value obtained with the pyrotechnical igniter is well in the range of results given by “round robin tests”. While for the electric spark igniter, the ratio between round robin measurements and our tests is 1.47 (Bernard, et al., 2017). For each experimental test, at least two runs were performed. **Fig. 6** present the evolution of the pressure and the k_{st} as a function of the dust concentration with both ignition sources. The highest value of P_{max} (6.64 bara) is obtained at a concentration of 500g/m^3 for the electric spark igniter and for the pyrotechnical igniter, the highest value of P_{max} (7.99 bara) is obtained at a concentration of 500g/m^3. While the Kst_{max} for the pyrotechnical igniter was 242bar.m/s at a concentration of 750g/m^3, it was 134 bar.m/s for the electric spark igniter at a concentration of 750g/m^3.

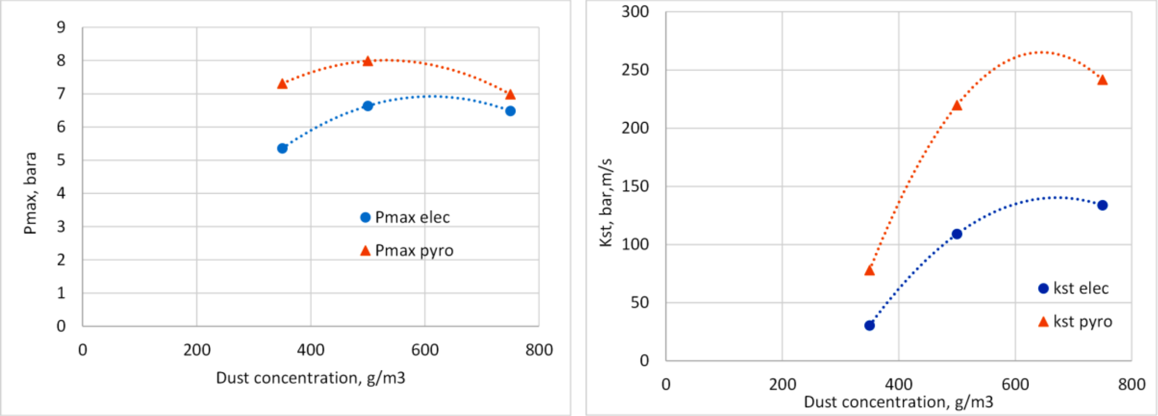

Fig. 6. *Severity parameters of CaRo 11 as function of concentration determined with electric spark igniter and pyrotechnical igniter*

The curves were fitted according to a polynomial of order 2 and the K_{st} is written as follows as a function of the concentration C: $K_{st} = a_0 + a_1.C + a_2.C^2$

Where the fitting coefficients for the electrical spark igniter are respectively a_0= -339.03, a_1=1.4275, a_2= -1.063 10^{-3} and for the pyrotechnical igniter are a_0 =-628.62, a_1 =2.76989 and a_2 =-2.144 10^{-5} .

3.1.2 Aluminium tested dusts

For each experimental test, at least two runs were performed. The severity of the explosion was measured in terms of the maximum pressure reached, reflecting the overall energy release, and the deflagration index K_{st}, reflecting the rate of pressure rise and thus the reaction rate. The dust concentration is an important factor that affects the severity of the explosion. (Jing, et al., 2021) present the determined explosion pressure P_{max} and K_{st} evolution as a function of the dust concentration with both ignition sources. Both curves show a comparable course. The highest value of P_{max} (8.2 bara) is obtained at a concentration of 1000g/m^3 for the electric spark igniter while for the pyrotechnical igniter, the highest value of P_{max} (9.5 bara) is obtained at a concentration of 750g/m^3. While K_{st} for the pyrotechnical igniter was 425 bar.m/s at a concentration of 750g/m^3, it was 317 bar.m/s for the electric spark igniter at a concentration of 1250g/m^3. (Millogo, et al., 2020) obtained around 7.7 bars for the overpressure and 317.58 bar.m/s for the k_{st} using the electric spark igniter. (Lomba, et al., 2015) also obtained around 8 bars for the overpressure.

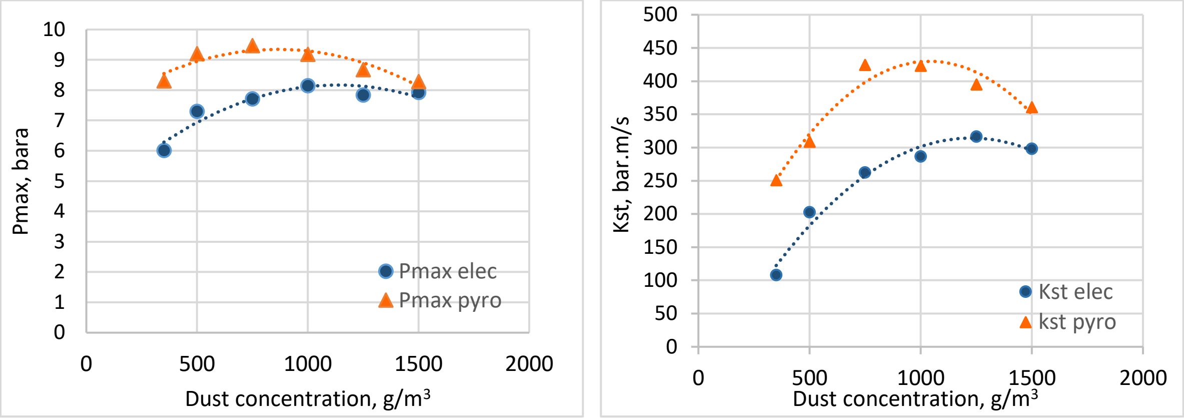

Fig. 7.*Severity parameters of AlF3915 as function of concentration determined with electric spark igniter and pyrotechnical igniter*

The curves were fitted according to a polynomial of order 2 and the K_{st} is written as follows as a function of the concentration C: $K_{st} = a_0 + a_1.C + a_2.C^2$

Where the fitting coefficients for the electrical spark igniter are respectively a_0 =-61.6641, a_1=0.6129, a_2= -2.4988 10^{-4} with R^2= 0.9717 and for the pyrotechnical igniter are a_0 = -628.62, a_1 =2.76989 and a_2 =-2.144 10^{-5} with R^2= 0.9456

As well the determined values for P_{max} as for Kst_{max} were markedly higher for tests with the pyrotechnical igniter.

3.1.3 Ti6Al4V

The parameters of the explosive combustion of Ti6Al4V were studied according to the concentrations between 350 g/m^3 to 1500 g/m^3. The highest value of P_{max} 7.1bara is obtained at a concentration of 1000g/m^3 for the electric spark igniter while for the pyrotechnical igniter, the highest value of P_{max} 6.7bara is obtained at a concentration of 1500g/m^3. While K_{st} for the pyrotechnical igniter was 100.8 bar.m/s at a concentration of 1000g/m^3, it was 89.7 bar.m/s for the electric spark igniter at a concentration of 1000g/m^3. (Millogo, et al., 2018) notice for high concentration an electric ignition the presence of TiN particles in combustion products, it means that after consume all oxygen the combustion continue with the exothermic nitration reactions.

DOI: 10.7795/810.20221124

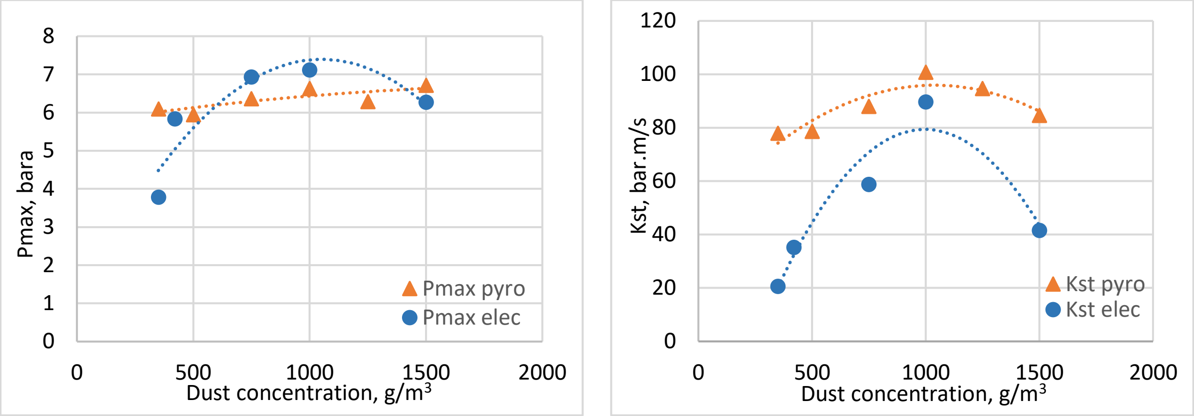

Fig. 8. *Severity parameters of Ti6Al4V as function of concentration determined with electric spark igniter and pyrotechnical igniter*

An attempt to fit curves by the same polynomial of order 2 as a function of the concentration C has been made: $K_{st} = a_0 + a_1.C + a_2.C^2$

The fitting coefficients obtained for the electrical spark igniter are respectively a_0 =-61.3128, a_1=0.2823, a_2= -1.4167 10^{-4} with R^2= 0.9067 and for the pyrotechnical igniter are a_0 = 46.6133, a_1 =0.09486 and a_2 =-4.5648 10^{-5} with R^2= 0.8178.

The Pmax is higher with the electric igniter than the pyrotechnical igniter. The cause for this may be, that the TiN particles were not presented in the combustion product with chemical ignitors compared to electrical ignitors. Probably the combustion stop just after consume all the oxygen, this causes a decrease in pressure therefore the Pmax is smaller for the pyrotechnical igniter , and the combustion kinetic seems to be affected by the chemical ignitor combustion.

Establishing a correspondence between severity parameters obtained for the same dust with two different ignition modes seems possible. Nevertheless, these 3 dusts with different behaviors show the difficulty of finding a relationship unifying all the data.

In fact, the combustion of aluminum powder only consumes oxygen from the air and does not produce gas in the combustion products, CaRo powder, like other organic powders although they consume when burning the oxygen also produces gases as combustion products and this contributes to the modification of the dp/dt. This increase is greater than the pressure gap introduced by the ignition system, as it is the case with chemical igniters.

Titanium powders, although not producing gas in the combustion products, seem to have their combustion kinetics affected by the combustion of chemical igniters, whereas this is not the case with electric ignition.

Probably, to establish this correspondence more precisely, it will be necessary to consider at least the three scenarios illustrated by this article.

4. Conclusions

In this work, the severity parameters of CaRo11, aluminium powder AlF3915 and titanium alloy Ti6Al4V were determined using both pyrotechnic and electric igniters and a correspondence is now possible between these two ignition sources over a wide concentration range. The results show that these severity parameters are higher using the pyrotechnic igniter compared to the electric igniter. The P_{max} values determined with electric igniter were less than 10% lower than values determined with pyrotechnic igniter. This can be explained by the use of a low ignition energy (electric spark of about 66 J) compared to the pyrotechnic igniter (5kJ). These results are not surprising since the pyrotechnic igniter accelerates the combustion with multi ignition points in a large volume and thus the Kst. It is partially due to the overpressure provided by the igniter just before the explosion really begins.

References

Askar, E. & Schröder, . V., 2019. The Influence of Strong Ignition Sources on the Explosion and Decomposition Limits of Gases. *Chemical engineering transactions ,* Volume 77, pp. 127-132.

Amyotte, P. R. & Eckhoff, R. K., 2010. Dust explosion causation, prevention and mitigation: An overview. *Journal of Chemical Health and Safety,* Volume 17, pp. 15-28.

Ballal, D., 1980. Ignition and flame quenching of quiescent dust clouds of solid fuels. *Proceedings of the Royal Society of London,* pp. 479-500.

Bernard, S., Gillard, P., Foucher, F. & MounaÏm-Rousselle, C., 2012. MIE and flame velocity of partially oxidised aluminium dust. *Journal of Loss Prevention in the Process Industries,* pp. 460-466.

Bernard, S., Gillard, P. & Frascati, F., 2017. Ignition and explosibility of aluminium alloys used in Additive Layer. *Journal of Loss Prevention in the Process Industries,* pp. 888-895.

Bernard, S. et al., 2010. Statistical method for the determination of the ignition energy of dust cloud-experimental validation. *Journal of Loss Prevention in the Process Industries,* pp. 404-411.

Boyle, A. & Llewellyn , F., 1950. The electrostatic Ignitability of Dust Clouds and Powders. *The Society of the chemicals Industry Transactions,* pp. vol 69,pp.173-181.

Jing, Q. et al., 2021. Inhibition effect and mechanism of ultra-fine water mist on CH4/air detonation: Quantitative research based on CFD technology. *Process Safety and Environmental Protection,* Volume 148, pp. 75-92.

Lomba, R. et al., 2015. Comparison of Combustion Characteristics of Magnesium and Aluminum Powders. *ICDERS,* pp. 1-6.

Millogo, M., Bernard, S. & Gillard, P., 2020. Combustion characteristics of pure aluminum and aluminum alloys powders. *Journal of Loss Prevention in the Process Industries,* Volume 68.

Millogo, M., Bernard, S., Gillard, P. & Frascati, F., 2018. Combustion properties of titanium alloy powder in ALM processes: Ti6Al4V. *Journal of Loss Prevention in the Process Industries,* Volume 56, pp. 254-261.

Parker, S., 1985. *Electric spark ignition of gases and dusts,,* The CityUniversity, London: s.n.

Proust, c., Accorsi, A. & Dupont, L., 2007. Measuring the violence of dust explosions with the ‘‘20 l sphere’’ and with the standard ‘‘ISO 1 m3 vessel’’ Systematic comparison and analysis of the discrepancies. *Journal of Loss Prevention in the Process Industries ,* Volume 20, pp. 599-606.

Scheid, M., Kusche, C., Schröder, V. & Barth, U., 2013. Suitability of ignition source “exploding wire” for determination of dust explosion characteristics in the 20-L-sphere. *Journal of Loss Prevention in the Process Industries,* Volume 26, pp. 1542-1548.

Spitzer, S., Askar, E., Krietsch, A. & Schröder, V., 2021. Comparative study on standardized ignition sources used for explosion testing. *Journal of Loss Prevention in the Process Industries.*

Van der Wel, P. G. J., 1993. *Ignition and propagation of dust explosions,* The Netherlands: Delft University Press.

Yuan, Z., Khakzad, N., Khan, F. & Amyotte, P., 2015. Dust explosions: A threat to the process industries. *Process Safety and Environmental Protection,* Volume 98, pp. 57-71.

DOI: 10.7795/810.20221124

Measurement of dust flame propagation and temperature with low wall influence

Christoph Spijker [a], Stefan Puttinger [b], Simon Schneiderbauer [b,c], Stefan Pirker [b], Georg Meyer[d], Christoph Buchner[d] & Tino Lindner-Silwester[d]

[a] Chair of Thermal Processing Technology, Montanuniversitaet Leoben, Leoben Austria

[b] Department of Particulate Flow Modelling, Johannes Kepler University Linz, Linz Austria

[c] Christian Doppler Laboratory for Multi-scale Modelling of Multiphase Proceses, Johannes Kepler University Linz, Linz Austria

[c] HOERBIGER Wien GmbH, Vienna, Austria

E-mail: christoph.spijker@unileoben.ac.at

Abstract

Earlier simulations of dust deflagration in ducts have shown that the flame is heavily influenced by the wall of the duct. To obtain evaluation data for future numerical models, an apparatus with low wall influence was developed. This apparatus creates a vertical dust cloud with sufficient distance to the walls. The dust cloud is ignited from the bottom. To create the vertical dust cloud, the apparatus works in two steps. First the dust is dispersed in a dispersion chamber by a primary air pulse, then a secondary air pulse transports the dust into the measuring chamber, creating a vertical cloud. The measuring chamber is translucent to obtain the dust dispersion and flame propagation by a high-speed camera. Additionally, 0.07 mm thermocouples are installed. By tracking the transient heat-up of those thermocouples, the temperature of the flame can be calculated.

Keywords: *dust deflagration, dispersion system, flame propagation, flame temperature*

1. Introduction

In previous studies of dust deflagrations, experimental setups with vertical ducts were often used. Ou-Sup (2000) studied the structure and propagation of Lycopodium dust clouds in a rectangular duct under atmospheric conditions. Kern (2015) was using a cylindrical vertical duct with atmospheric and non-atmospheric conditions to investigate the flame velocity and shape. Wieser (2015) investigated the flame temperature in atmospheric and non-atmospheric conditions in the duct apparatus of Kern (2015). For the duct apparatus of Kern (2015), two different Computational Fluid Dynamics (CFD) models were developed by Spijker. The first model (Spijker 2014) uses a burning velocity approach, where the laminar burning velocity is based on the concentration of lycopodium, described as Eulerian dust phase. After investigating the inner particle effects, Spijker (2019) created a pyrolysis-based model including the inner particle effects of lycopodium. Both models show that the dust deflagration in ducts is heavily influenced by the wall due to restriction of the flow and near wall turbulence. To avoid these near wall effects on the dust deflagration an experimental setup was designed that creates a column of dust surrounded by air and ignited at the bottom. The flame can expand in radial direction and does not touch the boundaries of the apparatus, except in the case of high dust concentrations in the column. The aim of this experimental setup is to obtain evaluation data for the development of new numerical models. Therefore, good reproducibility of the experiments and good optical access are important features to be desired in the experimental setup.

2. Description of the apparatus

The apparatus consists of two parts, the mixing chamber (***Fig. 1***. c.) and a rectangular observation chamber (***Fig. 1***. a., b.). The observation chamber has dimensions of 395 mm x 395 mm x 985 mm. The basic idea is that the dust is mixed with air by the dispersion system (***Fig. 2***) by the primary pulse of compressed air in the mixing chamber. The secondary pulse of compressed air pushes the dust into the observation chamber. The vertical cloud of dust in the observation chamber is ignited by a spark at the bottom of the device. The design aims to decouple the dust dispersion process in the mixing chamber and the dust injection into the measurement chamber. This allows a wide flexibility of the experimental setup and reduces the sensitivity of the dust concentration in the measurement chamber on the mixing process in the mixing chamber.

The observation chamber also contains 0.07 mm thermocouples at the height of 250 mm, 500 mm and 750 mm.

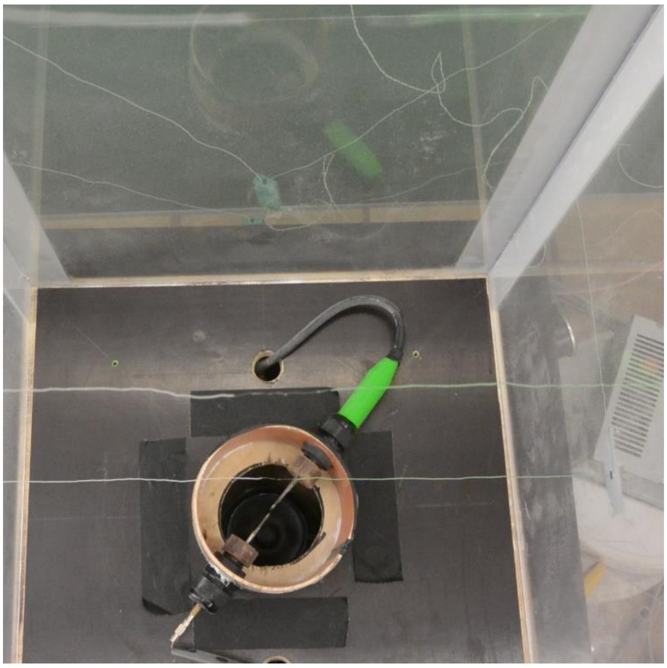

b.) top view

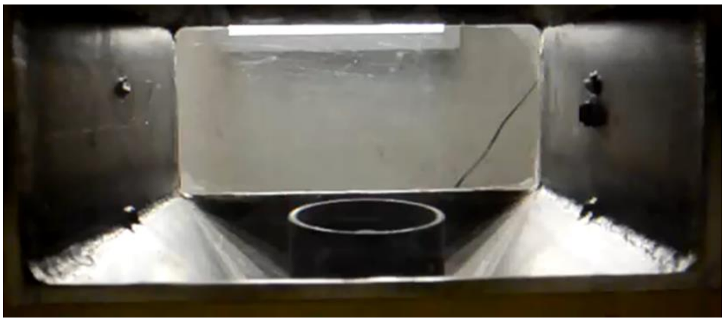

a.) front view

c.) side view of the mixing chamber

Fig. 1. *Photos of the apparatus. a.) Front of the apparatus, the measurement chamber sits on top of the expansion chamber. b.) Top view, shows the ignition electrodes and the support wires for the thermocouples. c.) Side view of the mixing chamber with the cup.*

DOI: 10.7795/810.20221124

2.1 Dust dispersion system

The dispersion system consists of a cup with a diameter of 100 mm, where the dust sample is placed. In the middle of the cup is a mushroom shaped nozzle for the dust dispersion. To avoid that dust adheres to the surface, the cup is equipped with five 0.3 W vibration motors. The baseplate below the cup contains a slotted pipe loop, that is fed from 8 ports for the secondary compressed air pulse.

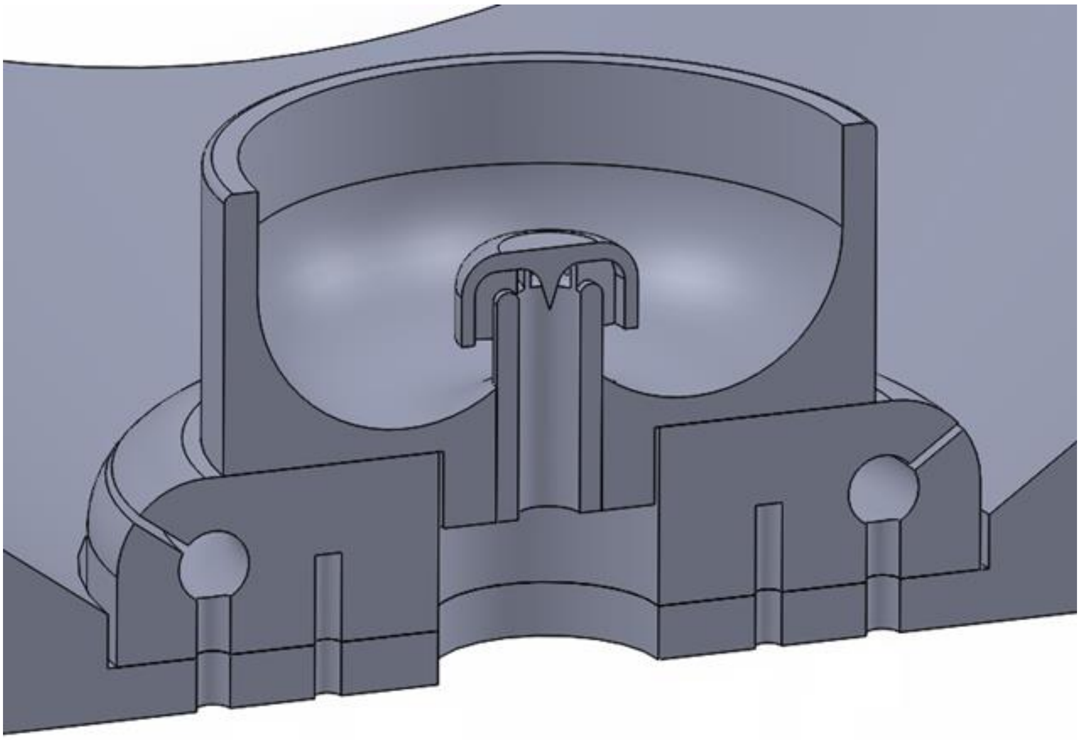

Fig. 2. *Sectional view of the dispersion system. The dust sample in the cup will be dispersed by the primary compressed air pulse though the mushroom nozzle. The secondary air pulse through the slotted pipe loop in the base plate pushes the dust cloud into the observation chamber.*

At the beginning of the dispersion process the vibration motors start. Three seconds later, the secondary air stream with 175 Nl/min is activated. At 5.5 seconds, the primary air pulse with 150 l/min is activated for 1 second. If the ignition has been enabled, the spark will start at 6.5 seconds for 250 ms.

2.1.2 High speed video analysis of the dispersion system

To analyse the dust cloud’s shape and reproducibility and to subsequently compare with the data of a CFD model, several experiments were conducted with the ignition mechanism deactivated. These experiments were filmed with a Chronos 1.4 high speed camera, triggered by the control system. In ***Fig. 3*** the shape of the dust cloud over time is shown, using 5 g of modified starch. The dust rises in an upward motion with decreasing velocity until, after 5.9 seconds, gravity forces the outer particles to settle down. Even then, the dust cloud remains centred. The repetition of these experiments shows nearly identical shapes until 5.8 seconds. After that, the top of the cloud starts to deform in slightly different shapes. In ***Fig. 3,*** at 5.8 seconds, the top part of the cloud starts leaning to the left. This influences the phase when the dust settles and the shape favours one side. In these experiments also dust clouds that stay basically centred could be observed.

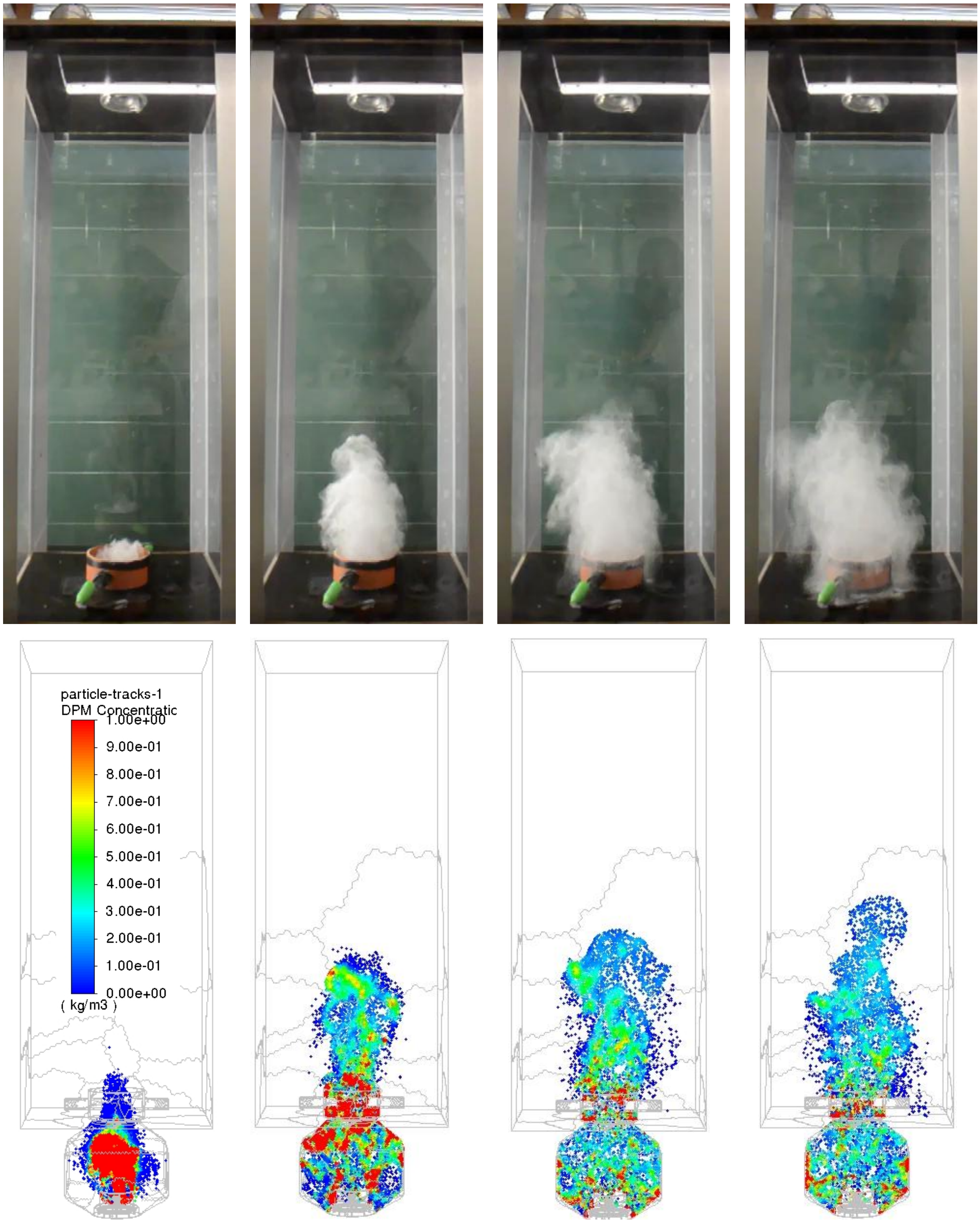

Time: 5.6 s Time: 5.8 s Time: 6.0 s Time: 6.2 s

Fig. 3. *Development of the dust cloud over time. The dust cloud is in an upward motion until 5.9 seconds, then the outer particles start to settle. This is an example for a dust cloud that is leaning left. In the CFD model the cloud stays centered.*

2.1.1 CFD model of the dispersion

For the numerical study of the particle dispersion, we used the commercial CFD package ANSYS Fluent 2021r1. The dispersion system and the measurement chamber are meshed using 321,171 polyhedral cells. To include the details of the dispersion system, the mesh is significantly finer in this region than in the measurement chamber. For the gas phase an ideal gas law is used, while the particle phase is described by the discrete particle model (DPM). Here, not every particle is considered since the total amount of maize starch is represented by 240,000 parcels. The particle density is assumed to be 1180 kg/m^3 and the particle size distribution was discretized using a logarithmic Rosin-Rammler distribution with 15 sampling points. Since the particle concentration was rather low in the measurement chamber, the drag correlation of Schiller and Naumann was used. The gas-phase turbulence was included by the WALE-LES model, where its impact on the particle trajectories was considered by discrete random walk approach. The LES approach required a bounded central differencing scheme for the convective term. The pressure was discretized by using the PRESTO! scheme and a time step size of 0.0002 s appeared to be sufficient for a proper integration of the parcel trajectories.

Fig 3 shows an example for a qualitative comparison between measured and simulated evolution of the dust-cloud in the measurement chamber. The CFD setup is able to reproduce the shape and height of the dust-cloud observed in the experiments over time. At this point the CFD simulation results were used to optimize the pre-design of the mixing chamber and to better understand the dust dispersion process in the experimental apparatus. The video analysis presented in section 3.1 will be the basis for a detailed quantitative comparison of the dust dispersion and flame propagation process between measurements and simulations.

2.2 Ignition- and control system

The core part of the control system is a relay board, which is controlled by LabView with an Arduino Nano as an interface. The relays close at a pre-programmed time and stay closed for a defined interval. This controls the two magnetic valves for the air pulses, the ignition, the vibration motors, and the trigger for the high-speed cameras. To monitor the flow of compressed air for the primary and secondary pulse, two Festo SFAH-200U flow sensors are used and linked into LabView. To monitor the temperatures of the 0.07 mm type K thermocouples, a National Instruments IN 9213 module with a sampling interval of 10 ms is used. The spark generator for the ignition consists of a function generator, switching an IGBT to create a square wave on the primary side of a neodymium transformer. The power of the spark is set to 300 W but can be adjusted by the input voltage. With a spark duration of 100 ms, the cloud is ignited by an energy of 30 J.

3. Experiments

3.1 Video analysis

It is generally difficult to visualize the unburnt dust cloud and the reacting zone in one single experimental setup, since the optimal settings for exposure time and lens aperture differ significantly for the phase before and after ignition of the dust particles. When the settings are chosen in a way that the camera chip does not fully saturate for the deflagration phase it is most likely that the dust cloud before ignition is underexposed, and thus, analysis of the particle dispersion is not possible. The limitations of this trade-off have been reduced by using a continuous wave (cw) laser with a wavelength of 532nm. The laser was used to illuminate the center plane of the experimental apparatus with a green light sheet. Hence, the scattered light of the dust particles and the reaction zone can be recorded with one single camera and sufficient quality for both areas. ***Fig. 4*** shows an image series recorded using this strategy again using 5 g of modified starch. The illumination with the laser light sheet allows to visualize the heterogeneous particle distribution in the dust cloud. These details are obviously not visible in images like the examples of ***Fig. 3***.

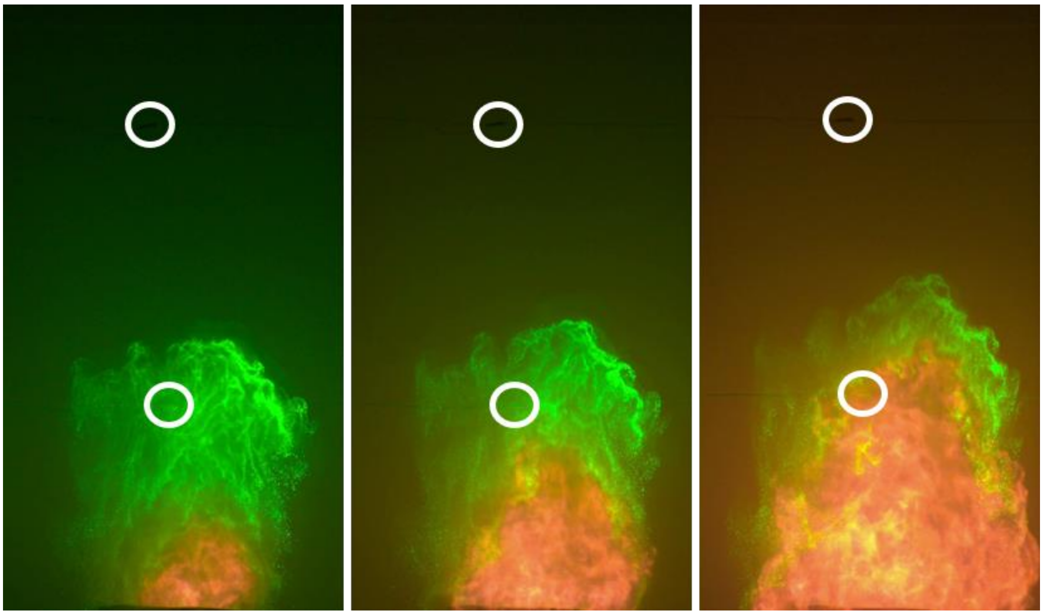

(a) Δt: 31ms (b) Δt: 59ms (c) Δt: 96ms

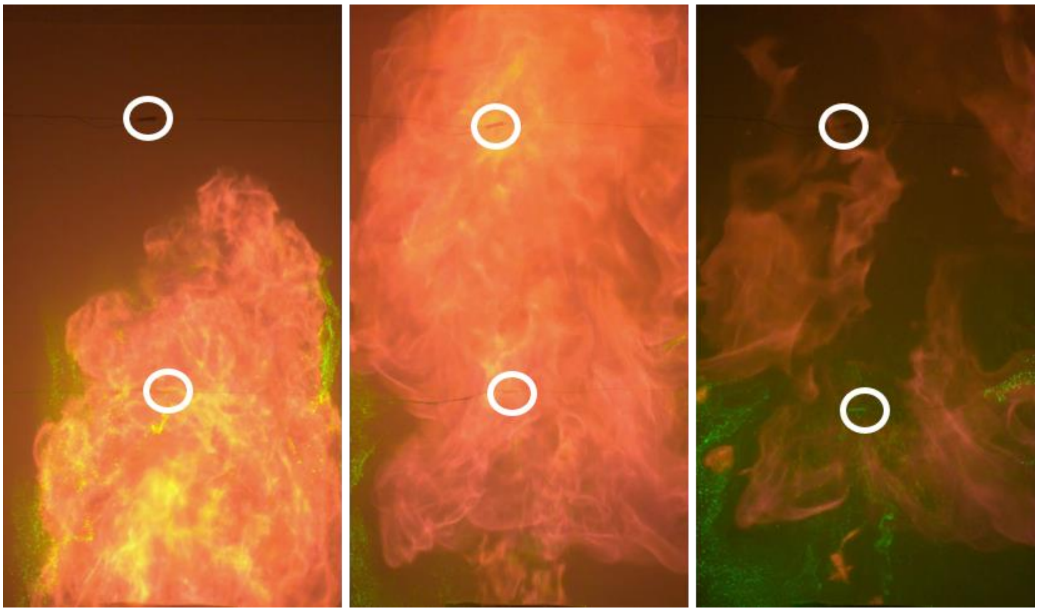

(d) Δt: 139ms (e) Δt: 342ms (f) Δt: 453ms

Fig. 4. *Dust cloud at certain times after ignition, illuminated with a green laser light sheet. The scattered light from the dust particles clearly shows the heterogeneous particle distribution that consequently influences the local temperatures in the reaction zone. The white circles indicate the locations of the thermocouples at z=250 and z=500mm.* $\boldsymbol{\Delta t}$ *is the time after triggering the ignition.*

As mentioned in section 2.1, the spark ignition is triggered 1s after the pressure pulse to disperse the particles. After roughly 1s the dust cloud has also reached its maximum extension in the observation chamber. Hence, the area of particles does not change in ***Fig. 4***(a) and (b) when the reaction zone is still small. Due to the expansion of the flame the size of the dust cloud finally increases (***Fig. 4***(c)) until the entire area is captured by the reaction zone (***Fig. 4***(d)). It is interesting to note that in the outer boundaries of the deflagration area a certain amount of particles remains unburnt (***Fig. 4***(d)-(f)). Due to the high light-scattering intensity from the laser sheet we can visualize these areas, which would not be possible by using ambient light or background illumination. In the final phase of the deflagration event (***Fig. 4***(f)) we can observe the heterogeneous structure of the decaying flame and remaining dust concentration.

This sort of qualitative data already provides a lot of valuable information to validate CFD modelling activities to simulate dust deflagration numerically. However, subsequent research will focus on the quantitative analysis of such experimental videos since they allow one to extract the velocity field of the unburnt dust particles and the flame expansion velocity by using particle image velocimetry (PIV) in combination with image processing methods. As a starting point for further processing, we need to identify a robust approach to separate the areas of the unburnt dust cloud and the deflagration zone from RBG images. Intuitively, one could assume that the red color channel is perfectly suited to separate the region of the flame. However, this is not the case, which can be discussed based on the example given in ***Fig. 5***.

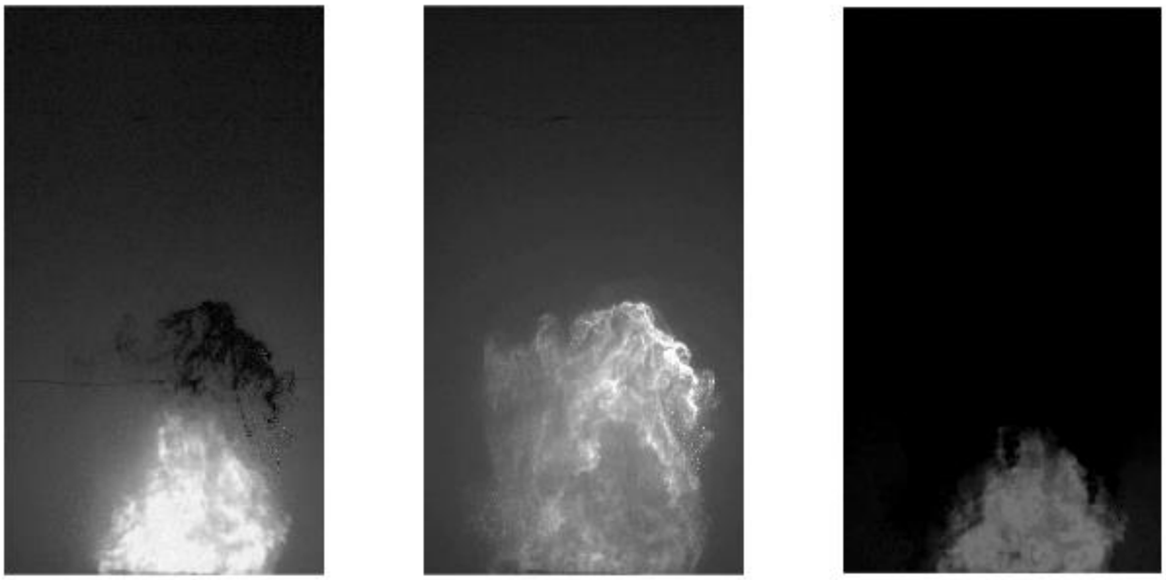

(a) Red color (b) Green color (c) Red - Green

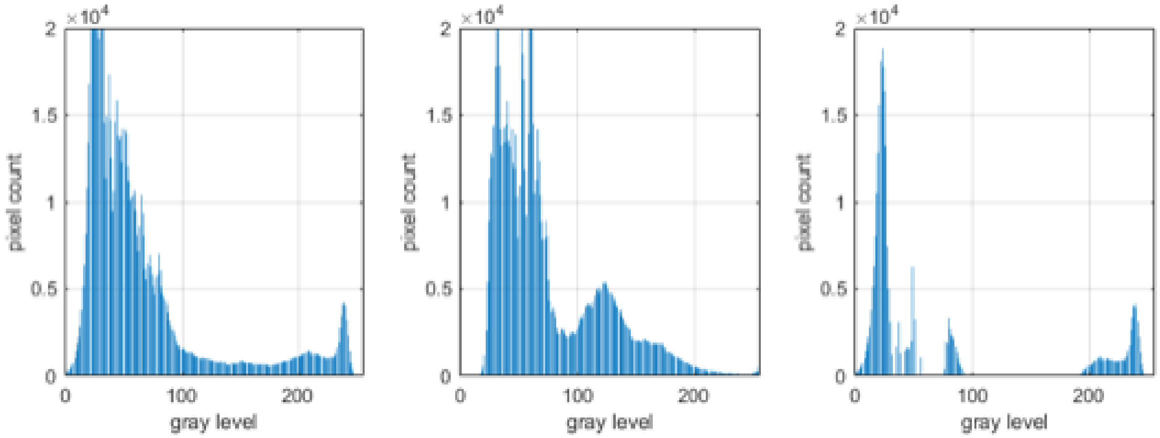

(d) Red histogram (e) Green histogram (f) R-G histogram

Fig. 5. *Separation of Fig. 4(b) into its color components red (a) and green (b). Subtracting the red and green channel delivers the actual deflagration zone. (d-f) show the corresponding 8-bit color channel histograms (color range 0-255). (f) shows the histogram of the red minus the green channel, this isn't equal to the difference between (d) and (e).*

Since the reaction zone illuminates the entire volume of the observation chamber, the background color changes with increasing flame area (c.f. ***Fig. 4***). Hence, the area with the lowest color levels in the red channel is actually not the background but the area of dust particles with the highest intensity of green light scattering. In contrast, the green channel of the images clearly shows the underlying particle cloud. A good separation of the flame area can be achieved by subtracting the green channel from the red channel (***Fig. 5***(c)). This combination of color channels is also less influenced by background illumination, as this essentially eliminates yellowish hues. Thus, we can use ***Fig 5***(b) and (c) as a basis for separating the dust cloud and the reaction zone for further processing.

3.2 Temperature measurements

The measurement of the temperature is based on the work of Wieser (2015). The idea is to observe the transient heat-up of small thermocouples. The basic equation for the transient heat-up of an object with a small Biot number is given in equation (1). By assuming that the heat transfer coefficient α, the heat capacity c_p, the mass m and the area A are constant, a linear function for the temperature of the thermocouple T_t can be derived, where the temperature of the gas phase T_∞ is the intercept (equation 2).

$$\frac{dT_t}{dt} = \frac{A\,\alpha}{m\,c_p}(T_\infty - T_t) \tag{1}$$

$$T_t = T_\infty - \frac{dT_t}{dt}\frac{m\,c_p\,\alpha}{A\,\alpha} \tag{2}$$

The time derivative of the thermocouple temperature $\frac{dT_t}{dt}$ is obtained by numerical differentiation. All temperatures below 100 °C and negative time differentiation of the thermocouple temperature are excluded from the data set before fitting. ***Fig. 6*** gives an example for the fitting process.

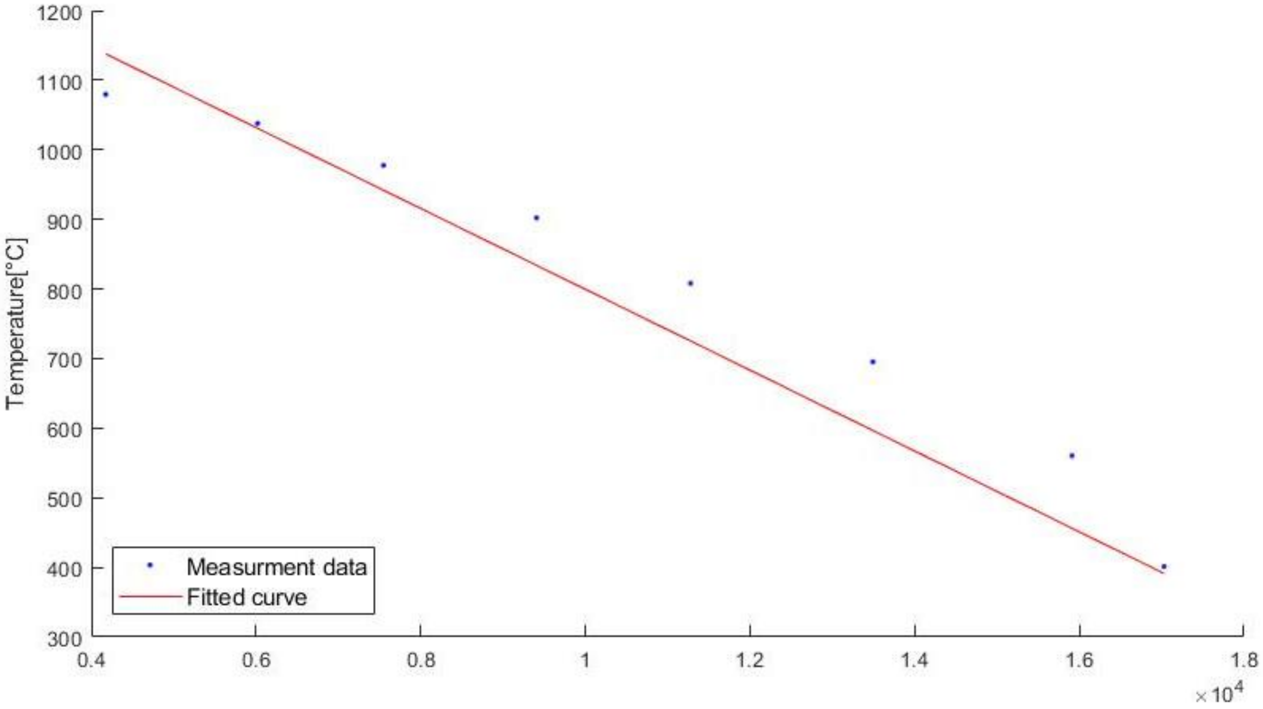

Fig. 6. *Example for the fitting to obtain the gas phase temperature* T_∞*. In this example the phase temperature* T_∞ *is 1293 +/-203 °C.*

In the first series of experiments, 4 g of modified corn starch were used. Not all temperature measurements produced sensible linear data in the fitting graph, obviously non-sensical ones were excluded in ***Fig 7***. At a height of 250 mm the experiments show temperatures, from approx. 1200 °C to 1430 °C. The high-speed footage shows structures of high heat radiation at this height, presumably with higher temperatures. These structures can pass or surround the thermocouple. Higher in the flame these structures disappear. So, the measurements at a height of 500 mm show consistent results at approx. 1250 °C. Also, the temperatures at the upper part of the flame are consistent at approx. 850 °C. At this point, the flame is diluted by air and the combustion temperatures decrease.

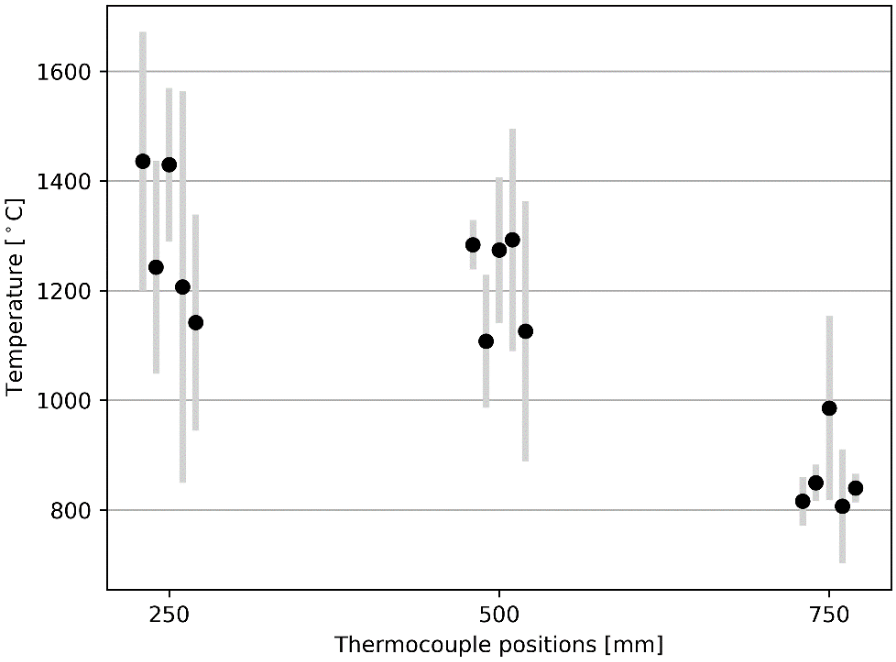

Fig. 7*. Calculated flame temperatures from the transient heat up of the thermocouples. 4 g of modified corn starch were used in the experiments. The error bars represent the 95 % confidence interval of the linear fitting.*

4. Conclusions

The presented apparatus was developed to obtain high-quality data for the evaluation of CFD models for flame propagation of dust flames. Older simulations (Spijker 2014, Spijker 2019) of dust deflagrations in ducts show that the flame is heavily influenced by the walls. Therefore, an apparatus with low wall influence was created allowing to observe freely propagating dust flames. The main goals of the experiments are to track the dust dispersion, track the flame front and to obtain temperature distributions for a comparison with numerical models. The dust dispersion shows good repeatability and can be described by the current CFD model. The major factors for this repeatability are the design of the apparatus relying on a mixing chamber and measurement chamber, the vibration motors, which break up granulates and evenly distribute the dust in the dispersion cup, and the precise timing of the air pulses. The setup also allows a wide flexibility for the investigation of different operating ranges in future experiments, e.g., the study of flame interaction with obstacles mounted in the measurement chamber. The high-speed video data, obtained by a Chronos 1.4 camera allows the separation of the particle and the flame by colour channels. This provides the basis for tracking the flame front and obtaining the particle velocities using PIV algorithms. This data is a key figure for the evaluation of future numerical models. Also, the combustion temperatures are an important parameter for evaluation of the model. To obtain the gas phase temperature, the transient heat up of thermocouples was used, an approach that previously showed promising results in a duct apparatus (Wieser,2015). In the presented setup with small wall influence and faster changes in temperature, the results show a broad confidence interval. Furthermore, the thermocouples can’t measure the inhomogeneity of the temperature field. Therefore, optical methods must be used. A combination of optical measurement and the existing thermocouples is planned.

References

Kern, H., Wieser, G. & Raupenstrauch, H. (2015). Flame propagation in lycopodium/air mixtures below atmospheric pressure. *Journal of Loss Prevention in the Process Industries*, 36: 281-286

Ou-Sup, H. (2000). Behaviour of flames propagating through lycopodium dust clouds in a vertical duct, *Journal of Loss Prevention in the Process Industries*, 6: 449–457

Spijker C., Kern, H. & Raupenstrauch, H. (2014). A CFD Approach for dust explosions based on

OpenFOAM, *10th International Symposium on Hazards, Prevention and Mitigation of Industrial Explosions*, Bergen, Norway

Spijker C., Kern, H. & Raupenstrauch, H. (2019). A model for dust deflagrations, considering inner particle transport effects, *17th International Conference on Numerical Combustion.*, Aachen, Germany

Wieser, G., Einflüsse der Temperatur und der Turbulenz auf die Flammenausbreitung in Staub/Luft-Gemischen unter reduzierten Druckbedingungen, *4. Magdeburger Brand- und Explosionsschutztag*, 2015, Magdeburg

DOI: 10.7795/810.20221124

Large-scale tests to investigate the consequences of exposing cryogenic storage vessels containing liquid hydrogen to a fire load

M. Kluge [a], A.K. Habib [a] and K. van Wingerden [b]

[a] Bundesanstalt für Materialforschung und –Prüfung, Unter den Eichen 87, 12205 Berlin, Germany

[b] Vysus Norway, Kokstadflaten 35, 5257 Kokstad, Norway

E-mail: Martin.Kluge@bam.de

Abstract

Large Scale Experiments have been performed to determine whether a storage vessel containing liquid hydrogen (LH2) and caught in a fire engulfing the vessel can result in a BLEVE (Boiling Liquid Expanding Vapour Explosion) and if so its consequences. The tests were performed at the Test Site Technical Safety of the Bundesanstalt für Materialforschung und –prüfung (BAM) in Germany at the Hydrogen Test Area (H2TA) within a research cooperation between BAM and Gexcon as part of the SH2IFT program. Three tests were performed using double-walled vacuum insulated vessels of 1 m^3 volume. The cylindrical Vessels differed in orientation (horizontal or vertical) and the insulation material used (perlite or multi-layer insulation (MLI)). The degree of filling of the vessels was approximately 35-40 % in each of the tests performed. The fire load was provided by a propane fed burner-system positioned under the storage vessel and designed to give a homogeneous fire load. The conditions in the vessel (temperatures and pressure) as well as external effects (heat radiation, blast waves, flame ball development and fragmentation) were measured. All vessels were equipped with K-type thermocouples at several locations at the inner and outer vessel shell. The pressure inside the inner vessel and in the space between the inner and outer vessels (vacuum pressure) was measured. Bolometers were used to measure the heat radiation generated by both the propane fire and that generated by a possible fireball/BLEVE. To measure blast generated by the vessel burst/BLEVEs blast pencils were positioned at up to three locations. Further several cameras were used to monitor the events: normal cameras, infrared (IR)-cameras, high-speed cameras also on board of an UAV. Two of these vessels, a horizontal and a vertical vessel both insulated with perlite withstood the fire loading for 1 hour 20 minutes and 4 hours respectively without catastrophic failure. A horizontal vessel insulated with MLI failed by bursting after 1 hour and 6 minutes resulting in a fireball, fragments, and blast wave.

Keywords: *prevention, industrial explosions, BLEVE, LH2, fire ball, fragments*

1. Introduction

Boiling Liquid Expanding Vapour Explosions (BLEVE) can occur when a vessel, containing a liquid phase and the corresponding gas phase, is heated up from the outside until the burst of the vessel. The consequences of such a BLEVE can be devastating and as several historical events show fatal consequences due to the generated blast waves and fragment generation. Is the vessel, involved in the BLEVE containing a flammable substance, a highly radiating fireball (Abbasi and Abbasi, 2007) can be formed. BLEVEs of flammable liquids have been seen for a wide range of fuels (Hemmatian et al, 2017) including liquefied natural gas (LNG) of which the effects of BLEVEs have recently been studied by Betteridge and Phillips (2015). The BLEVE phenomenon has already been the topic of many investigations and reviews (see e.g. (CCPS, 2016).

Nevertheless, there is still confusion on the definition of a BLEVE as discussed by van den Berg et al. (2004) and van den Berg et al. (2006). These authors refer to a BLEVE as an explosive evaporation of a liquified gas because of the rupture of a pressure vessel containing this liquefied gas. The consequences are directly related to the evaporation rate of the liquified gas which implies the temperature of the liquid and the disintegration speed of the pressure vessel. Other authors define a BLEVE to be the rupture of a vessel containing a liquid above the superheat limit. For temperatures above the superheat limit the evaporation rate of the liquid can be described as instantaneous. The super heat limit of hydrogen is 29.7 K (Ustolin et al, 2019).

Hydrogen is or will become one of the key energy resources in the future to replace energy generation by fossil fuels in many applications. Liquefaction of hydrogen is considered as one of the most promising means for transportation and storage of hydrogen in large volumes in the light of its low density and also allowing storage systems with a high gravimetric and low volumetric storage capacity as needed for mobile applications.

A BLEVE of a vessel containing liquid hydrogen (LH2) is hereby an accident scenario which must be considered then (Rigas and Sklavounos, 2005). On the other hand, only few experimental investigations of LH2 BLEVEs have been performed by now. The only investigation performed and available in open literature is the work performed by Pehr (1996). Small LH2 tanks designed for automobiles containing 1.8 to 5.4 kg of LH2 were destroyed by means of cutting charges. The lack of experimental data is most probably related to the limited application of liquefaction. Perhaps also because a LH2 BLEVE hazard was not viewed as a credible event thanks to its storage at cryogenic temperatures at relatively low pressure (Betteridge and Phillips, 2005). In fact, LH2 is stored in double walled vacuum insulated vessels which will contribute to the reduction of the probability of BLEVEs as recently shown by an experiment where such a vessel (3 m^3) filled with LNG (filling degree 66 %) proved to be resistant against a realistic accident fire scenario for a period of at least 2 hours (the test was aborted after 2 hours) (Kamperveen et al, 2016). The current paper presents LH2 experiments performed with three medium-scale 1 m^3 storage vessels exposed to a fire load. The vessels were double-walled vacuum insulated vessels with a filling degree of approximately 35 % - 40 % (corresponding to approx. 25 kg – 30 kg of LH2) and equipped with different types of thermal insulation (Perlite and MLI)

2. Experiments

2.1. General Setup

The experiments were performed at the Test Site Technical Safety (TTS) of the Bundesanstalt für Materialforschung und –prüfung (BAM) in Horstwalde, approximately 50 km south of Berlin. The former Blast Area 2, meanwhile rededicated as Hydrogen Test Area (H2TA), was used; a 400 m diameter flat circular area with an 80 m x 80 m concrete pad in the centre. On the H2TA an observation bunker, built to military standards, is used for controlling and monitoring the tests from a safe distance respectively a sheltered position (see figure 2).

The 1 m^3 storage vessels were purchased from and produced by INOXCVA in Vadodara, India. Three vessels were produced: two horizontal vessels, one with perlite as insulation material in between the outer and inner vessel, and the other with MLI (multi-layer insulation), and one vessel in vertical position insulated with perlite again (see figure 1).

The outer and inner vessels were made of low temperature resistant stainless steel (X5 CrNi 18-10). The thickness of the shell of the inner vessel is 3 mm and that of the outer vessel 4 mm. The thickness of the heads is always 5 mm. The maximum allowable working pressure of the vessels was 9 barg.

The vacuum insulation in the space between the two walls was a medium vacuum with a pressure of 0.3 mbar. The vessels were only equipped with basic instrumentation by the manufacturer. There were not safety valves installed. For the filling procedure a safety valve with shut-off feature was installed. This was closed during the fire load test itself.
Several measures were taken to protect vulnerable parts from the heat impact produced by the propane flames, including all valves directly connected to the vessel, thermocouple connections, flange gaskets and the piping in contact with flames. All these vulnerable parts were insulated using high temperature glass wool (Promaglaf). The thermocouples respectively the compensating cables were led away from the vessel using a scaffold (see figure 3).

***Figure 1**: The three LH2 storage vessels at the Hydrogen Test Area (H2TA) at BAM – TTS*

The liquid hydrogen was supplied by Air Liquide in a road trailer. The vessels were directly filled from this trailer via a flexible double-walled highly vacuum and MLI insulated hose. Before filling, the complete system was evacuated and flushed with helium for at least three times to avoid ignitable atmospheres within the filling system and the tank. During an initial phase the tanks had to be cooled down, which occurred by means of the flashing LH2 entering the tank. The filling was remote controlled by weighing system and pressure measurements using a valve arrangement assembled of highly insulated LH2-valves (see figure 2). During the filling process the vessel was placed on load cells and the amount of filled hydrogen was additionally monitored by a differential pressure sensor, measuring the hydrostatic pressure built-up inside the tank.

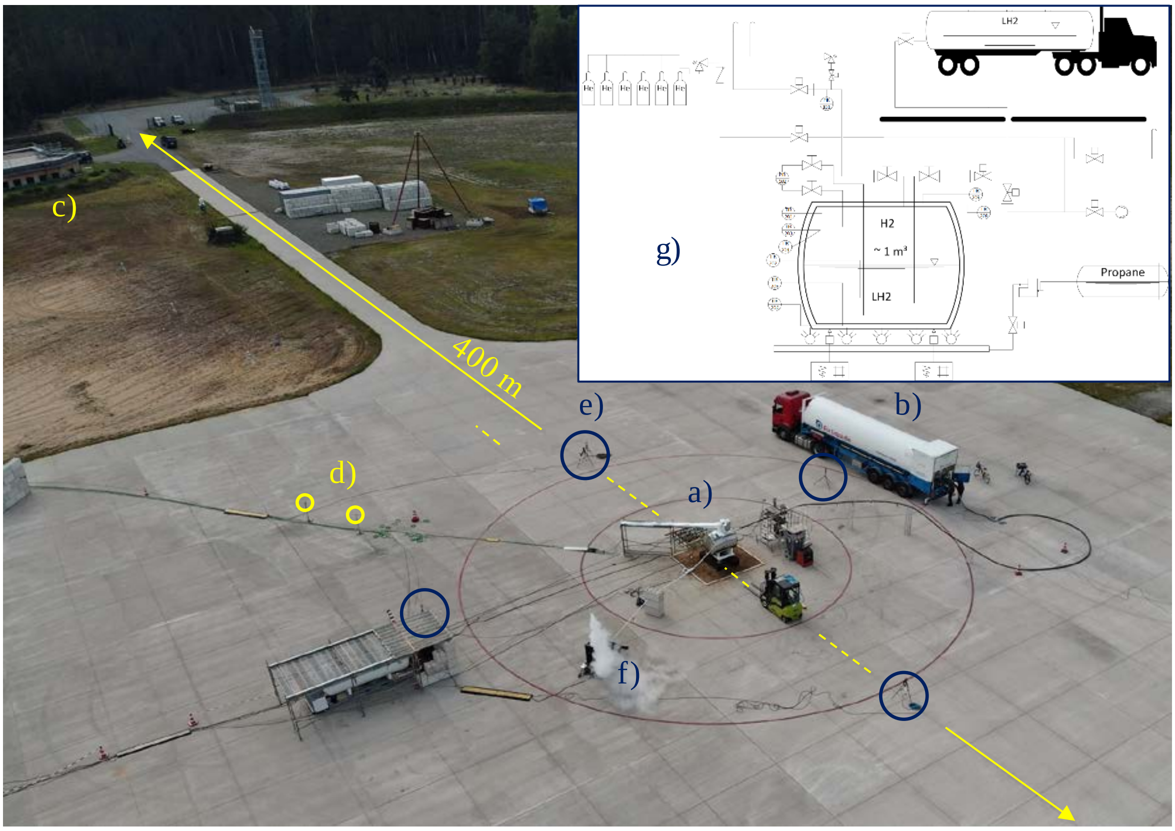

Figure 2: Setup of BLEVE test at H2TA of BAM- TTS; a) LH2-Vessel, b) road tanker, c) observation Bunker, d) blast probes, e) H2 Sensors and cameras, f) Box with safety valve and emergency release, g) flow diagram

The heat load applied to the vessels was generated by an array of 36 propane burners (see figure 3b) located underneath the vessels providing a heat load of approximately 100-150 kW/m^2 (mean propane consumption rate 4.3 kg/min) and designed to generate a homogenous fire load from all sides. Since the array of burners was considered to be at least damaged in case of a failing storage vessel, three such burner arrays were prepared for the tests. The propane was provided from a 5-m^3-storage vessel located at some distance from the LH2-vessel and protected by a concrete wall (see figure 3a)..

Three tests were performed with variation of the following parameters as shown in table 1:

***Table 1**: Test program for LH2 vessels in fire*

Degree of filling of vessel	Orientation of vessel	Insulation
35-40%	Horizontal	Perlite
35-40%	Horizontal	MLI
35-40%	Upright	Perlite

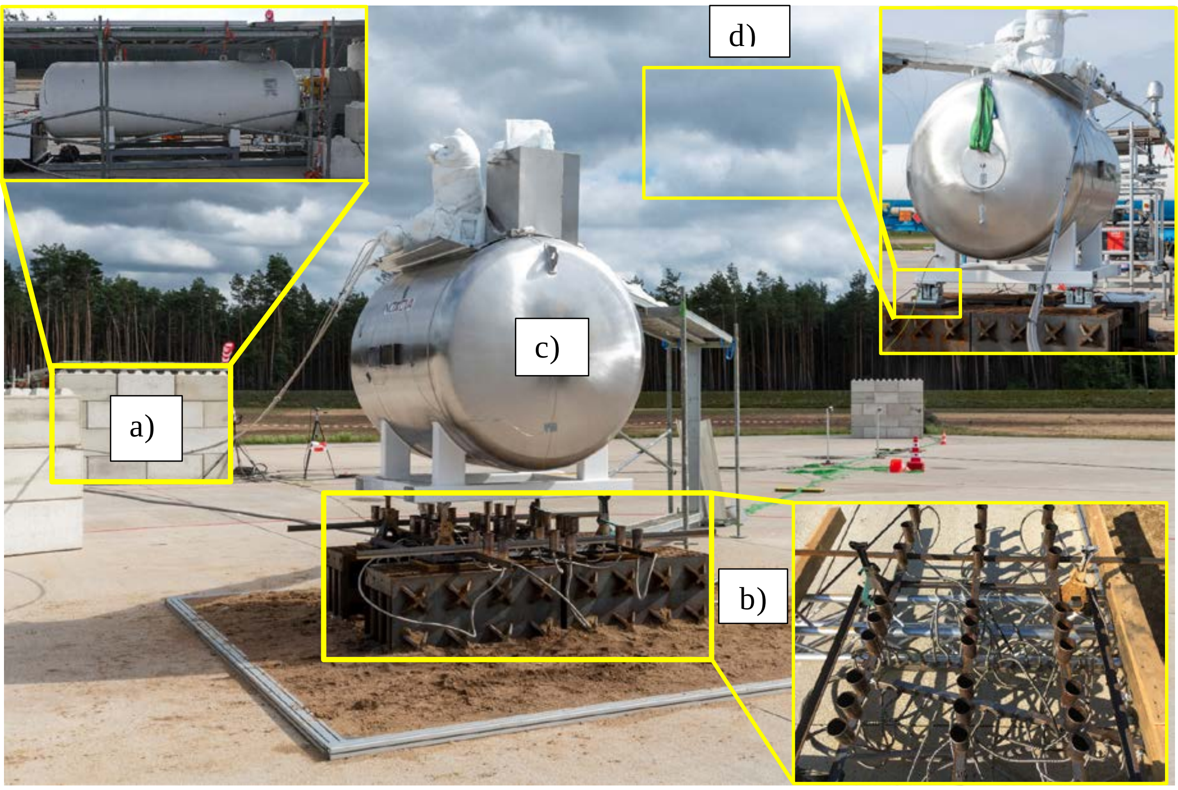

***Figure 3**: (a) propane tank, (b) propane burners and (c) one of the storage vessels (horizontal with MLI) before a BLEVE test showing the insulation used to protect valves and thermocouples on top of the vessel led away via scaffold, d) load cell of balance system for filling*

2.2. General Setup

For each test, similar instrumentation was used to record temperatures, pressures, heat radiation and video. All vessels were equipped with K-type thermocouples at several locations: inside the inner vessel in the gas phase and the liquid phase, on the inner and outer side of the inner vessel and on the inner and outer side of the outer vessel. The pressure inside the inner vessel (both in liquid, as a level indicator, and gaseous phase), and in the space between the inner and outer vessels (vacuum pressure) was measured (see figure 4).

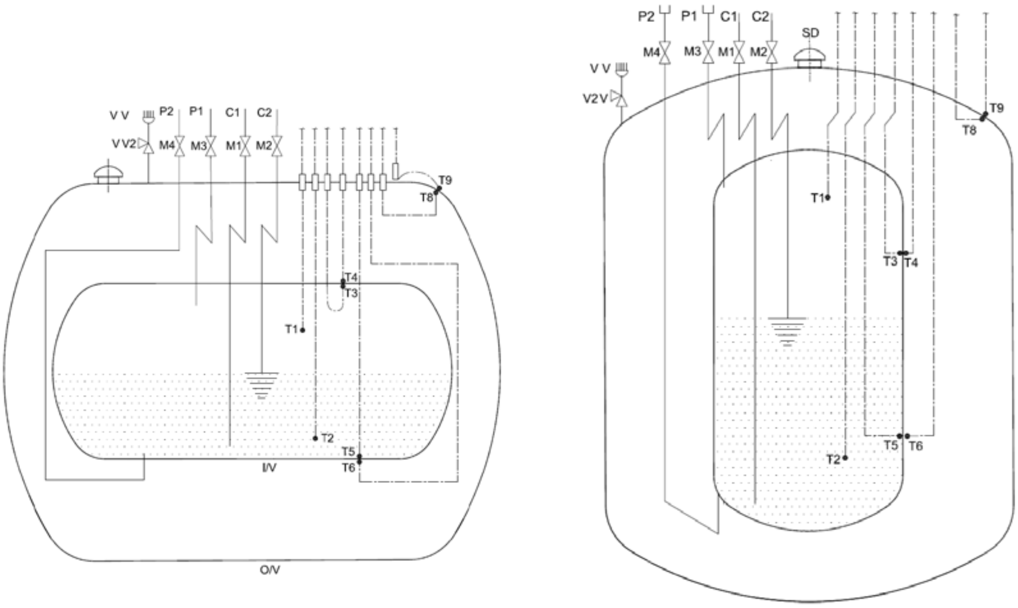

***Figure 4**: The layout of the two design types of LH2 storage vessels used during the BLEVE experiments.*

Bolometers were used to measure the heat radiation generated by both the propane fire and that generated by a possible fireball/BLEVE. To measure possible shockwaves generated by the vessel burst/BLEVEs, pencil probes were positioned at up to three locations. Further several cameras were used to monitor the events: normal cameras, infrared (IR)-cameras, high-speed cameras also on board of a UAV. In addition, 4 Hydrogen sensors were places around the vessel each in a distance of about 14 m to monitor the filling process and in case of a burst a possible formation of a hydrogen cloud.

***Table 2**: Sensors and equipment used for the fire tests*

Item/Sensor	Number	description
Gas sensor for H2	4, on in each orientation	NEOHYSENSE NEO974A
Heat radiation sensor	each in 70 m, 90 m and 110 m	Medtherm Model 64-XX-14
Inner pressure	2	1 absolute Keller PA-10 1 differential Keller PD-23
Thermocouple	14	Type K, 1.5 mm with Inconel mantle
UAV	1	DJI M300 RTK, optical and IR
IR-Camera	1	FLIR E95
Load cells	up to 4	MTS VC 3500
Blast sensor	up to 3	Kistler Pencil Probe Type 6233A
Action cams	up to 5	GoPro, 4K
Optical Camera	1	Canon EOS 1DX

DOI: 10.7795/810.20221124

3. Results and discussion

3.1. Fire test 1, horizontal Vessel with Perlite insulation

The first fire test was performed with the horizontally orientated vessel with perlite insulation. The fire was engulfing the vessel for a period of 1 hour and 20 minutes, after then the test was stopped. It could be observed that after approximately 50 minutes the outer shell imploded at several locations, most likely due to weakening of the material strength by the long exposure to high temperatures and the vacuum in the space between outer and inner shell.

After approx. 1 hour 15 minutes the vessel started leaking via the seal of the blind flange connection at the filling valve on top of the vessel. Thus also the main filling valve, which was closed before the test, must have failed too. This resulted in an upward orientated hydrogen jet fire which was visible on the IR cameras and also by regular video due to the propane fire still burning under the vessel. Upon abortion of the test by shutting down the propane supply and extinguishing the propane fire, the hydrogen jet fire continued but became invisible to the eye, detectable only with the IR-camera systems on site. The leakage caused the pressure inside the vessel to decrease considerably (from a maximum of 23.5 bar down to 10 bar within 300 s and down to 1 bar within 1000 s). This massive pressure loss led to the decision to stop the test, as the inner vessel pressure decreased so considerably that a vessel burst was impossible to achieve any more.

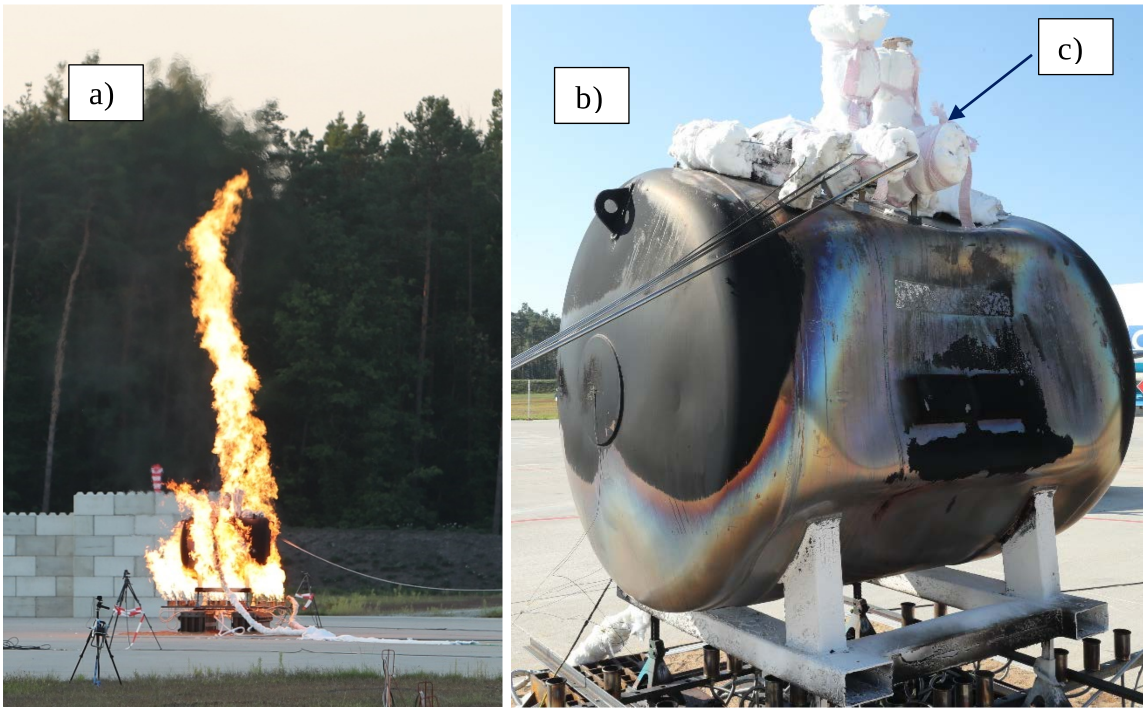

Figure 5*: a) H2-jet flame during fire test 2, b) deformation of outer shell, c) position of leakage*

In the next step the outer shell will be removed to prove several aspects, as there are: was the inner shell also deformed, what is the actual volume of perlite, what were the exact positions of the thermocouples and the inner piping etc.?

At the initial degree of filling with the perlite no free space for such observed deformation should be possible inside the insulation volume. Further investigations of the perlite itself will be done regarding possible shrinking effects due to thermal impact for example.

3.2. Fire test 2, horizontal Vessel with MLI

3.2.1. General observations

The second test was performed with the MLI insulated vessel positioned horizontally. This vessel was filled with about 27 kg of LH2 and started leaking after approximately 40 minutes. But this time the leakage happened far away from the fire at the box with the emergency release valve (see figure 2f). Reason for that was the design pressure of the installed cryogenic valve of only 40 bar. It was equipped with a pneumatic actuator, held in the normally closed position by a spring which opened at about 50 bar due to too low spring force. The leakage led to a stop of the increase of the inner pressure in the vessel, which then stayed constant at nearly 50 bar (see figure 6a).
Moreover, it could be observed that the vacuum pressure slightly increased during the test up to 56 millibar and rapidly increased in the moment of burst. So far it cannot be concluded whether the sudden loss of the vacuum caused the burst or vice versa. The data of pressure and temperature readings in combination with the different video sequences have to be analysed further. It is assumed, that the vessel failure might be closely linked to the loss of vacuum. The latter supposedly caused by the failure of an O-ring at the filling opening for the perlite, causing a possible sucking in of hot gases from the surrounding fire. Here a standard Viton ring was installed which is likely to be destroyed when exposed to temperatures above 300 °C for a long period of time.
Nevertheless, after 68 minutes the vessel failed, causing a fire ball, blast waves and fragments.

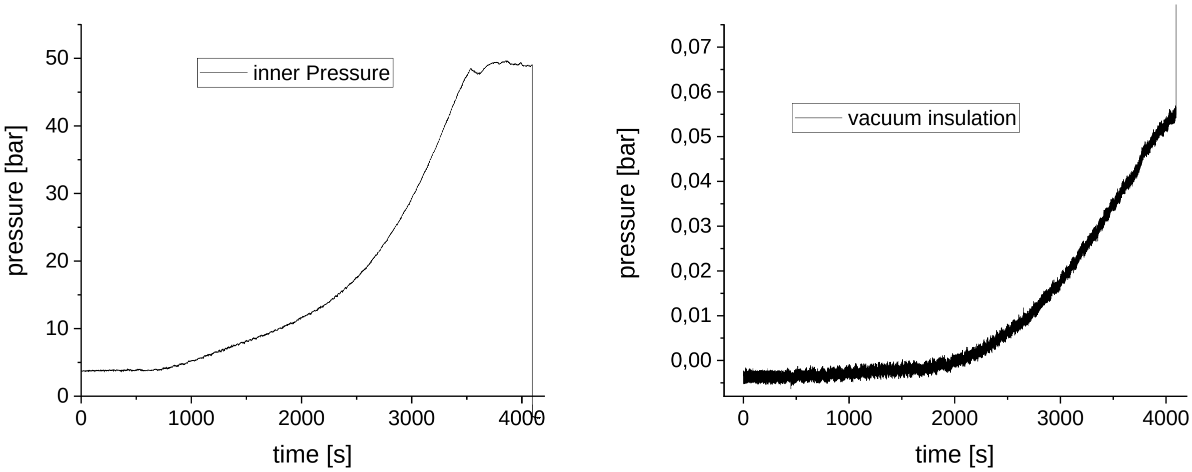

a) *b)*

***Figure 6**: a) Inner pressure over time at fire test 2, b) pressure inside vacuum insulation*

The correlating temperature readings to the presented pressure signal in figure 6 were recorded as amplified voltage signals and had to be calibrated with LN2 afterwards as the resulting thermoelectric voltage was not correlating to the tabled values for Type K sensors in the literature below about -100 °C. Therefore, an adapted polynomial of 9th degree was used with the similar progression of the standard polynomial for type K sensors. The temperature readings with the recent calibration method are shown in figure 7. The pressure inside the vessel is higher than expected on the basis of the measured temperature of the liquid (using the Antoine equation given in (NIST, 2021)) indicating a non-equilibrium condition. The measured temperature of the liquid hydrogen at the moment of failure of the vessel was below the superheat limit of hydrogen and below the critical temperature of hydrogen. The pressure was however above the critical pressure of 12.96 bar and hence the explosion might have been a supercritical BLEVE as explained by Ustolin et al. (2020). A final calibration of the thermocouples is planed with liquid Helium and LH2 soon.

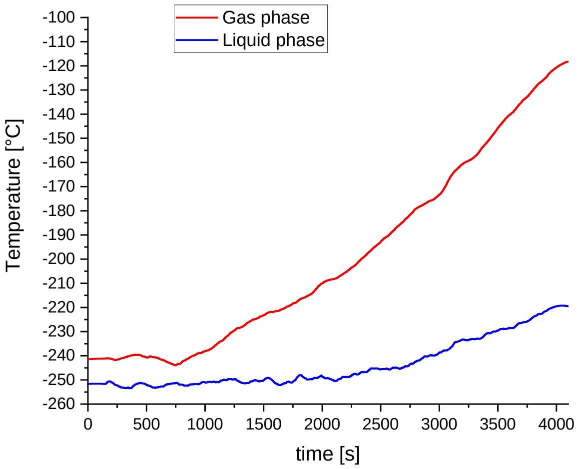

***Figure 7**: Temperatures measured in the gas and liquid phases of the MLI-insulated vessel positioned horizontally measured during the whole test duration.*

3.2.2. Fragments

The failure of the vessel resulted in fragmentation of the vessel, a fireball and a blast wave. All together 53 fragments were found but only 28 were generated by the vessel itself. Some of the fragments came from the burner system, the scaffold or metal labels of the instrumentation. Larger parts of the vessel were found at distances between 6 m and 167 m from the original position of the vessel. In figure 8 some relations of the mass and throw distances of the fragments as observed are presented.

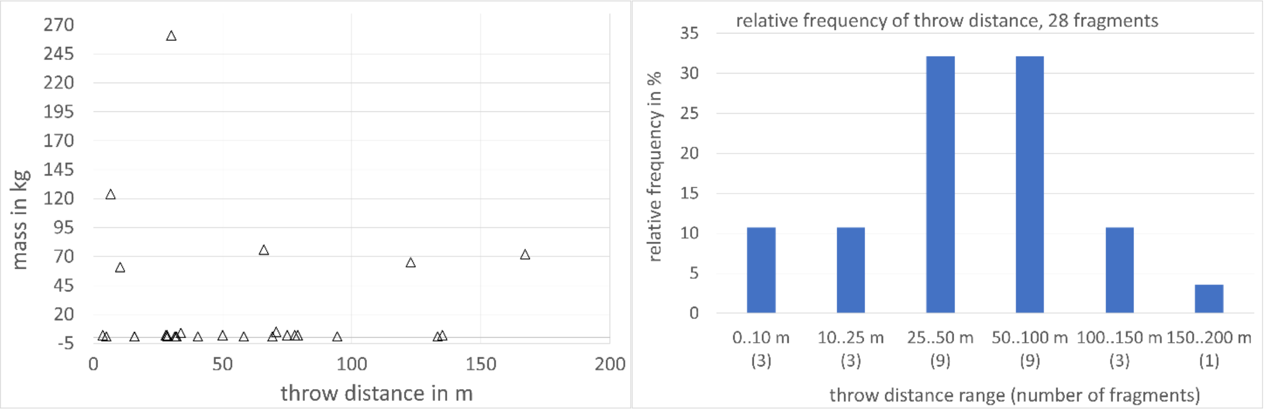

a) *b)*

***Figure 8:** a) mass of fragments via throw-distance, b) relative frequency of throw distance of fragments*

Moreover, from these 28 parts 11 parts were selected as relevant parts, coming directly from the vessel itself and not the additional instrumentation. Table 3 shows the relating parameters for these relevant fragments. By using the commercial software PRONUSS (v. 9.37) some calculations were done regarding the throw distance based on the initial experimental parameters. On the one hand a basic model by Lorenz and Radandt (1996) was used, describing the throw distance as parabola flight based on the initial impulse generated by the pressure at burst also considering substance-specific properties, like the isentropic coefficient, as well as the geometry and mass of the fragment.

***Table 3**: Parameters of relevant fragments generated at fire test 2*

fragment	description	throw distance in m	mass in kg
1	inner shell with bumped boiler end	7	124
4	inner bumbed boiler end	10	61
6	part of outer bumbed boiler end	34	4
19	large part of outer shell with stand	30	261
36	small valve	16	1
38	outer bumbed boiler end	167	72
41	instrumentation	135	2
43	large valve	71	5
47	outer bumbed boiler end	66	76
48	large part of outer shell	123	65
52	small part of outer shell	78	2

The second model used, formulated by TÜV Rheinland within the UBA Report 204 09 428 (2000), is independent of the substance-specific properties. The calculated results are compared in figure 9. The calculation was split into the fragments of the inner vessel and those of the outer vessel.

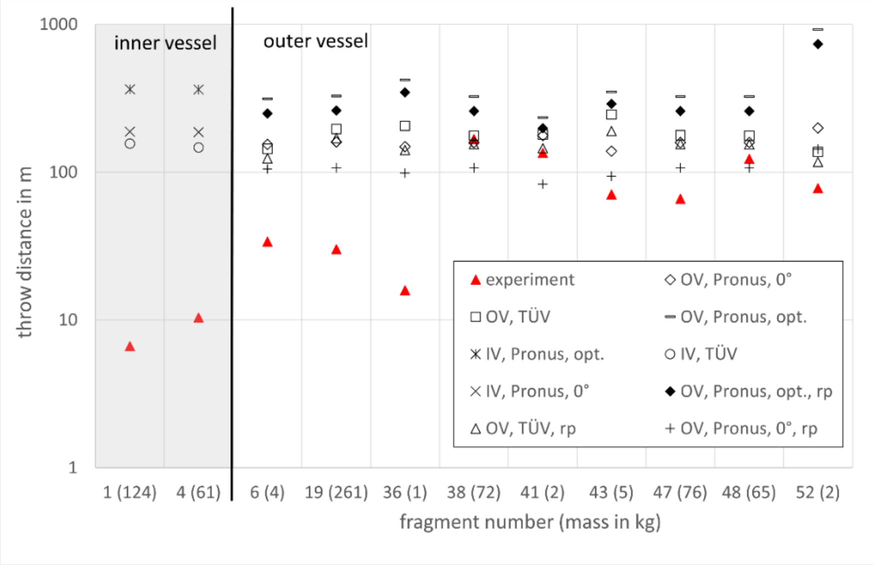

***Figure 9:** comparison of experimental found throw distances against calculated values*

The used shortcuts in the diagram are given in table 4.

***Table 4**: description of shortcuts used in figure 9*

shortcut	description
IV	Inner vessel containing the LH2
OV	Outer vessel, external shell
opt.	Optimum start angle of fragment, meaning 45°C
0°	Start angle of 0° for the fragment throw, as observed by video
rp	Reduced pressure, the pressure was reduced by including the vacuum volume
TÜV	Model described by TÜV Rheinland

The comparison of experimental and calculated throw distances show that the model often gives much larger throw distances than found. But in some cases, the models even underestimate the throw distances. From the safety related point of view the most reliable results were gained with the model of TÜV Rheinland. Nevertheless, the data show that the existing models can not handle a double walled vessel very well. Here an improvement of the models might be necessary.

3.2.3. Shockwaves and heat radiation

The burst of the vessel resulted in sharp shockwave and in the formation of a fireball with an irregular shape of about 24,2 m x 31.2 m. Blast waves show at least two peaks occurring shortly one after another as can be seen in figure 10a. At 22.5 m from the tank a maximum pressure of 133 mbar was measured and at 26.4 m 99 mbar.

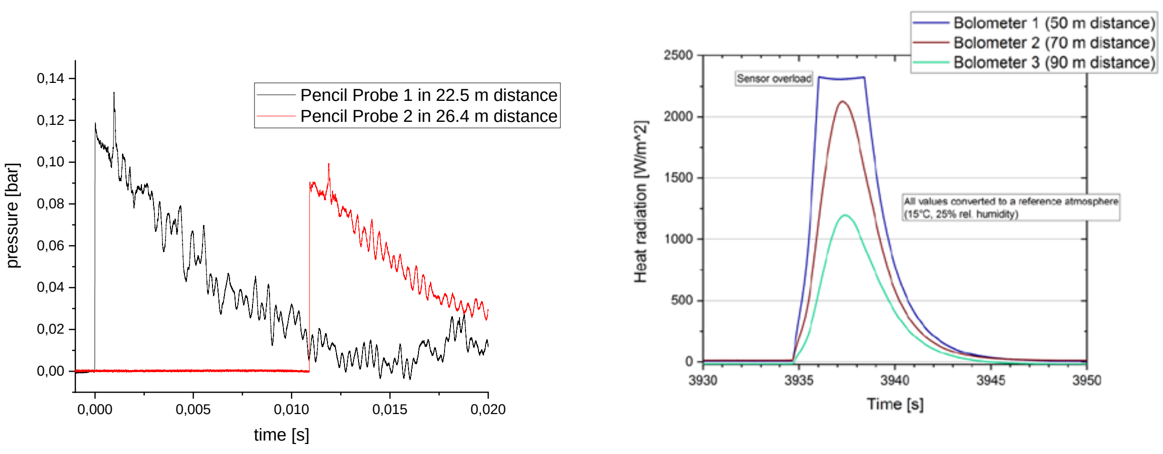

a) *b)*

Figure 10: *a) Blast waves measured at distances of 22.5 m and 26.4 m, right) heat radiation from the burst of the MLI-insulated vessel.*

The fireball development is shown in figure 11 (recording taken from an UAV).

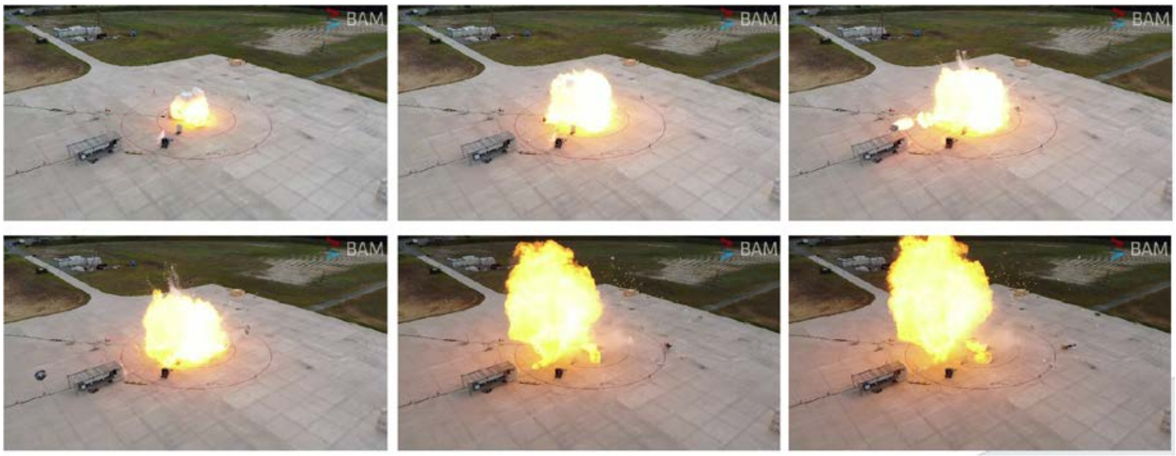

Figure 11*: Fireball development after the failure of an MLI-insulated vessel positioned horizontally filled with LH2 a seen from an UAV flying over the H2TA*

The maximum equivalent fireball diameter is about 25.8 m. The total duration of the fire ball is at least 5 s with lift-off occurring after 2s. Maximum incident heat radiation levels of 2.1 kW/m2 at 70 m and 1.2 kW/m2 at 90 m (the bolometer measurement results are presented in Figure 10b were reached. The Bolometer at 50 m distance was in overload mode with incident heat radiation exceeding 2.4 kW/m². The bolometer distances are measured from the vessel center point. The distances between radiating surface and bolometer have to be decreased by approx. 13 m, half the equivalent fireball diameter, at the beginning of the fireball and then increased due to the lift-off of the fireball. It is assumed that the reference distances of 50 m, 70 m and 110 m are good averages of the mean transient distances between sensor and fire ball hull.

3.3. Fire test 3, vertical Vessel with Perlite insulation

The third test was performed with the perlite-insulated vessel positioned vertically. The vessel was heated, exposed to the propane fire during 4 hours without failling. The setup was adapted due the leakage of fire test 2. Now there was a second remote controllable high-pressure valve installed behind the cryo-valve for emergency release. No leakage happened during this test.

After withstanding the fire for 4 Hours, the test was stopped. On one hand because such a long fire resistance time should never be necessary in reality and on the second hand because the propane tank feeding the flame was empty. As the test was stopped the pressure inside the vessel was 60 bar (see figure 12).

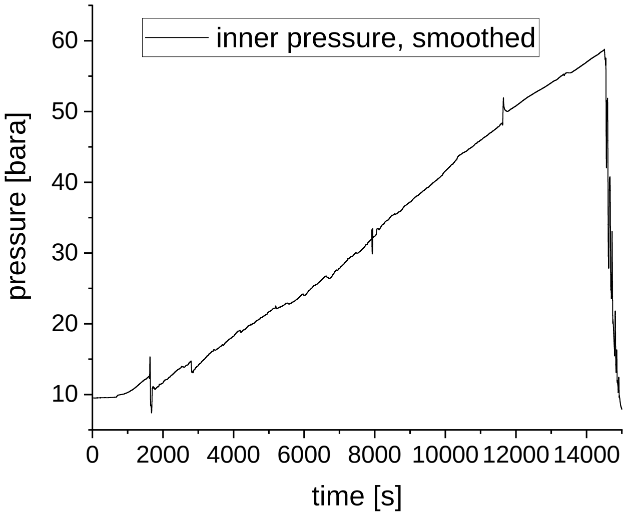

Figure 12*: Inner pressure over time at fire test 3*

Comparable to the horizontal perlite tank, this vessel's outer shell also imploded during the test after a relatively short period at several locations (see figure 13b). Similarly, to fire test 1 this vessel will also be disassembled to remove the perlite and examine the deformation of inner shell and the positions of piping and instrumentation.

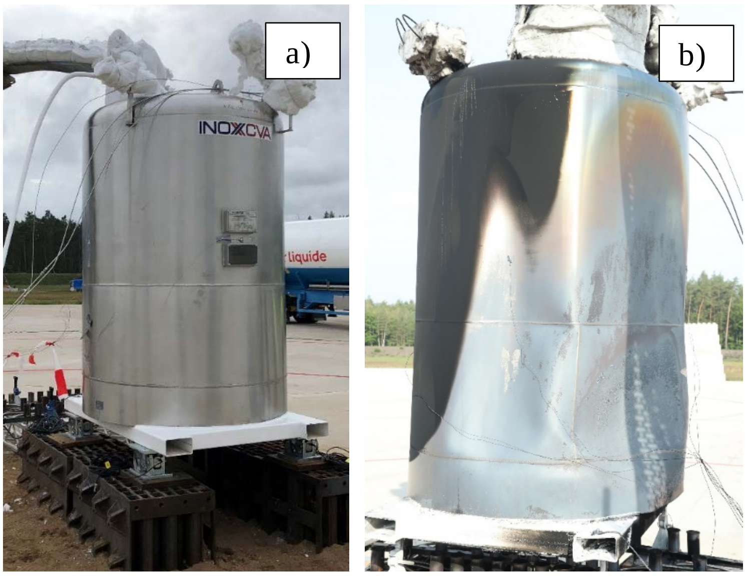

Figure 13*: a) Vessel before fire test 3, b) deformation of outer shell after test*

4. Conclusions

Three double-walled, vacuum insulated pressure vessels containing liquid hydrogen were exposed to a propane fire. Two of these cryo-vessels, a horizontal and a vertical one, both insulated with perlite, withstood the engulfing fire for 1 hour 20 minutes and 4 hours respectively without a catastrophic failing of the vessel but strong deformations of the outer shell.

The horizontal vessel insulated with MLI failed after 1 hour and 6 minutes resulting in a fireball, more than 30 fragments and blast waves. A fireball with a maximum equivalent diameter of about 25.8 m was formed. The total duration of the fire ball was about 5 s with lift-off occurring after 2s. The maximum incident heat radiation was measured with 2.1 kW/m2 at 70 m and 1.2 kW/m2 at 90 m distance.

Larger parts of the vessel were found at distances between 6 m and 167 m from the original position, the latter corresponding to the farthest throw distance of all fragments. Comparison of the throw distances with several models showed mainly a strong overestimation of the measured throw distances by the models indicating that there are further improvements of the models necessary for double walled vessels.

The resulting blast waves show at least two peaks occurring shortly one after another with maximum pressures of 133 mbar at 22.5 m from the vessel and 99 mbar at 26.4 m.

An assessment made on the basis of the preliminary results of internal pressure and temperature measurements at the moment of failure indicate that the liquid hydrogen inside the vessel had not reached the superheat limit of hydrogen at that moment.

Acknowledgements

This work was undertaken as part of the research project Safe Hydrogen fuel handling and Use for Efficient Implementation (SH2IFT). The authors would like to acknowledge the financial support of the Research Council of Norway, Air Liquide, Ariane Group, Equinor, Statkraft, Shell, Safetec, Total and a number of Norwegian municipalities.

References

Abbasi T., Abbasi S.A., (2007), The boiling liquid expanding vapour explosion (BLEVE): Mechanism, consequence assessment, management, Journal of Hazardous Materials, 141, 489–519

Berg A.C. van den, Voort M.M. van der, Weerheym J., Versloot N.H.A., (2004), Expansion-controlled evaporation: a safe approach to BLEVE blast Journal of Loss Prevention in the Process Industries, 17, 397–405

Berg A.C. van den, Voort M.M. van der, Weerheym J., Versloot N.H.A., (2006), BLEVE blast by expansion-controlled evaporation, Process Safety Progress, 25, 44-51

Betteridge S., Phillips L., (2015), Large scale pressurised LNG BLEVE experiments, IChemE Symposium Series no 160

Center for Chemical Process Safety (CCPS), (2016), Guidelines for Vapor Cloud Explosion, Pressure Vessel Burst, BLEVE, and Flash Fire Hazards

Hemmatian B., Casal J., Planas E., (2017), Essential Points in the Emergency Management in Transport Accidents which Can Lead to a BLEVE-Fireball, Chemical Engineering Transactions, 57, 439-444

Kamperveen J.P., Spruijt M.P.N., Reinders J.E.A., (2016), Heat load resistance of cryogenic storage tanks – Results of LNG Safety Program, TNO report no. TNO 2016 R10352

Lorenz D., Radandt S., (1996), Trümmerflug in der Umgebung von Staubexplosionsherden – Vergleich zwischen Modellrechnung und Explosionsereignissen. VDI Berichte Nr. 1272

NIST, (2021), NIST Chemistry WebBook 69, National Institute of Standards and Technology <webbook.nist.gov/cgi/cbook.cgi?ID=C1333740&Mask=4> accessed 01.12.2021.

Pehr, K., (1996), Aspects of safety and acceptance of LH2 tank systems in passenger cars, International Journal of Hydrogen Energy, 21, 387–395.

Rigas F., Sklavounos S., (2005), Evaluation of hazards associated with hydrogen storage facilities, International Journal of Hydrogen Energy, 30, 1501 – 1510

UBA Bericht, (2000), Ermittlung und Berechnung von Störfallablaufszenarien nach Maßgabe der 3. Störfallverwaltungsvorschrift; Forschungs- und Entwicklungsvorhaben 204 09 428.

Ustolin F., Song G., Paltrinieri N., (2019), The Influence of H2 Safety Research on Relevant Risk Assessment, Chemical Engineering Transactions, 74, 1393-1398

Ustolin F., Paltrinieri N., Landucci G., (2020), An innovative and comprehensive approach for the consequence analysis of liquid hydrogen vessel explosions, Journal of Loss Prevention in the Process Industries, 68, 104323.

DOI: 10.7795/810.20221124

Experimental investigation into the consequences of release of liquified hydrogen onto and under water

M. Kluge[1], A.K. Habib[1] and K. van Wingerden[2]

[1] Bundesanstalt für Materialforschung und –Prüfung, Unter den Eichen 87, 12205 Berlin, Germany

[2] Vysus Norway, Kokstadflaten 35, 5257 Kokstad, Norway

E-mail: karim.habib@bam.de

Abstract

Large-scale experiments have been performed to investigate the possible consequences of realistic amounts of liquified hydrogen (LH_2) encountering water. The experiments aimed at simulating an accidental release of LH_2 during especially the fuelling of a ship. For liquified natural gas (LNG) it has been demonstrated that when spilled onto water the evaporation rate can be that high that physical explosions occur which are referred as rapid phase transitions (RPTs). It cannot be excluded that RPTs are also possible in the case of LH_2. The tests were performed in a 10 m x 10 m x 1.5 m basin filled with water, at the Test Site Technical Safety of the Bundesanstalt für Materialforschung und –prüfung (BAM) in Horstwalde, Germany within a research cooperation between BAM and Gexcon as part of the SH2IFT program. LH2 releases were established releasing directly from a trailer carrying LH2 through a long flexible double vacuum insulated transfer line. The releases occurred from a height of 50 cm above and 30 cm under the water surface both pointing downwards and 30 cm under the water surface pointing along the water surface too. The release rate was determined based on the weight loss rate of the road tanker which was placed onto load cells. Special blast pressure sensors were used to measure the shock waves generated by the release processes both in the water and in the air. At several locations the gas concentration was measured. Heat radiation was measured at 3 distances from the point of release. High speed, Infrared (IR) and normal cameras were used to record events and to follow the gas cloud behaviour in time. This includes cameras mounted on a UAV and underwater cameras. Two weather stations were used to measure wind speed, wind direction, temperature and humidity during all tests performed. All investigated release configurations resulted in a very chaotic LH2-water mixing zone, causing considerable evaporation but only minor over pressures. The main phenomenon observed was an ignition of the released gas cloud, resulting in significant blast wave overpressures and heat radiation to the surroundings. The location of the ignition occurred in free air at some distance from the instrumentation and release location.

Keywords: *LH2, RPT, release, gas cloud explosion, heat radiation*

DOI: 10.7795/810.20221124

1. Introduction

When handling liquid hydrogen, especially for ships fuelled by or transporting LH2, a safety concern is the possibility of rapid phase transitions (RPTs) if a leak occurs, and the liquid hydrogen is spilled onto or under water. RPTs are strong physical explosions that can cause severe damage, as seen in the metal-casting industry when water comes into contact with liquid metal (Zielinski et al, 2011), or in the liquified natural gas (LNG) industry if LNG (boiling point at -160 °C) is accidentally released onto water where several accidents have been reported (Cleaver et al, 1998). For LNG RPTs one differs between *early RPT* and *late RPT*, signifying whether the RPT occurs in the LNG-water mixing zone (early) or away from the mixing zone where a pool has formed on top of the water surface (late) (Ustolin et al, 2020). In this work the possibility and consequences of LH_2 RPTs is studied.

LH_2 RPTs have received little attention, and experiments are limited to a study by Verfondern and Dienhart (2017) where the result of a low-impulse spill was investigated. Atkinson (2020) investigated a spray of water applied to LH_2. None of these experiments resulted in RPTs. A theoretical study reported by Odsæter et al. (2021) concluded that late LH_2 RPTs are very unlikely, and that early RPT is less likely to occur for LH_2 than for LNG. The conclusions are based on the understanding of the phenomenon of RPTs occurring when LNG comes into contact with water and is especially related to the low Leidenfrost temperature of LH_2 preventing a collapse of the vapour film separating LH2 and water. Moreover, Odsæter et al. (2021) demonstrated that overpressures generated will be considerably lower than for LNG, provided RPTs do occur when LH_2 is brought into contact with water.

The current paper presents a series of experiments performed to investigate whether RPTs are possible when releasing a LH_2 jet onto water or under water. The experiments aimed at simulating realistic conditions during LH_2 filling operations. The release rate was varied between 0.25 kg/ and 1.0 kg/s.

2. Experimental set-up

The experiments were performed at the Test Site Technical Safety (TTS) of the Bundesanstalt für Materialforschung und –prüfung (BAM) in Horstwalde, approximately 50 km south of Berlin. The former Blast Area 2, meanwhile rededicated as Hydrogen Test Area (H2TA), was used; a 400 m diameter flat circular area with an 80 m x 80 m concrete pad in the centre. On the H2TA an observation bunker, built to military standards, is used for controlling and monitoring the tests from a safe distance respectively a sheltered position.

To simulate realistic conditions, a 10 m x 10 x 1.5 m basin lined with tarpaulin was created to contain the water and provide a sufficiently large volume, behaving like open water with regard to the heat transfer during the short release durations of max. 2 minutes. The LH2 was supplied from a 40 m³ road trailer, providing a sufficient amount of liquid hydrogen for all releases.

DOI: 10.7795/810.20221124

Figure 1 shows the basin (on the left), the trailer carrying LH_2 (on the right) and a container for logging equipment (in the middle). Onto the basin a bridge construction was erected for fixing the release mechanism/point and measuring equipment.

Figure 1: *View of the test set-up to study the release of LH2 onto and under water. The picture shows the basin on the left with a bridge structure for holding the release mechanism and instrumentation. On the right the trailer, 1, carrying the LH2 and the cabin, 2, used for logging equipment.*

To protect the road trailer and the cabin with the logging equipment, concrete walls were erected between each of them and the water basin. A remote connection from the observation bunker to the cabin allowed for a complete remote control of the releases.

Figure 2 shows a schematic representation of the test setup. The LH_2 is released directly from the trailer carrying the LH_2 via an approximately 46 m long flexible double vacuum insulated transfer line (inner diameter 39 mm) connected to a remotely operated vacuum insulated valve. From there an approximately 10 m long flexible double vacuum insulated transfer line (inner diameter 39 mm) lead to the release nozzle. The nozzle could be moved up and downwards, enabling releases over and under the water surface. The transfer line was also connected to a second remotely operated vacuum isolated valve, allowing for an initial phase to release flashed LH_2. The release system was equipped with an emergency release point and was evacuated and purged with helium before starting a release for at least 3 times. The helium was also used as quenching system at the nozzle. A mouthpiece at the end of the release line as well as a manually operated valve at the trailer were used to vary the release rate. The release system was equipped with several pressure transducers and thermocouples to monitor the release conditions. A thermocouple directly at the nozzle was used to detect the release of liquid hydrogen. The road trailer was placed on a weighing system to determine the mass released during each release and the corresponding mass flow was calculated afterwards. Due to the fact, that the road trailer was equipped only with a manual release valve and no additional remotely controllable regulator for the mass flow, as well as the absence of any remotely monitorable readings of the inner pressure or filling level, the release rate could not be set to a defined point before the releases. Instead, a certain number of rotations of the main valve at the road trailer was realised and the release rate resulting from that setting deduced from the weighing system.

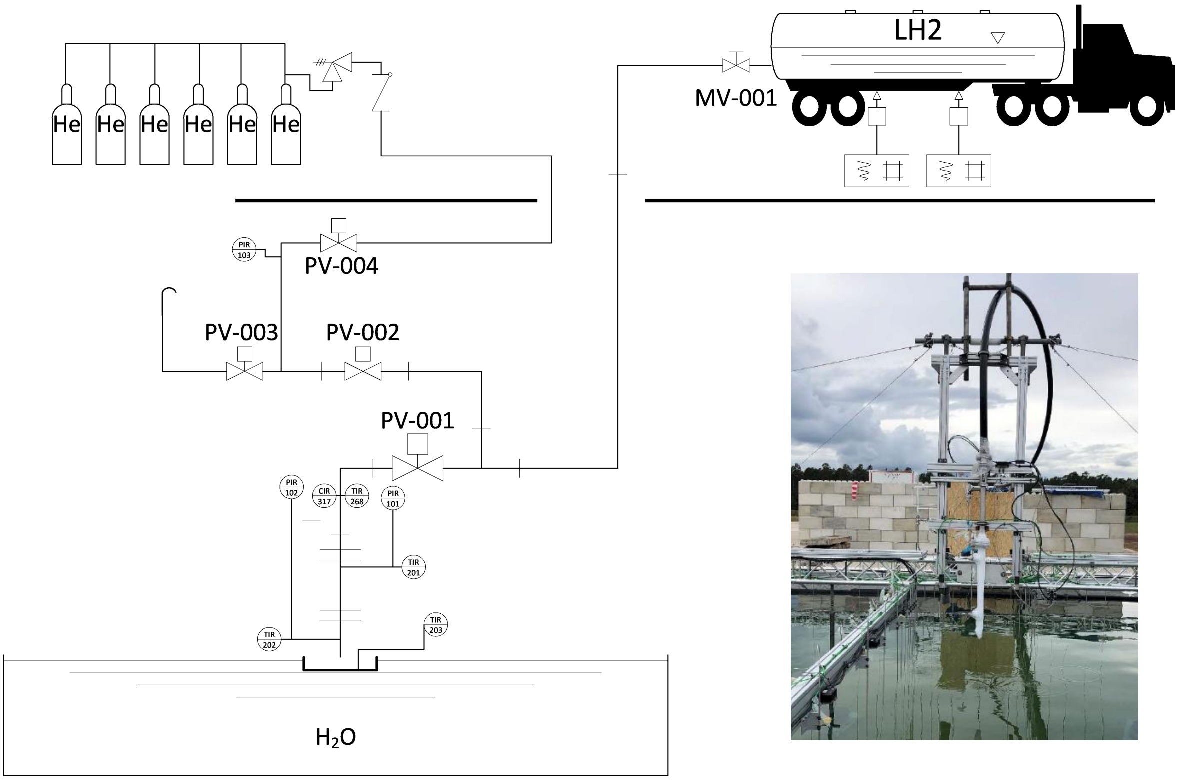

Figure 2: *Schematic showing the LH2 supply system. The system consists of double vacuum insulated hoses with valves designed for use with LH2. A special T-piece can be used as a safety system in case of freezing of the nozzle (due to contact with water) as well as for releasing flashed LH2 during the initial phases of a release. The system can be purged with helium before releasing LH2. The insert shows the release mechanism shortly after a release of LH2, 50 cm above the water level pointing downwards*

Figure 3 shows the road trailer on the weighing system. To determine the mass flow during each release, the mass of the road trailer had to be recorded. A weighing system has been installed consisting of four load cells with a maximum weighing range of 10 to each. The accuracy of the system was +/- 1,5 kg. The load cells were placed at the front and back of the road trailer. As can be seen on Figure 3, the load cells had to be placed on supports to reach a sufficient height for the road trailer not to touch ground anywhere else, then at the load cells. Although the whole measuring system was sensitive to higher wind loads, its accuracy was sufficient to determine the mass loss and calculate a mass flow for most of the releases.

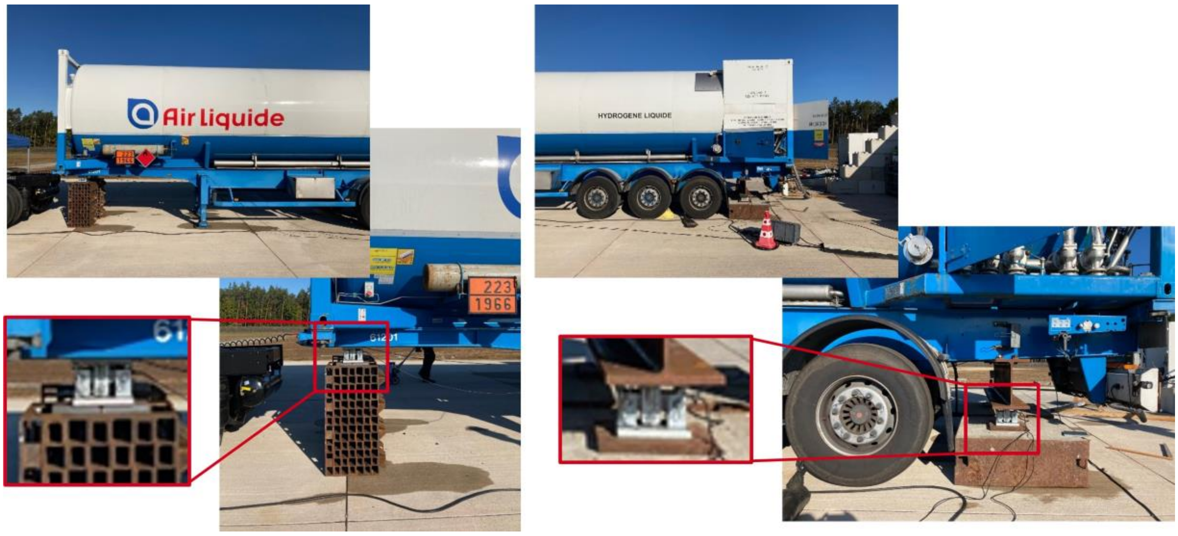

Figure 3: *Road trailer placed on the load cells, for mass loss measurements during the releases.*

3. Test program

As described earlier, the technical equipment of the road trailer did not allow for a "pre-setting" of an exact release rate. The release rate was determined afterwards, through the readings of the weighing system. The main parameters, that could be pre-set before each test, was the number of rotations of the main valve at the road trailer (up to a maximum of 16 rotations) and the location of the nozzle relative to the water surface. All other parameters that varied e.g., the back pressure in the road trailer hence the mass flow, could not be influenced and were only recorded.

Over 80 releases have been realized during the trials. 75 of them have been carried out and recorded successfully. Each trial consisted of more than one release. As the aim of the Experiments was to investigate the possibility of occurrence of RPTs when releasing LH2 on (or under) Water, the trails are named "RPT xxx".

Three positions of the release nozzle have been investigated in these trials:

- approximately 50 cm over the water surface, oriented vertically downward (A) with 31 releases
- approximately 30 cm under the water surface, oriented vertically downward (U) with 34 releases
- approximately 30 cm under the water surface, oriented horizontally parallel to the water (UH) with 10 releases.

The number of releases, the mass flow range and the type of release for each trial are shown in Table 1.

Table 1: *Release parameters of the RPT Trials*

Trial	Type of Release	Number of successful releases	Number of rotations of the main valve (max. possible: 16)	Released mass flow (range)
RPT 001	A	1	10	**4 kg/s
RPT 002	A	8	10	0,3 – 1 kg/s
RPT 003	A	1	10	**0,1 kg/s
RPT 004	U	3	10	0,35 – 0,85 kg/s
RPT 005	A	2	10	**0,25 kg/s
RPT 006	U	4	10	0,5 – 1,1 kg/s
RPT 007	U	5	10	0,35 – 0,65 kg/s
RPT 008	U	3	10	0,55 – 0,62 kg/s
RPT 009	U	3	16	0,35 – 0,7 kg/s
RPT 010	U	3	16	0,35 – 0,45 kg/s
RPT 011	A	3	16	0,45 – 1,1 kg/s
RPT 012	A	3	16	0,32 – 0,58 kg/s
RPT 013	A	3	5	0,25 – 0,4 kg/s
RPT 014	U	2	5	0,3 – 0,5 kg/s
RPT 015	U	3	16	0,5 – 0,75 kg/s
RPT 016	U	1	16	0,8 kg/s
RPT 017	A	5	16	0,4 – **1,4 kg/s
RPT 019	A	2	16	0,8 kg/s
RPT 020	A	3	16	1,1 kg/s
RPT 021	U	4	16	0,25 – 0,76 kg/s
RPT 022	U	3	16	0,27 – 0,37 kg/s
RPT 023	UH	3	16	0,53 – 0,78 kg/s
RPT 024	UH	3	16	0,36 - 0,55 kg/s
RPT 025	UH	4	16	0,38 – **0,93 kg/s

**RPT 018 is not listed, as this trial was not recorded due to a malfunction of the logging system, and is therefore considered as "failed"*

*** Values are not reliable and must be investigated further, as either the release duration was too short (<10s) or the released mass too low (<5kg) for the given sensitivity of the weighing system.*

4. Instrumentation

During the experiments several Data have been recorded:

- Temperatures
- Pressures
- Weight
- Wind speed and direction
- Heat radiation
- IR Video data
- Conventional video data
- Hydrogen concentration

Overall, 96 Sensors have been recorded for each trial as well as 8 Cameras, one IR Camera and a UAV-Camera were used. Figure 4 shows a schematic view of the sensor locations over the water surface. All sensors were mounted to a scaffolding spanning the water surface.

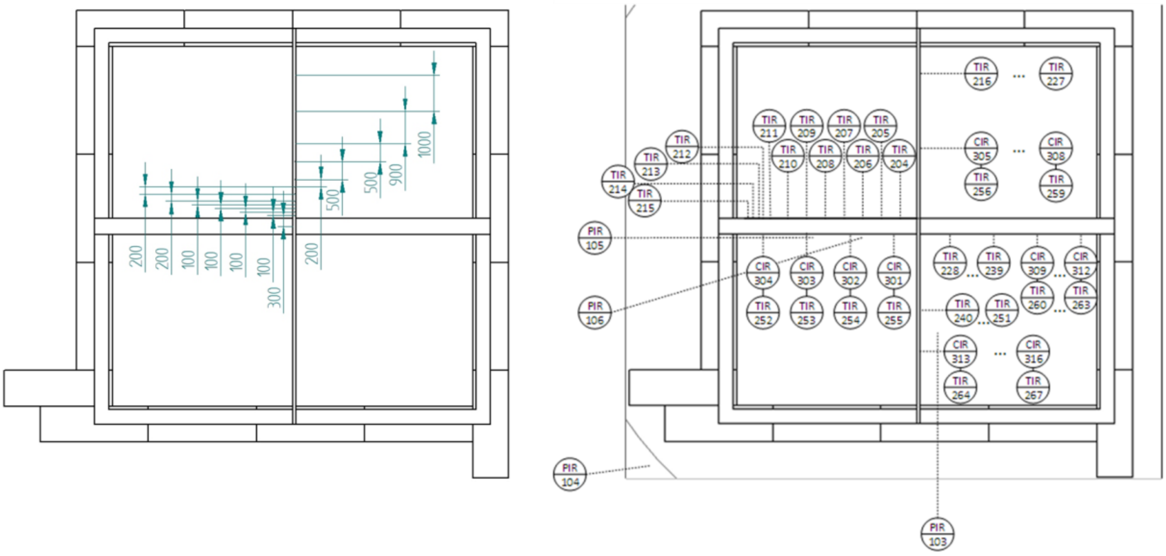

Figure 4: *Schematic view of the sensor positions over the water surface (TIR = Thermocouple, CIR = Gas Sensor, PIR = Pressure Sensor)*

The thermocouples shown in Figure 4, are placed alternatingly just above or just beneath the water surface. Thermocouples directly associated to a gas sensor were mounted directly beside the gas sensor. In addition, the temperature in the filling line was measured (1 at the outlet and 1 further down into the filling line). All thermocouples used were of Type K.

The four pressure sensors consisted of 2 underwater pressure transducers (Piezotronics, type PCB 138A01 underwater blast transducer) and 2 Blast wave sensors (Kistler Pencil Probe Type 6233A) measuring the pressure wave in air.

The concentration of hydrogen in air, was measured at 10 positions using NEOHYSENSE NEO974A, capable of detecting concentrations in the range of 0-100 Vol.%.
Heat radiation measurements at distances of 70, 90 and 110 m of the point of release were done with Bolometers (Medtherm Model 64-XX-14)
Wind speed and direction were recorded using ultra sonic anemometers (METEK USA-1 scientific). Video recordings were done with GoPro Cameras (Gen. 3- 8), a highspeed camera (Redlake Motion PRO X4), an IR-Camera (FLIR E 95) and by means of a UAV (DJI M300 RTK) equipped with regular and infrared camera systems (DJI Zenmuse H20T).
The load cells for weighing the road trailer were of type MTS VC 3500 with a maximum load of 10 t each.

5. Results

5.1 General

In the following observations applicable to all trials are presented. Detailed discussion about results will be done for selected trials but will be valid also for the other trials.

At the beginning of the tests the pressure in the road trailer was around 13,5 bar and varied throughout the trials only due to the releases (resulting in a decrease of the pressure) and the repressurisation of the road trailer due to boil-off between the trials. Due to the manual operation of the road trailer, setting a desired pressured in the trailer was not possible, as it would have required extended pre-tests, to investigate the correlation between the degree of opening of the main valve and the output of the vaporizer. The available amount of LH2 (limited to the volume of the road trailer) did not allow for such investigations. Therefore, most of the trials were carried out with a pressure of the road trailer around (or above) 10 barabs.

As a result, a relatively strong momentum LH2 jet was generated which penetrated quite deep into the water basin, even if the release occurred above the water surface (See Figure 5). From the underwater camera recordings an evaporation mechanism different from that explaining RPTs as seen for combination of water and molten metal and LNG and water can be recognised. The mechanism does not cause the high evaporation rates necessary to generate the overpressures as seen for the aforementioned combinations. From the camera recordings it is clear that there is massive evaporation, but no sudden bursts can be seen. The camera recordings reveal a very chaotic mixing zone that seem to pulsate due to the interplay between volume production from evaporation, insulating bubbles, buoyancy and the continuously incoming jet. The larger bubbles only form on the sides of the impact zone and the vapor layers between LH2 and water and the bubbles themselves are disintegrated due to what seems to be Taylor instabilities. The evaporation is not homogeneous and frequent Geysir-like jets propel out of the water.

Figure 5: *Multiphase jet penetrating the water (release rate 0.8 kg/s, release location 50 cm above the water pointing downwards). The left picture is taken very shortly after the jet entered the water surface. The one in the middle shortly later showing the penetration depth of the jet. The right picture shows the Geysir like behaviour over the water surface.*

For all trials, the detected peak overpressures were due to an unexpected severe gas cloud explosion, instead of the expected RPT phenomena. From all 75 releases, 80% showed an ignition (Table 2) occurring in the gas cloud formed over the water basin, leading to an unconfined vapor cloud explosion (UVCE). Releases with no ignition mostly occurred when releasing over the water surface. Also releases (over and underwater) at low pressures in the road trailer showed a tendency not to ignite which may be related to the lower release momentum.

Table 2: *List of total Number of releases per release type and corresponding number of observed ignitions*

Type of release	Total number of releases	Total Number of observed ignitions	Percent of releases with ignition
A	31	21	68 %
U	34	32	94 %
UH	10	7	70 %

The ignition source is unknown. The instrumentation bridge itself was duly grounded. To exclude the measuring equipment as possible ignition source, several tests (Trials RPT 015 – 017 with releases over and underwater) were performed with all electronic and electrical equipment on and at the basin switched off. Only far field camera recordings were done. Nevertheless, also in every of these releases an ignition was observed. Using the IR-cameras allowed to locate the ignition in “free-air” with a clear distance from the instrumentation bridge and any instrumentation (See Figure 6).

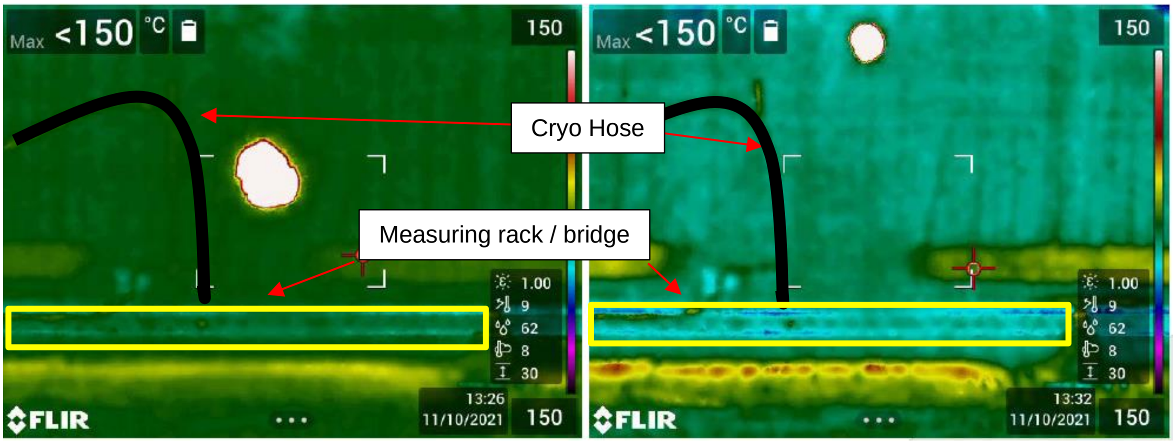

Figure 6: *Moment of initial flame propagation in hydrogen-air clouds generated by releases of LH2 onto and under water with all measuring equipment at the water basin switched off. The ignition location appears to be somewhere in the cloud at a distance from any physical object. The locations of the release point (cryo hose) and measuring rack/bridge have been indicated.*

DOI: 10.7795/810.20221124

Besides hydrodynamic dependencies between the ignition and the release momentum, influences of cavitation or other compressibility effects, electrostatic discharges and especially corona discharges at ice crystals (Petersen et al, 2015) evolving from the release/evaporation process may be an alternative explanation. Thus, a sufficiently strong electric field is needs to be generated by e.g., the freezing of water particles in the air generated by the sudden evaporation of LH2. At this point further analysis of the experimental results is required to investigate the mechanism or define what further experiments should be conducted to examine this phenomenon.

5.2 Consequences

H2 concentration readings during a 0.8 kg/s release for two selected gas sensors are shown in Figure 8. Although the selected sensors were not located directly at the release point and for the presented results also not on the centerline of the wind direction (see Figure 7), relevant concentrations of up to 25 Vol.% could be detected. Figure 8 shows the transient wind speed and wind direction during the whole trial (RPT 021) as well as the transient concentrations at the considered sensor locations. RPT 021 consisted of 4 underwater releases, which all ignited. That the transient concentration for the red sensor location does not reflect the 3rd and 4th release is due to the very short release duration until the ignition took place (respectively 4 s and 12 s). In addition, whilst the wind direction for the 1st and 2nd releases approximately corresponded to an orientation towards the red sensor location (see Figure 7 and Figure 8 a) and b)), the wind direction for the two last release was oriented in direction of the green sensor location. Therefore, the green sensor location shows a concentration peak for the 4th release and lower peaks than for the red sensor for the 1st and 2nd releases. Here as well, the 3rd release is not detected due to the too short duration.

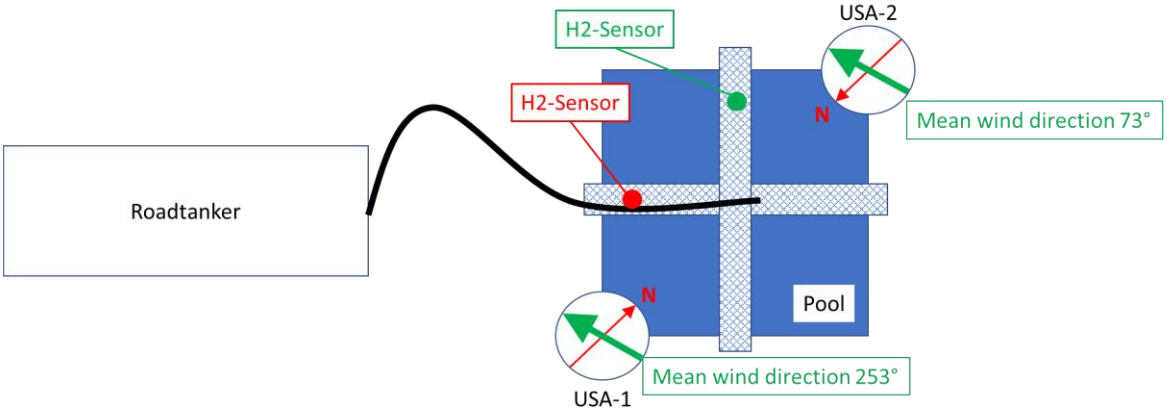

Figure 7: *Schematic view of the USA location and orientation and the emplacement of two H2-Sensors*

As shown the concentrations measured even in further distance of the point of release reach flammable concentrations more or less continuously during the release with some periods where the concentration is close to the stoichiometric concentration of 29.5 % (the minimum ignition energy of hydrogen is found at a concentration of about 33 % in air (Hankinson et al, 2009)). For all locations closer to the release point, the observed transient concentrations show higher values than in Figure 8 c) and can locally exceed the stoichiometric concentration of 29.5 Vol.%.

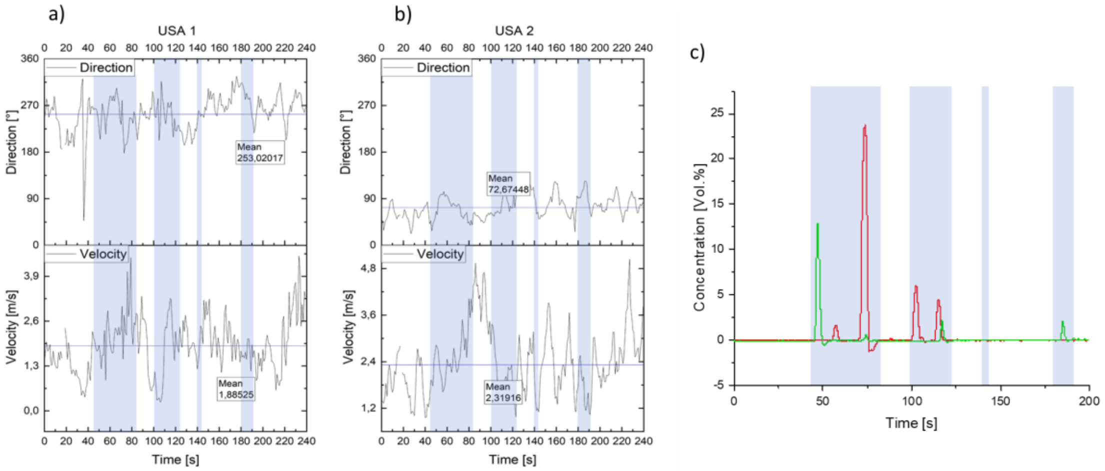

__Figure 8:__ Wind speed and direction over time of both USA and the corresponding recordings of the two gas sensors (red and green) marked in figure 7. Highlighted in light blue are the 4 releases.

The occurrence of RPT's can not be excluded, as there are overpressures noticeable at the pencil probes for the tests where no ignition was observed (see Figure 9 on the left). Measured overpressures associated to a possible RPT Phenomenon were all below 0.05 bar. The recorded pressure waves at the underwater blast sensors were mainly due to the release process and the waves generated in the water basin. These pressure effects were so high, that possible effects due to an RPT are not discernable (see Figure 9 on the right).

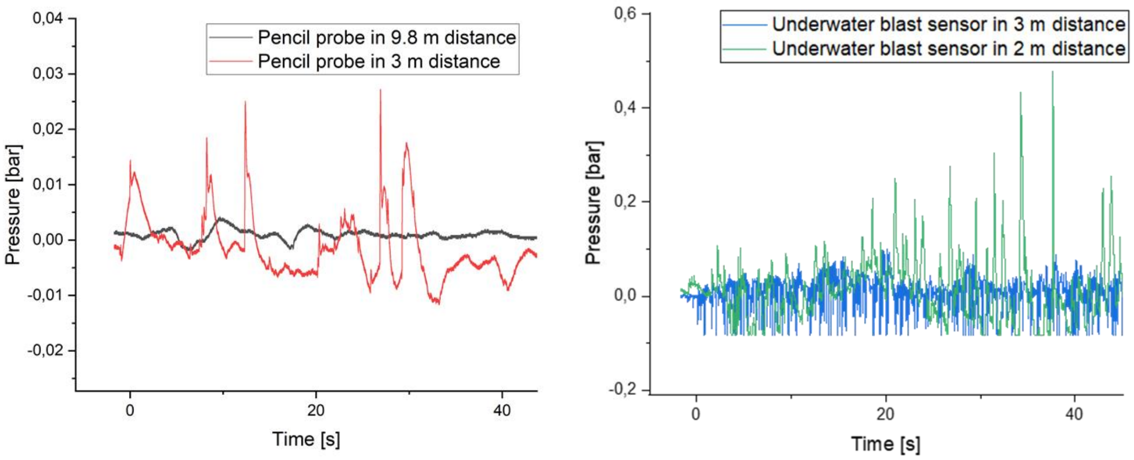

__Figure 9:__ Pressure signal recorded by the pencil probes on the left and by the underwater blast sensors on the right during a trail without ignition (RPT 013)

DOI: 10.7795/810.20221124

These pressure events associated to an RPT are more difficult to detect for the experiments with an ignition (see Figure 10) and are by far lower than the overpressures due to the UVCE. Overpressures recorded from the ignition and subsequent UVCE reached values up to 0.4 bar in the air and several bar underwater.

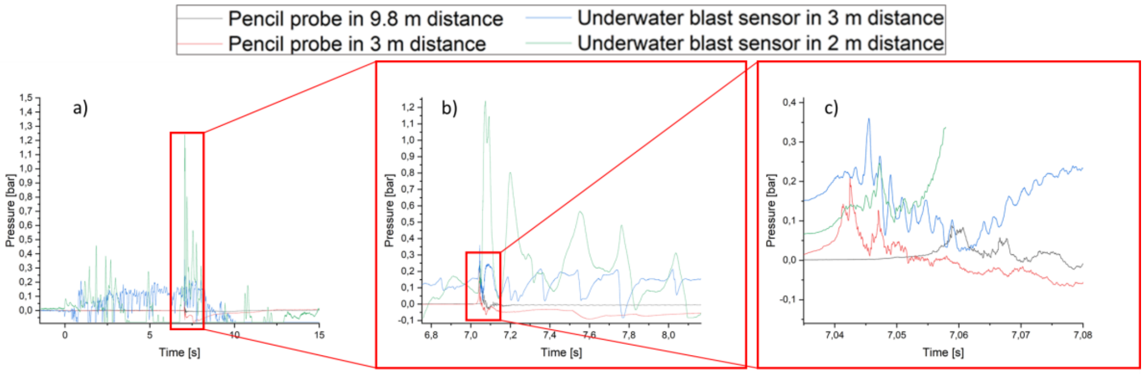

***Figure 10:** Recorded signals of the pencil probes and underwater blast sensors during a release with an ignition (extract of RPT 006)*

As can be seen in Figure 11, the overpressure generated underwater is to be divided in two phenomena. One peak with a short duration related directly to the UVCE and generally in the range of the values recorded by the pencil probe at 3m distance (around 0,2 bar in the considered case for Figure 10 and 11), followed by peaks with a much greater amplitude (in the considered case of Figure 11 up to 1.25 bar) and a significantly longer duration supposedly related to shock wave reflection at the walls and ground of the pool. Even if the latter phenomenon is not directly related to the UVCE, the presence of walls or structures able to reflect shock waves is a boundary condition, that should be investigated further and taken into account for hazard assessment.

DOI: 10.7795/810.20221124

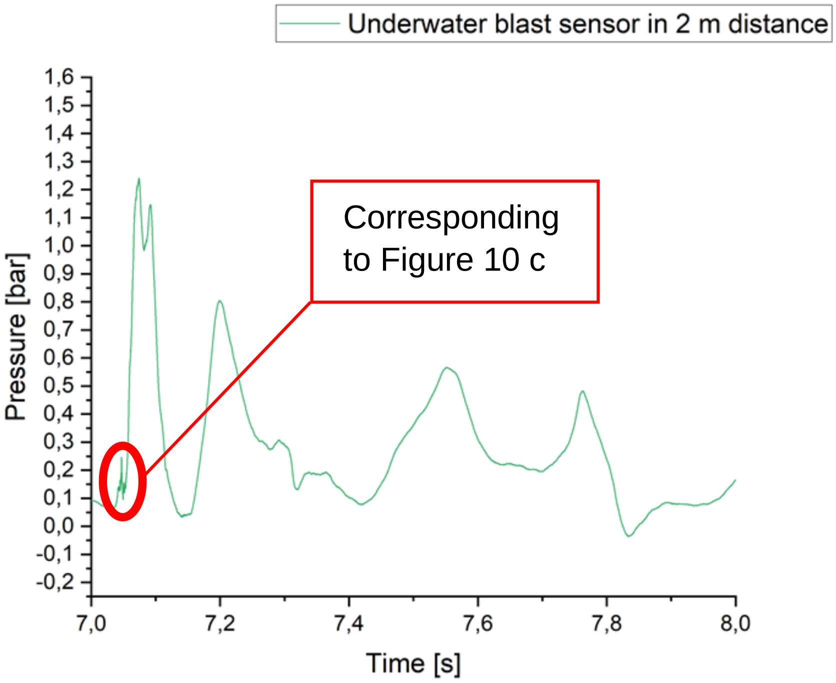

Figure 11:*Prressure signal of one underwater blast sensor during the release with ignition shown in Figure 10*

The UVCE also lead to heat radiation effects in the surroundings. Incident heat radiation measurements were performed at distances of 70m, 90m and 110m from the release point. At 70 m heat radiation peak values of up to 0.1 kW/m^2 were measured. Figure 7 shows the heat radiation profiles seen during the 4 ignitions in a test where 0.5 kg/s to 1 kg/s were released (RPT 006).

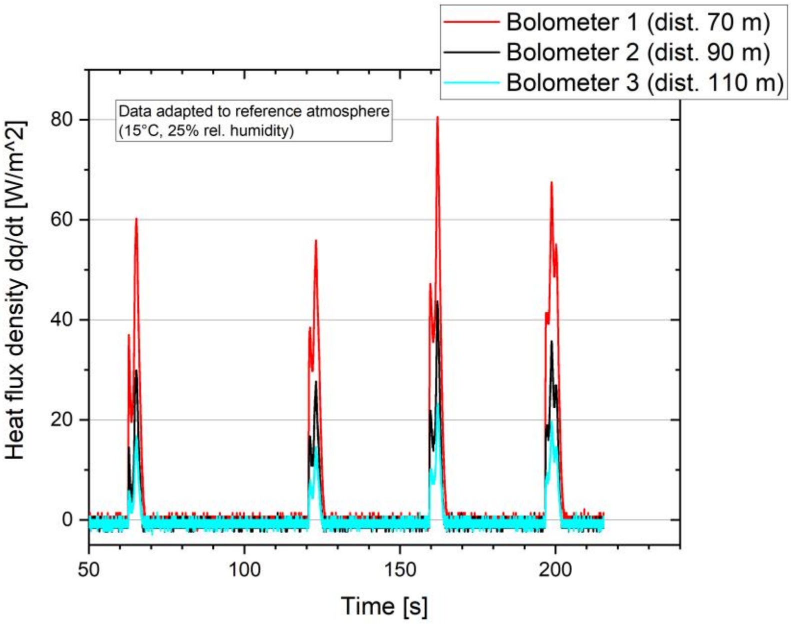

Figure 7: *Heat radiation measurements during a test where 4 ignitions occurred.*

6. Conclusions

Experimental investigations of the release of LH_2 onto and under water showed that the expected RPT phenomenon is not the hazard with the highest potential. Pressure waves generated in air are in the range of several 10 mbar. Against all expectations, the majority of the releases showed an ignition of the gas cloud followed by an UVCE producing much higher overpressures (up to several 100 mbar in air and under water), than recorded for the RPTs. Additionally, the UVCE results in hazard from heat radiation to the surroundings and the existence of a flame. The ignition itself took place in free air and the ignition mechanism is not identified yet. Further research on this topic seems necessary, as the ignition was reproduceable. Another finding of these experiments is, that although the UVCE produces significantly higher overpressures than the RPT, the highest pressures have been recorded underwater (up to several bar). Seemingly these high pressures are generated by reflected shockwaves from the walls and ground of the basin used. The dependency of the occurrence of such strong pressure waves from the geometry of the basin or existing obstacles in the water needs further investigation.

Acknowledgments

This work was undertaken as part of the research project Safe Hydrogen fuel handling and Use for Efficient Implementation (SH2IFT). The authors would like to acknowledge the financial support of the Research Council of Norway, Air Liquide, Ariane Group, Equinor, Statkraft, Shell, Safetec, Total and a number of Norwegian municipalities.

References

Atkinson G., 2020, Experiments and analyses on condensed phases, Report project Pre-normative Research for Safe use of Liquid Hydrogen (PRESLHY), Deliverable No. D4.8, Fuel Cells and Hydrogen Joint Undertaking (FCH JU)

Cleaver P., Humphreys C., Gabillard M., Nedelka D., Heiersted R.S., Dahlsveen J., 1998, Rapid phase transition of LNG, Proceedings 12th International congress on liquefied natural gas, Perth, Australia

Hankinson G., Mathurkar H., Lowesmith B. J., 2009, Ignition energy and ignition probability of methane-hydrogen-air mixtures, 3rd International Conference on Hydrogen Safety, Ajaccio, France.

Odsæter, L. H., Skarsvåg, H. L., Aursand, E., Ustolin, F., Reigstad, G. A., & Paltrinieri, N., 2021. Liquid Hydrogen Spills on Water—Risk and Consequences of Rapid Phase Transition. Energies, 14(16), 4789.

Petersen D., Bailey M., Hallett J., Beasley W., 2015, Laboratory investigation of corona initiation by ice crystals and its importance to lightning, Quarterly Journal of the Royal Meteorological Society, 141,1283–1293

Ustolin F., Odsæter L.H., Reigstad G., Skarsvåg H.L., Paltrinieri N., 2020, Theories and Mechanism of Rapid Phase Transition. Chemical Engineering Transactions, 82, 253–258

Verfondern K., Dienhart B., 2007, Pool spreading and vaporization of liquid hydrogen, International Journal of Hydrogen Energy, 32, 2106 – 2117

Zielinski S.M., Sansone A.A., Ziolkowski M., Taleyarkhan R.P., 2011, Prevention and Intensification of Melt-Water Explosive Interactions, Journal of Heat Transfer, 133, 071201-1/071201-8

DOI: 10.7795/810.20221124

Minimum diameters for CH_4/H_2-air mixtures: implications for natural gas cooktop burners

Cristian C. Mejía-Botero, Fernando Veiga-López & Josué Melguizo-Gavilanes
Institut Pprime, UPR 3346 CNRS, ISAE–ENSMA, Futuroscope Chasseneuil, France
E-mail: *cristian-camilo.mejia-botero@ensma.fr*

Abstract

The minimum detonation diameter for methane (CH_4)/hydrogen (H_2)-air mixtures is numerically evaluated to assess detonation risks in cooktops designed to work with natural gas. A one-dimensional mathematical model that considers heat and friction losses for detonations propagating in pipes is used for that purpose. The initial conditions are selected to emulate the operation of a commercial cooktop working with different CH_4/H_2 blends. Results show that for H_2 content in the blend higher than 45 %, a conventional cooktop air-fuel mixer may pose a detonation hazard since the minimum detonation diameters predicted by the model are smaller than the diameter of the mixing tube (i.e., $d_{\text{min}} < d_{\text{mixer}}$). Additionally, the individual effect of equivalence ratio, Φ, and hydrogen content, % H_2, in the fuel blend are evaluated separately. An increased risk of detonation is present for (i) CH_4/H_2-air mixtures with $\Phi \rightarrow 1$, and (ii) higher % H_2 content.

Keywords: *CH_4/H_2 blend, minimum diameter, detonation, cooktop*

1 Introduction

One of the strategies to reduce greenhouse gases emissions is the introduction of green hydrogen (H_2) into the world's energy matrix (Kong et al., 2021) but most current end-use equipment (e.g., industrial burners and residential/commercial heaters) is not designed to burn pure H_2. One of the interim strategies for a successful energy transition is to use natural gas (NG)/H_2 blends (Wojtowicz, 2019) on existing NG distribution networks. This provides the possibility of connecting H_2 producers with end-users in the short term and at a relatively low cost (Witkowski et al., 2018). The H_2 content (% $H_{2,\text{blend}}$) that could be safely added depends on the gas system of each country; Germany and The Netherlands have, to date, the highest authorized limits (% $H_{2,\text{blend}} = 10 - 12$) (Staffell et al., 2019).

The technology of cooktops designed to work with NG is quite simple (Figure 1). The fuel is injected from a small injector which increases the fuel discharge impulse, and in turn, draws air in from the surroundings resulting in a fuel-rich mixture. This mixture travels through the mixing tube to the combustion chamber, where ignition subsequently occurs and a partially premixed flame is generated. Cooktops are thus self-aspirating burners, similar to laboratory Bunsen burners. That is, part of the air (primary air) is mixed before combustion, and the rest (secondary air) is supplied by diffusion from the surroundings.

For safety reasons, the fuel concentration in the mixing tube must be higher than the upper flammability limit (UFL) in air to avoid accidental ignition and undesired flame propagation; the latter is known as flashback (Zhao et al., 2019a, Sayad et al., 2014). For this purpose, a primary air adjuster is used to control the amount of air that can be drawn in. The UFL of H_2 is higher (75 %vol) than that of CH_4 (15 %vol) which poses a safety hazard when increasing the content of H_2 in the fuel blend. If flashback occurs, the flame may potentially accelerate and transit to detonation, damaging the equipment and compromising the safety of end users.

Zhao et al. (2019b) studied the influence of H_2 addition to domestic natural gas burners, and evaluated the flashback limits for different CH_4/H_2 blends. The authors concluded that burners designed to burn NG are not suitable to work with % $H_{2,\text{blend}} \geq 20$. Literature addressing detonation risks in CH_4/H_2 blends seems scarce. Faghih et al. (2016) numerically evaluated explosions characteristics of these

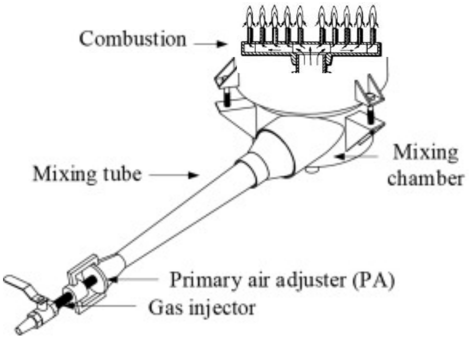

***Fig. 1**: Scheme of typical cooktop burner gas feed line including a gas injector, primary air adjuster, mixing tube/chamber and the combustion end. Adapted from (Chaelek et al., 2019).*

blends based on the deflagration index and maximum pressure increase, which are important indicators to assess the potential damage resulting from accidental explosions. They concluded that for % $H_{2,\text{blend}} > 70$, the deflagration index increases exponentially, and exhibits a strong/weak dependence on initial pressure/temperature. Pang and Gao (2015) evaluated the velocity deficit of CH_4-$2H_2$-$3O_2$, CH_4-H_2-$2.5O_2$, and CH_4-$4H_2$-$4O_2$ mixtures in a 36-mm inner diameter tube equipped with 2, 4, and 7.5-mm annular channels. A maximum velocity deficit of 7% from the ideal Chapman-Jouguet (CJ) velocity –mixture independent– was reported. Zhang et al. (2016) collected detonation cell size (λ) data for the same mixtures, concluding that detonation structure is irregular; a linear relationship between λ and the Zel'dovich-von Neumann-Döring (ZND) induction length, l_{ind}, was also reported.

A parameter of interest that could be applicable to NG burner design to avoid potential detonation hazard inside tubes is the minimum detonation diameter, d_{min}. It represents a limiting tube size below which detonation propagation is no longer possible. It is therefore good practice to have piping diameters that satisfy the later condition, i.e., $d < d_{\text{min}}$. Agafonov and Frolov (1994) performed a systematic study to derive a one-dimensional model capable of predicting d_{min} for pure and Ar/N_2-diluted H_2-O_2 mixtures. Their results were found to be in agreement with available experimental data showing that an increasing % $H_{2,\text{blend}}$ in the mixture results in a decrease in d_{min}. Gao et al. (2014) performed an experimental parametric study to determine d_{min} values for hydrocarbon-oxygen mixtures, i.e., acetylene (C_2H_2), propane (C_3H_8) and CH_4, using polycarbonate tubes (1.5 mm $< d <$ 50.8 mm). Their d_{min} results were shown to follow the $d_{\text{min}} = \lambda/3$ rule for the conditions evaluated. Surprisingly no study was found that reported d_{min} for CH_4/H_2 blends.

In the present work, the effect of the addition of H_2 to CH_4 on the minimum detonation diameter, d_{min}, is numerically evaluated. The paper is structured as follows. Section 2 introduces the physical model and the strategy followed to define the initial conditions for the simulations, which is based on the design and operating parameters of a commercial NG burner. Section 3 discusses the main results. Finally, section 4 presents the main conclusions applicable to the safe design of future cooktop burners working with CH_4/H_2 blends.

2 Methodology

2.1 Physical model

The flow is described by the compressible reactive Euler equations in a frame of reference attached to the shock. Here, the model presented in Veiga-López et al. (2022), which only included friction losses, is extended to account for heat losses. The system of equations thus reads:

$$\frac{\mathrm{d}\rho}{\mathrm{d}x} = -\frac{\rho}{\mathrm{w}}\left[\frac{\dot{\sigma}+F_q-Q+(\eta-1)F}{\eta}\right], \tag{1}$$

$$\frac{\mathrm{dw}}{\mathrm{d}x} = \left[\frac{\dot{\sigma}+F_q-Q+(\eta-1)F}{\eta}\right], \tag{2}$$

$$\frac{\mathrm{d}p}{\mathrm{d}x} = -\rho\mathrm{w}\left[\frac{\dot{\sigma}+F_q-Q-F}{\eta}\right], \tag{3}$$

$$\frac{\mathrm{d}Y_k}{\mathrm{d}x} = \frac{1}{\mathrm{w}}\frac{W_k\dot{\omega}_k}{\rho}, \ k=1,...,N. \tag{4}$$

ρ, w and $\dot{\sigma}$ sigma are the density, the axial velocity in the shock-attached frame and the thermicity. Y_k, W_k and $\dot{\omega}_k$ represent the mass fraction, molecular weight and net production/consumption rate of species k; $\eta = 1-M^2$ is the sonic parameter with $M = \mathrm{w}/a_f$ the flow Mach number computed based on the frozen speed of sound, a_f. The functions F_q, F and Q are given by:

$$F_q = \frac{(\gamma-1)}{a_f^2}c_f(D-\mathrm{w})^2|D-\mathrm{w}|; \quad F = c_f\left(\frac{D}{\mathrm{w}}-1\right)|D-\mathrm{w}|; \quad Q = \frac{(\gamma-1)q}{a_f^2\rho}, \tag{5}$$

with

$$q = \alpha c_f \rho |u| [c_p(T-T_w)+u^2/2]. \tag{6}$$

T, u, c_p and γ are the temperature, axial velocity in the laboratory frame, the specific heat at constant pressure of the gas and the ratio of specific heats; subscript w denotes conditions at the wall. In addition, the friction factor is defined as $c_f = P/(2A)\tilde{c}_f$, where P represents the perimeter of the tube, A its cross-sectional area, $\tilde{c}_f$ denotes a dimensionless skin-friction coefficient of the rough walls of the tube. α is the momentum-heat loss similarity factor, $\alpha = 1$, reproduces the Reynolds analogy for heat and momentum losses which is characteristic of smooth tubes.

The friction factor and the actual tube diameters are related through the Blasius approximation for smooth tubes (Equation 7), which has been used successfully in previous works to analyze experimental trends (Kitano et al., 2009, Tsuboi et al., 2013). In Equation 7 μ_s and ρ_s are, respectively, the dynamic viscosity and density of the mixture at post-shock conditions in Pa-s and kg/m^3, and u_s is the flow velocity measured relative to the shock wave, in m/s.

$$d = \left[\frac{0.6328}{c_f}\right]^{4/5}\left[\frac{\mu_\mathrm{s}}{\rho_\mathrm{s}u_\mathrm{s}}\right]^{1/5} \tag{7}$$

The output of system (1)-(7) are $D-d$ curves, that define the combination of detonation velocity (D) and tube diameter (d) that results in the steady propagation of a detonation wave. These curves exhibit a turning point, d_min, that indicates the minimum tube diameter for which a steady solution exists for a given set of initial conditions; the d_min value computed provides an estimate for detonation propagation limits. In Appendix A a comparison of the model's predictions with available experimental data for CH_4-O_2, H_2-O_2, and H_2-air mixtures is included.

2.2 Determination of initial conditions

2.2.1 Binary fuel mixture definition and upper flamability limit

The combustion reaction for a binary fuel mixture of CH_4/H_2 is shown in Equation 8. x denotes the mole fraction of H_2 in the blend ($x = n_{\mathrm{H}_2}/n_\mathrm{blend}$ where $n_\mathrm{blend} = n_{\mathrm{H}_2}+n_{\mathrm{CH}_4}$); $x = 0$ is thus pure CH_4 and $x = 1$ pure H_2. Close inspection of Equation 8 reveals that as x increases, less air is required for complete combustion of the mixture. Equation 9 expresses the equivalence ratio (Φ) of the mixture as a function of x and the mole fraction of fuel (X_{fuel}) and oxygen (X_{O_2}) in the reactive mixture.

$$xH_2 + (1-x)CH_4 + \frac{4-3x}{2}(O_2 + 3.76N_2) \rightarrow (1-x)CO_2 + (2-x)H_2O + 3.76\left(\frac{4-3x}{2}\right)N_2 \quad (8)$$

$$\Phi = \frac{\left(\frac{n_{\text{fuel}}}{n_{O_2}}\right)_{act}}{\left(\frac{n_{\text{fuel}}}{n_{O_2}}\right)_{stq}} = \left(\frac{X_{\text{fuel}}}{X_{O_2}}\right)\left(\frac{4-3x}{2}\right) \quad (9)$$

Equation 10 shows the Le Chatelier's mixing rule (L'Chatelier, 1891, Mashuga and Crowl, 2004) used to calculate the upper flammability limit for fuel blends ($\text{UFL}_{\text{blend}}$) in air, where x_i and UFL_i are the mole fraction and upper flammability limit of each component in the blend ($i = CH_4$ and H_2), respectively. Figure 2 (a)-(b) show $\text{UFL}_{\text{blend}}$ and its corresponding equivalence ratio ($\Phi_{\text{UFL,blend}}$) as the content of H_2 in the mixture increases. Expectedly, the plots are bounded by $\text{UFL}_{CH_4} = 15\%$ ($\Phi_{\text{UFL,blend}} = 1.68$) for pure CH_4 and by $\text{UFL}_{H_2} = 75\%$ ($\Phi_{\text{UFL,blend}} = 7.12$) for pure H_2.

$$\%\text{UFL}_{\text{blend}} = \frac{1}{\sum_{i=1}^{k} \frac{x_i}{\text{UFL}_i}} \times 100; \quad \sum_{i=1}^{k} \frac{x_i}{\text{UFL}_i} = \frac{x}{\text{UFL}_{H_2}} + \frac{1-x}{\text{UFL}_{CH_4}} \quad (10)$$

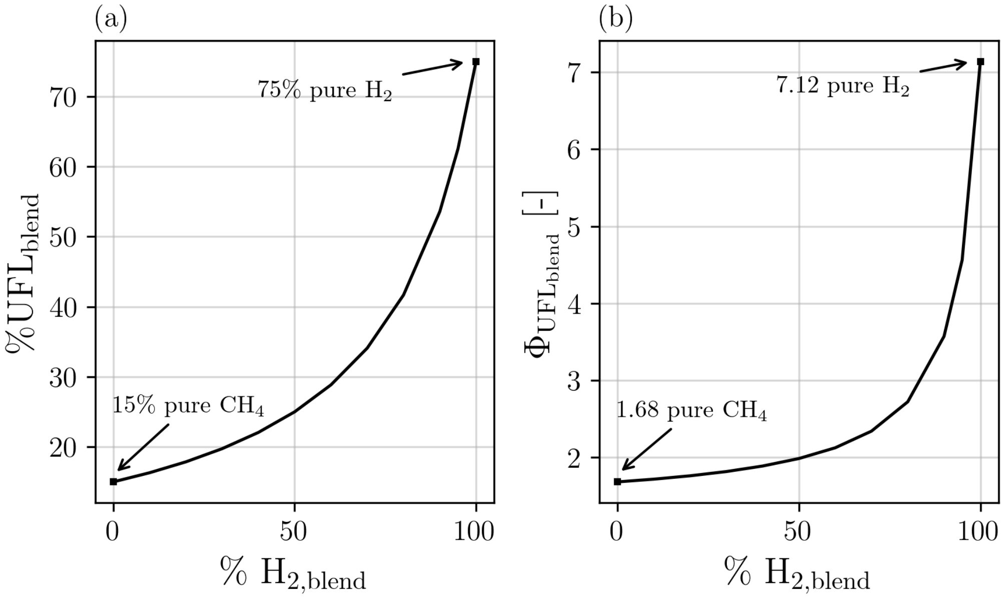

Fig. 2: *(a) Upper flammability limit of the CH_4/H_2 blend in air and (b) equivalence ratio for the corresponding UFL of the blend, for different H_2 blend composition.*

2.2.2 Commercial NG cooktop burner

The operating parameters of a commercial NG cooktop burner working at standard temperature and pressure (288 K and 101.325 kPa) are taken as the base case of our study. See Table 1.

In these burners, the fuel is injected through a nozzle whose diameter and supply pressure define the mass flow rate of fuel, $\dot{m}_{\text{fuel}}$. Equation 11 shows an expression derived using orifice discharge theory, where C is the injector discharge coefficient, A_{in} is the cross-sectional area of the injector, p_{in} is the gauge supply pressure and ρ_{fuel} is the fuel (CH_4/H_2) density. In the derivation of Equation 11, the

DOI: 10.7795/810.20221124

***Table 1**: Operational variables of a comercial NG cooktop*

Parameter	Values	Units
Injector diameter (d_{in})	0.8	mm
Injection pressure (p_{in})	35	mbar-g
Discharge coefficient (C)	0.9	-
Mixer diameter (d_{mixer})	15.9	mm

flow is assumed to be adiabatic, incompressible, steady and subsonic; the latter assumption holds for injection pressures below 100 mbar-g (North American Manufacturing Company et al., 1997).

$$\dot{m}_{\text{fuel}} = CA_{\text{in}}\sqrt{2p_{in}\rho_{\text{fuel}}} \tag{11}$$

To avoid operational risks, such as accidental ignition and flame propagation before reaching the combustion chamber, it is common practice to ensure that the fuel-air mixture in the mixing tube (see Figure 1) is always above the upper flammability limit (UFL). To meet this condition, NG cooktop burners are equipped with a primary air adjuster as shown in Figure 1. The mass of air, $\dot{m}_{\text{air}}$, drawn in by the fuel jet (Equation 12) is computed using free jet theory; PA is the primary air adjuster opening, I is the fuel injection impulse, and ρ_{mix} is the density of the mixture which decreases considerably with increasing hydrogen content in the fuel blend $\%\text{H}_{2,\text{blend}}$. Equation 12 is derived via a momentum balance and assuming that: (i) the radial velocity and mass concentration profiles have the same shape at each axial section examined, and (ii) the jet forms an angle of $\sim 11^\circ$ with the horizontal in line with experimental observations (North American Manufacturing Company et al., 1997).

$$\dot{m}_{\text{air}} = 0.3 \cdot PA\sqrt{I\rho_{\text{mix}}} - \dot{m}_{\text{fuel}}; \quad I = \frac{\dot{m}^2_{\text{fuel}}}{\rho_{\text{fuel}}A_{\text{in}}} \tag{12}$$

PA is the burner parameter that needs being determined. To do so, the value $\Phi_{\text{UFL,blend}} = 1.68$, which corresponds to the design condition of a conventional NG burner is used. Figure 3 shows how the equivalence ratio of a pure CH_4 mixture ($\Phi_{\text{mix,CH4}}$) varies for different PA openings. As PA increases, more air is drawn into the mixing tube, which according to Equation 9 results in a decrease of $\Phi_{\text{mix,CH4}}$. For $\Phi_{\text{mix,CH}_4}$ = $\Phi_{\text{UFL,blend}} = 1.68$, a $PA = 20$ mm is required; this value will be kept fixed for the remainder of the study.

2.2.3 Cases of practical interest

It is now possible to evaluate Φ_{mix} for different $\%\text{H}_{2,\text{blend}}$ and $PA = 20$ mm using the conditions listed in Table 1 (see Figure 4). Φ_{mix} decreases from 1.68 for $\%\text{H}_{2,\text{blend}} = 0$ to 1.27 for $\%\text{H}_{2,\text{blend}} = 88$. Further H_2 addition to 100% increases Φ_{mix} to 1.33. This behavior is due to the combined effect of increasing the fuel/air ratio and decreasing the air requirement for an increase of $\%\text{H}_{2,\text{blend}}$. Note that the values of Φ_{mix} obtained in Figure 4 are much lower than those shown in Figure 2 (b) for $\Phi_{\text{UFL,blend}}$, which represent unsafe operating conditions. To evaluate the burner performance under different % $\text{H}_{2,\text{blend}}$, six cases are considered. These are indicated as circular markers in Figure 4, and are listed in Table 2 for clarity.

3 Results and discussion

The results presented in this section were obtained using GRI 3.0 (Smith et al., 1994) with thermodynamic data extended to cover the range of 300 K - 5000 K.

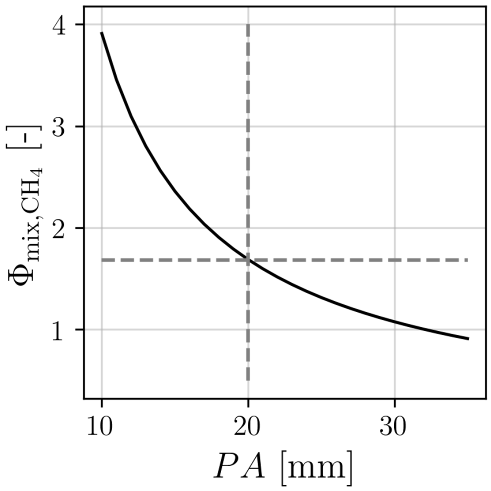

***Fig. 3**: Equivalence ratio for pure CH_4 in air as a function of the primary air opening using conditions of Table 1.*

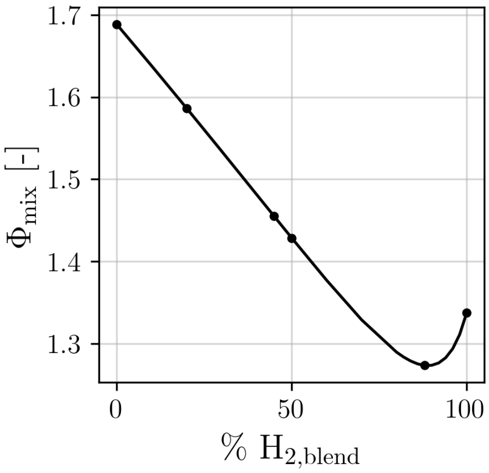

***Fig. 4**: Equivalence ratio of the CH_4/H_2 blend in air for conditions of Table 1 and $PA = 20$ mm.*

***Table 2**: Cases of practical interest*

	Case 1	Case 2	Case 3	Case 4	Case 5	Case 6
% $\mathbf{H}_{2,\mathbf{blend}}$	0	20	45	50	88	100
$\Phi_{\mathbf{mix}}$	1.68	1.58	1.45	1.42	1.27	1.33

3.1 Cases of practical interest

Figure 5 shows the $D-d$ curves for the cases listed in Table 2, and initial pressure and temperature of $p_0 = 100$ kPa and $T_0 = 300$ K. The maximum value of D for each condition corresponds to the CJ velocity, which is the ideal detonation velocity for a given initial pressure, temperature, and mixture composition. Due to heat and friction loses to the tube walls, a velocity deficit is observed as the tube diameter is decreased. All cases exhibit a turning point which indicate the minimum diameter capable of sustaining steady detonation propagation; d_{min} is thus the variable of interest in the present work. Detonation velocities at the turning point are much higher $D(d_{min}) = 1935$ m/s for case 6 (% $H_{2,blend}$ = 100, Φ_{mix} = 1.33) than for case 1 (% $H_{2,blend}$ = 0, Φ_{mix} = 1.68) where $D(d_{min}) = 1701$ m/s. Case 4 (% $H_{2,blend}$ = 50, Φ_{mix} = 1.42) yields the lowest propagation velocity $D(d_{min})$ = 1670 m/s.

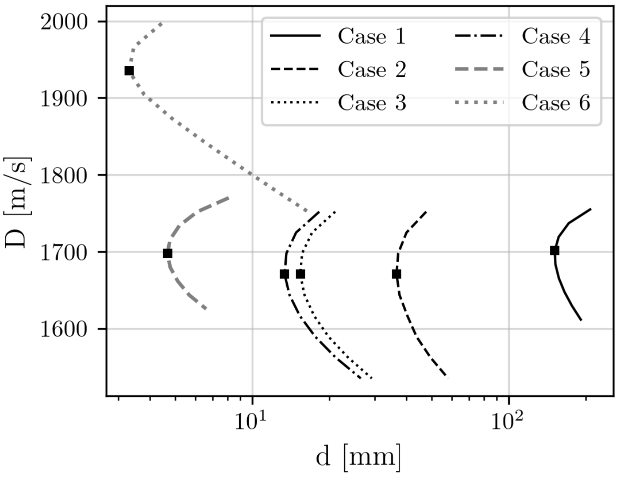

***Fig. 5**: $D-d$ curves for the cases of study presented in Table 2. Case 1: % $H_{2,blend}$ = 0, Φ_{mix} = 1.68; case 2: % $H_{2,blend}$ = 20, Φ_{mix} = 1.58; case 3: % $H_{2,blend}$ = 45, Φ_{mix} = 1.45; case 4: % $H_{2,blend}$ = 50, Φ_{mix} = 1.42; case 5: % $H_{2,blend}$ = 88, Φ_{mix} = 1.27; case 6: % $H_{2,blend}$ = 100, Φ_{mix} = 1.33.*

Figure 6 summarizes our results. d_{min} decreases with increasing % $H_{2,\text{blend}}$ content ranging from $d_{\text{min}} = 151.3$ mm (% $H_{2,\text{blend}}$ = 0) to $d_{\text{min}} = 3.3$ mm (% $H_{2,\text{blend}}$ = 100). Comparing d_{min} values with the mixing tube diameter, d_{mixer}, of a conventional NG burner, cases 3 to 6 do not meet the safety criterion since $d_{\text{min}} < d_{\text{mixer}}$. While the model predicts that a fuel blend with % $H_{2,\text{blend}} < 45$ would not in principle require a redesign of current NG burners, the risk of flashback and propagation of fast flames in the mixing tube remains because the fuel blends are always below the $\text{UFL}_{\text{blend}}$ (see Figure 2).

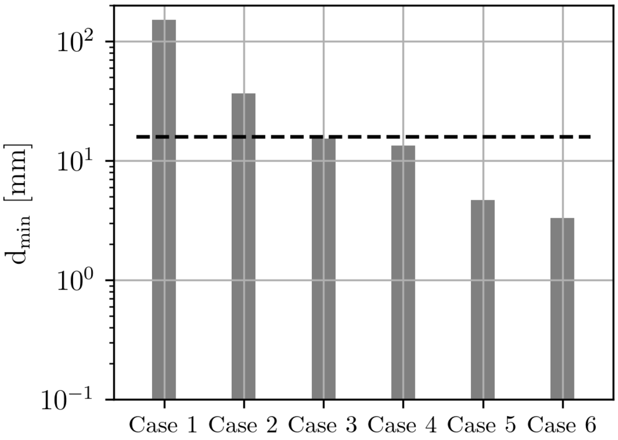

***Fig. 6**: Summary of d_{min} obtained for the cases of study presented in Table 2. Case 1: % $H_{2,blend}$ = 0, Φ_{mix} = 1.68; case 2: % $H_{2,blend}$ = 20, Φ_{mix} = 1.58; case 3: % $H_{2,blend}$ = 45, Φ_{mix} = 1.45; case 4: % $H_{2,blend}$ = 50, Φ_{mix} = 1.42; case 5: % $H_{2,blend}$ = 88, Φ_{mix} = 1.27; case 6: % $H_{2,blend}$ = 100, Φ_{mix} = 1.33. The horizontal dashed line is a visual indicator showing the mixer diameter, d_{mixer}, of a typical NG cooktop burner.*

Initial temperature (T_0) variations were also examined to evaluate seasonal changes, i.e., winter (0° C), summer (25° C), and standard conditions (15° C). d_{min} exhibits a very weak dependence on T_0 (not shown here).

Note that the results presented in this section do not allow to determine the sensitivity of d_{min} to individual changes in % $H_{2,\text{blend}}$, and Φ_{mix}, since leaving the burner operating parameters constant, both variables change simultaneously; subsection 3.2 addresses this issue.

3.2 *Effect of Φ_{mix} and % $H_{2,blend}$ on d_{min}*

Figure 7 (a)-(d) present the detonation velocity - tube diameter, $D-d$, curves for increasing values of equivalence ratio of the mixture, Φ_{mix}, –from stoichiometric to rich– and different levels of H_2 addition to the fuel blend, % $H_{2,\text{blend}}$. For all Φ_{mix} analyzed, the detonation velocity dependence on decreasing % $H_{2,\text{blend}}$ at the critical point is non-linear. The detonation velocity evaluated at the minimum diameter, $D(d_{\text{min}})$, is highest for % $H_{2,\text{blend}} = 100$ ($D(d_{\text{min}}) = 1881$ m/s for $\Phi_{\text{mix}} = 1$) and lowest for % $H_{2,\text{blend}} = 20$ ($D(d_{\text{min}}) = 1667$ m/s for $\Phi_{\text{mix}} = 1$). It recovers higher values at % $H_{2,\text{blend}} = 0$ ($D(d_{\text{min}}) = 1722$ m/s for $\Phi_{\text{mix}} = 1$). The behavior just described seems to be less pronounced for richest mixture considered, i.e., $\Phi_{\text{mix}} = 1.68$.

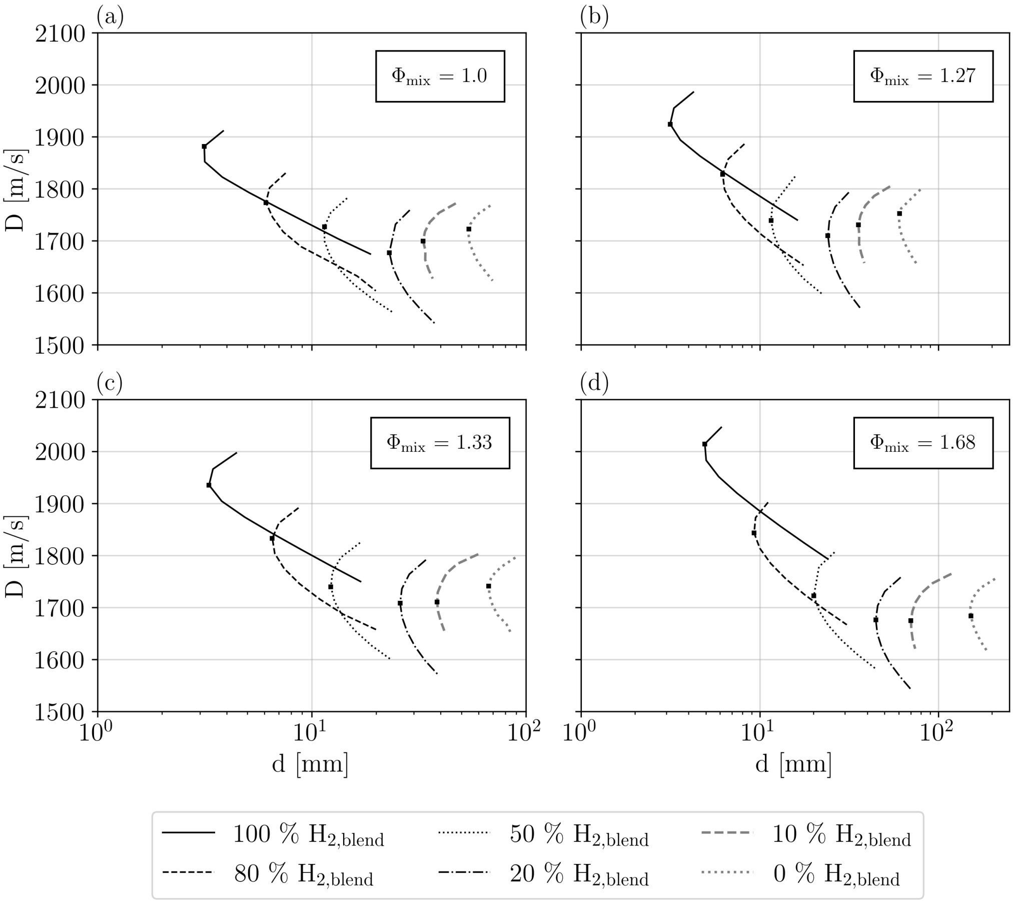

Fig. 7: *D - d curves for (a) Φ_{mix} = 1.0, (b) Φ_{mix} = 1.27, (c) Φ_{mix} = 1.33, and (d) Φ_{mix} = 1.68.*

Figure 8 summarizes the d_{min} values for the conditions evaluated. For all Φ_{mix}, a decrease in d_{min} is obtained as % $H_{2,\text{blend}}$ increases. d_{min} shows a modest dependence on equivalence ratio for $1.0 \leq \Phi_{\text{mix}} \leq 1.33$ and decreases as $\Phi_{\text{mix}} \to 1.0$. Also, the effect of Φ_{mix} on d_{min} is less pronounced for increasing $\%H_{2,\text{blend}}$.

Finally, to relate our results with the cellular structure of detonations, an empirical figure of merit for detonation limits in tubes can be used in which the arc length, πd_{min}, is compared with experimental cell sizes, λ. Since there seems to be no data available for CH_4/H_2 blends at the stoichiometry and initial pressure considered, the comparison is carried out for stoichiometric H_2-air ($\lambda = 8.18$ mm (Ciccarelli et al., 1994)) and CH_4-air ($\lambda = 349.53$ mm (Beeson et al., 1991)). πd_{min} for the former mixture is 9.17 mm ($\lambda/\pi d_{\text{min}} = 0.89$) whereas for the latter is 167.60 mm ($\lambda/\pi d_{\text{min}} = 2.08$). These ratios suggest that the model predictions provide reasonable values, taking into account that the cellular structures of the fuel-air mixtures are irregular, and the measured cell sizes can easily vary by a factor of two among different groups (Kaneshige and Shepherd, 1997).

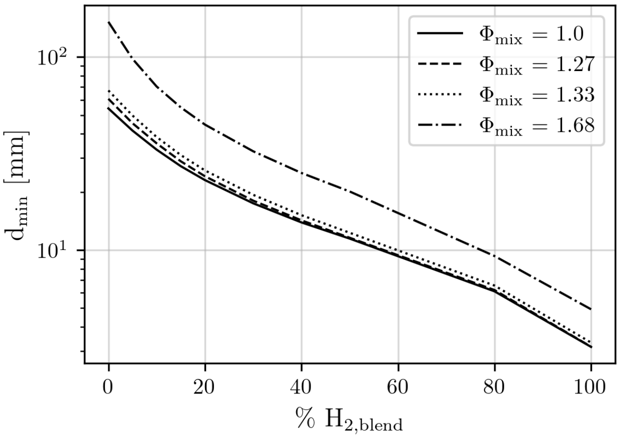

***Fig. 8**: Summary of d_{min} for different Φ_{mix} values for different CH_4/H_2 blendings.*

4 Conclusions

The minimum diameters, d_{min}, for different CH_4/H_2 fuel blends in air were determined using a one-dimensional model including friction and heat losses. Operating conditions relevant to a conventional NG burner were considered. The main learnings are:

- Keeping the operating parameters of a NG burner (i.e., injection pressure, discharge coefficient, injector diameter, and primary air regulator opening) constant: (i) the equivalence ratio of the mixture, Φ_{mix}, in the mixing tube decreases with increasing % $H_{2,\mathrm{blend}}$, going from 1.68 for 0 % $H_{2,\mathrm{blend}}$ to 1.27 for 88 % $H_{2,\mathrm{blend}}$, at which point, Φ_{mix} increases to 1.33 for 100 % $H_{2,\mathrm{blend}}$. All these mixtures lie below the UFL posing a potential ignition and flame propagation hazard inside the mixing tube that can potentially result in a detonation. (ii) For blends with % $H_{2,\mathrm{blend}} > 45$, the mixing tube diameter, d_{mixer}, is greater than d_{min}. This suggests that NG cooktops burners may need to be redesigned to work with CH_4/H_2 blends with high H_2 content. This has strong implications in achieving the final goal of a full transition to H_2 as all appliances in the residential/industrial sector may need to be replaced or retrofitted. Strong government-backed programs will need to be put in place.
- As the $H_{2,\mathrm{blend}}$ concentration increases, a considerable decrease in d_{min} for all Φ_{mix} evaluated was observed. Smaller mixing tubes are thus required to avoid potential ignition, flame propagation and detonation hazards when replacing NG with CH_4/H_2 blends.
- As $\Phi_{\mathrm{mix}} \to 1.0$, d_{min} decreases for all the CH_4/H_2 blends evaluated. As the % $H_{2,\mathrm{blend}}$ content increases, the effect of Φ_{mix} on d_{min} is weaker.

Future work will investigate the influence of the actual composition of NG (C_2H_6, C_3H_8, C_4H_{10}, N_2, CO_2, etc) on the minimum tube diamters predicted by our model.

Acknowledgements

The authors gratefully acknowledge the financial support from *l'Agence Nationale de la Recherche* Program JCJC (FASTD ANR-20-CE05-0011-01).

References

Agafonov, G., Frolov, S. (1994). *Computation of the detonation limits in gaseous hydrogen-containing mixtures*. Combustion, Explosion and Shock Waves, 30(1):91–100.

Beeson, H., McClenagan, R., Bishop, C., Benz, F., Pitz, W., Westbrook, C., Lee, J. (1991). *Detonability of hydrocarbon fuels in air*. Prog. Astronaut. Aeronaut, 133:19–36.

Chaelek, A., Grare, U. M., Jugjai, S. (2019). *Self-aspirating/air-preheating porous medium gas burner*. Applied Thermal Engineering, 153:181–189. ISSN 1359-4311. doi:https://doi.org/10.

1016/j.applthermaleng.2019.02.109.

Ciccarelli, G., Ginsberg, T., Boccio, J., Economos, C., Sato, K., Kinoshita, M. (1994). *Detonation cell size measurements and predictions in hydrogen-air-steam mixtures at elevated temperatures*. Combustion and Flame, 99(2):212–220. ISSN 0010-2180. doi:https://doi.org/10.1016/0010-2180(94)90124-4. 25th Symposium (International) on Combustion Papers.

Faghih, M., Gou, X., Chen, Z. (2016). *The explosion characteristics of methane, hydrogen and their mixtures: A computational study*. Journal of Loss Prevention in the Process Industries, 40:131–138. ISSN 0950-4230. doi:https://doi.org/10.1016/j.jlp.2015.12.015.

Gao, Y., Ng, H. D., Lee, J. H. (2014). *Minimum tube diameters for steady propagation of gaseous detonations*. Shock Waves, 24(4):447–454.

Kaneshige, M., Shepherd, J. (1997). *Detonation database*.

Kitano, S., Fukao, M., Susa, A., Tsuboi, N., Hayashi, A., Koshi, M. (2009). *Spinning detonation and velocity deficit in small diameter tubes*. Proceedings of the combustion institute, 32(2):2355–2362.

Kong, M., Feng, S., Xia, Q., Chen, C., Pan, Z., Gao, Z. (2021). *Investigation of mixing behavior of hydrogen blended to natural gas in gas network*. Sustainability, 13(8). ISSN 2071-1050. doi:10.3390/su13084255.

L'Chatelier (1891). *Estimation of firedamp by flammability limits*. Mines, 19:388–395.

Mashuga, C., Crowl, D. (2004). *Derivation of le chatelier's mixing rule for flammable limits*. Process Safety Progress, 19:112 – 117. doi:10.1002/prs.680190212.

North American Manufacturing Company, C., Reed, R., Schilster, R., Kobayashi, H. (1997). *North American combustion handbook: a practical basic reference on the art and science of industrial heating with gaseous and liquid fuels. Combustion equipment, controls, systems, heat recovery, process control optimization, pollution reduction, noise minimization, oxygen enrichment and oxy-fuel firing*. Number v. 2 in North American Combustion Handbook Vol. 2. North American Mfg. Company. ISBN 9780960159635.

Pang, L., Gao, Y. (2015). *Detonation limits in binary fuel blends of methane/hydrogen mixtures*. Fuel, 168:27–33. doi:10.1016/j.fuel.2015.11.073.

Pusch, W., Wagner, H.-G. (1962). *Investigation of the dependence of the limits of detonatability on tube diameter*. Combustion and Flame, 6:157–162. ISSN 0010-2180. doi:https://doi.org/10.1016/0010-2180(62)90085-8.

Sayad, P., Schönborn, A., Li, M., Klingmann, J. (2014). *Visualization of Different Flashback Mechanisms for H2/CH4 Mixtures in a Variable-Swirl Burner*. Journal of Engineering for Gas Turbines and Power, 137(3). ISSN 0742-4795. doi:10.1115/1.4028436. 031507.

Smith, G. P., Golden, D. M., Frenklach, M., Moriarty, N. W., Eiteneer, B., Goldenberg, M., Bowman, C. T., Hanson, R. K., Song, S., Gardiner, W. C., Lissianski, J. V. V., Qin, Z. (1994). *Gri-mech 3.0*.

Staffell, I., Scamman, D., Velazquez Abad, A., Balcombe, P., Dodds, P. E., Ekins, P., Shah, N., Ward, K. R. (2019). *The role of hydrogen and fuel cells in the global energy system*. Energy Environ. Sci., 12:463–491. doi:10.1039/C8EE01157E.

Tsuboi, N., Morii, Y., Hayashi, A. K. (2013). *Two-dimensional numerical simulation on galloping detonation in a narrow channel*. Proceedings of the Combustion Institute, 34(2):1999–2007.

Veiga-López, F., Faria, L. M., Melguizo-Gavilanes, J. (2022). *Influence of chemistry on the steady solutions of hydrogen gaseous detonations with friction losses*. Combustion and Flame, 240:112050. ISSN 0010-2180. doi:https://doi.org/10.1016/j.combustflame.2022.112050.

Witkowski, A., Rusin, A., Majkut, M., Stolecka, K. (2018). *Analysis of compression and transport of the methane/hydrogen mixture in existing natural gas pipelines*. International Journal of Pressure Vessels and Piping, 166:24–34. ISSN 0308-0161. doi:https://doi.org/10.1016/j.ijpvp.2018.08.002.

Wojtowicz, R. (2019). *An analysis of the effects of hydrogen addition to natural gas on the work of gas appliances*. Nafta-Gaz, 75(8):465–472.

Zhang, B., Pang, L., Shen, X., Gao, Y. (2016). *Measurement and prediction of detonation cell size in binary fuel blends of methane/hydrogen mixtures*. Fuel, 172:196–199. ISSN 0016-2361. doi:

https://doi.org/10.1016/j.fuel.2016.01.034.

Zhao, Y., McDonell, V., Samuelsen, S. (2019a). *Experimental assessment of the combustion performance of an oven burner operated on pipeline natural gas mixed with hydrogen*. International Journal of Hydrogen Energy, 44(47):26049–26062. ISSN 0360-3199. doi:https://doi.org/10.1016/j.ijhydene.2019.08.011.

Zhao, Y., McDonell, V., Samuelsen, S. (2019b). *Influence of hydrogen addition to pipeline natural gas on the combustion performance of a cooktop burner*. International Journal of Hydrogen Energy, 44(23):12239–12253. ISSN 0360-3199. doi:https://doi.org/10.1016/j.ijhydene.2019.03.100.

5 Appendix A

Figure 9 (a), (b) and (c) show a comparison between numerical and experimental data available in the literature for CH_4-O_2, H_2-O_2, and H_2-air mixtures, respectively; the ratio $d_{\text{min,num}}/d_{\text{min,exp}}$ is also presented.

For CH_4-O_2, good predictions are obtained in the range $0.33 < \Phi < 1.2$, whereas considerable deviations are present for $\Phi > 1.2$. Note that the experimental data for this mixture is quite dated (Pusch and Wagner, 1962), and the authors did not report error bars with their results.

For H_2-O_2, the agreement between experiments and model predictions is good in the range $0.15 < \Phi < 3.6$. Leaner mixtures ($0.1 < \Phi < 0.15$) exhibit large deviations. Note that $\Phi = 0.1$ is very close to the lower flammability limit of H_2-O_2.

For H_2-air, all data points within the range $0.8 < \Phi < 2.5$ show $d_{\text{min,num}}/d_{\text{min,exp}}$ ratios close to unity, but deviations exist for ultra-lean mixtures. Analogous to the experimental data for CH_4-O_2, the experiments reported by Agafonov and Frolov in 1994 do not include error bars.

The over predictions for H_2-O_2/air at ultra-lean conditions are somewhat not surprising since detailed kinetic models tend to be less reliable in these regions.

The validation exercise performed shows that the 1-D model is in agreement with experimental data as $\Phi \to 1.0$, which is the most stringent condition for detonation limits as shown in Figure 8 of the manuscript; this data point could thus serve as a target for future design of cooktop burners. While the model seems to provide acceptable results for safety engineering purposes, further validation against binary fuel mixtures (CH_4/H_2) is required when new experimental data becomes available.

DOI: 10.7795/810.20221124

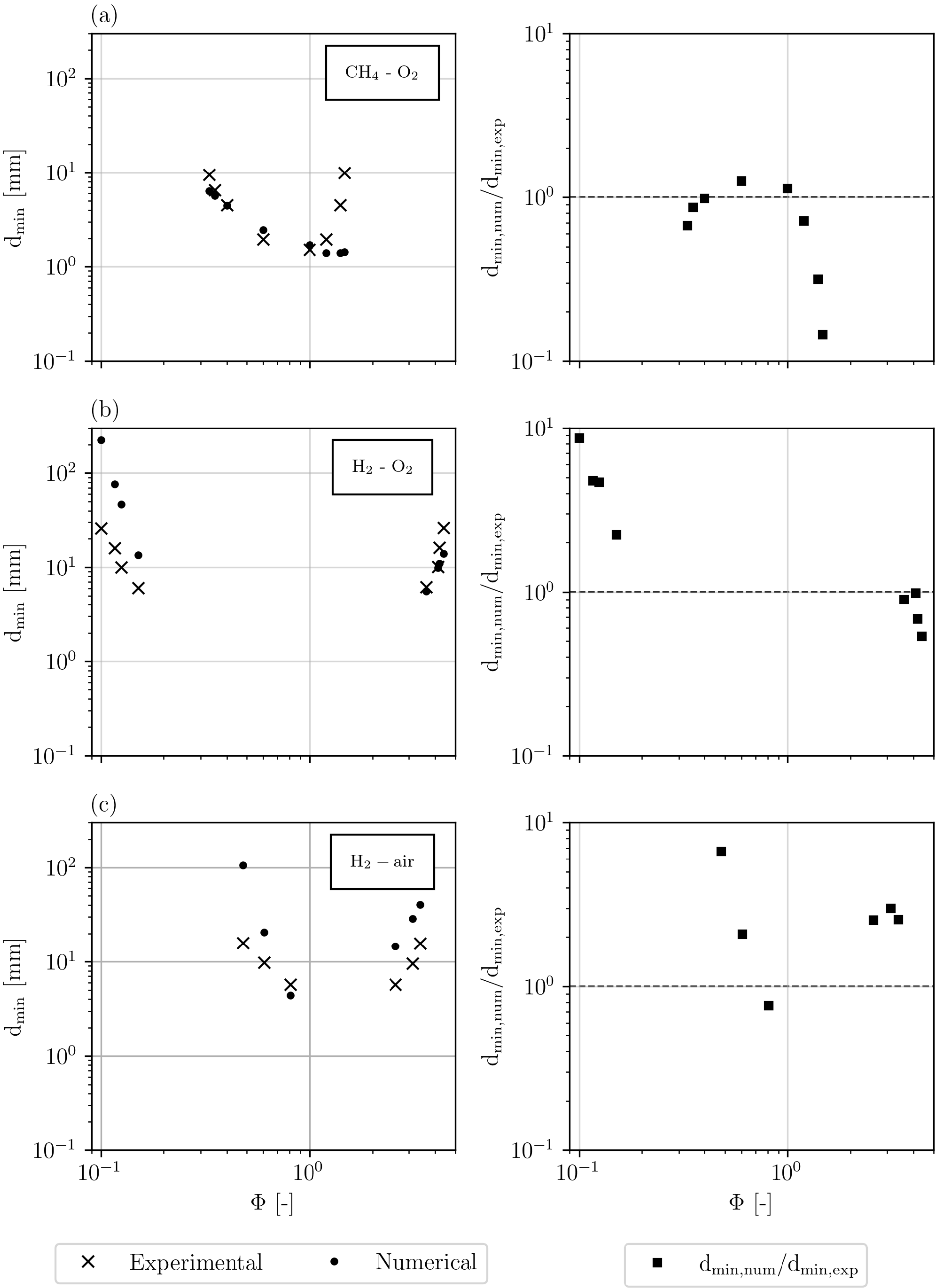

***Fig. 9**: Comparison between numerical and experimental results for the mixtures (a) CH_4-O_2 (Pusch and Wagner, 1962) (for $\Phi = 1.0$ Gao et al. (2014)), (b) H_2-O_2 (Agafonov and Frolov, 1994) and (c) H_2-air (Agafonov and Frolov, 1994).*

DOI: 10.7795/810.20221124

Experimental study of humidity influence on triboelectric charging of particle-laden duct flows

Wenchao Xu, Holger Grosshans

Physikalisch-Technische Bundesanstalt (PTB), Braunschweig, Germany
E-mail: *wenchao.xu@ptb.de*

Abstract

Electrostatic charge on powders arises during pneumatic transport due to particle-particle and particle-surface interactions via triboelectrification. This is a potential threat to the safety of industrial productions and the source of numerous fires and dust explosions in the past. Triboelectric charges are affected by environmental conditions, such as ambient temperature and relative humidity. In this work, we experimentally investigated the influence of ambient humidity on the particle charge of gas-solid flows in a square-shaped duct. Monodisperse PMMA particles are fed into a fully developed airflow in a PMMA duct and then pass through a metallic duct section. The charge of particles is measured at the outlet of the metallic duct via a Faraday cup. By measuring the electrostatic charge under various environmental conditions, we observed that the electrostatic charge first increases with the humidity and then decreases when the humidity becomes higher.

Keywords: *electrostatics, particle charge, triboelectricity, particle-laden flow*

1 Introduction

Dust explosion is one of the most serious and widespread explosion hazards in the processing industry. In an industrial production involving pneumatic conveyance of powders, electrostatics require to be paid particular attention (Abbasi & Abbasi, 2007). In the past, electrostatics has caused numerous fires and dust explosions (Eckhoff, 2003).

During pneumatic transport, powders undergo undesired charging via triboelectrification due to particle-particle and particle-surface interactions. The charge can accumulate on non-conductive materials. When such an insulator with a high concentration of charge moves close to a blunt grounded conductor, a "brush discharge" can happen and ignite dust clouds (Larsen et al., 2001). The charged particles can also agglomerate and deposit at the inner surface of pipelines or ducts due to particle-wall adhesion. These dust deposits can result in the plugging of conveyors and lead to a frequent cleaning of the system (Sippola et al., 2018). Moreover, the dust deposits can accumulate heat, develop high temperatures in a spot and even cause internal smouldering fires, which serve as another ignition source for dust explosions (Eckhoff, 2003).

Although the debate on the mechanism of triboelectrification is still ongoing (Lacks & Shinbrot, 2019), it is widely acknowledged that the triboelectric effect is an extremely sensitive phenomenon and differs from numerous conditions, including the material properties, methods by which the materials come into contact, temperature and humidity of the surrounding environment, and other properties.

The influence of environmental conditions on triboelectric charging of polymers, i.e. ambient temperature and humidity, has been reported in many publications. Kolehmainen et al. (2017) investigated the triboelectric charge of polyethylene (PE) particles in a glass container subjected to vertical vibration at different humidity levels. Applying the effective work function theory, they established a model predicting the effective work function difference regarding the humidity and showed the charge in the vibrating vessel, as well as fluidized bed, decreases non-linearly when the relative humidity increases. Jantač et al. (2019) reported that saturation charge of PE particles reduces with increasing air humidity in a shaking apparatus for a relative humidity ranging from 46% to 67% at 22 °C. Although electron pair interaction is widely acknowledged as the fundamental mechanism of triboelectric charging of polymers, Németh et al. (2003) proposed that the water adsorption of polymer particles influences the charging mechanism by introducing an additional ion conductivity into the process. Recent research reveals that the ambient humidity can even change the polarity of the tribocharge of non-polar polymers (PC and PVC) after rubbing with Aluminum samples (Tilmatine et al., 2022).

With the increase of humidity, the saturation charge of a particle can rapidly drop off after reaching a certain level of humidity. The experimental study by Cruise et al. (2022) shows that the cut-off humidity level is dependent on particle size. Smaller particles are more sensitive to humidity and begin to discharge at a lower humidity level than larger particles.

Despite the plentiful studies related to the influence of ambient humidity on triboelectric charging, most of them focus on the saturation charge under various humidity. The particles in this case are charged to saturation via sufficient frictions or collisions. However, the conclusions from these studies can not be directly applied to the scenario, in which particles are charged via a limited number of impacts instead of adequate collisions.

In this paper, we present an experimental study of the influence of humidity on triboelectric charging of particles in gas-solid flows in a short square-shaped duct. In this pneumatic conveying setup, the particle samples are charged by a limited number of collisions.

2 Experimental setup

2.1 Pneumatic conveying test bench

Figure 1a illustrates a schematic sketch of the experiment facility. The present configuration consists of an air blower, a powder feeder, a square test duct, and a Faraday cage. The air blower (Moro MHR 452) is placed at the inlet of the test duct to generate the conveying airflow. The blower is equipped with a frequency converter (Danfoss FC 51) to control the rotation speed of the blower, as well as the airflow velocity. A Pitot tube anemometer is installed along the channel center upstream of the particle inlet to measure the stream-wise air velocity.

The test duct includes two sections with the same inner side length of 45 mm×45 mm but different materials. The upstream section is made of polymethyl methacrylate (PMMA) and has a length of 1.8 m, whereas the downstream section is made of S195T steel section with a length of 0.5 m. Particles are fed into the duct in the PMMA section at the feeding position noted in fig. 1a with a distance of 0.3 m from the airflow inlet. In addition, a steel cylindrical obstacle with a diameter of 17 mm is placed at the middle of the entrance of the metallic section (see fig. 1b). The obstacle functions as a generic representation of components that are frequently built in pneumatic conveying systems, such as sensors, screws, or other pipes. The obstacle together with the metallic duct is grounded so that the electric potential of the metal surface remains constant.

2.2 Measurement equipment

To measure the charge of the particles, a 50 µm pore size filter bag is attached at the end of the duct and meanwhile covered by a Faraday cup (Monroe Electronics 284/22A). The Faraday cup is connected to a charge amplifier (PCB 44302). Particles are separated from the airflow by the filter and their

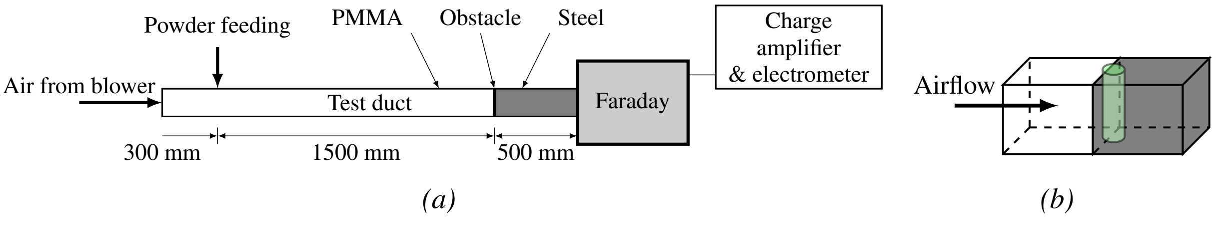

(a) (b)

Fig. 1: (a) Schematic sketch of the pneumatic conveying system (Grosshans et al., 2022). The Faraday measures the charge of the powder collected by a filter at the outlet of the metallic duct. (b) The green cylinder in the enlarged sketch shows the position of the obstacle in the metallic section.

charge is measured by the charge amplifier with a systematic error of 2%. It is worth mentioning that the charge of the electrical circuit leaks consistently. During the experiment, the time-scale of the charging measurement was set to be significantly smaller than the charge leakage time-scale of the electrical circuit, so that the error due to circuit leakage was negligible.

To reduce the error introduced by the leakage, the time-scale of the charging measurement is required to be significantly smaller than the charge leakage time-scale of the electrical circuit.

The temperature and relative humidity are measured by a high accuracy temperature and humidity sensor (Lascar EL-WiFi-TH+) with a tolerance of $\pm 0.2\,^{\circ}\mathrm{C}$ for temperature and 0.1% for relative humidity.

2.3 Experimental procedure

In the experiment, the airflow velocity is regulated to 13 m/s. Due to the character of the blower, the velocity fluctuates persistently with ± 0.15 m/s during the experiment. This velocity is measured by the Pitot tube anemometer at the centre-line, which corresponds to the maximum velocity in the cross-section of the airflow. The mean flow velocity, i.e. the mean conveying velocity, can be estimated by multiplying a coefficient of 0.8 (Susanti & Grosshans, 2020).

After the airflow is stabilized, particle samples are fed into the duct. In this study, we use monodisperse spherical PMMA particles from EPRUI Biotech with a diameter of 100 µm. The particles have a material density of 1.15 $\mathrm{g/cm^3}$ and a bulk density of 0.8 $\mathrm{g/cm^3}$. To avoid measurement error due to charge leakage and meanwhile not exceed the measurement range of the charge amplifier, we inject 0.5 g – 1.5 g particles into the PMMA duct within less than 10 s in each measurement.

Considering the short duration of each measurement, the feeding of particles is accomplished manually with a syringe instead of a vibrating feeder. Before and after each injection, the weight of the syringe is measured by a precise scale (Kern PCB 3500-2) with 0.01 g accuracy and the differential of the two measurements returns the weight of the fed powder. After a set of measurements, the particles collected by the filter are weighted to verify the measurement during each injection. Because the conveying system uses a positive pressure configuration, part of the particles might be blown away during the feeding process. The fine particles may also agglomerate on the inner wall of the duct. In our experiment, the ratio between the collected mass and the fed mass is higher than 95%, i.e., the mass loss during the feeding and the pneumatic conveying is less than 5%. Because the majority of the mass loss occurs during the feeding process due to the positive pressure in the conveying system, the influence of the mass loss on the charge measurement should be small.

3 Experimental repeatability

Being an extremely sensitive process, triboelectric charging is influenced by various conditions and parameters. To ensure the repeatability of the experiment, the whole process needs to be precisely controlled. In this section, we discuss the parameters we suspect to affect the repeatability of the charge measurement the most, namely the conveying velocity, powder mass flow rate, and the state of the duct's surface.

3.1 Conveying velocity

The impact velocity of particles on the conveying system, which increases with the conveying velocity, affects the electrostatic charging. This parameter is strongly correlated to the practical production process, since a high conveying speed during pneumatically transporting powdery materials is usually preferred to avoid deposition and stagnation of powders.

Figure 2 depicts the effect of conveying velocity on particle charge under the same environmental condition. For an air velocity of 15 m/s, the particles obviously receive more charge than the lower velocity of 13 m/s. This result is consistent with the experiments reported by Matsusaka et al. (2000) and Watanabe et al. (2006). Higher conveying velocity contributes to an increase of the normal com-

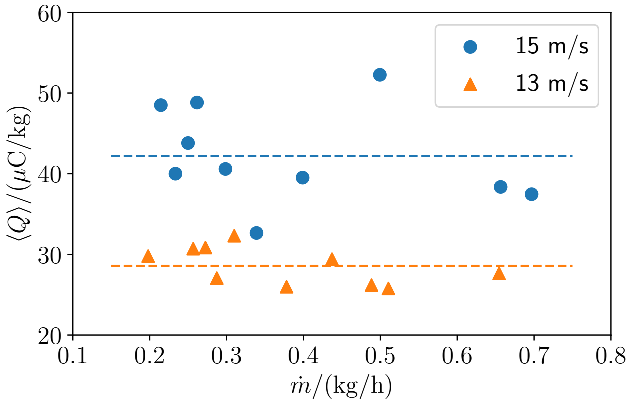

***Fig. 2**: Particle charge with different airflow velocities at the same ambient condition (RH* $= 54\%$*, T* $= 16.3$ *°C). The dashed line represents the average charge at each velocity.*

ponent of the impact velocity, which, according to Hertz theory, proportionally increases the maximal contact area of an elastically deformed particle impacting against a plane (Watanabe et al., 2006). Consequently, it increases the contact area between the particle and the and promotes triboelectrification.

Therefore, to receive repeatable results, the conveying velocity should remain constant during all the measurements.

3.2 Powder mass flow rate

To ensure a small feeding quantity and a short feeding duration in each measurement, we injected the powders into the duct manually using an syringe. In this case,the mass flow rate can not be precisely controlled and inevitably varies upon each attempt. Our previous study reported that the mass flow rate affects the powder charging in the particle-laden airflow (Grosshans et al., 2022). According to the numerical simulations presented by Grosshans et al. (2022), the wall-normal velocity of particles is faster for a higher mass flow rate in the dilute particle-laden flow. As a consequence, triboelectric charging is also promoted, which is analogous to the procedure of increasing conveying velocity. Moreover, when the mass flow rate further increases, a high concentration of charged particles can give rise to the surrounding electric field, and, according to the charge relaxation theory (Matsuyama & Yamamoto, 1995), reduce the charge a particle can hold.

In the experiment, to reduce the influence of varying mass flow rate, we repeated multiple times measurements for each experiment and meanwhile tried to cover a wide range of mass flow rates.

3.3 State of the duct's surface

We suspect the state of the conveying duct's surface, cleanliness and charge spots, to have a major impact on the experimental repeatability.

Fine particles can adhere or deposit on the inner wall of the pneumatic conveying system. With the presence of electrostatic force, particles adhere stronger (Hays, 1995). The adherence on the surface not only increases the energy loss during pneumatic transport by increasing surface friction, but also influences the triboelectric charge.

In our experiment, we occasionally observed significant drops of particle charge during successive measurements, see blue dots in fig. 3a. After properly cleaning the duct with ethanol and drying the test rig, the measured specific charge is recovered temporally and then continues decreasing (orange triangles in fig. 3a). Nevertheless, such a dramatic decrease of the charge seldom occurred in the experiment compared to the "normal" experiment (see fig. 3b), in which the measured charging is not correlated with the cumulative number of measurements.

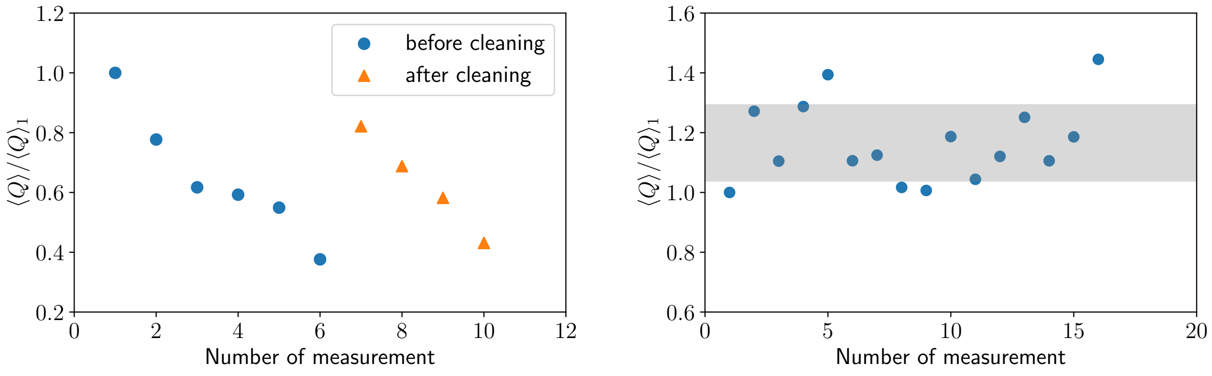

(a) *(b)*

Fig. 3: *Particle charge as a function of the measurement sequence. The charge of each measurement $\langle Q\rangle_i$ is normalized by the first measurement $\langle Q\rangle_1$. The gray area in (b) marks the measurements within one standard deviation of the mean charge.*

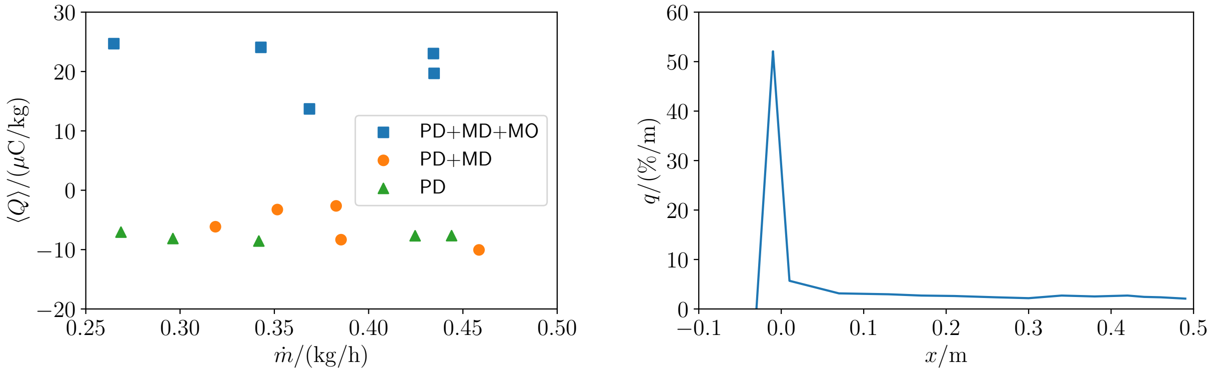

(a) *(b)*

Fig. 4: *(a) Particle charging with different setups. Squares: normal setup with PMMA duct (PD), metallic duct (MD), and metallic obstacle (MO); circles: test duct with PMMA duct and metallic duct (no obstacle); triangles: test duct only with the PMMA section. (b) Charge generation per meter as a fraction of the total powder charge along the streamwise direction with mass flow rate 0.091 kg/h and centre-line velocity 14.7 m/s from numerical simulation.*

To avoid the influence of surface contamination and deposition, the duct was cleaned with ethanol regularly. The experimental data, when such a phenomenon occurred, were regarded as invalid data and excluded from subsequent discussions.

4 Charging distribution in the conveying duct

In the reported configuration, particles are released upstream in the PMMA duct section, so that the particle-laden airflow is fully developed before entering the metallic section. The volumetric flow rate of the particles (10^{-1} cm^3/s) is much smaller than of the air (10^5 cm^3/s). In such a dilute phase gas–solid duct flow, the effect of particle–particle interactions on particle charging is negligible. Each particle can freely collide with the inner wall without hindering from surrounding particles. Although the study focuses on triboelectrics in the metallic section, charging in the PMMA duct is worth to be noticed.

Figure 4a shows the charge-to-mass ratio of particles, $\langle Q\rangle$, measured under different configurations with the same parameter. The blue squares represent the standard configuration, the orange dots correspond to the setup without the metallic obstacle at the entrance of the metallic duct, and the green triangles are the setup in which the metallic components, including the obstacle and the metallic duct, are completely removed. it is noticed that the charging differences between the orange dots and green triangles are very small, which indicates the triboelectrical charging between particles and the metallic duct is very weak. The blue squares, on the other hand, denote a much higher level of triboelectrical charging for the setup with the metallic obstacle compared to the setups without the obstacle. Obviously, the metallic obstacle plays an essential role in the triboelectrical process.

This result is consistent with our numerical simulations. Figure 4b shows the percentage of particle charges in the powder flow along the streamwise direction from simulations using our open-source CFD tool pafiX (Grosshans, 2022). Pafix uses an Eulerian–Lagrangian approach, in which the fluid and the particles are solved respectively in Eulerian and Lagrangian framework. The triboelectrification is calculated with an empirical charging model, which approximates the impact charge of a particle in the simulation directly from similar impacts measured in a single-particle experiment (Grosshans et al., 2022). A detailed description of the mathematical model and numerical methods implemented in pafiX was given by Grosshans et al. (2021). According to fig. 4b, more than half of the triboelectric charging occurs at contacts between the particles and the cylindrical obstacle.

This can be attributed to the following two reasons. First, due to the short length of the metallic duct (0.5 m), the particle-wall contacts in the metallic section occur less frequently on the inner wall of the duct than on the cylindrical obstacle. Second, the wall-normal velocity of particles is much higher when colliding with the cylinder compared with contacting the walls parallel to the stream direction.

Moreover, we observed that the PMMA particles are charged negatively in measurements without the cylindrical obstacle, see fig. 4a, which suggests the PMMA particles acquire electrons when colliding with a wall made by the same material. This phenomenon is analog to the scenario where particles of different sizes and the same insulating material contact with each other. Large particles usually tend to charge positively whereas small particles charge negatively (Waitukaitis et al., 2014). The PMMA particles can be regarded as "small particles" when colliding on the PMMA duct, therefore they get a negative charge after contact.

5 Influence of humidity

The laboratory for the experiment is not climate-controlled so that the room temperature is affected by the day-to-day weather variation. To study the influence of humidity on particle charge, we carefully recorded the temperature (T) and relative humidity (RH) variations in the lab and performed experiments under different weather conditions. Due to the slow variation of the room temperature and the short duration of each experiment (around 30 min), change of the ambient condition during an experiment can be neglected and the temperatures of the test rig and the room are considered identical. Thus, we were able to measure the influence of the air properties on the particle charge for a range of RH = 50% − 74.4% and T = 10.3 °C − 20 °C. The temperature and relative humidity during the experiments are plotted in fig. 6a. To exclude the influence of the fluctuating room temperature on the moisture content in the ambiance, we introduce the absolute humidity (AH), which is obtained from the following empirical equation (Ogino et al., 2019):

$$AH = \frac{217}{T+273.15} \times 6.1078 \times \exp\left(\frac{17.2694T}{T+237.3}\right) \times \frac{RH}{100} \tag{1}$$

where T is the room temperature in °C and RH is in %. The obtained AH is in the unit of $\mathrm{g/m^3}$. As shown in fig. 5b, the experiments are performed in an absolute humidity range of 4.97 $\mathrm{g/m^3}$ - 8.98 $\mathrm{g/m^3}$.

The experimental results are presented in fig. 6, which depicts charge-to-mass ratio against relative humidity and absolute humidity. In the diagram, each point represents one measurement by feeding a certain portion of particles in the duct flow. The feeding mass is not constant but varies with each attempt. The dots at the same humidity correspond to repeated measurements for each environmental condition.

In fig. 6, the charge-to-mass ratio is solely described by relative humidity and shows to be increasing monotonically with the rising relative humidity. However, given the varying room temperature, the

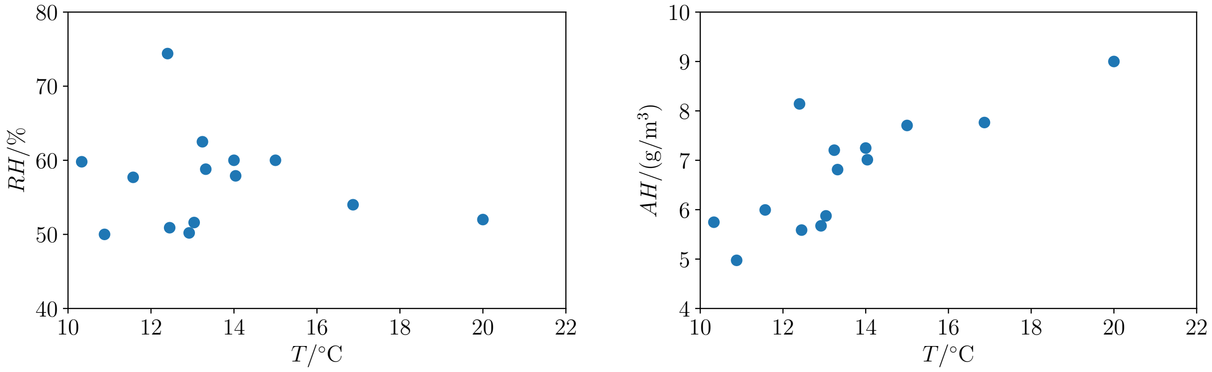

(a) *(b)*

***Fig. 5**: (a) Distribution of temperature and relative humidity of the experiment attempts; (b) distribution of temperature and absolute humidity of the experiment attempts.*

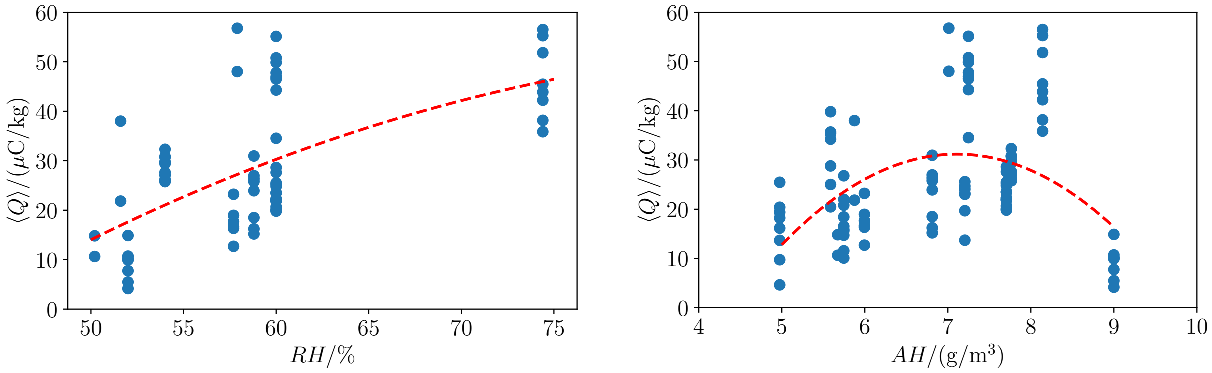

(a) *(b)*

***Fig. 6**: Charge-to-mass ratio as a function of (a) relative humidity and (b) absolute humidity. Each dot represents one measurement attempt. The red dashed curve represents a second order least squares polynomial fit.*

same relative humidity by different room temperatures does not represent the same moisture content in the ambient circumstance. Therefore, applying the relative humidity exclusively is not sufficient to compare the influence of the ambient moisture.

Figure 6b shows the charge-to-mass ratio as a function of absolute humidity, which is a measure of the actual amount of moisture in the air regardless of the air's temperature. As indicated with the polynomial fit curve, the charge-to-mass ratio first increases and then decreases with increasing absolute humidity. At first glance, the result seems to exhibit a trend inconsistent with the prevalent theory, that increased humidity reduces the saturation charge of polymer particles and increases the decay of electrostatic charge. However, the scenario in our experiment is different from the typical experiments with shakers or fluidized beds. Particles in the test duct acquire only a limited number of contacts or collides with other particles/surfaces. Therefore, the particles passing through the test rig might not be sufficiently charged and the measured charge must not be equal to the saturation charge.

Németh et al. (2003) proposed a theory of the function of water molecules on tribocharges, that the charge transfer is dominated by electrons at low humidity, whereas adhered water and ions in water promote triboelectric charging with increased humidity. This theory well explains the relationship between the specific charge and the humidity. Electron transfer is the fundamental process of polymer charging. At lower humidity, the tribocharging is marginally influenced by water molecules in the ambient. With increased humidity, the water can swell the surface of the polymer or form absorption layers onto polymer surfaces. Due to the auto-dissociation of water and the solvation of impurities on

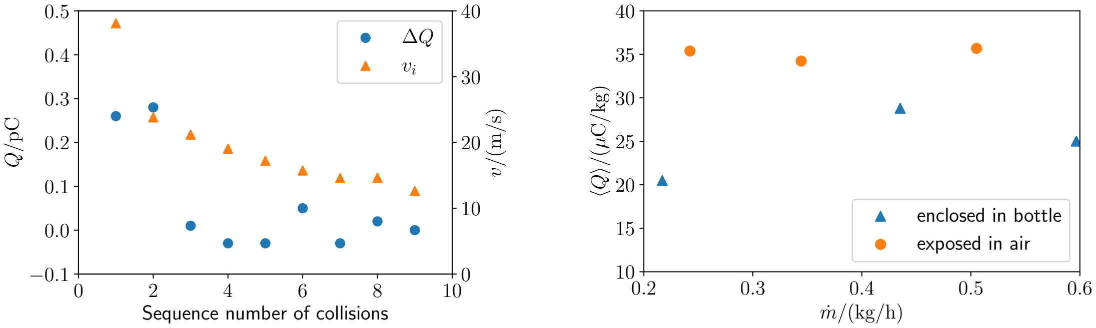

(a) *(b)*

***Fig. 7**: (a)Charge and velocity of a 200 µm PMMA particle in a single particle experiment (adapted from Grosshans et al. (2022)). (b)Charge-to-mass ratio of particles stored in different conditions. Blue triangles: particles stored in a hermetical container; yellow dots: particles exposed to air for 24 hours. ($RH = 50.9\%$, $T = 12.5$ °C).*

the particle surface during production, this formed water-containing layer introduces ionic species into the charging process. The ions can decrease the surface conductivity and intensify the triboelectric charging.

The thickness of the water-absorption layer is correlated to the amount of available water in the surrounding air. When the humidity further increases, the layers get thicker, thus, decrease the upper limit of the surface charge reduces and impedes the particles from obtaining more charge. Therefore the specific charge drops at $AH = 9\ \mathrm{g/m^3}$.

Moreover, PMMA is sensitive to the moisture in the surrounding atmosphere due to its good ability in absorbing water (Németh et al., 2003). Therefore the PMMA particles are able to quickly form water-containing swollen layers by absorbing water molecules from the air.

According to our previous single-particle experiment (Grosshans et al., 2022), in which a 200 µm PMMA particle was shot onto two parallel metallic plates, the charging of the particles heavily relies on the first few contacts when the particle fast collides with a surface. Figure 7a displays the charge and velocity of one particle in a succession of collisions. The charge transfer during the first two collisions is much stronger than the following collisions. This behavior suggests that the particle is saturated after the second impact. Such an efficient charge transfer might be also related the water-absorption layer on the particle surface, which increases the efficiency of the triboelectrical charge during an impact.

This effect can be also elucidated using the classical condenser model. In the condenser model, the charge transferred in a sequence of impacts is $\mathrm{d}q_c/\,\mathrm{d}n = kCV$, where n is the number of impacts, k is the electrification efficiency, C is the capacitance between the contact bodies and V is the potential difference between the contact bodies (Matsusaka et al., 2010). The existence of the water layer promotes the surface charge via increasing the electrification efficiency k, therefore increases the charge during a single contact.

To further validate the influence of the moisture on tribocharging, we prepared two particle samples for a comparison experiment. Both samples applied identical 100 µm spherical PMMA particles. One sample was stored in a shallow glass tray and exposed in the air at a room temperature of 12 °C − 16 °C and relative humidity around 50% for 24 hours, while the other sample was stored in a dry sealed container.

Both of the samples were fed into the test duct with the same operating parameter and the specific charge after conveying was measured, see fig. 7b. As expected, the water-contained layer due to the long-time exposure in the air results in a higher particle charge compared to the particles stored in the closed container. Moreover, the charge of the previous sample is seemly more stable, which implies the particles stored in a moister environment are closer to saturation at the outlet of the duct.

6 Conclusion and outlook

In this work, we reported a series of experiments on triboelectric charging of PMMA particles in a pneumatic conveying duct under various temperatures and humidities. To investigate the influence of humidity at different temperatures, instead of relative we applied absolute humidity, which provides a quantitative indication of the moisture content in the atmosphere.

According to the experimental results, the particle charge first increases with the rise of the absolute humidity and then decreases when the humidity exceeds a threshold. This phenomenon can be attributed to the surface layer of PMMA particles formed by absorbed water molecules from the surrounding air. This water-containing layer increases surface conductivity, promotes triboelectric charging, and meanwhile decreases the saturation of surface charge. In the conveying system with a limited number of collisions, the particles are not sufficiently charged, therefore the existence of water-containing layers increases the triboelectric charge. However, when the humidity becomes higher, the saturation charge decreases dramatically, thus resulting in a lower charge.

Moreover, we discussed several effects that can hinder reproducing the experiments. Changing conveying velocity and mass flow rate can influence particle charging. Adhesion on the inner surfaces of the conveying duct may reduce the charge of particles. For a repeatable experiment, the conveying velocity and the mass flow rate should remain consistent through all measurements, meanwhile, the duct should be cleaned regularly for a consistent surface state. Our results also reveal that increasing conveying velocity can raise risks of dust explosion due to stronger triboelectrification, particularly when there are surfaces or obstacles on the flow path, on which the particles can collide with a high wall-normal velocity. On the other hand, from the perspective of preventing static electricity, direct wall-normal collisions should be avoided by designing a pneumatic system.

The experiment shows that in a system where the particles are not sufficiently charged, increasing the humidity can intensify triboelectric charging. However, this study has only applied 100 µm PMMA particles for the measurements. It remains an open question if particles with different sizes or a material with different abilities to take up water can change the behavior of triboelectric charging in response to varying humidity. This will be part of a future investigation.

7 Acknowledgement

This project has received funding from the European Research Council (ERC) under the European Union's Horizon 2020 research and innovation programme (grant agreement No. 947606 PowFEct).

References

Abbasi, T., Abbasi, S. (2007). *Dust explosions–Cases, causes, consequences, and control*. J. Hazard. Mater., 140(1-2):7–44.

Cruise, R. D., Hadler, K., Starr, S. O., Cilliers, J. J. (2022). *The effect of particle size and relative humidity on triboelectric charge saturation*. J. Phys. D: Appl. Phys, 55(18):185306.

Eckhoff, R. (2003). *Dust explosions in the process industries: identification, assessment and control of dust hazards*. Elsevier.

Grosshans, H. (2022). *pafix*. `https://gitlab1.ptb.de/Holger/pafix`. Accessed: 2022-02-23.

Grosshans, H., Bissinger, C., Calero, M., Papalexandris, M. V. (2021). *The effect of electrostatic charges on particle-laden duct flows*. J. Fluid Mech., 909:A21.

Grosshans, H., Xu, W., Matsuyama, T. (2022). *Simulation of PMMA powder flow electrification using a new charging model based on single-particle experiments*. Chem. Eng. Sci., 254:117623.

Hays, D. A. (1995). *Adhesion of charged particles*. J. Adhes. Sci. Technol., 9(8):1063–1073.

Jantač, S., Konopka, L., Kosek, J. (2019). *Experimental study of triboelectric charging of polyethylene powders: Effect of humidity, impact velocity and temperature*. Adv. Powder Technol., 30(1):148–155.

Kolehmainen, J., Sippola, P., Raitanen, O., Ozel, A., Boyce, C. M., Saarenrinne, P., Sundaresan, S. (2017). *Effect of humidity on triboelectric charging in a vertically vibrated granular bed: Experi-*

ments and modeling. Chem. Eng. Sci., 173:363–373.

Lacks, D. J., Shinbrot, T. (2019). *Long-standing and unresolved issues in triboelectric charging*. Nat. Rev. Chem., 3(8):465–476.

Larsen, Ø., Hagen, J. H., van Wingerden, K. (2001). *Ignition of dust clouds by brush discharges in oxygen enriched atmospheres*. J. Loss Prev. Process Ind., 14(2):111–122.

Matsusaka, S., Ghadiri, M., Masuda, H. (2000). *Electrification of an elastic sphere by repeated impacts on a metal plate*. J. Phys. D: Appl. Phys, 33(18):2311–2319.

Matsusaka, S., Maruyama, H., Matsuyama, T., Ghadiri, M. (2010). *Triboelectric charging of powders: A review*. Chem. Eng. Sci., 65(22):5781–5807.

Matsuyama, T., Yamamoto, H. (1995). *Electrification of single polymer particles by successive impacts with metal targets*. IEEE Trans. Ind. Appl., 31(6):1441–1445.

Németh, E., Albrecht, V., Schubert, G., Simon, F. (2003). *Polymer tribo-electric charging: Dependence on thermodynamic surface properties and relative humidity*. J. Electrostat., 58(1-2):3–16.

Ogino, M., Naemura, K., Sasaki, S., Minami, J., Kano, T., Ito, N., Kasai, R., Kamijyo, F., Kusumoto, N., Akimoto, K., Tanaka, K., Shinohara, K., Yokoyama, K. (2019). *Triboelectric charging of polytetrafluoroethylene antithrombotic catheters*. Int. J. Artif. Organs, 22(4):300–306.

Sippola, P., Kolehmainen, J., Ozel, A., Liu, X., Saarenrinne, P., Sundaresan, S. (2018). *Experimental and numerical study of wall layer development in a tribocharged fluidized bed*. J. Fluid Mech., 849:860–884.

Susanti, N., Grosshans, H. (2020). *Measurement of the deposit formation during pneumatic transport of pmma powder*. Adv. Powder Technol., 31(8):3597–3609.

Tilmatine, O., Zeghloul, T., Medles, K., Dascalescu, L., Fatu, A. (2022). *Effect of ambient air relative humidity on the triboelectric properties of polypropylene and polyvinyl chloride slabs*. J. Electrostat., 115:103651.

Waitukaitis, S. R., Lee, V., Pierson, J. M., Forman, S. L., Jaeger, H. M. (2014). *Size-dependent same-material tribocharging in insulating grains*. Phys. Rev. Lett, 112(21):218001.

Watanabe, H., Samimi, A., Ding, Y. L., Ghadiri, M., Matsuyama, T., Pitt, K. G. (2006). *Measurement of charge transfer due to single particle impact*. Part. Part. Syst. Char., 23(2):133–137.

DOI: 10.7795/810.20221124

Assessment of explosion risks caused by cone discharges when filling silos and containers with pellets

Martin Glor [a] & Ute Hesener [b]

[a] Swiss Process Safety Consulting GmbH, Allschwil, Switzerland
[b] Covestro Deutschland AG, Leverkusen, Germany

E-mail: martin.glor@swisspsc.ch

Abstract

It is well known that during the filling of silos and containers with bulk material, so-called cone discharges can occur because of electrostatic charges. Whether or not cone discharges occur at all depends on whether the breakdown field strength of air under atmospheric conditions of 3 MV/m is reached at the silo or container inner wall. This in turn depends on the charge to mass ratio of the bulk, the bulk resistivity, the bulk density, the relative permittivity of the bulk material, the silo or container diameter and the filling rate. If cone discharges can´t be avoided, the energy of cone discharges can be estimated according to the formula given in the relevant guidelines TRGS 727 (2016) and IEC/TS 60079-32-1 (2013). Therefore, the coarse fraction must be considered. As soon as the energy of the cone discharge is greater than or equal to the minimum ignition energy of the bulk material introduced, there is a risk of dust explosion. Here the fine fraction of the bulk material is relevant.

In the investigations described, computer models are used to calculate for which silo or container diameters and filling rates the critical field strength of 3 MV/m is or is not reached, considering the charge relaxation during pneumatic filling with bulk material. The results of the computational modelling together with operational boundary conditions serve as a decision basis whether exclusion of incendive ignition sources is an adequate safety measure or whether further explosion protection measures must be considered. Finally, a brief overview of other possible explosion protection measures is given.

Keywords: *ignition source, static electricity, cone discharges, model calculations, industrial explosions*

1. Introduction

When pneumatically filling silos and/or containers with flammable bulk materials with a high electrical bulk material resistivity, the question arises again and again in practice as to whether an ignition hazard exists because of electrostatic charges and subsequent discharges.

Provided that all parts of the conveyor systems and silos are conductive, earthed and not coated with an insulating layer, spark and propagating brush discharges in the conveyor systems and in the silos incendive for dust/air mixtures can be ruled out. In the absence of flammable gases and/or vapours (no formation of hybrid mixtures), ignition by brush discharges can also be excluded. Brush discharges can occur due to the possibly charged product. However, according to the current state of knowledge TRGS 727 (2016) and IEC/TS 60079-32-1 (2013), brush discharges are not incendive for pure dust/air mixtures in the absence of flammable gases and vapours.

This leaves so-called cone discharges on top of the bulked product in the silo as the only possible ignition source generated by electrostatic charges. The energy of cone discharges can be calculated from the relevant by the relevant formula given in directives TRGS 727 (2016) and IEC/TS 60079-

32-1 (2013). As soon as this energy is greater than or equal to the minimum ignition energy of the dust cloud, an ignition hazard exists.

Cone discharges may occur as soon as the electric field in the upper part of the bulked product reaches the dielectric strength of air of approx. 3 MV/m under atmospheric conditions at the silo inner wall. In the present work, computer simulation calculations of the field strengths during the pneumatic filling of silos of different diameters from 1.0 m to 5.5 m with different filling rates from 10 t/h to 40 t/h (tonnes per hour) were carried out and described in the following. In these computer simulation calculations, the charge relaxation during the filling process has been taken into account.

2. Description of the computer simulation

2.1 General information

With the computer simulation, the real-time filling of the silo is simulated in detail on the computer. The silo is filled "slice by slice" or according to the filling procedure defined in practice. The new product entering the silo has the original charge to mass ratio, which can vary greatly depending on the product and the type of input. The longer the residence time of the product in the silo, the more the product in contact with the grounded silo wall becomes discharged according to its relaxation time τ. The relaxation time τ is determined by the resistivity of the bulk solid ρ, the permittivity of the vacuum ε_0 ($8.86 \cdot 10^{-12}$ As/Vm) and the relative permittivity ε_r of the bulk solid according to the formula

$$\tau = \varepsilon_r \cdot \varepsilon_0 \cdot \rho \qquad (1)$$

The lower the resistivity of bulk solid and the slower the silo is filled, the more the product already in the silo becomes discharged before new highly charged product is added.

2.2 Calculation of the electric field in the silo

In order to assess the electrostatic ignition hazards caused by cone discharges as a result of the accumulation and relaxation of charges on the product filled into the silo, the electric field in the silo during the filling process must be calculated.

The electric field E(x,y,z) in the silo can be calculated based on the charge distribution $\rho(x,y,z)$ in the silo due to the charged product and the geometry of the silo, which defines the boundary conditions for the electric potential. For the calculation, the Poisson equation (2) must first be solved,

$$\frac{\partial^2 \Phi}{\partial x^2} + \frac{\partial^2 \Phi}{\partial y^2} + \frac{\partial^2 \Phi}{\partial z^2} = -\frac{\rho}{\varepsilon_r \varepsilon_0} \qquad (2)$$

which describes the relationship between a spatial charge distribution $\rho(x,y,z)$ and the corresponding potential distribution $\Phi(x,y,z)$, taking into account the relevant boundary conditions (e.g. silo walls and silo bottom are at zero potential).

The electric field E(x,y,z) can then be calculated as the gradient of the potential distribution $\Phi(x,y,z)$ with the formula

$$\vec{E} = \frac{\partial \Phi}{\partial x}\vec{x} + \frac{\partial \Phi}{\partial y}\vec{y} + \frac{\partial \Phi}{\partial z}\vec{z} \qquad (3)$$

The Poisson equation is a partial differential equation. Analytical solutions of this equation are extremely complicated and only possible for simple geometries.

For complex geometric arrangements, the equations must be solved in 3 dimensions (3D). If the silo has cylindrical symmetry and the charge distribution in the silo is also cylindrically symmetric, the equations can be solved in 2 dimensions (2D). As soon as the charge relaxation in the silo has to be considered, the charge distribution is no longer homogeneous (it can still be cylindrically symmetric) and the equations (both 3D and 2D) can no longer be solved analytically. This means that the equations can only be solved numerically using iterative methods. One such numerical iterative method is the finite element method, which has been applied in the present model calculations. For that purpose, the commercially available software COMSOL® has been used.

2.3 Procedure in detail

To take into account the charge relaxation in the silo during filling, the silo must be filled step by step, i.e. "slice by slice", in the computer model. After the addition of each slice containing product with the initial charge to mass ratio, the charge relaxation of the already entered "product slices" must be recalculated and then the electric field in the silo must also be recalculated by solving the Poisson equation. With such a filling simulation, the maximum achieved electric field during the entire filling process can be determined. To avoid cone discharges, the electric field in the silo must not exceed 3 MV/m at any time.

Without conductive grounded structures inside the silo, the maximum field strength always occurs at the conductive grounded silo wall.

For the simulation of charge relaxation in the silo, a height-dependent space charge density was introduced according to equation (4):

$$\rho(z) = \rho_0 \cdot e^{-[H_{\text{Füll}}(z)\cdot\pi\cdot R(z)^2\cdot\frac{d}{m\cdot\tau}]} \qquad (4)$$

with

$R(z)$	Silo radius as a function of the current fill level z in m
$H_{\text{Füll}}$	Total filling height in m
z	Silo axis (height) in m
$H_{\text{Füll}}(z)$	$= H_{\text{Füll}} - z$ momentary filling height in m
ρ_{R0}	Resistivity of bulk material in $\Omega\cdot$m
d	Bulk density in kg/m^3
q	Charge to mass ratio in C/kg
ρ_0	$= q\cdot d$: space charge density before charge relaxation in C/m^3
$\rho(z)$	Space charge density as a function of the filling height, taking into account the charge relaxation in C/m^3
ε_0	Permittivity of the vacuum $8.86\cdot10^{-12}$ As/Vm
ε_r	Relative permittivity
τ	$= \varepsilon_0\cdot\varepsilon_r\cdot\rho_{R0}$ Relaxation time in s
m	Filling rate in kg/s

3. *Selected model parameters*

3.1 Equipment

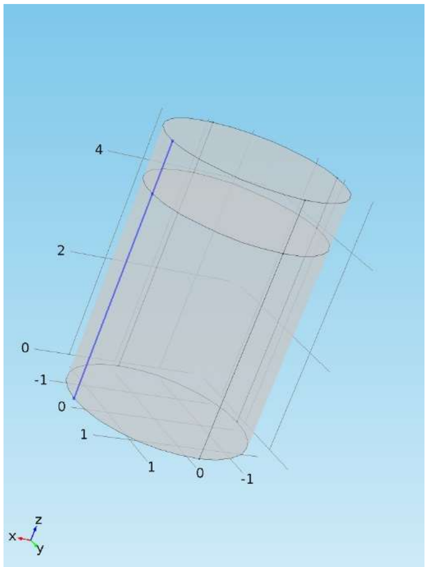

Fig. 1: *All equipment (silos and pipelines) is made from stainless steel and earthed. The cylindrical silos are filled pneumatically through pipelines of nominal diameter DN100. The silo diameter is varied between 1.0 m and 2.0 m in steps of 0.25 m and between 2.0 m and 5.5 m in steps of 0.5 m. The conveying rate is varied between 10 t/h (2.78 kg/s) and 40 t/h (11.11 kg/s) in steps of 5 t/h (1.39 kg/s). Due to charge relaxation of the product in the lower part of the silo, the electric field was only calculated for the upper 5 m of the silos and - as shown in this figure - the product filling height goes up to 1 metre below the total silo height(worst case).*

The blue line shown along the left side of the silo wall indicates the z-coordinate in Figures 6, 7 and 8.

3.2 Product

The transferred product are pellets with a median of the particle size distribution of 3 mm and a bulk density of 650 kg/m^3. The minimum ignition energy of the present fine dust is between 100 mJ and 300 mJ and has been determined without additional inductance in the discharge circuit as specified in the relevant guidelines TRGS 727 (2016) and IEC/TS 60079-32-1 (2013).

The relative permittivity ε_r of the bulked pellets is 2.

According to the tests in an accredited laboratory, the resistivity ρ of the bulked pellets is $8.3 \cdot 10^{11}$ Ωm.

According to the relevant guidelines TRGS 727 (2016) and IEC/TS 60079-32-1 (2013), the charge to mass ratio for pneumatic transfer extends over 4 orders of magnitude and lies between 10^{-7} C/kg to 10^{-3} C/kg. Experience shows that the charge to mass ratio for coarse-grained bulk solids, as in the case of pellets, tends to be at the lower end of this range, i.e., approx. 10^{-7} C/kg to 10^{-6} C/kg. This fact is also confirmed by the empirical values from the research project on the formation of cone discharges Glor et al. (1994) and in the final report on measures against dangerous effects of dust explosions in silos and containers: explosion pressure relief during filling by air conveyance Glor et al. (1988). In addition, it was confirmed in these later tests that the charge to mass ratio is further reduced at high mass flow (feed rate).

In the aforementioned research projects, HDPE granulate (pellets) with a diameter of approx. 3 mm was conveyed in delivery pipelines with a nominal diameter of DN100 and over delivery pipeline lengths of between 25 m and 105 m.

Based on the values from the above-mentioned research reports, the comparable operating modes and the fact that the charge to mass ratio decreases with higher mass flow, a charge to mass ratio of 10^{-6} C/kg was assumed for the model calculations.

Due to the short relaxation time of $\tau = \varepsilon_r \cdot \varepsilon_0 \cdot \rho$ = ca.15 s, the field distribution does not have to be calculated in the whole silo. A calculation for the last 4 m filling height in the cylindrical part of the silos is sufficient. Thus, a resolution with a mesh size of approx. 10 mm to 15 mm was achieved.

Based on the following explanations such a resolution is necessary and sufficient for the field strength calculation at the silo wall: In earlier research work the charge transferred in cone discharges has been measured (see Glor et al. (1988) and Glor et al. (1994)). The results showed that in cone discharges, which have energies comparable to the present evaluations and specified in the guidelines TRGS 727 (2016) and IEC/TS 60079-32-1 (2013), the transferred amount of charge equals the charge stored in a bulk material layer thicknesses in the silo of several centimetres.

4. Results of model calculations

Figures 2 to 5 show the distribution of the field strength along the inner surface of the silo wall for silo diameters of 0.5, 2.0, 3.5 and 5.0 m and fill rates of 10, 25 and 40 t/h. For each of the 4 silo geometries (Figures 1 to 4), a large-format picture is first shown for the 40 t/h filling rate and afterwards small format pictures for the 25 t/h and 10 t/h fill rates.

Figures 6 to 8 show the detailed field strength distributions along the inner surface of the silo wall for all silo geometries and all variations of the fill rate.

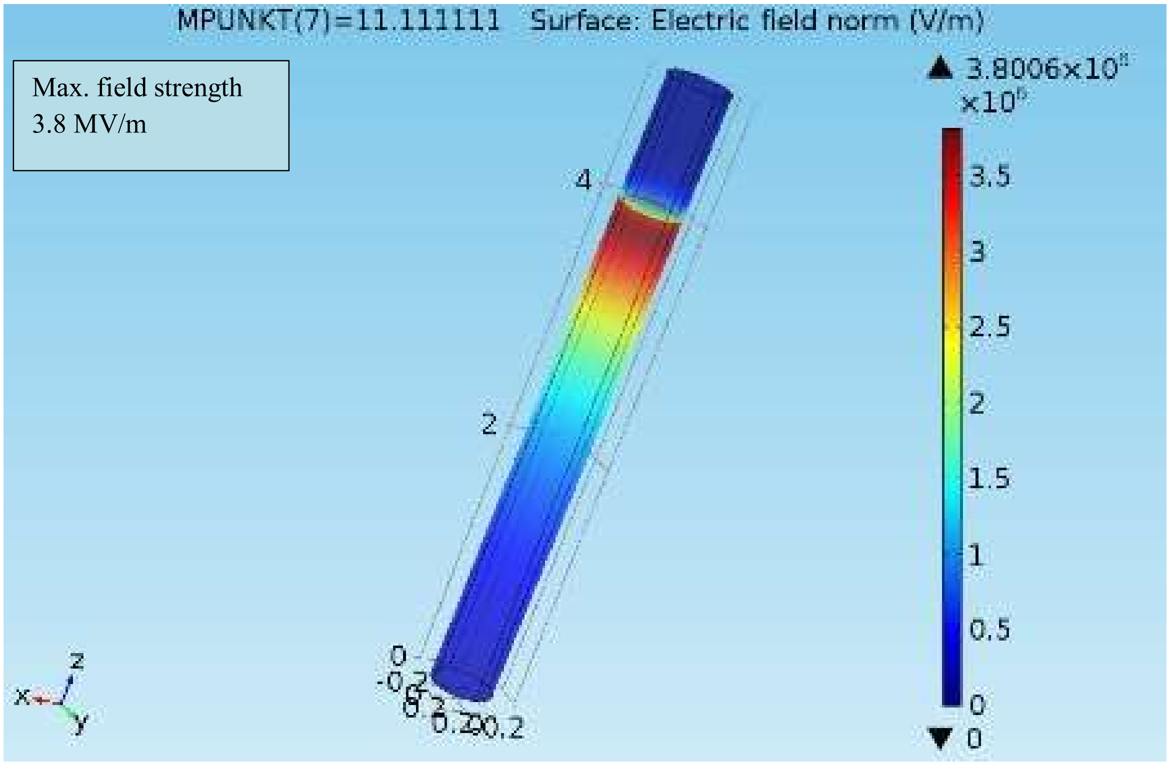

Max. field strength
3.8 MV/m

Fig. 2a:
Field strength distribution along the inner surface of the silo wall, selected model parameters see section 3, silo diameter 0.5 m, fill rate 40 t/h.

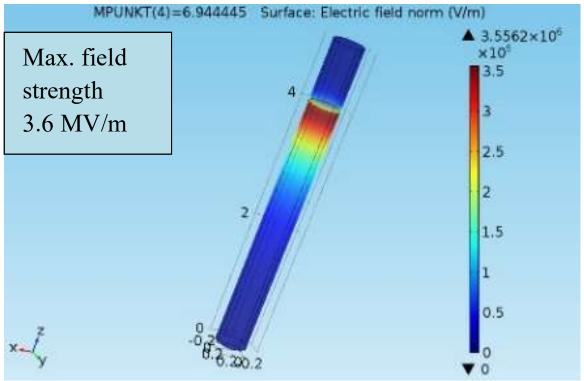 Max. field strength 3.6 MV/m	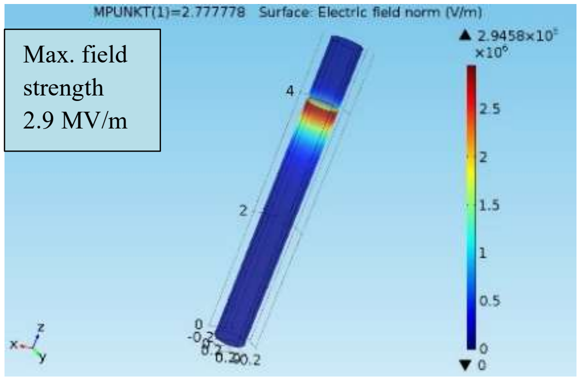 Max. field strength 2.9 MV/m
Fig. 2b: *Field strength distribution along the inner surface of the silo wall, selected model parameters see section 3, silo diameter 0.5 m, fill rate 20 t/h.*	***Fig. 2c:*** *Field strength distribution along the inner surface of the silo wall, selected model parameters see section 3, silo diameter 0.5 m, fill rate 10 t/h.*

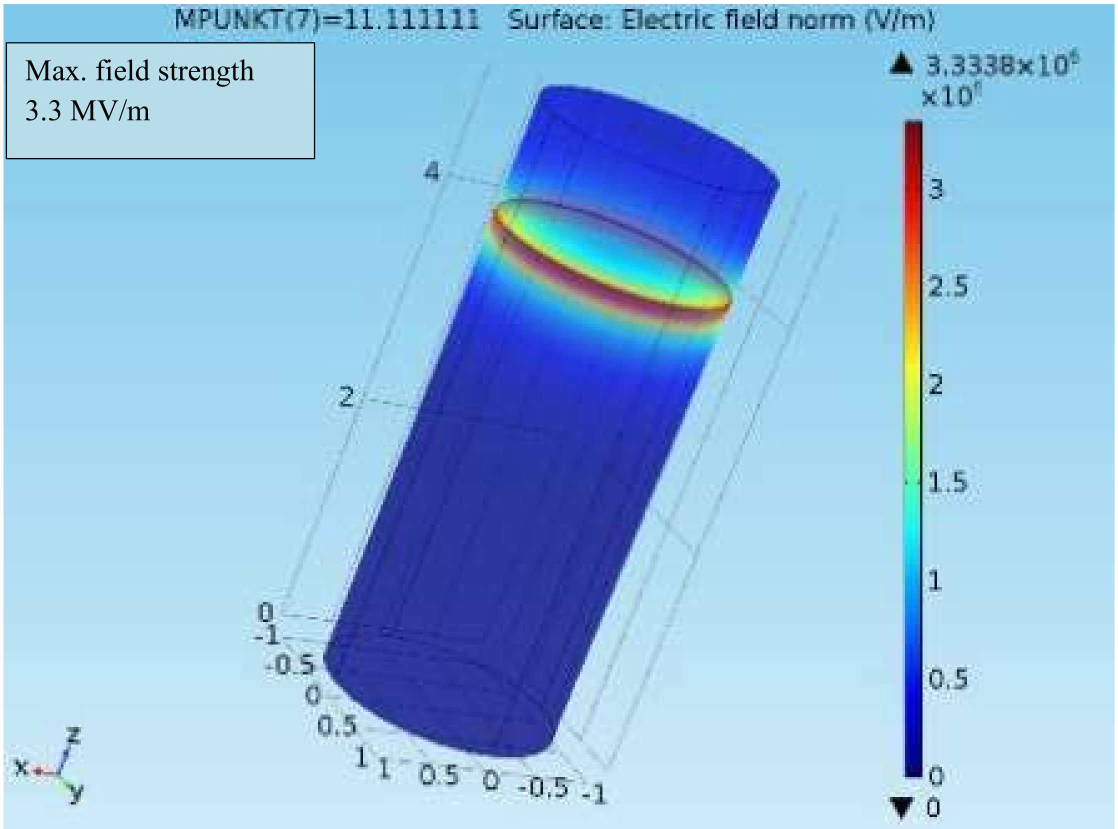

Fig. 3a:
Field strength distribution along the inner surface of the silo wall, selected model parameters see section 3, silo diameter 2.0 m, fill rate 40 t/h.

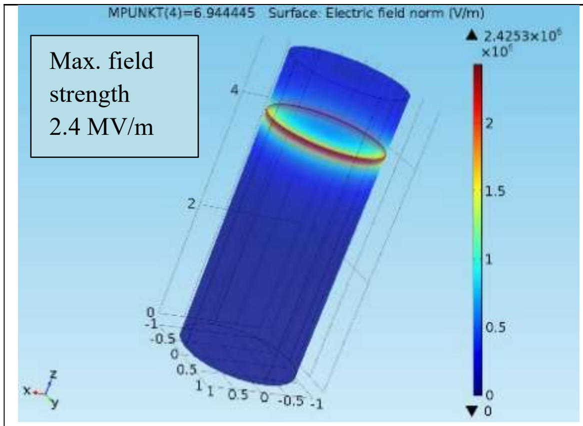

Fig. 3b: *Field strength distribution along the inner surface of the silo wall, selected model parameters see section 3, silo diameter 2.0 m, fill rate 20 t/h.*

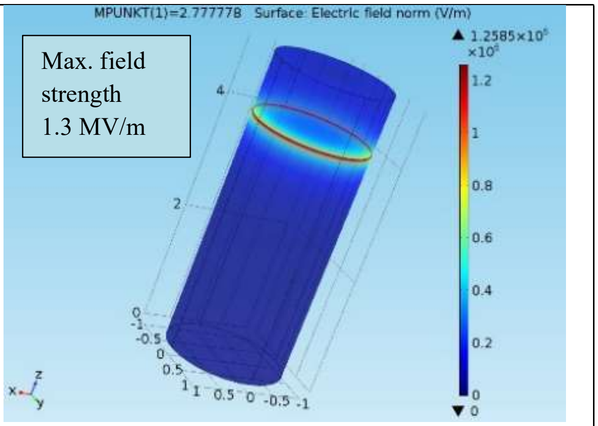

Fig. 3c: *Field strength distribution along the inner surface of the silo wall, selected model parameters see section 3, silo diameter 2.0 m, fill rate 10 t/h.*

DOI: 10.7795/810.20221124

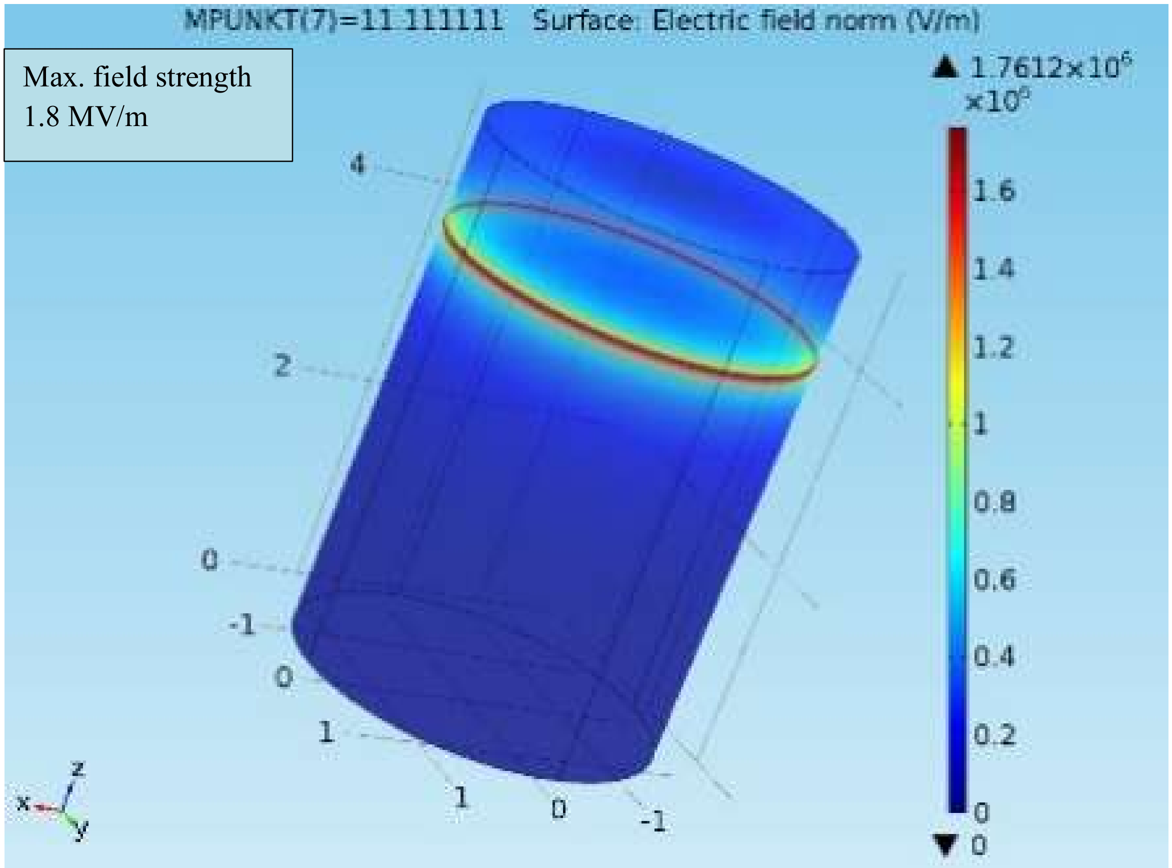

Max. field strength 1.8 MV/m

Fig. 4a:
Field strength distribution along the inner surface of the silo wall, selected model parameters see section 3, silo diameter 3.5 m, fill rate 40 t/h.

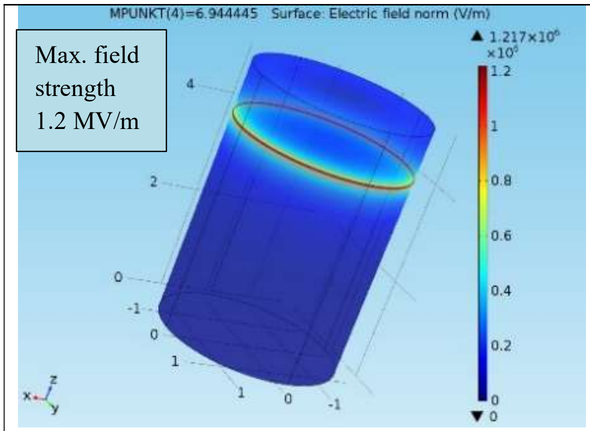 Max. field strength 1.2 MV/m	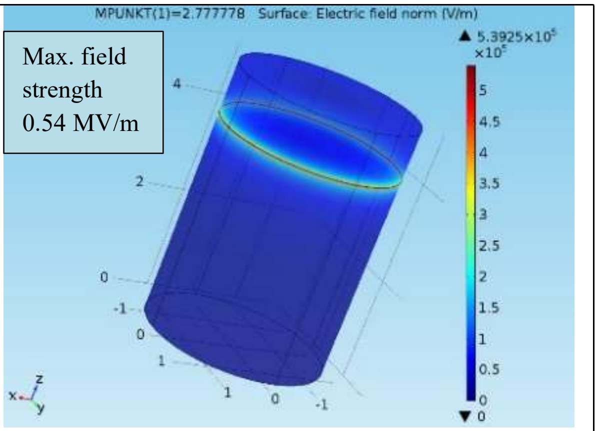 Max. field strength 0.54 MV/m
Fig. 4b: *Field strength distribution along the inner surface of the silo wall, selected model parameters see section 3, silo diameter 3.5 m, fill rate 20 t/h.*	***Fig. 4c:*** *Field strength distribution along the inner surface of the silo wall, selected model parameters see section 3, silo diameter 3.5 m, fill rate 10 t/h.*

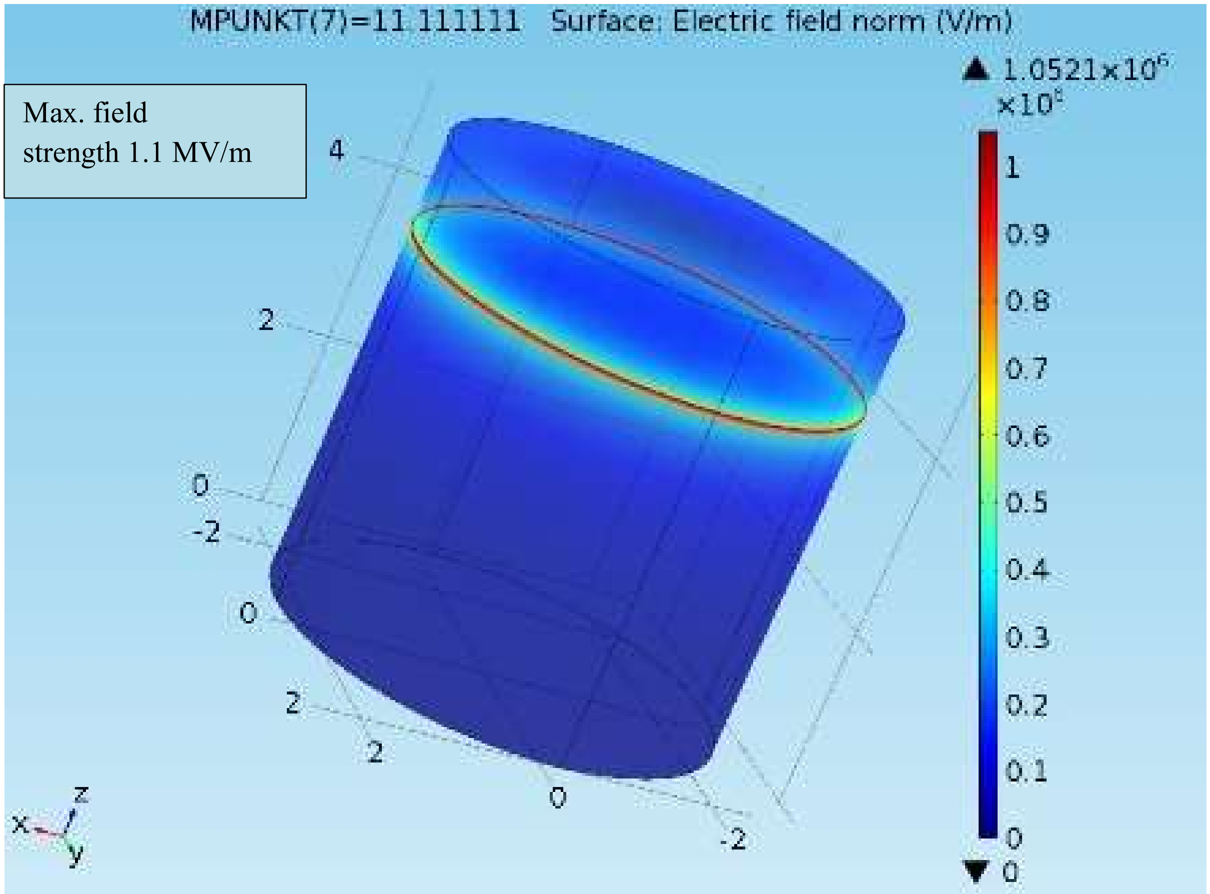

Fig. 5a:
Field strength distribution along the inner surface of the silo wall, selected model parameters see section 3, silo diameter 5.0 m, fill rate 40 t/h.

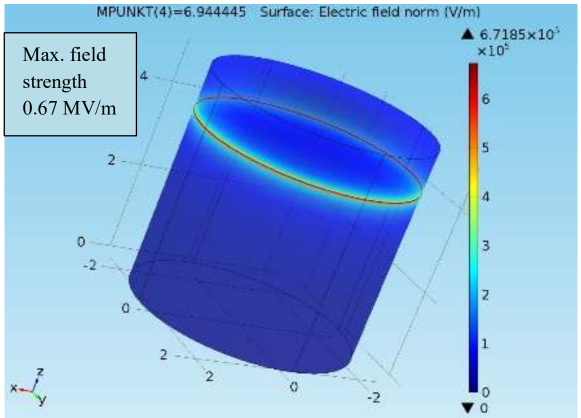

Fig. 5b: *Field strength distribution along the inner surface of the silo wall, selected model parameters see section 3, silo diameter 5.0 m, fill rate 20 t/h.*

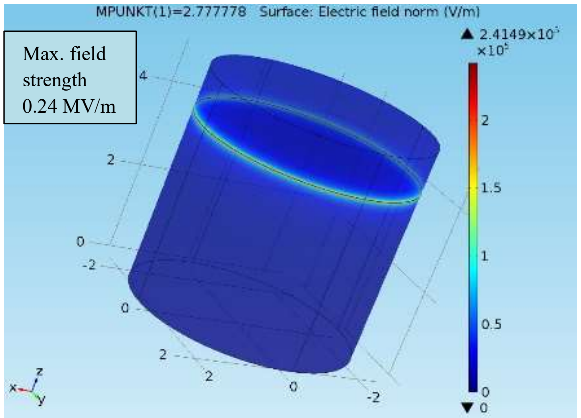

Fig. 5c: *Field strength distribution along the inner surface of the silo wall, selected model parameters see section 3, silo diameter 5.0 m, fill rate 10 t/h.*

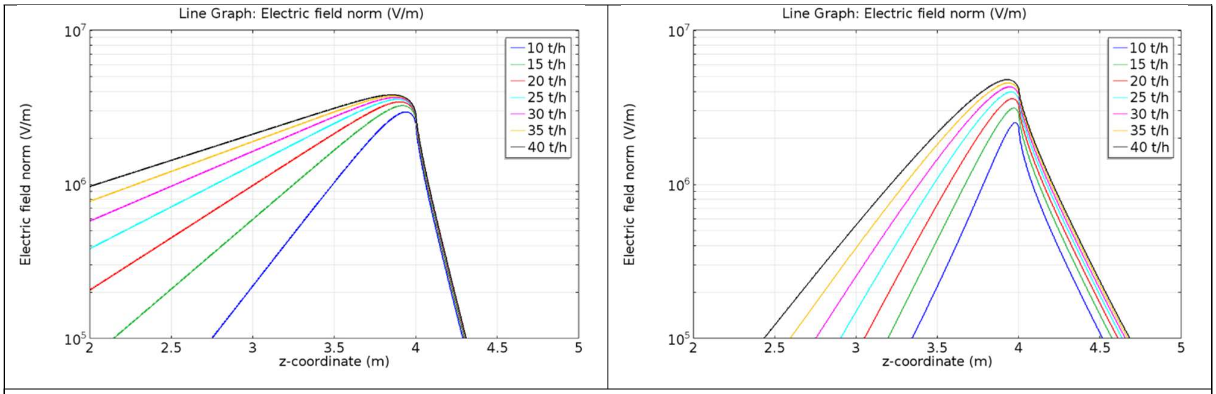

Fig. 6: *Field distribution along the silo wall (z-coordinate (m)) for a silo with 0.5/1 m (left/right) diameter at different fill rates under the assumptions mentioned in section 3.*

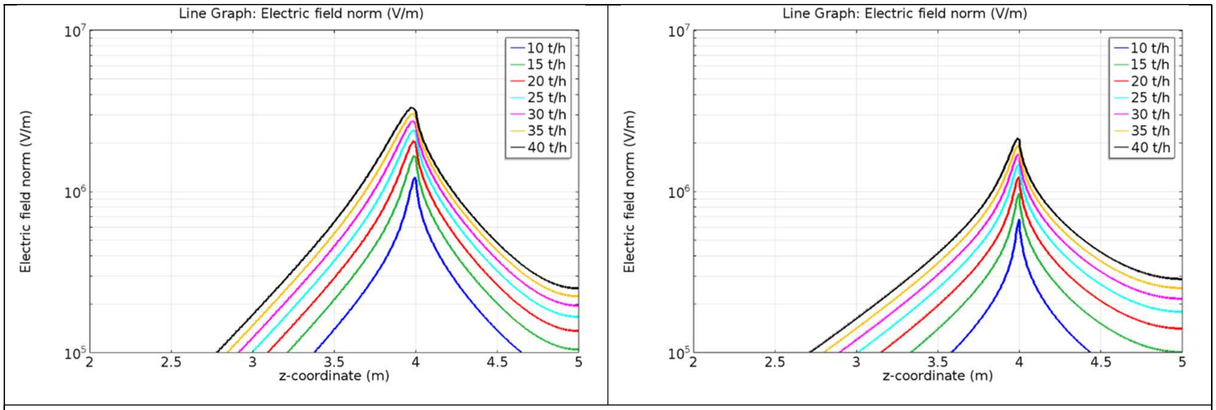

Fig. 7: *Field distribution along the silo wall (z-coordinate (m)) for a silo with 2/3 m (left/right) diameter at different fill rates under the assumptions mentioned in section 3.*

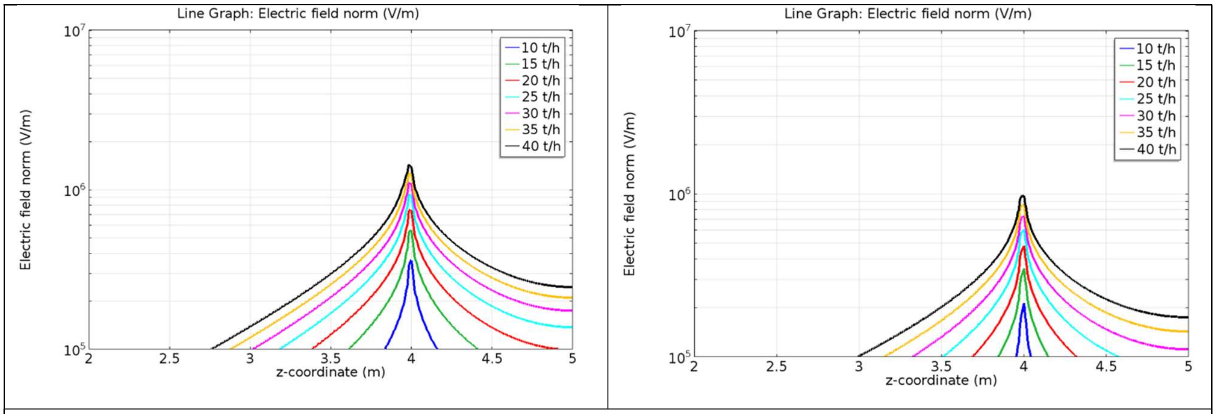

Fig. 7: *Field distribution along the silo wall (z-coordinate (m)) for a silo with 4/5 m (left/right) diameter at different fill rates under the assumptions mentioned in section 3.*

5. Interpretation of the results from the model calculations

Figure 9 summarises the results of the model calculations. The resulting maximum electric field strength at the silo wall can be read off for the silo diameters shown and for the corresponding mass flows during filling.

The field strength at the inner wall surface of a silo filled with charged product depends on 6 different parameters: The charge to mass ratio of the incoming product, the bulk density of the product, the relative permittivity of the bulked product, the charge relaxation time in the deposited product, the fill rate and the silo diameter. In the present model calculations, the first 4 parameters are kept constant, whereas the fill rate and the silo diameter are varied. For silos with a diameter larger than about 1 m the field strength decreases with the silo diameter because charge relaxation due to the long residence time of the product in the silo dominates the effect of field strength increase due to larger silo diameter. Below a silo diameter of about 1 m the effect of field strength decrease with smaller diameter dominates the effect of charge relaxation due to residence time of the product in the silo.

6. Conclusions

6.1 Occurrence of no or not incendive cone discharges

Rather conservative estimates and boundary conditions were used for the modelling. In addition, a safety margin of a factor of 2 was chosen for the maximum acceptable field strength (1.5 MV/m instead of the breakdown field strength in air under atmospheric conditions of approx. 3 MV/m).

Applying the above conditions, the following facts and statements apply to metallic silos as well as metallic conveying lines without internal coating for the storage of pellets with a median of the particle size distribution of 3 mm and a resistivity of bulked pellets of no more than $8.3 \cdot 10^{11}$ Ωm:

1) For all silos with silo diameter/mass flow constellations located in the green range of Figure 9 corresponding to a field strength < 1.5 MV/m, bulk cone discharges are not expected when such pellets are introduced.

2) For silos with a diameter ≥ 5.5 m, cone discharges are not to be expected if the mass flow of such pellets does not exceed 40 t/h during filling. For higher mass flows, an individual assessment is required.

3) In silos with a diameter ≤ 1.75 m, cone discharges may occur. The maximum energy of such cone discharges can be calculated by the corresponding formulas given in TRGS 727 (2016) and IEC/TS 60079-32-1 (2013) and will amount to about 100 mJ. Thus, an ignition hazard has to be expected if the minimum ignition energy of the fine dust present in the silo is equal or less than 100 mJ.

6.2 Conclusions in case of incendive cone discharges

In case the energy of possible cone discharges calculated by the corresponding formulas given in TRGS 727 (2016) and IEC/TS 60079-32-1 (2013) is larger than the minimum ignition energy of the dust cloud present in the silo, the energy of the cone discharges can be reduced by reduction of the striking distance of these discharges. In practice, this can be achieved by dividing the interior of the silo in vertical direction using conductive grounded pipes or ropes. In the relevant formula the maximum distance between these structures and their distance to the silo wall has to be considered. The fastenings of the pipes or ropes as well as the silo ceiling must be designed to withstand the expected tensile loads. Furthermore, the construction must be regularly maintained and checked for integrity, since electrically isolated parts present an ignition hazard in form of spark discharges within the silo.

Another measure to avoid ignition of dust/air mixtures by cone discharges has also proved successful in industrial practice. It is a known fact that even a small reduction of oxygen in the silo by a few percentage points drastically increases the minimum ignition energy of dust/air mixtures. Details can be found in the following literature Hesener et al. (2015).

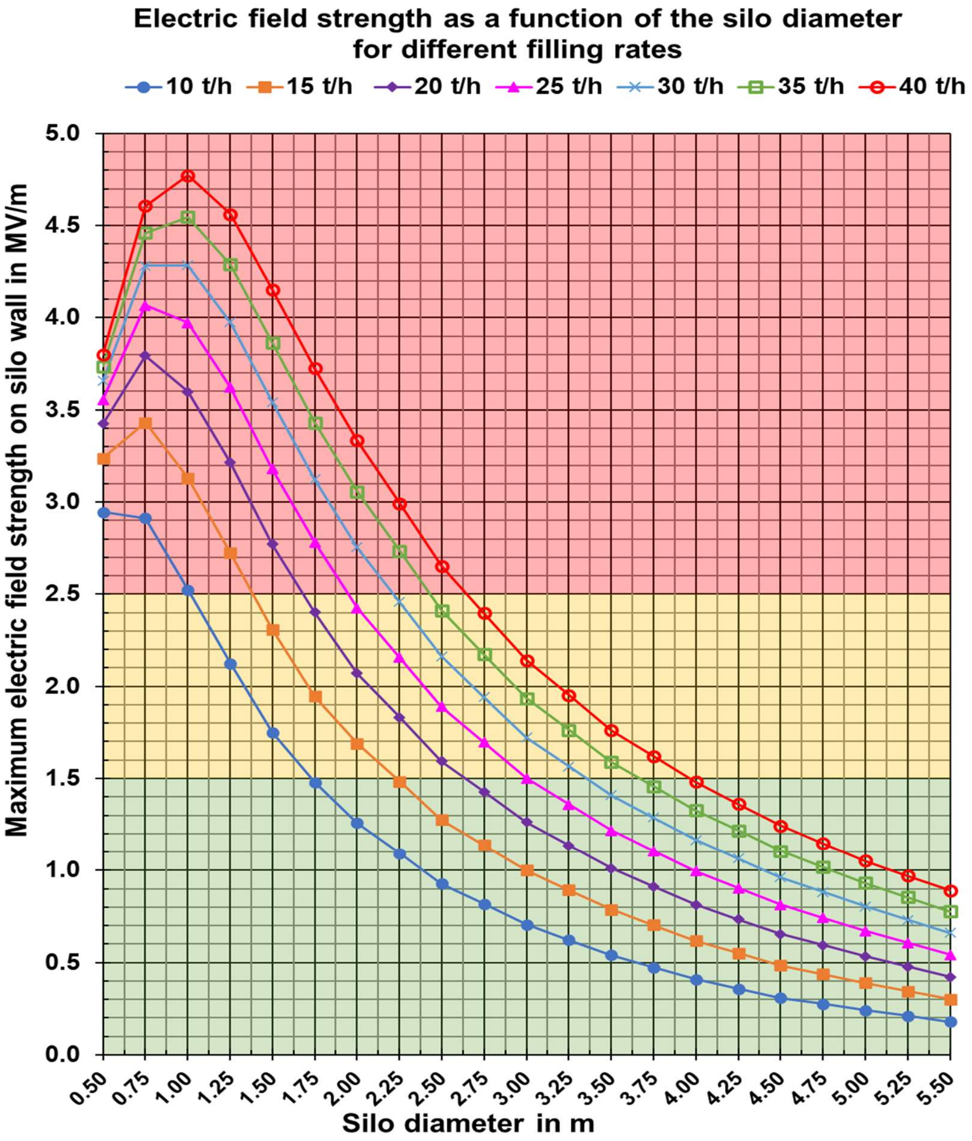

Fig. 9: *Summary of results shown in Figures 1 to 7.*

References

IEC/TS 60079-32-1 (2013). *Technical Specification, Explosive atmospheres - Part 32-1: Electrostatic hazards, guidance.* Edition 1.0, 2013-08.

TRGS 727 (2016). *Technische Regeln für Gefahrstoffe, Vermeidung von Zündgefahren infolge elektrostatischer Aufladungen*. Germany, 1. Edition April 2016.

Glor, M. & Maurer, B. (1988). *Maßnahmen gegen gefährliche Auswirkungen von Staubexplosionen in Silos und Behältern: Explosionsdruck-entlastung beim Befüllen durch Flugförderung.* Abschlussbericht Projekt-Nr.: 01 HK 664 A0 betreffend das Aufstockungsvorhaben Zündfähigkeit von Schüttkegelentladungen zum Forschungsvorhaben

Glor, M. & Maurer, B. (1994). *Zündfähigkeit von Schüttkegelentladungen*. Bundesministerium für Forschung und Technologie, Forschungsbericht (13 RG 9002).

Hesener, U. & al. (2015) *Forschungsbericht Sicherheitstechnische Kenngrößen von Stäuben bei nicht-atmosphärischen Bedingungen.* DEKRA EXAM GmbH.

DOI: 10.7795/810.20221124

Review on CFD modeling of electrostatic powder charging during pneumatic conveying

Holger Grosshans[a,b], Simon Jantac[a]

[a] Physikalisch-Technische Bundesanstalt (PTB), Braunschweig, Germany
[b] Otto von Guericke University of Magdeburg, Institute of Apparatus- and Environmental Technology, Magdeburg, Germany

E-mail: *holger.grosshans@ptb.de*

Abstract

Thus far, Computational Fluid Dynamics (CFD) simulations fail to reliably predict the electrostatic charging of powder during pneumatic conveying. The lack of a predictive tool is one reason for unwanted discharges and growing deposits that make a plant a prime candidate for an explosion. This paper reviews the numerical models' state-of-the-art, limitations, and progress in recent years. In particular, the discussion includes the condenser model, which is up to today most popular in CFD simulations of powder flow electrification but fails to predict most of its features. New experiments led to advanced models, such as the non-uniform charge model, which resolves the local distribution of charge on non-conductive particle surfaces. Further, models relying on the surface state theory predicted bipolar charging of polydisperse particles made of the same material. Whereas these models were usually implemented in CFD tools using an Eulerian-Lagrangian strategy, powder charging was recently successfully described in an Eulerian framework. The Eulerian framework is computationally efficient when handling complete powders; thus, this research can pave the way from academic studies to simulating powder processing units. Overall, even though CFD models for powder flow charging improved, major hurdles toward a predictive tool remain.

Keywords: *Simulation, electrostatics, pneumatic conveying, industrial explosions*

1 Introduction

One way to control powder charging would be to analyze an industrial process by simulations. Then, based on the results, one could adapt the facility's design or choose its operating parameters to limit the generating charge. However, the simulation of the charging of flowing powder is extremely challenging. It requires coupling the equations of fluid mechanics (turbulent conveying airflow), surface science (triboelectric charge exchange, adhesion), and electromagnetism (electrostatic attraction of charged particles). Each of these scientific sub-fields being complex by itself, their numerical coupling of these equations is yet more difficult. For some of the mentioned physical processes, the mathematical equations are not even clear to date.

In particular, particles change their charge through various physical mechanisms: through ionized gas or dissipation, but most often through contact with other surfaces. The lacking understanding of the physics and chemistry of particle charging explains the limited success of related numerical model formulation. These models usually require heavy tuning of parameters, or the predicted charge differs from experimental measurements by several orders of magnitude. For these reasons, CFD simulations are not mature enough to reliably evaluate the charging of particulates during processing.

Figure 1 compiles CFD predictions of powder charging by three groups using different codes. Whereas Tanoue et al. (2001) predicts the powder charge to decrease with increasing Reynolds number, the data of Grosshans and Papalexandris (2016a) suggests the opposite. According to Watanabe et al. (2006), the Reynolds number has nearly no influence. Even though each group simulated different particle material and sizes, the contradictory trend of the results is surprising since the flow Reynolds number is the dominating operation condition of pneumatic conveying.

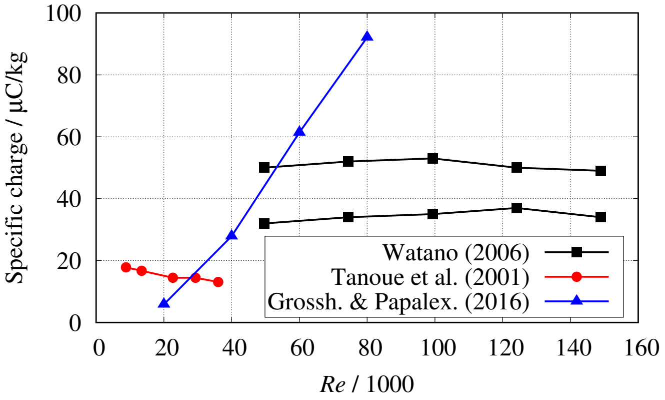

***Fig. 1**: CFD simulations of the powder charge after pneumatic conveying depending on the flow Reynolds number.*

It is emphasized that powder flow electrification is not simply the sum of the charging of the individual particles. Instead, fluid dynamics, electrostatics, and triboelectricity give rise to complex intertwined interactions, e.g.:

- The dynamics of a particle-laden flow determines the frequency and severeness of particle/surface and particle/particle contacts and, thus, the charge accumulation of powder (Grosshans and Papalexandris, 2017a, Jin and Marshall, 2017).
- The charge exchange during one contact does not only depend on the charge carried by the particle itself, but also on the electrostatic field generated by the charges of all other present particles and induced charges on surfaces (Matsuyama and Yamamoto, 1995, 1997).
- The electrostatic field significantly changes the powder flow pattern through electric forces and, thus, alters the dynamics of subsequent contacts (Dhodapkar, 1991).

These interactions cause perplexing phenomena, such as particles moving counter to the main gas flow due to the emerging electrostatic field (Myler, 1987). In other words, only having a correct particle charging model is not enough for a correct prediction of powder charging. In essence, the hazard of electrostatic charge accumulation to the operational safety of an industrial facility must be evaluated at a powder flow level.

This paper reviews the state-of-the-art, limitations, and progress in recent years of the numerical modeling of electrostatic charging of powder flows. Out of all industrial powder operations, pneumatic conveying, due to the high flow velocities, leads by far to the highest charge levels (Klinzing, 2018). Therefore, this review focuses on simulations of pneumatic conveying. Nevertheless, the research questions in pneumatic powder conveying are often similar to those of closely related fields, and their model development stimulates each other. In particular, this review summarizes advances in simulations, purely experimental studies are only included if they directly led to a model. Otherwise, the reader is referred to the reviews of Lacks and Shinbrot (2019) on general triboelectricity, of Chowdhury et al. (2021) on single particle charging models, of Matsusaka et al. (2010) on experimental electrostatics, of Mehrani et al. (2017) on charging in fluidized beds, and of Wong et al. (2015) on charging in pharmaceutics.

This paper is organized as follows: Sections 2 to 4 present the available numerical concepts to model the flow of charged powder in pneumatic conveying. More specifically, Section 2 gives an overview of the methods to simulate the carrier gas phase. Section 3 provides an outline of the different methods to simulate the dynamics of powder, including approaches to compute the electric field and the electrostatic forces on the particles. Section 4 summarizes the models of triboelectric charging on a single particle level. The final section gives the author's opinion on the future perspectives of the field.

2 Modeling the turbulent carrier gas flow

Given that particles collect most of their charge during contacts, and contacts are driven by aerodynamic forces, the simulation of the carrier gas flow plays a paramount role in powder charging. The gas flow in pneumatic conveyors is described by the Navier-Stokes equations. That means by the mass and momentum balance of incompressible Newtonian fluids in Eulerian framework,

$$\nabla \cdot \boldsymbol{u} = 0 \tag{1a}$$

$$\frac{\partial \boldsymbol{u}}{\partial t} + (\boldsymbol{u} \cdot \nabla)\boldsymbol{u} = -\frac{1}{\rho}\nabla p + \nu \nabla^2 \boldsymbol{u} + \boldsymbol{F}_{\mathrm{s}}\,, \tag{1b}$$

where $\boldsymbol{u}$ denotes the fluid's velocity, p its pressure, ρ its density, ν its kinematic viscosity, and t the temporal coordinate. The source term $\boldsymbol{F}_{\mathrm{s}}$ accounts for the momentum transfer from the particles to the carrier fluid. Both equations rely on a fundamental physical principle, Eq. (1a) on the assumption that mass can neither be created nor destroyed and Eq. (1b) on Newton's second law of motion extended to fluids. Since analytical solutions were found only for a few simple flow cases, solving the above equations requires numerical simulations.

Most of the time, pneumatic conveyors operate at high Reynolds numbers, which means in fully turbulent mode. The most exact method to simulate turbulence, termed *direct numerical simulation* (DNS), resolves all length- and time-scales of fluid motion on the numerical grid. However, turbulent flows of a high Reynolds number exhibit a wide range of scales. Resolving all spatial and temporal scales requires a fine grid and a small time-step, resulting in a high computational effort. Therefore, when simulating pneumatic powder conveying, turbulence is usually modeled instead of resolved.

In early computations of powder charging, not even the mean flow was solved but approximated by an analytical velocity profile. Afterward, the first simulations appeared using the *Reynolds-averaged Navier-Stokes* (RANS) approach (Kolniak and Kuczynski, 1989, Tanoue et al., 1999, 2001). In RANS, equations (1a) and (1b) are temporally or ensemble-averaged. Due to the averaging new unclosed terms arise, the so-called Reynolds stresses. Widespread closures include the mixing-length model (Baldwin and Lomax, 1978) and the standard $k-\varepsilon$ (Jones and Launder, 1972) and $k-\omega$ (Wilcox, 1998) models.

In other words, the RANS approach solves the mean flow but models all turbulence scales. This is reasonable when only time-averaged quantities are of interest rather than turbulent fluctuations. However, powder receives most of its charge when the particles reflect on the conveying duct's walls. Especially near-wall turbulence drives these impacts' frequency, velocity, and angle. Thus, the turbulence model's deficiency directly impairs the prediction of powder charging by RANS simulations.

For several years, *Large Eddy Simulation* (LES) of powder flow charging has been feasible (Grosshans and Papalexandris, 2016a, Korevaar et al., 2014). LES computes the filtered governing equations (1a) and (1b); only the turbulent motions larger than the filter size are resolved on the grid. Similar to RANS, new unclosed terms corresponding to the small (subfilter) scales appear through the filter operation. The rationale of LES stems from Kolmogorov's hypothesis that the small-scale structures are universal and can, thus, be modeled. Some of the most popular closures include the Smagorinsky (1963) model, the dynamic approach by Germano et al. (1991), the scale similarity model by Bardina et al. (1980), and the implicit approach by Boris et al. (1992). They all approximate the sub-filter terms from the resolved flow field, even though experiments showed the correlation is weak (Liu et al., 1994).

The computational effort of LES is much higher compared to RANS. But if the grid resolution is fine enough, a considerable part of the turbulence energy spectrum is resolved. Then, the influence of the turbulence model diminishes, and LES becomes exact. LES is especially reliable if the ratio of the characteristic particle to flow time is high. The ratio of the characteristic particle to flow time, which is the particle's Stokes number,

$$St = \frac{\tau_{\mathrm{p}}}{\tau_{\mathrm{f}}}, \tag{2}$$

DOI: 10.7795/810.20221124

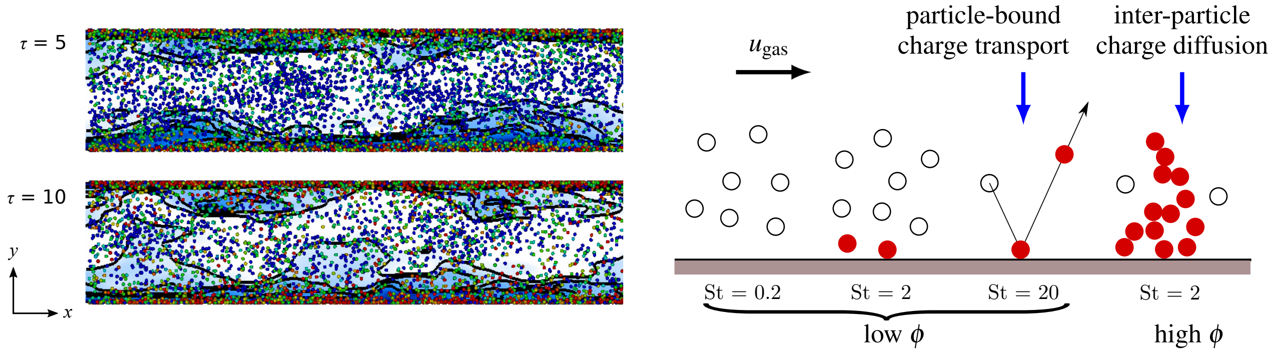

(a) *(b)*

***Fig. 2**: DNS of powder electrification in a channel flow depending on the Stokes number (St) and particle volume fraction (ϕ). (a) is for St = 20, the colors indicate the particles' charge. (adapted with permission from Grosshans and Papalexandris (2017a, 2018))*

determines the dynamics of the air-particle interaction. For those particles of a high Stokes number, inertial forces act as a high-pass filter. Their trajectories are influenced by large-scale but not by small-scale turbulence. Thus, the requirement to the grid resolution relaxes when simulating the charging of high Stokes number particles.

Only recently, the first DNS of electrifying powder flow was achieved (Grosshans and Papalexandris, 2017a). However, DNS can not simulate complete industrial unit operations. Instead, it is limited to generic domains and low Reynolds numbers, such as the channel flow of a friction Reynolds number of 360 in Fig. 2b. These DNS revealed, at a previously unknown level of detail, the small-scale mechanisms that determine the powder charging rate. More precisely, the mechanisms sketched in Fig. 2b dominate the charge transfer from the channel walls to and within the powder flow: *particle-bound charge transport* for highly inertial particles and *inter-particle charge diffusion* for low inertial particles in case of high particle volume fractions (ϕ). Identifying these mechanisms implies the possibility to control the electrification of powder flows by imposing flow conditions that purposely trigger these mechanisms.

3 Modeling electrostatically charged powder flow

Contrary to the carrier gas, which is continuous, the powder forms a dispersed phase. Powder consists of abundant particles. The amount of particles an their related solid/gas interface area restrict the choice of the numerical method. Those numerical methods for multiphase flows that resolve the phase interface on the grid, such as volumes-of-fluids, level-set, or marker-and-cell, are computationally too expensive. Instead, pneumatic conveying is usually modelled by the Eulerian-Lagrangian or the Eulerian-Eulerian approach. In both appoaches, the carrier gas is described in the Eulerian framework, as discussed in Sec. 2. The particulate phase is either described in Lagrangian framework, that means each particle is tracked individually, or in the Eulerian framwork, where the powder is modelled as a continuum.

3.1 Lagrangian

Most simulations of powder charging during pneumatic conveying use the Lagrangian framework to describe the particle flow. In the Lagrangian framework, each particle is treated individually as a point-mass whose motion is computed as

$$m_{\mathrm{p}} \frac{\mathrm{d}\boldsymbol{u}_{\mathrm{p}}}{\mathrm{d}t} = \sum \boldsymbol{F}\,, \tag{3}$$

where $\boldsymbol{u}_\mathrm{p}$ is the velocity and m_p the mass of the given particle. The term on the right-hand side represents the sum of all specific external forces acting on the particle which are elaborated in the following sub-section.

The advantage of the Lagrangian approach is that there is no limitation on St and polydispersity can be handled more easily compared to the Eulerian approach. However, the ratio of the average particle diameter to the characteristic flow scale is assumed to be low. Further, the numerical coupling of Lagrangian particles to the carrier phase poses a challenge.

The computational effort of the Lagrangian approach scales with the number of particles, N. Some sub-models scale linearly with N whereas others, such as collisions between particles, require the comparison of particle pairs. The computational effort of comparing particle pairs scales by $O(N^2)$. Advanced algorithm reduce the cost, for example, Fast Multipole Methods (FMM) (Rokhlin, 1990) to $O(N \log N)$. Nevertheless, operations that require evaluating particle pairs remain elaborative. Especially for pneumatic conveying systems, which consist of missions of particles, these operations can easily inflate the overall computational time. Therefore, the models describing Lagrangian particles have to be carefully chosen to optimize the equation system's accuracy and efficiency.

Further, the Lagrangian framework is limited to study the transport through one pipe instead of a complete pneumatic system, and for dilute or pulsed conveying where the particle number is low. Or for academical research, looking at fundamental charging methods in only a section of the complete pipe. For fundamental research, the Lagrangian approach plays out its strength, namely the resolution of individual particle trajectories.

3.2 Forces on a particle

The specific external forces acting on a particle are given by

$$\sum \boldsymbol{F} = \boldsymbol{F}_\mathrm{g} + \boldsymbol{F}_\mathrm{coll} + \boldsymbol{F}_\mathrm{ad} + \boldsymbol{F}_\mathrm{vdW} + \boldsymbol{F}_\mathrm{el}\,, \tag{4}$$

where $\boldsymbol{F}_\mathrm{g}$ denotes the gravitational, $\boldsymbol{F}_\mathrm{coll}$ the collisional, $\boldsymbol{F}_\mathrm{ad}$ the drag, $\boldsymbol{F}_\mathrm{vdW}$ the van der Waals, and $\boldsymbol{F}_\mathrm{el}$ the electric field forces acting on the particle.

The selection of forces included in the simulation model depends on the specific conveying system under consideration: for vertical conveying of high Stokes number particles, the particle dynamics with and without gravity is nearly identical (Marchioli et al., 2007); thus, the gravitation can be neglected. For horizontal conveying of low Stokes number particles, gravity determines the particles' trajectories and, thus, their charging. Therefore, gravitation is considered in all simulations of horizontal conveying.

The specific collisional force term $\boldsymbol{F}_\mathrm{coll}$ accounts for both inter-particle and particle-wall collisions. Collisions between particles requires the comparison of particle pairs, which is, as discussed above, computationally expensive. Therefore, inter-particle collisions are neglected whenever possible. During dilute conveying, particles collide seldom with each other (Elgobashi, 1994). Therefore, inter-particle collisions are usually only modelled when simulating dense conveying.

Due to the high flow velocities, the aerodynamic drag acting on a particle (Crowe et al., 2012),

$$\boldsymbol{F}_\mathrm{ad} = -\frac{\pi}{2} C_\mathrm{d}\, \rho\, r_\mathrm{p}^2\, |\boldsymbol{u}_\mathrm{rel}|\, \boldsymbol{u}_\mathrm{rel}\,, \tag{5}$$

is part of all pneumatic conveying simulations. In this equation, $\boldsymbol{u}_\mathrm{rel}$ the particle velocity relative to the gas, and C_d is the particle drag coefficient. The drag coefficient is computed according to the relation provided by Schiller and Naumann (1933) as a function of the particle Reynolds number,

$$C_\mathrm{d} = \frac{4}{Re_\mathrm{p}} \left(6 + Re_\mathrm{p}^{2/3}\right) \quad \text{with} \quad Re_\mathrm{p} = 2|\boldsymbol{u}_\mathrm{rel}|\, r_\mathrm{p}/\nu\,. \tag{6}$$

Originally, this expression was derived experimentally for idealized conditions, namely for isolated, spherical particles exposed to an undisturbed airflow. These idealizations generally do not hold for pneumatic conveying. Many new drag correlations were proposed in the recent years, reflecting non-spherical particles (Zastawny et al., 2012), shear flow due to the pipe's walls (Zeng et al., 2009), or the disturbance of the flow by nearby particles (Kravets et al., 2019, Tang et al., 2015). . However, the dynamics of charged particles is different from uncharged ones and so is their drag. The drag correlation for charged particles have, with the exception of the thesis of Ozler (2022), not been researched yet. Given that the near-wall dynamics of particles determines their charging during pneumatic conveying, choosing a suitable drag correlation is decisive for predicting powder flow charging.

There are other aerodynamic forces (besides drag) acting on a particle, summed up by the Basset-Boussinesq-Oseen (BBO) equation (Maxey and Riley, 1983). These include the virtual mass force that is required to drag along the surrounding fluid when the particle is accelerated. The virtual mass force is important for the case of a low solid-fluid density ratio which is not typical for pneumatic transport. The effect of a non-uniform flow around a particle is accounted for by the Faxen force. Further, the Saffman force is caused by the rotation of a particle due to large velocity gradients in shear flows. Both Faxen and Saffman forces, vanish if the particle size is small compared to the scale of the local flow gradients. The assumption of non-rotating particles also allows to neglect the Magnus force. The time delay in building up a boundary layer in the vicinity of the particles' surface is described by the Basset history term.

Also, the aerodynamic drag imposes a force on the fluid phase which is given by $\boldsymbol{F}_\mathrm{s}$ in equation (1b). Once again, for dilute conveying, where the number of particles is low, $\boldsymbol{F}_\mathrm{s}$ can be neglected.

Van der Waals forces can be stronger than gravitational forces if the particles are small (Tomas and Kleinschmidt, 2009). For airborne particles during pneumatic conveying, van der Waals forces play no role. They act only during a minuscule duration when the distance in-between particles or a particle and a wall is of the nanometer order, therefore, the particle's momentum change is negligible. Nevertheless, van der Waals forces can form dust deposits on the surfaces of pipes or other components. Thus, for the prediction of deposits, van der Waals forces need to be considered Klahn and Grosshans (2020).

Finally, the last term in Eq. (4) describes the electrostatic force acting on a particle that carries the charge Q,

$$\boldsymbol{F}_\mathrm{el} = Q\boldsymbol{E}\,, \tag{7}$$

which can dominate the dynamics of particles in pneumatic conveyors. The electric field strength, $\boldsymbol{E}$, is given by Gauss' law,

$$\nabla\cdot\boldsymbol{E} = \frac{\rho_\mathrm{el}}{\varepsilon_0}\,, \tag{8}$$

where ε_0 is the electrical permittivity and the electric charge density, ρ_el, reflects the charge carried by all particles in the system. Gauss' law involves only $O(N)$ operations and is, therefore, fast to solve. However, an extremely fine grid is required to resolve the gradient of the electric field caused by charged particles in close proximity.

Assuming the charge of each particle is located at its centre point, a mathematical equivalent formulation to Eq. (8) is Coulomb's law,

$$\boldsymbol{E}_m = \sum_{n=1,n\neq m}^{N} \frac{Q_n\,\boldsymbol{z}_{n,m}}{4\,\pi\,\varepsilon_0\,|\boldsymbol{z}_{n,m}|^3}\,. \tag{9}$$

Herein, $\boldsymbol{E}_m$ is the electric field at the position of particle m, N the number of all particles in the system, and $\boldsymbol{z}_{n,m}$ a vector pointing from the centre of particle n to the centre of particle m.

Equation (9) contains only Lagrangian variables and, therefore, requires no grid to solve. Drawback compared to Eq. (8) is that it involves comparisons of particle pairs, thus, $O(N^2)$ operations.

Similar solutions to this problem were independently proposed by Kolehmainen et al. (2016) and Grosshans and Papalexandris (2017b), combining the numerical advantages of Gauss' and Coulomb's law. More specifically, their hybrid approaches superimpose the far-field interactions computed with

Eq. (eq:gauss) and the Coulombic interactions between the particle and its neighboring particles. This approach is both fast and accurate and generally recommended for future simulations. In particular, it is more suitable for wall-bounded flows than the Ewald summation or the P^3M method (Yao and Capacelatro, 2016).

Nevertheless, the point charge assumption impedes the prediction of particle dynamics resulting from inhomogeneous charge distribution on the particles' surface. For example, the attraction of particles of the same polarity due to induced charges (Qin et al., 2016) cannot be captured. For fluidized beds, Kolehmainen et al. (2018a) recently included particle polarization due to surrounding charges. The development of advanced numerical models reflecting the surface charge distribution is expected to boost the accuracy of future pneumatic conveying simulations.

3.3 Eulerian

The Eulerian-Lagrangian approach suits especially numerical studies of laboratory-scaled systems. But even the expense of $O(N)$ operations limits the number of particles that can be computed simultaneously. Contrary, the description of powder in Eulerian framework opens the possibility to handle complete technical flows consisting of a vast amount of particles. In Eulerian description, the powder is treated as a continuum whose properties are averaged in each computational cell.

While the Eulerian-Eulerian approach is popular for general powder flow simulations, only recently a few studies appeared where it was employed to the charge generation of particle-laden flows. Kolehmainen et al. (2018b) developed a two-fluid model including the effect of electrostatic forces on the particles and charge diffusion through the random motion of particles. Ray et al. (2018) and Montilla et al. (2020) developed new formulations to compute electrostatic charging of particles in Eulerian framework. Whereas the mentioned works are limited to mono-disperse particle size distributions, Ray et al. (2020) expanded their earlier model to bi-disperse granular flows. Finally, Zeybek and Grosshans (2021) presented a description for the transport of charged poly-disperse powder in Eulerian framework using the direct quadrature method of moments (DQMOM) (Marchisio and Fox, 2005).

All these Eulerian formulations are steps toward the simulation of the charge build-up in technical flow facilities. Nevertheless, the accuracy of these models lacks way behind Lagrangian formulations.

4 Particle charging models

All methods discussed in the previous section to simulate pneumatic powder conveying assume the particles to be smaller than the cells of the computational mesh. In other words, the numerical grid does not resolve the gas-solid interfaces. Thus, all physical processes taking place on the particles' surface need to be modeled explicitly. These processes include, for example, aerodynamic drag, heat and mass transfer, collisions, phase change, adhesion, and chemical reactions. Often the underlying physics of these processes is complex and sometimes not even understood yet. Complex physical mechanisms needs to be simplified to obtain a computational efficient model suitable for CFD simulations. Usually, the uncertainty of the particle models defines the leading error to the overall simulation model.

This section reviews CFD models for the electrostatic charge transfer between a particle and an object. The implementation in a CFD approach requires the model to be accurate, computationally efficient to handle a vast amount of particles, able to predict charge transfer based on the data available in a CFD framework, and valid for conditions relevant to technical flows. These requirements impede the usage of detailed theoretical approaches, such as quantum mechanical or atomistic calculations (Fu et al., 2017).

For more than five decades, the most spread CFD model to predict particle contact charging is the so-called *condenser model* (John et al., 1980, Masuda et al., 1976, Soo, 1971). Its name refers to the analogy of particle charging to the temporal response of a capacitor (also known as a condenser) in a resistor-capacitor (R-C) circuit. Even though the condenser model appeared over the years in different variants, all formulations base on the same assumptions:

1. A particle charges upon contact with another surface.
2. The driving force for the charge transfer is the contact potential difference of the material pair, V, and the charge held by the particle before contact.
3. The polarity of the transferred charge is always the same.
4. The amount of transferred charge depends on the electrical properties and the contact kinematics.
5. The particle charge saturates asymptotically.

Thus, during collisions of two particles of the same material, which is the typical situation for particles being part of the same powder batch, no charge transfers because their contact potential is the same. Nevertheless, charge may exchange if at least one of the two particles carries a charge prior to the contact. In the original formulation by Soo (1971), the charge transfer between two particles, $\Delta Q_n = -\Delta Q_m$, during the collision contact time, Δt_p, reads

$$\Delta Q_n = \frac{C_n C_m}{C_n + C_m}\left(\frac{Q_m}{C_m} - \frac{Q_n}{C_n}\right)\left(1 - \mathrm{e}^{-\Delta t_\mathrm{p}/\tau_\mathrm{p}}\right) = -\Delta Q_m \,. \tag{10}$$

In the above equation, C_n and C_m denote the capacity of both particles and τ_p their charge relaxation time.

Afterward, John et al. (1980) expanded the model to the impact of a spherical particle with a plane surface such as a wall or a plate. In opposite to particle-particle collisions, in this situation, the two objects in contact are usually of dissimilar material. Thus, the total impact charge from the target to the particle, ΔQ, is given by the sum of the dynamic charge transfer to the particle caused by the contact potential, ΔQ_c, and the transferred pre-charge, ΔQ_t, i.e.,

$$\Delta Q = \Delta Q_\mathrm{c} + \Delta Q_\mathrm{t} \,. \tag{11}$$

The dynamic charge transfer during the wall-particle contact time Δt_pw is, as for a parallel plate condenser, given by

$$\Delta Q_\mathrm{c} = -CV\left(1 - \mathrm{e}^{-\Delta t_\mathrm{pw}/\tau_\mathrm{pw}}\right) \tag{12}$$

where C is the electrical capacity and τ_pw the charge relaxation time.

It is commonly assumed (John et al., 1980, Kolniak and Kuczynski, 1989) that the pre-charge is distributed uniformly on the particles' surface, A_p. Further, if the charge within the particle-target contact area, A_pw, is completely transferred, ΔQ_t equals

$$\Delta Q_\mathrm{t} = -\frac{A_\mathrm{pw}}{A_\mathrm{p}} Q_n \,. \tag{13}$$

Even though this concept holds only for the transfer of electrons during the contact of conductors, is was often successfully applied to the charging of insulators by assigning an effective work function (Chowdhury et al., 2018).

As mentioned above, the condenser model went through some evolutionary steps, one being the refinement of the contact potential difference to (Matsusaka et al., 2000)

$$V = V_\mathrm{c} - V_\mathrm{e} - V_\mathrm{b} + V_\mathrm{ex} \,. \tag{14}$$

Therein, the total contact potential difference is separated into contributions by the surface work functions (V_c), the image charge (V_e), the space charge by surrounding charged particles (V_b), and other external electric fields (V_ex).

The above formulations of the condenser model assume a uniform charge distribution on the particles surface. However, charge does not distribute uniformly on insulative surfaces, such as polymers.

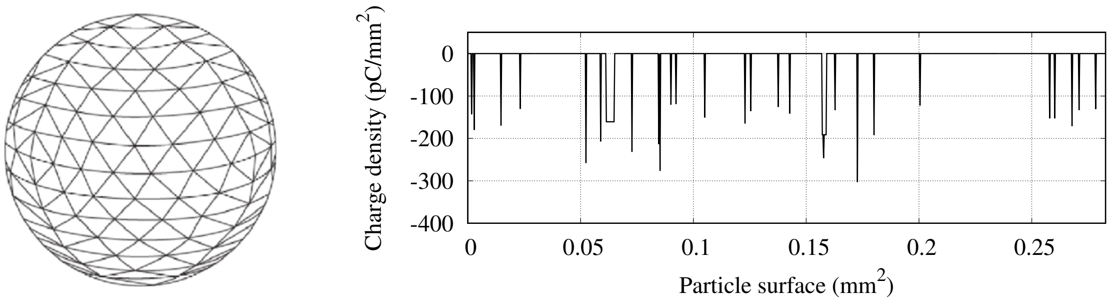

(a) *(b)*

***Fig. 3**: (a) Charging site concept of Yoshida et al. (2003). (b) Resolved charge density on a particle's surface after pneumatic conveying (Grosshans and Papalexandris, 2016b).*

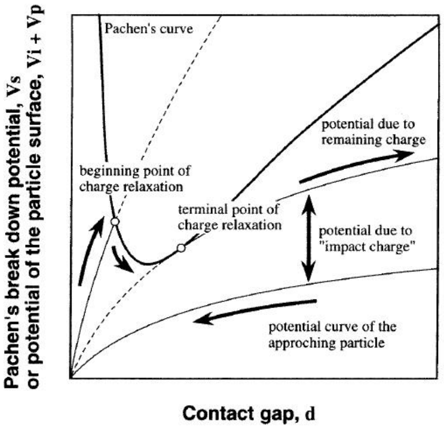

***Fig. 4**: Charge relaxation model (Matsuyama and Yamamoto, 1995).*

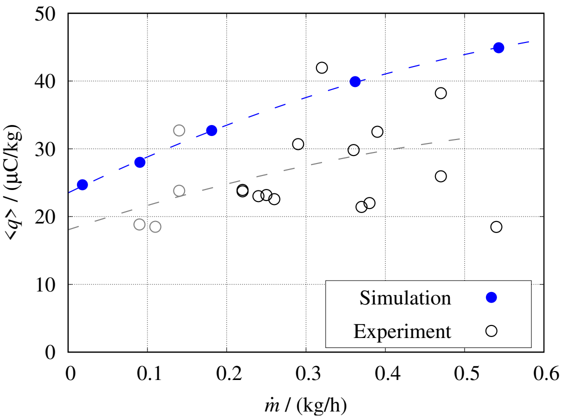

***Fig. 5**: CFD simulations of the electrification of PMMA particles during conveying using an empirical charging model.*

Therefore, the strong scatter of the impact charge in the single-particle experiments of Matsuyama et al. (2003) was attributed to a non-uniform charge distribution on the particle's surface.

As response to the observed scatter, several models resolve the charge location on particle surfaces. Yoshida et al. (2003) introduced the concept of charging sites which take up charge individually, see Fig. 3a. Using the concept of charging sites, (Grosshans and Papalexandris, 2016b) extended the condenser model to the *non-uniform charge model* for particle/surface and inter-particle collisions. This formulation leads to a wide range of possible outcomes of a contact event, which partially explains the scatter of the experimentally measured charging behavior of a single PTFE particle. The non-uniform charge model was used to simulate pneumatic powder transport. Figure 3b shows the resolved charge on the particle surface after leaving the duct. Each peak is caused by an impact. Some peaks even overlap each other, which means the particle impacted at a location of a charge spot left by a previous impact.

Another group of charging models relies on the surface state theory (Lowell and Truscott, 1986a,b). According to it, electrons with high energy levels exist only at the surface of insulators and can transfer to empty surface states of another insulator upon contact driven by their different effective work functions. These models aim to explain the charging of particles made of the same material. The low-density limit was recently utilized in models (Duff and Lacks, 2008), in a probabilistic version (Lacks and Levandovsky, 2007), and in a more general formulation considering the transfer of any charged species (Konopka and Kosek, 2017). By assuming the transfer of charge carriers from one particle to another until they are depleted, the results of this model agreed with two trends in observed in powder flows: particles charge stronger in highly poly-disperse systems, and big particles are usually positively and small particles negatively charged.

More a charge limitation than a generation model is the *charge relaxation model* (Matsuyama and Yamamoto, 1995) whose principle is visualized in Fig. 4. Therein, the arrows present the evolution of the potential difference between the particle and the wall, which increases after contact. Discharge takes place at the contact gap where the potential difference equals the gaseous breakdown limit potential, which is given by Paschen's law. Thus, this model limits the predicted charge exchange.

Finally, a purely empirical charging model was recently proposed by Grosshans et al. (2021) for spherical PMMA particles. The model bases on data from single-particle experiments using the precise same particles as in the simulations. The CFD simulations agree well with experiments, see Fig. 5, for 200 μm particles, but fail for 100 μm particles.

However, this model, just as all above-discussed charging models, handles only very specific situations. A generally predictive charging model that satisfies the requirements of a CFD tool is not in reach yet. Thus, in the foreseeable future, the particle charging model will remain the largest contributor to the overall error of CFD simulations of powder flow electrification.

5 Perspectives for future research

Due to its outstanding complexity, the CFD simulation of powder electrification fails so far. It requires the solution of an interdisciplinary mathematical model describing turbulence, electrostatics, and triboelectric charging. This paper reviewed the state-of-the-art and pinpointed toward the future research necessary to improve the numerical predictions. Highly-resolved direct numerical simulations of the carrier gas flow combined with Lagrangrian simulations of the particle dynamics offer insight in the detailed mechanics of powder charging. Understanding the dependence of powder charging rate on the conveyors operating parameters, such as velocity or powder mass flow rate, can guide the design of future, safe conveying systems. The largest contributor to the error of current simulations is the particle charging model. A generally valid, predictive model seems currently out of reach. But new single-particle experiments that deliver impact data tailored to pneumatic conveying can improve the accuracy of models for specific particles. Finally, recent Eulerian-Eulerian formulations open a way to the simulation of powder charging in complete flow facilities. The next step is to improve the handling of Euler-Euler models of polydisperse particle size distributions.

Acknowledgements

This project has received funding from the European Research Council (ERC) under the European Union's Horizon 2020 research and innovation programme (grant agreement No. 947606 PowFEct).

References

Baldwin, B. S., Lomax, H. (1978). *Thin-layer approximation and algebraic model for seperated turbulent flow*. AIAA Paper, 78(257).

Bardina, J., Ferziger, H., Reynolds, W. C. (1980). *Improved subgrid models for large eddy simulation*. AIAA Paper, 80(1357).

Boris, J. P., Grinstein, F. F., Oran, E. S., Kolbe, R. L. (1992). *New insights into large eddy simulation*. Fluid Dyn. Res., 10:199–228.

Chowdhury, F., Ray, M., Sowinski, A., Mehrani, P., Passalacqua, A. (2021). *A review on modeling approaches for the electrostatic charging of particles*. Powder Technol., 389:104–118.

Chowdhury, F., Sowinski, A., Ray, M., Passalacqua, A., Mehrani, P. (2018). *Charge generation and saturation on polymer particles due to single and repeated particle-metal contacts*. J. Electrostat., 91:9–15.

Crowe, C., Schwarzkopf, J. D., Sommerfeld, M., Tsuji, Y. (2012). *Multiphase Flows with Droplets and Particles*. CRC Press, Boka Raton, FL, second edition.

Dhodapkar, S. (1991). *Flow Pattern Classification in Gas-Solid Suspensions*. Ph.D. thesis, University of Pittsburgh.

Duff, N., Lacks, D. J. (2008). *Particle dynamics simulations of triboelectric charging in granular insulator systems*. J. Electrost., 66:51–57.

Elgobashi, S. (1994). *On predicting particle-laden turbulent flows*. Appl. Sci. Res., 52:309–329.

Fu, R., Shen, X., Lacks, D. J. (2017). *First-principles study of the charge distributions in water confined between dissimilar surfaces and implications in regard to contact electrification*. J. Phys. Chem. C, 121:12345–12349.

Germano, M., Piomelli, U., Moin, P., Cabot, W. H. (1991). *A dynamic subgrid-scale eddy viscosity model*. Phys. Fluids A, 3(7):1760–1765.

Grosshans, H., Papalexandris, M. V. (2016a). *Large eddy simulation of triboelectric charging in pneumatic powder transport*. Powder Technol., 301:1008–1015.

Grosshans, H., Papalexandris, M. V. (2016b). *A model for the non-uniform contact charging of particles*. Powder Technol., 305:518–527.

Grosshans, H., Papalexandris, M. V. (2017a). *Direct numerical simulation of triboelectric charging in a particle-laden turbulent channel flow*. J. Fluid Mech., 818:465–491.

Grosshans, H., Papalexandris, M. V. (2017b). *On the accuracy of the numerical computation of the electrostatic forces between charged particles*. Powder Technol., 322:185–194.

Grosshans, H., Papalexandris, M. V. (2018). *Exploring the mechanism of inter-particle charge diffusion*. Eur. Phys. J. Appl. Phys., 82(1):11101.

Grosshans, H., Xu, W., Matsuyama, T. (2021). *Simulation of PMMA powder flow electrification using a new charging model based on single-particle experiments*. subm. to Chem. Eng. Sci.

Jin, X., Marshall, J. S. (2017). *The role of fluid turbulence on contact electrification of suspended particles*. J. Electrostat., 87:217–227.

John, W., Reischl, G., Devor, W. (1980). *Charge transfer to metal surfaces from bouncing aerosol particles*. J. Aerosol Sci., 11(2):115–138.

Jones, W. P., Launder, B. E. (1972). *The prediction of laminarization with a two-equation model of turbulence*. Int. J. Heat Mass Transfer, 15:301–314.

Klahn, E., Grosshans, H. (2020). *An accurate and efficient algorithm to model the agglomeration of macroscopic particles*. J. Comput. Phys., 407:109232.

Klinzing, G. E. (2018). *A review of pneumatic conveying status, advances and projections*. Powder Technol., 333:78–90.

Kolehmainen, J., Ozel, A., Boyce, C. M., Sundaresan, S. (2016). *A hybrid approach to computing electrostatic forces in fluidized beds of charged particles*. AIChE J., 62:228.

Kolehmainen, J., Ozel, A., Gu, Y., Shinbrot, T., Sundaresan, S. (2018a). *Effects of polarization on particle-laden flows*. Phys. Rev. Lett., 124503:1–5.

Kolehmainen, J., Ozel, A., Sundaresan, S. (2018b). *Eulerian modelling of gas–solid flows with triboelectric charging*. J. Fluid Mech., 848:340–369.

Kolniak, P. Z., Kuczynski, R. (1989). *Numerical modeling of powder electrification in pneumatic transport*. J. Electrostat., 23:421–430.

Konopka, L., Kosek, J. (2017). *Discrete element modeling of electrostatic charging of polyethylene powder particles*. J. Electrostat., 87:150–157.

Korevaar, M. W., Padding, J. T., van der Hoef, M. A., Kuipers, J. A. M. (2014). *Integrated DEM-CFD modeling of the contact charging of pneumatically conveyed powders*. Powder Technol., 258:144–156.

Kravets, B., Rosemann, T., Reinecke, S., Kruggel-Emden, H. (2019). *A new drag force and heat transfer correlation derived from direct numerical LBM-simulations of flown through particle packings*. Powder Technol., 345:438–456.

Lacks, D. J., Levandovsky, A. (2007). *Effect of particle size distribution on the polarity of triboelectric charging in granular insulator systems*. J. Electrost., 65:107–112.

Lacks, D. J., Shinbrot, T. (2019). *Long-standing and unresolved issues in triboelectric charging*. Nature Rev. Chem., 3:465–476.

Liu, S., Meneveau, C., Katz, J. (1994). *On the properties of similarity subgrid-scale models as deduced from measurements in a turbulent jet*. J. Fluid Mech., 275:83–119.

Lowell, J., Truscott, I. (1986a). *Triboelectrification of identical insulators. I. An experimental investigation*. J. Phys. D: Appl. Phys., 19:1273.

Lowell, J., Truscott, I. (1986b). *Triboelectrification of identical insulators. II. Theory and further experiments*. J. Phys. D: Appl. Phys., 19:1281.

Marchioli, C., Picciotto, M., Soldati, A. (2007). *Influence of gravity and lift on particle velocity statistics and transfer rates in turbulent vertical channel flow*. Int. J. Multiphase Flow, 33:227–251.

Marchisio, D. L., Fox, R. O. (2005). *Solution of population balance equations using the direct quadrature method of moments*. J. Aerosol Sci., 36(1):43–73.

Masuda, H., Komatsu, T., Iinoya, K. (1976). *The static electrification of particles in gas-solids pipe flow*. AIChE J., 22:558–564.

Matsusaka, S., Gadhiri, M., Masuda, H. (2000). *Electrification of an elastic sphere by repeated impacts on a metal plate*. J. Phys. D: Appl. Phys., 33:2311–2319.

Matsusaka, S., Maruyama, H., Matsuyama, T., Ghadiri, M. (2010). *Triboelectric charging of powders: A review*. Chem. Eng. Sci., 65:5781–5807.

Matsuyama, T., Ogu, M., Yamamoto, H., Marijnissen, J. C. M., Scarlett, B. (2003). *Impact charging experiments with single particles of hundred micrometre size*. Powder Technol., 135–136:14–22.

Matsuyama, T., Yamamoto, H. (1995). *Charge relaxation process dominates contact charging of a particle in atmospheric conditions*. J. Phys. D: Appl. Phys., 28:2418–2423.

Matsuyama, T., Yamamoto, H. (1997). *Charge relaxation process dominates contact charging of a particle in atmospheric conditions: II. The general model*. J. Phys. D: Appl. Phys., 30:2170–22175.

Maxey, M. R., Riley, J. J. (1983). *Equation of motion for a small rigid sphere in a nonuniform flow*. Phys. Fluids, 26:883–889.

Mehrani, P., Murtomaa, A., Lacks, D. (2017). *An overview of advances in understanding electrostatic charge buildup in gas-solid fluidized beds*. J. Electrostat., 87:64–78.

Montilla, C., Ansart, R., Simonin, O. (2020). *Modelling of the mean electric charge transport equation in a mono-dispersed gas–particle flow*. J. Fluid Mech., 902:A12. doi:10.1017/jfm.2020.577.

Myler, C. (1987). *Use of Thermodynamic Analogy for Horizontal Pneumatic Conveying*. Ph.D. thesis, University of Pittsburgh.

Ozler, G. (2022). *Influence of Drag Force Modelling on the Flow of Electrically Charged Particles*. Master's thesis, Ege University, Turkey.

Qin, J., Li, J., Lee, V., Jaeger, H., de Pablo, J. J., Freed, K. F. (2016). *A theory of interactions between polarizable dielectric spheres*. J. Colloid Interface Sci., 469:237–241.

Ray, M., Chowdhury, F., Sowinski, A., Mehrani, P., Passalacqua, A. (2018). *An Euler-Euler model for mono-dispersed gas-particle flows incorporating electrostatic charging due to particle-wall and particle-particle collisions*. Chem. Eng. Sci., 197:327–344.

Ray, M., Chowdhury, F., Sowinski, A., Mehrani, P., Passalacqua, A. (2020). *Eulerian modeling of charge transport in bi-disperse particulate flows due to triboelectrification*. Phys. Fluids, 32(2):023302.

Rokhlin, V. (1990). *Rapid solution of integral equations of scattering theory in two dimensions*. J. Comput. Phys., 86:414–439.

Schiller, L., Naumann, A. Z. (1933). *A drag coefficient correlation*. Z. Ver. Dtsch. Ing., 77:318–320.

Smagorinsky, J. (1963). *General circulation experiments with the primitive equations: I. The basic equations*. Mon. Weather Rev., 91:99–164.

Soo, S. L. (1971). *Dynamics of charged suspensions*. In *Topics in Current Aerosol Research*, pages 71–73. Pergamon Press.

Tang, Y., Peters, E. A. J. F., Kuipers, J. A. M., Kriebitzsch, S. H. L., van der Hoef, M. A. (2015). *A new drag correlation from fully resolved simulations of flow past monodisperse static arrays of spheres*. AIChE J., 61(2):688–698.

Tanoue, K., Ema, A., Masuda, H. (1999). *Effect of material transfer and work hardening of metal surface on the current generated by impact of particle*. J. Chem. Eng. Jpn., 32:544–548.

Tanoue, K., Tanaka, H., Kitano, H., Masuda, H. (2001). *Numerical simulation of tribo-electrification of particles in a gas-solid two-phase flow*. Powder Technol., 118:121–129.

Tomas, J., Kleinschmidt, S. (2009). *Improvement of flowability of fine cohesive powders by flow additives*. Chem. Eng. Technol., 32:1470–1483.

Watanabe, H., Samimi, A., Ding, Y. L., Ghadiri, M., Matsuyama, T., Pitt, K. G. (2006). *Measurement of charge transfer due to single particle impact*. Part. Part. Syst. Char., 23:133–137.

Wilcox, D. C. (1998). *Turbulence Modeling for CFD*. DCW Industries, 2nd edition.

Wong, J., Kwok, P. C. L., Chan, H.-K. (2015). *Electrostatics in pharmaceutical solids*. Chem. Eng. Sci., 125:225–237.

Yao, Y., Capacelatro, J. (2016). *Competition between drag and coulomb interactions in turbulent particle-laden flows using a coupled-fluid–ewald-summation based approach*. Phys. Rev. Fluids, 3:034301.

Yoshida, M., Shimosaka, A., Shirakawa, Y., Hidaka, J., Matsuyama, T., Yamamoto, H. (2003). *Experimental and theoretical approaches to charging behaviour of polymer particles*. Powder Technol., 135/136:23–35.

Zastawny, M., Mallouppas, G., Zhao, F., van Wachem, B. (2012). *Derivation of drag and lift force and torque coefficients for non-spherical particles in flows*. Int. J. Multiphase Flow, 39:227–239.

Zeng, L., Najjar, F., Balachandar, S., Fischer, P. (2009). *Forces on a finite-sized particle located close to a wall in a linear shear flow*. Phys. Fluids, 21(3):033302.

Zeybek, M., Grosshans, H. (2021). *Eulerian formulation for the triboelectric charging of polydisperse powder flows*. Phys. Fluids, 33:63304.

DOI: 10.7795/810.20221124

Classification of Dispersibility for Combustible Dust based on Hausner Ratio

Yajie Bu [a,b], Albert Addo [c], Paul Amyotte [c] & Chunmiao Yuan [a]

[a] Fire & Explosion Protection Laboratory, Northeastern University, Shenyang, China
[b] College of Safety Science and Engineering, Nanjing Tech University, Nanjing, China
[c] Department of Process Engineering & Applied Science, Dalhousie University, Halifax, Canada

E-mail: yajiebu@foxmail.com

Abstract

Mixing of combustible dust and oxidant is one of five essential prerequisites in the dust explosion pentagon, requiring that particles originally in mutual contact within the deposits be separated and suspended in the air. However, dust dispersion never proceeds with 100% efficiency, with inevitable particle agglomeration, and an inherent trend toward settling out of suspension. Dispersibility is defined to describe the ease of dispersion of a dust and the tendency of the particulate matter to remain airborne once a dust cloud has been formed. Pioneers made contributions to classify dust dispersibility by introducing dustiness group (DG), dustability index (DI), NIOSH dispersion chamber and in-situ particle size analysis. Issues remained including the difficulty in comparing results from different methods, as well as the availability of some high-tech testing apparatus.

This study aims to provide a quick and universal testing method to estimate the dispersion property of combustible dust. A new dispersibility classification was developed based on dimensionless numbers Hausner ratio and Archimedes number. Four dispersibility classes (DCs) were proposed from one to four, with a larger number meaning better dispersibility. Results for more than a dozen dust samples and mixtures thereof showed the new method is useful in dust explosion research. The consistency in classifying dust dispersion properties between the DC method and previous methods was good. Changes in DC well explained our earlier findings on suppressant enhanced explosion parameter (SEEP) phenomenon attributed to the improvement in dust dispersibility. Hausner ratio, as one easily measured parameter, can be quite advantageous to assess dust dispersibility, permitting a proper risk assessment for the formation of explosible dust clouds.

Keywords: *dust explosion*, *dust dispersibility*, *Hausner ratio*, *explosion parameter*

1. Introduction

Dust explosion is a phenomenon resulting from the rapid chemical oxidation of particles dispersed in air that generates a sudden release of energy. Requirements for the occurrence of a dust explosion include the familiar prerequisites of a fuel, an oxidant, and an ignition source, augmented by mixing of the fuel and oxidant, as well as confinement of the resulting mixture. These five components are known to form the explosion pentagon, which provides fundamental level information about dust explosion causation in many respects (Amyotte, 2014).

Abundant research associated with dust explosions normally focuses on one of the five components or connections between the various pentagon elements. For instance, scores of hot keywords in the dust explosion field are listed as the following (labelled with the applicable pentagon element):

> dust chemistry (fuel), particle size (fuel), moisture content (fuel), explosible limit (fuel), hybrid mixture (fuel), inerting (fuel/oxidant), equivalence ratio (fuel/oxidant), oxygen content (oxidant),

oxidizing gas (oxidant), electric spark (ignition source), hot surface (ignition source), mechanical spark (ignition source), smoldering (fuel/ignition source), turbulence (mixing), degree of dispersion (mixing), dust concentration (fuel/mixing), dust layer fire (fuel/mixing), explosion venting (confinement), explosion isolation (confinement), overdriving (fuel/ignition source/confinement).

The explosion pentagon is practicable in gas and vapour explosions, yet mixing combustible solids and oxidants is a unique process for a dust explosion. One feature of the formation of a dust/air suspension is that dust particles are strongly influenced by gravity, showing an inherent trend toward settling out of suspension. Some degree of turbulence, as well as local variation in concentration, will always be present in combustible dust clouds before and after ignition. In addition, a factor that must be acknowledged is the real particle size distribution, since particles originally in mutual contact may not be fully separated after the suspension. Turbulence, dust concentration and actual particle size distribution interplay with each other in dust clouds. Variation in any of these parameters can affect the explosion characteristics of a dust. With the presence of a gravitational field, uniformity and stability of the dust cloud never occur, making research on dust explosions complicated and challenging.

It is easy to understand that the formation of dust clouds relies on dispersion boundary conditions, such as the pressure of the air blast used to disperse the dust, and the volume and geometry of the space where dust is involved. It is less known that the dust dispersion process is also highly sample-specific. The ease of deposited dust to form airborne clouds and the time it takes for redeposition differs from sample to sample, depending on material properties including density, size, morphology, and moisture content. Dust dispersibility (or dustiness) is defined to describe the dispersion property, indicating the tendency of a dust to form clouds and remain airborne.

Dispersibility classification of industrial dust was conducted regarding occupational health and safety in the workplace at the very beginning. Klippel et al. (2015) gave reviews and outlooks on dust dispersibility from the perspective of workplace safety and explosion protection. Inspired by these pioneers, the current paper aims to propose a convenient and universal method to preliminarily estimate the dispersibility of a given combustible dust. Results determined by this method are compared with other existing methods.

2. A brief review of current methods

To determine dust dispersibility, light attenuation measurement and gravimetric measurement are usually applied. The three main factors considered in current methods are:

- dust concentration as a function of time;
- in-situ particle size distribution of dispersed dust clouds;
- ratio of sample mass to filled-in mass.

Each of the factors represents an aspect of dispersion properties. Specifically, dust concentration versus time shows the ability of a suspended dust to remain airborne. In-situ particle size distribution gives evidence on the degree of particle agglomeration and breakage with comparison to pre-dispersion particle size distribution. The ratio of sample and filled-in mass can be used to assess the dust deposition and mass fractions at certain points. It should be clear that good dispersibility means a small declining rate in dust concentration, a small difference between in-situ and pre-dispersion particle size distribution, and a large sample to filled-in mass ratio.

On account of related industrial scenarios, existing methods for the determination of dust dispersibility may place emphasis on different parameters. This section briefly reviews the current methods, all of which are highly relevant to the dust explosion field.

2.1 Dustiness group

A German guideline VDI 2263 part 9 (2008) describes the measurement principle of a new safety parameter, dustiness, used in explosion protection (Klippel et al., 2013a, 2013b). Dustiness is determined in equipment consisting of a sample container with a feeding system, a dust chamber, a dust concentration meter, and a data acquisition computer. The local dust concentration over time is the targeted variable to calculate the dimensionless dustiness number S of each dust:

$$S = \frac{m^3/g}{t_F + t_s} \int_0^{t_F + t_s} c(t)dt \quad (1)$$

where $c(t)$ is the measured local concentration, t_F is the time in which the dust is conveyed (300 s) and t_S is the time of sedimentation (350 s), m^3/g is unit of dust concentration. Based on the dustiness number, a combustible dust can be assigned to a dustiness group (DG). There are six dustiness groups from one to six, with DG 1 representing the worst dispersibility, and DG 6 representing the best.

2.2. *Dustability index*

Marmo et al. (2018, 2019) developed a semi-quantitative method to evaluate the dispersibility of fibrous dust through a dustability index (DI). DI is calculated as the sum of the scores assigned to three properties:

- the tendency of dust to disperse fine particles in air when handled (considering the factor of dust concentration);
- the tendency of dust to settle as aggregates or fine particles (considering the factor of particle size distribution);
- the behaviour of dust when lifted by an air blast in the Hartmann tube (considering the factor of the mass fraction).

Each property has a score from 1 to 3, resulting in a reported DI from 3 to 9, where a small number represents poor dispersibility and a large number represents good dispersibility.

2.3 *NIOSH dispersion chamber*

Perera et al. (2016) designed a dust dispersion chamber with 15.24 cm height by 15.24 cm width by 152.4 cm length to conduct quantitative laboratory-scale dispersibility experiments (hereinafter referred to as NIOSH dispersion chamber). The test samples are placed in a tray and subjected to a reproducible 0.3 s air pulse from a 2.8 bar compressed air source. The concentration of the dispersed dust cloud and the mass of dust dispersed are targeted parameters, measured by a downwind optical dust probe and the mass loss of the dust tray, respectively. In comparison to a reference sample, the relative dispersibility of various types of dust samples is determined. Although the original intention of the NIOSH dispersion chamber was to evaluate the dispersibility of rock dust, there is no doubt that this methodology is applicable for combustible dust. It provides a repeatable dynamic pressure source and quantitative measure of two crucial parameters, *i.e.*, dust concentration and mass loss.

2.4 *In-situ particle size analysis*

The earliest in-situ particle size analysis of dispersed dust clouds probably goes back to 1978 when Eckhoff and Mathisen (1978) investigated the effect of dust moisture on the degree of maize starch dispersion in a 1.2-L Hartmann bomb. The main principle is to collect dispersed dust on double-stick tape mounted on a microscope slide fixed to an adjustable circular metal plate. The collected particles, whether individual units or agglomerates are further analyzed with respect to size either by light microscopy or scanning electron microscopy to cumulate the frequency distribution. The results obtained by representative counting and sizing of about 400 agglomerates are regarded as in-situ particle size and can be used to describe the dust dispersibility. Later, Eckhoff (2003) defined the global dispersibility parameter D for specific powder deposits as follows:

$$D = k/W_{min},\ 0<k<1 \quad (2)$$

where W_{min} is the total minimum work needed to break all inter-particle bonds in a unit of the dust cloud, and k is an efficiency factor describing the degree of dispersion. A perfect dispersion has k=1, which means every individual particle is dispersed as its primary size.

Continuing with this principle, Li (2000) investigated the dispersibility (which he called dust dispersion quality) of corn starch in the 1.2-L Hartmann bomb, 20-L spherical apparatus, and a vertical duct with a vibration sieve. The dust dispersion quality during the rapid dispersion process is measured using a special sampling setup and micro-photographic technique. Bu et al. (2020a, 2020b, 2021) developed a similar method to measure the effective particle size distribution of combustible dust clouds in the presence of inert solids. Several thousands of particles are analyzed by an image particle analysis software to give size distribution for one dispersed cloud. Changes in in-situ particle size distribution reveal the influence of admixed inertants on the dispersibility of combustible dust.

The optical measurement method is another major technique for in-situ particle size analysis. Murillo et al. (2013) used a laser diffraction sensor to determine the particle size distribution during the transient dispersion process. The apparatus has an optic system composed of a laser emission and a muti-element photodetector for diffraction acquisition at a frequency of 2 distributions per millisecond. Zhang et al. (2016) used a phase Doppler particle analyzer to measure the suspended particle size distribution of nano-sized PMMA dust clouds. The system consists of a pair of transmitting and receiving optical units, a laser generating and multicolour beam separating unit, a photodetector module, and a data analysis unit. Schweizer et al. (2020) applied high-speed digital in-line holography (DIH) for volumetric and in-situ characterization of dust clouds near the ignition zone of a Kühner MIKE3 MIE device. The recorded holograms around 120 ms after dispersion are analyzed on a workstation with DIH processing codes for in-situ particle diagnostics.

At present, in-situ particle size analysis is widely applied in determining the degree of agglomeration of combustible nanoparticles, and the dust cloud dynamics in specific vessels (Zhang et al., 2017; Murillo et al., 2018; Santandrea et al., 2019, 2020, 2021; Serrano et al., 2021; Prasad et al., 2021a, 2021b). It is foreseeable that the methodology will be highly desirable for dispersibility classification in the dust explosion and process safety research field.

3. A new dust dispersibility classification

The review shows different pathways toward addressing fundamental dust cloud formation within industry-relevant contexts. As dispersibility classification has become an interesting area for dust explosion research, the remaining issues require solutions. On the one hand, the targeted parameters are different in various test methods, leading to difficulties in comparing obtained results with each other. On the other hand, the availability and practicability of some above-mentioned high-tech testing apparatus should be considered before popularizing a worldwide methodology. This section gives a preliminary attempt to solve the issues by introducing a standardized dimensionless number in dust dispersibility classification.

3.1 Hausner ratio of combustible dust

Hausner ratio (HR), introduced by Hausner in 1967, is defined as the ratio between the tapped and aerated bulk densities. HR is commonly used to assess flow behaviour and to compare materials, being popular in industry and academia due to the simplicity and rapidity of measurement. A lower HR value indicates a powder system with better flowability, while a higher value means greater cohesion.

The logic of using HR to classify dust dispersibility is based on the particle interactions. HR is an indicator of the strength of particle interactions; it increases as the inter-particle forces increase. With increasing inter-particle forces, the total minimum work needed to break all the inter-particle bonds increases. As the same energy is available under a certain boundary condition, the degree of dust dispersion tends to be less complete as calculated by equation (2). It then follows that the HR value is a direct function of dust dispersibility.

To explore the connection between HR and dust dispersibility, more than a dozen combustible dusts and their mixtures are selected as test samples in this paper. HR measurement follows the ASTM D6393 standard. Aerated bulk density is measured after freely pouring the powder into a vessel, and tapped bulk density is considered as the asymptotic constant density obtained during tapping until no further volumes change occur. A more practical equation widely used to calculate HR is given by volume changes in a graduated cylinder after an adequate number of taps:

$$\mathrm{HR} = \frac{\rho_n}{\rho_0} = \frac{V_0}{V_n} \tag{3}$$

where ρ_0 and V_0 are the aerated bulk density and powder volume, and ρ_n and V_n are the tapped bulk density and powder volume after n taps, respectively. Results of HR values for selected dust samples are listed in Table 1.

Table 1: *Dispersion properties of selected combustible dust*

Dust sample	**D_{50}, μm**	**Hausner ratio**	**Dustability index**	**Dustiness group**
Acetaminophen (APAP)	32.7	2.08	3	-
APAP+1% nano-silica	-	1.59	6	-
Activated charcoal	35.7	1.59	6	-
Aluminum (Al)	33.5	1.18	8	-
Al+10% nano-alumina	-	1.41	6	-
Anthraquinone #1	45.9	1.39	7	-
Anthraquinone #2	6.4	1.88	4	-
Ascorbic acid	55.4	1.50	5	-
Corn starch	14.1	1.49	6	DG 4 (13.5 μm)
Lignite	54.8	1.35	8	DG 6 (37.7 μm)
Lycopodium #1	29.2	1.31	9	-
Lycopodium #2	37.6	1.26	9	-
Microcrystalline cellulose (MCC)	37.3	1.64	6	-
MCC+1% nano-silica	-	1.51	7	-
Nicotinic acid #1	42.6	1.48	6	-
Nicotinic acid #2	28.8	1.72	3	-
Polyethylene (PE)	56.0	1.68	5	-
Potato starch	32.3	1.38	6	DG 6 (45.7 μm)
Skimmed milk	91.8	1.21	7	DG 3 (45.4 μm)
Sulfur	34.3	1.59	4	-
Wheat flour	64.8	1.70	4	DG 1 (65.4 μm)
Wood dust #1	136.0	1.86	5	DG 2 (260.3 μm)
Wood dust #2	50.6	1.91	4	DG 2 (260.3 μm)

Note: Hausner ratio (HR) is measured by the current authors following ASTM D6393;
Dustablity index (DI) is determined by the current authors based on criterion proposed by Marmo et al. (2018);
Dustiness group (DG) data is quoted from Klippel et al. (2013a).

3.2 Comparison of different methods

In addition to HR, Table 1 gives dispersion properties determined by dustability index and dustiness group. The median particle sizes of samples are also given for reference. It should be noted that DI scores are based on the subjective judgement of the current authors.

Fig. 1 plots the dispersion properties determined by the different methods. The larger size of a plotted circle represents a larger median particle size of the sample. Generally, it is found that HR values monotonically decrease with increasing DI scores. Comparison between HR and DI shows consistency in classifying dust dispersibility. When taking DG into account, comparison becomes more difficult because the HR and DI values for samples used in Klippel et al.'s study (2013a) cannot be obtained. If replaced by HR data from the current study (as shown in Fig. 1), a less obvious trend is that a smaller HR value approximately corresponds to a higher DG. Exceptions are skimmed milk powder graded as DG 3 and wood dust graded as DG 2. Both materials have very different particle sizes in Klippel et al.'s research. For the remaining four materials (*i.e.*, wheat flour, corn starch, potato starch, and lignite), particle sizes of samples in the current study are much closer to Klippel et al.'s, leading to a confirmable correlation between HR and DG. It is speculated that the assessments on dispersibility based on HR value and DG number would be consistent for the same dust sample.

For the same material, dust dispersibility is not an intrinsic property but a sample-specific parameter. A decrease in particle size causes an increase in HR value, a decrease in DI score, and less tendency to form dust clouds. This is verified by the results for anthraquinone, lycopodium, nicotinic acid, and wood dust. Effects from other factors such as moisture content, particle shape and density on dispersibility can also be reflected in changes in HR value. The HR, therefore, appears to be a good metric of dust dispersion properties.

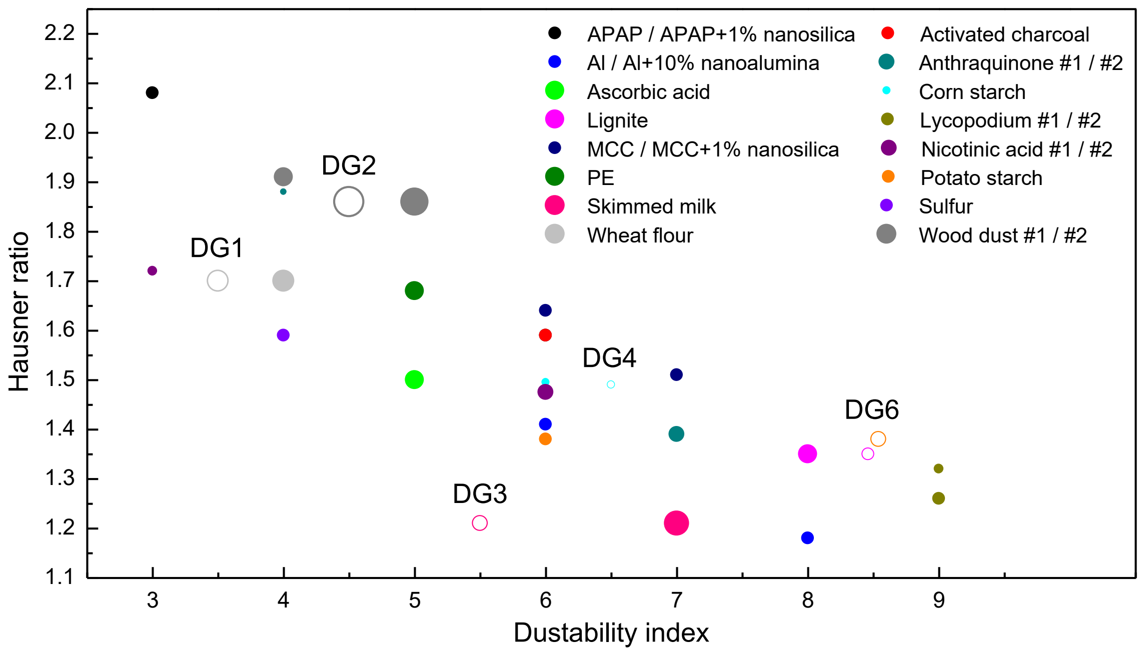

Fig. 1. *Comparison between Hausner ratio and dustability index*

3.3 *Dust dispersibility classification*

Table 2 gives the proposed new dispersibility classification based on the Hausner ratio and Archimedes number for combustible dust. Archimedes number (Ar) is defined as the ratio of the floating force to the viscous force and has been shown to accurately describe the behaviour of various powdered materials. Ar is involved to overcome some uncertainties in HR measurement, it takes particle size and density into account, as:

$$Ar = \frac{\rho(\rho_p - \rho) g d^3}{\mu^2} \tag{4}$$

where ρ is the fluid density, ρ_p is the particle density, d is the particle size, μ is the fluid viscosity, and g is the gravitational acceleration. Ar can also define the dust dispersibility and has an advantage that it requires no additional tests but only basic properties. As seen in equation (5), the HR is plotted as a function of the Ar (Kalman, 2021). This empirical equation provides the correspondence between HR and Ar in Table 2 and Fig. 2.

$$HR = 1.01 + 0.31Ar^{-0.21} \tag{5}$$

There are four dispersibility classes (DCs) ranging from DC 1 to DC 4, representing the degree of dust dispersion from very poor to good (Table 2). The borderline between good and fair is Ar=1, which is also the boundary for Geldart group A and group C powders. Most combustible dusts studied belong in group C powder, being difficult to fluidize and thereby disperse. In this study, an example of a DC 1 dust is acetaminophen, which is very cohesive and for that reason known to be difficult to handle in the pharmaceutical industry. Polyethylene with its electrostatic nature is shown to have poor dispersion as a DC 2 dust. Corn starch, a typical Geldart group C powder, is in DC 3 with fair dispersibility. Finally, lycopodium in DC 4 has good dispersibility and has been widely used as a reference dust for calibration in standard testing.

Table 2: *Dispersibility class for combustible dust*

Dispersibility class	HR	Ar	Tendency of dust dispersion	Description	Example
DC 1	>1.83	<0.01	Very poor	Severe particle agglomeration occurs; dust concentration declines rapidly in the formed dust clouds	Acetaminophen
DC 2	1.51~1.83	0.01~0.1	Poor	Moderate particle agglomeration occurs; dust concentration declines smoothly in the formed dust clouds	Polyethylene
DC 3	1.32~1.51	0.1~1	Fair	Slight particle agglomeration occurs; dust concentration is stable for a short period	Corn starch
DC 4	<1.32	>1	Good	Most particles exist as primary size; dust concentration is stable for a long period	Lycopodium

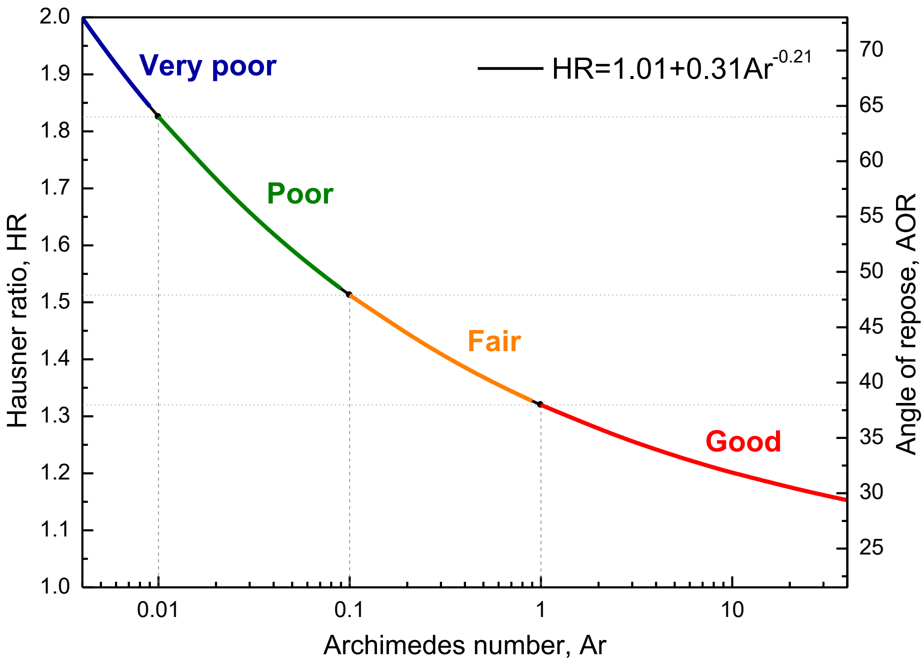

Fig. 2. *Dispersibility classification diagram*

In Fig. 2, the classification diagram for dust dispersibility is developed based on HR and Ar. Another parameter (*i.e.*, AOR, angle of repose) that corresponds to HR is also appropriate for classifying the tested materials. This diagram allows a quick assessment of the dispersion property of combustible dust. The criterion can be chosen among HR, Ar, and AOR, depending on which measurement is favoured by the user. The primary advantages of using HR are that it is relatively easy to conduct and serves to acquire a comparable engineering parameter. Using the more fundamental criterion "Ar" is prioritized if all basic properties of the sample are available or if there is difficulty in testing tapped bulk density. AOR is a substitute; it is also easy to determine but significantly affected by the test procedure.

4. Discussion of dispersibility class (DC) in dust explosions

This section gives a discussion on applying the current dispersibility classification method in dust explosion research. DC, as a new parameter, is proven to be useful in studying dust explosibility and conducting risk assessments.

4.1 Explanation of the suppressant enhanced explosion parameter (SEEP) phenomenon

For the prevention and mitigation of dust explosions, inert dusts (or suppressants) are sometimes used in industry to render the dust mixture incombustible. It has been proven that the use of inert dust in amounts less than that required for complete flame extinction can provide a false sense of safety but raise the level of consequence severity (Amyotte, 2014). Such a phenomenon is termed SEEP, where the explosion parameter is enhanced to a greater level than the pure dust.

The occurrence of SEEP is mainly attributed to the decomposition of insufficient suppressants that produce flammable gases and lead to more violent hybrid explosions. In other cases, the admixed inert solids can facilitate the ignition of the dust if notably improving its dispersion (Amyotte et al., 2005; Janès et al., 2014; Bu et al., 2021). Table 3 presents the explosibility and dispersibility class of several combustible dusts with and without small amounts of inert dusts. Among all the explosion parameters, MIE values are comparably susceptible to the additives. Enhancement in ignitability (*i.e.*, decrease in MIE) is observed for APAP, MCC and PE after admixing nano-silica. Minimal changes in MIT and P_{max} do not account for a lesser or greater explosion hazard. A 20 bar·m/s increase is found in K_{St} for APAP with 1% nano-silica, while a significant decrease occurs for Al in the presence of 10% nano-alumina.

Table 3: *Explosibility and dispersibility class of selected dust sample*

Dust sample	MIE, mJ	MIT, °C	P_{max}, bar	K_{St}, bar·m/s	HR	DC
Acetaminophen (APAP)	7	580	7.9	167	2.08	1
APAP+1% nano-silica	4	570	7.9	187	1.59	2
Aluminum (Al)	18	-	5.1	42	1.18	4
Al+10% micro-alumina	19	-	5.0	42	1.15	4
Al+10% nano-alumina	55	-	3.0	12	1.41	3
Lycopodium #1	11	440	-	-	1.31	4
Lycopodium #1+1% nano-silica	11	440	-	-	1.29	4
Microcrystalline cellulose (MCC)	17	420	8.6	154	1.64	2
MCC+1% nano-silica	15	430	8.5	148	1.51	3
Polyethylene (PE)	23	420	-	-	1.68	2
PE+1% nano-silica	20	420	-	-	1.43	3

Note: Some of the data is quoted from our previous studies.

Assuming the admixed inertants have little endothermic effect, it seemed SEEP occurs when there is a major decrease in HR or an upgrade in DC. In cases of APAP, MCC and PE, the coating nano-silica particles modify the interactions between combustible particles, easing the transformation of bulk powders into well-dispersed clouds. A better dispersibility ensures a larger total surface area for reaction available in a dust cloud. Finally, explosion enhances with upgrading DC, especially for those parameters which are highly dependent on the specific surface area of particles. An opposite example is aluminum admixed with 10% nano-alumina; the sharp increase in HR and downgrade in DC is due to the binding effect brought about by the nano-alumina as we previously reported (Bu et al., 2021). Nano-alumina with high surface energy functions as a caking agent, binding two or more Al particles together as larger-sized agglomerations. Meanwhile, the good inerting efficiency of nano-alumina accounts for the overall decline in the explosibility of aluminum. As for lycopodium, a welcome material for calibration, the explosibility stays consistent with the dispersibility.

From the current results, the dispersibility class is found to correlate quite well with the explosion parameters. This suggests the feasibility of the DC method in studying explosibility, being an addition to the previous DG, and DI classifications.

4.2 Potential application in dust hazard analysis (DHA)

After having an awareness of the process safety concerns in handling or processing combustible dust, DHA is a key step toward implementing appropriate controls to ensure the safety of operations. For identifying the hazard of atmospheres, IEC 60079-10-2 gives three zones that are associated with an environment: Zone 20, Zone 21, and Zone 22. These zones are classified considering the likelihood and duration of the presence of an explosive atmosphere in the form of a combustible dust cloud in air. The Zone system is popular around the world. However, the dispersion properties of combustible dust are not distinguished between Zones.

As dust dispersibility and boundary conditions are two key factors in the formation of dust clouds, an attempt is made to develop a two-dimensional risk matrix in this paper. The matrix uses ordinal scales for the evaluation of dispersibility and dispersion conditions. The dispersion property of specific combustible dust can be assigned a number rank in accordance with DC in Table 2. The number increases with increasing tendency to generate dust clouds, as discussed in section 3.3. The magnitude of the dispersion boundary condition is also assigned to four categories in increasing order of dispersion intensity in Table 4. Descriptions and examples are provided at the same time. The weakest dispersion condition could be the frequently occurring natural wind or artificial ventilation, while the most powerful condition is the pressure wave from a primary explosion which is not expected to occur in the lifetime of the unit.

Table 4: *Boundary conditions for dust dispersion*

Category	Description	Example
1	Frequently occur, weak dispersion condition	Natural wind, artificial ventilation
2	Occasionally occur, moderate dispersion condition	Particle lifting during normal processing
3	Barely occur, strong dispersion condition	Particle escape caused by system failure
4	Not expected to occur, extremely strong dispersion condition	Pressure wave from primary gas/dust explosion

Fig. 3 presents the matrix formatted with dispersibility classes forming the rows and boundary condition levels forming the columns. The strength of the dispersion condition increases from left to right, and the dust's tendency to disperse increases from the bottom to the top. For the ordinal measurement scale of risk, classic categories including acceptable, moderate, high, and unacceptable are used. The numerical value of the risk category increases as the risk magnitude increases. Descriptions are as follows:

- I: Acceptable risk from a dust cloud whose concentration barely reaches the MEC.
- II: Moderate risk from a small-scale explosible dust cloud which exists for a short period only.
- III: High risk from a large-scale explosible dust cloud which exists for a long period of time.

- IV: Unacceptable risk from an explosible dust cloud which fills the whole space and exists continuously.

It is observed that the risk level increases asymmetrically, influenced predominantly by the boundary condition category in the matrix. The authors believe that actual dispersion conditions play a bigger role than the dispersibility in the formation of dust clouds.

Admittedly, the use of a risk matrix is a subjective evaluation and may oversimplify the task. The DC classification is, however, shown to be a useful tool. More research is welcome to better assess the risk of combustible atmospheres that incorporate the concept of dust dispersibility.

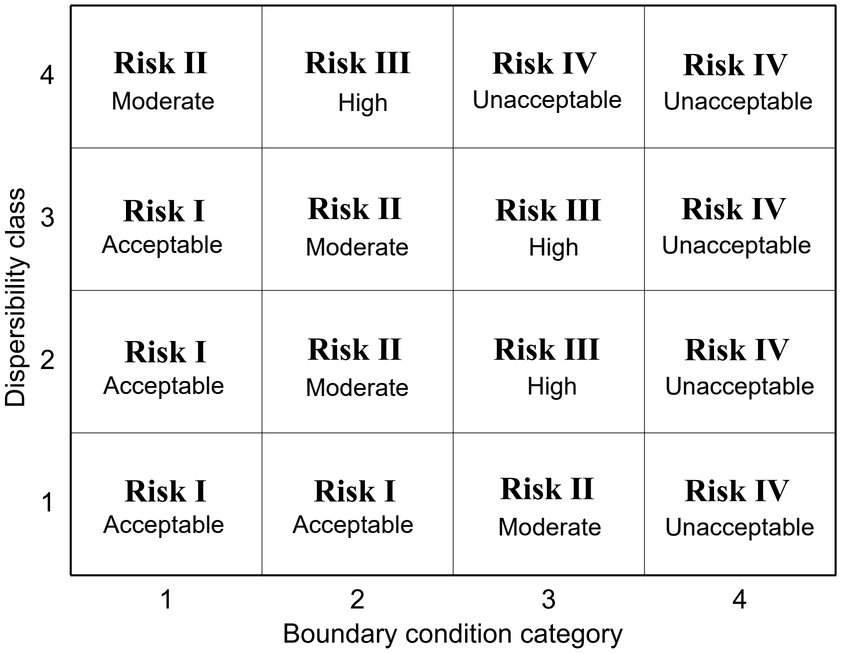

Dispersibility class \ Boundary condition category	1	2	3	4
4	**Risk II** Moderate	**Risk III** High	**Risk IV** Unacceptable	**Risk IV** Unacceptable
3	**Risk I** Acceptable	**Risk II** Moderate	**Risk III** High	**Risk IV** Unacceptable
2	**Risk I** Acceptable	**Risk II** Moderate	**Risk III** High	**Risk IV** Unacceptable
1	**Risk I** Acceptable	**Risk I** Acceptable	**Risk II** Moderate	**Risk IV** Unacceptable

Fig. 3. *Risk matrix of the formed combustible dust cloud*

5. Conclusions

Dust dispersibility is the tendency of dust to form clouds and remain airborne; this is an important safety parameter in preventing dust explosions. Previous studies prefer using light attenuation measurement and gravimetric measurement to determine dust dispersibility. A review of the existing methods shows difficulties in comparing results and accessing special high-tech apparatus. In this study, the Hausner ratio is proven to be a good indicator of the dispersion property of combustible dust. A lower HR value represents a dust with better dispersibility. Results obtained from more than a dozen of dust samples are consistent with those from previous DI and DG methods. A new classification with four dispersibility classes (DCs) is first developed based on the Hausner ratio and Archimedes number, allowing a quick and universal estimation of the dispersion property. It is expected that the proposed DC method will find usefulness in ongoing dust explosion research.

Acknowledgements

The authors gratefully acknowledge the financial contribution from the National Natural Science Foundation of China, the China Scholarship Council, and the Natural Sciences and Engineering Research Council of Canada.

References

Amyotte, P., Basu, A. & Khan, F. (2005). Dust explosion hazard of pulverized fuel carry-over. *Journal of Hazardous Materials*, 122: 23-30.

Amyotte, P.R. (2014). Some myths and realities about dust explosions, *Process Safety and Environmental Protection*, 92: 292-299.

ASTM D6393 (2014). Standard Test Method for Bulk Solids Characterization by Carr Indices.

Bu, Y., Ma, Z., Li, C., Amyotte, P., Yuan, W., Yuan, C. & Li, G. (2020a). Effect of admixed solid inertants on dispersibility of combustible dust clouds in a modified hartmann tube. *Process Safety and Environmental Protection*, 135: 1-11.

Bu, Y., Yuan, Y., Xue, S., Amyotte, P., Li, C., Yuan, W., Ma, Z., Yuan, C. & Li, G. (2020b). Effect of admixed silica on dispersibility of combustible dust clouds in a Godbert-Greenwald furnace. *Powder Technology,* 374: 496-506.

Bu, Y., Amyotte, P., Li, C., Yuan, W., Yuan, C. & Li, G. (2021). Effects of dust dispersibility on the suppressant enhanced explosion parameter (SEEP) in flame propagation of Al dust clouds. *Journal of Hazardous Materials,* 404: 124119.

Eckhoff, R.K. & Mathisen, K.P. (1978). A critical examination of the effect of dust moisture on the rate of pressure rise in Hartmann bomb tests. *Fire Safety Journal*, 1: 273-280.

Eckhoff, R.K. (2003). *Dust explosions in the process industries*. Third edition. Gulf Professional Publishing, Amsterdam.

Hausner, H. (1967). Friction conditions in a mass of metal powder. *International Journal of Powder Metallurgy*, 3: 7-13.

Janès, A., Vignes, A., Dufaud, O. & Carson, D. (2014). Experimental investigation of the influence of inert solids on ignition sensitivity of organic powders. *Process Safety and Environmental Protection*, 92: 311-323.

Kalman, H. (2021). Quantification of mechanisms governing the angle of repose, angle of tilting, and Hausner ratio to estimate the flowability of particulate materials. *Powder Technology*, 382: 573-593.

Klippel, A., Scheid, M., Koperski, J., Wappler, M. & Krause, U. (2013a). Influence of dustiness on small-scale vented dust explosions. *Journal of Loss Prevention in the Process Industries,* 26: 1433-1441.

Klippel, A., Scheid, M. & Krause U. (2013b). Investigations into the influence of dustiness on dust explosions. *Journal of Loss Prevention in the Process Industries*, 26: 1616-1626.

Klippel, A., Schmidt, M. & Krause, U. (2015). Dustiness in workplace safety and explosion protection - Review and outlook. *Journal of Loss Prevention in the Process Industries*, 34: 22-29.

Li, X. (2000). Vergleich Und Analyse Verschiedener Messverfahren Zur Bestimmung Der Mindestzundenergie Bei Staubexplosionen. Ph.D. Dissertation. Northeastern University, Shenyang, Liaoning, P.R. China, and Berufsgenossenschaft Nahrungsmittel Und Gaststatten, Mannheim, Germany.

Marmo, L., Sanchirico, R., Di Benedetto, A., Di Sarli, V., Riccio, D., & Danzi, E. (2018). Study of the explosible properties of textile dusts. *Journal of Loss Prevention in the Process Industries*, 54: 110-122.

Marmo, L. Ferri, A. & Danzi, E. (2019). Dust explosion hazard in the textile industry. *Journal of Loss Prevention in the Process Industries*, 62: 103935.

Murillo, C., Dufaud, O., Bardin-Monnier, N., López, O., Munoz, F. & Perrin, L. (2013). Dust explosions: CFD modeling as a tool to characterize the relevant parameters of the dust dispersion. *Chemical Engineering Science*, 104: 103-116.

Murillo, C., Amín, M., Bardin-Monnier, N., Muñoz, F., Pinilla, A., Ratkovich, N., Torrado, D., Vizcaya, D. & Dufaud, O. (2018). Proposal of a new injection nozzle to improve the experimental reproducibility of dust explosion tests. *Powder Technology*, 328: 54-74.

Perera, I.E., Sapko, M.J., Harris, M.L., Zlochower, I.A. & Weiss, E.S. (2016). Design and development of a dust dispersion chamber to quantify the dispersibility of rock dust. *Journal of Loss Prevention in the Process Industries,* 39: 7-16.

Prasad, S., Schweizer, C., Bagaria, P., Kulatilaka, W.D. & Mashuga, C.V. (2021a). Effect of particle morphology on dust cloud dynamics. *Powder Technology*, 379: 89-95.

Prasad, S., Schweizer, C., Bagaria, P., Saini, A., Kulatilaka, W.D. & Mashuga, C.V. (2021b). Investigation of particle density on dust cloud dynamics in a minimum ignition energy apparatus using digital in-line holography. *Powder Technology*, 384: 297-303.

Santandrea, A., Pacault, S., Perrin, L., Vignes, A. & Dufaud, O. (2019). Nanopowders explosion: Influence of the dispersion characteristics. *Journal of Loss Prevention in the Process Industries*, 62: 103942.

Santandrea, A., Gavard, M., Pacault, S., Vignes, A., Perrin, L. & Dufaud, O. (2020). 'Knock on nanocellulose': Approaching the laminar burning velocity of powder-air flames, *Process Safety and Environmental Protection*, 134: 247-259.

Santandrea, A., Pacault, S., Bau, S., Oudart, Y., Vignes, A., Perrin, L. & Dufaud, O. (2021). Safer and stronger together? Effects of the agglomeration on nanopowders explosion. *Journal of Loss Prevention in the Process Industries*, 69: 104348.

Schweizer, C., Prasad, S., Saini, A., Mashuga, C.V. & Kulatilaka, W.D. (2020). High-speed digital in-line holography for in-situ dust cloud characterization in a minimum ignition energy device. *Powder Technology*, 376: 612-621.

Serrano, J., Ratkovich, N., Muñoz, F. & Dufaud, O. (2021). Explosion severity behavior of micro/nano-sized aluminum dust in the 20L sphere: Influence of the particle size distribution (PSD) and nozzle geometry. *Process Safety and Environmental Protection*, 152: 1-13.

Verein Deutscher Ingenieure (2008). VDI-Richtlinie 2263 Part 9 "Dust Fires and Dust Explosions Hazards - Assessment - Protective Measures - Determination of Dustiness of Bulk Materials". Beuth Verlag.

Zhang, X., Yu, J., Sun, J. & Gao, W. (2016). Effects of turbulent intensity on nano-PMMA flame propagation behaviors. *Journal of Loss Prevention in the Process Industries*, 44: 119-124.

Zhang, X., Yu, J., Gao, W., Zhang, D., Sun, J., Guo, S. & Dobashi, R. (2017). Effects of particle size distributions on PMMA dust flame propagation behaviors. *Powder Technology*, 317: 197-208.

DOI: 10.7795/810.20221124

Moderation of Fe dust explosion by nano-sized Fe_2O_3 and Fe_3O_4 powders

Yongzheng Guo [a], Kaiyue Ren [a], Peng Zhao [b,c], Weixing Huang [a], Aizhu Wei [a], Dejian Wu [b,c*]

[a] School of Chemical Engineering, Sichuan University, Chengdu 610065, China
[b] Division 2.1 "Explosion Protection Gases and Dusts", Bundesanstalt für Materialforschung und -prüfung (BAM), Unter den Eichen 87, D-12205 Berlin, Germany
[c] Otto von Guericke University, Universitätsplatz 2, D-39106 Magdeburg, Germany
E-mail: dejian.wu@bam.de

Abstract: Iron powder, as one of the most abundant metal fuels that can be used as recyclable carriers of clean energy, is a promising alternative to fossil fuels in a future low-carbon economy. It may pose a potential explosion hazard during the process of processing, storage, transport and reduction/oxidation (redox). The explosion characteristics of iron dust in air were undertaken via a 20 L spherical explosion chamber with an emphasis on minimum explosion concentration (MEC) of iron dust. The alternative method of combustion duration time (t_c) was used to determine MEC, and compared with the standardized over pressure method. Two kinds of nano-sized iron oxides (Fe_2O_3 and Fe_3O_4) were used as inertants to determine the inhibition effect of different oxidation products. The experimental results showed that adding Fe_2O_3 or Fe_3O_4 could reduce the explosion severity and sensitivity of iron dust. The MEC data determined by both methods were comparable. The addition of 5 % oxide has obvious inhibition effect under 1500 g/m^3 concentration. With the increase of oxide concentration to 10 %, the inerting effect increases, and the MEC of iron dust increases more than 3 times. The increase of dust concentration will weaken the inerting effect. When the concentration increases from 500 g/m^3 to 3000 g/m^3, the weakening effect of 10 % Fe_2O_3 on the maximum explosion pressure decreases from 38.45 % to 2.24 %, and 10 % Fe_3O_4 decreases from 46.21 % to 10.63 %. These results provide a fundamental basis to mitigate the iron dust explosion via solid inerting method without adding extra elements.

Keywords: *iron; iron oxides; MEC; combustion duration time; overpressure*

1. Introduction

As a recyclable carrier of clean energy, metal fuels are expected to replace fossil fuels in the zero-carbon or extra low-carbon economy of the future (*Bergthorson 2018*). Among all materials, iron has been studied due to its abundance (*Popok et al. 2015; Lissianski et al. 2001*). Due to the heterogeneous combustion of iron on the surface, its oxidation products are easily captured and collected, and then used for reduction and recovery with clean energy such as solar energy to achieve the purpose of green recycling (*Bergthorson 2018; Bergthorson et al. 2015*). Metal fuels can be effectively kept indefinitely if they are protected from humidity and ambient air in airtight containers (*Bardsley 2008; Shkolnikov et al. 2011*), making them part of energy reserves or strategic reserves.

Fully understanding the combustion behavior of iron dust is of significance for industrial safety, combustion science and technology. Previous studies have shown that the dust explosion risk is related to many factors such as dust particle size (*Tascón 2018*), concentration (*Li et al. 2016; Zhang et al. 2018*), dispersion (*Di Sarli et al. 2014*), environmental oxygen content (*Li et al. 2009*) and ignition energy (*Going et al. 2000; Wu et al. 2009*). Among them, *Sun et al.* (*2001 & 2003*) conducted a series of studies on iron dust, such as the flame propagation mechanism, flame temperature and dust cloud behavior. They pointed out that there is no gas phase flame in the combustion of iron dust, and the number density of iron particles in the dust cloud varies with the distance from the leading edge of the combustion zone. The maximum value of number density is about 2.6 times larger than that at the region far ahead of the flame, which may affect the measurement of MEC. *Gao et al*. (*2017*) observed the high-resolution spectrum of iron combustion products and pointed out that the spectrum was decomposed into four pairs of spin orbit contributions, indicating that the combustion oxides contained Fe_2O_3, Fe_3O_4 and FeO. Dreizin (*2000*) revealed through the phase structure diagram of burning iron that in high concentration of oxygen, oxygen needs to be diffused twice from the phase interface to react with fresh iron, and the burning rate of iron at high temperature may be limited by the iron oxidation kinetics. Danzi et al. (*2021*) found that the laminar burning velocity of non-porous dust can be calculated by the maximum explosion pressure rise rate in a purely diffusive regime.

However, contact with air during processing, storage, transportation and reduction/oxidation (redox) is still unavoidable, resulting in a potential explosion hazard. *Krietsch et al.* (*2015*) even pointed out that spontaneous combustion occurs when iron powder particle size decreases to nanometer level. The US Chemical Safety Board has reported an accident that from January to May 2011, three iron dust explosions occurred at the Hoeganaes Corporation plant in Gallatin, Tennessee, resulting in four deaths and four injuries (*CSB 2011*). Therefore, it is necessary to adopt reasonable technology to prevent and mitigate explosion risk in industrial processes involving combustible metal dust.

The inerting of dust explosion based on the principle of intrinsic safety substitution and attenuation is the most commonly used method. Nitrogen, carbon dioxide and argon are common gas inertants (*Li et al. 2009*). However, the use of gas inertants is often limited by the environment, which is difficult to achieve in open spaces and can also cause asphyxiation risks (*Eckhoff 2005*). Solid inertants can well make up for this defect. Commonly used solid inertants include KCl, $CaCO_3$, $NaHCO_3$, $NH_4H_2PO_4$, etc. (*Amyotte 2006; Kuai et al. 2011a*). How to choose solid inertants depends on material properties. Experiments (*Chen et al. 2017; Dai et al. 2020; Dastidar and Amyotte 2002; Going & Snoeys 2002; Taveau et al. 2015*) show that kaolin, talcum, silicone oil, MET-L-X and Furex 770 cannot effectively inhibit the explosion of aluminum dust while the addition of carbonate and phosphate effectively inhibits the severity of explosion. In particular, metal oxides as combustion products are also a good choice for solid inerting agents (*Bu et al. 2020; Jin et al. 2021*). At the same time, the addition of metal oxides will not change the composition of products, which is a feature that other organic dusts do not have. In order to better understand the role of metal oxides in inhibiting metal dust explosion, the explosion characteristics of iron dust and its oxide dust mixed by 20 L explosion sphere chamber were studied. These results provide a basis for reducing iron dust explosion by solid inerting method without adding additional elements.

2. Experimental

2.1 Experimental Materials

The Fe dust and Fe_3O_4 dust used in the experiment were purchased from Chengdu Shengshi Technology Co., Ltd., and Fe_2O_3 dust was purchased from Chengdu Kelong Chemical Preparation Plant. The particle size distribution of dust obtained by laser particle size analyzer and Zeta nano particle size analyzer is shown in Fig. 1. The surface structure of the dust samples observed by scanning electron microscopy (SEM) is shown in Fig. 2. It can be seen from the diagram that Fe has a wide particle size distribution, irregular shape and no agglomeration, while Fe_2O_3 and Fe_3O_4 have regular spherical shapes and serious agglomeration.

In the experiment, the powder was well mixed by stirring, which was used to simulate the pre-mixing of combustible dust and inerting agent in practical work (*Dufaud et al. 2014*). Before the experiment, the experimental samples were dried at 50 °C in a vacuum oven for about 2 h to keep the moisture content below 5 wt.% (*ASTM 2007*). Then the required dust is weighed proportionally and mixed uniformly for testing.

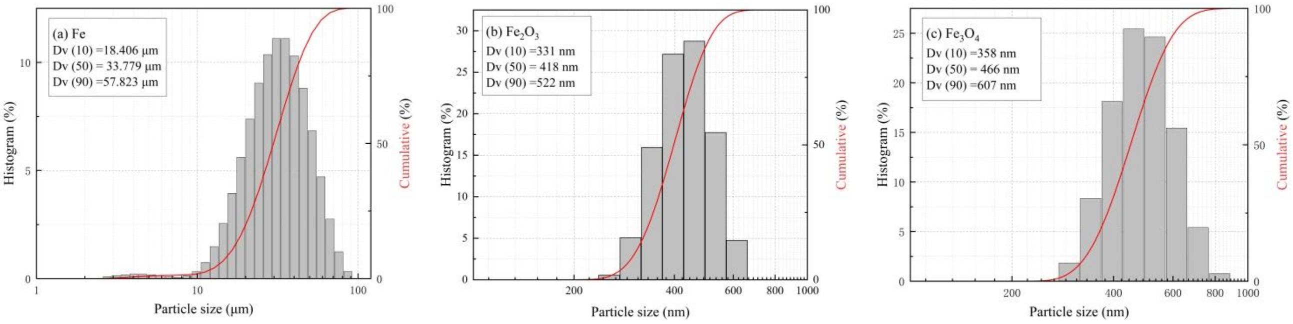

Fig. 1. *Particle size distributions of the dust samples: (a) Fe, (b) Fe_2O_3, (c) Fe_3O_4*

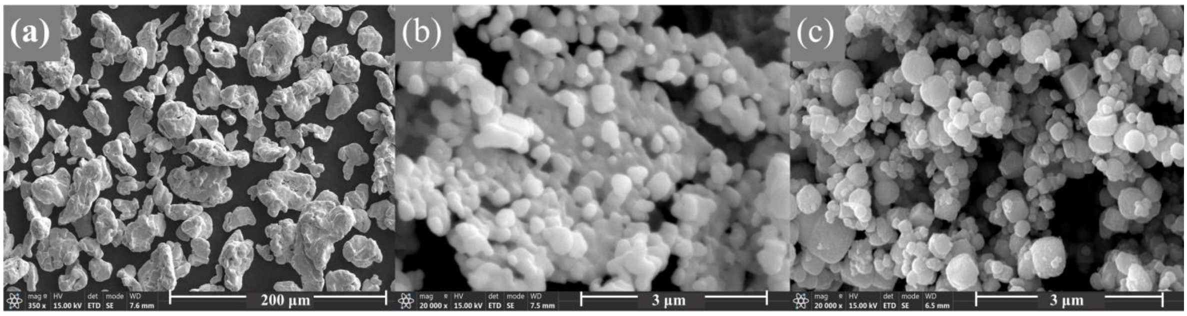

Fig. 2. *SEM images of the dust samples: (a) Fe, (b) Fe_2O_3, (c) Fe_3O_4*

2.2 Experimental apparatus, procedure and explosion criteria

The dust explosion occurs when the dust concentration exceeds a critical value, and the explosion below that concentration will not propagate. This concentration is defined as the lower explosion limit (LEL) or minimum explosion concentration (MEC) of dust. The European standard EN14034 (*EN 2006*) gives the classic MEC test method: namely, explosion overpressure method. When the measured explosion overpressure relative to the initial pressure P_i is ≥ 0.03MPa, dust suspension ignition or explosion is considered to occur. More detailed operation process is shown in Fig. 3. A series of combustion tests were carried out on iron dust using a standard 20L spherical explosive device as shown in Fig. 4. During the test, the pre-weighed dusts were filled into the dust container with a volume of 0.6 L, and then were dispersed into the 20-L spherical chamber that had been evacuated to 0.04 MPa with the help of premixed compressed gas mixture (2 MPa) and ignited by a 5-kJ chemical ignitor (*Taveau et al. 2017*). For the chemical ignitor used in the experiment, the measured average explosion pressure was 0.05MPa (i.e., P_i=0.05MPa).

In our previous study, a MEC discriminant method based on combustion duration time was proposed and used (*Yuan et al. 2012; Zhao et al. 2020 & 2021; Tan et al. 2019; Wu et al. 2022*). Dust explosions are time-dependent flame propagation processes. When the dust concentration is lower than MEC, the spacing between particles is too large, and the combustion of single particle cannot ignite its surrounding particles, and the combustion flame no longer propagates, so dust explosion will not occur. When the dust concentration reaches MEC, the spacing between particles decreases, and the spot flame formed by single particle combustion is sufficient to ignite the surrounding particles, forming a continuous combustion flame (producing flame propagation velocity), which forms a dust explosion. After that, with the increase of dust concentration, the total amount of combustible materials will gradually increase, and the flame propagation velocity will gradually increase. Therefore, there is a minimum value of flame propagation velocity at MEC, which indicates that MEC can be determined by finding the minimum value of flame propagation velocity of dust at low concentration. Using the inverse relationship between minimum flame propagation velocity and combustion duration, MEC can be determined by the maximum combustion duration.

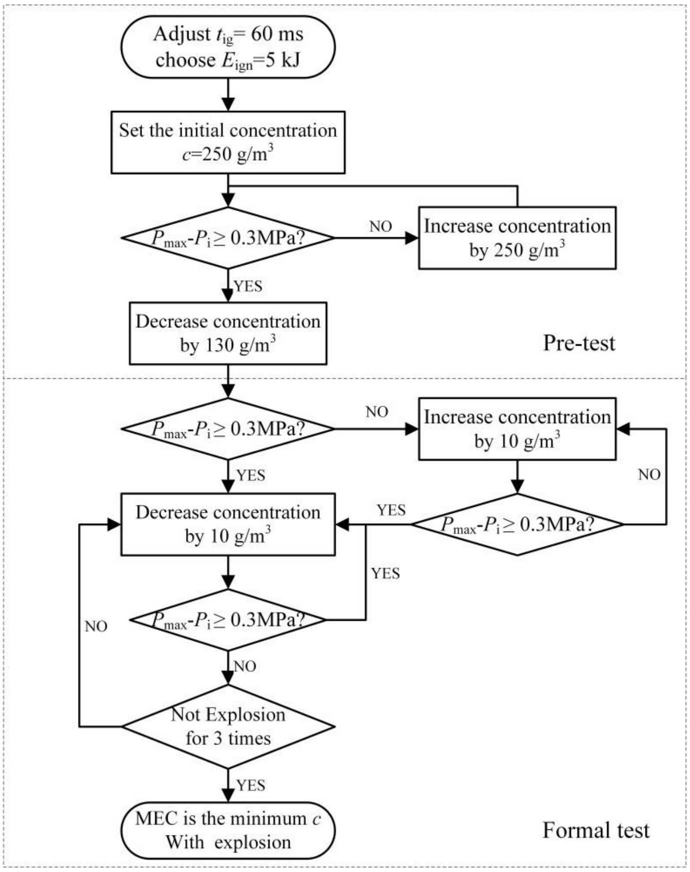

Fig. 3. *MEC test procedure*

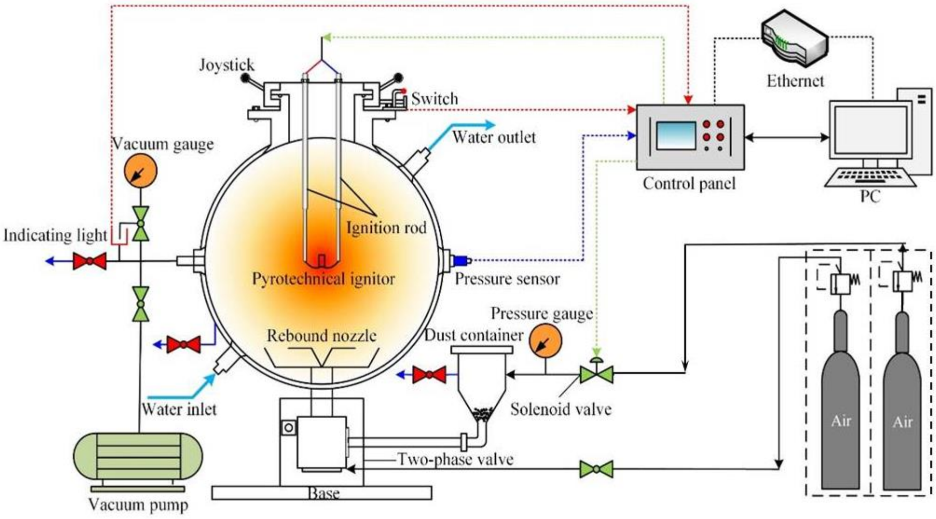

Fig. 4. *Schematic diagram of the 20-L spherical explosion test system*

Fig. 5 shows the explosion pressure-time (P-t) curve of iron dust at the concentration of 350 g/m^3 and the ignition energy of 5 kJ. It can be seen that the evolution process of dust explosion pressure can be divided into three stages. The first stage refers to the process of dust injection from t_1 to t_2, where t_{ig} is defined as ignition delay time. The second stage refers to the development of dust explosion from t_2 to t_3, where t_c is defined as combustion duration time. After t_3 the explosion ended, the pressure began to decay.

DOI: 10.7795/810.20221124

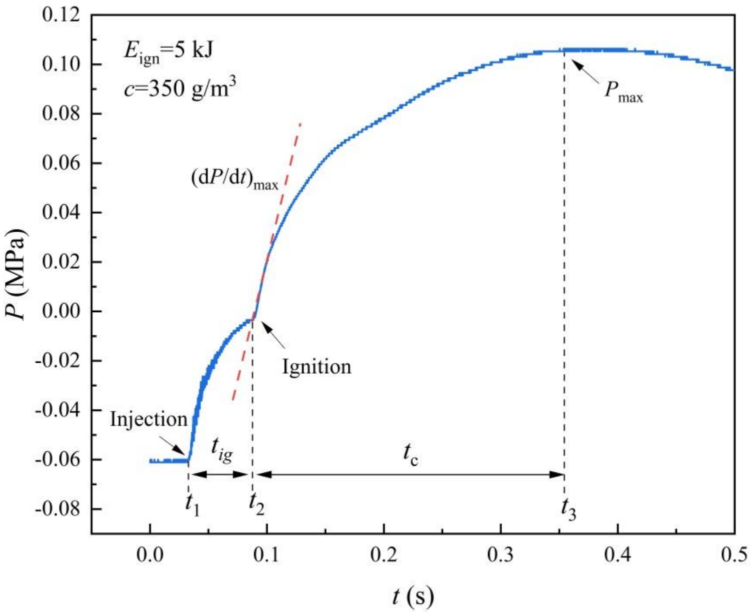

***Fig. 5.** Typical explosion process curve of iron dust in the standardized 20-L spherical chamber*

3. Results and discussion

3.1 Minimum explosion concentration of iron dust

Fig. 6 shows the MEC of iron dust in air measured by two methods, from which it can be seen that the MEC measured by the standardized over pressure method is 300 g/m^3, and measured by the combustion duration time method is 310 g/m^3. The relative error of the results obtained by the two test methods is within 5 %, indicating that the proposed combustion duration time method is also applicable to the judgment of MEC, and can be used as an alternative explosion criterion.

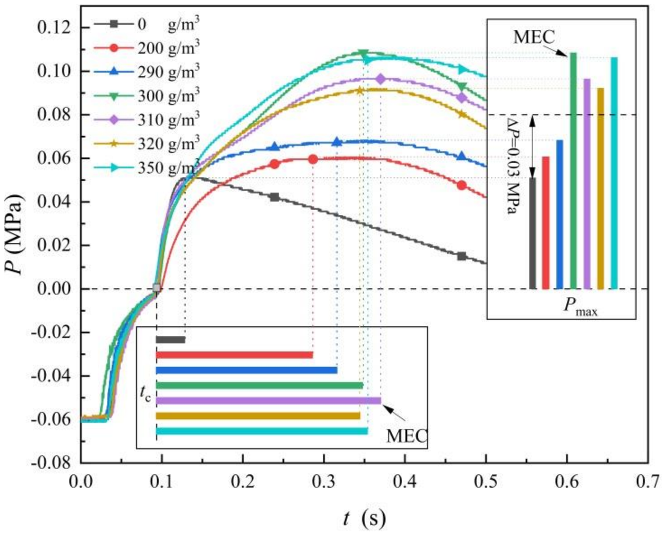

***Fig. 6.** The MEC of iron powder measured by two methods*

In fact, the combustion duration time criterion directly determines the MEC from the explosion dynamics, and the test repeatability is less affected by equipment. The standardized over pressure criterion determines the dust MEC from the thermodynamic point of view, which is related to the total heat released by the explosion. In the low concentration range, the measured explosion pressure fluctuates, and the repeatability of the test results is poor (*Tan et al. 2019*). Therefore, the combustion duration time criterion method for testing MEC has better stability and accuracy.

3.2 Severity of iron dust explosion

Fig. 7 shows the explosion characteristic parameters of iron dust at different concentrations. It can be seen from the figure that the maximum explosion pressure (P_{max}) and the maximum explosion pressure rise rate (($dP/dt)_{max}$) first increase and then decrease, which is very close to the experimental results of *Clouthier et al*. (*2019*). The difference is that the maximum value of P_{max} obtained by *Clouthier et al*. is at the concentration of 2000 g/m^3, while this experiment is at 2500 g/m^3, which may be caused by the over-driving effect of 10-kJ ignitor (*Taveau et al. 2017*). When the iron dust concentration is low, the oxygen content in the spherical chamber is sufficient, and the main influencing factor of P_{max} is iron dust concentration. With the increase of iron dust concentration, the energy released by combustion increases, so the P_{max} increases. When the concentration of iron dust reaches about 2500 g/m^3, the reaction between iron and oxygen is the most sufficient, and the released energy reaches the peak. When the dust concentration is too high, oxygen is relatively insufficient, which makes some iron particles cannot be fully burned. These iron dust will compete for the heat released by combustion, making the net energy released by explosion decreased.

Fe_2O_3, Fe_3O_4 and FeO are three oxides of iron. The calculation shows that the stoichiometric concentration of iron reacted with 20 L air for formation of Fe_2O_3 ($Fe+3/4O_2 \rightarrow 1/2Fe_2O_3$) is about 660 g/m^3, for formation of Fe_3O_4 ($Fe+2/3O_2 \rightarrow 1/3Fe_3O_4$) is about 740 g/m^3 and for formation of FeO ($Fe+1/2O_2 \rightarrow FeO$) is about 990 g/m^3 which is far less than the concentration when the P_{max} and $(dP/dt)_{max}$ are the largest in the experiment. This is because in the experiment, it is assumed that the added dust can be dispersed well in the 20-L spherical chamber, and it is often difficult to achieve in reality, especially for dust clouds with large density and concentration (*Cashdollar and Zlochower 2007*), which makes the actual explosion concentration less than the nominal concentration set. The same phenomenon was observed by Kuai et al. (2011b). In addition, incomplete combustion will also lead to this phenomenon.

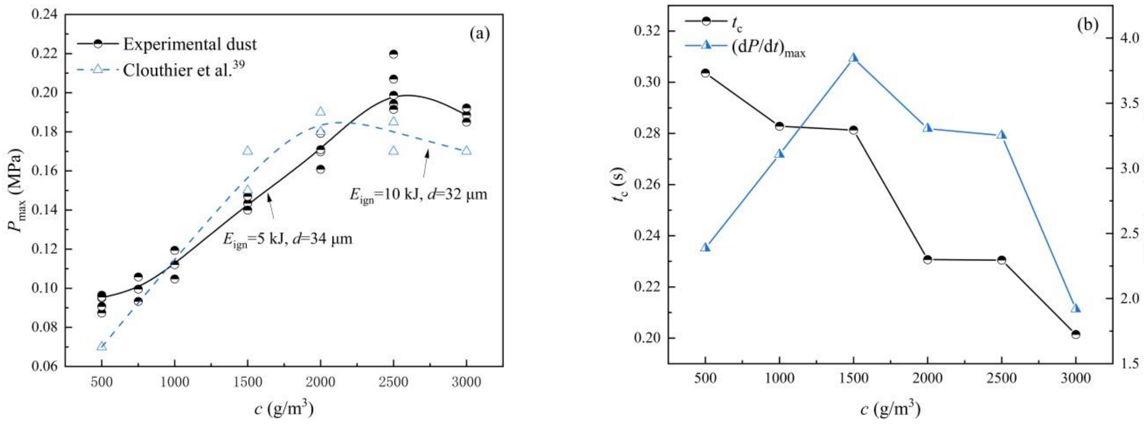

Fig. 7. *Effect of concentration on explosion characteristics of iron dust: (a) P_{max}, (b) t_c and $(dP/dt)_{max}$*

Combustion duration time (t_c) monotonically decreases with the increase of concentration in a higher concentration range. The qualitative reason is mentioned in Section 2.2. *Broumand et al*. (*2013*) deduced the combustion of dust under small Biot number through mass and energy conservation equations, and obtained the flame propagation velocity of iron dust:

$$v_f^2 = \frac{\lambda}{\rho c \tau}\left(C_{d,u}\frac{Q}{\rho c(T_i - T_\infty)} - 1\right) \tag{1}$$

where v_f is the flame propagation velocity, Q is the heat of reaction, $C_{d,u}$ is the dust concentration, T_i is the ignition temperature of the micron-sized particles, T_∞ is the temperature of unburned mixture, ρ, c, λ are the mixture density, heat capacity and thermal conductivity respectively and τ is the burning time of single particle dust:

$$\tau = \frac{\rho d^2}{8\rho_g D ln(1 + iY_\infty)} \tag{2}$$

where d is particle diameter, ρ_g is the gas density, D is the gas mass diffusivity, i is the mass stoichiometric fuel–oxidant ratio and Y_∞ is the mass fraction of oxygen in the preheat zone. Assuming that the products of each experiment is the same, then the burning time of single particle dust τ is a constant in the current experiments. Therefore, for equation (1), other parameters remain unchanged except for dust concentration $C_{d,u}$. The flame propagation velocity can be simplified as:

$$v_f^2 = \mathrm{A}C_{d,u} + \mathrm{B} \tag{3}$$

where A and B are two parameters related to other physical properties of iron dust. For 20-L spherical chamber, assuming that the characteristic combustion time is approximately equal to the combustion duration time, then the combustion duration time can be expressed as (*Zhao et al. 2021*):

$$t_c = \frac{\mathrm{R_{vessel}}}{v_f} \tag{4}$$

where $\mathrm{R_{vessel}}$ is radius of the spherical chamber. Taking Eq.(4) into Eq.(3) :

$$(\frac{\mathrm{R_{vessel}}}{t_c})^2 = \mathrm{A}C_{d,u} + \mathrm{B} \tag{5}$$

In order to simplify the calculation, the values of A and B can be obtained by substituting the experimental data with concentrations of 1000 g/m^3 and 3000 g/m^3 into the Eq.(5). The calculation results are shown in Table 1. Fig. 8 shows the distribution of calculation results and experimental results. It can also be seen from the calculation results that t_c decreases with the increase of concentration when other conditions remain unchanged. Since the dust is impossible to maintain a consistent size and perfect spherical shape, and the simplified calculation is affected by the deterministic conditions, these will lead to inevitable errors. The relative error of the formula is less than 20 % for the concentration range from 500 g/m^3 to 3000 g/m^3, which is within the acceptable range.

Table 1: *Deterministic conditions of solution and calculation results*

Deterministic conditions of solution	$\mathrm{R_{vessel}}$	A	B
$C_{d,u}$=1000 kg/m^3, t_c=0.2828 s $C_{d,u}$=3000 kg/m^3, t_c=0.2014 s	17 cm	1.7556	1857.9355

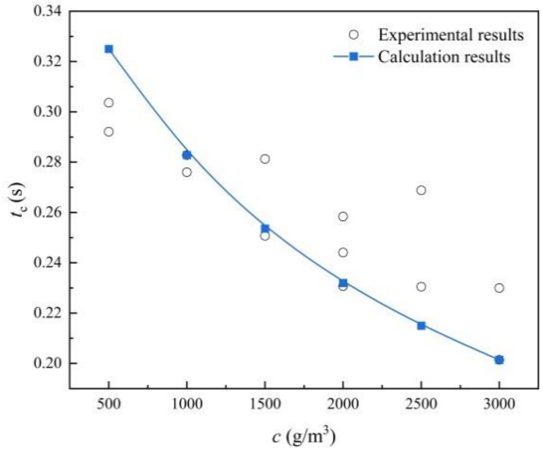

Fig. 8. *The distribution of calculation results and experimental results*

3.3 The inerting effect of oxides on iron powder

The inhibition effect of oxide on iron dust is shown in Fig. 9. The addition of Fe_2O_3 and Fe_3O_4

can reduce the P_{max} and the $(dP/dt)_{max}$ of iron dust. This is because, firstly, the nano-powders have strong inter-particle force and physical adsorption (*Bu et al. 2020*). The addition of nano-oxides promotes the agglomeration of iron dust into larger groups, resulting in poor dispersion. What's more, the aggregation makes the oxidant diffuse inward through the pores inside the aggregates. During the ignition process, the penetration depth of the oxidant inside the aggregates decreases rapidly, and the concentration of the oxidant decreases with the consumption of the reaction particles (Soo et al. 2018). There may even be a "dead" core inside the aggregates, where the particles stop the reaction due to the lack of oxidant. Secondly, the oxide itself has a certain cooling effect and thermal resistance effect, which can absorb the heat generated by partial combustion and increase the flame propagation resistance.

To better quantitatively analyze the inhibition effect of iron oxides, a weakening efficiency (WE) is defined as:

$$\mathrm{WE} = \frac{P_{\mathrm{max},1} - P_{\mathrm{max},2}}{P_{\mathrm{max},1}} \tag{6}$$

where $P_{max,1}$ is the maximum explosion pressure before inerting, and $P_{max,2}$ is the maximum explosion pressure after inerting. It is worth noting that for the addition of a small amount of oxides, when the concentration of combustible dust increases, the inerting effect decreases, as shown in table 2. When the concentration is lower than 1500 g/m^3, the addition of oxides decreases the P_{max} by more than 10 %. However, when the concentration is higher than 1500 g/m^3, the weakening effect of oxides decreases to less than 10 % except for 10 % Fe_3O_4. This may be because with the increase of dust concentration, the total heat released by combustion becomes larger, the energy proportion absorbed by oxide decreases, and the larger explosion pressure makes the turbulence in the 20-L spherical chamber stronger, so that some aggregates are separated and the reaction contact area of iron dust increases again. Of course, it may also be because the dust concentration increases, making oxide and iron dust not fully mixed, so that the inerting effect does not appear the desired effect.

Table 2: *Weakening efficiency of P_{max} by 5 % and 10 % oxides at different concentrations*

Solid inerts	proportion	500 g/m^3	1000 g/m^3	1500 g/m^3	2000 g/m^3	2500 g/m^3	3000 g/m^3
Fe_2O_3	5%	31.72 %	29.35 %	10.94 %	3.40 %	3.38 %	1.13 %
	10%	37.82 %	38.45 %	15.33 %	5.47 %	4.78 %	2.24 %
Fe_3O_4	5%	17.96 %	21.32 %	12.06 %	6.75 %	3.91 %	6.71 %
	10%	41.18 %	46.21 %	27.39 %	11.33 %	10.63 %	11.65 %

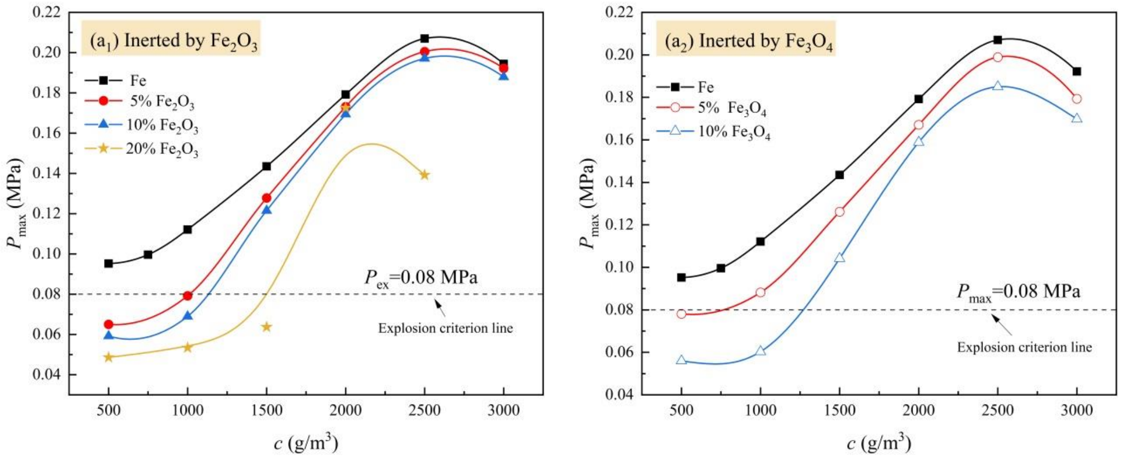

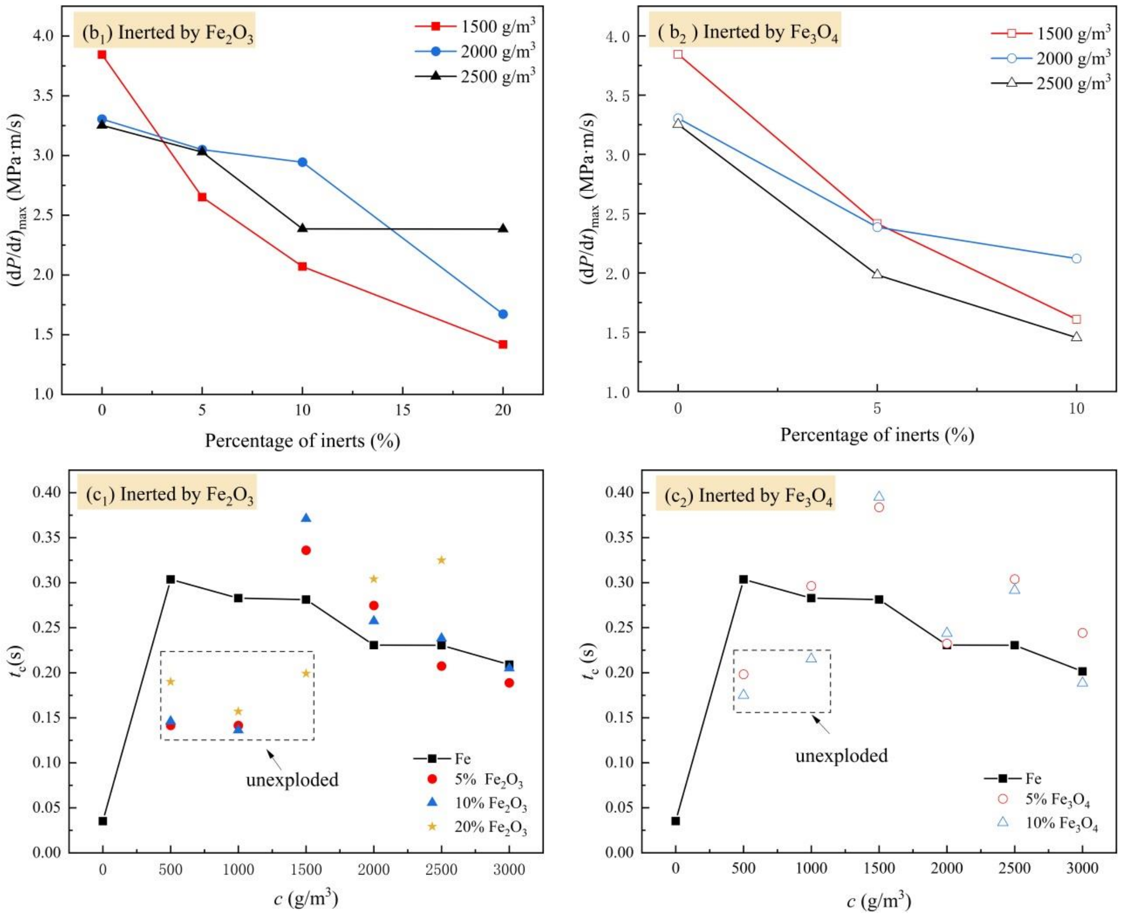

Fig. 9. *The inerting effect of oxides: (a) on P_{max} (b) on $(dP/dt)_{max}$ (c) on t_c*

As mentioned above, the particle agglomeration becomes stronger and the particle diameter *d* becomes larger with the addition of nano-oxide. From Eqs. (1), (2) and (4), it can be seen that the increase of particle size will lead to the increase of particle combustion time, the decrease of flame propagation velocity, and the overall combustion duration time becomes longer. It should be noted that t_c is much shorter than that without oxide in figure 9-c where the virtual coil comes out. This is because the addition of oxides causes the original explosion concentration to change into non-explosion concentration, which makes the combustion end earlier and forms a smaller t_c. The added oxide covers the surface of iron dust, which increases the resistance of oxygen diffusion to iron dust (*Chen and Yuen 2003*), thus slowing down the combustion process and prolonging the combustion duration time.

3.4 Comparison of inhibition effect

Fig. 10 shows the influence of the same content of oxides on the P_{max}. When 5 % oxide is added, there is a little difference between Fe_2O_3 and Fe_3O_4 for high concentration of inerting. However, it is worth noting that the addition of 5 % Fe_2O_3 makes the MEC of iron dust exceed 1000 g/m^3, while the addition of 5 % Fe_3O_4 still makes the MEC of iron dust remain below 1000 g/m^3. However, when the oxide content is added to 10 %, it is obvious that the inerting effect of Fe_3O_4 is better than that of Fe_2O_3, and both of them increase the MEC of iron dust to more than three times. 10 % Fe_3O_4 reduces the maximum value of P_{max} by 22 kPa, while 10 % Fe_2O_3 reduces the maximum value of P_{max} by only 9.9 kPa.

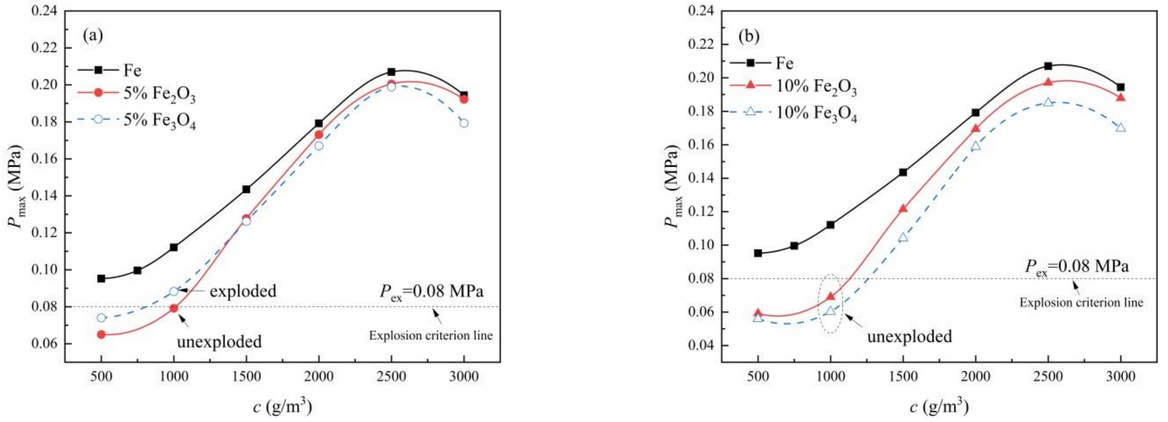

Fig. 10. *Comparison of iron oxide and ferric oxide inerting effect: (a) 5 % quality percentage, (b) 10 % quality percentage*

The reason for this difference may be related to the properties of iron and its oxides. First, the combustion temperature of iron is lower than its boiling temperature, which makes iron present the combustion mode of shrinking core combustion (*Bergthorson et al. 2015*). Secondly, Fe_2O_3 is stable in high partial pressures of oxygen, but is unstable and can be reduced to Fe_3O_4 under low partial pressures of oxygen (*Takeda et al. 2009*). Finally, the structure of Fe_2O_3 is loose while Fe_3O_4 is close, and the diffusion of oxygen in Fe_3O_4 is less than that in Fe_2O_3 (*Chen and Yuen 2003*).

Therefore, before the oxidant is added, the iron dust first combusts on the surface to form an Fe_2O_3 layer, and then shrinks to the internal combustion. Due to the decrease of oxygen, Fe_3O_4 layer and FeO layer are formed in turn. After adding iron oxide, a layer of Fe_2O_3 is formed on the edge of iron dust. Due to its resistance to oxygen diffusion, agglomeration and cooling effect, the P_{max} was reduced. When Fe_3O_4 is added, an oxide film was also formed on the edge of iron dust. Because of its greater resistance to oxygen diffusion, the Fe_2O_3 layer formed by surface combustion is under low partial pressures of oxygen. On the one hand, low partial pressures of oxygen make the internal combustion advance into the stage of Fe_3O_4. On the other hand, the low oxygen partial pressure causes the generated Fe_2O_3 layer to decompose into Fe_3O_4, which further increases the oxygen diffusion resistance and reduces the total heat generated by combustion.

In addition, the combustion heat of three oxides generated by iron combustion is (Gao et al. 2017):

$$\mathrm{Fe(s)} + 3/4\,\mathrm{O_2(s)} \rightarrow 1/2\mathrm{Fe_2O_3\,(s)} \quad \Delta \mathrm{H}^0_{\mathrm{comb}} = 412.1\ \mathrm{kJ/mol} \tag{I}$$

$$\mathrm{Fe(s)} + 2/3\,\mathrm{O_2(s)} \rightarrow 1/3\mathrm{Fe_3O_4\,(s)} \quad \Delta \mathrm{H}^0_{\mathrm{comb}} = 372.8\ \mathrm{kJ/mol} \tag{II}$$

$$\mathrm{Fe(s)} + 1/2\,\mathrm{O_2(s)} \rightarrow \mathrm{FeO(s)} \qquad \Delta \mathrm{H}^0_{\mathrm{comb}} = 272\ \mathrm{kJ/mol} \tag{III}$$

Mi et al. (*2022*) pointed out that the main products of iron dust combustion are Fe_4O_3 and FeO, Fe_2O_3 only generates a small layer on the surface, so there may be reaction competition between Fe_4O_3 and FeO in the combustion process. Therefore, in terms of chemical reaction, the addition of Fe_4O_3 will weaken the reaction (II) and promote the reaction (III), thus making the reaction (III) dominant, which will greatly reduce the total heat released by the iron combustion and reduce the P_{max}.

4. Conclusions

The explosion characteristics of iron dust and the inhibition effect of its two oxidation products were studied by using 20L spherical explosion chamber. The results show that the combustion duration time method is not only suitable for carbon-based dust, but also for metal dust, which provides a new idea for the test of the MEC. The addition of Fe_2O_3 and Fe_3O_4 can reduce the explosion severity of iron powder and weaken the combustion progress. The addition of a small

DOI: 10.7795/810.20221124

amount of oxides has a significant inerting effect on the low-concentration section, but the inerting effect on the high-concentration section is general. As the oxide concentration is increased to 10%, the inerting effect is significantly improved, and the MEC of iron dust is increased by more than three times. At the same time, the superior inerting properties of Fe_3O_4 are gradually revealed. These results provide new ideas for powder inerting technology as well as explosion protection and protection device design.

References

Amyotte, P.R. 2006. Solid inertants and their use in dust explosion prevention and mitigation, *Journal of Loss Prevention in the Process Industries*, 19: 161-73.

ASTM E1515. 2007. *Standard Test Method for Minimum Explosible Concentration of Combustible Dusts,* American Society of Testing Materials.

Bardsley, W.E. 2008. The Sustainable Global Energy Economy: Hydrogen or Silicon?, *Natural Resources Research*, 17: 197-204.

Bergthorson, J.M. 2018. Recyclable metal fuels for clean and compact zero-carbon power, *Progress in Energy and Combustion Science*, 68: 169-96.

Bergthorson, J.M., Goroshin, S., Soo, M.J., Julien, P., Palecka, J., Frost, D.L., and Jarvis, D.J. 2015. Direct combustion of recyclable metal fuels for zero-carbon heat and power, *Applied Energy*, 160: 368-82.

Broumand, M., and Bidabadi, M. 2013. Modeling combustion of micron-sized iron dust particles during flame propagation in a vertical duct, *Fire Safety Journal*, 59: 88-93.

Bu, Y., Li, C., Amyotte, P., Yuan, W., Yuan, C., and Li, G. 2020. Moderation of Al dust explosions by micro- and nano-sized Al2O3 powder, *Journal of Hazardous Materials*, 381: 120968.

Cashdollar, K.L., and Zlochower, I.A. 2007. Explosion temperatures and pressures of metals and other elemental dust clouds, *Journal of Loss Prevention in the Process Industries*, 20: 337-48.

Chen, R.Y., and Yuen, W.Y.D. 2003. Review of the high-temperature oxidation of iron and carbon steels in air or oxygen, *Oxidation of Metals*, 59: 433-68.

Chen, X., Zhang, H., Chen, X., Liu, X., Niu, Y., Zhang, Y., and Yuan, B. 2017. Effect of dust explosion suppression by sodium bicarbonate with different granulometric distribution, *Journal of Loss Prevention in the Process Industries*, 49: 905-11.

Clouthier, M.P., Taveau, J.R., Dastidar, A.G., Morrison, L.S., Zalosh, R.G., Ripley, R.C., Khan, F.I., and Amyotte, P.R. 2019. Iron and aluminum powder explosibility in 20-L and 1-m3 chambers, *Journal of Loss Prevention in the Process Industries*, 62: 103927.

CSB. 2011. CSB Continues Investigation of Fatal Fire at Hoeganaes Corporation Located Outside of Nashville, Tennessee.

Dai, L., Hao, L., Kang, W., Xu, W., Shi, N., and Wei, H. 2020. Inhibition of different types of inert dust on aluminum powder explosion, *Chinese Journal of Chemical Engineering*, 28: 1941-49

Danzi, E., Pio, G., Marmo, L., and Salzano, E. 2021. The explosion of non-nano iron dust suspension in the 20-l spherical bomb, *Journal of Loss Prevention in the Process Industries*, 71: 104447.

Dastidar, A., and Amyotte, P. 2002. Determination of Minimum Inerting Concentrations for Combustible Dusts in a Laboratory-Scale Chamber, *Process Safety and Environmental Protection*, 80: 287-97.

Di Sarli, V., Russo, P., Sanchirico, R., and Di Benedetto, A. 2014. CFD simulations of dust dispersion in the 20 L vessel: Effect of nominal dust concentration, *Journal of Loss Prevention in the Process Industries*, 27: 8-12.

Dreizin, E.L. 2000. Phase changes in metal combustion, *Progress in Energy and Combustion Science*, 26: 57-78.

Dufaud, O., Bideau, D., Le Guyadec, F., Corriou, J.-P., Perrin, L., and Caleyron, A. 2014. Self ignition of layers of metal powder mixtures, *Powder Technology*, 254: 160-69.

Eckhoff, R.K. 2005. Current status and expected future trends in dust explosion research, *Journal of Loss Prevention in the Process Industries*, 18: 225-37.

EN 14034. 2006. *Determination Of Explosion Characteristics Of Dust Clouds,* European Committee for Standardisation (CEN).

Gao, W., Zhang, X., Zhang, D., Peng, Q., Zhang, Q., and Dobashi, R. 2017. Flame propagation behaviours in nano-metal dust explosions, *Powder Technology*, 321: 154-62.

Going, J.E., Chatrathi, K., and Cashdollar, K.L. 2000. Flammability limit measurements for dusts in 20-L and 1-m3 vessels, *Journal of Loss Prevention in the Process Industries*, 13: 209-19.

Going, J.E., and Snoeys, J. 2002. Explosion protection with metal dust fuels, *Process Safety Progress*, 21: 305-12.

Jin, H., Zheng, L., Wang, J., Yu, S., Pan, R., Wang, X., Yang, W., and Fu, Y. 2021. Effect of Al2O3 particle size reduction on aluminum dust explosion, *Journal of Loss Prevention in the Process Industries*, 70: 104402.

Krietsch, A., Scheid, M., Schmidt, M., and Krause, U. 2015. Explosion behaviour of metallic nano powders, *Journal of Loss Prevention in the Process Industries*, 36: 237-43.

Kuai, N., Huang, W., Yuan, J., Du, B., Li, Z., and Wu, Y. 2011a. Experimental investigations of coal dust-inertant mixture explosion behaviours, *Procedia Engineering*, 26: 1337-45.

Kuai, N., Li, J., Chen, Z., Huang, W., Yuan, J., and Xu, W. 2011b. Experiment-based investigations of magnesium dust explosion characteristics, *Journal of Loss Prevention in the Process Industries*, 24: 302-13.

Li, G., Yuan, C.M., Fu, Y., Zhong, Y.P., and Chen, B.Z. 2009. Inerting of magnesium dust cloud with Ar, N2 and CO2, *Journal of Hazardous Materials*, 170: 180-83.

Li, Q., Wang, K., Zheng, Y., Mei, X., and Lin, B. 2016. Explosion severity of micro-sized aluminum dust and its flame propagation properties in 20L spherical vessel, *Powder Technology*, 301: 1299-308.

Lissianski, V.V., Maly, P.M., Zamansky, V.M., and Gardiner, W.C. 2001. Utilization of Iron Additives for Advanced Control of NOx Emissions from Stationary Combustion Sources, *Industrial & Engineering Chemistry Research*, 40: 3287-93.

Mi, X., Fujinawa, A., and Bergthorson, J.M. 2022. A quantitative analysis of the ignition characteristics of fine iron particles, *Combustion and Flame*, 240: 112011.

Popok, E.V., Levashova, A.I., Burlutskiy, N.P., Khudyakov, D.V., and Zhuravkov, S.P. 2015. Ultradispersed Electro-explosive Iron Powders as Catalysts for Synthesis of Liquid Hydrocarbons of CO and H2, *Procedia Chemistry*, 15: 225-30.

Shkolnikov, E.I., Zhuk, A.Z., and Vlaskin, M.S. 2011. Aluminum as energy carrier: Feasibility analysis and current technologies overview, *Renewable and Sustainable Energy Reviews*, 15: 4611-23.

Soo, M., Mi, X., Goroshin, S., Higgins, A.J., and Bergthorson, J.M. 2018. Combustion of particles, agglomerates, and suspensions – A basic thermophysical analysis, *Combustion and Flame*, 192: 384-400.

Sun, J., Dobashi, R., and Hirano, T. 2001. Temperature profile across the combustion zone propagating through an iron particle cloud, *Journal of Loss Prevention in the Process Industries*, 14: 463-67.

Sun, J., Dobashi, R., and Hirano, T. 2003. Concentration profile of particles across a flame propagating through an iron particle cloud, *Combustion and Flame*, 134: 381-87.

Takeda, M., Onishi, T., Nakakubo, S., and Fujimoto, S. 2009. Physical Properties of Iron-Oxide Scales on Si-Containing Steels at High Temperature, *Materials Transactions*, 50: 2242-46.

Tan, X., Zhao, P., Wu, D., Huang, W., and Yuan, J. 2019. Researchl on minimum explosible concentration of dust based on method of combustion duration, *China Safety Science Journal*, 29: 102-06.

Tascón, A. 2018. Influence of particle size distribution skewness on dust explosibility, *Powder Technology*, 338: 438-45.

Taveau, J., Vingerhoets, J., Snoeys, J., Going, J., and Farrell, T. 2015. Suppression of metal dust deflagrations, *Journal of Loss Prevention in the Process Industries*, 36: 244-51.

Taveau, J.R., Going, J.E., Hochgreb, S., Lemkowitz, S.M., and Roekaerts, D.J.E.M. 2017. Igniter-induced hybrids in the 20-l sphere, *Journal of Loss Prevention in the Process Industries*, 49: 348-56.

Wu, H.-C., Chang, R.-C., and Hsiao, H.-C. 2009. Research of minimum ignition energy for nano Titanium powder and nano Iron powder, *Journal of Loss Prevention in the Process Industries*, 22: 21-24.

Wu, W., Huang, W., Wei, A., Schmidt, M., Krause, U., and Wu, D. 2022. Inhibition effect of N2/CO2 blends on the minimum explosion concentration of agriculture and coal dusts, *Powder Technology*, 399: 117195.

Yuan, J., Huang, W., Ji, H., Kuai, N., and Wu, Y. 2012. Experimental investigation of dust MEC measurement, *Powder Technology*, 217: 245-51.

Zhang, Q., Liu, L., and Shen, S. 2018. Effect of turbulence on explosion of aluminum dust at various concentrations in air, *Powder Technology*, 325: 467-75.

Zhao, P., Schmidt, M., Krause, U., Duan, Q., Krietsch, A., and Wu, D. 2021. Experimental study on the minimum explosion concentration of anthracite dust: The roles of O2 mole fraction, inert gas and CH4 addition, *Journal of Loss Prevention in the Process Industries*, 71: 104490.

Zhao, P., Tan, X., Schmidt, M., Wei, A., Huang, W., Qian, X., and Wu, D. 2020. Minimum explosion concentration of coal dusts in air with small amount of CH4/H2/CO under 10-kJ ignition energy conditions, *Fuel*, 260: 116401.

DOI: 10.7795/810.20221124

Dust cloud behaviour in the modified Hartmann tube

Enrico Danzi [a], Olivier Dufaud [b], Fausto, Franchini [c], Luca Marmo [a] and Matteo Pietraccini [b]

[a] Dipartimento di Scienza Applicata e Tecnologia-Politecnico di Torino, C.so Duca degli Abruzzi 21, 10129, Torino, Italy
[b] Laboratoire Réactions et Génie des Procédés, Université de Lorraine, CNRS, LRGP, F- 54000 Nancy, France
[b] Department of Energy (DENERG), Politecnico di Torino, Viale T. Michel 5, 15121 Alessandria, Italy

E-mail: enrico.danzi@polito.it

Abstract

For a dust explosion to occur, a dispersion of fine particles in the air is needed: since an explosion is the fast combustion of particles in the air, if these are poorly dispersed, either agglomerated or remote one from another, the combustion velocity is slow, and deflagration will not occur. Dust concentration is related to the combustion velocity. The maximum explosion pressure rise occurs at dust concentration close to stoichiometric. On the other side, Minimum Explosion Concentration (MEC) is the lower limit at which a pressure rise is possible. Safety tests are designed to reproduce the dispersion and generation of dust clouds in industrial ambiences by using dispersion devices activated by pressure air pulses. The resulting dust cloud is considered representative of real clouds by standards. Still, several studies have dealt with some lacks and poor working of these devices (such as non-homogeneity in dispersion in 20 L sphere).

This work aims to investigate the actual behaviour of dust clouds inside the modified Hartmann tube through high-velocity video movies of the dust flow and post-treatment of the images.

A high-speed camera is coupled with LabVIEW® software to elaborate and process data, acquiring powder dispersions with a framerate of 2000 fps. Concentration (mass per volume) and dispersion pressure are varied to evaluate effects on dust flow. Maizee starch, iron powder and silica powder are chosen to investigate density, particle size and agglomeration. This approach could help investigate dust cloud structure, the shape and size of agglomerates, and the evolution of the concentration of dust in time. Considerations on the actual concentration of dust at the ignition location and delay time for MIE determination, while also comparisons with dust MEC and Stoichiometric value, could be drawn from this work. Furthermore, the intensity of light measured from video acquisition (in terms of pixels brightness) is correlated to dust particle concentration. It could also be related to turbulence intensity to identify the local turbulence scale and widen the characterisation of the cloud generated in the Hartmann tube.

Keywords: *dust cloud dynamics, Hartmann modified tube, dust concentration measurement, LabVIEW®*

1. Introduction

This work investigates the dust cloud dynamics inside the Hartmann modified tube used for flammability screening and MIE measurement. The idea is to extrapolate relevant information from high-speed movies of dust dispersion, elaborating the images to focus on the dust structure (see also Danzi et al., 2021).

It is well known today that the dust cloud's fluid dynamics has fundamental importance on the cloud's behaviour during the explosion. Several researchers have shown that the cloud's turbulence affects both the flame speed, the K_{St}, and the minimum ignition energy. In addition, it is well known that an increase in cloud turbulence determines the increase of the K_{St} and, at the same time, increases the MIE. The dust concentration also significantly affects the deflagrating parameters, which are maximum near the stoichiometric concentration and lower towards the MEC. These considerations are relevant, whatever the parameter is intended to measure, especially regarding MIE.

Current standards state that a Hartmann tube must be used to measure the MIE of dust. The cloud is created using an air pulse obtained by discharging the air stored in a tank at a pressure of 7 bar_g into the tube. The cloud is then subjected to an attempted ignition with an electric arc, which is triggered after a specific time (delay time): The ISO 80079 standard suggests adopting delay times between 60 and 180 ms, and it is known that the value of MIE is influenced by the ignition delay time, as is logical since the dust cloud thus created has a distinctly transitory character, and the turbulence decreases with time. Hartmann's tube is also used to carry out the flammability screening test, which effectively detects combustible dust in large sets of samples (Marmo & Danzi 2018, Marmo et al. 2018, 2019).

The literature contains some studies of cloud fluid dynamics in the Hartmann tube. Still, all focus primarily on the behaviour of the very early stages of cloud formation. For example, Murillo et al. (2013) studied the front of the cloud as it reaches the electrodes' position using high-speed films, while Hosseinzadeh et al. (2018) evaluated the flow field with PIV technology up to 120 ms. On the other hand, there are no studies on the behaviour of the cloud in the time interval suggested by the standard to ignite the cloud in the MIE measurement.

2. Experiments

The experimental setup is the same implemented in Danzi et al. 2021, while different powders were used in this work to evaluate the effect of varying PSD and density on the cloud structure: Iron powder (fine and coarse); Maizee starch (coarse) and Silica powder (fine and coarse). SEM images and PSD curves are reported in Figure. 1. Silica dust, as inert, is chosen as to identify inert powder behaviour in terms of motion in the tube and to analyse combustible-inert mixture dynamics in the next investigations.

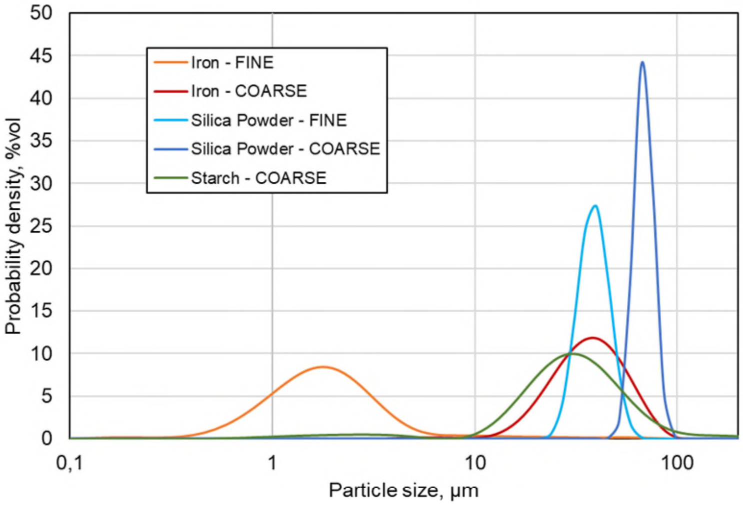

Figure. 1. *PSD curves for all samples*

The dust dispersion was recorded using a high-speed video camera (*MotionBlitz EoSens mini2*) at 2000 fps. The setup was modified to insert a black background behind the tube to limit reflections. In addition, a halogen lamp was used to avoid further light oscillations in the recording. The videos are synchronised assuming as "frame zero" the one at which the moving electrode shifts towards the fixed one. With the varying dispersion conditions (pressure, nominal concentration, PSD and type of dust), a total of 16 dispersion tests is realised (see Table 1), where the dispersion variables are summarised as:

- Air pulse pressure (3.5 and 7 bar_g);
- Nominal concentration (300 and 600 g/m^3);
- Dust PSD (fine and coarse, depending on the sample used);
- Dust nature.

Mixtures were realised to evaluate the interactions between powder particles with different densities (Iron-silica powder and Iron-starch).

Table 1: *Summary of dispersion tests*

Test	Dust	C [g/m^3]	P [bar]	PSD
1	Maize starch	300	3.5	Coarse
2	Maize starch	300	7	Coarse
3	Maize starch	300	3.5	Coarse
4	Maize starch	300	7	Coarse
5	Maize starch	600	3.5	Coarse
6	Maize starch	600	7	Coarse
7	Iron	600	3.5	Coarse
8	Iron	600	7	Coarse
9	Iron	600	3.5	Fine
10	Iron	600	7	Fine
11	Silica	300	3.5	Coarse
12	Silica	300	3.5	Fine
13	Silica	300	7	Coarse
14	Silica	300	7	Fine
15	Maize starch/Iron 1:1	300	3.5	Fine (both)
16	Maize starch/Iron 1:1	600	3.5	Fine (both)

2.1 Post-processing elaboration

This section describes the implementation of the digital elaboration of the videos performed with LabVIEW ®; the procedure is also described in Danzi et al., 2021. Each video was filmed at 2000 fps for about 500 ms, to describe the dust dynamics before the time suggested for ignition by current standards (from 60 to 180 ms). Since no ignition is performed, the dust dynamics is studied up to the time when the dust cloud front starts to settle towards the tube bottom.

The video processing is divided into successive phases, described in detail in Danzi et al., 2021. The first step aims to eliminate the noisy background signal to better highlight regions in which cloud dust movement occur: this is done by cancelling the background with a differential video signal acquisition, whether subtracting the initial video frame to all next frames or imposing a "delta frame" equal to *x*, subtracting to frame *n* the information acquired in frame *n-x,* see Danzi et al. 2021.

Different information on the cloud's dust displacement could be obtained depending on the number of subtracted frames. It will be referred to as "DeltaX" in the paper.

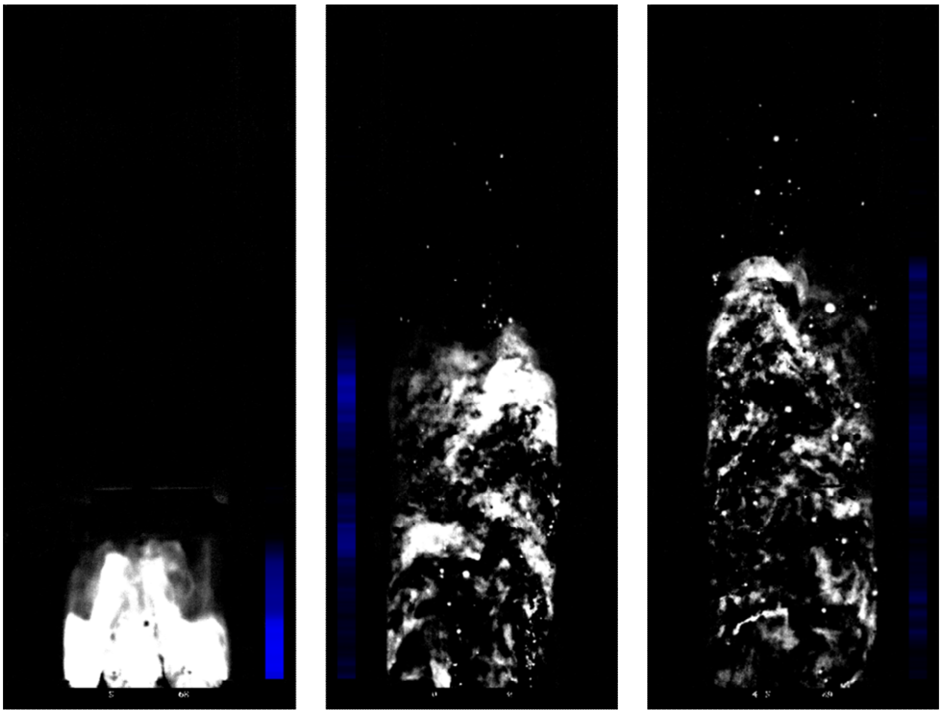

Fig. 2. *Visualisation of the cloud, Delta20 frames at respectively 50, 110, 155 ms, from test#1.*

In our previous paper (Danzi et al., 2021), the different DeltaX approaches were compared, with the following outcomes:

- At high cloud speed (early dispersion), a higher delta frame will cause loss of information and generate "blurry" images
- After 100 ms, the rise velocity starts to decay, a higher delta frame is needed to recover actual "clusters" movement.
- After 250 ms, the cloud begins to free fall, the highest delta frame would apply.

For these reasons, the video elaboration should be optimised depending on the cloud rise and the local speed velocity of clusters in the cloud. An attempt is made to overcome the "optimisation" problem due to the different DeltaX data recovering, raised in Danzi et al. (2021). Frames are elaborated with different colours for different approaches (see Fig. 3 to Fig. 5). This view helps to visualise the quality of the different elaboration of the collected data in terms of particles and clusters movement in time and space.

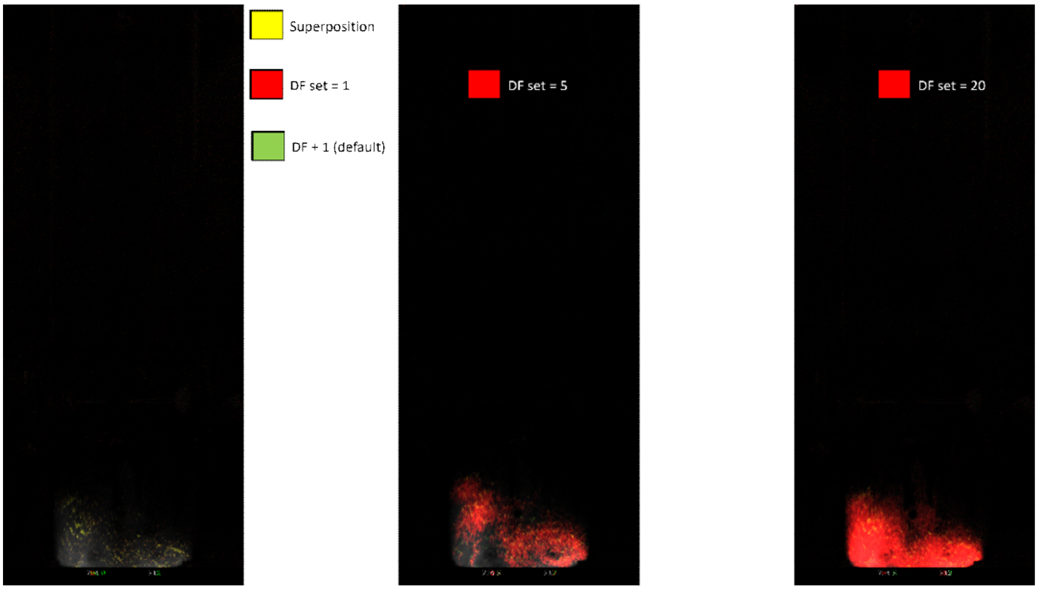

Fig. 3. *Visualisation of the cloud, different DeltaX, as in the legend, test#12 @50 ms.*

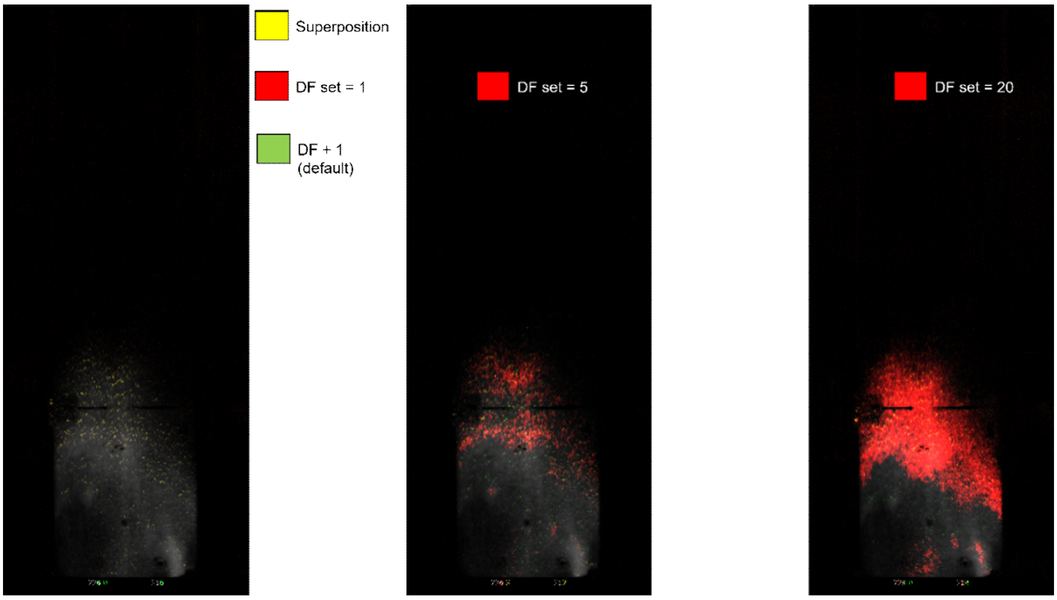

Fig. 4: *Visualization of the dust cloud, different DeltaX, as in the legend, test#12 @70 ms*

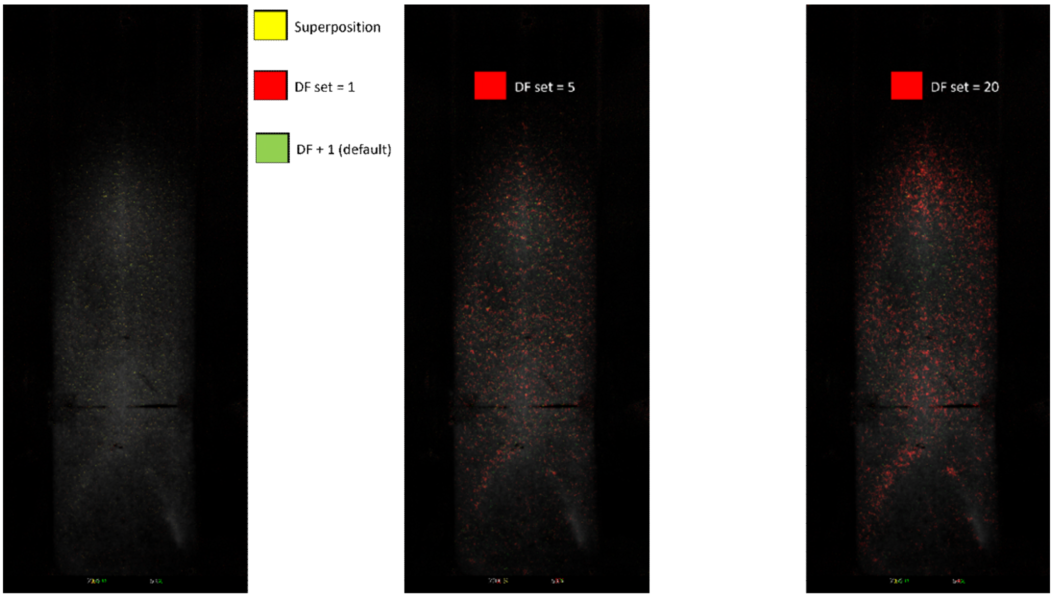

Fig. 5: Visualization of the dust cloud, different DeltaX, as in the legend, test#12 @125 ms

From the above images, it could be observed how the Delta20 is accurate in the final stage of the dispersion. At the same time, the Delta1 and 5 are likely more helpful to detect the cloud structure at the early stage of dispersion, when the cloud rise velocity is higher.

This difference likely occurs due to the actual DeltaX method functioning in the early phase of the dispersion, when the DeltaX is higher (x = 20), given the higher momentum of the dust cloud rise, the turbulence eddies would travel a great distance along with x frames (in the vertical direction) and change shape during the shooting, so they are no longer recognizable when X grows. Figure 6 shows the effect of the DeltaX choice with respect to the actual size of particle and their visualisation with time evolution.

On the contrary, when we consider the images taken after 0.1 s, when flow has reduced his initial momentum, the optimal choice would be Delta 5. As expected, the turbulence scale has significantly decreased with respect to early stage. Finally, the images taken after about 0.2 seconds from the dispersion, when the cloud is practically in free fall, are optimally processed by delta 20: turbulence scale has further decreased, eddies are barely visible, likely because the dust concentration is almost homogeneous.

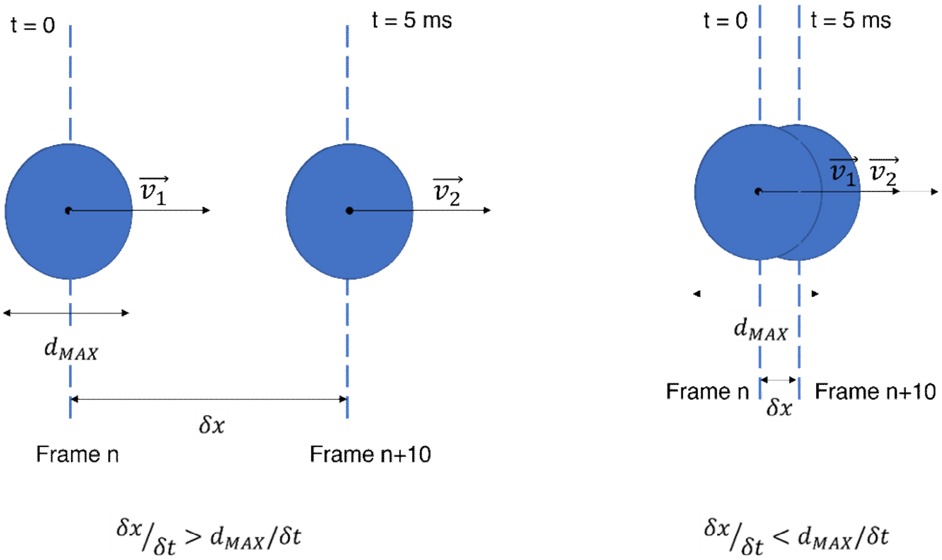

***Figure 6**: Schematic representation of DeltaX effect on particle motion and frame acquisition*

The second video-processing step allows detecting the luminance variation on a single row of the video framing. Thus, obtaining the luminance's maximum, average and standard deviation is possible during dust dispersion. Graphic representation is reported in Fig. 7, where a waveform graph and an intensity history are plotted.

From this post-processing, further information is obtained, such as:

- An estimate of dust cloud front rise velocity in the tube.
- The distribution of the dust clusters in height and time.

Cloud front was detected using a "detector value" (the average, maximum or standard deviation of luminance). In addition, a threshold value and a background value (when no particles are present) were defined. When values higher than the detector threshold are registered in the video, the arrival of the cloud front could be identified.

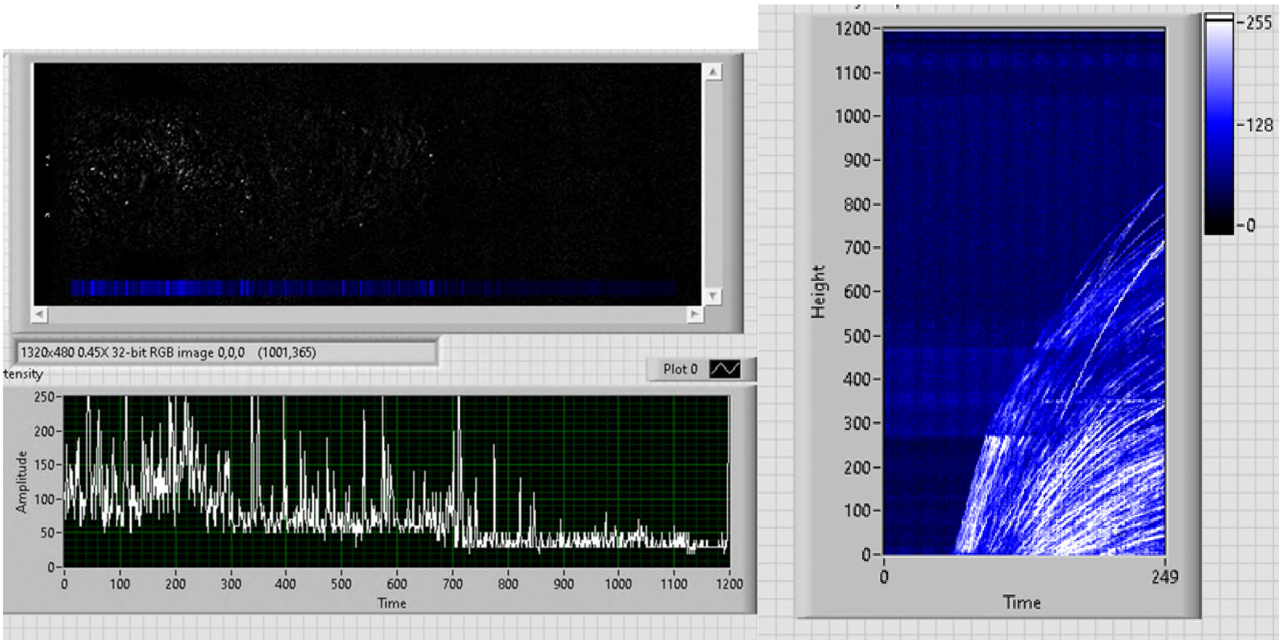

Fig. 7. Intensity history and waveform graph representation as in the LabVIEW application

This threshold is set differently depending on the dispersion tests. Finally, rise velocity is estimated as the derivative of the front rise in time.

3. Results and discussion

In the followings, the results of the different approaches adopted for the post-treatment are reported: intensity of the luminance of the pixels is firstly analysed as it is, in terms of peak and average of the values on the same pixels row in the video frame.

DOI: 10.7795/810.20221124

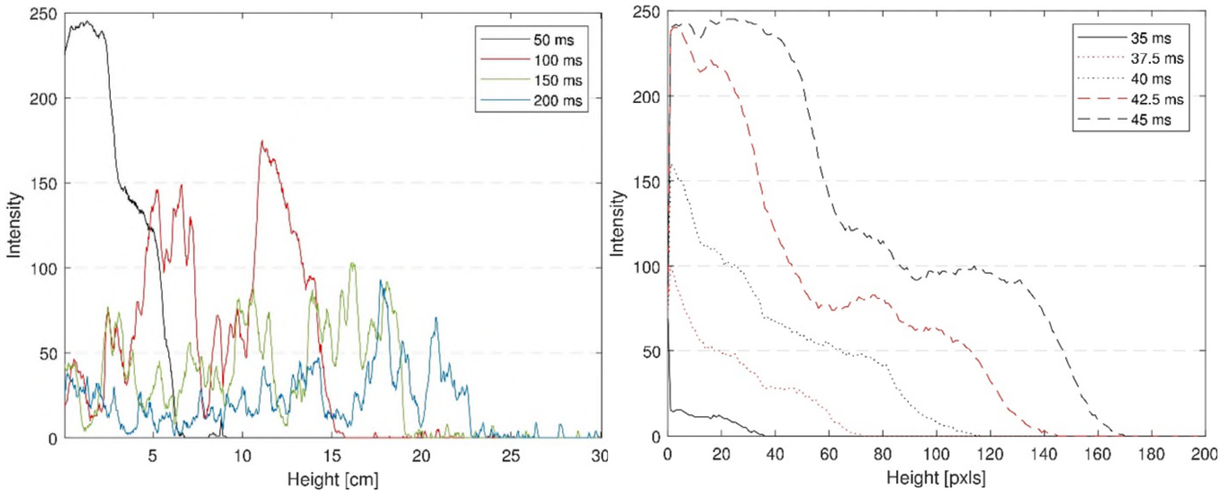

Fig. 8: *Intensity luminance peak vs height, Delta20 approach for three samples (300 g/m3, 3.5 bar).*

The intensity evolution in time shows the cloud concentration history. A luminance peak is evident at the early dispersion time (50 ms), while another peak is observed after 100 ms from dispersion at a higher location in the tube. After 100 ms the dust cloud seems to be more homogeneous in space and time. Any clearly defined peaks could be observed from this time on. Fig. 8 (right) reveals how the cloud front position and velocity may be studied with this elaboration.

Two approaches were initially adopted to identify the optimal solution regarding the amount of information recovered from the experimental tests: intensity average and intensity peak in time, respectively. From Fig. 9, some considerations may be drawn.

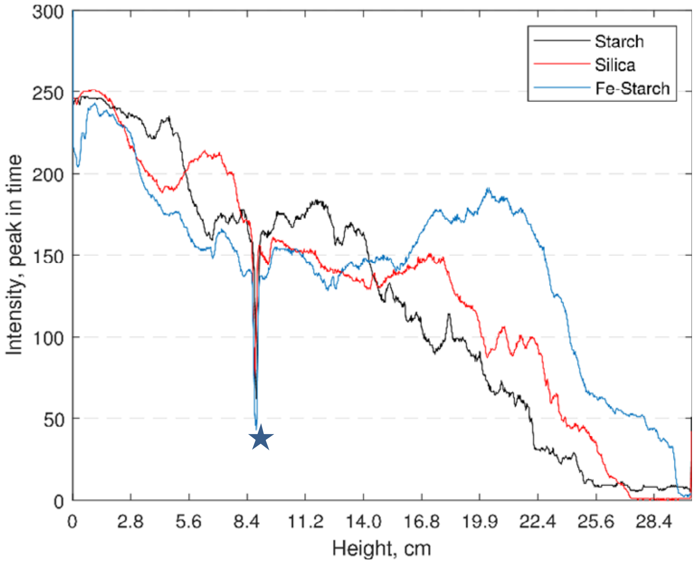

Fig. 9. *Intensity luminance peak vs. height, Delta20 approach for three samples (tests#1, 11, 15).*

The highest peak is in the lower part of the tube, below the electrodes (the star represents the luminance effect due to electrode movement; this peak should be brushed in the elaboration). Intensity is higher for Starch and Silica tests than Fe-Starch within the first half of the tube, while Fe-Starch intensity is higher afterwards. A clear second peak is observed for this test at about 20 cm from the bottom.

DOI: 10.7795/810.20221124

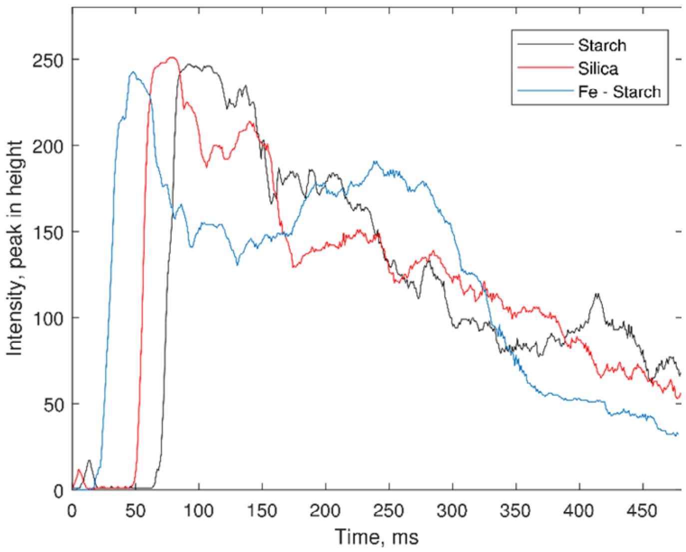

Fig. 10: *Intensity peak by height vs. time for three samples (tests#1, 11, 15).*

The intensity history is found if the maximum values according to tube height is calculated, as in Fig. 10. From these data, the maximum peak in intensity is reached for different samples at different times after the dispersion: maximum dust cloud "optical concentration" is reached at different time intervals depending on the dust sample nature. This first outcome reveals the variability of dust cloud dynamics inside the tube in terms of concentrations range and timing at the moment of ignition.

As observed in Danzi et al. (2021), it is necessary to optimise the delta frame (DeltaX, where X is the delta frame value) based on the local cloud speed or cloud rise steps.

When applying different Delta frames, the different information contained in the intensity graph could be observed in Fig. 11.

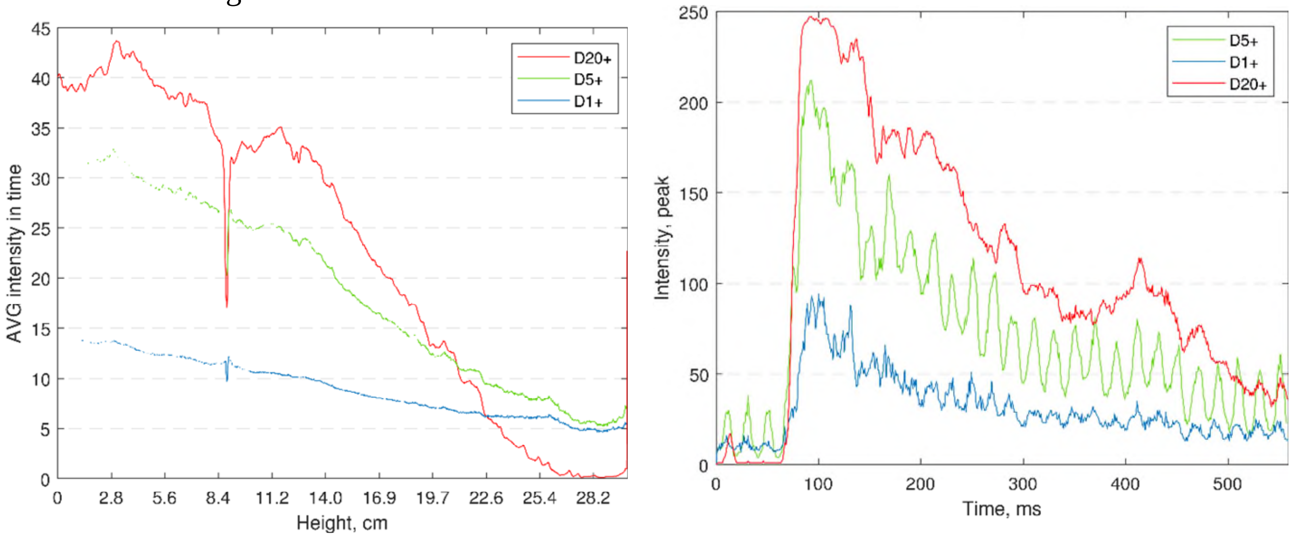

Fig. 11: *Intensity evolution in height (left) and time (right) for test#1, with different DeltaX approaches.*

The average intensity value is higher for Delta20 up to about 22 cm from the tube bottom; afterwards, its value decay rapidly, while Delta5 and Delta1 stay constant. If peak values are considered, Delta20 presents higher values in all dispersion time with respect to other Delta approaches.

The interruptions in Fig. 11: for Delta different than 20 are due to unexpected spikes at maximum intensity value (255) during dispersion time (likely due to lab light frequency oscillations).

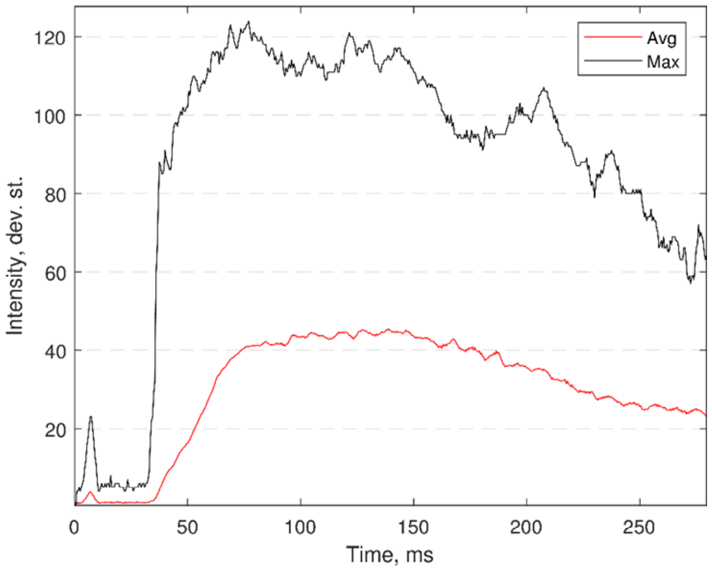

***Fig. 12:** Standard deviation values of intensity (peak and average of pixels rows) vs. dispersion time, for test#1.*

A different elaboration was performed, focusing on the Standard deviation value of intensity, intended to identify some correspondences between this value and the turbulent structure characteristics in terms of scale and velocity.

3.1 Dust cloud rise evaluation

The cloud front is detected with the LabVIEW routine as the rise of the luminance threshold is defined a priori (depending on background luminance). The purpose of the threshold is to distinguish between actual dust particles and fluctuations due to background or external lights. If adequate detection criteria are adopted (average, maximum or standard deviation values) and the luminance threshold is well-imposed, the cloud rise is extrapolated from video frames.

Fig. 13: reports the difference between the rise of an Iron/Maize starch cloud and a Silica powder cloud, at the same dispersion conditions (nominal concentration and pressure). Silica powder seems more easily lifted by the air blow, while fail to rise to the end of the tube, reaching a quasi-still condition and then starting to settle down in the last interval (from almost 0.16 seconds on).

Iron-Starch cloud rise less steeply, likely reaching the top of the tube, without any settling.

The different rise could be influenced by factors such as density of dusts, dispersion efficiency, agglomeration/breakage of clusters in the vertical direction. Hence, as estimated here, the dust cloud front reaches the electrode position at different times for different dusts, thus implying the maximum concentration will occur at different times close to the electrodes. The ignition delays should be related to these discrepancies.

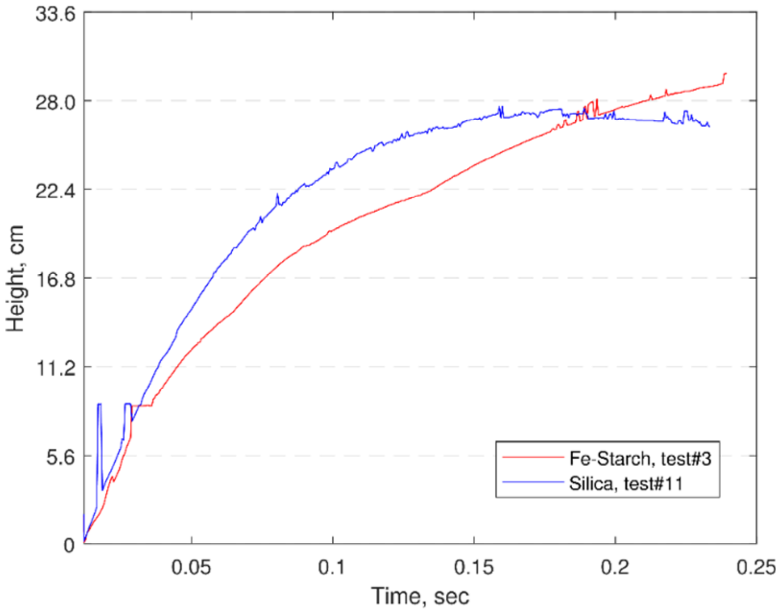

Fig. 13: *Cloud rise comparison, estimated with Initial difference detector on light intensity, tests#3 & 11.*

Rise velocity is calculated from the first derivative of the cloud height rise in time, Fig. 14 shows the different velocity estimation of three different powders. The comparison could be made among them.

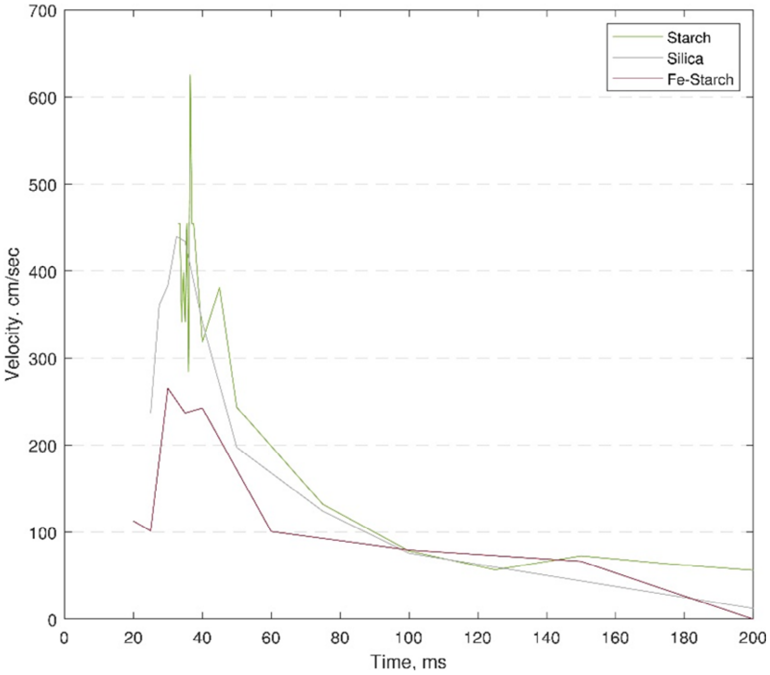

Fig. 14: *Cloud front rise velocity, estimated from elaboration, for three different powders (tests#1, 11, 15)*

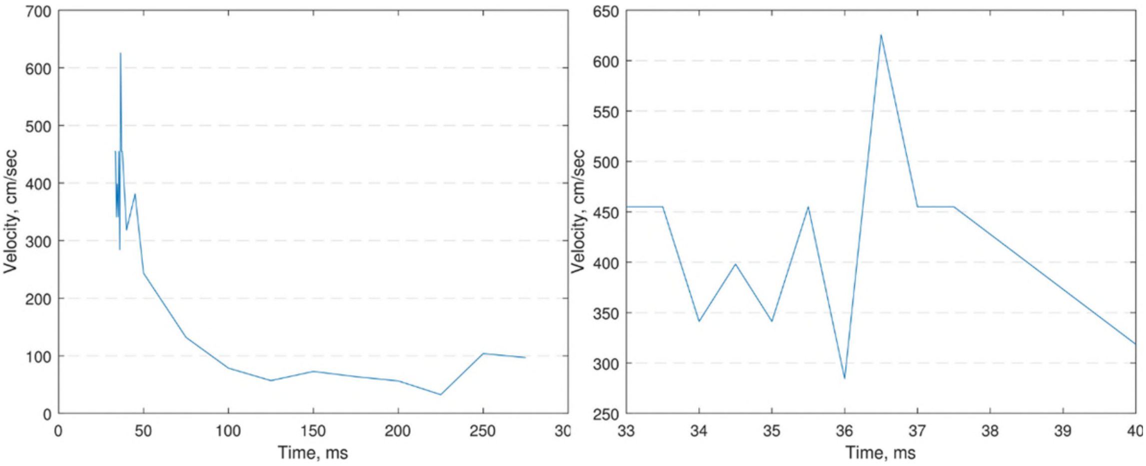

Figure 15: *Cloud rise velocity, test#1, with focus on the early step of dispersion (right).*

From Figure 15, rise velocity oscillations could be observed in the right-hand image: this could be correlated to the turbulence intensity in this interval, which is greater due to the air pulse contribute. This approach does not clearly identify the induced turbulence due to the electrode obstacles.

The turbulence course seems to peak in the early phase. At the same time, decay is observed, until an asymptotic value, near the end of the dispersion time.

Further investigations could support this evaluation, identify turbulent vortexes during the cloud rise, and help estimate the turbulence scale and velocity.

3.2 Dust cloud rise evaluation: comparisons with previous works

As reported above, similar experimentations on the fluid-dynamics of Hartman tube could be found in literature, although only minor investigations are present (with respect to 20L apparatus). Data from Hosseinzadeh et al. (2018) could be partially compared with the elaboration results from the present work on the particle velocity. If dust cloud rise velocity is compared to particle velocity vs. time in Hosseinzadeh et al., (2018) similar evolution in time could be observed: an early rise up to about 7 m/s and a rapid decrease to values smaller than 1 m/s after about 100 ms from the dispersion. The comparison is made between the front rise velocity obtained by applying the Initial Difference approach with a detector threshold on the average value (see section 3.1); data from Hosseinzadeh et al. (2018) are referred to the single particle velocity in 59 runs. Ensemble averaged velocity values reached a maximum value of about 3.9 m/s, which is about one half the maximum value obtained in this work.

4. Conclusions

This work aims to define a novel approach to studying the cloud behaviour and dynamics inside the Hartman modified tube, adopted for the flammability screening and the MIE determination in the combustible dust explosion risk assessment.

It implies high-speed movies post-treatment that reveal some fluid dynamics aspects of the dust cloud:

- The rise in time and space
- The dust cloud front rise velocity
- The distribution of clusters during the tube rise
- Information about the turbulence during the test

Once the method is finalised (optimisation of delta frame procedure and tuning concerning different powders), it will be a valid alternative to more time consuming and complex methods, such as PIV tracing of particles.

Further works will foresee the realisation of videos with a different camera setup, i.e., with two different cameras, set at different shooting angles, to register a wider section of the tube and realise a “quasi” 3D framing, close to the central axe of the tube. The images of the two-camera will be overlapped for this purpose.

The cloud particle size distribution need also to be focused on: a LabVIEW routine will be used with a digital imaging elaboration tool to identify the motion and size of the clusters during dust dispersion. The correlation between cluster size and an associated turbulence scale will be studied.

References

Danzi, E., Franchini, F., Dufaud, O., Pietraccini, M., Marmo, L. (2021). Investigation of the fluid dynamic of the modified Hartmann tube equipment by high-speed video processing. *Chemical Engineering Transactions*, 2021, 86, pp. 367–372

Hosseinzadeh, S., Vanierschot, M., Norman, F., Verplaetsen, F., Berghmans, J. (2018). Flame propagation and flow field measurements in a Hartmann dust explosion tube. Powder Technology, 323, 346–356. 10.1016/J.POWTEC.2017.10.001

ISO /IEC 80079-20-2:2016 Explosive atmospheres - Part 2 0-2: Material characteristics - Combustible dusts test methods

Marmo, L., Danzi, E. (2018), Metal waste dusts from mechanical workings - explosibility parameters investigation, Chemical Engineering Transactions, 67, pp. 205–210. 10.3303/CET1867035

Marmo, L., Ferri, A., & Danzi, E. (2019). Dust explosion hazard in the textile industry. Journal of Loss Prevention in the Process Industries, 62. https://doi.org/10.1016/j.jlp.2019.103935

Marmo, L., Sanchirico, R., Di Benedetto, A., Di Sarli, V., Riccio, D., Danzi, E. (2018), Study of the explosible properties of textile dusts Journal of Loss Prevention in the Process Industries, 54, pp. 110–122. 10.1016/j.jlp.2018.03.003

Murillo, C., Dufaud, O., Bardin-Monnie r, N., López, O., Munoz, F., & Perrin, L. (2013). Dust explosions: CFD modeling as a tool to characterise the relevant par ameters of the dust dispersion. Chemical Engineering Science, 104, 103–116. 10.1016/J.CES.2013.07.02

Proceedings of the 14th International Symposium
on Hazards, Prevention and Mitigation of Industrial Explosions

DOI: 10.7795/810.20221124

A CFD Based Methodology to Design an Explosion Prevention System for Li-Ion Based Battery Energy Storage System

Anil Kapahi, Alberto Alvarez-Rodriguez, Stefan Kraft, Jens Conzen, and Sunil Lakshmipathy

Jensen Hughes, Baltimore, MD USA

E-mail: *akapahi@jensenhughes.com*

Abstract

This work developed a performance-based methodology to design a mechanical exhaust ventilation system for explosion prevention in Li-Ion-based stationary battery energy storage systems (BESS). The design methodology consists of identifying the hazard, developing failure scenarios, and providing mitigation measures to detect the battery gas and maintain its global concentration lower than 25% of the lower flammability limit (LFL) to meet the prescriptive performance criterion of NFPA 69 – Standard on Explosion Prevention Systems. Representative UL 9540A test data is used to define the battery gas composition, release rate, and release duration to describe the failure scenario involving thermal runaway propagation. In addition, an exemplar BESS enclosure geometry is defined to model the failure scenarios using a computational fluid dynamics (CFD) solver. A grid convergence study is performed to estimate the grid resolution required to perform the CFD analysis. In addition, sensitivity studies for different input parameters are performed to understand the impact of inputs on the detection times and ventilation performance. The approach used in this work provides a systematic procedure for the fire protection engineering community to understand the explosion prevention requirement for a BESS installation. The explosion prevention system functionality presented in this work is limited to removing flammable battery gas generated due to the non-flaring decomposition of batteries.

1. Introduction

Energy storage is playing a pivotal role in empowering the decarbonization of transportation and enabling power grids to function with more resilience. Lithium-Ion based batteries have come a long way from their usage in consumer electronics with tens of Wh (watt-hour) capacity to approximate 100 KWh capacity battery systems in modern electric vehicles. Decarbonizing the electricity generation process is a big issue and critical to supporting the changing landscape in the automotive industry. Addressing this issue ensures we do not deal with greenhouse gases at the electricity generation source. Lithium-Ion based energy storage is one of the leading technologies for sustainable and emission-free energy. The advantage of storing green energy, such as solar or wind, during off-peak hours and using it during peak hours is gaining traction as various governments in the world look toward renewable sources of energy. The growth in the energy capacity is tremendous, with the United States having less than 1 GW of large energy storage installations in 2019 to adding a capacity of 6 GW in 2021 and forecasted to achieve an additional 9 GW in 2022 [1].

Like many other energy sources, Lithium-Ion based batteries present some hazards related to fire, explosion, and toxic exposure risk. Although the battery technology is considered safe and is continuously improving, the battery cells can undergo thermal runway when they experience a short circuit leading to a sudden release of thermal and electrochemical energy to the surroundings. Cyclical thermal/electrical loading and unloading, manufacturing defects, and thermal, mechanical, or electrical abuse are many reasons that can cause an exothermic reaction inside the batteries.

Typically, the Li-Ion cells are used as building blocks to form modules comprising cells and racks comprising modules placed inside an enclosure for BESS applications. The most common type of form factor for BESS is shipping-type containers and cabinet-type enclosures (NFPA 855 [2] defines cabinet type ESS as those systems where personnel cannot enter the enclosure other than reaching in to access components for maintenance purposes). BESS contain several battery racks for increased energy capacity. These modular designs allow high flexibility in deploying to match the clients' applications, scaling from neighborhood buildings as backup power sources to large-scale power utility facilities for grid peak shaving applications. BESS designs are moving toward more congested cabinets to optimize the storage capacity of its footprint. Although this strategy can increase heat loads, the reduced open volume can help in reducing the cooling costs; however, it also makes the design challenging from an explosion safety perspective.

NFPA 855 requires BESS installed within a room, building, or walk-in type unit shall be provided with either an explosion control system, i.e., deflagration vents according to NFPA 68 [3], or an explosion prevention system, i.e., a mechanical ventilation system according to NFPA 69 [4]. The standard was amended also to impose this requirement on cabinet-style BESS. This basically means that any BESS of the size of a small ISO container or larger is required to have some form of explosion control. This paper focuses on developing a procedure to design an explosion prevention system for a representative BESS.

While the scope of NFPA 69 is extensive and applies to the design, installation, operation, maintenance, and testing of systems to prevent explosions using a variety of methods, this work is limited to the conceptual design of an explosion prevention system by pursuing the performance-based design option that aims at controlling the combustible concentration. The system is designed using computational fluid dynamics and consists of an exhaust system to remove the flammable battery gas and supply louvers for outside makeup air. The usage of CFD for simulating an accidental release of flammable gas is well established. The CFD simulations can help demonstrate the evolution of gas release as a function of space and time.

A variety of metrics can be used to quantify the global parameters such as volume fraction and mass within an enclosure. In addition, displaying the gas cloud between the lower flammability limit (LFL) and upper flammability limit (UFL) can help quantify the size of the flammable cloud. This detailed information is very useful in understanding the consequence of a scenario and designing the mitigation measures such as gas detection and explosion prevention systems.

The usage of CFD for designing explosion prevention systems is prevalent in process safety industries dealing with flammable fluids [5] and explosible dust [6]. Different scenarios involving spills, buoyancy-driven leaks, momentum-driven leaks, and a sudden loss of containment can be prescribed using a source term in the CFD model. These different leak scenarios require a deep understanding of the flammable fluid, storage and operating conditions, and the associated hazards. The critical challenge in designing an explosion prevention system for a BESS is to quantify the source term that can describe the release of battery gas during a thermal runaway event. The highly non-linear and stochastic behavior of battery cells requires a different approach from other failure scenarios commonly seen in the process safety industry, with greater emphasis on the availability of UL 9540A test [7] data to describe a battery gas release rate. In addition, the released battery gas is a mixture of hydrogen, carbon dioxide, carbon monoxide, and several hydrocarbons, requiring an approach to quantify mixture properties and flammability limit. Furthermore, the HVAC system used to cool the batteries can impact airflows with the formation of hot and cold aisles that can impact the placement of detectors and supply and exhaust locations for the explosion prevention system.

2. Design Approach

2.1 Applicable standards

NFPA 855 [2] requires that an explosion prevention system must be installed in accordance with NFPA 69 [4] for buildings and walk-in containers housing an ESS. NFPA 855 also indicates that a UL 9540A test or equivalent full scale fire test shall be performed to evaluate the fire characteristics of an ESS that undergoes thermal runaway. NFPA 69 requires that the global combustible concentration shall be maintained at or below 25% of the LFL for all foreseeable variations in operating conditions and material loadings. The typical method to achieve this criterion is to use a ventilation/purge system that removes flammable battery gas from the container housing the ESS and replenishes it with outside clean air. For compliance with NFPA 855/NFPA 69 requirements to limit the flammable gas concentration, a representative release rate of battery gas during a thermal runaway scenario is developed for the input to the CFD model.

2.2 Design Inputs

2.2.1 UL 9540A thermal runaway testing

NFPA 855 recommends that a UL 9540A [7] test should be used to evaluate the fire characteristics of an ESS undergoing thermal runaway for explosion control safety systems. An approach to determine a flammable battery gas source term to design explosion control systems has been developed based on UL 9540A or similar test data. The goal of this approach is to ensure that the process is consistent regardless of the battery system being evaluated. Information from the cell, module, and unit level UL 9540A test reports or similar test data available in the literature is used to calculate the composition, properties, amount, and duration of the flammable gas release.

The UL 9540A cell level test defines a repeatable method for forcing a battery cell into thermal runaway. The standard requires measurements of the cell surface temperature as well as the temperature of the gas that is released from the cell during testing. Other important parameters used in the source term model include the gas volume released, gas composition, gas lower flammability limit, and the thermal runaway temperature of the cell. Typically, cells are forced into thermal runaway using film heaters and a steady temperature increase rate. The thermal runaway temperature is indicated as the sharp temperature rise that is significantly greater than what the film heater provides. The reported thermal runaway temperature is the average of four tests. In the fifth and separate test, the previously measured composition of the gas is synthetically replicated and used in a flammability test to determine the lower flammability limit (LFL), burning velocity, and maximum explosion pressure.

The module and unit level UL 9540A tests are required if the cell vent gas composition is flammable according to ASTM E918 [8]. As lithium ion batteries used in most commercial ESS systems use flammable liquid electrolytes and release flammable gases upon a thermal runaway, module and unit level tests must be performed. One or more cells in the initiating module are forced into thermal runaway using the same or similar methodology used in the cell level test. Thermal runaway initiation and propagation within the module, unit or target units are assessed in the respective module and unit level tests. For the development of the source term, the extent and timing of thermal runaway propagation are used to construct an appropriate rate and duration of flammable gas release.

Additional conservatism may be added to the source term to account for the various types of uncertainty present in this analysis. For example, this includes a test to test variability, the thermal runaway initiation method, and conditions compared to an actual scenario, as well as data uncertainty. This is achieved by using the actual cell release volumes and gas composition, but in combination with a shorter time to propagate thermal runaway. This results in a higher overall average gas release rate than was present in the UL 9540A test itself.

2.2.2 Flammable Battery Gas Release Model

Most UL 9540A data commissioned by manufacturers is proprietary. For this work, a set of representative thermal runaway data for a nickel manganese cobalt (NMC) chemistry battery cell was used to develop the input flammable gas model for the CFD model. The data used was from

DOI: 10.7795/810.20221124

experiments done by Archibald [9] and Huang et al. [10] . For a 94 Ah NMC cell thermal runaway test [9] performed in a pressure vessel in a nitrogen environment, a gas volume of 221.6 L was released, with the gas composition as shown in Table 1. For a 4-cell mockup NMC module thermal runaway propagation test [10] with 100 Ah NMC cells, a minimum time for thermal runaway propagation to occur was found to be 90 s, as shown in the temperature data in Figure 1. Note that thermocouples were placed on each side of the cells, and the thermal runaway time corresponded to the steep increase in the temperature of the side nearest the initiating cell 1. Although the cell and module test used different cells, the chemistry and dimensions were the same and were assumed to provide equivalent results for the purpose of this study.

***Table 1:** Gas composition of thermal runaway test on NMC 94 Ah cell performed in pressure vessel [9].*

Species	**Vol. Percent**
Hydrogen	30.60%
Carbon Dioxide	29.90%
Carbon Monoxide	21.30%
Methane	7.20%
Ethylene	5.60%
Propane/Propylene	2.00%
Ethane	1.80%
Others	1.60

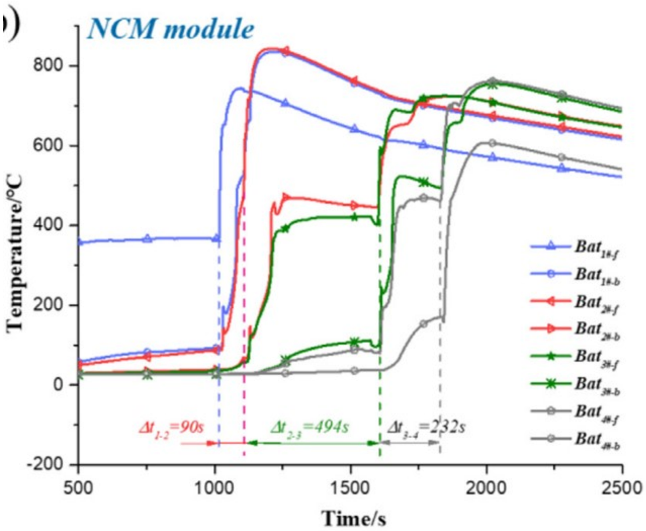

Figure 1: Temperature of 4 cell mockup module with 100 Ah NCM cells thermal runaway test showing minimum propagation time of 90 s [10].

The representative battery module used in the model is shown in Figure 2 and includes 24 cells total in two rows. The separation between the two rows of cells is thermal insulation. For the gas release model, it was assumed that thermal runaway would initially be in the center cell indicated and propagate to all other cells in the top row at a 90 s delay. It was assumed that the 2nd row cells would not experience thermal runaway. It was also assumed for the purpose of this model that no propagation to adjacent modules above, below, or to the side in other racks would occur.

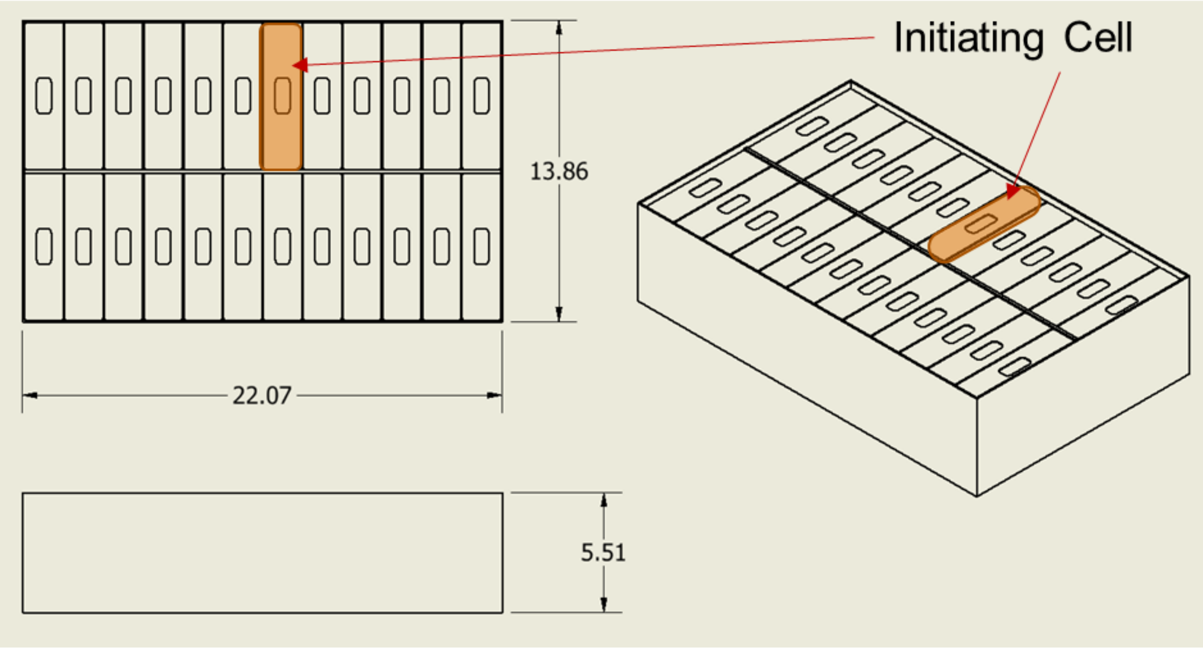

Figure 2: Representative battery module with 24 cells in two rows (units for the dimensions are in inches).

The thermal runaway propagation was assumed to proceed simultaneously in both directions from the initiating cell near the center. After 90 s from the thermal runaway of the initiating cell, the cells immediately adjacent to this cell undergo thermal runaway. This propagation occurs until all the cells in the row have undergone thermal runaway. The local gas released was modeled as a discrete release with all gases exiting the cell in 40 s. The amount of time for the gas to be released can vary based on the cell type and test conditions; Archibald showed that for the 94 Ah NCM cell, the gas release occurred within 10 s [9], whereas Huang et al. indicated the thermal runaway duration for the 100 Ah cells were 19-31 s [10]. Zhang et al. showed for a 50 Ah NCM cell that the maximum vent gas molar amount was released in about 1 minute [11]. For the purposes of this model, the duration of the gas release was assumed to be about 10 minutes for the 12 cells in one row. The average release rate was 4.9 g/s based on a 9.8 minute duration and 226 g of gas released per cell. See Figure 3 for the gas release models.

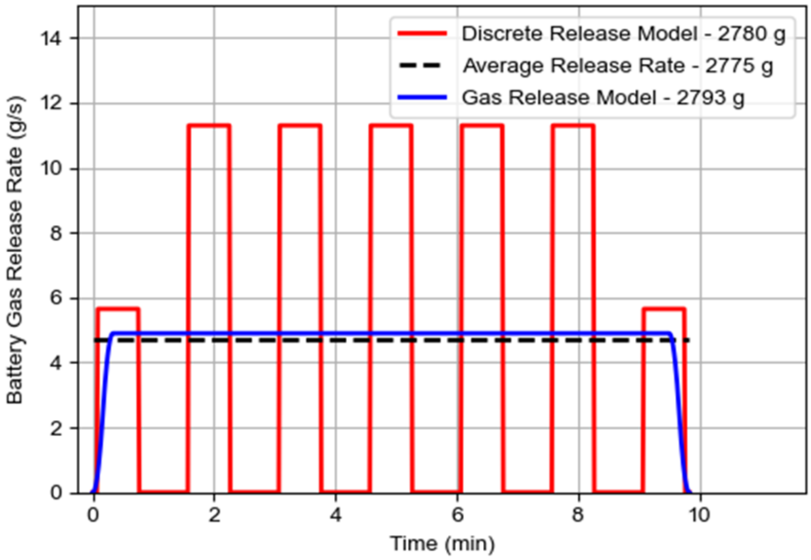

Figure 3: Gas release models for representative module undergoing thermal runaway.

Two battery gas compositions were considered using the composition presented in Table 2. The first battery gas composition was adjusted by combining hydrocarbons and others to propane. This battery gas composition is called composition 1 in this work. A second composition called Composition 2 distributed the others to the known components of battery gas. Both compositions used for the CFD analysis are presented in Table 2. In order to save computational time on the transport equation, air, as a mixture of nitrogen and oxygen, and battery gas are defined as "lumped species". A lumped species is defined as a group of species that transport and react together in the same proportion. This implies that the molecular diffusivities of each component of the mixture are the same, which is an approximation.

Table 2: *Battery gas compositions used in the CFD analysis*

Component	Battery Gas Composition 1	Battery Gas Composition 2
Hydrogen	30.60%	31.10%
Carbon Dioxide	29.90%	30.39%
Carbon Monoxide	21.30%	21.65%
Propane	18.20%	2.03%
Methane	-	7.32%
Ethylene	-	5.69%
Ethane	-	1.83%

The LFL of the gas compositions was calculated according to Le Chatelier's law. The method was modified to use the flammability-concentration curve for H_2-CO_2 as CO_2 is an inert gas. The process for calculating the LFL is explained by Baird [12]. The H_2-CO_2 flammability curve was obtained from Coward and Jones [13]. An approximate value of 5.83% was used for both compositions.

2.2.3 Representative enclosure

A representative container ESS mockup was designed for this modeling work based on general characteristics of solutions used in grid-scale energy storage. The overall dimensions of this container are 40 feet long, 8 feet wide, and 8.5 feet high. Figure 4 shows a section view of the 40 ft container with one row of battery racks shown and an auxiliary room in the unit separated from the other part of the ESS container. This auxiliary room is not considered for the CFD analysis. Two HVAC ducts provide cooling airflow with a total capacity of 2000 CFM to the batteries. There are a total of 22 battery racks, each having 12 modules. The total energy capacity of the ESS container is 4.29 MWh. The ESS container was augmented with two hydrogen detectors (1 and 2) located at the ceiling level, as shown in Figure 5. The detection threshold for each detector is 25% LFL of hydrogen, which corresponds to a 1% hydrogen concentration. The response time corresponding to each detector is 10 seconds. The container material is assumed to be stainless steel of thickness 3 mm. The contents of the container are also assumed to be stainless steel of thickness 3 mm with insulated backing, i.e., no heat loss to the backside boundary.

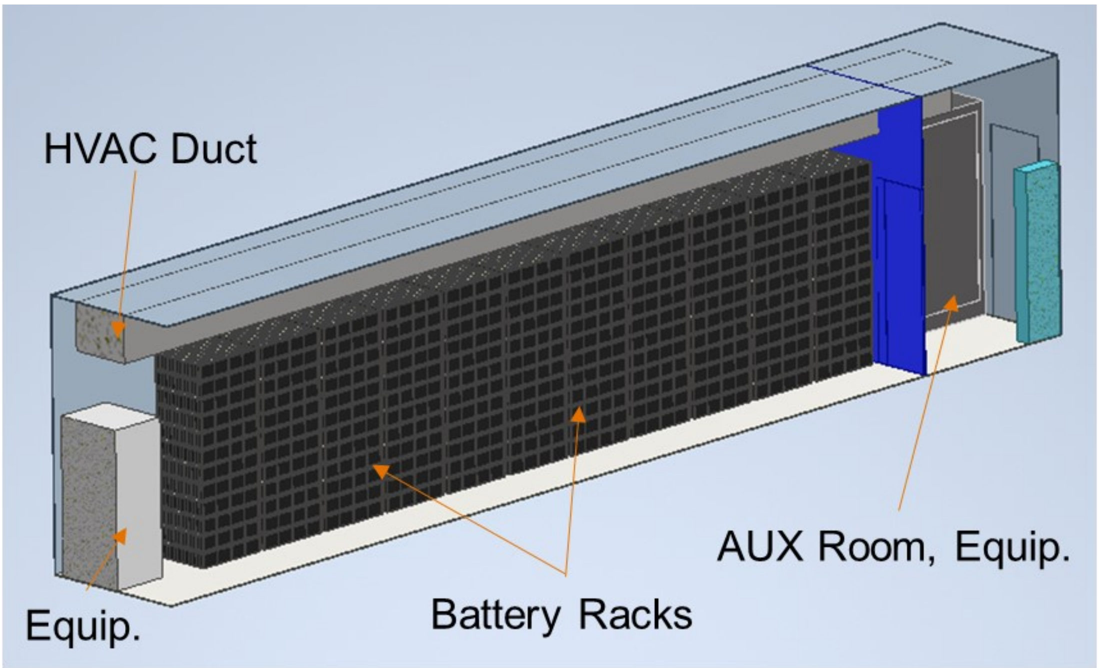

Figure 4: Representative 40 ft ESS container showing one of two rows of battery racks.

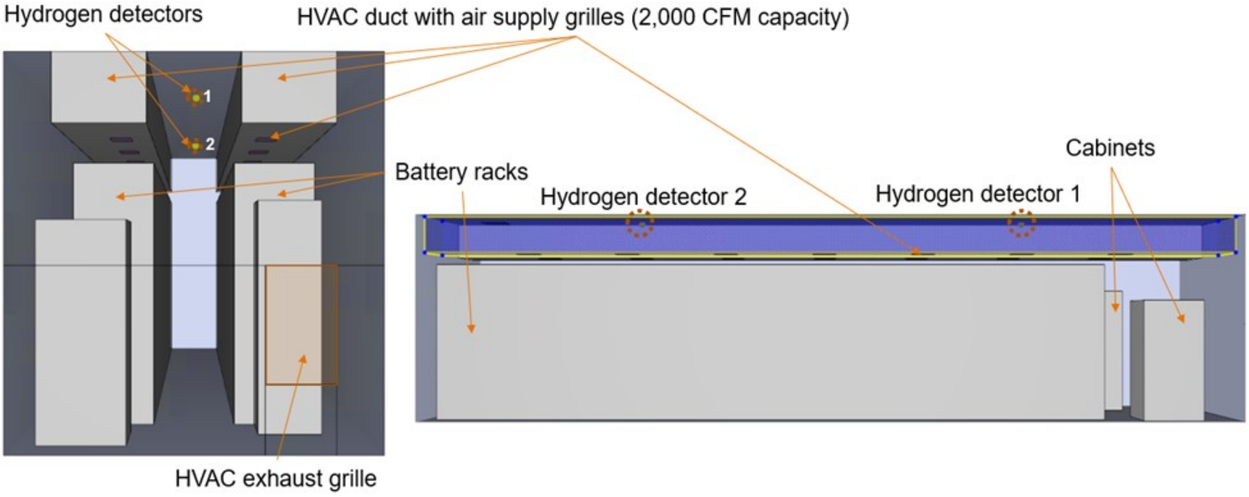

Figure 5: Enclosure showing hydrogen detector location and HVAC supply and exhaust locations

This enclosure will be augmented with an explosion prevention system using an exhaust fan and supply louvers. Note that the HVAC system described above is for the cooling of batteries, while the proposed exhaust and supply louvers will act as an emergency system that activates after detecting battery gas within the enclosure.

2.3 Design Tool

Fire dynamics simulator (FDS) is a computer fire model developed by the National Institute of Standards & Technology (NIST). It is widely used in the fire protection engineering industry to predict thermodynamic conditions for the surrounding environment resulting from an input fire or similar fluid flow-driven event and to evaluate the results against specific performance criteria. The FDS model has the capability to evaluate the evolving distribution of smoke and fire gases, including the resulting temperatures, visibility, and toxic products of combustion, throughout a compartment or building. For the type of analysis performed in work, FDS can evaluate the dispersion of the battery gas based on the different release scenarios while predicting the time when the detectors would actuate and activate the mechanical exhaust system, simultaneously deactivating the HVAC cooling system.

FDS can calculate the changes in said parameters over time. The model divides a given geometry into a series of small control volumes. Each of the volumes is then individually evaluated by the model via a series of conservation equations for mass and momentum transfer. Once the computations are completed for each time interval, the results are compiled to form the numerical and visual results of the model. The model can also consider the flow of air and gases through vents and other openings.

The FDS model presents an idealized representation of a real compartment or enclosure, but one that has proven to be very useful and accurate for many engineering applications. The model has been subjected to a wide range of engineering scrutiny and comparisons with experimental data. FDS has been developed by a recognized government authority and is not biased or influenced by any specific financial interest or association to a particular industry. Documentation of the model, including validation studies, is readily available [14].

2.4 Sequence of Operations

A sequence of operations is defined for the CFD model that results in the release of battery gas at the beginning of the simulation. The battery gas disperses in the container and is detected by one of the two hydrogen detectors. The hydrogen detection results in the activation of the explosion prevention system. A sequence of operations depicting the event and the corresponding event time is shown in **Table 3**.

Table 3: *Sequence of operations for the CFD analysis*

Event	Event Time (s)
Start of battery gas release	0
H_2 detection threshold is reached at one of the two H_2 detectors	t_1
Activation of the exhaust system	t_1 + 10 seconds
The exhaust system reaches its full capacity after a linear ramp of 20 seconds	t_1 + 30 seconds
Battery gas release stops	600 seconds

This event timeline is used for all of the simulations shown in this work except for the simulations involving the grid convergence study. The grid convergence analysis is limited to the detection of battery gas.

3. Modeling Methodology

This section provides an overall modeling methodology and a list of scenarios that were modeled. The 3D CAD geometry of the enclosure shown in Figure 5 was imported into FDS via the software PyroSim developed by Thunderhead Engineering. The model was augmented with point devices to monitor the hydrogen concentration with time. In addition, the HVAC module of FDS was used to set up the cooling HVAC supply and return nodes. At this point, the container had all of its original features captured that can be used for the CFD analysis.

The explosion prevention system required adding further details of a standalone exhaust and supply louvers to the model. The model added two supply louvers of size 1 ft wide by 2 ft high and a 1ft^2 opening for the exhaust fan. The exact locations for these openings are provided in Figure 6. The exhaust location was selected to be at the ceiling level as battery gas is expected to accumulate at the ceiling level as it is hot and buoyant. The supply locations are provided in the middle of the side walls. This results in the mixing of battery gas with supply air leading to exhaust of battery gas and air mixture. Free volume calculations were performed to quantify the amount of space where battery gas can accumulate inside the enclosure. These calculations were performed by assuming all of the obstructions within the container to be solid. The free volume for the enclosure was found to be 1338.5 ft^3.

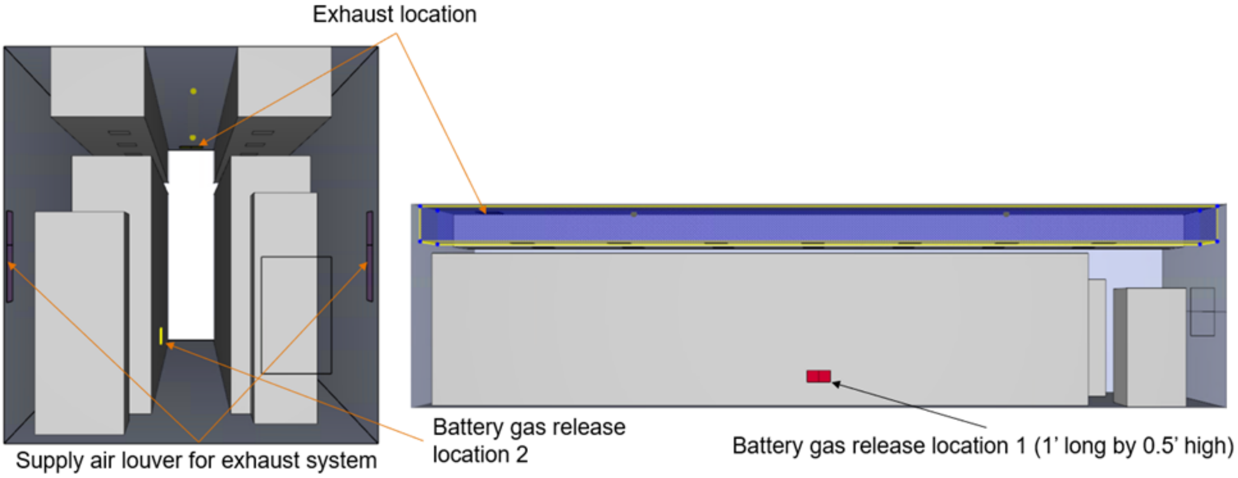

Figure 6. Enclosure showing exhaust system components and battery gas release locations

Before proceeding with the CFD calculations, well-mixed model calculations were performed to estimate the exhaust CFM for the explosion prevention system. These calculations were performed using CONTAM. CONTAM is a tool developed by the National Institute of Standards and Technology (NIST) that models airflow and contaminant dispersal in buildings. The well-mixed assumption refers to the treatment of the enclosure as a single control volume wherein the fluid (air or battery gas) has uniform (well-mixed) temperature, pressure, and battery gas concentration. The model does not consider buoyancy and thermal effects essential to understand the dispersion of hot battery gas in an enclosure filled with air at a significantly lower temperature. Nevertheless, CONTAM can provide reasonable estimates of the exhaust fan capacity needed at a fraction of the computational cost for a CFD model. It should be noted that the CONTAM model is not required to follow the exact layout of the container and the obstructions within the container. A graphically representative model that captures the free air volume of the container is used to quantify the results of the analysis.

The CONTAM model simulated the battery gas failure scenario using a 1000 CFM and 2000 CFM exhaust capacity. The sequence of operations described in Table 3 was used to quantify the detection times leading to the activation of the exhaust system. The evolution of global battery gas volume fraction as a function of time for both scenarios is shown in Figure 7.

DOI: 10.7795/810.20221124

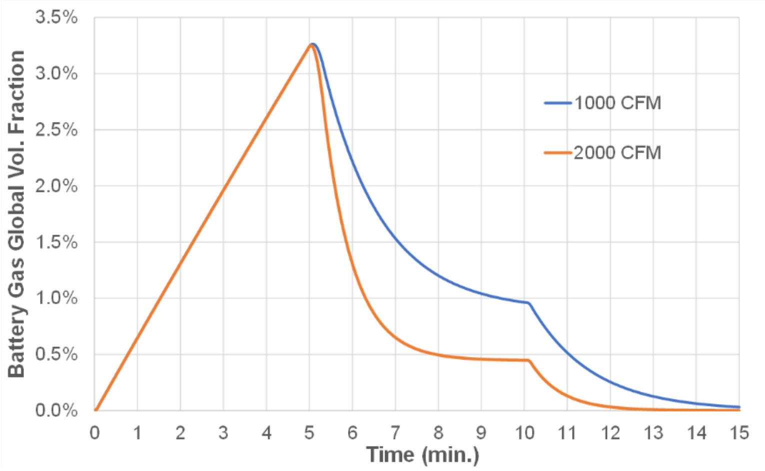

Figure 7. Global battery gas volume fraction calculated using CONTAM

The battery gas volume fraction increases steadily until it reaches a value of 3.3%, corresponding to a volume fraction of 1% for hydrogen resulting in the activation of the exhaust system. The volume fraction drops as soon as the exhaust system is activated for both scenarios. The exhaust capacity of 2000 CFM was selected for the baseline CFD case based on the steady-state 0.5% battery gas concentration, which is lower than 25% of the battery gas LFL.

3.1 Modeling scenarios

Once the estimated, required exhaust capacity is determined, a baseline scenario is defined, which is used to perform a grid convergence study. In addition, a simulation matrix is defined to understand the sensitivities associated with various input parameters and their impact on the detection times and ventilation performance. The simulation matrix with input parameters for baseline and sensitivity scenarios is shown in Table 4.

Table 4: *Input Parameters for Baseline and Sensitivity Scenarios*

Input Parameter	Baseline Scenario value	Sensitivity study value(s)
Battery Gas Composition	Composition 1	Composition 2
Battery Gas Release Location	Location 1	Location 2
Battery Gas Release Temperature	600 ºC	400 ºC, 800 ºC
Battery gas Release Rate	Average rate	Discrete Rate
Ambient (outside) temperature	30 ºC	20 ºC, 40 ºC
Location of Supply Louvers	Middle of the container	Top/Bottom of the container
Exhaust Fan Capacity	2000 CFM	1000 CFM, 1500 CFM
HVAC Configuration	OFF (20 ºC as inside air temperature)	ON[1]- 100% recirculation mode (20 ºC as inside air temperature)
Material of container components	Steel surfaces	Adiabatic

---

[1] Note that the HVAC system is switched off after the battery gas is detected. This scenario is different from rest of the scenarios that can be described using the sequence of operation presented in Table 3.

The battery gas release locations and supply louver locations for baseline and sensitivity scenarios are shown in Figure 6.

3.2 Modeling Results

This section describes the results of the CFD analysis used to design the explosion prevention system.

3.2.1 Grid Convergence Study

A critical component in any CFD analysis is the resolution of the simulation dictated by the size of the grid cell. A grid convergence study is performed to evaluate a grid size resulting in a converged solution to ensure the results are not dependent on the grid size. The study started with a grid size of 6 inches and reduced it by half until a converged solution was obtained. The study was limited to the detection analysis to save the computation resources, and the simulations were stopped as soon as the hydrogen concentration at the two detectors reached a volume fraction of 1%. The results for the evolution of hydrogen at two different detector locations for four different grid sizes are shown in Figure 8. The figure shows that the evolution profile of hydrogen at both locations is getting converged as the grid is refined.

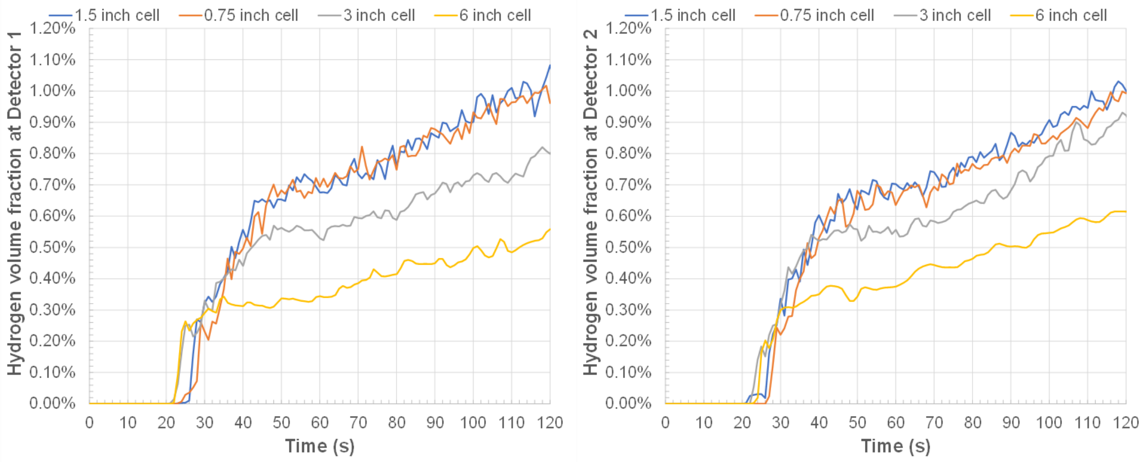

Figure 8. Time evolution of hydrogen concentration at both detectors for different grid resolutions.

In addition, global parameters such as battery gas mass greater than a certain percentage of LFL were evaluated to quantify the impact of numerical diffusion. This is an important parameter as it impacts the flammable cloud size inside the enclosure. The results for battery gas mass above 25% LFL, 50% LFL, and LFL for all four grid sizes are shown in Figure 9.

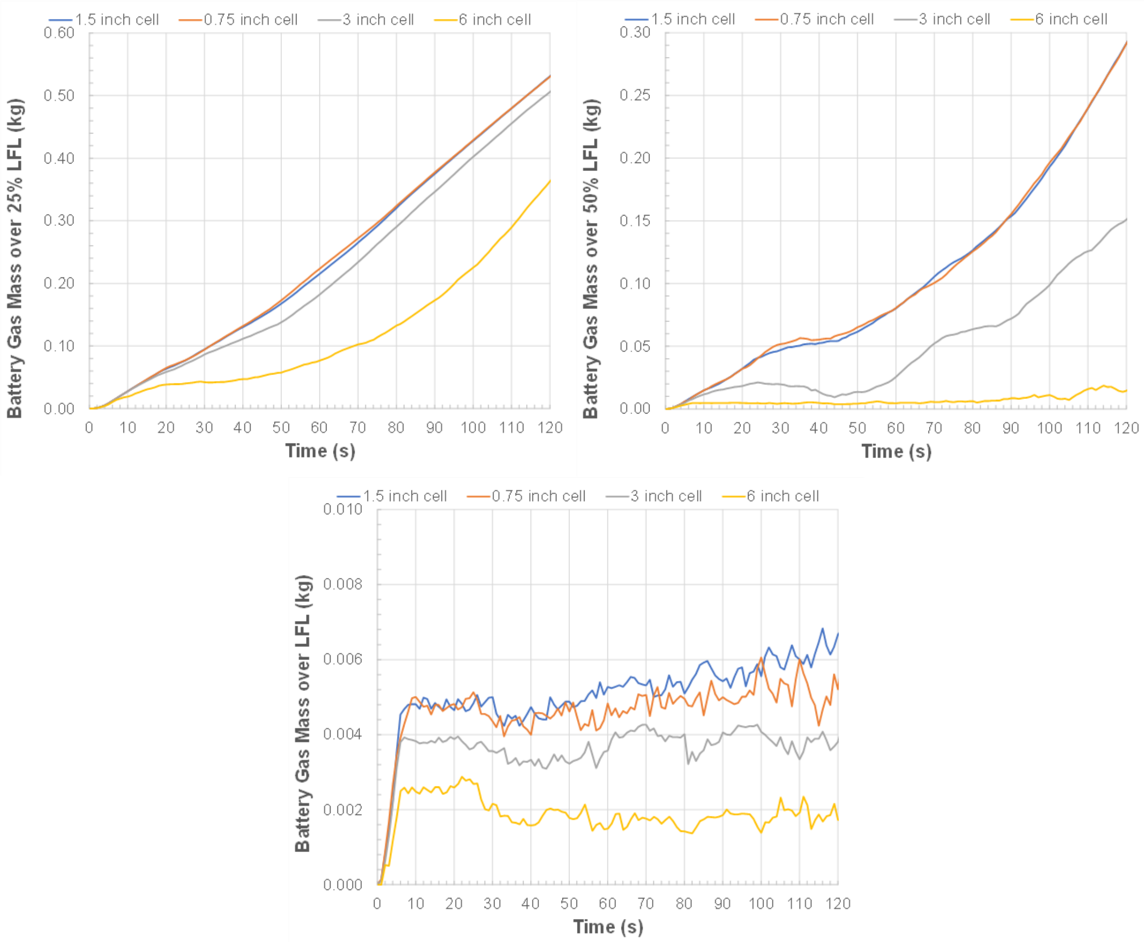

Figure 9. Time evolution of battery gas mass within the container for different grid resolutions (a) over 25% LFL (b) over 50% LFL (c) over LFL

The battery gas contours for a volume fraction greater than 25% LFL and LFL for all four grid resolutions are shown in Figure 10 and Figure 11, respectively. The figure shows the higher numerical diffusion with the coarser grids (3 inches and 6 inches), resulting in a reduction in the local concentration of battery gas compared to the finer grids (0.75 inches and 1.5 inches) scenarios. Note that the global volume fraction and the total mass of battery gas are identical for all cases as no amount of battery gas is leaving the enclosure.

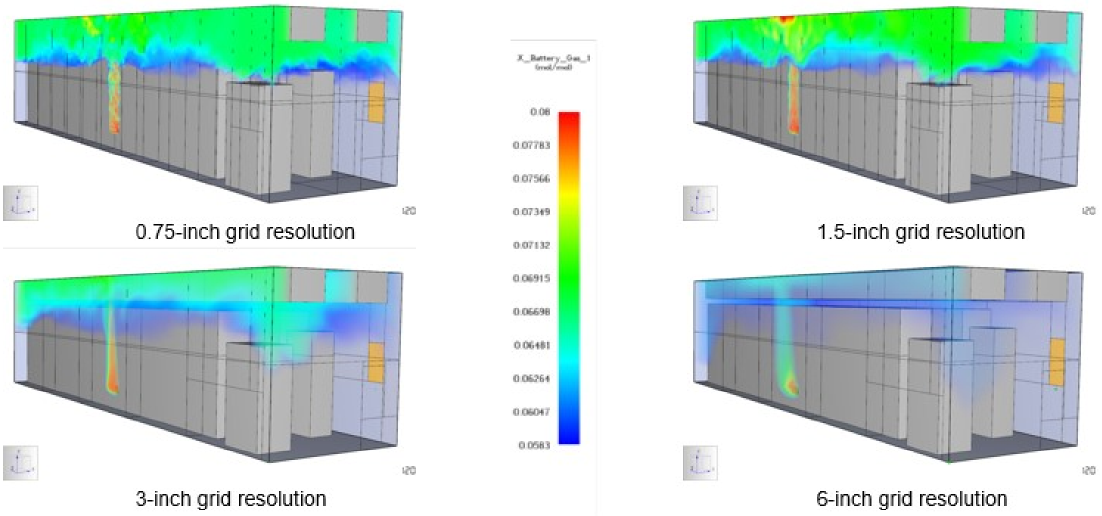
0.75-inch grid resolution

1.5-inch grid resolution

3-inch grid resolution

6-inch grid resolution

Figure 10. Battery gas contours for volume fraction greater than 25% LFL for the grid convergence study

DOI: 10.7795/810.20221124

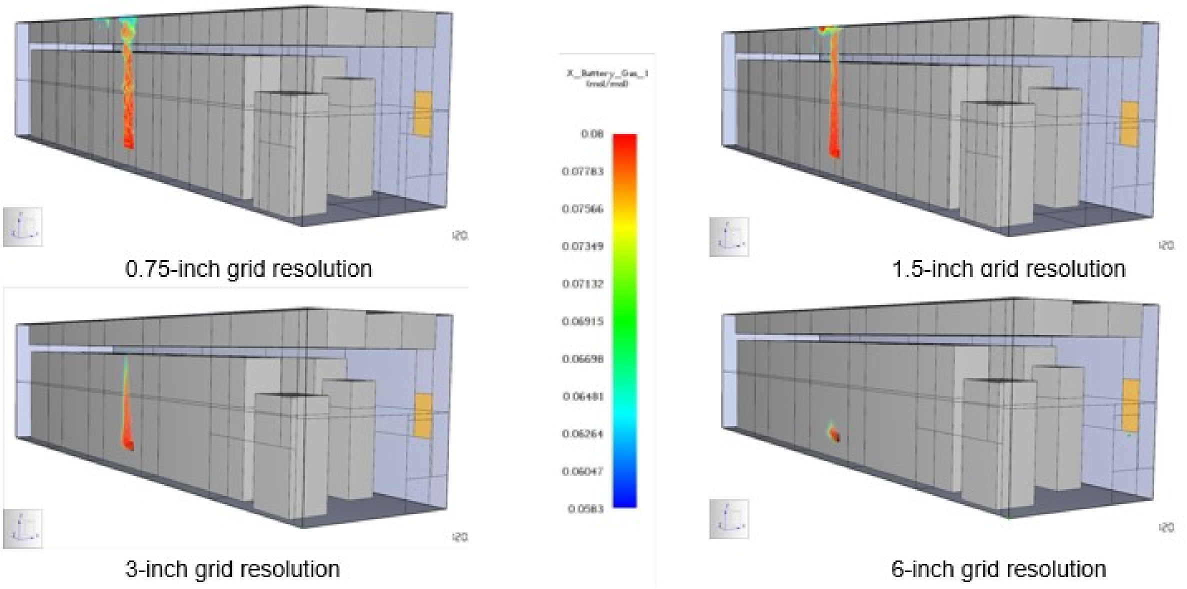

0.75-inch grid resolution

1.5-inch grid resolution

3-inch grid resolution

6-inch grid resolution

Figure 11. Battery gas contours for volume fraction greater than LFL for the grid convergence study

Based on the results obtained from the grid convergence study, it was decided that a grid resolution of 1.5 inches is sufficient for performing this analysis.

3.2.2 Baseline Scenario

This section describes the results for the baseline scenario using a grid resolution of 1.5 inches identified using the grid convergence study. The scenario was simulated using the sequence of operations presented in Table 3. Location 1 for the battery gas is selected as it is equidistant from both detectors and is close to the enclosure floor. The input parameters for the baseline scenario are listed in Table 4. The evolution of hydrogen concentration for both detectors is shown in Figure 12. The gas is detected at detector 1 at 107 seconds resulting in the activation of the exhaust fan at 117 seconds. Note that the local volume fraction shown in this paper is based on the CFD model's raw data. A time averaging is recommended to ensure a smooth evolution of local concentration can be obtained. This will require a two-step simulation process. The first step requires post-processing the detection data to obtain the detection time and the second step uses the time-averaged detection time to activate the exhaust system.

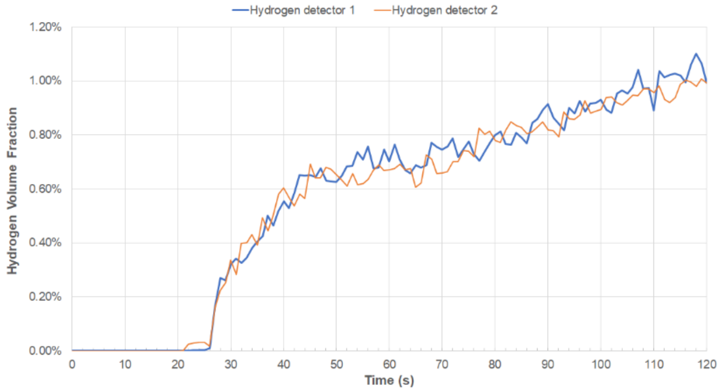

Figure 12. Time evolution of Hydrogen volume fraction at detector locations

The battery gas contours before the activation of the exhaust system are shown in Figure 13 (a). The figure shows the accumulation of battery gas at high in the enclosure. The global volume fraction of battery gas inside the enclosure is approximately 1.3% and is reduced immediately as the exhaust system ramps up to its full capacity of 2000 CFM at 137 seconds.

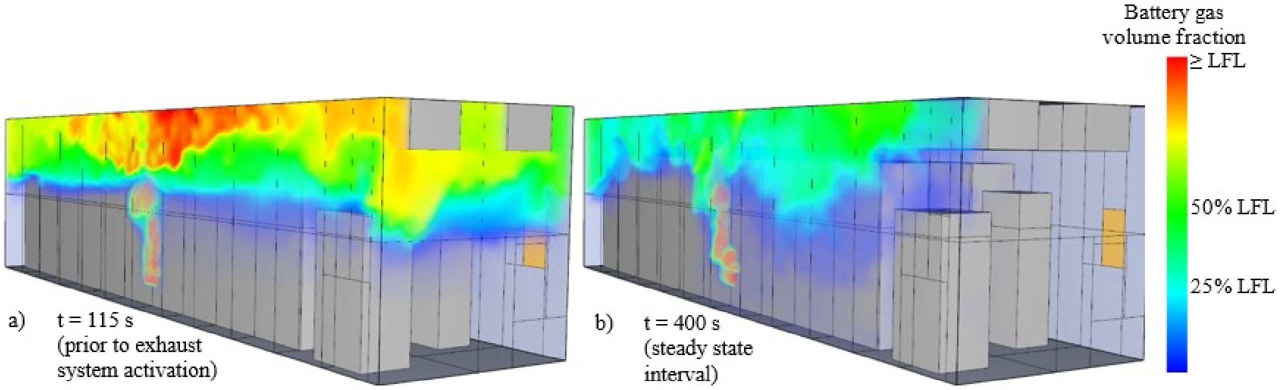

Figure 13. 3D contours of battery gas volume fraction inside the enclosure

The time evolution of battery gas global volume fraction for the whole analysis is shown in Figure 14. The battery gas contours at 400 seconds representing the steady-state interval, are shown in Figure 13(b). The evolution of battery gas in Figure 13 and Figure 14 shows that the explosion prevention system can remove the battery gas from the enclosure. The 3D contours of battery gas can also help identify local spots where battery gas can concentrate. In addition, the battery gas concentration during the steady-state is 0.31%, which is significantly lower than the 25% LFL (1.45%).

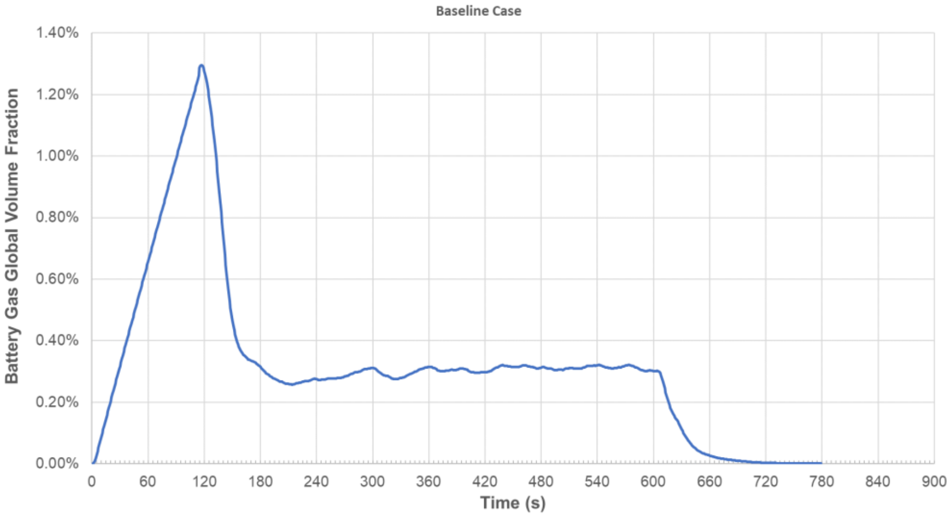

Figure 14. Time evolution of global battery gas volume fraction inside the enclosure

3.2.3 *Sensitivity Analysis*

This section describes the sensitivity analysis of each input parameter used for the baseline scenario. A sensitivity analysis is a study to understand the impact of uncertainty in the input parameters on the model's performance. Note that the input uncertainty is assumed to be known in this study, and the various values that each input variable can have are defined in **Table 4**. The model performance in this work can be assessed based on detection time, peak global battery gas volume fraction, and steady-state global battery gas volume fraction. These parameters were discussed for the baseline scenario in section 3.2.2.

The impact of input sensitivity on battery gas detection time for all scenarios is shown in Figure 15. In addition, the peak and steady-state global battery gas volume fractions are shown in Figure 16.

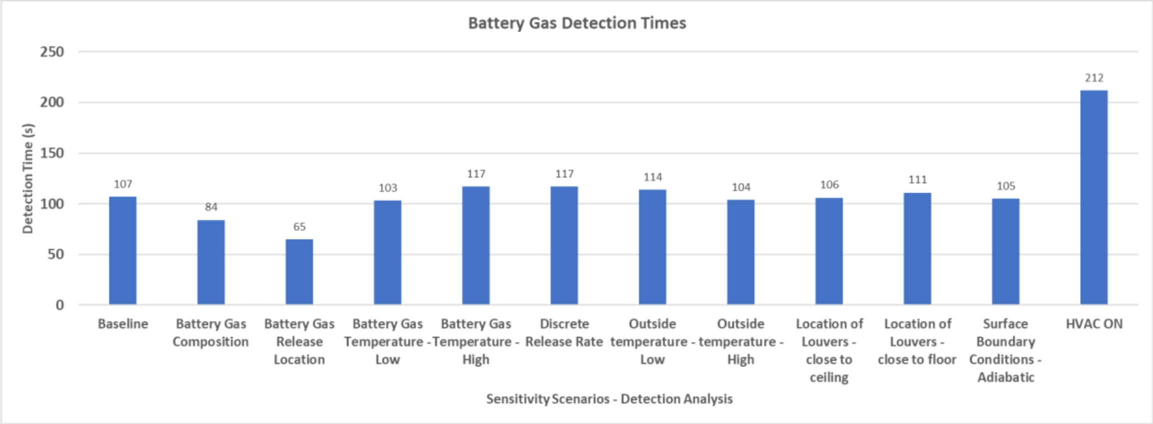

Figure 15. Battery gas detection times for all modeled scenarios for the sensitivity analysis

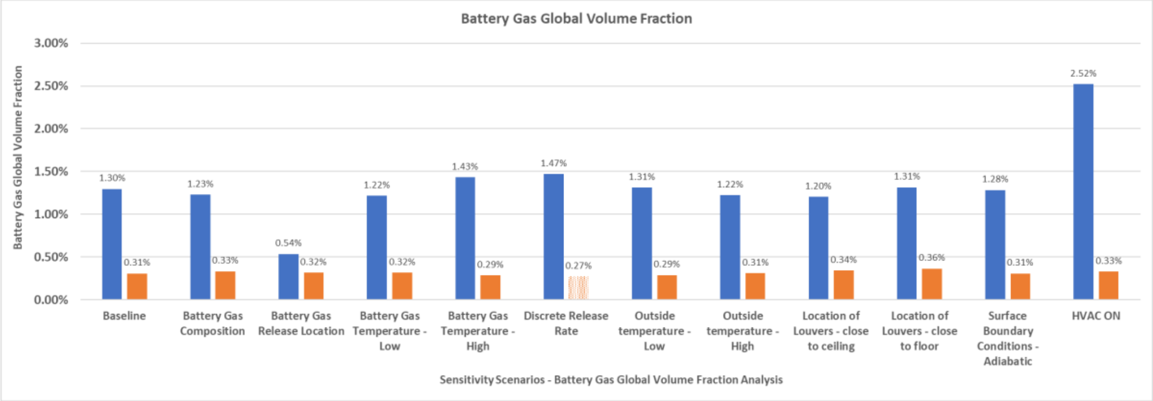

Figure 16. Battery gas global volume fraction metrics for all modeled scenarios for the sensitivity analysis

The change in battery gas composition (composition 2 – see section 2) results in a faster detection because of the higher volume fraction of hydrogen, i.e., 31.10 % compared to 30.60% (composition 1 – baseline scenario). In addition, the molar mass of battery gas is lower for composition 2, resulting in gas being more buoyant, leading to faster detection of hydrogen at the ceiling. There is no significant change in global volume fraction metrics.

The impact of detection time on battery gas release location is informative, with faster detection for a location closer to detectors. This analysis emphasizes the need to select a conservative battery gas release location for the explosion prevention system design. This is corroborated by lower peak global volume fraction metrics, as shown in Figure 16.

The uncertainty in the UL 9540A test can result in having a range of temperatures associated with battery gas release. The sensitivity analysis associated with varying the battery gas release temperature can impact the detection times with higher temperatures resulting in delayed detection and lower temperatures resulting in faster detection times for the studied configuration. The impact of detection times can be seen on the peak global volume fraction in Figure 16.

The discrete release rate is modeled using the profile presented in Figure 3. The comparison of the global battery gas volume fraction for this analysis with the baseline scenario is shown in Figure 17. The figure shows that using a discrete model can increase detection times and global battery gas

DOI: 10.7795/810.20221124

metrics. A discrete model with a shorter battery gas release duration than the cell to cell propagation time can result in a much higher peak release rate than the average release rate. This can result in local time instances having battery gas global volume fraction higher than the steady-state value observed during an averaged release.

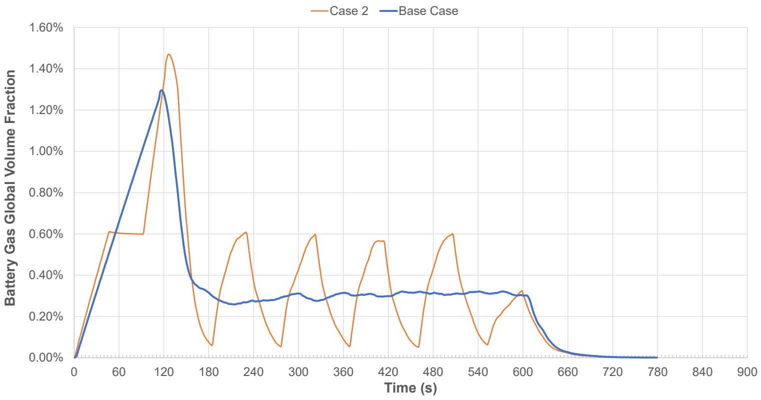

Figure 17. Comparison of global battery gas volume fraction for the averaged battery release model (baseline) and the discrete model

The impact of outside temperature on model performance is attributed to heat transfer through the enclosure boundaries and does not impact the overall performance significantly. The location of supply louvers at the ceiling level results in a lower peak global volume fraction but does not impact the steady-state value significantly.

A critical component of designing the explosion prevention system is understanding its interactions with the cooling HVAC unit. The interaction of the airflow created by the HVAC unit with the battery gas can influence the battery gas dispersion within the enclosure leading to a change in detection time. A sensitivity analysis was performed to quantify the detection time while the cooling HVAC unit was on and in 100% recirculation mode. The battery gas was released once the cooling HVAC unit established a steady airflow. The release of battery gas in a more turbulent environment than the quiescent conditions during HVAC system off resulted in a longer detection time. Enhanced mixing of battery gas with the air resulted in a relatively uniform concentration of battery gas within the enclosure. This is demonstrated in Figure 18 by comparing the contours of battery gas volume fraction inside the enclosure at 107 s for both HVAC ON and OFF scenarios. This time corresponds to the battery gas detection time for the HVAC OFF scenario (Baseline case). In addition, the figure also shows the battery gas contours at 212 s, which is the time corresponding to the detection of battery gas for the HVAC ON scenario.

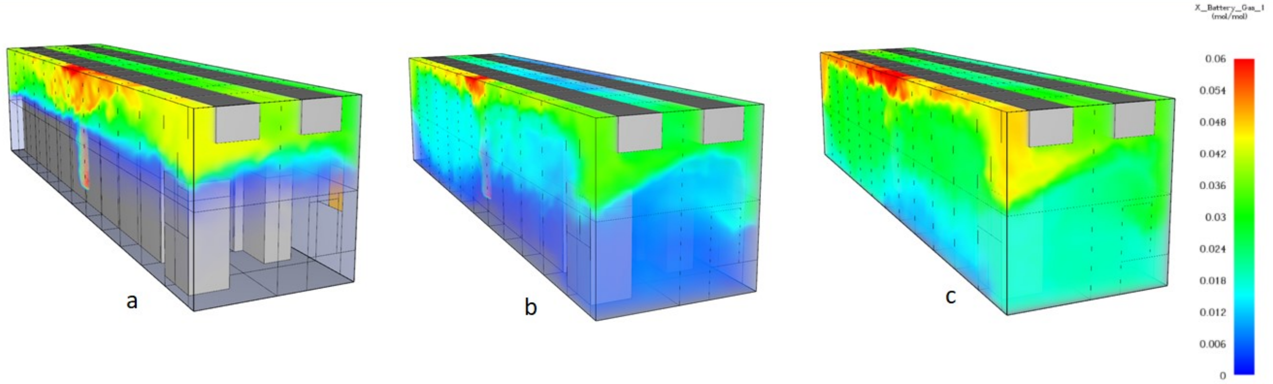

Figure 18. 3D contours of battery gas volume fraction (a) Baseline scenario at 107s (HVAC OFF) (b) HVAC ON scenario at 107 s (c) HVAC ON scenario at 212 s

The peak and steady state battery gas global volume fraction for the HVAC ON scenario was 2.52% and 0.33%, respectively.

The authors have observed that it is difficult to get accurate thermal properties for battery racks and other objects in the enclosure. A sensitivity analysis was performed assuming all surfaces within the enclosure, including the enclosure boundary, are adiabatic. This change did not impact the results significantly.

4. Conclusion

This work provides a methodology to design a conceptual explosion prevention system for an ESS enclosure according to the performance-based design option of NFPA 69. A procedure to construct the battery gas release rate based on different levels of UL 9540A test data is established. The release profile is assumed to present a hazard associated with flammable battery gas generated due to the non-flaring decomposition of batteries. A representative ESS enclosure with battery racks, HVAC ducts, and other representative equipment is augmented with a hydrogen detection system and an explosion prevention system. A methodology is provided to identify the exhaust and supply locations and evaluate the exhaust CFM required for the explosion prevention system. It is recommended to perform the grid convergence study to evaluate the grid size for a converged solution. Several input parameters are identified to understand the sensitivity associated with each parameter and its impact on the overall performance of the detection and explosion prevention system. The sensitivity study resulted in increased detection time and peak global battery gas volume fraction by 10% for a few scenarios. Most scenarios did not result in a significant change in steady-state battery gas global concentration.

A significant increase in detection time and battery gas peak global volume fraction was found for the HVAC ON case. This was due to the enhanced mixing of battery gas with air, resulting in delayed detection and increased volume fraction.

The discrete battery gas release rate resulted in battery gas concentration oscillating between 0.6% and 0.5% once the explosion prevention system was activated. The difference in the evolution of global volume fraction for an averaged release rate and a discrete release rate can be significant depending on the cell release duration and cell to cell propagation times. This shows the challenges in defining the battery gas release profile and its impact on the performance of the explosion prevention system.

Note that the work presented here did not consider the presence of a clean agent or an aerosol-based suppression system that may impact the performance of the detection system and the ventilation system.

In general, a CFD-based methodology can be effectively used with the performance-based design of an explosion prevention system. In addition to global statistics, the CFD model can provide detailed information on local hotspots where battery gas may concentrate. This study also highlighted the importance of sensitivity analysis on the input parameters to ensure the designed system functions as expected for all operational conditions. Overall, the methodology presented here can be extended to designing an explosion prevention system for any ESS enclosure.

DOI: 10.7795/810.20221124

Bibliography

[1] J. Blunt and K. and Hiller, "https://www.wsj.com/articles/," Wall Street Journal, 21 December 2021. [Online]. Available: https://www.wsj.com/articles/battery-storage-soars-on-u-s-electric-grid-11640082783?reflink=desktopwebshare_permalink.

[2] NFPA, *NFPA 855 Standard for the Installation of Stationary Energy Storage Systems,* National Fire Protection Association, 2020.

[3] NFPA, NFPA 68: Standard on Explosion Protection by Deflagration Venting, 2018 ed., National Fire Protection Association, 2018.

[4] NFPA, NFPA 69: Standard on Explosion Prevention Systems, 2019 ed., National Fire Protection Association, 2019.

[5] R. Shen, J. Zeren, P. Trent, S. Yue and W. Qingsheng, "Recent application of Computational Fluid Dynamics (CFD) in process safety and loss prevention: A review," *Journal of Loss Prevention in the Process Industries,* vol. 67, no. 104252, 2020.

[6] R. K. Eckhoff, "Dust Explosion Prevention and Mitigation, Status and Developments in Basic Knowledge and in Practical Application," *International Journal of Chemical Engineering,* vol. 2009, no. Article ID 569825, p. 12, 2009.

[7] ANSI/CAN/UL, UL 9540A: Standard for Test Method for Evaluating Thermal Runaway Fire Propagation in Battery Energy Storage Systems, 4th ed., Underwriters Laboratories Inc., 2019.

[8] ASTM E918, "Practice for Determining Limits of Flammability of Chemicals at Elevated Temperature and Pressure," 2011.

[9] E. J. Archibald, Fire & Explosion Hazards Due to Thermal Runaway Propagation in Lithium-Ion Battery Systems, The University of Texas at Austin, 2021.

[10] Z. Huang, X. Li, Q. Wang, Q. Duan, Y. Li, L. Li and Q. Wang, "Experimental investigation on thermal runaway propagation of large format lithium ion battery modules with two cathodes," *International Journal of Heat and Mass Transfer,* vol. 172, 2021.

[11] Y. Zhang, H. Wang, W. Li and C. Li, "Quantitative identification of emissions from abused prismatic Ni-rich lithium-ion batteries," *eTransportation,* vol. 2, 2019.

[12] A. R. Baird, E. J. Archibald, K. C. Marr and O. A. and Ezekoye, "Explosion Hazards from Lithium-Ion Battery Vent Gas," *Journal of Power Sources,* vol. 446, pp. 227-257, 2020.

[13] H. F. Coward and G. W. Jones, "Limits of Flammability of Gases and Vapors, Bulletin 503," U.S. Department of the Interior Bureau of Mines, Washington, D.C., 1952.

[14] K. McGrattan, S. Hostikka, R. McDermott, J. Floyd and M. and Vanella, "Fire Dynamics Simulator, User's Guide. National Institute of Standards and Technology, Gaithersburg, Maryland, USA, and VTT Technical Research Centre of Finland, Espoo, Finland," NIST Special Publication 1019, sixth edition (FDS Version 6.7.5), August 21, 2020.

[15] T. Fateh, T. Rogaume and F. Richard, "Multi-scale modeling of the thermal decomposition of fire retardant plywood," *Fire Saf. J.,* p. 36–47, 2014.

DOI: 10.7795/810.20221124

Modelling Methodology for Deflagration Vent Design of Battery Energy Storage Systems

Sunil Lakshmipathy [a*], Anil Kapahi [a], Jerome Taveau [a], Stefan Kraft [a], and Jens Conzen [a]

[a] Jensen Hughes, Baltimore, USA

E-mail: slakshmipathy@jensenhughes.com

Abstract

The objective of this study is to evaluate the design modeling methodologies utilized in deflagration vent sizing for Lithium-Ion based Battery Energy Storage Systems (Li-BESS). Design of Li-BESS which are typically confined and highly congested enclosures should include design of explosion mitigation systems such as deflagration vents. Practical and reliable deflagration vent design modelling is therefore an important requirement. The current study provides a comparative evaluation between the commonly used prescriptive code based engineering models such as NFPA 68 (2018) and EN 14994 (2007) and performance-based computational fluid dynamics (CFD) modelling for explosion vent design of Li-BESS. The analysis details the applicability of prescriptive code-based engineering models for Li-BESS geometries and CFD modeling considerations for these Li-BESS.

Deflagration analysis was performed for a hypothetical Li-BESS with the battery cells in thermal runaway.

Keywords: *Battery Energy Storage Systems (BESS), Explosion protection, NFPA 68, EN14994, CFD Modelling*

1 Introduction

Lithium-Ion based Battery Energy Storage Systems (Li-BESS) with their ability to store energy, help facilitate reliable supply from intermittent energy production sources such as wind and solar. Li-BESS are gaining increasing prominence as the landscape for energy production is shifting towards renewable resources. Li-BESS, with their inherent storage technology, pose hazardous threats that need to be minimized and managed. Explosions being one of the main hazards posed by Li-BESS, deflagration venting forms an important design consideration for these systems. Failure of BESS utilizing Lithium-Ion battery technology (Li-BESS) due to thermal runaway of the battery cell/module would result in battery gas which is flammable being released into the BESS enclosure. The release of the flammable battery gas can rapidly form an explosive atmosphere inside the BESS enclosure. Ignition of the flammable mixture inside the BESS enclosure will trigger a deflagration event. Deflagration venting is the most frequently used explosion hazard mitigation technique in the industry. Deflagration venting creates a pathway for the rapidly expanding vapors to exit the enclosure in the event of a deflagration. Vents must be designed to limit the maximum pressure (P_{red}) developed within the enclosure during the vented deflagration to be less than the enclosure strength by a sufficient margin of safety to prevent structural failure as per the requirements of NFPA 68 (NFPA 68, 2018, §4.2.1.2).

Deflagration analysis in the current study is performed by considering a representative hypothetical Li-BESS with the battery cells undergoing thermal runaway and releasing flammable gas into the Li-BESS enclosure. Section 2 of this paper presents the industry standard tools for deflagration vent design which are considered for comparative analysis in the current study. A discussion on the Li-BESS hazards and specifically the explosion hazards is presented in Section 3. Details of the Li-BESS are presented in Section 4. Section 5 presents the modeling considerations for this analysis while Section 6 and Section 7 discuss the results and conclusions from the deflagration vent sizing analysis performed for the BESS using NFPA 68, EN-14994 engineering models and CFD methods, respectively.

2 State of the Art for Explosion Vent Design Tools

The most commonly used methods in the industry to size explosion vents for an enclosure are based on the prescriptive-based vent design methodology presented in NFPA 68 (2018) and EN-14994 (2007) which are the regulatory standards for explosion vent design in North America and Europe, respectively.

2.1 NFPA 68 (2018)

Deflagration vent sizing in NFPA 68 is based on the peak pressure, which is affected by many factors such as enclosure characteristics i.e., size and shape of the enclosure, gas mixture, characteristics of the vent, congestion inside the enclosure, and the ignition location. Although easy to use, the correlations in NFPA 68 are conflicting in their setup party due to the complex nature of the explosion venting process itself (Dorofeev, 2011). The vent sizing correlations offered in NFPA 68 are found to be well suited for hydrocarbon mixtures in small and medium enclosures (Mokhtar 2020). However, they were not reliable for hydrogen-air explosions. The limited applicability range of the empirical correlations is due to the narrow validity range of the experimental data used to derive these.

2.2 EN-14994 (2007)

Deflagration vent sizing in EN-14994 is based on the concept of gas explosion constant, K_G. $K_G$which is determined experimentally, is the maximum rate of pressure rise inside a closed vessel under standard conditions. the empirical correlations in EN-14994 is only valid for empty enclosures. and flammable atmospheres with gas explosion constant, $K_G \leq 550\ bar\, m/s$. EN-14994 correlations for the vent size also includes the vent area as a function of the vessel volume, and the static vent burst pressure. EN-14994 does not account for presence of obstacles inside the enclosure which is a major limitation for application in Li-BESS deflagration vent sizing which generally are highly congested geometries.

2.3 CFD Analysis

Computational Fluid Dynamics (CFD) methods have been increasingly used for deflagration vent sizing analysis and are demonstrated to become suitable alternative approach as they provide higher resolution in capturing the physics of explosion venting (Woolley, 2013, Baraldi, 2010, Di Sarli, 2009). Limitations of the engineering models to account of congestions and fuel compositions suggest that CFD methods will be an important tool for deflagration vent sizing of complex geometries as considered in this study.

3 Battery Energy Storage Systems using Li-Ion Battery Technology

The most common type of form factor for BESS is shipping-type containers and small cabinet type enclosures. Li-BESS comprises several battery racks for increased energy capacity. To maintain a small footprint, BESS are highly congested geometries. The modular design bases and enclosure type form factor allow for these energy systems to allow for high flexibility in deploying these to match the clients' applications scaling from neighborhood buildings as back-up power sources to large-scale power utility facilities for grid peak shaving applications.

Cyclical thermal/electrical loading and unloading of Li-Ion batteries in BESS pose a high risk and hazards due to the increased possibility of thermal and electrical abuse. Battery failure that can occur due to many contributing factors such as manufacturing defects, thermal abuse, electrical abuse, and mechanical damage have a tendency to cause an exothermic reaction inside the sealed batteries. These batteries undergo thermal runaway which causes the battery cells to generate large amounts of flammable gas consisting of hydrogen (H_2), carbon monoxide (CO), carbon di-oxide (CO_2), and various hydrocarbons (THC) such as propane and methane (Baird, A.R., 2019). The release of these flammable gases in the BESS enclosures can create a rapidly growing explosive environment inside the BESS enclosure.

The need for deflagration venting for BESS enclosures is well documented. NFPA 855 §4.1.2.1 (NFPA 855, 2020) does not necessitate providing deflagration venting if it can be demonstrated that the flammable gas concentrations in the BESS enclosure are maintained below 25% lower flammability limit (LFL) in locations where the gas is likely to accumulate. However, these are recommended to minimize and mitigate explosion hazard. One of the lessons learned from the explosion accident at the BESS facility in Surprise Arizona (DNV-GL, 2020) which resulted in injuries to the firefighters was providing explosion vents following the NFPA 68 guidelines (NFPA 68, 2018). Explosion hazard mitigation for BESS enclosures typically includes fitting the enclosure geometry with explosion relief vents. Design criterion for these vents is to provide sufficient vent area to relieve the deflagration overpressure (P_{red}) inside the BESS enclosures to values below the ultimate strength of the enclosure.

4 Representative Li-BESS and Thermal Runaway Consideration

4.1 BESS Geometry

A representative container BESS mockup was designed for this modeling work based on general characteristics of solutions used in grid-scale energy storage. The BESS enclosure is considered to be a 40-ft ISO container geometry with all the essential internal components such as battery racks, control box, and HVAC ducting added to represent the congestion inside these geometries. Figure 1 shows a cut section of the BESS geometry providing details of the BESS interior and Figure 2 shows a cross-sectional view of the BESS. The auxiliary room at the end of the BESS enclosure is considered to be separated from the battery racks with a full wall partition.

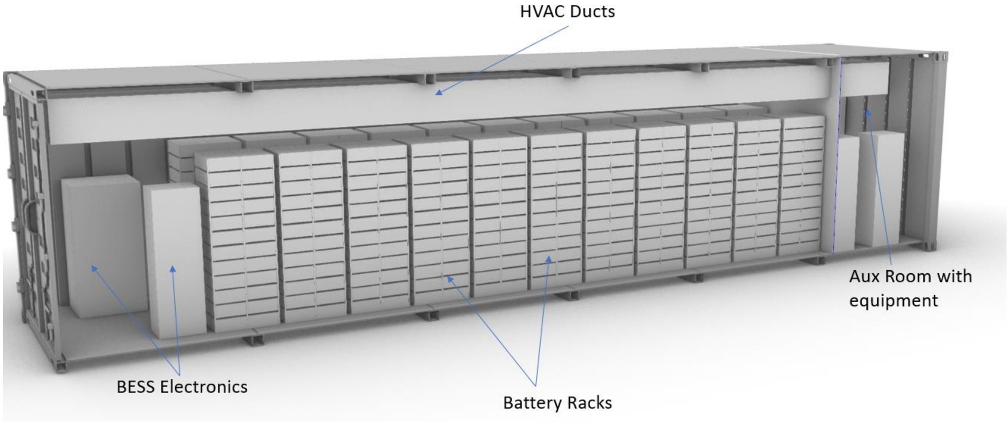

Figure 1: Representative 40-ft BESS container showing one of the two rows of battery racks

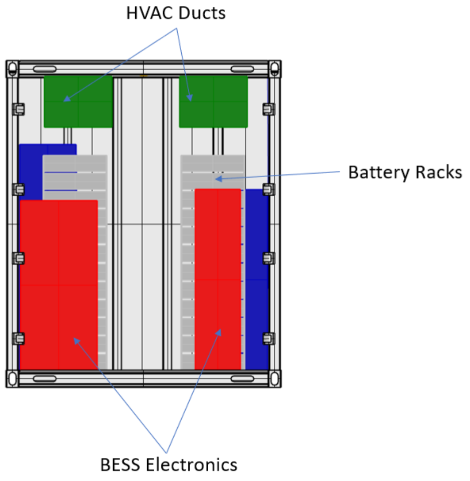

Figure 2: BESS cross-section details

The accompanying paper (Kapahi, 2022) presents detailed overview and background in developing this representative BESS geometry and the battery gas release scenarios which provide inputs to the current deflagration analysis. The BESS enclosure has a total of 22 battery racks.

4.2 Released Battery Gas Details

Existing research (Mikolajczak, C., 2011) has found that LFP batteries (individual cells) decompose into a gas mixture consisting primarily of hydrogen, carbon dioxide, carbon monoxide, and “total hydrocarbons” (THCs), which refers to various hydrocarbon gases such as ethane, methane, propane, etc. The ratio of these components varies depending on the type of cell. A battery “module” refers to a series of cells that are wired together and packaged into a modular unit. Battery modules are characterized by their design voltage and capacity; a module with a large number of cells will have a greater energy content (measured in kWh), characterized either by a greater voltage (measured in V) or a greater capacity (measured in Ah).

Characteristics of the released battery vent gas mixture are well summarized in a literature review done by Baird, A. R. (Baird, 2019). Vent gas quantity and composition vary with the state of charge (SOC) of the battery cells. Higher SOC produces a greater volume of vent gases along with a wider flammability range with a higher fraction of H_2, CO, and THC and a lower fraction of CO_2. In the industry, commercial BESS manufacturers perform the UL9540A (UL, 2019) tests to evaluate the vent gas characteristics of the batteries used in the BESS. Results from UL9540A which is performed for regulatory compliance, are proprietary to the BESS manufacturer and not available in the public domain. In the current analysis, following the discussion presented in the accompanying paper (Kapahi, 2022), a representative thermal runaway data with the composition of the released battery as provided in Table 1 is considered. Battery gas composition considered in the current analysis is consistent with the available literature (Archibald, 2021; Huang, 2021) for this data. The release model assumed in the current analysis considers battery gas to be released at a rate of 4.9 g/s for a period of 9.8 minutes releasing a total of 2793 g[1] of battery gas into the BESS enclosure. Detailed analysis on the conception of the battery gas release model is presented in Kapahi (2022).

---

[1] The total battery gas amount released is less than the theoretical value of 2881.2 g as the battery gas release model considers a ramp and ramp down of the battery gas release rate.

Table 1: Battery gas composition

Species	**Vol. %**
Hydrogen	30.60%
Carbon Monoxide	29.90%
Carbon Dioxide	21.30%
Propane*	18.20%

*All Hydrocarbons are lumped into a single species

5 Deflagration Vent Size Modelling Details

5.1 Deflagration Scenarios

Two deflagration scenarios are considering for evaluation. These include:

Scenario 1: Full volume deflagration. The entire BESS is filled with a stoichiometric concentration of battery gas-air mixture and deflagration venting analysis is performed by considering roof venting.

Scenario 2: Partial volume deflagration. In this scenario, the BESS enclosure is filled with a stoichiometric mixture of battery gas-air mixture flammable cloud where 2793 g of battery gas is mixed with air to form the flammable vapor cloud. For the partial volume deflagration scenarios, a sensitivity study was performed by varying the effective vent area at the roof and evaluating the generated overpressures.

5.2 CFD Modelling Methodology

5.2.1 CFD Tool

The CFD tool used for deflagration vent size in the current study is FLACS (Gexcon, 2021). FLACS is a 3D fully compressible, finite volume solver based on a single-block structured cartesian mesh. FLACS solver utilizes SIMPLE pressure correction algorithm for pressure-velocity coupling. The solver applies two-equation Reynolds-Averaged Navier Stokes (RANS) models for modelling turbulence together with Bray correlation for computing the turbulent burning velocity (Bray, 1990). FLACS CFD tool is a well-validated, widely used CFD tool for gas deflagration scenarios (Hansen 2010).

5.2.2 CFD Geometry

The CAD geometry shown in Section 4.1 is imported into the FLACS tool and refined for CFD analysis. The roof of the BESS enclosure is modified to allow for explosion venting. A total of eighteen (18) vent panels each with an area of $1m^2$ is implemented in the CFD model for analysis. To reduce the effective vent area, the roof panel at the vents are replaced by non-opening blind flange. Figure 3a shows the overall BESS geometry in FLACS with the 18 vent panels. Details of the internal geometry are shown in Figure 3b.

DOI: 10.7795/810.20221124

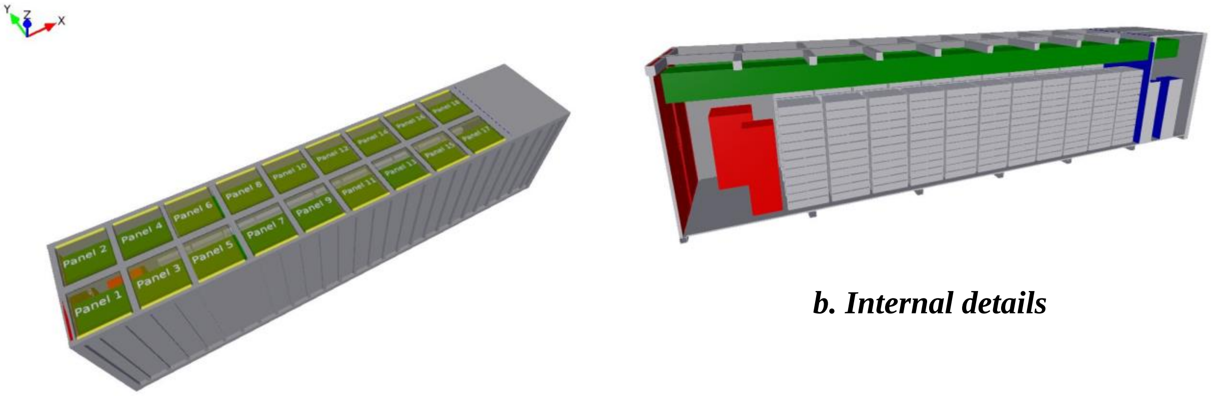

b. Internal details

a. Roof vents configuration

Figure 3: CFD geometry details of the BESS

6 Results

A comparative assessment of the generated overpressures from CFD analysis, NFPA 68, and EN 14994 are presented and discussed in this section. Five (5) CFD runs were performed. Effect of variation of the ignition location on the generated overpressures was performed for the full volume deflagration. For the partial volume deflagration, the sensitivity study was performed on the variation of the vent area on the generated overpressures. NFPA 68 (NFPA 68, 2018) analysis was performed considering the inputs for the burning velocity from the FLACS database for the gas mixture considered. P_{red}, the maximum pressure developed inside the vented enclosure during a vented deflagration was obtained following the methodology described in Section 7 of NFPA 68. EN 14994 results were obtained considering the gas constant, Kg, for the battery gas mixture to be the maximum allowable value. EN 14994 does not consider the effect of any internal obstructions. Appendix A in EN 14994 does provide guidance on considering the effect of turbulence inducing obstructions. Based on the EN 14994 guidance, it was established that for the BESS considered in the current analysis, EN 14994 would not produce reliable estimates for P_{red} as the vent area formulation in the Appendix A of EN 14994 produce smaller vent area compared to the vent area formulations in Section 5.2 of EN 14994. As per the recommendation of EN 14994, for such scenarios where the vent area from the formulations presented in Section 5.2 is higher than the vent area from the formulations presented in the Appendix of EN 14994, more sophisticated methods need to be considered to evaluate the reduced venting overpressure (P_{red}).

The five deflagration venting scenarios considered are presented in Table 2. Table 2 also presents the maximum overpressures (P_{red}) inside the BESS enclosure for the different venting scenarios considered.

Table 2: P_{red} data for the deflagration scenarios considered

Scenario	**Ignition location**	**Fill volume**	**Vent area available (in m^2)**	**P_{red} *(in psi)***		
				FLACS	**NFPA 68**	**EN 14994**
Scenario 1	Center	Full	18 m^2	111	21.5	1.3
Scenario 2	Corner	Full	18 m^2	61	21.5	1.3
Scenario 3	Center	Partial	18 m^2	17.5	14.4	1.3
Scenario 4	Center	Partial	10 m^2	22.3	33	3.5
Scenario 5	Center	Partial	6 m^2	26.1	50	8.4

DOI: 10.7795/810.20221124

EN 14994 data is presented in Table 2. However, as per the guidelines in the Appendix of EN 14994, the P_{red} data from EN14994 for this particular BESS enclosure considered is unreliable since the vent area calculated from the methodology presented in the appendix A is smaller. Results from EN 14994 will not be considered for further analysis

Ignition Location Sensitivity

A sensitivity study on the effect of ignition location variation on the explosion overpressures inside the BESS enclosure was performed. Two ignition locations were considered namely, Center ignition and Corner ignition. For the Center ignition, the ignition location was placed at the bottom center of the BESS enclosure in the middle of the battery aisle. For the Corner ignition, the ignition location was placed at the bottom corner in the middle of the battery aisle. The two ignition locations are illustrated in Figure 4.

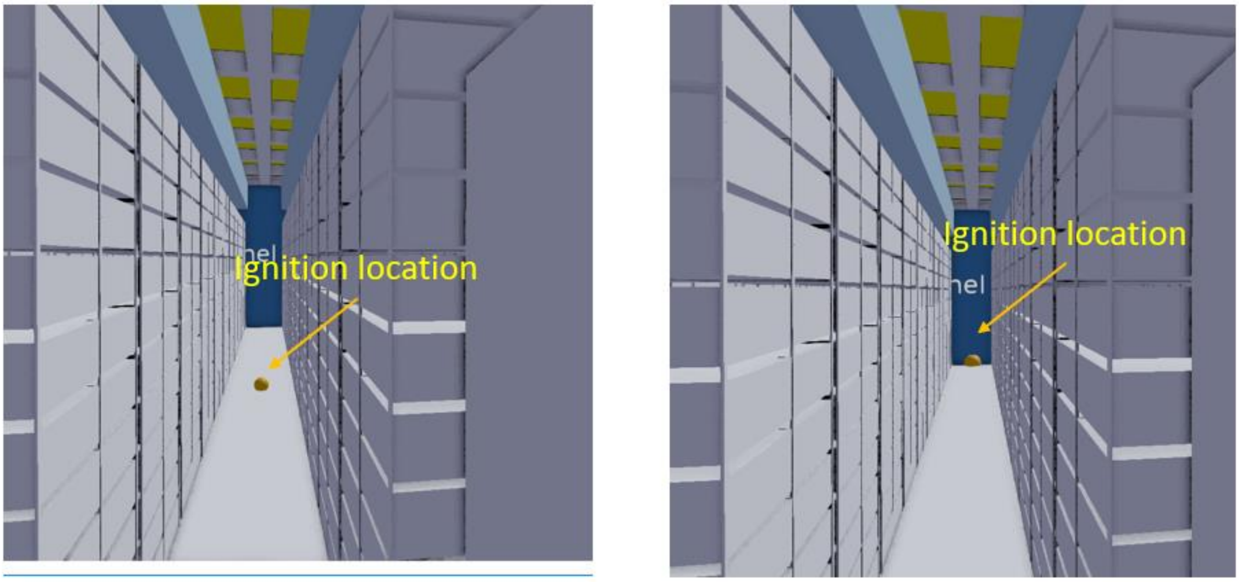

Center ignition

Corner ignition

Figure 4: Ignition location variation for the full volume deflagration cases

Figure 5 presents the maximum generated overpressures plot for the two ignition location variations comparing FLACS results and NFPA 68 results. NFPA 68 engineering model does not have formulations to account for change in the ignition location and therefore the NFPA 68 results remain unchanged for the two ignition location variation considered. For the Center ignition location, FLACS provides higher P_{red}. FLACS results are about five times higher than the NFPA 68 results. With Corner ignition, P_{red} inside the BESS enclosure is higher. FLACS results are generally overpredicted compared to NFPA 68 for the full volume deflagration scenarios.

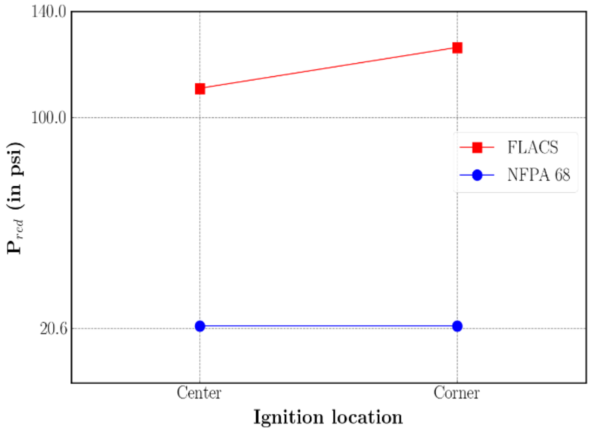

Figure 5: Full vol. deflagration venting – ignition location sensitivity plot

Vent Area Sensitivity

Partial volume deflagration scenarios represent a more realistic explosion hazard for the BESS enclosure due to the nature of the thermal runaway event. For the partial volume deflagration scenarios, effect of the available vent area on the explosion overpressures inside the BESS enclosure were evaluated. Three vent areas were considered in the current analysis. These are illustrated in Figure 6.

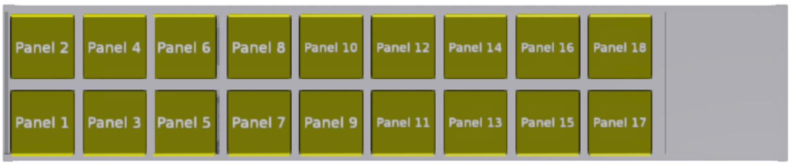

a. 18 m^2 vent area

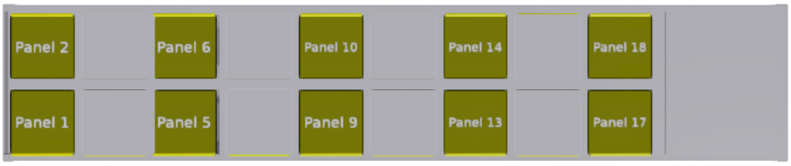

b. 10 m^2 vent area

c. 6 m^2 vent area

Figure 6: Vent configurations considered for the partial fill scenarios. Active vents are shown in yellow.

Comparison between NFPA 68 model results and FLACS results showing the variation of the enclosure overpressures with changing vent area is shown in Figure 7. Both FLACS and NFPA 68 produce the expected results in that the Pred reduces as the available vent area is increased. For the 18 m^2 vent area, both FLACS and NFPA 68 results are close with the FLACS slightly overpredicting P_{red}. With decreasing vent area, NFPA 68 results and FLACS results diverge with NFPA 68 over-predicting P_{red} compared to FLACS. Scatter plot shown in Figure 8 comparing the NFPA 68 results against FLACS show that FLACS results and the NFPA 68 results are within 50% of one another with the 18 m^2 vent area producing the closest agreement between the two models.

DOI: 10.7795/810.20221124

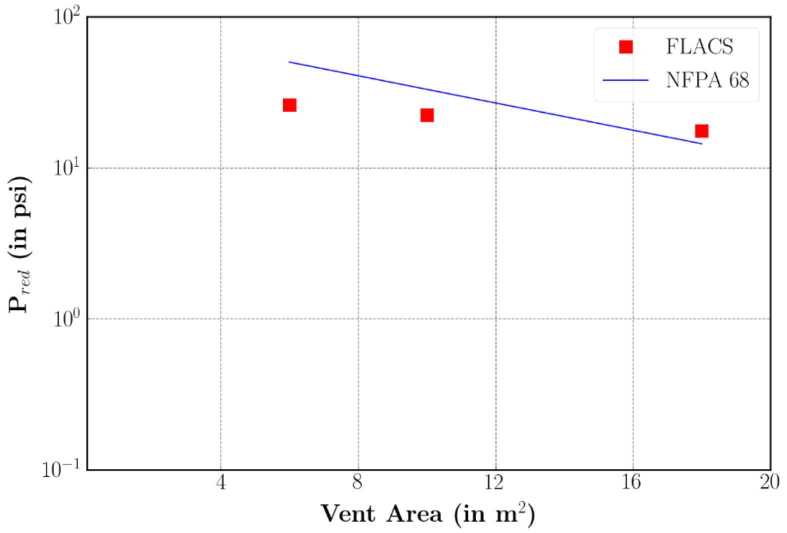

Figure 7: Variation of P_{red} with vent area for partial fill cases

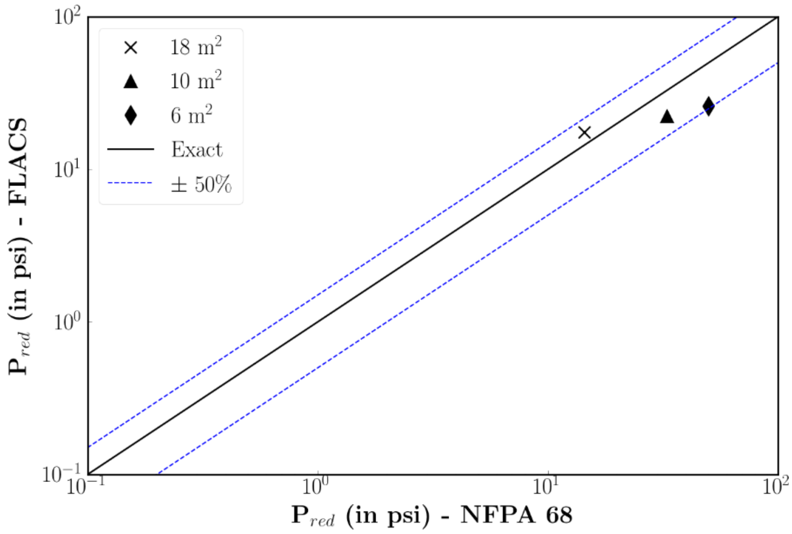

Figure 8: Scatter plot comparing P_{red} from NFPA 68 and P_{red} from FLACS

7 Summary

A comparative evaluation of NFPA 68 methodology and CFD using FLACS to obtain the required deflagration vent area for a given stoichiometric battery gas-air mixture volume is evaluated and discussed in this paper.

Typically engineering model are the most widely used for estimating the required deflagration vent area for a given P_{red}, the maximum overpressure experienced inside the BESS enclosure during an explosion venting event. P_{red} is generally the maximum allowable explosion pressure a given enclosure can withstand without experiencing any critical damage to the enclosure structure. Estimating the vent area using engineering models is challenging as discussed in this paper. Engineering models are typically calibrated on a limited set of experimental results have limitations in terms of their applicability as observed for EN 14994 model in the current study. Inputs to the engineering models are unclear especially for BESS structures as the released battery gas chemical characteristics are unknown. For e.g. using EN 14994 would require knowing the gas constant, K_g of the battery gas mixture. This information is generally determined experimentally and for most applications unknown. Also, EN 14994 assumes that the static opening pressure of the vents to be greater than 0.1 bar. In the current analysis the yield pressure of the explosion vents was considered to be 0.5 psi (0.034 bar). NFPA 68 has limitations in terms of its applicability to gas mixtures which have high burning velocity.

There are more sophisticated engineering models that are proposed in literature. These include the Molkov (Molkov, 2011) model, Molkov and Bragin (Molkov, 2015) model, and the FM Global (Bauwens, 2011) explosion venting models. These models consider an additional range of physical properties and phenomena and are found to be more accurate compared to NFPA 68 and EN 14994 (Lakshmipathy, 2019) when applied for Hydrogen-air mixtures. However, results from these models might not be acceptable by the Authority Having Jurisdiction (AHJ) as these results are not from acceptable regulatory commissions such as National Fire Protection Association (NFPA) or British Standard (BS). Performance-based design using CFD methods is generally accepted as an alternative method to NFPA 68 analysis.

CFD analysis using FLACS overpredict P_{red} for the full volume deflagration venting scenarios. For the partial fill scenarios, FLACS results are comparable to NFPA 68 analysis and are under-predicted compared to NFPA 68 results when the vent area is reduced. 3D CFD analysis using FLACS, is able to account for geometric complexity and effect of turbulence inducing obstructions. Also, the effect of changing ignition location, static opening pressure of the vent panels are more easily captured using CFD methods. Because the chemical properties of the battery-gas air mixture is generally not known, CFD modelling using FLACS provides for more trustworthy analysis due to less number of inputs needed. NFPA 68 and EN 14994 would require knowing the chemical properties such as the burning velocity (S_u), Maximum Pressure (P_{max}), and Gas Constant (K_g)of the battery gas as inputs to the engineering models. For the BESS the battery gas mixture chemical properties vary widely from one BESS to another and are dependent on many factors such as the cell type, Amperage of the battery cells, the thermal shielding and many other factors. Therefore NFPA 68 and EN 14994 methods cannot be practically used for deflagration vent sizing of the BESS and CFD modelling would be the most practical way to evaluate the deflagration vent size of the BESS.

DOI: 10.7795/810.20221124

References

Archibald, E. J., "Fire & Explosion Hazards Due to Thermal Runaway Propagation in Lithium-Ion Battery Systems," *Doctoral Dissertation,* The University of Texas at Austin, 2021

Baird, A. R., "A Framework for Characterizing the Safety of Li-BESS using Performance Based Code Analysis and Testing," *Masters' Thesis, U. of Texas at Austin,* 2019

Baraldi, D. et al., "An inter-comparison exercise on CFD model capabilities to simulate hydrogen deflagrations with the pressure relief vents," Int. J. of Hyd. Energy, 35 (22) pp 12381-12390, 2010

Bauwens, C. R., Chaffee, J., and Dorofeev, S. B., "Vented Explosion Overpressures from Combustion of Hydrogen and Hydrocarbons mixtures, *International Journal of Hydrogen Energy,* 2011, 36. 2329 - 2336

Bray, K.N.C, "Studies of the Turbulent Burning Velocity," *Proc. Math. and Phy. Sci.*, 431: 315 – 335, 1990

Di sarli, V. et al., "Using Large Eddy Simulation for Understanding Vented Gas Explosion in the presence of obstacles," J. of Hazardous Materials, 169(1-3), pp 433-438, 2009

DNV-GL, "McMicken Battery Energy Storage System Event Technical Analysis and Recommendations," *Arizona Public Service,* Document No. 10209302-HOU-R-01 Issue A, 2020

Dorofeev, S.B., "Flame acceleration and explosion safety applications," *Proc. Of Combustion Inst.*, 33, pp 2161-2175, 2011

Gexcon, "FLACS v21.3 User's Manual," Gexcon A.S., 2021

Hansen, O. R., Hinze, P., Engel, D., and Davis, S., "Using Computational fluid dynamics (CFD) for blast wave predictions," *J. Loss Prev., Process Ind.*, 23(6), 885 – 906, 2010

Huang, Z., Li, X, wank, Q., Duan, Q., Li, Y., Li, L, and Wang, Q., "Experimental investigation on thermal runaway propagation of large format lithium ion battery modules with two cathodes," *International Journal of Heat and Mass Transfer*," Vol. 172, 2021

Kapahi, A, Alvarez, A-R, Kraft, S., Conzen, J., and Lakshmipathy, S. "A CFD Based methodology to Design an Explosion Prevention System for Li-Ion based Battery Energy Storage System," ISPMIE 14, 2022

Lakshmipathy, S., Skjold, T., Hisken, H., and Atanga, G, "Consequence models for vented hydrogen deflagrations, CFD vs. engineering models," *International Journal of Hydrogen Energy* 44, 8699 – 8710, 2019

Malkov, V., "Primer: Hydrogen Deflagrations," Presentation Joint Summer School on Fuel Cell and Hydrogen Technology, Viterbo , Italy, 21-25 August 2011

Molkov, V., and Bragin, M. "Hydrogen Air Deflagrations: Vent Sizing correlation for Low Strength Equipment and Building," *International Journal of Hydrogen Energy,* 40, 1256 – 1266, 2015

Mikolajczak, C., Kahn, M., White, K., and Long, R. T., "Lithium-Ion Batteries Hazard and Use Assessment," national Fire Protection Association, Quincy, MA, USA, 2011

Mokhtar, K.M., Kasmani, R.M., Che Hassan, C. R., Hamid, M. D., Emami, S. D., and Mohamad Nor M. I., “Reliability and applicability of empirical equations in predicting the reduced explosion pressure of vented gas explosions,” *J. of Loss Prevention in the Proc. Ind.*, 63, 2020

NFPA 68, “Standard on Explosion Protection by Deflagration Venting,” National Fire Protection Association (NFPA), 2018

NFPA 855, “Standard for the Installation of Stationary Energy Storage Systems,” National Fire Protection Association (NFPA), 2020

UL, “Test Method for Evaluating Thermal Runaway Fire Propagation in Battery Energy Storage Systems”, ANSI/CAN/UL 9540A:2019, 4th ed., Underwriters Laboratories Inc., Northbrook, IL, USA, 2019

Woolley, R. M. et al., “Prediction of confined, vented methane-hydrogen explosions using a computational fluid dynamics approach,” Int. J. of Hyd. Energy, 38 (16) pp 6904-6914, 2013

DOI: 10.7795/810.20221124

Probabilistic Risk Assessment for domino effect due to Vapor Cloud Explosions using an integrated Petri-Bayesian network approach

Julio Ariel Dueñas Santana [a,b], Orelvis González Gómez [c] & Jesús Luis Orozco [b]

[a] Scuola Superiore Meridionale. University of Naples Federico II, Naples, Italy
[b] Department of Chemical Engineering. University of Matanzas, Matanzas, Cuba
[c] Centro de Ingeniería e Investigaciones Químicas (CIIQ), La Habana, Cuba

E-mail: *julioariel.duenassantana-ssm@unina.it* *or* *julio.duenas94@gmail.com*

Abstract

The domino effect has triggered serious and irreversible damages across several hydrocarbon facilities. Domino effect accidents are considered the most serious of possible accidents. Therefore, based on this, the European Commission considers the research and models of prediction of the domino effect a mandatory challenge for the years ahead. One of the possible scenarios which can trigger to domino effect phenomenon is the Vapor Cloud Explosion (VCE). For Probabilistic Risk Assessment, among all proposed methodologies in specialized literature, the use of Bayesian Networks and Petri nets have been prevalent in the last years. Moreover, these networks can be integrated with classical risk analysis techniques in order to obtain more reliable results. The present research focuses on the probabilistic risk assessment for the domino effect occurrence due to VCE in hydrocarbon storage sites. For this purpose, a new integrated methodology is proposed based on the accurate integration of Probabilistic Petri Nets, Bayesian Networks, Scenario Simulation (using the ALOHA software), Past Event Analysis and Event Tree technique in order to predict the likelihood of domino effect due to VCE. This methodology is applied in a real hydrocarbon storage site in Cuba. As main results, we obtain that the accident probabilities are high compared to those reported by specialized literature and that the joint probability can reach 100% if a real VCE occurs.

Keywords: *industrial explosions, explosion modelling, explosion prevention, Vapor Cloud Explosion, Bayesian networks, Petri nets, hydrocarbon storage, risk assessment.*

1. Introduction

Industrial development creates new challenges related to risk assessment and safety management in the process industries. Nowadays, the process complexity needs the integration of the present techniques for risk analysis in order to get more reliable results. Despite the major accidents prevention procedures established, a phenomenon known like "domino effect" might occur (Dueñas et al., 2021 a,b). If an explosion occurs in a process unit, the generated blast wave will affect the nearby target units and may cause new explosions and fires, in this case, the escalation vector is the overpressure (Mukhim et al., 2017; Atkinson 2017). One of the most devastating accidents related to this escalation pattern is the Buncefield major accident in 2005 (Atkinson et al., 2015).

The domino effect has triggered catastrophic and irreversible damages across many hydrocarbon facilities. When an accident occurs, this phenomenon might happen when its potential escalation vectors are enough to cause the equipment failure. Moreover, this is not the only condition for classifying a chain of events as domino effect, indeed, the consequences of this scenarios need to be higher than the effects of the single primary accident. This concept has been widely studied by Khan and Abbasi, (1998), Reniers and Cozzani, (2013) and Cozzani and Reniers, (2021).

Furthermore, the long-term consequences of domino effect accidents can affect also the economy, environment, and the society. According to Lees, (2012), this phenomenon is considered one of the most serious in hydrocarbon facilities. Then, the European Commission considers the models for simulating domino effect and its effects as a mandatory challenge for the years ahead (Poljanšek et al., 2017; Dueñas et al., 2021a).

Additionally, there is a tendency in specialized literature to the use of Bayesian Networks (BN) and Probabilistic Petri Nets (PPN) for representing the domino effect evolution (Kabir and Papadopoulos, 2019; Ramzali et al., 2015; Zhou and Reniers, 2017). Despite this, there are other classical risk analysis techniques which can be included into an integrated framework for this purpose, such as the Scenario Simulation, the Event Trees, and the Past Event Analysis (Taleb-Berrouane et al., 2020; Dueñas et al., 2021a).

This research proposed an integrated PPN-BN approach for the probabilistic risk assessment considering the domino effect occurrence due to VCE in hydrocarbon storage sites. For this purpose, a new integrated methodology is proposed based on the integration of Probabilistic Petri Nets, Bayesian Networks, Scenario Simulation (using the ALOHA software), Past Event Analysis and Event Tree technique in order to predict the likelihood of domino effect due to VCE. This methodology is applied in a real hydrocarbon storage site in Cuba.

2. Methodology

In this section, the proposed methodology in this research framework is explained. Figure 1 shows the six-step approach for predicting the domino effect probability due to VCEs. The first step is related to the division of the study area into process units depending on its capability to generate accidents. Secondly, it is necessary to simulate the VCE scenario for each process unit, in order to obtain the overpressure values. Thirdly, using a combination of Past Event Analysis and Event Tree, the initial probability for this scenario is obtained. Next, the fourth step is focused on quantifying the escalation probability using the Probit equations proposed by Reniers and Cozzani, (2013). The fifth step aims to determine the accident probability considering the possible interactions of these VCEs and their impact in the nearest process units using a PPN. Finally, we propose to develop a BN in order to predict the domino effect likelihood at different escalation levels.

2.1 Step 1: Selection of the process units

This step focuses on the division of the study area into process units, based on their hazardous potential. Then, each process unit must contain a hazardous material which can be involved if a VCE occurs. Also, a technological criterion should be considered to give priority to some parts which have been involved in previous accidents or have a higher risk for generating a VCE.

2.2 Step 2: Simulation of VCE scenarios

The VCE scenarios strongly depend on the flammability and volatility of the storage material (Gyenes et al., 2017, Jaderi et al., 2019). The main aim of these simulations is the determination of the generated overpressure in determined points which represent the other process units. ALOHA software is proposed for this purpose. ALOHA was developed jointly for the National Oceanic and Atmospheric Administration (NOAA) and the Environmental Protection Agency (EPA). Furthermore, ALOHA works by using LOC (Level of Concern) according to the scenario. In the case of VCE, ALOHA establishes the following LOCs:

- Red Threat Zone: 8.0 psi (55.2 kPa) destruction of buildings.
- Orange Threat Zone: 3.5 psi (24.1 kPa) serious injury is likely.
- Yellow Threat Zone: 1.0 psi (6.9 kPa) shatters glass.

For ALOHA© simulation, the meteorological conditions corresponding to the studied area must be provided by the user. It is strongly recommended using a period of ten years in order to analyze all possible variations. Moreover, the software requires information about the source of the spill, based on the process unit selection in Step 1. More information about the described software can be found in the ALOHA© User´s Handbook (2016).

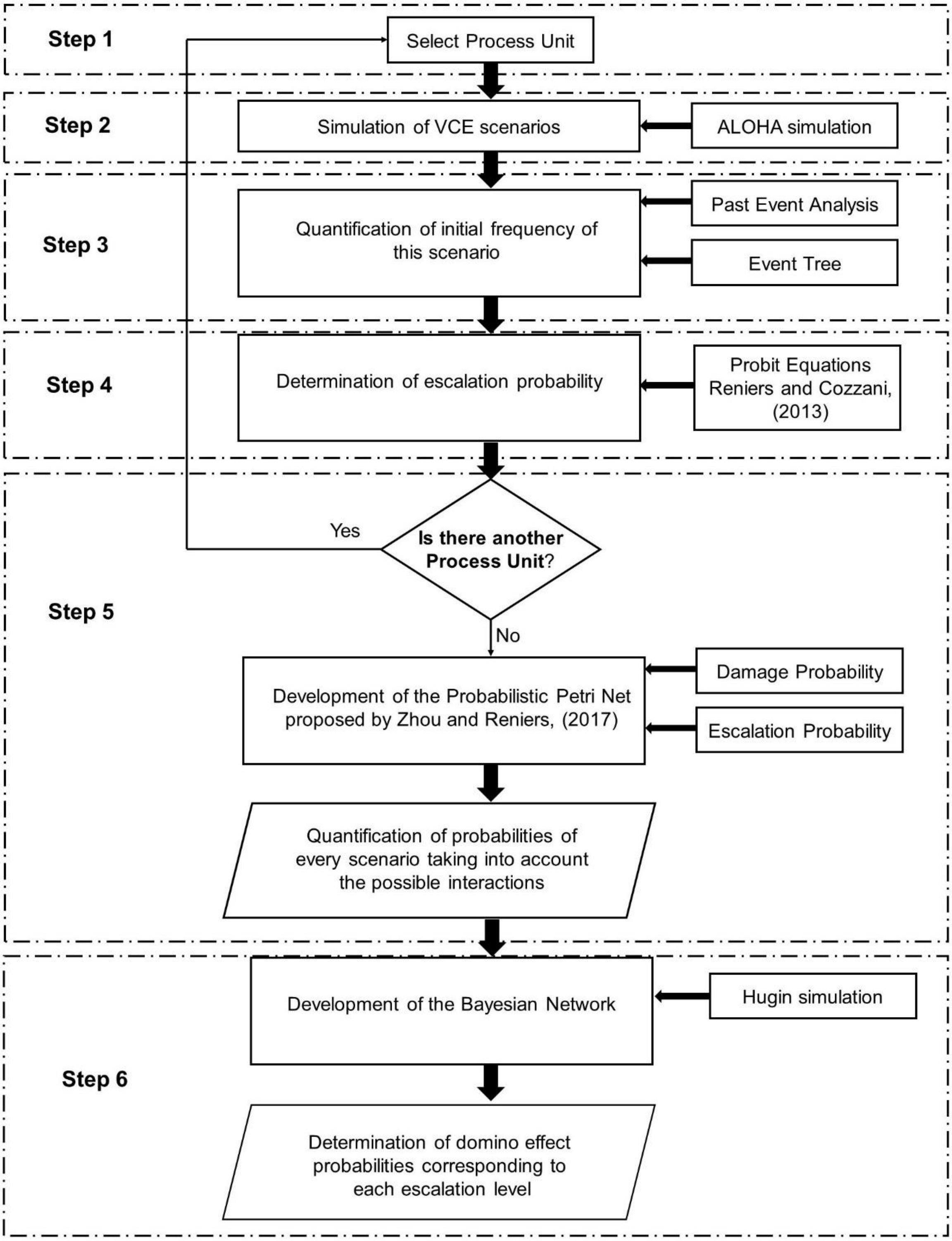

Fig. 1. *Proposed methodology in this research framework*

2.3 Step 3: Quantification of the initial frequency for the VCEs

For determining the initial frequency of each scenario, it is necessary to first analyse the scenarios that can be generated if a leak occurs in the process unit. Assuming that there are several ways of defining a scenario, all of these methodologies lead to the same result. More precisely, the physical and chemical properties of the material, operational conditions, and shape of the process unit all define the scenarios which can occur (Casal, 2008; Wells, 1997; Gyenes, 2017). For purposes of this research, Event Tree analysis is proposed for quantifying the initial frequency of each possible scenario. For the application of the Event Tree technique, the calculation of ignition probability is required. The ignition probability is referred to the possibility of occurrence of a fire when a leak takes place, taking into account the flow or spilled material quantity, spilled material, and surrounding characteristics or general conditions of the spill. The methodology proposed by Changlong et al. (2012) cuts through these parameters with the ability to control the process. Additionally, determination of separate probabilities is proposed and eventually, the ignition probability is quantified according to equation 1.

$$P_{IP} = max(P_{MP}, P_Q, P_{IS}) \cdot K_{IC} \tag{1}$$

Where P_{IP} is the final ignition probability, P_{MP} describes the ignition probability due to material properties, and P_Q, P_{IS} are the ignition probability due to the flow and ignition source respectively and K_{IC} is the factor referred to the control of the process. Specifically, this research focuses on a new way of study of the Event Tree, based on Past Event Analysis. The proposed technique must be applied when detailed incident reports are known for at least ten years in respect to each process unit. We assume that this will make it possible to determine the initial frequency of the spill or leak more reliably and specifically, on the basis of historic records of every process unit. The stated analysis leads to more credible and specific final results of the proposed model.

2.4 Step 4: Determination of escalation probability

The quantification of the escalation probability is an essential step in domino effect analysis. For this purpose, Probit equations which calculate necessary parameters are described in the literature (Reniers and Cozzani, 2013). The escalation probability represents the potential of a first leading accident (primary accident) that results in a chain of events. The Probit equation for determining the escalation probability for atmospheric storage vessels and the considered threshold value are shown in table 1. Further information can be found in the literature (Reniers and Cozzani, 2013).

Table 1: *Vulnerability models for atmospheric storage tanks*

Escalation vector	**Threshold value**	**Probability model**	**Equation**
Overpressure	P>22 kPa	$Y = -18.96 + 2.44 \cdot ln(P_S)$	2

Y, probit value for escalation given the primary scenario; Ps, peak static overpressure on the target equipment, kPa.

When the probit value is obtained, it is transformed into a probability value according to equation 3.

$$P = \frac{1}{\sqrt{2p}} \int_{-\infty}^{Y-5} exp\left[-\frac{V^2}{2}\right] dV \tag{3}$$

In the manner described, the proposed methodology determines the probability of escalation for further use.

2.5 Step 5: Development of the Probabilistic Petri Net

A Petri Net may be defined as a mathematical tool for modelling distributed systems, taking into account notions of concurrency, non-determinism, communication and synchronization (Baldan et al., 2018). With Petri net models, it is easy to model process synchronization of asynchronous events, concurrent operations, and conflicts or resource sharing (Baldan et al., 2018; Zhou and Reniers, 2018;

Lacerda and Lima, 2019). A Petri Net can be executed by firstly establishing an initial recording; secondly, by choosing a set of eligible transitions; thirdly, by firing a transition among the set of eligible ones and finally, by going back to step 2 until no more transitions are eligible (Baldan et al., 2018; Kabir and Papadopoulos, 2019). A transition is said to be eligible if all its input places contain one token. The transition occurs when one token is removed from each of its input places and one token is added to each of its output places (Vernez et al., 2003). According to Vernez et al. (2003), dynamic properties of Petri Nets can be used to model complex event sequences in safety analysis, such as parallel firing, successive firing, or concurrent transitions. The main objective of the development of a Petri Net is to quantify the probability of each accident due to the interactions of the possible VCEs. In the frame of this research, this extension of Petri Nets, which is called Probabilistic Petri Net, was adopted to calculate the probability of accidents.

The Probabilistic Petri Net can be defined as a 7-tuple according to equation 4.

$$PPN = (P, T, I, O, M, V, U) \tag{4}$$

One of the main advantages of the Petri Net is that the probability of a place can be updated when the probabilities of its previous places have changed. For more information about this Probabilistic Petri Net, see the article by Zhou and Reniers (2017).

2.6 Step 6: Development of the Bayesian Network

Bayesian Networks have become one of the most complete, coherent and sustainable tools among several used for knowledge acquisition, representation, and application in computer systems (Wang et al., 2018; Leoni et al., 2019; Simon et al., 2019; Zarei et al., 2019). A Bayesian Network is an acyclic graphic used for reasoning under uncertainty, in which nodes represent variables and are connected by addressing arcs (Leoni et al., 2019; Dueñas et al., 2021 a,b). Arcs denote dependencies of causal relations between nodes, while conditional probability tables determine the type and force of every dependency. One of the main advantages of Bayesian networks is their mathematical base in Bayes' rule according to equation 5.

$$P(A/B) = P(A) \cdot \frac{P(B/A)}{P(B)} \tag{5}$$

This means that the conditional probability of A given B, $P(A/B)$, also named posterior probability due to its derivation from the specified value of B probability; is equivalent to the product of the probability of A, $P(A)$, with the Bayes' factor or probabilities relation, which is defined as the probability of B given the event A, $P(B/A)$, divided by the probability of B, $P(B)$.

The development of a Bayesian Network has a main objective: the determination of domino effect probabilities corresponding to each escalation level. This is possible due to the inclusion of specific nodes proposed by Khakzad et al. (2012). However, the links among the nodes which represent process units are avoided because all of these possible interactions were included in the development of the Petri net.

3. Results and discussion

This section provides the results obtained after the application of the proposed methodology for an actual hydrocarbon storage area in Cuba. Moreover, we discussed these results with regard to those reported by specialized literature.

3.1 Selection of the process units (Step 1)

The first step corresponds with the accurate delimitation of the process units in the studied area, depending on how dangerous they might be in explosion accidents. For a better application of the model, the selected area is divided into three main sub-areas. Figure 2 shows the analyzed hydrocarbon storage station

Fig. 2. *Hydrocarbon storage site studied in this research framework*

This hydrocarbon storage site is divided into 17 process units which consist of two tanks containing naphtha (16, 17), five tanks containing jet fuel (18, 19, 20, 21, 74), five tanks containing diesel (1, 4, 24, 25, 26), two tanks containing fuel oil (30, 38), and three tanks containing kerosene (13, 22, 23).

3.2 Results for the VCEs simulations, initial frequency and escalation probability (Steps 2-4)

This research proposes to focus on tank 17 as a primary event because of its centralized position in the area, storage material of high volatility and flammability (naphtha), volume (4647 m^3) and potential to generate a VCE, which can lead to the occurrence of domino effects. Figure 3 shows the scope of the overpressure generated due to a VCE in tank 17. The scope of the overpressure reaches practically all the other process units into the analyzed area and a similar behavior is observed for the VCEs in the other process units. The orange threat zone (429 m) represents the overpressure higher than 3.5 psi (24.1 kPa) which can trigger serious injury, and the yellow threat zone (646 m), overpressure higher than 1.0 psi (6.9 kPa) which can trigger shatters glass. Moreover the maximum overpressure reached is 6.36 psi (43.85 kPa) (escalation probability 0.9830), this is because tanks are approximately at similar distances from each other, coinciding with the results obtained by Dueñas et al. (2021b). Thus, the analysis of the domino effect evolution starting by a VCE has a paramount importance in this area.

For determining the initial frequency of each scenario, we propose a combination of the Past Event Analysis and the Event Tree. For this analyzed area, ten years were studied considering the accidents which occurred in this period. The probability of the direct ignition is determined based on the methodology of Changlong et al., (2012). There is evidence which proves in the study that fires and electrical faults occurred with regularity. Hence, an ignition source can be probable if a release took place. However, the control of the process is good because of the control actions. Then, ignition probability is reduced to 0.25. Thus, the delayed ignition is 0.75. The explosion probability is 0.4 in this case (flammable liquid fuels) (Wells, 1997). After applying the Event Tree proposed by Wells (1997) we obtained that the VCE initial frequencies are 0.0135 and 0.0090 y^{-1} for naphtha and jet-fuel respectively.

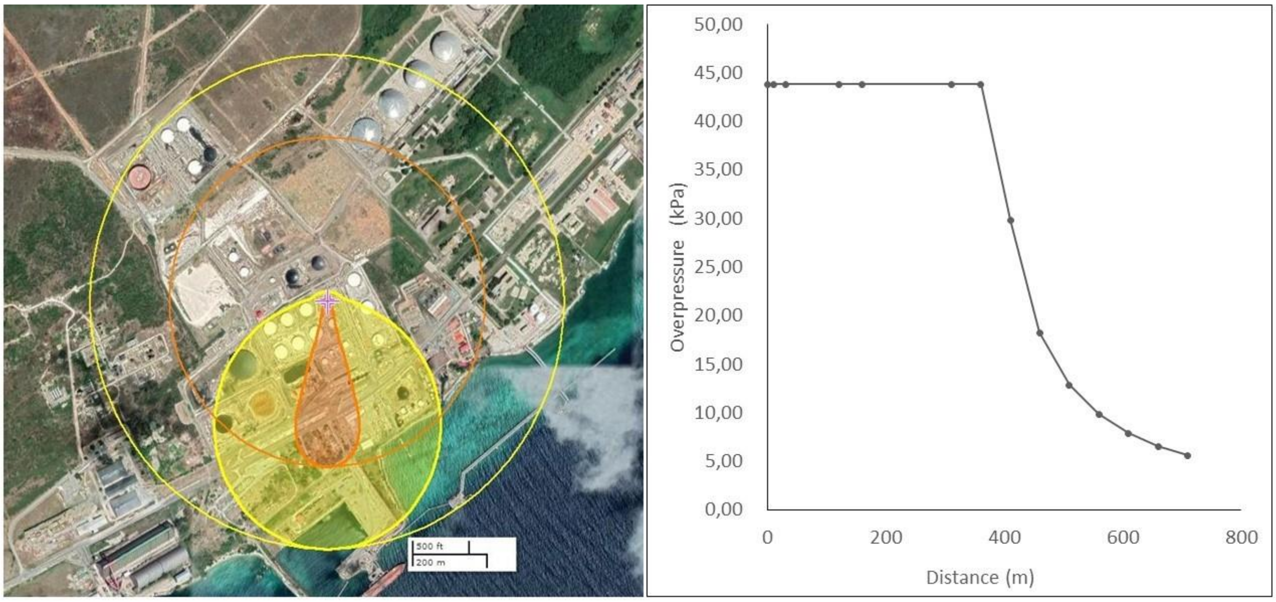

Fig. 3. *Overpressure generated if a VCE occurs in Tank 17*

3.3 Results for the development of Probabilistic Petri Net and Bayesian Network (Steps 5-6)

For quantifying the domino effect and the accident probabilities considering an initial VCE in tank 17, a combination of a Probabilistic Petri Net (PPN) with a Bayesian Network (BN) is proposed. The developed PPN is shown in figure 4. The PPN makes possible to model the propagation effect and the possible interaction among the process units in the area. For this, it is analyzed that within the area there are seven process units which can generate VCEs (TK17, TK16, TK18, TK19, TK20, TK21 and TK74). In the other process units, other types of scenarios can be generated, such as pool fires or BLEVEs plus fireballs. It can be seen that the overpressure levels generated are so high that if a VCE occurs, the other process units are directly affected. Then, the architecture of the network requires a large number of transitions for an adequate representation of the possible sequences that may occur (107 transitions and 33 places). A similar PPN was developed for Dueñas et al. (2021b) but in that research, an area of smaller extension was considered. Figure 5 illustrates the results obtained from the development of the PPN regarding to the accident probability.

Moreover, the highest accident probability values are those corresponding to tanks 25, 13 and 22 with a value of 0.0731 and tank 24 with a value of 0.0591. This is due to the synergistic effect and the influence of many explosions simultaneously. It is followed by tanks 74, 1, 4 and 23 with values close to 0.0500. The failure probabilities for most cases represent twice the probability of accidents, since the failure of the vessel does not always lead to the development of a new accident. These results are higher with respect to those reported by the specialized literature Dueñas et al. (2021b); Zhou and Reniers (2017).

DOI: 10.7795/810.20221124

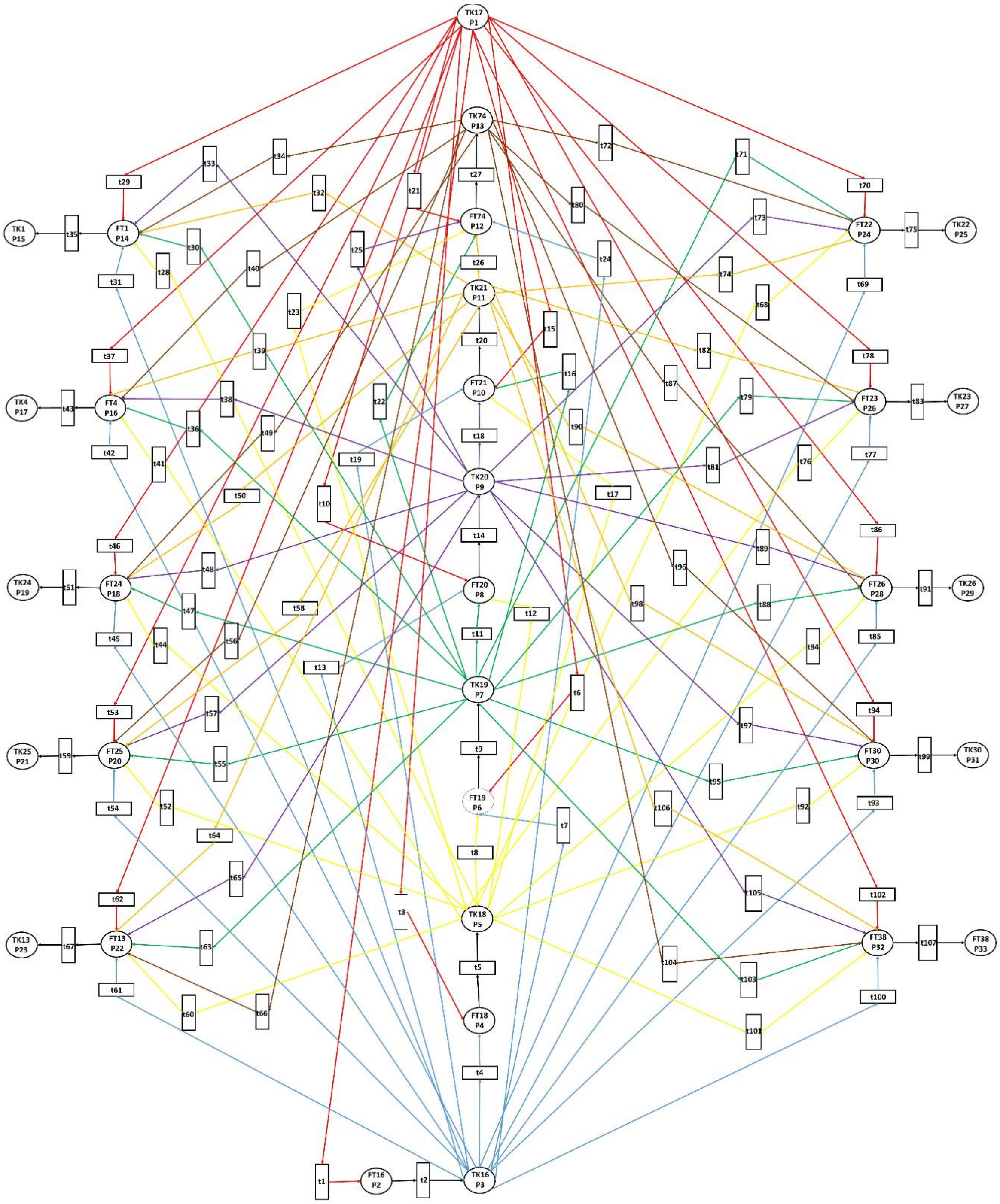

Fig.4. *Probabilistic Petri Net developed considering a primary VCE in Tank 17*

Note: FT represents the fault of the vessel, and T, the occurrence of a VCE or accident in the vessel. Transitions FT-T represent the occurrence of a VCE or accident in the vessel T; and T-FT, the overpressure T affects FT.

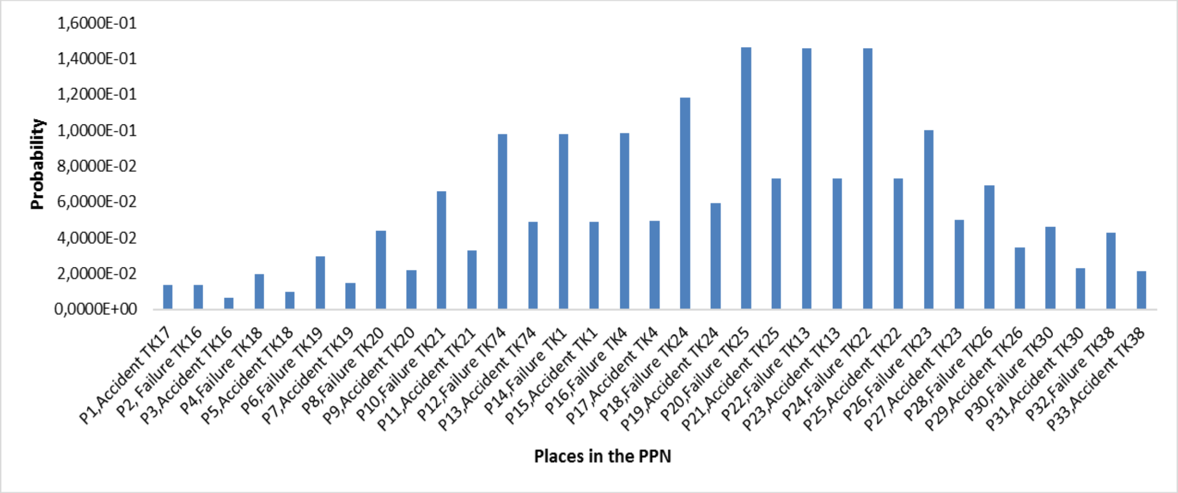

Fig.5. *Accident probabilities from the development of the PPN*

Bayesian networks allow for the quantification of the joint probability of the domino effect precisely because of their graphical ability to model this phenomenon. In this research, an ordinary Bayesian network is developed with the accident probability values obtained from the Probabilistic Petri Net for determining the joint probability due to the domino effect for an explosion. The joint probability of the domino effect if we know that a VCE in tank 17 is occurring is above 99%, because the intense propagation effect generated by the expansive wave due to overpressure. This value is considered high and agrees with that obtained by Dueñas et al. (2021b). Hence, the combination of PPN plus BN allows to quantify the accident probabilities due to explosions and the domino effect likelihood as well.

4. Conclusions

This research proposed an integrated PPN-BN approach with classical risk analysis techniques in order to quantify the domino effect probabilities in a hydrocarbon site. Overall, if a VCE occurs in tank 17, the probability of the domino effect phenomenon is very high due to the overpressure levels which can be reached in this case. We strongly recommend the use of this methodology for determining the domino effect likelihood due to VCEs in the process industries.

Acknowledgements

The authors gratefully acknowledge the financial contribution from the Modelling and Engineering Risk and Complexity (Ph.D. program) of the Scuola Superiore Meridionale, University of Naples Federico II.

References

Atkinson, G.; Cowpe, E.; Halliday, J.; Painter, D.. (2017). A review of very large vapour cloud explosions: Cloud formation and explosion severity. Journal of Loss Prevention in the Process Industries DOI: 10.1016/j.jlp.2017.03.021.

Atkinson, G; Coldrick, S; Gant, S; Cusco, L. (2015). Flammable vapor cloud generation from overfilling tanks: Learning the lessons from Buncefield. Journal of Loss Prevention in the Process Industries, 35, pp. 329-338. DOI: http://dx.doi.org/10.1016/j.jlp.2014.11.011.

Baldan, P.; Bocci, M.; Brigolin, D.; Cocco, N.; Heiner, M.; Simeoni, M. (2018). Petri nets for modelling and analyzing trophic networks. Fundamenta Informaticae XX 1-25 DOI: 10.3233/FI-2012-0000

Casal, J. (2008) Evaluation of the Effects and Consequences of Major Accidents in Industrial Plants. Industrial Safety Series., Volume 8. First Edition. Elsevier ISBN: 978-0-444-53081-3

Changlong, Z.; Juncheng, J.; Xiongjun, Y.. (2012). Study on ignition probability of flammable materials after leakage accidents. Procedia Engineering. Volume 45.DOI: 10.1016/j.proeng.2012.08.182.

Cozzani, V., Reniers, G., 2021. Dynamic Risk Assessment and Management Of Domino Effects And Cascading Events In The Process Industry. Susan Dennis, Radarweg 29, PO Box 211, 1000 AE Amsterdam, Netherlands The Boulevard, Langford Lane, Kidlington, Oxford OX5 1GB, United Kingdom 50 Hampshire Street, 5th Floor, Cambridge, MA 02139, United States.

Dueñas, J.A., Orozco, J.L., Furka, D., Furka, S., Boza Matos, Y.C., Febles Lantigua, D., González Miranda, A., Barrera González, M.C., 2021a. A new Fuzzy-Bayesian approach for the determination of failure probability due to thermal radiation in domino effect accidents. Engineering Failure Analysis 120. https://doi.org/10.1016/j.engfailanal.2020.105106

Dueñas, J.A., Orozco, J.L., Lantigua, D.F., Furka, D., Furka, D., Cruz, A.G., 2021b. Using integrated Bayesian-Petri Net method for individual impact assessment of domino effect accidents. Journal of Cleaner Production 294. https://doi.org/10.1016/j.jclepro.2021.126236

Gyenes, Z.; Wood, M.; Struckl, M.. (2017). Handbook of Scenarios for Assessing Major Chemical Accident Risks. JRC Technical Reports EUR 28518 EN p. 1-116 DOI:10.2760/884152

Jaderi, F.; Ibrahim, Z.; Reza, M. 2019. Criticality analysis of petrochemical assets using risk based maintenance and the fuzzy inference system. Process Safety and Environmental Protection. 121. 312-325. https://doi.org/10.1016/j.psep.2018.11.005

Kabir, S ; Papadopulos, Y. (2019). Applications of Bayesian network and Petri nets in safety, reliability and risk assessments: A review. Safety Science. Vol. 115 p 154-175. DOI: https://doi.org/10.1016/j.ssci.2019.02.009

Khakzad, N.; Khan, F.; Amyotte, P.; Cozzani, V. 2012. Domino Effect Analysis Using Bayesian Networks. Risk Analysis. https://doi.org/10.1111/j.1539-6924.2012.01854.x

Khan F.I., S.A. Abbasi, DOMIFFECT (DOMIno eFFECT): user-friendly sfotware for domino effect analysis, Environmental Modelling and Software 13, (1998) 163-177. PII: S1364-8152(98)00018-8.

Lacerda, B.; Lima, P. (2019) Petri net based multi-robot task coordination from temporal logic specifications. Robotics and Autonomous Systems Elsevier. DOI: https://doi.org/10.1016/j.robot.2019.103289.

Lees, F.P. (2012). Loss prevention in the process industries: Hazard identification, assessment and control, fourth edition. ED. Mannan S., Elsevier Butterworth-Heinemann. DOI: http://dx.doi.org/10.1016/B978-0-12-397189-0.00001-X

Leoni, L; Toroody, A.B; Carlo, F.D; Paltrinieri, N. (2019). Developing a risk-based maintenance model for a Natural Gas Regulating and Metering Station using Bayesian Network. Journal of Loss Prevention in the Process Industries, 57, pp. 17-24, DOI: https://doi.org/10.1016/j.jlp.2018.11.003.

Mukhim E.D., T. Abbasi, S.M. Tauseef, Domino effect in chemical process industries triggered by overpressure- Formulation of equipment-specific probits. Process Safety and Environmental Protection, 106. (2017) 263-273, http://dx.doi.org/10.1016/j.psep.2017.01.004

Poljanšek, K., Marin Ferrer, M., De Groeve, T., Clark, I. (2017). Science for disaster risk management 2017: knowing better and losing less. EUR 28034 EN, Publications Office of the European Union, Luxembourg. ISBN 978-92-79-60678-6, doi:10.2788/688605, JRC102482.

Ramzali, N; Miri, M. R.; Ghodousi, J. (2015). Safety barriers analysis of offshore drilling system by employing Fuzzy Event Tree Analysis. Safety Science. 78. 49-59. DOI: http://dx.doi.org/10.1016/j.ssci.2015.04.004

Reniers, G., Cozzani, V., 2013. Domino Effects in the Process Industries. Modeling, Prevention and Managing.

Simon, C.; Mechri, W.; Capizzi, G. (2019). Assessment of Safety Integrity Level by simulation of Dynamic Bayesian Networks considering test duration, Vol. 57. Journal of Loss Prevention in the Process Industries. DOI: 10.1016/j.jlp.2018.11.002.

Taleb-Berrouane, M.; Khan, F.; Amyotte, P. (2020). Bayesian Stochastic Petri Nets (BSPN)- A new modelling tool for dynamic safety and reliability analysis. Reliability Engineering and System Safety. V 193. DOI: https://doi.org/10.1016/j.ress.2019.106587

User´s Handbook ALOHA©. (2016). U.S. Environmental Protection Agency. Office of Emergency Washington, D.C.

Vernez, D.; Buchs, D.; Pierrehumbert, G. (2003) Perspectives in the use of coloured Petri nets for risk analysis and accident modelling. Safety Science.PII: S0925-7535(01)00078-9

Wang, Y; Yang, H; Yuan, X; Cao, Y. (2018) An improved Bayesian network method for fault diagnosis. IFAC. Elsevier. DOI: 10.1016/j.ifacol.2018.09.443.

Wells, G. (1997). Major Hazards and their management. Gulf Publishing Company. Houston, Texas.315 p. ISBN: 0 85295 368 2

Zarei, E ; Khakzad, N ; Cozzani, V ; Reniers, G. (2019). Safety analysis of process systems using Fuzzy Bayesian Network (FBN). Journal of Loss Prevention in the Process Industries. Vol. 57 p 7-16. DOI: https://doi.org/10.1016/j.jlp.2018.10.011

Zhou, J.; Reniers, G. (2017) Petri-net based cascading effect analysis of vapor cloud explosions. Journal of Loss Prevention in the Process Industries. V 48 p118-125. DOI: http://dx.doi.org/10.1016/j.jlp.2017.04.017

Zhou, J.; Reniers, G. (2018) Petri-net based evalaution of emergency response actions for preventing domino effects triggered by fire. Journal of Loss Prevention in the Process Industries. V 51 p94-101. DOI:https://doi.org/10.1016/j.jlp.2017.12.001

DOI: 10.7795/810.20221124

Inert gas influence on limiting experimental safe gap of fuel-air mixtures at various initial pressures

Maria Mitu [a], Thomas Stolz [b] & Sabine Zakel [b]

[a] "Ilie Murgulescu" Institute of Physical Chemistry, Romanian Academy, Bucharest, Romania
[b] Physikalisch-Technische Bundesanstalt (PTB), Braunschweig, Germany

E-mail: *maria_mitu@icf.ro*

Abstract

The Maximum Experimental Safe Gap (MESG) is an important criterion to assess the propagation of flames through small gaps. This safety-related parameter is used to classify the flammable gases and vapours in explosion groups, which are fundamental to constructional explosion protection. It is used both, for the safe design of flameproof encapsulated devices as well as for selecting flame arresters appropriate to the individual application. The MESG is determined experimentally according to the standard ISO/IEC 80079-20-1 at normal conditions (20 °C, 1.0 bar) with air as oxidizing gas. The aim of this work is to investigate the effect of inert gas addition on the MESG in order to assess the effectiveness of inertization in constructional explosion protection. The term limiting experimental safe gap (S_G) is used for the result of these measurements. The fuel-air mixtures used as representatives for the explosion groups in flame arrester testing were chosen and diluted with inert gas before testing. The initial pressure was varied up to 2.0 bar to include increased pressure conditions used in flame arrester testing. Apart from the well-known reciprocal dependence on the initial pressure, the added inert gas results in an exponential increase of S_G. This effect depends on the inertizing potential of the gas and is therefore different with nitrogen and carbon dioxide. The ranking of the fuels is the same as with MESG. As a result, various mixtures of the same limiting experimental safe gap can now be chosen and tested with an individual flame arrester to prove the concept of a constant and device-related limiting safe gap. The work was funded by BG-RCI in Heidelberg (PTB grant number 37056).

Keywords: *inert gas, hydrogen, methane, propane, ethylene, Maximum Experimental Safe Gap*

1. Introduction

The limiting experimental safe gap (S_G) reflects the property of flame propagation through small gaps. If the limit gap width is measured under ambient conditions in pure air, it is referred to as the standard gap width or MESG (maximum experimental safe gap). The standard MESG is one of the fundamental quantities in constructive explosion protection. It is used to minimize the effects on people, materials, and the environment to a safe level if explosion processes cannot be completely avoided. In a literature review commissioned by BG RCI in 2014, the need for research regarding the effect of inert gases on the limiting experimental safe gap was required (Hirsch and Brandes, 2015). In this regard, the experiments were carried out to determine whether the known pressure dependence of the gap width is also maintained when an inert gas is used, and to what extent the type of inert gas affects the flame transmission capability of the mixture. As the measurement result is not measured under standard conditions, the term limiting experimental safe gap (S_G) is used throughout this study.

According to IEC 80079-20-01:2019 the MESG is defined as the "maximum gap between the two parts of the interior chamber which, under the test conditions, prevents ignition of the external gas mixture through a 25 mm long flame path when the internal mixture is ignited, for all concentrations of the tested gas or vapour in air". The MESG depends on the initial concentration, pressure, and temperature. The explosion vessel for determining the experimental safe gaps according to this standard is shown in Figure 1. The test apparatus is made of stainless steel and consists of an inner volume and an outer volume, which are connected by a gap with a length of 25 mm and an adjustable distance. The inner volume is equipped with an ignition source (electrical spark ignition with a voltage $U_{max.} \approx 14$ kV and energy $E \approx 10$ J). Through a window, it can be observed whether the flame propagates into the outer volume.

The MESG serves to classify gases into explosion groups. The flammable gases and vapours may be classified into group I, which is a group of equipment for mines susceptible to firedamp, and group II of equipment used in places with an explosive gas atmosphere other than mines susceptible to firedamp (IEC 80079-20-01:2019). Group II equipment is subdivided and, for the purpose of classification of gases, the MESG limits are presented in Table 1.

The MESG is one of the characteristic data for explosion-proof equipment and is widely used for the design of flame arresters (Britton, 2000; Brandes and Redeker, 2002; Davies and Heidermann, 2013; Razus et al. 2019) considering that the flammable gas classification according to their MESG describes their capability to avoid flame transmission. Industrial standard conditions for flame arresters are only valid within so-called atmospheric conditions: temperatures from −20 °C up to +60 °C, pressures from 800 mbar up to 1100 mbar and air as the oxidizing gas (ATEX Directive 2014/34/EU, Brandes and Moller, 2008; Henkel et al. 2019). Conditions outside these intervals and oxidants other than air are therefore considered to be non-atmospheric conditions.

***Table 1**: Classification of flammable gases and vapors according to their MESG (IEC 80079-20-01:2019)*

Explosion group	
IIA	0.9 mm < MESG
IIB	0.5 mm ≤ MESG ≤ 0.9 mm
IIC	MESG < 0.5 mm

Usually, literature reports MESG of flammable gases at ambient initial conditions for pure substances (Brandes and Redeker, 2002; Brandes and Moller, 2088; CHEMSAFE, 2021; Redeker, 1981). Determination of the performance limits of flame arresters at increased oxygen concentrations is presented by Henkel et al. (2019). Limiting experimental safe gaps that are not measured under standard conditions are referred to as limiting experimental safe gaps (S_G).

The limiting experimental safe gap (S_G) decreases with increasing initial temperature. It was observed a linear correlation for temperatures up to 180 °C for many data sets of substances (CHEMSAFE, 2021). The temperature coefficient is substance-specific. There is a relative decrease of it between 5% and 12% per 100 K.

The pressure dependency of the limiting experimental safe gap (S_G) is much more pronounced than the temperature dependency (Hirsch and Brandes, 2014). For most substances, however, the S_G was only determined at normal pressure and in the negative pressure range, but not in the overpressure range. The following dependency on the pressure (p) was found (Redeker, 1981; Hirsch and Brandes, 2014), eq. (1):

$$S_G(p) = S_G(p_0) \cdot p^n \tag{1}$$

The exponent n is between -0.9 and -1.1. This is found to be in good agreement with the theoretical considerations because the quenching distance d_Q is directly proportional to the limiting experimental safe gap S_G. Equation (2) defines the relationship between these values:

$$S_G = 0{,}5 \cdot d_Q \tag{2}$$

According to Brokaw and Gerstein (1956), the quenching distance (d_Q) is:

$$d_Q \sim p^{-m/2} \tag{3}$$

where m refers to the reaction order. Assuming a second-order reaction, the exponent is $n \approx -1$. Since the real exponents only deviate slightly from this value, one can assume, as a good approximation, that the S_G is inversely proportional to the pressure. Experimental data up to an initial pressure of 2.8 bar are also available for short-chain alkanes. Here it is already indicated that the reciprocal pressure dependency in the overpressure values is the same as the values in the sub-atmospheric pressure.

The MESG decreases significantly with increasing initial pressure and oxygen enrichment (Lunn, 1984; Hirsch and Brandes, 2014; Henkel et al., 2019). An opposite effect is obtained when adding inert gas to flammable mixtures (Razus et al., 2019). At the same oxygen partial pressure but different nitrogen content (e.g. 0.5 bar at 100% O_2 or 1.0 bar at 50% O_2), the mixture without nitrogen content has a lower limiting gap width (Hirsch and Brandes, 2014). This is an indication of the additional inerting effect of nitrogen.

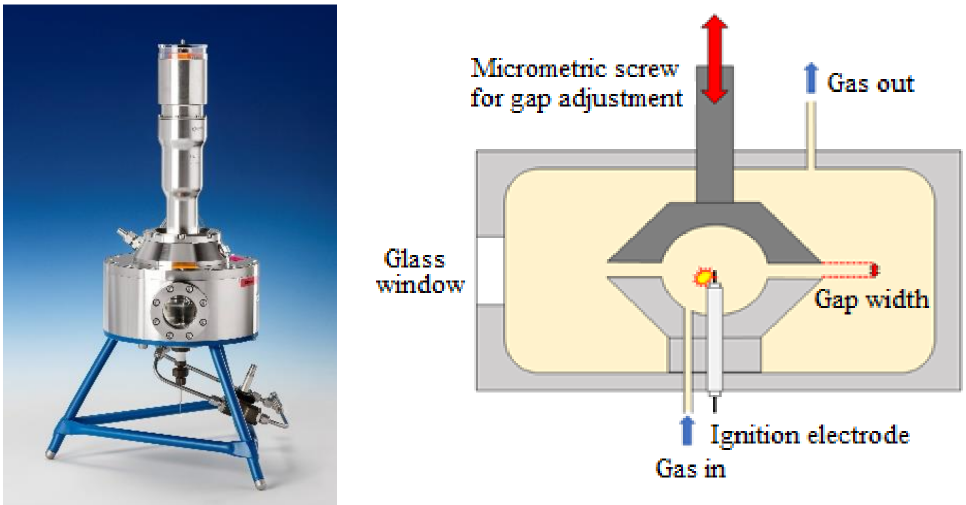

***Fig. 1.** Explosion vessel for determining the experimental safe gap according to ISO/IEC 80079-20-1 (2019).*

The current study presents data on the influence of increased inert gas content in an explosive mixture on the MESG in order to assess the effectiveness of inertization in constructional explosion protection. The term limiting experimental safe gap (S_G) is used for the result of these measurements.

2. Experiments

The tested combustible gases are specified as test gases for the classification of flame arresters in DIN EN ISO 16852:2017-04 (Table 2). In this standard, concentrations are defined at which limiting experimental safe gaps are measured that reflect the boundaries of the explosion groups. However, these values do not necessarily correspond to the MESG, i.e. the lowest value over the concentration range. In this study, however, measurements were made at the concentration at which the lowest value occurred, so that the concentrations differ slightly from those of the test gasses from the standard. For a fixed fuel/air ratio, the limiting experimental safe gap was measured at initial pressures of 1.0 bar; 1.5 bar and 2.0 bar with varying overall mole fractions of the inert gas up to 40%.

***Table 2**: Excerpt from the test gas table for deflagration and detonation tests (DIN EN ISO 16852:2017-04)*

Explosion group	MESG of real sample mm	Representative test gas	Mole fraction of test gas %	S_G of test gas mm
IIA1	≥ 1.14	Methane	8.4 ± 0.2	1.16 ± 0.02
IIA	> 0.9	Propane	4.2 ± 0.2	0.94 ± 0.02
IIB3	≥ 0.65	Ethylene	6.6 ± 0.2	0.67 ± 0.02
IIC	< 0.50	Hydrogen	28.5 ± 2.0	0.31 ± 0.02

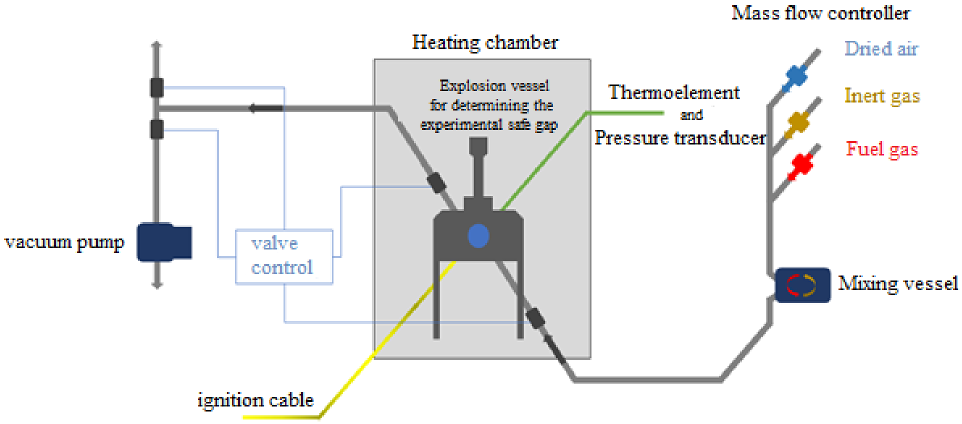

***Fig. 2.** Scheme of the experimental set-up.*

The test procedure deviates from the standard procedure described in ISO/IEC 80079-20-1. The experimental set-up is shown in Fig. 2. On the one hand, this procedure is used for the controlled setting of increased initial pressure and, on the other hand, for the removal of the unburned or burned mixture and water from the device. However, the cumbersome procedure limits the number of experimental tests compared to the standard procedure: Before each ignition test, the test vessel was evacuated to below 15 mbar to remove moisture and exhaust gases from the preliminary test. The inlet valve was then opened and the vessel was filled with the desired mixture up to the desired initial pressure. Dried air with a relative moisture content smaller than 2 % was used. According to the measurement uncertainty of the mass flow controllers, the associated measurement uncertainty for the gas mixtures is 1 % relative. The measurement uncertainty of the piezoresistive pressure sensors is 0.5 % relative.

The tested gap width was set with the micrometer screw. After a waiting time of 2 minutes, which serves to equalize the temperature the ignition in the inner volume was triggered manually. To check whether the ignition propagates through the gap into the outer volume, the viewing window of the test vessel was used. After that, regardless of whether the flame spread or not, the vessel was purged then five times with inert gas. Only then did the next test cycle begin.

The test series started with a small gap and was repeated with a larger gap in steps of 0.02 mm in the case of no flame transmission. If flame transmission occurred, the gap was reduced again and at least ten non-ignitions were measured one increment below the highest ignition. The limiting gap width of the mixture was the value at which no flame transmission occurred in ten successive tests. The tolerance of the limiting gap widths during verification is ± 0.02 mm (ISO/IEC 80079-20-1, 2019). It corresponds to the expanded measurement uncertainty of the individual measurement.

3. Results and discussion

The following diagrams show either the measured gap widths or limiting gap widths (S_G), i.e. the values of the largest gap widths at which flame transmission does not occur. The lowest value of a flame transmission was 0.02 mm above that.

3.1. Influence of initial concentration on *experimental safe gap*

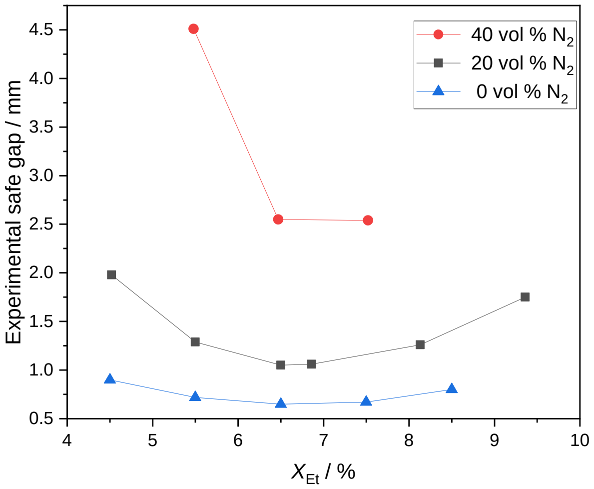

Fig. 3. *Experimental safe gaps of ethylene-air mixtures with various concentrations, at various initial concentrations of ethylene and initial pressure 1.0 bar.*

As shown in Figure 3, the experimental safe gaps of ethylene-air mixtures depend strongly on the composition. Generally, the curve is not a symmetric parabola. The experimental safe gap increases much more with smaller fuel concentrations, making the curve much steeper on the left side. This effect is more pronounced with higher nitrogen concentrations. When inert gas is added, the width of the gap increases, but it has been observed that the minimum S_G value is maintained at the same fuel concentration: 6.5 vol% C_2H_4. Therefore, the ratio of fuel gas/air concentrations was kept constant in all subsequent tests. For the following experimental determinations, if a proportion of additional inert gas is specified, it refers to the mixing ratio with the fuel gas/air mixture.

3.2. Influence of initial pressure on S_G by addition of inert gases

The experimental results are shown in Figure 4. For each of the four flammable gases, the proportion of inert gas (nitrogen or carbon dioxide) was varied at an initial pressure of 1.0 bar; 1.5 bar and 2.0 bar. The S_G of the pure fuel gas/air mixtures without the addition of inert gas was taken from the literature (Table 3). The limiting experimental safe gap for mixtures containing carbon dioxide is always higher than in nitrogen. The same behavior is observed even at increased pressure values. Furthermore, the limiting gap widths increase exponentially with the increasing content of inert gas in the mixture.

Regarding the already known pressure dependence of S_G in air, which is described in the introduction (Redeker, 1981) the experimental data for each composition of the mixture was also plotted as a function of the reciprocal pressure value (Figure 5). The regression lines show that this relationship is also valid for the inert gases.

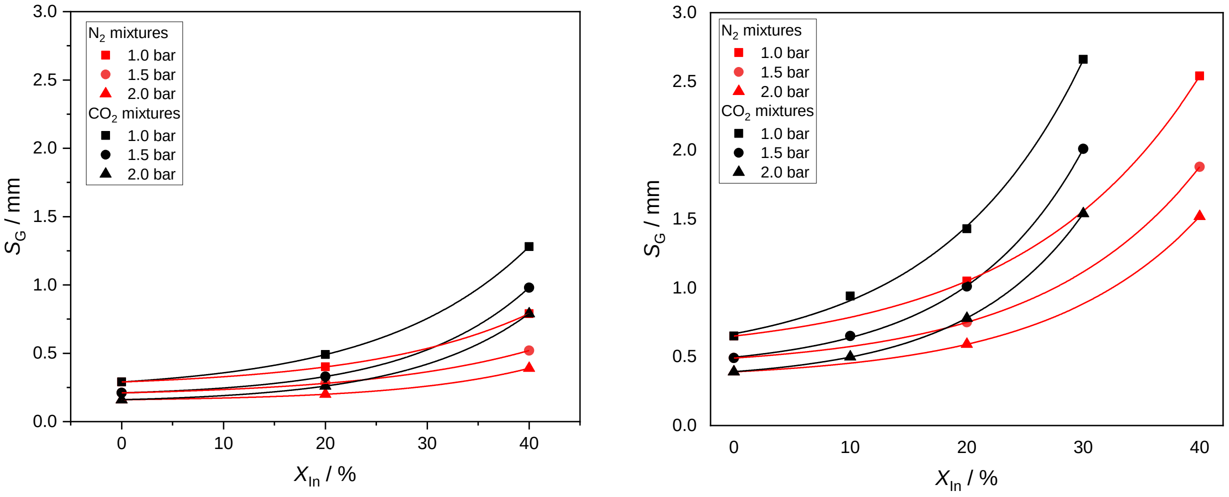

(a)

(b)

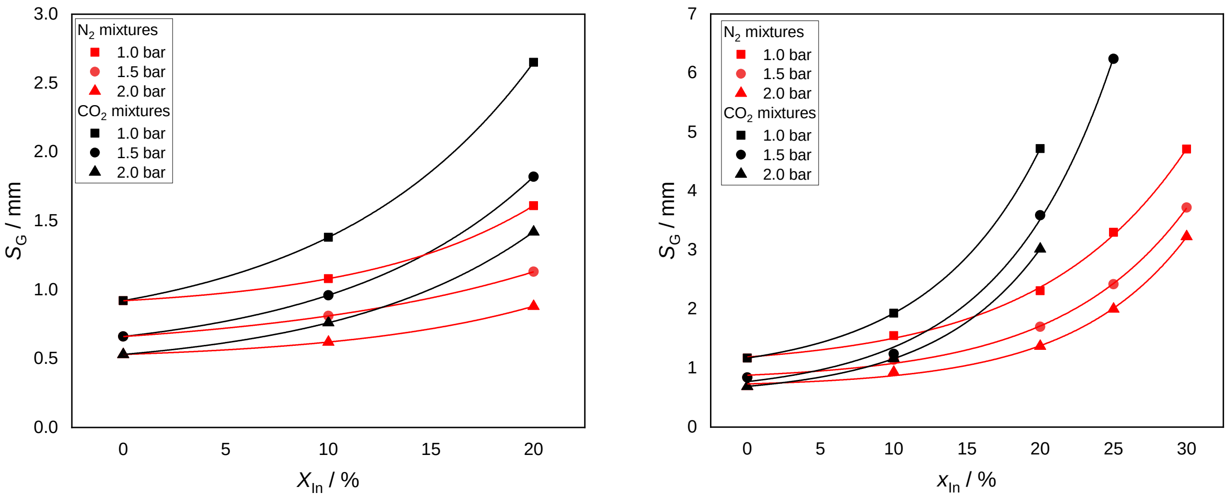

(c) (d)

Fig. 4. *Influence of inert gas concentration X_{In} on S_G of fuel-air- mixtures at different initial pressures: (a) 29.5 % hydrogen-air- mixtures; (b) 6.5 % ethylene-air- mixtures; (c) 4.4 % propane-air- mixtures; (d) 8.4 % methane-air- mixtures.*

Table 3*: Literature values for the limiting experimental safe gap widths (S_G) of the various fuel gases at various pressures and 20 °C without addition of inert gas. (ISO/IEC 80079-20-1; Redeker, 1981; Henkel et al., 2019; CHEMSAFE, 2021)*

	S_G / mm		
	1.0 bar	1.5 bar	2.0 bar
Hydrogen	0.29	0.21	0.19
Ethylene	0.65	0.49	0.39
Propane	0.92	0.66	0.53
Methane	1.14	0.83	0.65

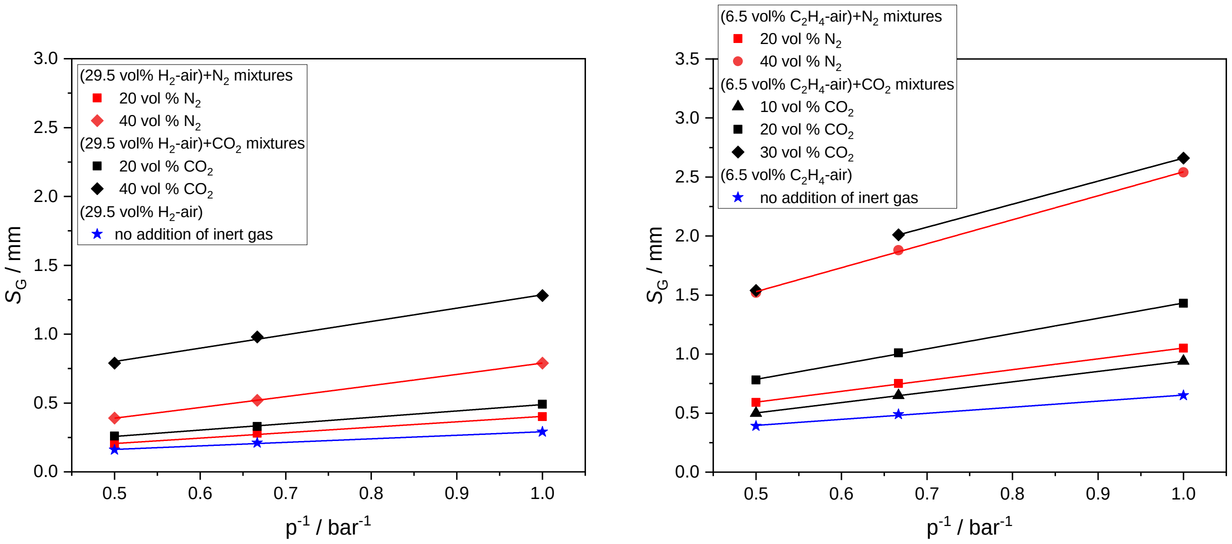

(a) (b)

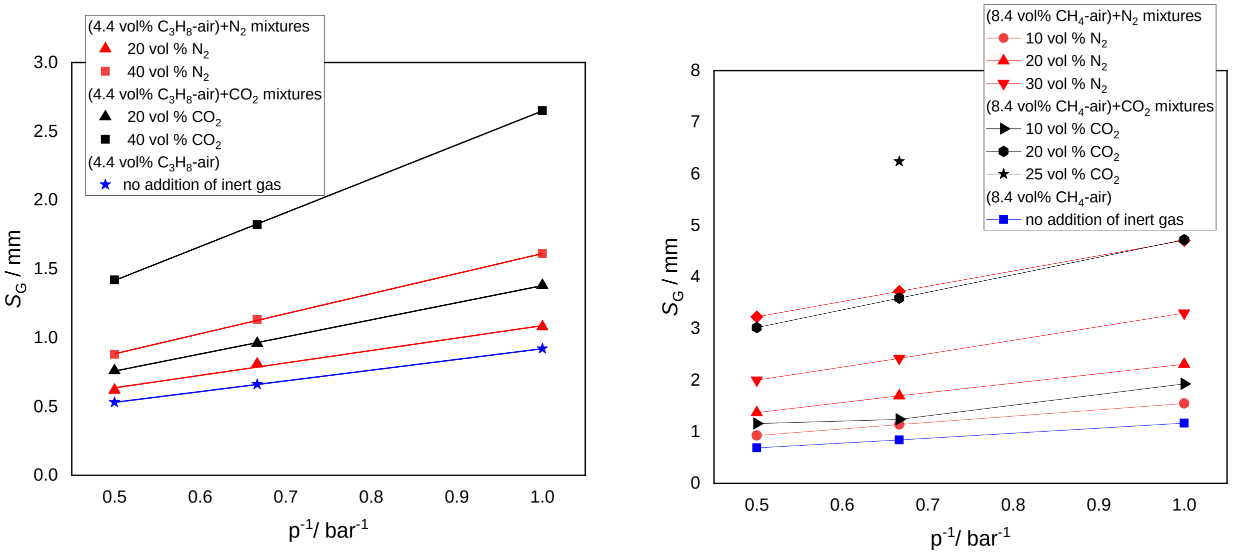

(c) (d)

Fig. 5. *S_G of mixtures with inert gas at various initial pressures and various concentrations of added inert: (a) 29.5 % hydrogen-air-mixtures; (b) 6.5 % ethylene-air-mixtures; (c) 4.4 % propane-air-mixtures; (d) 8.4 % methane-air-mixtures.*

The exponential increase of S_G with inert gas content is mainly due to the dilution of the explosive mixture, which leads to a lower energy release per unit volume of gas during combustion and reduces the flame velocity. However, the results show that S_G depends not only on the partial pressure of the oxygen or fuel gas in the gas mixture but also on the type of inert gas. When nitrogen is added to the hydrogen mixture, the heat capacity of the mixture hardly changes. For the methane/air, ethylene/air, and propane/air mixtures, the heat capacity decreases slightly with the addition of nitrogen.

Carbon dioxide has a stronger inerting effect compared to nitrogen. This effect is already known to result from a greater narrowing of the explosion ranges of flammable gases and vapors (Lewis and von Elbe, 1987). It is industrially used in inerting potentially explosive atmospheres to prevent explosions when the occurrence of an ignition source cannot be excluded (TRGS 722, 2012). European standard ISO 10156 (ISO 10156, 2017) gives a nitrogen equivalence coefficient of 1.5 for carbon dioxide. This is based on both a higher molar heat capacity (c_p) compared to nitrogen and the ability of a triatomic molecule to absorb thermal radiation. When carbon dioxide is added to the test mixtures, the molar heat capacity increases for all unburned test gas mixtures, so this effect amplifies the dilution effect.

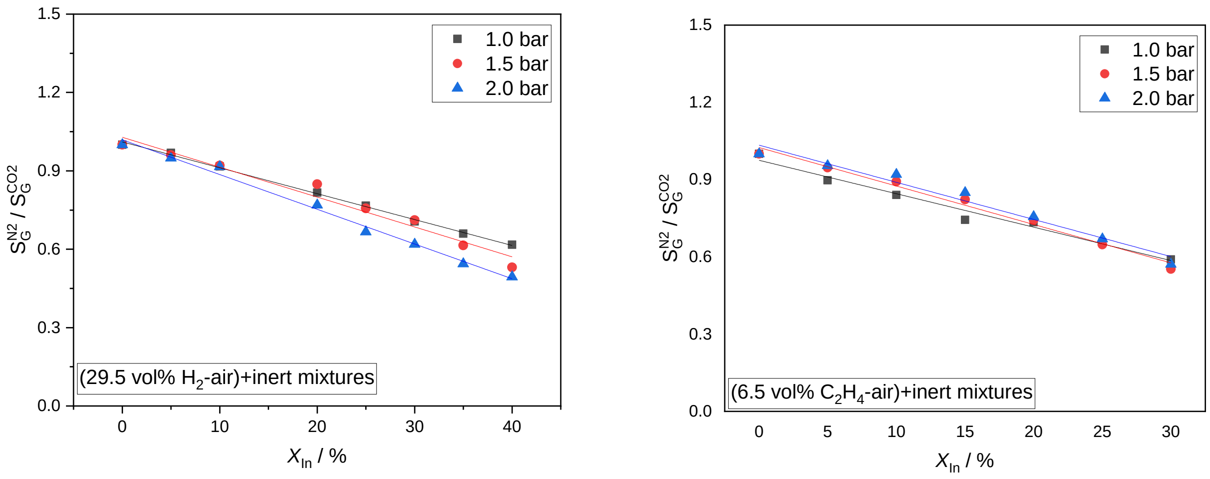

(a) (b)

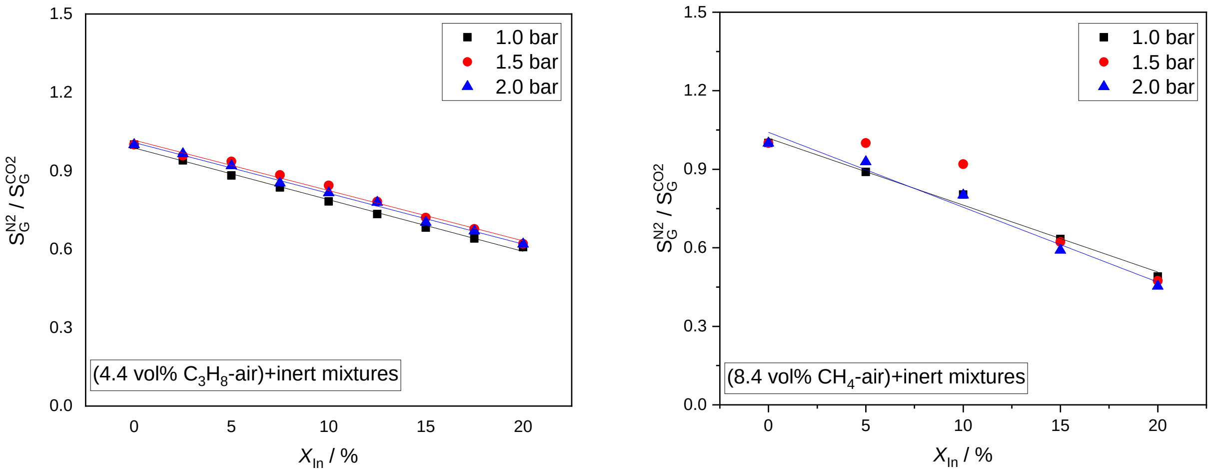

(c) (d)

Fig. 6. *Ratio of* S_G^{N2}/S_G^{CO2} *S_G of fuel-air-inert mixtures, at various initial pressures and various concentrations of added inert X_{In}: (a) (29.5 % hydrogen-air)-inert mixtures; (b) (6.5 vol % ethylene-air)-inert mixtures; (c) (4.4 vol % propane-air)-inert mixtures; (d) (8.4 vol % methane-air)-inert mixtures.*

Figure 6 presents the ratio between the limiting experimental safe gap determined for fuel-air mixture in presence of nitrogen and carbon dioxide (S_G^{N2}/S_G^{CO2}), at various initial pressures and various concentrations of added inert (X_{In}). It is observed that the (S_G^{N2}/S_G^{CO2}) ratio is not constant but decreases linearly for all combustible mixtures tested when the amount of inert gas increases. The behavior of methane seems to be different (much less linear) compared to the other gases. However, no plausible reason was found for this. Within the range of measurement uncertainty, the ratio is the same with different pressures. The (S_G^{N2}/S_G^{CO2}) ratio decreases between 1.0 (for mixtures without inert) and 0.5 (for mixtures with 40% inert). As the inert concentration increases, the pronounced dilution effect of carbon dioxide compared to nitrogen is observed. A comparison with the published measurements on ethylene mixtures with the addition of inert gases by Razus et al. (2019) shows significant deviations between the measured values. The limiting experimental safe gaps presented in this paper are lower (to the safe side) and consistent with the comparison values given in ISO/IEC 80079-20-1 (2019) and DIN EN ISO 16852 (2017).

4. Conclusions

In this study, the influence of inert gases on the limiting experimental safe gap (S_G) of various test gases in the overpressure range was investigated in hundreds of individual measurements. The S_G decreases inversely proportionally with increasing initial pressure, but it can be increased exponentially again by adding inert gas. Carbon dioxide has a stronger inerting effect than nitrogen. These data provide information about the mitigation effect of inert addition on flammable gas mixtures used in flame arrester testing at higher than atmospheric pressure. It can be pointed out that the statements on the influence of pressure and inert gas on S_G are of general nature as the test gases are representatives of the explosion groups IIA, IIB, and IIC and they show a fairly uniform behavior.

In the continuation of this work, the question could be clarified whether the results obtained here can be transferred to real flame arresters for example. For an individual flame arrester, the amount of inert gas in the test gas mixture can be determined, at which the arrester just not fails. The limiting experimental safe gap of this gas mixture can then be measured in the standard MESG apparatus. It would be beneficial to know, whether the arrester would not fail with other gas mixtures of the same limiting experimental safe gap.

Acknowledgments

The authors gratefully acknowledge the financial contribution from BG-RCI in Heidelberg (PTB grant number 37056).

References

Brandes, E., Redeker, T. (2002). Maximum experimental safe gap of binary and ternary mixtures. *J. Ohys. IV France* 12. Pt7-207. DOI: 10.1051/jp4:20020285.

Brandes, E., Möller, W. *Safety characteristic data. Vol.1: flammable liquids and gases.Bremerhaven*. Wirtschaftsverlag NW, Verlag fur neue Wissenschaft GmbH; 2008. ISBN 978-3-86509-811-5.

Britton, L.G. (2000). Using maximum experimental safe gap to selected flame arresters. *Process Saf Prog* 19, 140–5.

Brokaw, R.S., Gerstein, M. (1956). Correlations of burning velocity, quenching distances and minimum ignition energies of hydrocarbon-oxygen-nitrogen systems. *Proc. 6th Symp. Int. on Comb*., New Haven, 66.

CHEMSAFE *Database for Recommended Safety Characteristics, BAM, PTB, DECHEMA*, Germany; 2021. www.chemsafe.ptb.de

Davies, M., Heidermann T. (2013). Protect your process with the proper flame arresters. *Chemical Engineering Progress* 109, 16–22.

DIN EN ISO 16852:2017-04, Flammendurchschlagsicherungen - Leistungsanforderungen, Prüfverfahren und Einsatzgrenzen (ISO 16852:2016); Deutsche Fassung EN ISO 16852:2016, Beuth Verlag.

Henkel, S., Zakel, S., Stolpe, F. (2019). Determination of the performance limits of flame arresters at increased oxygen concentrations, *Journal of Loss Prevention in the Process Industries*; 58: 17-21.

Hirsch, W., Brandes, E. (2014). Sicherheitstechnische Kenngrossen von Gasen und Dämpfen bei nicht atmospharischen Bedingungen. *Abschlussbericht zum Forschungsvorhaben,* PTB.

IEC 80079-20-1:2019: *Explosive atmospheres – Part 20-1: Material characteristics for Gas and vapor classification – Test methods and da*ta. Beuth, 2019.

ISO 10156:2017-07, *Gasflaschen - Gase und Gasgemische - Bestimmung der Brennbarkeit und des Oxidationsvermögens zur Auswahl von Ventilausgängen*, Beuth Verlag.

Lewis, B., von Elbe, G. (1987). *Combustion, flames and explosions of gases*. Academic press inc., Orlando, Florida.

Lunn, G. A. (1984). The maximum experimental safe gap: The effects of oxygen enrichment and the influence of reaction kinetics. *Journal of Hazardous Materials* 8, Nr. 3, 261–270.

Razus, D., Mitu, M., Giurcan, V., Movileanu, C., Oancea, D. (2019). *Additive influence on maximum experimental safe gap of ethylene-air mixtures*. Fuel, 237, 888-894.

Redeker, T. *Classification of flammable gases and vapours by the flameproof safe gap and the incendivity of electrical sparks*. PTB-W-18 (1981), ISSN 0341-6739.

ATEX Directive 2014/34/EU: RICHTLINIE 2014/34/EU DES EUROPÄISCHEN PARLAMENTS UND DES RATES vom 26. Februar 2014 zur *Harmonisierung der Rechtsvorschriften der Mitgliedstaaten für Geräte und Schutzsysteme zur bestimmungsgemäßen Verwendung in explosionsgefährdeten Bereichen* (Neufassung), Amtsblatt der Europäischen Union, L96/309.

TRGS 722: *Vermeidung oder Einschränkung gefährlicher explosionsfähiger Atmosphäre, Technische Regel für Gefahrstoffe*, Ausgabe: März 2012, GMBl 2012 S. 398 [Nr. 22].

DOI: 10.7795/810.20221124

The capabilities of flame arresters on explosive mixtures with increased inert gas content

Frank Stolpe[a], Samah Bendada[a,b]

[a] Physikalisch-Technische Bundesanstalt (PTB), Braunschweig, Germany
[b] Otto-von-Guericke Universität (OvGU), Magdeburg, Germany

E-mail: *frank.stolpe@ptb.de*

Abstract

Flame arresters are widely used as a constructive protection measure against the propagation of explosions in the process industry. They are classified on the basis of the maximum experimental safe gap (MESG) of flammable gases under atmospheric conditions. However, many industrial processes operate outside this range. Therefore, the capabilities of flame arresters exposed to deflagrations of explosive mixtures diluted by increasing amounts of inert gas have been investigated by varying the initial pressure. The results have been reviewed by comparing the related MESGs to verify the applicability of the MESG as an appropriate measure of classification.

Keywords: *flame arresters, inert gas, perfomance, MESG*

1 Introduction

Flame arresters are a constructive measure of explosion protection by preventing the propagation of an ongoing gas or vapour explosion within an installation or plant. A multitude of different types of flame arresters for different applications is available. This investigation focuses on inline deflagration flame arresters. In practice, flame arresters are primarily classified and selected by the explosion group of the substances they are intended to be used with. The explosion group is defined by the MESG of these substances at atmospheric conditions. The MESG is determined using apparatus and method described in IEC 80079-20-1:2019 (2019) which originates from the work of Redeker (1981).

The dimensions of the channels of a flame arresting element do not correspond to the MESG directly, which interprets the need to test individual flame arrester setups under application-oriented conditions. Such test procedures are described in ISO 16852:2016 (2016). The testing is done with a gas-air mixture representing the intended explosion group. The standard tests are made under atmospheric condition, but often flame arresters have to be used under non-atmospheric conditions, like elevated temperature or pressure or at deviating oxygen content or oxidizer.

The present investigation focuses on reduced oxygen concentration by diluting air with inert gas.

2 Experimentental setup and method

The measurements carried out consist of two parts. At first the performance limits of the chosen flame arresters have been determined. In the second part additional MESG data were obtained.

2.1 Setup for flame arrester testing

The setup for testing the flame arresters was derived from ISO 16852:2016 (2016), section 7.3.2.2 figure 2. A customary, but modified, flame arrester was mounted between two pipe sections of DN 50 and 2500 *mm* length, representing a length to diameter ratio (L/D) of 50. The pipe section of the unprotected side was equipped with two pressure transducers, two photodiodes and a spark plug as an ignition source. One of the pressure transducers, a static pressure transducer, was used to measure the initial, pre-ignition, pressure. The second pressure transducer, a dynamic type, was used to measure the explosion pressure. The two photodiodes were used to determine the flame speed. On the protected side is another photodiode located to detect a flame transmission. The schematics of the setup is given in figure 1. To reduce the influence of temperature fluctuations, the entire setup was wrapped with heating tape (see figure 2). This way, the temperature of the setup and the gas mixture inside could be kept within a range of $20°C \pm 5°C$.

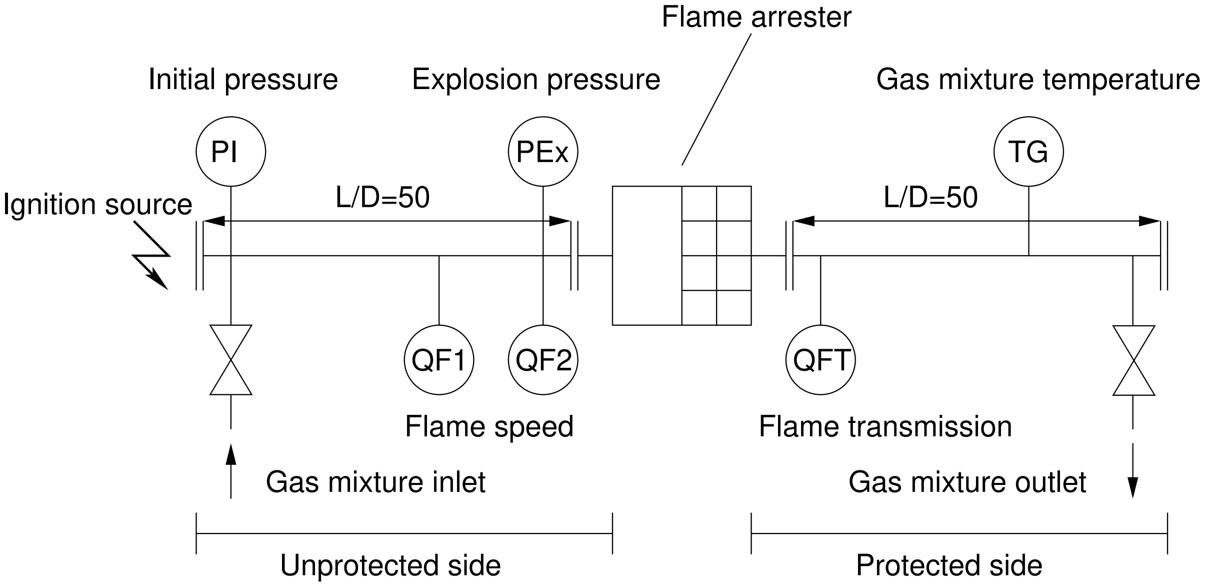

***Fig. 1**: Schematic of the flame arrester setup*

***Fig. 2**: View of the experimental setup*

The flame arresting element used was modified in such a way, that the flame arrester failed for atmospheric or nearly atmospheric conditions. This was achieved by reconfiguring the flame arresting element. Different configurations have been tested. Finally two different configurations were used, one for mixtures containing ethene and one for mixtures containing propane. For mixtures containing ethene a package of two flame arresting elements ($0.5\,mm$ triangle height, $10\,mm$ thickness, one with a right twist and one with a left twist) and an intermediate layer were used. Propane containing mixtures were tested with a single flame arresting element of $10\,mm$ thickness and a triangle height of $0.7\,mm$.

2.1.1 Preparing the gas mixtures

The gas mixtures used were stoichiometric propane-air and ethene-air mixtures diluted by argon, nitrogen or carbon dioxide as an additional inert component. The amount of inert gas added varied between 2 Vol% and 20 Vol%. The mixtures have been prepared by using appropriate calibrated mass flow controllers with a standard uncertainty of 1% relative. The gases used had a purity of 3.0 or better. The compressed air had a residual moisture content of $0.8\,g \cdot m^{-3}$.

2.1.2 Testing procedure

The inert gas concentration in ethene-air and propane-air stoichiometric mixtures were set to 2 Vol-%, 5 Vol-%, 10 Vol-%, 15 Vol-%, and 20 Vol-% . For fixed mixture concentration, if no flame transmission occurred, the inital pressure was increased by $0.1\,bar$ for the next test, finally up to $1.6\,bar$. If the flame was transmitted to the protected side, the initial pressure was decreased by $0.1\,bar$ and tested four times consecutively. After approximately a recovery time of $24\,h$, the initial pressure was increased by $0.05\,bar$ and tested; if no flame transmission occurred, again four tests were made to confirm the performance limit. The limiting pressure is the highest initial pressure at which no flame transmission has occurred in four successive explosion tests.

2.2 Maximum experimental safe gap

For those mixtures diluted by argon no previous MESG data were available and it was necessary to measure these MESG. These measurements were made using the apparatus and procedure described in IEC 80079-20-1:2019 (2019). The procedure was simplified by applying only five consecutive tests to confirm that no flame transmission has occurred. This resulted in a slightly higher uncertainty of measurement of $\pm 0.04\,mm$ of the MESG.

The MESG for gas mixtures diluted by nitrogen and carbon dioxide have been derived from the data published by Brandes and Hirsch (2014), Razus et al. (2018), Zakel et al. (2020) and Rodgers (2010).

3 Results and discussion

The tests of the flame arresters were carried out using stoichiometric ethene-air and propane-air mixtures diluted with argon, nitrogen or carbon dioxide. The MESG has a significant pressure dependence. By adjusting the initial pressure of a chosen gas mixture, the MESG of this mixture is adjusted to. The performance limit of the flame arrester is described by the maximum initial pressure when no flame transmission occurs and the minimum initial pressure when the flame arrester failed. The figures 3 and 4 illustrate and summarize this.

3.1 Related MESG

Tables 2 and 3 are showing the MESG and the corresponding initial pressure and inert gas content. Both values, for failure and prevention of propagation, are given. The true limit is assumed between those two values.

Table 1: *Table of the MESG related to inert gas*

flammable gas	inert gas	MESG range in mm	MESG mean in mm
ethene	Ar	0.5 – 0.60	0.52
	N_2	0.54 – 0.57	0.56
	CO_2	0.50 – 0.56	0.53
propane	Ar	0.89 – 1.01	0.95
	N_2	0.74 – 0.89	0.80
	CO_2	0.78 – 0.86	0.82

Adding inert gas resulted in a significant increase of the initial pressure before a failure of the flame arrester. These data are showing, the performance limit depends on the nature and concentration of the inert gas. But having a look to the corresponding MESG, shows only a narrow range of values (see table 1).

Please note, the range of the MESG for one combination of flammable gas and inert gas over the initial pressure is in most cases larger than the uncertainty of measurement. This means, there is not a simple mean value to assume.

4 Conclusions

The observations described before are leading to the assumption, the MESG seems to be a suitable candidate to describe the performance limit of a flame arrester within a certain pressure range. So the performance limit might be described by the MESG in general. This description gets more precise, when focusing on a certain inert gas added. From the measured data can be deduced, that the effect of increasing the MESG by adding inert gas is not of the same magnitude than the decrease if the MESG by increasing the initial pressure. Additionally this depends on the kind of inert gas added.

With respect to the observed uncertainties and the number of flame arresters and configuration tested the MESG can not be named as the quantity to described the performance limit exactly. But the knowledge of this data provides the information where to start additional testing and helps to keep time and effort moderate.

Summarizing this results: The MESG of a flame arresters performance limit under certain conditions is not a general value, but it indicates the range where to start testing for a certain application with different conditions. The MESG can not be enough alone to present reliable information about flame arrester classification under non-atmospheric conditions.

Acknowledgements

The authors would like to thank all their colleagues at the Physikalisch-Technische Bundesanstalt who have supported this study. The authors would like to thank also Dr. Thomas Heidermann and Braunschweiger Flammenfilter GmbH - PROTEGO® for providing the flame arrester equipment, as well as Jürgen Hübner and Uwe Block for constructing the flame arrester test setup and supporting the tests. Also many thanks to Uwe Hansen for his support of the MESG measurements.

This research did not receive any specific grant from funding agencies in the public, commercial, or not-for-profit sectors.

References

Brandes, E., Hirsch, W. (2014). *Abschlussbericht zum Forschungsvorhaben: Sicherheitstechnische Kenngrößen bei nichtatmosphärischen Bedingungen: Gase und Dämpfe.* Physikalisch-Technische Bundesanstalt, Braunschweig.

IEC 80079-20-1:2019 (2019). *Explosive atmospheres - part 20-1: Material characteristics for gas and vapour classification - test methods and data.* Standard, International Electrotechnical Commission, Geneva, CH.

ISO 16852:2016 (2016). *Flame arresters - performance requirements, test methods and limits for use.* Standard, International Organization for Standardization, Geneva, CH.

Razus, D., Mitu, M., Giurcana, V., Movileanua, C., Oanceab, D. (2018). *Additive influence on maximum experimental safe gap of ethylene-air mixtures.* Fuel, 237:888–894.

Redeker, T. (1981). *PTB Report PTB-W-18: Classification of flammable gases and vapours by the flameproof safe gap and the incendivity of electrical sparks.* Physikalisch-Technische Bundesanstalt, Braunschweig.

Rodgers, S. A. (2010). *A fuel ratio method for estimating the mesg of nitrogen-diluted and oxygen-enriched fuels, including the brandes-redecker method to estimate the mesg of mixed fuels.* In American Institute of Chemical Engineers (Ed.), The 44th Annual Loss Prevention Symposium, pages 11–15.

Zakel, S., Hansen, U., Stolz, T. (2020). *Ermittlung der Grenzspaltweite von Gasgemischen in Abhängigkeit von Inertgasanteil und Druck im Überdruckbereich.* Physikalisch-Technische Bundesanstalt, Braunschweig.

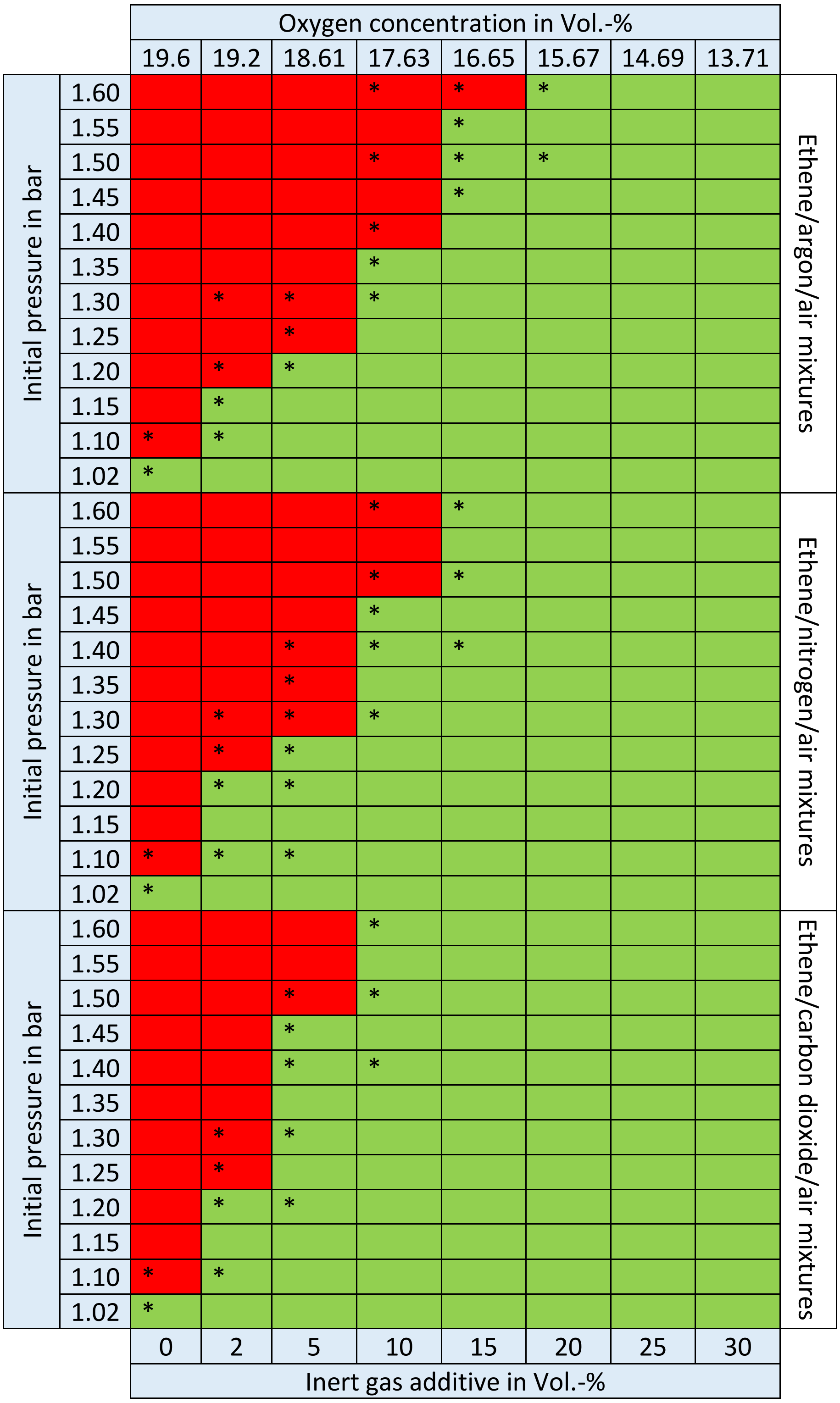

	Oxygen concentration in Vol.-%								
Initial pressure in bar	19.6	19.2	18.61	17.63	16.65	15.67	14.69	13.71	
1.60	🟥	🟥	🟥	🟥 *	🟥 *	🟩 *	🟩	🟩	Ethene/argon/air mixtures
1.55	🟥	🟥	🟥	🟥	🟩 *	🟩	🟩	🟩	
1.50	🟥	🟥	🟥	🟥 *	🟩 *	🟩 *	🟩	🟩	
1.45	🟥	🟥	🟥	🟥	🟩 *	🟩	🟩	🟩	
1.40	🟥	🟥	🟥	🟥 *	🟩	🟩	🟩	🟩	
1.35	🟥	🟥	🟥	🟩 *	🟩	🟩	🟩	🟩	
1.30	🟥	🟥 *	🟥 *	🟩 *	🟩	🟩	🟩	🟩	
1.25	🟥	🟥	🟥 *	🟩	🟩	🟩	🟩	🟩	
1.20	🟥	🟥 *	🟩 *	🟩	🟩	🟩	🟩	🟩	
1.15	🟥	🟩 *	🟩	🟩	🟩	🟩	🟩	🟩	
1.10	🟥 *	🟩 *	🟩	🟩	🟩	🟩	🟩	🟩	
1.02	🟩 *	🟩	🟩	🟩	🟩	🟩	🟩	🟩	
Initial pressure in bar									
1.60	🟥	🟥	🟥	🟥 *	🟩 *	🟩	🟩	🟩	Ethene/nitrogen/air mixtures
1.55	🟥	🟥	🟥	🟥	🟩	🟩	🟩	🟩	
1.50	🟥	🟥	🟥	🟥 *	🟩 *	🟩	🟩	🟩	
1.45	🟥	🟥	🟥	🟩 *	🟩	🟩	🟩	🟩	
1.40	🟥	🟥	🟥 *	🟩 *	🟩 *	🟩	🟩	🟩	
1.35	🟥	🟥	🟥 *	🟩	🟩	🟩	🟩	🟩	
1.30	🟥	🟥 *	🟥 *	🟩 *	🟩	🟩	🟩	🟩	
1.25	🟥	🟥 *	🟩 *	🟩	🟩	🟩	🟩	🟩	
1.20	🟥	🟩 *	🟩 *	🟩	🟩	🟩	🟩	🟩	
1.15	🟥	🟩	🟩	🟩	🟩	🟩	🟩	🟩	
1.10	🟥 *	🟩 *	🟩 *	🟩	🟩	🟩	🟩	🟩	
1.02	🟩 *	🟩	🟩	🟩	🟩	🟩	🟩	🟩	
Initial pressure in bar									
1.60	🟥	🟥	🟥	🟩 *	🟩	🟩	🟩	🟩	Ethene/carbon dioxide/air mixtures
1.55	🟥	🟥	🟥	🟩	🟩	🟩	🟩	🟩	
1.50	🟥	🟥	🟥 *	🟩 *	🟩	🟩	🟩	🟩	
1.45	🟥	🟥	🟩 *	🟩	🟩	🟩	🟩	🟩	
1.40	🟥	🟥	🟩 *	🟩 *	🟩	🟩	🟩	🟩	
1.35	🟥	🟥	🟩	🟩	🟩	🟩	🟩	🟩	
1.30	🟥	🟥 *	🟩 *	🟩	🟩	🟩	🟩	🟩	
1.25	🟥	🟥 *	🟩	🟩	🟩	🟩	🟩	🟩	
1.20	🟥	🟩 *	🟩 *	🟩	🟩	🟩	🟩	🟩	
1.15	🟥	🟩	🟩	🟩	🟩	🟩	🟩	🟩	
1.10	🟥 *	🟩 *	🟩	🟩	🟩	🟩	🟩	🟩	
1.02	🟩 *	🟩	🟩	🟩	🟩	🟩	🟩	🟩	
	0	2	5	10	15	20	25	30	
	Inert gas additive in Vol.-%								

***Fig. 3**: Summary of the test result with ethene-air mixtures. "*" indicate tests carried out. A green background indicates no flame transmission (safe conditions), a red background indicates a failure of the flame arrester (unsafe conditions).*

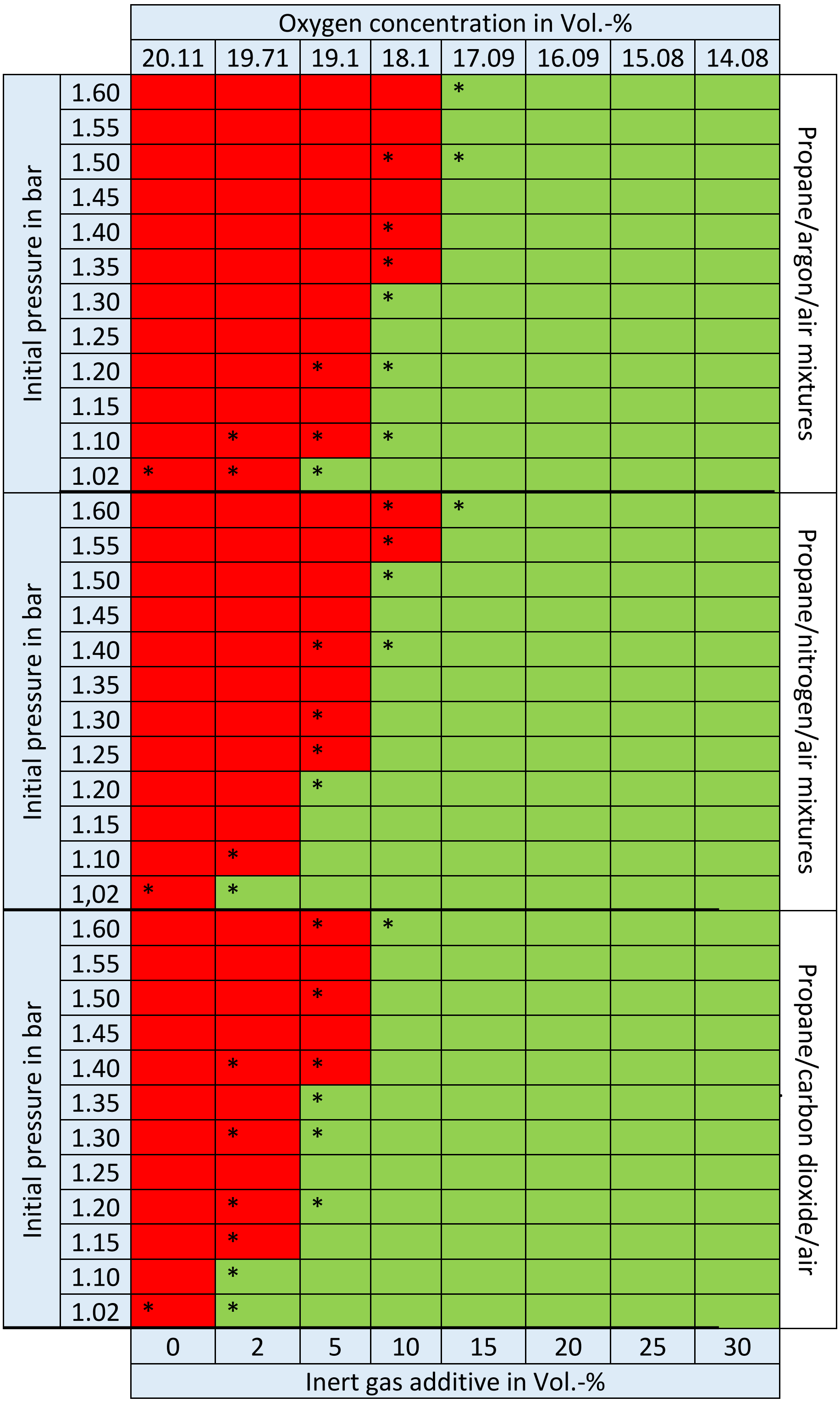

		Oxygen concentration in Vol.-%								
		20.11	19.71	19.1	18.1	17.09	16.09	15.08	14.08	
Initial pressure in bar	1.60	🟥	🟥	🟥	🟥	🟩 *	🟩	🟩	🟩	Propane/argon/air mixtures
	1.55	🟥	🟥	🟥	🟥	🟩	🟩	🟩	🟩	
	1.50	🟥	🟥	🟥	🟥 *	🟩 *	🟩	🟩	🟩	
	1.45	🟥	🟥	🟥	🟥	🟩	🟩	🟩	🟩	
	1.40	🟥	🟥	🟥	🟥 *	🟩	🟩	🟩	🟩	
	1.35	🟥	🟥	🟥	🟥 *	🟩	🟩	🟩	🟩	
	1.30	🟥	🟥	🟥	🟩 *	🟩	🟩	🟩	🟩	
	1.25	🟥	🟥	🟥	🟩	🟩	🟩	🟩	🟩	
	1.20	🟥	🟥	🟥 *	🟩 *	🟩	🟩	🟩	🟩	
	1.15	🟥	🟥	🟥	🟩	🟩	🟩	🟩	🟩	
	1.10	🟥	🟥 *	🟥 *	🟩 *	🟩	🟩	🟩	🟩	
	1.02	🟥 *	🟥 *	🟩 *	🟩	🟩	🟩	🟩	🟩	
Initial pressure in bar	1.60	🟥	🟥	🟥	🟥 *	🟩 *	🟩	🟩	🟩	Propane/nitrogen/air mixtures
	1.55	🟥	🟥	🟥	🟥 *	🟩	🟩	🟩	🟩	
	1.50	🟥	🟥	🟥	🟩 *	🟩	🟩	🟩	🟩	
	1.45	🟥	🟥	🟥	🟩	🟩	🟩	🟩	🟩	
	1.40	🟥	🟥	🟥 *	🟩 *	🟩	🟩	🟩	🟩	
	1.35	🟥	🟥	🟥	🟩	🟩	🟩	🟩	🟩	
	1.30	🟥	🟥	🟥 *	🟩	🟩	🟩	🟩	🟩	
	1.25	🟥	🟥	🟥 *	🟩	🟩	🟩	🟩	🟩	
	1.20	🟥	🟥	🟩 *	🟩	🟩	🟩	🟩	🟩	
	1.15	🟥	🟥	🟩	🟩	🟩	🟩	🟩	🟩	
	1.10	🟥	🟥 *	🟩	🟩	🟩	🟩	🟩	🟩	
	1,02	🟥 *	🟩 *	🟩	🟩	🟩	🟩	🟩	🟩	
Initial pressure in bar	1.60	🟥	🟥	🟥 *	🟩 *	🟩	🟩	🟩	🟩	Propane/carbon dioxide/air
	1.55	🟥	🟥	🟥	🟩	🟩	🟩	🟩	🟩	
	1.50	🟥	🟥	🟥 *	🟩	🟩	🟩	🟩	🟩	
	1.45	🟥	🟥	🟥	🟩	🟩	🟩	🟩	🟩	
	1.40	🟥	🟥 *	🟥 *	🟩	🟩	🟩	🟩	🟩	
	1.35	🟥	🟥	🟩 *	🟩	🟩	🟩	🟩	🟩	
	1.30	🟥	🟥 *	🟩 *	🟩	🟩	🟩	🟩	🟩	
	1.25	🟥	🟥	🟩	🟩	🟩	🟩	🟩	🟩	
	1.20	🟥	🟥 *	🟩 *	🟩	🟩	🟩	🟩	🟩	
	1.15	🟥	🟥 *	🟩	🟩	🟩	🟩	🟩	🟩	
	1.10	🟥	🟩 *	🟩	🟩	🟩	🟩	🟩	🟩	
	1.02	🟥 *	🟩 *	🟩	🟩	🟩	🟩	🟩	🟩	
		0	2	5	10	15	20	25	30	
		Inert gas additive in Vol.-%								

***Fig. 4**: Summary of the test result with propane-air mixtures. "*" indicate tests carried out. A green background indicates no flame transmission (safe conditions), a red background indicates a failure of the flame arrester (unsafe conditions).*

***Table 2**: Table of the MESG related to initial pressure and inert gas dilution for ethene*

ETHENE

		Initial pressure [bar]	MESG [mm]
Ar [Vol.-%]	0	1.02	0.62
		1.10	0.58
	2	1.15	0.54
		1.20	0.54
	5	1.20	0.56
		1.25	0.52
	10	1.35	0.50
		1.40	0.48
	15	1.55	0.46
		1.60	0.44
	20	1.60	-
		-	-
N_2 [Vol.-%]	2	1.20	0.57
		1.25	0.54
	5	1.25	0.58
		1.30	0.55
	10	1.45	0.55
		1.50	0.53
	15	1.60	0.57
		-	-
CO_2 [Vol.-%]	2	1.20	0.57
		1.25	0.54
	5	1.45	0.50
		1.50	0.49
	10	1.60	0.52
		-	-

DOI: 10.7795/810.20221124

***Table 3**: Table of the MESG related to initial pressure and inert gas dilution for propane*

		PROPANE	
		Initial pressure [bar]	**MESG [mm]**
Argon [Vol.-%]	2	-	-
		1.02	-
	5	1.02	1.07
		1.10	0.95
	10	1.30	1.00
		1.35	0.77
	15	1.60	-
		-	-
N_2 [Vol.-%]	0	-	-
		1.02	0.9
	2	1.02	0.91
		1.10	0.87
	5	1.20	0.78
		1.25	0.75
	10	1.50	0.75
		1.55	0.73
	15	1.60	0.79
		-	-
CO_2 [Vol.-%]	2	1.10	0.88
		1.15	0.84
	5	1.35	0.79
		1.40	0.76
	10	1.60	0.78
		-	-

DOI: 10.7795/810.20221124

Thermal evaluation of junction and connection boxes in explosion protection

Florian Koch [a], Peter Thurnherr [b], Detlev Markus [a] & Ulrich Krause [c]

[a] Physikalisch-Technische Bundesanstalt (PTB), Braunschweig, Germany
[b] thuba AG, Basel, Switzerland
[c] Otto-von-Guericke-Universität Magdeburg, Magdeburg, Germany

E-mail: *florian.koch@ptb.de*

Abstract

To reliably avoid potential ignition sources and thus ignition of the potentially explosive atmosphere in junction and connection boxes of type of protection Increased Safety 'e', the self-heating shall not exceed a specified level depending on the temperature class. For the conformity assessment of such products, complex thermal tests are necessary due to the great variety of mounting types and arrangements of terminal blocks in the enclosure, depending on the enclosure size. These tests are very time-consuming for the manufacturer of junction and connection boxes or for the testing laboratory and are therefore associated with considerable costs. To reduce this effort and to ensure a uniform assessment in the conformity evaluation by a certification body, it is therefore essential to create fitting charts depending on the enclosure size.

This work introduces a calculation tool by means of systematic investigations on different enclosure sizes and with different assemblies, which enables the calculation of fitting charts with justifiable effort. For this purpose, the maximum temperature in the enclosure was determined as a function of the current and the assembly. From this, electrical and enclosure-specific constants such as the maximum permissible current per conductor and a conductor specific factor were determined and combined with an exponential dependence of the power dissipation. It is shown that this relationship is valid for an overtemperature of 40 K for compliance with temperature class T6 up to an ambient temperature of +40 °C. Finally, to verify the reliability of the calculation tool, the results are compared with the enclosure-specific rated value of the maximum power dissipation according to IEC 60079-7, 5.7.

Keywords: *Thermal evaluation, Junction box, Temperature class, Fitting table, Increased safety*

Introduction

In many chemical and petrochemical industries, combustible gases, vapors or dusts are produced or emitted during the production, processing, transport and storage of combustible substances, creating an explosive atmosphere in combination with the oxygen in the air (Steen, 2004). An explosion caused by ignition of the combustible atmosphere must be prevented by explosion protection. For explosion protection of electrical equipment, the surface temperature of the equipment or components accessible to the explosive atmosphere and from which an explosion can propagate unhindered is of decisive importance. As the surface can become a source of ignition for combustible gases and vapors, the limit values in the IEC 60079-0 ff (IEC, 2017) standard must not be exceeded with respect to a specific temperature class. Combustible gases and vapors are categorized into these defined six temperature classes according to their flammability. E.g., for temperature class T6, the maximum surface temperature must not be higher than 80 °C.

For electrical installations, normally a junction and connection box is used to connect several electrical conductors by using through terminals. In terms of explosion protection, these are primarily designed in type of protection Increased Safety 'e', so that, among other things, measures have been taken to prevent the possibility of impermissibly high surface temperatures inside the electrical equipment. This type of equipment is certified in accordance with IEC 60079-7 (IEC, 2015). The maximum dissipated power method and defined arrangement method are specified in this standard under section 6.8 and Annex E to give the end user electrical data for installation.

1.1 Maximum dissipated power method according to IEC 60079-7, section 6.8.2

A way to ensure safe operation of junction and connection boxes is to inform the end user about the allowed maximum dissipated power. This is based on the fact that the enclosure surface can only dissipate a certain amount of power to the environment. As a result, the specification of the maximum dissipated power depends on the enclosure size. The maximum dissipated power is calculated for each terminal and its associated conductors by using the maximum rated current for the terminal and the contact resistance at 20 °C. For the calculation, a cable length per terminal is taken corresponding to the three-dimensional enclosure diagonal. A comparative measurement in the laboratory shows the maximum number of terminals n that may be installed with these electrical parameters for a specific temperature class

$$P = I^2 \cdot n \cdot \left\{ R_{TB} + \left(R_{W/D} \cdot \sqrt{L_B^2 + W_B^2 + D_B^2} \right) \right\}. \tag{1}$$

The maximum dissipated power P for a junction and connection box with the length L_B, width W_B and depth D_B is calculated by using the rated current I, the individual terminal contact resistance R_{TB} and resistance of the conductor $R_{W/D}$.

1.2 Defined arrangement method according to IEC 60079-7, section 6.8.3

An alternative method gives the end user the possibility to build up a junction and connection box with the help of a fitting chart. This fitting chart gives for a specific conductor cross section and an application related current the maximum allowed number of terminals to be installed in the box. It depends on the enclosure size and the enclosure material. A maximum conductor length is assumed that corresponds to the three-dimensional enclosure diagonal. For this method complex, time-consuming and cost-intensive thermal evaluations are required as part of the conformity assessment due to the great variety of mounting types and arrangements of terminals blocks in the enclosure, depending on the enclosure size.

A calculation tool already exists to generate these fitting charts (Wießner, 1993) (Bendel et al, 1993). However, this can only be used to a limited extent, since the scientific basis can no longer be completely reproduced. To keep the certification effort for the testing laboratory and the manufacturer as low as possible, a new calculation tool is to be developed that gives the same results and safety as this method. It will be tested for a temperature class T6. This allows a maximum temperature rise of 40 K to occur at an ambient temperature of +40 °C. The results will then be compared with outcome of the maximum dissipated power method.

2. Experimental setup

Systematic tests were carried out on junction and connection boxes to determine the allowable currents for the different conductor cross-sections and enclosure types. The test setup used for this purpose is shown in Figure 1. The experimental setup is supplied by an AC 230 V variable transformer T1 (Ruhstrat T-RSD), which allows stepless regulation of the voltage. Subsequently, the voltage is transformed to two times 12 V, 50 A each by the isolating transformer T2 (Ruhstrat Iii0). In order to use a current greater than 50 A, both secondary windings are connected in parallel so that with maximum 12 V a supply of 100 A is possible. The voltage and current are measured using a Power Analyzer P1 (FLUKE NORMA 4000) connected by a current transformer T3. The temperature measurement TC in the respective sample DUT is carried out with thermocouples type K, class 1 (IEC 60584-1) and temperature input modules (National Instruments TB-9212).

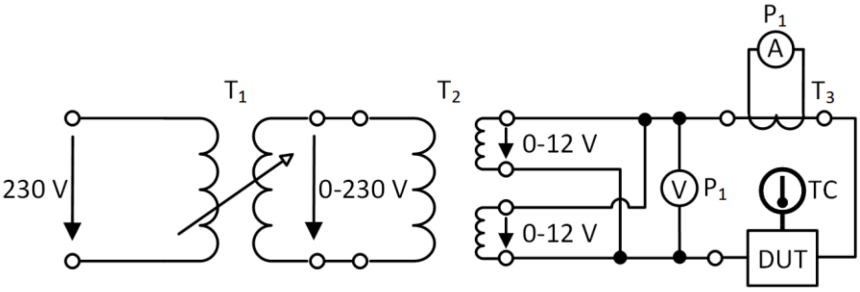

Figure 1: *Schematic test setup for a maximum power supply of 12 V, 50 A with transformer T1-T3, power analyzer P1, temperature measurement module TC and test sample DUT.*

The investigated samples with their dimensions and enclosure material are listed in Table 1. The enclosure contains a DIN rail on which the terminal blocks are mounted. The maximum number of installed terminals results from the enclosure and terminal block size. The installation is always horizontal. The terminals are connected in series with a conductor length corresponding to the three-dimensional diagonal of the enclosure per terminal block. Only the connecting cable at the beginning and at the end leaves the enclosure via cable entries (Figure 2a). This ensures that the completely generated power dissipation remains in the enclosure so that the measurements take place under worst case conditions. The standard for electrical installation design, selection and erection IEC 60079-14 (IEC, 2013) requires that for this type of equipment maximum six cables may be combined into one cable bundle. This was applied for the tests.

Table 1: *Examined samples and tested conductor cross sections*

No.	Enclosure material	Dimension	Tested conductor sizes
1	Polyester	270x270x135 mm (9,8 L)	2.5, 4, 6, 10, 16 mm²
2	Polyester	400x450x200 mm (36 L)	2.5, 16 mm²
3	Stainless Steel	270x270x135 mm (9,8 L)	2.5, 4, 6, 10, 16 mm²
4	Stainless Steel	395x300x195 mm (23,1 L)	2.5, 4, 6, 10, 16 mm²

One challenge of temperature measurements is the selection of the measurement points to get the most accurate information about the temperature distribution inside or on the outside of a sample. Since a complex heat distribution is already formed in an equipped junction and connection box, the hot spots are determined with a thermal imaging camera as a time saving solution (Figure 2b). In all samples used, it was found that the cable bundles and the clamping point between the cable and the terminal block are the hottest points. Accordingly, one or more thermocouples were placed in each cable bundle, at selected cables and terminal points, between the terminal blocks and on the inner wall of the enclosure (Figure 2a). The measurement points were kept the same on all samples so that the results are comparable with each other. To ensure the best possible heat transfer, a heat-resistant epoxy resin adhesive was used to attach the thermocouple to the measuring point.

Temperature measurements are performed at ambient temperature and ambient pressure. A measuring point consists of the combination of enclosure, number of installed terminals and conductor cross-section. Two temperature measurements were carried out per measuring point, so that the temperature rise of the hot spots is once just above 40 K and once just below 40 K. The current that leads exactly to a temperature rise of 40 K is then calculated by an exponential function (Bendel et al., 1993). This procedure is necessary because the exact determination of the current which leads to a temperature rise of 40 K is not possible due to the resistance reduction by heating of the conductors. According to IEC 60079-0 the final temperature is reached when the rate of temperature rise at all measuring points does not exceed a rate of 2 K/h (IEC, 2017).

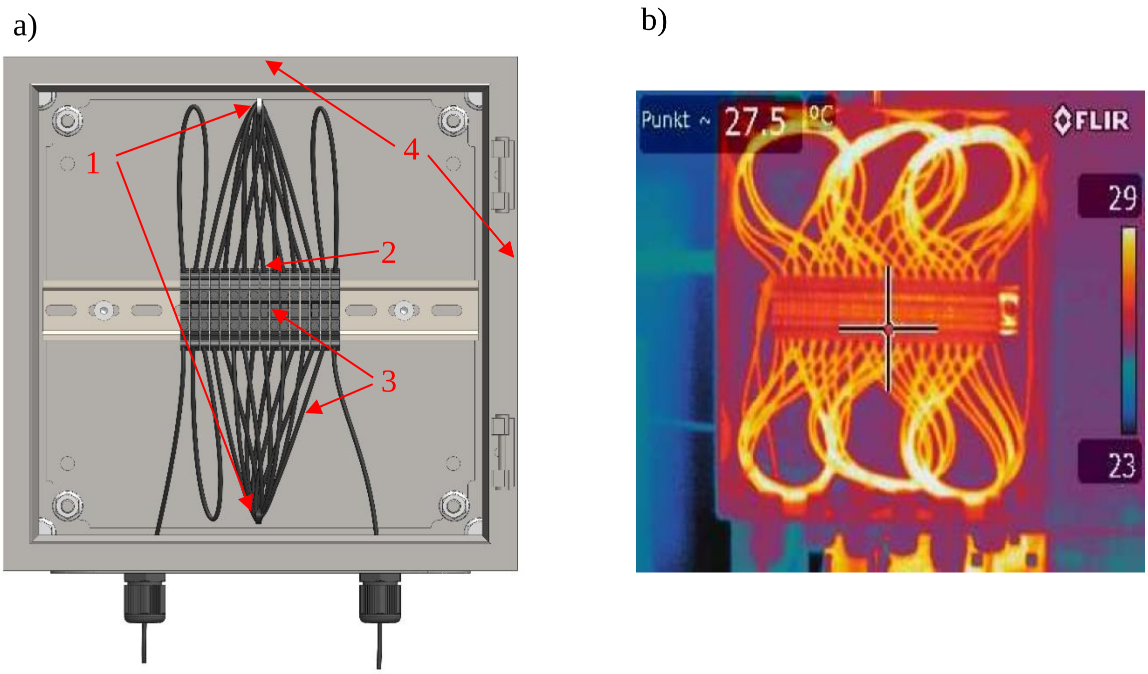

Figure 2: *a) Schematic layout with exemplary marking of the thermocouples in the cable bundles (1), at the contact point in the terminal (2), between the terminals and on the cable (3) and on the inner wall of the enclosure (4). b) Thermography image of a junction and connection box.*

3. Results and discussion

3.1 Detached type installation

Figure 3 shows the experimental results for the four tested enclosures for all five conductor cross sections. The number of installed terminals is shown as a function of the current that leads to a temperature rise of 40 K. The enclosures were installed on a rack allowing free convection to take place on all sides of the enclosure. It can be seen both in Figure 3a and Figure 3b that the permissible current decreases exponentially with increasing number of terminals installed and converges to a cross section specific constant value. This value is defined as I_u as the current value for a theoretical infinite number of terminals. An exponential fit can be used to determine the cross-section specific values (Wießner, 1993). With increasing conductor cross-section, the electric current density is reduced, so that the current I_{max} increases to reach a temperature rise of 40 K. Figure 3a shows the characteristics of the 9.8 L polyester enclosure for all five conductor cross-sections, the two hot spots in the cable bundle and at the contact point on the terminal. For a large number of terminals installed, I_{max} results in approximately equal temperature rise in the hotspots. As soon as the number of installed terminals is so low that six conductors in the cable bundle are no longer completely flown by current, the temperature in the cable bundle is much lower compared to temperature at the clamps. A temperature rise of 40 K results accordingly for a small number of installed terminals at different I_{max}. This is independent of the enclosure and cross-section.

I_{max} for a measurement point in the cable bundle for all enclosures and all conductor cross sections is shown in Figure 3b. For all tested enclosure sizes and materials, it can be seen that I_{max} decreases exponentially with increasing number of terminals installed. The size of the enclosure has no significant influence. It can be concluded that the enclosure material has an influence on the heat transfer and thus on the maximum current for a specific number of installed terminals. If the current for black polyester enclosures is set to 1, the value for the bare metal enclosures is constant at 0.9. The relatively small influence of the enclosure material on heat dissipation is also referred to in IEC TR 60890 (2014).

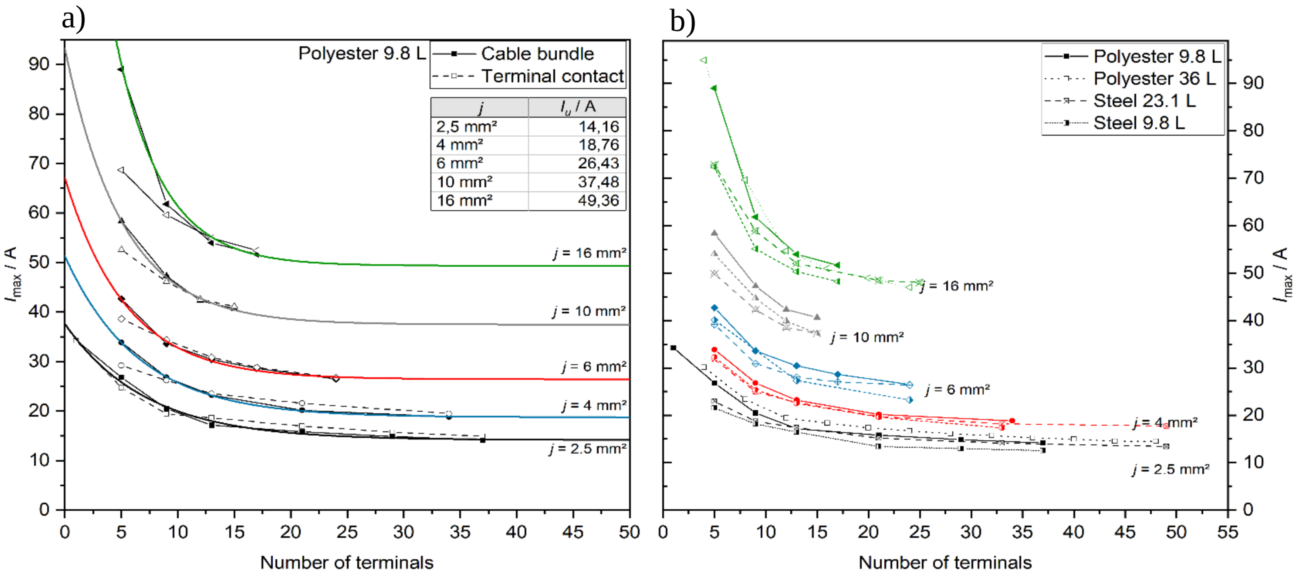

Figure 3: *a) Current I_{max} that leads to a temperature increase of 40 K as a function of the number of terminals and the resulting current I_u for the theoretically infinite number of terminals installed. b) I_{max} for all enclosures, enclosure materials and all conductor cross sections.*

3.2 Different types of installation

The heat transfer of the enclosure depends significantly on the freely available outer surface (Bergman et al., 2017), so further experiments were carried out on the influence of the insulation of one or more enclosure walls. For this purpose, the side walls of the 36 L polyester enclosure were covered with polystyrene foam sheets in various combinations to simulate different installation types. According to IEC TR 60890 (2014) the bottom surface of the enclosure has no significant influence on heat transfer, therefore it was not considered in the experiment. Six different types of installations were tested, each with a free backplane (e.g. installation on a rack) and with a covered backplane (installation on a wall). The results for I_{max} are set in relation to the enclosure installed freely in air (E = 1), an erection factor E is obtained for the different installation types which is given in Table 2. With increased coverage of the enclosure walls, I_{max} decreases because less energy can be dissipated and the temperature limit of 40 K is reached with less current, so that E also decreases.

Table 2: *Erection factor E for different installation types. Heat transport inactive surfaces marked in red and wall mounting marked in grey in the symbol.*

Symbol	Type of installation	*E*
□	Separate enclosure, detached on all sides	1
▨	Separate enclosure, wall-mounting type	0.95
□ □	First or last enclosure, detached type	0.95
▨ ▨	First or last enclosure, wall-mounting type	0.9
□	Central enclosure, detached type	0.9
▨	Central enclosure, wall-mounting type	0.85
□	Central enclosure, detached type with covered top surface	0.81
▨	Central enclosure, wall-mounting type with covered top surface	0.76
□	Separate enclosure, detached type with covered top surface	0.89
▨	Separate enclosure, wall-mounting type with covered top surface	0.85
□ □	First or last enclosure, detached type with covered top surface	0.9
▨ ▨	First or last enclosure, wall-mounting type with covered top surface	0.82

3.3 Calculation Tool

On the basis of the results from 3.1, 3.2 and on the calculations according to Bendel et al. (1993) the following equation was developed for the calculation of the maximum permissible number of terminals for a given current in a defined enclosure and a specific conductor cross-section according to IEC 60079-7, section 6.8.3,

$$n = \left\{F \cdot \left(K_j \cdot S_m \cdot E\right) \cdot \ln \frac{I_{0,j}-\left(I_{u,j} \cdot E\right)}{I-\left(I_{u,j} \cdot E\right)}\right\} \cdot M \cdot S_f \text{ with} \tag{2}$$

$$F = \frac{G_{f,n}}{G_{f,i}} \text{ and } G_{f,i} = \frac{D}{A_e}. \tag{3}$$

The maximum permissible number of terminals n for a current I is calculated by using a geometric factor of the enclosure F, a conductor-specific factor K, the erecting factor E, a heat dissipation factor for the enclosure material M and the ratio of the maximum permissible current $I_{0,j}$ (Table 11 (VDE, 2013)) to $I_{u,j}$ for a theoretically infinite number of installed terminals. For enclosures made of steel, K is multiplied by an empirically determined factor $S_m = 0.72$ (Bendel et al., 1993). It should be noted that all steps of this calculation contain approximations. From a safety point of view, a safety factor is additionally introduced with $S_f = 0.9$, so that exceeding the permissible temperature rise is excluded. F considers design properties of the enclosure. According to Wießner (1993), the unitless constant factor for a standard enclosure is $G_{f,n} = 0.0038\ \mathrm{m}^{-1}$. $G_{f,i}$ for the enclosure under calculated results from the ratio of the three-dimensional enclosure diagonal D to the enclosure surface A_e.

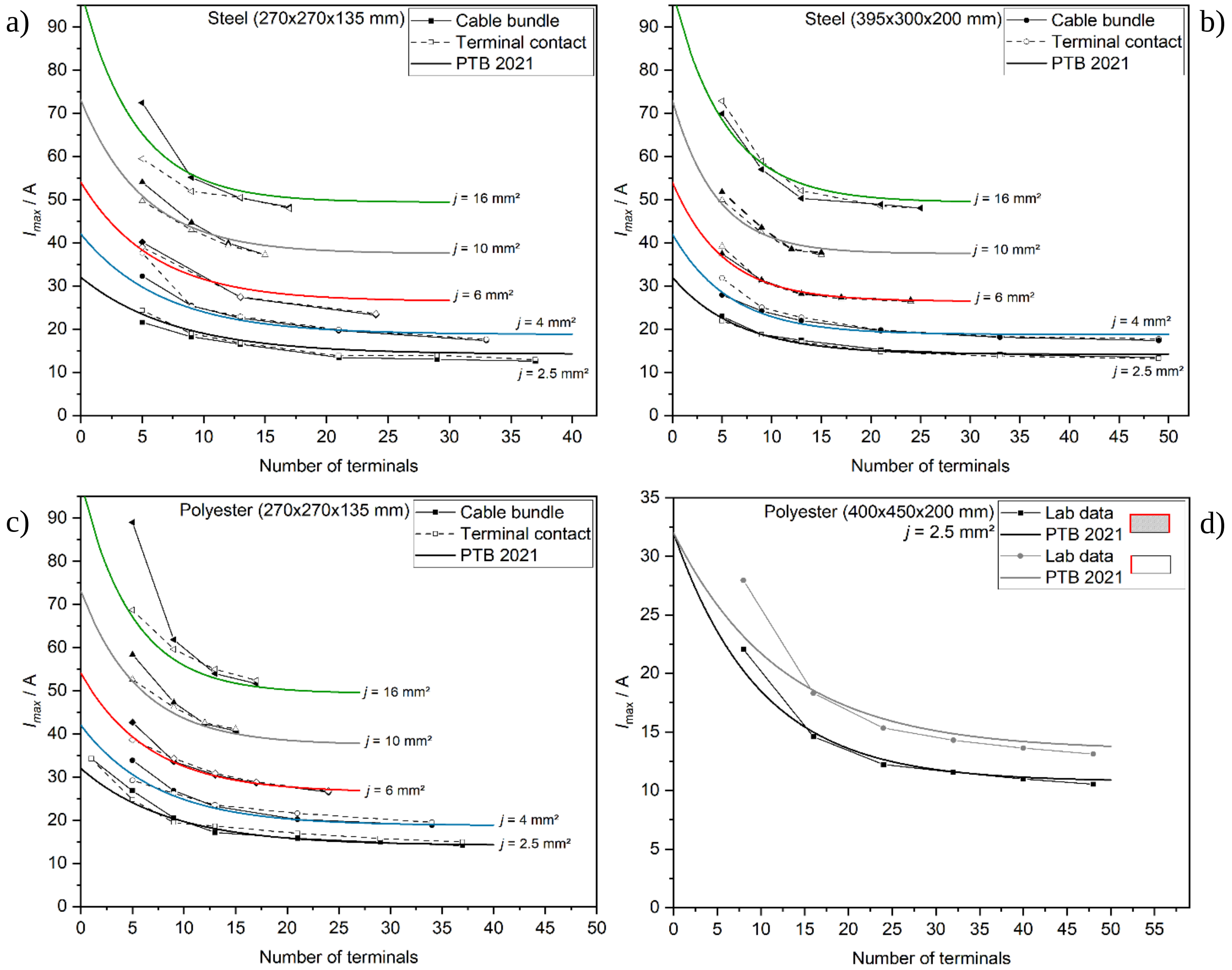

Figure 4: *Comparison of I_{max} of the measured values with the calculated values without S_f for the 9.8 L (a) and 23.1 L stainless steel enclosure (b) and the 9.8 L polyester enclosure (c) for the installation type 'Separate enclosure, detached on all sides' and for the 36 L polyester enclosure (d) for the installation type 'First or last enclosure, detached type' and 'Central enclosure, wall-mounting type'.*

Figure 4 shows calculated I_{max} using equation (2 as a function of the number of terminals compared to the measured values for all four enclosures and conductor cross-sections. Here, the safety factor S_f was not included in the calculation to show that the results agree well with the measured values even without this factor. Figure 4a – Figure 4c shows the values for three different enclosures free in air. It can be seen that the calculated values agree well with the measured values for the two enclosure materials polyester and steel and all conductor cross-sections. The maximum permissible current for a combination of enclosure size, terminal and corresponding cable is not exceeded, so that it is ensured that an exceeding of the maximum temperature rise of 40 K is not reached using equation 2. Furthermore, the calculation shows that the specified maximum current for a single conductor complies with the requirements given in DIN VDE 0298-4 (2013). This also generally ensures that the maximum current for a specific terminal is complied with. However, due to the large variance in different terminal designs, this must be checked in each individual case with the manufacturer's specifications.

Figure 4d shows exemplarily the comparison of the measured values with the calculation results for two different installation types for a conductor cross-section of 2.5 mm² in a 36 L polyester enclosure. For the installation type 'First or last enclosure, detached type' and 'Central enclosure, wall-mounting type' (see Table 2), there is a good correlation between the calculated results and the measured values. This graph also shows that it is important to consider the type of installation of the junction and connection box in the calculation. The difference of permissible current between these two types of installation is 20 %. The results for an enclosure installed free in air can therefore not be used for other types of installation. An individual calculation for the specific application is necessary.

3.4 Comparison of the two methods

To compare the calculation tool with the maximum power dissipation method, the results are analyzed for a cable cross-section of 2.5 mm² in the 36 L polyester enclosure. The calculation was made for the temperature class T6. The results are listed in Table 3. For the maximum dissipated power method, a rated current I = 21 A and a rated contact resistance per terminal $R_{TB,\,20°C}$ = 7 mΩ was used. This results in a temperature rise of 40 K at 38.7 W for eight installed terminals in a separate enclosure, detached on all sides. Compared to the calculation tool, the temperature increase of 40 K is already reached with 1.2 A less current for the same number of installed terminals. This difference is due to the use of resistance for conductors and terminals at an ambient temperature of 20 °C. With increasing temperature, the resistance decreases (Albach, 2011), which would result in lower power dissipation if a temperature-corrected resistance is used. This effect is already taken into account in the calculation tool. The maximum dissipated power method is not corrected for different installation types. This leads to the fact that with an installation as central enclosure, wall-mounting type with covered top surface a temperature rise of 40 K is reached with 18.7 A according to calculation tool. As both the experimental measurements and the calculation tool have shown, the temperature class T6 cannot be ensured with an applied current I_{max} = 21 A yielded from the maximum dissipated power method.

Table 3: *Maximum dissipated power P and rated current I_{max} for a conductor cross-section of 2.5 mm² in a 36 L polyester enclosure for three different installation types and temperature class T6.*

Method	**Power dissipation *P***	**Rated current I_{max}**	**Number of terminals**
Dissipated Power[1]	38.7 W	21.0 A	8
Calculation Tool[1]	33.4 W	19.8 A	8
Calculation Tool[2]	31.3 W	19.3 A	8
Calculation Tool[3]	28.1 W	18.7 A	8

[1] Separate enclosure, detached on all sides

[2] Central enclosure, wall-mounting type

[3] Central enclosure, wall-mounting type with covered top surface

4. Conclusions

Temperature measurements on junction and connection boxes were carried out for temperature class T6. Four different enclosures, two enclosure materials and five conductor cross-sections were examined. From the results, an exponential dependence of the installed terminals on the maximum current could be derived, from which a calculation tool was developed based on electrical and enclosure-specific parameters. Through further tests, a specific erection factor E could be derived for 12 different installation types of junction and connection boxes. It is shown that the results generated with the calculation tool agree well with the measured values. By applying a safety factor, it can be ensured that exceedances of the permissible temperature rise are excluded. A comparison with the maximum dissipated power method of IEC 60079-7, section 6.8.2 shows that a limit temperature rise of 40 K is already achieved with an at least 6 % lower current. There is therefore a possibility that the temperature class cannot be maintained with the maximum dissipated power method by using the rated current. However, the calculation tool can be used to calculate application-specific data for the fitting chart required by IEC 60079-7 in a very short time. This results in economic advantages in the design and installation of explosion-proof devices. The calculation method is suitable for proving permissible assemblies with current-loaded terminals in junction and connection boxes under the condition of a temperature rise up to 40 K.

Acknowledgements

The authors gratefully acknowledge the technical laboratory assistance of Andreas Piotrowski.

References

Albach, M. (2011). *Elektrotechnik*. First edition. Pearson Education Deutschland GmbH, München

Bendel, R., Fischle, M., Linström, H.-J. (1993). Klemmenanzahl in Abzweig- und Verbindungskästen der Zündschutzart EEx e. *etz*, Bd. 114: 918-920

Bergman, T. L., Lavine, A. S., Incropera, F. P., DeWitt, D.P. (2017). *Fundamentals of Heat and Mass Transfer*. Edition 8. Wiley-VCH Verlag GmbH & Co. KGaA, Weinheim

IEC (2013). *IEC 60079-14:2013 Explosive atmospheres - Part 14: Electrical installations design, selection and erection*. Edition 5.0. IEC Central Office, Geneva.

IEC (2014). *IEC TR 60890:2014 A method of temperature-rise verification of low-voltage switchgear and controlgear assemblies by calculation*. Edition 2.0. IEC Central Office, Geneva.

IEC (2015). *IEC 60079-7:2015-AMD1:2017 Explosive atmospheres - Part 7: Equipment protection by increased safety "e"*. Edition 5.1. IEC Central Office, Geneva.

IEC (2017). *IEC 60079-0:2017 Explosive atmospheres - Part 0: Equipment - General requirements*. Edition 7.0. IEC Central Office, Geneva.

Steen, H., Hattwig, M. (2004). *Handbook of Explosion Prevention and Protection*. First edition. Wiley-VCH Verlag GmbH & Co. KGaA, Weinheim

VDE (2013). *DIN VDE 0298-4:2013-06 Verwendung von Kabeln und isolierten Leitungen für Starkstromanlagen.* VDE Verlag GmbH, Berlin.

Wießner, R. (1993). Erwärmungsprüfungen in Abzweig- und Verbindungskästen. *etz*, Bd. 114: 914-917

DOI: 10.7795/810.20221124

Analysis of flanged joints for flameproof enclosed devices of gas group IIC according to the standard IEC 60079-1

Víctor Hugo Padrón Herrera [a], Jessica Dymke [a], Niels Springer [a], Detlev Markus [a]

[a] Physikalisch-Technische Bundesanstalt, Braunschweig, Germany

E-mail: *victor.h.padron-herrera@ptb.de*

Abstract

Due to the miniaturization of electronic components and circuits, as a result of the ever-advancing innovative optimization process, manufacturers of flameproof enclosures have the necessity to adapt their flameproof enclosures for smaller internal free volumes. The standard IEC 60079-1 for the type of protection Flameproof Enclosure “d” defines several internal free volume groups that go along with constructive requirements for the different types of joints. Nevertheless, the use of flanged joints for group IIC devices is very limited. Under the occurrence of acetylene containing atmospheres, they are only permitted if the internal free volume is $\leq 500\ \text{cm}^3$. However, the requirements are not suitable for enclosures with small internal free volumes.

This paper shows, after a first testing process, the minimum requirements for flameproof flanged joints of a small-internal free volume enclosure with a specific internal geometry. Here tests for non-transmission of an internal ignition and reference pressure tests with an enclosure with approximately $0.09\ \text{cm}^3$ internal free volume are presented. In the end, a deeper understanding of the flame transmission in flanged joints of Group IIC in flameproof enclosed equipment will be achieved.

Keywords: *Small volumes, flameproof enclosure, flanged joint, test for non-transmission of an internal ignition, reference pressure test*

1 Introduction

In recent years, there has been an increase in the use of electronics in explosion-proof areas. They are implemented, among other things, in the type of protection Flameproof Enclosure “d” according to the standard IEC 60079-1 (2014). The components that can trigger the ignition of an explosive combustible-air-mixture are to be installed inside an enclosure that can withstand an internal explosion pressure. Additionally, the gaps of the flameproof enclosures need to be designed and tested in such a way that the transmission of an internal explosion is reliably prevented. Therefore, an essential part of the safety assessment for the certification is the performance of the test for non-transmission of an internal ignition.

The minimum requirements for flameproof joints are categorized according to the gas groups (I, IIA, IIB or IIC), the internal free volume of the flameproof enclosure and the type of joint described in the standard. For gas group IIC flanged joints are allowed under the occurrence of acetylene containing atmospheres only if the internal free volume of the flameproof enclosure is $\leq 500\ \text{cm}^3$. The flanged joints must also comply with a minimum length L of 9.5 mm and a maximum gap i of 0.04 mm. An overpressure test and a test for non-transmission of an internal ignition must be passed for the certification of flameproof enclosures.

In the upcoming new edition of the standard IEC 60079-1 (Ed. 8) it will be established, however, that if a flameproof enclosure has an internal free volume of less than or equal to 10 cm^3, the minimum requirements for flameproof joints established in the standard do not apply. This means that for internal free volumes ≤ 10 cm^3, all types of flameproof joints are allowed, as long as the test for non-transmission of an internal ignition is passed successfully. The new standard IEC 60079-1 gives instructions for the construction of flameproof joints for enclosures with internal free volumes between 10 cm^3 and 2000 cm^3 for the gas group IIC, but no information or any guidelines for the construction of flameproof joints of enclosures with small internal free volumes. As many factors can affect the flame transmission, there is a need to test and evaluate various test samples with different internal free volumes, geometries and materials, in order to establish more precise information about the minimum requirements for flanged joints.

Therefore, in this work a series of tests for non-transmission of an internal ignition were carried out in an enclosure with an internal free volume of approximately 0.09 cm^3, a specific internal geometry, and a flanged joint. A systematic variation of the joint length and enlargement of the gap is essential to define the minimum requirements to avoid a flame transmission of the internal ignition to the outside of the enclosure. The aim is to enable statements to be made on the minimum constructive requirements for the design of flameproof enclosures with a small-internal free volume.

2 Background

A flameproof joint is made by the combination of two or more parts of the flameproof enclosure. Due to the simplicity of construction with respect to other more elaborate flameproof joints described in the standard IEC 60079-1, flanged joints are, in many cases, the easiest solution for the design and construction of flameproof enclosures. It is also one of the easiest joints to measure as you can survey the limits of the flameproof gap at every point of the joint.

The product certification process can be very difficult and costly for manufacturers, as they must ensure that all their products comply with the dimensions given in the technical documents. These challenges can be lessened when flanged joints are used instead of other types of joints established in the standard. However, because flanged joints represent a direct and free-flowing path for the flame to travel from the inside to the outside of the enclosure, this type of joint is very restricted in the standard.

The historical reason, why flanged joints are not widely allowed for the gas group IIC, is unclear. A possible reason is a difference in the kinetic energy of the different combustible-air-mixtures. The gases under group IIC have, in comparison to the gases of the other gas groups, a higher burning velocity and an easy ignitability of the explosive mixture (Steen, 2004). The generated pressure by explosion with gases under the group IIC can push the parts of the enclosure (e.g. enclosure and cover), thus opening the joints of the enclosure beyond the limits for a safe gap and compromising the safety of the flameproof enclosure. Due to their construction, flanged joints can be critical for gas group IIC.

The MESG (Minimum Experimental Safe Gap) data gives information about the flame transmission of different explosive combustible-air mixtures inside of an enclosure with spherical internal geometry and a flanged joint. The MESG for the gases under the gas group IIC is considerably lower in comparison to the explosive gases under the gas groups I, IIB and IIA (Redeker, 1981). For this reason, acetylene and hydrogen are classified under the gas group IIC.

The following Table 1 shows the different explosive gases for each gas group:

Gas group	Example of gas	MESG
I	Special group: Methane	
IIA	Propane	0.9 mm < MESG
IIB	Ethylene	0.5 mm < MESG < 0.9 mm
IIC	Acetylene, Hydrogen	MESG ≤ 0.5 mm

***Table 1:** Gas groups and their MESG (Steen, 2004)*

One of the tests relevant for the certification of flameproof enclosures is the performance of the reference pressure test or maximum explosion pressure test. The aim of this test is to generate the maximum explosion pressure possible inside of the flameproof enclosure in order to test via an overpressure test, the mechanical strength of the enclosure materials and the integrity of the flameproof joints. The required concentration of the explosive gas in a volumetric ratio with air for gas group IIC here is 31 ± 1 vol% for hydrogen, and 14 ± 1 vol% for acetylene.

With the aid of the test for non-transmission of an internal ignition we can verify if a joint of the flameproof enclosure can prevent an ignition of the combustible-air-mixture outside of the enclosure. For this test, following IEC 60079-1, the test sample is properly prepared and placed inside of a confinement area (e.g. explosion proof vessel). The given combustible-air-mixture with the exact volume concentration according to the standard is then introduced homogeneously inside and outside of the test sample. The test shall be made five times with each mixture of the intended gas group. The test is considered satisfactory if the internal ignition is not transmitted to the outside of the enclosure. The required concentration of the explosive gas in a volumetric ratio with air given by the standard for the test for non-transmission of an internal ignition is 27.5 ± 1.5 vol% hydrogen, and 7.5 ± 1 vol% acetylene for the gas group IIC.

3 Experimental setup

To perform the tests for reference pressure and non-transmission of an internal ignition, the test object needs to be in a confinement area in order to have a homogeneous and constant combustible-air-mixture outside as well as inside of the test sample. In this case an explosion-proof vessel was used. The combustible-air-mixture concentration according to the standard is pre-mixed and stored in a pre-mixture chamber connected to the inlet of the explosion-proof vessel by a valve. The concentration of the test mixture is controlled by an oxygen analyser (Servomex) at the outlet of the explosion-proof vessel.

In order to ensure a homogeneous combustible-air-mixture inside of the explosion-proof vessel and test sample, the experimental setup was connected to a vacuum pump. After applying vacuum to the system, the prepared test mixture can flow inside the vessel by opening the valve. The combustible-air-mixture then passed through all possible gaps or in the case of the reference pressure test, through the capillary into the free inner volume of the test sample due to the pressure difference between the pre-mixture chamber and the vessel.

The pressure measurements were captured with the piezo electric pressure sensor *type 601CAA*. A silicon layer was applied onto the sensor membrane to avoid a possible thermal shock effect (Krause, 2021). The piezoelectric pressure sensor generates a charge signal proportional to the pressure. The signal of the pressure sensor is converted into an electric voltage signal by an amplifier, which is then recorded by an oscilloscope. A low-pass filter with a 3 dB point of 5 kHz ± 0.5 kHz was used as required in the standard. The schematic experimental setup is shown in Fig. 1.

DOI: 10.7795/810.20221124

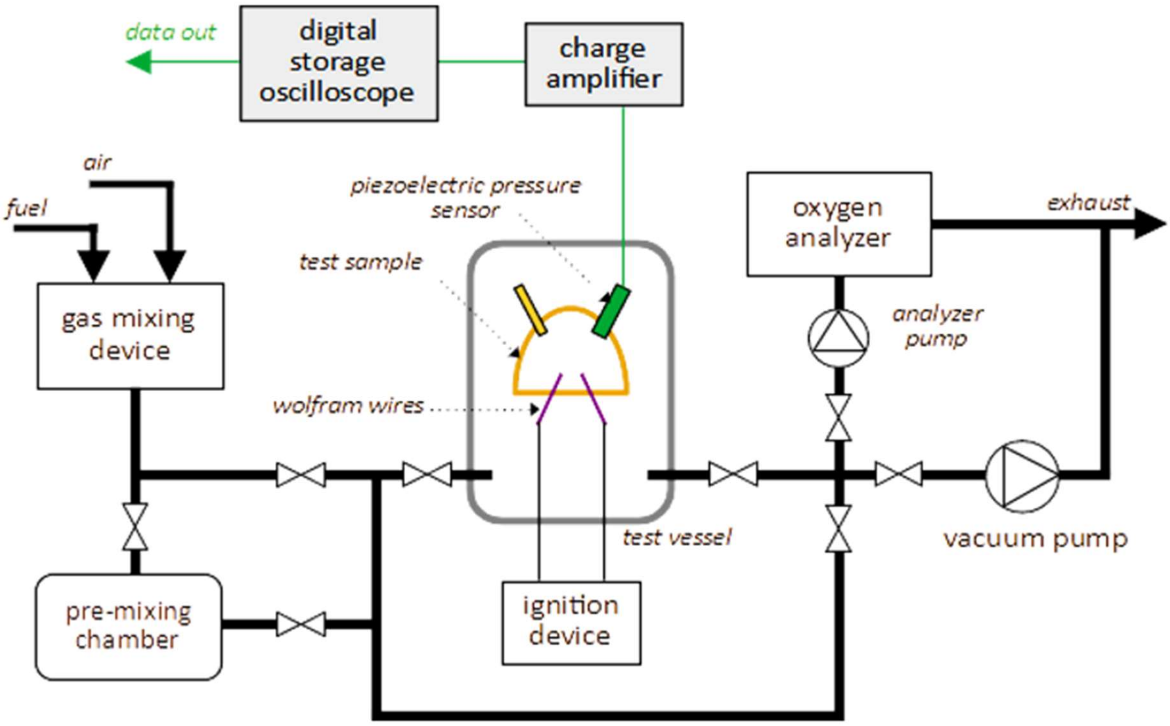

***Fig. 1** Experimental setup for the explosion test*

The vacuum method also saves the use of a gas inlet and outlet on the test sample in order to introduce the combustible-air-mixture and to avoid the addition of extra internal free volume to the sample thus altering considerably the measurements. Nevertheless, a capillary tube is used to ensure a homogeneous and constant explosive combustible-air-mixture in the test sample. This plays an important role for the maximum explosion pressure test, due to the tightness of the parts of the test sample. For the test for non-transmission of an internal ignition, the test mixture flows inside of the test sample without the aid of the capillary tube due to the enlargement of the test gap. Therefore, the opening M3 intended for the capillary tube can be sealed with a screw M3 for this test.

The detection of a flame transmission can be established by a visual detection through the windows of the explosion-proof vessel or by the acoustic sound when the explosive combustible-air-mixture outside of the test sample ignites. A flame transmission also can be detected by analysing the information of the pressure curves given by the sensor.

The test sample consists of a bottom and an upper part (Fig. 2). Between these two parts, a flanged joint is formed. The internal geometry of the test sample shapes a half sphere of approximately 0.09 cm^3 internal free volume representing an encapsulated LED flameproof enclosure with a small-internal free volume so that the test sample represents a real-life example.

The upper part of the test sample was made of two different materials in order to investigate the influence of different materials on the flame transmission such as thermal dissipation, roughness and mechanical strength. An upper part was made of metal (brass) as seen in Fig. 2 and the other one made out of a non-metallic material (PMMA - polymethylmethacrylat). The bottom part of the test sample was made of PVC - polyvinyl chloride (red part).

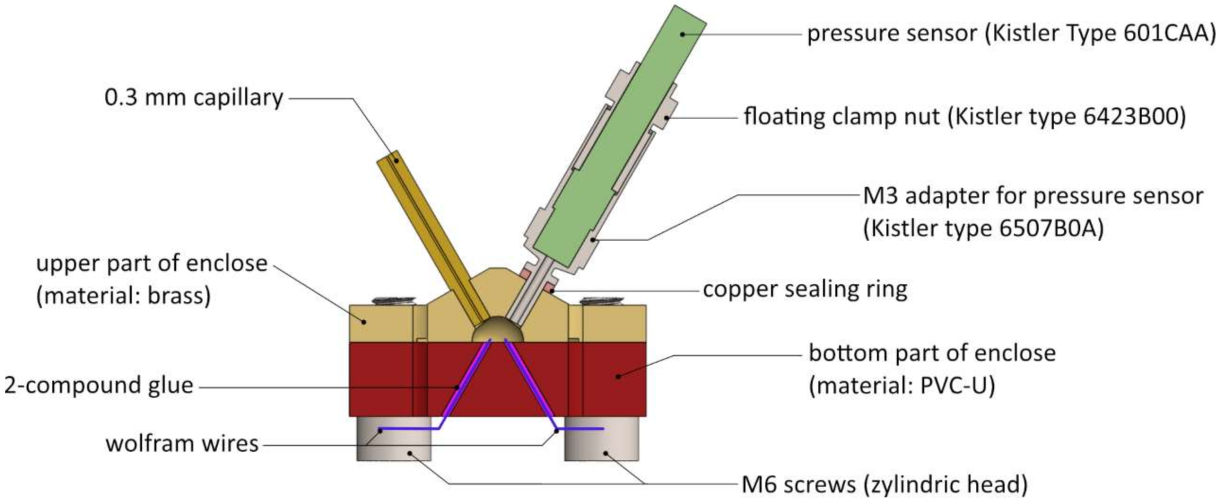

Fig. 2 *Test sample with brass upper part and no enlargement of the test gap (for reference pressure tests)*

The ignition inside of the test sample occurred via an electric spark. The electric spark takes place between two wolfram wires. The ignition source is located inside of the test sample. This configuration also gives a uniform distance from the ignition source to the beginning of the flanged joint from the inside of the test sample. There are two connection holes M3 on the upper part of the test sample. One connection hole was made for the capillary tube (M3) and the other one for the pressure sensor *type 601CAA* (M7). A reduction adapter was used, due to the size of the head of the pressure sensor for the small-internal free volume. An adapter *type 6423B00* from the company *Kistler* with a reduction from M7 to M3 was used to minimize an alteration of the internal geometry of the test sample. Acoustic resonances can take place through the use of the reduction adapter for the pressure sensor due to its construction and addition of free volume (Gosweiller, 2006) and were taken into consideration for this work.

To establish the limits for the constructive dimension of a flanged joint of an enclosure to prevent a flame transmission, a systematic enlargement of the gap and a variation of the flanged joint length was established for each test sequence. The length of the flanged joint can be adjusted by using a different bottom part of the test sample. By changing the bottom part, a different flanged joint length is formed when united with the upper part. The selected values of the flanged joint length for this first phase are 6 mm, 4 mm, and the shortest, 2 mm. The increase of the test gap is created by placing plates of a certain thickness between the bottom and upper part (Fig. 3).

DOI: 10.7795/810.20221124

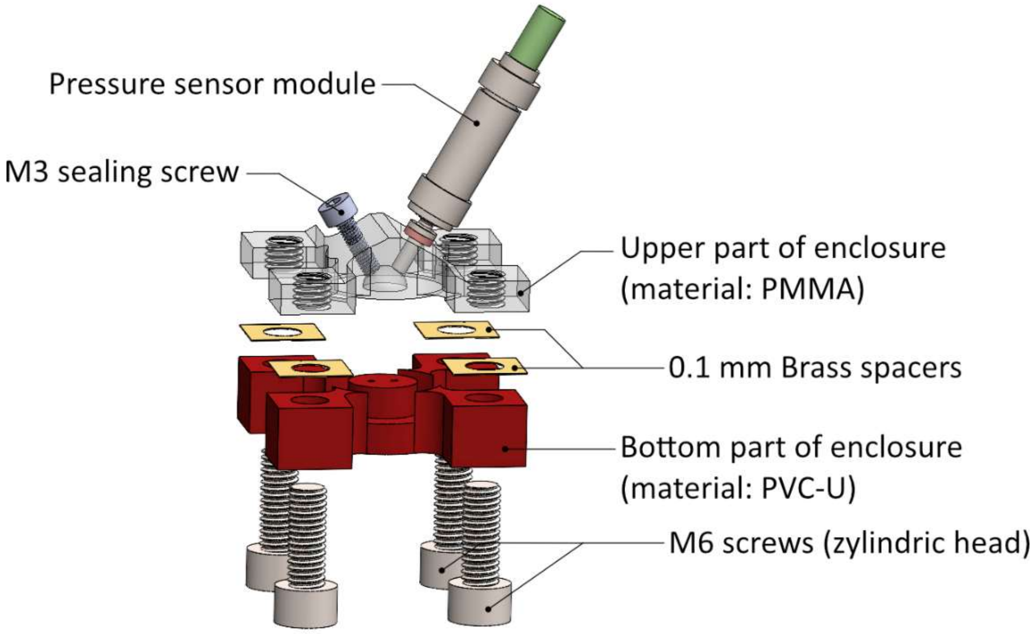

***Fig. 3** Test sample with the PMMA upper part and 2 mm bottom part length (for flame transmission test)*

The surface roughness of both sides of the enclosure (upper and bottom part) that form the flanged joint were measured in order to verify any correlation between the state of the surface of the flanged joint and the flame transmission (see Table 2). From the following measurements we can verify that the gap surface of the upper part made from PMMA is slightly smoother than the surface of the upper part made out of brass.

Test sample part		Roughness depth (Rz) in µm	Arithmetic average roughness value (Ra) in µm
	Gap length in mm		
Bottom part	6	3.95	0.730
	4	5.35	0.805
	2	7.00	0.515
Upper part	Material	Roughness depth (Rz) in µm	Arithmetic average roughness value (Ra) in µm
	Brass	1.70	0.195
	PMMA	1.05	0.060

***Table 2:** Roughness depth and arithmetic average roughness value of the test sample parts*

Additionally, an experimental Schlieren setup with a high-speed camera was added to the explosion tests installation in order to have a visual display of a flame transmission.

DOI: 10.7795/810.20221124

4 Results

The maximum explosion pressure tests were performed with no enlargement of the test gap of the test sample but at different lengths of the flanged joint. The tests were done with no pre-compression of the initial pressure (1.013 bar) and at ambient temperature (T ≈ 20 – 25 °C). The test mixture concentration used for the tests was 31 ± 1 vol% hydrogen. The following Fig. 4 shows the maximum explosion pressure curves as overpressure for each of the different test configurations. Only one pressure curve of the five performed tests was displayed due to the minor deviation of the pressure curves of the same configuration. At the moment of ignition (approximately $t = 7.5$ ms) a rapid pressure rise can be detected. The maximum peak of the pressure curves gives the maximum pressures relative to atmospheric pressure. After the maximum explosion pressure is achieved, the pressure inside of the test sample drops considerably. Due to the thermal shock effect, the pressure curve drops quickly to the negative area of pressure before stabilizing back to an overpressure of 0 bar. The height of the determined pressure peak is not influenced by the thermal shock effect due to the silicon layer applied onto the sensor membrane (Krause, 2021). The reference pressure tests were performed with the two different materials of the upper part of the test sample whereby the pressure curves were identical within the scope of the measurement accuracy.

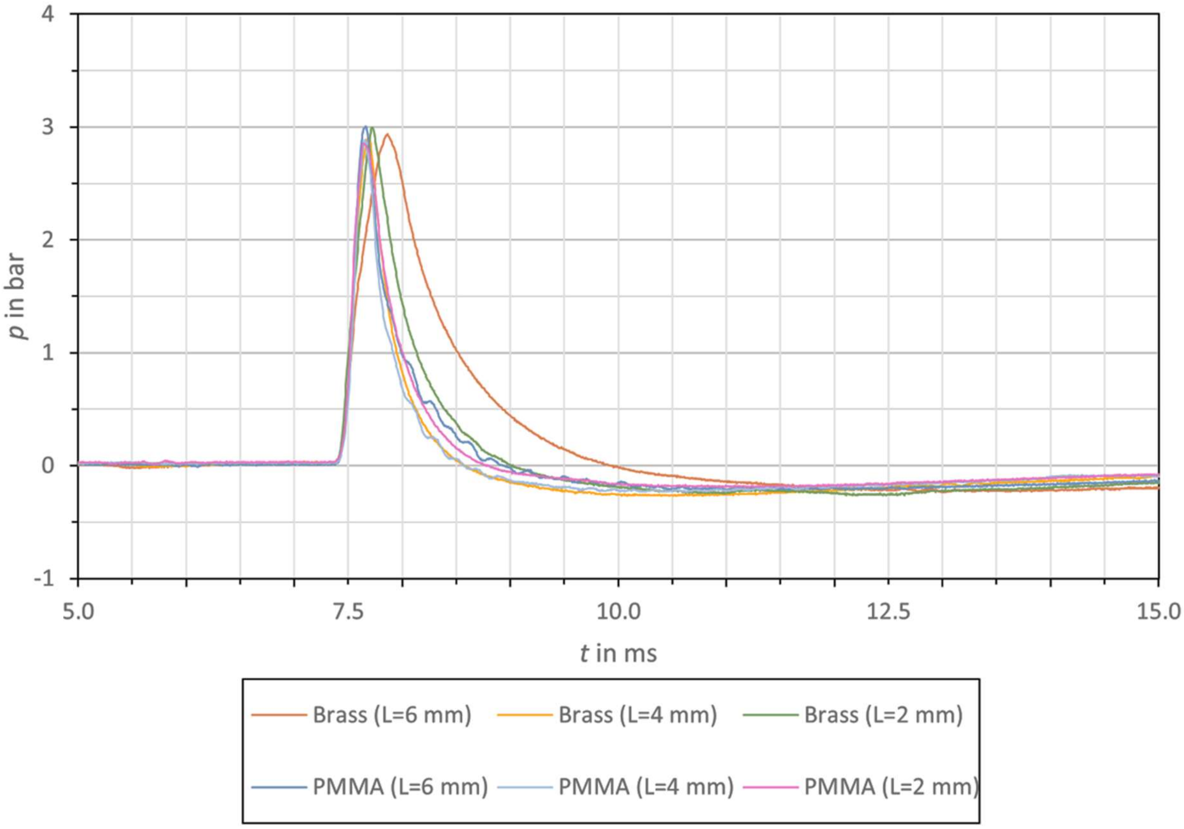

Fig. 4 *Pressure curves of the reference pressure test with different upper part materials of the test sample (gap length 6 mm and no enlargement of the test gap)*

For the tests for non-transmission of an internal ignition, a systematic enlargement of the test sample gap by 0.1 mm and a variation of the flanged joint length from 6 mm, 4 mm, and 2 mm was established for each test sequence of five tests. The same test configuration was performed with the two different materials of the upper part of the test sample to analyse any influence of different materials on the flame transmission. Each time a flame transmission occurred, the result was considered as failed and the used test configuration is considered as not safe. The tests for non-transmission of an internal ignition were performed with 27.5 ± 1.5 vol%

hydrogen combustible-air-mixture, no pre-compression of the initial pressure (1.013 bar) and at ambient temperature (T ≈ 20 – 25 °C).

Fig. 5 shows the minimum safe gap S_{min} as a function of the length of the flanged joint. The orange line represents the minimum safe gap S_{min} for the test sample with brass upper part and the blue line for the test sample with PMMA.

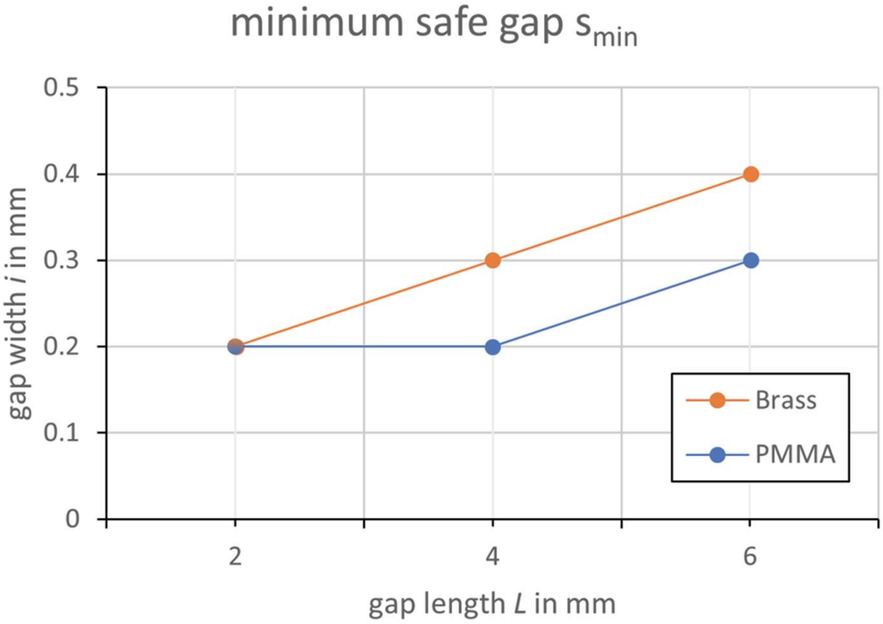

Fig. 5 *Minimum safe gap width yielded from tests for non-transmission of an internal ignition with different upper part materials of the test sample*

The results of Fig. 5 show a larger minimum safe gap width S_{min} compared to the MESG of hydrogen (0.29 mm) (Brandes, 2008), despite the fact we have used a much shorter flanged gap length compared to the MESG apparatus. As was shown by Redeker (1981), the value of the minimum safe gap increases with reducing inner volume. Due to the small-internal free volume, no significant pressure rise is generated inside of the test sample. The flame transmission is less effective at slower outflow velocities and therefore a larger safe gap than the MESG values can be enough to avoid a flame transmission, even using a gap length of only 6 mm. The smaller the internal free volume, the less critical the transmission of an internal ignition.

As can be seen in Fig. 6 the pressure inside the enclosure reduces significantly with increasing gap width. However, if a flame transmission occurs the pressure will rise due to the external explosion also inside the enclosure as shown in Fig. 7.

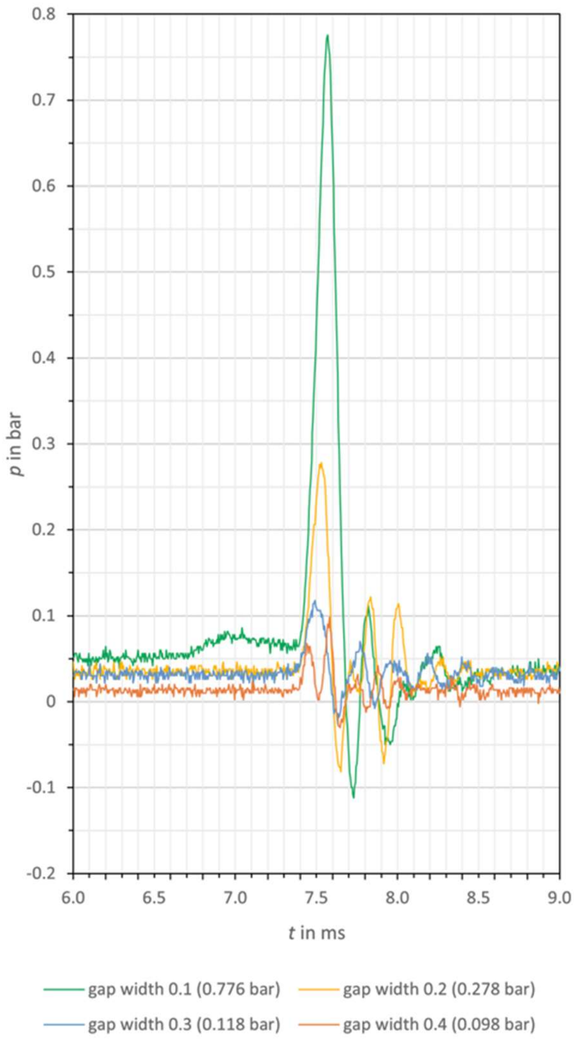

Fig. 6 *Pressure curves as a function of gap width without flame transmission (test sample with brass upper part and gap length 6 mm)*

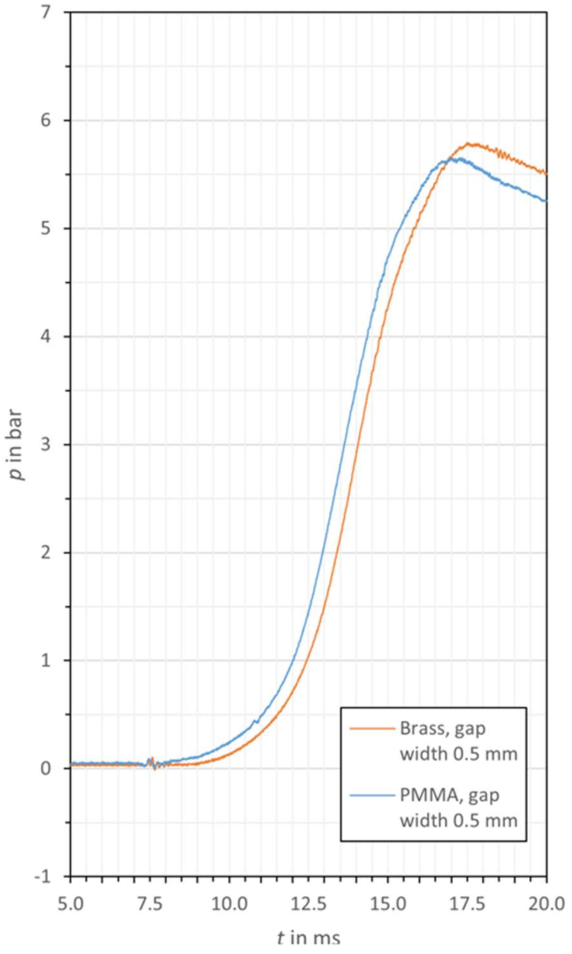

Fig. 7 *Pressure curves at the occurrence of a flame transmission*

With the help of the experimental Schlieren setup, the flame transmission can be analysed using a high-speed camera. The explosion-proof vessel is equipped with windows for optical access. The test sample was placed 90° in the direction of the camera in order to have a clear picture of the flow of hot gases from a flame transmission. Fig. 8 displays a temporal evolution of a flame transmission after an internal ignition using the test sample with brass upper part and the 6 mm bottom part and with a gap width of 0.5 mm. The test was performed with 27.5 ± 1.5 vol% hydrogen in air.

Fig. 9 shows the pressure curve during the flame transmission test and the point in time of the single images shown in Fig. 8. The first image represents the time of ignition *tz*. The ignition can be observed in the pressure curve as the first recorded pressure signal. After 0.166 ms (I) the first flow of hot gases coming out of the test sample (red circle) can be detected. The next image (II) shows how the hot flame passes through the sides of the test sample. As the time progresses, turbulence can be observed spreading around the test sample and the combustion propagates through the entire explosive test mixture inside the explosion-proof vessel.

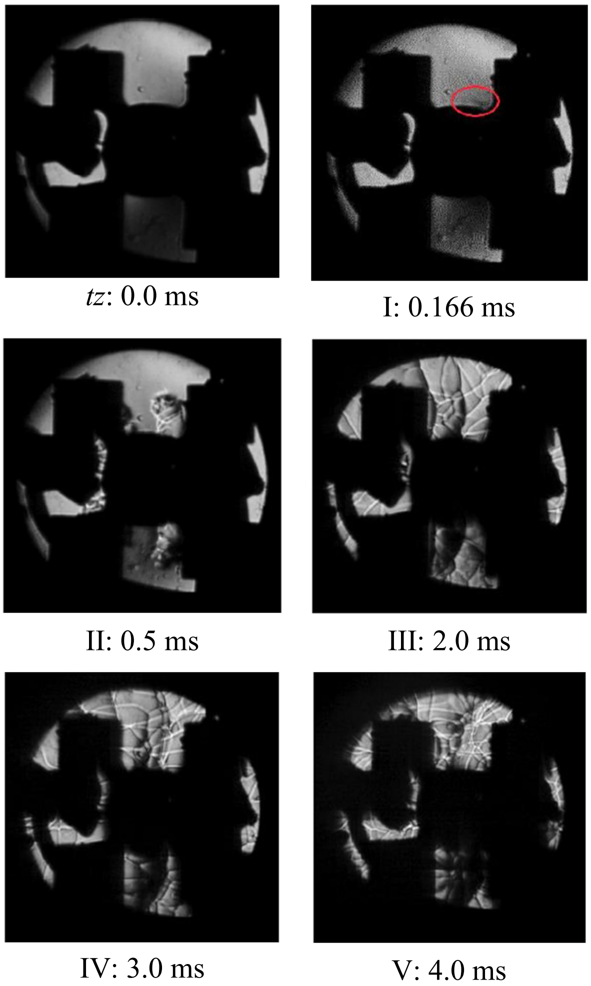

tz: 0.0 ms   I: 0.166 ms

II: 0.5 ms   III: 2.0 ms

IV: 3.0 ms   V: 4.0 ms

Fig. 8 *Schlieren photographs (real size of pictures approximately 70 mm x 70 mm)*

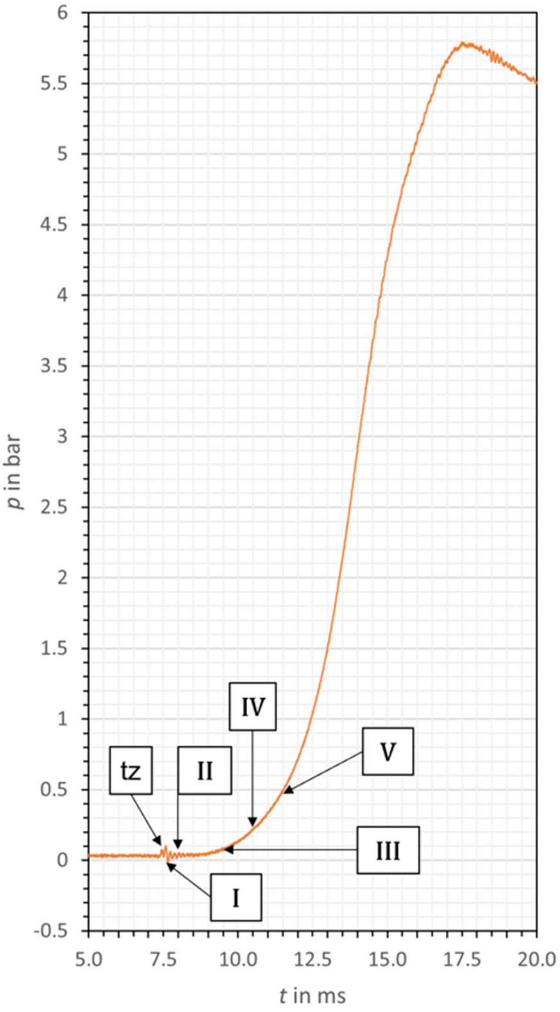

Fig. 9 *Pressure curve associated with Schlieren photographs*

5 Conclusions

The results of the reference pressure test or maximum explosion pressure test show no significant difference between the results with the two different upper part materials. Also, the variation of the gap length has no noticeable influence on the explosion pressure. According to the first results for non-transmission of an internal ignition, a slight difference can be noticed with the different brass and PMMA upper parts of the test sample. Nevertheless, there is no statistically significant value after performing only five tests for each test configuration and no statement can be established at this point.

The major outcome is the evidence that for small-internal free volume enclosures, the test for non-transmission of an internal ignition is sufficient to evaluate the safety of the flanged joints. The examined configuration shows clearly that the combination of small-internal volume and large gap opening results in safe gap widths significantly larger than the MESG. Due to the fact that there is no significant pressure rise inside the enclosure, only slow outflow velocities can occur. Therefore, cooling inside the gap is efficient here at avoiding a flame transmission. With the help of the Schlieren recordings and the pressure curves we can analyze visually the exact moment of the different stages of a flame transmission. The flame transmission does not occur uniformly throughout the entire flanged joint of the test sample but rather in specific areas of the joint, spreading rapidly throughout all sides of the test sample, igniting the outer explosive combustible-air-mixture.

Further tests shall be performed with hydrogen and a pre-compression of the initial pressure in order to simulate lower ambient temperatures. Also, further tests shall be performed with the explosive gas acetylene (with and without a pre-compression of the initial pressure) in order to cover all the explosive gases of the gas group IIC.

Acknowledgements

The tests were performed in the Ex-test laboratory at the PTB. The authors would like to thank Mr. Michael Paul, Mr. Fabian Reitmeier, Mr. Marc Shields and the working group 3.53 of PTB for their support.

References

IEC 60079-1 (2014). *Explosive Atmospheres - Part 1: Equipment Protection By Flame Proof Enclosures "d".*

Redeker, T. (1981). Certification of Flammable Gases and Vapours by the Flameproof Safe Gap and the Incendivity of Electrical Sparks, Physikalisch-Technische Bundesanstalt Report W-18.

Brandes, E., Möller, W. (2008), Safety characteristic data – Volume 1: flammable liquids and gases, 2nd ed., Wirtschaftsverlag NW, Bremerhaven.

Gosweiller, C., Willson, B., Walter, T. (2006). Application of an Improved Model for the Determination of Acoustic Resonances in Indicator Passages for Combustion Pressure Measurements, in: ASME 2006 Internal Combustion Engine Division Spring Technical Conference (ICES2006), 769–779.

Krause, T., Meier, M., Brunzendorf, J. (2021). Influence of thermal shock of piezoelectric pressure sensors on the measurement of explosion pressures, Journal of Loss Prevention in the Process Industry, 71:104523.

Steen, H. (2004). Handbook of Explosion Prevention and Protection, Wiley-VCH, Weinheim.

DOI: 10.7795/810.20221124

An experimental and a numerical study of a vented dust explosion in an 11.5 m^3 vessel

Chen Huang [a], Marius Bloching [b] & Andrei N. Lipatnikov [c]

[a] RISE Research Institutes of Sweden, Division Safety and Transport, Fire and Safety Department, Gothenburg, Sweden

[b] IND EX® - Intercontinental Association of Experts for Industrial Explosion Protection, Frankfurt am Main, Germany

[c] Chalmers University of Technology, Department of Mechanics and Maritime Sciences, Gothenburg, Sweden.

E-mail: *chen.huang@ri.se*

Abstract

A vented corn starch dust explosion in an 11.5 m^3 vessel is studied by comparing a dust explosion model with experiments. Unsteady three-dimensional Reynolds-Averaged Navier-Stokes simulations are performed using the Flame Speed Closure (FSC) model and its extended version. The FSC model predicts the influence of turbulence on premixed combustion, and the extended version allows for self-acceleration of a large-scale flame kernel, which is associated with the combustion-induced thermal expansion effect. Such an extension is highly relevant to large-scale industrial application. The explosion overpressure-time traces computed using the extended FSC model and both k-omega-SST and realizable k-epsilon turbulence models agree reasonably well with the experimental data using different initial rms turbulence velocities. It is recommended to have relative fine grid inside the vessel and on the vent opening wall together with a Courant number of 0.1 for the current case according to sensitivity studies. The developed code and model appear to be promising and deserve further study in research into large-scales dust or gaseous explosions.

Keywords: *corn starch, dust, vented explosion, experiments, Computational Fluid Dynamics, turbulent combustion, flame self-acceleration, open source, OpenFOAM, sensitivity study.*

1. Introduction

The three questions were asked in a pioneering German book of dust explosions in 1925 (Beyersdorfer, 1925). The first question, asked by common people, was "*Do dust explosions really exist?*". The second question, asked by the plant engineer, was "*Why are we having so many?*". The third question, asked by the researcher, was "*How do we not have more?*". These three questions were asked again in Rolf Eckhoff's book on dust explosions in the process industries first published in 1991 (Eckhoff, 2003). These three questions are still being asked today. In the role of a researcher, to answer the third question "*How do we not have more?*", we believe that one of the important solutions is to have access to physics-based, well-verified, well-validated, and efficient numerical models and tools. Specifically, the numerical tools can be used to quantitatively predict the consequences of dust explosions for the process plants where the current regulations and standards are not applicable.

The advanced Computational Fluid Dynamics (CFD)-based numerical code is one of the most promising solutions to the complex and challenging reality in the process industries (Eckhoff, 2015). Dust explosions were commonly simulated using the FLACS-DustEx code. This code was applied to large-scale industrial dust explosions with a focus on the overall explosion consequence, i.e., the maximum reduced explosion overpressures (Skjold et al., 2005; 2006; Skjold, 2007, 2014a). At the same time, there is still room for improvement of the FLACS-DustEx as discussed in detail elsewhere

(Skjold, 2014b). Apart from the FLACS-DustEx code, researchers also used other CFD tools for simulating dust dispersions and explosions (Li et al., 2020; Pico et al., 2020).

The present paper reports a part of results from a research project aiming at development of physics-based models and numerical tools for simulating dust explosions. The developed approach is based on an analogy between dust explosions and premixed turbulent flames. Accordingly, to simulate dust explosion, a model of the influence of turbulence on premixed combustion is adapted in the present work. More specifically, the so-called Flame Speed Closure (FSC) model (Lipatnikov and Chomiak, 1997; 2002) is used. In the preceding studies (Huang et al., 2020; 2022), (i) the FSC model was implemented into the OpenFOAM code, (ii) the implementation was verified using benchmark analytical solutions, (iii) the FSC model and the code were validated against experimental data on corn starch dust explosions obtained in a small-scale fan-stirred vessel (Bradley et al., 1989), and (iv) the FSC model was extended and computed results were compared with experimental data obtained from a large-scale vented dust explosion. The present paper reports new results computed by applying the model and code to the same experiments with additional sensitivity studies on the model and code. The code is available to the public (Huang and Lipatnikov, 2021).

The paper is organized as follows. Experimental and numerical method and setup are described in Sections 2 and 3, respectively. Results and discussions are presented in Section 4 followed by conclusions.

2. Experimental method and setup

An 11.5 m³ vessel at the REMBE® Research + Technology Center in Brilon, Germany was used to perform the vented corn starch dust explosions. The corn starch dust is characterized by a K_{St} value of 220 bar·m/s ± 15 % with a median diameter D_{50} of 97 µm and a moisture content of 9.87%. The calculated and applied vent area was set to 0.5 m² in a circular shape. The vent opening was closed with a layer of 70 µm low mass aluminium foil with a static activation pressure (p_{stat}) of 0.1 ± 15 %.

To create an explosive atmosphere inside the vessel, two pressurized dust containers were used for blowing the dust into the test vessel. A dust concentration of 750 g/m³ was chosen. An ignition delay of 800 ms was selected via multiple tests to achieve the required K_{St}-value with the above dust concentration.

The resulting explosive atmosphere was ignited using a pair of pyro-technique igniters with a total ignition energy of 10 kJ in the center of the test vessel. Two pressure detectors P1 and P2 were installed to measure the reduced maximum explosion overpressures (p_{red}) inside the vessel (see Figure 1). The data was recorded using an oscilloscope (Tektronix TDS 2014C). A snapshot of the vented corn starch dust explosion is shown in Figure 2.

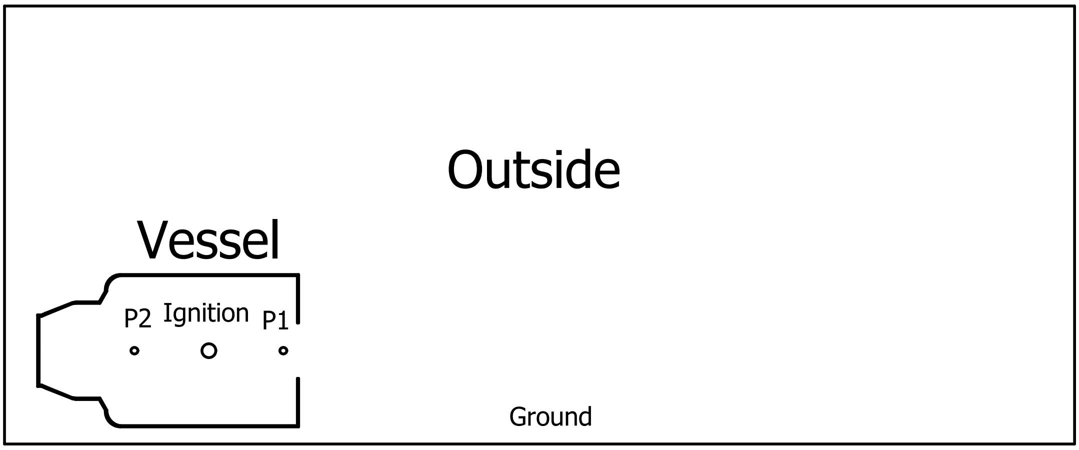

Fig. 1. *Illustration of the 11.5 m^3 explosion vessel and the computational domain.*

Fig. 2. *A snapshot of the vented corn starch dust explosion in the 11.5 m³ vessel with a circular vent opening.*

3. Numerical method and setup

In this section, the used combustion model, the input data for the simulation, and the numerical method are briefly discussed.

3.1 FSC turbulent combustion model

The FSC model (Lipatnikov and Chomiak, 1997; 2002) deals with the following transport equation

$$\frac{\partial \bar{\rho}\tilde{c}}{\partial t} + \nabla\cdot(\bar{\rho}\tilde{\mathbf{u}}\tilde{c}) = \nabla\cdot[\bar{\rho}(\kappa + D_t)\nabla\tilde{c}] + \rho_u U_t|\nabla\tilde{c}| + \frac{\bar{\rho}(1-\tilde{c})}{t_r(1+D_t/\kappa_b)}\exp\left(-\frac{\Theta}{\tilde{T}}\right) \quad (1)$$

for the Favre-averaged combustion progress variable $\tilde{c}$. Here, t is the time; $\mathbf{u}$ is the flow velocity vector; κ is the molecular heat diffusivity of the mixture; the Favre-averaged temperature $\tilde{T}$ is evaluated using the simplest form $\bar{\rho}\tilde{T} = \rho_u T_u$ of the ideal gas state equation; Θ is the activation temperature for a single reaction that the combustion chemistry is reduced to ($\Theta = 20000$ K in the present work); over-lines designate the Reynolds average, while $\tilde{q} = \overline{\rho q}/\bar{\rho}$ is the Favre-averaged value of q with $q" = q - \tilde{q}$; subscripts u and b designate unburned and burned gas, respectively; t_r is the reaction time scale, which is calculated following (Huang et al., 2016).

The turbulent diffusivity D_t and burning velocity U_t are closed as follows (Lipatnikov and Chomiak, 1997)

$$D_t = D_{t,\infty}\underbrace{\left[1-\exp\left(-\frac{t_{fd}}{\tau_L}\right)\right]}_{T_D}, \quad (2)$$

$$U_t = U_{t,ISP}\underbrace{\left[1-\frac{\tau_L}{t_{fd}}+\frac{\tau_L}{t_{fd}}\exp\left(-\frac{t_{fd}}{\tau_L}\right)\right]^{1/2}}_{T_1}\underbrace{\left(\frac{t}{t_{flacc}}\right)^{1/2}}_{T_2}. \quad (3)$$

In Eq. (2), t_{fd} is the flame development time counted starting from ignition; $D_{t,\infty}$ is the fully developed turbulent diffusivity given by a turbulence model; the time-dependent term T_D stems from the Taylor theory of turbulent diffusion, e.g., see section 14-4.F in a textbook by Brodkey (1967); $\tau_L = D_{t,\infty}/u'^2$ is the Lagrangian time scale of turbulence. In Eq. (3),

$$U_{t,ISP} = Au'Da^{1/4}, \quad (4)$$

is an intermediately steady turbulent burning velocity derived theoretically by Zimont (1979; 2000), where $Da = \tau_t/\tau_f$ is the Damköhler number; $\tau_t = L/u'$ and L are turbulent time and length scales, respectively; $\tau_f = \delta_L/S_L$ and $\delta_L = \kappa_u/S_L$ are the laminar flame time scale and thickness, respectively; A=0.4 (Lipatnikov and Chomiak, 1997; 2002) is the sole constant of the original FSC model. The time-dependent term T_1 belongs to that model and has been derived (Lipatnikov and Chomiak, 1997) by subsituting $D_{t,\infty}$ with D_t in the aforementioned Zimont model, i.e., T_1 is based on the term T_D, as discussed in detail elsewhere (Lipatnikov and Chomiak, 1997; 2002; Lipatnikov, 2012). The term T_2 has been added to the FSC model based on a study by Gostintsev et al. (1988) who discovered a self-similar regime of flame kernel growth by analysing large-scale gaseous flames. In this work, the timing t_{flacc} for activating the flame acceleration mechanism in simulations is tuned to get a reasonable maximum reduced explosion overpressure as compared to the experiments.

The interested reader is referred to papers (Lipatnikov and Chomiak, 1997; 2002; Lipatnikov, 2012; 2018; Huang et al., 2020; 2022) for more detail information on the extended FSC model.

3.2 Thermophysical properties of corn starch dust

Thermophysical properties are required to calculate the combustion and heat transfer process in a dust explosion. They include the chemical formula, heat of reaction, standard heat of formation, specific heat capacity, and adiabatic flame temperature. The chemical formula of $C_6H_{7.88}O_{4.98}$ and the heat of reaction $\Delta H_{reaction}$=2 521 kJ/mol for corn starch are taken from Bradley et al. (1989), whereas the specific heat capacity is taken from Tan et al. (2004). Accordingly, the absolute enthalpy H_a [J/kg] is evaluated using the following NIST-JANAF polynomial equation

$$H_{a,cs} = R_{spec,cs}\left(\frac{a_{4,cs}}{5}T^5 + \frac{a_{3,cs}}{4}T^4 + \frac{a_{2,cs}}{3}T^3 + \frac{a_{1,cs}}{2}T^2 + a_{0,cs}T + a_{5,cs}\right). \tag{5}$$

Here, $R_{spec,cs}$ is the specific gas constant for corn starch measured in J/(kg·K); $a_{0,cs}$, $a_{1,cs}$, $a_{2,cs}$, $a_{3,cs}$, $a_{4,cs}$ and $a_{5,cs}$ are the JANAF coefficients of corn starch. A summary of the thermophysical properties of corn starch dust is shown in Table 1.

Table 1. *Summary of thermophysical properties of corn starch dust.*

Name	Symbol	Value
Chemical formular	$C_6H_{7.88}O_{4.98}$	-
Molecular weight	W_{cs}	0.16 kg/mol
Standard heat of formation	$H^{\Theta}_{f,cs}$	-792.6 kJ/mol
JANAF coefficients	$a_{0,cs}$	-3.2726
	$a_{1,cs}$	0.10056
	$a_{2,cs}$, $a_{3,cs}$, $a_{4,cs}$	0
	$a_{5,cs}$	-9 9808

3.3 The laminar burning velocity of corn starch dust

Contrary to gaseous flames, available data on the laminar burning velocities for corn starch dust is limited and controversial. In the present study, the laminar burning velocity S_L measured by Dahoe et al. (2002) is used, and the data is fitted using Gülder's correlation (Gülder, 1984) (see Figure 3) as follows

$$S_L = W\phi^{\eta}e^{-\xi(\phi-\sigma)^2}, \tag{6}$$

Here, the coefficients $W = 0.2145$ m/s, $\eta = -0.2774$, $\xi = 39.1832$, $\sigma = 0.6$ for corn starch dust. Note that the corrected equivalence ratio includes only the dust which participated in the explosion. The dust concentration is converted to a corrected equivalence ratio using data on burnt mass fraction reported by Skjold et al. (2005; 2006).

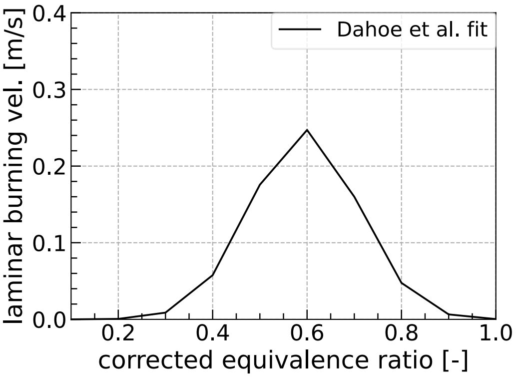

Fig. 3. *Laminar burning velocity measured by Dahoe et al. (2002), and fitted using Gülder's correlation versus corrected equivalence ratio.*

3.4 Numerical setup

The vented corn starch dust explosion was simulated in two stages. First, the dust explosion was simulated in a closed vessel. When the computed overpressure in the vessel reached a critical value of 0.1 bar (recall that, in the experiments, the vent panel ruptured at a static activation pressure p_{stat} equal to 0.1 bar ± 15%), the simulation was stopped, and the results were saved. These computed results were then mapped to a new computational mesh created for a larger computational domain to simulate the venting process. The computational mesh covering the closed vessel (see the vessel part in Figure 1) has a mesh number of 1.4 million and a mesh size of 6.25 – 25 mm; the computational mesh covering the whole domain (see Figure 1) has a mesh number of 2.4 million and a mesh size of 12.5 – 100 mm. Note that only half of the physical domain was simulated to save computational time by taking advantage of symmetry on a vertical plane with respect to the ground cutting through the centre of the vessel and along the length of the vessel. The computational domain size is 15.5 ×5×6.355 m. One simulation of the initial flame growth and the flame venting process of a duration 0.35 s took around three days using 2 nodes with 56 cores on a supercomputer. The initial temperature and pressure are 273 K and 1 atm., respectively. The initial turbulence velocity fluctuation u' was equal to 0.75 m/s in combination with the k-omega-SST turbulence model, and the value was set equal to 0.5 m/s in combination with realizable k-epsilon turbulence model. The initial integral length scale L was equal to 0.1 m in all cases. Due to the lack of experimental data on the flow characteristics, these initial turbulence characteristics were chosen by comparing measured and computed pressure curves during the first explosion stage (before rupture of the vent panel).

The developed numerical tool *FSCDustFoam* (Huang and Lipatnikov, 2021) was based on a standard solver *XiFoam* in OpenFOAM-version 1812. Several modifications were made including (i) calculations of turbulent diffusivity and turbulent velocity in Equations (2, 3), (ii) ignition source term, (iii) extra source term (last term in Eq. 1), (iv) calculation of Favre-averaged temperature due to the inaccurate way in the standard thermophysical library in OpenFOAM (Yasari 2011), and (v) removing of the transport equation of *Xi*. Note that a balance equation for the mixture fraction is solved to track the transportation of the dust-air cloud. The boundary conditions for solving different variables in OpenFOAM is shown in Table 2. A blend of first and second order numerical schemes were used to obtain a stable solution including (i) CrankNicholson with a coefficient of 0 for the time scheme, (ii) Gauss linearUpwind and Gauss limitedLinear for divergence schemes and (iii) Gauss linear limited for Laplacian schemes.

Table 2. *Boundary conditions used in OpenFOAM.*

	Walls	**Open boundaries**
P [Pa]	zeroGradient	totalPressure
$\tilde{\mathbf{u}}$ [m/s]	noSlip	pressureInletOutletVelocity
$\tilde{T}_u$ [K]	fixedValue 273	fixedValue 273
$\tilde{b}$ [-]	zeroGradient	zeroGradient
$\tilde{k}$ [m^2/s^2]	kqRWallFunction	zeroGradient

4. Results and discussions

Table 3 shows time-evolution of the computed fields of the Reynolds-averaged combustion progress variable which has a physical meaning of the probability of finding the burned products. Note the image at the time instance 0.1 s covers only the domain inside of the vessel because this first-stage calculation, mentioned in Section 3.4, covers only the burning inside of the vessel.

Table 3. *Mean combustion progress variable fields computed at different time instants.*

Time [s]	**Reynolds-Averaged progress variable $\bar{c}$ [-]**
0.1	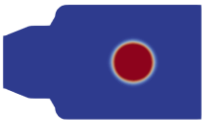
0.2	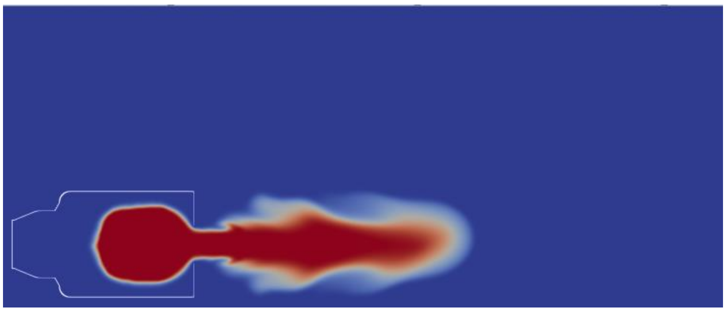
0.3	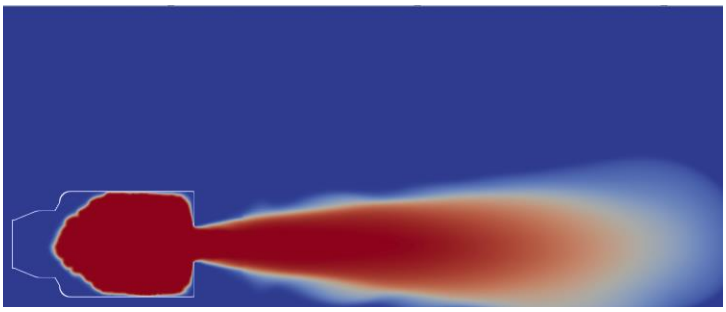
scale $\bar{c}$ [-]	

4.1 *Comparison with experiments*

The explosion overpressure-time traces computed using the extended FSC model and both k-omega-SST (Hellsten, 1998; Menter and Esch, 2001; Menter et al., 2003) and realizable k-epsilon turbulence models (Shih et al., 1994; 1995) (see red curves in Figure 4) agree reasonably well with the experimental data (black solid lines in Figure 4). The experimental data (black solid lines) was obtained by calculating the averaged value of two dust explosion tests, whereas the grey areas (see Figure 4) cover mean values ± the standard derivations based on the data of the two tests. Note that different initial rms turbulence velocities u' and different flame acceleration timings were used to achieve good agreement with the experiments when adopting the two turbulence models. The use of the conventional FSC model without the acceleration factor T_2 in Eq. (3) yields significantly underpredicted overpressure when compared to the experimental data, cf. cyan dash-dotted lines with black solid lines in Figure 4.

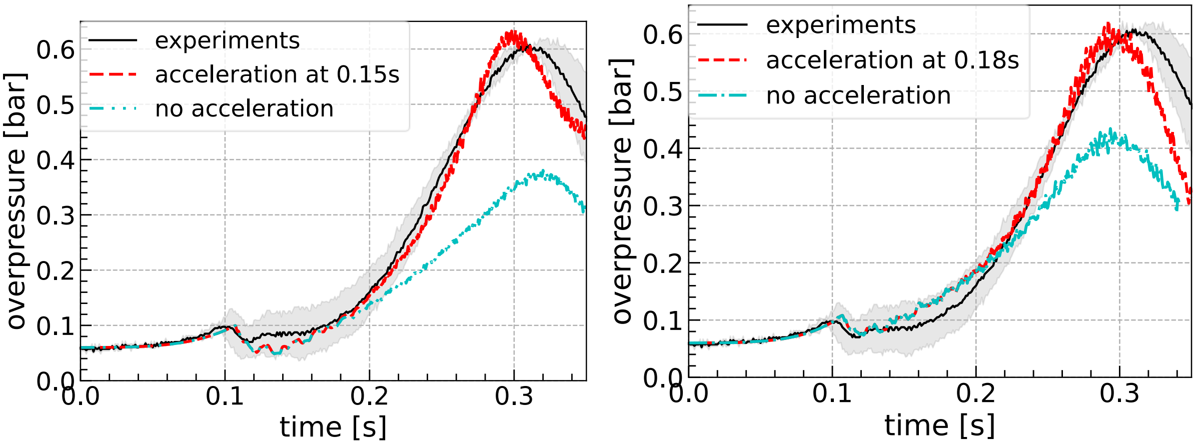

(a), k-omega-SST, u'=0.75 m/s (b), realizable k-epsilon, u'=0.50 m/s

Fig. 4. *Comparison between measured (mean value in the black solid line and the standard derivation in the grey area) and simulated (with and without flame accelerations) explosion overpressures.*

4.2 Sensitivity studies

CFD-based simulations involve a substantial number of parameters including model constants, initial and boundary conditions, domain size, grid size, numerical schemes and so on. It is a tremendous task to perform sensitivity studies on each input parameters. Therefore, it is of importance to make a proper choice of these parameters and be aware of the appropriate values of the simulations. At the same time, it is worth understanding the influence of critical parameters on the computed results. The following parameters were tested to yield a little impact on the computed explosion overpressure based on the case setup in Figure 4 (a):

(i) Progress variable boundary conditions on the walls being zeroGradient or fixedValue.
(ii) Pressure boundary condition from totalP till Tlnf0.2
(iii) Far-field mesh size
(iv) Temperature boundary conditions on the walls being zeroGradient or a fixed heat flux
(v) Domain size being 15.5, 25.5, or 35.5 m in the horizontal direction.

Turbulence model has a significant influence on the computed results, see a study by Huang et al. (2022). In addition, the mesh size and the Courant number are found to have a substantial impact on the computed results.

4.2.1 Grid size

Grid size is a constant concern for CFD simulations. Figure 5 compares the computed explosion overpressures using two different grid size resolutions in the vessel. A finer grid size yields a lower pressure as compared to a coarser grid size (c.f. red dash-dotted line and cyan dashed line in Figure 5). Figure 6 compares the explosion overpressures computed using two different grid size resolutions on the walls. A finer grid size on the wall yields a higher explosion overpressure as compared to a coarser grid size on the vent wall (c.f. red dash-dotted line and cyan dashed line in Figure 6). It is recommended to have a relatively fine grid in the vessel and on the walls (especially on the vent wall) to better capture the propagation of the flame and the flow through the vent opening, which was used as case setups in Figure 4.

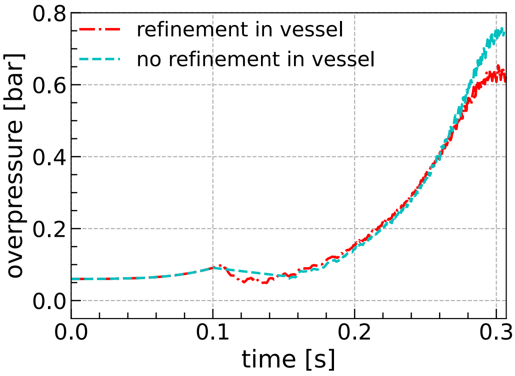

Fig. 5. *The effect of the mesh refinement on the computed explosion overpressure using k-omega-SST turbulence model. The red dashed curve was computed using a mesh size of 25 mm inside of the vessel, whereas the cyan dash-dotted curve was computed using a refined mesh size of 12.5 mm in a 0.7 m radius sphere inside of the vessel.*

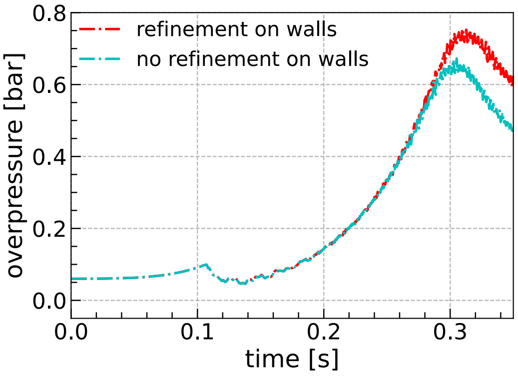

Fig. 6. *The effect of the mesh refinement on walls on the computed explosion overpressures using k-omega-SST turbulence model. The red dashed curve was computed using 5 layers mesh on the wall of the vessel and the venting wall, whereas the cyan dash-dotted curve was computed using no refinement on the walls of the vessel.*

4.2.2 Courant number

The Courant number *Co* is a measure of how fast a particle travels across a computational mesh, and therefore, the *Co* is proportional to the ratio of time step divided by grid size. It is preferable to have a reasonable *Co* value to accurately capture the solution within an acceptable computational time. Three *Co* were used to study the effect of time step on the computed results. Figure 7 shows that the computed explosion overpressure increases with the reduction of the *Co* number. It is worth noting that *Co*=0.1 is recommended for the current case since too low *Co* number requires long simulation time and worse agreement with experiments.

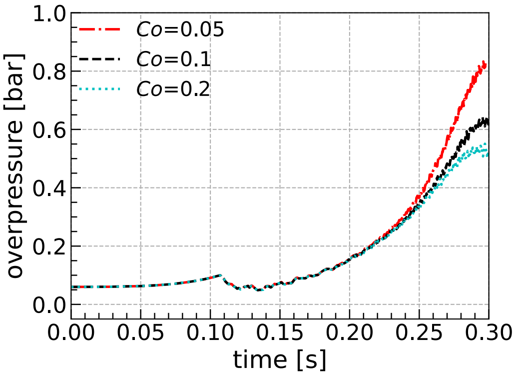

Fig. 7. *The effect of the Courant number on the computed explosion overpressure using k-omega-SST turbulence model.*

5. Conclusions

Vented corn starch dust explosion in an 11.5 m^3 vessel was studied experimentally and numerically. The numerical approach is based on unsteady three-dimensional RANS simulations using the FSC model of the influence of turbulence on combustion and various turbulence models implemented into OpenFOAM. The k-omega-SST and realizable k-epsilon turbulence models yield reasonable results with experiments using different initial rms turbulence velocities. While the use of the conventional FSC model yields underpredicted overpressure when compared to the experimental data, an excellent agreement between measurements and simulations was obtained by phenomenologically extending the FSC model to allow for the well-known self-similar regime of acceleration of large flame kernels, see Eq. (3). It is recommended to have relatively fine grid inside the vessel and on the vent wall together with a Courant number of 0.1 for the studied case. Therefore, this simple and numerically efficient extension of the FSC model looks promising and deserves further study in simulations of other large-scales dust or gaseous explosions.

Acknowledgements

The authors would like to acknowledge AFA-Försäkring for financial support of this project (grant number 180028). The computations were enabled by resources provided by the Swedish National Infrastructure for Computing (SNIC) at HPC2N partially funded by the Swedish Research Council through grant agreement no. 2018-05973 and RISE Simulation Lab. The SNIC projects SNIC2021-22-217, SNIC2021-5-185 and SNIC2021-22-821 are acknowledged. The authors would like to acknowledge IND EX® for providing the real scale test data of the IND EX® research project "Influence of the Explosion Relief Device Geometry on its Venting Efficiency".

References

Beyersdorfer, P., 1925. Staub-explosionen. T. Steinkopff.

Bradley, D., Chen, Z., Swithenbank, J., (1989). Burning rates in turbulent fine dust-air explosions. *22nd Symp. (Int.) on Combust., The Combust. Inst., Pittsburgh,* 1767-1775.

Brodkey, R.S., 1967. The Phenomena of Fluid Motions, Addison-Wesley Publ. Comp., London.

Dahoe, A.E., Hanjalic, K., Scarlett, B., (2002). Determination of the laminar burning velocity and the Markstein length of powder–air flames. *Powder Technol.* 122, 222-238.

Eckhoff, R.K.,(2003). *Dust explosions in the process industries: identification, assessment and control of dust hazards*. Elsevier.

Eckhoff, R.K., (2015). Scaling of dust explosion violence from laboratory scale to full industrial scale – A challenging case history from the past. *J. Loss Prev. Process Ind.* 36, 271-280.

Gostintsev, Y.A., Istratov, A., Shulenin, Y.V., (1988). Self-similar propagation of a free turbulent flame in mixed gas mixtures. *Combust. Explos. Shock Waves* 24, 563-569.

Gülder, Ö.L., (1984). Correlations of laminar combustion data for alternative SI engine fuels, SAE Technical Paper 841000.

Hellsten, A., (1998). Some improvements in Menter's k-omega SST turbulence model, in: 29th AIAA, Fluid Dynamics Conference, pp. 2554.

Huang, C., Bloching, M., Lipatnikov, A.N., (2022). A vented corn starch dust explosion in an 11.5 m3 vessel: Experimental and numerical study. *J. Loss Prev. Process Ind.* 75, 104707.

Huang, C., Lipatnikov, A.N., (2021). FSCDustFoam - a solver for premixed/partially-premixed combustion and explosion of dust and gas based on OpenFOAM (Version 1812). Zenodo. https://doi.org/10.5281/zenodo.5795161.

Huang, C., Lipatnikov, A.N., Nessvi, K., (2020). Unsteady 3-D RANS simulations of dust explosion in a fan stirred explosion vessel using an open source code. *J. Loss Prev. Process Ind.* 67, 104237.

Huang, C., Yasari, E., Johansen, L., Hemdal, S., Lipatnikov, A., (2016). Application of flame speed closure model to RANS simulations of stratified turbulent combustion in a gasoline direct-injection spark-ignition engine. *Combust. Sci. Technol.* 188, 98-131.

Li, H., Chen, X., Deng, J., Shu, C.-M., Kuo, C.-H., Yu, Y., Hu, X., (2020). CFD analysis and experimental study on the effect of oxygen level, particle size, and dust concentration on the flame evolution characteristics and explosion severity of cornstarch dust cloud deflagration in a spherical chamber. *Powder Technol.* 372, 585-599.

Lipatnikov, A., (2012). *Fundamentals of premixed turbulent combustion.* CRC Press.

Lipatnikov, A., Chomiak, J., (2002). Turbulent flame speed and thickness: phenomenology, evaluation, and application in multi-dimensional simulations. *Prog. Energy Combust. Sci.* 28, 1-74.

Lipatnikov, A.N., (2018). RANS simulations of premixed turbulent flames, in: Modeling and Simulation of Turbulent Combustion, Springer, pp. 181-240.

Lipatnikov, A.N., Chomiak, J., (1997). A simple model of unsteady turbulent flame propagation. *SAE Transactions, Section 3, Journal of Engines, 106,* 2441-2452.

Menter, F., Esch, T., (2001). Elements of industrial heat transfer predictions, in: 16th Brazilian Congress of Mechanical Engineering (COBEM), pp. 650.

Menter, F.R., Kuntz, M., Langtry, R., (2003). Ten years of industrial experience with the SST turbulence model. *Turbulence, heat and mass transfer* 4, 625-632.

Pico, P., Ratkovich, N., Muñoz, F., Dufaud, O., (2020). Analysis of the explosion behaviour of wheat starch/pyrolysis gases hybrid mixtures through experimentation and CFD-DPM simulations. *Powder Technol.* 374, 330-347.

Shih, T.-H., Liou, W.W., Shabbir, A., Yang, Z., Zhu, J., (1994). A new k-epsilon eddy viscosity model for high Reynolds number turbulent flows: Model development and validation. NASA Sti/recon Technical Report N 95, 11442.

Shih, T., Liou, W., Shabbir, A., Zhu, J., (1995). A New k-epsilon Eddy-Viscosity Model for High Reynolds Number Turbulent Flows-Model Development and Validation. *Computers Fluids,* 24 (3): 227-238.

Skjold, T., (2007). Review of the DESC project. *J. Loss Prev. Process Ind.* 20, 291-302.

Skjold, T., (2014a). Simulating vented maize starch explosions in a 236 m3 silo. *Fire Saf. Sci.* 11, 1469-1480.

Skjold, T., (2014b). *Flame propagation in dust clouds. Numerical simulation and experimental investigation,* PhD thesis. University of Bergen.

Skjold, T., Arntzen, B.J., Hansen, O.R., Storvik, I.E., Eckhoff, R.K., (2006). Simulation of dust explosions in complex geometries with experimental input from standardized tests. *J. Loss Prev. Process Ind.* 19, 210-217.

Skjold, T., Arntzen, B.J., Hansen, O.R., Taraldset, O.J., Storvik, I.E., Eckhoff, R.K., (2005). Simulating dust explosions with the first version of DESC. *Process Saf. Environ. Prot.* 83, 151-160.

Tan, I., Wee, C.C., Sopade, P.A., Halley, P.J., (2004). Estimating the specific heat capacity of starch-water-glycerol systems as a function of temperature and compositions. *Starch-Stärke* 56, 6-12.

Yasari, E. (2011). Modification of the Temperature Calculation Library for Premixed Turbulent Combustion Simulation. In 6th OpenFOAM Workshop, PennState University, USA, 13-16 June, 2011.

Zimont, V.L., (1979). Theory of turbulent combustion of a homogeneous fuel mixture at high Reynolds number. Combustion, Explosions, and Shock Waves, 15:305-311.

Zimont, V.L., (2000). Gas premixed combustion at high turbulence. Turbulent flame closure combustion model. *Exp. Therm. Fluid Sci.* 21, 179-186.

DOI: 10.7795/810.20221124

Dust Particle Sedimentation in the 20 L Standard Vessel for Dust Explosion Tests

Maria Portarapillo,[a] Marco Trofa, [a] Roberto Sanchirico, [b] Almerinda Di Benedetto,[a]

[a] Department of Chemical, Materials & Production Engineering, University of Naples Federico II, Naples, Italy

[b] CNR - Institute of Sciences and Technologies for Sustainable Energy and Mobility (STEMS), Naples, Italy

E-mail: maria.portarapillo@unina.it

Abstract

Dust explosion/flammability tests are performed in 20 L and/or 1 m^3 standard vessels. According to the current international standards, in order to perform the correct evaluation of the explosion and flammability parameters, a uniform distribution of the dust particles should be achieved inside the vessel.

Our CFD simulations have shown that in both standard test vessels (20 L and 1 m^3), the dust particles are not uniformly dispersed, being mostly concentrated at the edge of the macro-vortices generated by the injection of the fluid and particle through the nozzle. In addition, only a partial fed of the particles is obtained and dust particles sedimentation phenomena can occur.

As a result, the dust actually participating to the reactive process may be much lower than the expected nominal concentration in the vessel due to sedimentation and incomplete feeding. Consequently, misleading values of the flammability/explosion parameters could be measured.

Particle sedimentation and incomplete feeding depends both on the Stokes number and on the Reynolds number, whereas the concentration distribution depends on the turbulence level, the fluid flow maps, and the amount of particles which enter into the vessel through the nozzle.

The aim of this work is to evaluate the key parameters (particle size, particle density, and fluid velocity) affecting sedimentation and incomplete feeding in 20 L vessel. To this end, CFD simulations of dust dispersion are performed at varying the particle density and size. Operating maps, in terms of the key parameters and/or their dimensionless combinations, are eventually developed.

Keywords: *Standard test vessels; Dust explosion; Dust sedimentation; Partial feeding*

1. Introduction

To quantify the explosibility of combustible dusts, explosion testing is carried out in spherical closed vessels of 20 L and/or 1 m^3. Whatever the vessel used, the measured explosion parameters must be the same. However, several discrepancies were found among the results obtained in the two vessels although standard procedures were followed (ASTM E1226-19, 2019; BS EN 15967:2011, 2012).

Results strongly depend on several factors:

- Dust size (Di Sarli et al., 2013; Portarapillo et al., 2021c);
- Dust shape (Di Sarli et al., 2019);
- Pre-ignition turbulence level (Portarapillo et al., 2021a);
- Chemical ignitors explosion (Portarapillo et al., 2021b).

In addition to the above listed issues, dust distribution inside the testing vessel has been found to be dependent on the vessel size. In both vessels, dust dispersion is obtained by using compressed air at 21 bar which transports the dust loaded in the container to the test vessel once the electro-pneumatic valve is opened. In this way, the dust is shot into the test volume and macro-vortices are generated with the formation of dead volumes (Di Benedetto et al., 2013; Portarapillo et al., 2020b). A homogeneous level of concentration in every point of the vessel is never guaranteed, whatever the volume, even if it is a strict requirement in standard procedures (ASTM E1226-19, 2019; BS EN 15967:2011, 2012). In a previous work regarding the dispersion of mixtures of niacin and anthraquinone, we showed that due to the different properties (size and density) of the two pure dusts, there were some zones richer in niacin and poor in anthraquinone concentration and vice versa compromising the reliability of the test and the evaluation of any parameter relating to the mixture (Portarapillo et al., 2020a). We then concluded that the powder temporal/spatial dispersion strongly depends on the properties of the dust such as diameter and density. Once the dust particles are fed from the container to the test vessel, other mechanisms arise such as partial feeding and sedimentation and. In this work we investigate the role of diameter and density of dust particles on partial feeding and sedimentation. To this end we simulated the dust dispersion in the 20 L sphere at changing the dust size and density, eventually evaluating the particle sedimentation and partial feeding.

2. Methodology

CFD simulations were carried out under the operating conditions contained in Table 1 with a nominal dust concentration set at 250 g/m^3. In particular, we considered monodispersed dusts with diameter from 10 to 400 microns. In the case of size distribution the conclusions achieved by this work can be extended since the system can be considered ad dispersed (Elghobashi, 1994). The details of CFD simulations are reported in a previous work (Di Benedetto et al., 2013). Theoretically, the effect of concentration should also be investigated. Indeed, the dust concentration does not seem to have a direct effect on the sedimentation phenomenon but indirectly affects it by modifying the flow field of the continuous phase. It is worth underlining that the dust aliquot that remains dispersed in the form of a cloud inside the sphere is the one that, once triggered the explosion, contributes to it. The rest of the powder will form a layer on the base of the vessel and on the rebound nozzle. To this aim, the mass fractions of dispersed (y_{disp}) and deposited (y_{dep}) dust present in the sphere at different instants of time (0.02,0.04,0.06 s) were calculated as a function of the dimensionless relaxation time τ^+. In particular, to consider if a particle sedimented or not, the particles where tracked in terms of position and velocity in the entire domains. The criterium used for sedimentation was position<10% of the domain size and velocity<0.01 m/s.

y_{disp}, y_{dep} and τ^+ were defined as

$$y_{disp} = \frac{m_{disp}}{m_{tot}} = \frac{m_{disp}}{C_{nom} \cdot V} \tag{1}$$

$$y_{dep} = \frac{m_{dep}}{m_{tot}} = \frac{m_{dep}}{C_{nom} \cdot V} \tag{2}$$

$$\tau^+ = \frac{\tau}{t_d} = \frac{\rho_p d_p^2}{18 \cdot \mu \cdot t_d} \tag{3}$$

where τ (s) is the relaxation time, m_{disp} (kg) is the dispersed dust mass within the 20 L sphere and m_{dep} (kg) is the deposited dust mass. It is the characteristic time for the particle to approach steady motion.

It characterizes the time required for a particle to adjust or "relax" its velocity to a new condition of forces. It is an indication of the particle ability to quickly adjust to a new environment or condition. Since relaxation time is proportional to the square of particle diameter, it increases rapidly with the increase of particle size. Usually, small particles "relax" to new environments (i.e., following the flow well) in a very short time, while larger particles are more "stubborn" and tend to stick to their original path.

Table 1: *Dust properties used for simulation*

Diameter (μm)	Density (kg/m^3)
10	500-7000
60	500-7000
100	500-7000
200	500-7000
400	500-7000

3. Results and discussion

In Fig.1 the dimensionless relaxation time is shown as function of the dust diameter, at different values of the dust density.

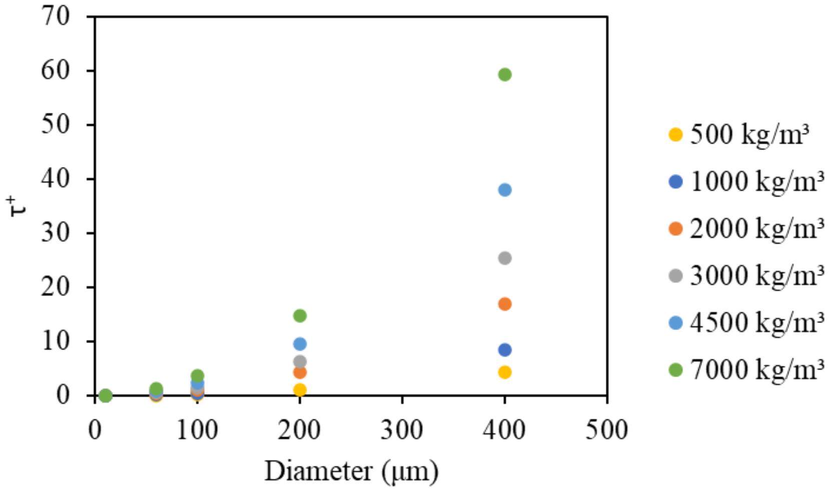

Fig. 1. *Dimensionless relaxation time as a function of the diameter and parametric in the density*

Fig. 2 shows the mass-to-nominal mass ratio present within the vessel, the tube, and the container at the ignition delay time, as computed at different values of diameter and density. As can be seen, at low values of diameter (<100 μm) the mass-to-nominal mass ratios within all the three parts of the whole domain are less sensitive to density variations. As the diameter increase, the dependence on the density is more relevant, the ratio in the explosion vessel decreases while increases both in the tube and in the container.

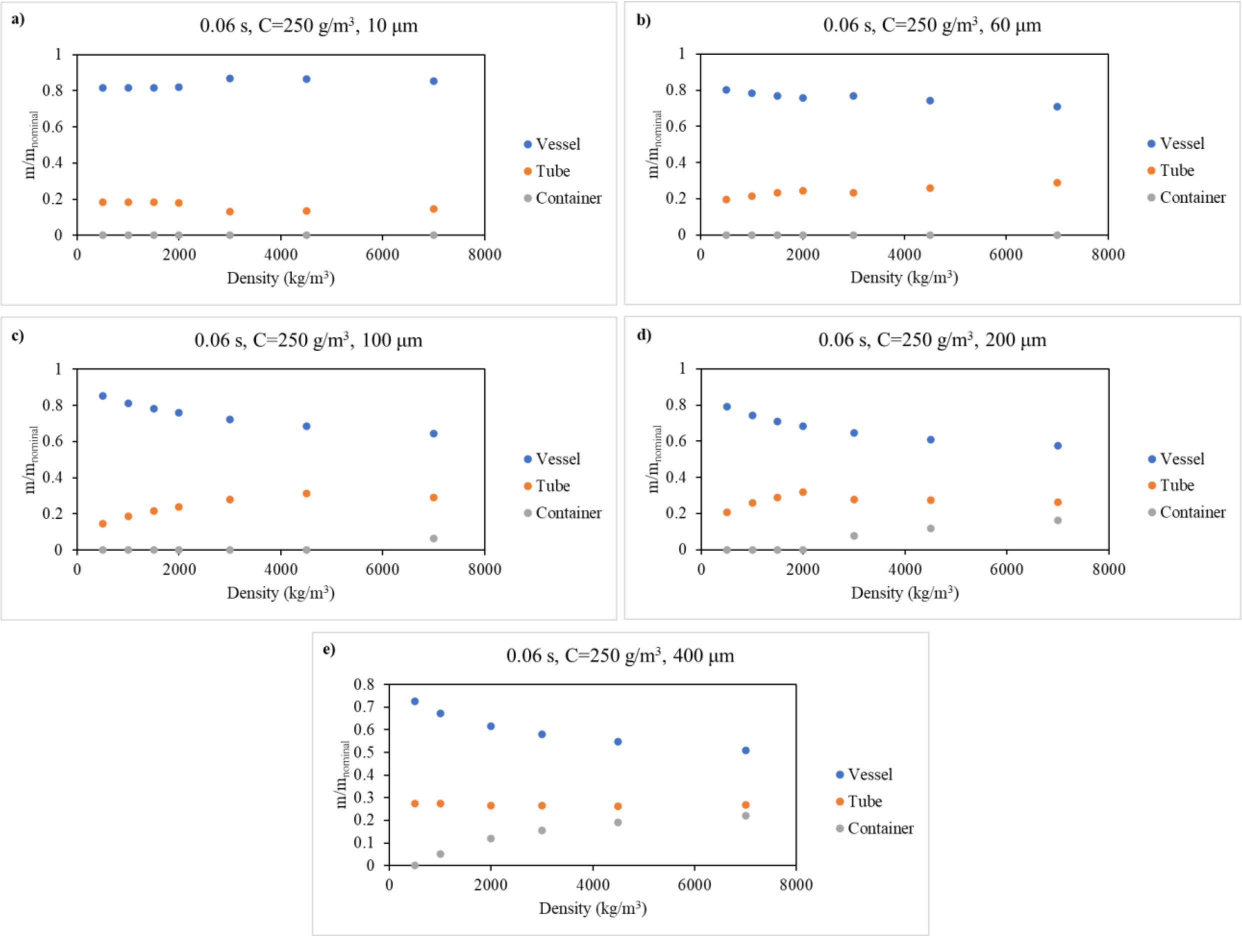

Fig. 2. *Mass-to-nominal mass (C_{nom}=250 g/m^3) ratio at 10 μm (a), 60 μm (b), 100 μm (c), 200 μm (d), 400 μm (e) as a function of density at the ignition delay time in the vessel (blue scatter plot), the tube (orange scatter plot) and the container (grey scatter plot)*

The same behavior was found at low values of density (<1000 kg/m^3) where the mass-to-nominal mass ratios within all the three parts of the whole domain are less sensitive to diameter variations (Fig. 3).

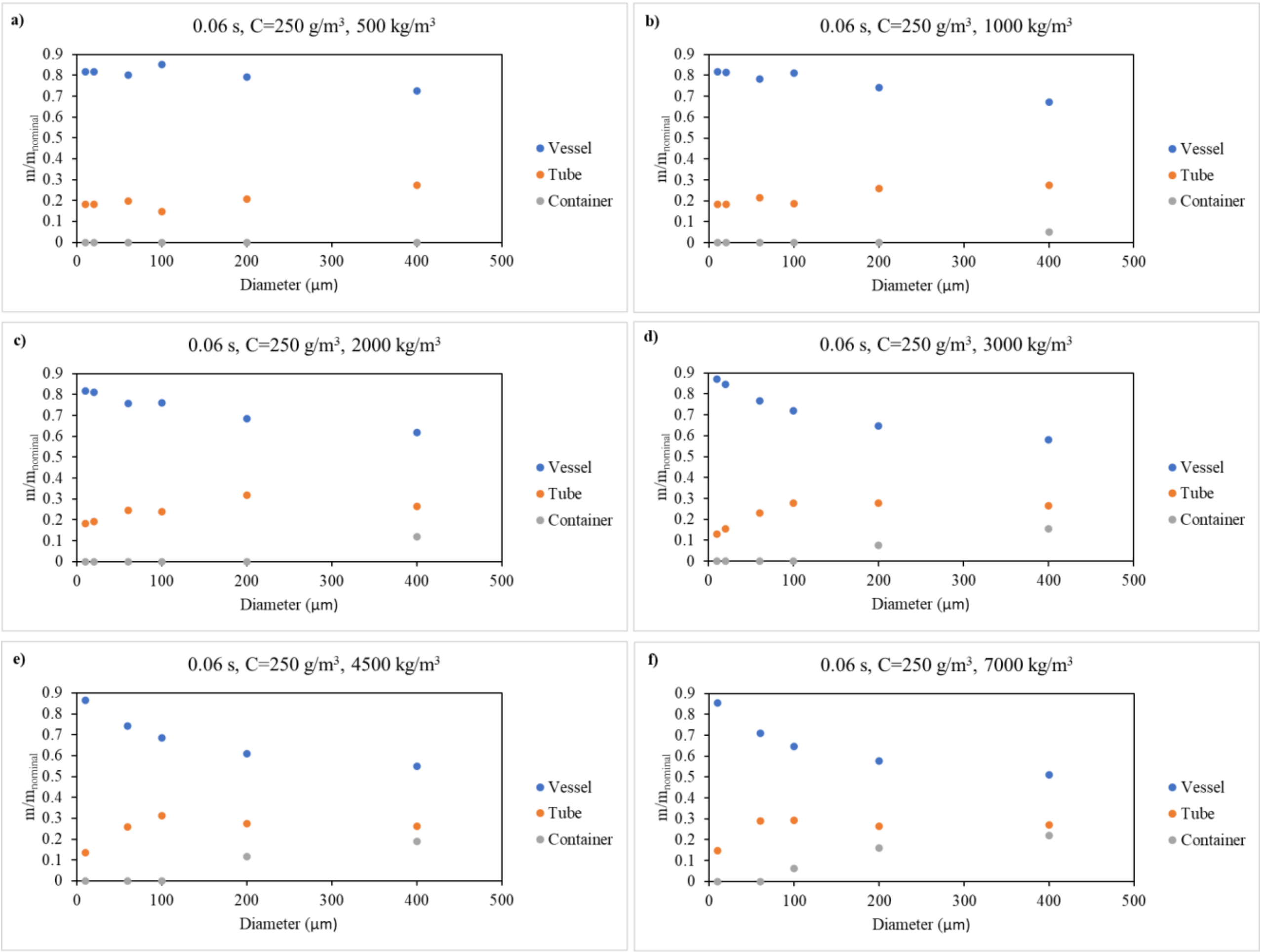

Fig. 3. *Mass-to-nominal mass (C_{nom}=250 g/m^3) ratio at 500 kg/m^3 (a), 1000 kg/m^3 (b), 2000 kg/m^3 (c), 3000 kg/m^3 (d), 4500 kg/m^3 (e) and 7000 kg/m^3 (f) as a function of diameter at the ignition delay time in the vessel (blue scatter plot), the tube (orange scatter plot) and the container (grey scatter plot)*

The trends of y_{disp} within the explosion vessel are reported as function of density at different value of diameter (Fig. 4) and as function of diameter at different value of density (Fig. 5), parametric in time. The following phases can be identified:

- feeding phase: the fraction of dust dispersed in the vessel increases from 0.02 s to 0.04 s
- sedimentation phase: the fraction of dust dispersed in the vessel decreases from 0.4 s to 0.06

It is also found that y_{disp} dramatically decreases as density and diameter increase, starting from a maximum value equal to 0.86 and reaching a plateau value at 0.50

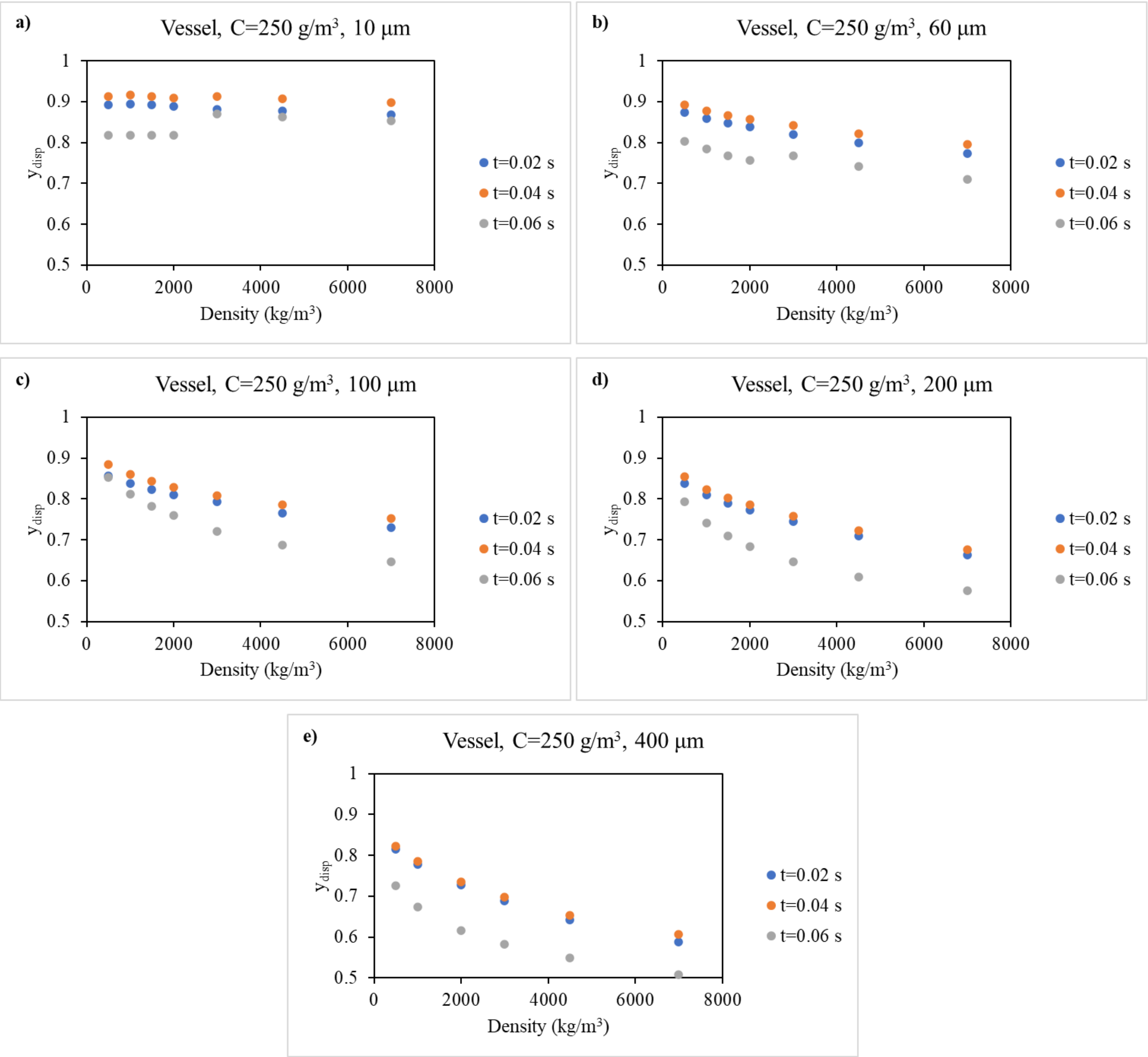

Fig. 4. *y_{disp} (C_{nom}=250 g/m^3) at 10 µm (a), 60 µm (b), 100 µm (c), 200 µm (d), 400 µm (e) as a function of density within the explosion vessel at 0.02 s (blue scatter plot), 0.04 s (orange scatter plot) and 0.06 s (grey scatter plot)*

DOI: 10.7795/810.20221124

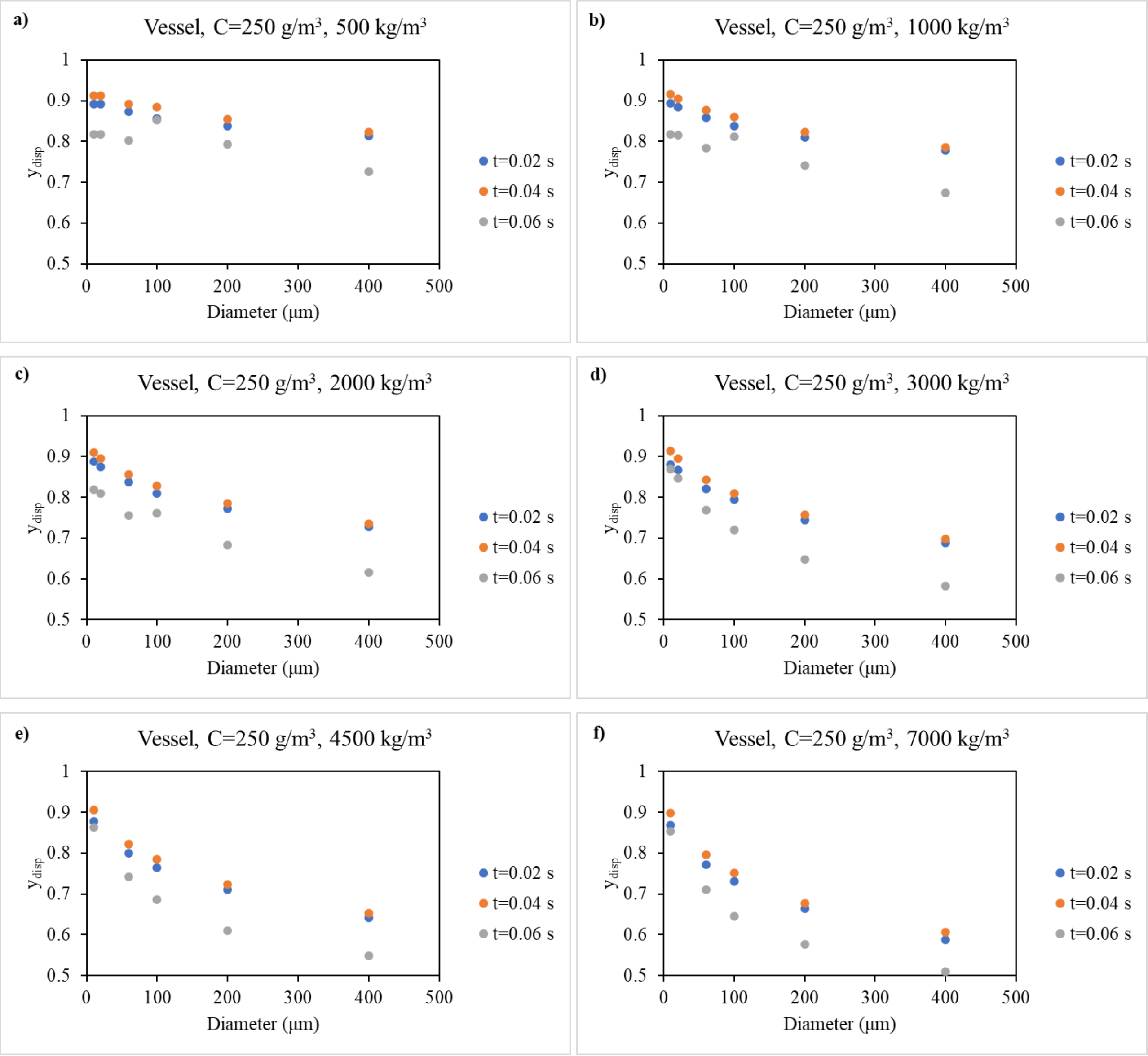

Fig. 5. *y_{disp} (C_{nom}=250 g/m^3) at 500 kg/m^3 (a), 1000 kg/m^3 (b), 2000 kg/m^3 (c), 3000 kg/m^3 (d), 4500 kg/m^3 (e) and 7000 kg/m^3 (f) as a function of diameter within the explosion vessel at 0.02 s (blue scatter plot), 0.04 s (orange scatter plot) and 0.06 s (grey scatter plot)*

Fig. 6 shows the fraction of dust dispersed inside the vessel versus the dimensionless relaxation time, parametric in time. Notably, the fraction increases during the feeding phase (up to 0.04 s the pressure gradient still allows the dust to enter from the container and the tube within the 20 L vessel) and then decreases to 0.06 s due to sedimentation phenomenon. As can be seen in Fig. 6 and Fig. 7 the fraction of dust dispersed in the form of a dust cloud decreases as τ^+ increases: the higher the τ^+, the longer the time required for the fluid to involve the dust particles in the turbulent motion generated by the pressure gradient. If the dust is not involved in the swirling motion generated in the sphere, it will tend to settle on the bottom of the vessel and will not participate to the flame propagation. In the case of dusts characterized by high relaxation time values, the fraction dispersed at the ignition delay time is equal to 50% of the nominal value. This turns out to be very critical both for the evaluation of P_{max}

and K_{St} (which would be underestimated) but above all in the evaluation of the *MEC* which could be largely overestimated.

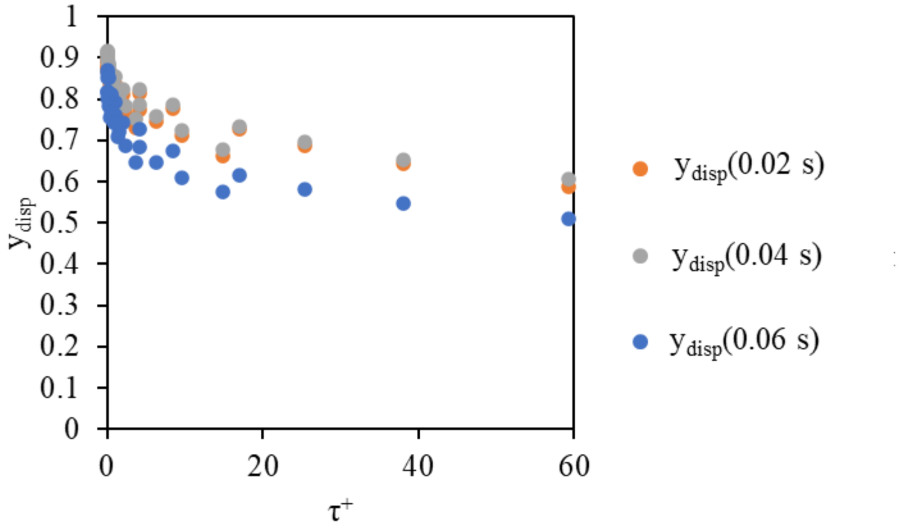

Fig. 6. *Mass fraction of dispersed dust as a function of the dimensionless relaxation time and parametric in time*

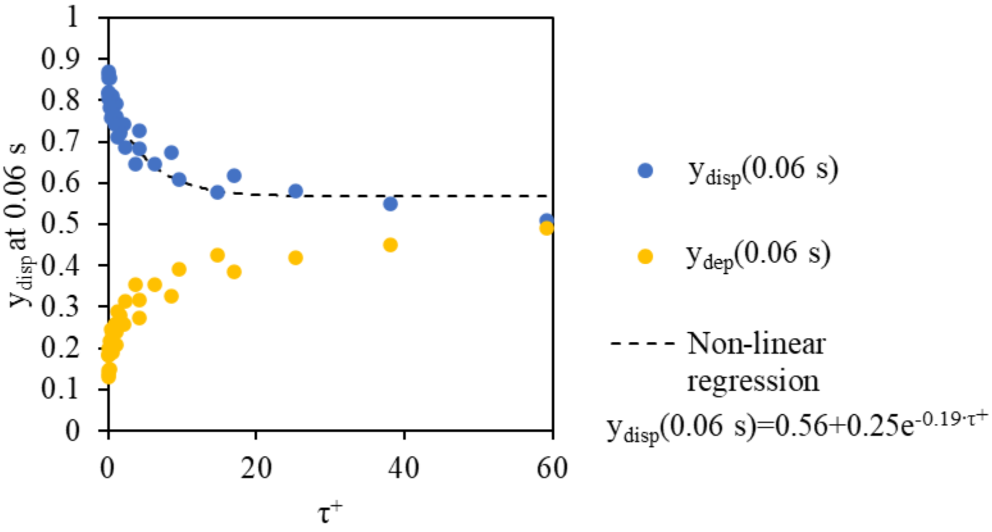

Fig. 7. *Mass fraction of dispersed and deposited dust at 0.06 s as a function of the dimensionless relaxation time. A non-linear regression (3-factors exponential decay) for y_{disp} is also shown ($R^2=0.91$)*

Combining the obtained results, Figure 8 highlights the zones where density does not play any effect (blue zone, diameter<100 μm), where diameter does not play any effect (yellow zone, density<1000 kg/m^3) and the area in which the effects of the two parameters are combined (grey zone). Some combustible dusts are reported in the Figure to show that typically the dusts can fall into each of the areas described above.

By using the operational map of Fig. 8, to consider the phenomena of sedimentation and partial feeding, we should proceed in this way:

1. Before testing the dust, it is necessary to know the diameter and density to evaluate the relaxation time
2. Once the relaxation time is calculated, it is possible to calculate the fraction of dust dispersed through the non-linear regression reported in Figure 7 to assess the maximum deviation of the nominal concentration and, if necessary, to proceed with the correction
3. Check from Figure 8 if, in the case of non-monodispersed sample, changes in diameter due to fragmentation or formation of agglomerates and changes in density, the fraction of material needs to be modified.

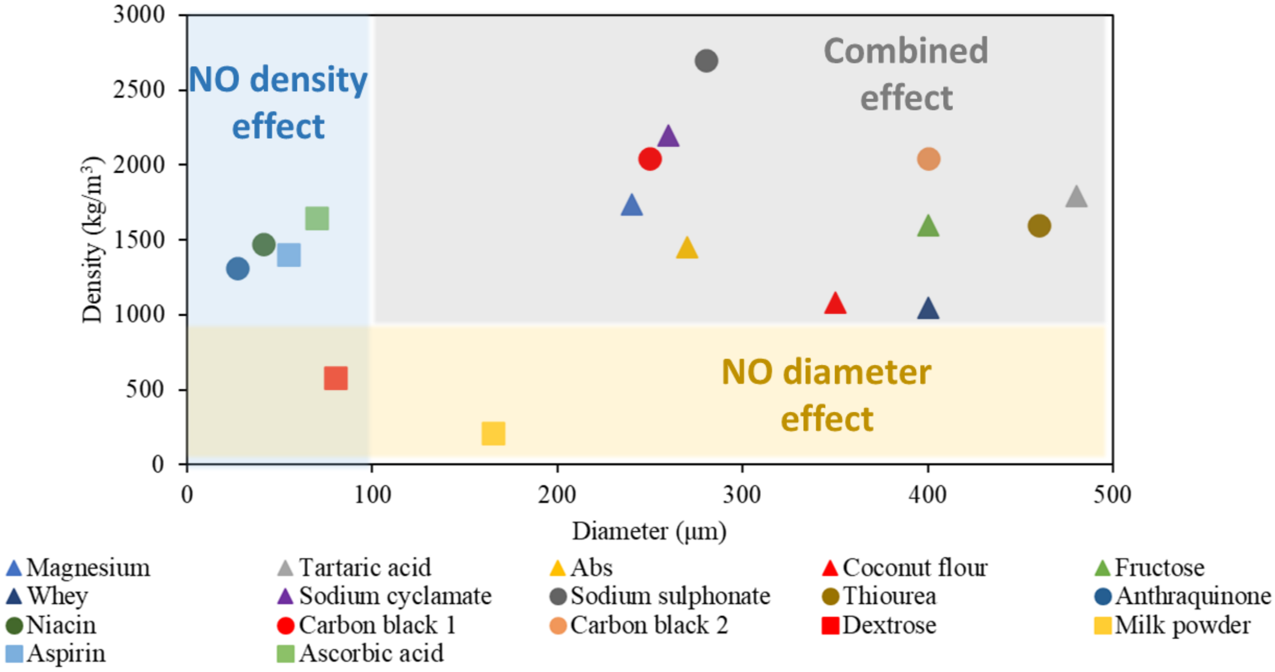

Fig. 8. *Density-diameter plane with areas of influence of the parameters highlighted in different colours: no density effect (blue), no diameter effect (yellow) and combined effect (grey). Typical combustible dusts are also reported.*

4. Conclusions

In this work the effect of sedimentation and partial feeding was quantified through CFD simulation of the dust dispersion obtained inside the 20 L vessel. In particular, several simulations by changing diameter and density (and consequently by changing relaxation time) were performed. Due to sedimentation and partial feeding, a lower dust aliquot than the nominal value is tested and the results in terms of explosivity parameters cannot be considered reliable. Results showed that at lower values of diameter, density does not play any effect on the fraction of dust dispersed inside the vessel at the ignition delay time as well as at low density, diameter has no effect on the same variable. To correct the concentration present in the vessel during an explosion test, a correction should be applied. In this work, we proposed a correlation between the fraction of dust that actually participates in the explosive phenomenon and the relaxation time of the dust.

References

ASTM E1226-19, 2019. Standard Test Method for Explosibility of Dust Clouds. ASTM Int. West Conshohocken, PA 1–15. https://doi.org/10.1520/E1226-19

BS EN 15967:2011, 2012. Determination of maximum explosion pressure and the maximum rate of pressure rise of gases and vapours.

Di Benedetto, A., Russo, P., Sanchirico, R., Di Sarli, V., 2013. CFD Simulations of Turbulent Fluid Flow and Dust Dispersion in the 20 Liter Explosion Vessel. AIChE 59, 2485–2496. https://doi.org/10.1002/aic

Di Sarli, V., Danzi, E., Marmo, L., Sanchirico, R., Di Benedetto, A., 2019. CFD simulation of turbulent flow field, feeding and dispersion of non-spherical dust particles in the standard 20 L sphere. J. Loss Prev. Process Ind. 62, 103983. https://doi.org/10.1016/j.jlp.2019.103983

Di Sarli, V., Russo, P., Sanchirico, R., Di Benedetto, A., 2013. CFD simulations of the effect of dust diameter on the dispersion in the 20L bomb. Chem. Eng. Trans. 31, 727–732.

Elghobashi, S., 1994. On predicting particle-laden turbulent flows. Appl. Sci. Res. 52, 309–329. https://doi.org/10.1007/BF00936835

Portarapillo, M., Di Sarli, V., Sanchirico, R., Di Benedetto, A., 2020a. CFD Simulation of the Dispersion of Binary Dust Mixtures in the 20 L Vessel. J. Loss Prev. Process Ind. 67, 104231. https://doi.org/10.1016/j.jlp.2020.104231

Portarapillo, M., Sanchirico, R., Di Benedetto, A., 2021a. Effect of turbulence spatial distribution on the deflagration index: Comparison between 20 L and 1 m3 vessels. J. Loss Prev. Process Ind. 71. https://doi.org/10.1016/j.jlp.2021.104484

Portarapillo, M., Sanchirico, R., Di Benedetto, A., 2021b. On the pyrotechnic ignitors role in dust explosion testing : Comparison between 20 L and 1 m 3 explosion vessels. Process Saf. Prog. 1–7. https://doi.org/10.1002/prs.12249

Portarapillo, M., Trofa, M., Sanchirico, R., Di Benedetto, A., 2021c. CFD simulations of the effect of dust diameter on the dispersion in the 1 m3 explosion vessel. Chem. Eng. Trans. 86.

Portarapillo, M., Trofa, M., Sanchirico, R., Di Benedetto, A., 2020b. CFD simulations of dust dispersion in the 1 m3 explosion vessel. J. Loss Prev. Process Ind. 68, 104274. https://doi.org/10.1016/j.jlp.2020.104274

DOI: 10.7795/810.20221124

Improved modelling of hydrogen explosions – representing effects of varying concentration and reduced oxygen atmospheres

Melodia Lucas[a,b], Helene Hisken[a,b], Trygve Skjold[b] & Bjørn J. Arntzen[a,b]

[a] Gexcon, Bergen, Norway

[b] Department of Physics and Technology, University of Bergen, Bergen, Norway

E-mail: *melodia.lucas.perez@gexcon.com*

Abstract

This paper evaluates the predictive capabilities of the advanced consequence model FLACS-CFD for deflagrations involving hydrogen. Two premixed combustion modelling approaches are presented: the extensively validated model originally developed for hydrocarbons included in FLACS-CFD *21.3* and a Markstein number dependent model implemented in the in-house development version FLACS-CFD *21.3 IH*. The predictive capabilities of the models for scenarios with different concentrations of hydrogen, and thus different Lewis and Markstein numbers, is assessed. Furthermore, the effect of atmospheres with added nitrogen on overpressure is investigated. The purpose is to evaluate how different scenarios affect the performance of the two model versions for different regimes of premixed combustion. The validation dataset includes deflagrations in the open, deflagrations in a congested open area, vented deflagrations in an empty enclosure and vented deflagrations in congested enclosures. The overpressure predictions by FLACS-CFD *21.3 IH* are found to be more accurate than those obtained with FLACS-CFD *21.3* for scenarios with varying hydrogen concentrations and/or added nitrogen in the mixture. The predictions by FLACS-CFD *21.3 IH* for lean hydrogen mixtures are within a factor of 2 of the values observed in the experiments. Improvements of the model are needed for more accurate prediction of deflagrations involving rich hydrogen mixtures.

Keywords: *CFD modelling, validation, hydrogen safety*

1 Introduction

If used within their validated range of applicability, consequence models are valuable tools for investigating the effects of various explosion protection measures as well as for designing systems where hydrogen is produced, transported, and used. Relevant examples are installations for hydrogen production by electrolysis, fuel-cell stacks in ships, and pipeline networks previously used to distribute natural gas to homes. Meanwhile, hydrogen is the most reactive and easily ignitable of all energy carriers ever considered for widespread use in society, and the propensity of hydrogen-air mixtures to undergo deflagration-to-detonation-transition has severe implications for explosion protection and safety distances (Skjold, 2020). The high reactivity of hydrogen-air mixtures implies that minor inaccuracies in modelling approaches, mainly developed for and validated against explosion scenarios involving 'conventional' fuels, can have an unacceptable impact on the model's capability of representing hydrogen-related accidents. This suggests that quantifying the uncertainty associated with model predictions for hydrogen applications potentially is more challenging than for applications involving conventional hydrocarbons. For example, the results from the second HySEA blind-prediction study showed that the spread in predicted maximum overpressures from seven different modellers using four different computational fluid dynamics (CFD) models for the same scenario covered two orders of magnitude (Skjold et al., 2019).

The FLACS-Hydrogen module in the CFD tool FLACS-CFD has been developed to represent accident scenarios involving hydrogen through several research programmes and projects over the last two decades. Middha (2010) carried out an extensive validation study for hydrogen dispersion and explosion scenarios, including blind-prediction benchmarks. Most of the hydrogen explosion validation work was done as part of the Network of Excellence HySafe. The validation work included experiments in a tube with different obstacle configurations (Breitung et al., 2005, Middha et al., 2007), in a mockup refuelling station (Makarov et al., 2009), in unconfined explosion scenarios with various degrees of congestion (Royle et al., 2007) and in a one-fifth scale traffic tunnel model (Sato et al., 2006). Hisken (2018) implemented and presented the validation of new sub-grid models in an in-house development version of FLACS. The model version was validated against the combined dispersion and explosion experiments performed as part of the HySEA project (Lucas et al., 2021). The performance of the new model was significantly better than that of the latest release version at the time (FLACS *v*10.9). However, an extensive validation study for different fuels and scenarios showed worse representation of the experimental results for some cases. This paper analyses the performance of two frameworks for premixed combustion modelling in FLACS-CFD: FLACS-CFD *21.3* and FLACS-CFD *21.3 IH*. FLACS-CFD *21.3* is a commercial version of FLACS-CFD released in 2021, while FLACS-CFD *21.3 IH* is an in-house development version that replaces the burning velocity correlations in FLACS-CFD *21.3* with the Markstein number dependent combustion model implemented by Hisken (2018). The aim of this work is to expand the validated application range of the tool and increase the modelling accuracy for scenarios with various equivalence ratios (ER), mixtures of hydrogen with other fuels, and flame propagation in non-standard atmospheres.

2 CFD modelling

FLACS-CFD is a CFD tool for assessing the consequences of fires, explosions or dispersion of flammable or toxic gases and liquids. FLACS-Hydrogen is a submodule of the CFD tool for pure hydrogen or hydrogen mixed with other fuels. The Favre-averaged Navier-Stokes equations are solved on a structured grid. The k-ε turbulence model (Launder and Spalding, 1974) is used. The combustion modelling includes sub-models for flame folding, burning velocity and combustion length scale. More details about the standard models used in FLACS-CFD can be found in the User's Manual (Gexcon AS, 2021). The modelling differences between FLACS-CFD *21.3* and FLACS-CFD *21.3 IH* are only related to the burning velocity models. In the following, the two different approaches for computing the burning velocity are described in detail.

The laminar burning velocity, s_L, in FLACS-CFD is tabulated for different fuels and equivalence ratios. For hydrogen, the data is taken from the experimental study done by Taylor (1991) with s_L obtained from outwardly propagating spherical flames. The uncertainty in measuring s_L for hydrogen-air can reach ±50% for ER<0.5 (±20% for ER>3 and ±10% for 1<ER<3) and is most likely related to ignition effects and the extrapolation model used (Han et al., 2020). For modelling the cellular flame propagation, a quasi-laminar burning velocity correlation is used. For hydrogen explosions, the transition from laminar to cellular flame propagation occur shortly after ignition. The quasi-laminar burning velocity model dominates for uncongested scenarios where the turbulence level is low. The empirical model for the quasi-laminar burning velocity, s_{QL}, in FLACS-CFD reads

$$s_{QL} = s_{L,Le}(1 + C_{QL} r_F^a). \tag{1}$$

Here C_{QL} is a mixture-dependent model constant, r_F is the flame radius and a is a model constant. $s_{L,Le}$ is the laminar burning velocity corrected for thermal-diffusive instabilities. In the in-house development version of FLACS-CFD, s_{QL} is modelled as

$$s_{QL} = max\left(s_L, s_L C_{QL}^{\star} \frac{r_F}{r_{F,cr}}^{a^{\star}}\right), \tag{2}$$

where $r_{F,cr}$ denotes the critical radius of the appearance of a cellular flame, and the model constants C_{QL}^* and a^* are both concentration- and mixture-dependent.

For the turbulent regime, the turbulent burning velocity, s_T, is expressed in terms of the effective root-mean-square turbulence velocity, u', and the Karlovitz stretch factor K (Bradley et al., 2013) as

$$\frac{s_T}{u'} = \alpha K^{-\beta}. \tag{3}$$

In FLACS-CFD *21.3*, α and β are constant parameters. In FLACS-CFD *21.3 IH* α and β are empirical parameters explicitly expressed in terms of the strain rate Markstein number, Ma_{sr}. The expressions are based on the correlations given by Bradley et al. (2013) with

$$\begin{aligned} \alpha = C_\alpha 0.023(30 - Ma_{sr}) \text{ and } \beta = 0.0103(Ma_{sr} - 30) \text{ if } Ma_{sr} > 0, \\ \alpha = C_\alpha 0.085(7 - Ma_{sr}) \text{ and } \beta = -0.0075(30 + Ma_{sr}) \text{ if } Ma_{sr} < 0. \end{aligned} \tag{4}$$

Here C_α is a constant model parameter. Ma_{sr} is determined from the stretched and unstretched flame speeds using extrapolation models. The values are highly dependent on the extrapolation method and the uncertainty is estimated to be about one order of magnitude larger than for the s_L (Han et al., 2020).

K is given by (Bradley et al., 2013)

$$K = 0.25\frac{u'^2}{s_L}\frac{u' l_C}{\nu}^{-0.5}, \tag{5}$$

where ν is the kinematic viscosity and l_C is the combustion length scale. l_C is proportional to the distance from the point of ignition to the flame front. For confined geometries, this growth is bounded by a parameter that is proportional to the distance between the enclosing walls. In FLACS-CFD *21.3*, s_L in Equation 5 includes the Lewis-number correction.

3 Experiments

This section introduces a collection of experimental campaigns relevant for validation of the burning velocity models used for representing accidental hydrogen deflagrations.

3.1 Deflagration in the open

A 20 m diameter hemispherical balloon filled with a stoichiometric hydrogen-air mixture experiment performed by the Fraunhofer Institut Chemische Technologie (Fh-ICT) in 1983 (Becker and Ebert, 1985) is used for the validation of the quasi-laminar burning velocity regime.

3.2 Deflagration in an open congested area

The 3D corner geometry consists of three perpendicular square steel plates of 37 cm x 37 cm mounted to form a corner. For the experiments studied here, two different obstacle sets were used consisting of different numbers of 36.5 cm long tubes as shown in Figure 1. The 4x4 obstacle set (1a) was formed using four layers with four tubes of 50 mm diameter, while the 9x9 obstacle set (1b) was formed using nine layers with nine tubes of 20 mm diameter. The rows of tubes were collocated perpendicularly to each other. The gas used as fuel was either 100 vol.% hydrogen or a mixture of 75 vol.% hydrogen and 25 vol.% nitrogen. The ignition source was mounted on the floor at the inner corner. Four pressure transducers were mounted at the steel walls. The coordinates in meters from the inner corner of the rig are (0.00, 0.045, 0.047) for P1, (0.00, 0.176, 0.315) for P2, (0.270, 0.000, 0.110) for P3 and (0.350, 0.355, 0.000) for P4.

3.3 Vented deflagrations in an empty enclosure

FM Global performed hydrogen explosion experiments in an empty chamber with different vent sizes, ignition locations and hydrogen concentrations (Bauwens et al., 2012). The vented chamber was 4.6 m x 4.6 m x 3.0 m. The experiments with the 2.7 m^2 vent size and centre ignition are studied here. The hydrogen concentration varied from 12.1 to 19.7 vol.%.

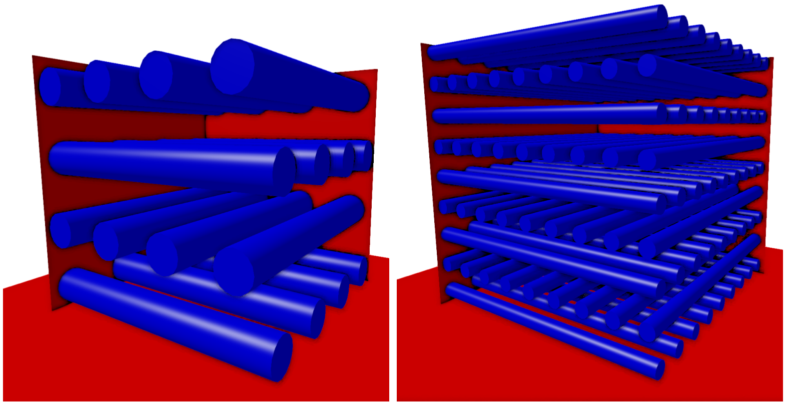

(a) 4x4 configuration. (b) 9x9 configuration.

Fig. 1*: Geometry models for 3D corner.*

3.4 Vented deflagrations in congested enclosures

Laboratory scale experiments performed in a 1.44 m x 0.3 m x 0.3 m rectangular channel are also considered. The channel was closed at one end and contained baffle plate obstructions. The baffles were 0.3 m wide, 0.05 m high and 0.005 m thick. The selected tests had either two baffles located at 0.48 and 0.96 m from the closed end of the channel or four baffles at 0.24, 0.48, 0.96 and 1.44 m from the closed end of the channel. The gas used as fuel was either 100 vol.% hydrogen or a mixture of 75 vol.% hydrogen and 25 vol.% nitrogen. The mixtures were ignited near the centre of the closed end of the channel. Pressure transducers were mounted on the side-wall of the vessel at 0.06 m from the floor, P1 at 0.135 m, P2 at 0.65 m and P3 at 1.135 m from the end of the channel. Figure 2 illustrates the four baffles configuration and the location of the pressure transducers and the ignition source.

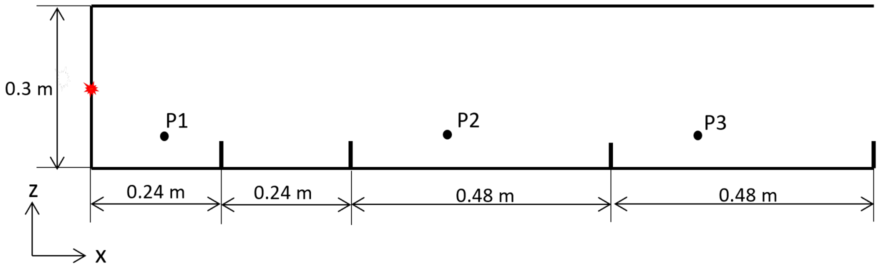

Fig. 2*: Sketch of the 1.44 m long explosion channel.*

Hydrogen deflagrations in 20-foot shipping containers were investigated as part of the HySEA project (Skjold, 2018) at the Gexcon test site outside Bergen, Norway. The tests with venting from the roof and a pipes rack located at the centre of the container are used in this work for validation of the models. Details about the geometry are given by Skjold et al. (2017). The hydrogen concentration was either 21 vol.% or 24 vol.%. The vent openings on the roof of the container were covered with either commercial panels or plastic sheets and the number was either four, six or eight. The ignition source was located at the centre of the floor. The pressure sensors inside the container were located symmetrically 0.2 m above the floor of the container and 0.085 m from the side walls. P01-P02 were located at 0.58 m, P03-P04 at 2.153 m, P05-P06 at 3.690 m, and P07-P08 at 5.245 m from the back wall of the container.

4 Results and discussion

This section summarizes the results for each experimental campaign. Only one grid size is used for discussion since the focus of this paper is to compare the model predictions when using different burning velocity models. The grids used follow the current guidelines in the FLACS-CFD User's Manual (Gexcon AS, 2021).

4.1 Deflagration in the open

Figure 3 shows the flame radius with time for the hemispherical balloon tests. The experimental flame propagation with time was derived from video analysis from three high-speed cameras. The flame radius of the flame was derived by averaging the values of the flame position along the radial paths between 45° and 135° respect to the ground. The uncertainty related to the determination of the flame position from picture analysis was estimated to be ±5% (García et al., 2010). The grid size used for the simulations is 60 cm. The predicted flame arrival time by both FLACS-CFD versions is higher than observed in the experiments. The observed initial flame speed is about 40 m/s and increases to about 80 m/s when the flame radius is about 8 m. The flame speed decreases after the flame radius is about 15 m. The estimated simulated flame speed varied from about 60 m/s to about 80 m/s.

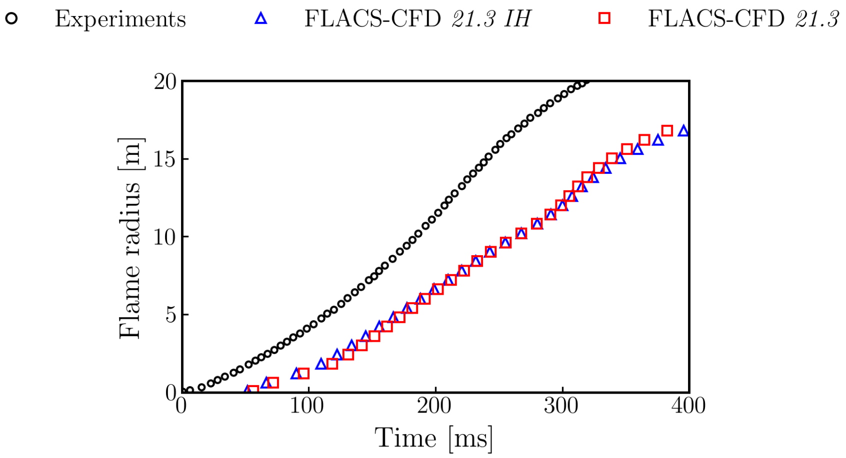

***Fig. 3**: Flame position with time for the balloon test.*

4.2 Deflagration in an open congested area

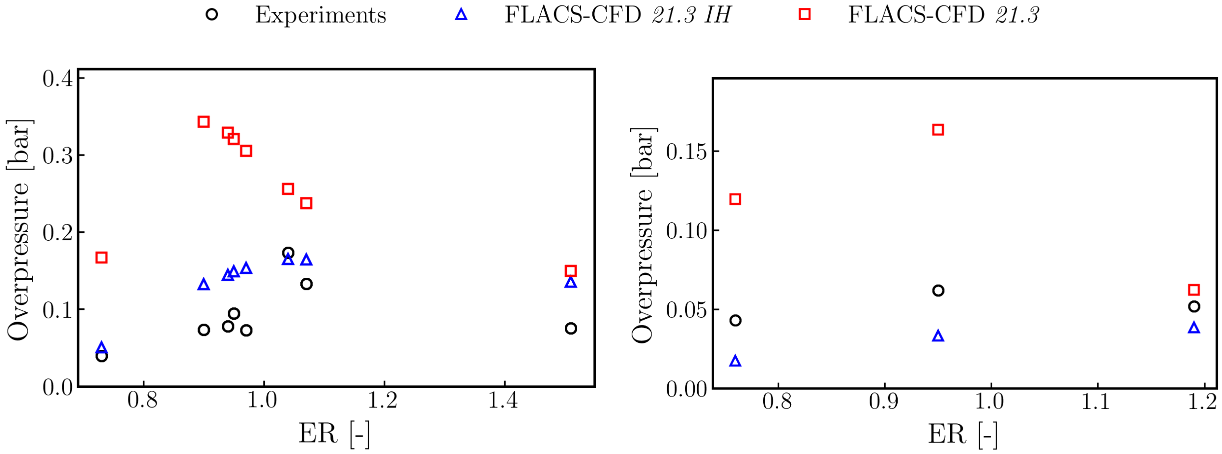

(a) Hydrogen. *(b) 75 vol.% hydrogen and 25 vol.% nitrogen.*

***Fig. 4**: Maximum overpressure with equivalence ratio for the 3D corner experiments.*

Figure 4 shows the maximum overpressure with equivalence ratio for the congested unconfined experiments, the 3D corner, for the hydrogen (a) and the hydrogen-nitrogen tests (b). The grid resolution used in simulations is 2.3 cm. Both experiments and FLACS-CFD *21.3 IH* predict an increase in maximum overpressure with increasing equivalence ratio for the pure hydrogen tests with ER varying from 0.73 to 1.04. The maximum overpressure predicted by FLACS-CFD *21.3* is highest for the test with ER=0.9 and decreases with increasing ER. Simulations with both FLACS-CFD versions predict a decrease in maximum overpressure for the tests with ER of 1.07 and 1.51 relative to the test with ER=1.04. Figure 4b shows the variation of the maximum overpressure with equivalence ratio for the congested unconfined experiments with 75 vol.% hydrogen and 25 vol.% nitrogen. The maximum overpressure increases with the equivalence ratio for the lean hydrogen-nitrogen-air mixtures tested, as for the hydrogen-air mixtures.

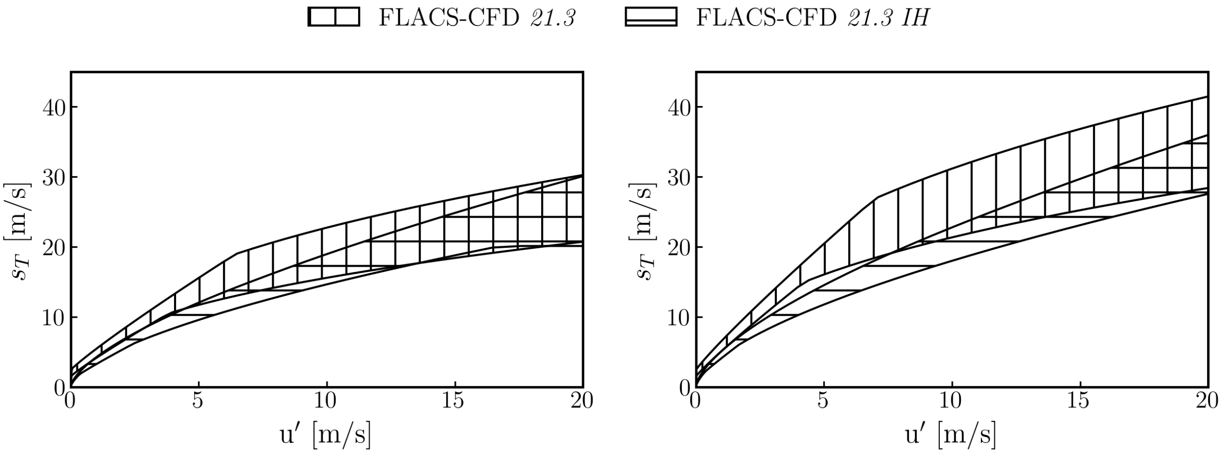

(a) l_C *= 2 mm.*

(b) l_C *= 10 mm.*

***Fig. 5**: Turbulent burning velocities as a function of* u' *for hydrogen-air mixtures with ER in the range [0.6, 1.6].*

The maximum overpressure occurs when the flame reaches the end of the rig. For the lean hydrogen-air mixture tests, the laminar burning velocity in FLACS-CFD *21.3* is higher than in FLACS-CFD *21.3 IH*. The initial flame propagation is driven by the quasi-laminar regime and the flame speed predictions by both FLACS-CFD versions are similar. Once the flame reaches the first rows of obstacles, the turbulent burning regime dominates and FLACS-CFD *21.3* predicts a faster flame propagation, resulting in a higher pressure peak. For the test with ER=1.51, the laminar burning velocity of FLACS-CFD *21.3 IH* is higher than for FLACS-CFD *21.3*, the computed quasi-laminar burning velocity is also higher, resulting in a faster initial flame propagation and higher turbulence levels. However, the difference in turbulent burning velocity is not significant and the maximum overpressure predicted by FLACS-CFD *21.3* is slightly higher. Figure 5 shows the turbulent burning velocity computed by the models in both versions for l_C=2 mm and 10 mm (on the order of the value predicted for these scenarios) and varying u'. This suggest that the overpredictions by FLACS-CFD *21.3* for lean hydrogen-air mixtures are related to the use of the Lewis number correction to the laminar burning velocity that is used in the turbulent burning regime calculations. In FLACS-CFD *21.3 IH* the Markstein number effects on the burning velocity are different for the different regimes.

4.3 Vented deflagrations in an empty enclosure

Figures 6 and 7 show the pressure-time curves and flame speed vs distance from ignition for the vented explosion tests in the empty enclosure (FM Global tests). The pressure-time curves were filtered using a 80 Hz low pass filter. The grid resolution used in simulations is 10 cm. Figure 6a

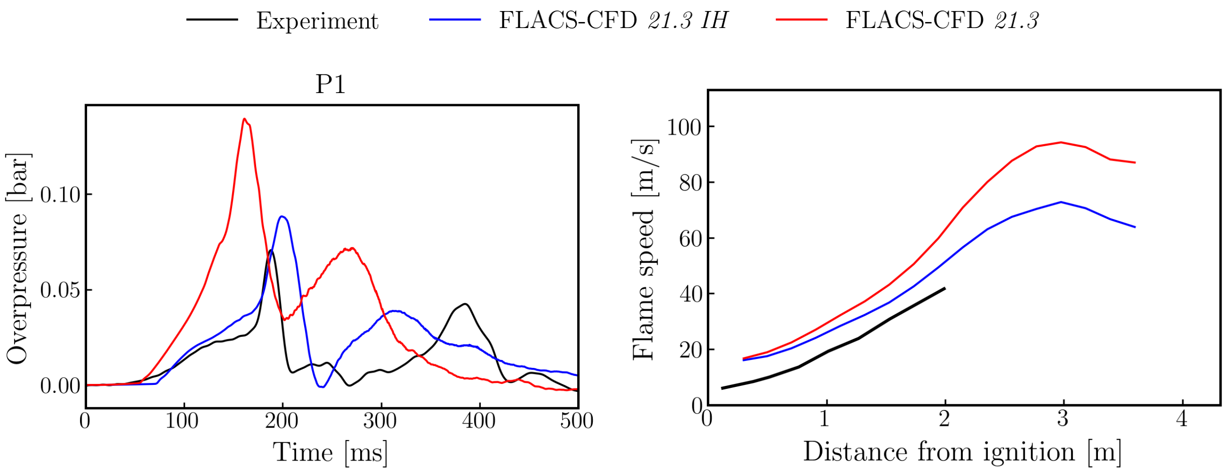

(a) Pressure-time curves. *(b) Flame speed vs distance from ignition.*

***Fig. 6**: FM Global test with 18 vol.% hydrogen.*

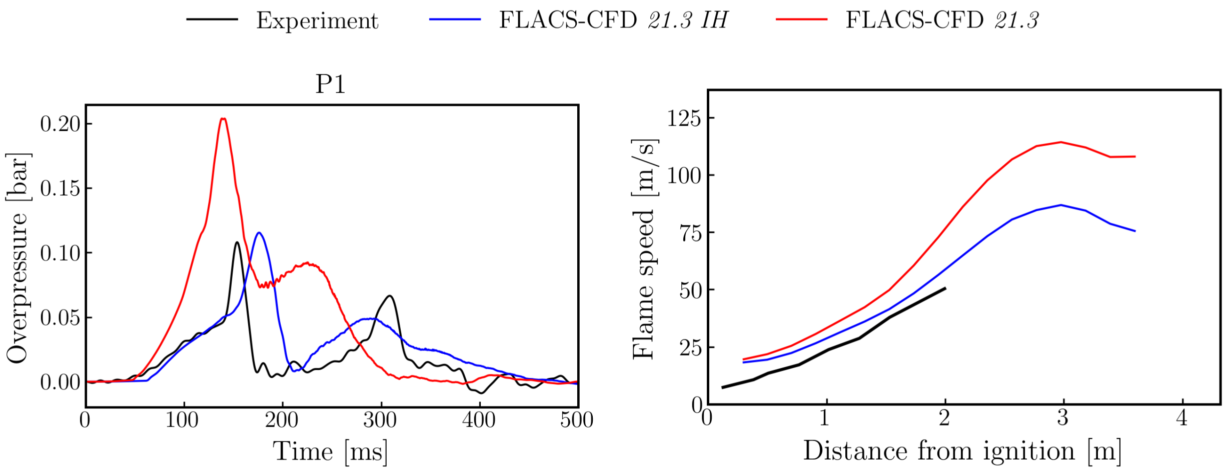

(a) Pressure-time curves. *(b) Flame speed vs distance from ignition.*

***Fig. 7**: FM Global test with 19 vol.% hydrogen.*

shows the pressure-time curves for the tests with a concentration of 18 vol.% hydrogen in air. Both FLACS-CFD versions predict two pressure-peaks as observed in the experiments. The increase in overpressure slows down at about 100 ms after ignition in the experiments and after about 150 ms in the predictions by FLACS-CFD *21.3 IH*. When the flame reaches the vent opening, the rate of pressure rise increases and the expelled hydrogen burns outside of the chamber. The first peak occurs when the fuel outside the chamber is burned. The second peak occurs when the flame reaches the side walls of the chamber. Figure 6b shows the flame speed vs distance from ignition for the test with 18 vol.% hydrogen-air. The initial flame speed is overpredicted by ±60-80% by FLACS-CFD *21.3* and by ±40-60% by FLACS-CFD *21.3 IH*. The simulated burning velocity inside the chamber is governed by the quasi-laminar regime, while for the external explosion, the turbulent burning velocity governs the flame propagation. The maximum flame speed predictions by FLACS-CFD *21.3* are about 23 m/s higher than the predictions by FLACS-CFD *21.3 IH* and occur outside of the chamber. The first peak, related to the external explosion, is therefore higher for the simulations with FLACS-CFD *21.3*. The flame propagation inside the chamber is also faster in the predictions by FLACS-CFD *21.3* and results in a higher second peak.

The two pressure peaks for the scenario with 19 vol.% hydrogen are higher than for the 18 vol.%

hydrogen scenario. The time between the occurrence of the peaks is also shorter.

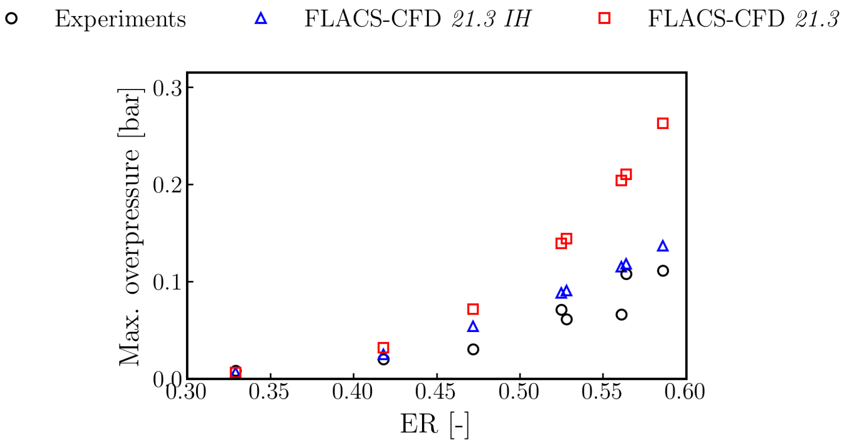

***Fig. 8**: Maximum overpressure with equivalence ratio for the FMGlobal experiments.*

Figure 8 shows the maximum overpressure, due to the external explosion, with equivalence ratio for the FM Global experiments in the empty chamber. The increase in maximum overpressure with the equivalence ratio for the lean hydrogen-air mixtures presented is more pronounced in the simulations than in the experiments. For the highest equivalence ratios considered, the predictions by FLACS-CFD *21.3* are more than two times higher than the maximum overpressure observed in the experiments.

4.4 Vented deflagrations in congested enclosures

Figure 9 shows the pressure-time curves for Test09/Test47 and for Test32/Test34 at the three pressure transducers located in the 1.44 m channel. The pressure-time curves are filtered using a Savitzky-Golay filter of zero order with a time window of 0.1 ms. Test09 and Test47 were performed in the channel with two baffles filled with a stoichiometric hydrogen-air mixture. Similar trends were observed for simulations and experiments. The pressure starts to increase at P1, the increase starts earlier for the simulations with FLACS-CFD *21.3 IH* because of higher predictions of s_{QL}, which is dominant before the flame passes the first baffle. When the unburnt fuel starts being pushed out of the channel, the pressure increase flattens for a short period. After the flame passes the second baffle, the turbulent burning regime dominates and FLACS-CFD *21.3* predicts higher overpressures due to higher predictions of s_T. The first peak occurs when the flame reaches the open end of the channel. The second peak occurs when the expelled fuel burn outside of the channel. The second peak travels inwards in the channel and is less visible for P3 pressure transducer located closest to the exit of the channel. Test32 and Tests34 were performed in the channel with four baffles and a hydrogen mixture with an equivalence ratio of 0.6. The pressure development is similar to that of Test09 and Test47 with two baffles. However, for ER=0.6 the s_{QL} predictions by both versions are alike and the initial flame propagation is similar.

Figure 10 shows the maximum overpressure inside the channel as a function of the equivalence ratio for the tests with two baffles (a) and for the tests with four baffles (b). Both FLACS-CFD versions capture the trends of maximum overpressure with equivalence ratio observed in the experiments. The predicted overpressures by FLACS-CFD *21.3 IH* for the two geometry configurations are within a factor of two of the values observed in the experiments for lean hydrogen-air mixtures, for rich hydrogen-air mixtures, the overprediction increases with the equivalence ratio

Results for the HySEA experiments are shown in Figure 11. The filtered pressure-time curves (using a 50 Hz filter) for the two scenarios with repetitions (venting through eight and six commercial panels) are presented. The maximum overpressure was similar at the different sensors and only P4 is shown in

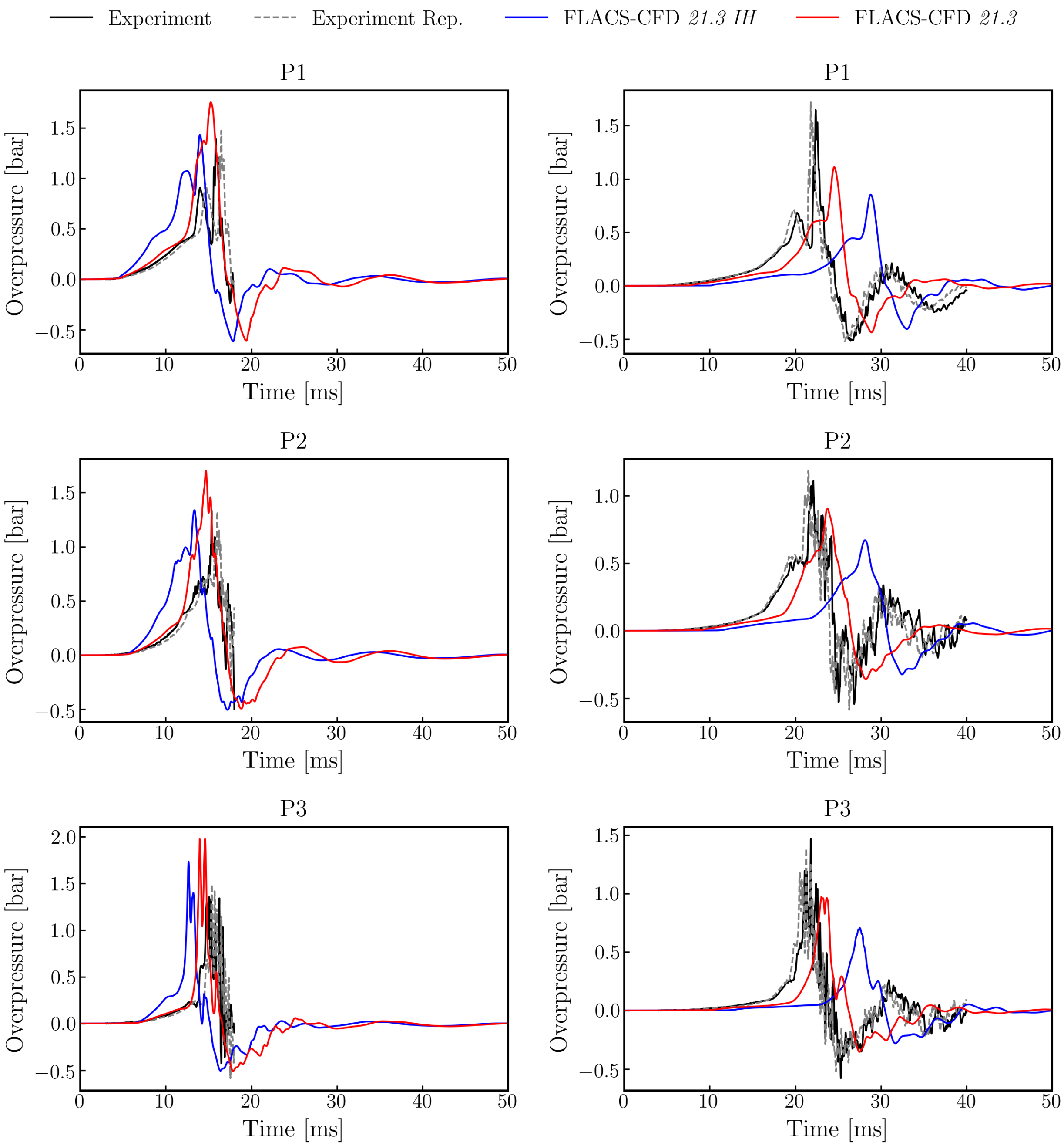

(a) Two baffles and ER=1. *(b) Four baffles and ER=0.6.*

***Fig. 9**: Pressure-time curves for the tests in the 1.44 long channel.*

the figure. The pressure starts increasing slowly until the flame moves through the first row of pipes. In this phase, the flame propagation is governed by the quasi-laminar regime. The flame propagation is faster in the FLACS-CFD *21.3* than in the FLACS-CFD *21.3 IH* predictions because of the higher laminar burning velocity used in the quasi-laminar burning velocity model. When the flame passes through the obstacles, the turbulent regime dominates. The maximum overpressure occurs when the flame reaches the vent opening. Figure 12 shows the predicted vs the measured maximum overpressure for the HySEA experiments in a scatter plot. Each point correspond to a pressure transducer for a given test. The overall overpredictions of the peak overpressures are considerably reduced using the FLACS-CFD *21.3 IH* instead of the FLACS-CFD *21.3* version. The FLACS-CFD *21.3 IH* predictions that do not fall within a factor 2 correspond to the tests with commercial vent panels. The predictions are quite sensitive to the modelling of the panels and overprediction in those scenarios may be related

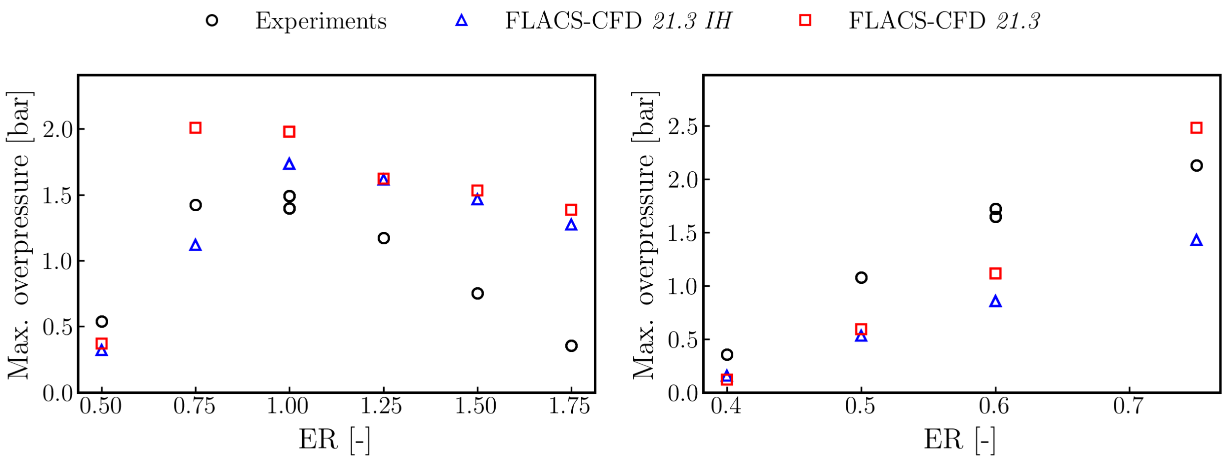

(a) 4 baffles. *(b) 2 baffles.*

Fig. 10: *Maximum overpressure with equivalence ratio for the 1.44 m long channel experiments with hydrogen.*

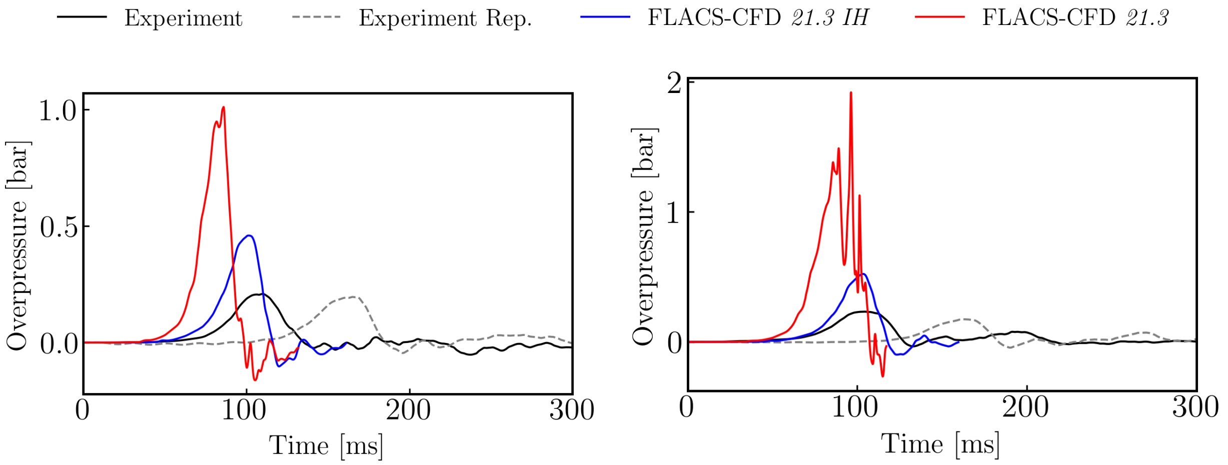

(a) Eight commercial panels. *(b) Six commercial panels.*

Fig. 11: *Pressure-time curves at pressure transducer P4 for the HySEA experiments.*

to the representation of the opening of the panels (Skjold et al., 2019). The severe overpredictions in FLACS-CFD *21.3* seem to be related to the Lewis correction applied to the laminar burning velocity that enhances the burning velocity in all regimes for the equivalence ratios used in these experiments.

5 Conclusions

A set of relevant experimental campaigns for evaluating the validity of the burning velocity models used in advanced consequence tools has been presented. The performance of two versions of the CFD tool FLACS, FLACS-CFD *21.3* and FLACS-CFD *21.3 IH*, has been evaluated. FLACS-CFD *21.3 IH* predicts the maximum overpressure for the experiments in this paper with better accuracy than FLACS-CFD *21.3*. Except for the HySEA experiments, the predictions by FLACS-CFD *21.3 IH* for lean hydrogen mixtures are within a factor 2 of the values observed in the experiments. Improvements of the model are needed for more accurate prediction of deflagrations of rich hydrogen mixtures. FLACS-CFD *21.3 IH* uses empirical correlations expressed in terms of the Markstein strain number to compute the quasi-laminar and the turbulent burning velocities. Even though the model predicts the maximum overpressure trends observed in the experiments with better accuracy than FLACS-CFD

DOI: 10.7795/810.20221124

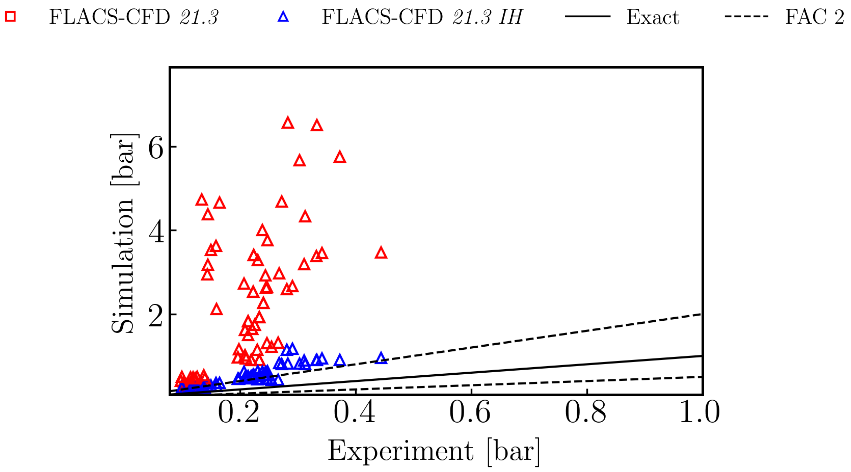

***Fig. 12**: Scatter plot of maximum overpressure at each sensor for the HySEA experiments.*

21.3, the model has important limitations. The correlations were implemented to be valid only for initially atmospheric pressures and standard ambient temperatures, and for mixtures of hydrogen with air (no added inerts). For mixtures with other fuels, a simple volume fraction-weighted approach was used. There is no available data for all fuels in the literature and the correlations used here might not be equally valid for other fuels or pressure and temperature conditions. Thus, further work should focus on studying the possibility of model improvements to include more fuels and mixtures. The strain-rate Marsktein number datasets could be computed from one-dimensional detailed chemistry flame solvers such as CosiLab or Cantera. New mixture rules and correlations for pressure and temperature might be needed. Alternative models with less dependency on datasets should also be considered.

Acknowledgements

The authors gratefully acknowledge the financial contribution from the Research Council of Norway (project number 317782) through the Industrial Ph.D. scheme.

References

Bauwens, C., Chao, J., Dorofeev, S. (2012). *Effect of hydrogen concentration on vented explosion overpressures from lean hydrogen-air deflagrations*. International Journal of Hydrogen Energy, 37(22):17599 – 17605.

Becker, T., Ebert, F. (1985). *Vergleich zwischen experiment und theorie der explosion grober, freier gaswolken*. Chemie Ingenieur Technik, 57(1):42 – 45.

Bradley, D., Lawes, M., Liu, K., Mansour, M. (2013). *Measurements and correlations of turbulent burning velocities over wide ranges of fuels and elevated pressures*. Proceedings of the Combustion Institute, 34(1):1519 – 1526.

Breitung, W., Dorofeev, S. A., Kotchourko, A., Redlinger, R., Scholtyssek, W., Bentaib, A., Heriteau, J.-P., Pailhories, P., Eyink, J., Movahed, M., Petzold, K.-G., Heitsch, M., Alekseev, V., Denkevits, A., Efimenko, A., Okun, M., Huld, T., Baraldi, D. (2005). *Integral large scale experiments on hydrogen combustion for severe accident code validation-hycom*. Nuclear Engineering and Design, 235:253–270. doi:10.1016/j.nucengdes.2004.08.063.

García, J., Baraldi, D., Gallego, E., Beccantini, A., Crespo, A., Hansen, O., Høiset, S., Kotchourko, A., Makarov, D., Migoya, E., Molkov, V., Voort, M., Yanez, J. (2010). *An intercomparison exercise on the capabilities of cfd models to reproduce a large-scale hydrogen deflagration in open atmosphere*. International Journal of Hydrogen Energy, 35(9):4435 – 4444.

Gexcon AS (2021). *FLACS-CFD v*21.2 *User Manual*. Technical report, Gexcon AS, Bergen, Norway.

Han, W., Dai, P., Gou, X., Chen, Z. (2020). *A review of laminar flame speeds of hydrogen and syngas* *measured from propagating spherical flames*. Applications in Energy and Combustion Science, 1:100008.

Hisken, H. (2018). *Investigation of instability and turbulence effects on gas explosions: experiments and modelling*. Ph.D. thesis, University of Bergen.

Launder, B. E., Spalding, D. B. (1974). *The numerical computation of turbulent flows*. Computer Methods in Applied Mechanics and Engineering, 3(2).

Lucas, M., Atanga, G., Hisken, H., Mauri, L., Skjold, T. (2021). *Simulating vented hydrogen deflagrations: Improved modelling in the cfd tool flacs-hydrogen*. International Journal of Hydrogen Energy, 46(23):12464–12473. ISSN 0360-3199. doi:https://doi.org/10.1016/j.ijhydene.2020.09.073. ICHS 2019 Conference.

Makarov, D., Verbecke, F., Molkov, V., Roe, O., Skotenne, M., Kotchourko, A., Lelyakin, A., Yanez, J., Hansen, O., Middha, P., Ledin, S., Baraldi, D., Heitsch, M., Efimenko, A., Gavrikov, A. (2009). *An inter-comparison exercise on cfd model capabilities to predict a hydrogen explosion in a simulated vehicle refuelling environment*. International Journal of Hydrogen Energy, 34(6):2800 – 2814. ISSN 0360-3199. doi:https://doi.org/10.1016/j.ijhydene.2008.12.067.

Middha, P. (2010). *Development, use, and validation of the CFD tool FLACS for hydrogen safety studies*. Ph.D. thesis, Department of Physics and Technology, University of Bergen.

Middha, P., Hansen, O., Groethe, M., Arntzen, B. (2007). *Hydrogen explosion study in a confined tube: Flacs cfd simulations and experiments*. In *Twenty-first International Colloquium of Dynamics of Explosions and Reactive Systems*.

Royle, M., Shirvill, L., Roberts, T. (2007). *Vapour cloud explosions from the ignition of methane/hydrogen/air mixtures in a congested region*. In *Second International Conference on Hydrogen Safety*.

Sato, Y., Merilo, E., Groethe, M., Colton, J., Chiba, S., Iwabuchi, H. (2006). *Homogeneous hydrogen deflagrations in a sub-scale vehicle tunnel*. In *Fifteenth World Hydrogen Energy Conference*.

Skjold, T. (2018). *Vented hydrogen deflagrations in 20-foot iso containers*. Twelfth International Symposium on Hazards, Prevention and Mitigation of Industrial Explosions, pages 823 – 846.

Skjold, T. (2020). *On the strength of knowledge in risk assessments for hydrogen systems*. Proceedings of the Thirteenth International Symposium on Hazards, Prevention and Mitigation of Industrial Explosions, pages 72 – 84.

Skjold, T., Hisken, H., Bernard, L., Mauri, L., Atanga, G., Lakshmipathy, S., Melodia, L., Carcassi, M., Schiavetti, M., Rao, V., Sinha, A., Wen, J., Tolias, I., Giannissi, S., Venetsanos, A., Stewart, J., Hansen, O., Kumar, G., Krumenacker, L., Laviron, F., Jambut, R., Huser, A. (2019). *Blind-prediction: Estimating the consequences of vented hydrogen deflagrations for inhomogeneous mixtures in 20-foot iso containers*. Journal of Loss Prevention in the Process Industries, 61:220 – 236.

Skjold, T., Hisken, H., Lakshmipathy, S., Atanga, G., van Wingerden, M., Olsen, K.L.and Holme, M., Turøy, N., van Wingerden, K. (2017). *Experimental investigation of vented hydrogen deflagrations in containers. phase 1: Homogeneous mixtures*. Technical report, Report HySEA-D2-04-2017: 314pp.

Taylor, S. C. (1991). *Burning velocity and the influence of flame stretch*. Ph.D. thesis, University of Leeds, UK.

Proceedings of the 14th International Symposium
on Hazards, Prevention and Mitigation of Industrial Explosions

DOI: 10.7795/810.20221124

Characterizing the Reactivity of Large-Scale Dust Explosions Using a Dimensionless Two-Parameter Combustion Model

C. Regis L. Bauwens, Lorenz R. Boeck & Sergey B. Dorofeev

FM Global, Research Division, Norwood, USA

E-mail: carl.bauwens@fmglobal.com

Abstract

Explosion protection is a critical safety measure to mitigate and prevent dust explosions at facilities handling combustible dusts. It is a great challenge, however, to adequately design these protection systems, as the severity of the explosion depends on both the inherent reactivity of the dust, as well as the specific configuration of the enclosure and the level of turbulence present. Currently, the most commonly used parameter to assess the reactivity of a dust is its deflagration index, K_{st}, which is related to the maximum rate of pressure rise measured in a standardized test apparatus. It is important to note, however, that this quantity is entirely empirical in nature and only assesses the relative hazard presented by a combustible dust. The lack of a comprehensive dust reactivity measure creates a significant issue for interpreting the results of the large-scale experimental work that has been performed to develop engineering guidelines used to protect enclosures or evaluate the performance of explosion protection devices.

This work describes the dimensionless formulation of a simple dust combustion model that considers two main parameters, an effective turbulent burning velocity, $S_{T,0}$, and a dimensionless reaction time, χ. By fitting the model results with the pressure-time series obtained during an explosion experiment, these two parameters can fully characterize the reactivity of a specific test. Using this approach, the values of these parameters have been obtained for a collection of over 170 large-scale dust explosion experiments performed in vessels ranging from 2.5 to 25 m^3. Based on these results, a model for predicting χ using dust properties is being developed, which shows good general agreement with the experimentally fitted values.

Keywords: *dust explosions, dust reactivity, large-scale testing*

1. Introduction

Dust explosions present a severe hazard at facilities where combustible dusts are present. To mitigate the consequences of these events, explosion protection measures are commonly deployed, such as explosion venting, suppression, and isolation. It is a great challenge, however, to adequately design these explosion protection systems, as the severity of a dust explosion depends on both the inherent reactivity of the dust, which can vary significantly (Eckhoff, 2003), as well as the specific configuration of the enclosure and the level of turbulence present.

Extensive work has been performed to characterize the reactivity of dusts. Many of these studies have attempted to quantify a fundamental laminar burning velocity for different combustible dusts (Bradley et al., 1989, Van Wingerden et al. 1996, Goroshin, 1996, Julien et al., 2015), analogous to those obtained for gaseous flame. These measurements, however, are challenging to perform, and do not capture the effect of turbulence, which significantly affects the propagation rate of a dust flame and the severity of an explosion (Amyotte et al., 1988). Furthermore, as the reactivity of a dust is highly dependent on properties that are specific to a given dust sample, such as particle size distribution (Di Benedetto et al., 2010), these velocities cannot be effectively used for practical applications.

Instead, a parameter referred to as the dust deflagration index, K_{st}, is much more commonly used to characterize the reactivity of a specific dust sample. The value of K_{st} is determined by the maximum rate of pressure rise, $(dP/dt)_{\max}$ for a vessel volume, V, obtained in a standardized test apparatus with a fixed level of initial turbulence:

$$K_{st} = \left(\frac{dP}{dt}\right)_{\max} V^{1/3} \tag{1}$$

It is important to note, however, that this quantity is entirely empirical in nature and only assesses the relative hazard presented by a combustible dust, as the actual severity is strongly affected by the level of initial turbulence present. Furthermore, while the use of K_{st} may be effective for assessing the relative hazard presented by different dusts, it is often inadequate at describing the overall behavior of large-scale dust explosions (Eckhoff, 2015).

The lack of a comprehensive dust reactivity measure creates a significant issue for interpreting the results of large-scale experimental work that has been performed to develop engineering guidelines used to protect enclosures or evaluate the performance of protective devices. Currently, these tests are characterized by an effective deflagration index, referred to as K_{eff}, which is tuned by varying the level of initial turbulence to obtain a value that is equivalent to the K_{st} of a specific class of dust. The deflagration index K_{eff}, however, only characterizes the reactivity at a single time, typically late in the combustion process when the flame approaches the vessel walls. As a result, experiments performed with consistent values of K_{eff} can produce significantly different rates of pressure rise at the critical early phase of the explosion when an explosion protection device must activate.

This work describes the development of a simple constant volume dust combustion model that considers both the effect of initial turbulence and the physical properties of the dust that can be used to characterize the effective reactivity of large-scale dust explosions. The model is then compared with an extensive collection of large-scale experiments performed in vessels ranging from 2.5 to 25 m^3 to demonstrate how this two-parameter model can accurately reproduce the pressure transients that develop during large-scale dust explosion experiments.

2. Model development

The model used in this study is an extension of a previously developed dust reactivity model, (Bauwens et al., 2020), that has been rederived based on the same underlying assumptions and expressed in dimensionless terms. In this model, turbulent dust flame propagation is considered where the dust within the burning region is consumed over a finite reaction time. The model assumes that the propagation of the leading edge of the flame front is governed by turbulent mixing, which entrains a mixture of unburned dust/air into the flame or burning region. Within this region, which is characterized by an effective flame radius, r_f, the unburned mixture is not consumed instantaneously, and a mixture of burned and unburned dust is present. As typical dust explosions are fuel-rich, the reaction time within the burning region is modeled by considering the consumption rate of the oxidizer using a simple mass balance. The general model formulation is similar to that proposed by Tamanini (Tamanini, 1993), with a different treatment of the underlying model assumptions, as described below.

The model equations are derived considering mass and energy conservation, consistent with previously developed models (Chao et al., 2015, Boeck et al. 2021) for gas flames, where the rate of combustion is evaluated on a mass basis (Boeck et al. 2021). The mass fraction of oxidizer is split into three quantities that are tracked individually: the unburned mass fraction upstream of the flame,

x_u; the unburned mass fraction within the flame region, $x_{f,u}$; and the burned mass fraction within the flame region, $x_{f,b}$. As the total mass of oxidizer is conserved in a closed volume, the mass balance is given by:

$$1 = x_u + x_{f,u} + x_{f,b}. \tag{2}$$

Assuming spherical flame propagation, the rate of change of the unburned mass fraction is governed by the rate at which unburned mass enters the flame region:

$$\frac{dx_u}{dt} = -\frac{3r_f^2 S_T \rho_u^*}{R^3}, \tag{3}$$

where S_T is the turbulent propagation velocity of the leading edge of the flame, ρ_u^* the gas density of the oxidizer in the unburned region normalized by the initial gas density, and R is the effective radius of the vessel, $R = (3V/4\pi)^{1/3}$. The propagation velocity of the leading edge of the flame is assumed to be governed by turbulent mixing at the scale of the flame radius and is proportional to the turbulent fluctuation velocity at this scale. For a Kolmogorov cascade, this yields an increase of S_T with flame radius due to the increased range of turbulent length scales involved in mixing as the flame grows:

$$S_T = ku'\left(\frac{r_f}{R}\right)^{\frac{1}{3}}, \tag{4}$$

where u' is the turbulent fluctuation velocity at an integral scale and k is a proportionality coefficient. As both the level of initial turbulence, u', and the proportionality factor, k, are not typically known, and are difficult to characterize independently, they are combined into a single reactivity parameter, $S_{T,0} = ku'$, which represents a characteristic turbulent burning velocity. Note that this quantity is specific to a given dust and experimental setup, as it depends on both the dust properties and the level of turbulence present. For the purpose of this model, it is assumed that $S_{T,0}$ is an effective value that remains constant throughout the explosion. It is also important to note that this model formulation has an intrinsic characteristic time:

$$\tau' = \frac{R}{S_{T,0}}, \tag{5}$$

which is proportional to the time needed for the flame front to reach the vessel boundary. To generalize the solution to various vessel sizes, one can define a dimensionless time, $t^* = t/\tau'$, and a dimensionless flame radius, $r_f^* = r_f/R$. In dimensionless terms, Eq. (3) becomes:

$$\frac{dx_u}{dt^*} = -3r_f^{*\,7/3}\rho_u^*. \tag{6}$$

The accumulation of unburned mass within the flame region depends on the balance between the rate at which upstream gas enters the flame region, and the rate unburned gas within the flame region is consumed:

$$\frac{dx_{f,u}}{dt^*} = 3r_f^{*\,7/3}\rho_u^* - \frac{dx_{f,b}}{dt^*},\ r_f^* < 1 \tag{7}$$

$$\frac{dx_{f,u}}{dt^*} = -\frac{dx_{f,b}}{dt^*},\ r_f^* = 1. \tag{8}$$

For the conditions typically present in a dust explosion, it can be shown that both the Taylor and Kolmogorov scales of turbulence significantly exceed the dust particle radii, and the local transport of fuel and oxidizer in the vicinity of the particle are in the laminar regime. As a result, it is assumed that the consumption rate of the oxidizer is governed by molecular diffusion and the dust properties, and the consumption rate is proportional to both the dust concentration and the molecular diffusion coefficient:

$$\frac{dx_{f,b}}{dt^*} = \frac{\tau'}{\tau}\frac{{T_f^*}^{1.75}}{P^*}\left(\frac{x_{f,u}}{x_{f,u}+x_{f,b}}\right), \tag{9}$$

where τ is a characteristic burning time, which is dependent on various dust material properties, such as particle size and the molecular diffusion coefficient; P^* is the vessel pressure normalized by the initial pressure; and T_f^* is the average temperature within the flame region normalized by the initial temperature. The pressure and temperature dependence of the diffusion coefficient is explicitly retained in Eq. (9) such that the characteristic time τ is invariant to the change in pressure and temperature that occurs during a constant volume dust explosion. The average temperature within the flame region is approximated as:

$$T_f^* \approx \frac{\sigma x_{f,b}+x_{f,u}}{x_{f,b}+x_{f,u}}, \tag{10}$$

where the expansion ratio σ is the ratio of unburned to burned gas density at ambient pressure, estimated as $P_\mathrm{m}/P_0 - 1$, where P_m is the constant volume explosion pressure. Assuming isentropic compression, the unburned and burned gas densities at a given pressure can be expressed as:

$$\rho_u^* = P^{*\frac{1}{\gamma_u}}, \quad \rho_b^* = \frac{1}{\sigma}P^{*\frac{1}{\gamma_b}}, \tag{11}$$

where γ_u and γ_b are the unburned and burned specific heat capacity ratios, respectively. As these values are poorly defined for a dust/air mixture, it is assumed that $\gamma_u = \gamma_b = \gamma'$ to simplify the calculation, where γ' is an effective specific heat ratio. The value of γ' that yields the correct constant volume explosion pressure, P_m, and expansion ratio is calculated using the following expression (Boeck et al., 2021):

$$\gamma' = \frac{\log(P_0/P_m)}{\log(1/\sigma)}. \tag{12}$$

To evaluate the instantaneous vessel pressure from the mass balance within the enclosure, we first note that the total vessel volume is constant:

$$1 = \frac{x_{f,b}}{\rho_b^*} + \frac{x_u+x_{f,u}}{\rho_u^*}, \tag{13}$$

and Eqs. (11) and (13) can be combined to yield the following expression for the normalized pressure:

$$P^* = \left[(\sigma-1)x_{f,b}+1\right]^{\gamma'}. \tag{14}$$

The flame radius is then obtained from the flame volume, $V_f^* = x_{f,b}/\rho_b^* + x_{f,u}/\rho_u^*$:

$$r_f^* = \left(1 - \frac{x_u}{(\sigma-1)x_{f,b}+1)}\right)^{1/3}. \tag{15}$$

In dimensionless terms, a single parameter, $\chi = \tau/\tau'$, representing the ratio of consumption to propagation time, characterizes the overall behavior of the model, as shown in Fig. 1. Although the general solution depends on this parameter, any comparison with experimental data requires converting the time and length scales through $V^{1/3}$, $S_{T,0}$ and σ. The model suggests that, for a given shape of the pressure rise curve, the maximum rate of pressure rise scales with $V^{1/3}$, which is consistent with the volume scaling of K_st and K_eff.

DOI: 10.7795/810.20221124

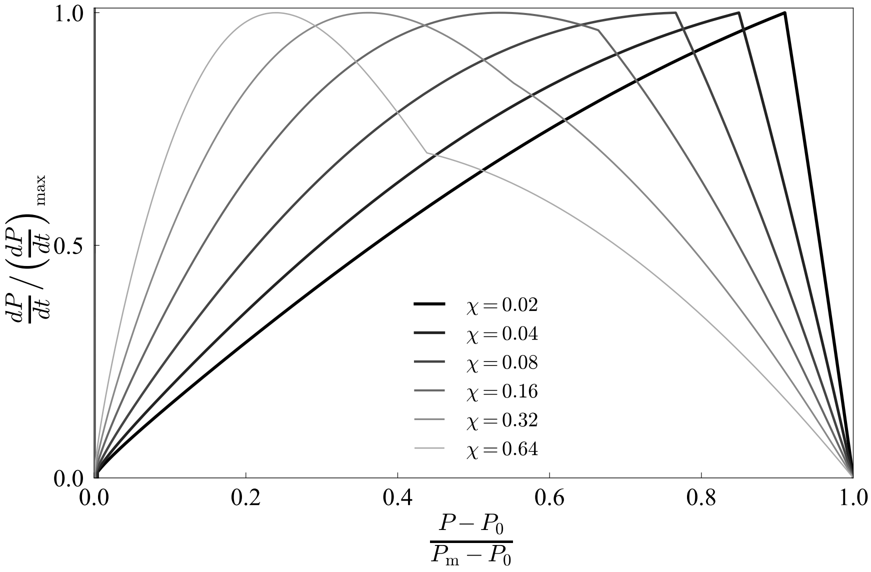

Fig. 1: *Generalized model results as a function of normalized pressure over a range of the dimensionless parameter,* χ.

3. Comparison of model results with experimental data

In order to create a consistent method of extracting values of χ and $S_{T,0}$ from the experimental test data, an automated fitting routine was developed. The routine first compares the normalized rate of pressure rise with the model results to find the value of χ that minimizes the difference between the model and experimental curves, as a function of the dimensionless pressure. Next the routine compares the rate of pressure rise in dimensional terms to obtain a best fit value for $S_{T,0}$.

To illustrate the performance of the dust combustion model and the automated fitting routine, a comparison is made with closed volume dust explosion experiments performed in an 8-m^3 vessel with a height-to-diameter ratio of 1.45, shown in Fig. 2, as described in previous studies (Chao, 2015b, Boeck et al., 2021).

DOI: 10.7795/810.20221124

Fig. 2: *Image of the 8-m^3 test vessel showing the location of three dust injectors.*

Representative model results are compared with experimental data in Fig. 3, for two dusts, powdered sugar and cornstarch, where the ignition delay was tuned to produce similar values of the maximum rate of pressure rise, and the deflagration index K_{eff}. This figure illustrates how two experiments that produce the same value of K_{eff} can display significantly different pressure rise profiles and how the two-parameter model can effectively reproduce the rate of pressure rise and characterize the overall shape of the pressure profile.

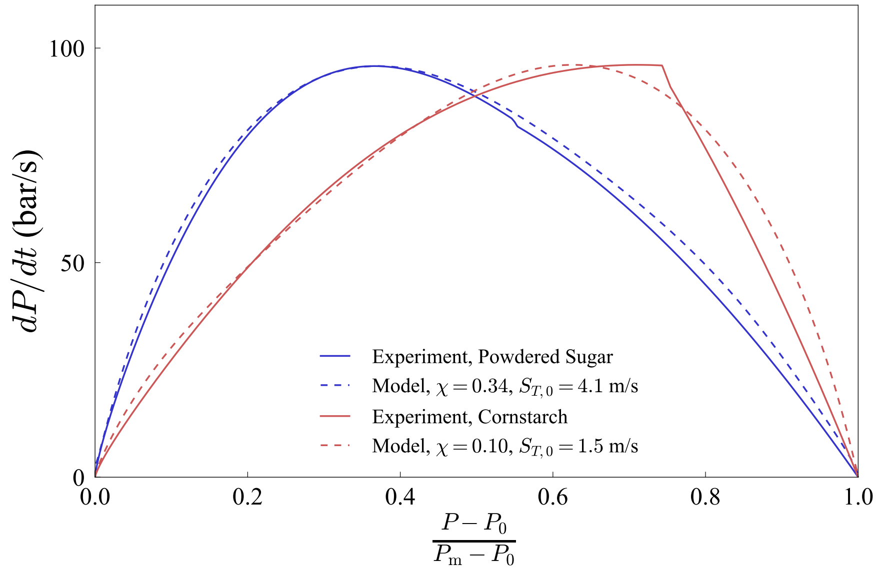

Fig. 3: *Illustrative model comparison with cornstarch and powdered sugar experiments performed in an 8-m^3 vessel.*

A dimensionless dust deflagration index, K^*_{eff}, can also be defined relating the overall maximum rate of pressure rise, analogous to K_{eff}:

$$K^*_{\text{eff}} = \frac{K_{\text{eff}}}{\sigma P_0 S_{T,0}}. \tag{16}$$

By exercising the model, it was found that the dimensionless deflagration index is weakly dependent on the constant volume explosion pressure, roughly scaling with $(P_m/P_0)^{1.08}$. This dimensionless dust deflagration index was compared with a collection of 176 large-scale experiments performed in three geometrically similar vessels with volumes of 2.5, 8, and 25 m^3 over a wide range of ignition delays, for several different dusts, and at multiple dust loadings, and the results are shown in Fig. 4. A monotonic relationship between the dimensionless dust reactivity parameter K_{eff}^* and the dimensionless parameter χ was found, where the maximum rate of pressure rise decreases with χ for a given value of $S_{T,0}$. These results show good agreement between the model calculations and experiments when the values of K_{eff}^* and χ were automatically fitted to each experimental pressure profile.

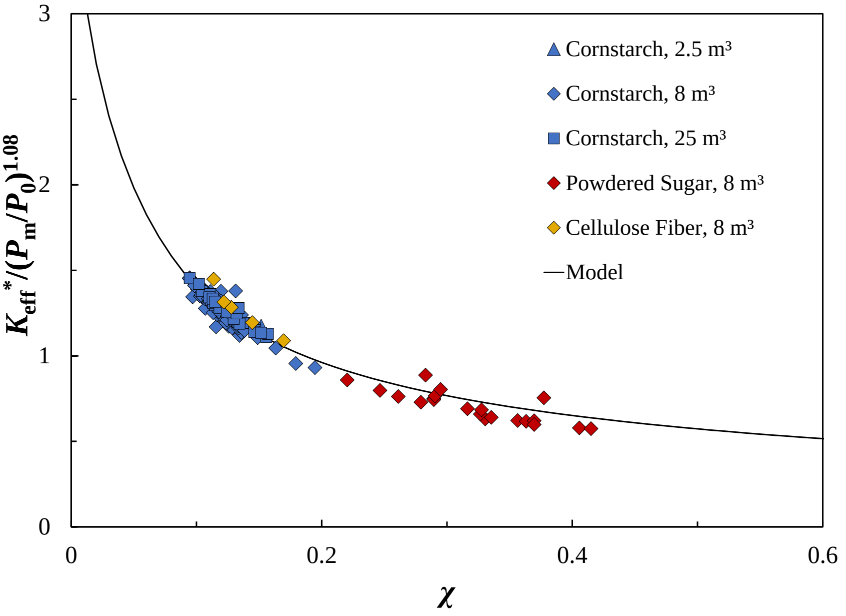

Fig. 4. *Variation of K_{eff}^* as a function of parameter χ.*

4. Estimation of parameter χ from dust properties

Parameter χ is defined as the ratio of the characteristic time τ given by the complex two-phase burning process, generally at length scales that are below the inertial turbulent cascade, and the characteristic time τ' of the transport of oxidizer to these scales, which is governed by the inertial cascade.

To examine the effect of dust properties on the characteristic time, τ, it is necessary to estimate the length scales present within the dust cloud itself. For a typical dust loading of 750 g/m^3, which was found to maximize the reactivity of cornstarch in a 20-L sphere, and a particle density of 1.6 g/m^3, the average distance between particles is approximate 13 particle radii and is independent of the particle size. It can be assumed that the oxidizer consumption starts with entrainment of oxidizer at large scale, proceeds through turbulent transport and ends with laminar transport to the individual particles.

For an ensemble of particles with a number density N in a burning cloud of radius r_f, the total mass flux of oxidizer transported to the particle scale is given by the total entrainment flux divided by the number of particles:

$$\dot{m}_T \sim \frac{4\pi\rho_g S_T r_f^2}{\frac{4}{3}\pi r_f^3 N}, \tag{17}$$

where ρ_g is the local gas density.

For the combustion of an individual particle, we will qualitatively follow a classical approach describing the gasification and burning of fuel particles or liquid droplets (Law, C. K., 1982). This approach is based on the conservation of steady one-dimensional mass and energy flows to and from a fuel particle. The flame is formed at a distance from the particle where the evaporated fuel and oxidizer are consumed in a thin flame sheet. As there are several simplifying assumptions in this model, some of which, if applied directly, may not be valid for nonstationary dust explosion conditions, the following discussion will be focused on qualitative relationships and general functional dependences.

According to the classical particle burning model, the fuel mass flux from gasifying a particle is a combination of the fuel evaporation flow (blowing) and molecular diffusion. Thus, the total fuel mass flow rate is higher than the flux driven purely by diffusion, and the same is true for the total mass flow rate $\dot{m}$ of the oxidiser and its diffusive mass flux, $\dot{m}_D$, at the particle scale. The ratio between these flow rates is given by:

$$\frac{\dot{m}}{\dot{m}_D} \sim \ln(1+B), \tag{18}$$

where B is the Spalding transfer number:

$$B = \frac{C_{pg}(T_\infty - T_S) + \left(\frac{Y_{O\infty}}{s}\right)Q}{H}. \tag{19}$$

In Eq. (19),C_{pg} is the gas phase heat capacity, T_∞ and T_s are the temperatures far from particle and of the particle, respectively, $Y_{\text{O}\infty}$ is the oxidizer mass fraction far from the particle, s is the stoichiometric oxidizer to fuel mass ratio, Q is the heat of combustion of the fuel, and H is the heat of gasification of the fuel.

The diffusion mass flux of oxidizer to a single particle is proportional to the particle size and the molecular diffusion coefficient:

$$\dot{m}_D \sim 4\pi\rho_g D r_s. \tag{20}$$

where r_s is the particle radius.

Combined with Eq. 18, this yields the total oxidiser mass flux at the particle scale:

$$\dot{m} \sim 4\pi\rho_g D r_s \ln(1+B). \tag{21}$$

Thus, the ratio of the transport mass flux to the burning mass flux is given by the ratio of the right-hand sides of Eqs. 17 and 21:

$$\frac{\dot{m}_T}{\dot{m}} \sim \frac{3S_T}{4\pi r_f N D r_s \ln(1+B)}. \tag{22}$$

Replacing the number density N with the dust loading m, $N = 3m/4\pi r_s^3 \rho_s$, where ρ_s is the density of an individual particle, Eq. 22 yields:

$$\frac{\dot{m}_T}{\dot{m}} \sim \frac{S_T \rho_S r_S^2}{m D r_f \ln(1+B)}. \tag{23}$$

Noting that when the flame touches the vessel walls $r_f = R$ and $S_T = S_{T,0}$ and recognizing that $S_{T,0}/R$ is defined as $1/\tau'$ in Eq. (5), we can see that Eq. (23) is inversely proportional to τ'. As the remaining terms, $\rho_S r_S^2/mD \ln(1+B)$, are proportional to τ, Eq (23) can be rewritten as:

$$\frac{\dot{m}_T}{\dot{m}} \sim \frac{S_{T,0}}{R} \cdot \frac{\rho_s r_s^2}{mD\ln(1+B)} \sim \frac{\tau}{\tau'} \sim \chi, \tag{24}$$

making the ratio of the transport mass flux of oxidizer to the burning mass flux proportional to χ. The term ρ_s/m in τ represents the mass of oxidizer reacting with a single particle, where higher values of m increase the consumption rate of the oxidizer. The term $\ln(1+B)$ represents the material properties captured by the Spaulding number, however, the logarithmic function makes the influence of these properties weak relative to the quadratic scaling of the particle size. It is worth noting that, although χ is considered a model constant, in reality $\dot{m}_T/\dot{m}$ varies with the flame radius due to changes of S_T/r_f.

Thus far, the material properties for cornstarch (CS) and powdered sugar (PS) were obtained through testing at an external laboratory, as summarized in Table 1. Using these properties, the values of χ extracted from the experimental results were compared with the predictions of Eq. 24 in Fig. 5 for all 176 experiments that were previously described. These results also include a small number of experiments performed using cellulose fiber (CF). Note that only the proportionality of fitted and estimated values of χ is evaluated here and, without introducing a model constant, only the general trend is compared.

Table 1: *Summary of dust properties used*

Dust	r_s (μm)	ρ_s (kg/m^3)	H_v (kJ/kg)	H_c (kJ/kg)
Cornstarch	7	1,450	257	16,496
Powdered Sugar	12.5	1,500	276	17,698
Cellulose Fiber	65	50	67	16,496

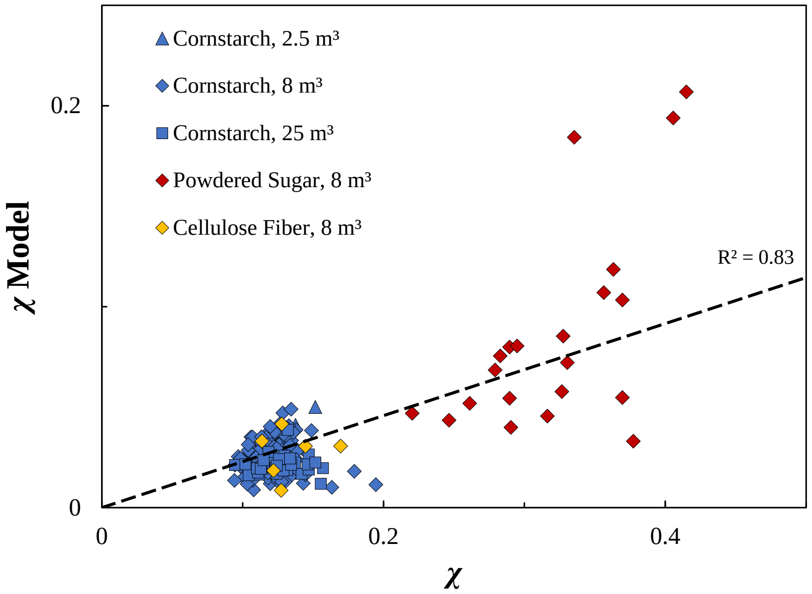

Fig. 5. *Comparison of χ fitted by the model and estimates by Eq. 23.*

While the scatter of data is significant, due to the inherent variability of dust explosion experiments performed across a range of test volumes and injection systems, the overall trend is in good agreement, particularly the general trend between CS and PS dusts. Current research is focusing on extending this study to a wider range of fuels and dust loadings, which will be performed using a single consistent test apparatus.

5. Conclusions

In this study, a dimensionless dust-flame combustion model is derived based on a characteristic turbulent burning velocity and a finite reaction time. Using an automated fitting routine considering only two parameters, the model was able to reproduce the entire experimental pressure time-histories of over 170 experiments performed for a range of dusts in volumes ranging from 2.5-25 m^3. The results also showed that the shape of the rate of pressure rise curve can vary significantly for experiments performed in the same apparatus, where the maximum rate of pressure rise can occur at considerably different pressures in tests producing the same effective deflagration index. This demonstrates how the use of a single parameter, such as K_{eff}, is insufficient to characterize the behavior of large-scale explosions and the need for a better method to characterize dust explosions.

Based on this modelling approach, a framework for estimating how the parameter χ varies with fundamental dust properties has been developed, which reproduces the overall trends seen in experiments performed using cornstarch and powdered sugar dusts. With this model, equivalency between different experimental setups can be established by fitting the model parameters $S_{T,0}$ and χ to the measured pressure profiles. Furthermore, this model can also provide a basis for future methods of explosion hazard evaluation that consider the level of initial turbulence and the material properties of the specific dust present.

Acknowledgements

The work presented in this paper was funded by FM Global and performed within the framework of the FM Global Strategic Research Program on Explosions and Material Reactivity. The technical assistance of Kevin Mullins, Thomas Lapierre, and Joseph Marte in preparing and conducting the tests is greatly appreciated.

References

Amyotte, P. R., Chippett, S., & Pegg, M. J. (1988). Effects of turbulence on dust explosions. Progress in Energy and Combustion Science, 14(4), 293-310.

Bauwens, C.R., Boeck, L.R., & Dorofeev, S.B. (2020). A simple dust combustion model for characterizing reactivity in large-scale experiments. *13th ISHPMIE, Braunschweig, Germany.*

Boeck, L. R., Bauwens, C. R., & Dorofeev, S. B. (2021). Modeling of explosion dynamics in vessel-pipe systems to evaluate the performance of explosion isolation systems. Journal of Loss Prevention in the Process Industries, 71, 104477.

Bradley, D., Chen, Z., & Swithenbank, J. R. (1989). Burning rates in turbulent fine dust-air explosions. In *Symposium (International) on Combustion* (Vol. 22, No. 1, pp. 1767-1775). Elsevier.

Chao, J., Lee, J. H., Bauwens, C. R., & Dorofeev, S. B. (2015a). Laminar burning velocities of various silanes. Journal of Loss Prevention in the Process Industries, 36, 471-477.

Chao, J., & Dorofeev, S. B. (2015b). Evaluating the overall efficiency of a flameless venting device for dust explosions. Journal of Loss Prevention in the Process Industries, 36, 63-71.

Di Benedetto, A., Russo, P., Amyotte, P., & Marchand, N. (2010). Modelling the effect of particle size on dust explosions. *Chemical Engineering Science*, 65(2), 772-779.

Eckhoff, R.K. (2003). Dust explosions in the process industries. Third edition. Gulf Professional Publishing, Amsterdam.

Eckhoff, R. K. (2015). Scaling of dust explosion violence from laboratory scale to full industrial scale–A challenging case history from the past. Journal of Loss Prevention in the Process Industries, 36, 271-280.

Goroshin, S., I. Fomenko, and J. H. S. Lee. "Burning velocities in fuel-rich aluminum dust clouds." In *Symposium (International) on Combustion*, vol. 26, no. 2, pp. 1961-1967. Elsevier, 1996

Julien, P., Vickery, J., Goroshin, S., Frost, D. L., & Bergthorson, J. M. (2015). Freely-propagating flames in aluminum dust clouds. *Combustion and Flame*, *162*(11), 4241-4253.

Law, C. K. (1982). Recent advances in droplet vaporization and combustion. Progress in energy and combustion science, 8(3), 171-201.

Tamanini, F. (1993). Characterization of mixture reactivity in vented explosions. 14th International Colloquium on the Dynamics of Explosions and Reactive Systems (pp. 1-6). Coimbra, Portugal: University of Coimbra.

Van Wingerden, K., Stavseng, L., & Bergen, N. (1996). Measurements of the laminar burning velocities in dust-air mixtures. *VDI-Berichte*, *1272*, 553-564.

DOI: 10.7795/810.20221124

The role of vapor fraction in hydrocarbon mist explosion

Stephanie El-Zahlanieh [a], Amélie Jean [a], Alexis Vignes [b] & Olivier Dufaud [a]

[a] Université de Lorraine, CNRS, LRGP, Nancy, France
[b] INERIS, Parc Technologique ALATA, BP 2, F-60550, Verneuil-en-Halatte, France

E-mail: stephanie.el-zahlanieh@univ-lorraine.fr

Abstract

The modern world depends greatly on hydrocarbons which are ubiquitous, indispensable fuels used in nearly every existing industry. Although important, their use may trigger dangerous incidents, whether in their production, handling, storage, or transporting phase, especially when aerosolized. In light of proposing a standard procedure to assess the flammability and explosivity of fuel mists, a new test method was established based on the EN 14034 standard. For the previous purposes, a gravity-fed mist generation system was designed and employed in a modified 20 L explosion vessel. This test method allowed the determination of the ignition sensitivity of several fuels. In addition, their explosion severity was represented by the explosion overpressure P_m, and the rate of pressure rise dP/dt_m, two thermo-kinetic parameters determined with a specifically developed control system and custom software. Nonetheless, a noticeable difference in the ignition sensitivity and the explosion severity was perceived when changing suppliers or petroleum cuts of some fuels. Moreover, sensitivity studies showed that both the droplet size distribution and the temperature of the droplets play a significant role in fuel mist explosion. These parameters can be directly related to the vapor fraction surrounding a droplet during its ignition. Consequently, this study focuses on the influence of varying the composition of three well-known and abundantly used fuels. Different petroleum cuts were introduced in different fractions into isooctane, Jet A1 aviation fuel, and diesel fuel mixtures which were then aerosolized into a uniformly distributed turbulent mist cloud and ignited using spark ignitors of 100 J. Subsequently, the same tests were executed in a vertical flame propagation tube coupled with a high-speed video camera allowing the visualization of the flame and the determination of the spatial flame velocity, and estimation of the laminar burning velocity. The latter was also estimated from the pressure-time evolution in the 20 L sphere using existing correlations. Indeed, the determination of the laminar burning velocity can be useful in modeling such accidents. Finally, highlighting the essential role of the mist and vapor fraction during their ignition has led to a better understanding of their explosion mechanisms.

Keywords: *mist, aerosol explosion, petroleum cuts, flame propagation, explosion severity, hybrid explosion*

1. Introduction

Over the years, the chemical and petrochemical sectors have seen a substantial number of explosions caused by liquid aerosol dispersions (Santon, 2009). These mist explosion incidents do not cease to take place and lead to human and material losses. Concerns over such incidents have grown as it became evident that they can occur at temperatures below the flashpoint of the aerosolized liquid (Eichhorn, 1955), and that, although the ATEX standards recognize the dangers of flammable mists, their categorization is still limited to this flashpoint. Indeed, while the classification of flammable gases and dust clouds is well-established, that of liquid aerosols remains less so. This is mainly due to a lack of scientific data and knowledge in such a matter.

The increased interest and concern in mitigating mist explosion incidents call for a standardized test method to evaluate such risks and for a greater understanding of the influence of external conditions. To address this issue, a test procedure based on the EN 14034 standard is proposed allowing the assessment of fuel mists' flammability and explosivity in a confined explosion vessel, well-known as the 20 L explosion sphere. Experiments were performed mainly on Jet A1 aviation fuel, B7 diesel fuel, and isooctane mists generated into the 20 L sphere using a Venturi-based spray nozzle. A considerable difference in ignitability was perceived, as fuel suppliers were changed or with the aging of the fuels. Therefore, in addition to the determination of the explosion severity, represented by the explosion overpressure (P_m) and the rate of pressure rise (dP/dt_m), and the ignition sensitivity, represented by the lower explosive limit (LEL) and the minimum ignition energy (MIE), this study emphasizes the influence of varying vapor fractions in the mist clouds on their ignitability and explosivity. Experiments were coupled with an evaporation model based on the d^2-law allowing the quantification of the liquid/vapor ratio in the 20 L sphere under specified conditions. Moreover, Jet A1 – methane hybrid mixtures were tested in order to specify different explosion regimes and highlight the contribution of the mist in such explosions. Complementary tests will be performed in a flame propagation tube allowing the estimation of the laminar burning velocity and its comparison to theoretical values calculated from the thermo-kinetic parameters.

2. Experiments

In the light of studying the influence of the vapor fraction on fuel mist ignitability and explosivity, experiments were carried out on binary isooctane-diesel blends, isooctane-Jet A1 blends, and hybrid mixtures of Jet A1 and methane gas. The blends were characterized by their flashpoint and compared by their ignition time $\tau_{ignition}$ and their explosion thermo-kinetic parameters P_m and dP/dt_m. MIE experiments were also performed to assess the ignitability of the mentioned blends. Hybrid explosion (Jet A1 + CH_4) experiments were, as well, carried out to identify explosion regimes and to pinpoint the contribution of mist in such explosions.

2.1 Tested fuels

The proposed test method, detailed in Section 2.2, was established using a variety of fuels (ethanol, isooctane, diesel, kerosene, biodiesel, light fuel oil, hydraulic oil). For this study, however, Jet A1 aviation fuel, B7 diesel fuel, and isooctane were the main focus as they are widely used in industries, and as they exhibit different physicochemical and thermodynamic properties. One should not overlook the involvement of these fuels in mist explosions. Indeed, diesel mist releases have caused a considerable number of explosions, notably in the marine sector (Reina del Pacifico, 1974, Miss Dorothy towing vessel, 2021, etc.) (Eckhoff, 2005; NTSB, 2022). Kerosene mist releases were involved in seven out of the 29 incidents reported by Santon (2009). Both fuels appeared in many incident reports, such as Lees et al. (2019) and Yuan et al. (2021). However, commercially available fuels, such as Jet A1 aviation fuel and B7 diesel fuel, have a wide range of compositions, making them difficult to investigate in-depth (Dumitrescu et al., 2011). Therefore, isooctane was introduced to both fuels to form a constant, easily quantifiable, vapor fraction allowing the comparison and understanding of their ignitability and explosivity.

Table 1 demonstrates the separate physicochemical properties of the three fuels following characterization tests such as the Hoeppler Falling-Ball viscometry, the Pendant Drop surface tension measurement, and the flashpoint determination using the Setaflash Series 3 flashpoint apparatus.

The following blends were prepared for this study:

- B7 diesel + 5, 7, 9, and 15 $\%_{v/v}$ isooctane
- Jet A1 + 2, 5, 10, and 25 $\%_{v/v}$ isooctane

Preliminary tests showed that the addition of isooctane had negligible effects on the physical properties of the mixture, and hence on the droplet size distribution. On the other hand, this addition triggered an important decrease in the flashpoint as shown in Figure 1 in the case of diesel-isooctane blends. Similar tendencies were observed for Jet A1-isooctane blends. It should be noted that the final point at 100 $\%_{v/v}$ isooctane is not experimental, as the flashpoint apparatus does not test for temperatures lower than 0 °C.

***Table 1:** Physicochemical properties of Jet A1, diesel, and isooctane*

Fuel	**Jet A1**	**Diesel B7**	**Isooctane**
Density (kg.m^{-3})	840	880	690
Dyanmic viscosity (mPa.s)	1.2	2.95	0.45
Surface tension (kg.s^{-2})	0.026	0.027	0.018
Flashpoint (°C)	40	65	-12
Boiling point (°C)	130-300	150-390	99

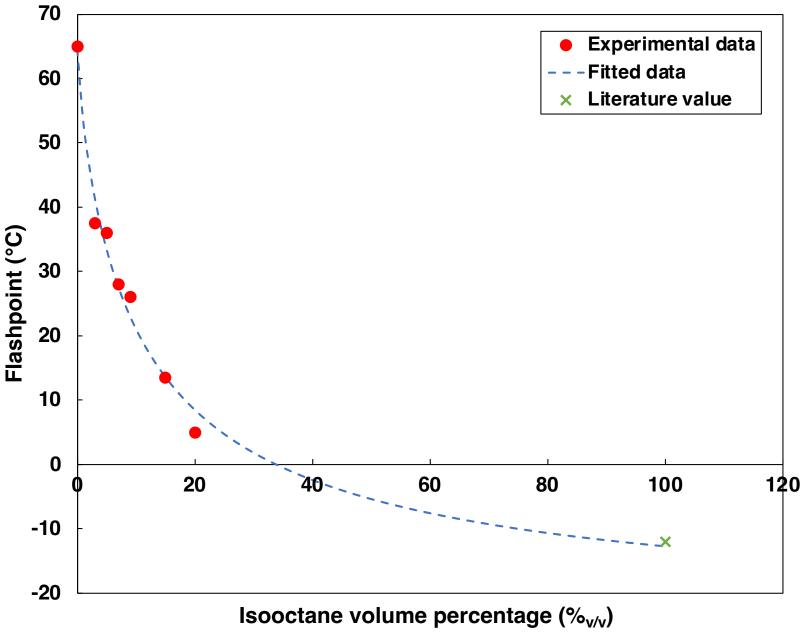

***Fig. 1.** Evolution of the flashpoint as a function of the volumetric percentage of isooctane in an isooctane-diesel blend*

For the evaporation model detailed in Sections 2.4 and 3.4, the vapor pressure of each of the three fuels was required to determine their vapor fractions. For these purposes, the following equations, found in literature, were used for each fuel:

- Jet A1:

$$P_{vap} = 5.76 \times 10^6 . \exp\left(\frac{-4191}{T}\right) \qquad \text{(Shepherd et al., 1997)}$$

where P_{vap} is the vapor pressure in mbar, and T is the absolute temperature in K

- Diesel fuel:

$$\ln(P_{vap}) = 99.4943 - \frac{7332.14}{T} - 12.8127 \ln(T) + 0.0128504T \qquad \text{(Safarov et al., 2018)}$$

where P_{vap} is in Pa, T is in K

- Isooctane:

$$\log P_{vap} = 3.93679 - \frac{1257.84}{T-52.415} \qquad \text{(Willingham et al., 1945)}$$

where P_{vap} is in bar and T is in K

In the case of a mixture, Raoult's law $P = \sum_i P_i x_i$ is applied to measure the total vapor pressure with the assumption of an ideal solution based on the basic microscopic premise that intermolecular interactions between dissimilar molecules are equal to those between similar molecules and that their molar volumes are equal.

2.2 Ignitability and explosivity of fuel mist

As advised by the EN 14034 standard, the test apparatus employed in this study is the standardized 20 L explosion sphere. To mimic industrial leaks, a spray nozzle equipped with a Venturi junction was used to aerosolize the fuel into the sphere from the bottom. The injection duration and pressure were controlled using electronic valves, allowing the regulation of the mist's concentration, its droplet size distribution, and its level of turbulence, as well as the ignition delay. After injection, the mist cloud would then be instantaneously ignited (t_v = 3 ms) with a permanent spark of 100 J. Two piezoelectric pressure sensors allow the tracking of the pressure-time evolution during an explosion and then the determination of P_m and dP/dt_m using a specifically developed control and data acquisition system allowing the full control and safe operation of the explosion vessel and the optimal interpretation of the experimental data. An ignition is considered to take place when an overpressure of at least 0.5 bar relative to the initial pressure occurs, permitting the determination of both the lower explosive limit (LEL) and the minimum ignition energy (MIE).

All the experiments performed for this study were carried out using a spray nozzle of an orifice diameter of 0.45 mm and an injection pressure of 2.9 bar, ensuring a uniformly distributed mist cloud of median diameters varying between 8 and 10 µm and a constant turbulence level. Concentrations were limited to about 160 $g.m^{-3}$ in order to avoid long injection durations, which enhance coalescence, sedimentation, or droplet-droplet interactions. Indeed, concentrations in this study are expressed as the injected mass divided by the vessel's volume. However, an exact estimation of the concentration in the sphere is required.

2.3 Flame propagation

Researchers like Burgoyne & Cohen (1954), and Polymeropoulos & Das (1975) were interested in studying the effect of droplet sizes on flame propagation in a liquid aerosol. Indeed, it is of interest to visualize eventual flame deformations by the presence of droplets on the flame front and any change to the flame propagation speed. Moreover, the laminar burning velocity of a fuel-air combination is an inherent, intrinsic parameter that may be employed in sophisticated simulations to assess the effects of an explosion under specified conditions. This parameter was evaluated via flame propagation visualization in a 1-meter-long flame propagation tube with a square cross-section of 7 cm^2. The latter was coupled with a high-speed video camera (Phantom VEO 410L) to analyze the first moments of the flame kernel growth, before touching the tube's walls. Video analyses were carried out using a model developed by Cuervo et al. (2017). The propagation speed was first estimated using models that suppose that the flame expands spherically and is driven by a one-step exothermic process with the mixture's thermodynamic parameters, such as molecular weight, specific heat, and thermal conductivity, remaining constant and allowing the estimation of the laminar burning velocity.

Values found using the flame propagation tube were then compared to calculations of the laminar burning velocity S_u^0 obtained by Silvestrini's correlation (Silvestrini et al., 2008):

$$S_u^0 = 0.11 \frac{\left(\frac{dP}{dt}\right)_m V^{\frac{1}{3}}}{P_m \left(\frac{P_m + 1}{P_0}\right)^{0.14} \left(\frac{P_m}{P_0}\right)^{\frac{1}{\gamma}}}$$

where *dP/dt*$_m$ is the rate of pressure rise and P_m the explosion overpressure at a specific concentration, P_0 is the atmospheric pressure, and γ is the ratio of specific heats.

Such comparisons may permit to evaluate the appropriate method supplying reliable values of the laminar burning velocity of a mist cloud.

2.4 Droplet evaporation model

A droplet evaporation model, detailed in El – Zahlanieh et al. (2022), was utilized in this study in order to quantify the vapor fraction in the 20 L sphere before ignition. This model was based on the d^2-law, which is a simplified law, developed by Godsave (1953), that represents the evaporation of a single spherical droplet in a uniform-temperature environment, neglecting all exterior interactions. Some modifications were applied to the d^2-law in order to take into account a cloud of mists, its turbulence level, and the possible saturation that might occur in the confined vessel. The main equations used for this model are:

$$d^2 = d_0^2 - Kt$$

where d is the droplet diameter at time t, d_0 is the initial droplet diameter, and K is the evaporation rate constant and is calculated as follows:

$$K = 8D\frac{\rho}{\rho_l}\ln(1 + B_T)$$

where D is the vapor diffusion coefficient, ρ and ρ_l are the vapor and liquid densities respectively, and B_T is the thermal transfer Spalding number.

In order to take into account the turbulence level, K_t is calculated:

$$K_t = K\left(1 + 0.0276Re^{\frac{1}{2}}Sc^{\frac{1}{3}}\right)$$

where Re and Sc are the Reynolds and Schmidt numbers respectively.

Finally, combustion was also considered by including the combustion enthalpy, the oxygen mass fraction in the surrounding environment, and the mass stoichiometry coefficient in the calculation of the thermal and mass transfer Spalding numbers.

3. Results and discussion

3.1 Explosion severity tests

For a range of concentration reaching about 160 $g.m^{-3}$, diesel mists were tested and exhibited explosivity as of 92 $g.m^{-3}$ at 27 °C. However, the same tests were performed with a new batch of diesel from the same supplier, and no explosion took place under the same conditions. This raised the question about the petroleum cut and the vapor fraction of commercial fuels. Isooctane-diesel blends were then tested and showed an increase in explosivity parameters from 4.2 bar and 31 $bar.s^{-1}$ to 5.1 bar and 100 $bar.s^{-1}$ as the isooctane percentage was increased from 5 to 15 $\%_{v/v}$ respectively. Complementary tests will be performed on high turbulence levels and higher concentrations.

The same tests were also carried out on Jet A1 and isooctane blends. As seen in Figure 2, the addition of isooctane increased both P_m and dP/dt_m considerably. Another observed influence would be on the lower explosive limit which shifted from about 80 $g.m^{-3}$ for Jet A1 only to about 45 $g.m^{-3}$ for Jet A1 + 25 $\%_{v/v}$ isooctane. Indeed, the presence of an increased vapor fraction surrounding the droplets facilitated the ignition of the mist cloud. As it can also be seen, the most noticeable difference is observed in the rates of pressure rise at relatively high mist concentrations, showing the influence of an important vapor fraction on the kinetics of the mist explosion.

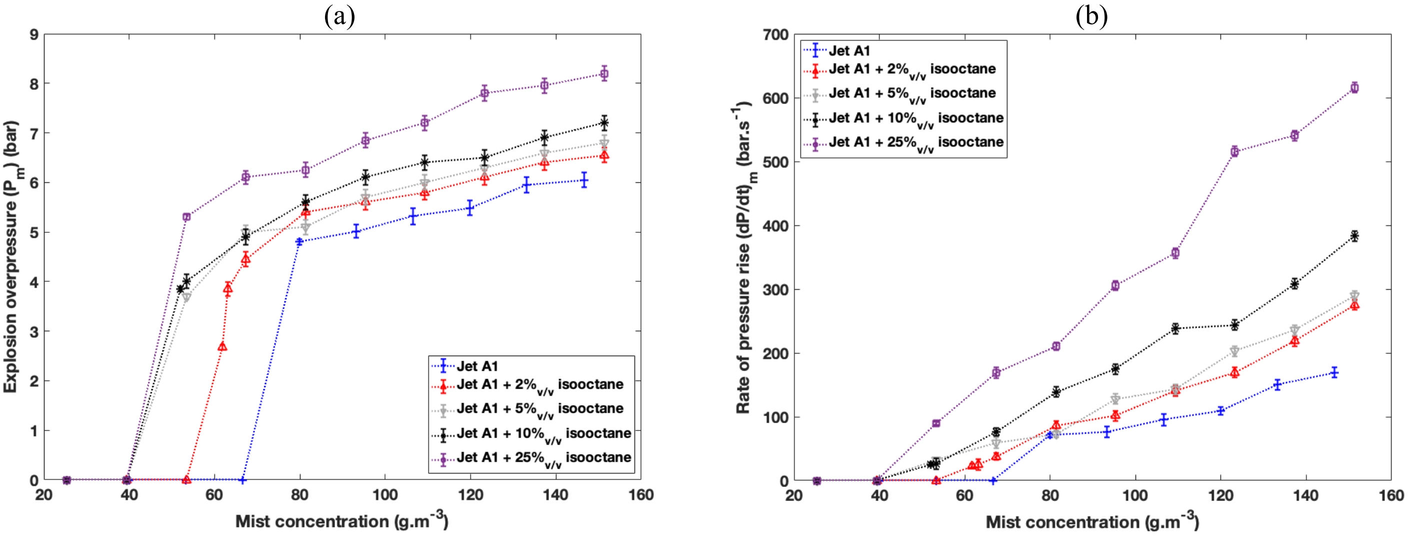

Fig. 2. *Evolution of the explosion overpressure (a) and the rate of pressure rise (b) with mist concentration and isooctane volume percentage*

3.2 Ignition time

For a total mist concentration of about 125 g.m^{-3}, the time necessary to ignite the mist cloud of the five blends was compared. An ignition delay time (IDT) is usually a crucial parameter used by engine designers and can be usually measured at high temperatures and pressures in a shock tube. This parameter is an important macro indicator of a fuel's reactivity (Khaled et al., 2017). When a certain fuel combination is subjected to specific thermodynamic circumstances of pressure and temperature, it takes a certain amount of time for it to oxidize and produce heat. In the current study, this ignition time τ_{ignition} is defined as the time needed for the mist cloud to ignite and reach a maximum rate of pressure rise P_m after the actuation of the ignition source in the 20 L sphere (see Figure 3).

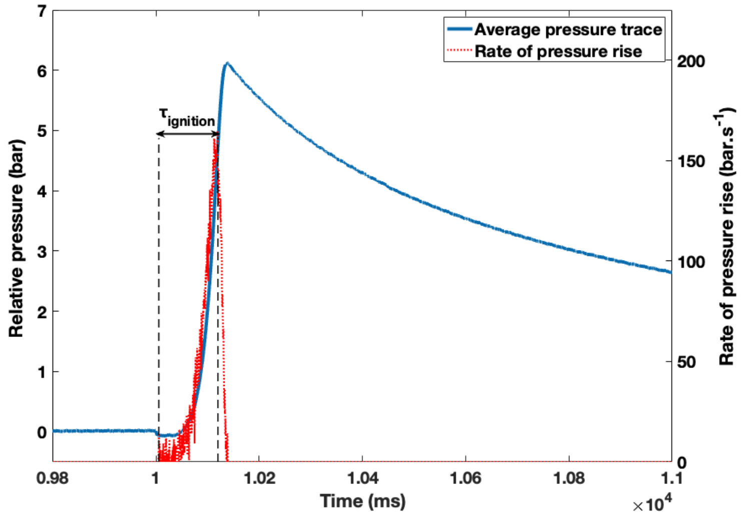

Fig. 3. *Evolution of the explosion pressure and the rate of pressure rise with time*

Figure 4 demonstrates the pressure-time evolution of Jet A1 mist alone, as well as Jet A1-isooctane blends of varying isooctane percentages (2, 5, 10, and 25 $\%_{v/v}$). These tests were all performed at a sphere temperature of 27 ± 0.5 °C and with a 100 J permanent spark that lasts for about 445 ms. The decrease in τ_{ignition} was evident as the isooctane volume percentage increased, showing a significant enhancement and an acceleration of the reactivity with faster rates of pressure rise. Indeed, as shown in Table 2, a Jet A1 mist cloud of 125 g.m^{-3} required 121 ms after the actuation of the spark to ignite and reach 161 bar.s^{-1}. On the other hand, 25 %$_{v/v}$ of isooctane reduced this duration to about its half (59 ms) to reach a dP/dt$_m$ about three times faster (516 bar.s^{-1}). Another observed influence is that on the explosion overpressure, which increases from 5.9 bar to 7.8 bar which could be explained by the higher energy density of isooctane and the domination of a high-temperature energy release governing its ignition (Dumitrescu et al., 2011).

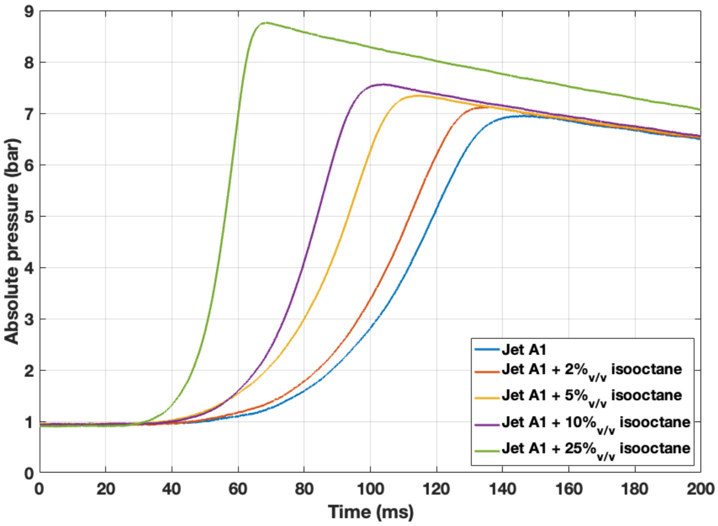

Fig. 4. *Evolution of the explosion pressure for Jet A1 and isooctane blends with time*

Table 2: *Evolution of the ignition delay time as a function of isooctane volume percentage (mist mass concentration 125 g.m^{-3})*

Fuel blend	**$\tau_{ignition}$ (ms)**	**P$_m$ (bar)**	**dP/dt$_m$ (bar.s^{-1})**
Jet A1	121	5.9	161
Jet A1 + 2%$_{v/v}$ isooctane	113	6.1	170
Jet A1 + 5%$_{v/v}$ isooctane	94	6.3	203
Jet A1 + 10%$_{v/v}$ isooctane	85	6.5	244
Jet A1 + 25%$_{v/v}$ isooctane	59	7.8	516

3.3 Minimum ignition energy

Along with the ignition time, the lower explosive limit, and the thermo-kinetic explosion parameters, the minimum ignition energy was influenced by the addition of isooctane. A high-voltage spark ignition system with control of both the voltage and the spark duration was designed to measure this parameter. This system consisted of a Brandenburg 3590-1320 DC/DC converter with a 12 V to 10 kV voltage range, total power of 5 W, and a maximum input current of 0.5 mA. The output of this converter may be changed, allowing for fine-tuning of the energy sent to the mist cloud. To get an exact estimate of the provided ignition energy, the total spark duration and the continuous delivered current would be determined. Table 3 shows the evolution of the MIE with the increase of isooctane volumetric percentage in a 65 g.m^{-3} Jet A1-isooctane blend. As it can be seen, increasing isooctane in the mist cloud renders it easily ignitable as the MIE decreased from a value greater than 900 mJ for Jet A1 mist to a value less than 160 mJ when the mixture contained 25 %$_{v/v}$ of isooctane. This can be explained by the help of isooctane molecules in facilitating the flame kernel's growth and propagation within the mist cloud.

***Table 3:** MIE of Jet A1 – isooctane blends (mist mass concentration of 65 g.m^{-3})*

Fuel blend	**MIE (mJ)**
Jet A1	> 900
Jet A1 + 2%$_{v/v}$ isooctane	630
Jet A1 + 5%$_{v/v}$ isooctane	380
Jet A1 + 10%$_{v/v}$ isooctane	250
Jet A1 + 25%$_{v/v}$ isooctane	< 160

3.4 Evaporation model

Following the evaporation model based on the d^2 law and detailed in Section 2.4, Figure 5 represents the ratio of the vapor fraction and the corresponding lower explosive limit of both Jet A1 and isooctane mists. As it can be seen, at 300 K corresponding to 27 °C, the amount of Jet A1 vapor in a confined mist cloud, of a mean diameter of 8 µm, is not sufficient to sustain an explosion; nonetheless, at this concentration (3 g ➔ ~ 150 g.m^{-3}) an explosion occurs (See Figure 2) showing the contribution of the Jet A1 mist. A big difference is seen for the same mass of injected isooctane as its LEL is easily reached at this temperature.

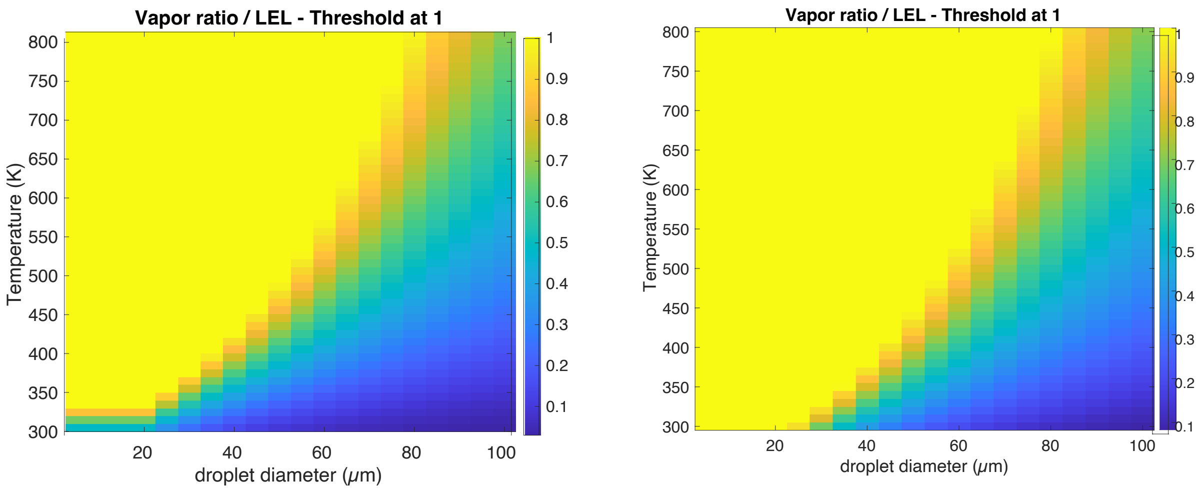

***Fig. 5.** Evolution of the vapor fraction / LEL ratio as a function of ambient temperature and droplet diameter for 3 g injected of: (a) Jet A, (b) isooctane*

Current work is in progress to apply the evaporation model on a multicomponent mist cloud and link findings to experimental data.

3.5 Hybrid mixtures

Interest in hybrid dust-gas explosions has been rising throughout the years. Nevertheless, a hybrid mixture can be defined as an aerosolized liquid and gas mixture capable of being ignited and can indeed trigger an explosion. Moreover, it was seen as interesting to highlight the contribution of the mist in a mist-gas cloud to its explosivity. For these reasons, experiments were first performed at a sphere temperature of 27 ± 0.5 °C while varying Jet A1 mist concentrations between 67 and 120 g.m^{-3} to quantify the explosion severity of hybrid mixtures containing 3%$_{v/v}$ of methane. As seen in Table 4, the addition of a low percentage of methane first influenced the LEL of the mist cloud by facilitating ignition at a concentration lower than 80 g.m^{-3}. Rates of pressure rise were also seen to accelerate by at least 3.6 times their initial values, even though the percentage of CH_4 did not exceed its LEL which is about 5.5 %$_{v/v}$. An explosion occurring when both components were found in lower quantities than their LELs shed light on the importance of understanding the explosion behavior of gas-mist hybrid mixtures and determining the explosion driving regime. It is indeed important to determine whether a mist is sufficient to drive an explosion even when the gas content is not enough. Methane concentrations were therefore varied between 0 and 12 $\%_{v/v}$ and Jet A1 mists between 0 and 120 g.m^{-3}. The same level of turbulence was maintained throughout the series of experiments to ensure that no influence, other than the Jet A1 – CH_4 mixture composition, occurred on the explosivity.

Figure 6 represents a bubble chart expressing the rates of pressure rise obtained for varying concentration to explosive limits ratios as inspired by Russo et al. (2012), who evaluated the explosion severity of methane and nicotinic acid.

Here we differentiate between the LEL of CH_4 expressed in volumetric percentage, experimentally measured to be 5.5 $\%_{v/v}$, and the minimum explosion concentration (MEC) of Jet A1 mist expressed in g.m^{-3}, experimentally measured to be 80 g.m^{-3}. As can be seen in Figure 6, the diameter of dP/dt_m circles is proportional to their values raging between 52.5 bar.s^{-1} to 613 bar.s^{-1}. The figure also demonstrates the existence of five different explosion regimes. A "mist-driven explosion" zone can first be identified for explosions taking place at mist concentrations above the MEC and CH_4 concentrations below the LEL. Inversely, when the CH_4 concentration is maintained above its LEL, and the contrary for Jet A1, the explosion becomes more "gas-driven". On the other hand, when both concentrations are above the lower limits, both fuels are considered to have contributed to the explosion leading to a "dual-fuel explosion" zone. Note that explosions with the same CH_4 concentration were more severe when more Jet A1 was introduced to the mixture, demonstrating the contribution of the mist cloud. Finally, the last two zones were seen to be divided into a "no explosion" zone and a "synergic explosion" zone. The latter was identified because it was seen that the interaction of the two components resulted in a total impact bigger than the sum of their individual effects, even when below both their flammability limits. The former can be separated from the explosion regime by either Le Chatelier's mixture flammability limit rule (Mashuga & Crowl, 2000), usually applied for homogeneous gas mixtures, or the Bartknecht curve (Addai et al., 2016), usually applied for hybrid dust-gas mixtures.

Le Chatelier's law, which shows a linear relationship between the MEC of the mist and the LEL of the gas both weighed by their concentrations, is as follows:

$$LEL_{mixture} = \frac{1}{\frac{C_{mist}}{MEC_{mist}} + \frac{y_{CH_4}}{LEL_{CH_4}}}$$

Bartknecht curve, which shows that, by a second order equation, the MEC of the hybrid mixture decreases with increasing gas concentrations, is as follows:

$$MEC_{mixture} = MEC_{mist}\left(\frac{y_{CH_4}}{LEL_{CH_4}} - 1\right)^2$$

Figure 4 shows that the Bartknecht curve may better delimit the two zones as no explosions occurred under the curve. Nevertheless, complementary tests are required to better quantify and understand liquid-gas explosions. Preliminary experiments on hybrid mixtures have, however, highlighted the role that mists can take in an explosion.

Table 4: *Influence of methane gas on Jet A1 mist explosions at T = 27 °C*

	Mist concentration (g.m^{-3})	**67**	**80**	**93**	**107**	**120**
P_m (bar)	**Jet A1**	0	4.8	5	5.3	5.5
	Jet A1 + 3$\%_{v/v}$ methane	6.5	6.7	7	7.2	7.4
dP/dt_m (bar.s^{-1})	**Jet A1**	0	71	76	95	109
	Jet A1 + 3$\%_{v/v}$ methane	264	274	379	350	416

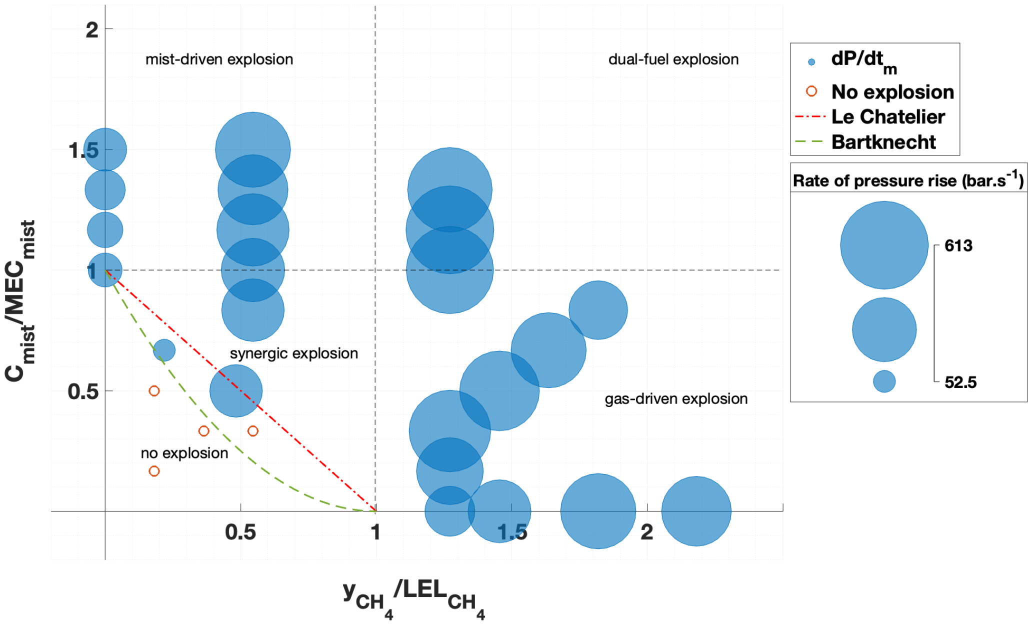

Fig. 6. Explosion experimental results as a function of Jet A1 mist and methane concentrations

3.6 Laminar burning velocity

Calculations based on the correlation of Silvestrini allowed obtaining laminar burning velocities, as shown in Figure 7, for the Jet A1 and isooctane blends at 27 °C. Due to the dependence of S_u^0 on P$_m$ and dP/dt$_m$, it follows their evolution as it increases with increasing mist concentrations and accelerates with increasing isooctane percentages. Pre-evaporated and premixed Jet A1-air mixtures were tested by Vukadinovic et al. (2013) and exhibited a laminar burning velocity of about 35 cm.s^{-1} at stoichiometric conditions and an initial temperature and pressure of 27 °C and 1 bar respectively. Such a higher value can be explained by the fact that the Jet A1 was pre-evaporated before ignition, hence facilitating the propagation of the flame.

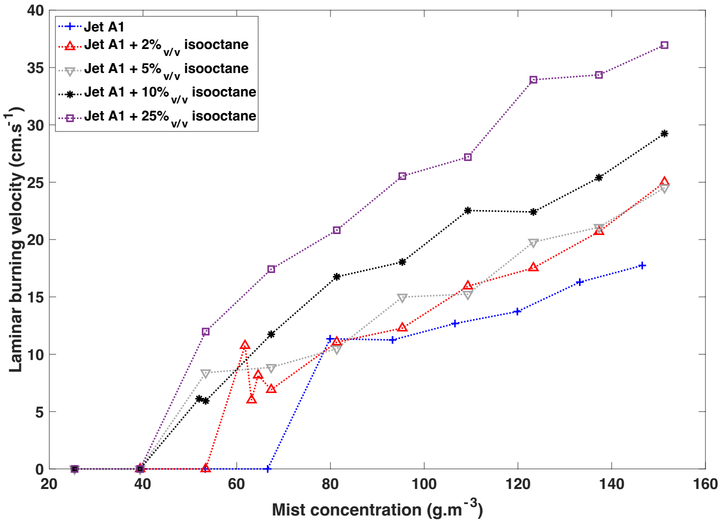

Fig. 7. Evolution of the calculated laminar burning velocity as a function of Jet A1 - isooctane mist concentration

Experimental values of the laminar burning velocity obtained from the flame propagation tube are currently being calculated and will be presented soon. Figure 7 demonstrates two different flame propagations in isooctane and Jet A1 mist clouds. As it can be seen in Figure 7a, the flame front was not perfectly smoothed indicating its deformation due to present isooctane droplets. Further analyses are under development.

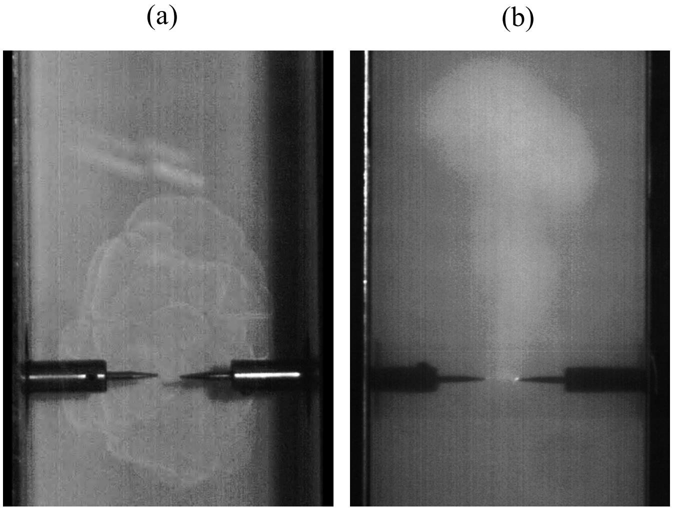

Fig. 8. *Flame propagation in (a) isooctane mist cloud at 120 ms ignited by a 3 J spark (b) Jet A1 mist cloud at 100 ms ignited by a 200 J spark*

4. Conclusions

This study proposed a new test method that can be used for the assessment of mist ignitability and explosivity. Indeed, it was proven that, in a single apparatus, it is possible to determine the explosion overpressure P_m, the rate of pressure rise dP/dt_m, the lower explosive limit LEL, and the minimum ignition energy MIE.

Experiments showed that commercialized fuels can behave differently depending on petroleum cuts, aging, or suppliers. Tests were, therefore, conducted on B7 diesel and Jet A1 with the addition of flammable isooctane. The latter increased the explosivity of both fuels and enhanced their ignitability. Indeed, in the case of Jet A1 – isooctane blends, the LEL of the mist cloud decreased from 80 $g.m^{-3+to}$ about 45 $g.m^{-3}$. Another influence was the considerable acceleration of the rate of pressure rise. Moreover, a significant decrease in the MIE was observed from a value above 900 mJ for pure Jet A1 to a value below 160 mJ for Jet A1 + 25 $\%_{v/v}$ isooctane. In addition, an evaporation model based on the d^2 law was developed to quantify the vapor fraction in a confined mist cloud and take into account the saturation that could take place. This model will also be applied to multicomponent droplets to be more adaptable to fuels or fuel blends. Furthermore, experiments were conducted on hybrid mixtures of Jet A1 mist and methane gas, allowing the distinction of five explosion regimes. A “no explosion” zone that is delimited by the Bartknecht curve, a synergic explosion zone where both fuels complemented each other, a mist- and a gas-driven explosion zone where the explosions were dominated by the presence of Jet A1 mists and methane gas, respectively, and finally, a dual-fuel explosion zone where both mist and gas contributed to the explosion. An interesting finding is the more severe explosions observed in the dual-fuel explosion zone, highlighting the contribution of the mist cloud. Finally, the laminar burning velocity was calculated using existing correlations and explosion severity parameters and was shown to reach values between 15 and 38 $cm.s^{-1}$ for Jet A1 mists and Jet A1 + 25$\%_{v/v}$ isooctane mist, respectively. In addition, flame propagation tests performed in a flame propagation tube will soon be used to compare to this velocity’s calculated values.

Complementary analyses are under development to better quantify the contribution of the vapor fraction to the ignitability and explosivity of a fuel mist cloud.

References

Addai, E. K., Gabel, Dieter, & Krause, Ulrich. (2016). Models to estimate the lower explosion limits of dusts, gases and hybrid mixtures. *Chemical Engineering Transactions*, *48*, 313–318. https://doi.org/10.3303/CET1648053

Burgoyne, J. H., & Cohen, L. (1954). The Effect of Drop Size on Flame Propagation in Liquid Aerosols. *Proceedings of the Royal Society of London. Series A, Mathematical and Physical Sciences*, *225*(1162), 375–392. JSTOR.

Cuervo, N., Dufaud, O., & Perrin, L. (2017). Determination of the burning velocity of gas/dust hybrid mixtures. *Process Safety and Environmental Protection*, *109*, 704–715. https://doi.org/10.1016/j.psep.2017.06.009

Dumitrescu, C. E., Guo, H., Hosseini, V., Neill, W. S., Chippior, W. L., Connolly, T., Graham, L., & Li, H. (2011). The Effect of Iso-Octane Addition on Combustion and Emission Characteristics of a HCCI Engine Fueled With n-Heptane. *Journal of Engineering for Gas Turbines and Power*, *133*(11). https://doi.org/10.1115/1.4003640

Eckhoff, R. K. (2005). Chapter 3—Explosions in Clouds of Liquid Droplets in Air (Spray/Mist). In R. K. Eckhoff (Ed.), *Explosion Hazards in the Process Industries* (pp. 149–173). Gulf Publishing Company. http://www.sciencedirect.com/science/article/pii/B9780976511342500087

Eichhorn, J. (1955). Careful! Mist can explode. *Petroleum Refiner*, *34(11)*, 194–196.

El – Zahlanieh, S., Sivabalan, S., Dos Santos, I. S., Tribouilloy, B., Brunello, D., Vignes, A., & Dufaud, O. (2022). A step toward lifting the fog off mist explosions: Comparative study of three fuels. *Journal of Loss Prevention in the Process Industries*, *74*, 104656. https://doi.org/10.1016/j.jlp.2021.104656

Godsave, G. A. E. (1953). Studies of the combustion of drops in a fuel spray—The burning of single drops of fuel. *Symposium (International) on Combustion*, *4*(1), 818–830. https://doi.org/10.1016/S0082-0784(53)80107-4

Khaled, F., Badra, J., & Farooq, A. (2017). Ignition delay time correlation of fuel blends based on Livengood-Wu description. *Fuel*, *209*, 776–786. https://doi.org/10.1016/j.fuel.2017.07.095

Lees, P., Gant, S., Bettis, R., Vignes, A., Lacome, J.-M., & Dufaud, O. (2019). *Review of recent incidents involving flammable mists*. *166*, 23.

Mashuga, C. V., & Crowl, D. A. (2000). Derivation of Le Chatelier's mixing rule for flammable limits. *Process Safety Progress*, *19*(2), 112–117. https://doi.org/10.1002/prs.680190212

NTSB. (2022). *Engine Room Fire aboard Towing Vessel Miss Dorothy* (MIR-22/05; p. 15). National Transportation Safety Board. https://www.ntsb.gov/investigations/AccidentReports/Reports/MIR2205.pdf

Polymeropoulos, C. E., & Das, S. (1975). The effect of droplet size on the burning velocity of kerosene-air sprays. *Combustion and Flame*, *25*, 247–257. https://doi.org/10.1016/0010-2180(75)90091-7

Russo, P., Benedetto, A. D., & Sanchirico, R. (2012). *Theoretical evaluation of the explosion regimes of hybrid mixtures*. https://doi.org/10.3303/CET1226009

Safarov, J., Ashurova, U., Ahmadov, B., Abdullayev, E., Shahverdiyev, A., & Hassel, E. (2018). Thermophysical properties of Diesel fuel over a wide range of temperatures and pressures. *Fuel*, *216*, 870–889. https://doi.org/10.1016/j.fuel.2017.11.125

Santon, R. C. (2009). *Mist fires and explosions—An incident survey*. *155*, 5.

Shepherd, J. E., Krok, J. C., & Lee, J. J. (1997). *Jet A Explosion Experiments: Laboratory Testing*. 74.

Silvestrini, M., Genova, B., & Leon Trujillo, F. J. (2008). Correlations for flame speed and explosion overpressure of dust clouds inside industrial enclosures. *Journal of Loss Prevention in the Process Industries*, *21*(4), 374–392. https://doi.org/10.1016/j.jlp.2008.01.004

Vukadinovic, V., Habisreuther, P., & Zarzalis, N. (2013). Influence of pressure and temperature on laminar burning velocity and Markstein number of kerosene Jet A-1: Experimental and numerical study. *Fuel*, *111*, 401–410. https://doi.org/10.1016/j.fuel.2013.03.076

Willingham, C. B., Taylor, W. J., Pignocco, J. M., & Rossini, F. D. (1945). Vapor pressures and boiling points of some paraffin, alkylcyclopentane, alkylcyclohexane, and alkylbenzene hydrocarbons. *Journal of Research of the National Bureau of Standards*, *35*(3), 219. https://doi.org/10.6028/jres.035.009

Yuan, S., Ji, C., Han, H., Sun, Y., & Mashuga, C. V. (2021). A review of aerosol flammability and explosion related incidents, standards, studies, and risk analysis. *Process Safety and Environmental Protection*, *146*, 499–514. https://doi.org/10.1016/j.psep.2020.11.032

DOI: 10.7795/810.20221124

Where one plus one equals three: the MIT of hybrid mixtures

Paul Geoerg[a], Stefan Spitzer[b], Dieter Gabel[a] & Ulrich Krause[a]

[a] Otto-von-Guericke University, Magdeburg, Germany
[b] Bundesanstalt fuer Materialforschung und -pruefung, Berlin, Germany

E-mail: *dieter.gabel@ovgu.com*

Abstract

The knowledge of ignition parameters is of great importance for safety processes in chemical, petrochemical, and process plants. Standards to develop benchmarks are determined by standardized procedures. However, these procedures are only applicable for gases or solids (single-phase systems). Hybrid mixtures (multi-phase systems) are not considered in standard operating procedures. Therefore, the Nex-Hys project aimed to develop such procedures, ready for standardization.

To determine minimum ignition temperatures for frequently used hybrid mixtures, first, the minimum ignition temperatures and ignition ratios were determined in the modified Godbert-Greenwald furnace for solids (Lycopodium, Corn starch), liquids (n-Heptane), and gases (Methane, Hydrogen). Second, the minimum ignition temperature and ignition ratios were determined for several combinations as hybrid mixtures of dust and liquid or gas.

A noticeable decrease of minimum ignition temperatures below the MIT of the pure gases was observed for the hybrid mixtures. For vapors, the effect is not that strong. The MIT of the hybrid mixture is in the region of the MIT of the dust component. Additionally, more widely dispersed areas of ignition can be achieved. Following previous findings, the results demonstrate a strong relationship between the likelihood of explosion and the amount of added solvent or gas. Consequently, the hybrid mixture is characterized by a different minimum ignition temperature than that of the single components.

These findings and the conclusions during the development of the GG oven are summarized in recommendations for further progressing the underlying standards.

Keywords: *Hybrid mixture, Minimum ignition temperature, Dust, Gas, Vapour*

1 Introduction

Starting in Spring 2019, the Nex-Hys project aimed at the introduction of standardized determination methods for safety parameters of explosion protection for hybrid mixtures. Besides other explosions parameters determined in the 20-liter vessel, like the maximum explosion pressure and the maximum pressure rise, the Minimum Ignition Temperature (MIT) was the parameter of interest in a separated work package.

The before-mentioned hybrid mixtures consist of a combination of combustible dust and an ignitable gas or vapor phase. These occur in industrial processes and are partially neglected in safety assessments. Reasons, therefore, are the fact that they are not treated in the standard, the assumption that a concentration below the ignition limits is not relevant, or the tendency to consider the more dangerous gas phase only. But all three factors need to be considered. Regulations force an operator of an installation to ensure safety in all cases; it has already been proven, that mixture where both components are below their respective ignition limit can be ignitable (Bartknecht, 1981); increased turbulence due to the dust might increase the explosion severity and synergistic effects cannot be excluded, yet. Thus, Tan et al., 2020 also focus on carbonaceous dusts in their studies and conclude that the proportion of combustible gas has significant effects on the MIT of dust samples and that the content of volatile matter in the dust plays an important role in the ignition process. On the other hand, mixtures are possible in which the hybrid MIT does not drop below the MIT of the gas component (i.e. Kosinski et al., 2013).

The Minimum Ignition Temperature is defined as the lowest temperature of a hot surface that leads to a self-propagating exothermal reaction in a combustible system. Following international standards (DIN EN 50281-2-1 (Deutsches Institut für Normung, November 1999)) two different apparatuses can be used. Due to its greater application in safety laboratories (Eckhoff, 2019) and its easier usability, the Godbert Greenwald (GG) oven was focussed in this project and the BAM furnace is not considered.

This paper summarizes the modification made to the apparatus and the experimental results provides a suggestion for a future testing procedure and an outlook to overcome the weaknesses of the MIT in its present state.

2 Materials and experiments

2.1 Dusts, gases, and vapours

Within the Nex-Hys Project a standard dust - a corn starch (Fig. 1 a) - was used for all experiments performed within project. To guarantee equal quality and behavior round-robin tests were regularly made throughout the project duration. This although ensures the statement to be true that variations found in the experimental result are not due to differences in material properties. Additionally Lycopodium clavatum was used in the experiments. As can be seen in the images by the scanning electron microscope (Fig. 1 b) the spores are all of the equal size and do not tend to agglomeration.

Following, the particle size distribution of the two dust (Fig. 2) reflects these findings with a very narrow span for Lycopodium (blue) and broader distribution for starch (red). The dust sample was characterized by a median particle size of approximately 0.017 mm (Nex-Hys corn starch) and 0.031 mm (Lycopodium). The particle size distribution was determined for the two samples using Camsizer (Retsch Technology) according to ISO 13322-2:2006-11 (International Standards Organisation, 2006). The residual humidity was determined by Satorius MA 100 for the dust samples. The median residual moisture was approximately 7.7 % for Nex-Hys corn starch and 3.2 % for Lycopodium.

As can be seen in Figure 1 a) the starch contains agglomerates. Nonetheless, as this starch was used and tested by all members of the Nex-Hys project independently it always shows a comparable particle size distribution. During the experiments in the GG oven neither an agglomeration nor a break up of agglomerates is to be expected. For the experiment in the 20 liter sphere this phenomenon should be regarded.

As gases, Methane and Hydrogen were used, as well as n-Heptane as a combustible liquid to be

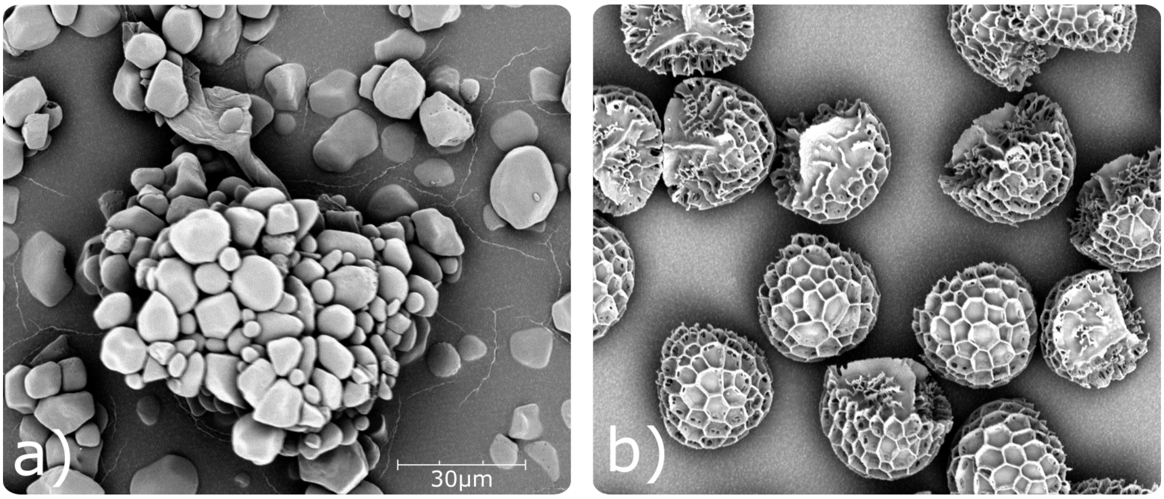

***Fig. 1**: Images captured at 2000x magnification with a scanning electron microscope of (a) Nex-Hys Starch and (b) Lycopodium.*

vaporized. All are standard high-grade pure chemicals. Their standard MITs and ignition ranges are summarized in Tab. 1.

***Table 1**: MIT and ignition range of gases and vapors according to* CHEMSAFE - Database for Safety Characteristics in Explosion Protection *(2022).*

Substance	**MIT**	**LEL**	**UEL**
Methane	595°C	4.4%	17.0%
Hydrogen	560°C	4.0%	77.0%
Heptane	220°C	0.8%	6.7%

2.2 Experimental setup development

Experiments on hybrid mixtures at the the Otto-von-Guericke University already started some years ago and were extensively published by Addai et. al. who has focused on the lower explosion limits (Addai, Gabel, and Krause, 2015a; Addai, Gabel, and Krause, 2015b; Addai, Addo, et al., 2017; Addai, Gabel, and Krause, 2017; Abbas et al., 2019), minimum ignition temperature (Addai, Addo, et al., 2017; Addai, Gabel, and Krause, 2016a; Addai, Gabel, and Krause, 2016b), the minimum ignition energy (Addai, Gabel, Kamal, et al., 2016; Addai, Gabel, and Krause, 2016b) and the minimum explosion concentration (Addai, Gabel, and Krause, 2015a; Addai, Gabel, and Krause, 2017) of hybrid mixtures. Findings of the minimum ignition temperature for premixed dust-solvent mixtures were published as well by Gabel and Krause (2019). All findings are in line with other literature, a comparison is not made here in detail as this was already made in our previous work Gabel, Geoerg, et al., 2021. The argument clearly is that we need as standardized setup and procedure to generate comparable results in the future.

The approach to generate the hybrid mixture for the MIT at that time was set up as serial: the solvent reservoir is placed in line with the dust chamber and the heated furnace (setup described in more detail in Gabel, Geoerg, et al. (2020)). Practically, the MIT of hybrid mixtures could be determined that way, but some disadvantages were identified:

- dust is pushed into the furnace before the gas,
- moisture of the vapor phase can interact with the dust - agglomeration possible,
- permanent change to the standardized apparatus unavoidable.

DOI: 10.7795/810.20221124

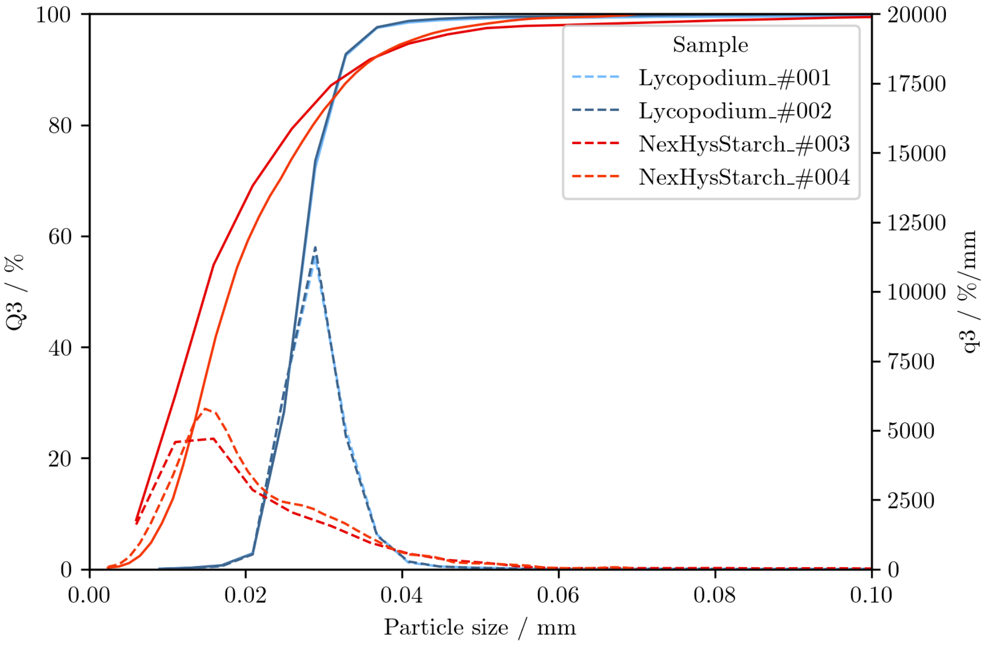

Fig. 2*: Particle size distribution of Nex-Hys corn starch (red) and Lycopodium (blue), two measurements each.*

The burnable gas was mixed directly into the air in the gas reservoir. This might be challenging as well if the setup is not authorized for combustible substances (explosions protected equipment). These considerations led to the final setup described in the next section.

As mentioned, experiments are done in the standard oven as well as in a furnace with twice the original length. The MIT depends on the apparatus and is often lowest in the BAM oven. As this could not be used within this project an oven with double length is used, to show how the increased residence time in the oven might decrease the measured MIT.

2.2.1 Final setup and procedure

To overcome the disadvantages mentioned above the setup was optimized: the admixture of the gas/vapor phase was separated from the dust part. The mixing directly takes place in the tube as presented in Fig. 3. By this, the original standardized setup is practically unchanged with only a slight modification of the top section of the furnace. The dust, as well as the gas/vapor, are not blown into the tube directly in the center, but two tubes are arranged side by side closed to the middle of the furnace.

In comparative measurements, it was ensured that the modification does not influence the MIT. Even if not used in this research project anymore the possibility to introduce different gases in the 'air / gas reservoir' is still given in the setup.

Minor changes in the applied pressure (±0.1 bar) or quantities (±0.1 g) are necessary to achieve equal values, but these parameters are not relevant as the final MIT is a temperature value only. Additionally, high-speed video recordings with a transparent plastic tube (Fig. 4, left) were captured to get a qualitative visual impression of the distribution and mixing effect (Fig. 4, right). We did not observe any substantial differences in the distribution behavior for the different setups and in all cases a good contact of the dust phase along the tube walls was confirmed. Practically, no differences in the different setup could be found for the MIT that lays outside the expected variation. The video recordings gave interesting insides of how the dust is distributed in the head of the tube that some when might be of interest when comparing to dust distribution simulations.

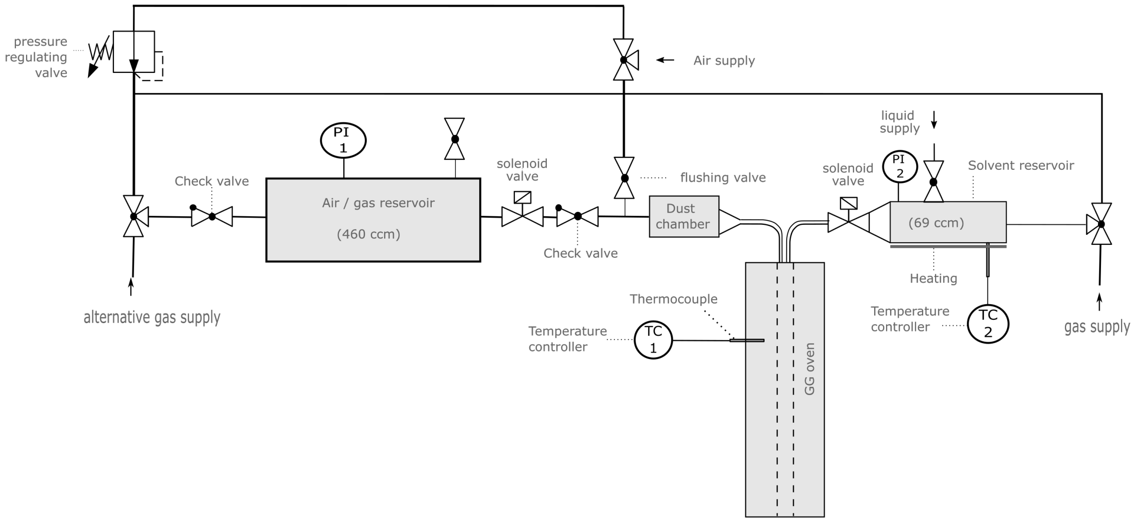

***Fig. 3**: Schematic drawing of the modified Godbert-Greenwald-apparatus.*

The measuring procedure does not need to be further changed and is described in detail in Gabel, Geoerg, et al. (2020). Only the number of repetitions suitable for a standard needs to be discussed.

2.2.2 Alternative ignition criterion

As already discussed in Gabel, Geoerg, et al., 2020, the idea to introduce a more reliable and verifiable ignition criterion is still followed. While the automatic video analysis showed promising results the setup and handling are error-prone. The big advantage still is that a capture offers an ex-post visual control, as the video is stored and can be replayed.

The alternative ignition criterion comparable to other safety characteristics would either be the pressure or the temperature during an experiment. The pressure measurement can be discarded as we have an open setup with only a low-pressure rise and already an air blast that is used to distribute the materials. The high temperature in the oven would increase the price of pressure sensors as well.

On the other hand, using the temperature as a criterion increase in the tube seemed to be a straightforward idea. The question of why this was not used in the beginning might be historical. The fast temperature change could not be detected with classical thermometers as a consequence of their inertia. Modern thin thermocouples react sufficiently fast to the temperature change induced by an ignition. The temperature measured is not the real flame temperature of the reaction zone but the absolute value is of no interest, only a clear differential signal is needed to detect ignition. Fig 5 shows the typical temperature changes in the tube during ignition in a Lycopodium experiment.

Therefore three thermocouples were introduced in the middle of the tube at different heights. Only temperature differences are shown in Fig 5, as the absolute temperature changes with the height in the tube. It is lowest at the open end and this thermocouple shows the least reaction on the ignition, too. Within the framework of the Nex-Hys project, these temperature measurements were conducted in much more detail. These findings will be part of the final considerations for further developing the standard, too. (Franken, 2021; Schwerdt, 2021)

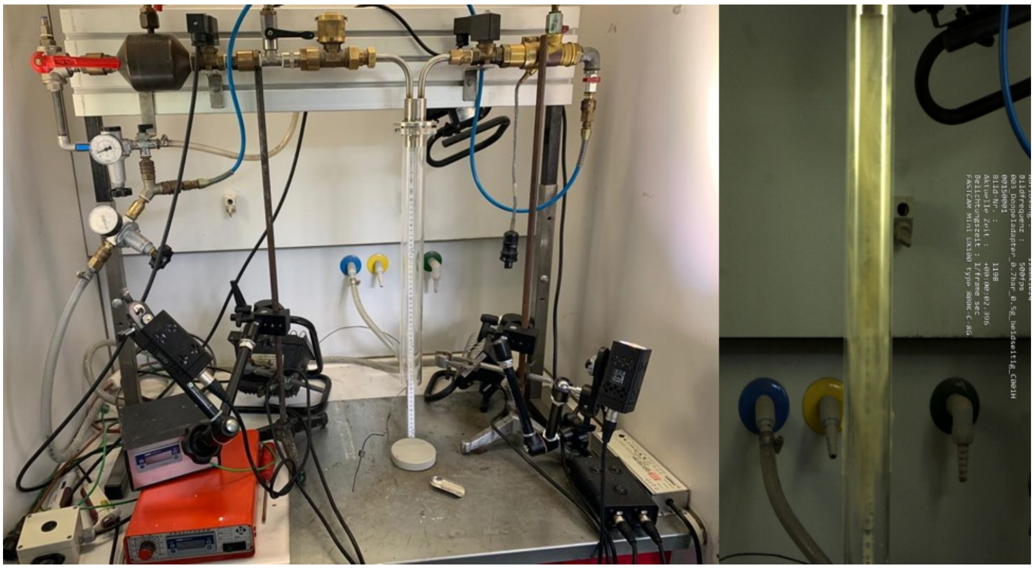

***Fig. 4**: Setup for the high-speed camera recordings (left) and visual impression of the Lycopodium distribution inside the tube (right).*

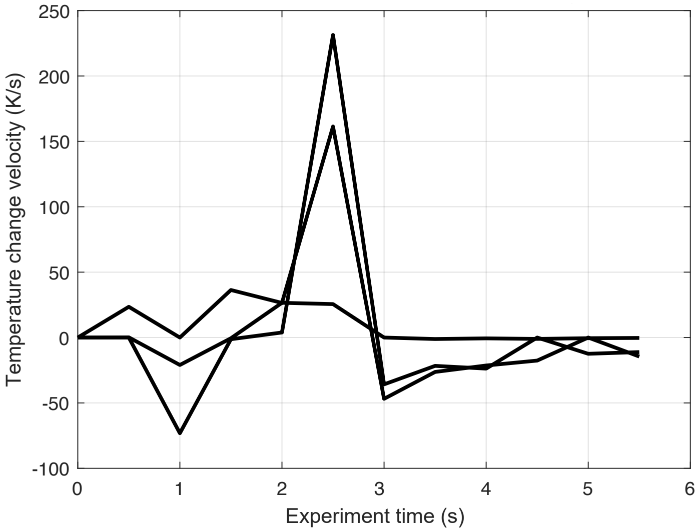

***Fig. 5**: Exemplary plot of the speed of temperature change during ignition.*

3 Results and discussion

First, the MIT of the pure dust was determined. Unlike the standard procedure, additional repetitions per measurement point were made to count for the ignition ratios. This is visualized by the size and the color of the scatter points in Fig. 6 - Fig. 8. Additionally, the Frequencies in the x- and y-direction are shown in the histogram plots at the margins of the diagrams. The accumulated ignition ratio counts of pure corn starch (Fig. 6) depending on the mass and the temperature of the GG furnace is presented. As expected, the ratio of ignitions decreases depending on temperature, and the probability to ignite increases with an increasing amount of dust. It can be observed that there is a dust concentration level at which the ignitability cannot be increased by further increasing the dust mass (c_{Starch} = 0.5 g). Theoretically, one would expect a decrease in the likelihood of ignitions if the amount of dust increases. This expectation could not be confirmed in the experiments presented here, as the injection pressure would need to be higher and the remaining dust amount in the chamber is increasing differently in practice.

A well-defined non-ignition temperature is observed for corn starch at 380 °C. These limits are confirmed by 27 repetitions without any ignitions.

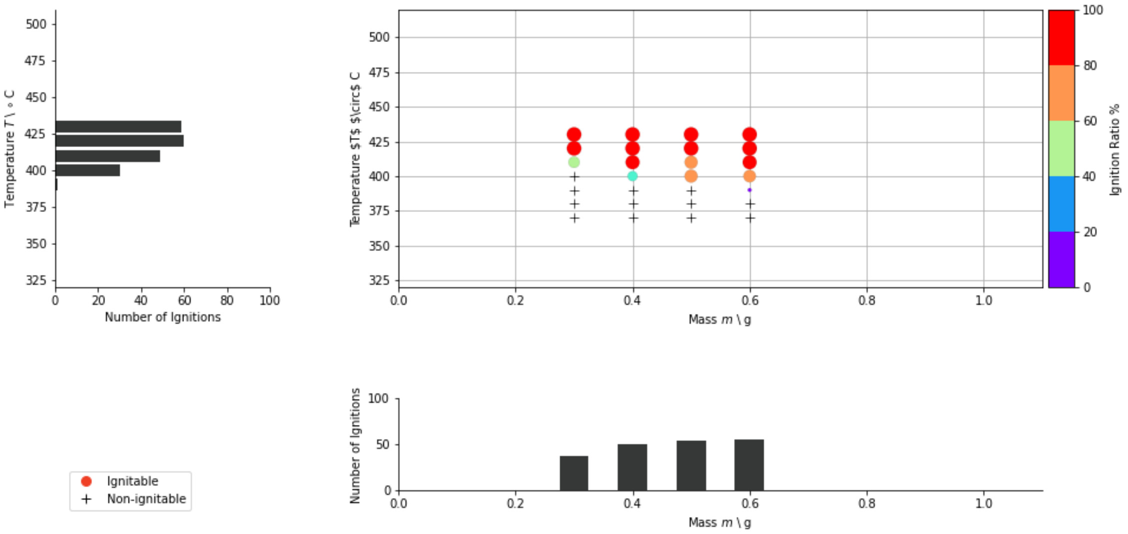

Fig. 6: Ignition ratio counts of pure corn starch depending on mass and temperature of the GG furnace. Please note that the number of ignitions can be greater than five, as the data has been grouped by the varied injection pressures (p+ = [0:3; 0:5; 0.7] bar).

The MIT of Methane is measured to be 660 °C in this experimental setup (Fig. 7) and recognizable above the standard value of 595 °C (Tab. 1). As presented in Fig. 7, the optimal concentration for ignition is 5 %, which is half of the stoichiometric concentration. As a higher dilution can be predicted in the experiment, it can be assumed that the effective gas concentration in the combustion chamber is even lower. The determining influence of the high temperature on the combustion process is highlighted here.

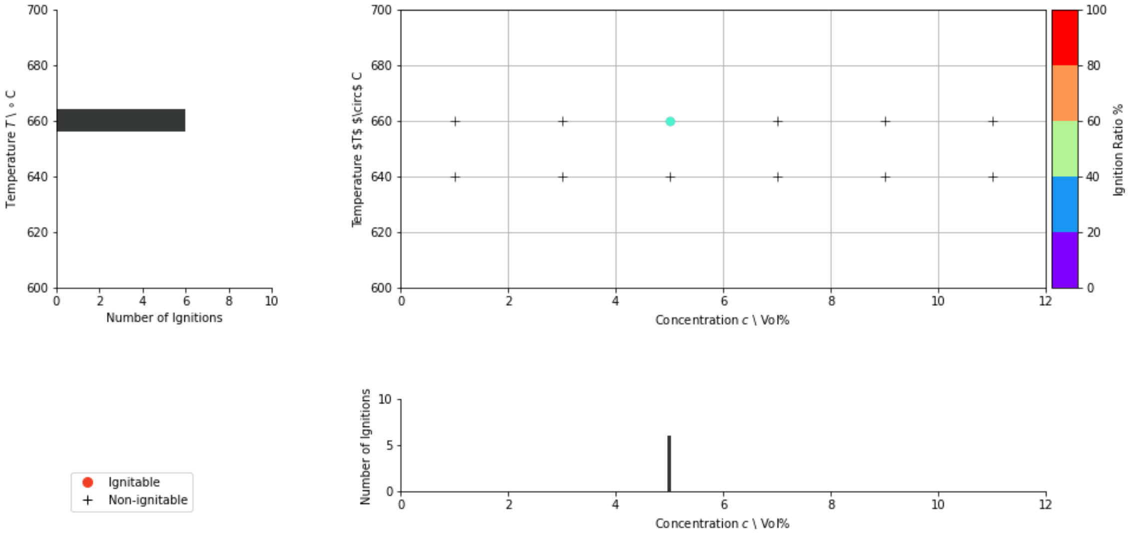

Fig. 7: Ignition ratio counts of pure Methane depending on concentration and temperature of the GG furnace. Frequencies in the x- and y-direction are presented in the histogram plots at the margins.

Due to the higher MIT of the gas, a decrease in MIT was not expected for the hybrid mixture system. The focus was on whether the amounts of dust required to achieve an ignition would change compared to the pure dust experiments. To also limit the parameter space to be tested for research pragmatic concerns, the injection pressure was set as constant by 0.5 bar. This is in line with a series of preliminary tests (Ernst (2020) and Hofmann (2020)) and following the findings of the experiments with pure dust systems. As part of the research project, the entire parameter range was systematically tested. The slight increase of the MIT detected for both systems might be due to the reduced level of oxygen in the system, but still lies within the measurement uncertainty.

Regarding the systems from the side of the gas, it can be shown, that even very low gas concentrations lead to an ignition where the pure gas system needs higher concentration to allow self-sustaining flame propagation.

A comparison of the MIT of hybrid mixtures is shown in Fig. 8 slight increase in ignition temperatures with an increasing gas concentration in the hybrid mixture is observed compared to the pure substances.

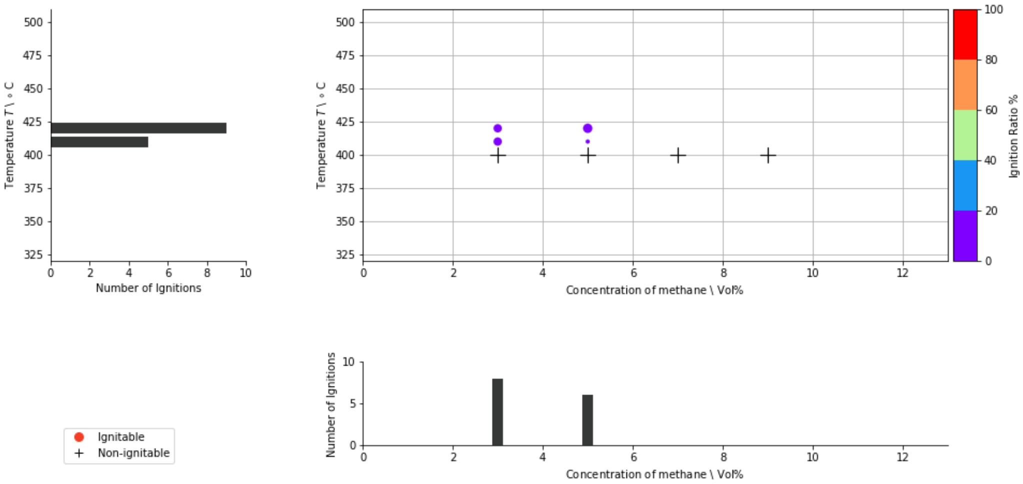

***Fig. 8**: Cumulative ignition counts of a hybrid mixture consisting of m = [0.4, 0.5] g corn starch and a variable concentration of methane in a temperature interval of T = [400; 420]* °C.

The MIT of vapor can be determined under variation of the introduced amount. It can be shown, that the lower explosion limit of n-Heptane is depending on the temperature. Decreasing the amount of n-Heptane the MIT is increasing as shown in Fig. 9. For bigger amounts, an MIT of 260 °C is found. A concentration cannot be stated here as it is not known how the vapor distributes in the tube.

It appears that the shifted ignition limit is displayed here and not the MIT of the substance is measured. Consequently, a lower explosion limit can only be determined with the standardized procedure and not be found in the GG oven.

The same behavior could be shown when testing pure gases, even if not published here in detail.

DOI: 10.7795/810.20221124

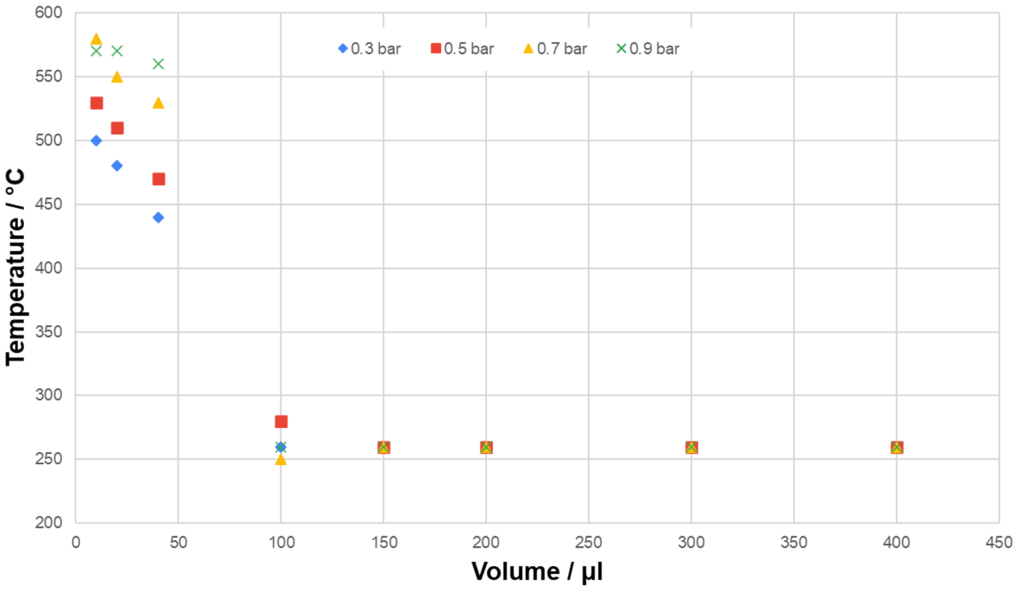

Fig. 9: *Ignition temperatures of n-Heptane under variation of volume and distributing pressure.*

The result obtained within the Nex-Hys project is partially summarized in the following graphical representation (Fig. 10). The results are grouped by the different experimenter and compare different pure substances and their combinations.

The shortened findings are:

- testing for dust, gases, vapors, and their (hybrid) mixtures is possible,
- the length of the oven has an influence, but not equally on all substances,
- a deviation of ± 10 K is at least to be expected,
- nor synergistic effect could be found, yet - no $\mathrm{MIT}_{mixture}$ below the MITs of the single substances is to be expected.

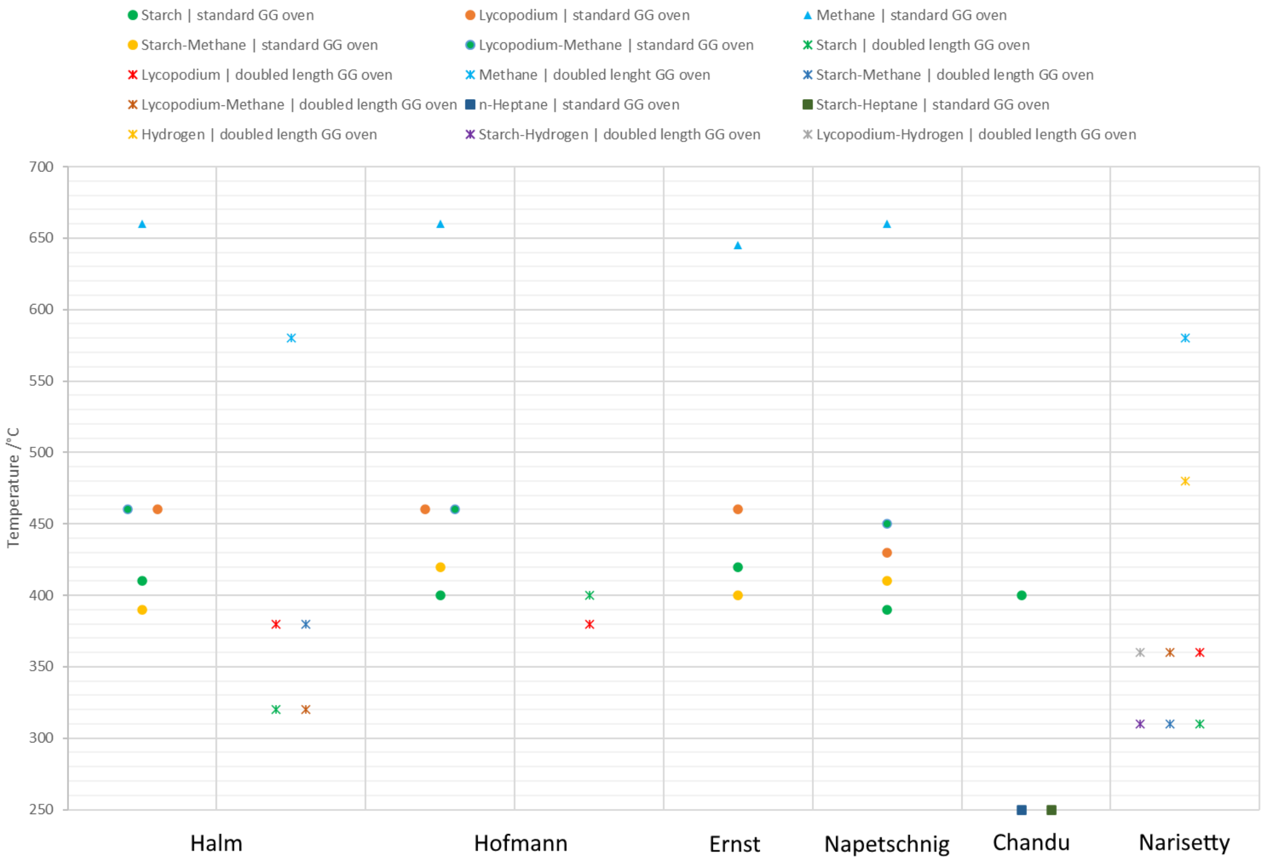

***Fig. 10**: Comparison of MITs (according to Napetschnig, 2022) determined by different experimenters Halm, 2021; Hofmann, 2020; Ernst, 2020; Narisetty, 2021; Napetschnig, 2022 within the Nex-Hys project.*

4 Conclusions and Outlook

Within the Nex-Hys project, an improved setup for determining the MIT of dust, gases, vapors, and their (hybrid) mixtures was developed and extensively tested. The presented modifications do not influence the standard procedure for pure dust. The number of required non-ignitions to be stated in a revised standard still needs to be discussed and is a function of the step width of the parameters of the experiment. For the temperature as a key parameter, even 10 K seems to be too strict. The authors here reference the original intention of MIT testing (Eckhoff, 2019) and prefer temperature classes comparable to the gas-standard as ab alternative approach for discussion.

One aim of the NexHys is to generate a scientific basis to justify a low number of repetitions for the standard procedure. Systematic measurements of the MIT in the GG oven can be very expensive and time-consuming if parameter variations and more repetition are realized.

The MIT of the hybrid system is located close to the component with the lower ignition temperature. An influence of the gas concentration on the ignition probability could not be shown in the experiments: even a small concentration of methane favored ignition (which, however, is still higher than the MIT of the pure dust). Additionally, a more wide region of transition between ignition and non-ignition can be achieved. In consequence, a hybrid mixture system consisting of gas and solid is characterized by a different minimum ignition temperature than that of the single components.

The key result still is that no synergistic effect could be found, with no MIT_{hybrid} below the MITs of the single components.

Acknowledgements

This work has been performed within the research program 'Development of standardised determination methods for safety parameters of explosion protection for hybrid mixtures (NEX-HYS)' funded by the German Federal Ministry of Education and Research - BMBF (grant number 03TNH006A).

References

Abbas, Zaheer et al. (2019). "Theoretical evaluation of lower explosion limit of hybrid mixtures". In: *Journal of Loss Prevention in the Process Industries* 60, pp. 296–302. ISSN: 09504230. DOI: `10.1016/j.jlp.2019.05.014`.

Addai, Emmanuel Kwasi, Albert Addo, et al. (2017). "Investigation of the minimum ignition temperature and lower explosion limit of multi-components hybrid mixtures in the Godbert-Greenwald furnace". In: *Process Safety and Environmental Protection* 111, pp. 785–794. ISSN: 09575820. DOI: `10.1016/j.psep.2017.09.003`.

Addai, Emmanuel Kwasi, Dieter Gabel, Mustafa Kamal, et al. (2016). "Minimum ignition energy of hybrid mixtures of combustible dusts and gases". In: *Process Safety and Environmental Protection* 102, pp. 503–512. ISSN: 09575820. DOI: `10.1016/j.psep.2016.05.005`.

Addai, Emmanuel Kwasi, Dieter Gabel, and Ulrich Krause (2015a). "Explosion characteristics of three component hybrid mixtures". In: *Process Safety and Environmental Protection* 98, pp. 72–81. ISSN: 09575820. DOI: `10.1016/j.psep.2015.06.013`.

– (2015b). "Lower explosion limit of hybrid mixtures of burnable gas and dust". In: *Journal of Loss Prevention in the Process Industries* 36, pp. 497–504. ISSN: 09504230. DOI: `10.1016/j.jlp.2015.02.014`.

– (2016a). "Experimental investigation on the minimum ignition temperature of hybrid mixtures of dusts and gases or solvents". In: *Journal of hazardous materials* 301, pp. 314–326. DOI: `10.1016/j.jhazmat.2015.09.006`.

– (2016b). "Experimental investigations of the minimum ignition energy and the minimum ignition temperature of inert and combustible dust cloud mixtures". In: *Journal of hazardous materials* 307, pp. 302–311. DOI: `10.1016/j.jhazmat.2016.01.018`.

– (2017). "Lower explosion limit/minimum explosible concentration testing for hybrid mixtures in the Godbert-Greenwald furnace". In: *Process Safety Progress* 36.1, pp. 81–94. ISSN: 10668527. DOI: `10.1002/prs.11825`.

Bartknecht, Wolfgang (1981). *Explosions: Course, Prevention, Protection*. Berlin, Heidelberg: Springer Berlin Heidelberg. ISBN: 9783642677496. DOI: `10.1007/978-3-642-67747-2`.

CHEMSAFE - Database for Safety Characteristics in Explosion Protection (2022). URL: `https://www.chemsafe.ptb.de/`.

Deutsches Institut für Normung (November 1999). *Elektrische Betriebsmittel zur Verwendung in Bereichen mit brennbarem Staub. Teil 2-1: Untersuchungsverfahren - Verfahren zur Bestimmung der Mindestzündtemperatur von Staub*.

Eckhoff, Rolf K. (2019). "Origin and development of the Godbert-Greenwald furnace for measuring minimum ignition temperatures of dust clouds". In: *Process Safety and Environmental Protection* 129, pp. 17–24. ISSN: 09575820. DOI: `10.1016/j.psep.2019.06.012`.

Ernst, Matthias (2020). "Vergleichende Bestimmung der MZT von Gemischen und Reinstoffen". Master thesis. Magdeburg: Otto-von-Guericke-University.

Franken, Fabian (2021). "Einwicklung eines neuen Zündkriteriums bei der Bestimmung der Mindestzündtemperatur". Master thesis. Magdeburg: Otto-von-Guericke-University.

Gabel, Dieter, Paul Geoerg, et al. (2020). "Nex-Hys – Minimum Ignition Temperature of Hybrid Mixtures". In: *13th International Symposium on Hazards, Prevention and Mitigation of Industrial Explosions, Proceedings*. Ed. by Florian Baumann et al. Physikalisch-Technische Bundesanstalt (PTB), pp. 484–493.

– (2021). “Nex-Hys: minimum ignition temperature of hybrid mixtures”. In: *Journal of Loss Prevention in the Process Industries* 72, p. 104502. ISSN: 09504230. DOI: `10.1016/j.jlp.2021.104502`.

Gabel, Dieter and Ulrich Krause (2019). “Minimum ignition temperature of hybrid mixtures”. In: *Chemical engineering transactions* 75, pp. 1–6.

Halm, Jonas (2021). “Mindestzündtemperatur von hybriden Gemischen im GG-Ofen”. Bachelor thesis. Magdeburg: Otto-von-Guericke-University.

Hofmann, Tobias (2020). “Variation der Gemischbildung für hybride Gemische im GG-Ofen”. Bachelor thesis. Magdeburg: Otto-von-Guericke-University.

International Standards Organisation (2006). *ISO 13322-2:2006-11. Partikelgrößenanalyse - Bildanalyseverfahren - Teil 2: Dynamische Bildanalyseverfahren ISO*. Berlin.

Kosinski, Pawel et al. (2013). “Explosions of carbon black and propane hybrid mixtures”. In: *Journal of Loss Prevention in the Process Industries* 26.1, pp. 45–51. ISSN: 09504230. DOI: `10.1016/j.jlp.2012.09.004`.

Napetschnig, Philipp (2022). “Zündtemperatur von hybriden Gemischen”. Bachelor thesis. Magdeburg: Otto-von-Guericke-University.

Narisetty, Anvesh (2021). “Ignition Temperature of Hybrid Mixtures”. Master thesis. Magdeburg: Otto-von-Guericke-University.

Schwerdt, Lennard (2021). “Wege zu einem Normenvorschlag für die Bestimmung der MZT hybrider Gemische”. Masters thesis. Magdeburg: Otto-von-Guericke-University.

Tan, Xin et al. (2020). “Minimum ignition temperature of carbonaceous dust clouds in air with CH4/H2/CO below the gas lower explosion limit”. In: *Fuel* 264, p. 116811. ISSN: 00162361. DOI: `10.1016/j.fuel.2019.116811`.

DOI: 10.7795/810.20221124

Dust Explosions in Vessel-Pipe Systems at Large Scale

Lorenz R. Boeck, C. Regis L. Bauwens & Sergey B. Dorofeev

FM Global, Research Division
Norwood, MA, USA

E-mail: lorenz.boeck@fmglobal.com

Abstract

This study investigates dust explosions in vessel-pipe systems to develop a better understanding of dust flame propagation between interconnected vessels and implications for the proper application of explosion isolation systems. Cornstarch dust explosions were conducted in a large-scale setup consisting of a vented 8-m^3 vessel and an attached pipe with a diameter of 0.4 m and a length of 9.8 m. The ignition location was varied between experiments. The experimental results are compared against previous experiments with initially quiescent propane-air mixtures, demonstrating a significantly higher reactivity of the dust explosions due to elevated initial turbulence, leading to higher peak pressures and faster flame propagation. In addition, a physics-based model developed previously to predict gas explosion dynamics in vessel-pipe systems was extended for dust combustion. The model successfully predicts the pressure transients and flame progress recorded in the experiments and captures the effect of ignition location.

Keywords: *dust explosions, explosion isolation, large-scale experiments, vessel-pipe systems*

Nomenclature

Symbol	Description	Units
A	Area	(m^2)
a	Speed of sound	(m/s)
k	Model parameter	(-)
K_{St}	Deflagration index	(bar·m/s)
L	Length	(m)
m	Mass	(kg)
p	Pressure	(Pa; bar-g)
R, r	Radius	(m)
S	Burning velocity	(m/s)
t	Time since ignition	(s)
T	Temperature	(K)
u	Velocity	(m/s)
V	Volume	(m^3)
x	Axial position	(m)
γ	Ratio of heat capacities	(-)
ν	Kinematic viscosity	(m^2/s)
ρ	Density	(kg/m^3)
σ	Expansion ratio	(-)
τ	Characteristic combustion time	(s)

Superscripts

‘	Turbulent fluctuation

Subscripts

0	Initial condition
b	Burned
e	External (outside the vent)
f	Flame
i	Inertia
p	Pipe
t	Turbulent
u	Unburned
v	Vent

1. Introduction

Explosions propagating between interconnected vessels often produce more severe consequences than those in individual vessels due to effects such as pressure piling, flame acceleration in the interconnecting pipes, and flame-jet ignition in secondary vessels (Bartknecht, 2021; Eckhoff, 2016; Taveau, 2017) and can result in widespread damage to industrial facilities. Explosion isolation systems are used to contain and mitigate such events (Hattwig and Steen, 2008). These systems can be either passive or active in nature, operating based on the pressure build-up and flow generated by the explosion directly or through the use of detection and control systems. For effective isolation, however, these systems must activate rapidly. A thorough understanding of flame propagation through vessel-pipe systems is needed to ensure these systems are designed, installed, and tested appropriately.

To develop engineering guidance and a methodology to certify explosion isolation systems, an extensive research program is underway at FM Global. Large-scale experiments are being conducted to study the dynamics of both gas and dust explosions in vessel-pipe systems and physics-based models are being developed to predict flame propagation.

Previous work within this program (Boeck et al., 2018; 2021) focused on gas explosions in vessel-pipe systems, performed large-scale experiments, and developed physics-based models to predict explosion dynamics across a wide range of geometries and mixture reactivities. While gas explosions provided an ideal first scenario to consider, since experiments can be controlled precisely and models can be formulated based on fundamental combustion properties, dust explosion applications present the majority of scenarios where explosion isolation is deployed.

This study addresses dust explosions in vessel-pipe systems. Large-scale experiments were performed and a recently developed dust reactivity model was incorporated into the modeling framework for vessel-pipe systems. The experimental results for dust are compared against previous experiments with gases and the updated model is evaluated against experimental data.

2. Experiments

Experiments were conducted in a vessel-pipe system, see Fig. 1, which includes an 8-m^3 vessel vented at the top (vent diameter: 0.8 m) and a pipe attached to the side of the vessel (diameter: 0.4 m; length: 9.8 m). Sheets of aluminium foil (thickness: 0.076 mm) were used to simulate a low-inertia explosion vent panel, where the vent deployment pressure was controlled by the number of foil layers. For this study, all experiments were performed with four layers, which resulted in a static deployment pressure of 0.34 bar-g.

The vessel-pipe system was purged with dry air prior to each test, and combustible dust was introduced using a system of four dust injectors installed at the vessel. The injection system provided sufficient dust to achieve flame propagation throughout the entire system without the need for supplemental dust injection directly into the pipe. Cornstarch dust was used in the present work as a representative St-1 dust (K_{St} = 155–166 bar·m/s; $p_{\max}$ = 7.9–8.1 bar-g according to ASTM E1226 tests of multiple samples). The dust was dried prior to each test to ensure a moisture content less than 1%. Ignition was affected after a defined ignition delay time, measured from the start of dust injection, using two 5-kJ chemical igniters (Sobbe EBBOS ChZ) located at one of three locations: at the vessel center (x = 0 m), at the vessel back-wall (x = – 0.9 m), or at the front near the pipe entrance (x = 0.9 m), see Fig. 2.

Fig. 1: *Experimental setup including vented 8-m^3 vessel and attached pipe. Image taken during a dust explosion experiment showing flame exiting through the vent and the pipe*

Reference closed-volume experiments were conducted in the 8-m^3 vessel, without venting or an attached pipe, to determine the appropriate ignition delay that yields the desired dust reactivity. For all dust experiments discussed in this work, a delay of 0.65 s was used to obtain an effective deflagration index of K_{eff} = 200 bar·m/s, which signifies the upper bound of the St-1 dust reactivity class.

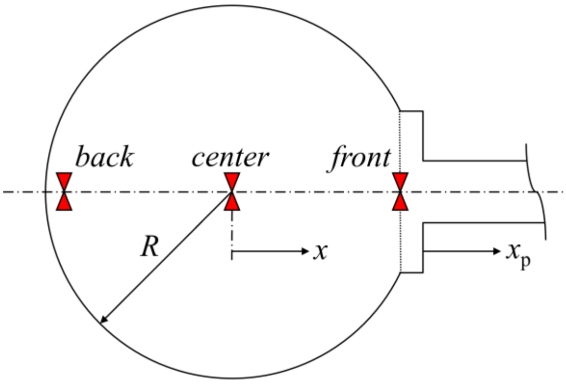

Fig. 2: *Schematic of explosion vessel, plan view, including ignition locations (red markers)*

Diagnostics included pressure measurements at the vessel (three redundant Kistler 4260A transducers), as well as pressure measurements (Kistler 211B transducers) and optical flame detectors (Thorlabs PDA36A2 detectors) distributed along the pipe.

3. Physics-based model

A physics-based model was developed previously to simulate gas explosions in vessel-pipe systems. This model considers three elements: (1) a vessel; (2) a vent installed at the vessel; and (3) a pipe attached to the vessel. For each element, equations are solved numerically using a Runge-Kutta method to determine the parameters of interest, including the vessel pressure and the location of the flame front inside the vessel and in the pipe, as a function of time. The model details are provided in Boeck et al., 2021, and a brief summary is given in the following.

- In the vessel, a mass balance equation is solved for the unburned and burned mixture considering combustion and flow through the vent and pipe. Equations for isentropic compression are solved to determine the vessel pressure. The flame expands either spherically or hemi-spherically, depending on the ignition location, and the flame tip is advected toward the vent or pipe.
- The vent deploys at a specified pressure, and both unburned and burned gases are vented at a ratio that depends on the size of the flame. The total venting rate is calculated assuming constant-enthalpy flow, which depends on the vessel pressure and the ambient pressure. Once the flame exits from the vent, an external explosion is considered that temporarily increases the ambient pressure and reduces the venting rate.
- Flow and turbulent combustion in the pipe are modeled using the momentum equation integrated for incompressible flow, including terms for pressure loss due to wall friction, inlet and outlet losses, and flow inertia.

This model is modified in the present study to capture dust explosions, which necessitates several changes to parts of the model that describe combustion in the vessel, venting and external explosion, and flame propagation in the pipe. The following sections summarize these changes.

3.1 Combustion inside the vessel

A key requirement for modeling explosions in vessel-pipe systems is to accurately capture the rate of combustion inside the vessel as a function of time. The existing gas combustion model (Boeck et al., 2021) is not suitable to describe dust explosions as the physics controlling the propagation of turbulent dust flames are fundamentally different.

It is important to note that turbulent dust flames cannot be described accurately by a constant turbulent burning velocity. Figure 3 shows a comparison of experimental and simulated pressure traces of a cornstarch explosion in the closed 8-m^3 vessel. Two simulations are shown, which assume spherical flame propagation and constant burning velocities of 0.95 m/s or 1.45 m/s. While the former value captures the early combustion and the early pressure rise (pressures below about 0.1 bar-g) and the latter captures the maximum rate of pressure rise, neither one captures the entire process, clearly demonstrating the need for a physics-based dust combustion model.

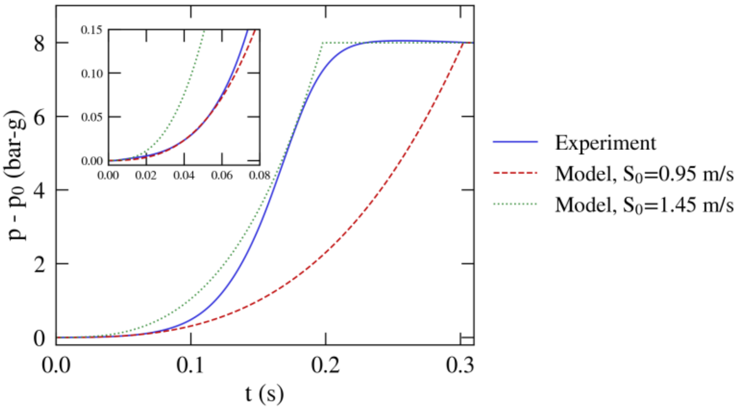

Fig. 3: *Comparison between cornstarch explosion experiment in the 8-m*^{3} *vessel and simulations assuming constant turbulent burning velocities, demonstrating inaccurate model predictions*

In this study, turbulent dust flame propagation inside the vessel is modeled using the approach developed by Bauwens et al. (2020) for characterizing dust reactivity in large-scale explosions, which considers an expanding turbulent flame that entrains unburned dust-air mixture across its leading edge and consumes the mixture within a flame zone at a finite rate. The mass balance inside the vessel considers the unburned mass ahead of the flame, m_u, the unburned mass in the flame zone, $m_\mathrm{f,u}$, and the burned mass, m_b:

$$\frac{dm}{dt} = \frac{dm_\mathrm{u}}{dt} + \frac{dm_\mathrm{f,u}}{dt} + \frac{dm_\mathrm{b}}{dt}. \tag{1}$$

This mass balance only considers the oxidizer as the limiting component during combustion at optimum dust concentration. The change in unburned mass in the flame zone is the balance of the entrained unburned mass and conversion to burned mass in the flame zone,

$$\frac{dm_\mathrm{f,u}}{dt} = S_\mathrm{t}\rho_\mathrm{u}A_\mathrm{f} - \frac{dm_\mathrm{f,b}}{dt}. \tag{2}$$

The turbulent burning velocity, S_t, is governed by turbulent mixing and increases as the expanding flame, with flame radius r_f, interacts with growing turbulent length scales,

$$S_\mathrm{t} = S_\mathrm{t,0}\left(\frac{r_\mathrm{f}}{R}\right)^{\frac{1}{3}}, \tag{3}$$

where $S_\mathrm{t,0}$ represents the characteristic burning velocity of the mixture and R is the vessel radius. The burning rate within the flame zone is limited by the rate of oxygen diffusion toward the dust particles,

$$\frac{dm_\mathrm{f,b}}{dt} = \frac{p_0}{p}\left(\frac{T_\mathrm{f}}{T_0}\right)^{1.75}\frac{m}{\tau}\left(\frac{m_\mathrm{f,u}}{m_\mathrm{f,u}+m_\mathrm{b}}\right), \tag{4}$$

where τ is a characteristic combustion time. Further assumptions made to evaluate Eq. (4) are given in Bauwens et al. (2020). In summary, dust reactivity is described by two parameters, $S_\mathrm{t,0}$ and τ, which are determined by fitting model predictions to the pressure histories from experiments conducted in closed vessels. The compression of gases inside the vessel is assumed to be isentropic, which allows for calculating the unburned and burned gas densities and the vessel pressure.

Figure 4 shows experimental and simulated pressure traces for a cornstarch explosion conducted in the closed 8-m^3 vessel. The two-parameter dust combustion model closely captures the entire pressure trace using the reactivity parameters $S_{t,0}$ = 1.71 m/s and τ = 0.062 s, expansion ratio σ = 8, and maximum explosion pressure p_{max} = 8 bar-g.

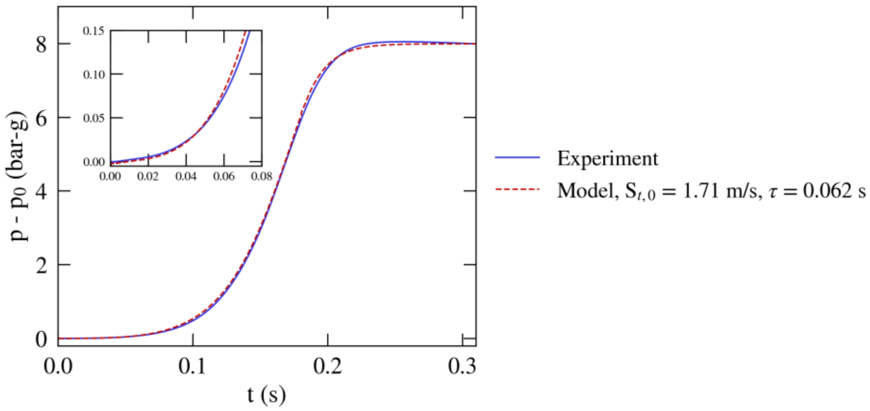

Fig. 4: *Comparison between cornstarch explosion experiment in the 8-m³ vessel and simulation using the dust combustion model (Bauwens et al., 2020), demonstrating close agreement*

3.2 Venting and external explosion

The existing vessel-pipe explosion model describes venting based on constant-enthalpy flow, which results in an expression for the velocity of the vented gases, u_v, as a function of the vessel pressure, p, and the external pressure outside the vent, p_e. The effect of flow inertia on the venting rate is considered in the present work as an additional pressure loss/gain across the vent,

$$\Delta p_{v,i} = L_v \rho_v \frac{du_v}{dt}, \tag{5}$$

where L_v is the effective length of the vent throat and ρ_v is the density of the vented mixture including unburned dust loading. The effective length of the vent throat is estimated at $L_v = 2R_v$ based on the vessel geometry and end corrections.

The external explosion, which occurs when the flame exits the vent and consumes the previously vented unburned mixture, is modeled according to Strehlow (1979) based on acoustic theory applied to an expanding flame. This yields a relation for the external pressure outside the vent, p_e,

$$\frac{p_e}{p_{e,0}} - 1 = \frac{\gamma(\sigma - 1)}{4\pi a_{e,0}^2 R_e} \frac{d}{dt}\left(S_e A_{f,e}\right). \tag{6}$$

To evaluate this relation, the present work describes the burning velocity S_e of the flame within the external cloud analogous to the combustion inside the vessel,

$$S_e = S_{t,0} \left(\frac{r_{f,e}}{R}\right)^{\frac{1}{3}}, \tag{7}$$

where the $r_{f,e}$ is the radius of the external flame, and a thin flame is assumed ($\tau \rightarrow 0$, *cf.* Sec. 3.1).

3.3 Flow and combustion in the pipe

Flow and combustion in the pipe are described based on the momentum equation integrated for incompressible flow. The present work continues to use this approach and modifies the treatment of combustion using a simple scaling for the turbulent burning velocity inside the pipe, $S_{t,p}$, as a function of the characteristic turbulent burning velocity, $S_{t,0}$, the turbulent fluctuation velocities in the pipe and vessel, $u'_{p,2}$ and u', and the radii of the pipe and vessel, R_p and R,

$$S_{\mathrm{t,p}} = S_{\mathrm{t,0}} \left(\frac{R_{\mathrm{p}}}{R}\right)^{\frac{1}{3}} \left(1 + \frac{u'_{\mathrm{p,2}}}{u'}\right). \tag{8}$$

The turbulent fluctuation velocity in the pipe is related to the bulk flow velocity in the pipe ahead of the flame, $u_{\mathrm{p,2}}$, the pipe radius, R_{p}, and the kinematic viscosity, $\nu_{\mathrm{p,2}}$ (Basse, 2017),

$$u'_{\mathrm{p,2}} \propto u_{\mathrm{p,2}} \left(\frac{u_{\mathrm{p,2}} R_{\mathrm{p}}}{\nu_{\mathrm{p,2}}}\right)^{-0.11}. \tag{9}$$

Hence, the turbulent burning velocity in the pipe is calculated as

$$S_{\mathrm{t,p}} = S_{\mathrm{t,0}} \left(\frac{R_{\mathrm{p}}}{R}\right)^{\frac{1}{3}} \left[1 + k_{\mathrm{t,p}} \frac{u_{\mathrm{p,2}}}{u'} \left(\frac{u_{\mathrm{p,2}} R_{\mathrm{p}}}{\nu_{\mathrm{p,2}}}\right)^{-0.11}\right], \tag{10}$$

where $k_{\mathrm{t,p}}$ is a model parameter. A turbulent fluctuation velocity $u' = 4.1$ m/s was assumed based on measurements inside the vessel after an ignition delay time of 0.65 s using a bidirectional probe.

4. Results and model comparisons

This section discusses the results from two series of gas and dust explosion experiments conducted in the same vessel-pipe setup introduced in Sec. 2 and evaluates the model predictions for dust explosions against experiments.

4.1 Qualitative comparison of gas and dust explosions

Qualitative comparison of experimental observations is the first step to identify key physics of gas and dust explosions in the vessel-pipe setup described in Sec. 2. Figure 5 shows the results of gas explosion experiments performed under initially quiescent conditions with mixtures of 3.5% propane in air, where pressure traces (left) and flame-arrival times along the pipe (right) were obtained from experiments with different ignition locations. Markers in the pressure plot identify the times and vessel pressures at vent deployment.

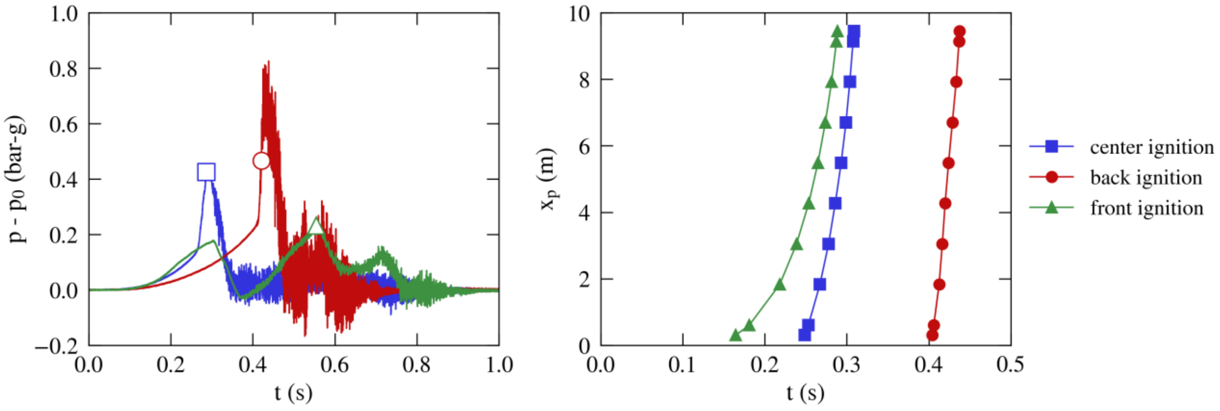

Fig. 5: *Gas explosion experiments with initially quiescent 3.5% propane-air mixture, for three different ignition locations. Vessel pressure (left) with markers indicating vent deployment, and flame-arrival times along the pipe (right)*

DOI: 10.7795/810.20221124

The main observations from these gas explosion experiments are:

- Back ignition led to the highest peak pressure of 0.83 bar-g inside the vessel, followed by center (0.46 bar-g) and front ignition (0.23 bar-g). Note that only two vent foil layers were used with front ignition, compared to three layers for center and back ignition, *i.e.*, the peak pressure for front ignition is not directly comparable.
- Back ignition led to clearly slower early pressure rise than center or front ignition.
- Significant acoustic oscillations occurred in each test, which appear to be triggered by vent deployment. The highest acoustic pressure amplitudes were observed for back ignition, followed by center and front ignition.
- A characteristic sharp rise in vessel pressure was observed for center and back ignition when the flame entered the pipe, at 0.24 s and 0.41 s, respectively, which is related to high turbulent combustion rates in the pipe resulting in significant thermal expansion and reduced venting of gases through the pipe with potential back-flow from the pipe into the vessel.
- Front ignition led to the earliest flame arrival at the pipe entrance and at all sensor locations along the pipe, followed by center and back ignition.

Experiments shown in Fig. 6 were conducted with cornstarch dust using an ignition delay of 0.65 s and four vent foil layers.

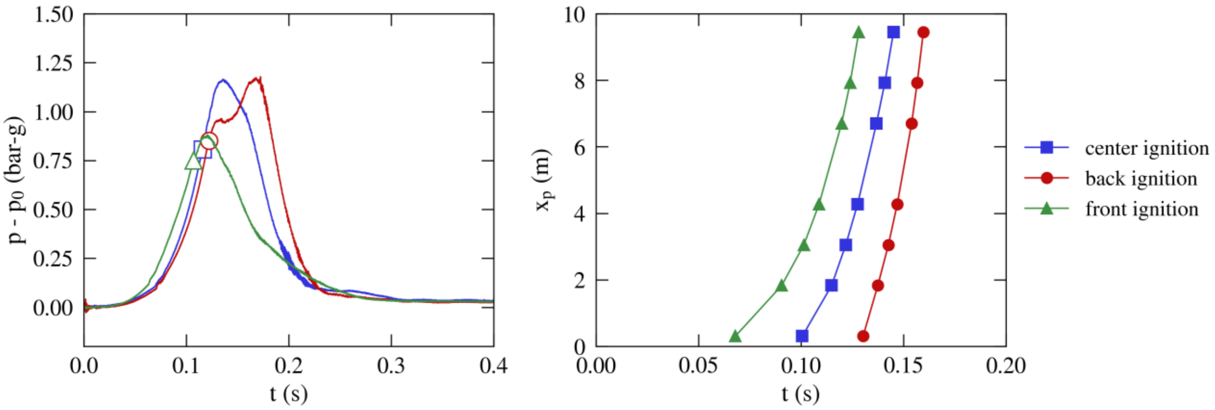

Fig. 6: *Dust explosion experiments with cornstarch and an ignition delay of 0.65 s, for three different ignition locations. Vessel pressure (left) with markers indicating vent deployment, and flame-arrival times along the pipe (right)*

The main observations from these dust explosion experiments are:

- All three dust explosions showed significantly higher reactivities than the previous gas explosions, with consistently faster pressure rise and earlier flame arrival along the pipe.
- The evolution of pressure showed smaller differences between all three ignition locations compared to gas explosions. Front ignition led to slightly faster early pressure rise compared to center or back ignition, whereas peak pressure was the lowest for front ignition (0.88 bar-g) compared to center (1.16 bar-g) and back (1.18 bar-g) ignition.
- No significant acoustic oscillations occurred with only minor amplitudes observed toward late times, t ≈ 0.2 s.
- No significant change in the rate of pressure rise in the vessel was observed upon flame entrance into the pipe, in contrast to previous gas explosions.
- Front ignition led to the earliest flame arrival along the pipe, followed by center and back ignition.

The qualitative comparison between gas and dust explosion experiments reveals significant differences in pressure and flame dynamics with practical implications for explosion isolation applications. Gas experiments and modeling were discussed in detail in previous work (Boeck et al., 2021). The following sections therefore focus on further analyses of dust explosion experiments and modeling.

4.2 Analysis of dust explosion experiments and model predictions

All three experiments shown in Fig. 6 are further analyzed and used in this section to evaluate model predictions. The vessel-pipe explosion model described in Sec. 3 is exercised using the dust reactivity parameters $S_{t,0}$ = 1.71 m/s and τ = 0.062 s, which captured dust reactivity accurately for the closed 8-m^3 vessel, see Fig. 4. The vessel-pipe dust explosions were conducted using the same dust injection parameters, including an ignition delay of 0.65 s, with the goal of maintaining the reactivity from the closed-vessel reference experiments.

Figure 7 shows experimental and simulated pressure traces (left) and flame-arrival times along the pipe (right) for center ignition. The model predictions generally show good agreement with the experimental pressure traces and flame-arrival times. Especially before vent deployment at $t = 0.11$ s, pressure traces show excellent agreement indicating that the dust reactivity is comparable to the closed-vessel reference experiments. Experimental and simulated traces diverge after vent deployment where venting rates are slightly over-predicted by the model at $0.12 \text{ s} < t < 0.19$ s. The simulated flame reaches the vessel walls at $t = 0.19$ s, resulting in a fast drop in vessel pressure until all remaining unburned mass in the flame zone is consumed at $t = 0.2$ s. In the experiment, the final burnout process appears to be slower, leading to a more gradual drop in pressure at later times ($t > 0.19$ s). Flame-arrival times along the pipe are predicted accurately with differences between model and experiment less than 3 ms at all sensor locations. The accurate prediction of flame arrival at the pipe entrance suggests accurate prediction of flame advection (advection model described in Boeck et al., 2021), which assumes that the leading edge of the flame inside the vessel is advected toward the pipe entrance and therefore arrives significantly before burnout. Flame acceleration along the pipe is captured well by the model and is governed by the evolution of flow velocity ahead of the flame, $u_{p,2}$, which affects the turbulent burning velocity in the pipe, $S_{t,p}$. The parameter $k_{t,p}$ used in Eq. (10) is taken as $k_{t,p} = 1$ in this simulation and kept constant for the following simulations of back and front ignition scenarios.

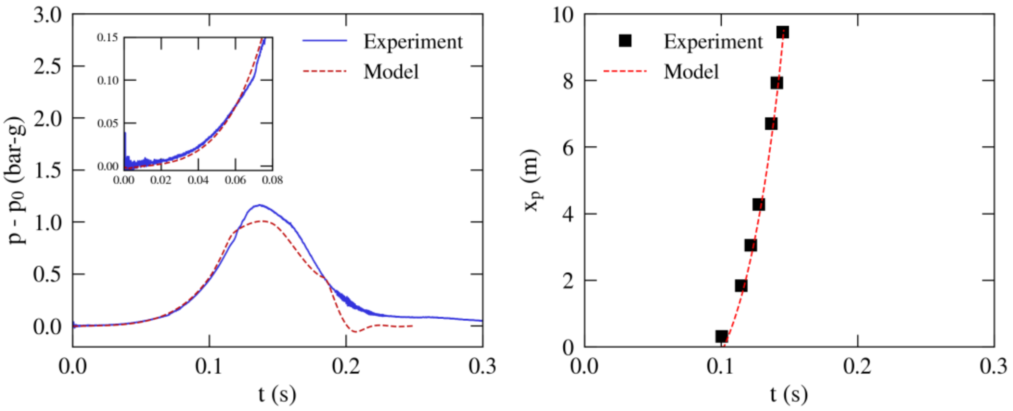

***Fig. 7:** Comparison of experimental and modeled pressure traces (left) and flame-arrival times (right), center ignition*

For modeling back ignition of gas explosions, previous work (Boeck et al., 2021) assumed a hemispherical flame geometry, which led to model predictions that closely captured the experimental results. Figure 8 shows that using this assumption (dotted lines), the present model for dust explosions under-predicts the pressure rise and therefore over-estimates flame-arrival times along the pipe in the case of back ignition. The assumption of a hemispherical flame geometry appears to under-estimate the generation of flame surface area as a function of flame radius. Dashed lines in Fig. 8 show model predictions assuming a spherical flame geometry, resulting in better agreement of pressure and flame arrival predictions with experiments.

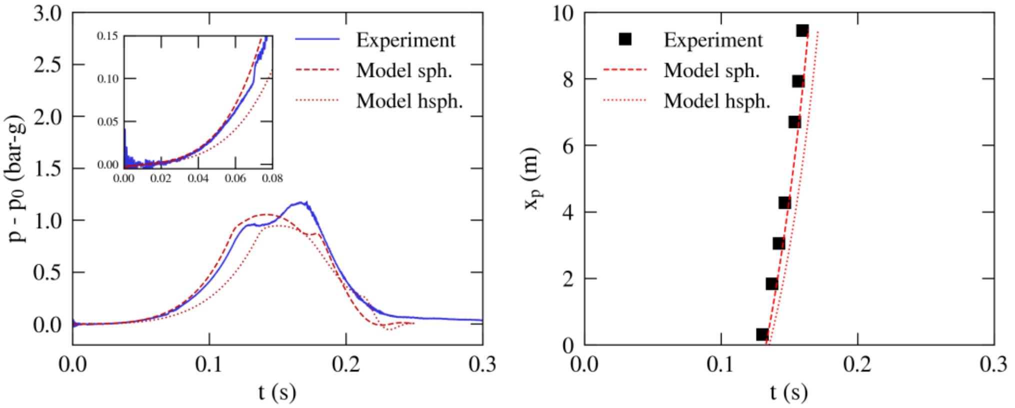

Fig. 8: *Comparison of experimental and modeled pressure traces (left) and flame-arrival times (right), back ignition*

Also for front ignition, see Fig. 9, a hemispherical flame geometry assumption (dotted lines) under-predicts early combustion rates in the vessel compared to experiments, whereas a spherical flame geometry (dashed lines) produces better agreement at early times but slightly over-predicts the peak pressure. While previous gas explosion tests were performed using initially quiescent conditions and low-energy spark ignition, the present experiments use elevated initial turbulence and chemical igniters. It appears that the combination of turbulence with the relatively large initial flame kernel produced by a high-energy ignition source may result in flame development that resembles a spherical flame rather than a hemispherical flame with regard to the overall rate of combustion.

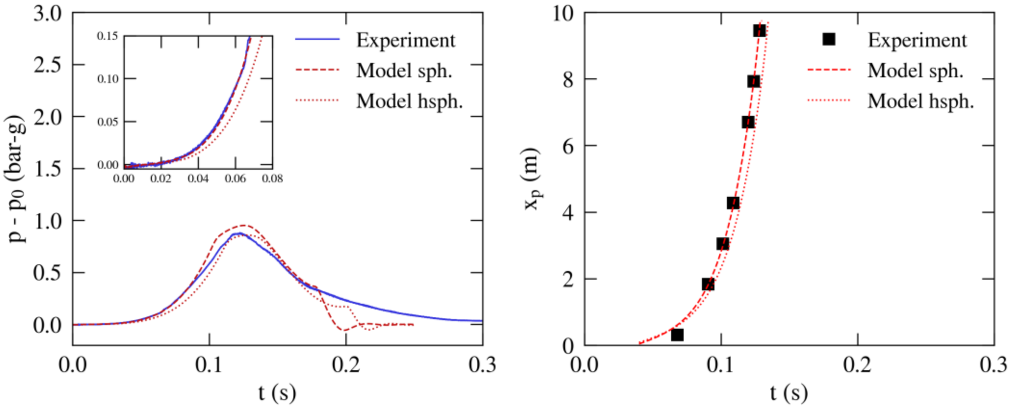

Fig. 9: *Comparison of experimental and modeled pressure traces (left) and flame-arrival times (right), front ignition*

The model captures early flame arrival at the pipe entrance in the case of front ignition, with initially slower flame velocities followed by significant acceleration, see Fig. 9, right panel, capturing flame-arrival times to within ±8 ms at all sensor locations.

5. Conclusions

Large-scale dust explosion experiments were conducted in a vessel-pipe system including an 8-m^3 vented vessel and an attached pipe with a diameter of 0.4 m and a length of 9.8 m. The experimental conditions included the use of cornstarch dust and elevated initial turbulence, resulting in a representative St-1 explosion hazard. Pressure transients and flame progress were recorded.

A previously developed vessel-pipe explosion model was extended to consider dust combustion and model predictions were compared against the experimental results. Across all three investigated ignition locations, the model was able to capture the principal features of the pressure transients and predicted flame-arrival times to within ±8 ms at all sensor locations along the pipe. Further model validation will be performed using additional experimental data from both experiments performed at FM Global and literature studies, focusing on the effects of geometric scale and reactivity.

References

Bartknecht, W. (2012). *Explosions: course, prevention, protection*. Springer Science & Business Media.

Bauwens, C.R., Boeck, L.R., & Dorofeev, S.B. (2020). A simple dust combustion model for characterizing reactivity in large-scale experiments. *13th ISHPMIE, Braunschweig, Germany.*

Boeck, L.R., Bauwens, C.R., & Dorofeev, S.B. (2018). A physics-based model for explosions in vented vessel-pipe systems. *12th ISHPMIE, Kansas City, USA.*

Boeck, L.R., Bauwens, C.R., & Dorofeev, S.B. (2021). Modeling of explosion dynamics in vessel-pipe systems to evaluate the performance of explosion isolation systems. *Journal of Loss Prevention in the Process Industries*, 71: 104477.

Eckhoff, R. K. (2016). *Explosion hazards in the process industries*. Gulf Professional Publishing.

Hattwig, M., & Steen, H. eds. (2008). *Handbook of explosion prevention and protection*. John Wiley & Sons.

Strehlow, R. A. (1979). *The blast wave from deflagrative explosions, an acoustic approach*. Tech. rep., University of Illinois.

DOI: 10.7795/810.20221124

Thermal structure of Aluminum Dust Explosion with Additional Carbon Dioxide

Po-Jul Chang [a], Toshio Mogi [a] & Ritsu Dobashi [a]

[a] Department of Chemical System Engineering (The University of Tokyo, Tokyo, Japan)

E-mail: dobashi@chemsys.t.u-tokyo.ac.jp

Abstract

Temperature of aluminum dust explosion involving different percentages of CO_2 were investigated. The results show that as CO_2 higher than 40%, ignition temperature decreases for near 400 K in the case of micro-scale aluminum. Moreover, the time for igniting nano-Al dust clouds reduced to half (from 120 msec to 60 msec) as part of N_2 was replace by CO_2 compared to O_2/N_2 composition, while O_2 % kept the same. The condensation of its oxide was used to explain the change of flame temperature and ignition time. Thermal equilibrium products were calculated to conjecture the possible condensed products. The results suggest that under O_2/N_2 environment, flame temperature of micro aluminum is limited by the boiling point of Al_2O_3, on the other hand, flame temperature of nano aluminum is limited by the reaction of AlN. The replacement of N_2 by CO_2 can change the dominated products to Al_4C_3 for both micro and nano scale aluminum, and the flame temperature is determined by the dissociation or reduction of Al_4C_3. Finally, dust explosion was conducted under Ar/O_2 to exclude the possible condensation of AlN and Al_4C_3, and significant increase of flame temperature was observed.

Keywords: *aluminum, dust explosion, flame temperature*

1. Introduction

In dealing with dust explosion, one can consider a very quick response of suppressant injection to suppress explosion (Taveau et al., 2015), or adding CO_2 to N_2/O_2 mixture creates an inert environment (Eckhoff, 2005). Nevertheless, it is interesting to note that combustion of aluminum under CO_2 is also considered as an energetic fuel for rocket engine (Shafirovich and Varma, 2008). Although, the combustion of propellants is normally conducted under much higher pressure (a few MPa) than dust explosion (usually around one atmosphere), question may still arise that can CO_2 be used as an oxidizer meanwhile as a fire extinguisher for aluminum dust explosion. Moreover, the recent increase of nano-particle application, due to its high surface area, makes the potential risk more uncertain.

It has been generally accepted that the combustion temperature of aluminum can be strongly affected by the characteristics of its oxide, such as Al_2O_3 or AlO (Yetter, 2009). For example, the non-volatile of Al_2O_3 requires the heat released from chemical reactions higher than its heats of gasification, otherwise, the condensed oxide to the particle surface can limit the equilibrium flame temperature. As a result, flame temperature is determined by the characteristics of oxide. Those fragmentations of oxide which diffuses back to the burning particle is known as “oxide cap”, and the products of aluminum oxidation are not limited to the reaction with O_2. For instance, Dreizin (1999) has found that the size of oxide caps under Ar/O_2 and He/O_2 environment was considerably smaller than under N_2/O_2. This result implies that nitrogen was involved in the combustion of aluminum, and a one-dimensional equilibrium calculation suggests that NO was formed in the fuel-lean regime. Moreover, Glorian et al. (2016) simulated heterogeneous reactions on burning aluminium particle, the results also show that in O_2/Ar environment, the residue size is considerably smaller than pure CO_2

environment. On the other hand, Yuasa (1997) indicated that only traced amount of AlN spectrum can be identified in the condensed smoke, thus it was concluded that the influence of N_2 is insignificant to the combustion of aluminum. Zhang (2021) suggested that the dilution of O_2 by N_2 or CO_2 can suppress dust explosion, but the kinetic model show N_2 did not involve in reactions. The question remains that whether nitrides change the flame temperature and whether the replacement of N_2 by CO_2 is effective for supressing aluminum combustion.

In current work, dust explosions were conducted under N_2/O_2, CO_2/O_2, and Ar/O_2 mixtures. With the help of a two-color pyrometer, it allowed us to observe flame temperature. Based on the equilibrium calculations, we tried to propose possible dominated products during dust explosion.

2. Experiments

2.1 *Materials*

Experiments were conducted using two aluminum particle sizes. Micron size Al (High Purity Chemicals, Japan) was sieved to the range between 10-20 µm, and 100 nm Al (uncoated, Alex) were used as received from the makers. For 100 nm Al, the surface area was determined by BET method (Nova 4200e, Quantachrome), and the calculated BET equivalent diameter is 240 nm. The samples were confirmed by thermogravimetric analysis (RIGAKU, Thermoplus TG8120) under air atmosphere, and the sample powders were under well-dried condition without significant mass change at water boiling point.

2.2 *Gas compositions*

For gas mixtures, oxygen concentrations were all the same at ~22 %, and the rest part (~78%) was mixtures of CO_2, N_2, or Ar. Volumetric gas fractions were calculated by its partial pressure ratio. The prepared mixing gases were then confirmed by an oxygen monitor (JIKCO, JKO-A Ver.3). Results show that the variation of O_2 % in each test was around ±1 %.

2.3 *Experimental apparatus*

Dust explosions were performed with a half-open system as illustrated in Figure 1. The dispersion procedures of powders follow the JIS standard (JIS Z 8818, 2002) as for the procedure of minimum explosible concentration (MEC) measurement. Initially, the sample powders were placed on the bottom of tube (diameter = 70 mm, length = 290 mm), and at top of the tube was covered by a paper filter to prevent powder from following out. At first, the inside air was purged by mixing gas from tank A for 15 sec. As long as purging had stopped, a blast of air (from a 0.0013 m^3 premixing tank B at pressure 0.07 MPa) dispersed the sample forming a dust cloud in the tube. After 0.5 sec delay from blast, a 15 kV neon transformer was arcing for 0.2 sec to generate an ignition spark (around 60 J). In the middle of cylinder tube, a view port was made of quartz glass which allows a high-speed camera to record the explosion process. The dust clouds were under fuel-rich condition at concentration of 670 g/m^3 (equivalent ratio = 2.2) for all experiments.

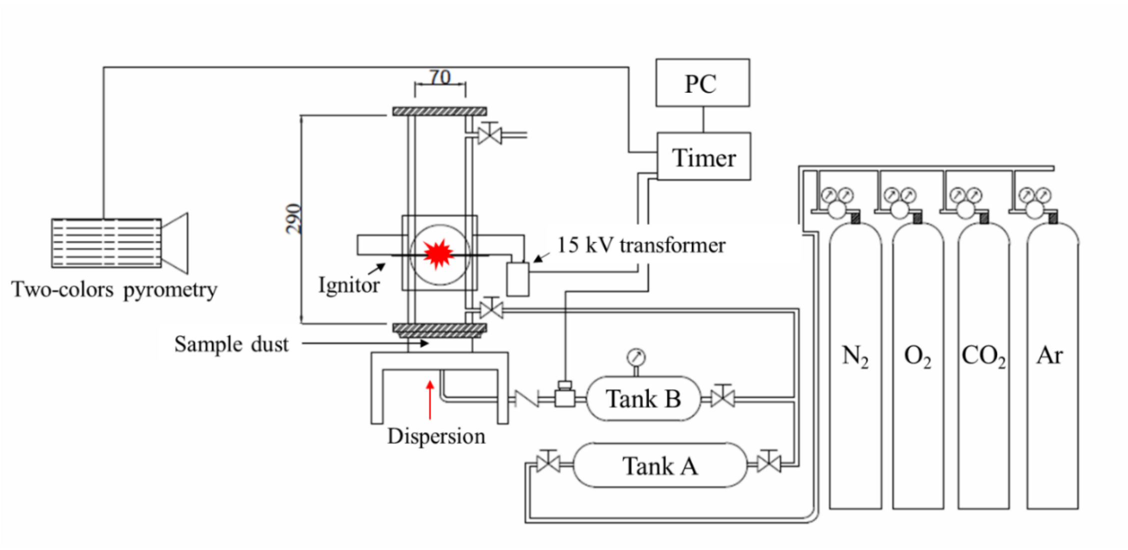

Fig. 1. *Experimental setup*

2.4 Two-color pyrometer

A broadband two-color ratio was measured by a high-speed camera (Photron, FASTCAM SA2). ND filter was set in front of lens to prevent signal from saturation. The unprocessed raw data were recorded in 8bits Bayer filter as RGGB pattern. Due to relative weak intensity of blue (B) light in the current work, red (R) and green (G) were chosen for temperature measurement. The average G/R ratio at each pixel was calculated from the surrounding 3x3 matrix (Chang et al., 2021). Temperatures were calibrated by Tungsten Halogen lamp (Newport, QTH 20w) from 1000~2500 K under air atmosphere. In order to make sure that different atmosphere does not affect the ratio of selected broadband wavelength, the calibrations were also conducted under 100 % of CO_2, Ar, and N_2 as showed in Figure 2. The results indicated that different gas mixtures did not affect G/R ratio. Emissivity is assumed to be constant at the detection range of wavelength (Gray body assumption), and temperature can be measured as the function of two-color ratio (Goulay et al., 2010). A computer code (python 3.8) was written to solve for the temperature in 2048x2048 pixel pictures.

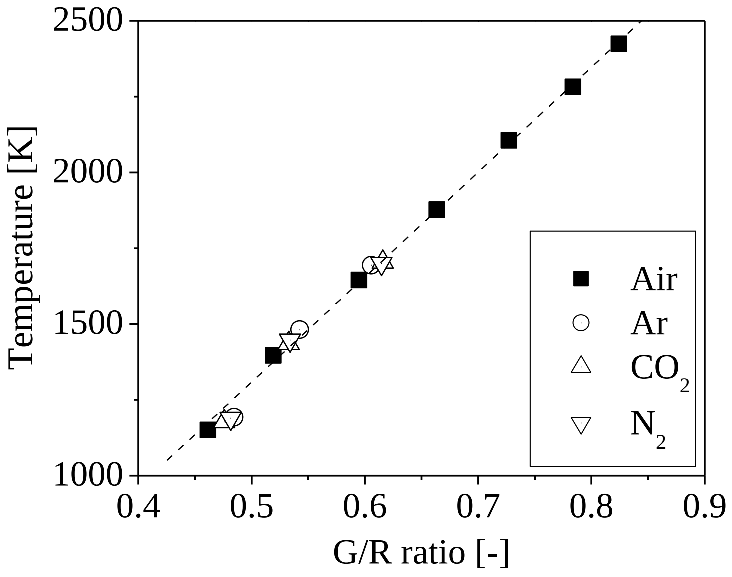

Fig. 2. *Temperature calibration under different atmosphere*

3. Results and discussion

3.1 Inerting by Adding CO_2 gas

3.1.1 10-20 μm Al

Figure 3 summarizes the temperature history under three gas mixtures (1) 22 % O_2 + 78 % N_2 (2) 22% O_2 + 41 % CO_2 + 37 % N_2 (3) 22% O_2 + 78 % CO_2. Without additional CO_2, average dust cloud temperature kept at ~3000 K for initial 10 msec, and gradually decreased to ~2600 K as flame propagated away from the electrode. By contrast, with additional CO_2, aluminum dust clouds can be ignited slightly faster, and the temperatures decreased quickly as flame propagated away from the electrode. After successful ignition for 20 msec, the average temperatures were stable and maintained at ~2770 K and ~2580 K under 41 % CO_2 and 78 % CO_2, respectively. For comparison, Figure 4 shows the average temperature of initial 10 msec after aluminum dust clouds were ignited. The error bar displays the standard deviation. Once CO_2 is higher than 40%, the temperature significantly drops for ~370 K.

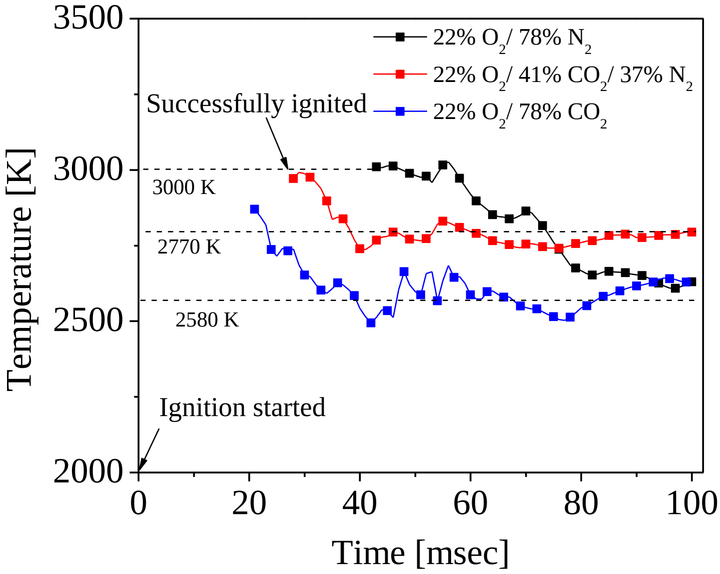

***Fig. 3.** Comparison of temperature history by different gas mixtures*

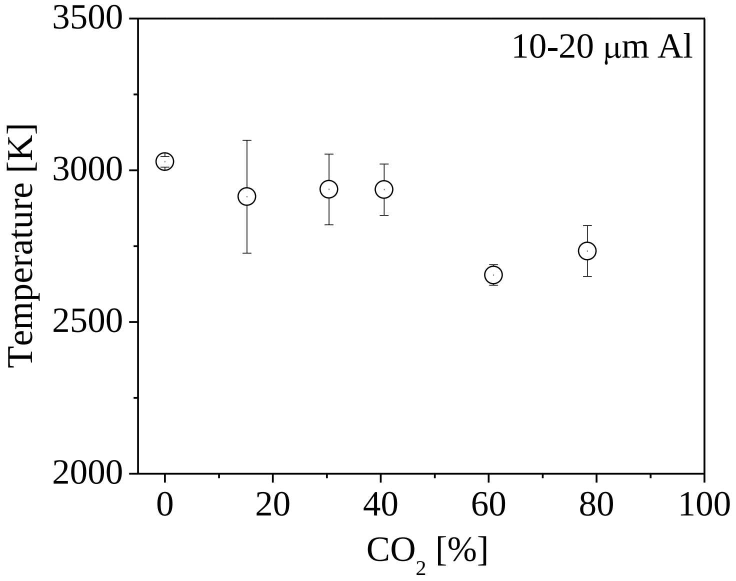

Fig. 4. *The initial temperature of 10-20 μm Al by* CO_2*%*

Figure 5, 6, and 7 show the temperature image of 10-20 μm Al during dust explosion. After electrode discharging, without additional CO_2 it took around 45 msec for dust cloud to be ignited, and then a stable flame propagation started. At flame front, there was a notable temperature difference between top edge and bottom edge as showed in Figure 5. This can be explained by the continuous discharging of electrode during the whole explosion, and dust clouds near electrode should be likely to have higher external energy. On the other hand, partial replacement of N_2 by CO_2 made the flame propagation become fragile. In addition, as flame propagated upward there was no burning dust left behind near electrode, so no significant temperature difference between top edge and bottom edge was observed as showed in Figure 6. Figure 7 shows the temperature profiles when N_2 was completely replaced by CO_2. The flame propagation was stable, and there was also no burning dust left behind, which suggests that particle burning time was shorter under O_2/CO_2 than O_2/N_2. Rossi et al. (2000) and Bucher et al. (1999) also concluded that a single aluminum particle is burning faster under pure CO_2 than air atmosphere.

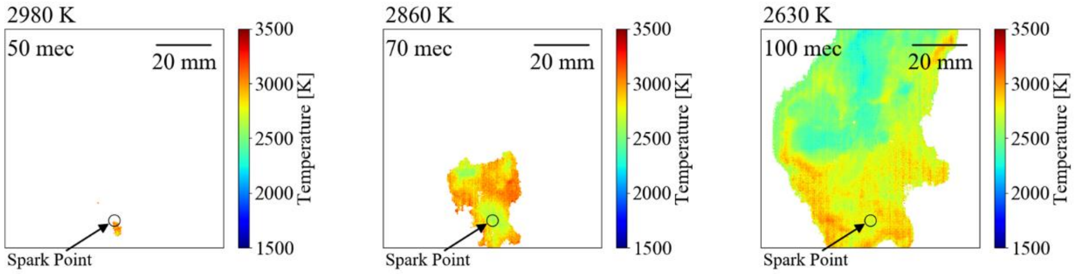

Fig. 5. *The temperature images of 10-20 μm Al dust explosion under 22 %* O_2 *+ 78 %* N_2

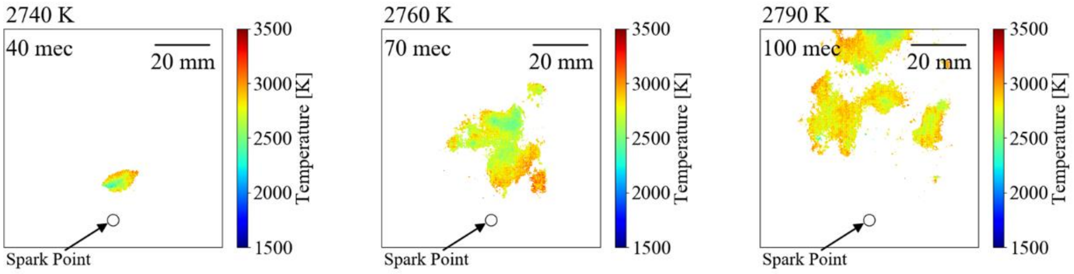

Fig. 6. *The temperature images of 10-20 µm Al dust explosion under 22 %* O_2 *+ 41 %* CO_2 *+ 37 %* N_2

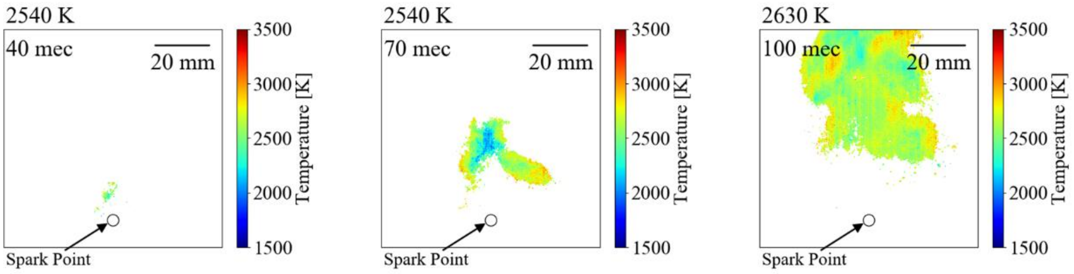

Fig. 7. *The temperature images of 10-20 µm Al dust explosion under 22 %* O_2 *+ 78 %* CO_2

3.1.2 100 nm Al

Figure 8 shows the temperature history of 100 nm Al under (1) 22% O_2 + 78% N_2 (2) 22% O_2 + 63% N_2 + 15 % CO_2 (3) 22% O_2 + 17% N_2 + 61% CO_2 (4) 22% O_2 + 78% CO_2. In the case without CO_2, the ignition started at lower temperature of around 2400 K. After 20 msec, the average temperature gradually increased to a stable plateau of around 2700 K. On the other hand, as CO_2 higher than 61%, the temperature was stable from the beginning of ignition. It is interesting to note that without CO_2, it took around 120 msec for ignition which was around twice longer than the case of 61% and 78% CO_2 of around 60 msec. Moreover, even though N_2 was completely replaced by CO_2, the maximum temperature difference was less than 200 K.

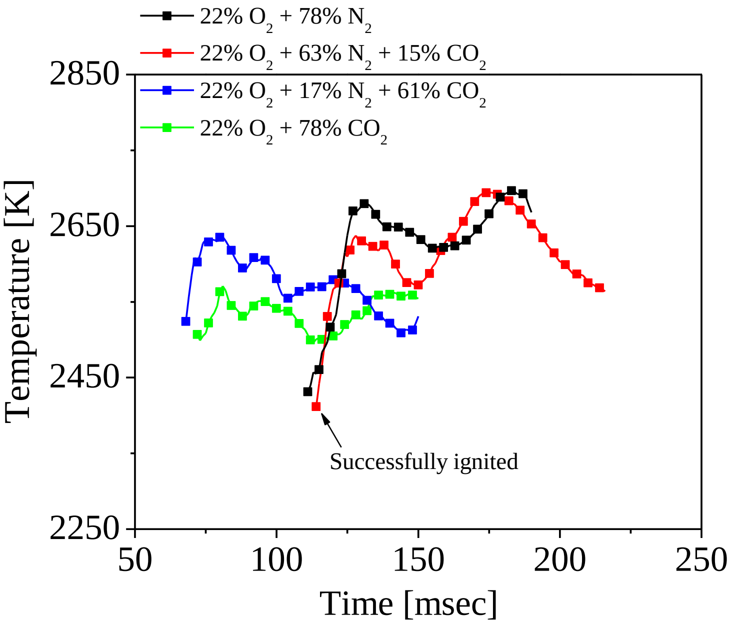

Fig. 8. *Temperature histories of 100 nm Al under different gas compositions*

Figure 9 shows the temperature images of 100 nm Al under 22% O_2 + 78% N_2. At first, aluminum dust was ignited by arcing spark. However, the reaction rate initially was slow, and it took around 120 msec to have a notable light emission; meanwhile dust clouds flowed upward by inertia of dispersion gas. As a result, a stable flame was built far away from the spark point. By contrast, without N_2 the ignition started much faster as showed in Figure 10. As flame propagation, similar to micro size aluminum, no tail was left behind, and it also suggests that the combustion rate was faster without N_2.

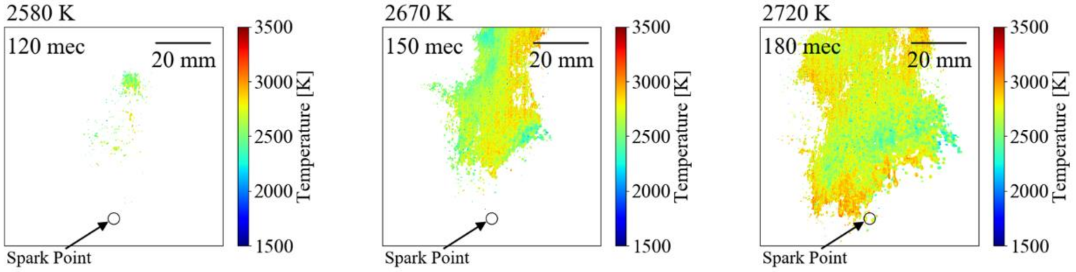

Fig. 9. *The temperature images of 100 nm Al dust explosion under 22%* O_2 *+ 78%* N_2

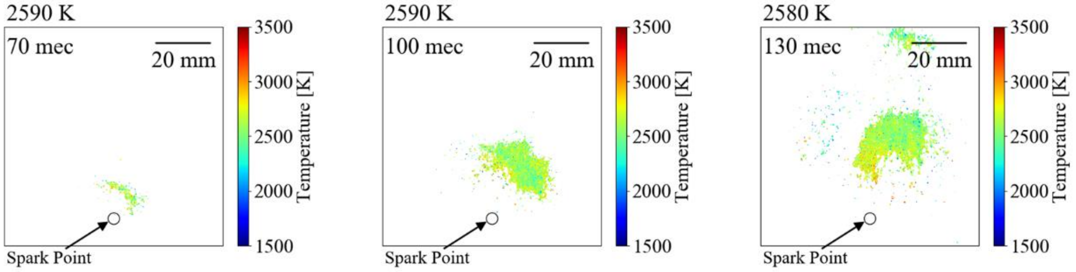

Fig. 10. *The temperature images of 100 nm Al dust explosion under 22%* O_2 *+ 78%* CO_2

To sum up, CO_2 can decrease the equilibrium flame temperature of micro-scale aluminum dust clouds, but the concentration needs to be higher than 40%. For nano-scale aluminum dust clouds, the flame temperature has no significant different even if N_2 has been totally replaced by CO_2. In addition, the involvement of CO_2 largely decreases the necessary time for ignition. Considering the heat capacity of N_2 (29.12 kJ/kmol-K) is lower than CO_2 (37.14 kJ/kmol-K), one may expect that the flame temperature should be lower with CO_2 which by calculation is around 2350 K under 78% of CO_2. However, the measured flame temperature with CO_2 is notably higher than the exaptation. Thus, we can infer that the chemical reactions with CO_2 or N_2 also partly contribute to the combustion.

3.2 Transition of Flame Temperature

3.2.1 Air environment

Figure 11 shows the equilibrium calculation of reaction products under air atmosphere of aluminum reach condition (equivalent ratio = 2.0) using NASA-CEA (Gordon and McBride, 1996) code (a similar calculation results can also refer to Bucher et al., 1999). For micro aluminum, because the flame temperature was observed around 3000 K as showed in Figure 3, it is straightforward to conjecture that the dominated products would be Al_2O (g) or Al_2O_3 (l). This result is well consistent with the boiling point of Al_2O_3 (3250 K), because to reach a higher flame temperature needs to vaporize the condensed oxide. As a result, the flame temperature is limited by the necessary heat for phase change. On the other hand, nano aluminum has the flame temperature between 2400 K~2700 K, which suggests that the dominated products should be AlN (l), Al_2O_3 (l) and Al2O (g). Under a lower equilibrium temperature, additional high percentage of condensed AlN (l) must limit the diffusion rate of oxygen and further limit the reaction rate of fresh aluminum within oxides. As a result, flame temperature is determined by the decomposition of AlN (l).

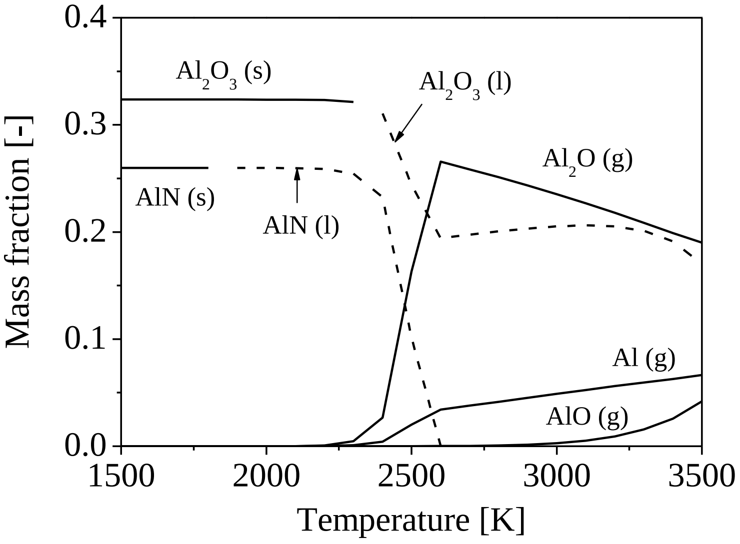

Fig. 11. *Equilibrium products under air environment by different temperature*

3.2.2 With Additional CO_2

Figure 12 shows the equilibrium calculation of reaction products under 22% O_2 + 78% CO_2 gas mixtures of aluminum reach condition. As indicated in Figure 3 and 8, both micro and nano scale aluminum have equilibrium temperatures at around 2600 K. It is interesting to note that the calculation shows only additional gaseous CO was produced, and it should not limit the reaction rate on the burning surface. Thus, one may expect a higher flame temperature than 2600 K. This is because CO was considered as a final product in equilibrium calculation. One thermodynamically reasonable mechanism is that high concentration of CO diffuses through to the burning surface and reacts with aluminum producing carbon element as follows (Breakspere, 1970).

$$2Al + 3CO \rightarrow Al_2O_3 + 3C \quad (1)$$

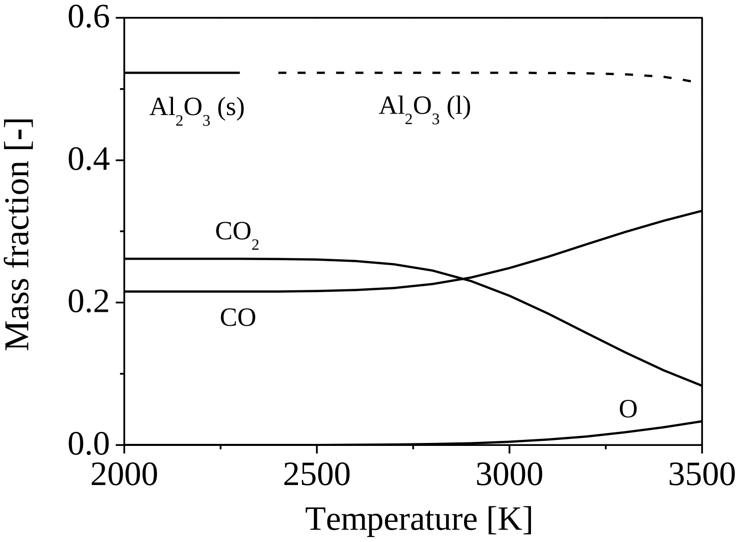

Fig. 12. *Equilibrium products under 22%* O_2 *+ 78%* CO_2 *gas mixtures by different temperature*

The evidence for carbon element was found by Sarou-Kanian et al. (2006). During combustion, carbon appeared on the burning aluminum surface, and it was captured by a high-speed CCD. In addition, with the deposited Al_2O_3, carbon reacts further to form Al_4C_3 (Hocking, 2005):

$$2Al_2O_3 + 9C \rightarrow Al_4C_3 + 6CO \text{ (> ~2300 K)} \tag{2}$$

Or through the pathway as follows (Breakspere, 1970):

$$4\text{Al} + 3C \rightarrow Al_4C_3 \text{ (> 673 K)} \tag{3}$$

Therefore, one can infer that involving of CO_2 results in the increase of Al_4C_3 covering on particle surface, and the condensed Al_4C_3 would significantly reduce the reaction rates. As a result, the flame temperature was determined by the dissociation 2500-2800 K (Foster et al., 1958) or reduction of Al_4C_3 2400-2500 K (Warren, 2003, in Encyclopedia of physical science and technology), which is consistent with the current result of 2600 K.

$$Al_4C_3 \rightarrow 4Al + 3C \text{ (2500-2800 K)} \tag{4}$$

$$Al_4C_3 + Al_2O_3 \rightarrow 6Al + 3CO \text{ (> ~2400-2500 K)} \tag{5}$$

Since the ignition of nano aluminum in CO_2 (> 40%) becomes much faster, we can infer that the replacement of molten AlN to Al_4C_3 can much improve the surface reaction rate. This is because further reaction of AlN forms quite stable gaseous Al_2O. By contrast, decomposition of Al_4C_3 produces Al which is still reactive. The transition of flame temperatures is illustrated in Figure 13.

DOI: 10.7795/810.20221124

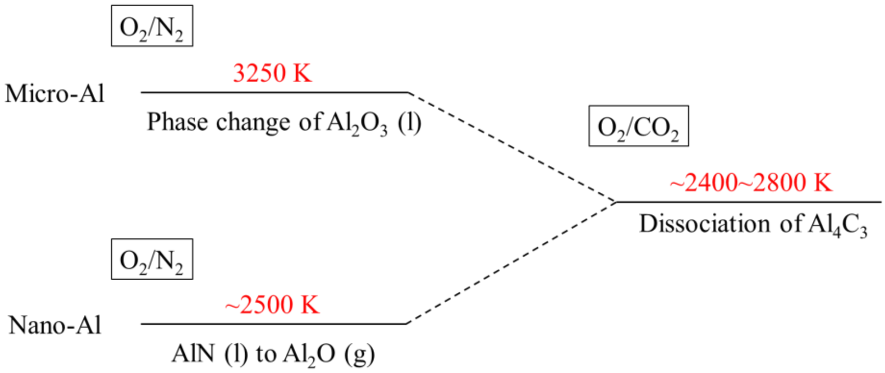

Fig. 13. *Determining of flame temperature by dominated condensed products*

3.3 *Inerting by Adding Ar Gas*

In order to confirm the assumption of dominated products, experiments were conducted under 22% O_2 + 78% Ar to exclude the possible condensation of AlN or Al_4C_3. Figure 14 and 15 show temperature the images of 10~20 μm and 100 nm Al, respectively.

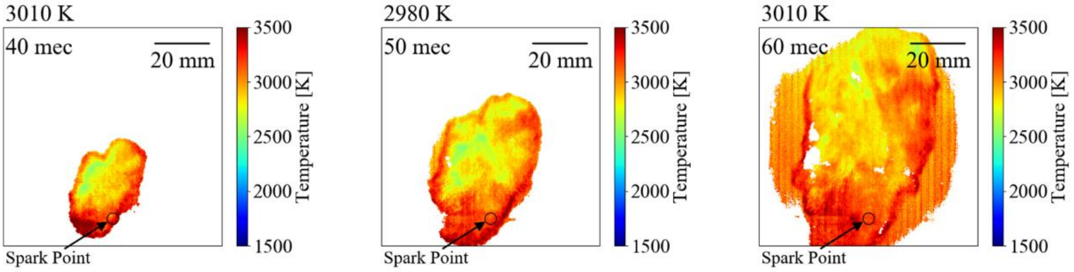

Fig. 14. *The temperature images of 10~20 μm Al dust explosion under 22%* O_2 *+ 78% Ar*

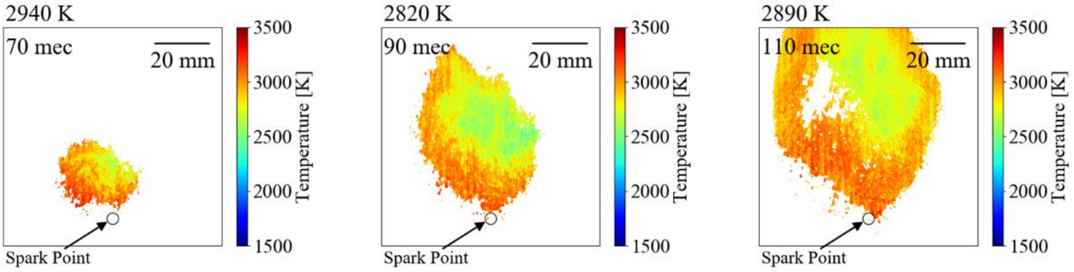

Fig. 15. *The temperature images of 100 nm Al dust explosion under 22%* O_2 *+ 78% Ar*

For micro aluminum, the flame temperature kept at 3000 K all the time without notable decrease, and flame propagated much faster through the chamber. For nano aluminum, around 300 K increased in flame temperature comparing to under O_2/N_2 composition, and average flame temperature kept at around 2900 K all the time. The results provide an evidence for the assumption of condensation of N and C related products, and the restriction of growing oxide cap by Ar somewhat improve the reaction rate on aluminum surface.

4. Conclusions

Current works confirm that the influence of N_2, CO_2 and Ar on particle temperature during dust explosion are notable, and the transition of flame temperature under different atmospheres were measured by a two-color pyrometer. For micro scale dust clouds, CO_2 can decrease equilibrium flame temperature if the concentration is higher than 40 %; however, for nano scale dust clouds, CO_2 has only minor influence on flame temperature, and the maximum difference is less than 200 K. In addition, CO_2 largely decreases the time for ignition in the case of nano aluminum.

Flame temperatures were then compared with the calculation of equilibrium products. The results suggest that under O_2/N_2 environment, flame temperature of micro aluminum is limited by the boiling point of Al_2O_3, on the other hand, flame temperature of nano aluminum is limited by the reaction of AlN. The replacement of N_2 by CO_2 can change the dominated products to Al_4C_3 for both micro and nano scale aluminum, and therefore the flame temperature is determined by the dissociation or reduction of Al_4C_3. Unlike AlN, the reaction rate of nano aluminum can be somewhat promoted by the dissociation of Al_4C_3 due to the formation of reactive Al. Finally, the experiments were conducted in O_2/Ar atmosphere to exclude the possible condensation of AlN and Al_4C_3, and the resulting flame temperature has significant increase for both micro and nano aluminum.

At this time, we do not have directly evidence to confirm the condensed products on particle surface, and it needs to be elucidated by further experiments. However, according to the influence of CO_2 or Ar on the temperature of burning aluminum, they may not be an effective way to distinguish or suppress aluminum dust explosion.

References

Breakspere, R.J., (1970). High-Temperature Oxidation of Aluminum in Various Gases. *J. Appl. Chem*. 20, 208–212.

Bucher, P., Yetter, R.A., Dryer, F.L., Vicenzi, E.P., Parr, T.P., Hanson-Parr, D.M., (1999). Condensed-phase species distributions about Al particles reacting in various oxidizers. *Combust. Flame* 117, 351–361.

Dreizin, E.L., (1999). On the mechanism of asymmetric aluminum particle combustion. *Combust. Flame* 117, 841–850.

Eckhoff, R.K., (2005). Current status and expected future trends in dust explosion research. *J. Loss Prev. Process Ind*. 18, 225–237.

Foster, L.M., Long, G., Stumpf, H.C., (1958). PRODUCTION OF GRAPHITE SINGLE CRYSTALS BY THE THERMAL DECOMPOSITION OF ALUMINUM CARBIDE. *Am. Mineral*. 43, 285–296.

Glorian, J., Gallier, S., Catoire, L., 2016. On the role of heterogeneous reactions in aluminum combustion. *Combust. Flame* 168, 378–392.

Gordon, S. and McBride, B. J., (1996). NASA Reference Publication 1311.

Goulay, F., Schrader, P.E., Michelsen, H.A., (2010). Effect of the wavelength dependence of the emissivity on inferred soot temperatures measured by spectrally resolved laser-induced incandescence. *Appl. Phys. B* Lasers Opt. 100, 655–663.

Hocking, M. B., (2005). Handbook of Chemical Technology and Pollution Control. Academic Press, 2nd ed.

Japanese Industrial Standard, (2002). Test method for minimum explosible concentration of combustible dusts. JIS Z 8818.

Meyer. R. A., (2001). Encyclopedia of physical science and technology. Academic Press, 3rd ed.

Rossi, S., Dreizin, E.L., Law, C.K., 2000. Combustion of aluminum particles in carbon dioxide. *Combust. Sci. Technol*. 164, 209–237.

Sarou-Kanian, V., Rifflet, J.C., Millot, F., Gökalp, I., (2006). Aluminum combustion in wet and dry CO_2: Consequences for surface reactions. *Combust. Flame* 145, 220–230.

Shafirovich, E., Varma, A., (2008). Metal-CO_2 propulsion for Mars missions: Current status and opportunities. *J. Propuls. Power* 24, 385–394.

Taveau, J., Vingerhoets, J., Snoeys, J., Going, J., Farrell, T., 2015. Suppression of metal dust deflagrations. *J. Loss Prev. Process Ind*. 36, 244–251.

Yetter, R.A., Risha, G.A., Son, S.F., (2009). Metal particle combustion and nanotechnology. *Proc. Combust. Inst*. 32 II, 1819–1838.

Yuasa, S., Zhu, Y., Sogo, S., (1997). Ignition and combustion of aluminum in oxygen/nitrogen mixture streams. *Combust. Flame* 108, 387–390.

Zhang, S., Bi, M., Jiang, H., Gao, W., (2021). Suppression effect of inert gases on aluminum dust explosion. *Powder Technol*. 388, 90–99.

DOI: 10.7795/810.20221124

Ageing effect on ignition sensitivity of lignocellulosic dusts

Maria Portarapillo[a], Almerinda Di Benedetto[a], Roberto Sanchirico[b], Enrico Danzi[c], Luca Marmo[c]

[a] Dipartimento di Ingegneria Chimica, dei Materiali e della Produzione Industriale, Università degli Studi di Napoli Federico II, Piazzale V. Tecchio 80, 80125 Napoli, Italy
[b] Istituto di Ricerche sulla Combustione, Consiglio Nazionale delle Ricerche (CNR), Piazzale V. Tecchio 80, 80125 Napoli, Italy
[c] Dipartimento di Scienza Applicata e Tecnologia-Politecnico di Torino, C.so Duca degli Abruzzi 21, 10129, Torino, Italy

E-mail: maria.portarapillo@unina.it

Abstract

Hydrothermal treatment is one method for the accelerated ageing of wood and lignocellulosic material. The ageing may reduce hygroscopicity, enhance stiffness and brittleness, and change the chemical composition. Consequently, it may affect the flammability and the ignition susceptibility of combustible dust samples.

Several lignocellulosic dusts from industrial processes were chosen and submitted to accelerated ageing to investigate its influence on the flammability properties. Grape pomace, cork flour, olive pomace, wood dust and lignocellulosic residual from process waste were selected for morphology, chemical characterisation, and lignin/cellulose content. According to literature references, ageing temperature and moisture conditions were chosen to reproduce naturally aged materials. Chemical composition changes in terms of pseudo-components (cellulose, hemicellulose, and lignin) are likely to alter the flammability properties of samples. This study investigated the ageing effect on Minimum Ignition Energy (MIE) and combustion/pyrolysis behaviour. Thermogravimetric analysis and differential scanning calorimetry (TGA and DSC) in inert atmosphere were used to characterise the materials. Maximum weight loss Temperature (MWLT) was also registered. Air tests were performed to identify exothermic reactions and detect combustion onset from Initial Exothermic Temperature (IET), Onset Temperature and Final Exothermic Temperature (FET).

Results showed how ageing could vary the ignition hazards. MIE of grape pomace reduces, while wood-based samples do not ignite after the hydrothermal procedure. The case of pomace is consistent with the decrease in lignin content and moisture. At the same time, passivation of particle surface could explain wood samples behaviour. Hence it is relevant to consider the different behaviour to ignition and combustion of aged biomass samples in dust explosion risk assessment.

Keywords: *prevention, mitigation, industrial explosions, biomass, ageing effect*

1. Introduction

1.1 Biomass dust explosion hazards

The risk of dust explosion for biomass materials has been recently investigated by several research groups overwide. This is likely due to some severe episodes that occurred in the last years, as reported by Ennis (2016), Krause U. (2009), Hedlund et al. (2018), IEA (2013). If statistical data collected by Cloney C. (2021) is reviewed, the category "wood & wood products" and "agriculture & food products" account for 68.5% of the total combustible dust fire and explosions in 2021.

Biomass materials could be likely considered under these categories: whether in the form of wood pellets/fine powder adopted as fuel in combustors directly or as a mixture in co-firing plants with coal (Fernandez-Anez N. et al., 2015 & Kukfisz, B., 2018). Besides this, biomass cumulation as waste from agricultural production could constitute an issue in terms of environmental and safety issues (see Portarapillo et al., 2021, Danzi et al., 2021 & Petraccini et al., 2021).

1.2 Factors influencing flammability

Several factors may modify the ignition susceptibility, the flammability as well as the explosibility of dusty samples, apart from particle size and moisture content. More specifically, for non-traditional biomass dusts, a crucial role can be played by the lignocellulosic components content. Biomass energetic content is related to its Net Heating Value (NHV), which is dependent on pseudo-components share (cellulose, hemicellulose, lignin) and moisture degree. If biomass is present in the form of fine dust, an explosion is regarded as the main concern. Its dynamics may be influenced by several factors.

If pseudo-components are considered, some recent results indicate that hemicellulose and cellulose do have a positive effect on maximum pressure rise and maximum rate or pressure rise, respectively, while lignin limits the pressure peak (Liu et al., 2021). Pyrolysis rate is influenced hence by components share and could be evaluated through thermogravimetric analysis (TGA) and coupled gas chromatography (Zhao et al., 2017): lignin likely decrease rate, while cellulose and hemicellulose have a positive influence. Concerning biomass-coal mixtures, a synergistic effect is found, by adding corn starch to coal (Lin et al., 2019), while the addition of functional O_2 containing groups enhances coal explosibility. Fernandez-Anez et al. (2015) reported how the addition of biomass to coal/waste mixture increases the rate of pressure rise and flame length, while reactivity is slightly reduced as shown by an increase of the minimum explosive concentration (MEC).

Ignition sensitivity is also influenced by different factors. Lignin content is considered likely negligible on the MIE values (Castells et a., 2020), while volatile matter content (VM) is dependent on lignin share and other components (Andrews, G.E., 2014); generated pyrolysis gases in turn influence the flammability, depending on whether flammable (e.g., CH_4, CO) or inert gases (e.g. CO_2) are produced.

Since biomass samples will experience ageing while stored, the maturity of samples may have a role in their combustion/explosion properties. Lignin tends to decrease with wood maturity (Berrocal et al., 2004). Consequently, storage lifetime is another variable affecting the chemical-physical properties of biomasses. It may influence their attitude to combustion (this could affect the efficiency of energy production whether in the form of pellets or raw material, Lee et al., 2015). The ageing of the samples may be obtained through artificial and accelerated treatment such as hydrothermal treatments (Endo et al., 2016). The hydrothermal treatment causes several modifications in the samples. Thus, an aged sample theoretically will contain a small amount of hemicellulose and lignin and a higher amount of cellulose. As a consequence, a chemically altered sample could have its explosion risk increased because its flammability properties are enhanced by the transformation (Portarapillo et al., 2021).

In this work, these factors will be evaluated on different biomass samples having different origins (woody, agricultural, industrial waste). The purpose of the procedure described here is to define some experimental tests, parallel to flammability tests, to identify critical properties on the ignition sensitivity, i.e. through the calorimetry analysis and applied them on samples aged by laboratory conditioning, simulating storage time effect.

2. Material and methods

Samples tested in this work are all lignocellulosic biomass, derived both from production processes and waste streams. The microscopic images of the samples are reported in Fig.1 and the different morphologies can be easily captured. However, all were characterised in-depth by their size, morphology, thermal behaviour and chemical composition before and after the hydrothermal ageing process. Five different materials were studied in this work and tested as received. Sample I is a residue of olive pomace, analysed in detail in Pietraccini et al. (2018), sample II is cork flour, used as fuel in a facility combustor, sample III is wood sawdust, sample IV is a waste product of a wood recycling plant, sample V is a grape pomace dust, described in Portarapillo et al. (2020). Table 1 reports the experimental tests carried out to study the samples' combustion behaviour (both in air and in inert atmosphere, as to simulate oxidation and pyrolysis mechanisms), chemical composition and volatile/ashes content.

Table 1: *Tests used to characterize the samples*

Analysis	Output parameters	Standard
Laser diffraction granulometry	d_{10}, $D_{4,3}$	-
Ultimate analysis	Carbon, Hydrogen, Nitrogen, Oxygen	ASTM D3176-15
FTIR analysis	Spectra	-
Thermogravimetric analysis (TGA) – Inert atmosphere	DTG	-
Thermogravimetric analysis (TGA) – Oxidant atm.	IET, FET	-
Differential Scanning Calorimetry (DSC)	MWL Temperature	-
Proximate analysis	VM, A, M,FC	ASTM D7582-15

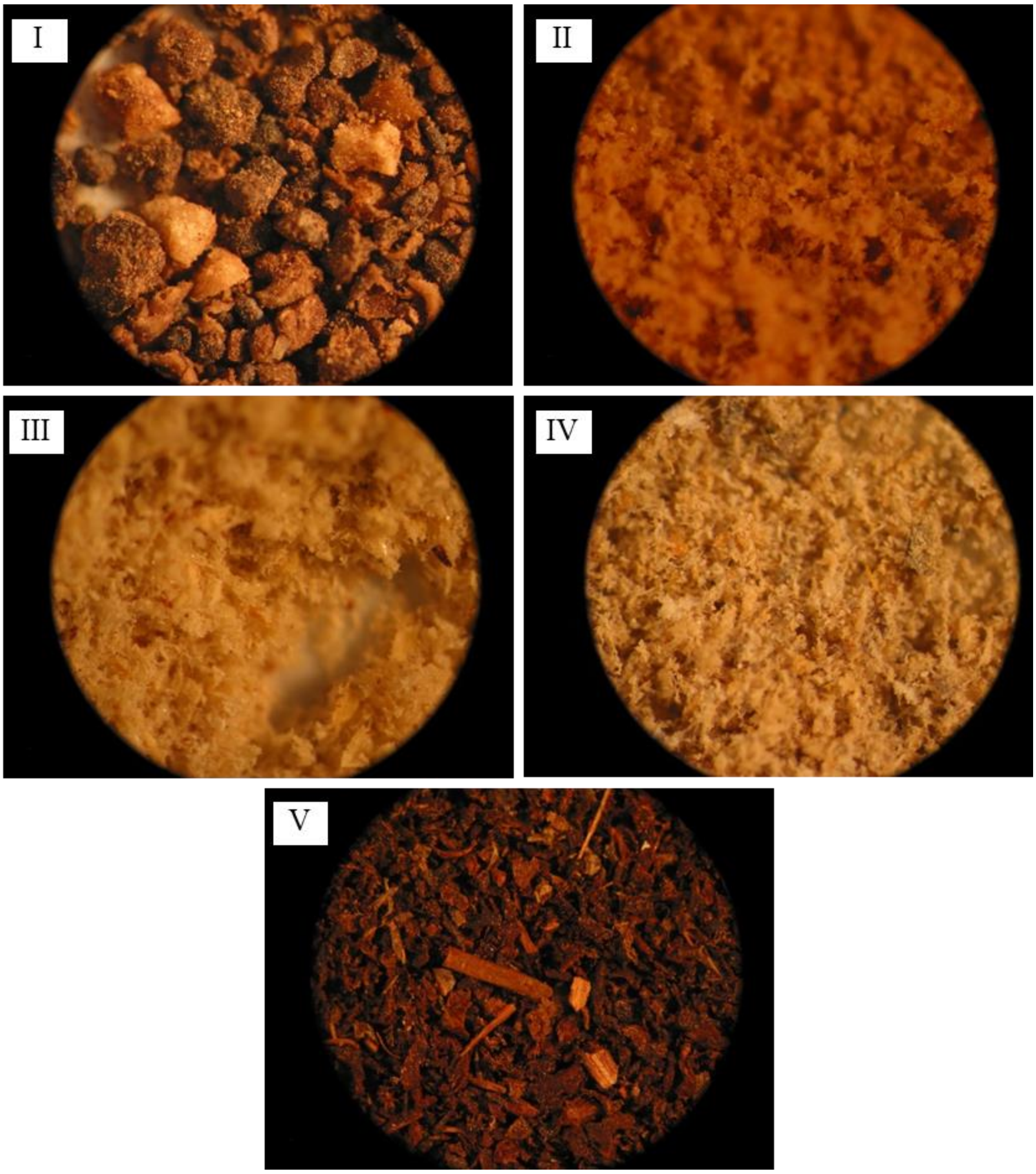

Fig. 1. *Optical microscopic images of samples (before ageing treatment).*

TGA analysis is carried out here (as in Portarapillo et al., 2021) to evaluate the pseudo-components share from the deconvolution of the first derivative of TG signal (DTG curve) in an inert atmosphere (ASTM D7582-15). The procedure is derived from Hu et al. (2016). The associated DSC aims to study the pyrolysis steps according to different characteristic temperatures, such as Maximum Weight Loss Temperature (MWLT). Other Temperature thresholds are detected by the test in oxidant atmosphere (TGA/DSC up to 1000 °C with a heating rate equal to 10 °C/min), such as the Initial Exothermic Temperature (IET) and the Final Exothermic Temperature (FET), which reveal the exothermic reactivity of the samples. Moreover, the thermogravimetric furnace was used to carry out the proximate analysis for the evaluation of moisture (M), volatiles matter (VM), ash (A) as well as fixed carbon (FC) contents, according to the standard procedure (ASTM D7582-15).

Alongside characterisation tests, Minimum Ignition Energy (MIE) was measured for all the samples before and after ageing. MIE analysis is carried out with a MIKE III instrument according to UNI EN 13821:2004. To evaluate the effect of the diameter, we used laser diffraction granulometry

(Malvern Instruments Mastersizer, 2000) to characterize the granulometric distribution on both the samples, before and after the dispersion within the MIKE3.

2.1 Ageing treatment

Hydrothermal treatment is one method to perform accelerated ageing of wood and lignocellulosic material. In this work, it is used to simulate the storage time effect on the samples. The treatment conditions are derived from literature (Endo et al., 2016). Samples are thermally treated at 120 °C and relative humidity (RH) 60% for 7 days in an autoclave. The hygroscopicity of non-treated samples may be affected by ageing. Ageing causes the conversion of hemicellulose compounds in less hygroscopic elements. At the same time, the sample mechanical properties (strength, elasticity) are modified: the sample could become more fragile. This is crucial for dust explosion risk assessment: fragile and brittle solids likely generate fines if handled/transported or fall by chute, such as in standard operations in biomass treatment facilities. Particle size could also be modified by the ageing treatment: this is a direct consequence of altering the water content/hygroscopic behaviour of samples by drying, but also is related to the effect of some physical reactions (decomposition, recrystallisation and cross-linking of ligneo-cellulosic constituents) which modify the morphology of samples (Sandberg et al., 2013), induce partial passivation of the outer surface, or tend to agglomerate the particles in larger clusters. All the parameters as well as their effect on the samples ignition sensitivity are reported in Table 2. These physical effects can be observed qualitatively in the microscopic images of the aged samples reported in **Error! Reference source not found.** Quantitative results as well as their effect on the safety parameters are going to be discussed in the following section.

Table 2: *Likely effects of parameter variation after ageing application on samples ignition sensitivity*

Parameters variation	***Ignition sensitivity***
Moisture reduction	Enhance
Particle size reduction	Enhance
Chemical composition variation	Enhance/Reduce
Structural characteristics (brittleness, stiffness)	Enhance
Hygroscopic reduction	Enhance/Reduce

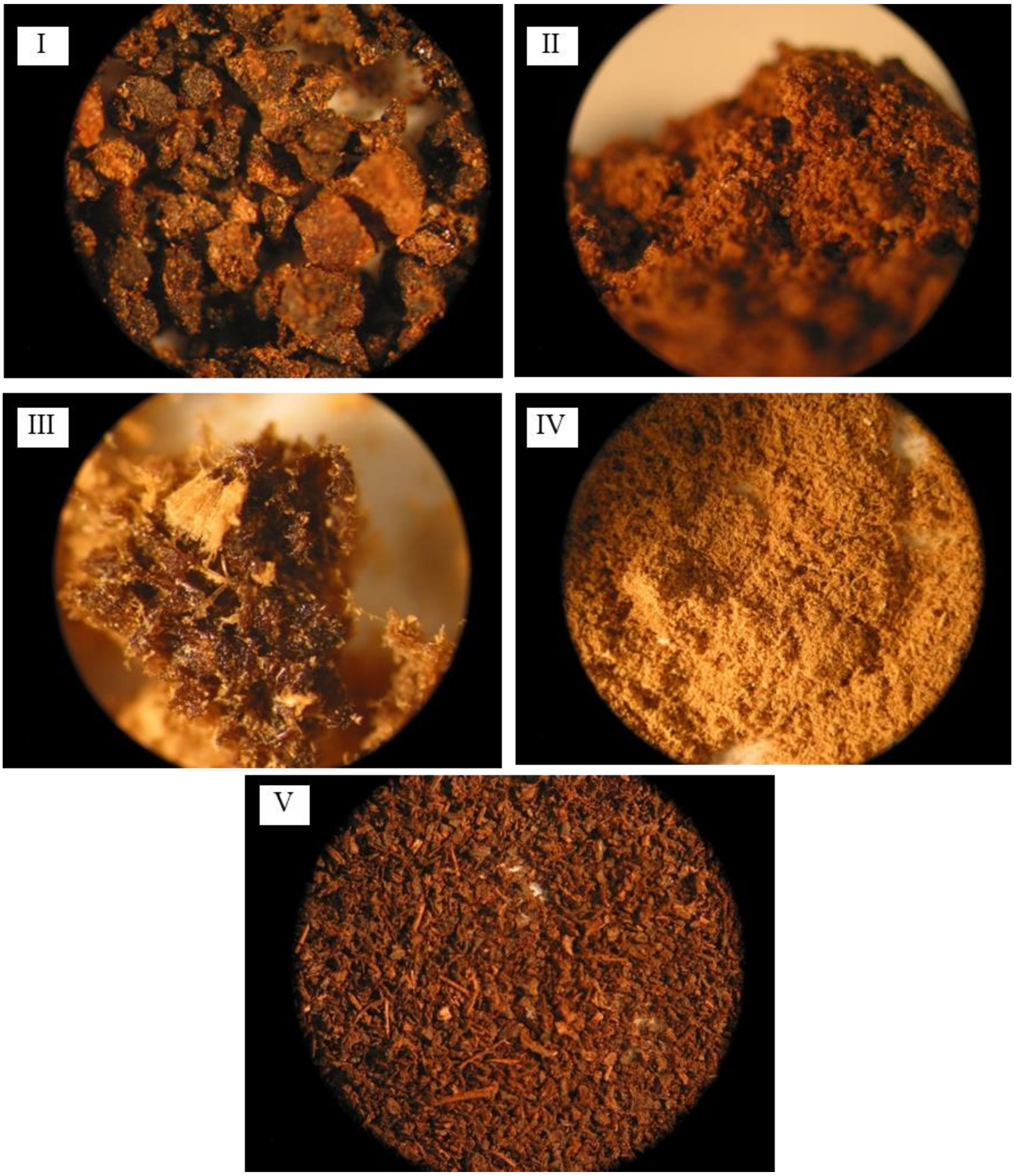

Fig. 2. *Optical microscopic images of samples (after ageing treatment).*

3. Results and discussion

In the followings, results of the characterisation and MIE measurements on samples subjected to treatment are compared to original samples.

3.1 Particle size distribution (PSD) and morphology variation

Fig. 3 shows the results of laser diffraction granulometry. Ageing affects the morphology of samples differently from one to another: while sample I seemed to remain unchanged in shapes of particles, aged sample V lost its flakes-like shape. Finer samples (II to IV) undergo an agglomeration phenomenon and likely passivation of their outer particles layers (as clearly observed for sample II, where large agglomerates did appear and fines reduced greatly).

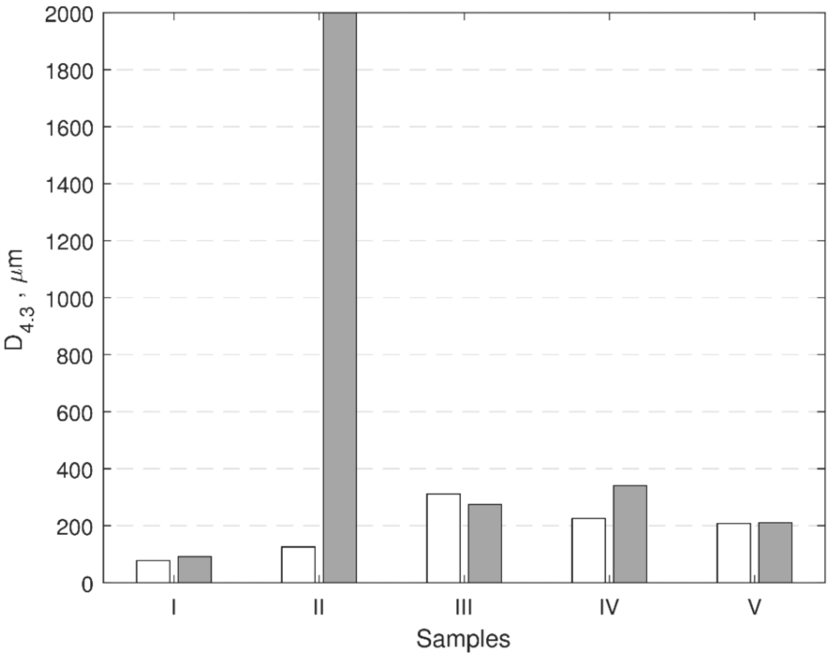

Fig. 3. *Effect of ageing on particle size distribution, where raw materials are reported with white columns and aged materials with grey ones.*

Afterwards, a PSD measurement (in terms of volume-weighted mean diameter $D_{4,3}$) was effectuated on all samples, after dispersion in the Hartman tube to detect any PSD change, likely due to the impact of particles on tube walls, collisions and abrasion (Sanchirico et al., 2015). Some indications could be obtained from the results of this test: samples with finer particles (II, III) likely went through some agglomeration process during the dispersions ($D_{4,3}$ slightly higher), while aged coarser samples (I and IV) did behave differently, likely due to the embrittlement of aged particles which are more prone to fracture and size reduction. Sample V $D_{4,3}$ grew after dispersion both for non-treated and aged samples (Table 3).

Table 3: *Volume-weighted mean diameters (pre- and post-dispersion) for all the samples.*

Sample	D(4,3) (μm)	D(4,3) Post Dispersion (μm)
I	77.6	78.7
I aged	91.5	76.3
II	125.4	131.5
II aged	>2000	>2000
III	311.1	335.4
III aged	274.7	298.9
IV	225.6	225.8
IV aged	340.9	321.5
V	208	324
V aged	211	254

DOI: 10.7795/810.20221124

3.2 Physico-chemical composition

Ultimate analysis results provide an overview of the elemental chemical composition of the samples. They are plotted into a Van Krevelen diagram (Van Krevelen, 1950) as to evaluate their Carbon to Oxygen and Hydrogen ratios (Fig. 4). For each sample, an increase of both H/C and O/C can be observed, moving from low values characteristic of fresher biomass with high lignin content (black square) to aged biomass more similar to cellulose (green rhombus).

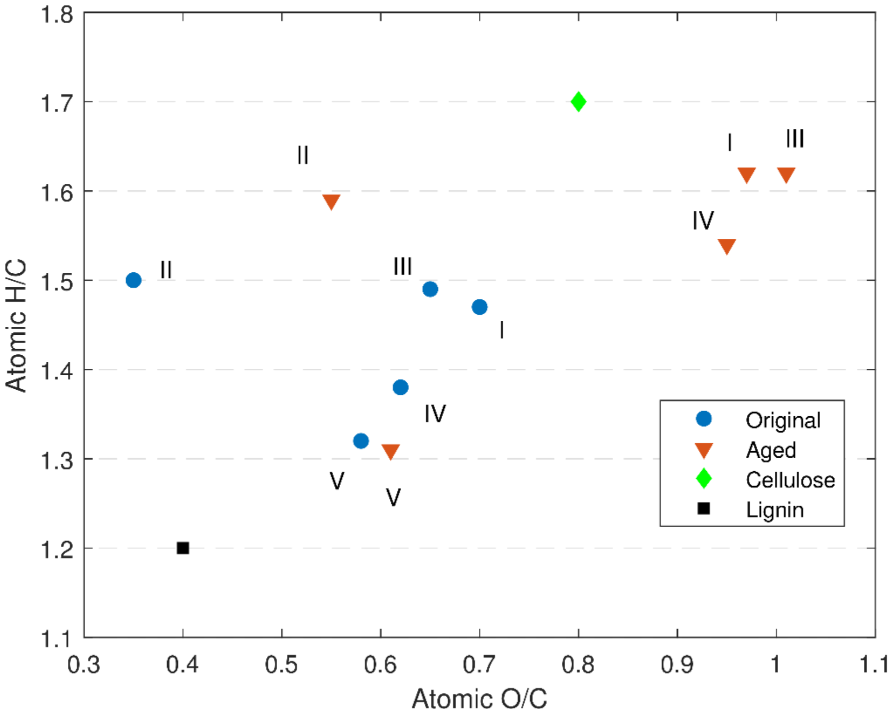

Fig. 4. *Van Krevelen plot for the sample tested (original and aged), compared to pure cellulose and lignin.*

Furthermore, FTIR spectra are qualitatively affected by ageing (not reported). Indeed, after ageing, spectra have the same fingerprint of original samples ones, but the peaks intensities are different in particular those relative to hemicellulose and cellulose components. These peaks show a reduced intensity after ageing likely due to a reduction of their contents.

3.3 Combustion behaviour and pseudo-components variation

Fig. 5 shows the DTG curves as a function of temperature for the TG/DSC analysis in N_2 flow (left) and in airflow (right). For all the samples the trends were quite similar in terms of quality, while the quantitative effects were highlighted by evaluating the characteristic temperatures and the amount of lignocellulosic components (Table 4). For all the samples the reduction of the lignin and hemicellulose components was highlighted with an increase of the cellulose component. The increase in the cellulose content can explain an increase in the reactivity in the homogeneous phase of the samples as its decomposition occurs at intermediate temperatures (about 320 °C) with the formation of flammable gases (especially CO). In the case of sample I, the maximum mass loss is anticipated at lower temperatures (i.e., low MWLT) which could explain a greater flammable character.

Table 4: *MWLT, IET, FET and lignocellulosic components.*

Sample	MWLT (°C)	IET (°C)	FET (°C)	Hemicellulose %	Cellulose %	Lignin %
I	310	203	500	58	15	27
I aged	287	206	500	19	72	9
II	413	270	458	18	58	24
II aged	410	244	489	10	70	20
III	354	268	442	59	36	5
III aged	354	275	414	44	53	3
IV	350	284	530	6	67	27
IV aged	360	294	530	0	72	27
V	320	240	460	31	14	55
V aged	330	250	481	29	23	48

Proximate analysis results provide an overview of the share of each material that could favour combustion (volatiles and carbon matter with respect to ashes). As shown in Table 5, Samples I, II and IV show a reduction in the volatile content and an increase in the ash content while for the other samples an increase in the volatile content is found. In any case the aged samples are drier than the original samples. It is worth noting that due to the increase in cellulose content it is likely that the volatiles produced are more flammable than the original samples.

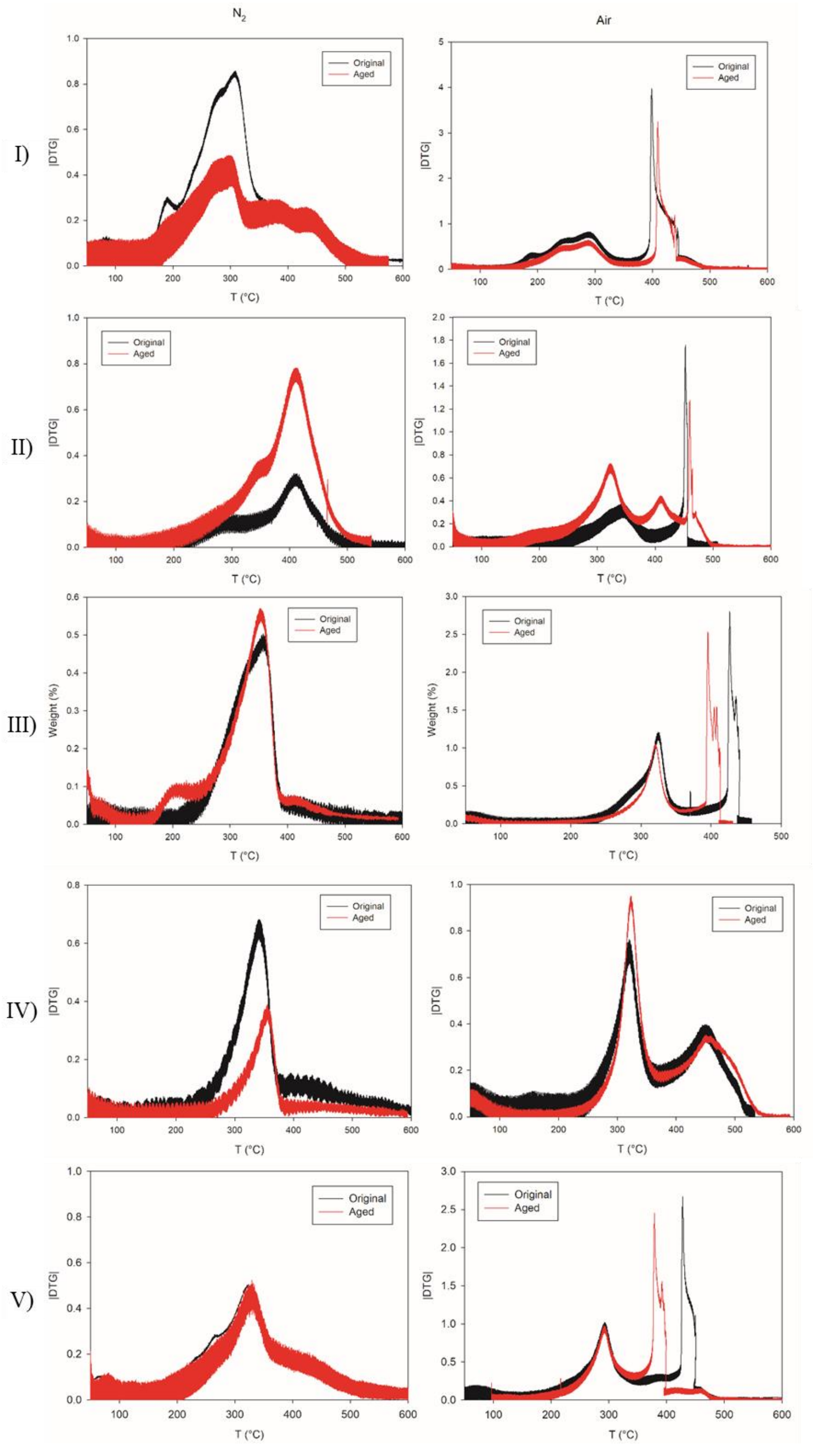

Fig. 5. *DTG curves as a function of temperature for all the samples (I-V) in inert (left) and oxidative atmosphere (right).*

Table 5: *Proximate analysis results.*

Sample	M %	V %	A %	FC %
I	7.2	70.1	16.5	6.2
I aged	4.6	67.9	20.8	6.7
II	3.4	86.1	10.5	0
II aged	3.6	76.4	19.5	0.5
III	7.1	75.2	15.6	2.0
III aged	6.6	76.9	16.5	0.0
IV	5.4	69.6	20.3	4.8
IV aged	5.1	68.1	21.7	5.1
V	5.6	67.4	21.3	5.7
V aged	≈0	70.1	24.9	5.0

3.4 Ignition Energy

After the ageing treatment, some variations on the ignition sensitivity to electric spark could be observed when measuring MIE in the modified Hartman tube. Results are reported in Table 6. Original samples less reactive to ignition (I and V) seemed to demonstrate some enhancements in their sensitivity, with hotspots and sparks generations at each concentration, although no flame propagation is reported. Sample V sensitivity is enhanced after ageing since its MIE is reduced by 26%. This is coherent with the moisture reduction due to drying (as seen in TG analysis) and to a visible (from optical microscope) change in morphology, where quasi-spherical agglomerates are observed, at the expense of flake-like particles. Original more reactive samples (II, III, IV) do behave conversely: MIE is raised by ageing for samples II to IV, by respectively 15% and 85%. This effect could be explained by the passivation of the outer particle surface during ageing, which prevents the sample from igniting at lower energies. This could be observed in Fig. 2 (IV) for sample IV. Sample II undergoes a greater agglomeration phenomenon, with the consequence that aged sample cannot be tested for MIE since PSD is too coarse for testing in Hartman device ($D_{4.3}$ > 2000 um).

Table 6: *MIE measurements results.*

Sample	MIE (mJ)	Comments after ageing
I	>1000	Sparks and hotspots at each concentration
I aged	>1000	
II	13.7	Not possible, D>500 microns, disk
II aged	Unknown	
III	193.3	-
III aged	227.9	
IV	79	-
IV aged	547.7	
V	>1000	Sparks and hotspots at each concentration
V aged	740	

4. Conclusions

Biomass-derived fuels may be stored for a long time before their use in power plants or energy recovery facilities. In storage facilities, ageing may occur. Ageing is a chemical-physical process that may affect the chemical composition, morphology, and brittleness of the material. The natural consequence is that ageing affects the reactivity and the ignition susceptibility of these materials. The ageing does not influence material properties equally. Some materials demonstrated a decrease in the overall reactivity, while other samples behaved the opposite. The complex trend is likely due to the interaction of many variables affected by ageing: hemicellulose to lignin ratio, particles size and brittleness, moisture content. The results of this work suggest that if the dust explosion risk need to be assessed in biomass power plants and facilities, the ageing of the fuel has to be taken into account. More specifically, in this work, a complete procedure, including a chemico-physical characterization as well as a thermal screening is proposed to get insight into any modification caused by the lignocellulosic components content variation.

Acknowledgements

This work is dedicated to the memory of Prof. Rolf Kristian Eckhoff, who we did have the honour to meet in person at conferences, his presence was always inspiring, both from a professional and a human point of view.

References

Andrews, G.E. Pulverised biomass flame propagation and explosion characteristics: Problems and solutions. In Proceedings of the meeting on Biomass Dust Explosions University of Leeds, Leeds, UK, 23 September 2014

Berrocal, A.; Baeza, J.; Rodriguez, J.; Espinosa, M.; Freer, J. Effect of tree age on variation of pinus radiata D. Don chemical composition. J. Chil. Chem. Soc. 2004, 49, 251–256

Castells, B.; Amez, I.; Medic, L.; Garcia-torrent, J. Preliminary Study of Lignocellulosic biomass ignition properties estimation from Thermogravimetric Analysis. J. Loss Prev. Process. Ind. 2020, 71, 434–445. https://doi.org/10.7795/810.20200724

Cloney, Chris (2021). "2020 Combustible Dust Incident Report - Version #1" DustEx

Danzi, E., Di Benedetto, A., Sanchirico, R., Portarapillo, M., & Marmo, L. (2021). Biomass from winery waste: Evaluation of dust explosion hazards. Chemical Engineering Transactions, 86(September 2020), 301–306. https://doi.org/10.3303/CET2186051

Endo, K.; Obataya, E.; Zeniya, N.; Matsuo, M. Effects of heating humidity on the physical properties of hydrothermally treated spruce wood. Wood Sci. Technol. 2016, 50, 1161–1179. https://doi.org/10.1007/s00226-016-0822-4

Ennis, T. (2016). Fire and explosion hazards in the biomass industries. Institution of Chemical Engineers Symposium Series, 2016 (161), 1–9.

Ennis, T. (2016). Fire and explosion hazards in the biomass industries. Institution of Chemical Engineers Symposium Series, 2016-Janua(161), 1–9.

Fernandez-Anez, N., Slatter, D., Saeed, M. A., Phylaktou, H. N., Andrews, G. E., & García Torrent, J. (2015). Ignition Sensitivity of Coal / Waste / Biomass Mixtures. In Sustainable Energy and Environmental Protection SEEP2015, Paisley (UK).

Hedlund, F. H. (2018). Carbon dioxide not suitable for extinguishment of smouldering silo fires: Static electricity may cause silo explosion. Biomass and Bioenergy, 108, 113–119. https://doi.org/10.1016/J.BIOMBIOE.2017.11.009

I E A Bioenergy. (2013). Health and Safety Aspects of Solid Biomass Storage, Transportation and Feeding. IEA Bioenergy, (May), 4.

Krause, U. Fires in silos. In Hazards, Prevention, and Fire Fighting; WILEY-VCH Verlag GmbH & Co. KGaA: Weinheim, Germany, 2009.

Kukfisz, B. (2018). The potential fire and explosion hazards in biomass co-firing with conventional fossil fuels based on data obtained during testing. E3S Web of Conferences, 45. https://doi.org/10.1051/e3sconf/20184500039

Lee, J. S., Sokhansanj, S., Lau, A. K., Jim Lim, C., Bi, X. T., Basset, V., … Melin, S. O. (2015). The effects of storage on the net calorific value of wood pellets. Canadian Biosystems Engineering / Le Genie Des Biosystems Au Canada, 57, 8.5-8.12. https://doi.org/10.7451/CBE.2015.57.8.5

Lin, S., Liu, Z., Zhao, E., Qian, J., Li, X., Zhang, Q., & Ali, M. (2019). A study on the FTIR spectra of pre- and post-explosion coal dust to evaluate the effect of functional groups on dust explosion. Process Safety and Environmental Protection, 130, 48–56. https://doi.org/10.1016/j.psep.2019.07.018

Liu, A.; Chen, J.; Lu, X.; Li, D.; Xu, W. Influence of components interaction on pyrolysis and explosion of biomass dust. Process. Saf. Environ. Prot. 2021, 154, 384–392.

Pietraccini, M., Danzi, E., Marmo, L., Addo, A., & Amyotte, P. (2021). Effect of particle size distribution, drying and milling technique on explosibility behavior of olive pomace waste. Journal of Loss Prevention in the Process Industries, 71, 104423. https://doi.org/10.1016/j.jlp.2021.104423

Portarapillo, M., Danzi, E., Sanchirico, R., Marmo, L., & Di Benedetto, A. (2021). Energy recovery from vinery waste: Dust explosion issues. Applied Sciences (Switzerland), 11(23). https://doi.org/10.3390/app112311188

Sanchirico, R., Di Sarli, V., Russo, P., Di Benedetto, A., 2015. Effect of the nozzle type on the integrity of dust particles in standard explosion tests. Powder Technol. 279, 203–208. https://doi.org/10.1016/j.powtec.2015.04.003

Sandberg, D., Haller, P., & Navi, P. (2013). Thermo-hydro and thermo-hydro-mechanical wood processing: An opportunity for future environmentally friendly wood products. Http://Dx.Doi.Org/10.1080/17480272.2012.751935, 8(1), 64–88. https://doi.org/10.1080/17480272.2012.751935

Van Krevelen, D.W. Graphical-statistical method for the study of structure and reaction processes of coal. Fuel 1950, 29, 269– 284.

Zhao, C.; Jiang, E.; Chen, A. Volatile production from pyrolysis of cellulose, hemicellulose and lignin. J. Energy Inst. 2017, 90, 902–913. https://doi.org/10.1016/j.joei.2016.08.004

DOI: 10.7795/810.20221124

Waste and Recycling of plastics: dust explosion risk evaluation

Enrico Danzi [a], Luca Marmo [a], Maria Portarapillo[b], Roberto Sanchirico[c] & Almerinda Di Benedetto[b]

[a] Department of Applied Science and Technology-Politecnico di Torino, C.so Duca degli Abruzzi 21, 10129, Torino, Italy

[b] Dipartimento di Ingegneria Chimica, dei Materiali e della Produzione Industriale, Università degli Studi di Napoli Federico II, Piazzale V. Tecchio 80, 80125 Napoli, Italy
c Istituto di Ricerche sulla Combustione, Consiglio Nazionale delle Ricerche (CNR), Piazzale V. Tecchio 80, 80125 Napoli, Italy

E-mail: enrico.danzi@polito.it

Abstract

Most plastic waste currently goes to landfills or incineration. As for 2016, only 16% of global polymer flows (from virgin monomer to end-use) is processed for recycling (Geyer et al., 2016). However, global concerns about environmental and health impacts of plastic proliferation have risen in the last 30 years, promoting the recovery of these materials. As a result, global non-fibre polymer recycling constantly increased over the previous two decades. With this trend assumed to continue, in 2050 recycling rate would reach 44% of total waste flows, meaning a significant impact in terms of quantity (Geyer et al., 2016). The mechanical sector is leading among different recycling processes, mostly involving the recovery of polyolefins such as PE and PP and PET and PVC (Hopewell et al., 2009).

Size reduction limiting volumetric flow is a common step of all recycling plants, which generate a high percentage of fine particles. Handling these materials will produce dusty and granular particles due to friction that occurs during transportation along pipelines, conveyors or chutes from hoppers and silos. Cutting/shredding will reduce materials to small flakes, while milling aims to homogenise mono-material waste flow, granulation will change scraps to their final chip-form (or even in powdered directly).

The rising recycling rate is potentially linked to the rising of accidents. From the '90s, plastic dust explosions and fires began to be reported and accounted for (14% of the total events from 1980 to 2005) (CSB, 2010). Materials are mostly thermoplastic derived dust (PE above all) and mixtures containing thermosets (PUR, phenolic resins).

This work will attempt to give an overview of the explosive potential of the polymer recycling sector. Recent case histories, statistical reports, and dust explosions will be investigated, and plastic dust will be analysed and tested. Dust generation and deflagration likelihood of mechanical operations materials will be the outputs to cover the explosion risk assessment of this specific sector.

Keywords: *polymers, recycling process, dust explosion*

1. Introduction

Mechanical recycling (see Fig. 1) is defined as “primary” recycling, or closed-loop recycling, which indicates the mechanical reprocessing of waste into a product with equivalent properties. Closed-loop recycling is feasible for almost all thermoplastics, although it is effective only if (i) an optimal separation of polymers from contaminating elements is possible, such as from other material layers, inks, adhesives and (ii) the constituent polymer could be stabilised against degradation during reprocessing (Hopewell et al., 2009). In this view, PET and LHDPE bottles are considered as the few materials which could undergo mechanical closed-loop recycling.

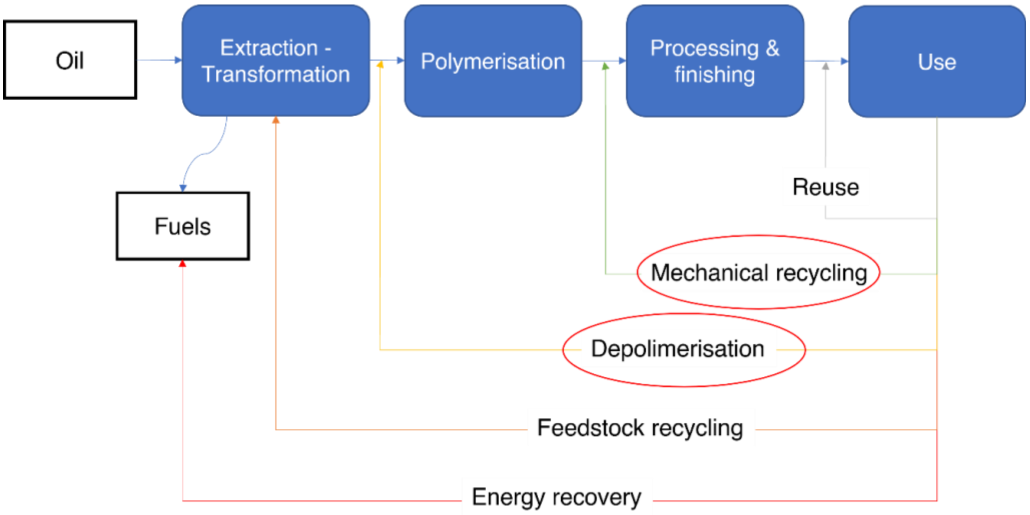

Fig. 1. *Polymer recycling loop*

Following pre-sorting, the (almost) pure polymer material is fragmented to reduce particle size and thus enable further processing. This is usually done in a cutting mill which consists of counter-rotating or fixed – blades, afterwards a perforated plate or grill screen material by particle size. The particle dimensions, hence, the flammability properties of the powdered resulting materials is directly related to the mechanical operation adopted to reduce plastic waste volume: waste flow could be constituted by a mixture of granules, flakes, agglomerates or very fine quasi-spherical particles. The morphology is also dependent on the type of polymer matrix, as in the followings. PET and PE film recycling process are reported in Fig. 2 and Fig. 3 below.

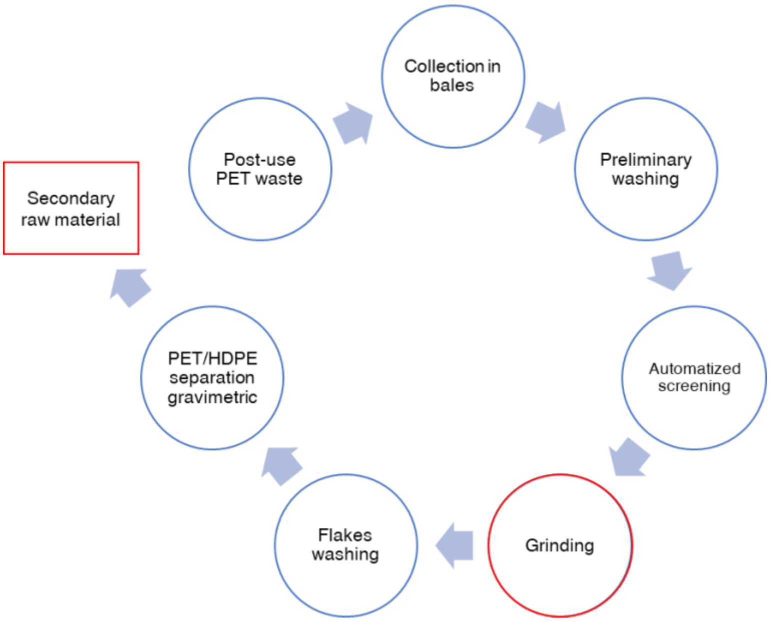

Fig. 2. *PET recycling process flow*

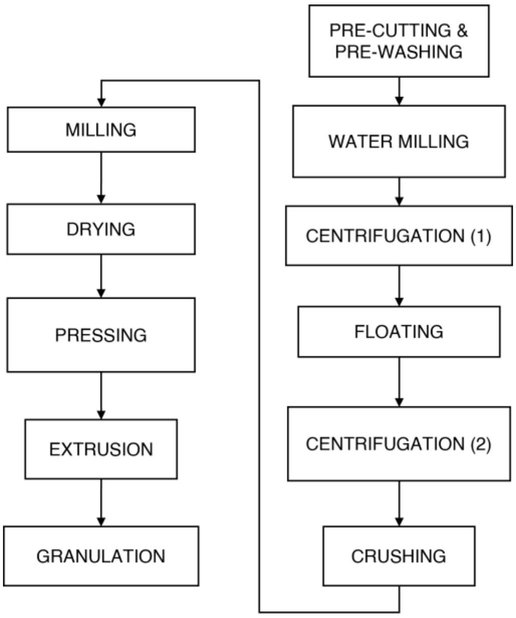

Fig. 3. *PE film recycling process flow*

2. Dust explosions

The recycling industry of polymer materials is relatively young with respect to pulp and paper/glass technologies. The quantitative amount of recycled plastic is relatively low compared to other materials, such as paper and glass, respectively 73.9 in EU (EPRC, 2021) and about 50% world averaged (CTCN, 2022). Accordingly, the dust safety science community concentrated on the polymer manufacturing industry rather than recycling plants. A focused paper was published by Stern et al. (2015), with a general overview of dust explosion in the plastic industry.

However, a relatively lower amount of data and papers could be found with respect to metal or wood/coal biomass powders explosion study. In pioneering work, Jacobson et al. (1962) dealt with the plastic dust industry and explosibility tests. Recently polymer dust has gained interest in several studies on the explosibility properties of some specified materials, such as nano-powder of PMMA

(Zhang et al., 2020), the inhibition effect on various polymer powders (Zhou et al., 2019 & Yang et al., 2019), the explosibility behaviour of nylon dust fibres (Marmo et al., 2018).

If dust explosion data are regarded, it could be seen how introducing a new material (i.e., the recycled polymer) could lead to severe enhancement of the explosion risk. Statistics account for polymer dust explosions only starting from 1982 (Fig. 4). A relevant episode is witnessed by CSB in their report (2008), involving “Plastic” as dust fuel in a chemical manufacturing plant, leaving 9 injured (MN, USA). The severity and number of polymer dust accident episodes did grow lately, starting from the 90s.

Plastic primary recycling could enhance dust explosion risk mainly because of the volume reduction operations generating flakes and smaller particles. It could be seen how this has influenced the dust explosion scenario. Since the rising of polymer recycling, a corresponding rise in industrial accidents in recycling facilities has been observed. Data from 1980 are gathered in 5-years intervals, and dust explosions numbers could be compared to plastic recycling flowrate on the total plastic waste produced (recovered from Ritchie & Roser, 2018). The dust explosion accidents share associated with “polymer and rubber” in the datasets (see Fig. 4:) seems to be directly related to the increase in recycling rate, referred to the total plastic fate (i.e., recycled, incinerated or discarded in landfills). An accidents peak is observed in the 2001-2005 interval where plastic dust episodes account for 21% of the total, while the recycling rate was 13%. In 1980-1985 polymer dust explosions were not registered, while the share of plastics recycling on total plastic waste fate was at its lowest (4%).

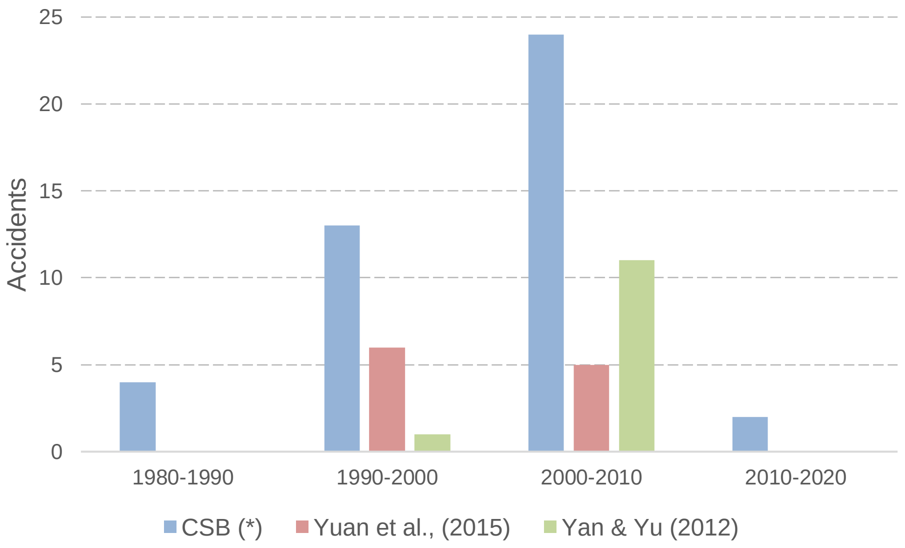

Fig. 4: *Statistics of polymer dust explosions*

In recent years an accident drop has been observed while the recycling rate is still increasing. This could be explained by the increased consciousness in facing dust explosion issues as a consequence of some severe episodes (West Pharmaceuticals and CTA Acoustics cases in Table 1), and, at least in the US, after the beneficial effect of the countermeasures contained in the CSB Call to Action (CSB, 2018). On the other hand, it is also likely the consequence of an under-reporting due to delays in collecting data and investigation course still to be concluded for the latest years episodes.

Table 1: *Recent cases of polymer dust explosions, I/F stands for injuries and fatalities.*

Date	Case	Location	Dust	I/F	Ref

1994	Kanaya Shoe Factory	JAP	Rubber waste	22/5	G. Vijayaraghavan, 2004
1995	Malden Mills	US	Nylon flock	27/0	CSB report
1997	Hunstman Polypropylene Corporation	US	PP	0/1	OSHA, Report ID: 0213900, 1997
1999	Jahn Foundry	US	Phenolic resin	9/3	CSB, 2009
2001	Finelvo	IT	Nylon flock	3/0	Marmo et al., 2018
2002	Rouse Polymerics International, Inc	US	Rubber	6/5	McKee, 2016
2002	Liaoyang Petrochemical Company	PRC	PE	19/8	Gan et al. (2018)
2003	West Pharmaceutical Services	US	Polyethylene	38/6	CSB, 2004
2003	CTA Acoustics	US	Phenolic resin	37/7	CSB, 2005
2011	Polymer Partners, LLC	US	Carbon black resin	3/1	McKee, 2016
2017	Yeosu Industrial Complex	SKOR	PP	-/-	Pak et al., 2019
2017	Arakawa Chemical Industries Ltd	JAP	Resin	11/1	Cloney, Chris (2018)

Table 1 reports the main accidents involving polymer dust in the late years: as could be observed, thermoplastics and thermosets are both involved, while most episodes are related to polyolefins (PE, PP). Yan & Yu (2012) report polymer dust explosion cases in the PRC, and the totality of episodes is correlated to PE dust.

Dust safety science report (Cloney, 2020 & 2021) reported a case of an explosion in a plastic bottle manufacturing plant involving the extruder system (US), a dust collector fire in a recycling site (OH, USA) and a plastic dust explosion in Germany in 2021. Evidence from this report and from OSHA citations (also referred to in Cloney 2020) indicate the involvement of an increasing number of recycling and waste management facilities in fire and explosion hazards due to combustible dust. Increased awareness about the issue is reported in different works, dealing with Refuse Derived Fuel (RDF) risk assessment, as in Januszewski & Brzezinska, 2021, while focus on recycling plants is reported by industrial associations, such as Dust Safety Science and OSHA.

3. Testing dust from plastic waste

In the followings, it is reported a summary of the tests performed in this study. Samples are identified according to their polymeric nature and type of process industry.

Dust originating from the waste flow of recycling facilities are compared to samples deriving from manufacturing plants (such as plastic powder products). The first samples have variable morphology; both fine particles and flakes could be present, depending on the mechanical treatment to which plastic waste is subjected and on the polymer mechanical characteristics.

Samples were characterised by optical microscopy, PSD through laser granulometry, moisture determination. FTIR analysis was adopted to identify their chemical nature (polymer or main polymers in the blend) by comparing the obtained spectra to known polymer spectra (Fig. 5).

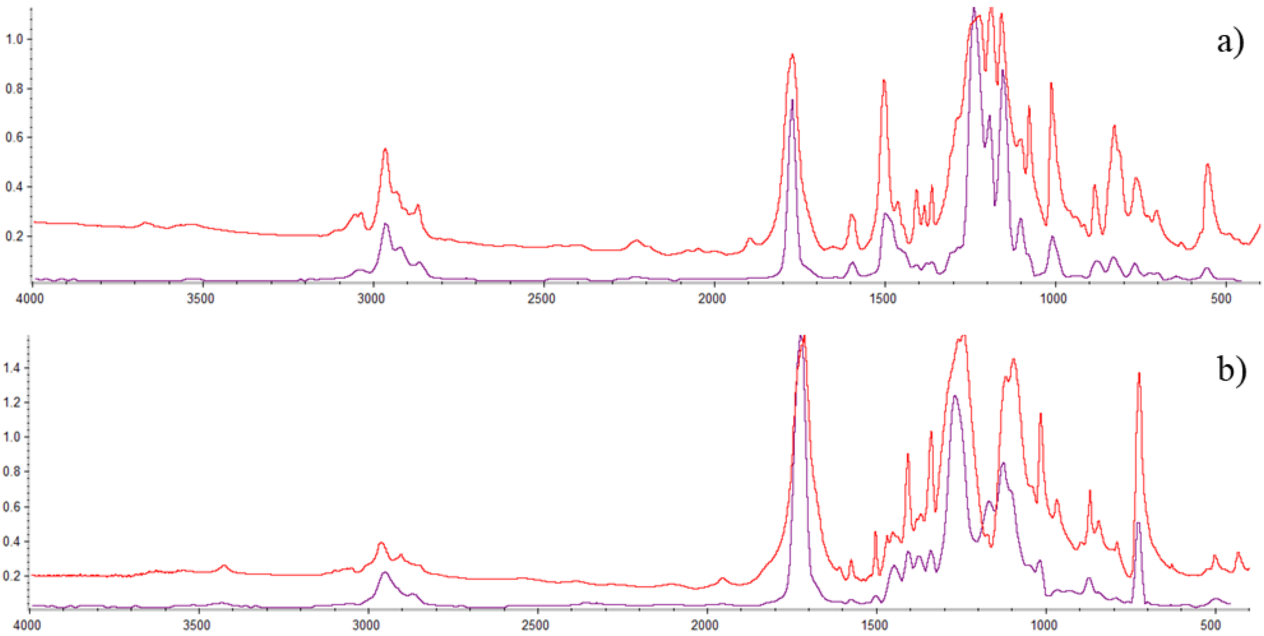

Fig. 5: *FTIR spectra for two samples in purple compared to dataset spectra in red: Polycarbonate (a) and Polyethylene terephthalate (b).*

The morphology of these samples could greatly vary according to sample origin. In Fig. 6 and Fig. 7, different samples are presented: dusts originated from industrial waste are mostly composed by coarser particles or fiber-like particles, while dusts from recycling process are finer and smaller flakes are present.

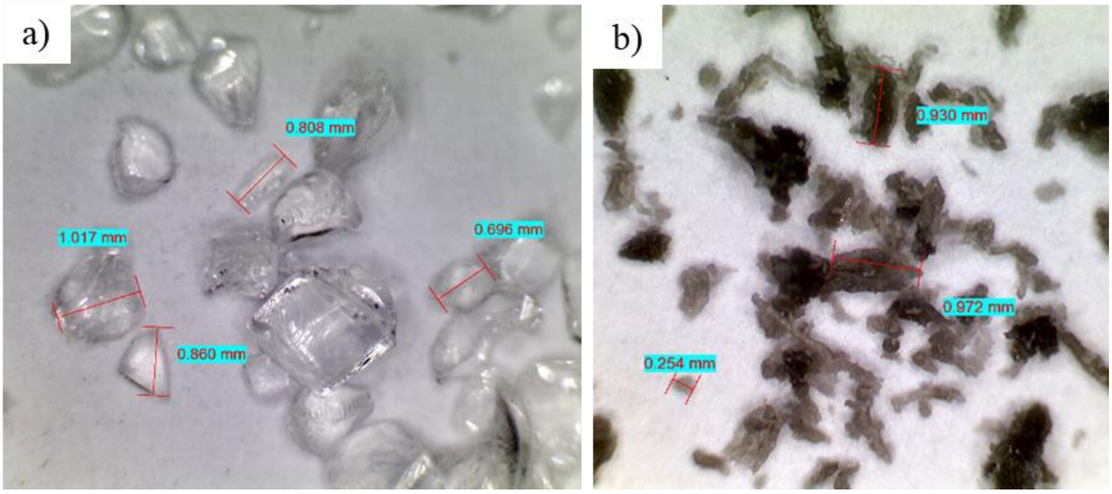

Fig. 6: *Optical microscopic images of samples defined as "Non-Explosive" PET granules (a) and plastic fibres from automotive, industrial waste (b).*

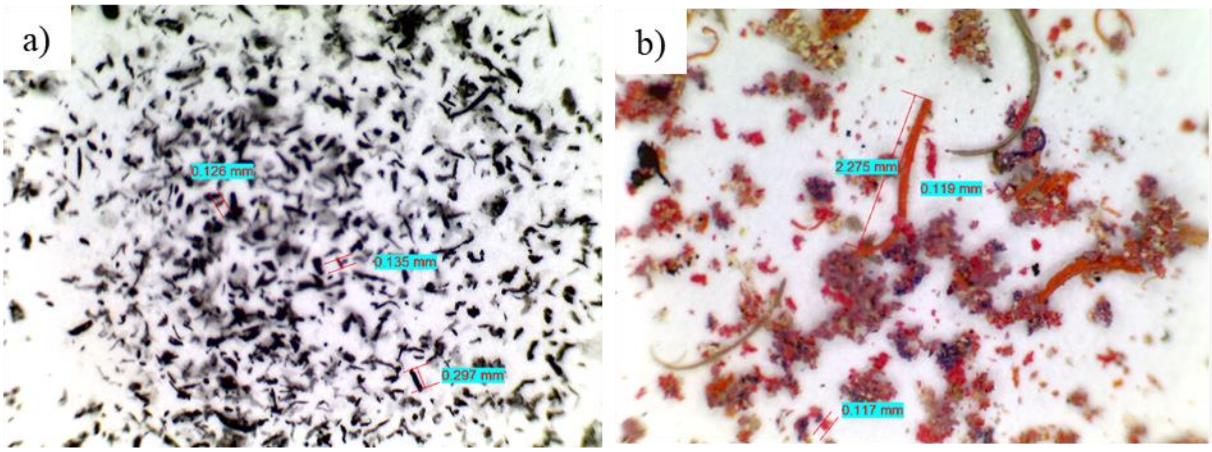

Fig. 7: *Optical microscopic images of explosible samples: Polycarbonate dust (a) and Rubber dust from recycling processes (b).*

Flammability tests are performed on all samples, in particular: Flammability screening (ISO 80079-20-2:2016), Minimum Ignition Energy (UNI EN 13821), Deflagration parameters (UNI EN 14034), Minimum Ignition Temperature (ISO 80079-20-2:2016).

4. **Results and discussion**

The FTIR analysis allowed to identification of the main polymer matrix of all samples. Most were composed of a pure polymer, while some were made up of a blend of different polymers or are copolymers samples. Fig. 8 reports the polymer distribution among the samples tested in this work. The rubber category defines thermoset samples that were not furtherly identified (mainly polyurethane resins or elastomers, like NBR).

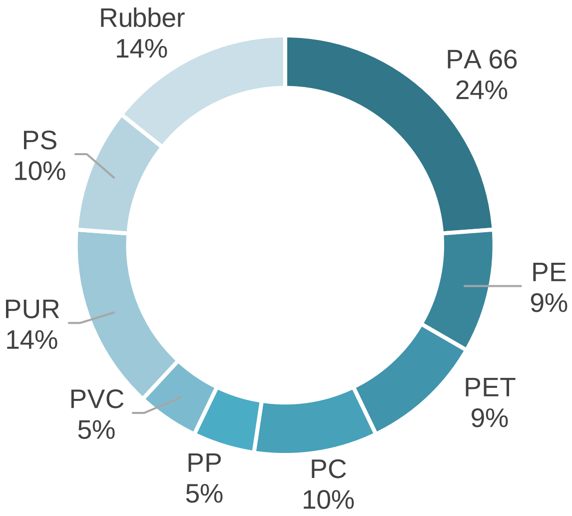

Fig. 8: *Main polymer distribution among samples.*

About 90% of the sample tested demonstrated a flammable behaviour when exposed to the ignition sources provided by the flammability screening (Fig. 9), according to ISO 80079-20-2:2016.

Samples that did not meet the ignition criteria of the test (“Non-Explosible”) are relatively coarser than the others. One among them is a fibrous dust sample, which could not be ignited in Hartman tube tests and not dispersible neither in the G-G furnace or the standard dispersion cup of the 20L sphere for deflagration parameters determination (see Fig. 6b).

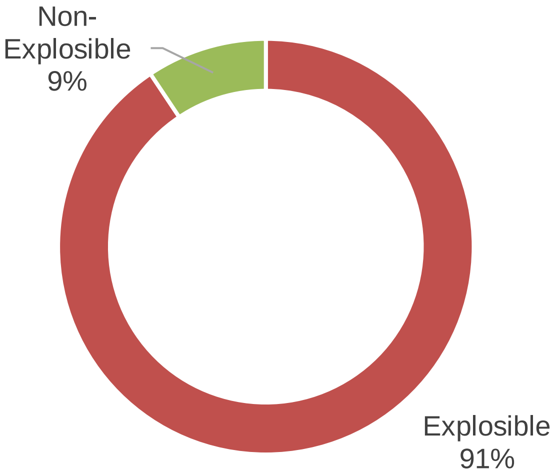

Fig. 9: *Screening test outcomes for all samples (ISO 80079-20-1:2016).*

Among samples defined as Explosibles, about 72% ignite at the beginning of the screening test, i.e., a flame propagation occurred in the Hartman modified tube with electric arc or glowing wire as an ignition source, indicating a high ignition sensitivity. Deflagration index (K_{St}) and maximum pressure (P_{max}) of all samples were measured in the 20L sphere (with 10kJ Sobbe chemical igniters), according to UNI EN 14034-1 and 2 (2004). As expected, the deflagration index is much higher in the case of finer samples, as shown in Fig. 10.

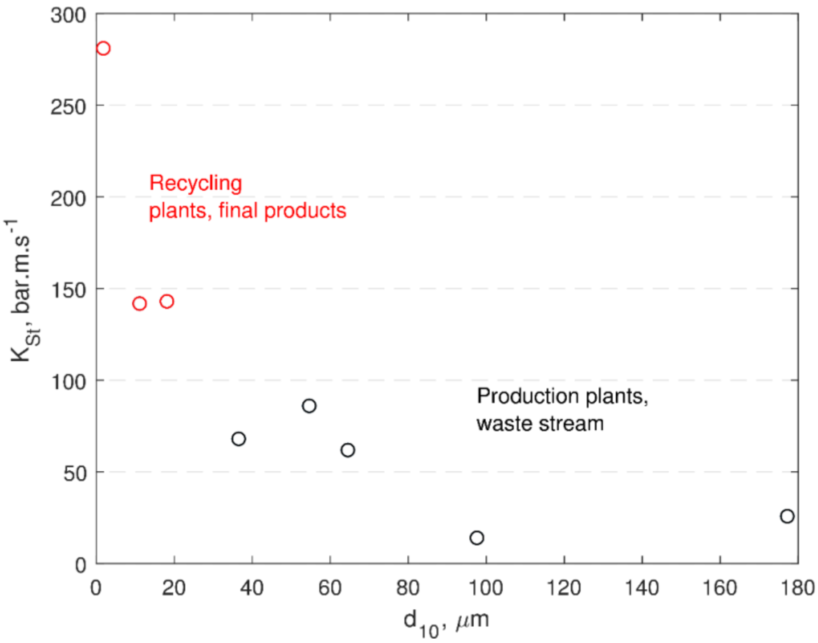

Fig. 10: *K_{St} values vs. d10 percentiles.*

MIE and MIT results are also reported, respectively, in Fig. 11 and Fig. 12. MIE of polymer dust is likely dependent on particle size, in this case, referred to the finest fraction identified by the tenth percentile (d_{10}). MIE increases with (d_{10}), according to fundamental dust explosion science literature (Echkoff, R. K., 2003 & Addai et al., 2016).

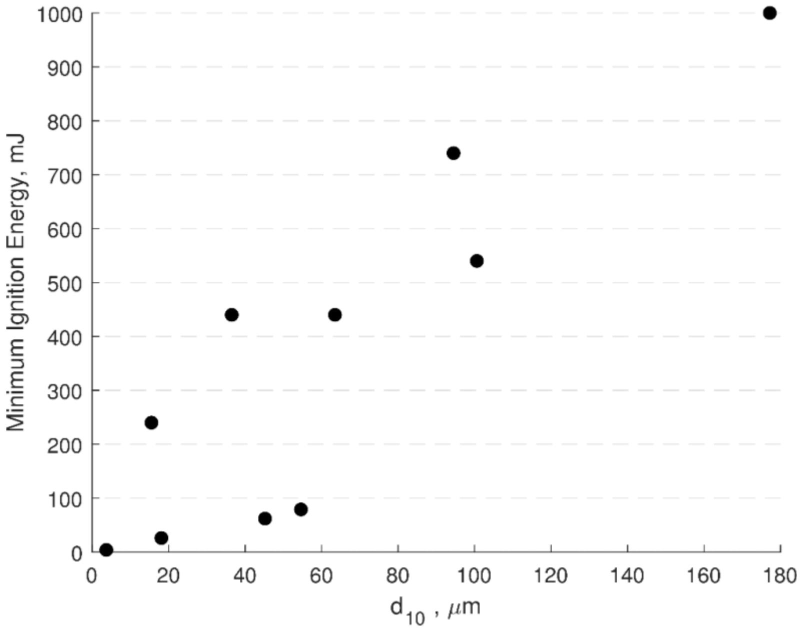

***Fig. 11:** Minimum ignition energy of samples, vs d10.*

Conversely, MIT values are close for all samples, there are some exceptions: higher MIT is obtained by Polycarbonate matrix dust, while lower values are associated with PE dust and PVB (polyvinyl butyral) dust. MIT of polymer dust also seemed not to rely entirely on PSD or other variables measured in this work. Hence, further tests are needed to clarify their behaviour, such as calorimetric analysis, to reveal decomposition and combustion energy of samples or any exothermic/endothermic process which could influence the ignition mechanism (work in progress). Further studies could investigate the effect of sample nature on the MIE values, as in Portarapillo et al. (2022).

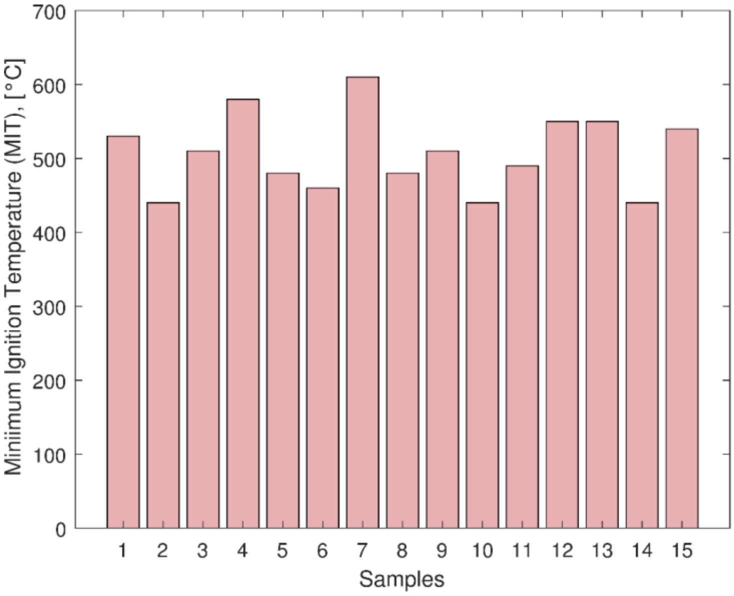

***Fig. 12:** Minimum ignition temperature of samples.*

To summarize, waste samples deriving from recycling operations demonstrated an higher ignition sensitivity and explosibility (Table 2), hence these facilities should be considered at high explosion risk, if proper countermeasures are not provided.

***Table 2:** Most hazardous samples identified in this work.*

Polymer	**d10**	**K_{St}**	**P_{max}**	**MIE**	**MIT**	**Origin**
PET	18.1	143	6.3	26	510	Recycling plant
PC	11.1	141.8	7.2	440	580	Recycling plant
PS-PVC mix	1.8	281	8.0	1.9	480	Recycling plant
Cellophane	54.6	86	6.8	79	440	Manufacturing industrial waste
PEA[a]	3.7			4	440	Automotive industrial waste
PUR	36.5	68	7.0	440	530	Automotive industrial waste

[a] polyethylacrilate

5. Conclusions

The purpose of the present work was to identify ignition sensitivity and deflagration properties of polymer-based dust, originating from industrial waste and recycling processes, to support explosion risk assessment where these kinds of materials are present, such as in recycling plants, plastic manufacturing waste flow, energy generation from waste fuel premises.

Based on the outcomes of the experimental tests, some considerations could be drawn:

- Deflagration parameters (K_{St}) of recycling-derived dust are higher than those of plastic waste powders (as in Fig. 10).
- Morphology and PSD are leading factors that should be carefully considered in the explosion risk assessment of these materials, focusing on finer particles and flakes.
- MIE values are mostly dependent on the finest fraction of samples (d_{10});
- MIT may depend on some properties other than PSD or dust nature.

References

Addai, E. K., Gabel, D., & Krause, U. (2016). Experimental investigations of the minimum ignition energy and the minimum ignition temperature of inert and combustible dust cloud mixtures. Journal of Hazardous Materials, 307, 302–311. https://doi.org/10.1016/j.jhazmat.2016.01.018

Cloney, Chris (2021). “2020 Combustible Dust Incident Report - Version #1” DustEx

CSB, 2010. Investigation Report, Combustible Dust Hazard Study. U. S. Chem. Saf. Hazard Investig. Board. REPORT n° 2006-H-1.

Eckhoff, R.K. (2003). *Dust explosions in the process industries*. Third edition. Gulf Professional Publishing, Amsterdam.

EPRC. (2021). Monitoring Report 2020. European Declaration on Paper Recycling 2016-2020. Retrieved from https://www.paperforrecycling.eu/publications/

Gan, B., Gao, W., Jiang, H., Li, Y., Zhang, Q., & Bi, M. (2018). Flame propagation behaviors and temperature characteristics in polyethylene dust explosions. Powder Technology, 328, 345–357. https://doi.org/10.1016/j.powtec.2018.01.061

Geyer, R., Jambeck, J. R., & Law, K. L. (2017). Production, use, and fate of all plastics ever made. Science Advances, 3(7), 25–29. https://doi.org/10.1126/sciadv.1700782

Hannah Ritchie and Max Roser (2018) - "Plastic Pollution". Published online at OurWorldInData.org. Retrieved from: 'https://ourworldindata.org/plastic-pollution' [Online Resource]

Hopewell, J., Dvorak, R., & Kosior, E. (2009). Plastics recycling: Challenges and opportunities. Philosophical Transactions of the Royal Society B: Biological Sciences, 364(1526), 2115–2126. https://doi.org/10.1098/rstb.2008.0311.

https://dustsafetyscience.com/fire-hazards-waste-recycling-ryan-fogelman/, last accessed on the 10th March 2022

https://www.csb.gov/csb-releases-call-to-action-on-combustible-dust-hazards/ last accessed on the 10th March 2022.

https://www.osha.gov/combustible-dust, last accessed on 10th March 2022.

Hundertmark, T., Mayer, M., McNally, C., Simons, T. J. & Witte, C. (2018). How plastics waste recycling could transform the chemical industry - McKinsey & Company. McKinsey Insights, (December).

Jacobson, M., Nagy, J., & Cooper, A. R. (1962). Explosibility of Dusts used in the Plastic Industry. U.S. Dept. of Interior, Bureau of Mines.

Januszewski, J.; Brzezinska, D. RDF Fire and Explosion Hazards at Power Plants. Sustainability 2021, 13, 12718. https://doi.org/10.3390/su132212718

Marmo, L., Sanchirico, R., Di Benedetto, A., Di Sarli, V., Riccio, D., & Danzi, E. (2018). Study of the explosible properties of textile dusts. *Journal of Loss Prevention in the Process Industries*. https://doi.org/10.1016/j.jlp.2018.03.003

Marmo, L., Sanchirico, R., Di Benedetto, A., Di Sarli, V., Riccio, D., & Danzi, E. (2018). Study of the explosible properties of textile dusts. Journal of Loss Prevention in the Process Industries. https://doi.org/10.1016/j.jlp.2018.03.003

McKee, Johnna Denise, "Comparative Case Study Analysis of Combustible Dust Explosions: Determining the Need for an OSHA Combustible Dust Standard" (2016). Online Theses and Dissertations. 400. https://encompass.eku.edu/etd/400

Pak, S., Jung, S., Roh, C., & Kang, C. (2019). Case studies for dangerous dust explosions in South Korea during recent years. Sustainability (Switzerland), 11(18). https://doi.org/10.3390/su11184888

Portarapillo, M., Danzi, E., Guida, G., Luciani, G., Marmo, L., Sanchirico, R., & Di Benedetto, A. (2022). On the flammable behavior of non-traditional dusts: numbers evaluation for nylon 6 , 6 short fibers. Accepted by Journal of Loss Prevention in the Process Industries, March 2022.

Research Ltd. Retrieved from http://dustsafetyscience.com/2020-Report

Stern, M. C., Ibarreta, A., & Myers, T. J. (2015). Abetment and mitigation of combustible dust hazards in the plastics industry. AIP Conference Proceedings, 1664(May). https://doi.org/10.1063/1.4918527

UN Climate Technology Centre & Network (CTCN), https://www.ctc-n.org/technologies/glass-recycling, last accessed 08/06/2022.

UNI CEI EN ISO /IEC 80079-0-2:2016 Explosive atmsospheres - Part 20-2: Material characteristics: Combustible dust test methods. CEN-CENELEC Management Centre: Avenue Marnix 17, B-1000 Brussels

UNI EN 14034-1:2011 Determination of explosion characteristics of dust clouds - Part1: Determination of the maximum explosion pressure P_{max} of dust cloudsUNI EN 14034-2:2011 Determination of explosion characteristics of dust clouds – Part 2: Determination of the maximum rate of explosion pressure rise(dP/dt_{max} of dustclouds

U.S. Chemical Safety and Hazard Investigation Board. (2005). Investigation Report, COMBUSTIBLE DUST FIRE AND EXPLOSIONS. U. S. Chemical Safety and Hazard Investigation Board, Report N°(CTA Acoustic, INC.), 1–127. Retrieved from https://www.hsdl.org/?view&did=234907%0Ahttps://www.csb.gov/recommendations/?F_InvestigationId=3530

Vijayaraghavan, G., Engineering, C., & College, A. E. (2011). EMERGING EMERGENCY DUE TO DUST EXPLOSIONS IN PROCESS INDUSTRY Journal of Engineering Research and Studies, II (IV).

Yan, X. Q., & Yu, J. L. (2012). Dust explosion incidents in China. Process Safety Progress, 31(2), 187–189. https://doi.org/10.1002/prs.11482

Yang, J., Yu, Y., Li, Y., Zhang, Q., Zheng, L., Luo, T., … Jiang, J. (2019). Inerting effects of ammonium polyphosphate on explosion characteristics of polypropylene dust. Process Safety and Environmental Protection, 130, 221–230. https://doi.org/10.1016/j.psep.2019.08.015

Yuan, Z., Khakzad, N., Khan, F., & Amyotte, P. (2015). Dust explosions: A threat to the process industries. Process Safety and Environmental Protection, 98, 57–71. https://doi.org/10.1016/j.psep.2015.06.008

Zhang, X., Gao, W., Yu, J., Zhang, Y., Zhang, J., Huang, X., & Chen, J. (2020). Effect of flame propagation regime on pressure evolution of nano and micron PMMA dust explosions. *Journal of Loss Prevention in the Process Industries*, *63*. https://doi.org/10.1016/j.jlp.2019.104037

Zhou, J., Jiang, H., Zhou, Y., & Gao, W. (2019). Flame suppression of 100 nm PMMA dust explosion by KHCO3 with different particle size. *Process Safety and Environmental Protection*, *132*, 303–312. https://doi.org/10.1016/j.psep.2019.10.027

DOI: 10.7795/810.20221124

Schlieren imaging investigations of hot gas kernel expansion caused by slow contact break discharges

Carsten Uber[a], Niklas Schüler[a], Steffen Franke[b], Michael Hilbert[a], Dirk Uhrlandt[b]

[a] Physikalisch-Technische Bundesanstalt, Braunschweig, Germany
[b] Leibniz-Institut für Plasmaforschung und Technologie, Greifswald, Germany

E-mail: carsten.uber@ptb.de

Abstract

In potentially explosive atmospheres, electric contact break discharges, which are typically generated at low voltages < 30 V and low currents in a range of 30 mA up to 80 mA, are a potential ignition source. Such locally small and fast discharges (typically 150 µm) generate a hot gas kernel relevant to the ignition process between electrodes in motion within 200 µs and are dominated by metal vapor from the cadmium cathode. However, it is essential to understand the transition from a contact discharge to a hot gas kernel and then to a thermochemical ignition. This has not been sufficiently investigated so far.

Schlieren imaging can be applied to study the hot gas kernel; however, this analysis of hot gas kernels here is demanding. Specifically, it requires good spatial resolution and sufficient time resolution (20 000 fps) while using a suitable parallel light beam. The test setup developed for this purpose will be described in this article. Moreover, examples of the expansion of a hot gas kernel with and without successful ignition in an H_2/air mixture will be shown. This includes an evaluation of the expansion dynamics and the dynamic evolution to power input. The aim is to draw conclusions on criteria that lead to ignition by investigating the processes of contact discharges that may or may not result in ignition.

The results obtained will be integrated into a multi-physical model to assess potential ignition.

Keywords: *contact break discharges, hot gas kernel, schlieren imaging, spark test apparatus, metal vapor discharge*

1. Introduction

Knowledge of the development of the hot gas kernel and flame front caused by an electrical discharge is necessary for basic understanding of an ignition as well as for modelling a possible ignition in order to predict it. The development of the hot gas kernel has been explored in diverse investigations documented in the basic literature (Lewis and von Elbe 1951, Babrauskas 2003, Steen 2000). However, previous investigations differ from those presented in this work – which concern ignitions in H_2/air mixtures (H_2 volume fraction 21 %) caused by electric contact break discharges at the ignition limit – because the previous investigations used different gas mixtures, electrode types, methods and investigation goals. Nevertheless, the investigations contained here also signify gains in knowledge in certain areas of the investigations performed in this field to date.

Using Töpler's schlieren technique and Dvorak's shadowgraph method, Lewis and von Elbe (1951) documented many basic investigations on combustion and ignition. Lintin and Wooding (1959)

DOI: 10.7795/810.20221124

focused more specifically on the development of a flame front ignited by a high-voltage spark in a methane/air mixture. The critical phase of a growing flame front between electrodes in fixed positions was investigated and documented. Here, the radius and duration were estimated in order to determine the point in time when the flame front continues to expand or begins to contract. For methane, a critical radius of 1 mm was determined and compared to the quenching radius. Via the schlieren technique, other authors such as Bane (2010), Xu (2014) and Essmann (2019) investigated the hot gas kernel and the ignition of various gas mixtures via low-energy discharges but with a fixed arrangement of electrodes and with high-voltage.

Discharges as a source of ignition were used by Thedens (2002) to investigate the flame front in a H_2/air mixture via the schlieren technique, albeit with an anode 4 mm in diameter. Zborovsky (1969) also used contact discharges in methane and with currents > 1.6 A for schlieren imaging investigations of a hot gas kernel. In schlieren imaging investigations, the lead author of this work observed the flame front of an ignition caused by rapid contact openings (Uber 2016).

However, the critical phase in which the hot gas kernel either expands or contracts has not yet been investigated thoroughly enough to be sufficiently understood. This phase may occur during or after an electrical contact break discharge. A particular challenge that arises during investigations of this nature is to determine the location (typical discharge length 150 µm) and the point in time when the given gas kernel begins to develop (typically within 200 µs, see section 4) during the discharge process. However, this is necessary in order to understand the ignition and create a corresponding model.

To this end, the contact situation including the electrical source and the schlieren technique are first focused on more closely. After the setup used is described, example schlieren images of the hot gas kernel including the corresponding electrical processes and the initial results are shown. This is then followed with a discussion of the results and a conclusion.

2. Background

To generate ignitions that have low voltage and current values, slow contact break discharges and special conditions are required (Holm 1967, Slade 2014, Babrauskas 2003). The following conditions refer to discharges at the ignition limit of H_2/air mixtures that are comparable to the standardized spark test apparatus (cf. IEC 60079-11 (2012)).

The contact apparatus is supplied with energy by a constant current source with limited maximum voltage; at $U_{\text{max}} = 30$ V and $I = 60$ mA, it is close to the ignition limit. The constant current source is used to ensure that the discharges can be investigated independently of circuit-related mechanisms and effects. The contact process is presented in detail in Fig. 1.

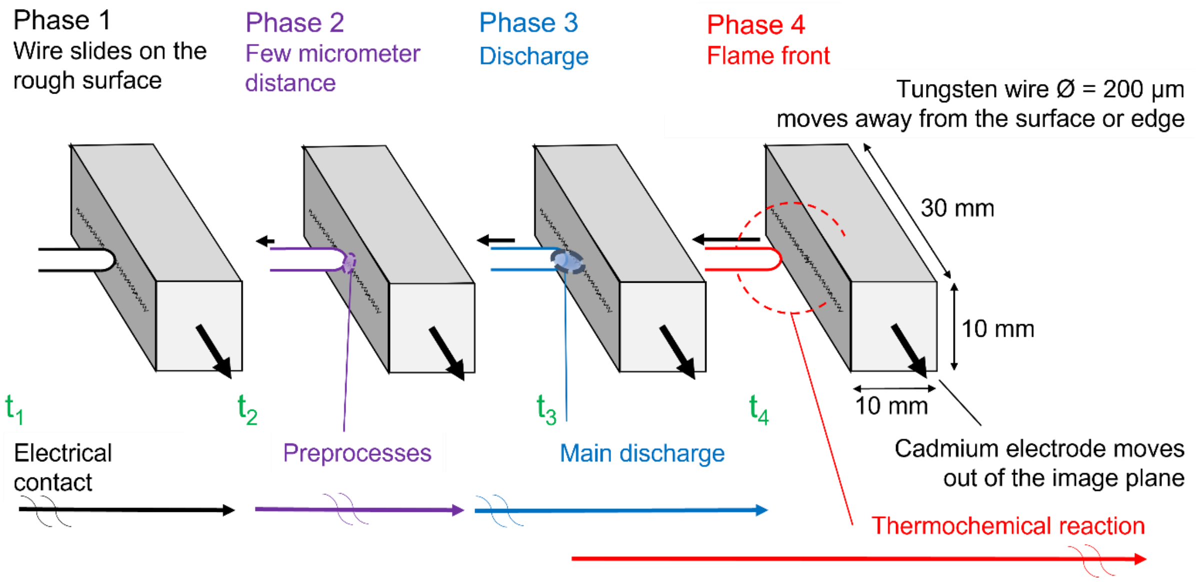

Fig. 1. *Schematic representation of processes that take place during an ignition caused by a contact break discharge in the experimental contact apparatus*

In the first phase, the wire slides along the rough surface and an electrical contact takes place between the tungsten wire (anode) and the cadmium block (cathode). In the second phase, the wire is a short distance (a few micrometers) away from the surface; between the two phases, preprocesses take place with continuous discharges. If the wire moves further away during the third phase, the main discharge takes place; this discharge lasts several hundred microseconds and has a typical maximum length of 150 µm under the chosen parameters. The discharge is dominated by metal vapor. Here, the principal energy transfer takes place in the hot gas kernel; the thermochemical reaction starts if the ignition is successful. More detailed characteristics of electrical contact discharges can be found in Uber (2019).

For the investigations of the hot gas kernel and the flame front in H_2/air mixtures, the schlieren technique can be used; here, a field of irregular density is visualized (Settles (2001), Schardin (1942)). In this investigation, the schlieren technique is used for the qualitative observation necessary to visualize the temperature changes of the hot gas kernel and flame front, including the observation of the initiation process (cf. Lewis and von Elbe (1951)). Fig. 2 depicts a typical schlieren system with lenses. The light from the light source is used to generate a parallel light beam via Lens 1, a pinhole and Lens 2. In the observation area, the light beam is focused at the focal point of Lens 3. In this way, a light spot is generated at the position of the knife-edge. The schlieren knife-edge partially conceals this light spot. When passing through the observation area, the light beam is deflected due to the physical condition of the medium (for example, a change in density). Then the light point on the image layer will move. The deflection creates grey-scale values in the schlieren images.

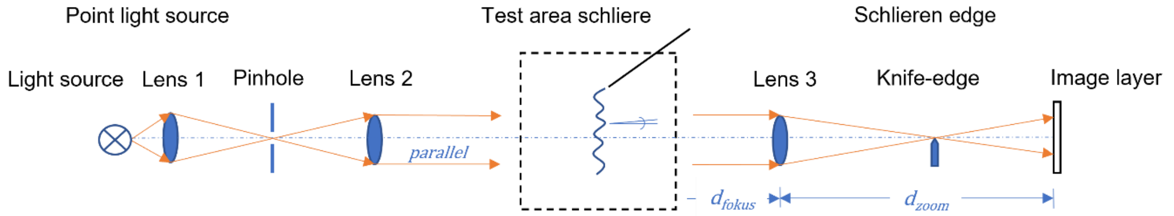

Fig. 2. *Basic schlieren array with parallel transmission through the object and lenses (cf. Settles (2001), Schardin (1942))*

The angle of deflection, which is determined via the refractive index, reacts relative to the parallel light, thus allowing a qualitative observation of the hot gas kernel.

A challenging aspect not present in the discharges investigated in the literature to date is (Lewis and von Elbe 1951, Bane 2010, Essmann 2019), on the one hand, the smallness of the observation area for the relevant discharges (0-150 µm in length) in contrast to the distances between the electrodes, which are in the millimeter range. On the other hand, the relevant transition process takes place over a few hundred microseconds and requires a suitable light intensity for the high-speed image recording process.

3. Setup

In basic terms, the setup consists of a contact device in an explosion chamber, a control mechanism, a supply of electricity for the contact device and measurement equipment, as well as the schlieren setup (comparable to that in Fig. 2) used to observe the hot gas kernel (see Fig. 3).

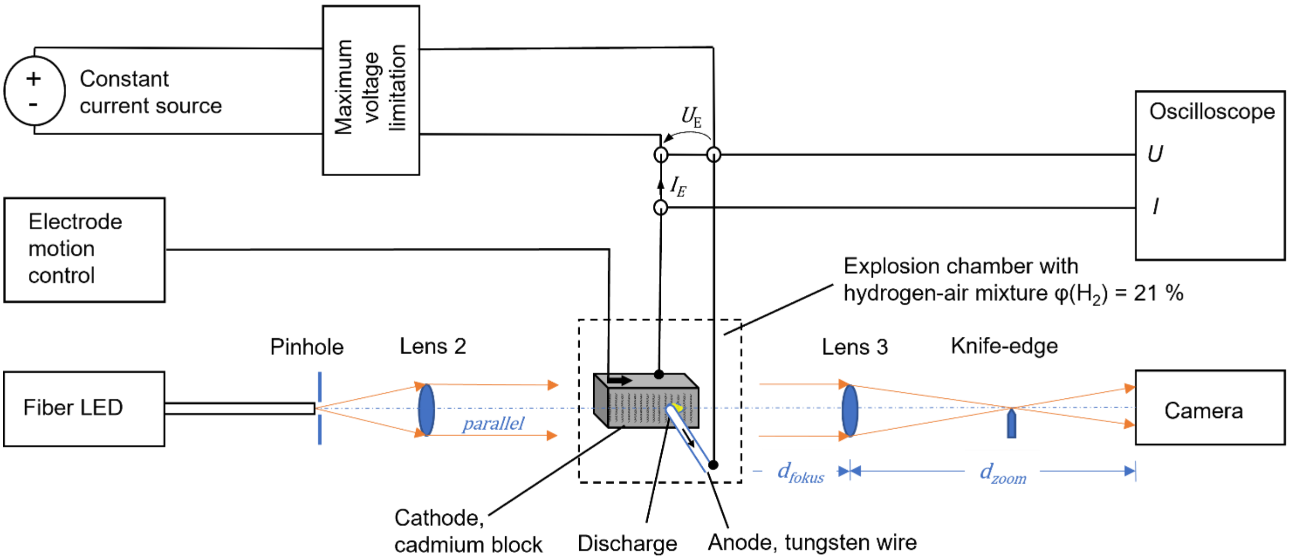

***Fig. 3.** Experimental setup for the schlieren imaging investigations of contact discharges*

As shown in Fig. 3, a constant current source with a limited maximum voltage is used to supply electricity; this source quickly re-adjusts the required current up to the maximum voltage and its quality can be seen in the current and voltage curves of the oscilloscope. This circuit is used because, in contrast (for example) to a resistive circuit (cf. Zborovsky 1969), the electrical values can be determined simply and directly without conversion. The control element of the contact device in the test setup described here allows contact break processes to be carried out in which the wire is slowly raised to a distance of ca. 150 µm within 1 ms following a defined period of preprocesses and with a distance between the electrodes of a few micrometers. A 30 mm long cadmium block with a rough surface is used as a cathode; this block moves at an average speed of 0.002 m/s perpendicular to the movement direction of the anode. The anode is a tungsten wire with a diameter of 200 µm that moves away from the cadmium block according to the slow contact break movement of the cadmium block (cf. Uber (2019)).

For the setup used as shown in Fig. 3, a compromise was found in the form of a multi-mode fiber LED that had a sufficient light intensity with relatively even distribution (multi-mode fibers with a core diameter of 200 µm, LED 554 nm, 21 mW). However, observing objects that are this small requires a correspondingly parallel light from a point-shaped light source; this is realized via a pinhole with a diameter of 200 µm and via Lens L2 (f = 60 mm). In the setup, a lens with f = 60 mm is used as L3. On the one hand, this focal length determines the distance to the object d_{fokus} and the distance to the knife-edge. On the other hand, the distance d_{fokus} to the object as determined by the focal length is of critical importance for the intensity of the dark and light areas in the image plane, as is the location of the deflection. Also of relevance for the contrast of the schlieren is the percent of the beam covered by the knife-edge. Approx. 45 % of the intensity was demonstrated to be a feasible value (cf. Zang et al. (2021)). The low signal-to-noise ratio is improved via post-processing of the images. Here, based on the current image, a difference image is created with a background image at the start of the recording process; this difference image is generated via a half-automated process using OriginLab. For the half-automated process, the image with the schliere is subtracted from a reference image without a schliere in order to then determine the edges from this calculated difference image with profile lines. In this way, the target schliere becomes more visible and evaluable, even though the measurement accuracy is slightly reduced.

For this test setup, a resolution normal (Negative 1951 USAF Resolution Text Target Ø1" (Thorlabs)) was used to calculate an object length of 6.2 µm x 6.2 µm per pixel in the video image; this length was determined via the distance d_{zoom}. This resolution standard was also used to resolve the lines of Group G3E6 with a line thickness of 35 µm; this line thickness was included in the measurement uncertainty (see Fig. 9).

A H_2/air mixture (hydrogen volume fraction 21 %) was used as the explosive atmosphere. This corresponds to Group IIC of the standard (IEC 60079-0:2017).

4. Experiments and Results

When an ignition takes place due to a contact break discharge, the expansion of the hot gas kernel can be observed as dark and bright areas via a schlieren image (see Fig. 4).

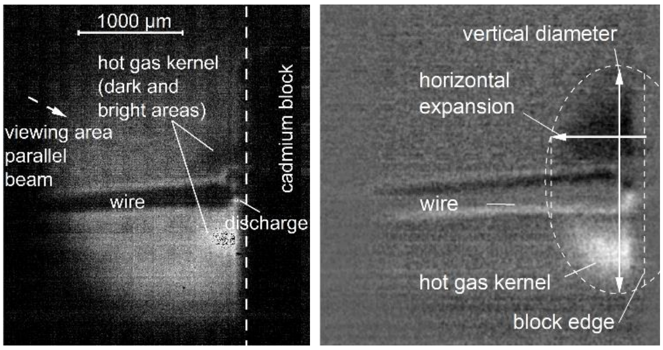

Fig. 4. *Left: schlieren image of hot gas kernel with cathode (Cd block), wire and discharge, size: 0.33 mm x 0.33 mm; right: evaluated image (difference to reference image) with visible hot gas kernel and size indications, size: 0.25 mm x 0.25 mm*

In the typical schlieren image shown in Fig. 4 (left), the wire can be seen in the field of the parallel light; the edge of the cadmium block is also shown. Between the wire and the block, the bright discharge can be seen and, around the discharge, the bright and dark areas of the schlieren image generated by the hot gas kernel. Between the cadmium block and the viewing area, a dark area can be seen; this is the result of the parallel light beam being concealed by the block, whose arrangement is not perfectly parallel. This concealment changes depending on the position of the block and was determined for all measurements using the image with the least concealment. In the evaluated image in Fig. 4 (right), an elliptical line has been added as the boundary between the ambient temperature and the hot gas kernel. The horizontal expansion and the vertical diameter indicated are applied in later evaluations. Fig. 5 shows a typical image series with a corresponding voltage and current curve.

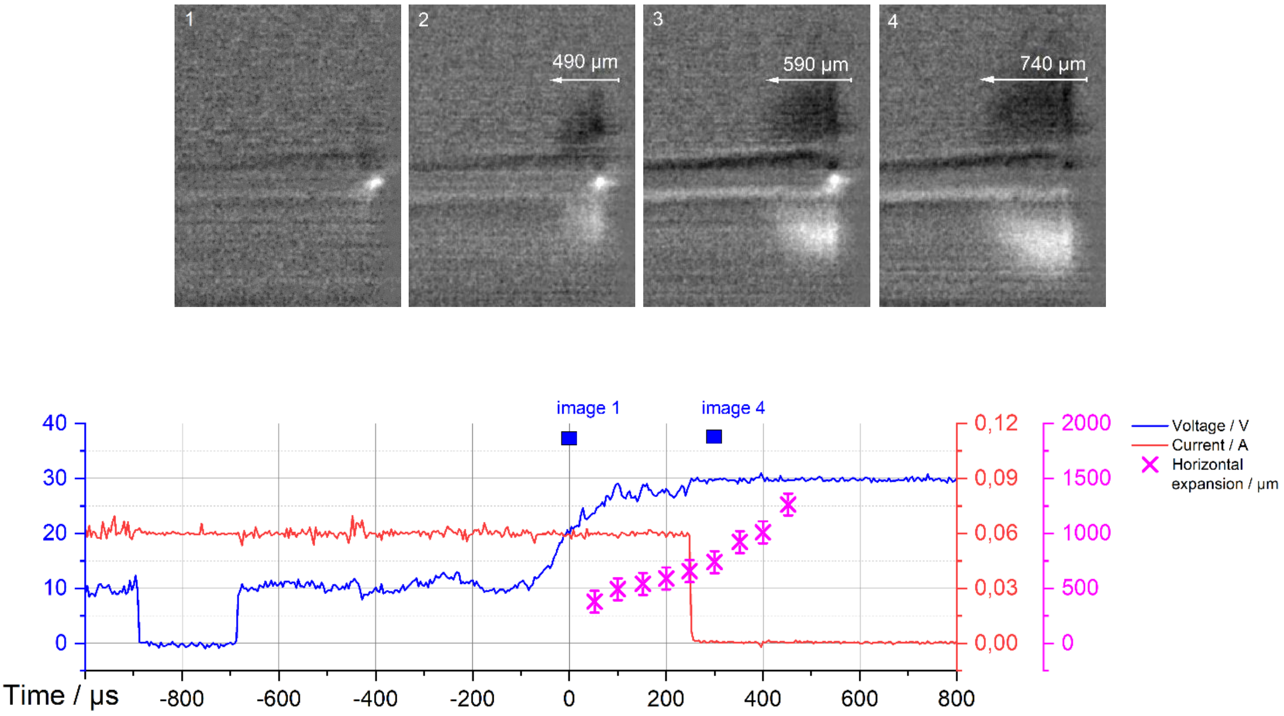

Fig. 5. *Top: Schlieren images, processed images. Bottom: Voltage/current curves and horizontal expansion of the hot gas kernel with ignition*

In the schlieren image series at the top of Fig. 5, the discharge can be seen in images 1-3 as a small bright point between the wire tip and the cadmium block; in image 4, the discharge has already ended. A semicircular hot gas kernel forms around the discharge and increases in size; due to the position of the knife-edge, this gas kernel is darker at the top and brighter at the bottom than its surroundings. The semicircular gas kernel is still barely recognizable in image 1 and grows in images 2, 3 and 4 until it has a radius of approx. 500 µm, 600 µm and 750 µm, respectively.

In the current curve below these images in Fig. 5, the constant current of I = 60 mA can be recognized, which is visible for as long as the discharge takes place. The voltage during the discharge increases at the beginning to between approx. 8.6 V and 11 V; this discharge takes place when the distance between the electrodes is small (preprocesses). The longer the discharge lasts, the more the voltage increases up to a maximum voltage of 30 V until the discharge breaks down when the required source voltage is no longer available for the increasing discharge length. In this example, the hot gas kernel can be identified starting at approx. 200 µs and a voltage of > 20 V. At the end, the hot flame front forms as soon as the thermochemical reaction starts and the expansion increases sharply. As revealed by observations of the hot gas kernel during rapid contact openings, the flame front of the H_2/air mixture expands at a rate of approx. 7.3 m/s (cf. Uber (2016)); this also agrees well with the data provided by Essmann (2019, P. 85), although his data concerned high-voltage discharges.

One of the greatest challenges entailed by this test setup is to maintain a parallel orientation between the surface of the moving cadmium block and the parallel light beam. For the images, the orientation that can be realized in practice means that the rearmost or forwardmost part of the block can protrude into the image, leaving part of the gas kernel in the shadow or otherwise concealed. Furthermore, given the rough surface involved, which has peaks and valleys, the discharge and the gas kernel are not always fully visible in the images.

A hot gas kernel was also observed for discharges without a successful ignition; however, the size of this kernel remains at a maximum value and does not increase further. This is illustrated in the following example in difference image 4 (see Fig. 6).

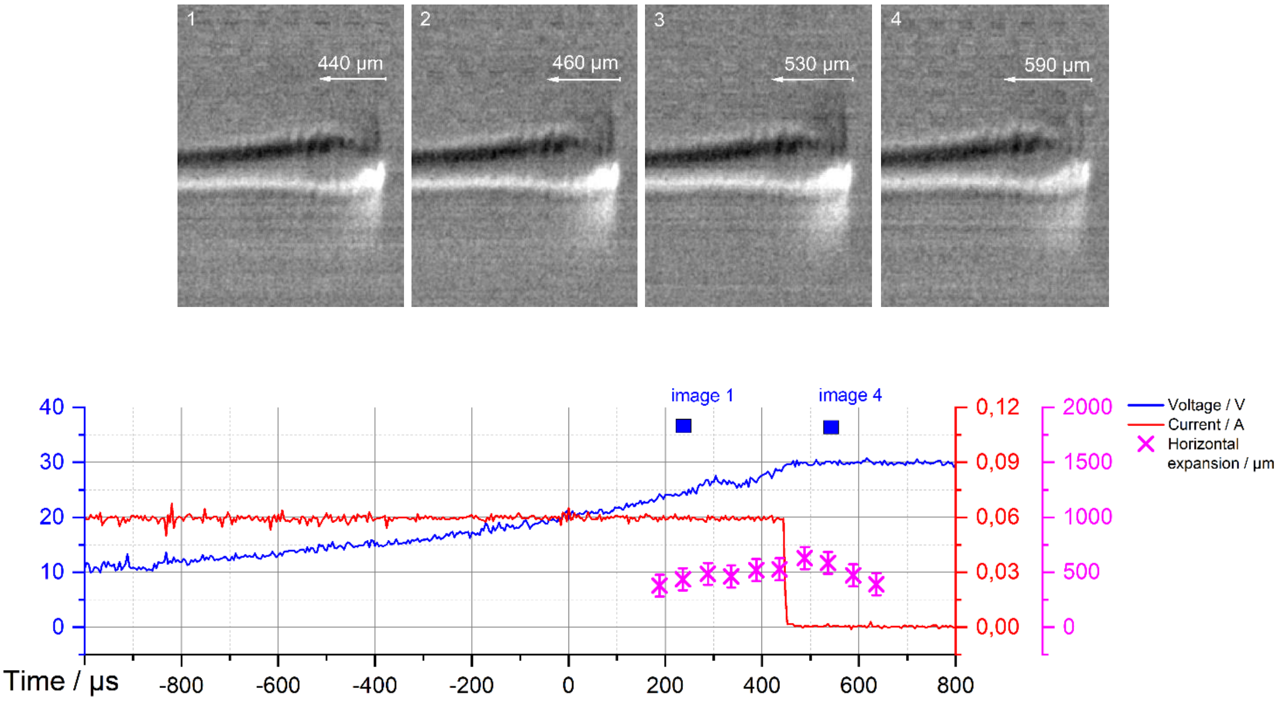

Fig. 6. *Top: Schlieren images, processed images. Bottom: Voltage/current curves and horizontal expansion of the hot gas kernel without ignition*

For image 4, the horizontal expansion of the gas volume in this example is estimated to be 500 µm. The volume of an assumed rotationally symmetrical semicircle without a wire is approx. 0.23 mm^3 and remains in this approximate order of magnitude. This volume is larger than the minimum ignition volume of 0.1 mm^3 defined by Steen (2000); however, the anode and cathode have a larger cooling surface.

By comparison, the measurements performed in these investigations showed that there is a significant region in the voltage curve during the critical phase. In this significant region (from ca. 20 V to around 30 V, where the collapse takes place), the discharges with ignition differ from the discharges without ignition because the former have a larger gas kernel; in this example, the discharges with ignition also have a higher voltage and thus power in the critical phase (see Fig. 7).

DOI: 10.7795/810.20221124

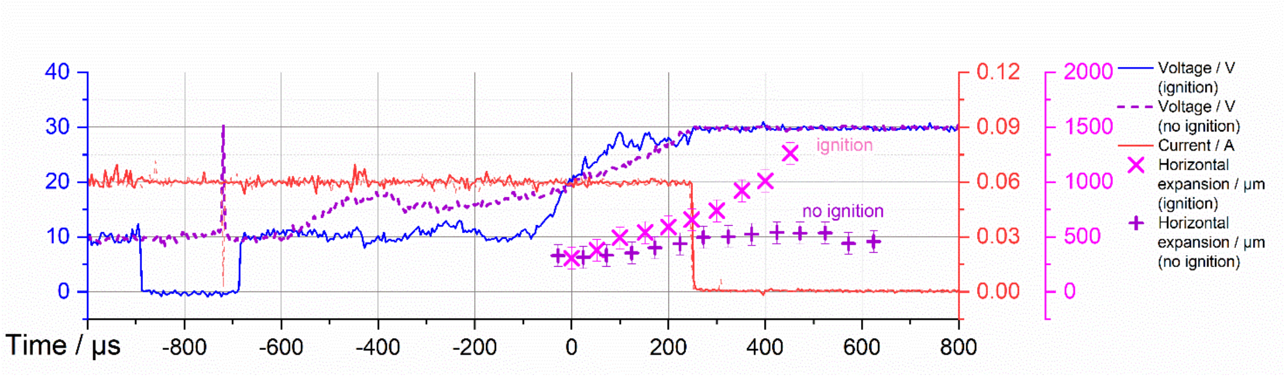

Fig. 7. *Comparison of the horizontal expansion of the hot gas kernel with and without ignition for 60 mA, max. 30 V and 1 ms contact-opening time up to 150 µm.*

In Fig. 7, starting at 0 µs and lasting approx. 200 µs, a difference can be seen in the voltage curves of the example discharges with and without ignition. At 0 µs, the voltage is between approx. 20 V and 24 V, corresponding to a discharge length of 100 µm (Uber (2019)). For all measurements performed within the scope of this work, a voltage of 20 V was roughly estimated to be the start of the critical phase; thus, for all the diagrams contained in this work, 0 µs was set for a voltage of 20 V. The horizontal expansion of the gas kernel (crosses) is also visible in the curve. Ultimately, if the ignition is successful, the expansion increases at the speed of the flame front. If the discharge takes place without an ignition, the hot gas kernel increases in size to less than 500 µm and does not exceed this size. Observing the smaller hot gas kernel confirms that the ignition is quenched at small discharge sizes; this was also determined using the model for these contact discharges (Uber et al. (2022)).

Given a voltage of approx. 22-30 V, the measurements performed in these investigations were associated with a duration (dashed line in Fig. 8) of approx. 150 µs (usually up to 200 µs). Because of the constant current used, this corresponds to a power range of approx. 1.44-1.8 W.

To estimate the quality of the measurand, the factors contributing to the measurement uncertainty were compiled in an Ichikawa diagram (Fig. 8).

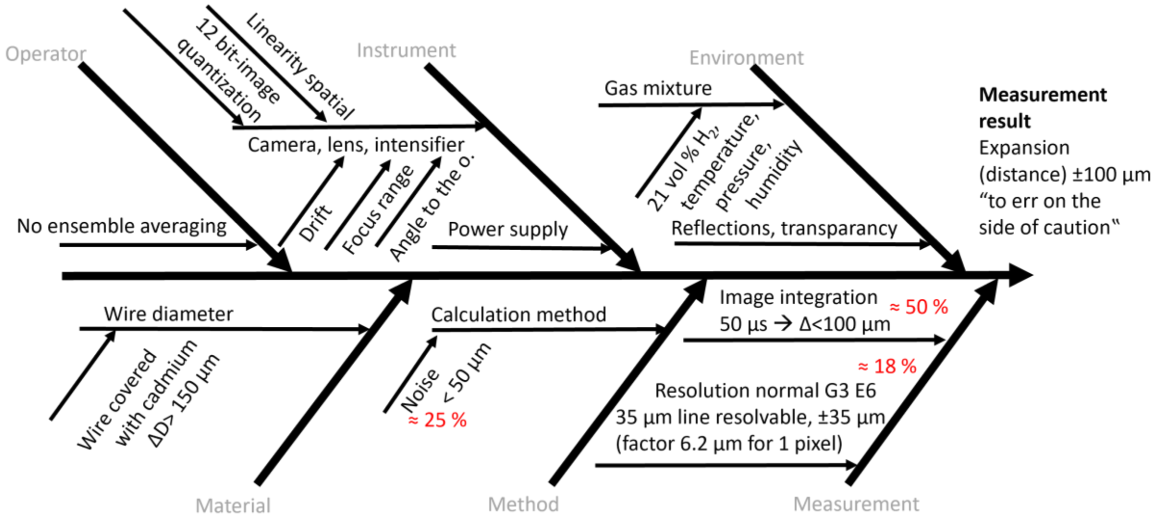

Fig. 8. *Evaluation of the factors contributing to the measurement uncertainty*

The possible factors contributing to the measurement uncertainty during the investigation of the expansion of the hot gas kernel are shown in Fig. 8. The relevant contributing factors include deviations during the schlieren edge evaluation caused by the noisy signal, changes due to the images being integrated while they are being captured and the optical resolution measured with the resolution normal. Here, it should be noted that, because it is not possible to precisely align the block with the parallel light beam, part of the gas kernel may be concealed; this will mean the gas kernel cannot always be evaluated. For the initial measurements performed here, the measurement uncertainty of the expansion is estimated to be ±100 µm in order to err on the side of caution. Despite this, there is still a temporal correlation between the expansion of the gas kernel and the electrical curve.

5. Discussion

During the critical phase, the expansion of the gas kernel caused by contact break discharges is observed and the corresponding electrical curve is recorded by means of the test setup presented here; these elements are shown in the paper. For an ignition caused by a discharge, the expansion of the hot gas kernel during the discharge can be seen in the schlieren images. It has a semicircular shape corresponding to examples known from the literature that feature a small electrode and a spherical expansion. An increasing expansion of the hot gas kernel up to the flame front can be seen and measured.

The volume of the hot gas kernel increases with increasing power, corresponding to the model in (Uber et al. 2022). This volume in the critical limit range of an ignition/no ignition at a radius of approx. ca. 500 µm is larger than the known minimum ignition volume of 0.1 mm (Steen 2000); this is attributed to the larger cooling electrodes. The minimum duration, significant voltage and minimum power of the critical phase has been estimated for the reference situation using the examples from these measurements; this corresponds to an optimal energy transfer at an optimal electrode distance (Wähner et al. 2013). In contrast to a spark discharge with a very short duration and minimum ignition energy, this concerns a minimum energy transfer for a period of time during which losses due to the cooling electrodes must be compensated.

6. Conclusion

Using a test setup for schlieren measurements, successful observations of the development of a hot gas kernel caused by a contact discharge in the micrometer range were carried out. Initial findings were obtained concerning the duration of the energy transfer in the critical phase.

The specific relationship between the energy transferred (power consumed) and the increasing volume of the hot gas kernel is yet to be investigated. For the required statistical accuracy, the minimum duration and power must be improved by means of additional measurements. To err on the side of caution, these measurements should be validated by means of parameter variations such as those of the electricity or the contact break times. The distinctive voltage curves for ignitions that correspond to the discharge length must be analyzed in greater detail (cf. Zborovsky and Cotugno 1974). The additional measurements required will allow a better understanding of the relationships inherent in an ignition caused by a contact discharge.

The current setup, in which a plane of the cadmium block is aligned parallel to the light beam, was shown to be suboptimal. A slightly rounded surface should potentially reduce the concealed area of the gas kernel.

Acknowledgements

The authors thank Rilana Rohde, Lia Benedix, Robin Abraham, Thomas Uehlken for their experimental work and Markus Höhnen (Fa. Additive) support to the calculation method. We also thank Detlev Markus for his expertise. Financial support by the Deutsche Forschungsgemeinschaft (DFG), Germany Grant number GE3146/1-1 is gratefully acknowledged.

References

Babrauskas, V. (2003), Ignition handbook. Fire Science Publishers, Issaquah (WA, USA).

Bane, S. (2010). Spark Ignition: Experimental and Numerical Investigation with Application to Aviation Safety, PhD thesis, California Institute of Technology, Pasadena, California.

Essmann, S., Markus, D. and Maas (2015), Investigation of the pressure wave and hot gas kernel induced by low energy electrical discharges. 25th International Colloquium on the Dynamics of Explosions and Reactive Systems, Leeds, Paper 167.

Essmann, S.; Markus, D. und Maas, U. (2016). Investigation of the spark channel of electrical discharges near the minimum ignition energy. Plasma Physics and Technology 3, pp. 116–121.

Essmann, S. (2019). Experimentelle Untersuchung der Zündung durch elektrostatische Entladungen geringer Energie, Dissertation, Karlsruher Institut für Technologie (KIT), doi: 10.7795/110.20190709.

Holm, R. (1967), Electric Contacts. Theory and applications. Springer-Verlag, Berlin, Heidelberg, 1967, DOI: 10.1007/978-3-662-06688-1.

IEC 60079-0:2017 (2017). Explosive atmospheres - Part 0: Equipment - General requirements.

IEC 60079-11:2011 Corr 2012, (2012). Explosive Atmospheres Part 11: Equipment Protection by Intrinsic Safety “i”. Lewis, D. R. and von Elbe, G. (1951). Combustion, Flames and Explosion of Gases. Academic Press, New York.

Lintin, D. R. and Wooding, E.R. (1959). Investigation of the ignition of a gas by an electric spark. British Journal of Applied Physics, Vol. 10, April 1959.

Merzkirch, W. (2007). Density-based techniques Handbook of Experimental Fluid Mechanics. Hrsg. Von Tropea, C., Yarin, A.L. und Foss, J.F., eds., Springer, Berlin.

Schardin, H. (1942). Die Schlierenverfahren und ihre Anwendungen. Ergebnisse der exakten Naturwissenschaften. Trendelenburg, F., Hund, F., eds., Springer, Berlin pp. 303 – 439.

Settles, G.S. (2001). Schlieren and shadowgraph techniques: visualizing phenomena in transparent media, Springer, Berlin.

Slade, P. G. (2014), Electrical contacts. Principles and applications. CRC Press, Boca Raton (FL, USA).

Steen, H. (2000), Handbuch des Explosionsschutzes. Wiley-VCH, Weinheim.

Thedens, M. (2002). Funkenzündung von Gasgemischen bei erhöhten Drücken und Temperaturen für die Zündschutzart Eigensicherheit, Dissertation TU Carolo-Wilhelmina zu Braunschweig.

Uber, C.; Shekhar, R.; Gerlach, U. (2016). Ansatz zur Modellierung von Zündfunken durchelektrische Kontaktvorgänge für die Zündschutzart Eigensicherheit. 14.BAM-PTB-Kolloquium zur chemischen und physikalischen Sicherheitstechnik, pp.76–83.

Uber, C. (2019). Charakterisierung elektrischer Kontakt-Entladungen im Bereich niedriger Spannungen im Zündgrenz-Bereich von Wasserstoff-Luft-Gemisch, Dissertation TU Ilmenau.

Uber, C.; Franke, S.; Barbu, B., Hilbert, M.; Berger, F.; Uhrlandt, D.; Lienesch, F. (2022), Correlation between the electrical power of a slow contact break discharge and the ignition of an H_2/air mixture, Journal of Loss Prevention in the Process Industries, Volume 74, doi.org/10.1016/j.jlp.2021.104620

Wähner, A., Gramse, G., Langer, T., Beyer, M. (2013): Determination of the minimum ignition energy on the basis of a statistical approach. Journal of Loss Prevention in the Process Industries, Vol. 26, P.1655–1660, doi.org/10.1016/j.jlp.2013.06.002

Zborovszky, Z. (1969). Ignition criteria and flame kernel development between breakflash electrodes in explosive gas mixtures, PhD. University of Surrey, Guildford.

Zborovsky, Z. and Cotugno, L. (1974). Evaluation of the cadmium disk breakflash in testing electrical circuits, University of Denver, Bureau of Mines Washington D.C. Open File Report 68-76.

Xu, D.A.; Shneider, M.N.; Lacoste, D.A. and Laux, C. O. ((2014). Thermal and hydrodynamic effects of nanosecond discharges in atmospheric pressure air, Journal of Physics D: Applied Physics 47, 235202. doi:10.1088/0022-3727/47/23/235202

DOI: 10.7795/810.20221124

Investigating the influence of additional inductivity in electrical circuits during ignition caused by contact break discharges

Bogdan Barbu[a], Carsten Uber[b] & Frank Berger[a]
[a] Technische Universität Ilmenau, Ilmenau, Germany
[b] Physikalisch-Technische Bundesanstalt, Braunschweig, Germany
E-mail: *bogdan.barbu@tu-ilmenau.de*

Abstract

Real electrical networks will always possess a certain inductance (L) and capacitance (C) generated either by the electrical system itself or by additional L/C components that are built in the electrical network. During a switching procedure, which might consist even in the disconnection of a plug-in connector, electrical discharges will be generated between the contact pieces. These discharges may lead to an explosion within an explosive atmosphere. Currently, the consent-based curves presented in standard IEC 60079-11 (2011) are being used for the evaluation of ignition processes. These ignition curves describe the maximum voltage and current allowed in the electrical circuit for defined inductance and capacitance values so that when a discharge is created no ignition occurs and the explosion is prevented . However, a correlation between the electrical parameters and their influence on the discharge development and its ignition has not been researched in detail up to the present time.

In this article, we will analyze the effects produced by a change in the electrical network inductance upon the discharge stability and its power distribution over time. Starting with a reference configuration, where no additional inductance and capacitance are considered, the circuit parameters (L and C) are modified and their correlation with the thermochemical ignition process is investigated and presented. The results obtained from our study show a significant change in the temporal distribution of discharge energy in relation to the electric network parameters.

Keywords: *Contact break discharges, Electrical circuit parameters, Inductance*

1 Introduction

Ignition limits for contact discharges within simple electrical circuits with variable circuit elements, i.e. variable resistor, inductor or capacitor, are given in the IEC 60079-11 (2011) standard and in PTB report ThEx-10 from Johannsmeyer and Krämer (1999). These characteristics are based on measurements with the so called spark test apparatus (STA). However, the results obtained in this manner are scattered (see Proficiency Testing Report from Physikalisch-Technische Bundesanstalt (2012)) and for this reason consensus-based ignition curves with safety factors are published in the standard. These ignition curves refer to exact values set for the circuit inductance (L) and capacitance (C), do not allow the use of intermediate values and, if intermediate values should occur, then, for the electrical circuit evaluation the next higher value will be considered. The ignition curves, presented in Fig. 1, refer to a probability of ignition of 10^{-3} and consider a safety factor $SF = 1.5$, as defined in the standard. The ignition curves are plotted for different inductance values varying from 0 mH, i.e no inductance, up to 5 mH. It can be observed that contact discharges produced in electrical circuits without an additional inductor present higher electrical limits of the ignition curves (Johannsmeyer and Krämer (1999), Magison (1978)). Nonetheless, it must be considered that real electrical circuits will always possess a certain parasitic inductance and capacitance that has to be taken into consideration. Additionally, the electrical circuit parameters might vary over time due to changes in the wiring, in the measurement equipment or in the electrical devices that are connected in the circuit, as described in Babrauskas (2003, p. 547). As the inductor value increases, the electrical values required for ignition will decrease and discharges can occur with as low as 2 V and 100 mA considering

DOI: 10.7795/810.20221124

an additional inductor of 5 mH coupled in the circuit. For the nominal current and voltage used in the presented experiments, i.e. 60 mA and 30 V, it can observed that discharges with ignition can be generated starting from 10 V at 60 mA or starting from 18 mA at 30 V for an additional inductor of 5 mH .

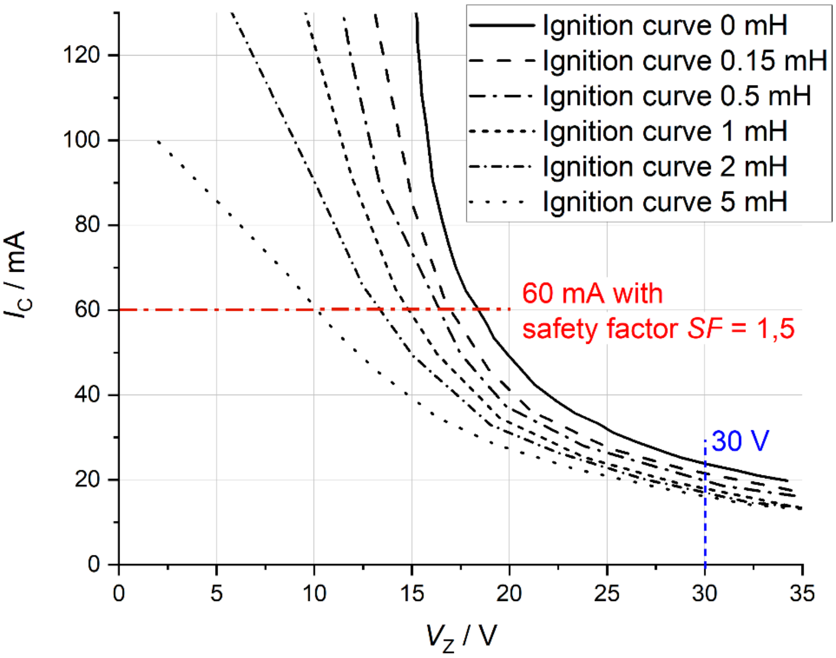

***Fig. 1**: Ignition limits for inductance values between* 0 mH *and* 5 mH *considering an electrical source with rectangular current characteristic and a safety factor of* 1.5

In scientific publications, the contact opening discharges are intensively researched in connection with the electrical contacts research for different classes of switchgear. The discharge behavior associated with the presence of inductors in the electrical circuit, the induced voltage peaks generated at the discharge quenching time point or the discharge stability is studied in this research field in detail. It is established that any current variation will cause an increase in the induced voltage meant to counteract the current change and stabilize the discharge (Borchert (1957), Holm (1967), Slade (2014), Vinaricky (2016)). Suhara (1991) published a simulation method for contact opening discharges in inductive circuits considering the minimum current for a discharge, showing in detail the effects of inductance on the discharge. The parameters are in a comparable range with our experiments (e.g. 24 V, 0.2 A, 10 mH), but only one discharge without ignition is treated. The publications from this research field provide a solid base for understanding the circuit parameters influence on different types of discharges, mainly thermal electric arcs, but the experimental research is done under different conditions and usually neglects several physical effects, e.g. power distribution for specific time intervals, that are important in the field of explosion protection.

In a publication analyzing ignitions by contact opening discharges in a methane-propane explosive atmosphere, Litchfield et al. (1967) concluded that an important quantity for this type of discharges is the minimum ignition current (MIC). This differs from electrostatic spark ignitions, generated between fixed electrodes, where the quantity that has to be accounted for is the minimum ignition energy (MIE). It was shown that circuits with larger inductance require a lower MIC for ignition. This behavior was justified by the additional energy stored in the inductance (Magison, 1978, p. 345). Vogt (1980) investigated ignitions in methane with different inductance values and developed a comparison method between the MIC and the energy stored in the inductance. This method was further used in order to estimate the MIC for a gas mixture.

A detailed investigation regarding the factors influencing the power transfer to the discharge, including the electric circuit parameters, was done by Zborovszky and Cotugno (1974). Unfortunately, in this study the author focused, in a first step, only on purely resistive circuits. The effect of additional lumped circuit elements, forming either an RC, RLC or RL circuit, was only theoretically analyzed based on the differential circuit equations (see (Zborovszky and Cotugno, 1974, p. 140)). For an RC circuit the conclusions were that an additional capacitor could make the power transferred to the discharge temporarily higher, thus increasing the danger of ignition. For an RL circuit, the author concluded that the power transfer from the inductor to the discharge is strongly influenced by the ratio between the value of the circuit resistance and the discharge resistance. Another important fact that must be accounted for is that the inductor will release its energy only when the discharge requires and this will be done in a gradually manner.

In the PTB-W-16 report by Johannsmeyer (1979), the contact discharge behavior inside an electrical circuit powered by a constant voltage source with an electronic current limiting circuit is investigated for different inductor and capacitor values. The calculations are based on the PTB-W-11 report of Schebsdat (1978) , where the maximum current and power as well as their arithmetic mean values are computed. For the evaluation of an ignition, in case of a capacitive circuit the maximum values where considered to be important while, for an inductive circuit, the mean values where decisive. The arithmetic mean value of the current was used as a substitute current in order to transfer the ignition curves to inductive circuits and could also be used for voltage sources with current limiting devices.

From the above technical and scientific publications it can be concluded that the power transfer from the electrical circuit into the discharge will affect the discharge development and its ignition. Therefore, a detailed investigation of the correlation between the circuit parameters and the discharge development is important for a better understanding of the underlying physical effects governing the discharge as well as of the normative ignition curves. Besides that, these investigations shall lead to a mathematical model able to predict the ignition by a contact break discharge.

2 Experimental setup

The experimental setup is schematically presented in Fig. 2 and contains a constant current source, the electrical circuit and the experimental contact device (ECD) enclosed in the explosion chamber (EC). The structure of this experimental circuit is typical for electrical circuits used in the field of explosion protection as described in IEC60079-25 (2010). The constant current source includes a voltage source and an electronic current limiting circuit. This combination ensures that at the output of the constant current source, point 1 in Fig. 2, only current values up to a user pre-set value are delivered for the chosen source voltage. The electrical circuit, connecting the constant current source and the ECD, is represented by two groups of electrical elements: one representing the parasitic circuit elements (L_{par}, C_{par}) and the second representing the variable circuit elements (L_{var}, C_{var}). The resulting circuit inductance and capacitance will be: $L = L_{par} + L_{var}$ and $C = C_{par} + C_{var}$. For our experimental circuit, the parasitic elements measurement showed that the values for both parameters were small enough to be neglected in the present study. Based on this fact, from this point forward, the total circuit inductance and capacitance will be defined and referred as: $L = L_{var}$ and $C = C_{var}$.

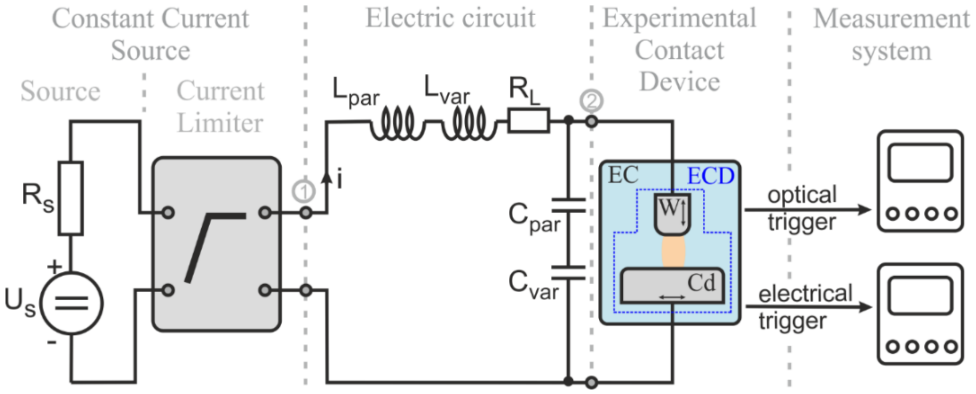

Fig. 2: Experimental circuit with lumped electrical elements

The ECD represents a modified version of the spark test apparatus, defined in IEC 60079-11 (2011), containing several modifications meant to improve the research on contact break discharges. A detailed description of the ECD can be found in Uber (2019).

The measurements where performed by using two oscilloscopes that recorded the discharge current and voltage. One oscilloscope was triggered by optical signals and recorded only signals from the discharge that produced an ignition. The second oscilloscope was triggered by electrical signals and kept a history of maximum 120 no-ignition discharges prior to the ignition discharge in order to analyze and compare their characteristics.

The main purpose of our research was to investigate how the circuit parameters influence the discharge development and its ignition. For this reason, during the entire measurement campaign, the constant current source parameters as well as the ECD parameters were kept constant. All experiments were conducted at a nominal voltage $U_s = 30\,\mathrm{V}$ and a nominal current $i = 60\,\mathrm{mA}$.

For the electrical circuit parameters, the following variations were performed: $L = 0\,\mathrm{mH}$, 0.15 mH, 0.5 mH, 1 mH, 2 mH, 5 mH and 10 mH and $C = 10\,\mathrm{pF}$. Due to the negative impact of the capacitor on the discharge development, the main focus of or investigations was set on the inductor influence on the discharge.

3 Results and discussion

From the physical point of view, an inductor is a two terminal passive network element that stores energy in its magnetic field when a current pass through it and use it in order to quickly counteract any current variation by developing a counter voltage across its terminals. The amount of energy stored in the inductor and the resulting voltage variation are computed by eq. (1) and (2). Based on eq. (1) it can be estimated that the amount fo energy stored in the inductor for the above mentioned values lies between 0.27 µJ, for L =0.15 mH, and 18 µJ, for L =10 mH.

$$E_L = \frac{1}{2} L \cdot i^2 \tag{1}$$

$$u_L = -L \cdot \frac{di}{dt} \tag{2}$$

The influence of an additional inductor is exemplary shown in Fig.3, where typical current and voltage characteristics from experiments with $L = 0\,\mathrm{mH}$ and $L = 10\,\mathrm{mH}$ are presented. All characteristics are synchronized at the discharge quenching time point, i.e. the time point where the current crosses the 0 A value for the last time. Fig. 3a presents an overview of the discharge behavior from ignition to its quenching, while Fig. 3b displays a zoomed image of a 300 µs interval at the discharge quenching.

In the following, the presented current and voltage characteristics will be analyzed in detail in order to obtain a better understanding of how the inductance influences the discharge development over time. For comparison purpose the discharge development will be separated in 4 phases and for each phase the measured characteristics for $L = 0\,\mathrm{mH}$ and $L = 10\,\mathrm{mH}$ will be discussed against each other. It must be mentioned that, the following analysis should be regarded as a phenomenological description and all presented values reference only the diagrams presented as example in Fig. 3.

The first phase, P1 in Fig.3, is represented by the discharge formation, i.e. the time point when the electrode separation begins. In Fig. 3 this phase takes place at approximately $-2.8\,\mathrm{ms}$ for both inductance values. The voltage characteristics are similar and present a sudden increase up to approx. 10 V corresponding to the anode and cathode voltage drop. In contrast, on the current characteristics we can notice a strong decrease down to 26 mA for $L = 0\,\mathrm{mH}$, and a small decrease down to 55 mA for $L = 10\,\mathrm{mH}$.

In the second phase (P2), the discharge continues its development at electrode gaps up to several tens of micro-meters. At this stage the discharge column is very small and the discharge voltage drop is mainly given by the anode-cathode voltage drop. Therefore, in this phase we can observe a relatively constant discharge voltage in the range 10 V to 12 V. For the $L = 0\,\mathrm{mH}$ graph, a very short

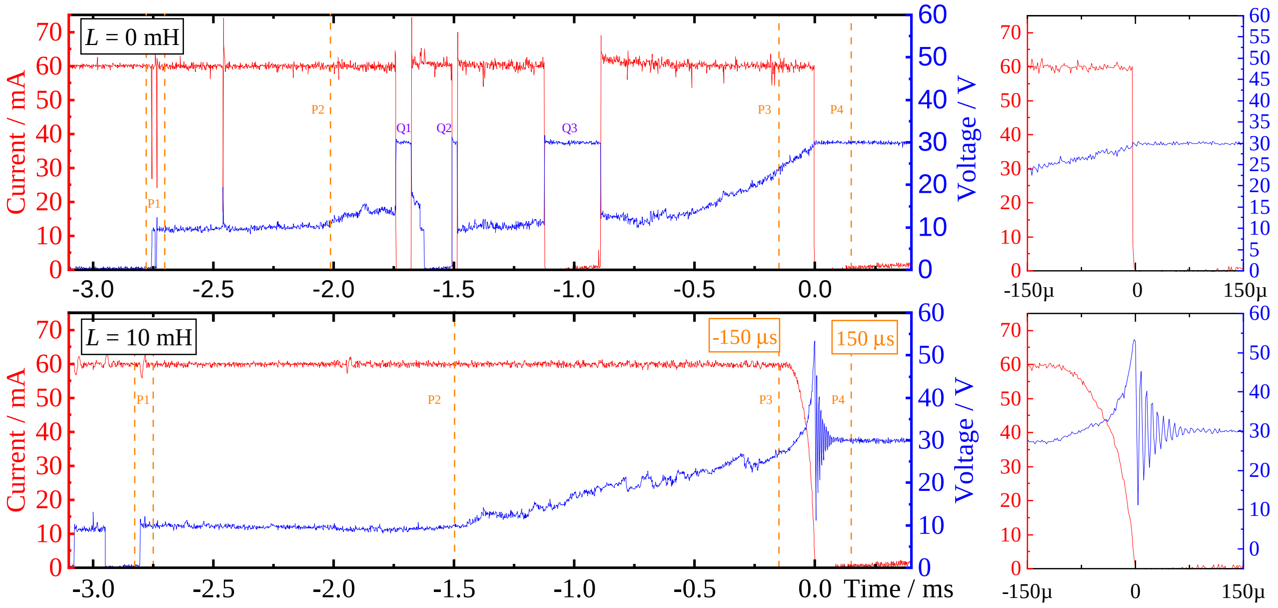

(a) *(b)*

***Fig. 3**: a) Typical current and voltage characteristics for discharges with L = 0 mH and L = 10 mH; b) zoomed current and voltage characteristics for the region of discharge quenching*

voltage spike at -2.45 ms with a corresponding current decrease down to 17 mA can be observed. For $L = 0$ mH this phase takes place up to approximately -2 ms while for the $L = 10$ mH up to -1.5 ms.

As the electrode gap increases the discharge column develops and expands between the electrodes. This third phase (P3), representing the discharge elongation, can be observed from -2 ms, for $L = 0$ mH, and from -1.5 ms , for the $L = 10$ mH, onward. Unlike in the first two phases, when the main energy losses where represented only by conduction in the electrode bulk, in the third phase, changes in the surrounding conditions (e.g. gas flow, electrode surface) will affect to a higher degree the discharge energy balance. These additional losses, if not compensated, will destabilize or even quench the discharge. Such a behavior can be observed on the current and voltage characteristics for $L = 0$ mH starting from -1.73 ms up to -0.9 ms. In this time interval we notice how the initial discharge is quenched, for $\approx$70 µs, then reignited, quenched again for $\approx$15 µs, reignited and quenched again for $\approx$220 µs. For a better understanding the quenching points have been marked with Q1, Q2 and Q3 in Fig. 3a. After -0.9 ms , for $L = 0$ mH, a new discharge is formed and develops between the electrodes. In comparison, this behavior is not present at all for the $L = 10$ mH case.

The last phase (P4), detailed in Fig. 3b, represents the discharge quenching. In this phase the discharge voltage approaches the source nominal voltage and limits the current flow through the circuit. For $L = 0$ mH it can be observed that as soon as the discharge voltage reaches 30 V, the current drops from its nominal value of 60 mA to 0 A within 5 µs. For $L = 10$ mH the current drop presents an exponential decrease that starts when the discharge voltage reaches $\approx$28 V. For the presented case, the current drop from 60 mA to 0 A takes $\approx$120 µs. In this time interval, the discharge voltage crosses the source nominal voltage at -80 µs and the increases exponentially up to 53 V at 0 s.

From the detailed analysis of the measured current and voltage characteristics for $L = 0$ mH and $L = 10$ mH it can be concluded that, during the different phases of the discharge development, the additional inductance will stabilize any current variations caused by sudden changes in the discharge voltage. Compared to a power source, the energy stored in the inductor magnetic field can be released into the circuit much faster and, most important, in controlled amounts depending on the discharge requirements. In this manner, very strong current variations can be quickly attenuated. As a result, it can be stated that an increased circuit inductance leads to longer discharges able to accumulate more energy over time. This fact is presented in Fig. 4, where the discharge net input power for several

DOI: 10.7795/810.20221124

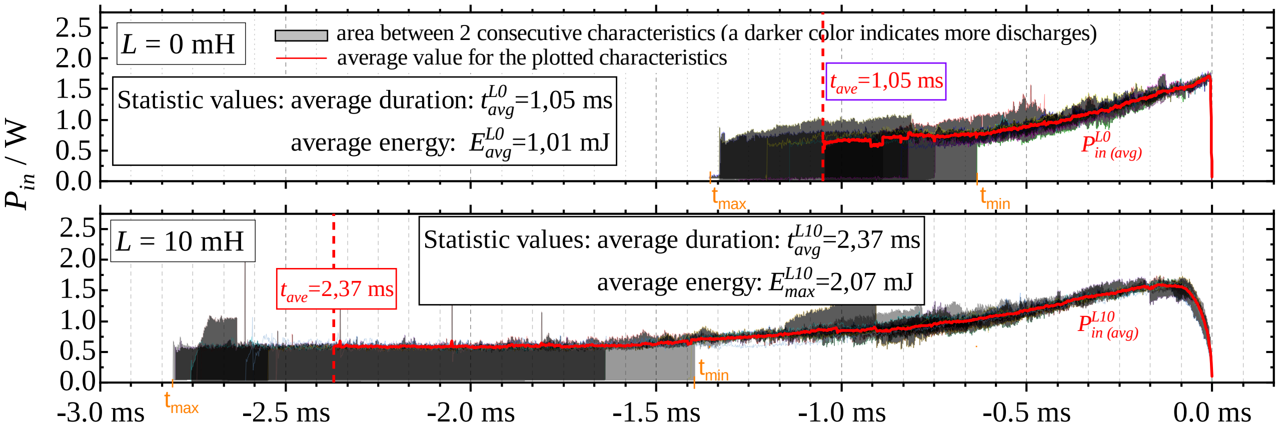

***Fig. 4**: Discharge power input for electrical circuits without and with an additional inductor*

ignition discharges is compared for $L = 0\,\text{mH}$ and $L = 10\,\text{mH}$. The statistical analysis shows that the average duration for discharges with $L = 0\,\text{mH}$ is 1.05 ms while for $L = 10\,\text{mH}$ reaches 2.37 ms. The average energy is 1.01 mJ for $L = 0\,\text{mH}$ and doubles to 2.07 mJ for $L = 10\,\text{mH}$.

Nonetheless, for a correct evaluation of the discharge ignition in an explosive atmosphere, the energy content computed for the entire discharge duration should not be regarded as the only factor. This statement is based on two conclusions drawn during our research and presented in Uber et al. (2022). The first one states that for break discharges, as the ones presented in this study, a certain power density for a specific time period is required to cause ignitions. Considering that in this study, based on the measured electrical signals, we analyze only the variation of the input energy, it is difficult to make assumptions on the power density in the discharge volume. For such an analysis further research is required. The second conclusion is that for a certain time period after its formation, the discharge quenching is very strong and most of its energy is not used to heat the surrounding gas in order to produce an ignition. According to the estimations, published in Uber et al. (2022) for an example discharge, the electrode gap up to which this happens is 100 µm and this corresponds to a discharge voltage of approx. 22 V. For this reason, in the following, we will analyze in detail the discharge characteristics in the range 20 V up to the discharge quenching when the current zero occurs.

Based on these conclusions, the following chapters will focus on three main aspects, namely: the effect of the voltage peak generated at the discharge extinction, the energy content for the interval starting from 30 V up to current zero and the energy content for the interval 20 V to 30 V.

3.1 Comparison of the measured voltage peak with the normative voltage values

The ignition curves shown in Fig. 1 are based on the standard IEC60079-25 (2010) or the PTB report W-16 by Johannsmeyer (1979) and are used for an evaluation of the ignition probability according to the state of the art. In these curves a safety factor $SF = 1.5$ is considered. For scientific research and a correct comparison with the presented investigations, the ignition curves without safety factor, i.e. $SF = 1$, were calculated maintaining the ignition probability of 10^{-3}. These theoretical ignition curves are presented in Fig. 5a for several inductor values. For the nominal current of 60 mA, the ignition curves indicate that the minimal discharge voltage required for ignition is 22 V for $L = 0\,\text{mH}$ and 15 V for $L = 5\,\text{mH}$. One hypothesis developed from analyzing these characteristics was that the voltage difference between the ignition curves could be attributed to the voltage peak generated at the discharge quenching. In order to evaluate this hypothesis, in Fig. 5b are compared for different inductor values the voltage difference between the ignition curves, taking as reference the $L = 0\,\text{mH}$ curve, with the voltage difference between the voltage peak and the nominal voltage, i.e. 30 V, obtained in our experiments. It can be concluded that the two datasets present only a qualitative behavior, because in all cases the voltage difference increases with the inductor value, but no quantitative behavior.

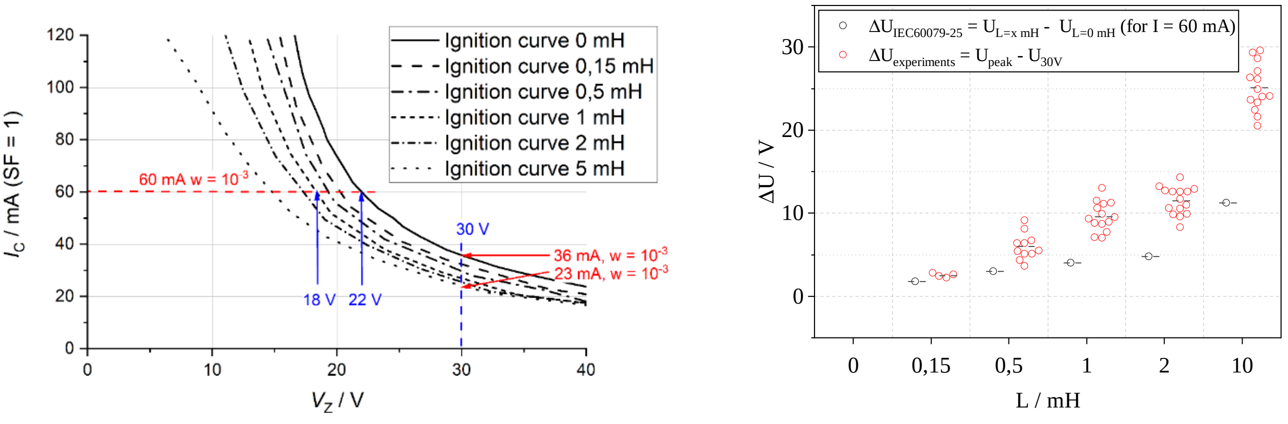

(a) *(b)*

***Fig. 5**: a) Ignition curves for selected inductances with a probability of* 10^{-3} *and a safety factor SF = 1 (cf. IEC 60079-25 (2010)); b). Comparison of the voltage difference for the IEC ignition curves and the voltage difference obtained from the experiments*

3.2 Energy input for the voltage interval above 30 V

As shown in Fig. 3, one difference between the current and voltage behavior for discharges without and with an additional inductor is represented by the time interval in which the current drops to zero after the voltage reached the source nominal voltage of 30 V. For the voltage characteristic presented in Fig. 3 for $L = 10\,\text{mH}$ this happens at $\approx -80\,\mu\text{s}$. The energy delivered from this time point until the discharge quenching into the discharge can only come from the energy stored in the inductor magnetic field. When compared with the $L = 0\,\text{mH}$ case, this additional energy could be another cause for the lower electrical values required for the discharge ignition in circuits with additional inductance. In our experiments this additional energy varies between 60 µJ and 94 µJ for $L = 10\,\text{mH}$.

3.3 Energy input for the voltage interval 20 V – 30 V

Unlike the previous cases, for the voltage interval starting from 20 V and up to 30 V there are two sources responsible for the energy input into the discharge. One is the circuit source and the second is the energy stored in the inductor magnetic field. By comparing the discharge development and its power distribution over this time interval we can better asses the influence of the additional inductor.

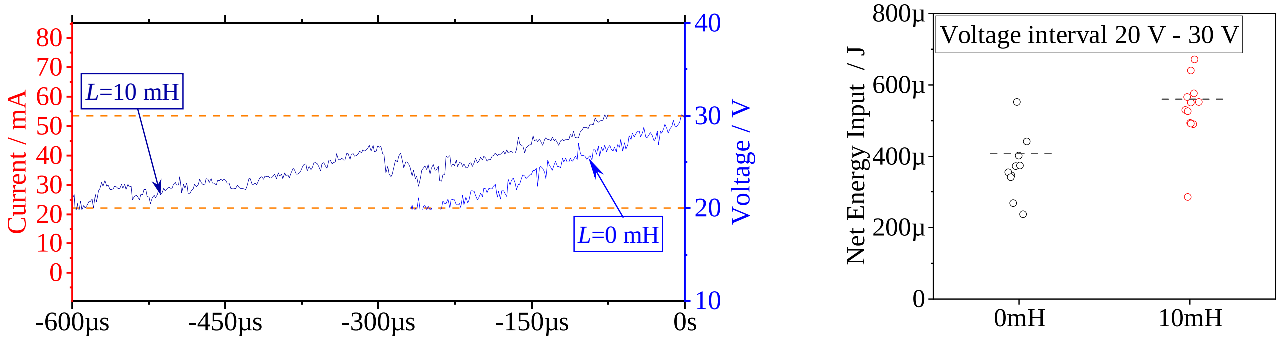

(a) *(b)*

***Fig. 6**: a) Discharge voltage development in the in the interval* 20 V – 30 V *; b) computed net energy input for the discharges at* $L = 0\,\text{mH}$ *and* $L = 10\,\text{mH}$

In Fig. 6a is plotted the discharge voltage development corresponding to the characteristics presented in Fig. 3 for the voltage interval 20 V – 30 V. For a better view, and because the current values are

DOI: 10.7795/810.20221124

similar for the mentioned interval, the current characteristics are not presented. It can be observed that for $L = 10\,\text{mH}$ the discharge voltage rises over the 20 V limit much earlier and increases up to 30 V over ≈550 µs. In contrast, for $L = 0\,\text{mH}$ the voltage increase is much stepper, reaching the 30 V limit in ≈270 µs. The net energy input computed for this voltage interval for several ignition discharges is presented in Fig. 6b. It can be observed that in almost all experiments conducted with $L = 10\,\text{mH}$ the discharge energy is higher than for $L = 0\,\text{mH}$. On average between the two datasets there is a difference of 200 µJ.

4 Energy input for discharges with ignition and without ignition

Beside the energy input for the ignition discharges, presented up to this point, we have computed also the net energy input for discharges without ignition and compared it with the net energy of the discharge with ignition. As mentioned in section 2 , the no-ignition discharges were recorded by using an electrical trigger based on the discharge voltage. During all experiments the trigger condition was that the voltage is between 13.7 V and 24.7 V for at least 0.4 ms. Based on this condition, only temporally long discharges were recorded and used for the analysis. All other discharges were neglected. The results are presented in Fig. 7. It can be observed that in all experiments the net energy of the ignition discharge is not significantly higher than the net energy of the discharges without ignition. This comparison shows that for this type of discharges other factors, like the gas chemical composition, gas flow or the electrode surface, play an important role in the discharge ignition.

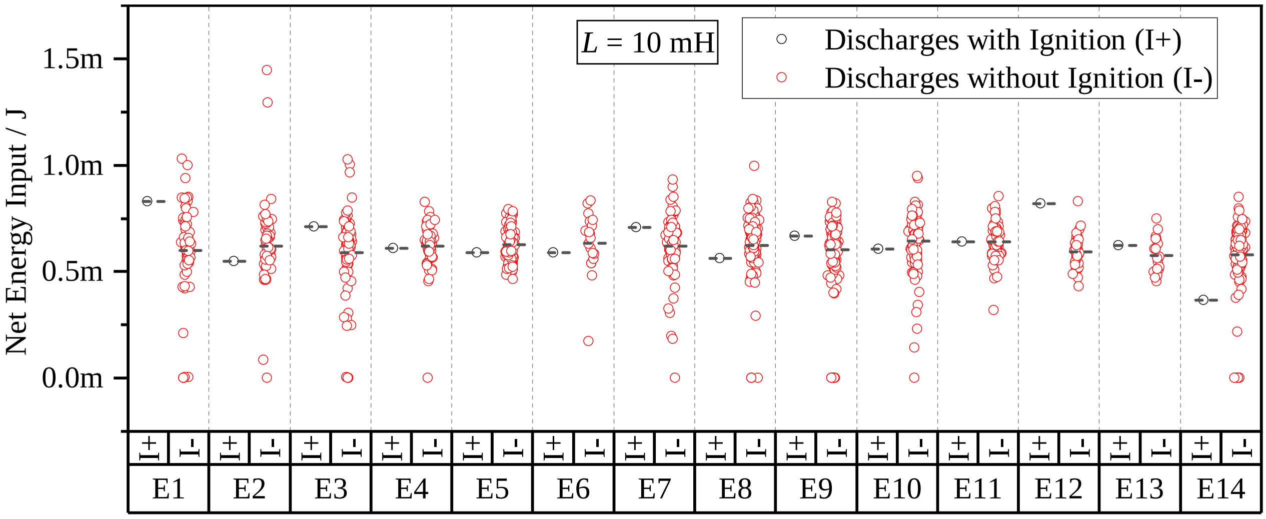

Fig. 7: Comparison of the net energy for discharges with ignition (black) and without ignition (red)

5 Conclusions

By using an experimental circuit typical for electrical circuits used in the field of explosion protection the present study performed a detailed analysis of how the circuit inductance variation influences the discharge energy input and its development. The study analyzed the entire discharge input energy distribution as well as specific regions considered important for the ignition process. The main conclusion of this study are:

1. A higher inductance in the electrical circuit will create temporally longer and stable discharges that will receive more energy.
2. For the ignition relevant voltage range, i.e. above approx. 20 V, the following statements can be made:
    - In the voltage range 20 V to 30 V, our analysis showed that the discharge energy input will be increased by increasing the inductor value. For $L = 10\,\text{mH}$, the energy increase was estimated to be ≈ 200 µJ ;

  - For the voltage range above 30 V up to current zero, our analysis showed that the discharge energy input will be increased by increasing the inductor value. For $L = 10\,\mathrm{mH}$, the energy increase was estimated to be $\approx 94\,\mu\mathrm{J}$;
  - The voltage peak generated at the discharge quenching has only a qualitative but no quantitative correlation with the voltage difference between the IEC60079-25 (2010) ignition curves for different inductance values.

3. The comparison of the discharges with and without ignition revealed that the discharge energy for discharges without ignition is not always smaller than that of discharges with ignition; this proves that other factors (e.g. gas flow, surface conditions) play an important role in the discharge ignition.

A very important remark that must be made is that the input energy alone can not be used for the estimation of the ignition process. For break discharges, as the ones presented here, the most important factor for the ignition process is represented by the power density for a specific time period. Currently, investigations using schlieren imaging are undergoing (Uber 2022b) in order to draw conclusions on the criteria that may lead to ignition or not.

Acknowledgements

The authors thank Rilana Rohde, Niklas Schüler and Thomas Uehlken for their experimental work and Alexandru Balan for data evaluation software development. Special thanks are due to Dr. Michael Hilbert for the critical remarks and helpful discussions during the development of this publication. The authors gratefully acknowledge the financial support of the Deutsche Forschungsgemainschaft (DFG), Grant Number 411446115.

References

Babrauskas, V. (2003). *Ignition handbook*. Fire Science Publishers, Issaquah (WA, USA). ISBN 978-0-9728111-3-2.

Borchert, L. (1957). *Ursachen der zerstörung von schwach belasteten kontakten der nachrichtentechnik und kontaktschutz durch eine funkenlöschung*. ETZ-A, Bd. 78(Nr. 19):702–712.

Holm, R. (1967). *Electric Contacts: Theory and applications*. Springer-Verlag, Berlin, Heidelberg. ISBN 978-3-642-05708-3. doi:10.1007/978-3-662-06688-1.

IEC 60079-11 (2011). *IEC 60079-11 explosive atmospheres - part 11: Equipment protection by intrinsic safety "i"*.

IEC60079-25 (2010). *IEC 60079-25 explosive atmospheres - part 25: Intrinsically safe electrical systems*.

Johannsmeyer, U. (1979). *Zündverhalten von Netzwerken eigensicherer Stromkreise mit elektronischen Strombegrenzungseinrichtungen: PTB-W-16*. Braunschweig. ISBN 0341-6739.

Johannsmeyer, U., Krämer, M. (1999). *Zusammenschaltung nichtlinearer und linearer eigensicherer stromkreise*. PTB-Bericht PTB-ThEx-10.

Litchfield, E., Hay, M. H., Kubala. T. A., Monroe, J. S. (1967). *Cover art minimum ignition energy and quenching distance in gaseous mixtures: Techniques and apparatus*.

Magison, E. C. (1978). *Electrical instruments in hazardous locations*. Instrument Society of America, Pittsburgh, 3d ed., rev. and enl edition. ISBN 9780876643761.

Physikalisch-Technische Bundesanstalt (2012). *Final report for test round d/i of the ptb ex proficiency testing program (pilot phase). summary analysis of the results and graphical dispalys*.

Schebsdat, F. (1978). *Zündverhalten von Netzwerken eigensicherer Stromkreise mit konzentriert auftretender Kapazität und Induktivität bei Gleichstrom*. Braunschweig.

Slade, P. G. (2014). *Electrical contacts: Principles and applications*. CRC Press, Boca Raton (FL, USA), 2. ed. edition. ISBN 978-1439881309.

Suhara, K. (1991). *Break arcs in inductive circuits and the minimum arc current*. IEEE Transactions on Components, Hybrids, and Manufacturing Technology, 14(1):118–123. ISSN 01486411. doi:

10.1109/33.76520.

Uber, C. (2019). *Charakterisierung elektrischer Kontakt-Entladungen im Bereich niedriger Spannungen im Zündgrenz-Bereich von Wasserstoff-Luft-Gemisch*. Doctoral thesis.

Uber, C., Schüler, N., Franke, S., Hilbert, M., Uhrland, D. (2022). *Schlieren imaging investigations of hot gas kernel expansion caused by slow contact break discharges*. In *International Symposium on Hazards, Prevention and Mitigation of Industrial Explosion*. Braunschweig.

Vinaricky, E. (2016). *Elektrische Kontakte, Werkstoffe und Anwendungen: Grundlagen, Technologien, Prüfverfahren*. Springer Vieweg, Berlin, 3. edition. ISBN 978-3-642-45426-4.

Vogt, G. (1980). *Untersuchungen der Zündung von explosionsfähigen Methan/Luft-Gemischen durch elektrische Entladungen in induktiven Stromkreisen von eigensicheren Betriebsmitteln für den Steinkohlebergbau: Doctoral Thesis, TH Aachen*. Mitteilungen der Westfälischen Berggewerkschaftskasse.

Zborovszky, Z., Cotugno, L. A. (1974). *Evaluation of the cadmium disc breakflash in testing electrical circuits: A comprehensive study of intrinsic safety criteria, denver research institute - university of denver*. Bureau of Mines Open File Report 68-76.

DOI: 10.7795/810.20221124

Investigation of safety related ignition processes of laminar strained premixed NH_3-H_2-air flames

Chunkan Yu[a], Sven Eckart[b], Stefan Essmann[c], Detlev Markus[c],Agustin Valera-Medina[d], Robert Schießl[a], Bo Shu[c], Hartmut Krause[b] & Ulrich Maas[a]

[a] Institute of Technical Thermodynamics, Karlsruhe Institute of Technology, Karlsruhe, Germany
[b] Institute of Thermal Engineering, TU Bergakademie Freiberg, Freiberg, Germany
[c] Physikalisch-Technische Bundesanstalt (PTB), Braunschweig, Germany
[d] College of Physical Sciences and Engineering, Cardiff University, Cardiff CF24 3AA, United Kingdom

E-mail: *chunkan.yu@kit.edu*

Abstract

The ignition properties of ammonia (NH_3) / hydrogen (H_2) mixtures are important because of the abundance of these mixtures in chemical engineering processes, and also for the prospective role of H_2 and NH_3 as fuels in future energy systems. In particular, the question arises if and how important characteristics like ignition limits and minimum ignition energies in NH_3/H_2 mixtures are related to the ignition properties of the pure substances. The present work studies safety-related ignition process in ammonia /hydrogen mixtures with different level of H_2 addition by numerical simulations involving detailed chemistry and molecular transport. A detailed study on the influence of strain rate and the pre-heat temperature on the ignition is performed, aiming at insight into the understanding of a reliable ignition process and prevention of hazard. Numerical simulations of premixed flame in counterflow configurations are employed. The findings are useful for assessing the ignitability of ammonia and its mixtures with hydrogen, which provides insight view for the design of ammonia-based combustion processes and also in safety related processes, where spontaneous ignition of ammonia/hydrogen gas mixtures in production plants is a concern.

Keywords: *hazards, ammonia, industrial explosions, spark ignition, strained premixed flame*

1 Introduction

Spark ignition is not only an important aspect to address in fundamental and applied combustion, but also a complex topic including the strong interaction between the physical and chemical processes. For example, flame propagation is impaired for mixtures with Lewis numbers greater than unity. Here, additional energy must be expended to overcome this impeding effect. As a result, induced flow fields gain strength and may interfere with the ignition process, leading to a larger degree of variation in the ignition process (Essmann et al., 2020). Therefore, flame propagation for mixtures with a Lewis number considerably greater than unity can be dominated by flow effects (spark assisted flame propagation) during the critical phase (Bradley and Lung, 1987).

Although the spark ignition process has been intensively investigated for various hydrocarbon fuels under a wide range of conditions, the knowledge base on spark ignition properties related to ammonia is still scarce, which becomes more and more attracting in the recent years. This is because ammonia as a carbon free carrier offers a high energy density and could provide a practical next generation system for energy transportation, storage and use for power generation (overview see e.g.Valera-Medina et al. (2018)).

It is well known that the ignition energy of the pure ammonia gas is orders of magnitude higher than that of the pure hydrogen gas, this has major implications in the efficient usage of the ammonia in combustion devices. The addition of hydrogen is a common way to improve the combustion property of ammonia gas. If NH_3 is used as an energy carrier in the future, the ignition processes when using

NH_3/H_2/air mixtures must therefore be investigated in detail.

The present work will focus on investigation the safety related ignition process of ammonia with different level of H_2 addition. A detailed discussion on the strain rate effect and the pre-heat temperature effect on the system will be proposed, aiming at providing more insight into the understanding of a reliable ignition process and prevention of hazard.

2 Mathematical Numerical Modeling

The strained premixed flame considered in the present work is presented in Fig.1. The unburnt premixed mixtures from both sides are operated with identical conditions. Depending on the flow velocity, the system can lead to a stable flame or flame extinguish.

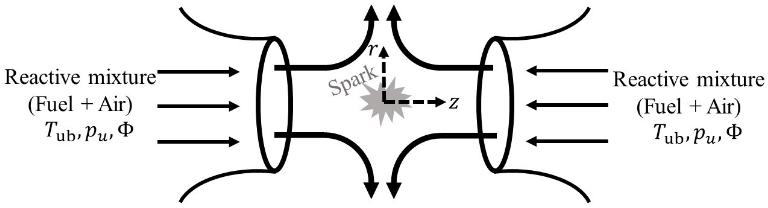

Fig. 1: *Schematic illustration of the strained premixed laminar flame.*

In order to perform the numerical simulation of the present model, the in-house code INSFLA (Maas and Warnatz, 1988) is used. This code solves the one-dimensional flame in counterflow configuration by using the two-parameter formulation (tangential pressure gradient J and radial velocity gradient G), which is described in detail in Stahl and Warnatz (1991). The simulation depends only on one spatial variable (z-axis in the normal direction of the flame surface) with infinite extent in other two directions (slab geometry) with the domain $z \geq 0$ due to symmetry.

The strain rate imposed in the flow describes the "strength" of the flow which is constant throughout the whole flow, and can be determined by means of the tangential pressure gradient J as (Stahl and Warnatz, 1991):

$$a = \sqrt{-\frac{J}{\rho_{\mathrm{ub}}}}, \tag{1}$$

where ρ_{ub} is the density of the unburnt gas mixture.

For the spark ignition energy, the following model for the power density $\dot{q}_s$ is used according to Maas et al. (1988) as:

$$\dot{q}_s(z,t) = \begin{cases} \frac{D_{\mathrm{s}}}{\tau_{\mathrm{s}}} \cdot \exp\left[-\left(\frac{z}{\delta_{\mathrm{W}}}\right)^8\right] & \text{for } 0 \leq t \leq \tau_{\mathrm{s}}, \\ 0 & \text{otherwise} \end{cases} \tag{2}$$

where D_{s} is the maximum energy density (J/m^3) at $z = 0$, and δ_{W} is the spark width. τ_s is the spark duration time describing how long the spark energy is provided into the system. Note that this reflects the spark energy of practical device, as shown in Maas et al. (1988), and no energy exists for $r \to \infty$. Based on $\dot{q}_s(z,t)$, one can also calculate the total deposited energy E_{s} per surface (in J/m^2), which can be determined as:

$$E_{\mathrm{s}} = \int_{z=-\infty}^{+\infty} \int_{t=0}^{\tau_{\mathrm{s}}} \dot{q}_s(z,t) \mathrm{d}t\mathrm{d}z = 2 \cdot D_{\mathrm{s}} \cdot \delta_{\mathrm{W}} \cdot \Gamma\left(\frac{9}{8}\right) \tag{3}$$

where $\Gamma(\cdot)$ is the gamma function ($\Gamma(9/8) \approx 0.94174$).

Simulations are initialized with a homogeneous distribution of species mass fractions ($w_i(z, t = 0) = w_{i,\mathrm{ub}}$) and temperature ($T(z, t = 0) = T_{\mathrm{ub}}$), with index "ub" specifying the unburnt gas. The pressure for the present work is assumed to be constant during the whole spark and combustion processes with $p = 1$ bar. The constant pressure considered in the present work is a good approximation if the spark duration is longer than 0.01 ms (Maas et al., 1988). The left boundary is specified at the the symmetry

	mole fraction			
α_{H_2}	H_2	NH_3	O_2	N_2
0.0	0.0	0.2188	0.1641	0.6171
0.1	0.0225	0.2021	0.1628	0.6162
0.2	0.0462	0.1846	0.1615	0.6077
0.3	0.0712	0.1661	0.1602	0.6025
0.4	0.0977	0.1465	0.1587	0.5971
1.0	0.2958	0.0	0.1479	0.5563

***Table 1**: Mole fractions of species concentrations for stoichiometric unburnt NH_3-H_2-air gas mixture*

axis ($z = 0$) where a Neumann condition (zero gradient) is applied for the species mass fractions and temperature, and the velocity is $v = 0$. On the right side, a Dirichlet boundary condition (fixed value) is used for species mass fractions and temperature. Furthermore, the tangential pressure gradient J is also given as input into the system for the specification of the strain rate imposed to the flame.

A detailed transport model including the thermal diffusion (Soret effect) (Hirschfelder et al., 1964) is considered in the simulation. Furthermore, the thermal radiation is neglected. However, it is worth studying the radiation effect on the NH_3 combustion system in the future.

3 Gas mixture and the chemical mechanism

The H_2-enriched ammonia gas mixture, NH_3-H_2-air mixture, is considered in this study. The level of H_2 addition in the fuel is described by the mole fraction α_{H_2} of H_2 in the fuel:

$$\alpha_{H_2}H_2 + (1-\alpha_{H_2})NH_3 + \frac{1}{\Phi}\left(0.75 - \frac{\alpha_{H_2}}{4}\right)(O_2 + \frac{79}{21}N_2), \tag{4}$$

where Φ is the fuel/air equivalence ratio.

In this work, we focus on stoichiometric mixtures with varying H_2 content, as $0 \le \alpha_{H_2} \le 0.4$. This is because of the following three issues:

- previous works performed by Božo et al. (2019) have suggested the use of blends with less than 40% hydrogen concentration to keep stability in turbulent, swirling flames.
- The work, expanded recently to various equivalence ratios (Marhruk et al., 2022), also suggests that the increase to 50% hydrogen leads to hydrogen overtaking the combustion profile, even creating two flame fronts (Valera-Medina et al., 2018, Goldmann and Dinkelacker, 2021).
- Finally, with increasing hydrogen content, the high temperature hydrogen attack (HTHA) might become serious and destroy the material in real applications (Cesaro et al., 2021). This in return leads to lower efficiencies.

Therefore, it was decided that values from 0 to 40% hydrogen would be investigated in the present work, as these would keep ammonia-based features whilst being more representative to future industrial systems working on ammonia/hydrogen blends. Pure hydrogen gas ($\alpha_{H_2} = 1.0$) is also considered as a reference, comparing the performance with the hydrogen enriched ammonia gas mixture. Tab.1 lists mole fractions of species concentrations for stoichiometric unburnt NH_3-H_2-air gas mixture for different H_2 addition levels (α_{H_2}).

To perform the numerical simulation, the Li-2019 detailed chemical mechanism is used for the numerical simulation of the considered combustion system (Li et al., 2019). This mechanism, which is originally designed for NH_3-H_2-CH_4 air combustion system, consists of 128 reactive species and 957 reactions and has been validated against recent literature experimental data such as ignition delay times, laminar burning velocities, and speciation. Good performance has been reported (Li et al., 2019). Removing all species including hydrocarbon and inertgas such as AR and HE, the remaining mechanism has 34 species and 252 reactions.

Figure 2 gives the representative performance of the Li-2019 mechanism for the prediction of laminar burning velocity (LBV) with varying fuel/air equivalent ratio (left figure) and extinction strain rate a_E of strained premixed flame (right figure) under $p = 1$bar and stoichiometric condition. It can be observed clearly that the Li-2019 mechanism gives a good agreement compared with experimental measurement.

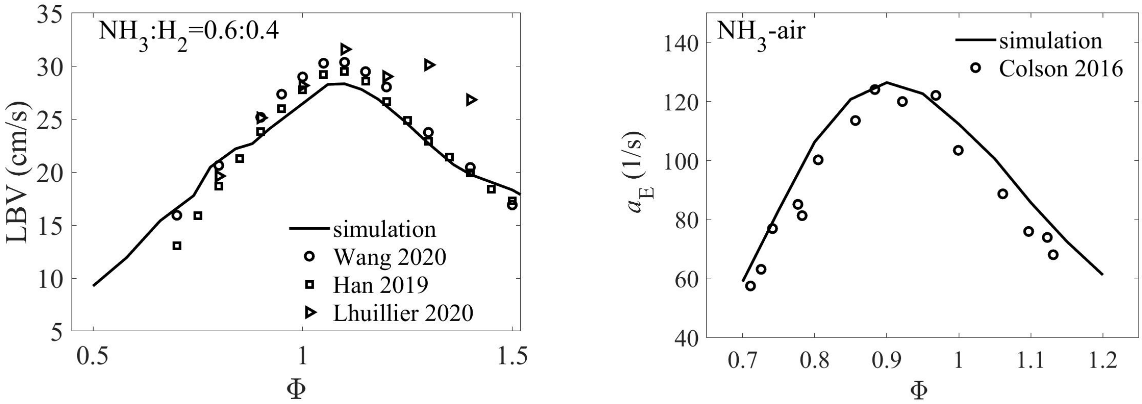

***Fig. 2**: Validation of Li-2019 mechanism for laminar burning velocity (left) and extinction strain rate (right). Wang 2020: Wang et al. (2020); Han 2019: Han et al. (2019); Lhuillier 2020: Lhuillier et al. (2020); Colson 2016: Colson et al. (2016).*

4 Results and Discussion

In this section, the effect of the spark ignition energy on different parameters such as spark duration time τ_s, spark width δ_w, strain rate a, H_2 content α and the unburnt gas mixture temperature T_ub is investigated. We only focus the pressure to be 1 bar, and the spark duration times above 0.01ms. Furthermore, we only consider stoichiometric gas mixtures.

Moreover, we are focusing on the minimum energy E_s^min and minimum energy density D_s^min for a successful ignition, an important safety characteristic used to quantify the ignitability of fuels. In practice, safety characteristic data is used to assess process safety in industrial applications.

4.1 Effect of spark igniter parameters

In this section, we first investigate the effect of spark duration τ_s and spark width δ_W on D_s^min. A typical dependence is represented in Fig.3 for a strain rate $a = 100\mathrm{s}^{-1}$ at 1 bar. It is observed that higher D_s^min is required for a longer spark duration τ_s and a wider spark width δ_w. Lower D_s^min can be achieved by decreasing the spark duration time and spark width. In order to understand this behavior, we have a closer look at the temperature profile at the end of the spark duration $T = T(t = \tau_s)$ with varying spark igniter parameters, as shown in Fig.4. Note that in the figure, we only show the positive z-axis because of the symmetry at $z = 0$. The maximum of the spark ignition energy occurs at $z = 0$.

Figure 4 (left) shows the temperature profiles $T = T(t = \tau_s)$ for different spark width δ_w, and the maximum of the temperature is observed at $z = 0$, corresponding to the position of maximum of spark ignition energy. In general, for a narrower spark width, spark ignition energy is used to heat up a smaller amount of gas mixture. Therefore, the spark temperature T_s (maximum of the temperature at $t = \tau_s$) increases with decreasing spark width δ_w. For T_s to reach sufficiently high temperature for fast reaction rate, more spark ignition energy must be provided to the system.

Figure 4 (right) shows temperature profiles $T = T(t = \tau_s)$ for different spark duration time τ_s. It is observed that with increasing spark duration, the spark temperature T_s decreases. The reason is attributed to the competition between the heating-up rate caused by spark ignition and energy dissipation rate caused by heat conductivity:

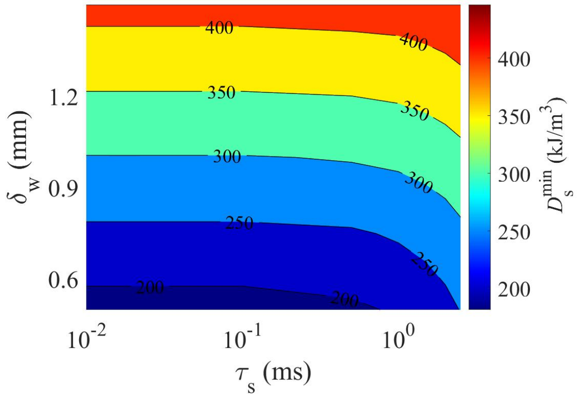

Fig. 3: Contour-plot showing the dependence of D_s^{min} on spark duration τ_s and spark width δ_W for flows with strain rate $a = 100s^{-1}$ under $p = 1$ bar. Stoichiometric with NH_3:H_2=0.9:0.1. $T_{ub} = 300K$.

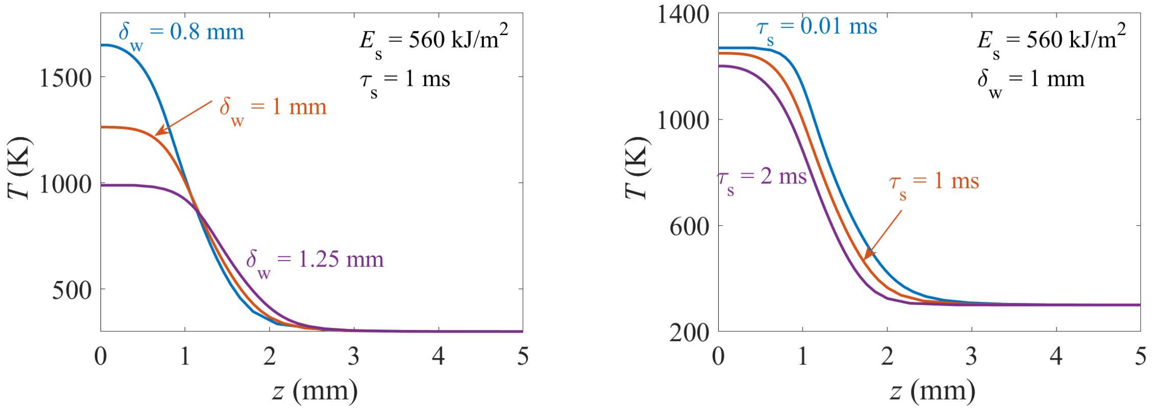

Fig. 4: The temperature profiles at $t = \tau_s$ for flows with strain rate $a = 100\ s^{-1}$ under $p = 1$ bar for varying spark width (left) and spark duration time (right). Stoichiometric with NH_3:H_2=0.9:0.1. $T_{ub} = 300K$.

- for a short spark duration, almost no energy can be dissipated due to slow heat conductivity process, and the heat conductivity therefore has almost no influence of the temperature profile. Therefore, the $E_s^{\rm min}$ remains almost unchanged for short spark duration (c.f. Fig.3).
- for a long spark duration, the energy dissipation rate becomes important. The longer the spark duration is, the more energy can be dissipated and, consequently, a lower T_s is observed. Therefore, with longer spark duration, more $E_s^{\rm min}$ is necessary (c.f. Fig.3).

4.2 Effect of the H_2 content

In this section, we investigate the effect of H_2 content in the gas mixture on the ignition energy. $\alpha_{\rm H_2}$ is selected to be 0.0, 0.1, 0.2, 0.3, 0.4 and 1.0.

Figure 5(left) compares the $D_s^{\rm min}$ over strain rate for different levels of H_2 addition. Furthermore, the results for pure NH_3-air and pure H_2-air gas mixtures are presented as reference values. The very right points correspond to the extinction strain rates (ESR), above which no stable burning flame solution can be observed. It can be clearly seen that the ESR increases with increasing H_2 content. Such tendency of the ESR is consistent with observed in e.g. Lee and Kwon (2011), and the effect of H_2 addition on ESR is beyond scope of this work. Concerning the minimum energy for a successful ignition $D_s^{\rm min}$, we observe that the pure NH_3-air gas mixture required much higher spark energy. More precisely, for flow imposed with the same strain rate, around 15% more $D_s^{\rm min}$ is required compared to a H_2 addition of only 10% in fuel (blue line versus red line). For NH_3-H_2-air gas mixture, the $D_s^{\min}$ decreases monotonically with increasing H_2 content in fuel, as shown in Fig. 5(right) for flows with strain rate $a = 100\text{s}^{-1}$ with solid line. Also shown is the characteristic reaction rate k at T_s, which is defined as the inverse of the ignition delay time:

$$k(T_s) = \frac{1}{\tau_{\text{ign}}(T_s)}. \tag{5}$$

This characteristic reaction rate is a suitable quantity to measure how fast the reaction of a combustion system takes place, which was discussed in detail in Livengood and Wu (1955).

We mainly observe that less spark energy is required for a successful ignition with increasing H_2 content in the gas mixture. This is because the heat capacity decreases with increasing H_2 content, therefore less energy is required for the system to reach sufficient high temperature required for a successful ignition. However, the dashed line in Fig.5(right) shows that the corresponding required reaction rate at T_s increases monotonically with H_2 content. This is because if the system is blended with more H_2, the H-radicals diffuse away from the flame zone faster which may result in extinction. Therefore higher reaction rate is necessary to compensate the higher molecular diffusivity of H-radicals.

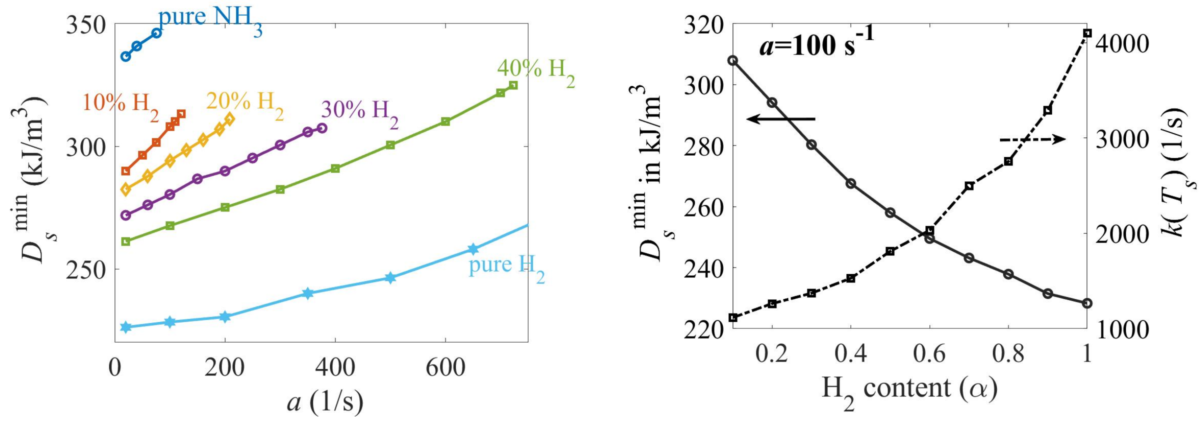

Fig. 5*: Dependence of the* D_s^{min} *against strain rate for different levels of* H_2 *in the fuel. Igniter:* $\delta_w = 1mm$ *and* $\tau_s = 1ms$*;* $p = 1bar$*,* $T_{ub} = 300K$*.*

4.3 Effect of the strain rate

As seen in Fig.5, for all cases, $D_s^{\min}$ increases with increasing strain rate, until the strain rate exceeds the extinction strain rate (ESR), above which no stable burning solution can be obtained. Such dependence can be attributed to two main reasons:

- the higher the strain rate is, the higher the flow velocity (and consequently the mass flux) is. Therefore, if the flow is imposed with higher strain rate, more unburnt gas mixture per time unit passes the spark ignition regime. Therefore, at the end of the spark duration, the temperature becomes lower with increasing strain rate, as shown in Fig.6(left). In order to reach sufficient ignition temperature T_s, more spark energy must be provided to heat up the unburnt gas mixture for flow with increasing strain rate.
- the higher the strain rate is, the higher the rate of energy transport (convection and heat conductivity) is: high convection due to high flow velocity; and high rate of heat conductivity due to high spatial gradient of temperature. As shown in Fig.6(right), a higher reaction rate $k(T_s)$ is required with increasing strain rates to compensate increasing rate of energy transport.

In the practical combustion devices, flows with higher turbulence intensity impose higher strain rates, indicating that more spark energy is required for flows with higher turbulence. This is also observed in e.g. Huang et al. (2007), De Soete (1971), Shy et al. (2017).

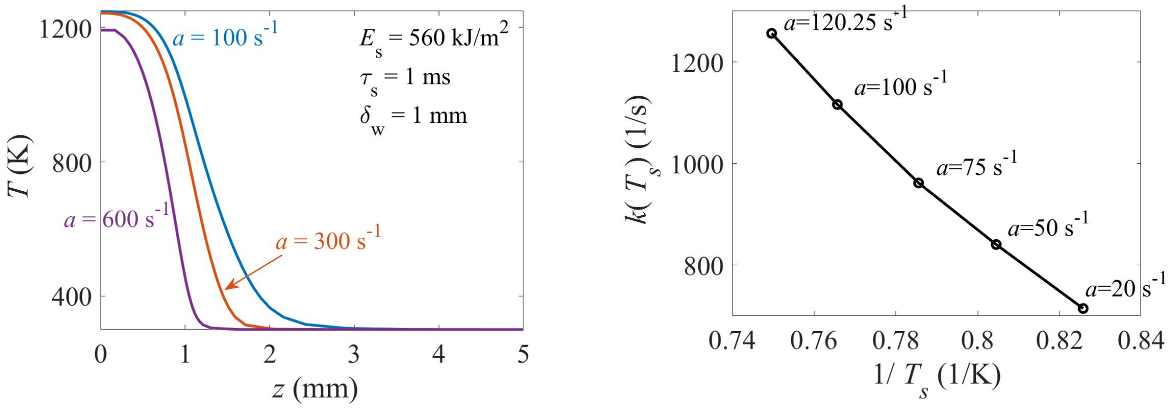

***Fig. 6**: The temperature profiles (left) and the characteristic reaction rate (right) at $t = \tau_s$ for flows with different strain rates under $p = 1$ bar. Stoichiometric with NH_3:H_2=0.9:0.1. $T_{ub} = 300K$.*

4.4 Effect of the gas temperature

Figure 7 shows D_s^{min} against strain rate for various initial gas temperatures. It is straightforward and also well known that with increasing gas temperatures, gas needs less spark ignition energy to be heated up to reach the necessary ignition temperature. However, if we further increase the gas temperature, we would expect that the gas mixture can be either self-ignited due to its high temperature or ignited only we provide the external spark energy, depending on the flow strength. This can be observed through the blue line in Fig.7. Therefore, at low strain rate regime (here $a < 674$ s^{-1}), no external spark energy is required ($D_s^{\text{min}} = 0$) and the gas mixture can self-ignite due to its own fast reaction rate. At high strain rate regime (here $a > 674$ s^{-1}) the required minimum spark energy increases, as already discussed above, with increasing strain rate.

There, at high gas temperature, there exists a so-called transition strain rate a_{trans} which distinguishes between the self ignition and the spark ignition. For all $a < a_{\text{trans}}$, the gas mixture can be self-ignited, without external spark energy. For strain rate above the transition strain rate $a > a_{\text{trans}}$, spark ignition energy is required for a successful ignition.

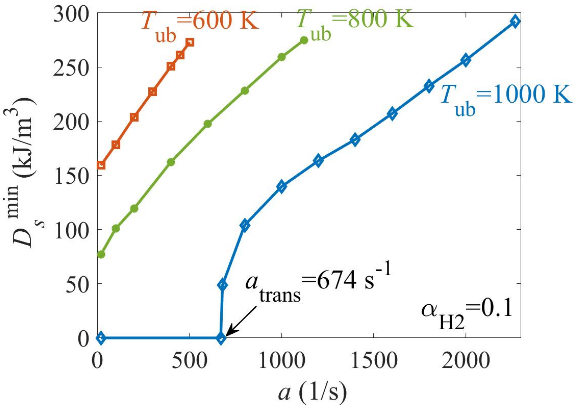

***Fig. 7**: The dependence of D_s^{min} on gas temperature T_{ub} for flames under $p = 1$ bar. Stoichiometric gas mixture with NH_3:H_2=0.9:0.1. Igniter parameter: $\delta_w = 1mm$, τ_s =1.5 ms.*

The dependence of a_{trans} on the gas temperature T_{ub} is represented in Fig.8 (left) for different levels of H_2 addition and pure H_2 and pure NH_3 gas mixture under stoichiometric condition and $p = 1$ bar. We observe that pure NH_3-air has a very low a_{trans} while a_{trans} of pure H_2-air gas mixture increases exponentially with T_{ub}. This provides two very important issues concerning the safety-related ignition:

- For a pre-heated pure NH_3-air gas mixture, it can be very difficult to achieve self-ignition due to its low reaction rate and burning rate (Valera-Medina et al., 2019). A reliable combustion is achievable only when one provides external spark ignition. From the other side, the pure NH_3-air gas mixture has the lowest possibility of hazardous explosion danger.
- For a pre-heated pure H_2-air gas mixture, it can be extremely easily self-ignited even under higher strain rates, which is well-known and important for the safety process.

In order to investigate how the reaction rate affects the transition strain rate, Fig.8(right) shows the a_{trans} against the characteristic reaction rate $k(T_{\text{ub}})$ for all points shown in Fig.8(left). It is observed that there is a linear correlation, and the linear regression models the relationship between the transition strain rate a_{trans} and the characteristic reaction rate $k(T_{\text{ub}}) = 1/\tau_{\text{ign}}$ as

$$a_{\text{trans}} = 4.4 \cdot k(T_{\text{ub}}) = \frac{4.4}{\tau_{\text{ign}}}. \tag{6}$$

If the reaction rate tends to zero ($k \to 0$), corresponding to an infinite reaction time, the gas mixture cannot also be self-ignited and $a_{\text{trans}} \to 0$. This simple linear correlation provides the information that if one knows the ignition delay time of the gas mixture at one temperature, the transition strain rate a_{trans} can be easily determined. This could be important information for the process safety that a) the hazardous explosion can be generated at elevated temperatures without providing external spark energy if the flow is imposed with small strain rates; b) a spark ignition can fail if the flow is imposed with high strain rate.

However, there is a lack of experimental measurement for the ignition study with heated gas mixture under various strain rates. It is therefore interesting to be compared with experiment results, if there exists in the future. Furthermore, more numerical simulations with various system parameters (e.g. pressures and fuels) will be performed to confirm this linear correlation between ignition delay time of the gas mixture and the transition strain rate.

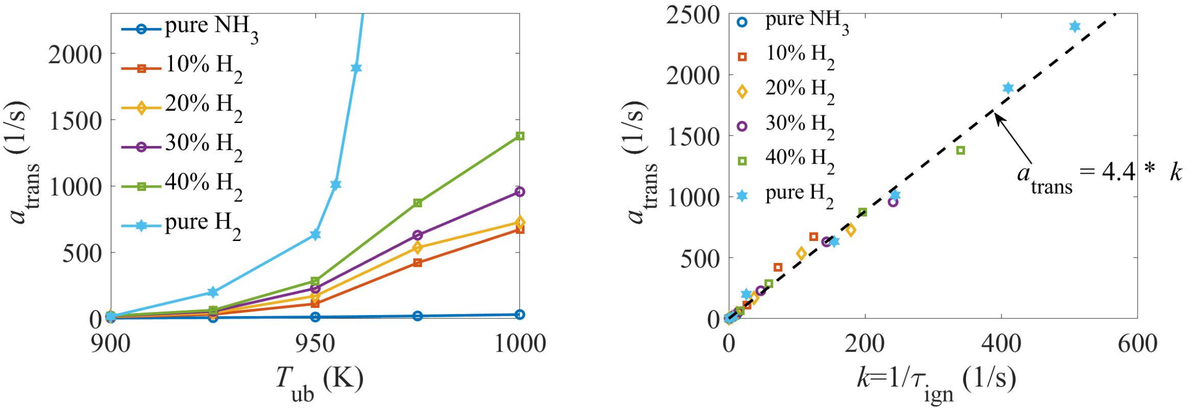

Fig. 8: *Dependence of the* a_{trans} *over the gas mixture temperature* T_{ub} *(left) and the reaction rate* $k = 1/\tau_{ign}$ *under* $p = 1$ *bar.*

5 Conclusions

In this work, the ignition process of the hydrogen enriched ammonia gas mixture (NH_3-H_2-air) was studied. It was found that the minimum spark ignition (SI) energy required for a successful ignition decreases monotonically with increasing H_2 content. Furthermore, the numerical experiment showed that the minimum SI energy increases with increasing strain rate, which reflects the turbulence intensity. Moreover, it was observed that with increasing gas mixture temperature, there exists a transition strain rate a_{trans}, below which the gas mixture can be self-ignited and above which it can be successfully ignited only through spark ignition. It was interesting to see that there is a quasi-linear correlation between the a_{trans} and the characteristic reaction rate (inverse of the ignition delay time).

DOI: 10.7795/810.20221124

This work yields insight into the ignition process of the ammonia-hydrogen gas, which supports a knowledge-based prevention of hazardous explosion and understand the safety process in ammonia-hydrogen related combustion devices.

Acknowledgements

The State of Lower Saxony / Germany for funding within the H2-WaVe project Grant number ZN3772 is grateful acknowledged by Stefan Essman, Detlev Markus and Bo Shu.

References

Božo, M. G., Vigueras-Zuniga, M., Buffi, M., Seljak, T., Valera-Medina, A. (2019). *Fuel rich ammonia-hydrogen injection for humidified gas turbines*. Applied Energy, 251:113334.

Bradley, D., Lung, F. K.-K. (1987). *Spark ignition and the early stages of turbulent flame propagation*. 69:71–93. ISSN 0010-2180.

Cesaro, Z., Ives, M., Nayak-Luke, R., Mason, M., Bañares-Alcántara, R. (2021). *Ammonia to power: Forecasting the levelized cost of electricity from green ammonia in large-scale power plants*. Applied Energy, 282:116009.

Colson, S., Hayakawa, A., Kudo, T., Kobayashi, H. (2016). *Extinction characteristics of ammonia/air counterflow premixed flames at various pressures*. Journal of Thermal Science and Technology, 11(3):JTST0048–JTST0048.

De Soete, G. (1971). *The influence of isotropic turbulence on the critical ignition energy*. In *Symposium (International) on Combustion*, volume 13, pages 735–743. Elsevier.

Essmann, S., Markus, D., Grosshans, H., Maas, U. (2020). *Experimental investigation of the stochastic early flame propagation after ignition by a low-energy electrical discharge*. 211:44–53.

Goldmann, A., Dinkelacker, F. (2021). *Experimental investigation and modeling of boundary layer flashback for non-swirling premixed hydrogen/ammonia/air flames*. Combustion and Flame, 226:362–379.

Han, X., Wang, Z., Costa, M., Sun, Z., He, Y., Cen, K. (2019). *Experimental and kinetic modeling study of laminar burning velocities of nh3/air, nh3/h2/air, nh3/co/air and nh3/ch4/air premixed flames*. Combustion and Flame, 206:214–226.

Hirschfelder, J. O., Curtiss, C. F., Bird, R. B., Mayer, M. G. (1964). *Molecular theory of gases and liquids*, volume 165. Wiley New York.

Huang, C., Shy, S., Liu, C., Yan, Y. (2007). *A transition on minimum ignition energy for lean turbulent methane combustion in flamelet and distributed regimes*. Proceedings of the Combustion Institute, 31(1):1401–1409.

Lee, S., Kwon, O. C. (2011). *Effects of ammonia substitution on extinction limits and structure of counterflow nonpremixed hydrogen/air flames*. International Journal of Hydrogen Energy, 36(16):10117–10128. doi:10.1016/j.ijhydene.2011.05.082.

Lhuillier, C., Brequigny, P., Lamoureux, N., Contino, F., Mounaïm-Rousselle, C. (2020). *Experimental investigation on laminar burning velocities of ammonia/hydrogen/air mixtures at elevated temperatures*. Fuel, 263:116653. ISSN 00162361. doi:10.1016/j.fuel.2019.116653.

Li, R., Konnov, A. A., He, G., Qin, F., Zhang, D. (2019). *Chemical mechanism development and reduction for combustion of nh3/h2/ch4 mixtures*. Fuel, 257:116059.

Livengood, J., Wu, P. (1955). *Correlation of autoignition phenomena in internal combustion engines and rapid compression machines*. Symposium (International) on Combustion, 5(1):347–356.

Maas, U., Raffel, B., Wolfrum, J., Warnatz, J. (1988). *Observation and simulation of laser induced ignition processes in o2- o3 and h2- o2 mixtures*. Symposium (International) on Combustion, 21(1):1869–1876.

Maas, U., Warnatz, J. (1988). *Ignition processes in hydrogen oxygen mixtures*. Combustion and flame, 74(1):53–69.

Marhruk, S., Vigueras-Zuniga, M., Tejeda-del Cueto, M., Xiao, H., Yu, C., Maas, U., Valera-Medina,

A. (2022). *Combustion features of ch4/nh3/h2 ternary blends*. International Journal of Hydrogen Energy, under review.

Shy, S., Shiu, Y., Jiang, L., Liu, C., Minaev, S. (2017). *Measurement and scaling of minimum ignition energy transition for spark ignition in intense isotropic turbulence from 1 to 5 atm*. Proceedings of the Combustion Institute, 36(2):1785–1791.

Stahl, G., Warnatz, J. (1991). *Numerical investigation of time-dependent properties and extinction of strained methane- and propane-air flamelets*. Combustion and flame, 85(3-4):285–299.

Valera-Medina, A., Gutesa, M., Xiao, H., Pugh, D., Giles, A., Goktepe, B., Marsh, R., BOWEN, P. (2019). *Premixed ammonia/hydrogen swirl combustion under rich fuel conditions for gas turbines operation*. International Journal of Hydrogen Energy, 44(16):8615–8626.

Valera-Medina, A., Xiao, H., Owen-Jones, M., David, W., Bowen, P. J. (2018). *Ammonia for power*. Progress in Energy and Combustion Science, 69:63–102. doi:10.1016/j.pecs.2018.07.001.

Wang, S., Wang, Z., Elbaz, A. M., Han, X., He, Y., Costa, M., Konnov, A. A., Roberts, W. L. (2020). *Experimental study and kinetic analysis of the laminar burning velocity of nh3/syngas/air, nh3/co/air and nh3/h2/air premixed flames at elevated pressures*. Combustion and Flame, 221:270–287.

DOI: 10.7795/810.20221124

Experimental and numerical modelling of igniting hydrogen/air mixtures in inter-connected vessels

Bisham McCarthy-Singh[a,b], Manideep Manchikatla[c], Tim Krause[c], Detlev Markus[c], Holger Grosshans[c,d] & Alberto Gambaruto[a]

[a] University of Bristol, Bristol, UK
[b] Rotork Controls Ltd, Bath, UK
[c] Physikalisch-Technische Bundesanstalt, Braunschweig, Germany
[d] Otto von Guericke University, Magdeburg, Germany

E-mail: *bm15605@bristol.ac.uk*

Abstract

In Physikalisch-Technische Bundesanstalt (PTB), Braunschweig, experiments have been conducted on the pressure piling phenomenon when igniting a stoichiometric hydrogen-air mixture in inter-connected compartments. Two sets of experimental results are presented; single chamber and a dual inter-connected chamber. Moreover, PTB simulated both experiments using the pressure-based OpenFOAM solver *XiFoam*. In collaboration, the experiments were simulated at the University of Bristol using the density-based OpenFOAM solver *rhoReactingFoam*. From the experimental data, pressure piling was not observed in the single chamber set-up due to the size and shape of the geometry. However, in the dual chamber set-up pressure piling did occur. Within the single chamber experiment, the mixture is ignited at one end and the flame propagates laminar through the unburnt gas. Within the dual-chamber experiment, as the flame propagates towards the second chamber, the unburnt gases ahead of the flame are compressed and three flame regimes are achieved. Once the flame reaches the second chamber, the unburnt gases are at a higher than atmospheric pressure. The ignition of the unburnt high-pressure gases causes an explosion and, hence, pressure piling. Due to the number of flame regimes and the wide range of temporal and spatial flow-scales, simulating this event has many challenges, especially when pressure piling occurs. Considerable attention is given to validating the numerical setup and discretisation schemes, and the two solvers are compared. The numerical results are in good qualitative and quantitative agreement with the experimental data. This is evident from the pressure curves which show that the computed solution can accurately capture the pressure magnitude and its rate of increase. The single chamber experiment and numerical results are presented. The dual inter-connected chamber simulations are presented as preliminary work-in-progress.

Keywords: *pressure piling, CFD, OpenFOAM, industrial explosions*

1 Introduction

Explosions within relatively small confined geometries can be extremely destructive given the correct conditions. When two volumes are connected through a small pipe or orifice a phenomenon known as pressure piling can occur. Simulating such an event is important within many applications, such as certification testing of commercial electric valve actuators, as it can produce up to *eight times* (CCPS, 2006) the standard combustion pressures causing design failures and ultimately a non-certifiable product.

A typical pressure trace of the pressure piling effect can be seen in Fig. 1. The pressure in the second chamber peaks significantly higher than in the first chamber, which can be extremely destructive as this is usually over a very short period of time. Ignition occurs within the first chamber and compresses the unburnt mixture within the second chamber as the flame propagates towards the interconnecting

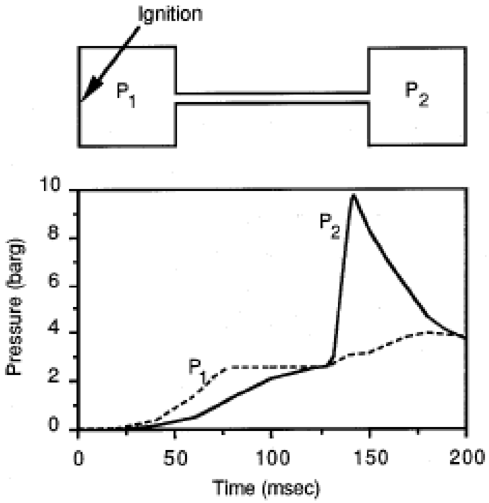

Fig. 1*: Typical pressure piling set-up and pressure trace (Heinrich, 1988).*

tube. The pressure piling phenomenon can be replicated with two linked vessels as seen within this study.

There have been numerous studies, both experimental and numerical, investigating the topic of pressure piling. Phylaktou and Andrews (1993) & Singh (1977) have both previously completed experiments on pressure piling using two interconnected vessels. Benedetto and Salzano (2010) have simulated both experiments using a modified solver achieving reasonable accuracy. There are significant differences in characteristics between a confined geometry that can produce pressure piling compared to one that cannot. Within a single chamber geometry a relatively uniform pressure wave is formed in front of a combustion front which will then be reflected by the internal walls. An interconnection between chambers adds a further layer of complication to the flow physics. The pressure waves created are normally accelerated through the interconnecting tube or orifice plate, producing a pressure buildup and high turbulence intensity within the secondary chamber. This usually produces large over-pressures in the secondary chamber, as shown by curve P_2 Fig. 1, while the single chamber geometry will produce a curve similar to P_1 in Fig. 1.

The main aim of this study is to validate two numerical methods to simulate the pressure piling phenomenon within the presented geometry. It is also to compare the two different OpenFOAM solvers and note any advantages or differences.

The subsequent sections outline results gathered from the experiment and presents simulation results in comparison to the set of discussed experimental results.

2 Experimental data

The experimental part of this work is largely based on the test specifications of IEC 60079-1 (2014) for the determination of the explosion pressure of flameproof enclosures. Two different configurations consisting of two stainless steel chambers of different lengths and an orifice plate are used as test cases (see Fig. 2). The experiments without the occurrence of pressure piling are conducted on a single 250 mm long chamber which is closed on both sides by flanges of 22 mm thickness.

For the test with pressure piling, the short chamber is combined with the 500 mm long chamber using the orifice plate, and closed at each end with end flanges. The inner diameter of both chambers is 161.5 mm, the diameter of the orifice plate hole is 15 mm. All tests are carried out with a fuel-air mixture of 31 vol.% H_2 in air which is prepared with mass flow controllers and verified by an oxygen analyser. After ignition by the centred spark plug at the end flange of the long chamber, the explosion pressure is measured by a piezoelectric pressure sensor (Type: Kistler 601CAA) at the opposite flange side at the centre of the short chamber. In linear correlation to the pressure caused by the explosion, the pressure sensor generates a charge which is subsequently converted into a voltage signal by a

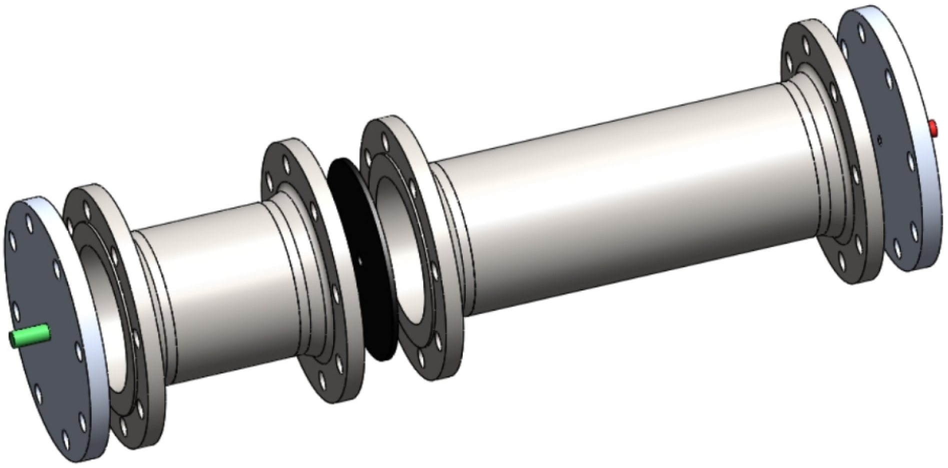

***Fig. 2**: Components of the test samples - short and long chamber, orifice plate and end flanges. The spark plug (red) and the pressure sensor (green) are positioned centrally and opposite each other.*

charge amplifier (Type: Kistler LabAmp 5167A). The voltage signal is also linear to the pressure and is recorded via transient recorder with a sampling rate of 1 MS/s. A low-pass filter (3 dB, Butterworth, 2nd order) with a cut-off frequency of 5 kHz is used as signal filter.

3 Numerical simulations: OpenFOAM

OpenFOAM is a C++ based, open source toolbox for the development of customized numerical solvers, and pre-/post- processing utilities for the solution of continuum mechanics problems, including combustion (Foundation, 2022). The version used within this study is *OpenFOAM-dev v4*, the weekly updated development line from The OpenFOAM Foundation.

The Navier-Stokes (N-S) for a compressible fluid, the advection-reaction-diffusion and other equations which collectively model fluid motion and chemical reactions, can only be solved analytically in some restricted situations. Otherwise, numerical methods are used to solve them, such as the finite volume method (FVM). After spatial and temporal discretization of the coupled equations, the resulting system of algebraic equations is commonly solved by iterative solvers.

In the present work, two important variables to set correctly for simulation initiation are the Courant-Friedrichs-Lewy (CFL) condition and the initial turbulence variables. The CFL condition is described by the following equation:

$$Co = \frac{U\ \Delta t}{\Delta x} \tag{1}$$

where Co, U, Δt and Δx are Courant number, flow velocity, time step and grid spacing respectively (Morton and Mayers, 1994). This equation controls the time step to ensure stability of hyperbolic type PDEs, according to the flow velocity and grid spacing. Within OpenFOAM the time step can be automatically controlled adaptively by the solver according to a maximum Courant number set by the user. The time step is adapted to maintain a Courant number below the maximum value set by using the flow velocity at that iteration and the grid spacing used.

The initial conditions for the turbulence variables are also important as this ensures the mixing is initiated correctly. Within this study both solvers use the standard $k-\varepsilon$ turbulence model (Launder and Spalding, 1974) as previous studies have shown this to be sufficient in describing the fluid dynamics for similar setups. Equation 2 calculates the turbulent kinetic energy which includes the turbulence intensity (I) and flow velocity (U). The turbulent kinetic energy dissipation rate is calculated with equation 3 and utilises a constant from the model ($C_\mu = 0.09$), the turbulent kinetic energy (k) as previously calculated and the turbulent length scale (L).

DOI: 10.7795/810.20221124

$$k = 1.5(I\,U)^2 \tag{2}$$

$$\varepsilon = \frac{C_\mu^{0.75} k^{1.5}}{L} \tag{3}$$

The over-arching differences between an pressure based and density based solver is the solution process of the main equations. Pressure based solvers are mainly used for low speed, incompressible flows where density is constant (or for compressible flows density is calculated from both the continuity and momentum equations). Pressure is then calculated from a pressure correction equation. On the other hand, density based solvers are used more commonly for high speed, compressible flows. Density is calculated directly from the continuity equation and the pressure from the equation of state. Both solvers used within this study employ the PIMPLE (Pressure Implicit Method for Pressure-Linked Equations) algorithm for the solution process of the main coupled equations for transient simulations, Barton (1998) first introduced this algorithm. This is a combination of PISO (Pressure Implicit with Splitting of Operator) and SIMPLE (Semi-Implicit Method for Pressure-Linked Equations) schemes.

3.1 Pressure based: XiFoam

The XiFoam solver in OpenFOAM is mainly used for modelling the premixed combustion process involving turbulence. It is a transient solver where a progress variable is calculated and used in a transport equation to model the flame front propagation. The value of the progress variable is 1 in burnt gas and 0 in fresh gas. As the flame propagates, it varies from 0 to 1. The progress variable is calculated using the following relation:

$$c = \frac{T - T_f}{T_b - T_f} \tag{4}$$

where c, T, T_b, T_f are progress variable, temperature, burnt gas temperature and unburnt gas temperature respectively. The mean reaction regress variable is: $b = 1 - c$. The transport equation is written as follows:

$$\frac{\partial}{\partial t}(\rho b) + \nabla(\rho \mathbf{U} b) - \nabla\left(\frac{\mu_t}{Sc_t}\nabla b\right) = -\rho_u S_u \Xi |\nabla b| \tag{5}$$

where ρ, $\mathbf{U}$, μ_t, Sc_t, ρ_u are density, gas velocity, turbulent viscosity, turbulent Schmidt number and unburnt gas density respectively. The terms S_u and Ξ in the transport equation need to be calculated and for that, there are different models available in XiFoam.

To calculate the laminar flame speed S_u, we have models: Unstrained, Equilibrium and Transport (equation 6):

- **Laminar flame speed transport model:**

$$\frac{\partial S_u}{\partial t} + U_s \nabla S_u = -\sigma_s S_u + \sigma_s (S_u)^\infty \frac{({S_u}^0 - S_u)}{(S_u - {S_u}^\infty)} \tag{6}$$

Both Equilibrium and Transport models are preferable compared to the Unstrained model because they consider the curvature of the flame surface. The Equilibrium model delays in estimating the heat release from the flame leading to lower flame front curvature and Markstein length. The transport equation is the most effective of the three models.

To calculate the value of Ξ we have the models: Fixed, Algebraic and Transport (equation 7):

- **Ξ transport model:**

$$\frac{\partial \Xi}{\partial t} + U_s \nabla \Xi = G\Xi - R(\Xi - 1) + (\sigma_s - \sigma_t)\Xi \tag{7}$$

  where the rate coefficients ($G = R\frac{\Xi_{eq}-1}{\Xi_{eq}}$), ($R = \frac{0.28\Xi^*_{eq}}{\tau_n \Xi^*_{eq}-1}$), U_s is the surface flame velocity and

  $\Xi_{eq} = 1 + 0.62\sqrt{\frac{u^{|}}{S_u}}R_n$ and $\Xi^*_{eq} = 1 + 2(1-b)(\Xi^*_{eq} - 1)$.

  When using the transport model for calculating the flame wrinkling factor (Ξ), the turbulent generation rate GΞ and turbulent removal rate R(Ξ – 1) of the flame front are used for better evaluation.

After going through all the models, the *transport* equations 6 and 7, for solving S_u and Ξ are proven to be efficient in the XiFoam solver and are used in this paper (Weller et al., 1998) .

3.2 Density based: rhoReactingFoam

rhoReactingFoam is a solver for combustion with chemical reactions (Foundation, 2022) and operates on a Eulerian description, fixed space and time through volume, unlike Lagrangian solvers. In this study, a reliable numerical method is developed to simulate pressure piling utilising *OpenFOAM-dev (v4)* (Foundation, 2022). The numerical method has the capability to capture shocks robustly as well as resolve combustion phenomena in a stable manner. The equations employed are the equations of mass, momentum, energy, gas species to model the combustion process.

The governing equations utilised within the rhoReactingFoam solver are as follows and are similar to that described by Oran and Borris (2001):

- **Conservation of Mass Equation**:

$$\frac{\partial \rho}{\partial t} + \nabla \cdot (\rho \mathbf{U}) = 0 \tag{8}$$

- **Conservation of Momentum Equation**:

$$\frac{\partial}{\partial t}(\rho \mathbf{U}) + \nabla \cdot (\rho \mathbf{U}\mathbf{U}) = -\nabla p + \nabla \cdot \tau \tag{9}$$

$$\tau = \mu \left[(\nabla \mathbf{U} + \nabla \mathbf{U}^T) - \frac{2}{3}\nabla \cdot \mathbf{U} I \right] \tag{10}$$

- **Conservation of Energy Equation**:

$$\frac{\partial}{\partial t}(\rho E) + \nabla \cdot (\rho \mathbf{U} E) + \frac{\partial}{\partial t}(\rho K) + \nabla \cdot (\rho \mathbf{U} K) - \frac{\partial p}{\partial t} = \nabla \alpha_{eff} \nabla E + \dot{Q}_{heat} \tag{11}$$

- **Conservation of Chemical Species Number Densities**:

$$\frac{\partial}{\partial t}(\rho Y_i) + \nabla \cdot (\rho \mathbf{U} Y_i) = \nabla \mu_{eff} \nabla Y_i + \dot{R}_i \tag{12}$$

- **Equation of State** - Perfect Gas:

$$P = \rho RT \tag{13}$$

where ρ, p, $\mathbf{U}$, τ, E, Y_i, Q_i, R, K, α_{eff}, μ_{eff}, $\dot{R}_i$, I and T are respectively the density, the pressure, the velocity, the viscous stress tensor, the total energy density, the number density of species, heat release, gas constant, kinetic energy, effective thermal diffusivity, effective thermal viscosity, the chemical production rate of species, turbulence intensity and the temperature.

The rhoRectingFoam solver requires a mechanism to be applied for the chemistry to be solved. This can be with either a single-step or a multi-step mechanism and one is chosen over the other depending on accuracy and computational effort. The accuracy of single-step mechanism is sufficient but multi-step is more accurate in terms of flame speed prediction. When setting the initial conditions for the chemical species, OpenFOAM operates using mass fraction. It is also useful to note that XiFoam does not implement chemistry.

Charles K. Westbrook (1981) made a comparison of a number of methane mechanisms proving that the multi-step mechanisms predicted the flame velocity more accurately. Single-step or global reaction mechanisms summarise the combustion process while multi-step or detailed mechanisms outline the process on a molecular level. However, from an industry perspective and for this particular application a single-step mechanism is sufficient, as verified from the results we gather. Kim and Kim (2019) have also completed similar work but on hydrogen combustion mechanisms, also showing that multi-step models produce more accurate results. They also successfully modelled denotative combustion using OpenFOAM.

The reaction rate for a specific reaction can be described by the following Arrhenius type equation:

$$k = AT^b \exp\left(-\frac{E_a}{RT}\right) C_{H_2} C_{O_2} \tag{14}$$

where k, A, b and E_a are respectively the rate constant, pre-exponential factor, temperature exponent, activation energy and gas constant.

To control the turbulence-chemistry interaction, there are two available combustion models within rhoReactingFoam: Eddy-Dissipation Concept (EDC) and Partially Stirred Reactor (PaSR, equation 15) which are both based on turbulent mixing:

- **PaSR model:**

$$\overline{R_i} = \kappa \frac{C_{i,1} - C_{i,0}}{\Delta t} \tag{15}$$

where κ and C_i are respectively mixed fraction that can react in a cell and mixture concentration. Within this model a parameter known as C_{mix} can be calculated by the following equation and sets the level of turbulence where as $C_{mix} \rightarrow 0$ the more turbulent the flow:

$$C_{mix} = \sqrt{\frac{1}{1 + C_\mu Re_t}} \tag{16}$$

where Re_t is the turbulent Reynolds number.

Within this study the PaSR combustion model was selected along with an ODE solver for the chemistry, a numerical method has been developed for this type of combustion and is applied to this study.

Both solvers discussed have the initial/boundary conditions as shown in Table 1:

Property	Initial Value	Boundary Condition
p	1 bar	zeroGradient
$\mathbf{U}$	0 m/s	noSlip
T	300 K	fixedValue
k	0.0015 m^2/s^2	wall function
ε	0.00687 m^2/s^3	wall function
S_u^0 (XiFoam only)	2.089 m/s	zeroGradient

***Table 1**: Numerical setup - initial and boundary conditions*

4 Results and discussion

A comparison of results obtained with the two numerical solvers and the experimental data is presented within this section. The comparison is of the single chamber experiment with the dual chamber results a work-in-progress. It is noted that gauge pressure (atmospheric pressure is removed) is used throughout all of the results presented.

4.1 Mesh convergence study using XiFoam

To determine a suitable mesh size for the geometry based on accuracy, a mesh independence study was carried out on the single chamber experiment using XiFoam to evaluate the pressure error approximation. The computational domain was discretised into approximately 0.1 million, 0.25 million, 0.5 million, 1 million and 2 million cells, and the pressure curve was plotted as shown in Fig. 3 and reported in Table 2. From these simulations, the discretisation with 1 million cell was considered suitable as a trade off based on the computational time and accuracy, and this discretisation was adopted for further simulations using both solvers discussed.

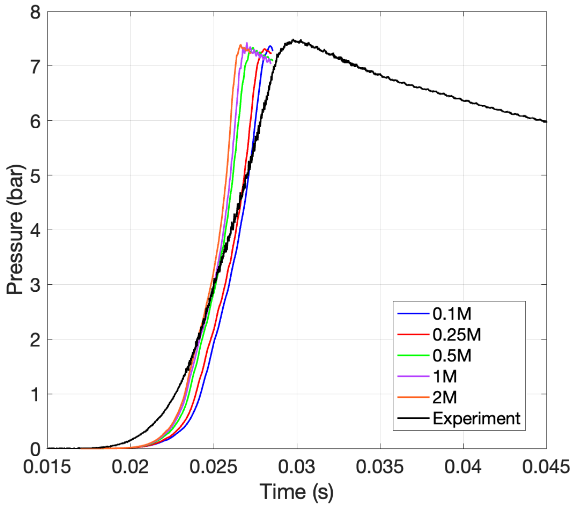

***Fig. 3**: Mesh independence study.*

Number of Cells	Peak Pressure (bar)	Error Percentage (%)
109,760	6.9318	6.68
253,265	7.0700	5.06
519,115	7.2518	2.92
1,080,000	7.4598	0.47
1,945,085	7.4792	0.25
Experimental:	7.5000	(reference)

***Table 2**: Pressure error approximation.*

4.2 Single chamber

We first present the results of the single chamber experiments, where pressure piling was not observed. This can be seen from Fig.4 in which the experimental data taken on the opposite end face of the chamber is plotted. There is a peak pressure of 7.49 bar at $t = 30$ ms. The pressure gradient between $t = 23$ ms and $t = 28$ ms is $\Delta p/\Delta t \approx 1054$ bar/s and shows a gradual increase until peak pressure is reached. By this point all of the unburnt hydrogen gas will have been consumed and the pressure decays back toward atmospheric.

The heat release rate (HRR) was calculated from the experimental pressure curve using the following equation and shown in Fig. 5:

$$\frac{dQ}{dt} = \frac{1}{\gamma - 1} V \frac{dp}{dt} \tag{17}$$

where γ, V and p are specific heat ratio of the oxidiser, volume of the chamber and pressure respectively. It must be noted that the specific heat ratio changes with temperature, however, it is considered to be constant: $\gamma = 1.35$. To obtain the HRR the pressure signal was interpolated and then a Savitzky–Golay filter (polynomial order = 4, window = 50) was utilised during differentiation. The HRR is usually used to investigate the ignition delay properties of the experiment. The maximum HRR is 16.5 kW and occurs gradually over a period of time.

The numerical comparison is made in Fig. 6. This shows good correlation between both numerical results and the experimental data. The peak pressure and pressure gradient are both simulated well and are within an approximate percentage error of 4%. The initial pressure gradient between $t = 20$ ms

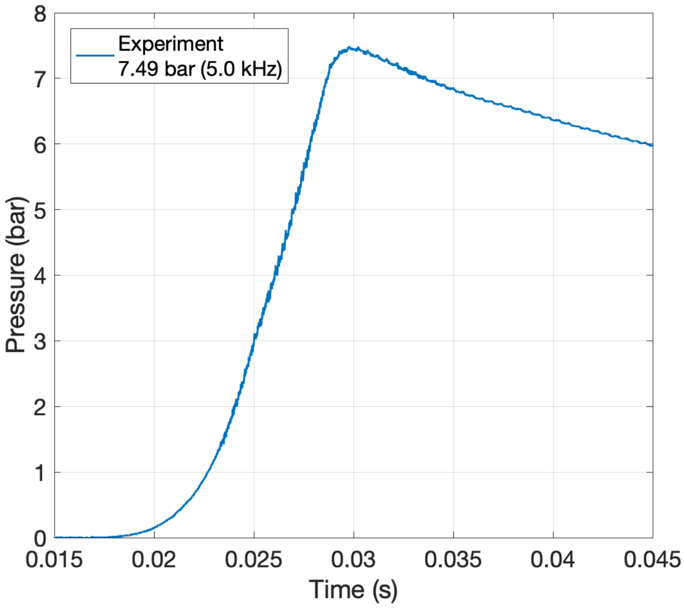

***Fig. 4**: Single chamber experiment.*

DOI: 10.7795/810.20221124

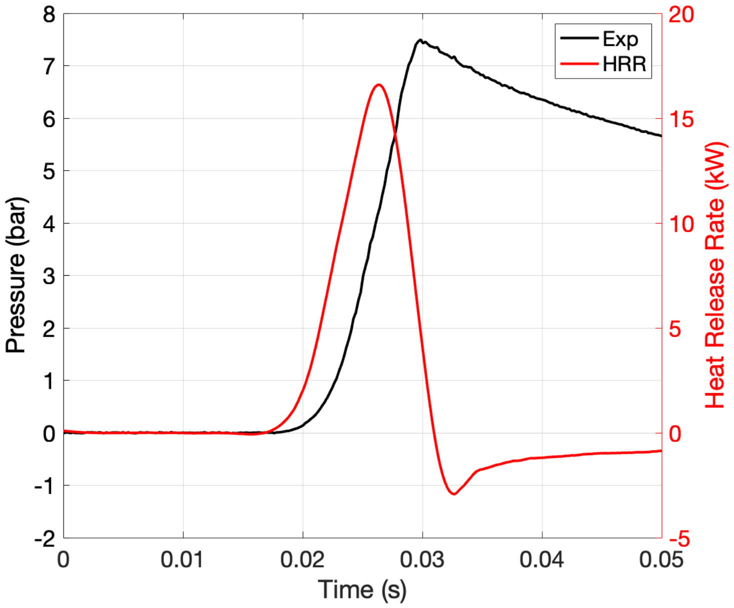

__Fig. 5__: Single chamber heat release rate.

and $t = 25$ ms is captured very well by both solvers. A small amount of deviation is then seen before the peak pressure is reached. The XiFoam result is in very good agreement in terms of peak pressure localisation and magnitude. The rhoReactingFoam result does not capture the peak as accurately but is still in good agreement.

Fig. 7 presents the XiFoam results comparing contour plots of pressure, velocity (line integral convolution) and temperature over various time steps. From the first time step presented ($t = 20.8$ ms) it can be seen that the pressure wave front is travelling ahead of the combustion front. At $t = 23.8$ ms the unburnt hydrogen is compressed at the opposite end of the chamber from the ignition point and the pressure wave is then reflected from that wall. Half of the flow is reversed increasing the amount

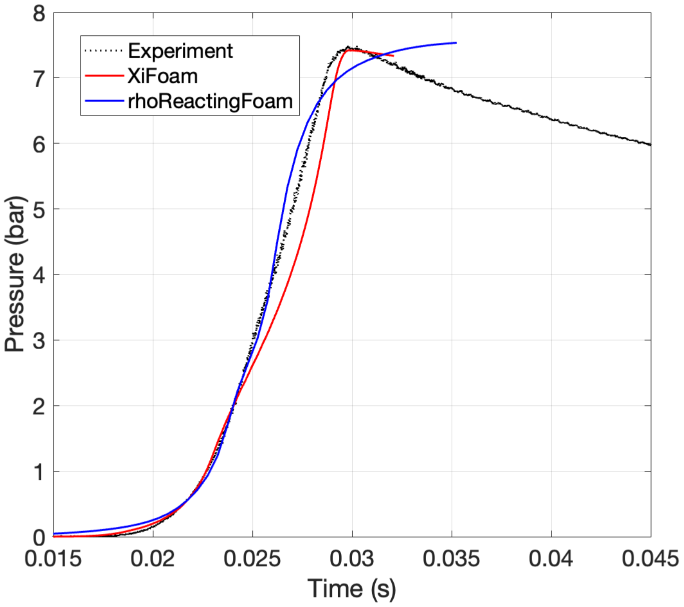

__Fig. 6__: Single chamber experiment and simulation comparison.

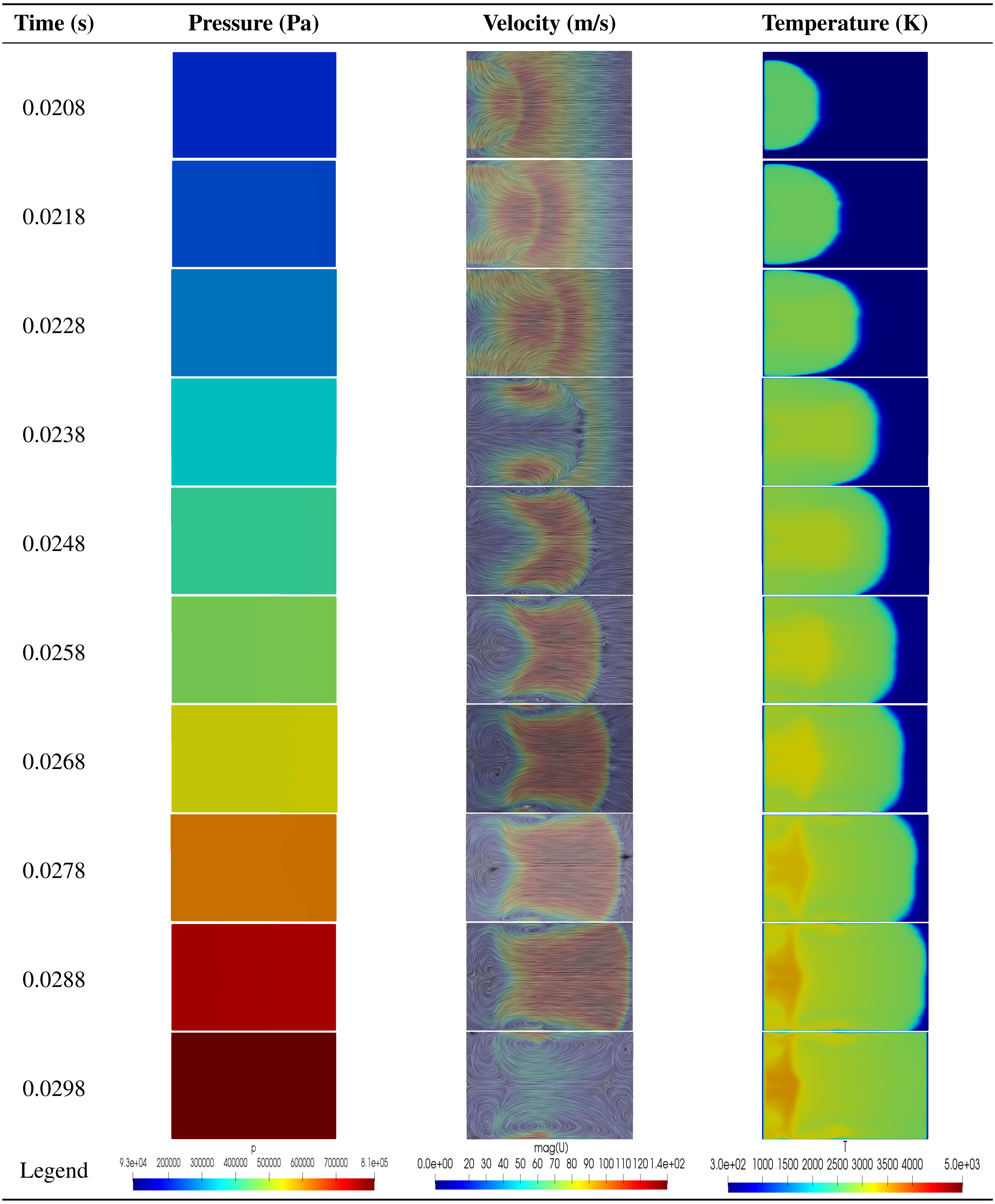

Fig. 7*: Pressure (p), velocity (U) and temperature (T) numerical comparison of various time steps (XiFoam result).*

DOI: 10.7795/810.20221124

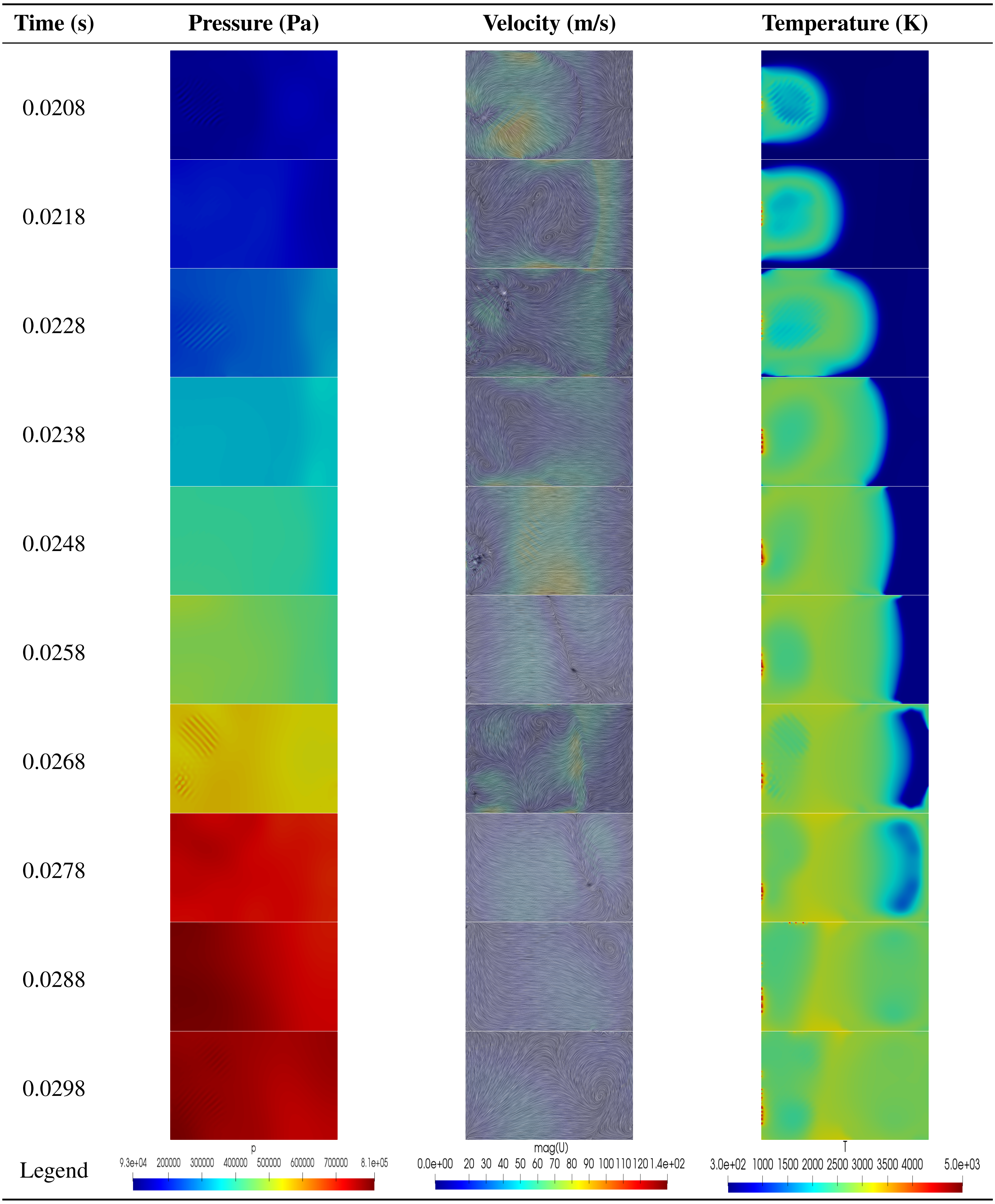

***Fig. 8**: Pressure (p), velocity (U) and temperature (T) numerical comparison of various time steps (rhoReactingFoam result).*

of turbulence in the burnt gas. As the pressure wave is reflected from the end wall, it will interact with the combustion wave initially slowing it down. However, the increase in turbulence will then help to accelerate it again. The hydrogen is mostly combusted at $t = 29.8$ ms just as the peak pressure is reached. A thin section of unburnt gas can be seen at either end of the domain which is due to the boundary conditions. A peak velocity of $U = 45$ m/s is achieved along with a peak temperature of $T = 3500$ K.

In comparison Fig. 8 presents the rhoReactingFoam results comparing pressure, velocity and temperature at the same time steps as before. The pressure wave formed is not as visible in these results, due to the scale range used. Again, at $t = 22.8$ ms the unburnt gases are compressed ahead of the combustion wave meaning the pressure wave is leading in time and in front of the flame front. The pressure contour plots are very different to the XiFoam results showing a much more uniform distribution. There is a lack of symmetry shown in the velocity vector plots also when compared to the XiFoam results. The flow behind the combustion wave can be seen to have revered at $t = 22.8$ ms as the pressure wave is reflected from the end wall. The maximum temperature reached is $T = 5000$ K which is the limit of the mechanism model. This is a numerical related effect and such temperature is observed at the boundaries, caused by the ignition source and can be corrected by using a different method of ignition, however this did not seem to affect the present results. A similar issue is found with the velocity as the maximum velocity reached is $U = 140$ m/s which is only observed near the boundary walls, and may be corrected by changing the boundary condition from *slip* to *noSlip* for example, however again the effects on the whole are localised and did not affect the computed solution. Comparing both sets of results shows good correlation in terms of pressure gradient and flame propagation.

The two solvers XiFoam and rhoReactingFoam utilises different equations as explained in section 3. In XiFoam when considering equations 2 and 3, the initial turbulent kinetic energy and turbulent kinetic energy dissipation rate values have been varied and tested. When using the initial values $k = 1.5$ m^2/s^2, $\varepsilon = 217.55$ m^2/s^3, the turbulent length scale (defines the size of the smallest eddy) was 7.6×10^{-4}. When lowering the initial k and ε ($k = 0.0015$ m^2/s^2, $\varepsilon = 0.00687$ m^2/s^3) and keeping the turbulent length scale the same, the pressure rise was slower as both the initial turbulent kinetic energy was low and turbulent length was the same. The two tests are compared in Fig. 9, where the pressure rise can be observed. Within the XiFoam solver, the pressure rise is affected based on the initial k and ε values.

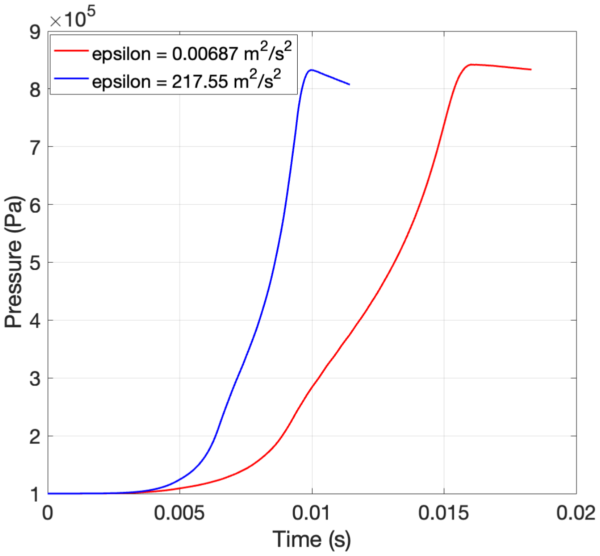

***Fig. 9**: Comparison of the pressure rise when varying k and ε*

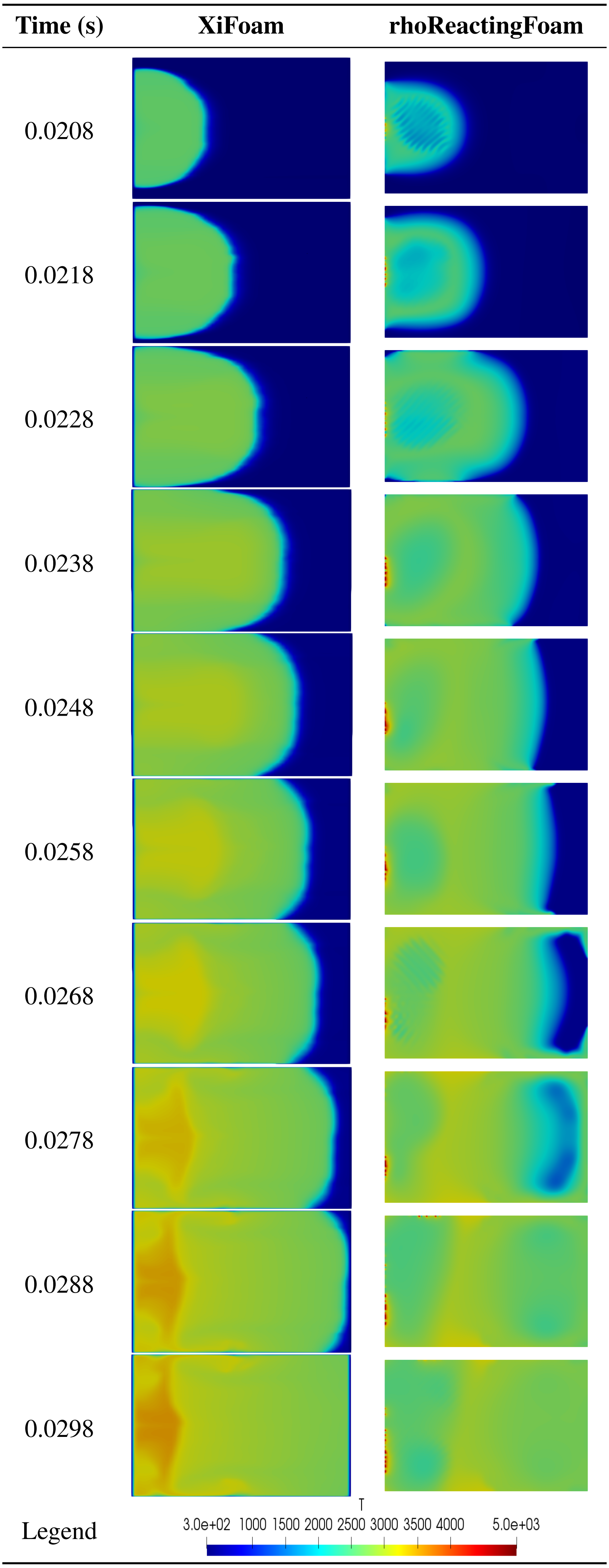

Fig. 10*: Temperature (K) contour plot, solver comparison over certain time steps*

4.3 Solver comparison

Fig. 10 presents a comparison of temperature profiles between both solvers, over a series of time steps ($t = 20.8$ ms to $t = 29.8$ ms). It can be seen that just after ignition the flame front propagates from the ignition source on the left towards the end wall on the right (where the pressure transducer is located). The location of the ignition source is where the hottest point is found, which is approximately $T = 3500$ K. At $t = 28.8$ ms most of the hydrogen has been consumed and the peak pressure has already been reached. In terms of flame propagation both solvers are in good agreement with one another. However, from the rhoReactingFoam results at $t = 27.8$ ms a small pocket of unburnt gas is formed due to the gas flow velocities, but which is then eventually consumed. This does not occur in the XiFoam result. The shape of the flame front also differs between the solvers with the rhoReactingFoam result seemingly being more diffusive than the XiFoam result. At $t = 20.8$ ms from the rhoReactingFoam results, at the ignition point an inconsistency can be seen which most likely to be induced by the mesh and the numerical discretisation. The main differences between the two solvers is the near wall results. The flame front at the walls from rhoReactingFoam at $t = 25.8$ ms can be seen to accelerate at the walls and starts to overtake the flame front. The burning temperature of both results is similar at approximately $T = 3000$ K. Overall the energy in both systems are similar as the peak pressure from both solvers are also similar and in good agreement with the experiment even though the transients in the two simulations are different. Within the XiFoam results a hot spot is formed from $t = 27.8$ ms where ignition occured. The rhoReactingFoam results, a small patch of high temperature cells on the left wall reach $T = 5000$ K which is the reaction mechanism limit which is most likely non-physical. In general, both results are in good agreement in terms of flame propagation and flame temperature.

4.4 Dual chamber

A comparison of both experimental results is shown in Fig. 11 where the peaks have been aligned. This highlights the differences between both sets of results and brings to evidence the challenge that both solvers have in order to simulate pressure piling. The dual chamber result has a much steeper and quicker rise time to a larger peak pressure than the single chamber result. The dual chamber

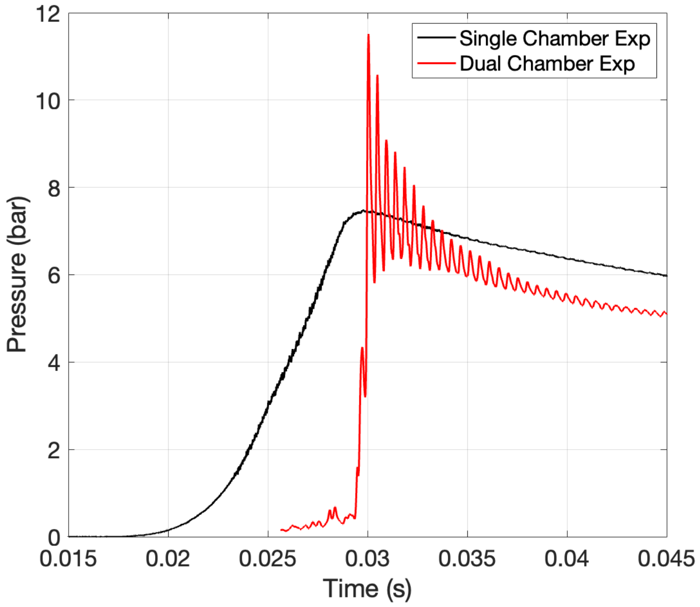

***Fig. 11**: Single and dual chamber experimental results comparison (filtered signals) with peak pressures aligned.*

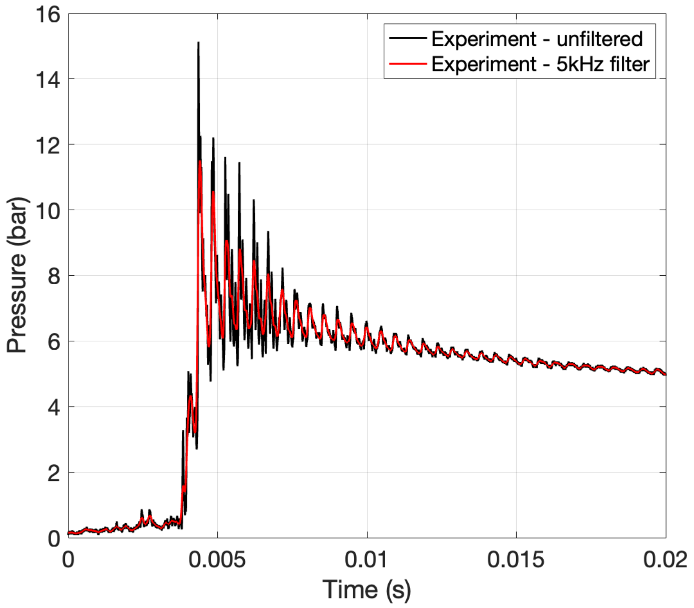

***Fig. 12**: Dual chamber experimental result including filtered signal.*

simulations are extremely difficult and are currently a work-in-progress by both solvers. As evident by Fig. 11, the solvers need to handle an extremely sharp pressure gradient, essentially a shock wave.

The dual chamber experiment and simulation results are presented as preliminary in this section. Within this geometry, pressure piling was observed as seen in Fig. 12. Within the secondary chamber a peak pressure of $p = 11.5$ bar occurred at $t = 4.4$ ms. It can be seen that the pressure gradient before the peak pressure is much steeper when compared to the single chamber experiment. This pressure gradient is $\Delta p/\Delta t \approx 16341$ bar/s between $t = 4.2$ ms and $t = 4.3$ ms which constitutes to the pre-compression occurring before the peak pressure. The pressure then decays as previously back to atmospheric.

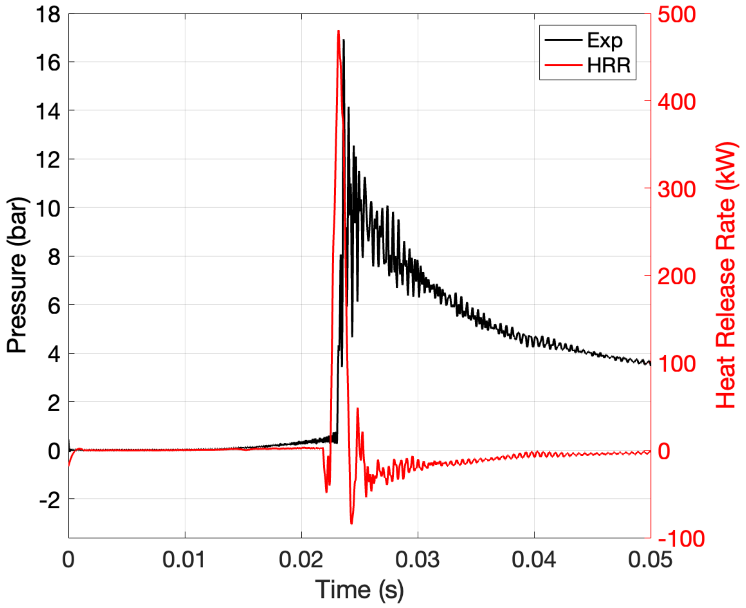

***Fig. 13**: Dual chamber heat release rate.*

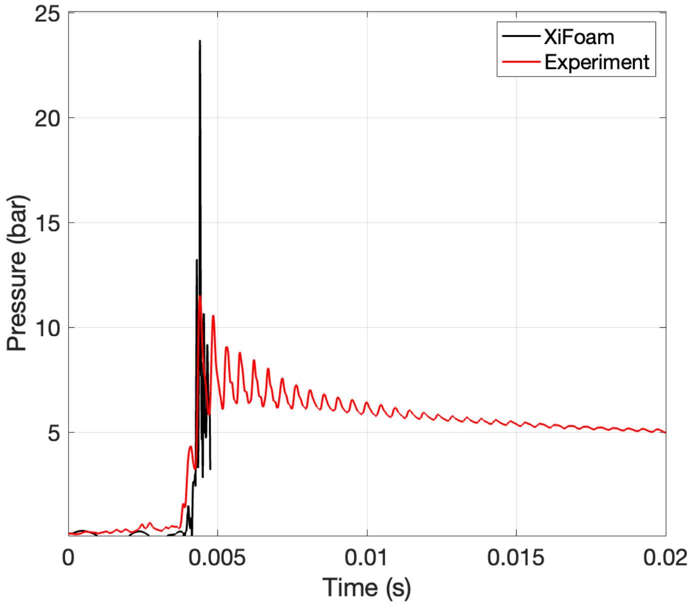

Fig. 14: *Dual chamber comparison (XiFoam result).*

As previously presented, the HRR is calculated from the dual chamber pressure signal and shown in Fig. 13. The maximum HRR is approximately 480 kW which is a factor of 30 larger when compared to the single chamber experiment. The combination of a larger volume but also the pressure piling phenomenon has a large effect on the HRR.

An initial comparison between the numerical (XiFoam) and experimental results are shown in Fig. 14. There is a large overshoot from the XiFoam result after which the solver failed. The overshoot can be controlled by using higher order discretisation schemes for the gradient terms where gradient limiters can also be employed. Similar results were gained with the rhoReactingFoam solver. However, in a similar to the XiFoam result the simulation crashed due to the Courant number exploding and the time step crashing. This is mostly likely due to an ill-defined mesh where nonphysical velocities are created and the time step plummets to very low numbers. The k-ΩSST turbulence model was also trailed due to near wall improvements, the simulation improved but the combustion rate was very slow. Therefore, the mesh is required to be improved and the simulations are a work-in-progress.

5 Conclusions

Explosions within small confined enclosures can produce large over-pressures especially when the phenomenon of pressure piling is involved. Pressure piling is only seen within the dual chamber experiment which is yet to be fully simulated. However, simulations of the single chamber have proven to be successful. The dual chamber simulations have proven difficult, however, the initial results are encouraging. Effort needs to focused on capturing the pressure shock front accurately as this is one of the most difficult to simulate. Overall, the simulation results of the single chamber are in good agreement with the experimental. The main attributes of the experimental data; peak pressure and pressure gradient are captured well. Both solvers utilised simulate the pressure curves well but there are a number of differences that can be seen. The experimental results of the single and dual chambers prove the effects that the pressure piling phenomenon has on the maximum over-pressure of the system. Understanding pressure piling through simulation is key to explosion safety, for example, power plants.

Acknowledgements

The primary author gratefully acknowledges the sponsorship from Rotork Controls Ltd.

References

Barton, I. E. (1998). *Comparison of simple and piso-type algorithms for transient flows*. Int. J. Numerical methods in fluids, 26:459–483.

Benedetto, A. D., Salzano, E. (2010). *Cfd simulation of pressure piling*. Journal of Loss Prevention in the Process Industries, 23:498–506.

CCPS (2006). *Safe Design and Operation of Process Vents and Emission Control Systems*. John Wiley Sons, Ltd, combustion and flammability edition.

Charles K. Westbrook, F. L. D. (1981). *Simplified reaction mechanisms for the oxidation of hydrocarbon fuels in flames*. Combustion Science and Technology, 27:31–43.

Foundation, T. O. (2022). *Openfoam ltd.*

Heinrich, H. (1988). *Ablauf von gas und staubexplosionen gemeinsamkeiten und unterschiede*. VDI Berichte, (701).

IEC 60079-1 (2014). *Explosive atmospheres part 1: equipment protection by flameproof enclosures "d"*.

Kim, D., Kim, J. (2019). *Numerical method to simulate detonative combustion of hydrogen-air mixture in a containment*. Engineering Applications of Computational Fluid Mechanics, pages 938–953.

Launder, B. E., Spalding, D. B. (1974). *The numerical computation of turbulent flows.* Computer methods in applied mechanics and engineering, 3:269–289.

Morton, K. W., Mayers, D. F. (1994). *Numerical solution of partial differential equations*. Cambridge University Press.

Oran, E. S., Borris, J. O. (2001). *Numerical Simulation of Reactive Flow*. Naval Research Laboratory. ISBN 0-521-58175-3.

Phylaktou, H., Andrews, G. E. (1993). *Gas explosions in linked vessels*. Journal of Loss Prevention in the Process Industries, 6(1).

Singh, J. (1977). *Gas explosions in single and comparmented vessels*.

Weller, H. G., Tabor, G., Gosman, A. D., Fureby, C. (1998). *Applications of a flame-wrinkling les combustion to a turbulent mixing layer*. The Combustion Institute.

DOI: 10.7795/810.20221124

Research on the flame stability of biodiesel/diesel blends in small-scale combustion based on data fusion

Gongping Mao[a], Huan Mao[a], Zhijian Xu[a], Chunkan Yu[b] & Ulrich Maas[b]

[a] School of Automotive and Traffic Engineering, Jiangsu University, Zhenjiang, China
[b] Institute of Technical Thermodynamics, Karlsruhe Institute of Technology, Karlsruhe, Germany

E-mail: gongping.mao@kit.edu

Abstract

The flame stability has an important influence on the equipment safety and combustion efficiency of small-scale combustors. In this study, the flame images of different biodiesel/diesel blends combustion under different conditions were captured by using a small-scale combustion test apparatus and charge-coupled device (CCD) camera. Through digital image processing technology, the structure sizes and effective areas of combustion flame were acquired and presented as the experimental characteristic parameters of flame stability. The mass fractions of CO_2 and chemical reaction rates of global reaction of the blends combustion, which was presented as the simulated characteristic parameters of flame stability, were calculated by using Fluent software and analysed. Furthermore, another simulated characteristic parameter, extinction temperature of the blends was also investigated numerically because it is especially important for flame stability and safety. And then the flame stability index, which could directly reflect the combustion flame stability, was obtained by fusing the data of all the characteristic parameters through the data fusion technology. The results show that with the increase of air flow rate, the flame height, effective area and extinction temperature increased first and then decreased, the flame width decreased gradually, the CO_2 concentration and chemical reaction rate increased gradually, the flame stability index increased first and then decreased. With the increase of the blending ratio of biodiesel, the extinction temperature increased first and then decreased, the other characteristic parameters of flame stability and flame stability index decreased gradually.

Keywords: *flame stability, blending biodiesel, data fusion, flame stability index, extinction temperature*

DOI: 10.7795/810.20221124

1. Introduction

In combustion systems, the combustion instability would bring some challenges when designing internal combustion engines (Liu et al., 2022), industrial boilers (Yan et al., 2021), rockets (Guo et al., 2021) and other industrial systems. For examples, the combustion instability in engine cylinder may lead to knock, and result in poor emissions and serious environmental pollution. The unstable combustion of pulverized coal in boilers reduces the boiler thermal efficiency, and in serious cases, it would lead to the accumulation of pulverized coal and occurrence of an explosion. Combustion flame could directly reflect the combustion state, so research on the flame stability could be conducive to enhance the combustion stability and reduce the unexpected explosion, environmental pollution, and other safety hazards.

In recent years, the rapid development of micro-electronic mechanical systems (MEMS) has attracted widespread attention (Nastro et al., 2020). With the characteristics of small volume, lightweight, and high energy density, the small-scale combustor fueled with liquid hydrocarbon fuels is applied to MEMS for energy supply (Yang et al., 2019). However, large surface-to-volume ratio and the small chamber size may cause the large heat loss, short residence time, easy radical quenching and thermal quenching. Therefore, the flame of small-scale combustors is less stable, which would lead to low combustion efficiency, equipment damage, and potential safety hazard. Thus, the flame stability of small-scale combustor is of great interest, which is the focus of this work.

The flame stability of gas hydrocarbon fuels in small-scale combustors has been studied by many researchers via experimental or numerical methods. Bagheri et al. studied the flame stability of hydrogen–air mixture in different miniature blunt-body combustors. They concluded that when the inlet velocity of the blending gas is increased from 20 m/s to 30 m/s, the flame of the mini-wall blade bluff body combustion chamber is more stable than the flame of other shapes of bluff body combustion chambers (Bagheri et al., 2014). In addition, Yan et al. found that the controllable slotted bluff body produced a double backflow zone and made the high-temperature field expand, which could enhance the combustion efficiency and flame stability of hydrogen (Yan et al., 2019). Hu et al. experimentally studied the flame stability of blending biogas and hydrogen in the constant volume combustion bomb. The results show that the flame instability increases with the decrease of equivalence ratio, and the global flame stability decreases with the increase of CO_2 fractions (Hu et al., 2019). Tang et al. studied the effect of hydrogen addition on the small-scale combustion of pure propane and found that the addition of hydrogen could overcome the inertia of inlet velocity and inhibit the change of flame morphology so that the flame could maintain symmetrical and stable combustion (Tang et al., 2021). Askari et al. studied the laminar burning velocity and the flame instability of $H_2/CO/O_2/He$ in cylindrical and spherical cavity vessels by differential multi-shell thermodynamic models. They reported that He thinner can significantly improve the flame stability because He can increase the thermal diffusivity (effective Lewis number) and the flame thickness (Askari et al., 2017). Davani et al. used the Reynolds stress model (RSM) to simulate the flow and the eddy dissipation model (EDM) to simulate the CH_4/Air combustion system with two-step chemical reaction. The calculation results show that when the circular jet is used in the inlet, increasing the number of air intakes can enhance the forced vortex field in the central and secondary refluxed areas, thus making the flame more stable and rigorous (Davani et al., 2019).

Compared with gaseous fuels, liquid fuels have the advantages of high energy density and easy storage. Therefore, they are more suitable for micro-energy systems. However, as far as the authors are aware, only Gan's group has carried out research on the ethanol combustion in small-scale at present (Gan et al., 2015 and 2017). They analyzed the effect of alternating current (AC) electric field on flame behaviors of ethanol combustion in small-scale stainless-steel tubes experimentally and found that the increase of AC frequency and strength was beneficial to the enhancement of flame stability. They also investigated the effect of direct current (DC) electric field and found that the increase of DC strength could accelerate the chemical reaction and enhance the flame stability.

Biodiesel, with the advantages of renewable, easy biodegradation, non-toxic, low sulfur content, could be used as fuel alone or combined with diesel fuel, and has great application potential in small-scale combustion (Karami et al., 2020 and 2021). However, in the published literatures it is rarely reported the study on flame stability of biodiesel combustion in small-scale. The diffusion capacity of biodiesel is lower than that of diesel fuel, which would lead to combustion instability. Hence, it is meaningful to research the flame stability of biodiesel in small-scale combustor.

In addition, many existing studies mainly focus on analyzing the relationship between different single factors and flame stability. In fact, some factors may not have a strict linear relationship with flame stability, and there are even contradictory effects of different factors on flame stability, and even diametrically opposite conclusions (Wang et al., 2020). In other words, due to the large number of influencing factors, it is difficult to make a comprehensive evaluation of the effects on flame stability. Therefore, it is necessary to use a comprehensive research strategy on flame stability. Data fusion, an emerging research discipline of data processing, could analyze, handle, control, and use the information to describe the state of the tested object, make the system each part or overall performance achieve better decision and provide the reference for the process of estimating mission. Especially, it could combine intelligently multiple data to improve the accuracy of observation or identification, and has been widely applied in many fields (Castanedo et al., 2013; Chen et al., 2021). For instance, Jiang et al. firstly classified Jinhua ham by using distance-probability classification according to multiple sensory technology data of Jinhua ham at different aging times and then established a prediction model of sensory properties of Jinhua ham by data fusion (Jiang et al., 2021). Similarly, Yu et al. used digital image processing to calculate and extract the five characteristic parameters (The flame area, average gray, the area ratio, connectivity, and rectangular fullness) from the flame images. Based on the SOM neural network and SVM algorithm, they fused these characteristic parameters and constructed a flame stability diagnosis model (Wang et al., 2020). The prediction accuracy of the diagnosis model could become more than 90%, which could detect the gas combustion state according to the collected flame image. In the same way, this study presented a new method of evaluating flame stability, that used data fusion to fuse several evaluation indicators of flame stability, then got the flame stability index to the comprehensive judgment of flame stability, which is advantageous to judge the flame stability more accurately.

In this study, multiple evaluation indicators from experiment and numerical simulation were used to diagnose the flame stability of biodiesel/diesel blends in the small-scale combustor. The evaluation indicators were proposed via digital image processing and numerical simulation, and then based on the weighted average, the decision-level with the highest fault tolerance rate and accuracy was selected to fuse them to obtain the flame stability index, which could directly reflect the flame stability. It was conducive to better analysis of flame stability and could provide a certain theory for the better application of biodiesel in small-scale combustors and the enhancement of combustion stability and equipment safety.

2. Methodology

In general, data fusion is a method for data processing, which analyzes, handles, controls, and uses the sensor information to describe the state of the tested object, thus to make the system each part or overall performance achieve better decision and provide the reference for the process of estimating mission. Data fusion can be divided into three levels (Golrizkhatami et al., 2018; He et al., 2021) according to the fusion objects: data level-fusion, feature-level fusion, and decision-level fusion. Data-level fusion refers to the direct fusion of the original data. Feature-level fusion requires feature extraction from original data, and then the extracted feature values are fused. Decision-level fusion is based on feature-level fusion for analysis and recognition and then fusion.

In this study, the decision-level fusion with the highest fault tolerance rate and accuracy is selected to fuse the flame stability indicators. Fig.1 shows the step diagram of decision-level fusion. As shown in Fig.1, the height, width, and effective area of combustion flame, obtained by experiments and presented as the experimental characteristic parameters of flame stability, were considered as Feature

1, Feature 2, and Feature 3 (named F1, F2, and F3), respectively. The CO_2 concentration, chemical reaction rate of global reaction, and extinction temperature, obtained by numerical simulation and presented as the simulated characteristic parameters, were taken as Feature 4, Feature 5 and Feature 6 (named F4, F5, and F6), respectively. And then, the relationships between the identified features and flame stability were analyzed. Finally, the weighted average was applied to decision-level fusion and the flame stability index (named M) would be calculated according the formula (1).

$$M = \sum_{i=1}^{6} \beta_i B_i \quad \left(\sum_{i=1}^{6} \beta_i = 1 \right) \tag{1}$$

where B_i is the normalization of the value of Feature i, β_i is the weight of Feature i and equal to 1/6 in this study.

B_i could be calculated according the formula (2).

$$B_i = A_i / A_{i\max} \quad (i = 1, 2, ..., 6) \tag{2}$$

where A_i is the value of Feature i, $A_{i\max}$ is the maximum value of A_i.

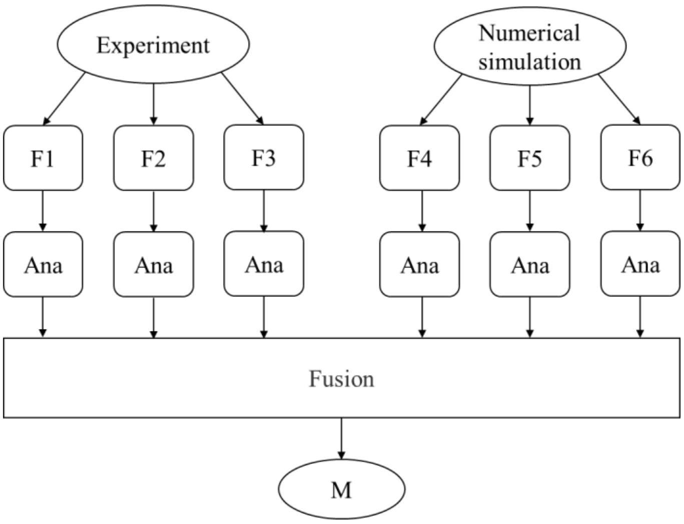

Fig. 1. *The step diagram of the decision-level fusion*

2.1 Methods for acquiring the experimental characteristic parameters

Fig.2 shows the schematic diagram of the experimental setup. The main parameters of the small-scale combustor are shown in Table 1.

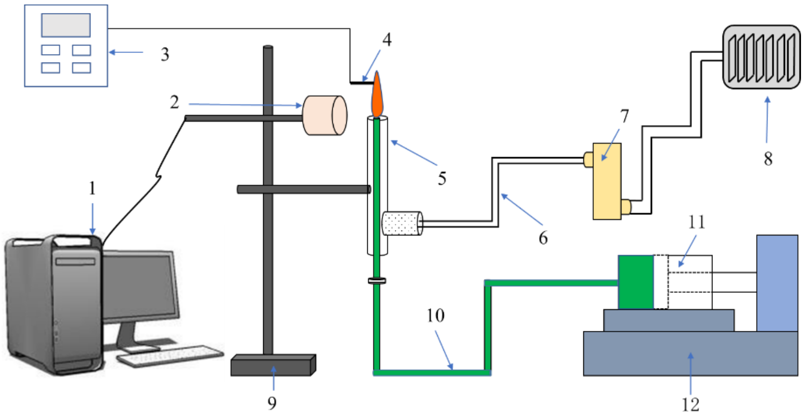

1-Computer; 2-High-speed camera; 3-Temperature indicator; 4-Thermocouple; 5-Small-scale combustor; 6-Intake tube 7-Air flow meter; 8-Air pump; 9-Steel stand; 10-Fuel inlet pipe; 11-Syringe; 12-Micro fuel pump

Fig.2. *The structure diagram of the experimental system*

The test fuels were the mixture fuel consisted of 0# diesel (bought from China National Petroleum Corporation) and homemade soybean biodiesel fuel, named B0, B25, B50, B75 and B100, in which the numerals represent the volume ratio of biodiesel in the blends. Table 2 shows their main properties. The flow rates of the fuels were a fixed volume flow of 0.8 mL/min. The flow rates of air were from 0 to 12 L/min. A K-type thermocouple with 0.1 mm diameter is used to measure the flame temperature, and a high-speed camera (Canon F0816) was used to capture the combustion flame images. Median filtering method (Aguiar et al., 2019) were used to denoise the original images to remove the interference of noise and make the images clearer. To separate the flame image from the background and make the image edge outline is clearer, Otsu method (Xiao et al., 2019) were used to enhance the denoised images. Finally, the processed images facilitate the calculation for the experimental characteristic parameters, such as the height, width and effective areas of combustion flame, which could effectively reflect the combustion state of the flame (Gan et al., 2016; Wang, et al., 2020).

Table 1: *Relevant dimension parameters of burners*

Parameters	Unit	Value
Quartz tube inner diameter	mm	5
Quartz tube outer diameter	mm	7
Double-pass stainless steel tube inner diameter	mm	20
Double-pass stainless steel tube outer diameter	mm	23
Plug thickness	mm	12

Table 2: *Comparison of physicochemical characteristics between soybean biodiesel and diesel*

Physical and chemical properties	Unit	Diesel fuel	Soybean biodiesel fuel
Calorific value	$MJ\cdot kg^{-1}$	42.5	37.5
Density	$g\cdot mL^{-1}$(20 °C)	0.837	0.885
Oxygen content	%	0	10.89
Kinematic viscosity	$mm^2\cdot s^{-1}$(20°C)	3.2	4.5
Flash point	K	328	>422
Cetane number	-	45	47.1
Sulfur content	$\mu L\cdot L^{-1}$	196	<3

The flame height H_y, flame width W_y and effective flame areas could be calculated by formula (3), Formula (4), and Formula (5) respectively.

$$H_y = k[\max(y_1, y_2, ..., y_n) - \min(y_1, y_2, ..., y_n)] \tag{3}$$

$$W_y = k[\max(x_1, x_2, ..., x_n) - \min(x_1, x_2, ..., x_n)] \tag{4}$$

$$S = k^2 \sum_{i=1}^{m} \sum_{j=1}^{m} F(g(i,j) - th) \tag{5}$$

where, x and y are the horizontal and vertical coordinates corresponding to pixel points respectively, k is the scale coefficient of object and image, m and n are the pixel points in the horizontal and vertical directions, g (i, j) is the gray value at point (i, j), th is the segmentation threshold, Fx is the step function, which is defined as Formula (6).

$$Fx = \begin{cases} 1, x \geq 0 \\ 0, x < 0 \end{cases} \tag{6}$$

The error of the flame structure size and effective area calculated by MATLAB is controlled at 1%

2.2 Methods for acquiring the simulated characteristic parameters

2.2.1 CO2 concentration and chemical reaction rate of global reaction

The Fluent software was used to calculated the CO_2 concentration and chemical reaction rate of global reaction. The sizes of the combustor were the same as Table 1. The height of the burner is set as 10 mm. Since the combustor model is symmetrical, only half of the physical model needs to be established. The width and height of the grid model was 30 mm and 60 mm. The grid had 50800 cells and meet the grid independence verification. Table 3 showed the boundary names and boundary types of the grid model, where boundary slip is not considered for the inner and outer walls of the combustor. The inner and outer walls of the burner are made of quartz and stainless steel, respectively. Table 4 showed the thermophysical properties of quartz and stainless steel at 298.15 K. Table 5 listed the relevant models selected in the calculation.

Table 3: *Boundary names and boundary types of the grid model*

Serial number	Boundary name	Boundary type
1	Fuel inlet	Velocity-inlet
2	Air inlet	Velocity-inlet
3	Inner wall of the combustor	Wall
4	Outer wall of the combustor	Wall
5	Axis of symmetry	Symmetry
6	Free boundary	Pressure-outlet

Table 4: *Thermophysical properties of quartz and stainless steel at 298.15K*

Material	Density(kg/m^3)	Thermal conductivity[w/(m·k)]	Cp (Specific heat) [j/(kg·k)]
Quartz	2650	1.4	750
Stainless steel	8030	16	502

Table 5: *The relevant calculation models**

Models	Model selection
1 Radiation model	P-1 Radiation Model
2 Viscous model	RANS with K-epsilon
3 Species model	Species Transport Model
4 Reaction model	Eddy Dissipation Concept (EDC)

*The P-1 radiation model is the simplest type of P-N model. The starting point of the P-N model is to expand the radiation intensity into orthogonal spherical harmonic functions. The Species Transport Model is one of the calculation methods for the gas reaction provided by FLUENT, which involves the processes of the chemical reaction, mixing, and transportation.

The mechanism for biodiesel/diesel fuel was a skeletal mechanism with 115 species and 460 reactions for a tri-component biodiesel surrogate, which consists of methyl decanoate, methyl 9-decenoate and n-heptane (Luo et al., 2012). The second-order upwind scheme was adopted to discretize the set of differential equations. Meanwhile, the “SIMPLE” algorithm was applied to coupling the pressure and velocity. Iteration convergence was judged based on a criterion that the residuals of all variables drop below 1.0×10^{-3}. The flow and combustion process of working medium followed the conservation equation of mass, momentum, energy, and continuity. The accuracy of the model was verified by comparing the calculated and experimental values of temperature and flame structure sizes. The maximum errors of flame height, width and top temperature are 6.9%, 6.1% and 9.2% respectively.

2.2.2 Extinction temperature

The numerical simulations for the extinction temperature were performed using the in-house HOMREA code (Maas et al., 1988; Yu, et al., 2021). The mechanism of biodiesel/diesel was the same as that used in Fluent software. To illustrate the extinction times, the Perfectly Stirred Reactors (PSR) configuration corresponding to the inlet conditions was considered. The fuels are B0, B25, B50, B75, B100, and all conditions are operated under 1 bar with 300 K as inlet temperature. The oxidizer was the 100% air, and their pressure and temperature were the same as the fuels. The equivalent ratio was from 0.5 to 1.5, and the flow rate of the mixture were from 0.1 to 0.3 mol/s. To facilitate comparison, based on the equivalence ratio of fuel and air, molecular formula, density and other properties, the air flow rates corresponding to the molar flow rates of the mixture were calculated.

3. Results and discussions

3.1 Extinction temperature

Fig.3 showed the effects of the blends and air flow rates on the extinction temperature. It could be seen from Fig.3 (a), Fig.3 (b) and Fig.3 (c), with the increase of the blends flow rates, the extinction temperature reduced gradually. When the rate limit was reached, the extinction temperature dropped sharply. When the equivalence ratio was increased by 0.5, the limit of the fuel flow rate increased by about 0.1 mol/s. In addition, the proportion of biodiesel in the blend had little effect on the extinction temperature, and the maximum difference in the maximum extinction temperature of the blends with different proportions was about 20 K. It could be seen from Fig.3 (d) that with the increase of air flow rate, the extinction temperature increased first and then decreased. When the air flow rates were 6~8 L/min, the extinction temperature reached maximum value, which indicated the flame stability was strong. In addition, the lower the air flow and the higher the proportion of biodiesel in the blended fuel, the higher the extinction temperature. Conversely, when the air flow rates were higher and the proportion of biodiesel in the blends was higher, the extinction temperature decreased. This was mainly because biodiesel had a higher oxygen content about 10%. When the air flow rate was low (below 6 L/min), less oxygen was supplied, and the oxygen in the biodiesel could make up for the deficiency, helping to promote combustion. As the air flow continued to increase (at 6-8 L/min), the combustion tended to be stable and the extinguishing temperature increased. However, when the air flow was further increased (above 12L/min), the air would take away a lot of heat, resulting in a lower extinction temperature, even lower than when the air flow rate was lower than 6~8 L/min.

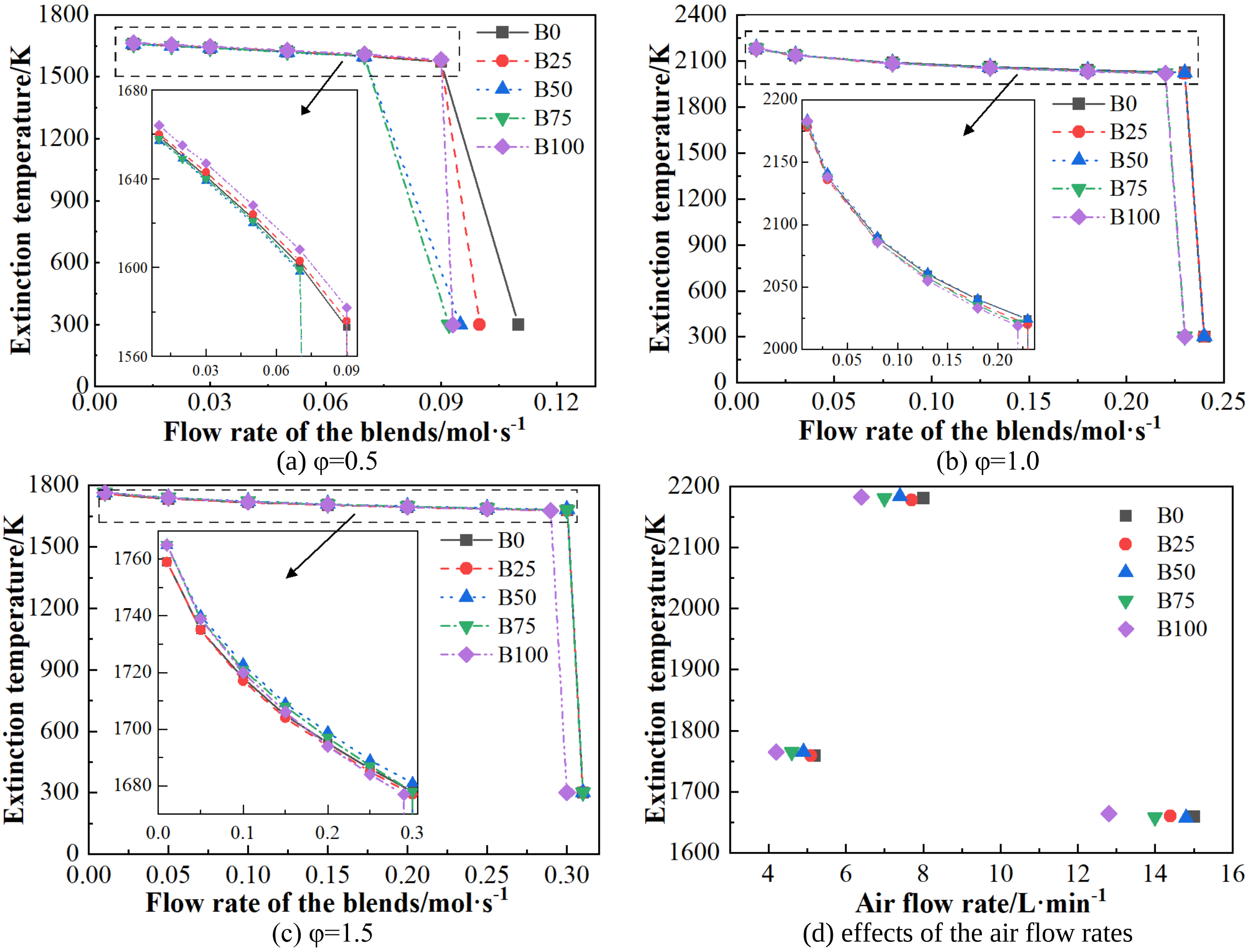

(a) φ=0.5

(b) φ=1.0

(c) φ=1.5

(d) effects of the air flow rates

Fig.3. *The regularity of the extinction temperature*

3.2 Evaluation indicators of flame stability

Fig.4(a), Fig. 4(b), and Fig. 4(c) respectively showed the effects of air flow rates on the flame height, and flame width, and flame effective areas of the different blending ratios of biodiesel and diesel fuel combustion. It could be found that the flame height and flame effective area increased first and then decreased, the flame width decreases gradually. When the air flow rate was 3 L/min, the flame height and flame effective area reached maximum. Thus, the flame stability was the strongest at the air flow rate of 3 L/min, the reason might be that when the air flow rate was below 3 L/min, the oxygen was supplemented by air flow to the benefit of combustion, which made the ability of the flame to diffuse to the outside enhance gradually (Li et al., 2018), resulting in the increase of flame height and flame effective area. But the large air flow rate would reduce the mixing time of fuel and air, and disturb the flame, which would reduce the intensity of combustion and make the unstable flame (Zargar et al., 2020). The pressure on the side of the flame decreased as the air flow increased, so the flame width decreased as the side of the flame was squeezed by the air.

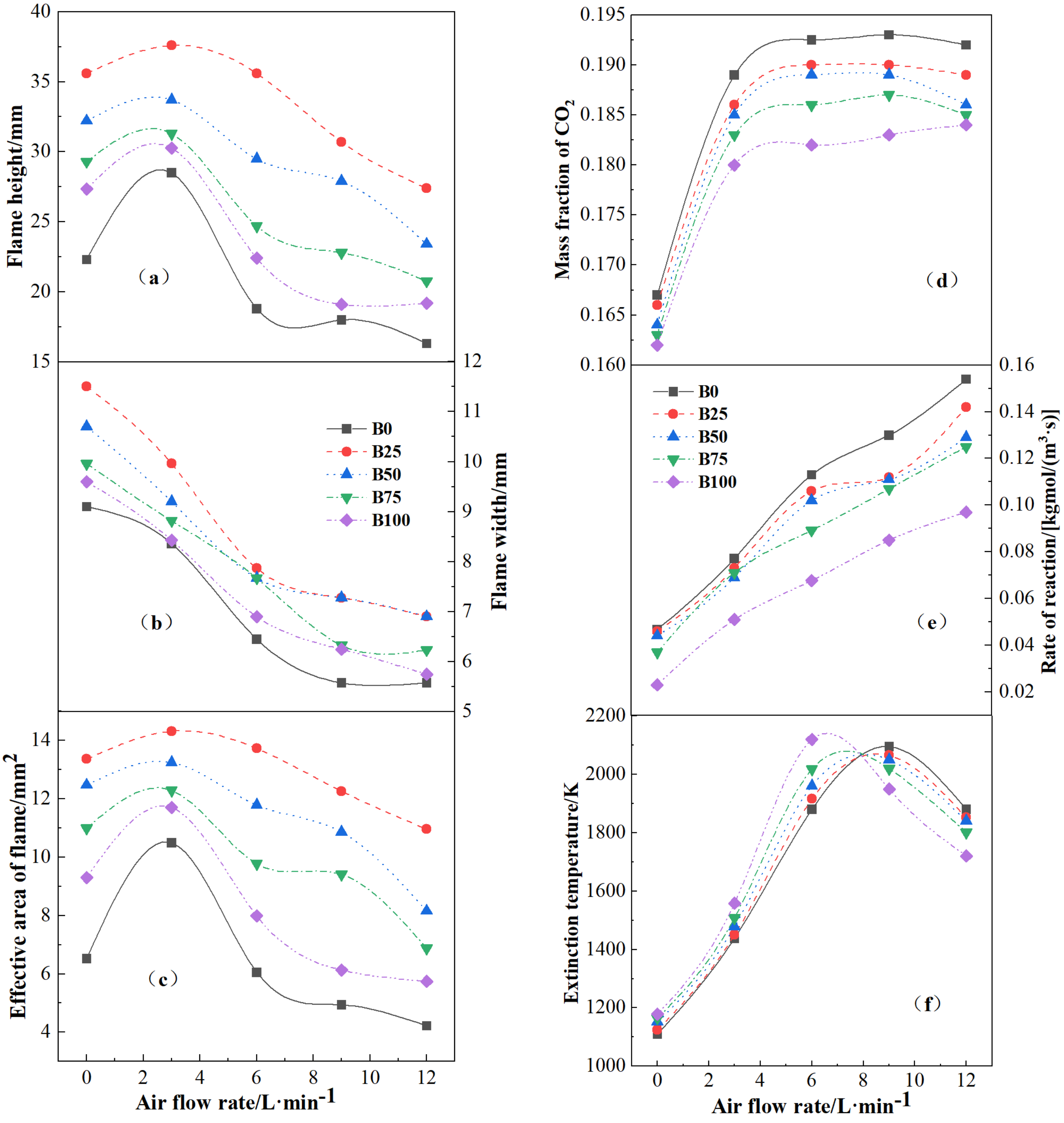

Fig.4. *The regularity of the evaluation indicators of flame stability*

It could be seen from Fig.4(d) that when the air flow rate was in the range of 0 to 3 L/min, with the increase of air flow, maximum CO_2 concentration increased rapidly, indicating that the increase of oxygen content improved the combustion. And when the air flow rate increased from 3 to 12 L/min, a maximum CO_2 concentration increased more slowly, because a larger air flow rate made the combustion disturbance and poor combustion stability. The reason why the increase of the maximum value of CO_2 concentration when the air flow rate above 3 L/min was that the combustion zone was more concentrated (Jiang et al., 2017). Fig.4(e) showed the chemical reaction rate where the maximum value of the chemical reaction rate increased gradually with the increase of air flow rate. This was because the higher the air flow rate is, the higher the oxygen content is, and the faster the chemical reaction rate is. In addition, a larger air flow rate speeds up the diffusion rate of fuel and enhances diffusion combustion (Sujith et al., 2020). Because the numerical simulation was an ideal state, when the air flow rate increases, the fuel diffusion rate, and oxygen content increased, so the chemical reaction rate would always increase with the increase of the air flow rate. However, in the experimental research, the larger air flow rate would have a strong adverse impact on flame, causing the oscillating flame, thereby leading to the weakness of the flame stability (Yuasa et al., 2005; Lu et al., 2019). Fig.4(f) showed that the extinction temperature increased first and then decreased with the increase of air flow. When the air flow rate was 6 L/min, the extinction temperature of B75 and B100 was the highest, and the extinction temperature of B0, B25and B50 was the highest at the air flow rate of 8 L/min.

Simultaneously, it could also be seen from Fig.4 that with the increase of blending ratio of biodiesel, except for the extinguishing temperature, the value of the evaluation indicators of flame stability decreased gradually which indicates that flame stability became poor gradually. When the flow rate was below 6 L/min, the extinction temperature increased. When the flow rate was higher than 8 L/min at first, the extinction temperature decreased. This result may be explained that the lower heat value of the biodiesel causes the reduction of heat released by the combustion (Elkelawya, et al., 2019). The higher viscosity of the biodiesel was unfavorable to evaporation of the fuel, which made the uniformity of the blends decrease and caused the decrease of the released heat by the combustion. Thus, the ability for the flame to extend outward was reduced, resulting in a reduction of the flame effective area and chemical reaction rate (Zhang, et al., 2018). The decrease of the released heat also made the differential pressure between the flame and the outside world decrease, resulting in the decrease of flame height and flame width. In addition, the carbon content of diesel was higher than biodiesel at the same combustion conditions, so the higher the diesel content was, the more CO_2 would be generated (Devarajana, et al., 2020).

3.3 Flame stability index

Fig.5 showed the effects of air flow rates on the flame stability indexes. It could be seen that for B50, B75, and B100, when the air flow rate increased from 0 to 3 L/min, the flame stability indexes all increased, and then the flame stability index decreased gradually as the flow rate continued to increase to 12 L/min. At the air flow rate of 6 L/min, the flame stability indexes of B0 and B25 reached maximum value. At the same air flow rates, when the blend ratios of biodiesel increased, the flame stability indexes decreased gradually. Taking a comprehensive analysis of the flame stability index and the evaluation indicators of flame stability, there were similar change regularities between the stability index and flame stability, which indicated that there was a good linear relationship between the flame stability index and flame stability, and flame stability index could directly and accurately reflect the change regularity of flame stability. Thus, it can be seen from Fig.5 that as the air flow rate increased from 0 to 3 L/min, the flame stability of B50, B75, and B100 gradually increased, then the flame stability gradually weakened when the air flow rates were above 3 L/min, and the flame stability was the strongest when the air flow rate was 3 L/min. In the same way, the flame stability of B0 and B25 was the strongest at the air flow rate of 3 L/min. The reasons for these differences in peak of flame stability indexes were mainly due to that there was about 10% oxygen content in biodiesel fuel, while there was nearly no oxygen in diesel fuel. As a result, the diesel fuel required more oxygen for full combustion than biodiesel did. The flame stability became weak with the increase of the biodiesel blending ratios, which indicated that the addition of biodiesel would weaken the flame stability. Therefore, when the biodiesel fuel was applied in a small-scale burner, an appropriate amount of diesel fuel should be added, which was beneficial to improve combustion stability and equipment safety.

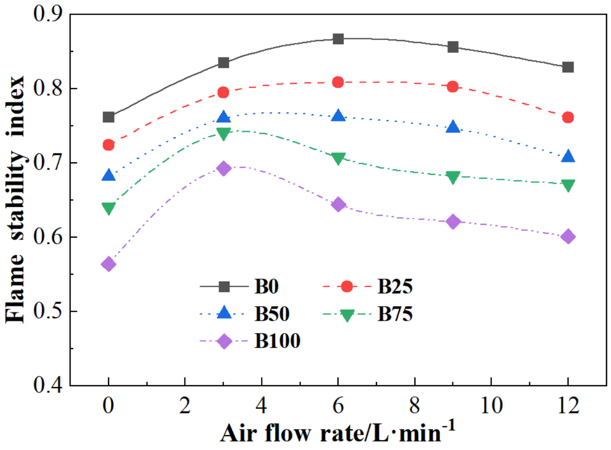

Fig.5. *Variation law of flame stability index*

4. Conclusions

(1) For the blends of diesel fuel and biodiesel fuel burning in small-scale, with the increase of air flow rates, the height, effective areas, and extinction temperatures of the flame increased first and then decreased, the flame width decreased, and the CO_2 concentration, and chemical reaction rate of global reaction increased gradually. With the increase of biodiesel blending ratio, the height, width, and effective areas of the flame, CO_2 concentration, and chemical reaction rate decreased, while the extinction temperature increased gradually when the flow rate was below 6 L/min, then decreased gradually when the flow rates was higher than 8 L/min.

(2) With the increase of air flow rates, the flame stability index increased first and then decreased. When the air flow rates were 3~6 L/min, the flame stability index reached the maximum. With the increase of biodiesel blending ratios, the flame stability index decreased gradually. The flame stability indexes of B0 reached the minimum, and B100 reached maximum.

(3) For the mixture of B0 and B25, when the air flow rate was 6 L/min, the flame stability would become strongest. For B50, B75, and B100, the flame would be the most stable when the air flow rate was 3 L/min. In addition, adding the proportion of diesel could help to enhance the stability and safety of the combustion flame of the blends.

Acknowledgements

The authors gratefully acknowledge the financial contribution from the China Scholarship Council (CSC) (No. 202108320154).

References

Aguiar, G. J., Mantovani, R. G., Mastelini, S. M., de Carvalho, A. C., Campos, G. F., & Junior, S. B. (2019). A meta-learning approach for selecting image segmentation algorithm. *Pattern Recognition Letters*, 128, 480-487.

Askari, O., Wang, Z., Vien, K., Sirio, M., & Metghalchi, H. (2017). On the flame stability and laminar burning speeds of syngas/O_2/He premixed flame. *Fuel*, 190, 90-103.

Bagheri, G., Hosseini, S. E., & Wahid, M. A. (2014). Effects of bluff body shape on the flame stability in premixed micro-combustion of hydrogen–air mixture. *Applied Thermal Engineering*, 67(1-2), 266-272.

Castanedo, F. (2013). A review of data fusion techniques. *The scientific world journal*, 2013.

Chen, C., Chen, Q., Li, G., He, M., Dong, J., Yan, H., ... & Duan, Z. (2021). A novel multi-source data fusion method based on Bayesian inference for accurate estimation of chlorophyll-a concentration over eutrophic lakes. *Environmental Modelling & Software*, 141, 105057.

Davani, A. A., Amini, R., & Kashfi, M. (2019). Effects of reactor design parameters on stability and emissions of vortex flames: A numerical study. *Applied Thermal Engineering*, 155, 584-591.

Devarajan, Y., Nagappan, B., Mageshwaran, G., Kumar, M. S., & Durairaj, R. B. (2020). Feasibility study of employing diverse antioxidants as an additive in research diesel engine running with diesel-biodiesel blends. *Fuel*, 277, 118161.

Elkelawy, M., Bastawissi, H. A. E., Esmaeil, K. K., Radwan, A. M., Panchal, H., Sadasivuni, K. K., Ponnamma, D., & Walvekar, R. (2019). Experimental studies on the biodiesel production parameters optimization of sunflower and soybean oil mixture and DI engine combustion, performance, and emission analysis fueled with diesel/biodiesel blends. *Fuel*, 255, 115791.

Gan, Y., Luo, Y., Wang, M., Shi, Y., & Yan, Y. (2015). Effect of alternating electric fields on the behaviour of small-scale laminar diffusion flames. *Applied Thermal Engineering*, 89, 306-315.

Gan, Y., Wang, M., Luo, Y., Chen, X., & Xu, J. (2016). Effects of direct-current electric fields on flame shape and combustion characteristics of ethanol in small scale. *Advances in Mechanical Engineering*, 8(1), 1687814015624846.

Golrizkhatami, Z., & Acan, A. (2018). ECG classification using three-level fusion of different feature descriptors. *Expert Systems with Applications*, 114, 54-64.

Guo, K., Ren, Y., Chen, P., Lin, W., Tong, Y., & Nie, W. (2021). Analysis of spontaneous longitudinal combustion instability in an O_2/CH_4 single-injector rocket combustor. *Aerospace Science and Technology*, 119, 107209.

He, B., Cao, X., & Hua, Y. (2021). Data fusion-based sustainable digital twin system of intelligent detection robotics. *Journal of Cleaner Production*, 280, 124181.

Hu, Z., & Zhang, X. (2019). Experimental study on flame stability of biogas/hydrogen combustion. *International Journal of Hydrogen Energy*, 44(11), 5607-5614.

Jiang, S., Ni, C., Chen, G., & Liu, Y. (2021). A novel data fusion strategy based on multiple intelligent sensory technologies and its application in the quality evaluation of Jinhua dry-cured hams. *Sensors and Actuators B: Chemical*, 344, 130324.

Jiang, Y. H., Li, G. X., Li, F. S., Sun, Z. Y., & Li, H. M. (2017). Experimental investigation of correlation between cellular structure of the flame front and pressure. *Fuel*, 199, 65-75.

Karami, R., Rasul, M. G., & Khan, M. M. (2020). CFD simulation and a pragmatic analysis of performance and emissions of tomato seed biodiesel blends in a 4-cylinder diesel engine. *Energies*, 13(14), 3688.

Karami, R., Rasul, M. G., Khan, M. M. K., Salahi, M. M., & Anwar, M. (2021). Experimental and computational analysis of combustion characteristics of a diesel engine fueled with diesel-tomato seed oil biodiesel blends. *Fuel*, 285, 119243.

Li, H. M., Li, G. X., Jiang, Y. H., Li, L., & Li, F. S. (2018). Flame stability and propagation characteristics for combustion in air for an equimolar mixture of hydrogen and carbon monoxide in turbulent conditions. *Energy*, 157, 76-86.

Liu, J. J., Ding, S. F., Ding, S. L., Gao, J. S., Song, E. Z., & Yang, F. Y. (2022). Effects of gas injection timing on combustion instability for a spark ignition natural gas engine under low load conditions. *Applied Thermal Engineering*, 206, 118144.

Lu, Q., Gou, J., Pan, J., Zhang, Y., Zhu, J., & Quaye, E. K. (2019). Comparison of the effect of heat release and products from heterogeneous reaction on homogeneous combustion of H2/O2 mixture in the catalytic micro combustor. *International Journal of Hydrogen Energy*, 44(59), 31557-31566.

Luo, Y., Gan, Y., & Jiang, X. (2017). Investigation of the effect of DC electric field on a small ethanol diffusion flame. Fuel, 188, 621-627.

Luo, Z., Plomer, M., Lu, T., Som, S., Longman, D. E., Sarathy, S. M., & Pitz, W. J. (2012). A reduced mechanism for biodiesel surrogates for compression ignition engine applications. *Fuel*, 99, 143-153.

Maas, U., & Warnatz, J. (1988). Ignition processes in hydrogen oxygen mixtures. *Combustion and flame*, 74(1), 53-69.

Nastro, A., Ferrari, M., & Ferrari, V. (2020). Double-actuator position-feedback mechanism for adjustable sensitivity in electrostatic-capacitive MEMS force sensors. *Sensors and Actuators A: Physical*, 312, 112127.

Sujith, R. I., & Unni, V. R. (2021). Dynamical systems and complex systems theory to study unsteady combustion. *Proceedings of the Combustion Institute*, 38(3), 3445-3462.

Tang, A., Ni, Q., Deng, J., & Huang, Q. (2021). Role of hydrogen addition in propane/air flame characteristic and stability in a micro-planar combustor. *Fuel Processing Technology*, 216, 106797.

Wang, Y., Yu, Y., Zhu, X., & Zhang, Z. (2020). Pattern recognition for measuring the flame stability of gas-fired combustion based on the image processing technology. *Fuel*, 270, 117486.

Xiao, L., Ouyang, H., & Fan, C. (2019). An improved Otsu method for threshold segmentation based on set mapping and trapezoid region intercept histogram. *Optik*, 196, 163106.

Yan, R., Chen, Z., Zhang, B., Zheng, Y., & Li, Z. (2022). Impact of radial air staging on gas-particle flow characteristics in an industrial pulverized coal boiler. *Energy*, 243, 123123.

Yan, Y., Liu, Y., Li, L., Cui, Y., Zhang, L., Yang, Z., & Zhang, Z. (2019). Numerical comparison of H_2/air catalytic combustion characteristic of micro–combustors with a conventional, slotted or controllable slotted bluff body. *Energy*, 189, 116242.

Yang, X., Zhao, L., He, Z., Dong, S., & Tan, H. (2019). Comparative study of combustion and thermal performance in a swirling micro combustor under premixed and non-premixed modes. *Applied Thermal Engineering*, 160, 114110.

Yu, C., Breda, P., Minuzzi, F., Pfitzner, M., & Maas, U. (2021). A novel model for incorporation of differential diffusion effects in PDF simulations of non-premixed turbulent flames based on reaction-diffusion manifolds (REDIM). *Physics of Fluids*, 33(2), 025110.

Yuasa, S., Oshimi, K., Nose, H., & Tennichi, Y. (2005). Concept and combustion characteristics of ultra-micro combustors with premixed flame. *Proceedings of the Combustion Institute*, 30(2), 2455-2462.

Zargar, O. A. (2020). Effects of the jet pulsation intensity on flame behavior, thermal structure and combustion product concentration of a gas turbine model with swirl combustor. *Thermal Science and Engineering Progress*, 19, 100560.

Zhang, B., Liu, Z., Li, W., Luan, B., He, J., & Dong, J. (2018). Characteristic visualization of the micro/mesoscale liquid ethanol diffusion flame by using deflection tomography. *International Communications in Heat and Mass Transfer*, 96, 43-52.

DOI: 10.7795/810.20221124

Influence of the flammable cloud geometry on the gas explosion effects

Jérôme Daubech[a], Jérôme Hebrard[a] & Emmanuel Leprette[a]

[a] Institut National de l'Environnement Industriel et des Risques, Parc Technologique ALATA, BP 2, 60550 Verneuil-en-Halatte, France

E-mail: *jerome.daubech@ineris.fr*

Abstract

In the context of industrial large cloud explosions such as the Buncefield accident (SCI, 2009), it is commonly accepted that the flammable cloud spreads over a large area on the ground but has a limited height. This can therefore be considered as the limiting dimension of the cloud. In this work at a small scale, Leyer (1982) highlights the influence of the limited height of the flammable cloud in the case of cylindrical cloud explosions. Without prejudging the combustion mechanisms, the objective of this paper is to present the influence of this limited dimension of the flammable cloud on the flame dynamics to assess more precisely the overpressure distances of a UVCE by a better determination of the energy involved in the explosion. The analysis is based on the comparison of the flame position over time from the fast video films and the overpressure signals recorded in the flammable clouds. The explosions examined are methane and hydrogen free jet (Sail, 2014; Daubech, 2015), methane jet interacting with the ground and rows of obstacles (Sail, 2014), and large propane clouds obstructed by rows of tree trunks (SCI, 2014).

Keywords: *UVCE, flammable cloud geometry, overpressure effects*

1. Introduction

The history of industrialization is punctuated by major unconfined explosions that have left their mark on the scale of the caused damage. The accidental sequence of this type of accident can be summarised as follows. An unconfined gas/vapor/air cloud is formed, its size, composition, and internal level of agitation (the "turbulence") depend on the type of leak that caused it. If an effective ignition source is introduced into the flammable area of the cloud, the cloud ignites and a flame starts to spread. In its path, the flame almost instantaneously transforms the cold reactants into very hot combustion products (from 1000 to 2000°C), which results in a strong volume expansion of the burnt gases. This volume expansion, which sets the atmosphere in motion like a piston (or a loudspeaker), is responsible for the pressure effects. In the open air and at a given distance from the explosion, the greater the expansion velocity of flame is, the greater the overpressure effects are. Among the well-known accidents, we can mention the UFA (Russia, 1989), Port Hudson (USA, 1970), more recently Buncefield (England, 2005), and Jaipur (India, 2009). All of the above accidents have the singularity that the flammable cloud spreads over a large area on the ground but has a limited height. For instance, an analysis of the Buncefield accident (SCI, 2009) shows that the winter-grade gasoline flammable cloud occupied an area of 120000 m^2 with a height of about 2 m. The Jaïpur gasoline cloud spreads over a radius of 350 m around the release point with a limited height giving a pancake shape to the flammable atmosphere (Oran, 2020). It appears that the flammable cloud has a much smaller characteristic size than the others.

One of the first to experimentally investigate the influence of flammable cloud geometry on the effects of an explosion was Leyer (1982). He has studied at the lab scale the pressure fields produced by the explosion of a cylindrical cloud. Leyer extends the soap bubble technique of creating a hemispherical deflagration to cylindrical geometry. The soap films are held together by a cylindrical metal structure filled with an oxygen-doped ethylene-air mixture. This cylindrical volume is characterized by a radius R0 (9, 22 et 35 cm) and a height h_0 (2.4 cm ≤ h_0 ≤ 9 cm), which represents a volume between 0.6 to 17 liters. The flame dynamic is captured by a fast video camera (1500 frames/s) and a schlieren system. The overpressure is registered by microphone-type sensors. The analysis of fast video images shows a flame development in three successive steps.

The first step consists of a spherical development of flame until the burnt gases are allowed to escape toward the surroundings. The maximum radius r_{max} reached by the flame at the end of this spherical phase is given by the initial height of the cloud multiplied by the expansion ratio E raised to the power of one-third ($r_{max} = h_0 . E^{1/3}$).

The second step is a radial propagation of the flame. The flame shape is a truncated hemisphere of nearly constant height which can be estimated as $h_0 . E^{1/3}$. Above the flame front, an ascending convective motion of combustion products is observed. The flame propagation speed is slightly lower than in the first phase.

The last step is reached when the flame extends to the radial boundaries of the cloud which coincides with the end of combustion. The boundaries of the flammable cloud are materialized by the presence of a supporting ring which might be considered as an obstacle. The fast video images show that the ring induces a swirling motion of the outward expanding fresh mixtures. The flame front is considerably affected by this vortical structure inducing a strong flame area increase.

This dynamic flame development is visible on the pressure signal (Fig.1). The cylindrical pressure signal is compared to a hemispherical pressure signal with quite the same volume and the same flammable mixture ($C_2H_4 + 3O_2 + 12N_2$). Until 20 ms, the pressure rise-up is the same for the cylindrical and hemispherical volume. After, while the pressure continues to rise for the hemispherical cloud, the pressure reaches an almost constant plateau for the cylindrical cloud. For the cylindrical cloud, the end of the pressure signal is affected by a strong pressure peak which reflects the interaction of the flame front with the ring.

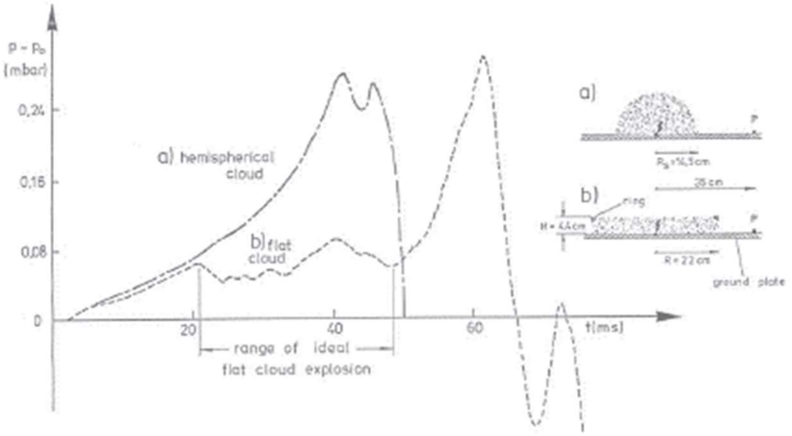

Fig. 1. Pressure signals (Leyer, 1982) obtained in soap bubble experiments from the explosion of a hemispherical cloud and of a flat cloud of equal volume (a – hemispherical cloud – Radius = 14.5 cm – Volume: 6385 cm^3 / b – cylindrical cloud – Radius = 22.5 cm, height = 4.4 cm – Volume = 6690 cm^3)

This pressure signal compared with a spherical cloud underlines the role of the flammable cloud geometry and more particularly the limited dimension (height of cloud) on the overpressure pressure and the flame dynamic.

The objective of this paper is to present the influence of this limited dimension of the flammable cloud on the flame dynamics and the overpressure effects by an analysis of several explosion configurations at intermediate or large scales like:

- methane and hydrogen free jet explosion (Sail, 2014; Daubech, 2015),
- methane jet interacting with the ground and rows of obstacles (Sail, 2014),
- large propane clouds obstructed by rows of tree trunks (SCI, 2014).

The analysis is based on the comparison of the flame position versus time from the fast video films and the overpressure signals recorded in the flammable clouds.

2. Flame dynamics and overpressure effects

The purpose of this section is to describe the experimental bench which provided experimental data to allow us to evaluate the influence of a flammable cloud limited dimension on flame dynamics and associated overpressure effects in several experimental configurations of UVCE.

2.1 Methane and hydrogen free jet explosion

The same experimental installation is used for methane and hydrogen jet release and jet explosion. Sail (2014) and Daubech (2015) present in detail the experimental setup. The release was produced by a 12 mm diameter orifice fuelled by a 5 m^3 tank (Fig.2). The tank is filled with methane or hydrogen initially pressurized at 40 bar. This configuration ensures a low decrease of the 5 m^3 tank pressure and a low decrease of the mass release rate during the tests (only a few seconds for jet explosion tests).

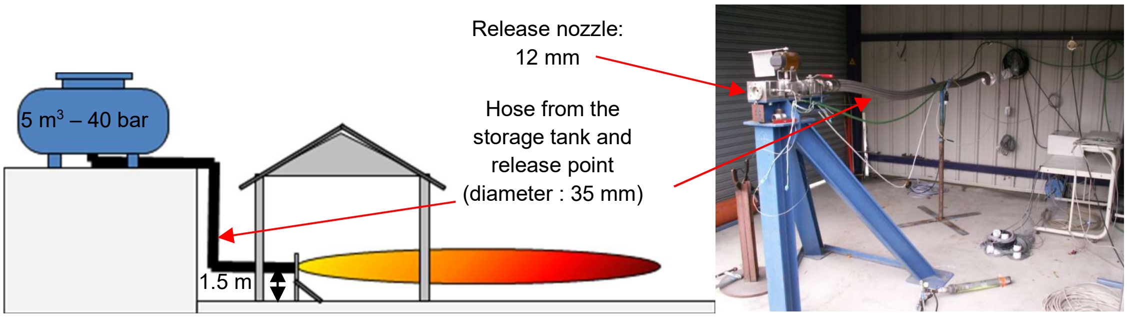

Fig. 2. Scheme of experimental device and release point

The ignition source is a vertical steel tube (diameter: 5.5 cm – length: 50 cm) filled with an H2/O2 stoichiometric mixture ignited by a pyrotechnical match (60 J). The measurement of overpressure is performed using 3 piezoresistive pressure sensors Kistler 0-2 bar. These sensors are embedded in lens support which allows the measurement of incident pressure waves without any reflection effect. Fig. 3 presents the overall repartition of pressure gauges. The flame dynamic is captured by image processing from fast videos. The image processing is the BOS method. A reference image is subtracted from the image sequence. To obtain more detail on the burnt gas pocket, the greyscale of each pixel is multiplied by 10. A Boolean rule is applied to keep the pixel above a specifically defined grayscale level for each test. The value of pixel grayscale is changed to 255 for pixels above de specific grayscale level and 1 for the others.

Fig. 3. Overall repartition of pressure gauges and flame image processing

For methane jet explosion, the chosen explosion configuration is for an ignition realized at a concentration of around 13 % (Sail, 2014). The axial lower flammability limit (LFL) distance is around 5.5 m from the release point and the maximal radial LFL distance is around 0.4 m from the axis of the jet. Fig.4 presents the pressure signal registered by the L3 gauge sensor located at 3 m from the ignition source, flame position, and flame velocity deduced from the fast video. The flame velocity in four directions (upstream, downstream, upwards, and downwards from ignition) is presented versus time and distance from the ignition source.

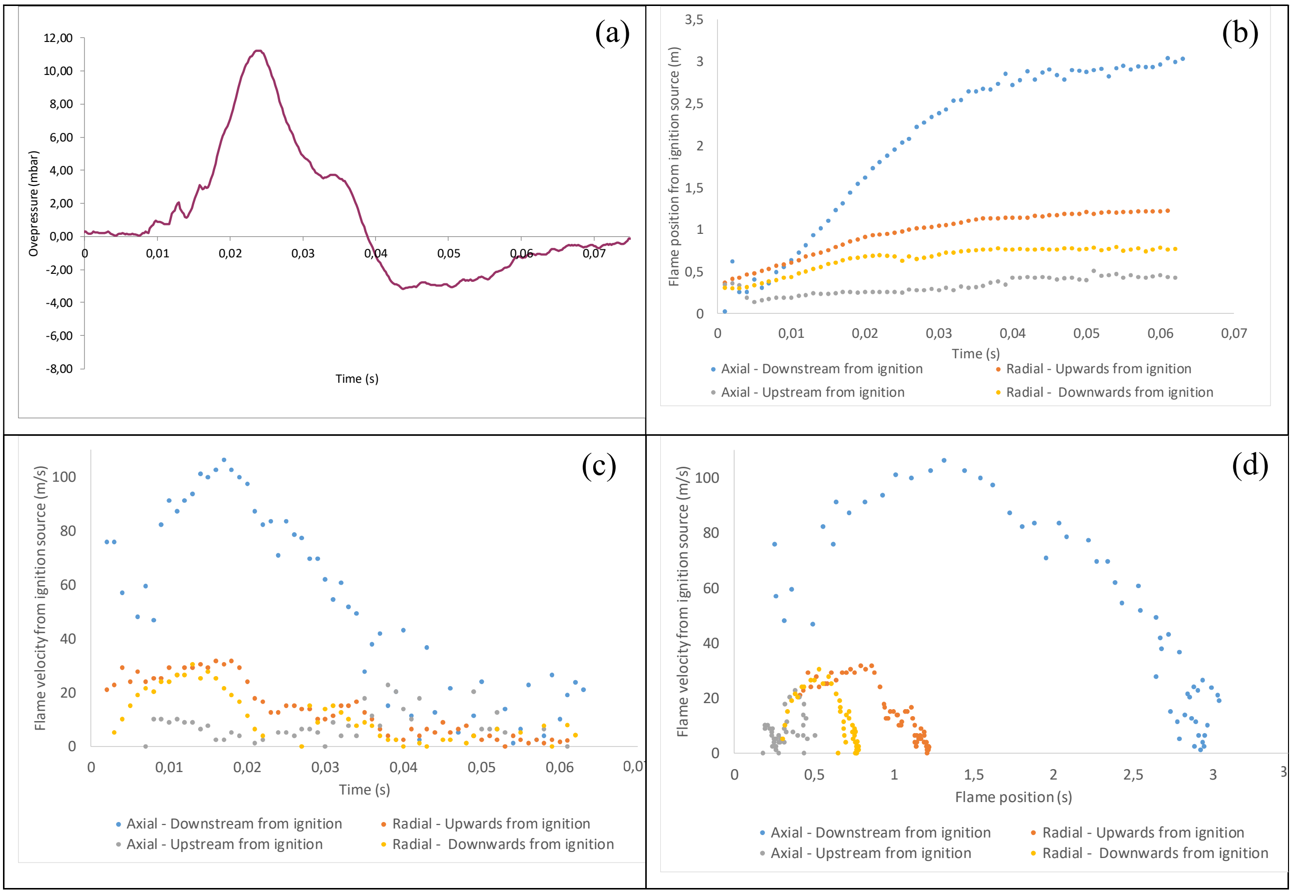

Fig. 4. Pressure signal registered by L3 gauge sensor located at 3 m from ignition source (a), the flame position (b) and flame velocity(c), and flame velocity versus flame position (d) deduced from the fast video movie

The maximum overpressure registered at 3 m from ignition is around 12 mbar and occurs at 23 ms. Radial upwards and axial downstream flame velocities are maximum at 18 ms, respectively around 30 m/s and 105 m/s (figure 4c). After 18 ms, the flame velocities decrease. When both velocities are maximum, the downstream flame position is around 1.35 m and the upward flame position is around 0.85 m (figure 4d).

The time between the flame velocity and overpressure peak is 5 ms. If we consider that pressure waves propagate at the speed of sound (340 m/s), the distance traveled by a pressure wave in 5 ms is 1.7 m, i.e. *ca.* the distance from the flame to the sensor, thus pressure peak might occur when the flame velocities are maximum. But, when flame velocity is maximum, the radial flame position is 0.85 m, which corresponds approximately to the maximum flame radius calculated by Leyer at the end of spherical flame propagation for a cylindrical cloud[1] ($r_{max} = h_0 \times E^{1/3}$). It seems also to show that the overpressure peak occurs when the flame reaches the radial boundary of the flammable cloud whereas the downstream flame propagation is still possible (LFL distance = 5.5 m). Thus, the overpressure effects develop when the flame is fully subjected to thermal expansion. When the burnt

---

[1] Here, $h_0 = 0.45$ m and $E \approx 7.5$.

gas pocket is punctured as the flame reaches the cloud boundary, the flame speed decreases sharply. So, It also implies that only one part of the cloud is involved in the overpressure effects.

For hydrogen jet explosion, Daubech (2015) presents in detail the experimental set-up and the experimental work on hydrogen dispersion. This work shows that, for an initial tank pressure of 40 bar through a 12 mm hole, the axial LFL distance is around 20 m. The same release setup is used (replacing methane with hydrogen). The two main differences between methane and hydrogen configurations are ignition (100 mJ spark instead of 60J) and the pressure sensors' positions (see Fig. 5). The ignition occurs at 0,8 m from the release hole where the concentration is 50 % of H2 in air and the radial LFL distance is around 0,2 m from the jet axis. As sensor L1 is located right next to the ignition source, all the overpressure history is registered by this gauge.

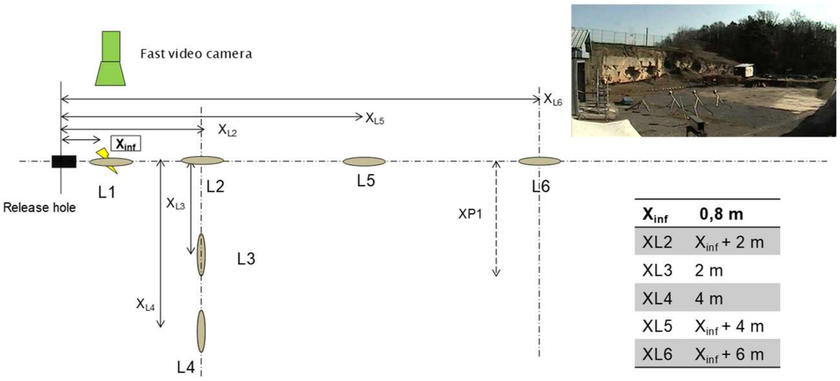

X_{inf}	0,8 m
XL2	X_{inf} + 2 m
XL3	2 m
XL4	4 m
XL5	X_{inf} + 4 m
XL6	X_{inf} + 6 m

Fig. 5. Overall repartition of pressure gauges

Fig.6 presents the pressure signal registered by L1 and L2 sensors, the flame position, and flame velocity deduced from the fast video movie. The flame velocity in four directions (upstream, downstream, upwards, and downwards from ignition) is presented versus time and versus distance from the ignition source.

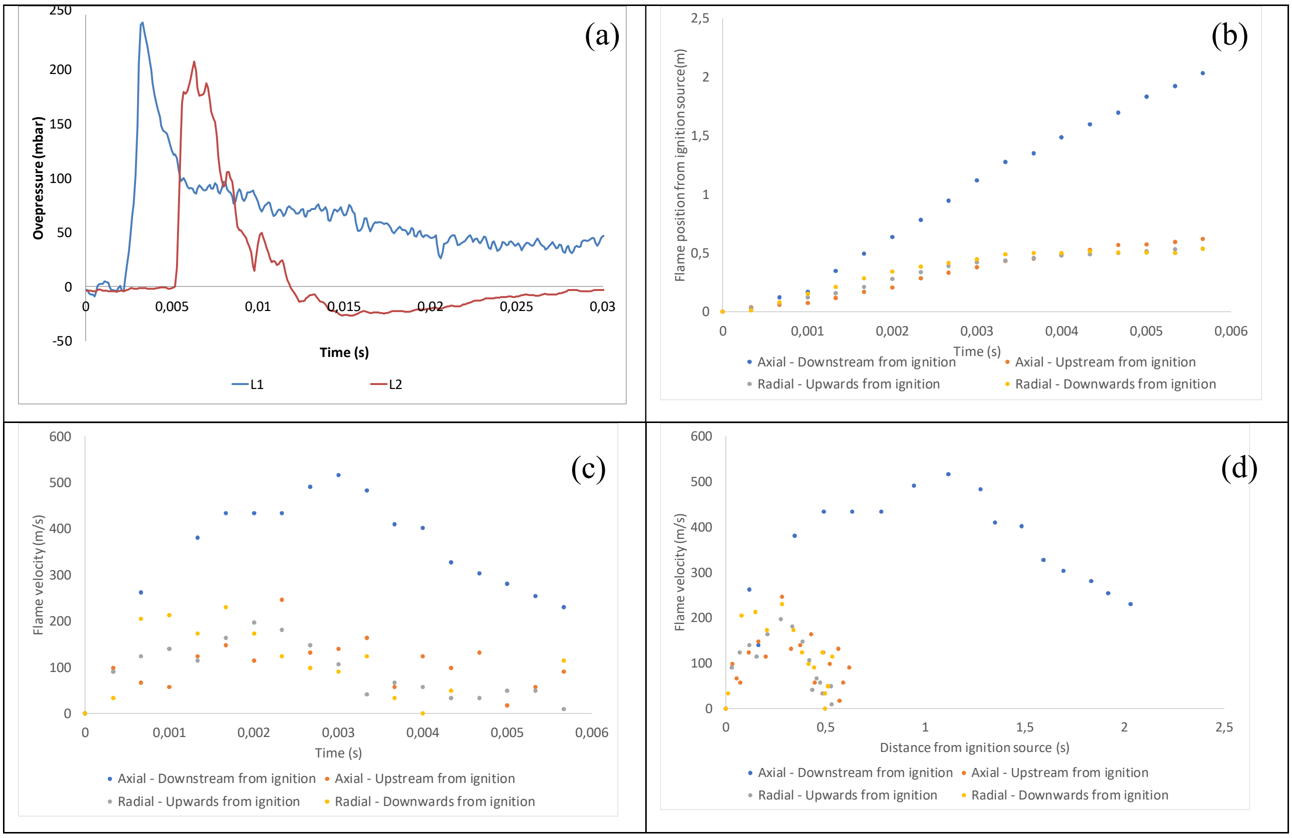

Fig. 6. Pressure signal registered by L1 and L2 gauge sensor (a), the flame position (b) and flame velocity(c), and flame velocity versus flame position (d) deduced from the fast video movie

The maximum overpressure is around 240 mbar and occurs at 3 ms. If we focus on flame dynamics, we notice that the radial and the axial downstream flame velocities are maximum at 3 ms, respectively around 200 m/s and 450 m/s. After 3 ms, the flame velocities decrease. When the velocities are maximum, the downstream flame position is around 1.2 m and the upward flame position is around 0.35 m.

As previously presented for methane jet explosion, this test confirms that the overpressure peak occurs when the flame velocities are maximum. The flame velocities are maximum when the radial position is around 0,35 m, which has also the same order of magnitude as the maximum flame radius calculated by Leyer at the end of spherical flame propagation[2] ($r_{max} = 0{,}2 \times (5{,}4)^{1/3}$). Even with a more reactive gas, the overpressure peak seems also occurs when the flame reaches the radial boundary of the flammable cloud where the flame is fully subjected to thermal expansion. After, the flame velocity and the overpressure decrease. Here, only a small part of the cloud is involved in the overpressure effects.

2.2 Methane jet interacting with the ground and rows of obstacles

The following configuration has been already presented by Sail (2014). This is a methane release under an initial pressure of 40 bar through a 12 mm circular orifice. The release is horizontal at 25 cm from the ground. The flammable cloud that is formed interacts with a wire mesh of welded 2 cm tube 30 cm high, 3 m long, and 1 m wide (Fig.7). The ignition of this flammable cloud is achieved using a pyrotechnic match (60 J) located in a 10 cm high, 15 cm long, and 12 cm deep containment with an open wall directed towards the axis of the release (Fig.7). The containment is filled with a flammable mixture. A flame of about ten centimeters in diameter ignites the external flammable cloud.

Fig. 7. Experimental configuration and ignition box

The pressure instrumentation shown in Fig. 8 consists of 6 pressure sensors, 3 of which are located in the wire mesh at 0.3 m (L3), 1 m (L5), and 2.1 m from the igniter. Two high-speed cameras film the explosion to capture the flame trajectory. Two pressure sensors are located outside the wire mesh: sensor L6 at 1 m from the end of the wire mesh and sensor L7 at 2.5 m from the axis of the discharge aligned with sensor L4.

The dispersion study in this configuration (Sail, 2014) shows that the wire mesh is filled with a stoichiometric methane/air mixture.

---

[2] Here , $h_0 = 0.2$ m and $E \approx 5.4$

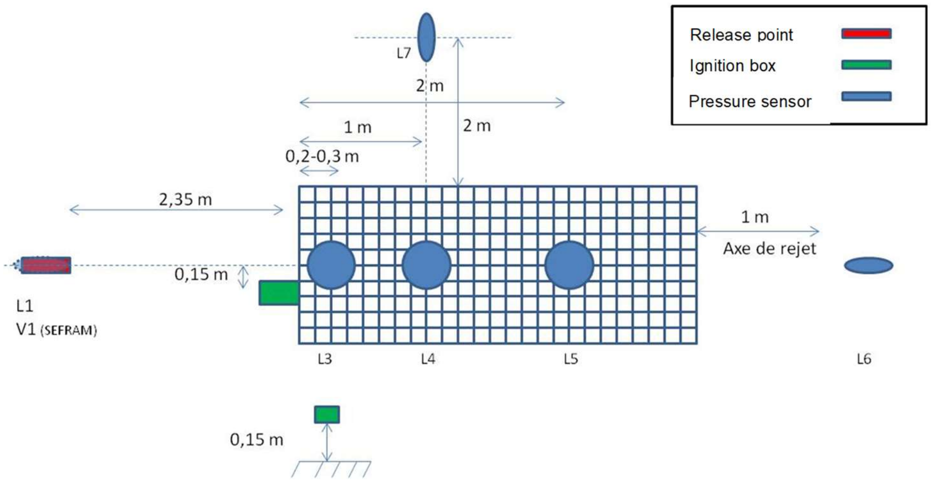

Fig. 8. Instrumentation

Fig.9 presents the pressure signal registered by L1 and L2 sensors, the flame position, and flame velocity deduced from the fast video movie. The flame velocity in four directions (upstream, downstream, upwards, and downwards from ignition) is presented versus time and distance from the ignition source.

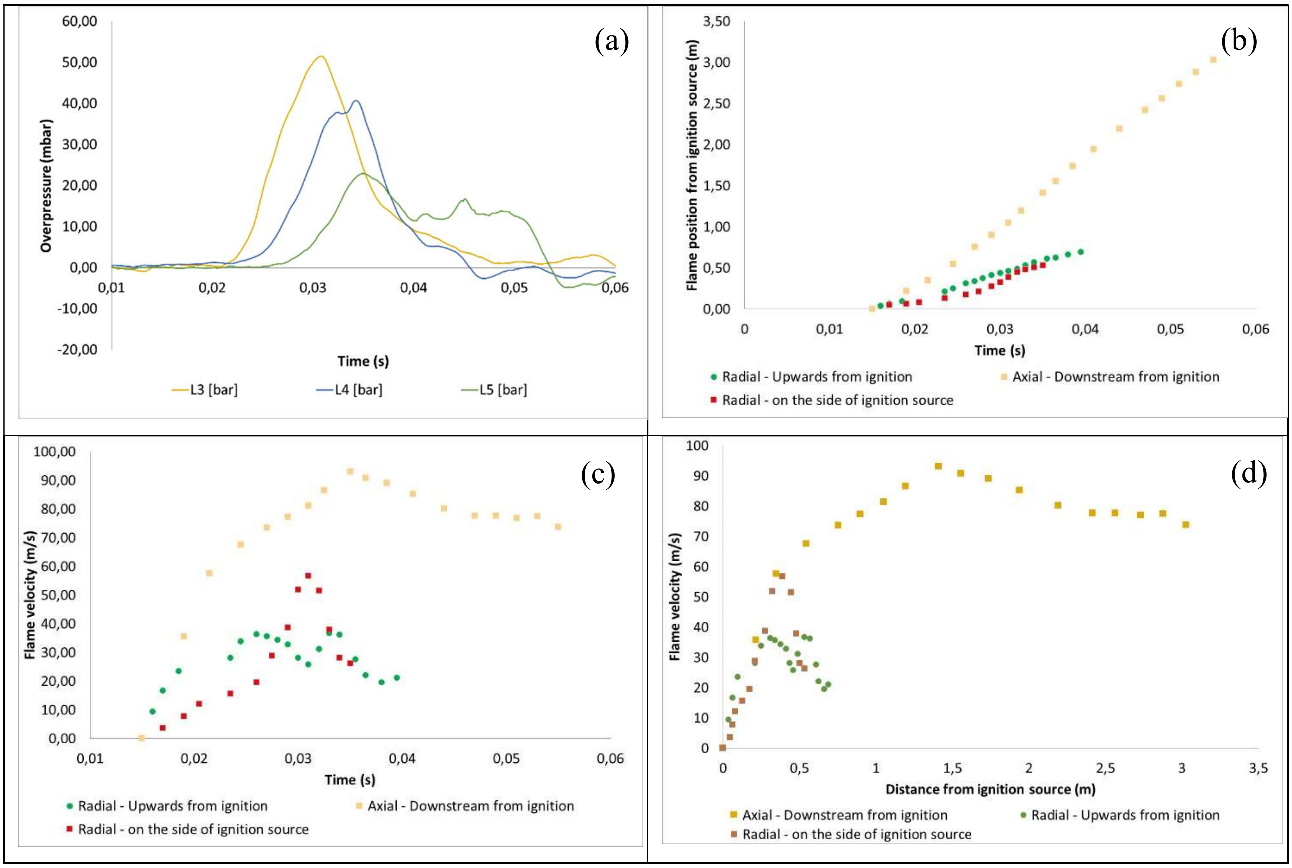

Fig. 9 Pressure signal registered by L3, L4, and L5 gauge sensors (a), the flame position (b) and flame velocity(c), and flame velocity versus flame position (d) deduced from the fast video movie

The flame travels axially 1.1 m, vertically 50 cm, and radially 40 cm when the peak of the overpressure is reached at 31 ms. Only a small part of the cloud burned at the time of the overpressure peak. If we analyze the evolution of the flame velocities in a little more detail, we can see that :

- when the flame reaches vertically 30 cm, i.e. when it reaches vertically the upper limit of the cluttered area, the flame slows down, passes through a minimum at 46 cm, re-accelerates before waiting for the upper limit of the cloud, and goes out when the flame reaches 60 cm, i.e. twice the height of the cloud (as observed earlier). This re-acceleration of the flame causes an increase in velocity on the axial velocity and a slight increase in pressure visible on the L4 sensor signal,
- When the flame reaches 40 cm radially, i.e. when it reaches the edge of the clogged area radially, the flame slows down,
- When the flame reaches 1.5 m axially, the flame velocity decreases and propagates at a constant speed. This directly impacts the pressure signal, where the pressure becomes constant at around 15 mbar (sensor L5).

2.3 Large propane clouds obstructed by rows of tree trunks

These tests were realized (SCI, 2014) by DNV GL on the experimental site of Spadeadam (UK). The objectives of these large-scale experiments are to study the different parameters that influence the acceleration of flames in vegetation: length, width, density, and type of vegetation and to verify that the transition to detonation is possible in a hedge (unconfined and very crowded environment). The stoichiometric propane/air mixture was contained in a tarpaulin-covered metal structure (Fig.10) whose length varies from 51 to 120 m depending on the experimental configurations. The width of the metallic structure is 4,5 m and its height is 3 m. Tarpaulin is cut by a pyrotechnic device just before ignition The congested areas are shorter than the total length of the cloud. Trees used for congestion are spruce, alder, and birch. The ignition is realized by a spark generator located on the centreline of the tree row at 1 m from the congested area edge and at 100 mm from ground level.

Fig. 10. Tarpaulin-covered metal structure and example of congestion

The overpressure is measured by piezo-electric pressure transducers deployed inside and outside the flammable cloud. Twelves pressure sensors are spaced 3 m apart on the axis of the ignition cloud at 1.75 m. Flame arrival time was measured through the test rig using an array of ionization probes located at the same position as pressure sensors.

Video footage from each experiment was recorded using both high-speed and normal-speed digital video cameras.

It is chosen here to present and compare two tests (3 and 4) carried out under similar conditions. In both cases, the dimensions of the flammable cloud are 51 m x 4.5 m x 3 m, and the dimensions of the congested area are 30 m x 4.5 m x 3 m. The difference between the two tests comes from the nature of the congestion. The congestion of test 3 consists of alders with 2 trees/m^2 and 15 fence posts of 8" on the center separated by 2 m. The congestion of test 4 is alder with 1.5 trees/m^2.

Test 3 remained in deflagration while Test 4 led to a deflagration detonation transition. The difference between the two explosion dynamics comes from the difference in the congestion. The congestion analysis by DNV GL shows that the average surface blockage rate is similar in both cases and the volume blockage rate in test 3 is 1.5 times higher than in test 4. However, the analysis shows that the density of small diameter obstacles is greater in Test 4 than in Test 3, which would have favored the acceleration of the flame and the deflagration-detonation transition.

Let us analyze the dynamics of the development of the flame in more detail thanks to the fast videos. The analysis of the videos is less precise than those carried out previously because of the dimensions of the experiment. However, it allows us to draw the main trends. The Fig.11. presents the pressure signals registered by P1 to P6 located between 3 and 18 m from the ignition source (SCI, 2014), the flame position, and flame velocity deduced from the fast video movie for Test 3. Fig.12 presents the same data for Test 4.

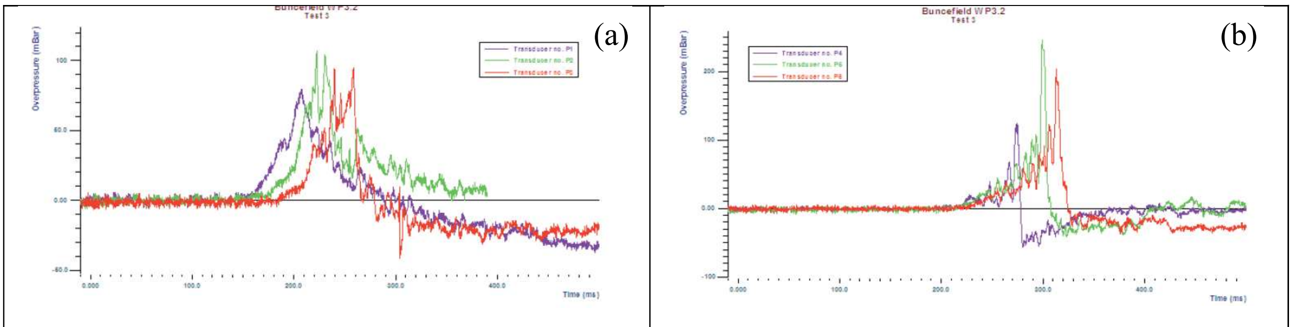

Pressure signals P1 (blue), P2 (green), P3 (red)

Pressure signals P4 (blue), P5 (green), P6 (red)

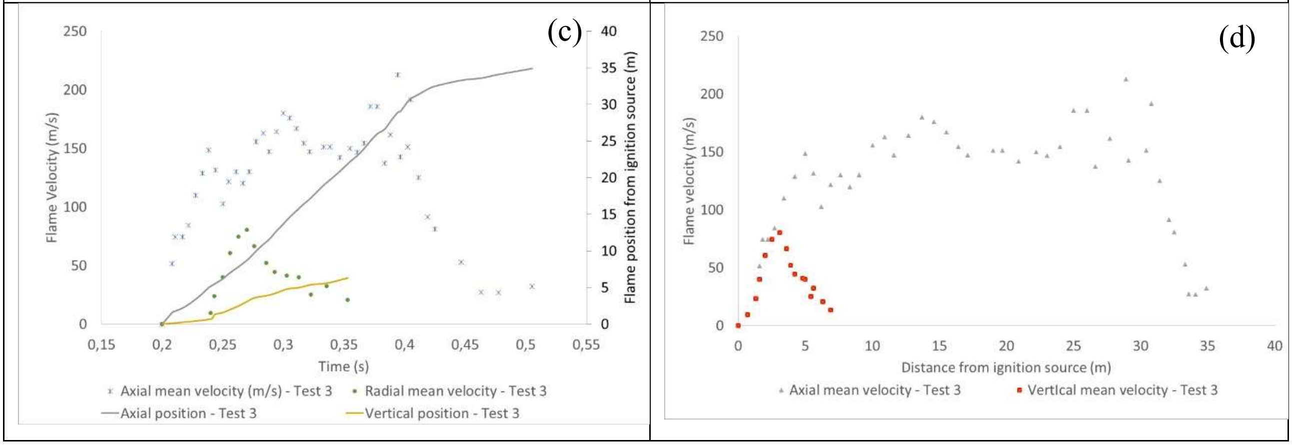

Fig. 11. Test 3 - Pressure signals registered by P1 to P6 gauge sensors located between 3 and 18 m from ignition source (a-b), the flame position and flame velocity(c), and flame velocity versus flame position (d) deduced from the fast video movie

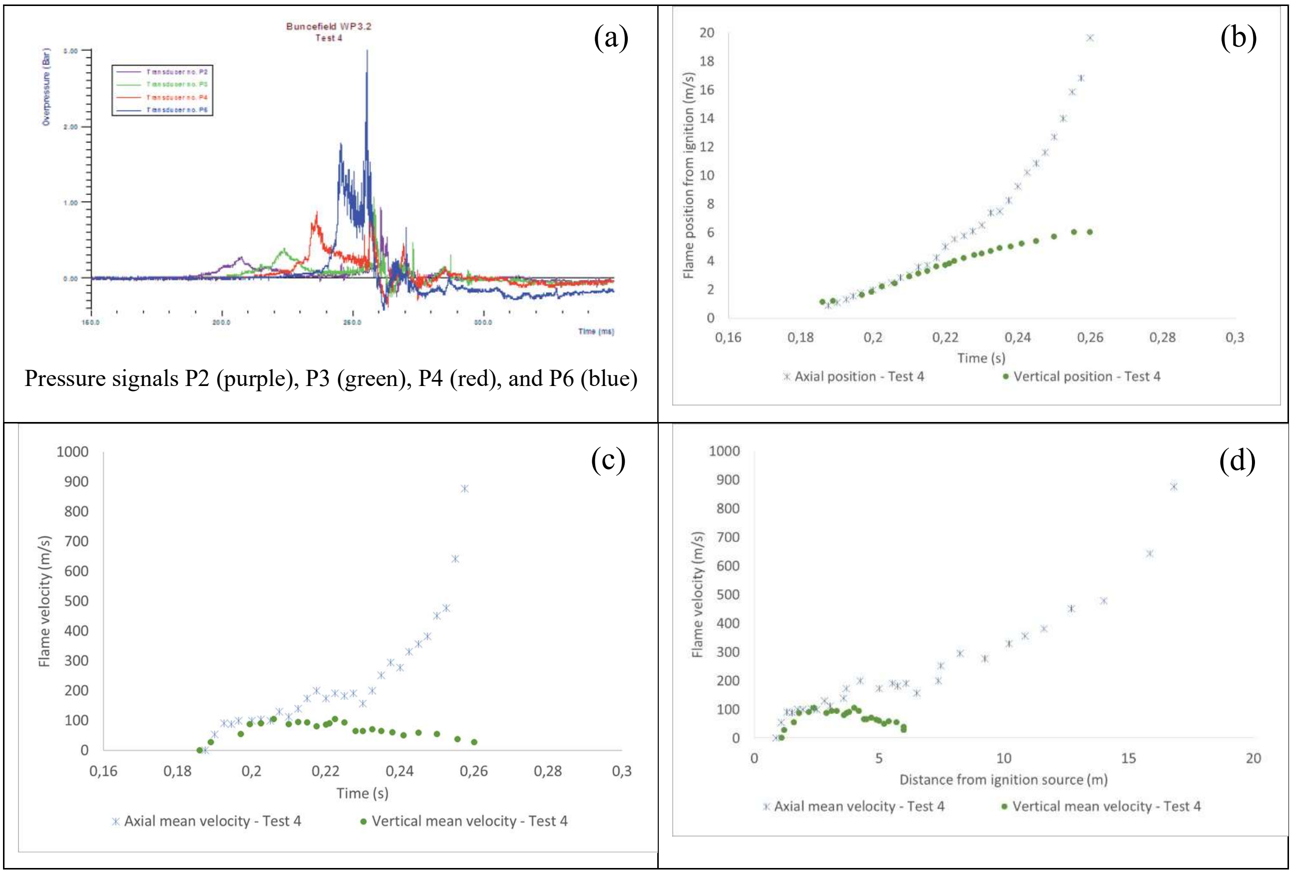

Pressure signals P2 (purple), P3 (green), P4 (red), and P6 (blue)

Fig. 12. Test 4 - Pressure signal registered by P2 to P6 gauge sensors located between 6 and 18 m from ignition source (a), the flame position (b) and flame velocity(c), and flame velocity versus flame position (d) deduced from the fast video movie

For test 3, the maximum overpressure is recorded at 245 mbar at sensor 5 located 15 m from the ignition source. At 15 m the flame reaches a peak speed of around 180 m/s. At this point, the flame is located vertically at 5.5 m, i.e. about twice the distance between the ignition source and the initial position of the top of the cloud. This corresponds to the height that could be calculated with the Leyer relation used previously. Afterward, the flame slows down and seems to propagate at a constant speed of about 150 m/s until it reaches the end of the cluttered area at 30 m. In this zone, a quasi-constant pressure of about 100 mbar is established (SCI, 2014). After 30 m, the flame speed drops significantly to around 25 m/s. It can therefore be seen that when the flame reaches the upper boundary of the cloud, the axial flame propagation velocity and the overpressure are at their maximum. Afterward, the flame slows down to a constant speed. This flame behavior is similar to the one presented in the previous experimental configuration.

For Test 4, it appears that the deflagration-detonation transition occurs around a distance of the order of 15 m where the flame speed reaches 500 m/s. The pressure sensors P4 and P6 show this deflagration detonation transition with the appearance of a steep pressure front between 240 and 250 ms. At this moment, the flame altitude is about 5.5 m, the maximum vertical flame propagation height (Leyer relation). This shows that the deflagration-detonation transition occurs when the flame is still fully subjected to the thermal expansion of the burnt gases.

3. Discussion

Analysis of the flame propagation dynamics and pressure signals of the experimental set-ups presented above shows the impact of the limiting dimension of the flammable cloud. When the flame reaches the cloud boundaries, the flame velocity is maximal in the case where a deflagration detonation transition does not occur. The pressure peak occurs at this point. Then the flame slows down, and the pressure drops to a constant value.

We can wonder what the impact of these flame dynamics on the pressure effects outside the cloud is. For this purpose, we try to reconstruct the pressure signals ΔP at the distance r thanks to the acoustic source model of Leyer (1982):

$$\Delta P(\tau, r) = \rho_0 . \frac{(1 - E^{-1})}{4.\pi.r} . \frac{\partial^2 V_{BG}}{\partial \tau^2}$$

With $\tau = t + \frac{r - r_f}{c}$

V_{BG} is the volume of burnt gases, r_f is the flame position, r is the target position and c is the speed of sound.

The flame path diagram makes it possible to reconstruct the volume of burnt gases. Thus, the volume change of the acoustic source is known.

First, this exercise is made on the hydrogen jet explosion regarding the pressure signal registered at 4 m from the axis of the release (Fig. 5). Fig. 13 presents a comparison between the estimated and experimental signals and the evolution of burnt gas volume. There is good agreement on both the shape and amplitude of the estimated pressure signal. The overpressure peak occurs at 15 ms, which corresponds to a time of 3 ms without the time lag due to the propagation of the pressure wave. At this moment, the volume of burnt gases is around 0,6 m^3, the flame velocity is maximum. As mentioned earlier, it coincides with the moment when the flame reaches the radial boundary of the flammable cloud. Considering a mean expansion ratio of burnt gas equal to 5,4, the volume of fresh gases implies in the explosion effects is around 0,1 m^3, whereas the total flammable volume above the LFL is around 40 m^3. Thus, only a small part of the flammable cloud participates in the overpressure effects at distance.

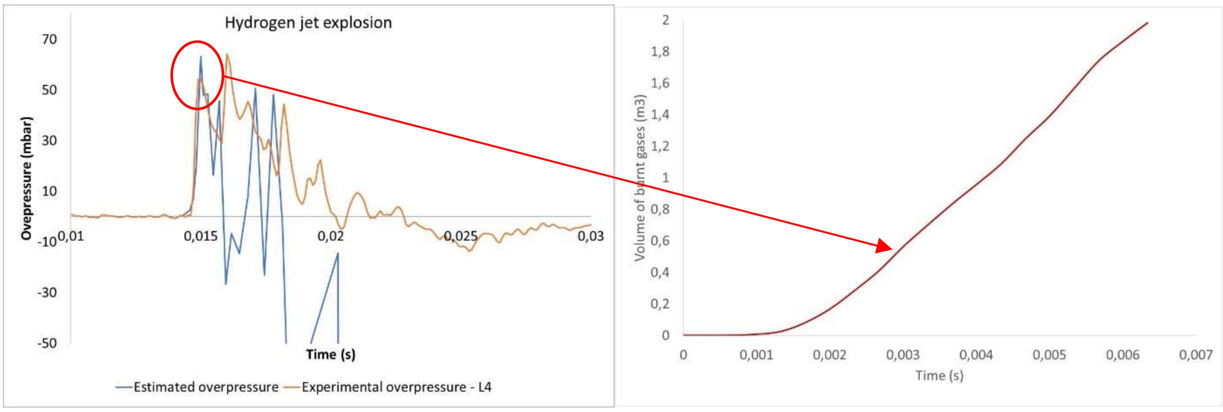

Fig. 13. Estimated and the experimental L4 pressure signals of hydrogen jet explosion and evolution of burnt gases volume

The same approach is made to the Methane jet explosion interacting with the ground and rows of obstacles. The reference pressure signal is the L6 sensor registered at 4 m from the ignition source on the axis of the release (Fig. 8). Fig. 14 presents a comparison between the estimated and the experimental signals and the evolution of burnt gases volume. There is also good agreement on both the shape and amplitude of the estimated pressure signal. The overpressure peak occurs at 45 ms, which corresponds to a time of 34 ms without the time lag due to the propagation of the pressure wave. At this moment, the volume of burnt gases is around 0.5 m^3. With a mean expansion ratio of burnt gas of about 6.4, the volume of fresh gases implies in the explosion effects is around 0,08 m^3, whereas the total flammable volume above the LFL is around 0.9 m^3. Thus, this shows again that only a small part of the flammable cloud participates in the overpressure effects at distance.

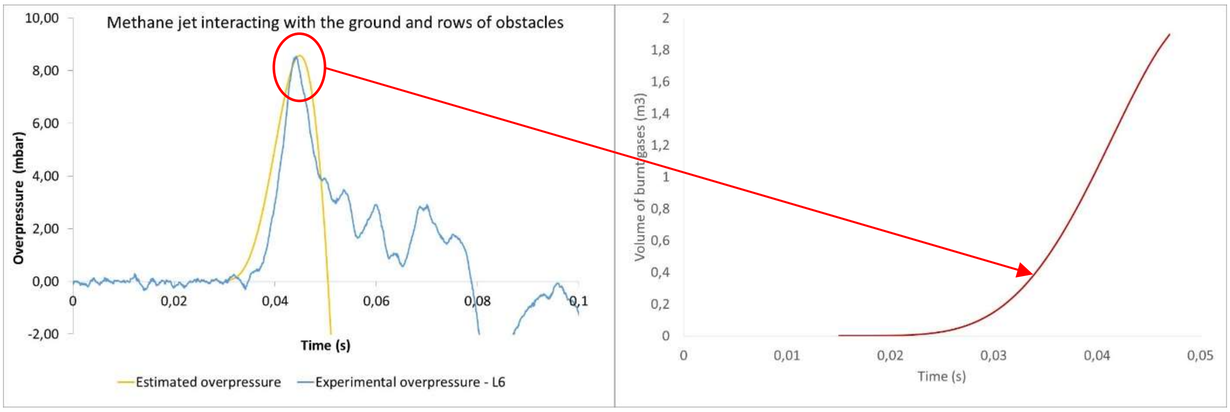

Fig. 14. Estimated and the experimental L6 pressure signals of hydrogen jet explosion interaction with the ground and obstacles and evolution of burnt gases volume

4. Conclusions

Flame dynamics analysis shows that when the flame reaches the cloud boundary (generally the smallest of the characteristic dimensions of the flammable cloud), the flame speed is at its maximum. It is at this point that the peak overpressure occurs. Then, when the pocket of burnt gases bounded by the flame is punctured, the burnt gases escape and the flame slows down to a constant speed if the mixture is homogeneous. It appears that the pressure is constant in the area where the flame propagates at a constant speed. If a deflagration-detonation transition occurs, it appears to occur when the flame is fully subjected to the thermal expansion of its combustion products. Large-scale tests would be interesting to see if turbulent and obstructing conditions can lead to a deflagration-detonation transition when the flame is no longer subject to its volume expansion, as in the case of Test 3 of the SCI tests.

The analysis of the pressure signals that can be made about the evolution of the volume of the burnt gas pocket shows that a part of the flammable cloud participates in the overpressure effects. This has direct consequences on the evaluation of the combustion energy involved in an explosion and on the calculation of the overpressure effect distances that could be estimated using the multi-energy method, for example.

References

Steel Construction Institute (2009). Buncefield Explosion Mechanism Phase 1 - Volume 1.

Oran E, Chamberlain G, Pekalski A, (2020), Mechanisms and occurrence of detonations in vapor cloud explosions, Progress in Energy and Combustion Science, vol 77, 100804

Leyer J.C (1982) An Experimental Study of Pressure Fields by Exploding Cylindrical Clouds, Combustion and flame, vol 48, pp 251-263

Sail J, Blanchetiere V, Geniaut G, Osman K, Daubech J, Jamois D, Hebrard J. (2014). Review of knowledge and recent works on the influence of initial turbulence in methane explosion. Proceeding of X. ISHPMIE, Bergen, Norway.

Daubech J, Hebrard J, Jallais S. Vyazmina E, Jamois D, Verbecke F, (2015), Un-ignited and ignited high pressure hydrogen releases: Concentration – turbulence mapping and overpressure effects, Journal of Loss Prevention in the Process Industries Volume 36, July 2015, Pages 439-446

Steel Construction Institute (2014). Dispersion and Explosion Characteristics of Large Vapour Clouds Volume 1 – Summary Report

DOI: 10.7795/810.20221124

Explosive properties of selected aerosols determined in the spherical 5-L test chamber

Adrian Toman[a], Wojciech Adamus [a]
[a]Central Mining Institute (Katowice, Poland)
E-mail: a.toman@gig.eu

Abstract

Combustible liquids in a form of aerosols are important to many industrial processes. Therefore the problem of explosion hazard posed by the aerosols appears more and more often. To properly assess the explosion risk and meet the requirements of the ATEX directive information on the flammable and explosive properties of the aerosols are necessary. Unlike in the case of gases and dusts no standard procedures aimed to obtain quantitative information of this type exists. Among the factors that influence the explosion dynamics of aerosols are: concentration, droplet size, temperature etc. Some of those factors strongly depend on methods of the aerosol generation. In the paper an attempt to determine the basic explosion parameters of flammable liquid aerosols are described. The measurement procedure has been developed and the prototype test equipment consisting of the 5-L spherical vessel equipped with pump-injection system for generating an aerosols and spark ignition source has been built. A wide variety of injection settings were tested to select the most useful conditions across a wide range of concentrations and liquids of different properties. The tests were carried out for the liquids frequently used in industry: Isopropanol and Kerosene.

Keywords: *aerosol, spray, explosion, flame propagation*

Introduction

The combustion of atomized liquids is the a subject of numerous studies, many of which are aimed at optimization of a combustion processes as well as an identification of the risk associated with an explosion. In order to avoid incidents related to an explosion of aerosols, it is necessary to know, preferably – quantitatively, their explosive properties. Many ideas and research methods have emerged, however, there are no standard measuring procedures or equipment for an assessment of parameters describing aerosol explosion Betis (2017).

Typically, an aerosol generation is accomplished by atomizing a liquid. The acting mechanical force disperses the liquid through the nozzle and transform it into an aerosol with particle sizes dependent on a type of the nozzle. Research J.H. Burgyone, L. Cohen (1954), C.E. Polymeropoulos (1984) R. Thimothée et al (2016) indicate that the dispersed liquid particles are more sensitive to a potential ignition source than liquid due to the higher surface to volume ration. Moreover, as noted by Burgoyne and Cohen (1954), dispersed liquid with a droplet diameter < 10 μm may already behave like a vapour. Gant et al. (2013) suggested that if the sprayed droplets are very small (with a diameter of less than 10 μm), they evaporate in front of the flame and the flame essentially propagates as in a vapour-air mixture. Therefore, he suggested the examination of an aerosol particles ranging in size from about 15 μm to 30 μm. Formally, an aerosol is defined in the European Standard EN 60079-10 as small (less than 50 μm) liquid particles suspended in the atmosphere.

The standardization of the assessment of aerosols explosive properties has been discussed by Shuai Yuan et al (2019) or Stephanie El-Zahlanich et al. (2021). As mentioned in the review by Shuai Yuan et al (2021), experimental research is carried out using various methods and devices, what makes comparison of the results difficult. These differences appear primarily in the initial conditions, aerosol fragmentation, ignition source and the volume in which the studies were carried out.

Similarly as in the case of gases and dust the measurements performed in a laboratory scale and in a larger scale show a dependence of the explosion dynamics on the volume in which the explosion takes place. In order to obtain volume-independent information about the dynamics of the explosion the well-known constant K (K_{St} for dusts, K_G for gases) was introduced. The constant K is defined as the maximum rate of pressure build-up in a volume of 1 m^3. If the tests are carried out in a different volume, the so-called volume law could be applied to determine the constant K. It is believed that in the case of dusts the volumetric law can be applied to a volume equal to or greater than 20 dm^3, while for gases and liquid vapours~~,~~ this law applies from a volume of 5 dm^3. It seems that the specificity of the aerosol tests is rather closer to testing gases than air-dust mixtures. In addition, the formation of an aerosol cloud is more difficult in case of larger volumes than for smaller ones.

Bearing in mind the above considerations, the prototype equipment for measuring aerosol explosion parameters was constructed. Its design takes into account the following main requirements: closed spherical combustion chamber with a volume of 5-L, shape, range and quality of aerosol cloud droplets size 10-50 μm. The paper presents a description of the prototype equipment, the testing procedure and the obtained results of the explosion parameters of selected aerosols. As in Shuai Yuan et al (2019) or Stephanie El-Zahlanich et al. (2021) the first stage of the research consisted in defining aerosol properties, such as droplet size distribution, concentration and obtaining homogeneity of aerosol cloud in the studied space. Then tests with the ignition source have been carried out in a pressure-resistant test chamber. A procedure was developed for determining the maximum explosion pressure p_{max} and the maximum rate of explosion pressure increase $(dp/dt)_{max}$. The tests were performed on Isopropanol and Kerosene.

1. Materials and Methods

1.1 Experimental apparatus

The principle of operation and the construction of the apparatus designed to measure aerosol explosion indices is based on the concept of gas and dust explosion equipment. The main part of the apparatus (Fig. 1) is the modified 5-L spherical chamber manufactured by Adolf Kühner equipped with two piezoresistive pressure transducers, aerosol generation system, spark generator and temperature control unit.

Fig 1 *Research stand*

Block diagram of the whole stand is presented in Fig. 2.

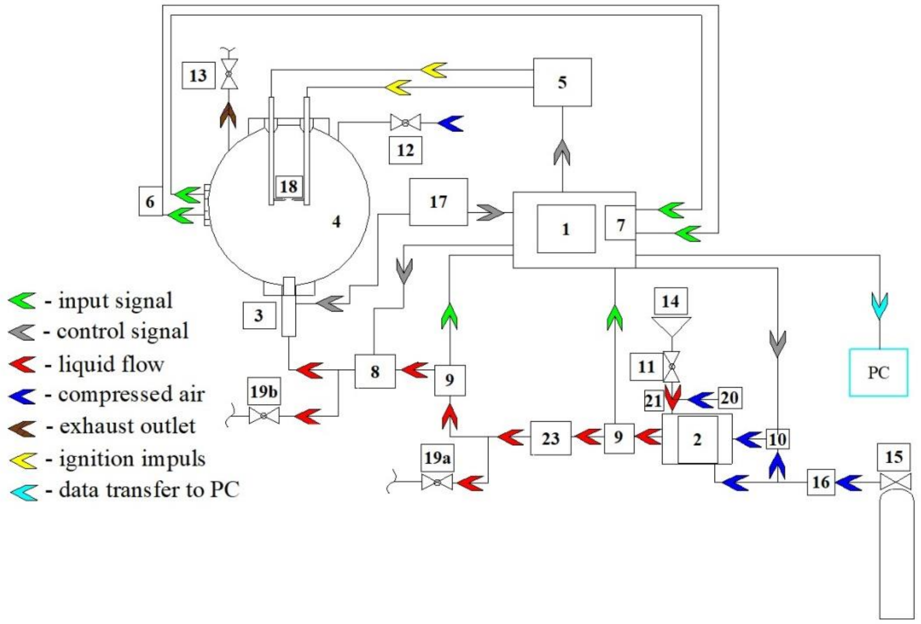

1	control and acquisition system
2	high pressure pump
3	electromagnetic injector
4	5L spherical chamber
5	spark generator
6	pressure sensors
7	amplifiers
8	electric valve
9	pressure transducers
10	compressed air solenoid valve, pump control air
11	pump main valve
12	compressed air valve for ventilating the chamber
13	chamber purge outlet valve
14	liquid dosing
15	compressed air cylinder
16	pressure reducer
17	injection control system
18	electrodes
19	technological valves
20	compressed air connection in the flooding throat
21	flooding throat
22	PC
23	needle valve

***Fig. 2** Block diagram of the apparatus with the flow of media and signals*

The aerosol generation system consists of the Maximator GSF 35 high-pressure pump, the Bosch electromagnetic injector 0 261 500 109 (Fig. 3) and the precise injection control system Motoelektron.

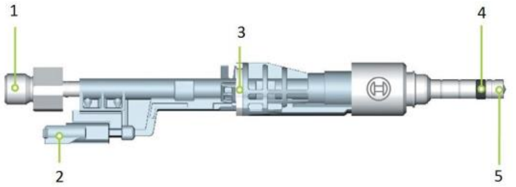

***Fig**. **3.** Bosch HDEV 5.2L* electromagnetic injector

The pump is designed for flammable liquids and is able to generate working pressure up to 400 bar. More efficient and stable operation of the pump may be ensured by a 250 ml liquid buffer included in the injection section with a pressure transducer that stabilize liquid pressure in the section. The total capacity of the injection unit is 350 ml.

The 5-L sphere is a smaller copy of the standard 20-L sphere described in the European and American Standards. To measure explosion pressure two Kistler 4624 piezoresistive pressure transducers with amplifiers were used. Signals were gathered by NI USB 6009 data acquisition system. As in larger version the sphere is surrounded with a water jacked that enables control of the sphere temperature. To enable reference to the results available in the literature (e.g. Addai (2016)) as an ignition source a generator with a constant maximum spark energy of 7 J was used. The distance between tungsten electrodes was 3,3 mm used by Bane (2013).

The most difficult part of designing the experimental stand was a choice of the injector. The geometry of the testing volume impose restrictions on the shape of the aerosol cloud. It was critical to avoid significant settlement of the droplets on the vessel's walls and at the same time fill uniformly the volume with aerosol. After testing many types of injectors six-hole Bosch HDEV electromagnetic injector was selected (Fig. 3). This injector allows generation of aerosol droplets within the range 10-50 μm. Wide spraying angle (110˚) ensures even aerosol distribution in the test vessel. The injection was controlled by Motoelektron injection system. The amount of injected liquid and therefore the aerosol concentration in the vessel was controlled by the number of doses, injection pressure or the injector opening time.

The operation of the injection control system allows to:

- • adjust injection pulse time in range of 100-10000μs
- • adjust pulse frequency 1-50Hz (resolution 1Hz)
- • select the number of generated pulses from 1 to 60000
- • generate of a single pulse with an adjustable time 0.1-2 seconds (resolution 0.1s)

1.1.1 System calibration

To check quality of the generated aerosol cloud for single and sequential injection in a pressure range of 100-200 bar before injection a transparent 5-L sphere (Fig. 4) was utilized. A high-speed camera enabled visualization of the process. The analysis of the injection time sequence showed that the sequential injection and the liquid pressure of 150 bar are the most favorable conditions for the system used to generate an aerosol in a given volume.

Visual analysis of films from a high-speed camera also allowed to estimate the formation time of a homogeneous aerosol-air mixture. It was assumed that after approx. 20 ms from the end of single injection (or over 150 ms in case of 10 injections sequence) the aerosol evenly filled the entire volume.

Measurements of the explosion parameters of Kerosene for different ignition delay times and fix concentration are shown in Fig. 5. The same results for Isopropanol are presented in Fig. 6. In the case of Kerosene, the results suggest that relatively stable and repeatable maximum values of the explosion pressure and the rate of pressure rise can be obtained when ignition occurs after about 160 ms (28 ms after the last injection). Further Kerosene and Isopropanol tests were performed with these settings.

It was checked that the repeatability of the pulse sequence is very good. Sequences of the same length in the same conditions disperse the same liquid volume. That observation allows to control amount (volume or mass) of the liquid dispersed in the vessel. For each tested liquid the relationship between a nominal aerosol concentration and parameters of a sequential injection was found. Using the relationship the amount of injected fluid could be controlled by the injection pulse time and by the number of generated pulses. The constant pressure before injection must also be kept.

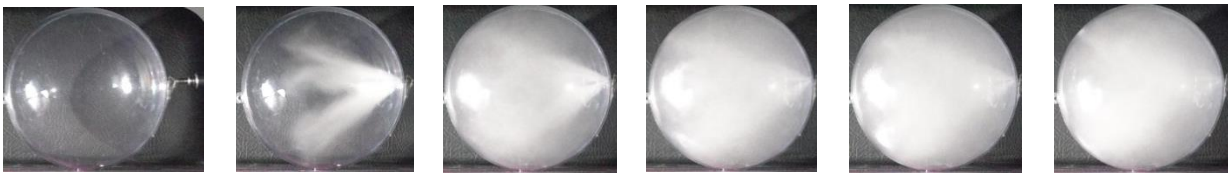

0ms 7ms 34ms 55ms 66ms 88ms

End of injection 132ms | 144ms | 152ms | Ignition 160ms | 182ms | 232ms

***Fig. 4** Dispersion of Kerosene in the transparent spherical 5-L chamber; aerosol concentration 336g/m^3, 10 pulses*

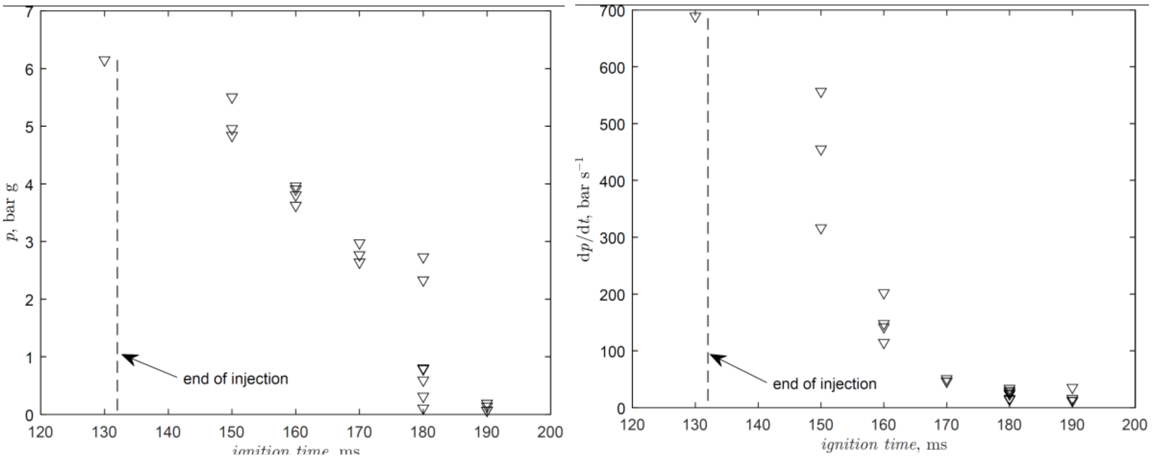

***Fig. 5** Time dependence of kerosene ignition delay for concentration 336g/m^3 [ms] in 20℃*

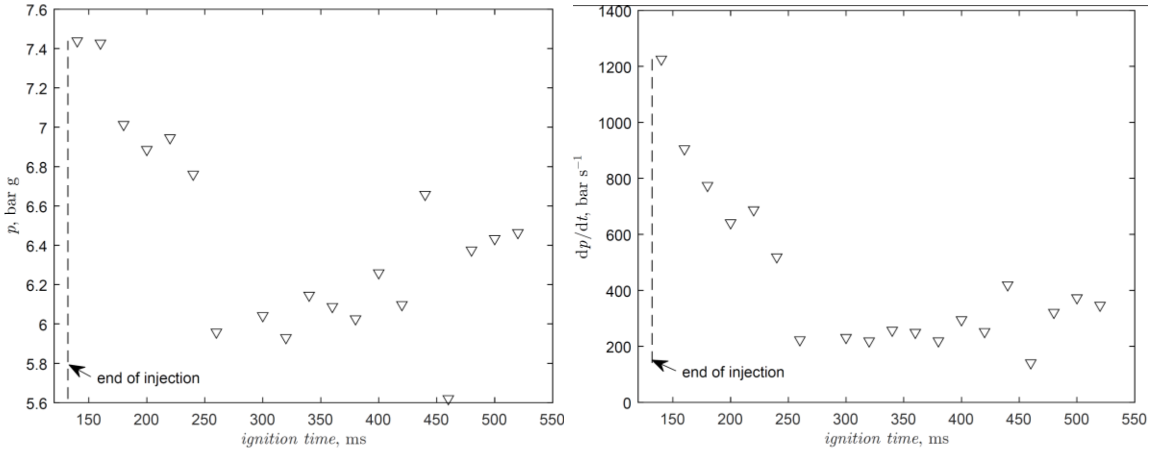

***Fig. 6** Time dependence of Isopropanol ignition delay for concentration 312g/m^3 [ms] in 20℃*

1.2 Properties of selected liquids

In order to verify operation of the prototype equipment, it was decided to begin with an assessment of explosive properties for kerosene and isopropanol.

The most important properties of liquid affecting the aerosol generation process are: density, surface tension and viscosity. Also important should be boiling temperature as it provides information on a rate of evaporation at room temperatures. Density may also influence a dispersion process. According (Orzechowski and Thriver, 1991) for liquids of higher density smaller drops can be obtained.

***Table 2** Physical properties of different fluids*

	commercial Kerosene for lamps (DRAGON)	**Isopropanol**	**Water**
Density (g/cm^3)	0.84	0.78	1.0

Viscosity (cSt)	< 3 mm^2/s in +40°C	2.43 (ASTM D-4052)	0.89
Surface tension (kg.s^{-2})	0.027	0,022	0.073
Flammability limits (%Vol.)	0.5–6,5%	2 – 12%	-
LTL/ UTL (lower temperature limit/ upper temperature limit)	38 - 83°C	11-34°C	-
Boiling point (^{o}C)	180 – 310	85.5	100

1.2.1 Characterization of aerosols

A laser diffraction particle analyser Malvern Panalytical Spreytec was used to obtain droplet size distributions of the aerosols generated by the equipment. Measurements for water were performed for comparison. Due to technical limitations the measurements were made outside the experimental chamber varying number of injections without any changes in the setting of the aerosol generation system. Plots in Fig. 7 present results of the measurements.

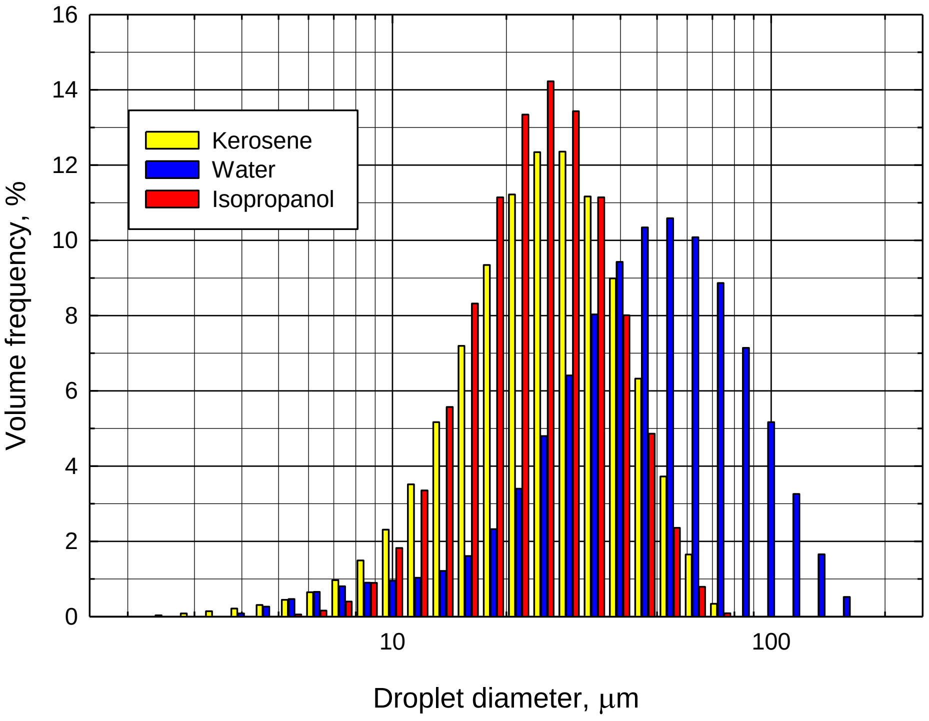

Fig. 7 *Droplet size distribution of the aerosols; liquid pressure 150 bar*

Table 3 contains one-value parameters describing the distributions. Generated aerosols of Kerosene and Isopropanol have very similar droplet size distributions. Water droplets are larger even though its density exceeds densities of the tested liquids. Apparently, other properties, surface tension and/or viscosity, play here a decisive role.

Table 3 *Parameters of droplet size distribution*

	Dv_{10}	**Dv_{50}**	**Dv_{90}**	**$D_{[3][2]}$**
Kerosene	14.18	26.85	46.54	22.48
Isopropanol	13.59	25.11	39.81	22.02
Water	19.42	51.98	103.2	34.73

2. Results and discussion

Several series of tests with aerosols were carried out in the constructed equipment. The main goal was to measure maximum explosion pressure p_{max} and maximum rate of pressure rise $(dp/dt)_{max}$ as a function of the aerosol concentration. In all tests an explosion development was registered by measurement of an explosion pressure. From those results a rate of pressure rise was calculated.

2.1 Preliminary tests of Kerosene

Preliminary series of tests were performed with Kerosene aerosol. The tests were done to check operation of the prototype equipment.

Unexpectedly, the values of a maximum explosion pressure had a large spread. It was suspected that the spread is caused by changes of the vessel's temperature. Therefore, an additional series of tests was carried out to obtain a temperature dependence of the results.

2.2.1 Temperature dependence of explosive properties of Kerosene aerosol

Tests were carried out for a single aerosol concentration of 336 g/m^3. In the tests temperature of the explosion vessel was controlled. The results of that part of an experiment are presented in Fig. 8. Both maximum pressure and maximum rate of pressure rise increased with an increase of the temperature of the vessel. Pressure p_{ex} rises from a value slightly above 3 bar up to almost 6 bar when the temperature changes from 20^{o}C to 54^{o}C. The rise of maximum rate of pressure rise is even faster. In that range of the temperature $(dp/dt)_{ex}$ increases 4.5 times.

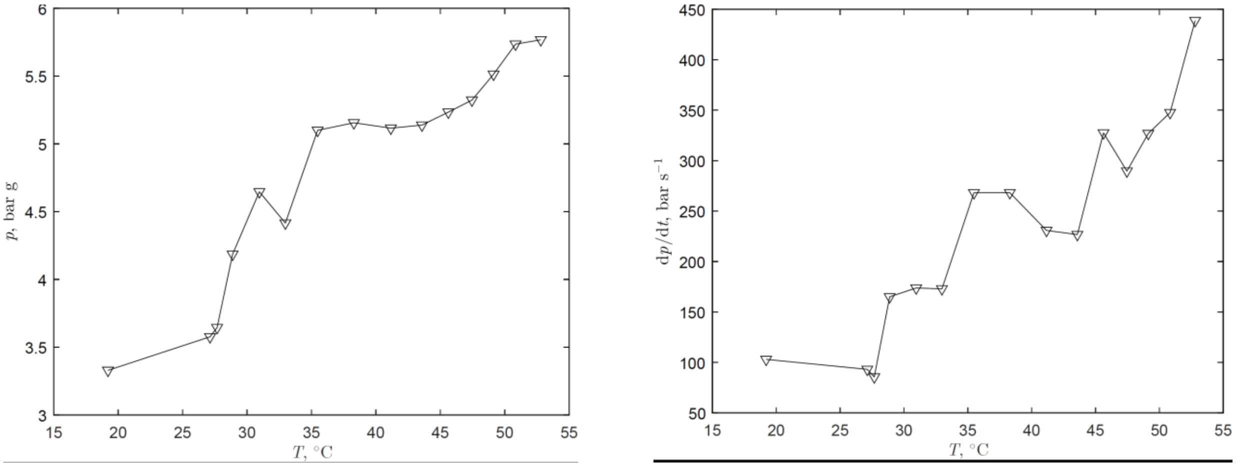

Fig. 8 *Dependence of explosion parameter on temperature for Kerosene aerosol; concentration 336* g/m^3

This effect should probably attributed to Kerosene evaporation. The observation confirms results of Shepherd (1997) and Stephanie El-Zahlanich et al. (2022).

After that tests a cooling system was attached to the vessel. All subsequent research program was carried out with that system, at constant temperature of 20°C.

2.2.3 Explosive characteristics of Kerosene aerosol

Under the conditions established as a result of the tests described Kerosene aerosol was tested. An injection lasted 132 ms in a sequence of 10 pulses. A concentration of the aerosol in the vessel was controlled by a length of the pulse. The tests covered a range of the concentrations 45 g/m^3 to 336 g/m^3. The results are presented in Fig. 9&10.

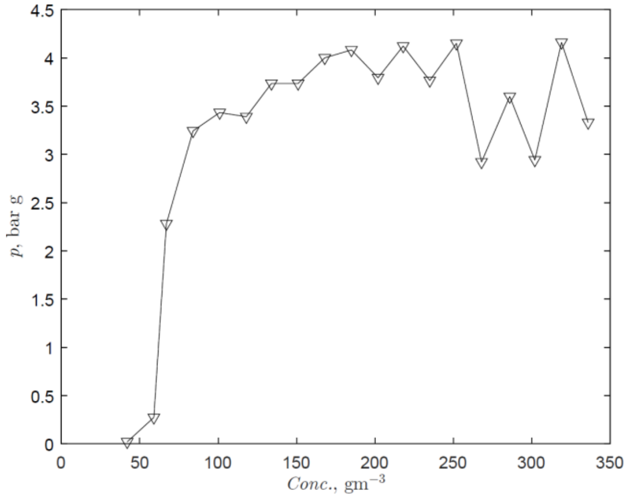

Fig. 9 *p_{max} for Kerosene in 20℃*

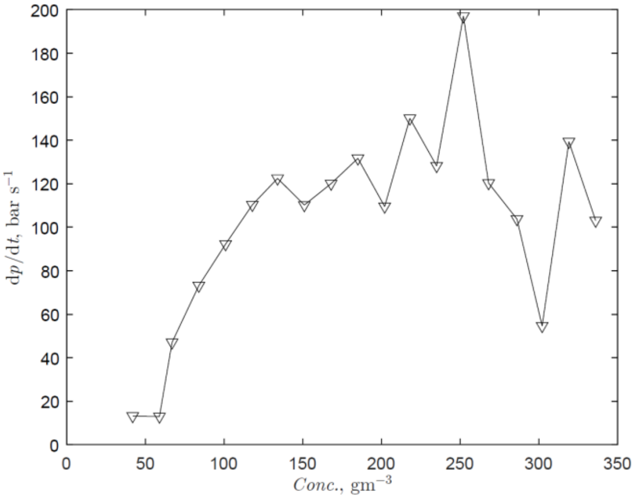

Fig. 10 *dp/dt_{max} for Kerosene in 20℃*

Maximum explosion pressure (p_{max} = 4.1 bar), was measured at a concentration between 200 g/m^3 – 250 g/m^3. Further a spread of the experimental points becomes large. As expected, in Fig. 11 a spread of experimental points in Fig. 10 is large. Basically, a maximum value of $(dp/dt)_{max}$ is about 160 bar/s, but in one test it is 200 bar/s.

2.2.4 Explosive characteristics of Isopropanol aerosol

In the same conditions testing of explosive properties of Isopropanol aerosols were carried out. Initially, a similar range of concentrations was assumed: 50 g/m^3 – 315 g/m^3. However, at the highest concentration a maximum value of p_{max} and $(dp/dt)_{max}$ was not reached. Tests at higher concentrations required a modification of the injection sequence. To obtain higher concentrations the sequence of pulses was extended to 20 or 30 in time of 274 ms and then farther elongated to 30 pulses in 418 ms. The modification of the settings is shown in the diagram Fig. 11. That way a maximum concentration of 1000 g/m^3 was obtained. Results presented in Fig. 12&13 indicate that even in such a high concentrations a maximum values of pressure and rate of pressure rise are not apparent. In case of p_{max}, starting at about 700 g/m^3 pressure seems to level off and stays a bit over 8 bar. For $(dp/dt)_{max}$ its maximum value might be in the range of concentrations 800 g/m^3 – 1000 g/m^3 but a spread of experimental points makes it difficult to confirm.

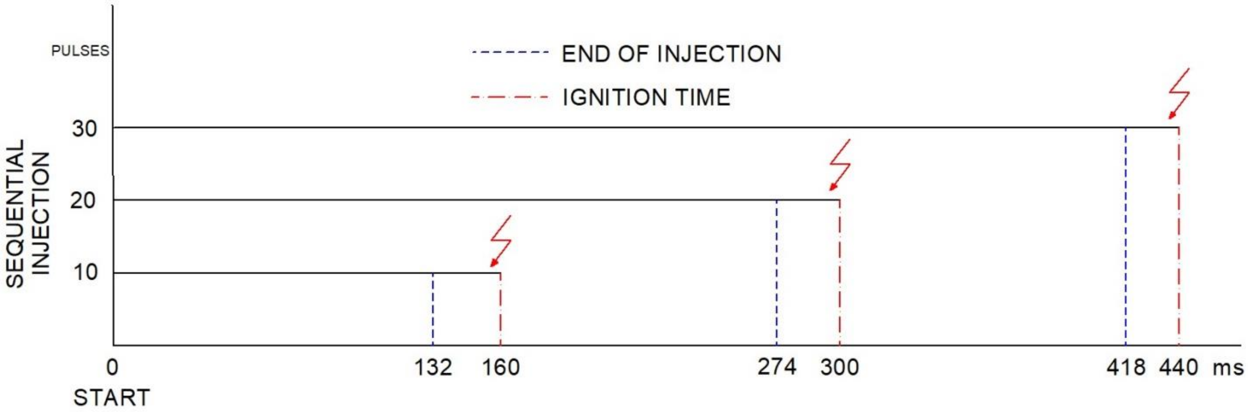

Fig. 11 *Injection and ignition time modification diagram*

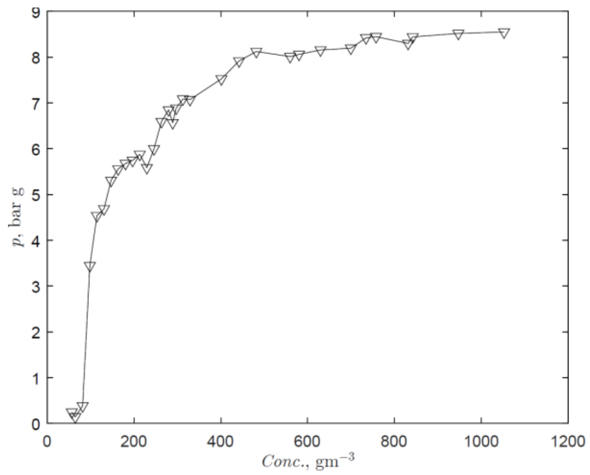

Fig. 12 *p_{max} for Isopropanol in 20℃*

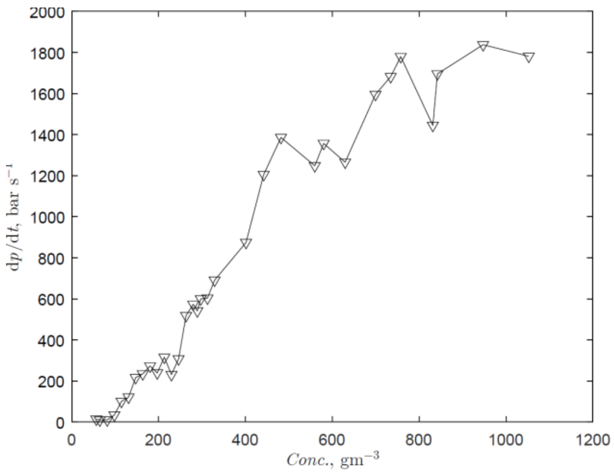

Fig. 13 *dp/dt_{max} for Isopropanol in 20℃*

Both maximum pressure and maximum rate of pressure rise obtained in those tests are smaller than reported by Addai (2016). The difference may be explained by a difference in the method of aerosol generation. Addai did it with use of pressurized air. Such a method is inevitably bounded with generation of a certain level of turbulence which results in an increase of explosion dynamics. A movement of droplets in air may also increase a rate of evaporation.

3. Conclusions

In the paper the prototype equipment intended to use for testing explosive properties of aerosols is described. Preliminary tests allowed to develop a test procedure. The design of the measuring equipment enables:

- Creating of a homogeneous aerosol with a droplet size described by the Sauter diameter in the range of 10 – 30 μm,
- Precise control of the aerosol concentration,
- Measurements under conditions of constant temperature.

When creating aerosol a crucial part is the appropriate selection of the elements making up the aerosol generating system.

The pump-injection system used in this work allows for formation of ~~a~~ homogeneous aerosol in the entire test volume. With this method of aerosol formation, a pressure increase in the test space is caused only by the aerosol volume introduced into the test space. The theoretical maximum pressure rise with the highest isopropanol concentration is about 0.1% of the initial pressure.

By appropriately adjusting the injection opening time in a ten-injections sequence, it is possible to obtain concentrations up to 336 g/m^3 for Kerosene and 314 g/m^3 for Isopropanol. For kerosene that concentration range seems to be sufficient. In the case of Isopropanol, the range has been extended to 1052 g/m^3 by changing the sequence - extending the injection time.

In order to avoid the influence of changes in aerosol concentration resulting from agglomeration or evaporation of droplets, the shortest possible ignition time was chosen. On the basis of a series of measurements of the explosion pressure and the rate of pressure rise at different ignition times for Kerosene aerosol, the ignition time equal to 28 ms after the last injection was selected. The analysis of film frames and the obtained results indicate that the use of a shorter ignition time causes much greater scattering of the measurements.

The explosion parameters of aerosol strongly depend on the temperature at which they are determined. With increasing temperature p_{max} and $(dp/dt)_{max}$ increase.

For Kerosene as well as for Isopropanol at the highest tested concentrations, the measurement results show fluctuations. This may be due to the greater tendency to agglomerate aerosol droplets in high concentrations. For Kerosene, around p_{max} and $(dp/dt)_{max}$, the scattering of the results was the greatest.

With use of the equipment, preliminary assessment of explosive properties of a few aerosols have been carried out. The results suggest that the equipment might be a useful tool for of explosive properties of aerosols. To further check its usefulness additional tests and an interpretation of the results are being performed.

As the next stages of work, determination of other flammability and explosiveness parameters, such as minimum ignition energy are planned.

References

Addai E. K. – (2016) *Investigation of Explosion Characteristics of Multiphase Fuel Mixtures with Air*. Dissertation for the award of the degree Doktor ingenieur

ASTM Standard D3065-01 *Standard Test Methods for Flammability of Aerosol Products* ASTM International, West Conshohocken, PA (2013)

ASTM E1620 – 97 (2016) *Standard Terminology Relating to Liquid Particles and Atomization*

Bane, S.P.M., Ziegler, J.L., Boettcher, P.A., Coronel, S.A. & Shepherd, J.E. (2013). *Experimental investigation of spark ignition energy in kerosene, hexane, and hydrogen*. Journal of Loss Prevention in the Process Industries, 26(2): 290-294.

Bettis, R., Burrell, G., Gant, S. & Coldrick, S. (2017). *Area classification for oil mists* - final report of a Joint Industry Project. RR1107 HSL report, Buxton, UK.

Borowski P. *Identification of the mixing and combustion system in the system of two gasoline direct injection nozzles* (in Polish) Dissertation

Bradley D, Lawes M, Liao S, Saat A, *Laminar mass burning and entrainment velocities and flame instabilities of i-octane, ethanol and hydrous ethanol/air aerosols*. Combust. Flame. 2014, 10.1016/j.combustflame.2013.12.011

Burgyone J.H,. Cohen L, *The effect of drop size on flame propagation in liquid aerosols*. Proc. R. Soc. London. Ser. A. Math. Phys. Sci.. 225, 1954, 375-39210.1098/rspa.1954.0210

Burrell, G. & Gant, S. (2017). *Liquid classification for flammable mists*. RR1108 HSL report, Buxton UK.

Dufaud, O., Charvet, A., Mougel, G., Molière, M., Luthun, S., Brunello, D., Perrin, L., Delimoges, S. & Couchot, M. (2015). *Generation, Characterization and Ignition of Lube Oil Mists*, ASME Turbo Expo 2015, Combustion, Fuels and Emissions. ASME, Montreal, Canada, Paper No. GT2015-43524, p. V04BT04A039.

Eckhoff, R.K. (2016). *Explosion Hazards in the Process Industries*. Gulf Professional Publishing

Eckhoff R.K, *Dust explosions in the process industries: identification, assessment and control of dust hazards.* 2003: Gulf professional publishing.

Eckhoff, R.K. (1995). *Generation, ignition, combustion and explosion of sprays and mists of flammable liquids in air: a literature survey,* Offshore Technology Report OTN 95 260, Health and Safety Executive, Bootle, UK.

Eichhorn, J. (1955). *Careful! Mist can explode. Petroleum Refiner*, 34 (11): 194-196.

EN 13673-2 *Determination of maximum explosion pressure and the maximum rate of pressure rise of gases and vapours - Part 2: Determination of the maximum rate of explosion pressure rise*

Gant, S. (2013). *Generation of flammable mists from high flashpoint fluids*: Literature review. Research Report RR980, HSL report, Buxton, UK.

Gant, S., Bettis, R., Coldrick, S., Burrell, G., Santon, R., Fullam, B., Hill, H., Mouzakitis, K., Giles, A. & Bowen, P. (2016). *Area classification of flammable mists: summary of joint-industry project findings*, Symposium series n°161, IChemE Hazards 26, 24-26 May, Edinburgh, UK.

Gieras M, Klemens R, Kuhl A, Oleszczak P, Trzciński W, Wolański P, *Influence of the chamber volume on the upper explosion limit for hexane-airmixtures*. J. Loss Prev. Process Ind.. 2008, 10.1016/j.jlp.2008.02.006

Hayashi S, Kumagai S, *Flame propagation in fuel droplet-vapor-air mixtures*. Symp. Combust.. 1975, 10.1016/S0082-0784(75)80318-3

Hayashi S, Kumagai S, Sakai T, *Propagation velocity and structure of flames in droplet-vapor-air mixtures*. Combust. Sci. Technol.. 1977,10.1080/00102207708946782

National Fire Protection Association. NFPA 30: *Flammable and combustible liquids code* NFPA (2021)

Mouzakitis, K. & Giles, A. (2017). *Experimental investigation of oil mist explosion hazards,* Research Report RR1109, HSL report, Buxton, UK.

Polymeropoulos C.E. *Flame propagation in aerosols of fuel droplets, fuel vapor and air*. Combust. Sci. Technol.. 1984, 10.1080/00102208408923807

Schick R. *Spray technology reference guide: understanding drop size. Spraying systems* Co. Bulletin, 2008 (459C)

Shuai Yuan, Chenxi Ji, Haitian Han, Yue Sun, Chad V. Mashuga (2021) *A review of aerosol flammability and explosion related incidents, standards, studies, and risk analysis* Process Safety and Environmental Protection Volume 146, February 2021, Pages 499-514

Shuai Yuana, ChenxiJi, Andrew Monhollen, Joseph Sang-II Kwon, Chad Mashuga *Experimental and thermodynamic study of aerosol explosions in a 36 L* Fuel Volume 245, 1 June 2019, Pages 467-477

SKOWRON M. PIELECHA I. (2015) *Comparative analysis of fuel spray behaviour of selected types of liquid fuel injectors* (in Polish) Journal Logistik No.3

Stephanie El - Zahlanieha, Augustin Charveta, Alexis Vignesb, Benoit Tribouilloyb & Olivier Dufauda (2020) *Hydrocarbon aerosol explosion: towards hazardous area classification* Proceedings of the 13th ISHPMIE DOI: 10.7795/810.20200724

Stephanie El - Zahlanieha, Shyarinya Sivabalan a, Idalba Souza Dos Santos a, Benoit Tribouilloy b, David Brunello a, Alexis Vignes b, Olivier Dufaud (2022) *A step toward lifting the fog off mist explosions: Comparative study of three fuels J*. Loss Prev. Process Ind. 74 (2022) 104656

Thimothée, R. (2017) *Experimental characterization of a laminar flame propagation in a two-phase medium (aerosol) in microgravity conditions*, PhD thesis, Université d'Orléans, France (in French).

Williams A. Combustion of liquid fuel sprays. 2013: Butterworth-Heinemann

Graco, Inc. P.O. Box 1441 Minneapolis, MN 55440-1441 ©1995 Graco Inc. Form No. 321-027 8/95 Rev 2 SL Training 11/14

Shepherd J. E., Christopher Krok J. C. and Julian J. Lee *Graduate Jet A Explosion Experiments: Laboratory Testing Aero nautical* Laboratories California Institute of Technology Pasadena, CA 91125 June 26, 1997 corrected on November 21, 1997

C. D. Martin and J. E. Shepherd. "Low temperature autoignition of Jet A and surrogate jet fuel". Journal of Loss Prevention in the Process Industries (2021)

J.T. Edwards, "Reference Jet Fuels for combustion testing". In 55th AIAA Aerospace Sciences Meeting. American Institute of Aeronautics and Astronautics, (2017)

DOI: 10.7795/810.20221124

Coloured Powder potential dust explosions

Blanca Castells [a,b], Isabel Amez [a,b], David León[a,b] & Javier García-Torrent [a,b]

[a] ETSI Minas y Energía, Universidad Politécnica de Madrid, Madrid, Spain
[b] Laboratorio Oficial JM de Madariaga, Universidad Politécnica de Madrid, Getafe, Spain

E-mail: b.castells@upm.es

Abstract

The use of Coloured powder (Holi powder) (colour dust) has been largely used in India for their festivities. Due to their popularity is extensive around the world since the popularity of the parties and events with this kind of show is increasing considerably. Despite the fact of its extensive use, its highly flammable nature is poorly known. Currently, some serious accidents related to the Coloured powder (Holi powder) have been registered (Liao et al., 2016). Coloured powder (Holi powder) organic nature implies a significant increase in the probability to form an explosive atmosphere as their use includes dust dispersion, leading to explosion hazards as has been previously reported (Kukfisz and Piec, 2021). Moreover, it is important to take into account the effects on the flammability of the additives and the colourings existing in the Coloured powder (Holi powder) as they might increase hazard. To properly understand Coloured powder (Holi powder) potential for producing explosive atmosphere, and the attached risk of dust explosions, several samples were tested. Coloured powder (Holi powder) from 6 different manufacturers were gathered. Each manufacturer provided several colours (between 5 and 8) which were characterized through moisture content and particle size determination. Once each sample was characterized, screening tests were performed on each sample setting test conditions and determining whether ignition was produced or not. Those screening test were carried out using the equipment for minimum ignition temperature on cloud determination (0,5 g set at 500 ºC and 0,5 bar), and minimum ignition energy determination (using 100 and 300 mJ energies and 900 and 1200 mg). From those test results, important differences were seen between manufacturers, but most important, differences between colours of the same manufacturer were observed. The screening tests allowed the selection of 11 samples that were fully characterized through thermogravimetric analysis, maximum pressure of explosion, Kst, minimum ignition temperature on cloud, and minimum ignition energy. When carrying out thermogravimetric analysis, some samples increased mass when reaching a temperature between 250 and 350 ºC in a fast process that destabilizes the internal balance and leads to negative mass report. In the flammability and explosion tests, again, important differences were noticed between manufacturers and colours, and so it was possible to determine which of the samples could be used more safely and which poses a serious risk of accident as all combustible powders pose a serious flash fire risk if dispersed near people.

Keywords: *Coloured powder (Holi powder), prevention, dust explosions*

1. Introduction

Dust explosions have been studied for decades due to the high explosion hazard associated to the use, storage and transport of finely divided solids (Eckhoff, 2009, 2003; Fernandez-Anez et al., 2020). Because of that fact its safe use requires deep knowledge regarding material properties and industrial safety measures, preventive and protective. Dust explosions are produced when five factors take place simultaneously: combustible dust, oxygen, confinement, dispersion and ignition source. Indeed, if combustible dust is dispersed into the air in a confined space an explosive atmosphere is generated, if an ignition source is applied to the explosive atmosphere with energy enough it will lead to dust explosion (Amyotte, 2014; Eckhoff, 2005).

Besides those factors, dust explosion risk mainly depends on dust material (physical and chemical properties) and thus, on its chemical composition, moisture, particle size, compaction, etc., (Zhang et al., 2018) as these parameters present an effect on the flammability properties of dusts (Amyotte et al., 2007; Castro et al., 2013; Hassan et al., 2014).

Due to the wide variety of combustible dust, their associated problems take place in several sectors such as the manufacturing, food processing industry, pharmaceutical products, power generation industry (solid fuels), etc., as the processes that take place in those industries can produce small particles that might produce explosive atmospheres. Even more, the risk increases when accumulation and dispersion are not controlled (Medic et al., 2014; Wu et al., 2019). Indeed, nowadays industrial accidents related to dust explosions are still a crucial issue for companies due to their consequence severity: dust explosions produce important human, economic and environmental losses (Taveau, 2017). Although dust explosion principles and prevention measures have been largely studied, and so a decrease in the number of industrial accidents in the last years took place, dust accidents still happen (Abbasi and Abbasi, 2007; Dobashi, 2017) as new materials (such as biofuels, chemical products, etc.) are used every day without having a deep knowledge of their ignition behaviour (Krigstin et al., 2018).

However, dust explosions are not limited to process industries or mines, but also to other scenarios that may affect civil safety. Some daily products such as organic food or medicines can generate explosive dust clouds, but its regular use does not imply a risk for citizens. Nevertheless, in the last years Coloured powder (Holi powder) has become popular, due to the expansion around the world of one of the most popular festivals in India, the Holi party. This type of powder can involve a serious risk that must be studied, as its use typically consists of generating a dust cloud by means of suspended coloured (or Holi) powder. These festivals started in India as a cultural celebration, but nowadays, its colourful attractive effects have involved a big increase in its use throughout the world. Such festivals originally were celebrated outdoors, nevertheless, nowadays these events take part also indoor. When the Coloured powder (Holi powder) material is susceptible to ignition, these confined conditions pose a higher probability to produce an explosion (Taveau, 2017).

The most typical composition of Coloured powder (Holi powder) is based on organic matter, being manufactured from organic substances such as corn starch or rice starch, although they can also be composed by inorganic substances such as talcum ((FOPH), 2017). In order to obtain a colour powder, synthetic pigments and chemical dyes are added. There are some research works regarding the effect of Coloured powder (Holi powder) on health or air quality (Bossmann et al., 2016; Gupta et al., 2019, 2018; Liao et al., 2016; Velpandian et al., 2007) as its use might be harmful and toxic; however, their flammability properties were poorly studied, and a lack of safety measures has led to accidents during those events (Kukfisz and Piec, 2021). Considering that the Coloured powder (Holi powder) main raw matters have been largely studied (mainly as biomass) due to their flammability (Addai et al., 2015; Han et al., 2020; Jiang et al., 2014; Zhang et al., 2017) and the industrial accidents produced by their use are well known (Chen et al., 2017; Han et al., 2020; Randeberg and Eckhoff, 2006; Zhang et al., 2017), it is important to evaluate the flammability of the Coloured powder (Holi powder) in order to prevent further accidents.

Some of the parameters that influence dust flammability and ignition, such as particle size, moisture, ash content or flammable additives vary depending on the manufacturer (Amez Arenillas et al., 2019) which means that the flammable nature of the powder may, therefore, change considerably from one manufacturer to another. The Coloured powder (Holi powder) organic nature gives a hint regarding its flammable behaviour, however, not every Coloured powder (Holi powder) is composed by organic matter, and the additives and dyes directly affect the flammability of this kind of dust.

Indeed, Kukfisz et al. carried out a study comparing flammability and explosion severity parameters for three different Coloured powder (Holi powder) (Kukfisz and Piec, 2021). It was found that minimum ignition energy values were lower than 300 mJ and minimum ignition temperatures were

DOI: 10.7795/810.20221124

between 430 and 450 ºC; characteristics that showed the flammable nature of these kind of dust. Furthermore, they also carry out explosion severity tests finding out that corn starch powders meet the requirements to be considered not only flammable but explosive dusts.

In order to characterize Coloured powder (Holi powder) according to its flammable nature, the present research work departs from a previous study (Amez Arenillas et al., 2019) where a preliminary assessment was carried out and differences between manufacturers and colours were found. The study proved the existence of high flammability properties on this kind of dust developing a risk analysis for different samples from six different manufacturers. In the present research, the authors intend to determine further ignition and explosion severity characteristics in order to provide the needed knowledge to fulfil the safety measures required to assure public safety when handling coloured powder.

To reach this purpose samples from 6 different manufacturers and different colours were collected. Each sample was characterized through particle size determination and moisture content. Afterwards, ignition screening tests were performed to find differences between manufacturers and colours. Furthermore, from the screening tests results, 11 samples were selected to perform ignition and severity explosion characterization tests. Through this characterization, ignition sensitivity was assessed, and safety recommendations and prevention measures can be concluded.

2. Experiments

The manufacturers selected for the present study were commercially available. Most of those manufacturers did not provide enough information regarding its composition. Furthermore, some of them even labelled Coloured powder (Holi powder) packages as “non-flammable” (manufacturer 2). A total of 6 manufacturers were selected from which different colours were collected. Table 1 shows each manufacturer’s studied colours, together with composition and safety recommendations. Regarding its origin, only manufacturers 3 and 4 provides information (made in India).

Table 1: *Selected colours and manufacturers*

	Red	**Orange**	**Yellow**	**Purple**	**Blue**	**Pink**	**Green**	**Dark blue**	**Composition**	**Safety recommendations**
Manufacturer 1		X		X	X				Corn-starch, talcum and FD&C Approved Dyes	To use in open air or ventilated spaces
Manufacturer 2	X	X			X	X	X		Corn-starch and food colouring	To use in open air. Not intended for use in small, confined, poorly ventilated spaces
Manufacturer 3	X	X	X		X	X	X		Corn-starch and food colouring	Do not use indoors
Manufacturer 4	X	X	X	X	X	X	X	X	Corn-starch (99%) and safe dyes (1%)	To use in open air or ventilated spaces
Manufacturer 5	X	X	X	X	X	X	X	X	Corn-starch (99%) and food colouring (1%)	Do not use in enclosed or poorly ventilated areas
Manufacturer 6		X	X	X	X	X	X		Corn-starch, bicarbonate, sodium chloride and food dyes	For use in outdoor or well-ventilated areas

Each sample was characterized through particle size distribution and moisture content. Particle size distribution was determined using Malvern Mastersizer 2000 instrument that provides results using laser diffraction technique and Fraunhofer approximation (assumes that the particle is much larger than the light wavelength). From this technique d10, d50 and d90 parameters were obtained, together with the particle size distribution curve.

On the other hand, moisture content was determined using a Mettler Toledo HB43-S halogen moisture analyser. A disposable pan is tared and filled with 1±0.1 g of sample as a uniform layer and placed inside the analyser. For each sample, moisture content was determined 3 times and the average result was reported.

2.1 Screening tests

The screening tests were carried out using the equipment for Minimum Ignition Energy (MIE) and Minimum Ignition Temperature on cloud (MITc) determination. Screening tests were carried out in order to find significant differences between colours and manufacturers applying economic and fast tests. Because of that, not the complete standardized procedure was carried out, but defined conditions. In particular, for minimum ignition temperature on cloud determination, 0.5 g of sample were set at 500 ºC and using 0,5 bar pressure for dust dispersion. The result of the test is defined as positive if the ignition was produced at those fixed conditions, and negative, if no ignition was observed.

Also, a simplified procedure was used for MIE determination, using a Kuhner Mike-3 equipment; however, two sample concentrations were used. First test was carried out placing 900 mg of sample and applying 100 mJ sparks, second one was set at 900 mg but increasing the energy up to 300 mJ. The third test was carried out using 1200 mg of sample and applying 300 mJ. In each test, and ignition delay of 120 ms was applied. Again, the result of the test is considered positive if the ignition was produced at those fixed conditions, and negative, if no ignition was observed.

Screening tests results allowed the selection of the samples that underwent the complete ignition sensitivity and explosion severity test. For each manufacturer, two samples were selected except for manufacturer 1, whose screening test provide preliminary non-flammable results, so only one colour was selected.

2.2 Ignition sensitivity

Materials ignition sensitivity is typically defined through four tests: lower explosion limit (LEL), minimum ignition temperature on layer (MITl), minimum ignition temperature on cloud (MITc) and minimum ignition energy (MIE); all of them defined by the standard ISO/IEC 80079-20-2:2016 (European committee for standardization CEN-CENELEC, 2016). However, MITl was not carried out as this study focusses on dust explosions in which dust clouds needs to be produced, which only takes place in MIE and MITc. Neither was LEL as explosion severity provides more detailed information.

For MIE, the standard defines the required procedure to determine the material's minimum ignition energy, which is the minimum energy required to ignite a cloud produced by material's suspension in the air. The test was carried out using a Mike 3 apparatus, which is based on a Hartmann Tube equipment. The apparatus consists of a vertical cylindrical glass tube provided with two opposing ignition electrodes separated 6 mm between each other. The tube is connected to a 50 mL air reservoir pressurized that disperses the sample and produces the cloud inside the tube. Different concentrations were tested, applying an ignition delay of 120 ms and spark energies of 1, 3, 10, 30, 100, 300 and 1000 mJ. The software calculates minimum ignition energy by applying the following equation:

$$\log(MIE) = \log(E_2) - I_{E_2} \cdot \frac{\log(E_2) - \log(E_1)}{(NI+I)_{E_2} + 1}$$

Where:

- MIE is the minimum ignition energy expressed in millijoules.
- E_2 is the energy at which the ignition is produced expressed in millijoules.
- I_{E2} is the number of tests at which the ignition is produced at E_2 energy.
- $(NI+I)_{E2}$ is the total number of tests carried out at E_2 energy.

- E_1 is the highest energy at which no ignition takes place expressed in millijoules.

On the other hand, MITc is determined using a vertical furnace, based on the Godbert-Greenwald Apparatus (Eckhoff, 2019) whose temperature can be controlled. A silicon tube is place vertically placed in the furnace with its bottom open to the air. The top is connected to a glass adapter where the sample is placed, which is connected to a valve that releases compressed air in order to disperse the dust and produce the dust cloud inside the furnace. For the test, 0.3 g of sample are placed on the glass tube and the furnace temperature is set at 500 ºC. If ignition is not produced, the test is repeated increasing temperature 50 K until ignition takes place or up to 900 ºC. After ignition is produced, mass and dispersion pressure are varied until the most vigorous ignition is produced. Afterwards, using the same mass and dispersion pressure, further tests are carried out reducing temperature in steps of 20 K until no ignition is obtained after 10 attempts.

2.3 Explosion severity

Explosion severity parameters are defined using 20-L sphere equipment, in which dust is dispersed to form a dust cloud under standard conditions of pressure and temperature and applying ignition using two 5000 J igniters. Again, the procedure is standardized through SO/IEC 80079-20-2:2016 (European committee for standardization CEN-CENELEC, 2016).

The apparatus is equipped with pressure sensors that record explosion pressure and time, so maximum explosion pressure (P_{max}) and pressure-time rate (dP/dt) are defined. The definition of P_{max} provides important information regarding flash fire severity, as is a surrogate for the flame temperature which is the main parameter for flash fire severity characterization. The maximum rate of explosion pressure rise $(dP/dt)_{max}$ allows the determination of the standard constant (K_{st} or K_{max}) as:

$$K_{st} = (dP/dt)_{max} \cdot \sqrt[3]{V}$$

Where V represents the volume expressed in m^3. Furthermore, K_{st} provides information regarding explosion severity as shows Table 2:

Table 2: *Rating explosion severity according to Kst*

Dust Explosion Class	K_{st} (bar · m/s)	Characteristic
St 0	0	No explosion
St 1	(0, 200]	Weak explosion
St 2	(200, 300]	Strong explosion
St 3	>300	Very strong explosion

2.4 Simultaneous thermal analysis (STA)

Simultaneous thermal analysis (STA) consists of perform TGA and DSC simultaneously. Thermogravimetric analysis (TGA) is an analytical technique that monitors samples weight changes while applying heat so thermal stability and volatile fractions can be determined. On the other hand, differential scanning calorimetry (DSC) is a thermal technique that measures the energy exchanged from a sample that undergoes a physical or chemical change. The technique measures the difference in the amount of heat required to increase the temperature of a sample and reference as a function of temperature. In other words, DSC analysis calculates the amount of energy required to increase sample's temperature by comparing it to a reference material.

In the present study, Mettler Toledo TG-DSC T50 apparatus was used, together with 70 µL alumina crucibles where 30±2 mg of sample is place. The test is carried out controlling the atmosphere inside the furnace, the initial and final temperature (30 and 800 ºC respectively), and the heating rate (β=50K/min), and records temperature, mass, heat flow and time during the whole procedure. The furnace atmosphere was air, so one of the key reactions was oxidation.

3. Results and discussion

3.1 Samples characterization

As mentioned above, each sample was characterized trough particle size and moisture content. Table 3 shows the results obtained for each sample, together with standard deviation for each parameter and manufacturer (calculated considering every colour).

Table 3: *Samples characterization*

Manufacturer	Colour	d10 (µm)	d50 (µm)	d90 (µm)	Moisture (%)
1	Orange	1.341	12.069	67.568	3.52
1	Purple	1.851	12.044	56.058	2.10
1	Blue	1.242	7.97	39.578	1.97
Standard Deviation (σ_1)		**0.33**	**2.36**	**14.07**	**0.87**
2	Red	9.329	14.39	22.034	10.25
2	Orange	8.933	13.686	20.747	10.34
2	Blue	2.756	10.158	25.811	1.91
2	Pink	2.195	8.477	32.34	0.67
2	Green	8.877	13.338	19.83	10.57
Standard Deviation (σ_2)		**3.61**	**2.56**	**5.11**	**5.00**
3	Red	8.515	14.255	24.197	9.90
3	Orange	8.603	14.496	26.919	10.20
3	Yellow	8.159	15.335	60.137	10.24
3	Blue	8.309	15.001	33.838	9.70
3	Pink	8.57	14.321	26.493	10.14
3	Green	8.496	15.522	37.841	9.78
Standard Deviation (σ_3)		**0.17**	**0.54**	**13.38**	**0.23**
4	Red	9.100	14.024	21.424	11.26
4	Orange	8.943	13.285	19.546	10.72
4	Yellow	9.382	13.984	20.689	10.60
4	Purple	9.428	14.050	20.782	10.64
4	Blue	9.661	13.700	19.324	10.44
4	Pink	9.461	14.062	20.779	10.66
4	Green	9.497	13.587	19.334	10.55
4	Dark Blue	9.317	13.906	20.596	10.18
Standard Deviation (σ_4)		**0.23**	**0.28**	**0.79**	**0.31**
5	Red	9.309	13.808	20.281	10.06
5	Orange	9.095	13.797	20.719	11.21
5	Yellow	9.16	14.043	21.388	13.65
5	Purple	9.526	13.619	19.346	12.79
5	Blue	9.541	13.614	19.289	12.02
5	Pink	9.105	13.558	20.003	11.52
5	Green	8.949	13.635	20.593	9.93
5	Dark Blue	9.279	13.885	20.608	10.25
Standard Deviation (σ_5)		**0.21**	**0.17**	**0.71**	**1.35**
6	Orange	10.41	79.575	335.672	5.24
6	Yellow	9.971	21.907	335.22	5.95
6	Purple	10.889	62.955	334.409	11.02
6	Blue	10.17	26.634	301.045	5.68

6	Pink	11.332	127.304	391.097	4.37
6	Green	10.408	110.53	328.108	10.46
Standard Deviation (σ_6)		**0.50**	**43.01**	**29.35**	**2.86**

Particle size does never exceed 500 μm which is the nominal size under which dust can produce explosive atmospheres. It is remarkable the colour effect in both particle size and moisture, as for the same manufacturer, samples heavily differ depending on colour. Those differences are clearly seen when assessing standard deviation (σ_i). When comparing manufacturer 1, 2, 3 and 6 colours, it can be noticed that high σ_i values are obtained for particle size determination, especially d90. On the other hand moisture is a more homogeneous parameter besides samples 2 and 6, where differences between colours are clearly noticed. This fact means that for the same raw material composition, the applied dyes produce significant physical changes. For example, when considering manufacturer 2 moisture content, it is noticed that blue and pink colours present low moisture content, while the remaining colours show >10% moisture. On the other hand, manufacturers 3, 4 and 5 presented more homogeneous results. As physical parameters affect explosion severity and flammability parameters (Castells et al., 2020; Eckhoff and Mathisen, 1978; Pietraccini et al., 2021; Rifella et al., 2019; Russo et al., 2013; Zhang et al., 2017), it can be deduced that not every colour from the same manufacturer will behave identically in subsequent tests. Samples from manufacturer 6 show much higher d90 values.

3.2 Screening tests

The screening tests results were considered positive if ignition was detected, and negative on the other hand. Figure 1 plots the results for each sample, where the bars are coloured in the colour they represent.

DOI: 10.7795/810.20221124

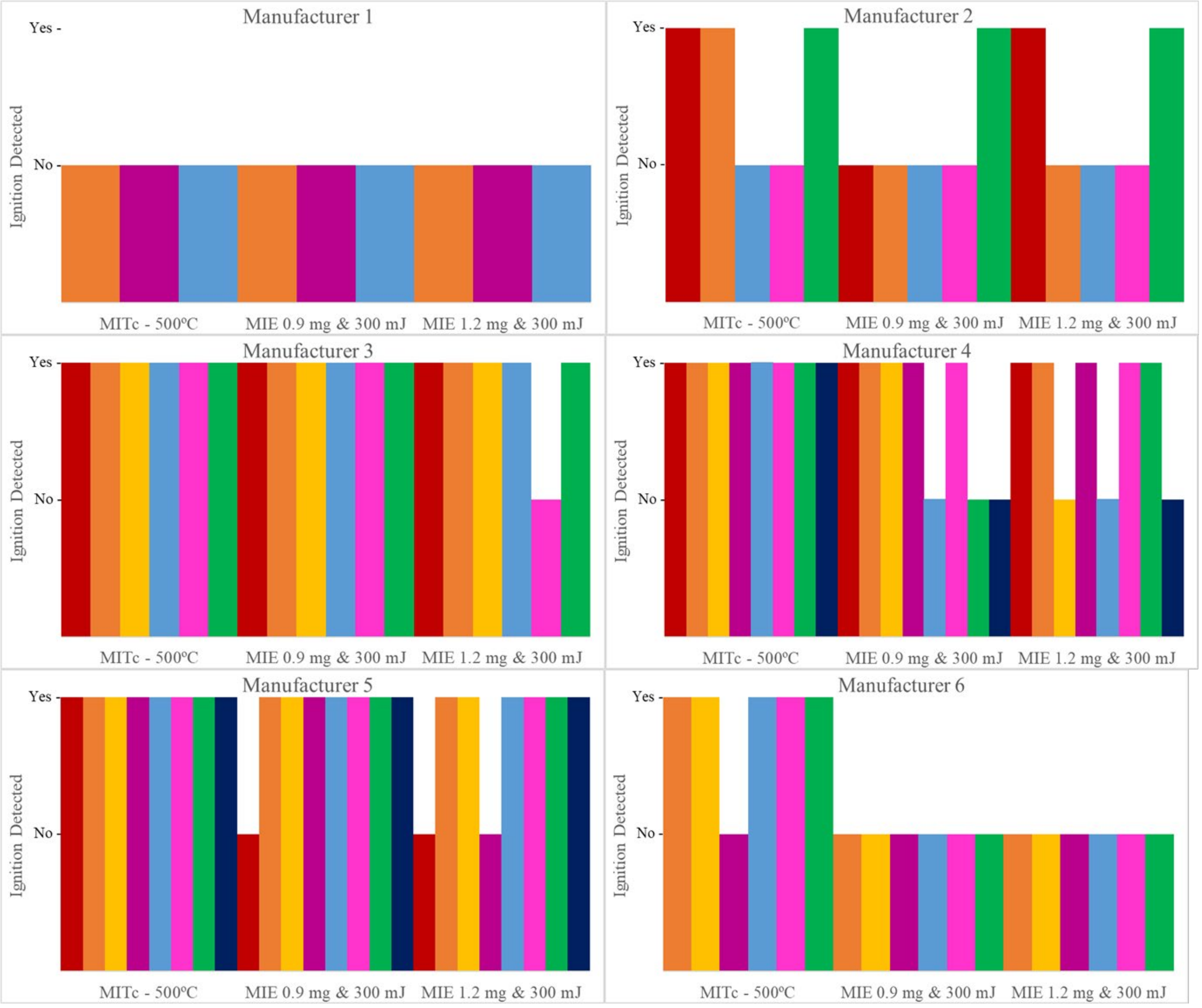

Fig. 1. *Screening test results*

From the screening test can be noticed that samples have a tendency to produce more positive results when testing MITc than MIE, as no positive result was found in MIE if not found previously in MITc. Furthermore, from the results it is shown that manufacturers 1 and 6 preliminary produce the less flammable products. This fact can be explained due to its composition. Manufacturer 1 raw material composition is not only corn-starch, but also talcum which is an inert material and reduces flammability sensitivity. On the other hand, manufacturer 6 is composed by corn-starch, bicarbonate, and sodium chloride, being these last two inert materials. However, for this manufacturer, the adding of inert material does not completely erase flammability risks as 5 of 6 samples resulted positive when testing MITc.

The screening tests allowed the selection of 11 samples for complete characterization. For each manufacturer two samples were selected: one with significant flammable sensitivity and another with less sensitivity (besides manufacturer 1, from which only one sample was selected). Those samples were characterized through proximate analysis, in order to have a better knowledge of their composition. Those results are shown in table 4.

Table 4: *Selected samples proximate analysis*

Manufacturer	Colour	Moisture (%)	Volatiles (%)	Ash (%)
1	Purple	2.05	29.838	66.815
2	Blue	1.91	61.155	31.432
2	Green	10.57	58.916	23.812
3	Yellow	10.24	84.973	0.253
3	Blue	9.70	86.418	0.137

4	Red	11.26	84.928	0.202
4	Blue	10.44	85.460	0.331
5	Red	10.06	91.244	1.380
5	Yellow	13.65	95.715	0.604
6	Yellow	5.95	47.179	26.731
6	Purple	11.02	43.617	26.649

The high ash contents for samples produced by manufacturer 1, 2 and 6 preliminary indicates that lower explosivity severity will be obtained when testing those samples, especially manufacturer 1 whose ash content is the highest. When carrying out ash test, some kind of explosion was detected when temperature reached around 300ºC, as important amount of smoke was produced inside the furnace together with low explosion sounds. As it is shown in figure 2, some of the samples heavily increased their mass overflowing the crucible. However, this phenomenon will be addressed through TGA as it will detect the mass increase and the temperature at which is produced, together with heat flow transfer.

Fig. 2. *Ash content analysis*

3.3 Ignition sensitivity and explosion severity

The obtained results from MITc and 20-L sphere are shown in table 5. It can be noticed that, according to K_{st} characterization, every sample classifies to “weak explosion” besides manufacturer 1, where no explosion was detected.

It might seem that complete test results are not consistent with screening test results, especially regarding MITc as some samples did not produce ignition when carrying out MITc screening test at 500ºC but when carrying out the complete procedure MITc below 500ºC were found. It can be explained since complete procedure not only modifies temperature but also sample weight and pressure, so that concentration and turbulence are thoroughly modified. Because of that, MITc could be lower than 500ºC. Similar situation takes place when considering manufacturer 4-blue sample, whose MIE is set at 190 mJ and it was found negative when testing MIE screening tests at 300 mJ. Again, the complete procedure modifies concentration and ignition delay, so the MIE can be lower than the energy applied when performing screening tests.

Table 5: *Flammable and explosion severity results*

Manufacturer	**Colour**	**MIE (mJ)**	**MITc (ºC)**	**P_{max} (bar)**	**$(dP/dt)_{max}$ (bar/s)**	**K_{st} (bar · m/s)**
1	Purple	150	480	0	0	0
2	Blue	>1000	490	6.5	71	19
2	Green	55	420	7.5	218	59
3	Yellow	79	400	8.2	351	95
3	Blue	55	390	8.1	344	93
4	Red	380	400	8.5	373	101

4	Blue	190	380	8.4	354	96
5	Red	>1000	420	7.8	376	102
5	Yellow	240	400	8.8	518	141
6	Yellow	>1000	510	6.5	307	83
6	Purple	>1000	460	6.6	43	12

Overall MITc results are consistent with results published by Kukfisz and Piec, 2021, as temperature range varies between 400 and 500 ºC. However, they found the lowest MITc value for the sample containing talcum, while in the present study talcum, as inert material, difficulties ignition leading to greater temperatures. Between colours of the same manufacturer, no significant differences of MITc were found, besides manufacturer 6, whose samples differ 50K.However, the same cannot be said about MIE, as some manufacturers (1 and 5 mainly) show really low energies for one of their samples, and greater than 1000 mJ for the other one. Even if, according to packaging specifications, manufacturers 4 and 5 present the same composition, different behaviour was noticed between both, even considering the same colour.

As it has been said, week explosions were detected, as the maximum pressure rate rarely increases over 400 bar/s. However, significant pressures were detected, especially for manufacturers 3, 4 and 5, which also produce the greatest pressure rates and, therefore, K_{st}. As previously mentioned, this fact is related to samples ash content. Indeed, as it was suggested in the previous section, manufacturer 1 high ash content leads to no explosion detection when performing the test. If compared to the results obtained by Kukfisz and Piec, 2021, samples 3, 4 and 5 behaves similar to their results for corn-starch. According to packaging specifications, samples 4 and 5 present a composition 99% corn-starch, which explains the similar results. For sample 3, no exact composition was provided by the manufacturer, however the results clearly show that corn-starch is present in high concentrations. On the other hand, manufacturer 1, which includes talcum in their samples, did not generate explosion while the talcum sample tested by Kukfisz and Piec, 2021, did. It can be deduced that manufacturer 1 samples presented higher talcum concentrations which lead to no explosion.

Nevertheless, the obtained results show that most of the samples present a high content of corn-starch and, therefore, a true explosion and flash fire risk is implied when using Coloured powder (Holi powder), particularly considering that its use involve dust dispersion in the air, and so, producing explosive atmospheres.

From the ignition sensitivity and explosions severity results it is noticed that applied dyes produce significant differences in those parameters, and therefore, in their ignition and explosion associated risk. Furthermore, some samples present low ignition values both for energy and temperature, which means that its use might require safety measures.

Overall, manufacturers 3,4 and 6 showed the most homogeneous results considering different colours results. However, manufacturers 2 and 5 showed important discrepancies especially when assessing MIE. Furthermore, those samples show significant Kst discrepancies and 1 bar maximum pressure differences. Those differences cannot be explained by particle size as samples present similar average values, and neither by moisture as differences are noted in manufacturer 2 but not in number 5. From those results it can be deduced that discrepancies are produced by the ash content, as in both samples, greater ash percentage lead to higher flammable and explosion severity parameters.

3.4 Thermogravimetric Analysis and Differential Scanning Calorimetry

TGA results can be divided into two groups: samples that progressively loss mass when increasing temperature and samples that increase mass when increasing temperature. Those results are plotted in figure 3. On the other hand, DSC behaviour is similar for every sample, so DSC curves are plotted all together in figure 4.

DOI: 10.7795/810.20221124

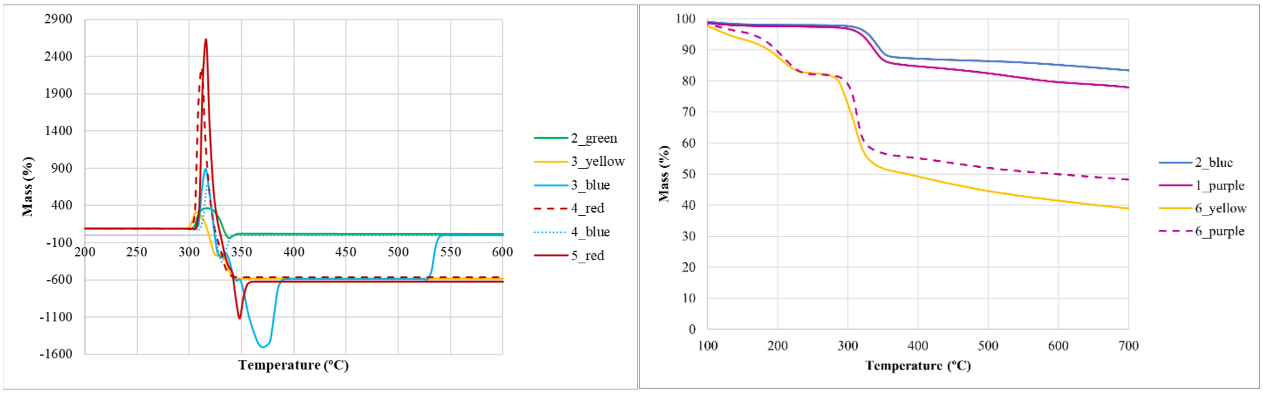

Fig. 3. *TGA curves from 200ºC to 600ºC*

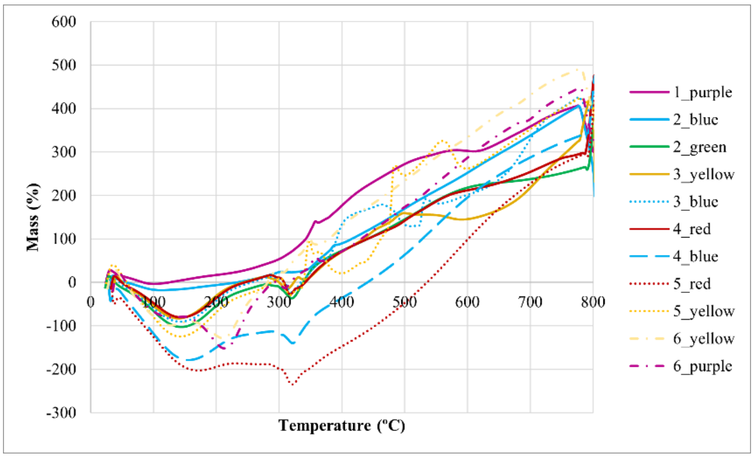

Fig. 4. *DSC curves*

According to the effects noticed during ash analysis, an explosion was preliminary though to be happened. However, when carrying out STA it was noticed that the heat flow during mass increase was negative, in other words, reaction was found to be endothermic, so no explosion nor deflagration was produced. For those samples that experiment mass increase, temperature at which mass begins its increase (T_0), together with temperature at which mass reaches its maximum ($T_{m,max}$) and the percentual mass increase can be seen in table 6. Furthermore, heat absorbed (negative values) or released (positive values) during mass increase process can be calculated integrating heat flow curve and it is also provided in this table.

Table 6: *Mass increase STA values*

Manufacturer	**Colour**	**T_0 (ºC)**	**$T_{m,max}$ (ºC)**	**Mass increase (%)**	**Heat (mJ)**
2	Green	300.63	317.02	363.42	-622.19
3	Yellow	297.71	307.11	296.08	-316.75
3	Blue	305.65	315.03	887.89	-563.74
4	Red	300.95	310.96	2243.10	-934.12
4	Blue	309.42	316.95	692.37	-327.46
5	Red	305.21	315.13	2621.98	-792.82
5	Yellow	304.42	313.5	1892.57	-789.43

Clearly, the higher the mass increase, the higher the heat absorbed. DSC plot shows that samples that increased mass, showed a heat flow negative peak around 300K while the others, showed a progressive increase as samples combustion releases heat. The samples that did not produce mass increase are the ones that show better flammability and explosion severity results, which means that TGA analysis can provide preliminary information regarding samples characterization prior to carry out the complete test procedures. The samples that presented a regular behaviour (mass progressively decreases) are the ones that presented higher ash content, which again, shows the importance of composition on those parameters.

Moreover, the samples that showed the greatest mass increase correspond to those that showed the highest $(dP/dt)_{max}$ values, so if several samples are tested and compared a correlation might be found, and preliminary behaviour predictions can be stated.

Nevertheless, the mass increase when performing STA was a non-usual result, as mass increase only takes place when buoyancy effect is produced (Bottom, 2008; Menczel and Prime, 2009) and not great mass increase percentage is produced, and the present results show more than 500% mass increase. Furthermore, from figure 2 it was noticed that volume increased took place around 300 ºC, which could be related to thermal expansion, and it was a fast process, as the maximum mass percentage was reached after temperature increased ~10K. Indeed, solid's molecules have a reasonably fixed position within it, although each atom of the crystal lattice vibrates (and therefore moves), and the amplitude will depend on the total energy of the atom or molecule. When heat is absorbed, the average kinetic energy of the molecules increases and with it the average amplitude of vibrational motion and the combined effect of this increase is what gives the increase in body volume called thermal expansion. Considering that the thermal expansion was produced quickly, the fast volume increase could produce a serious buoyancy effect which completely destabilizes equipment balance and leads to mass negative values when buoyancy phenomenon is over. Moreover, oxidation of some of the inorganic dyes and pigments (or possible metals in the powder) can contribute to the mass increase noticed when performing TGA. This oxidation is also a fast process, whose characteristics meet the buoyancy effect, so a mix of both process can take place.

4. Conclusions

Several samples were characterized in the present study. The screening test allowed to see differences between manufacturers and colours, which allowed estimating that dyes would affect flammability properties. Indeed, when carrying out ignition sensitivity and explosion severity characterization, those difference were remarkable, and also dyes effects.

The results provided in this research can be very useful as it characterizes different samples and parameters, comparing compositions, physical parameters such as particle size, and flammability characterization. It was noticed that proximate analysis provides important information, as the ash content heavily influenced explosion severity results.

The use of Coloured powder (Holi powder) constitutes a serious risk when dispersed in enclosed spaces, as it produces a dust explosive atmosphere. Furthermore, the ignition conditions of these atmospheres are not very demanding, and therefore, the explosion can be easily produced. It was noticed that manufacturers did not take this fact into account as the safety recommendations seem not to consider the further consequences that could happen if used in a confined space. Its flammable nature should be addressed and indicated in the package instead of avoiding this information. Moreover, manufacturer 2 package specified "non-flammable", however the obtained results differ from this statement, which may incur into fatal accidents.

Due to the tests carried out in this study it was noticed that some manufacturers (1 and 6) presented higher ignition parameters, so the flammable conditions are more difficult to reach. The addition of inert materials to composition produced the ignition parameters increase, which means that manufacturers that incorporate inert materials to corn-starch produce a safer Coloured powder (Holi powder). Between both manufacturers that meet this condition, manufacturer 1 showed better results, which means that talcum addition better reduces ignition than bicarbonate and sodium chloride, and high ash content reduces explosion risk.

Although this study has focused on air dispersion in order to produce dust clouds, TGA and ash content analysis were carried out on non-dispersed sample. Furthermore, an initial relationship between TGA and explosion rate was found, so further studies could focus on a better definition of this relation.

From TGA tests it was noticed that around 300ºC the dust undergoes thermal expansion which rapidly enlarges volume. This fact should also be addressed, and Coloured powder (Holi powder) safe storage conditions should be defined in order to avoid accidents due to thermal expansion.

References

Boilard, S.P., Amyotte, P.R., Khan, F.I., Dastidar, A.G. & Eckhoff, R.K. (2013). Explosibility of micron- and nano-size titanium powders. *Journal of Loss Prevention in the Process Industries*, 26(6): 1646-1654.

Eckhoff, R.K. (2003). *Dust explosions in the process industries*. Third edition. Gulf Professional Publishing, Amsterdam.

(FOPH), S.F.O. of P.H., 2017. Holi powders: factsheet for importers and distributors.

Abbasi, T., Abbasi, S.A., 2007. Dust explosions-Cases, causes, consequences, and control. J. Hazard. Mater. 140, 7–44. https://doi.org/10.1016/j.jhazmat.2006.11.007

Addai, E.K., Gabel, D., Krause, U., 2015. Explosion characteristics of three component hybrid mixtures. Process Saf. Environ. Prot. 98, 72–81. https://doi.org/10.1016/j.psep.2015.06.013

Amez Arenillas, I., Garcia-Torrent, J., Castells, B., Medic, L., 2019. RISK ANALYSIS OF THE FLAMMABILITY OF THE COLOUR DUST (HOLI POWDER), 32. MEĐUNARODNI KONGRES O PROCESNOJ INDUSTRIJI.

Amyotte, P.R., 2014. Some myths and realities about dust explosions. Process Saf. Environ. Prot. 92, 292–299. https://doi.org/10.1016/j.psep.2014.02.013

Amyotte, P.R., Pegg, M.J., Khan, F., Nifuku, M., Yingxin, T., 2007. Moderation of dust explosions. J. Loss Prev. Process Ind. 20, 675–687. https://doi.org/10.1016/j.jlp.2007.05.011

Bossmann, K., Bach, S., Höflich, C., Valtanen, K., Heinze, R., Neumann, A., Straff, W., Süring, K., 2016. Holi colours contain PM10 and can induce pro-inflammatory responses. J. Occup. Med. Toxicol. 11, 1–11. https://doi.org/10.1186/s12995-016-0130-9

Bottom, R., 2008. Thermogravimetric Analysis, Principles and Applications of Thermal Analysis, Wiley Online Books. Blackwell Publishing Ltd. https://doi.org/https://doi.org/10.1002/9780470697702.ch3

Castells, B., Amez, I., Medic, L., Torrent, J.G., 2020. Particle size influence on the transport classification labels and other flammability characteristics of powders. Appl. Sci. 10, 1–14. https://doi.org/10.3390/app10238601

Castro, Z.S., Gauthier-maradei, P., Hernández, H.E., 2013. Effect of particle size and humidity on sugarcane bagasse combustion in a fixed bed furnace. Rev. Ion 26, 73–85.

Chen, T., Zhang, Q., Wang, J.X., Liu, L., Zhang, S., 2017. Flame propagation and dust transient movement in a dust cloud explosion process. J. Loss Prev. Process Ind. 49, 572–581. https://doi.org/10.1016/j.jlp.2017.03.022

Dobashi, R., 2017. Studies on accidental gas and dust explosions. Fire Saf. J. https://doi.org/10.1016/j.firesaf.2017.04.029

Eckhoff, R.K., 2019. Origin and development of the Godbert-Greenwald furnace for measuring minimum ignition temperatures of dust clouds. Process Saf. Environ. Prot. 129, 17–24. https://doi.org/10.1016/J.PSEP.2019.06.012

Eckhoff, R.K., 2009. Understanding dust explosions. The role of powder science and technology. J. Loss Prev. Process Ind. 22, 105–116. https://doi.org/10.1016/j.jlp.2008.07.006

Eckhoff, R.K., 2005. Explosion hazards in the process industries. Gulf Professional Publishing, Norway (University of Bergen). https://doi.org/https://doi.org/10.1016/C2014-0-03887-7

Eckhoff, R.K., 2003. Dust Explosions in the Process Industries: Identification, Assessment and Control of Dust Hazards: Third Edition, Dust Explosions in the Process Industries: Identification, Assessment and Control of Dust Hazards: Third Edition. Elsevier Inc. https://doi.org/10.1016/B978-0-7506-7602-1.X5000-8

Eckhoff, R.K., Mathisen, K.P., 1978. A critical examination of the effect of dust moisture on the rate of pressure rise in Hartmann bomb tests. Fire Saf. J. 1, 273–280. https://doi.org/10.1016/0379-7112(78)90016-4

European committee for standardization CEN-CENELEC, 2016. ISO/IEC 80079-20-2:2016 Explosive atmospheres - Part 20-2: Material characteristics - Combustible dusts test methods.

Fernandez-Anez, N., Castells Somoza, B., Amez Arenillas, I., Garcia-Torrent, J., 2020. Explosion Risk of Solid Biofuels, 1st ed, SpringerBriefs in Energy. Springer International Publishing. https://doi.org/10.1007/978-3-030-43933-0

Gupta, A., Gautam, S., Mehta, N., Patel, M.K., Talatiya, A., 2019. Association between changes in air quality and hospital admissions during the holi festival. SN Appl. Sci. 1, 1–8. https://doi.org/10.1007/s42452-019-0165-5

Gupta, S., Selvan, H., Markan, A., Gupta, V., 2018. Holi colors and chemical contact keratitis. Eye 32, 1–3. https://doi.org/10.1038/eye.2017.223

Han, B., Li, G., Yuan, C., Wang, Q., 2020. Flame propagation of corn starch in a modified Hartmann tube with branch structure. Powder Technol. 360, 10–20. https://doi.org/10.1016/j.powtec.2019.10.014

Hassan, J., Khan, F., Amyotte, P.R., Ferdous, R., 2014. A model to assess dust explosion occurrence probability. J. Hazard. Mater. 268, 140–149. https://doi.org/10.1016/j.jhazmat.2014.01.017

Jiang, J., Liu, Y., Mannan, M.S., 2014. A correlation of the lower flammability limit for hybrid mixtures. J. Loss Prev. Process Ind. 32, 120–126. https://doi.org/10.1016/j.jlp.2014.07.014

Krigstin, S., Wetzel, S., Jayabala, N., Helmeste, C., Madrali, S., Agnew, J., Volpe, S., 2018. Recent Health and Safety Incident Trends Related to the Storage of Woody Biomass : A Need for Improved Monitoring Strategies. Forests. https://doi.org/10.3390/f9090538

Kukfisz, B., Piec, R., 2021. The Fire and Explosion Hazard of Coloured Powders Used during the Holi Festival. Int. J. Environ. Res. Public Health 18, 11090. https://doi.org/10.3390/ijerph182111090

Liao, Y.L., Yeh, L.K., Tsai, Y.J., Chen, S.Y., 2016. Colored corn starch dust explosion-related ocular injuries at a Taiwan water park: A preliminary report from a single medical center. Taiwan J. Ophthalmol. 6, 123–126. https://doi.org/10.1016/j.tjo.2016.05.004

Medic, L., Fernandez-Anez, N., Montenegro Mateos, L., Garcia-Torrent, J., Ramírez, Á., 2014. Characterization of spontaneous combustuion tendency of dried sewage sludge. Proc. Tenth Int. Symp. Hazards, Prev. Mitig. Ind. Explos. (X ISHPMIE) 1453–1462.

Menczel, J.D., Prime, R.B., 2009. Thermal Analysis of Polymers: Fundamentals and Applications. John Wiley & Sons, Inc, Hoboken, NJ, USA.

Pietraccini, M., Danzi, E., Marmo, L., Addo, A., Amyotte, P., 2021. Journal of Loss Prevention in the Process Industries Effect of particle size distribution , drying and milling technique on explosibility behavior of olive pomace waste. J. Loss Prev. Process Ind. 71, 104423. https://doi.org/10.1016/j.jlp.2021.104423

Randeberg, E., Eckhoff, R.K., 2006. Initiation of dust explosions by electric spark discharges triggered by the explosive dust cloud itself. J. Loss Prev. Process Ind. 19, 154–160. https://doi.org/10.1016/j.jlp.2005.05.003

Rifella, A., Setyawan, D., Chun, D.H., Yoo, J., Kim, S. Do, Rhim, Y.J., Choi, H.K., Lim, J., Lee, S., Rhee, Y., 2019. The effects of coal particle size on spontaneous combustion characteristics. Int. J. Coal Prep. Util. 0, 1–25. https://doi.org/10.1080/19392699.2019.1622529

Russo, P., Amyotte, P.R., Khan, F., Di Benedetto, A., 2013. Modelling of the effect of size on flocculent dust explosions. J. Loss Prev. Process Ind. 26, 1634–1638. https://doi.org/10.1016/j.jlp.2013.07.012

Taveau, J., 2017. Dust explosion propagation and isolation. J. Loss Prev. Process Ind. 48, 320–330. https://doi.org/10.1016/j.jlp.2017.04.019

Velpandian, T., Saha, K., Ravi, A.K., Kumari, S.S., Biswas, N.R., Ghose, S., 2007. Ocular hazards of the colors used during the festival-of-colors (Holi) in India-Malachite green toxicity. J. Hazard. Mater. 139, 204–208. https://doi.org/10.1016/j.jhazmat.2006.06.046

Wu, D., Schmidt, M., Berghmans, J., 2019. Spontaneous ignition behaviour of coal dust accumulations: A comparison of extrapolation methods from lab-scale to industrial-scale. Proc. Combust. Inst. 37, 4181–4191. https://doi.org/10.1016/j.proci.2018.05.140

Zhang, H., Chen, X., Zhang, Y., Niu, Y., Yuan, B., Dai, H., He, S., 2017. Effects of particle size on flame structures through corn starch dust explosions. J. Loss Prev. Process Ind. 50, 7–14. https://doi.org/10.1016/j.jlp.2017.09.002

Zhang, J., Xu, P., Sun, L., Zhang, W., Jin, J., 2018. Factors influencing and a statistical method for describing dust explosion parameters: A review. J. Loss Prev. Process Ind. 56, 386–401. https://doi.org/10.1016/j.jlp.2018.09.005

DOI: 10.7795/810.20221124

Investigation of Marginally Explosible Dusts

Albert Addo [a], Maria Portarapillo [b], Almerinda Di Benedetto [b], Yajie Bu [c], Yuan Chunmiao [c],
Ashok Dastidar [d], Faisal Khan [e] & Paul Amyotte [a]

[a] Department of Process Engineering & Applied Science, Dalhousie University, Halifax, NS, Canada
[b] Department of Chemical, Materials & Production Engineering, University of Naples Federico II, Naples, Italy
[c] Fire & Explosion Protection Laboratory, Northeastern University, Shenyang, China
[d] Fauske & Associate LLC, Burr Ridge, IL, USA
[e] Mary Kay O'Connor Process Safety Center, Texas A&M University, College Station, TX, USA

E-mail: al246147@dal.ca

ABSTRACT

This investigation is focused on a group of combustible dusts that have been referred to as “marginally explosible” in previous studies. Marginally explosible dusts (MEDs) are distinguished by relatively low volume-normalized maximum rate of pressure rise (K_{St}) and maximum explosion pressure (P_{max}) values. Earlier studies have suggested that dusts with K_{St} values less than 45 bar·m/s in the laboratory-scale 20-L chamber would not explode in the 1-m^3 chamber and therefore not on an industrial scale. Conversely, for some metallic dusts, significantly higher K_{St} values are generated in the 1-m^3 chamber. The problem of classifying these materials continues to exist, and industries that handle them continue to search for answers to the questions “are they explosible or not?” and “should we protect or not protect against explosions of these dusts?”. The research follows an earlier campaign that tested two different particle sizes of polyethylene dust in the 20-L chamber (with 2.5-, 5-, and 10-kJ chemical ignitors) and the 1-m^3 chamber (with only 10-kJ ignitors). From this previous study, it was surmised that as the particle diameter increased, the coarser polyethylene dust approached its limit of flammability. This accounted for the low K_{St} value < 45 bar·m/s in the 20-L chamber as well as insensitivity to spark ignition. Despite these results, the coarser polyethylene sample was determined not to be a marginally explosible dust because it clearly exploded in the 1-m^3 chamber.

In order to provide a clear judgement on the question of whether such dusts are explosible or not, the current study involves additional, well-characterized materials that cover a range of industries. The materials tested were carbon black, oat grain flour, urea, and zinc. Five ignition energies (i.e., 0.5, 1, 2.5, 5 and 10 kJ) were used in the 20-L chamber tests. The current results show a clear case of overdriving (as a result of the high ignition energy density in the 20-L chamber) with respect to urea and carbon black dusts. According to the data from the lower ignition energies, 1-m^3 chamber, MIKE-3 apparatus, and BAM oven, the urea dust is non-explosible. For zinc dust, the small size of the 20-L sphere and reaction time therein, restrict full combustion development, which is not the case in the 1-m^3 chamber. The data also suggests that generally, for dusts whose flame propagation is dictated by a homogeneous combustion path, the 20-L chamber is recommended. Also, generally, for dusts whose flame propagation is controlled by heterogeneous combustion, the 1-m^3 chamber is recommended. However, some materials deviate from their expected combustion behaviour, and thus influence the choice of test chamber. With reference to urea dust, a new definition for MEDs has been suggested as dusts having P_{max} < 3.0 bar(g), K_{St} < 20 bar·m/s (in the 20-L chamber), MEC > 500 g/m^3, MIE > 1000 mJ, and MIT > 600 ^{o}C. This work provides guidelines to industries that handle MEDs on the explosibility classification of these dusts, thus addressing the existing difficulty, and informing industry on the safety strategies required when handling this group of dusts.

Keywords: *marginally explosible dusts, explosibility, energy density, overdriving*

DOI: 10.7795/810.20221124

1. Introduction

Proper classification of combustible dusts as explosible or non-explosible is the first step in the dust explosion hazard and risk assessment process (Ebadat, 2010). In recent times, one group of combustible dusts that has received increased attention as a result of the uncertainty that surrounds its classification (as being explosible or non-explosible) is “marginally explosible dusts”. The term was firstly adopted by Palmer & Tonkin in 1968, when the explosibility of phenol formaldehyde resin and magnesium oxide dusts, and their mixtures, were investigated in a vertical explosion tube and concluded that marginally explosible dusts have a comparatively narrow range of flammable concentrations, generate only moderate explosion pressures, and are unlikely to cause severe explosions. Several studies have been undertaken to investigate and understand the behavior of dusts considered to be “marginally explosible” in terms of their explosibility (Cashdollar & Chatrathi, 1993; Proust et al., 2007; Cloney et al., 2013; Thomas et al., 2013). This group of combustible dusts present a peculiar challenge when designing dust explosion prevention and mitigation strategies. While they may appear to explode during laboratory scale tests, their explosion characteristics in industrial-size facilities can be less certain. For instance, ambiguities have been found in the results for some materials as determined in different-size chambers and in accordance with standardized test protocols (Proust et al., 2007; Cloney et al., 2013; Thomas et al., 2013). For example, Proust et al. (2007) concluded that a dust having a value of $K_{St} < 45$ bar·m/s measured in a standard 20-L sphere might not be explosible in a 1-m^3 chamber.

Several studies have attributed this behavior largely to the phenomenon of over-driving leading to false positives in smaller explosion chambers (Going et al., 2000, Rodgers and Ural, 2011, Kuai et al., 2011, 2013, Thomas et al., 2013). Although several studies have been conducted to understand the behavior of this group of dusts, the question of “whether these dusts are explosible or not” still remains unanswered. Hence, the industries that handle such dusts either continue to employ the same prevention and mitigation measures as severely explosible dusts, or do not put in place any explosion safety measures because the dusts are deemed non-explosible on an industrial scale. Other studies (Proust et al., 2007; Bucher et al., 2012; Myers et al., 2013; Cloney et al., 2013; Taveau et al., 2014; Taveau et al., 2015a & 2015b; Taveau & Seidel, 2015) have suggested the existence of another complication associated with the different behavior of metallic marginally explosible dusts relative to non-metallic marginally explosible dusts. For instance, as found by Bucher et al. (2012), out of the 13 metallic dust samples tested, a significant majority of 12 dusts that tested to be explosible in the 20-L chamber with K_{St} values below 50 bar·m/s, were found to have greater values of both P_{max} and K_{St} in the 1 m^3 vessel. Similarly, Taveau et al. (2019) indicated that K_{St} values of iron, zinc and aluminum dusts can be much more severe when measured in the 1-m^3 chamber relative to values measured in the more commonly used 20-L chamber. The K_{St} value of aluminum, in particular, can double in the larger vessel. This assertion has been further confirmed by Puttick (2017).

The current experimental study investigates the explosion behavior of marginally explosible dusts observed in the 20-L and the 1-m^3 chamber to attempt to provide answers to the questions “are marginally explosible dusts explosible or not?” and “should we protect or not protect against explosions of these dusts?”. Answers to these questions would help bring clarity to industries handling these dusts. The research further seeks to suggest a working definition for the term marginally explosible dusts.

2. Experiments

Testing was performed to determine two sets of explosion characteristics namely, explosion severity parameters and explosion likelihood parameters. Explosion severity parameters, which included the maximum explosion pressure (P_{max}) and maximum rate of pressure rise $(dP/dt)_{max}$, were determined on two test scales: the 20-L and 1-m^3 explosion chambers. On the other hand, explosion likelihood parameters (i.e., minimum ignition energy (MIE), minimum explosible concentration (MEC), and minimum ignition temperature (MIT) were determined with the MIKE-3 apparatus, both 20-L and 1-m^3 chambers, and BAM oven respectively.

2.1 *Experimental materials*

This section presents the four experimental materials used in the testing program. These include carbon black, oat grain flour, urea, and zinc powders. Carbon black was supplied by Michelin Canada and is mainly used in the rubber industry, mostly in the automotive field; oat grain flour, used as an ingredient and antioxidant in a variety of food products; and urea, a nitrogen fertilizer widely used due to its high nitrogen content. Zinc is used to galvanize metals and alloys such as brass and in the form of powder to produce zinc oxide. The selected materials represent different types of dust materials with distinct reactivities, handled by various processing industries across the globe. All four materials were procured in powder form and were tested as received. Prior to determining the explosion parameters in this study, all experimental apparatuses and procedures were verified by testing against a well-established standard dust (niacin), and the results produced are consistent with previously published data. The niacin sample was obtained from an international round robin campaign in 2017 (CaRo17), in which the Dalhousie Dust Explosion Lab participated. Prior to testing, the dust samples were placed in a desiccator to prevent moisture absorption.

2.2 *Material characterization*

Before testing was conducted, selected physical and chemical properties of the dust samples were determined. The properties investigated include particle size distribution given in terms of the median diameter, D_{50}, as well the 10% and 90% boundaries (i.e., D_{10} and D_{90} respectively), polydispersity (σ_D) (which was calculated from the particle size distribution), and bulk density (ρ_{bulk}). Microscopic images of all the dusts were obtained via scanning electron microscopy (SEM). Figure 1 shows the SEM images of all four dusts, while Table 1 presents some of the physical properties determined. The thermal behavior of dusts was also assessed by thermogravimetric (TG) analysis using a simultaneous TG/DSC TA Instrument Q600SDT. Tests were performed in open alumina pan. Briefly, 10 mg sample was placed in the crucible and was heated up with heating rate β = 10.0 °C/min, in both N_2 and airflow (100 mL/min) to assess the influence of different atmospheres. To analyze gases produced from samples degradation, an FTIR gas was carried out through TGA/FTIR interface linked by transfer line to TGA furnace. The cell and transfer line of the TGA/FTIR interface were heated and kept at 220 °C. In this way, product gases from samples degradation could not condense. The output of this analysis is a Gram-Schmidt diagram and the attribution of FTIR peaks was carried out by using the OMNIC library and literature data. Additionally, proximate (in accordance with ASTM D7582-15 (2015)) and ultimate analyses (using the equipment, CHN 628 LECO) were performed for each sample and the results are presented in Table 2. All measurements were conducted using calibrated apparatus and standard procedures according to the respective ASTM standards.

DOI: 10.7795/810.20221124

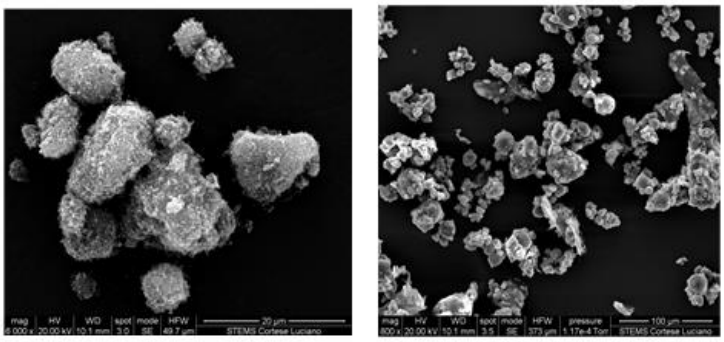

(A) Carbon black (B) Oat grain flour

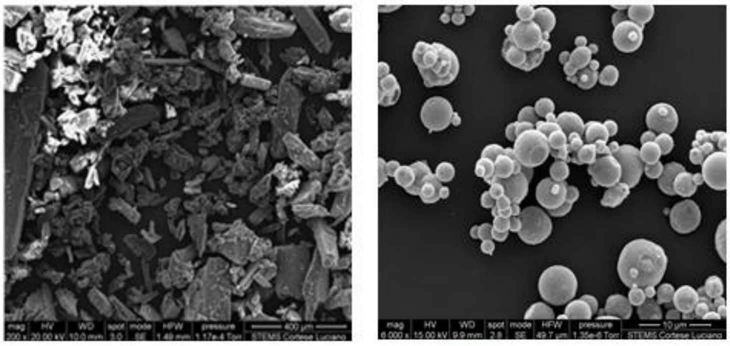

(C) Urea (D) Zinc

Figure 1: Scanning Electron Microscopy (SEM) images of all four dust samples

Table 1: *Test material properties*

Material	**Particle Size (µm)**			σ_D	ρ_{bulk} **(kg/m³)**
	D_{10}	D_{50}	D_{90}		
Carbon black	22	78	678	8.4	380
Oat grain flour	8	46	424	9.0	330
Urea	14	94	373	3.8	1340
Zinc	4	9	22	2.0	7130

Table 2: *Proximate and ultimate analysis of the tested samples*

Material	**Proximate analysis**				**Ultimate analysis**					
	M%	*VM%*	*A%*	*FC%*	C%	H%	N%	O%	H/C	O/C
Oat grain flour	4.0	77.6	15.7	2.7	43.27	7.21	1.45	48.06	2.00	0.83
Carbon black	0.5	3.8	94.1	0.9	94.63	0.25	0.02	5.11	0.03	0.04
Urea	0.0	99.5	-	-	19.51	6.65	44.58	29.26	4.09	1.12
Zinc	0.0	-	-	-	-	-	-	-	-	-

2.3 Experimental apparatuses and procedures

Measurement of explosion parameters was performed using standardized equipment and following standardized test protocols. Explosion severity parameters investigated were maximum explosion pressure, P_{max}, and volume-normalized maximum rate of pressure rise, K_{St} (determined with the maximum rate of pressure rise, $(dP/dt)_{max}$). For explosion likelihood parameters, the minimum explosible concentration, MEC, minimum ignition energy, MIE, and minimum ignition temperature, MIT were determined. The test apparatuses and procedures used in this research have been described in detail in a previous study (Addo et al., 2019). Table 3 gives a summary of the equipment used, standard procedure followed, and equipment location. Five different ignition energies (i.e., 0.5, 1, 2.5, 5, and 10 kJ) were used for the determination of explosion severity parameters (P_{max} and K_{St}) in the 20-L explosion chamber. In the 1-m^3 explosion chamber, all explosion severity testing was conducted with an ignition energy of 10 kJ and using a delay time of 600 ms, which departs from the previous study (Addo et al., 2019) where a choice between 550 ms or 600 ms was made depending on the sample's bulk density.

Table 3: *Summary of standard test equipment, standards, and equipment location*

Equipment	**Explosion parameter(s)**	**Test standard**	**Apparatus location**
20-L explosion chamber	P_{max}, K_{St} MEC	ASTM 1226-12a, 2018 ASTM 1515-14, 2018	Dalhousie Dust Explosion Lab
1-m^3 explosion chamber	P_{max}, K_{St} MEC	ASTM 1226-12a, 2018 ASTM 1515-14, 2018	Fauske and Associates LLC
MIKE 3	MIE	ASTM 2019-03(2013), 2018	Dalhousie Dust Explosion Lab
BAM oven	MIT	ASTM 1491-06(2012), 2018	Dalhousie Dust Explosion Lab

3. Results and discussion

Results from the experimental work are presented in this section. Discussion focuses on both the qualitative and quantitative trends observed in the extensive material characterization and experimental testing.

3.1 Effects of material characteristics

This section discusses the results of the material properties or characterizations determined in this work and how these characteristics influence the explosion behaviour of marginally explosible dusts.

3.1.1 Chemico-physical properties analysis

In order to fully appreciate all the phenomena and issues occurring during the testing of a specific combustible dust, it is imperative to understand the flame propagation mechanism. A complete chemico-physical and thermal characterization is required to understand their influence on the combustion behavior and, consequently, make a judgement of which explosion vessel leads to the most realistic evaluation of explosion parameters. Through the chemico-physical characterization, that consists of the determination of particle size distribution, shape, density and molecular composition, the relaxation time can be calculated, and the role of oxygen diffusivity can be assessed. With thermal characterization, the decomposition and combustion phenomena can be investigated, and the proximate analysis can be used to mainly evaluate the moisture and volatile content. Moreover, the gaseous species produced can be distinguished by Fourier transform infrared spectroscopy (FTIR) analysis. The thermal analysis is important to understand which combustion path is predominant during flame propagation and whether a selected dust fits the definition of a marginally explosible dust. Once the predominant flame propagation path of the dust and the controlling step have been identified, it is possible to determine the vessel to be used for the explosion tests in order to obtain the most practical explosion parameters that can be applied in the design of safety strategies. If the volatiles evolved are a mixture of flammable and inert species, a phenomenon of marginal explosibility may occur if the amount of inert gases evolved is significantly high. In the case of dusts whose flame propagation is controlled by phenomena in the heterogeneous phase, the dust requires time and space for full combustion development; thus, the use of the 1-m^3 chamber is recommended. On the other hand, for dusts whose flame propagation is controlled by phenomena in the homogeneous phase, the 20-L chamber can produce a good estimation of the explosion characteristics. However, there are some exceptions where some materials do not follow the expected combustion mode.

3.1.2 Thermal analysis

To explain the behavior of the organic dusts, a thermal analysis both in inert and oxidant atmosphere was performed together with the proximate analysis and the FTIR analysis of gaseous products. As can be seen from Table 2, both oat grain flour and urea are characterized by a high amount of volatiles that can be produced during the combustion reaction. Then, oat grain flour and urea were tested with TG/FTIR analysis and results are reported in Figure 2 and Figure 3. For oat grain flour, the *TG* and the first-derivative of TG (*DTG)* profiles are similar in nitrogen and air in the low temperature section and then differ from 450 °C (Figure 2). From this behavior, it can be said that the heterogeneous combustion path can take place, but at a lower temperature, 60% of the dust is already devolatilized forming a mixture of flammable gases (hydrocarbons, carboxylic acids, and CO) and inert gases such as water and CO_2. These flammable volatiles are released during heating and then reacts in the gas phase with air. It is therefore possible to conclude that the combustion of oat grain flour is mainly homogeneous, and the low K_{St} value is mainly linked to the formation of a mixture containing inert materials which slows down flame propagation.

This concept is even stronger in the case of urea. The profiles in an inert and oxidizing environment are identical (Figure 3); only the homogeneous combustion path is present in the case of urea. When subjected to heat, urea produces a mixture of flammable (isocyanic acid and ammonia) and large amounts of inert (CO_2) gases. The large amount of inert CO_2 gas produced impedes flame propagation through the reacting gas phases, thus, making urea non-explosible.

In the case of carbon black, the scenario differs from both oat grain flour and urea. As can be seen in Figure 4, the *TG* and *DTG* profiles in an inert and oxidizing environment are different. In inert atmosphere, carbon black loses a percentage by weight corresponding to the sum of the moisture and volatile contents measured during the proximate analysis. In the case of an oxidizing atmosphere, the sample is instead totally consumed following two reactive and strongly exothermic phenomena at 250 °C and 650 °C. The mixture of volatiles produced in inert atmosphere is again composed of a mixture of flammable species (ammonia, isocyanic acid) and CO_2. In this case, the interaction with oxygen is present and active already at low temperature with the formation of the typical combustion products. From the results, it can be said that in the case of carbon black both reactive paths are active. However, due to the molecular structure of carbon and its reactivity, a surface reaction is strongly favoured: i.e., flame propagation is controlled by a heterogenous combustion path. Although this organic sample presents a heterogeneous path predominant over the homogeneous one (volatile matter is only 3.8% of the total solid mass), it still seems to show a behavior similar to marginally explosible organic dusts: i.e., the explosion parameters are greater inside the 20-L sphere while there is a decrease of explosion severity in terms of both P_{max} and K_{St} values in the larger vessel. This may be due to overdriving in the smaller 20-L chamber.

With respect to the zinc dust, it is known that zinc, like many metals, oxidizes spontaneously in air because of the diffusion of oxygen species over the surface. Consequently, the solid particles are coated with a layer of ZnO covering their entire surface. While approaching the flame front, solid Zn particles are heated and the Zn core inside the solid-phase oxide layer starts to melt (melting point 420 °C). The melting point of ZnO is much higher (melting point 1970 °C) which prevents the particle from igniting immediately. Sundaram et al. (2016) suggested that ignition of metallic dusts results from the layer-by-layer destruction, attributed to the thermomechanical stresses produced during the heating phase, and the melting of the oxide shell. Differently from zinc, the interaction between carbon black and oxygen is faster and active at low temperature.

The rate of flame propagation can also be related to the molecular structure. In fact, carbon black is made up of amorphous granules characterized by high surface-to-volume ratio. Unlike zinc, whose combustion is controlled by the melting of the core and the fracture of the shell that allows the diffusion of oxygen, carbon black reacts quickly with oxygen. For these reasons, the flame propagation is not controlled by particle preheating as occurs in the case of metal powders. This may account for the different behaviours of carbon black and zinc dusts in the two explosion chambers.

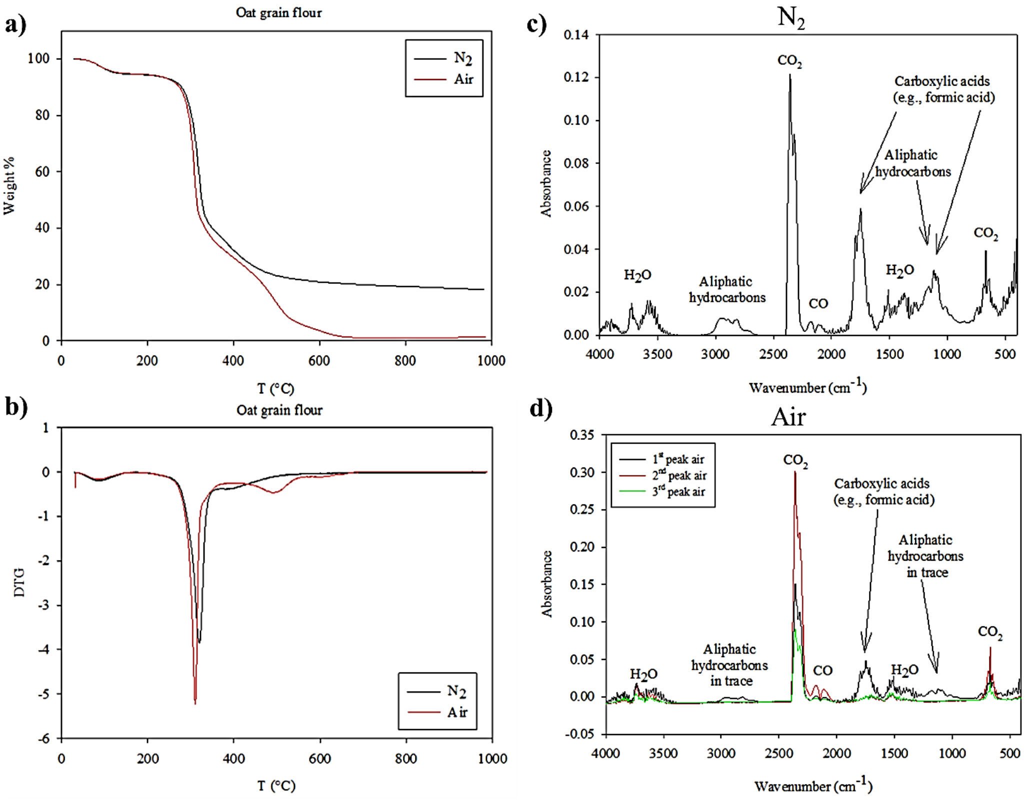

Figure 2: Weight % (a) and DTG curves (b) as a function of temperature (°C) in nitrogen (black line) and air (red line) flow of oat grain flour. FTIR on gaseous species in nitrogen (c) and air (d) flow. In the case of more than one peak, black line is for the 1st peak, red line for the 2nd peak, green line for the 3rd peak and blue line for the 4th peak

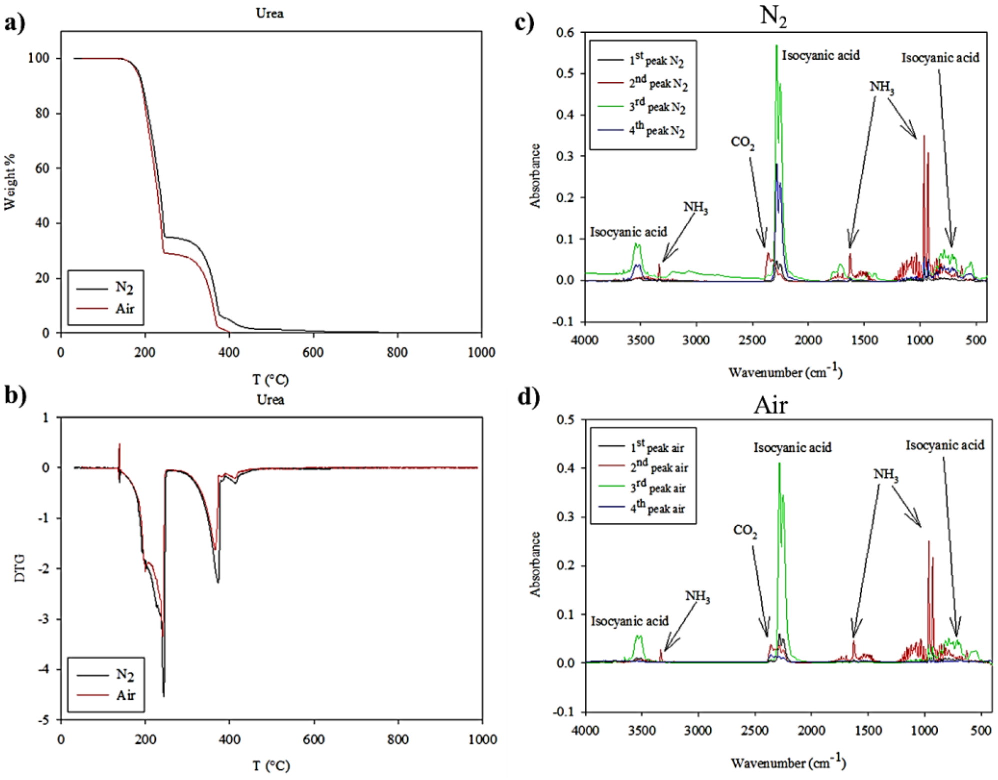

Figure 3: Weight % (a) and DTG curves (b) as a function of temperature (°C) in nitrogen (black line) and air (red line) flow of urea. FTIR on gaseous species in nitrogen (c) and air (d) flow. In the case of more than one peak, black line is for the 1st peak, red line for the 2nd peak, green line for the 3rd peak and blue line for the 4th peak

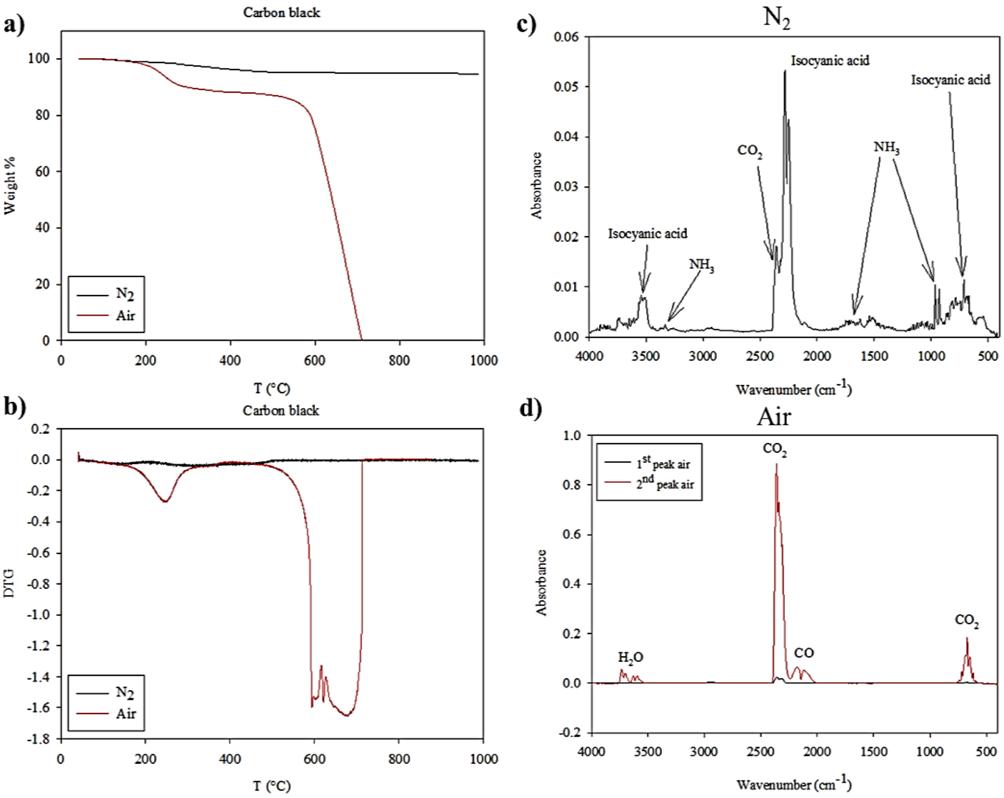

Figure 4: *Weight % (a) and DTG curves (b) as a function of temperature (°C) in nitrogen (black line) and air (red line) flow of carbon black. FTIR on gaseous species in nitrogen (c) and air (d) flow. In the case of more than one peak, black line is for the 1st peak, red line for the 2nd peak, green line for the 3rd peak and blue line for the 4th peak*

3.2 Explosion severity results

This section presents results of the explosion severity measurements in the two different sized explosion chambers.

3.2.1 Explosion in the 20-L chamber

The explosion severity data obtained from the small scale 20-L sphere is presented and discussed in this section. Table 4 gives a summary of the explosion severity results as indicated by the parameters of interest, P_{max} and K_{St}. In the 20-L sphere, the measurement of these parameters for each of the dusts was conducted with five different ignition energies (i.e., 0.5, 1, 2.5, 5, and 10 kJ). However, it is imperative to note that, according to the standard (ASTM E1226-12a (2018)), only P_{max} and K_{St} values determined with 10-kJ ignition energy are considered in the design of safety strategies (i.e., preventive and mitigative measures). As a consequence, data obtained with 10-kJ ignitors will be emphasized while data obtained with the other ignition energies will be considered for the purpose of comparison. It can be seen that all four dusts produced an explosion when an ignition energy of 10 kJ was used. This is indicated by all four dusts recording P_{max} values greater than the threshold value of 1 bar(g). In terms of P_{max} and K_{St} values, carbon black recorded the most severe explosion while urea recorded the least. Oat grain flour also generated a higher maximum overpressure than zinc although its volume-normalized maximum rate of pressure rise was lower than the latter. The behavior of carbon black in the small chamber may be attributed to the incomplete combustion of the carbon to form more intermediate carbon monoxide (CO) gas. The relatively short reaction time coupled with the small volume mean that the dust cannot develop its full reactivity and burn completely to form more inert gases such as CO_2. Oat grain flour exploded in the 20-L chamber generating a P_{max} value of 6.9 bar(g). The explosion pressure recorded is typical for organic materials, so it is as expected. Although the K_{St} value for oat grain flour fits into the definition of what constitutes a marginally explosible dust, the relatively high P_{max} value does not make it straightforward to classify this dust as marginally explosible. To make a correct judgement, the dust was tested within the 1-m^3 chamber, and the results will be discussed in the next section.

With respect to urea, the explosion produced the lowest P_{max} and K_{St} values. The K_{St} value of 7 bar·m/s suggests that there was barely any propagation of the flame through the dust. These values further suggests that urea may be marginally explosible, but the P_{max} value recorded does not make it straightforward to classify. Similar to the case of oat grain flour, it is imperative to test the urea dust in the 1-m^3 chamber for verification. A close look at the SEM image (in Figure 1) of urea shows a non-porous, flaky structure that may behave like fibrous materials. The low K_{St} of urea may be attributed to the combustion of urea to produce large volumes of inert gases such as CO_2 that inhibit flame propagation. In the case of zinc, the P_{max} and K_{St} values indicate an explosion in the 20-L chamber. The microscopic image of zinc shows spherical particles with some degree of agglomeration. For dust materials with very low volatile content like zinc and iron, heterogenous combustion is responsible for ignition and flame propagation. Here, due to the low flame temperature and high evaporation temperature of zinc, there is no release of flammable volatiles during combustion, and the reaction occurs at the surface of the solid zinc particles. The combustion of zinc is complicated by the formation of a protective film ZnO which prevents further particle to particle combustion. More reaction time and volume will be required for the propagating flame to reach more of the particles and be sustained, thus, a larger chamber will be most suitable to produce explosion data that is most representative of industrial situations. The behavior of zinc dust in the 20-L chamber is consistent with the work of Taveau et al., (2019).

Table 4: *Explosion severity results*

Material	**Ignition Energy (kJ)**	**20 L* 60 ms**		**1 m^{3*} 600 ms**	
		***P_{max}* bar(g)**	***K_{St}* (bar·m/s)**	***P_{max}* bar(g)**	***K_{St}* (bar·m/s)**
Carbon black	10.0	7.2	63	6.4	44
	5.0	7.0	59	–	–
	2.5	7.0	59	–	–
	1.0	6.7	42	–	–
	0.5	6.4	22	–	–
Oat grain flour	10.0	6.9	40	6.8	59
	5.0	6.6	29	–	–
	2.5	6.4	27	–	–
	1.0	6.3	25	–	–
	0.5	6.0	16	–	–
Urea	10.0	3.0	7	0	0
	5.0	0.0	0.0	–	–
	2.5	0.0	0.0	–	–
	1.0	0.0	0.0	–	–
	0.5	0.0	0.0	–	–
Zinc	10.0	6.2	57	6.0	129
	5.0	6.7	45	–	–
	2.5	6.4	43	–	–
	1.0	6.2	41	–	–
	0.5	5.5	40	–	–

*equipped with rebound nozzle

3.2.2 Role of ignition energy

Some authors have shown that decreasing ignition energy results in a reduction of both P_{max} and K_{St} values in the 20-L sphere, although this effect is more significant for K_{St} values. This behavior has been largely attributed to a phenomenon called preconditioning where the dust mixture is preheated by the strong ignition source prior to combustion (Cloney et al., 2013; Portarapillo et al., 2021; Clouthier et al., 2019). The relatively large 10-kJ ignition energy used in the 20-L chamber may cause the explosion characteristics to be overestimated (Cloney et al, 2013; Portarapillo et al., 2021). After testing was completed with the 10-kJ Ignitors, the ignition energy was reduced to 5 kJ, 2.5 kJ, 1 kJ, and 0.5 kJ. This was done to examine the influence of decreasing the ignition energy on the P_{max} and K_{St} data, suggesting the most appropriate ignition energy to use, and in what chamber volume to use it. Figure 5 presents the effect of varying the ignition energy on the P_{max} and K_{St} values of all four dusts. It can be noticed from both plots that decreasing the ignition energy from 10 kJ to 0.5 kJ also caused a decrease in both severity parameters. Furthermore, the effect of varying ignition energy is more profound for K_{St} values than for P_{max} values. This trend is as expected.

Choosing an appropriate ignition source is important to make sure that it is energetic enough to initiate the combustion process without actively forcing an explosion by preheating the dust mixture. Previous work by Addo et al (2019) suggested that, for severely explosible dusts, decreasing ignition energy from 10 kJ to 2.5 kJ in the 20-L chamber did not affect both P_{max} and K_{St} significantly. In such a case, a 5- or 2.5-kJ ignitor can give a good estimation of the explosion severity of such dusts. On the other hand, for hard-to-ignite or marginally explosible dusts, the suggestion is to use an ignition energy that is just enough to initiate the ignition process without forcibly triggering the explosion of the dust by preheating it.

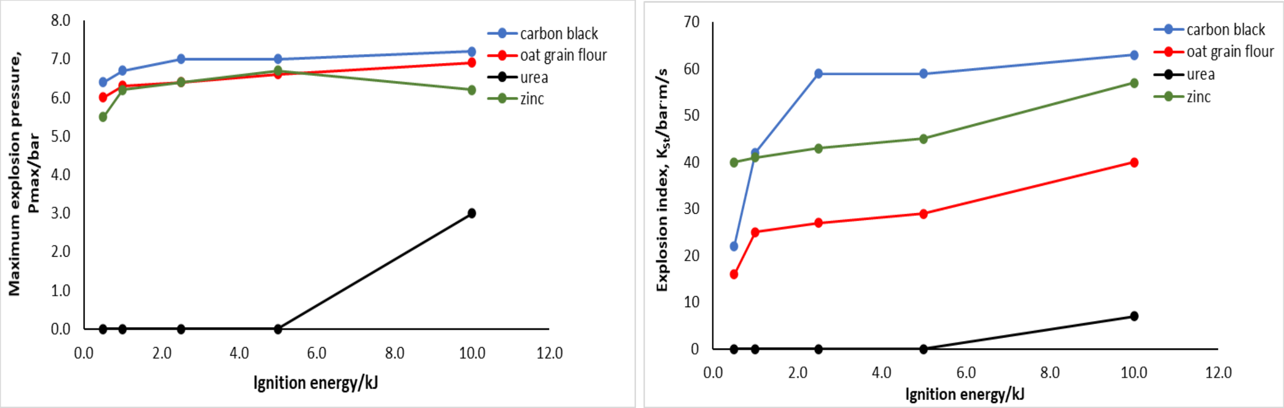

***Figure 5**: Effect of varying ignition energy on P_{max} and K_{St} values in the 20-L sphere*

3.2.3 Explosion in the 1-m^3 chamber

Table 4 also shows the summary results of explosion severity parameters measured in the 1-m^3 chamber with an ignition delay time of 600 ms. From Table 4, it can be seen that three dusts (i.e., carbon black, oat grain flour, and zinc) out of the four dusts produced an explosion in the 1-m^3 chamber according to their P_{max} and K_{St} values. Among the three dusts that exploded, oat grain flour recorded the highest P_{max} value while zinc recorded the lowest. The P_{max} values of both carbon black and oat grain flour are as expected for organic materials. The pyrolysis of oat grain flour evolves more combustible gases for homogenous combustion, thus, the relatively higher P_{max} and K_{St} values than carbon black. As explained earlier (in section 3.1), the combustion of carbon black may not be entirely homogenous although it may be considered as an organic dust. In fact, the very low amounts of volatile matter present and its structure suggests that the combustion process may be dominated by heterogenous combustion at the surface of the carbon black dust. In terms of zinc dust, the P_{max} value of 6.0 bar(g) is similar to the value reported by previous authors (Taveau et al, 2019) although K_{St} value in this research is about 25% higher. This may be attributed to the difference in particle size distribution and the degree of passivation on the metal dust surface.

The K_{St} value of zinc in the 1-m^3 increased by more than two-fold relative to the 20 L value. The relative increase of the K_{St} value of zinc in the 1-m^3 may be attributed to the large chamber volume and the longer reaction time which allowed the zinc dust to develop its full reactivity during the combustion process. Additionally, these conditions present in the 1-m^3 enhance a layer-by-layer heterogenous combustion of the ZnO covering the surface of the solid particle. Unlike the other three dusts, urea did not explode in the larger 1-m^3 chamber. The P_{max} value indicates that there was no flame propagation through the urea dust particles. Clearly, the behaviour of urea in the smaller chamber was as a result of overdriving and testing in the 1-m^3 chamber has confirmed that the urea dust is non-explosible. Hence, in the case of urea, although it follows a homogenous combustion mode, the larger 1-m^3 chamber gives a more practical estimation of the explosion severity parameters.

3.2.4 Role of chamber volume

Tables 4 also shows a comparison of the 20-L and 1-m^3 results in both test chambers. Also, the reproducibility values for each dust sample have been presented in Table 5. For three of the dusts (i.e., carbon black, oat grain flour, and zinc), the values of P_{max} did not vary significantly and are within the reproducibility limits as outlined in ASTM E1226-12a (2018). However, the K_{St} values varied markedly and do not fall within the 30% reproducibility limits. Considering the P_{max} and K_{St} values in the 1-m^3 chamber, it can be concluded that the three dusts are explosible. The only exception was urea, whose P_{max} and K_{St} values in the 1-m^3 chamber indicated that an explosion did not occur. The larger chamber volume played an important role. The 1-m^3 chamber offers a volume that is 50 times that of the 20-L chamber. This means that the combustion process now has enough reaction volume available for a dust sample to develop its full reactivity. There is also adequate time for the combustion reaction to proceed. The larger volume requires that a longer delay time (i.e., 600 ms) is used which allows the turbulence generated to be distributed over the entire volume of the chamber (Portarapillo et al., 2021).

Table 5: *Reproducibility limits for explosibility testing*

Samples	**Reproducibility limits (%)**	
	P_{max} (bar(g)) (± 10%)	**K_{St} (bar·m/s) (± 30%)**
Carbon black	12.5	43
Oat grain flour	1.5	32
Urea	-	-
Zinc	3.3	56

-no reproducibility value calculated due to no explosion recorded in 1-m^3 chamber

Although the same amount of ignition energy (10 kJ) is used in the 1-m^3, the corresponding increase of dust material (i.e., 50 times the amount of dust used in 20-L chamber) causes a dilution of the energy release (Ogle, 2016). This dilution behavior is absent in the 20-L chamber, thus its susceptibility to overdriving effect. Table 4 also shows more than a twofold increase of the K_{St} value of zinc. This is because the zinc dust needed more time to attain its stabilized combustion regime; the 1-m^3 chamber provides both adequate time and volume for reaching this regime. The behavior of zinc is typical of metallic dusts and similar behavior has been reported in other studies (Taveau et al., 2019).

It can therefore be suggested that scaling 20-L results for some dusts (such as metals) may not be straightforward. This conclusion agrees with the previous work by Addo et al. (2019), whereby K_{St} results for coarse polyethylene in the 1-m^3 chamber at an ignition delay time of 600 ms did not vary significantly from testing at an ignition delay time of 550 ms. From the results presented in this work (i.e., Table 4), a suggestion could be made for a working definition of marginally explosible dusts. Using the urea as an example, marginally explosible dusts may be defined as dusts with $P_{max} < 3.0$ bar(g), $K_{St} < 20$ bar•m/s in the 20-L chamber and will not explode with a 5-kJ Ignitor. This definition is a more detailed one that considers the very important conditions that affect the explosion characteristics of these dusts. As per the characteristics of marginal explosibility discussed together with the 1-m^3 results presented in this study, the urea dust is a marginally explosible dust.

3.3 Choice of explosion chamber for practical results

The strategy of assessing the explosion risk of dusts has been to present the worst-case scenario, or the worst conditions under which the dust being tested can cause an explosion. The problem here is that there is the possibility to over-estimate the explosion characteristics when all test conditions and procedures are not carefully considered. One important consideration in the measurement of explosion characteristics, especially in the case of marginally explosible dusts is the effect of scaling the data from the small 20-L chamber. The results of the current study (i.e., chemico-physical, thermal analysis, and experimental analysis) have suggested that the type of combustion phenomenon exhibited by a particular dust strongly dictates the choice of appropriate explosion chamber to produce acceptable explosion data. Preliminary analysis of the results in the current research has suggested that generally, dusts whose deflagration is predominantly influenced by homogenous combustion (Path A) (such as oat grain flour in this work, and other traditional organic dusts) may produce reliable results in the 20-L chamber. Homogeneous combustion is characterized by the devolatilization of the organic dust particles followed by a gas phase combustion reaction with air. In other words, they obey the “cubic root relationship” and the data obtained from the 20-L chamber correlates well with that of the 1-m^3 chamber. Conversely, for dusts whose combustion phenomenon is largely dictated by heterogenous combustion (Path B) (such as zinc dust in the current research), the 1-m^3 chamber may be the best choice to provide the closest evaluation of the explosion risk to the industrial scenario. Heterogeneous combustion is characterized by surface burning of solid dust particles. Here, there is no release of volatiles.

However, not all materials (either organic or metallic) follow the expected combustion paths. An example is carbon black which is considered as an organic material but reacts in a heterogenous combustion mode, thus, making the 1-m^3 chamber the most suitable. For urea, although, flame propagation is controlled by a homogenous combustion mode, measuring the explosion characteristics according to the current standard procedure (ASTM E1226, 2018) will overestimate its explosion severity. In this case, it is recommended to test the urea dust in the 1-m^3 to generate explosion data that is more practical. An example of a metallic dust that deviates from the expected combustion path is aluminium. The combustion of aluminium has been explained by Cloney (2019). Table 6 shows a summary of the dusts analysed in the current work together with the relative flame propagation paths as well as the vessels to be used to obtain the most realistic K_{St} values.

Table 6: *Summary of investigated dusts and relative flame propagation path*

Material	**Flame propagation path**		**Comments**	**Most practical *K_{St}* value**
	PATH A	PATH B		
Carbon black	No	Yes	Low flammable volatile content and rapid heterogeneous combustion	1-m^3
Oat grain flour	Yes	No	Mainly homogeneous combustion	20 L
Urea	Yes	No	Homogeneous combustion but overdriven	1-m^3
Zinc	No	Yes	Layer-by-layer heterogeneous combustion	1-m^3

3.4 Explosion sensitivity

This section presents and discusses the explosion likelihood results. Table 7 gives a summary of the explosion likelihood test results in terms of MEC in the 20-L and 1-m^3 chambers, MIE (without and with inductance) in the MIKE 3 apparatus, and MIT in the BAM oven respectively.

Table 7: *Explosion likelihood results*

Material	***MIE* (mJ)**		***MIT* (°C)**	***MEC* (g/m^3)**	
	With Inductance	**Without Inductance**		**20 L 2.5 kJ 60 ms**	**1 m^3 10 kJ 600 ms**
Carbon black	> 1000	> 1000	> 600	80	250
Oat grain flour	100 – 300 E_s = 140	300 – 1000 E_s = 540	400	250	500
Urea	> 1000	> 1000	> 600	750*	> 3000
Zinc	300 – 1000 E_s = 720	> 1000	> 600	650	750

* is *MEC* determined with ignition energy (I.E) of 10 kJ since no explosion occurred with 2.5 kJ I.E.

3.4.1 Minimum explosible concentration (MEC) in both 20-L and 1-m^3 chambers

From Table 7, a comparison between MEC values obtained in both chambers indicates a general increase of MEC values obtained in the 1-m^3 chamber. Also, it can be seen that in the 20-L chamber, carbon black dust recorded the lowest MEC values followed by oat grain flour and zinc, while urea dust did not record a measurable MEC value in both the 20-L sphere (with 2.5- and 5-kJ Ignitor) and 1-m^3 chamber (with 10-kJ Ignitor). Out of the three dusts that recorded measurable MEC values, these values were very high for oat grain flour and zinc, indicating that relatively thick layers of these dusts are required to form combustible dust clouds if dispersed in air. The only exception was carbon black dust which recorded an MEC value less than 100 g/m^3 in the 20-L chamber. However, the MEC value of 250 g/m^3 recorded in the 1-m^3 indicates a case of overdriving in the smaller 20-L chamber even with an ignition energy of 2.5 kJ. One solution to the problem of overdriving will be to measure the MEC of carbon black and dusts with similar combustion behaviours in the larger 1-m^3 explosion chamber. Another case of overdriving the MEC value was observed for urea whereby a measurable MEC value was only recorded in the 20-L chamber when the ignition energy was increased from 2.5 to 10 kJ. Even with this large ignition energy, the MEC value of 750 g/m^3 is very high, thus, thick layers of urea are needed to form combustible dust clouds if dispersed in air. The fact that there was no explosion recorded in the 1-m^3 chamber confirms that the MEC value for urea dust in the 20-L is as a result of overdriving. For a metallic dust like zinc, the high MEC value is as expected. This can be attributed to the relatively high density of the zinc dust. This implies that to form an explosible dust cloud, a significant number of the metal particles must be suspended in air. Due to the high density of individual particles, the resultant bulk density of the metal dust becomes very high. The greater the number of particles required to form an explosible dust/air cloud, the greater the amount of dust (in grams) needed. The results in Table 7 suggest that there is no agreement between MEC values measured in the two chambers as they did not fall within the reproducibility limits outlined in ASTM 1515-14 (2018). Testing on the larger scale confirmed that all the dusts tested in this work have very high MECs $\geq$ 500 g/m^3 thus indicating that thin layers of these dusts could not readily form combustible dust clouds if dispersed in air. In addition to the proposed definition of MEDs in section 3.2.4, it can be suggested that marginally explosible dusts have MEC values greater than 500 g/m^3 (i.e., MEC > 500 g/m^3).

3.4.2 Minimum ignition energy (MIE)

The summary results obtained for the minimum ignition energy of all dusts tested are also presented in Table 7. MIE values were determined with inductance and without inductance. It can be seen that oat grain flour recorded the lowest MIE values both without and with inductance. Without inductance, the remaining three dusts did not ignite at the maximum ignition energy that can be measured with the equipment (i.e., MIE > 1000 mJ or 1 J). However, with inductance, the MIE value of oat grain flour decreased, while the zinc dust also ignited at an MIE < 1000 mJ (i.e., 720 mJ). This behavior is evidence of the impact of inductance in producing sparks with longer duration which in turn decreases the MIE of a given sample (von Pidoll, 2001; Eckhoff, 2017). The two other dusts (carbon black and urea) still did not ignite with the addition of an inductance of 1 mH since the MIE values remained unchanged (i.e., MIE > 1000 mJ). The minimum ignition energy of dusts is dependent on factors including the size distribution of the dust particles, dustiness (or the ease of forming a combustible dust cloud), ease of evolution of volatile matter, electrical conductivity of dust, etc. The behavior of oat grain flour with respect to spark ignition may be attributed to the ease of evolving volatiles for combustion as well as its dispersibility, while that of zinc may be largely attributed to its electrical conductivity. Despite the formation of the ZnO film on the surface of zinc, prolonged application of spark ignition is able to breakdown the film and cause the particles to ignite. The MIE results imply that oat grain flour is more sensitive to electric sparks as relative to the other three dusts, followed by zinc which is weakly sensitive when exposed to prolonged electric sparks. Both carbon black and urea were insensitive to spark ignition. From the MIE results from the current study, it can be concluded that dusts that exhibit marginal explosibility may be insensitive to spark ignition energies less than or equal to 1000 mJ (i.e., MIE ≤ 1000 mJ).

3.4.3 Minimum ignition temperature (MIT)

The summary results of the minimum ignition temperature (MIT) tests for all dusts are also presented in Table 7. The majority of the dusts (i.e., 3 out of 4) did not show an ignition when exposed to the hot surface at a temperature of 600 °C. The minimum ignition temperature of combustible dusts is strongly dependent on the ease of evolution of combustible volatiles from the dust. Generally, the greater the volume of combustible gases released relative to time, the more sensitive the material is when exposed to hot-surface ignition. The MIT results reflect the fact that hot-surface ignition processes involve different physical and chemical phenomena than those in spark ignition scenarios. Additionally, the 5-s ignition criterion for the BAM oven could lead to a sample material emitting sufficient volatiles for combustion as it sits on the bottom surface of the heated furnace. Overall, the MIT results show that only oat grain flour, out of the four dusts, can undergo hot-surface ignition at temperatures around 400 °C. This behavior is typical of traditional organic dusts like oat grain flour with respect to hot-surface ignition. From the results presented in Table 7, an MIT threshold value of 600 ^{o}C can be suggested for marginally explosible dusts.

3.5 Industrial implications

This work has provided data and explanations that are aimed at providing guidance to process industries that handle marginally explosible dusts (MEDs). The behavior of urea in this work has provided a basis for the explosibility classification of these dusts, thus addressing the existing difficulty of handling MEDs. However, it is important to evaluate the risk of more dusts that are truly marginally explosible to make a firmer conclusion. With the current behavior of urea in both chambers, it can be suggested that marginally explosible dusts are indeed capable of propagating a dust flash fire but not an explosion. Based on this information, it can be suggested that process industries put in place safety measures and strategies required to prevent flash fires when handling urea. It must be stressed that, the most accurate method of classifying any dust as explosible or non-explosible is by testing in standard test apparatuses and using standard procedures. Thus, the explosion characteristics of individual dusts must be measured to assess their risk of explosion.

4. Conclusions

The discrepancy that results from scaling 20-L explosion data is real, especially for marginally explosible dusts. The current study investigated the problem posed by marginally explosible dusts by assessing the explosion risk of four well-characterized combustible dusts in the 20-L and 1-m^3 chambers. The research also conducted detailed chemico-physical and thermal analyses to further understanding the fundamental behaviors that underly the mechanisms of flame propagation with respect to MEDs. The effect of varying the ignition energy in the 20-L chamber, and the effect of scaling the 20-L data were investigated as well. Finally, this work considers (though preliminary at this point) how the type of combustion phenomenon influences the choice of appropriate test chamber in order to produce conservative results. This study contributes to our understanding of the fundamental mechanisms which govern the explosion behavior of MEDs and the implications on industry. The following points summarize the major findings from the current study:

- Both chemico-physical and thermal analyses are important to understand the explosion behavior of MEDs.
- Carbon black and urea dusts are clearly overdriven in the 20-L chamber with a 10-kJ ignitor.
- Although carbon black and urea seem to fit the definition of MEDs in the 20-L chamber, carbon black is explosible while urea is non-explosible as indicated by data obtained from the 1-m^3 chamber.
- Oat grain is explosible and has explosion characteristics typical of a traditional organic dust.
- Comparing the explosion data from both chambers shows good agreement in terms of P_{max} values, but no agreement in terms of K_{St} values.
- Explosion severity of metal dusts such as zinc may be under-estimated in the 20-L chamber. Explosion severity of metal dusts can more than double in the 1-m^3 chamber due to factors such as increased volume and time to develop full explosibility.
- Marginally explosible dusts have low ignition sensitivity as can be seen by the MEC, MIE and MIT results for urea.
- With reference to urea dust, a new definition of MEDs has been suggested: $P_{max} < 3.0$ bar(g), $K_{St} < 20$ bar•m/s, MEC > 500 g/m^3, MIE > 1000 mJ, and MIT > 600 °C.
- For dusts whose flame propagation is dictated by a homogeneous combustion (Path A), the 20-L chamber is recommended. However, for dusts whose flame propagation is controlled by heterogeneous combustion (Path B), the 1-m^3 chamber is recommended. However, there are dust materials such as carbon black (from the current work) and aluminum whose combustion mode deviates from what is expected. The possibility of overdriving can also affect the choice of an explosion test chamber.

Acknowledgements

The authors gratefully acknowledge the financial contribution from the Natural Sciences and Engineering Research Council of Canada. They are also thankful to Jensen Hughes Dust and Flammability Testing Laboratory located in Halifax, Nova Scotia, for access to their material characterization equipment. Also, our appreciation goes to Fauske and Associates, LLC, Burr Ridge, IL, USA for use of its 1-m^3 explosion chamber and the availability of personnel for testing purposes. Finally, sincere gratitude goes to Andrew Adamson from Michelin Canada, for supporting this work in terms of material provision.

References

Addo, A., Dastidar, A. G., Taveau, J. R., Morrison, L. S., Khan, F. I., & Amyotte, P. R. (2019). Niacin, lycopodium, and polyethylene powder explosibility in 20-L and 1-m^3 test chambers. *Journal of Loss Prevention in the Process Industries*, 62, 103937.

Amyotte, P.R. (2014). Some myths and realities about dust explosions, *Process Safety and Environmental Protection*, 92: 292-299.

ASTM D7582-15 (2015), *Standard Test Methods for Proximate Analysis of Coal and Coke by Macro Thermogravimetric Analysis*. ASTM International, West Conshohocken, PA.

ASTM E1226-12a (2018). *Standard test method for explosibility of dust clouds*. ASTM International, West Conshohocken, PA.

ASTM E1515-14, 2018. *Standard Test Method for Minimum Explosible Concentration of Combustible Dusts*. ASTM International, West Conshohocken, PA.

ASTM E2019-03(2013), 2018. *Standard Test Method for Minimum Ignition Energy of a Dust Cloud in Air*. ASTM International, West Conshohocken, PA.

ASTM E1491-06(2012), 2018. *Standard test Method for Minimum Autoignition Temperature of Dust Clouds*. ASTM International, West Conshohocken, PA.

Bucher, J., Ibarreta, A.F., Marr, K. & Myers, T.J. (2012). Testing of marginally explosible dusts: evaluation of overdriving and realistic ignition sources in process facilities. *Proceedings of 15th Annual Mary Kay O'Connor Process Safety Center Symposium*, College Station, TX.

Cashdollar, K. L. & Chatrathi. K. (1993). Minimum explosible dust concentrations measured in 20-L and 1-m^3 chambers. *Combustion. Science Technology*, 87, 157–171.

Cloney, C.T., Ripley, R.C., Amyotte, P.R. & Khan, F.I. (2013). Quantifying the effect of strong ignition sources on particle preconditioning and distribution in the 20-L chamber. *Journal of Loss Prevention in the Process Industries*, 26, 1574-1582.

Cloney, C. T. (Host). (2019). DSS042: Fundamental Burning Characteristics of Five Combustible Dusts [Audio podcast]. https://dustsafetyscience.podbean.com/e/dss042-fundamental-burning-characteristics-of-five-combustible-dusts/ Accessed: 27-05-2022.

Clouthier, M. P., Taveau, J. R., Dastidar, A. G., Morrison, L. S., Zalosh, R. G., Ripley, R. C., Khan, F. I. & Amyotte, P. R. (2019). Iron and aluminum powder explosibility in 20-L and 1-m^3 chambers. *Journal of Loss Prevention in the Process Industries*, *62*, 103927.

Ebadat, V. (2010). Dust explosion hazard assessment. *Journal of loss prevention in the process industries*, *23*(6), 907-912.

Eckhoff, R. K. (2017). Ignition of combustible dust clouds by strong capacitive electric sparks of short discharge times. *Zeitschrift für Physikalische Chemie*, *231*(10), 1683-1707.

Going, J.E., Chatrathi, K. & Cashdollar, K.L. (2000). Flammability limit measurements for dusts in 20-L and 1-m^3 vessels. *Journal of Loss Prevention in the Process Industries*, 13, 209-219.

Kuai, N., Li, J., Chen, Z., Huang, W., Yuan, J. & Xu, W. (2011). Experiment-based investigations of magnesium dust explosion characteristics. *Journal of Loss Prevention in the Process Industries*, 24, 302-313.

Kuai, N., Huang, W., Du, B., Yuan, J., Li, Z., Gan, Y. & Tan, J. (2013). Experiment-based investigations on the effect of ignition energy on dust explosion behaviors. *Journal of Loss Prevention in the Process Industries*, 26, 869-877.

Myers, T.J., Ibarreta, A.F. & Marr, K. (2013). Assessing the hazard of marginally explosible dusts. *Proceedings of 9th Global Congress on Process Safety*, San Antonio, TX.

Ogle, R. A. (2016). *Dust explosion dynamics*. Butterworth-Heinemann.

Palmer, K. N. & Tonkin, P. S. (1968). The explosibility of dusts in small-scale tests and large-scale industrial plant. *International Chemical Engineering Symposium Series* (Vol. 25).

Portarapillo, M., Sanchirico, R., & Di Benedetto, A. (2021). On the pyrotechnic ignitors role in dust explosion testing: Comparison between 20-L and 1-m^3 explosion vessels. *Process Safety Progress*, *40*(4), 289-295.

Proust, C., Accorsi, A. & Dupont, L. (2007). Measuring the violence of dust explosions with the "20-L sphere" and with the standard "ISO 1-m^3 vessel". Systematic comparison and analysis of the discrepancies. *Journal of Loss Prevention in the Process Industries*, 20, 599-606.

Puttick, S. (2017). Issues with the conflicts in the determination of K_{St} in 20-litre and 1-m^3 vessels. Letter to CEN TC305 WG1 members, N556. Huddersfield, 30th January.

Rodgers, S. A. & Ural, E. A. (2011). Practical issues with marginally explosible dusts – evaluating the real hazard. *Process Safety Progress*, 30, 266-279.

Sundaram, D. S., Puri, P., & Yang, V. (2016). A general theory of ignition and combustion of nano- and micron-sized aluminum particles. *Combustion and Flame*, *169*, 94-109.

Taveau, J. R. (2014). Combustible metal dusts: a particular class. In: Mary Kay O'Connor Process Safety Center, Seventeenth International Symposium, pp. 594–606.

Taveau, J. R., (2015a). Scaling-up metal dusts explosion severity. In: Presentation to NFPA 68 committee, September 9th, Quincy, MA.

Taveau, J. R., (2015b). Metal Dusts Explosibility Testing in 20-L Sphere and 1-m^3 Vessel. Presentation to ASTM E27 committee, November 19th, Tampa, FL.

Taveau J., Lemkowitz S., Hochgreb S., Roekaerts D., 2019, Metal Dusts Explosion Hazards and Protection, *Chemical Engineering Transactions*, 77, 7-12 DOI:10.3303/CET1977002.

Thomas, J. K., Kirby, D. C. & Going, J. E. (2013). Explosibility of a urea dust sample. *Process Safety Progress*, 32, 189-192.

DOI: 10.7795/810.20221124

Turbulence generated by dust dispersion in the standard 1 m^3 vessel

Zdzisław Dyduch[a]

[a] Experimantal Mine Barbara of Central Mining Institute, Mikołów, Poland
E-mail: *zdyduch@gig.eu*

Abstract

The standard 1 m^3 vessel is an apparatus recommended for an assessment of dust explosion indices by ISO, European and American standards. However the definition of the vessel construction given in the Standards leaves some room when designing it. That may lead to significantly different results obtained in vessels built in different laboratories even when all of them meet the requirements of the Standards. One of key parameters that should be controlled in the tests is the turbulence intensity. Several authors reported measurements of turbulence intensity in the 1 m^3 vessel. However, all of those results were obtained for pure air dispersed from the dust dispersion system. The paper presents results of turbulence measurements performed in the 1 m^3 vessel built and used at Experimental Mine Barbara of Central Mining Institute, Poland. Unlike in previous measurements transient flow velocity in the vessel was generated by dust injection from the dust dispersion system. For the measurement the Bi-Directional Velocity Probe developed by McCaffrey and Heskestad (McCaffrey B.J. (1976)) was used. The construction of the probe was modified to improve its performance in the dusty conditions. The tests were performed for several nominal dust concentrations of two dust. From the measurements the root-mean-square of instantaneous velocity u'_{rms} was calculated. The results were compared with the results obtained for pure air in the dust dispersion system. The presence of dust modifies turbulence in the vessel. Its intensity is reduced and the flow development is delayed.

Keywords: *dust explosion, test methods, turbulence measurement, Bi-Directional Velocity Probe*

1 Introduction

In the process safety assessment of dust explosion hazard in industry important role play dust parameters that quantify explosive properties of dust. Among those parameters most widely used are maximum explosion pressure and maximum rate of pressure rise scaled with the volume of a test equipment (Eckhoff, 2003). As the value of those parameters depend not only on properties of dust tested but also on method of the assessment it is crucial to precisely define both the equipment and the test procedure. Such information are included in European EN14034+A1 (2011), American ASTM-E-1226 (2012) and international ISO6184/1 (1985) Standards. The equipment of first choice is a compact ($L/D \simeq 1$) 1 m^3 vessel but other apparatus of different volumes are allowed as long as they are able to give comparable results. As there is no standard 1 m^3 vessel commercially available those who want to construct such equipment should be provided with sufficiently precise design instructions. Several author suggested that the information in the standards mentioned are insufficient. Among the factors that should be defined more precisely is the construction of the system of dust dispersion, the process that generates turbulence in the vessel's interior prior to the ignition. The turbulence in turn strongly influences the explosion dynamics and therefore the value of maximum rate of pressure rise $(dp/dt)_{max}$. Usually, the turbulence intensity is quantified by root-mean-square of the velocity fluctuations.

In accordance with the Standards, in 1 m^3 vessel dust/air mixture should be ignited at 600 ms after a dust dispersion was initiated. The turbulence intensity measured by van der Wel (1993) at that time, quantified by root-mean-square velocity was u'_{rms} 0.5 m/s. Measurements reported by Proust Ch. (2007) in his 1 m^3 vessel show fast turbulence decay after injection, however at the time of typical explosion duration, between 600 ms and 1000 ms, the turbulence intensity levels off at the value of

2 m/s. Hauert F. (1994) measured both horizontal and vertical components of the velocity after 600 ms and obtained the values of 1.2 m/s and 5.36 m/s respectively. Dyduch et al. (2016) reported the results of the velocity measurements in their 1 m^3 vessel. They showed that during the time of interest turbulence in the vessel is isotropic and homogeneous. At that time the rms velocity was in the range between 0.5 m/s and 1 m/s. The difference between the measured turbulence intensities might be due to differences in engineering factors like shape of the test vessel, dispersion system or dispersion nozzle used.

All the results mentioned above were obtained for the dispersion of pure air. Tamanini (1998) made limited measurements with dust charge in the injection flow concluding that the major effect of the dust in the injection charge is to delay the flow development leading to higher turbulence during the time of interest for the explosion tests. Hauert F. (1994) measured transient flow in the ISO 1 m^3 vessel with dust concentration 30-120 g/m^3 but he did not report results for pure air. Therefore an assessment of influence of dust presence is not possible. Portarapillo et al. (2022) developed a CFD model and simulated turbulent flow in 1 m^3 vessel caused by dispersion of air and air with dust. They reported a good agreement of computed turbulent kinetic energy with experimental data at times higher than 300 ms.

The paper presents a continuation of the work described in Dyduch et al. (2016). A similar methodology was applied to assess turbulence intensity generated by the dust dispersion system of the 1 m^3 vessel. Both the system and the measuring equipment were modified. To obtained reference values the measurements of the velocity fluctuations were carried out for the dispersion of pure air. Than measurements were performed with different amounts of two dusts often used in experiments when a new equipment is tested.

2 Experimental setup

The equipment was prepared for measurement of transient flow velocity generated inside the standard 1 m^3 vessel by air outflow from the dust dispersion system. The vessel, together with the dispersion system, meets the requirements of the European Standards EN14034+A1 (2011). The only difference was the dispersion nozzle. The Standards recommends Perforated Dispersion Ring as a first choice, allows however the usage of Rebound Nozzle for dusts difficult to disperse. Nowadays Rebound Nozzle is probably used most often both in the standard 20-l sphere and 1 m^3 vessel. This type of nozzle was used in all tests described in the paper. In Figure 1 an outline of the whole apparatus is presented.

The vessel consists of cylindrical part closed at both ends with ellipsoidal bowls. A shape of the vessel is nearly spherical ($L/D \simeq 1$). Several ports at the vessel's wall were used to mount required equipment. At the wall a dust dispersion system is mounted. In all tests described in this paper two identical dispersion units were used. The outlets of the units, terminated with dispersion nozzles are located on opposite sides in the center of the cylindrical part, at half of the vessel's height.

2.1 Dust properties

For the tests two well-known dusts were chosen: Cornstarch and hard coal dust - Barbara d38. The latter is often used in tests at EM *Barbara* of Central Mining Institute as a reference coal dust of known properties and behavior. In Figure 2 particle size distribution of the dusts are presented. Both have well defined particle sizes with most of their mass within a range 10-300 μm and 5-30 μm in case of Barbara d38 and Cornstarch respectively. The volume-weighted mean size D[4,3] is 107 μm and 14 μm.

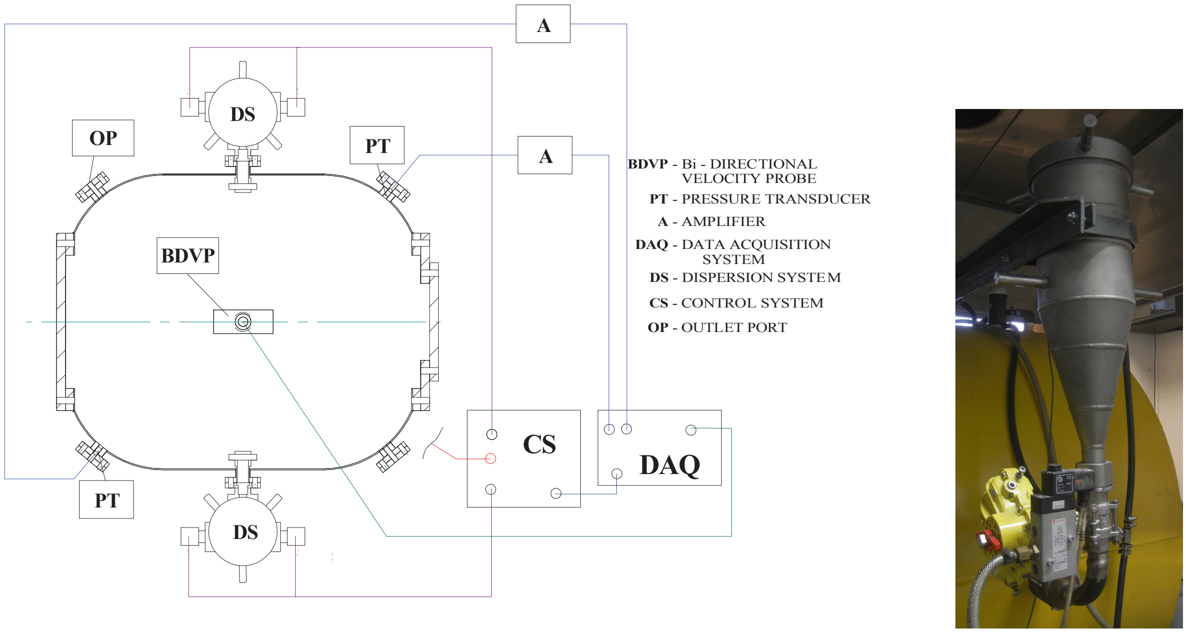

(a) Test stand diagram (BDVP's sensing head not to scale) *(b) Dispersion system*

***Fig. 1**: Setup of the* $1m^3$ *vessel*

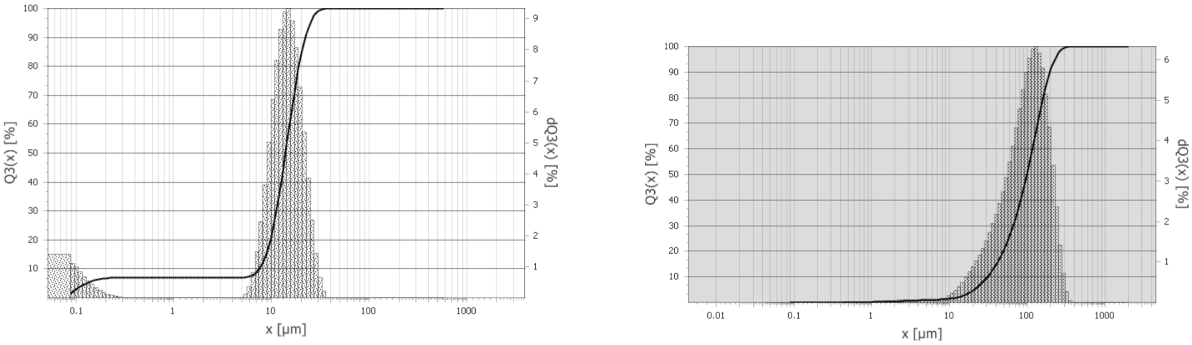

(a) Cornstarch *(b) Barbara d38*

***Fig. 2**: Particle size distribution of dusts used in tests*

2.2 Dispersion system

A dispersion system consists of a dust canister, fast acting valve, connecting tube and dispersion nozzle. The canister has a volume of 5.4 L and form factor 3:1, as required by the Standards. Its lower part is cone-shape to facilitate dust outflow. The bottom of the canister is connected to a fast-acting valve via a short tube. That part of the system has been modified. Piston-like fast-acting valve, similar to that used in the standard 20-L sphere has been replaced with a typical 1-inch ball valve. The valve is driven by a pneumatic driver controlled by an electromagnetic valve. The length of the tube connecting the fast acting valve with the dispersion nozzle is 210 mm with inner diameter 24 mm. As a disperser so-called Rebound Nozzle was used. The design of the nozzle complies with the precise drawing included in the Standards EN14034+A1 (2011). Before dispersion, the canister was filled with compressed air up to 20 bar g, and in further tests also with dust. Air injection was initiated by opening the fast acting valve. The valve remained open throughout the experiment. One unit of the dispersion system is shown in Figure 1.

Two such units mounted on opposite walls were used in all tests. The operation of the dispersion system was checked by measuring the pressure in one of the dust canisters. In Figure 3 pressure drop in the dust canister during the dispersion of pure air is shown together with the reference curves from the Standards EN14034+A1 (2011).

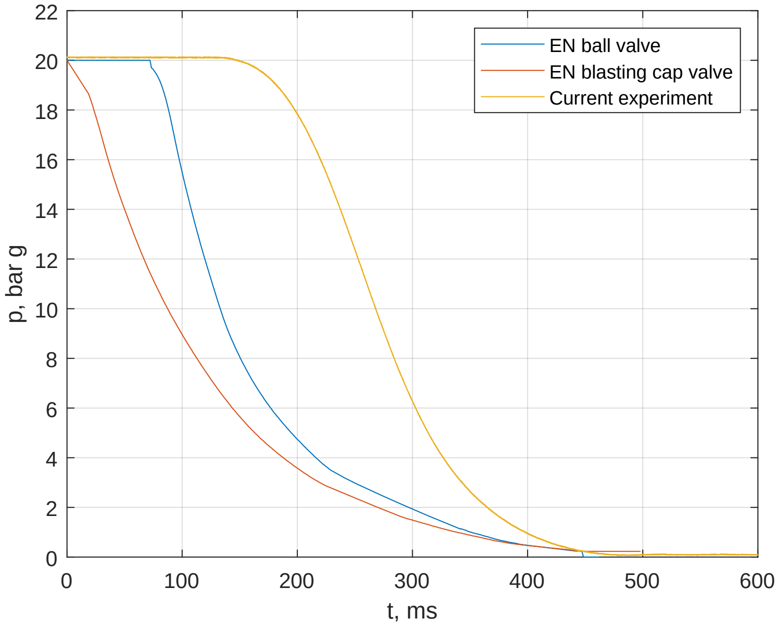

Fig. 3: *Air discharge from the dust container - measured and recommended*

Generally, the shape of the pressure-time curve is consistent with the reference curves of the Standards, but the time required to open the ball valve is longer by almost 100 ms. That time is represented by initial, flat part of the pressure curve. Despite that the pressures in the canister and in the vessel align practically at the same time as in case of the reference valves. This happens well before the ignition (600 ms). Longer opening time does not cause any problem as long as the entire process is repeatable. Then the moment $t = 0$ may be chosen at any point of the flat part of the pressure-time plot. In the tests described here the repeatability was very good.

2.3 Bi-Directional Velocity Probe

The Bi-Directional Velocity Probe (BDVP) is an impact probe similar to the pitot-static probe. The probe (Figure 4) was constructed based on the design of McCaffrey B.J. (1976). The original design was slightly modified to better suit current purposes. Unlike in the original probe the differential pressure transducer was located directly inside the sensing head and used to divide the head into two zones. The size of the sensing head is 20 mm in diameter with 40 mm length. The probe blocks the flow and that generates pressure difference between front and rear surfaces of the pressure differential transducer. By use of the well-known relationship for pitot-static probes, the flow velocity is inferred from the local differential pressure and gas density.

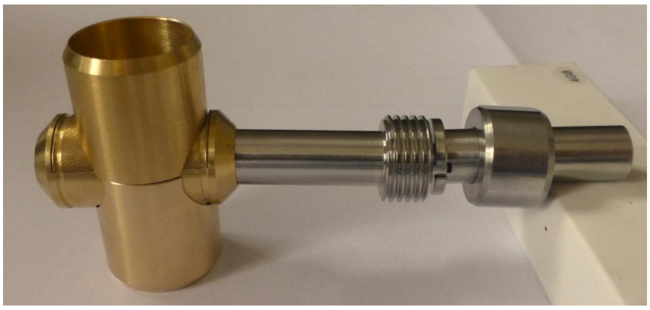

Fig. 4: *Bi-Directional Velocity Probe*

Results obtained in the previous work (Dyduch et al. (2016)) indicate that the turbulence generated by air dispersion from the dust canisters is isotropic and homogeneous. Therefore the BDVP was positioned in central part of the vessel and directed along the vessel's axis, perpendicularly to the axis of the dispersion nozzles.

3 Results and discussion

To obtain reference turbulence intensity the experiments were began with tests of pure air dispersion. Then a series of test was carried out with Cornstarch and Barbara d38 coal dust.

3.1 Dispersion of pure air

The first part of measurements was carried out for turbulence generated by air-only dispersion. Five such tests were performed. In Figure 5 the average values of u'_{rms} are plotted as a function of time. For comparison results of previous the work (Dyduch et al. (2016)) are also included.

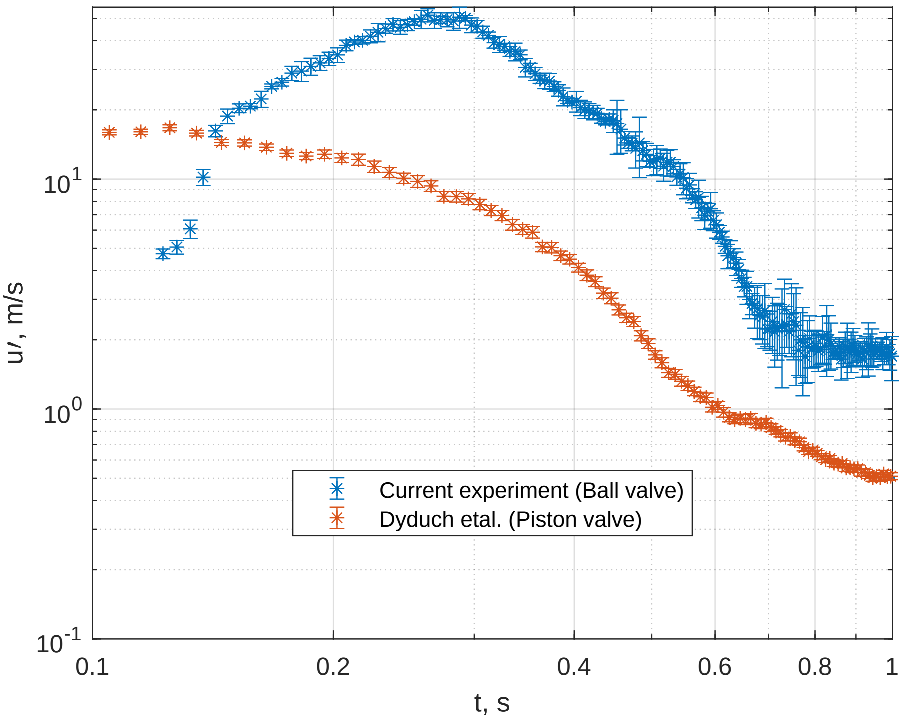

***Fig. 5**: Averaged root-mean-square of fluctuation velocity*

Moderate sizes of the error bars, even though only five tests were performed, suggest fairly good reproducibility of the turbulence intensity. Its maximum value, described by u'_{rms}, turbulence reaches just before 300 ms. Then it decays and in the period of time between 600 ms and 900 ms the values of u'_{rms} are in the range 2-5 m/s. When compared to the results obtained previously (Dyduch et al. (2016)), turbulence intensity changes differently. In the previous tests u'_{rms} reaches maximum value earlier, just after 100 ms. This value is smaller than in current tests. Then turbulence slowly decay down to $u'_{rms} = 0.5$ m/s. The difference in the discussed relationships should related to the exchange of the fast-acting valve. This is the only change made to the system. The change of the valve resulted in a change in the flow conditions at this point. The valve piston obstructed the flow while the ball valve opens the entire cross-section.

3.2 Dispersion of dust/air mixture

After the tests with air-only dispersion measurements of the turbulence generated by dust dispersion were carried out. In the tests different amounts of dust covering the range of nominal dust concentra-

tion 125 g/m^3 - 1000 g/m^3 were used. Results of those tests are presented in Figure 6 together with the results for pure air included for comparison.
To have a better insight into the dispersion process in Figure 6 changes of conditions in one of the dust canister were plotted too. Instead of pressure the rate of pressure changes is shown as this is a parameter more sensitive to changes.

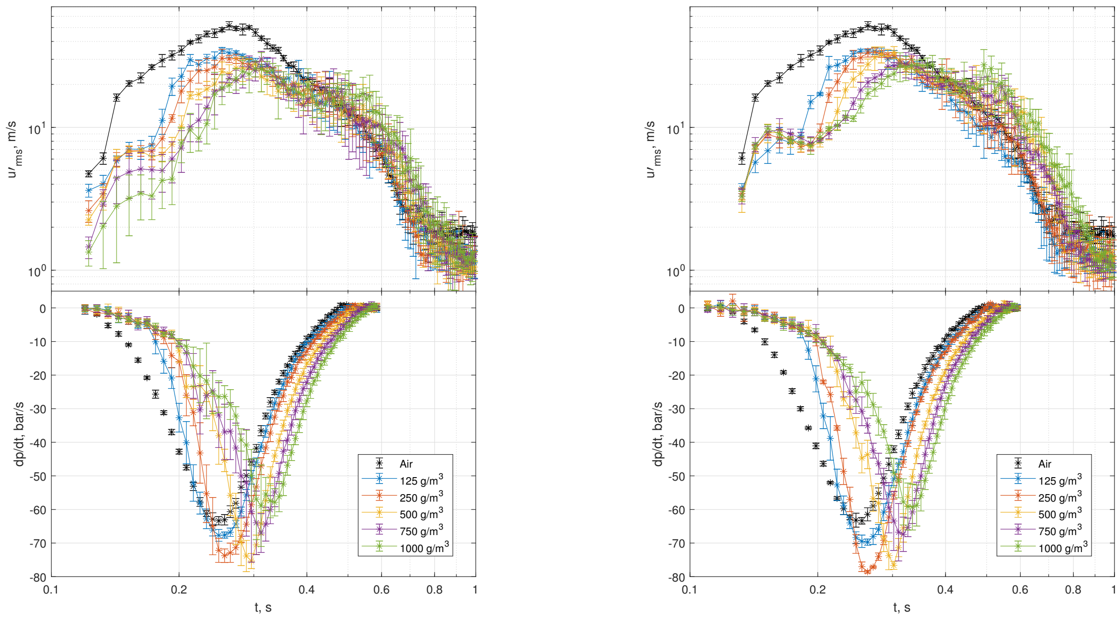

(a) Cornstarch *(b) Barbara d38*

***Fig. 6**: Root-mean-square of fluctuation velocity in dust/air mixtures and rate of pressure rise in the dust container*

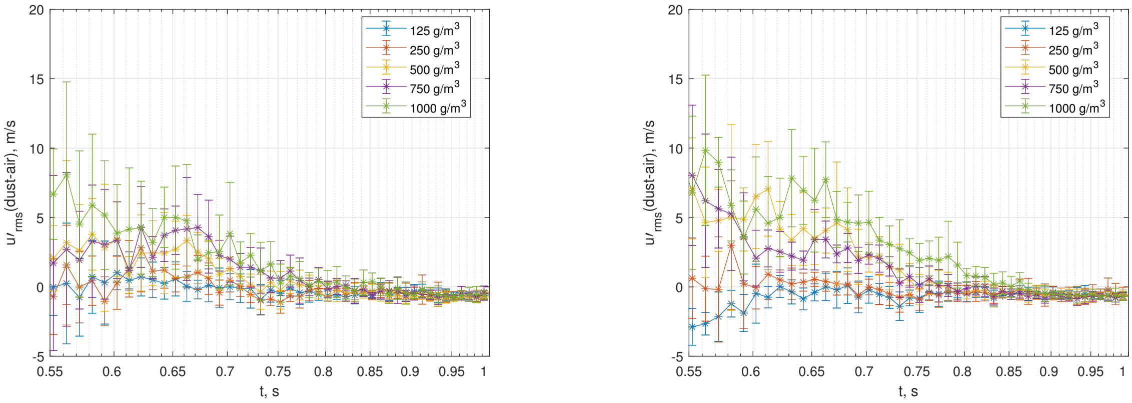

(a) Cornstarch *(b) Barbara d38*

***Fig. 7**: Differences of u'_{rms} values measured in experiments with dusts and with pure air*

Generally, plots representing results for two tested dusts are rather similar. For all tested dust concentrations, the intensity of turbulence, maximum value of u'_{rms}, is lower than in the test with pure air. After initial rise, up to about 6 m/s u'_{rms} stays at the same level for several tens of milliseconds. The larger the dust concentration the longer this period. That is probably time when pure air and a small portion of the dust in lower part of the canister is injected into the vessel. The rate of pressure change in the canister is small and identical for all amounts of dust used in the tests. Air in the upper part "does not know" about the injection yet. Then turbulence rises abruptly to its maximum values, smaller than in case of air dispersion. Again, the rate of rms velocity rise depends on the dust concentration. For larger amounts of dust the rate is smaller. Then for all tests with dust another small rise of rms velocity appears followed by fast decrease. Beginning at about 400 ms plots of u'_{rms} that represent different dust loads together with error bars are close to each other and that practically disable any reasonable observation. That is especially so for the most important period of time, between 600 ms and 900 ms, when main part of an explosion take place.

To better visualize most interesting time period, between 600 ms and 900 ms, in Figure 7 rms velocity is presented with reduced number of experimental points. Instead of the velocity alone plots represent differences of u'_{rms} obtained in tests with dust and pure air. In case of small dust loads the difference are close to zero within accuracy of the measurements. For larger loads the differences are of a few meters per second. Interestingly, for both dusts used beginning at about 750 ms all the values approaches zero.

4 Conclusions

In the paper results of measurement of turbulence generated in the standard 1 m^3 vessel by the dispersion of dust/air mixtures are presented. The turbulence was quantified by root-mean-square of fluctuation velocity. Prior to the main test measurement of turbulence generated by air dispersion were performed to obtain a point of reference. Tests with use of two well-know dusts indicate a modification of the turbulence development and decay. Initially dust presence delays outflow from the dust canister. The delay rises with increase of the dust load. These results correspond to observation made by Tamanini (1998) that the effect of the dust in the injection charge is to delay the flow development. Then the intensity of turbulence increases, but its maximum is lower than in the case of pure air and seems to be independent of the dust charge. At the end of the canister emptying stage, the turbulence intensity increases slightly. That might be attributed to an outflow of air with a little amount of dust that does not obstruct the outflow significantly. Subsequent turbulence decay is similar to the decay in dustless dispersion. Interestingly, after about 750 ms combined effect of the delayed outflow and lower maximum value of u'_{rms} results in very similar turbulence intensity caused by dispersion with and without dust. It might suggest that after that time turbulence assessed in test of dustless dispersion is also valid for actual dust tests.

The above observations suggest that the main effect of the presence of dust is to change the outflow from the dust canister. The main outflow starts with a delay and is slower, thus generating less intense turbulence.

It should be emphasised that in all tests described in the paper two dispersion units were used. If only one such unit is used an amount of dust in the canister will be doubled. Undoubtedly, the observed effects will then be more pronounced.

All observations and conclusions are based of results obtained for two well-known dusts. Tests with other dusts e.g. with large bulk densities may provide different results. Metal powders are obvious candidates for such tests. Also important are experiments with other dispersion nozzles, especially Perforated Dispersion Ring recommended as a first choice in the Standards.

Acknowledgments

The author gratefully acknowledge the contribution of his co-workers, co-authors of the previous paper.

References

ASTM-E-1226 (2012). *Standard test method for explosibility of dust clouds*. American Standard.

Dyduch, Z., Toman, A., Adamus, W. (2016). *Measurements of turbulence intensity in the standard* $1m^3$ *vessel*. Journal of Loss Prevention in the Process Industries, 40:180–187.

Eckhoff, R. K. (2003). *Dust Explosions in the Process Industries*. Gulf Professional Publishing, Amsterdam, third edition.

EN14034+A1 (2011). *Determination of explosion characteristics of dust clouds*. European Standard.

Hauert F., Vogl A., R. S. (1994). *Measurement of turbulence and dust concentration in silos and vessels*. Proceedings of the 6th International Colloquium on Dust Explosions, Shenyang.

ISO6184/1 (1985). *Explosion protection systems – part 1: Determination of explosion indices of combustible dusts in air*. ISO Standard.

McCaffrey B.J., H. G. (1976). *A robust bidirectional low-velocity probe for flame and fire application*. Combustion and Flame, 26:1125–127.

Portarapillo, M., Trofa, M., Sanchirico, R., Di Benedetto, A. (2022). *Cfd simulation of turbulent fluid flow and dust dispersion in the 1 m3 explosion vessel equipped with the rebound nozzle*. Journal of Loss Prevention in the Process Industries, 76:104755.

Proust Ch., Accorsi A., D. L. (2007). *Measuring the violence of dust explosions with the "20 l sphere" and with the standard "iso* $1m^3$ *vessel". systematic comparison and analysis of the discrepancies*. Journal of Loss Prevention in the Process Industries, 20:599–606.

Tamanini, F. (1998). *The role of turbulence in dust explosions*. Journal of Loss Prevention in the Process Industries, 11(1):1–10.

van der Wel, P. (1993). *Ignition and propagation of dust explosions*. Ph.D. Thesis.

DOI: 10.7795/810.20221124

Qualification in explosion protection - use of an adaptive learning platform

Patrick Dyrba, Prof. Dr. Thomas Köhler, Torsten Meyer-Efland

Dyrba Explosionsschutz Bildung und Beratung, Bad Schönborn, Deutschland
Technische Universität Dresden, Dresden, Deutschland
Area 9 Lyceum GmbH, Leipzig, Deutschland

E-mail: patrick.dyrba@exinfos.de

Abstract

Nowadays, specialists and managers are subject to high time pressure. When problems arise, they have to react quickly and find the right solution. This requires a high level of professional and personal responsibility. Constant adaptation of knowledge is required, lifelong learning is now standard. This applies in particular to specialists and managers for explosion-protected plants, where wrong decisions can have extreme consequences for human life and the destruction of plants.

The pressure on companies to provide training in this area is steadily increasing. Companies increasingly want education and qualification offerings that differ from conventional offerings. In view of demographic change, too, qualification offerings must be adapted to the needs of participants. This represents a major challenge for educational institutions that want to survive or remain leaders in the market in the wake of digitization. Last but not least, the competencies of learning facilitators may have to be completely rethought and trained.

In the context of a doctoral thesis, supervised by Professor Thomas Köhler at the TU-Dresden at the Institute for Vocational Education of the Faculty of Education, the effectiveness and efficiency of the use of an adaptive learning platform that enables personalized learning is investigated. The learning platform Area9 Rhapsode is used. Two modules, on zoning and maintenance in explosion protection, were developed specifically for the study. By using artificial intelligence, each participant goes through only the knowledge content that is relevant to them. The program automatically determines which knowledge gaps the participant has and then plays the appropriate learning resources to them. The learners can self-assess whether they are "beginner", advanced" or "expert". In the background, a continuous adaptation to the learner's knowledge level takes place. This results in different processing times for the participants, depending on the prior knowledge they already possess. According to studies by Area9 Lyceum, a time saving of up to 50% is possible compared to conventional e-learning. A big advantage compared to conventional e-learning is a proven data analysis, which allows individual evaluations. In this way, individual "nuggets" can be fed to each learner to effectively support them in their qualification. Greater efficiency is achieved as the learner's willingness to concentrate is higher when they can focus on learning content that is new and important to them. As learners discover and remedy their unconscious incompetence themselves, their enjoyment of the learning process increases. The first evaluations of the test subjects already show positive results.

The study comprises four test groups of 20 experimentees each. The sample of test persons consists of persons who have had their first contact with the topic of "explosion protection", such as students or people just starting out in their careers, as well as persons from occupational health and safety and experts in explosion protection. In the presentation, the international state of research on the topic will be discussed and the approach and initial research results will be reported.

Keywords: Adaptive learning, Qualification, E-Learning

DOI: 10.7795/810.20221124

1. Introduction

Nowadays, specialists and managers are subject to high time pressure. When problems arise, they have to react quickly and find the right solution. This requires a high level of professional and personal responsibility.

As digitization continues to advance, changes in the production process often have to be made at short notice. Different competencies are increasingly required of specialists and managers. Expert knowledge in a specific field, which used to be valued, is increasingly being displaced by the knowledge of generalists. Constant adaptation of knowledge is required; lifelong learning is now standard practice.

This is particularly true for specialists and managers for explosion-protected systems, where wrong decisions can have extreme consequences in terms of the destruction of human lives and systems. Thus in the field of explosion protection possess

- Planners and designers,
- manufacturers and installers,
- operators and maintenance personnel,
- engineering offices and consultants,
- testing organizations and authorities

an extremely high level of responsibility.

The pressure on companies to provide further training in this field is steadily increasing. The German legislator requires, for example, in the Hazardous Substances Ordinance, that the operator of explosion-protected systems must have specialist knowledge in his or her respective field and must keep this specialist knowledge up to date through appropriate training measures.

Solutions tailored to the specific problem are increasingly being sought. For example, for the repair of equipment, protective systems or safety, controlling or regulating devices in the sense of explosion protection (Directive 2014/34/EU), the operator must ensure that persons are deployed who, on the basis of their technical training, special knowledge and corresponding skills as well as experience with the repair of the equipment, protective systems, safety, controlling or regulating devices, can assess and carry out the assigned work and recognize the possible relevance for explosion protection within the scope of their activities.

Education and qualification offers are desired that differ from conventional offers. Volume 65 of the book series "Media in Science - Postgraduate Education with Digital Media" points out the need for high-quality and economically viable continuing education offerings. New target groups are to be reached and problem situations in the everyday working life of companies are to be mastered through practical knowledge (Fischer et al., 2014). Also with regard to demographic change, qualification offers have to be adapted to the needs of the participants. This represents a major challenge for educational institutions that want to survive or remain leaders in the market in the wake of digitization. This is also underpinned by the current corona situation. Last but not least, the competencies of learning facilitators may need to be completely rethought and trained. The focus of this work will be on adaptive learning. As a method the software "Area9 Rhapsode" will be tested and evaluated. It is taken into account that a homogeneous group of participants is not to be assumed. Area9 calls their learning platform the most advanced learning platform in the world (Area9, 2019). It is used specifically for adaptive and personalized learning. Benefits include (Area9, 2019):

- personalized learning, content adapted according to prior knowledge;
- learner self-assessment, i.e. learners receive just-in-time feedback on answered knowledge questions;
- detailed learning analytics of the participants, so the "Adaptive Learning Engineer" can provide appropriate content to each individual to ensure efficient knowledge transfer and
- according to Area9's internal studies, a possible reduction of participants' learning time by up to 50% compared to traditional e-learning systems.

The goal of adaptive learning is to move the learner from unconscious incompetence to conscious competence as efficiently as possible. The learner should be shown whether he is competent or incompetent. A learner with unconscious incompetence is thus led to believe that he or she possesses appropriate knowledge or certain skills, although this is not the case. According to Area9, learners are typically 15-40% unconsciously incompetent on a topic. It is concluded that many errors in practice occur due to unconscious incompetence. People think they know exactly how to proceed, but in reality they do not.

Area9 speaks here of four types of competence:
1. the unconscious incompetence,
2. the conscious incompetence,
3. the unconscious competence and
4. the conscious competence.

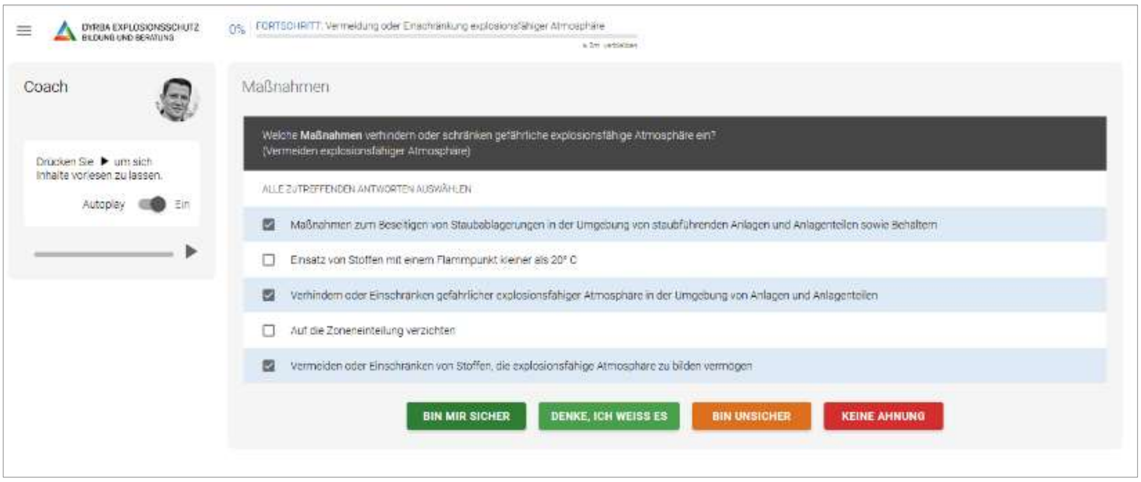

Welche **Maßnahmen** verhindern oder schränken gefährliche explosionsfähige Atmosphäre ein? (Vermeiden explosionsfähiger Atmosphäre)

ALLE ZUTREFFENDEN ANTWORTEN AUSWÄHLEN

☑ Maßnahmen zum Beseitigen von Staubablagerungen in der Umgebung von staubführenden Anlagen und Anlagenteilen sowie Behältern
☐ Einsatz von Stoffen mit einem Flammpunkt kleiner als 20° C
☑ Verhindern oder Einschränken gefährlicher explosionsfähiger Atmosphäre in der Umgebung von Anlagen und Anlagenteilen
☐ Auf die Zoneneinteilung verzichten
☑ Vermeiden oder Einschränken von Stoffen, die explosionsfähige Atmosphäre zu bilden vermögen

Figure 1. Self assessment in Area9 Rhapsode (Area9)

Which competence a learner belongs to is influenced by the learner's self-assessment (Figure 1). This helps the learner to gain more self-knowledge. Learners must independently assess how confident they are in answering the knowledge questions for each learning objective. In addition, automaticity allows us to move through our daily lives without cognitive overload. We need to internalize what we learn. We accomplish this through learning, repetition, and practice (Area9, 2019).

To get to a level of 100% competency, each learner needs their individual processing time. In this process, he goes through the course and he holds additional information if necessary, depending on his level of knowledge. Thus, as can be seen in Figure 2, it results that learner one, for example, only needs about 8 minutes to get to one hundred percent competence. Learner two needs about 19 minutes and learner three even invests about 33 minutes.

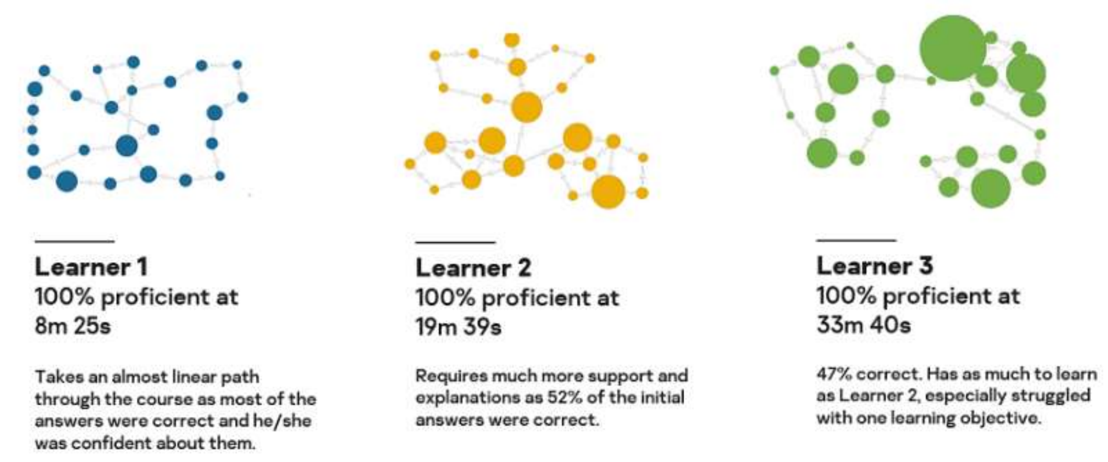
Learner 1
100% proficient at
8m 25s

Takes an almost linear path through the course as most of the answers were correct and he/she was confident about them.

Learner 2
100% proficient at
19m 39s

Requires much more support and explanations as 52% of the initial answers were correct.

Learner 3
100% proficient at
33m 40s

47% correct. Has as much to learn as Learner 2, especially struggled with one learning objective.

Figure 2. Individual learning path are based on an employee`s answers and their level of confidence (Area9)

2. Experiments

2.1 Preliminary work for the doctoral project

In the course of the doctoral project, questionnaires on continuing education were made available to all participants in continuing education courses between February 2019 and February 2020. Of 300 questionnaires, 273 were completed and returned immediately after the respective course. The target group was specialists and managers who have a high level of responsibility in the field of explosion protection.

The aim of this survey was to obtain relevant statements about the learning behavior of the participants. These statements should form a well-founded starting point for the doctoral thesis. The research method to be used is a learning platform that allows adaptive personalized learning. By means of different experimental groups the efficiency and the effectiveness of the learning shall be determined.

2.2 State of research Qualification in explosion protection

When considering current teaching and learning concepts, it was analyzed which qualifications - specifically for explosion protection - are offered (Dyrba, 2021). As German market leaders, the following providers are in the foreground: (alphabetical order)

1. BARTEC GmbH
2. BG RCI
3. DEKRA
4. DMT GmbH
5. Haus der Technik e.V.
6. IBExU
7. INBUREX
8. R. Stahl Schaltgeräte GmbH
9. TÜV (Nord, Rheinland, Saarland, Süd)

The presentation will address the international state of research on the topic.

2.3 Evaluation of qualified personnel in explosion protection

As a further step towards the PhD project, graduates of a training course in explosion protection were surveyed with regard to the knowledge imparted. In the process, 66 people who successfully completed their training in the period from 2017 to 2020 were evaluated via telephone interview. In this survey, the graduates were asked technical questions about the training and the answers were compared with the results of the two-hour final examination at the time.

2.4 Evaluation of the use of adaptive learning for qualification in explosion protection.

Four heterogeneous groups, beginners to experts, were put together to carry out the tests. In advance, two adaptive courses zoning and maintenance in explosion protection were specifically developed for the tests. These courses were worked on by two groups each (á 20 persons). Included in the final evaluation were two interviews conducted by telephone with specialist questions on the subject of explosion protection. The first test was conducted before the start of the respective course in Area 9 Rhapsode and the second test after the completion of a course. The results will be compared with the "Learning Analytics", the learning platform used by Area 9 Rhapsode.

3. Results and discussion

3.1 Essential core statements of the questionnaires on the subject of further training

The analyses of the questionnaires show a clearly heterogeneous group of people. The respondents ranged from persons without a high school diploma to those with an academic degree.

A large proportion of respondents (41.8%) had experience with classroom-based training events. Approximately 36% have already had contact with e-learning content. Only about 10% of the respondents have completed a webinar or blended learning content.

When it comes to the positive attributes of training events, immediate feedback from the learning facilitator was mentioned the most, at 36.6%. Next, respondents rated receiving topic-relevant information as most positive at 32.8%. A predetermined structure and program-guided learning were less relevant.

On the question of preferred end devices for online learning, the PC was named with 68.8%. The use of a tablet was mentioned by 24.5% and the smartphone by only 9.7%. When asked which media are best for learning, the most popular choices were instructional videos at 23.7%, PowerPoint presentations at 21.4%, PDFs at 20.9%, and interactive content at 13.3%. In order to work on a "building block" (smallest unit of a course), 52.1% mentioned a time frame of 15-30 minutes as being goal-oriented.

In order for a training event to be successful, it should meet the following requirements in the context of this survey: (indication of the five most frequently mentioned answers)

- Practical relevance with 13.9%
- Varied with 13.2%
- State of the art with 12,8%
- It must pick me up from my world of experience with 9.7%.
- Work on sample problem cases incl. solutions with 9,6%

When it comes to the individualization of e-learning content, the respondents' desire is for self-directed learning with 56.5%. Adaptive learning was named with 43.6%.

These statements were used to develop the adaptive courses for the studies. Thus, courses were created with the smallest possible building blocks.

If what has been learned is to be maintained, expert exchange is in first place with 20.4%. With 16.6%, e-learning is mentioned and followed by about 14%, the respondents would like to see presence phases, learning videos and expert conferences.

Augmented reality content is in first place with 35.8% as a target-oriented method for supporting training events. With 24.7%, the respondents also consider the use of learning analytics to be a target-oriented method for optimizing learning and the learning environment.

3.2 *Results of the evaluation of qualified personnel in explosion protection*

Figure 3 shows a comparison that includes the explosion protection training test result, the telephone interview test result, and the self-assessment from the telephone interviews.

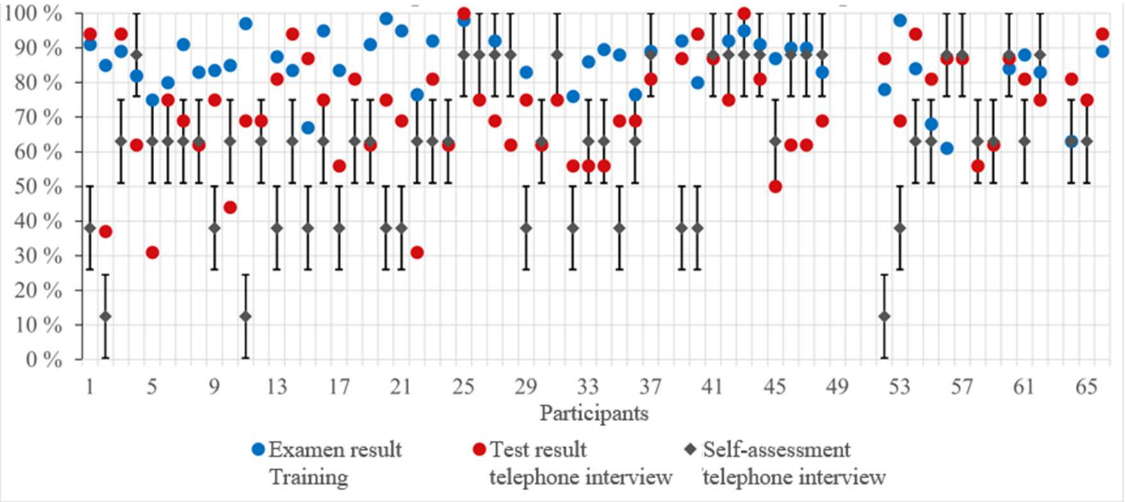

Figure 3. Comparison - Examen and telephone interview with self-assessment

It can be clearly seen here (red and blue dots in the graph) that - if there is no continuous further training on the subject - the knowledge acquired is quickly forgotten again due to lack of application/practice and can no longer be recalled.

The presentation of the self-assessment (black bars in the graph) shows the percentage range in which the participants see themselves, how they personally assess their skills in the field of explosion protection at the time of the survey. They could select the following ranges: 0-25%, 26-50%, 51-75%, and 76-100%.

Figure 4 shows the number of self-assessments across all participants in each percentage range. The range of 51-75% was cited as the most frequent with 20 votes in the self-assessment. The graphic line is intended to illustrate that a higher range - namely 76 - 100 % (green) should be targeted through the application of adaptive, personalized and mobile learning.

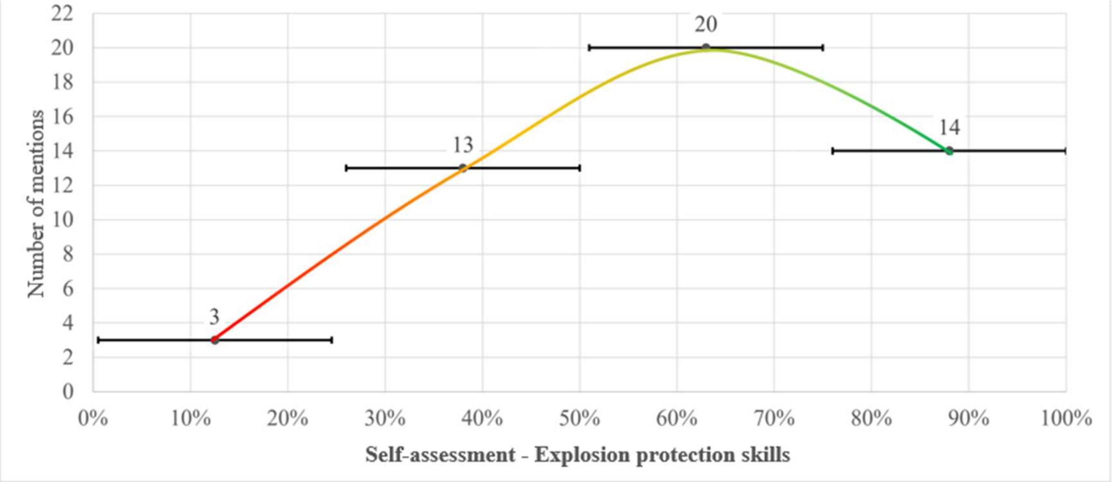

Figure 4. Number of self-assessments across all participants in each percentage area

Figure 5 shows the percentage of explosion protection activities and the self-assessed explosion protection skills of all participants. Again, participants could indicate ranges of 0-25%, 26-50%, 51-75%, and 76-100%. Although on average little time is spent on explosion protection issues, participants estimate their knowledge in the field of explosion protection at around 60%.

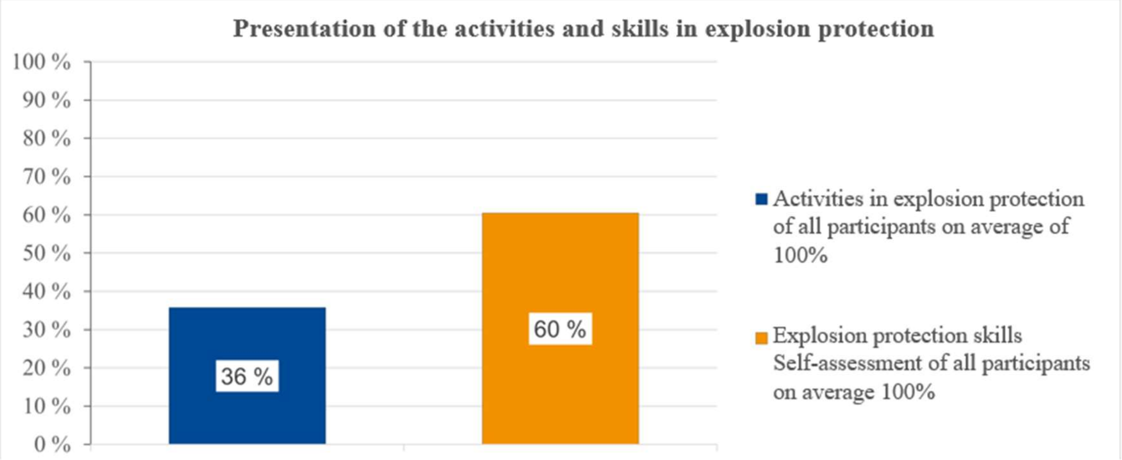

Figure 5. Presentation of the activities and skills in explosion protection

3.3 Results of the evaluation of the use of adaptive learning for qualification in explosion protection.

The first results of the study will be presented. The learning analytics of the test subjects will be discussed. Figure 6 shows a comparison of the evaluations of a test person. It can be seen that this person's knowledge level before completing the adaptive course was 40% of 100%. After completing the course and the offered refresher in Area 9, a knowledge level of 100% is achieved. A final telephone interview, one month after the completed course shows that the person still has a knowledge level of 80%.

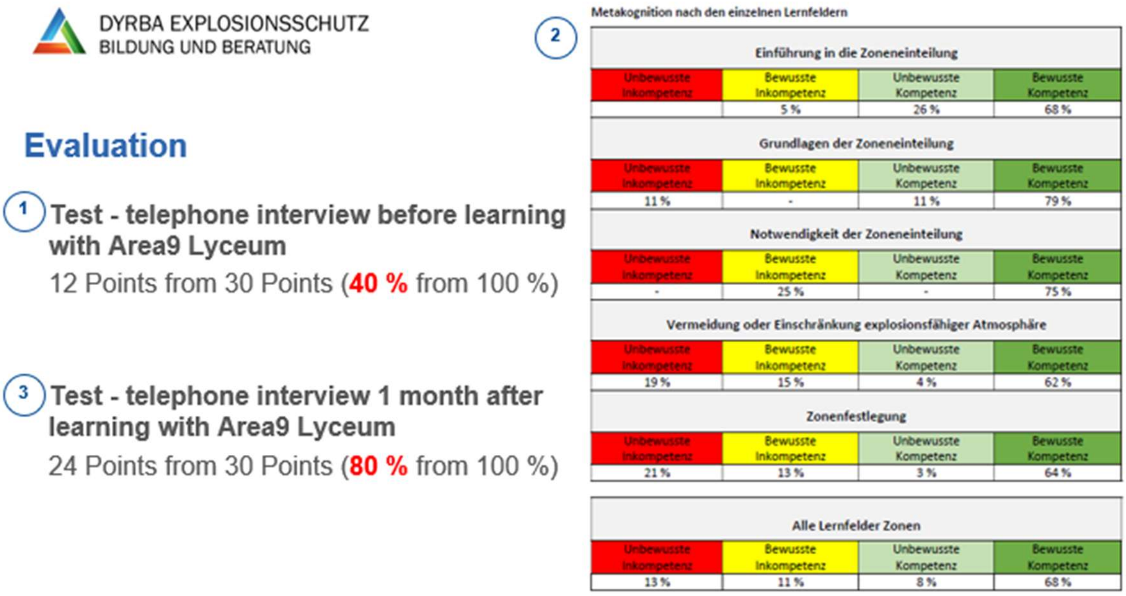

DYRBA EXPLOSIONSSCHUTZ
BILDUNG UND BERATUNG

Evaluation

① **Test - telephone interview before learning with Area9 Lyceum**
12 Points from 30 Points (**40 %** from 100 %)

③ **Test - telephone interview 1 month after learning with Area9 Lyceum**
24 Points from 30 Points (**80 %** from 100 %)

② Metakognition nach den einzelnen Lernfeldern

Einführung in die Zoneneinteilung			
🟥 Unbewusste Inkompetenz	🟨 Bewusste Inkompetenz	🟩 Unbewusste Kompetenz	🟩 Bewusste Kompetenz
	5 %	26 %	68 %

Grundlagen der Zoneneinteilung			
🟥 Unbewusste Inkompetenz	🟨 Bewusste Inkompetenz	🟩 Unbewusste Kompetenz	🟩 Bewusste Kompetenz
11 %	-	11 %	79 %

Notwendigkeit der Zoneneinteilung			
🟥 Unbewusste Inkompetenz	🟨 Bewusste Inkompetenz	🟩 Unbewusste Kompetenz	🟩 Bewusste Kompetenz
-	25 %	-	75 %

Vermeidung oder Einschränkung explosionsfähiger Atmosphäre			
🟥 Unbewusste Inkompetenz	🟨 Bewusste Inkompetenz	🟩 Unbewusste Kompetenz	🟩 Bewusste Kompetenz
19 %	15 %	4 %	62 %

Zonenfestlegung			
🟥 Unbewusste Inkompetenz	🟨 Bewusste Inkompetenz	🟩 Unbewusste Kompetenz	🟩 Bewusste Kompetenz
21 %	13 %	3 %	64 %

Alle Lernfelder Zonen			
🟥 Unbewusste Inkompetenz	🟨 Bewusste Inkompetenz	🟩 Unbewusste Kompetenz	🟩 Bewusste Kompetenz
13 %	11 %	8 %	68 %

Figure 6. First view of evaluation

In addition, other data will be taken from the learning analytics and presented, such as:

- the learning progress,
- the time to complete the course,
- the status after finishing the course,
- how many answers are correct or incorrect
- how often the learner was correct in learning in percent and
- the length of stay per module of a course.

3. Conclusions

Learning analytics is used to show which competencies the respective learner possesses. The goal is to lead the learner to conscious competence. This is illustrated by means of meta-analysis. The focus here is on self-knowledge in learning.

Meta-cognition and the development of a growth-oriented attitude are differentiated. Meta-cognition is thinking about one's thinking - an activity that refers to the continuous reflection of oneself as a learner through learning goals, strategies, and outcomes. A growth mindset encourages development, both in individuals and within organizations. By continuously completing refreshers and individualized nuggets over a period of one year, long-term knowledge retention could be enabled. This is demonstrated by the first applications of the in-house training program for explosion protection managers. This is a hybrid event in which adaptive learning is used in the run-up to the classroom event. This means that difficult topics can be dealt with efficiently during the classroom training.

References

Area9 Rhapsode, (2019). *Adaptives Lernen – In 4 Dimensionen;* PDF

Dyrba, (2021). *Qualifizierung im Explosionsschutz*; Sicherheitsingenieur; Dr. Curt Haefner-Verlag GmbH

Fischer, H., Köhler, T. (2014). *Postgraduale Bildung mit digitalen Medien – Medien in der Wissenschaft;* Band 65. Waxmann Verlag GmbH, Münster

DOI: 10.7795/810.20221124

Learning From the Past: The Importance of Risk Assessment in Aluminium Dust Processes

Barozzi Marco[a], Derudi Marco[b], Scotton Martina Silvia[a] & Copelli Sabrina[a,*]

[a]University of Insubria, Department of Science and High Technology, via Valleggio 9, Como (Italy)

[b]Politecnico di Milano, Department of Chemistry, Materials and Chemical Engineering, via Mancinelli 7, Milan (Italy)

*e-mail: sabrina.copelli@uninsubria.it

Abstract

Dust explosions are among the causes of the most severe industrial accidents that occur worldwide. Dust explosions from metal dust can be particularly hazardous. Unfortunately, the level of concern in the industrial panorama does not often reflect the danger represented by these dusts. The Hayes Lemmerz International, Huntington, Indiana (US), a company dedicated to manufacturing cast aluminium alloy wheels, witnessed a severe accident in 2003, when a dust explosion destroyed the plant. According to the reconstruction performed by the Chemical Safety Board, it was found that operators used to shut down a protective device, a slide valve installed in the 50.8 cm line outside the building, as they were not aware of its purpose. In this work, a quantitative risk analysis is proposed for this plant, showing the importance of the proper use of safety devices. The approach proposed is based on the Recursive Operability Analysis in combination with Failure Mode and Effect Analysis to define and compute Fault Trees. From accident reconstruction and plant information, a P&ID was constructed, detecting safety devices and main process components. Such a method is particularly suited for the construction of Fault Trees and highlights the importance of protective means. From the analysis, several Top Events were identified, including fires inside dust-collecting cyclones, the drop box and the bag filter. In some parts of the plant, overpressure may occur, due to an aluminium dust explosion. Probabilities of occurrence were estimated on the plant assuming both regular cleaning, housekeeping, safety devices installed and their shortcomings. From results, it was found that protective systems designed poorly do not remarkably affect system safety, and correct housekeeping is instead essential to avoid unfortunate events in this type of process.

Keywords: *aluminium dust, risk assessment, industrial explosions*

1. Introduction

Dust explosions are extremely severe phenomena that deeply impact process safety (Amyotte, 2013). According to the Combustible Dust Incident Report (Cloney, 2021), almost 300 dust explosions occurred between 2017 and June 2021 among U.S.A, Canada and the rest of the world. Fig. 1 shows the trend of dust explosions that occurred worldwide in the latter period on a yearly base. The accident trend does not suggest a remarkable decrease in industrial dust explosions, highlighting a need of improvement in process safety (Abbasi, 2007). Also, note that this datum covers accidents officially recorded; many other unknown accidents may have impacted chemical plants. While knowledge about dust explosion phenomena has increased in the latter years, thanks to the development of new models and studies, the same aspect is not necessarily reflected on process safety in industries handling these hazardous substances. The scope of this work is to focus on basic but important elements of process safety when handling with dust explosions, remarking the importance of risk assessment. The main target is to remark, through the application of Recursive Operability Analysis (ROA) (Piccinini and Ciarambino, 1997), the importance of the correct implementation of safety devices and procedures. This study is focused on the accident that involved the Hayes Lemmerz International site in 2003, when a dust explosion led to a casualty, injured workers and severe plant damage.

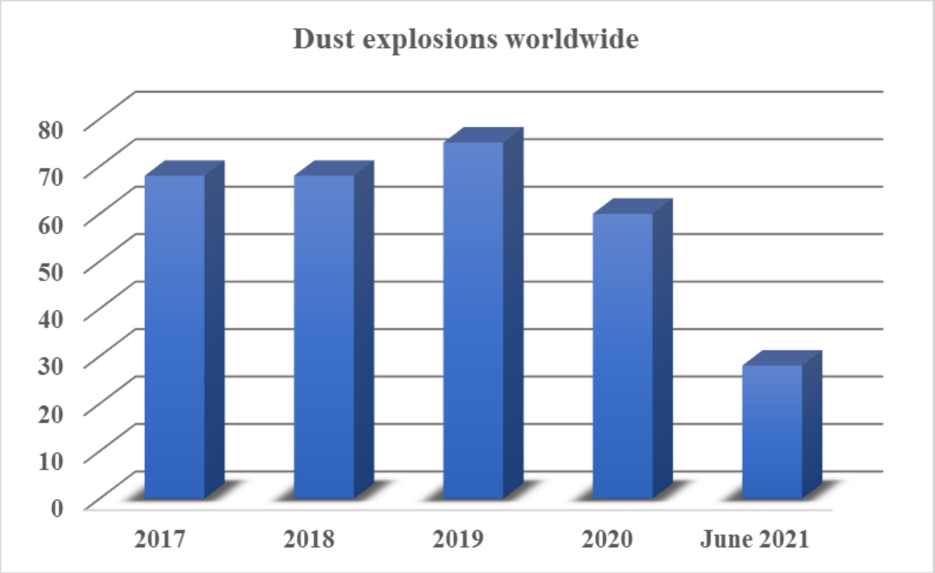

Figure 1 *Total number of dust explosions recorded worlwide over the period 2017-June 2021 (adapeted from Cloney, 2021)*

According to the accident reconstruction carried out by the Chemical Safety Board (CSB), the main root causes of the accident can be summarized as a general lack of knowledge in both process safety and safety devices installation. Unfortunately, this condition is not an outlier, but a general behaviour associated with process safety management, because safety is too often felt as a money and time expenditure with a non-direct economic gain. However, CSB never performed a Quantitative Risk Analysis on the process. The target is to estimate the probabilities of occurrence for the events involving dust explosions in the plant, to evaluate numerically which have been the most impactful errors on process safety. The analysis is performed based on a ROA. ROA is a risk assessment tool, originally derived from HazOp that can be used to assess the risk in chemical plants (Demichela et al., 2002), e.g. due to dust explosions (Barozzi et al., 2020a) and maintenance planning (Marmo et al., 2009). Its main strength is the capability of automatically generating Fault Trees, after a correct compilation of a ROA table (very similar to the HazOp one). The analysis will be executed on the main process involved in the accident, considering the impact of protective measures on process safety.

1.1 Accident description

An aluminium dust explosion occurred on October 29, 2003 at the Hayes Lemmerz International−Huntington, Inc. (Huntingtion, Indiana, U.S.A.) facility, leading to a casualty, two employees with major burns and 4 with minor injuries (CSB, 2004). Fig. 2 shows the plant after the explosion occurred.

DOI: 10.7795/810.20221124

Figure 2 *Hayes Lemmerz's facility after the explosion (CSB, 2004)*

The plant was dedicated to the manufacturing of cast aluminium alloy wheels. It appears that the explosion originated in a scrap re-melting system, that was used to improve aluminium use efficiency. However, an officially acknowledge ignition source of this accident is still unknown (Taveau et al., 2018). The event blew the dust collection equipment outside the building and damaged the internal equipment. Witnesses confirmed that, during the accident, a portion of the building roof above one furnace was lifted up and the fire burned for several hours. Aluminium dust is well-known for its extremely severe explosivity but, despite this, it is still today subject to severe industrial accidents (Danzi and Marmo, 2019). For this reason, it is extremely important to constantly inform and highlight companies and workers about the risk represented by explosive dusts, and how to correctly mitigate it.

2. Methods and Case Study

2.1 ROA – FMEA - FTA

The approach followed in this work is similar to the analysis carried out in a previous work, where a combination of these techniques was effectively used to estimate the risks associated with a biogas process (Barozzi et al., 2021). By combining the Recursive Operability Analysis with Failure Mode and Effect Analysis, it is possible to describe an accidental scenario with a more factual idea of all the basic events that can impact an industrial process, which are mainly components failures or human errors (risks posed by NATECH events or sabotage are not actually considered). However, the specific study on this case required to implement some modifications on the model to better describe the events involved. At first, a basic ROA was performed, so the plant states with protections working correctly were not considered (hence, Cause-Consequence-Diagrams were not computed). The ROA table structure is reported in Table 1.

Table 1 *ROA table used for the analysis (adapted from Barozzi et al., 2021)*

Record	**Node Deviation Variable (NDV)**	**Causes**	**Consequences due to protections failure**	**Protections**			**Notes**	**Top Event**
				Manual		Automatic safety systems actions		
				Alarm (optical/acoustic)	Operator actions on components			
	1	2	3	4	5	6		

From the table, Incidental Sequences Diagrams (ISD) can be generated according to the scheme shown in Fig. 3. From the union of all the ISDs, a Fault Tree for each Top Event is automatically generated. In this case, FMEA acts as a database: failures of basic components are retrieved from the table generated pre-emptively. It is also necessary to evaluate human errors and some process-specific basic events that will be explained in the following.

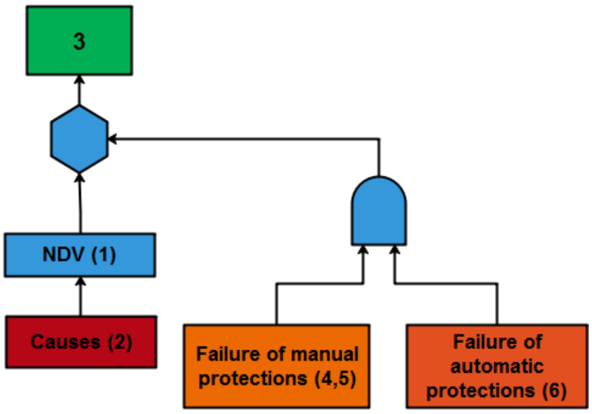

Figure 3 *ISD structure starting from a ROA record*

The most crucial part to be included in the analysis is the presence of secondary explosions. Unfortunately, a standard ROA is not suited to account for such events, because it would eventually create an internal loop where temperature and pressure deviations are forcibly linked. For this reason, the ROA will be applied at two separated stages:

1. Primary explosions: each device that can potentially host a primary explosion is analysed, considering it as independent from other explosions
2. Secondary explosions: probabilities of occurrence derived from the first part will be used as basic events to describe chain effects.

With this approach, the ROA remains well-structured at the cost of considering primary explosions as independent events, which is usually reasonable for relatively low probability events such as explosions.

2.2 Case Study

The risk assessment is carried out on the Hayes Lemmerz facility, which was dedicated to the re-melting of aluminium scraps. Process scheme and P&ID were reconstructed mainly basing on the information provided by a CSB report (CSB, 2005). From the report, the following information was taken. The aluminium scrap recycling process is performed on furnace 5, which receives the scraps after several cleaning steps, with the aim of removing other substances that can be mixed in the main wheel manufacturing process. The aluminium chips flow is then purified with the use of a cyclone, which removes the coarser particles mixed with the chips. At this point, chips are fed into a furnace, while the gas phase is furtherly treated, by passing through a spark box, a drop box, and a dust collector (a baghouse). The final treated gas phase is released into the atmosphere. The baghouse and the drop box are located outside the main building. Meanwhile, aluminium chips are fed into the furnace, where a fume hood is installed and connected with another dust collector system, based on a 2-units multi cyclone. The final treatment units are located outside the building. Fig. 4 shows the P&ID reconstructed based on this information. Equipment labelling is related to the corresponding node.

DOI: 10.7795/810.20221124

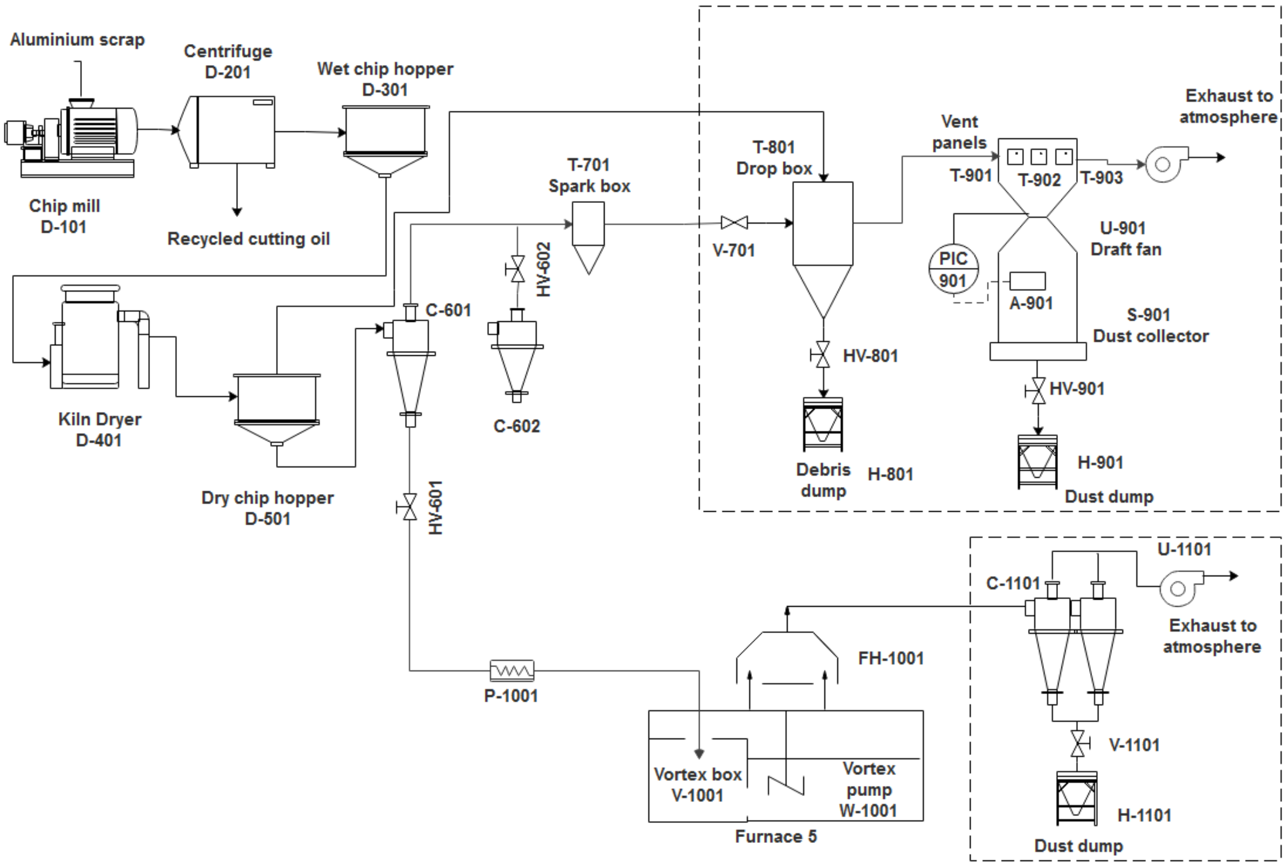

Figure 4 *Scheme and P&ID of the whole aluminium scraps recycling facility. Parts inside dashed boxes are located outside of the main building.*

According to literature (Eckhoff, 2003), the Minimum Ignition Temperature for aluminium dust is about 426.6 °C (800° F), and Minimum Ignition Energy (Eckhoff, 2003), could be reasonably considered about 60 mJ (Hong-Chun et al., 2010) according to the particle size analyzed by the CSB (MIE was not tested directly on the samples). The Minimum Explosive Concentration is about 50 g/m³ (CSB, 2005). These data are extremely important to define where and how dust clouds can be generated and, eventually, ignited. To apply a ROA, the process should be divided into nodes. For the purposes of this analysis, 11 nodes were identified:

1. Chip mill
2. Centrifuge
3. Wet chip hopper
4. Kiln dryer
5. Dry chip hopper
6. Dust cyclones
7. Spark box
8. Drop Box
9. Dust collector
10. Aluminium scrap furnace
11. Furnace venting line

Many components are involved in the process, and they are listed in Table 2.

Table 2 List of components involved in the analysis

ID	Description	ID	Description
D-101	Chip mill	T-901/2/3	Venting panels
D-201	Centrifuge	PIC-901	Pressure indicator/controller

D-301	Wet chip hopper	A-901	Pulse jet system
D-401	Kiln dryer	HV-901	Hand valve
D-501	Dry chip hopper	H-901	Dust dump
C-601	Dust cyclone	U-901	Draft fan
C-602	Dust cyclone	P-1001	Screw pump
HV-601	Hand valve	V-1001	Vortex box
HV-602	Hand valve	W-1001	Vortex pump
T-701	Spark box	FH-1001	Fume hood
V-701	Isolation valve	C-1101	Multi cyclone
T-801	Drop box	V-1101	Automatic valve
HV-801	Hand valve	H-1101	Dust barrel
H-801	Debris dump	U-1101	Draft fan
S-901	Baghouse		

It is important, to carry out the analysis, to identify also where dust fire, ignition and explosion can take place. Aluminium dust ignition could have reasonably occurred in the following plant sections:

- Draft fans
- Spark box or cyclone C-601
- Furnace
- Dust collector
- External dust aluminium barrels

Such zones are the most likely to represent an initial trigger for the following reasons: draft fans, mainly due to wearing, can overheat or generate electrical sparks. However, it was found that no electrical connections were close to the dust streams, and it is unlikely that a fan would reach aluminium MIT by simple overheating due to a worn impeller. Spark box, cyclones C-601 and C-602 exhibit the potential to intercept floating burning embers that would be generated during routine operation of the aluminium melt furnace. In addition, such devices must withstand flows with a high content of dust and chips, so they are very likely to experience wearing, leading to dust leakage and entrainment of air from the outside. The spark box acts as a device to minimize friction sparks due to the impact of floating chips. The furnace works at extremely high temperatures, so the ignition of dust deposits exposed to hot surfaces is a potential issue. A baghouse is a well-known source of dust ignition, due to overheating or accumulated static charge on the dust, especially when the equipment is not grounded properly. Additional issues may also arise in case of excessive pressure drops when bags are extremely fouled and the cartridges themselves can catch fire and trigger dust ignition. In this case, the dust collector also naturally creates dust clouds as it is also equipped with air pulse jets for cleaning operations. Finally, the dust collector systems are located outside (baghouse, dropbox and multi cyclone). This aspect makes an additional ignition source as a point of attention. This accident occurred before the explosion at the Zhong Rong Metal Products Co in 2014, which was deeply studied by Li et al. (2016). The company was dedicated to polishing aluminium wheel hubs, and it was then quite similar to the Hayes Lemmerz facility. It was found that if water enters the barrel (i.e., corroded bottom), it may trigger an extremely exothermic reaction with aluminium, which can lead to a fire, with potential subsequent explosions, as it happened in 2014. This aspect will be also considered.

Variables investigated for the analysis are:

- Temperature
- Flow
- Concentration (aluminium)

- Pressure
- Level

Level is associated with the level of dust, chips or debris accumulated at the bottom of the dust collector systems, so they are associated with C-601/C-602, S-901, T-801 and C-1101. About deviations, the most important are high concentration, which indicates a concentration above the MEC, and high pressure (>1 bar, the system is supposed to work at a slight underpressure), indicating an explosion.

2.3 FTA

A standard Fault Tree Analysis (FTA) was performed for each Top Event Identified. The FTs were solved using failure rates of components and human error probabilities recovered from literature databases. Probabilities of basic events were calculated using a Poisson distribution (Crowl and Louvar, 2002), hence neglecting the presence of maintenance and repairs. This hypothesis is reasonable with a mission time of 1 year. From FTA, analysis of Minimal Cut Sets (MCS), probabilities of occurrence and most critical events are reported.

3. Results and discussion

The analysis was carried out by assuming at first that the company would carry out the minimum necessary actions to handle aluminium dust: regular cleaning of ducts and devices, housekeeping, and the isolation valve V-701 is supposed to be active on the plant. In this way, it was possible to finally analyse the impact of the most severe errors that were handled by the company, namely the shutdown of V-701 and the lack of housekeeping and regular cleaning.

3.1 ROA tables

Before starting with ROA, FMEA must be compiled. Table 3 reports the failure analysis for the devices involved in the process. Failure rates were recovered from literature databases (Lees, 2005),(Smith, 2017).

Table 3 *FMEA analysis for nodes 6-11 (Cons.: Consequences, Prot.: protections)*

Component	Description	Failure mode	Failure cause	Cons.	Prot.	Failure rates [1/h]	Notes
C-601	Dust cyclone	Dust loss	Wearing	Loss in efficiency		$3\cdot10^{-6}$	
				Dust leakage		$3\cdot10^{-6}$	
C-602	Dust cyclone	Dust loss	Wearing	Loss in efficiency		$3\cdot10^{-6}$	Usually closed from HV-602
				Dust leakage		$3\cdot10^{-6}$	
HV-601	Hand valve (butterfly)	Failure to open	Shutter wearing	Dust accumulation on the C-601 hopper		$10\cdot10^{-6}$	
		Failure to close	Actuator wearing	Issues during mainteneance		$15\cdot10^{-6}$	Should be closed under maintenance
HV-602	Hand valve (butterfly)	Failure to open	Shutter wearing	-		$10\cdot10^{-6}$	Usually closed
		Failure to close	Actuator wearing	C-602 starts operating		$15\cdot10^{-6}$	
T-701	Spark Box	Does not extinguish sparks	Wearing	Dust leakage	Housekeeping	$1\cdot10^{-7}$	Chips stream erodes

						components surfaces -Safety device
V-701	Isolation Gate valve	Failure to open	Shutter wearing	Flow blocked	$10\cdot10^{-6}$	Safety device, normally opened
		Failure to close	Actuator wearing	Missed fire/explosion protection	$10\cdot10^{-6}$	
T-801	Drop Box (Settling chamber)	Box worn	Panels wearing	Dust leakage	$3\cdot10^{-6}$	No housekeeping (outside)
HV-801	Hand valve (slide)	Failure to open	Shutter wearing	T-801 clogged	$10\cdot10^{-6}$	
		Failure to close	Actuator wearing	Issues during maintenance	$15\cdot10^{-6}$	Closed in case of maintenance
H-801	Dust barrel	Barrel worn	Wearing	Dust leakage	$3\cdot10^{-6}$	No housekeeping (outside)
U-901	Draft fan	Failure in activation	Failure of elecritcal motor	No flow	$10\cdot10^{-6}$	
		Low flow	Worn impeller	Loss in efficiency	$2.57\cdot10^{-6}$	
S-901	Baghouse	Low flow	Cartridge clogged	High pressure drops	$3\cdot10^{-6}$	
		Dust flowing from the outlet	Cartridge torn	Dust dispersed in the atmosphere Wearing of fan	$3\cdot10^{-6}$	
HV-901	Hand valve (butterfly)	Failure to open	Shutter wearing	S-901 clogged	$10\cdot10^{-6}$	
		Failure to close	Actuator wearing	Issues during maintenance	$15\cdot10^{-6}$	Closed in case of maintenance
H-901	Dust barrel	Barrel worn	Wearing	Dust leakage	$3\cdot10^{-6}$	No housekeeping (outside)
PIC-901	Pressure indicator-controller	Fail low P	Failure of electrical components	Pulse jet activates too often	$10\cdot10^{-6}$	
		Fail high P	Failure of electrical components	S-901 clogged	$10\cdot10^{-6}$	
T-901/2/3	Venting panel	Does not open	Failure of mechanical components	Pressure rises in case of fire/explosion	$10\cdot10^{-6}$	

A-901	Pulse jet	Failure in activation	Failure of electrical components	S-901 cannot be cleaned (high pressure drops)	$6.3\cdot10^{-8}$	
P-1001	Screw pump	Failure in activation	Bearings wearing	Cannot send chips to the furnace, chips and dust accumulate under C-601	$20\cdot10^{-6}$	
			Screw wearing		$5\cdot10^{-7}$	
			Failure of electrical motor		$10\cdot10^{-6}$	
FH-1001	Fume hood	Failure in fumes containment	Wearing	Dust leakage		
W-1001	Vortex pump	Failure in activation	Transmission failure	Chips accumulate vertically on the box	$40\cdot10^{-6}$	
			Failure of electrical components		$10\cdot10^{-6}$	
U-1101	Draft fan	Failure in activation	Failure of electrical motor	No flow	$10\cdot10^{-6}$	
		Flow is low	Worn impeller	Low flow	$2.57\cdot10^{-6}$	
		Overheating	Worn impeller	Fan rupture	$1\cdot10^{-8}$	
C-1101	Dust multi cyclone	Dust loss	Wearing	Loss in efficiency	$3\cdot10^{-6}$	
				Dust leakage	$3\cdot10^{-6}$	
V-1101	Automatic valve	Failure to open	Shutter wearing	C-1101 clogged	$10\cdot10^{-6}$	
		Failure to close	Actuator wearing	Issues during maintenance	$15\cdot10^{-6}$	Closed in case of maintenance
H-1101	Dust barrel	Barrel worn	Wearing	Dust leakage	$3\cdot10^{-6}$	No housekeeping (outside)

ROA was then developed under these hypothesises local fires occur in case of presence of ignition, as it is assumed that some aluminium deposit (even if small), is always available during the process. If concentration is then greater than the MEC, an ignition can lead to a dust explosion. Table 4 reports the ROA for node 6, involving the cyclone. The most critical TE identified are a dust fire (TE1), and an explosion (TE3). Fire and explosions are associated with dust accumulation, which is basically due to a blockage of the lower cyclone outlet, allowing dust and debris to deposit on its bottom. An ignition is given by a floating ember, which can be pulled by the system that is opened to the outside. It is assumed that dust leakage and accumulation overtime can be effectively avoided by implementing a proper housekeeping.

Table 4 *ROA table for node 6*

Rec.	**NDV**	**Causes**	**Protections**		**Notes**	**Top Event**
			Manual			

			Consequences due to protections failure	Alarm (optical/acoustic)	Operator actions on components	Automatic safety systems actions		
6.0	6.1hC	6.1hL	6hT (in case of ignition)					
6.1	6.1hL	P-1001 blocked OR HV-601 closed	6.1hC		Housekeeping			
6.2	6.1hT	Embers pulled	6.1hhT Dust fire					TE1
6.3	6.1hhT	6.1hT AND 6.1hC	6.1hP					
6.4	6.1hP	6.1hhT	Dust Explosion					TE2
6.5	6.1lF	C-601 (worn) OR 9lF	Dust leakage (C-601) 10hF (9lF)		Housekeeping			TE3
6.6	6.1nF	V-701 (closed) OR 9nF	No flow					TE4

Table 5 reports the analysis for the drop box, which is basically a settling chamber. This device was lately connected with the dryer D-501, so it receives dust and debris from 2 connections. From these points several ignition sources are foreseen: debris from the dryer exhibit the potential of creating an impact spark that could ignite aluminium. In addition, embers may bypass the spark box and be pulled inside T-801. Since the dropbox is connected to an external barrel, it is possible that the deposits located here, whether not removed and treated correctly, develops a fire, which can be an additional triggering event.

Table 5 *ROA table for node 8*

Rec.	**NDV**	**Causes**	**Consequences due to protections failure**	**Protections**			**Notes**	**Top Event**
				Manual		Automatic safety systems actions		
				Alarm (optical/acoustic)	Operator actions on components			
8.0	8hC	8hL	8hT (in case of ignition)					
8.1	8hL	Dust accumulation OR HV-801 closed	8hC		Regular cleaning			
8.2	8hT	Embers pulled OR Impact spark from D-501 OR H-801 (fire)	8hhT Dust fire			T-701 (Embers)		TE5
8.3	8hhT	8hT AND 8hC	8hP					

8.4	8hP	8hhT	Dust Explosion					TE6
8.5	8lF	9lF	8hL					
8.6	8nF	9nF	No flow					TE7

Table 6 reports results for the dust collector. In this case, concentrations above critical values are always possible, due to the presence of a frequent air pulse jet for cleaning operations. The most likely ignition sources are a static charge accumulated overtime, a fire from the debris dump or embers pulled from the main flow.

Table 6 *ROA table for node 9*

Rec.	**NDV**	**Causes**	**Consequences due to protections failure**	**Protections**			**Notes**	**Top Event**
				Manual		Automatic safety systems actions		
				Alarm (optical/acoustic)	Operator actions on components			
9.0	9hC	Air pulse jet	9hT (in case of ignition)					
9.1	9hL	HV-901 closed OR Human error	Static charge Clogging		Grounding Check cartridges fouling and pressure			TE8
9.1	9hT	9hC AND (Static charge OR Embers pulled OR H-901 (fire))	9hhT Dust fire			System grounded (static charge) T-701		TE9
9.2	9hhT	9hT	9hP					
9.3	9hP	9hhT	Dust Explosion			T-901/2/3		TE10
9.4	9lF	U-901 worn OR Clogging	Efficiency loss AND 6.1lF AND 8lF					TE11
9.5	9nF	U-901 failure	No flow AND 6.1nF AND 8nF					

For what concerns the furnace, Table 7 reports a possible sequence of events. From the company, it was known that this was the process part most subjected to minor internal fire and accidents. In this case, temperature is almost always above MIT, so each dust clump or cloud that touches the molten surface can catch fire. Dusts naturally deposit on the fume hood over time, and proper housekeeping is necessary to protect from hazardous events. It is interesting to notice that a filled feed pipe from the dryer acts as a flame arrestor, so it can stop eventual minor fires from spreading into the rest of the facility.

***Table 7** ROA table for node 10*

Rec.	**NDV**	**Causes**	**Consequences due to protections failure**	**Protections**			**Notes**	**Top Event**
				Manual		Automatic safety systems actions		
				Alarm (optical/acoustic)	Operator actions on components			
10.0	10hC	Dust accumulation	10hhT (in case of ignition)		Housekeeping			
10.1	10hT	10hF	10hhT Dust fire				Dust is instantly ignited given the furnace temperature	TE12
10.2	10hhT	10hT AND 10hC	10hP					
10.3	10hP	10hhT	Dust Explosion					TE13
10.4	10lF	Low chip load	Missed protection in case of fire				The duct pipe acts as a flame arrestor in case of fires in the furnace	
10.5	10hF	6.1lF	10hT					

The final node describes the multi cyclone C-1101. In this case, embers may be pulled from the furnace, or fire can be developed to the dust dump located outside, under the right conditions. In this case, the filling of the barrel is controlled by an automatic valve (V-1101). In the other dust collecting systems, these valves are manual.

***Table 8** ROA table for node 11*

Rec.	**NDV**	**Causes**	**Consequences due to protections failure**	**Protections**			**Notes**	**Top Event**
				Manual		Automatic safety systems actions		
				Alarm (optical/acoustic)	Operator actions on components			
11.0	11hC	11hL	11hT (in case of ignition)					
11.1	11hL	Dust accumulation OR V-1101 closed	11hC		Regular cleaning			
11.2	11hT	Embers pulled OR H-1101 (Fire)	11hhT Dust fire					TE14
11.3	11hhT	11hC AND 11hT	11hP					
11.4	11hP	11hhT	Dust Explosion					TE15

11.5	11lF	C-1101 (worn) OR U-1101 worn	Dust leakage (C-1101)	Regular cleaning	TE16
11.6	11nF	U-1101 failure	No flow		TE17

To summarize, the most important TEs found were dust fires (TE1,5,9,12,14) and primary dust explosions (TE2,6,10,13,15). Some additional events were found, such as dust leakage around the plant, loss in efficiency of removal and flow absence. Now, if these events are considered completely independent from each other, it is possible to use them as triggering events for secondary explosions. Hence, it was possible to generate a ROA for secondary explosions, as shown in Table 9. Logically, each device may exhibit a secondary explosion if exposed to a primary explosion from the closest source. C-601 can be triggered by an explosion in the fume hood or in the drop box, the drop box can be triggered by C-601 or the dust collector and so on. Of course, to propagate the explosion, fuel must be present, hence a high concentration of dust must be available. Due to the nature of explosions, each deposit instantly becomes a dispersed dust cloud in case of exposition to a pressure wave.

Table 9 *ROA table for secondary explosions*

Rec.	**NDV**	**Causes**	**Consequences due to protections failure**	**Protections**			**Notes**	**Top Event**
				Manual		Automatic safety systems actions		
				Alarm (optical/acoustic)	Operator actions on components			
12.0	6.1hP	(TE13 OR TE6) AND 6.1hC	Secondary Explosion in C-601			V-701 (TE6)		TE18
12.1	8hP	(TE2 OR TE10) AND 8hC	Secondary Explosion in T-801 AND 9hP			V-701 (TE2)		TE19
12.2	9hP	TE6	Secondary Explosion in S-901					TE20
12.3	10hP	(TE2 OR TE15) AND 10hC	Secondary Explosion in FH-1001 AND 11hP					TE21
12.4	11hP	TE13 AND 11hC	Secondary Explosion in C-1101 AND 10hP					TE22

3.2 FTA

From each record, ISDs can be generated, and Fault Trees for the definition of the accidental scenario can be found. Figures 5-7 reports the results for the most relevant TE (namely, dust explosions). From the trees structure, it is important to notice how regular maintenance, housekeeping and cleaning are extremely important for enhancing process safety, acting as protective measure on the generation of dangerous dust deposits (see all the saturated inhibit gates).

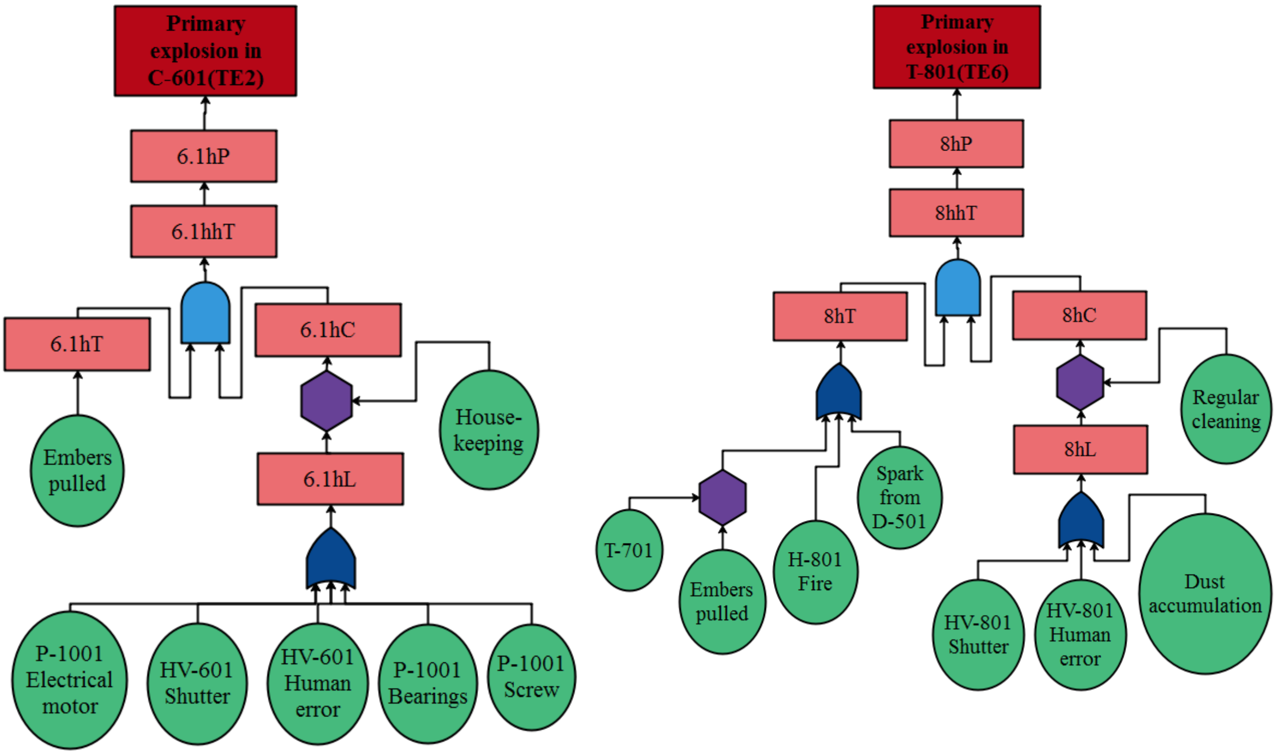

Figure 5 *FTs for a primary explosion in cyclone C-601 (left) and in the drop box T-801 (right)*

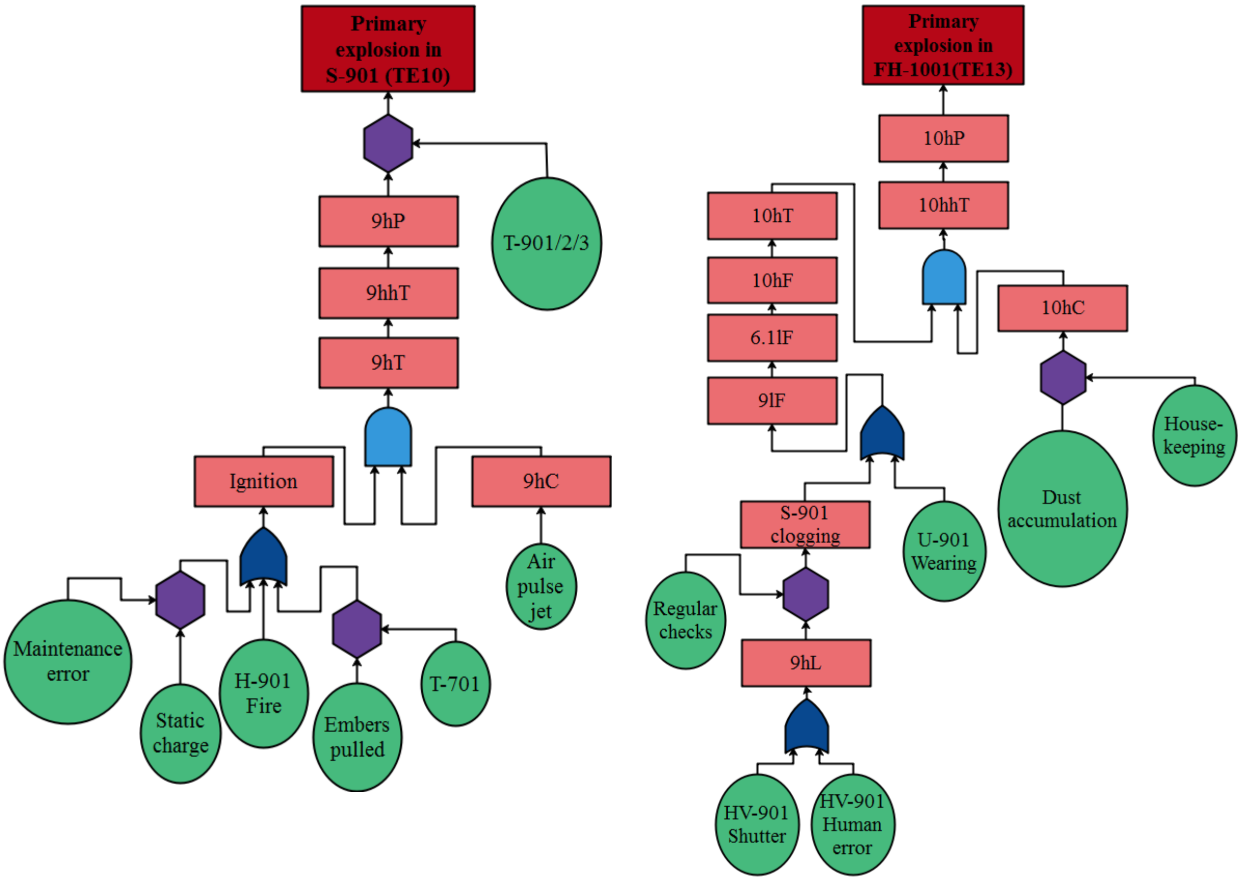

Figure 6 *FTs for a primary explosion in S-901 (left) and in the fume hood FH-1001 (right)*

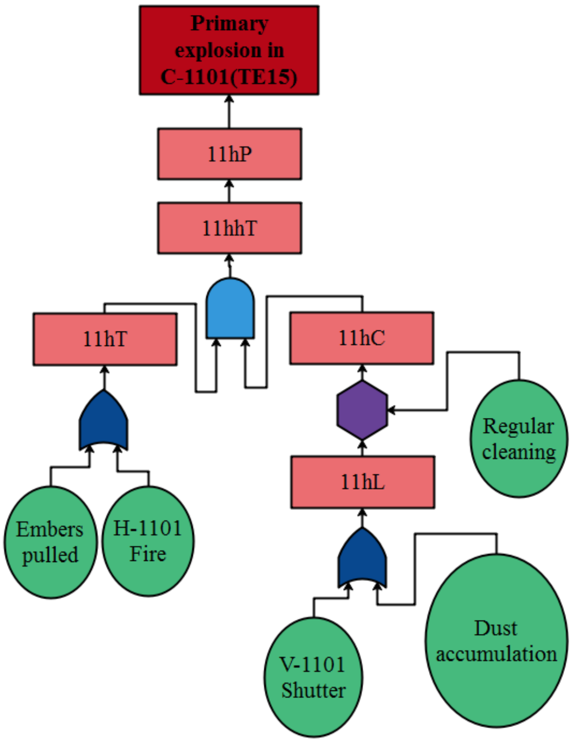

Figure 7 *FTs for a primary explosion in multi cyclone C-1101*

Finally, Fig.8 reports the structure of the Fault Tree describing the occurrence of secondary explosions. All high concentration deviations were reported as transfer gates to simplify the structure.

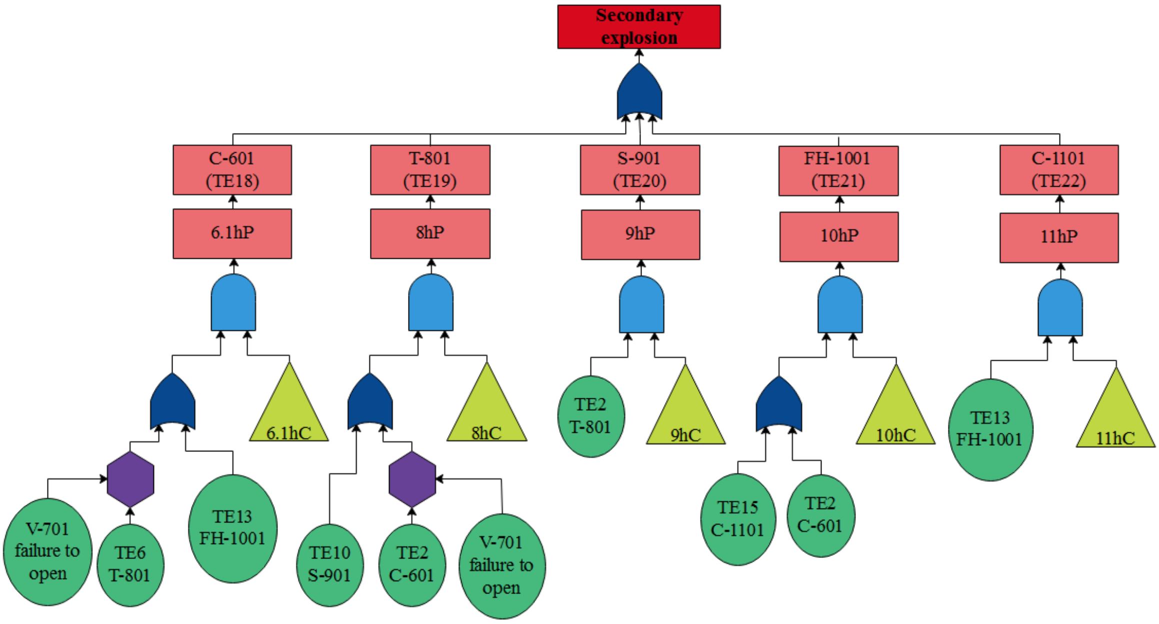

Figure 8 *FTs for the occurrence of a secondary dust explosion*

Now it is possible to numerically solve the FTs, identifying the probability of occurrence of such events and the most critical components. However, other additional events require an estimation of their probability of occurrence: human errors and some particular event. Human errors foreseen in the process are quite simple, so detailed modelling is not necessary. It will be used a database to represent the human errors that most likely describe the actions involved in the dedicated actions. The values used are listed in Table 10.

Table 10 *Probabilities of human errors involved (Bello and Colombari, 1980)*

Event	**Error type**	**Probability [-]**
HV-601 opened	Error in manual operation	$5\cdot10^{-3}$
HV-901 opened	Error in manual operation	$5\cdot10^{-3}$
Regular cleaning not performed	Omission of regular procedure	$2\cdot10^{-3}$
Error during grounding maintenance	Error in manual operation	$5\cdot10^{-3}$
Housekeeping not performed	Omission of regular procedure	$2\cdot10^{-3}$
Checks on bags not performed	Omission of regular procedure	$2\cdot10^{-3}$

But other particular events still require specific attention. Dust accumulation is associated to a probability equal to 1 over the year, due to the high amount of dust generated according to CSB information about the plant. This event is regulated by the presence of regular housekeeping, which acts as protection. The air pulse jet is extremely frequent (every 90 s), so the explosive concentration of dust inside the baghouse is kind of regular over time. The probability of embers getting pulled from spark box or cyclone is hard to be estimated, due to lack of essential information. However, since CSB stated that this is a potential source of ignition, it was assumed that such an event can occur at a rate of 1 event per year. The same assumption was considered for the occurrence of an impact spark in T-801 from D-501. For what concerns the possibility of a fire from dust and debris dumps, even in this case the evaluation is problematic. In a former work dedicated to the estimation of this event for the Zhong Rong accident (Barozzi et al., 2020b), it was estimated that such an event had a very low probability of occurrence ($< 10^{-8}$ over a mission time of 1 year) according to the information available about the company. Detailed information on how barrels substitution and inspection were performed at the Hayes Lemmerz are not known, but it makes sense to assume that the operation was handled in a very similar way compared to Zhong Rong Metal Products Co. So, it will be considered a similar probability. Finally, a static charge may effectively build up in the baghouse: aluminium indeed tends to dissipate the charge quickly but considering the variegated size distribution of material and the lack of attention towards correct handling of such devices, along with the low MIE of such dust, it will be considered as certain that at least one spark that can trigger a dust explosion can develop over a year. However, this ignition source is kept under control via a proper grounding, which is assumed to be associated with regular maintenance. Finally, failure of protective systems (spark box and venting panels), should be reasonably low. It was assumed for them a failure rate of $1\cdot10^{-7}$, compatible with a failure of an automatic protective device (Lees, 2005). Table 11 resumes the value used for the estimation.

Table 11: *Probabilities of basic events over 1 year of mission time*

Event	**Probability [-]**	**Event**	**Probability [-]**
Dust accumulation	1	H-901 fire	1E-8
Air pulse jet	1	H-1101 fire	1E-8
Embers pulled	0.63	Static charge in S-901	1
Impact spark	0.63	T-701 failure	$8.756\cdot10^{-3}$
H-801 fire	1E-8	T-901/2/3	$8.756\cdot10^{-3}$

Now it is possible to retrieve the probabilities of occurrence of the involved explosions. Table 12 summarizes the results. For all the equipment involved, the number of MCS is between 3 and 8, with orders of MCS about 3 and 4, highlighting a decent number of safety levels. Probabilities of primary explosions range between $1\cdot10^{-3}$ and $5\cdot10^{-6}$, with the dust collector being the safest device, and the multi cyclone and dropbox the devices most exposed to primary events. However, it is important to notice that such values have been found according to regular housekeeping and duct cleaning.

Table 12 *FTA for primary explosions*

Primary explosion	# mcs	max order mcs	Highest importance	Probability [-]
C-601	5	3	Embers pulled	$3.807 \cdot 10^{-4}$
T-801	8	4	Dust accumulation	$1.26 \cdot 10^{-3}$
S-901	3	4	Embers pulled	$4.86 \cdot 10^{-6}$
FH-1001	3	4	U-901 and dust accumulation	$4.495 \cdot 10^{-5}$
C-1101	4	3	Embers pulled and dust accumulation	$1.26 \cdot 10^{-3}$

By joining these events, the probability of having at least a single explosion over a year is equal to $2.943 \cdot 10^{-3}$, which already highlights some issues for a plant treating with extremely hazardous materials such as aluminium dust. This value is very close to the result provided by the analysis carried out by Yuan et al. (2015). They estimated the probability of occurrence of a dust explosion with no safety measures installed of $6.81 \cdot 10^{-3}$. This aspect is extremely related to the almost complete shortcoming of automatic protective devices. Also, variables are not monitored along the different devices, which would greatly help for better process handling.

For what concern the secondary explosions, the FT represented in Fig. 8 was resolved, leading to a probability of $1.2865 \cdot 10^{-3}$. This value is of the same order of magnitude of having at least an isolated explosion. This means that, despite foreseeing housekeeping, secondary explosions are very likely to occur in the plant. This aspect is severely related to the amount of non-isolated connections among the devices. Isolation valves and flame arrestors should be placed among the most critical components, to dampen the effect of secondary explosions. This aspect was also remarked in the work from Yuan et al. (2015), where it was shown that the most important aspect to improve the safety of the plant was the lack of isolation devices (referred to as X28).

It was also performed an additional FT analysis with assumptions that would be more related to the actual Hayes Lemmerz working conditions. At first, the absence of the isolation valve V-701 was studied, since operators would shut it down (CSB, 2004). Since it affects secondary explosions only, FT in Fig. 8 was resolved by removing the presence of the safety barrier represented by this valve. The final probability estimated is $1.3895 \cdot 10^{-3}$, differing by less than 10% than when it is active. This is due to a couple of factors: at first, the most important event in the triggering of secondary explosions is the drop box, which explosion automatically propagates to the baghouse, that always has amounts of dust to reach the MEC. In additions, multiple connections among the devices makes a single isolating valve of minor importance since a primary explosion can basically propagate to any other device. This aspect, though, highlights how safety devices should be installed correctly and according to the system structure. Finally, the probabilities of the primary explosions have been evaluated by omitting the presence of dust cleaning in the plant, which was more likely to the real process handling. Table 13 lists the values obtained. It is extremely interesting to show how the presence of dust cleaning procedures positively impacts process safety, lowering between 2 and 3 orders of magnitude the probabilities involved.

Table 13 *Comparison among probabilities considering lack of housekeeping*

Primary explosion	Probability without housekeeping and cleaning	Probability	Ratio
C-601	$1.904 \cdot 10^{-1}$	$3.807 \cdot 10^{-4}$	$5 \cdot 10^{2}$
T-801	$6.302 \cdot 10^{-1}$	$1.26 \cdot 10^{-3}$	$5 \cdot 10^{2}$
S-901	$4.86 \cdot 10^{-6}$	$4.86 \cdot 10^{-6}$	1
FH-1001	$2.247 \cdot 10^{-2}$	$4.495 \cdot 10^{-5}$	$4.5 \cdot 10^{2}$
C-1101	$6.30 \cdot 10^{-1}$	$1.26 \cdot 10^{-3}$	$5 \cdot 10^{2}$

Table 13 definitely shows the impact of abatement devices, as remarked in the literature (Danzi and Marmo, 2019). The fume hood is the only process element that is not dedicated to aluminium dust cleaning. S-901 does not depend upon housekeeping, since it is located completely outside the plant. Also, it appears that S-901 is the safest device. This is due to the contribution of multiple factors related to the foreseen ignition sources: since static charge has a negligible impact according to CSB, pulled embers and sparks from D-501 are likely explosion-triggering events. Between these, sparks from D-501 should have a relatively large size, so it was supposed that they are completely contained from the drop box. This is way T-801 shows a way greater probability compared to the bag filter. From the comparison of the probabilities with and without housekeeping, it should be extremely evident how relatively simple procedures can reduce casualties and accidents.

4. Conclusions

A Quantitative Risk Assessment was carried out for the old Hayes Lemmerz company, where aluminium scraps were recycled through remelted. The Recursive Operability Analysis proved as a versatile tool that can be used to carry out an assessment on processes handling dust explosions, although it required some modification and assumptions to be adapted for a system involving secondary explosions. The coupling with FMEA makes an even more useful tool, which can help in identifying the most likely accident scenarios. Due to the lack of information, it was necessary to make some assumptions, especially for what concerned the probabilities associated with the ignition sources. Scenarios identified are similar and definitely comparable to those found by the CSB (CSB, 2004), and probabilities of most significant top events (primary and secondary dust explosions), were estimated and studied. From results, shutting down the isolation valve surprisingly affects very mildly process safety, leading to almost the same probability of occurrence for secondary explosions. This aspect is related to the fact that a single isolating device is not suited for a system where 5 potential explosion sources are connected. From this, it is reasonable to assume that the choice of operators to shut down this valve, did not impact in a remarkable way their safety. By the other hand, completely different conclusions for dust cleaning procedures are drawn. On this plant, where automatic protective systems are almost absent, a correct housekeeping can reduce the risk associated with an explosion up to 500 times.

References

Abbasi, T., Abbasi, S.A., (2007). Dust explosions e cases, causes, consequences, and control. *Journal of Hazardous Materials* 140:7-44.

Amyotte, P. (2013). *An Introduction to Dust Explosions e Understanding the Myths and Realities of Dust Explosions for a Safer Workplace*. Butterworth-Heinemann, Oxford.

Barozzi, M., Copelli, S., Scotton, M.S., Torretta, V. (2020a). Application of an enhanced version of recursive operability analysis for combustible dusts risk assessment. *International Journal of Environmental Research and Public Health* 17.

Barozzi M., Scotton M. S., Derudi M., Copelli S. (2020b). Recursive Operability Analysis as A Tool for Risk Assessment in Plants Managing Metal Dusts, *Chemical Engineering Transactions*, 82: 43–48.

Barozzi, M., Contini, S., Raboni, M., Torretta, V., Casson Moreno, V., Copelli, S. (2021). Integration of Recursive Operability Analysis, FMECA and FTA for the Quantitative Risk Assessment in biogas plants: Role of procedural errors and components failures, *Journal of Loss Prevention in the Process Industries*, 71: 104468.

Bello, G.C., Colombari, V. (1980). The human factors in risk analyses of process plants: the control room operator model ‘TESEO. *Reliability Engineering* 1:3–14

Chemical Safety Board (2004). *Investigation Report: Aluminum Dust Explosion*, Report NO. 2004-01-I-IN, available at https://www.csb.gov/hayes-lemmerz-dust-explosions-and-fire/ (last accessed, 14/03/2022).

Cloney, C. (2021). *2021 Mid-Year Combustible Dust Incident Report - Version #1*. DustEx Research Ltd. Retrieved from http://dustsafetyscience.com/2020-Report.

Crowl, D. A., Louvar, J. F. (2002). *Chemical process safety: fundamentals with applications*. Prentice-hall International Series in the Physical and Chemical Engineering Sciences, second ed. Prentice Hall PTR, Upper Saddle River, N.J.

Danzi, E., Marmo, L. (2019). Dust explosion risk in metal workings. *Journal of Loss Prevention in the Process Industries*, 61: 195-205.

Demichela, M., Marmo L., Piccinini, N. (2002). Recursive operability analysis of a complex plant with multiple protection devices, *Reliability Engineering & System Safety*, 77(3): 301-308

Eckhoff, R.K. (2003). *Dust Explosions in the Process Industries*. Elsevier B.V.: Amsterdam, NL.

Hong-Chun, W., Hsin-Jung, O., Hsiao-Chi, H., Tung-Sheng, S. (2010). Explosion Characteristics of Aluminum Nanopowders, *Aerosol and Air Quality Research*, 10: 38–42.

Lees, F. (2005). *Lees' Loss Prevention in the Process Industries: Hazard Identification, Assessment and Control*. Elsevier.

Li, G., Yang, H.-X., Yuan, C. M., Eckhoff, R. K., (2016) A catastrophic aluminium-alloy dust explosion in China. *Journal of Loss Prevention in the Process Industries* 39: 121–130.

Marmo, L, Crivelletto, V., Starace, A. (2009) Recursive Operability Analysis as a decision support tool for Risk-Based Maintenance. *Journal of Loss Prevention in the Process Industries*, 22(5): 557-565

Piccinini, N., Ciarambino, I. (1997). Operability analysis devoted to the development of logic trees. *Reliability Engineering & System Safety*, 55:227–241.

Smith, D.J., 2017. *Reliability, Maintainability and Risk: Practical Methods for Engineers*. Butterworth-Heinemann.

Taveau, J., Hochgreb, S., Lemkowitz, S., & Roekaerts, D. (2018). Explosion hazards of aluminum finishing operations. *Journal of Loss Prevention in the Process Industries*, 51, 84–93.

Yuan, Z., Khakzad, N., Khan, F., & Amyotte, P. (2015). Risk-based optimal safety measure allocation for dust explosions. *Safety Science*, 74, 79–92.

DOI: 10.7795/810.20221124

The maximum rate of pressure rise of hybrid mixtures

Stefan H. Spitzer [a,b], Enis Askar [b], Kristin J. Hecht[b,c], Paul Geoerg [c], Dieter Gabel [c], Ulrich Krause [c], Olivier Dufaud[d] & Arne Krietsch [b]

[a] Physikalisch Technische Bundesanstalt, Braunschweig, Germany

[b] Bundesanstalt für Materialforschung und -prüfung, Berlin, Germany

[c] Otto-von-Guericke University, Magdeburg, Germany

[d]Université de Lorraine, Nancy, France

E-mail: stefan.spitzer@ptb.de, stefan.spitzer@bam.de

Abstract

The maximum rate of pressure rise $(dp/dt)_{max}$ and the corresponding K-value of hybrid mixtures containing flammable gases and dusts are important for constructive explosion protection measures. Since the safety characteristics of dusts and gases are determined under different conditions, there has been a lot of confusion about the influence of flammable gas on the (dp/dt) of dusts and vice versa. While some investigations showed comparably higher values for hybrid mixtures, others stated that the highest value for the gas component alone is the worst case.

The first part of this paper focuses on the confusion around the different statements about $(dp/dt)_{max}$ of hybrid mixtures and where they come from. In the second part of this paper experimental results are presented that elaborate how to clarify the different findings of past research and show what to expect as a real worst-case-value for hybrid mixtures.

Keywords: *Hybrid mixtures, 20L-sphere, turbulent combustion, maximum rate of pressure rise*

DOI: 10.7795/810.20221124

1. Introduction

When combustible substances are handled, produced or transported in a plant or process, safety precautions are essential to prevent unintended ignition. For this reason, safety characteristics such as the minimum explosible concentration (MEC, ASTM E1515), the maximum explosion pressure p_{max} or the maximum rate of pressure rise $(dp/dt)_{max}$ are determined. For this purpose, tests are carried out over a wide concentration range and, at the point where the highest values are obtained, repeated twice and averaged (ASTM E1226a, EN 14034 – 1, EN 14034 – 2). The highest values of a single test are called p_{ex} and $(dp/dt)_{ex}$ (Fig. 1).

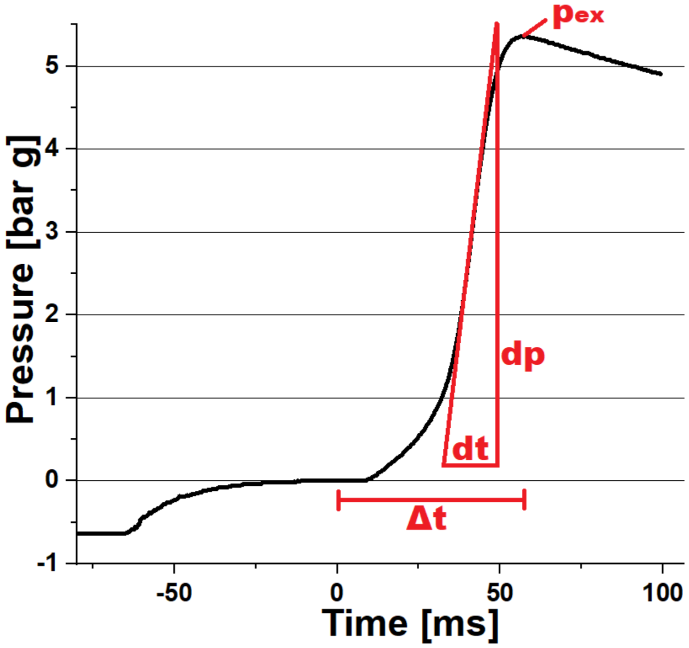

Fig. 1: *Pressure vs. time curve of an explosion with the highest explosion pressure (p_{ex}), the time until this pressure occurs after activation of the ignition source (Δt) and the highest (dp/dt) outlined*

However, this procedure is just valid for dusts. For gases and in the European dust standard the MEC is called lower explosible limit (LEL, EN 1839, EN 14034-3). The other two safety characteristics are also called p_{max} and $(dp/dt)_{max}$, but they are the highest measured value at the concentration with the highest values, not an average and are repeated five times (EN 15967). So the confusion about the safety characteristics of hybrid mixtures actually starts with the definitions, even before testing.

Even though first observations on hybrid mixture explosions were made almost two centuries ago (Faraday and Lyell (1844)), structured research on safety characteristics of hybrid mixtures containing flammable gas and dust is still scarce, reliable data even more. Especially when it comes to an often-used safety characteristic, the rate of pressure rise (dp/dt) or rather the volume-normalised K-value, statements in the rare literature are more confusing than clarifying, some are even conflicting:

- Khalil (2013) investigated the safety characteristics of activated carbon and hydrogen. He stated that the $(dp/dt)_{max}$ of the hybrid mixture is **more than twice** the $(dp/dt)_{max}$ of hydrogen alone
- Wang et al. (2020) investigated the safety characteristics of coal dust and methane. They found that the $(dp/dt)_{max}$ of the hybrid mixture is **always lower** than that of the gas alone

Other statements were made about the (dp/dt) of hybrid mixtures (Table 1) but the conclusions vary and leave the reader or the person responsible for the safety measures for a process plant or a facility behind with no clear suggestion about the behaviour of hybrid mixtures. This problem is especially intensified since there are no standard testing methods[1] and hardly any testing laboratories for determining the $(dp/dt)_{max}$ of a hybrid mixture.

Table 1: *Selected conclusions about the rate of pressure rise of hybrid mixtures*

Statement	**Dust/Gas/Vapour**	**Reference**
The $(dp/dt)_{max}$ of the hybrid mixture is 2.3 times greater than of the hydrogen-air mixture alone and 10.4 times greater than of activated carbon alone*	Activated Carbon / Hydrogen	Khalil (2013)
The $(dp/dt)_{max}$ of hybrid mixtures is usually as high as of the stoichiometric gas mixture under turbulence. It might be 15 % higher*,**	Many tested	Bartknecht (1985)
The $(dp/dt)_{max}$ of methane/coal dust mixtures at any methane concentration are higher than those of pure coal dust but lower than those of pure methane*	Methane / Coal dust	Wang et. al. (2020)
The optimum (e.g. worst-case-value) of the pure compounds for (dp/dt) is approximately 800 bar/s for 750 g/m³ of niacin, 1300 bar/s for 2.5% of diisopropyl ether and 1600 bar/s for certain hybrid mixtures (e.g. 23 % higher)*	Niacin / Diisopropyl ether	Dufaud (2008)

*all statements are shortened by the corr. author, the values and core findings were not changed
**translation by the corr. author

Taking a closer look at the literature, some factors that might lead to the contradicting conclusions were identified.

Different systems and different test methods

First of all, different components might lead to different conclusions and most of the authors stated, that their observations are not necessarily universal for other combinations of dusts and gases. Indeed, both the chemical reactivity of the fuels and the physico-chemical properties of the powders (e. g. refractive index, density, melting point) can strongly modify the explosion severity of such mixtures. There are also several other experimental parameters such as the ignition source, ignition energy and ignition delay time to name just a few, that affect the results. Considering some experimental parameters, the standard methods for determining safety characteristics of combustible dusts differ significantly from the standard methods for determining safety characteristics of flammable gases.

Usually, hybrid mixture explosion testing laboratories are either specialised dust explosion laboratories, that apply the standard methods for combustible dusts adding some gas to the experiments or gas explosion laboratories that apply the standard methods for flammable gases adding some dust. Because of the more complicated installation for the dispersion of the dust component and the wide range of industrial applications implying powders mixed with traces (or small amount) of gases, the first named variant is common.

Turbulence while igniting

The dispersion process of dusts is realized by means of turbulence, otherwise the dust would just lay on the bottom of the explosion vessel. Turbulence leads to an increase of the rate of pressure rise of flammable gases compared to quiescent mixtures which has long been known (Harris (1967)) but might have been overseen by some of the researchers. A good way to come around this difficulty is to first compare the safety characteristics of the gas component from quiescence to turbulence, by applying the same standard procedure adopted for dusts to gases (same ignition delay time, energy, ignition source) (Chatrathi (1994), Dufaud et. al. (2009)). Wang et. al. (2020), Ji et. al. (2022) and Bartknecht (1985) also referred to the (dp/dt) of gases under turbulence when comparing it to the

---

[1] ISO 6184-3 is officially under revision since 2005 and with 4 pages too short to be applicable

hybrid mixtures, but still have differing statements on the $(dp/dt)_{max}$. While Wang et. al. (2020) and Ji et. al. (2022) state this value for hybrids is lower, Bartknecht (1985) states it is the same or higher.

A similar finding to the one from Bartknecht (1985) can be seen in a research paper by Sanchirico et. al. (2011), where a stoichiometric mixture of acetone mixed with a low concentration of nicotinic acid of 30 g/m³ (optimum of niacin for $(dp/dt)_{max}$ is around 500 g/m³) showed a higher dp/dt than the acetone alone. Unfortunately, this is just shown in the figures and not pointed out clearly or discussed.

Kosinski et. al. (2013) found the same behaviour with propane and carbon black. Around the stoichiometric values of the gas component, a very low amount of dust raised the dp/dt value by about 15 %.

Chatrathi (1994) also observed for hybrid mixtures of propane and corn starch, that the highest value for (dp/dt) was obtained slightly above the stoichiometric value (5 Mol-% instead of 4.2 Mol-%) being about 10 % (at one single test even 26 %) higher, than the propane tested alone at 5 Mol-% under turbulent conditions.

Influence of the step-size

For the determination of safety characteristics of dusts, it is common to start with a concentration of 250 g/m³. If the highest value of (dp/dt) occurs at higher concentrations, the amount is increased in steps of 250 g/m³ (500 g/m³, 750 g/m³, 1000 g/m³, …), if it occurs at lower concentrations the steps are bisections e.g. 125 g/m³, 60 g/m³, 30 g/m³…(EN 14034-series, ASTM 1226a)[2]. Typically for combustible dusts, the increase of the explosion pressure and (dp/dt) is steep with increasing dust concentrations but after the maximum is reached the decrease is flat. An upper explosion limit is seldomly determined for combustible dusts because usually it is not of use for safety measures related to combustible dusts.

For gases the starting point and the step-size for determining $(dp/dt)_{max}$ is neither defined explicitly in given concentrations nor is it universal for all types of gases. For example, the upper explosion limit for butane is 9.4 Mol-% while the lower explosion limit of carbon monoxide is 10.9 Mol-%. A static starting point might be above or under the explosible region and with that of no use. If the gas component is known, the tests for determining $(dp/dt)_{max}$ start at the stoichiometric point, if the gas is unknown the tests start at a point chosen by experience, estimation or twice the lower explosion limit. The concentration is decreased and increased by factors of 0.8 or respectively 1.2. The step-sizes are further narrowed by steps of min. 0.2 Mol-% (EN 15967).

Because there is no standardized step-size for determining $(dp/dt)_{max}$ of hybrid mixtures, the intuitively chosen step-size by the researchers might be too coarse to find the maximum value in the explosion region. Banhegyi and Egyedi (1983) chose a very fine step-size for the dust and the gas on the lower end and a large one with higher concentrations, presenting their data in a logarithmic scale for the dust component. This unusual choice for the step-size and the presentation of the data showed an optimum in the explosion region around the stoichiometry of the gas component and very low dust concentrations (Fig. 2).

Unfortunately, for the explosion intensity Banhegyi and Egvedi (1983) defined an own unit and called it "k_{ex}", not to be confused with the K-value. This k_{ex}-value is the square-root of the (dp/dt) multiplied with the highest occurring pressure for the chosen concentration (p_{ex}) divided by the time from ignition to the highest pressure (Δt), so a comparison to new data is difficult.

---

[2] In both the steps from 125 g/m³ to 60 g/m³ are incorrectly described as "halved", presumably because of an unnecessary complicated division to 62,5 g/m³ and the following 31,25 g/m³

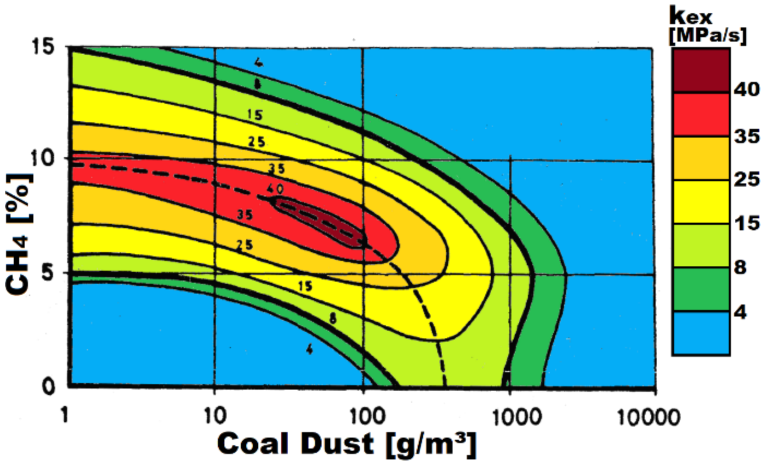

Fig. 2: *Explosion intensity of hybrid methane-coal-dust mixtures, taken from Banhegyi and Egyedi (1983), p. 11, colors and legend added by the author*

2. Experiments

Ignition tests involving three combustible dusts (corn starch, niacin and lycopodium) and one inert dust (quartz sand) were carried out in the 20L-sphere based on the procedures of the EN 14034-series. However, two 1 kJ chemical igniters (Fa. Sobbe) were used as ignition source throughout all test series instead of two 5kJ igniters. This lowers both, the chance of overdriving the system and the scattering of the data. At the concentrations with the highest values for (dp/dt) and around these concentrations the tests were repeated twice. The pre-ignition pressure rise was kept constant at 0.64 bar ± 0.02 bar according to Spitzer et. al. (2022a) in all the tests. The gas was filled into the explosion chamber of the 20L-sphere before injecting the air-dust mixture (Fig. 3).

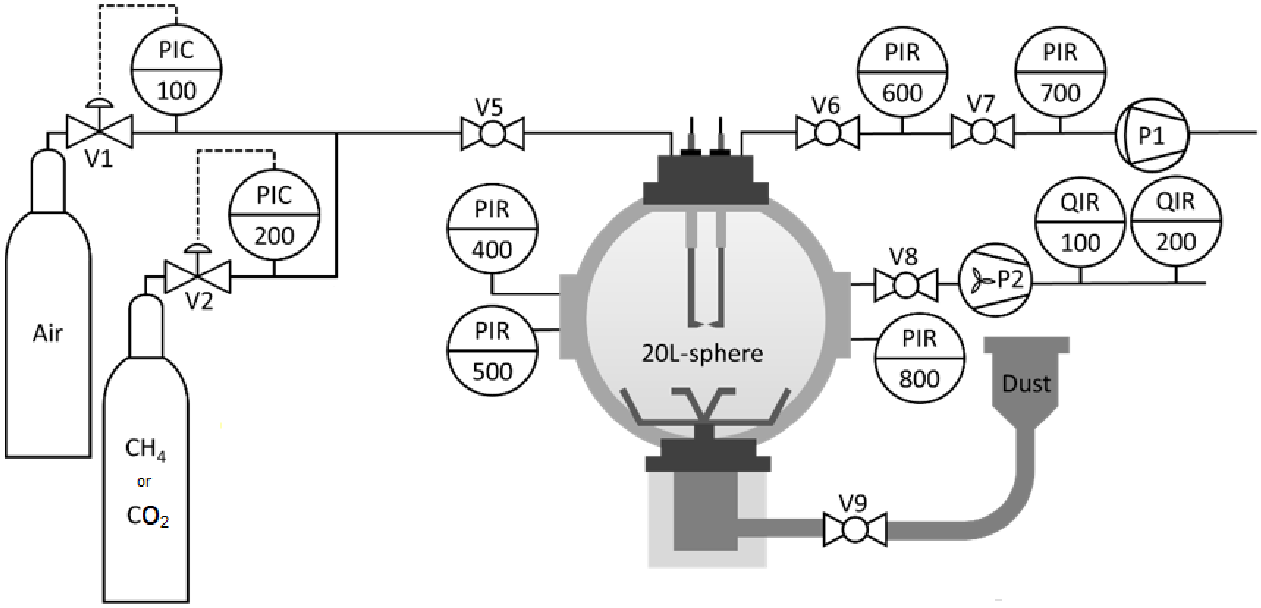

Fig. 3: *Schematic of the standard 20L-sphere with adaptations for hybrid mixture testing,gas amount inside the 20L sphere*

To determine the accuracy of the gas concentrations, pre-tests were performed on every testing day and/or when the concentration was changed within the day. The pre-tests were tests with a gas component in the 20L-sphere but no dust and no ignition source (Spitzer et. al. (2022b)). After the injection the valve V8 in Fig. 3 was opened and the gas was pumped through QIR100 for measuring the amount of the gas component and QIR200 for measuring the amount of oxygen. By this means an overall absolute uncertainty of maximum ± 0.2 Vol-% was determined. The presented values for

p_{max} in Fig. 4 and Fig. 6 were corrected with the following equations (1, 2) derived from the standard for dusts, EN 14034-1 and ASTM 1226a, simplified for a constant ignition energy of 2 kJ:

If the measured overpressure was below 5.5 bar g:

$$\mathrm{p}_{max} = \frac{5.5 \cdot \mathrm{p}_{max,20L} - 0.32}{5.18} \; [bar\ g] \qquad [1]$$

If the measured overpressure was above 5.5 bar g:

$$\mathrm{p}_{max} = 0.775 \cdot \mathrm{p}_{max,20L}{}^{1.15} \; [bar\ g] \qquad [2]$$

This correction is not done when testing safety characteristics of flammable gases and is one source of confusion when comparing data from different sources.

The K_H-values (H for hybrid), the volume-normalized rates of pressure rise, are calculated with the following equation (3) according to EN 14034-2:

$$\mathrm{K}_H = (0.02\, m^3)^{1/3} \cdot \left({}^{dp}\!/_{dt}\right)_{20L} \left[bar \cdot {}^{m}\!/_{s}\right] \qquad [3]$$

Niacin and lycopodium dusts were tested at the following concentrations: 0 g/m³, 20 g/m³, 60 g/m³, 125 g/m³, 250 g/m³, 500 g/m³, 1000 g/m³, 1500 g/m³ and 2000 g/m³, each with 0 Vol-%, 3 Vol-% and 9 Vol-% methane. The same original sample weights of corn starch were tested but with methane concentrations from 0 Vol-% to Vol-10% in steps of one percent and an additional 9.5 Vol-%, 12 Vol-% and 15 Vol-%.

The quartz sand was only tested at lower concentrations of 0 g/m³, 20 g/m³, 40 g/m³, 60 g/m³ and 125 g/m³, each with 7 Vol-%, 8 Vol-%, 9 Vol-%, 9.5 Vol-%, 10 Vol-% and 11 Vol-% methane.

3. Results and discussion

The particle size distributions for all four dusts were tested optically (MALVERN Mastersizer 2000). The 10th percentile (d(0.1)), the median value (d(0.5) and the 90th percentile (d(0.9)) related to the particle size respectively as well as the highest values for p_{max} and $(dp/dt)_{max}$ respectively the K_H-value for all substances and combinations are listed in Table 2.

Table 2: *Tested single materials and hybrid mixtures and their maximum values*

Hybrid mixture	**Particle Size distribution [µm]**			**p_{max} [bar g]**	**$(dp/dt)_{max}$ [bar/s]**	**K_H-value [bar*m/s]**
	d (0.1)	**d (0.5)**	**d (0.9)**			
Corn Starch	9	13	21	9.2	629	171
Corn Starch - Methane				9.2	1556	422
Niacin	4	17	54	8.5	865	235
Niacin - Methane				8.5	1515	411
Lycopodium	23	32	43	7.8	606	164
Lycopodium - Methane				7.9	1506	409
Methane	-	-	-	7.9	1471	399
Quartz sand	117	198	306	-	-	-
Quartz sand - Methane				7.9	1518	412

Values in grey indicate, that the value is from a single substance. It lies on the X- or Y-Axis in the hybrid field of Fig. 4 and Fig. 6 and no additional effect could be observed

DOI: 10.7795/810.20221124

The results for the hybrid maximum explosion overpressure values were as expected: Since the p_{max} for corn starch and niacin are higher than the p_{max} for methane, the value for the hybrid mixtures is the same as for the dust component alone and occurred when no gas was added to the system (Fig. 4).

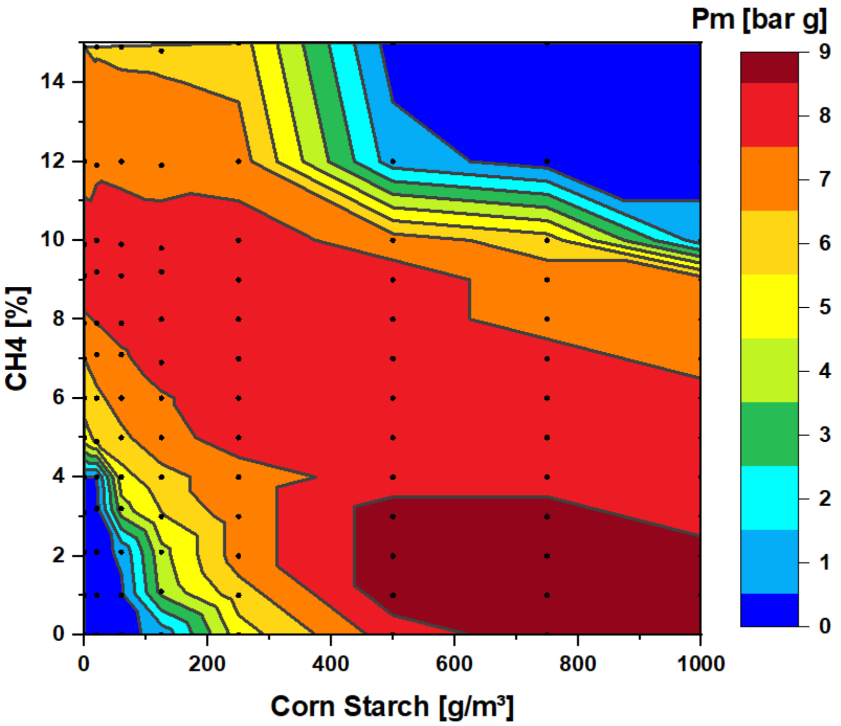

Fig. 4: *Explosion overpressure for hybrid mixtures of methane and corn starch, black dots indicate the measuring points or their average*

For lycopodium the pressure was almost constant over a straight line between the stoichiometric mixture of air and methane and the point with the highest explosion pressures of lycopodium alone (Fig. 5).

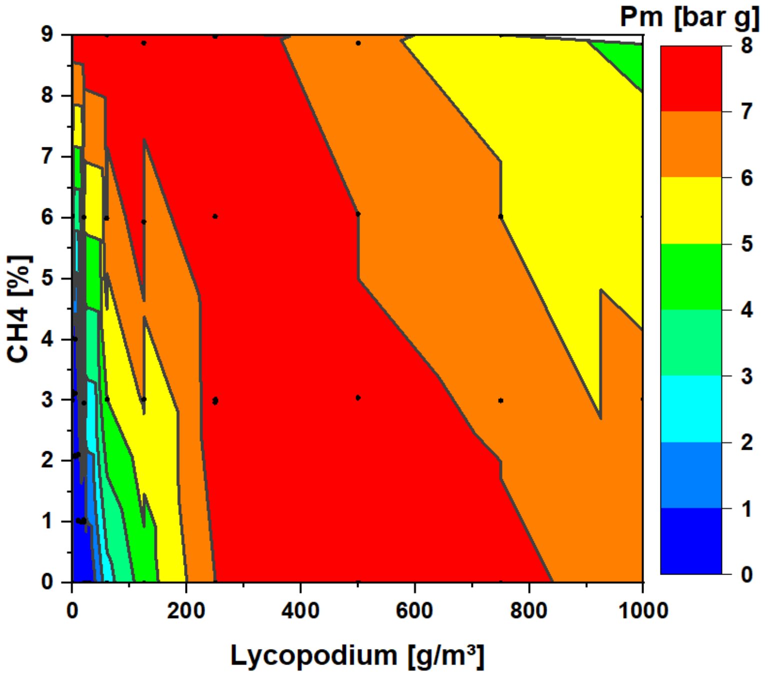

Fig. 5: *Explosion overpressure for hybrid mixtures of methane and Lycopodium, black dots indicate the measuring points or their average*

For the non-combustible quartz sand, the highest value was the same as the value for methane alone which is consistent from a thermodynamical point of view as the chemical contribution of sand to the combustion process is zero (Fig. 6).

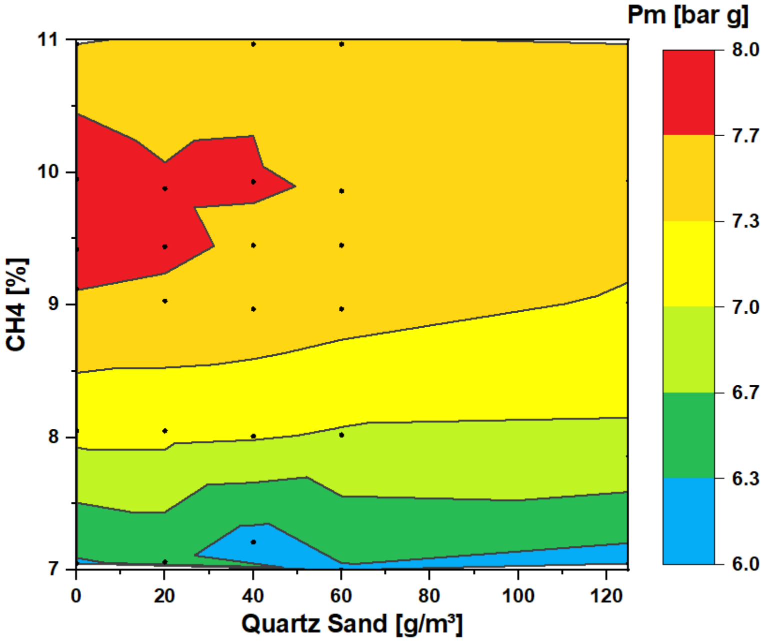

Fig. 6: *Explosion overpressure for methane and quartz sand, black dots indicate the measuring points or their average*

The values for $(dp/dt)_{max}$ were nearly double the values of the hybrid mixtures compared to the combustible dusts alone. The values for $(dp/dt)_{max}$ of the hybrid mixtures were all even slightly higher than the $(dp/dt)_{max}$-value of turbulent methane alone, though the effect is with three to twelve percent relatively small. It seems not to matter, which one of the four dusts is added, The methane concentration with the highest dp/dt-value was always found at 9 Vol-% to 10 Vol-% of methane (stoichiometric) and at 0.4 g to 2.5 g of combustible dust in the 20L-sphere (20 g/m³ to 125 g/m³) (Fig. 7 to Fig. 9). It shall be mentioned, that especially for Fig. 7 and Fig. 8 the colouring of the scale had to be adjusted, otherwise the difference would have been too small to see.

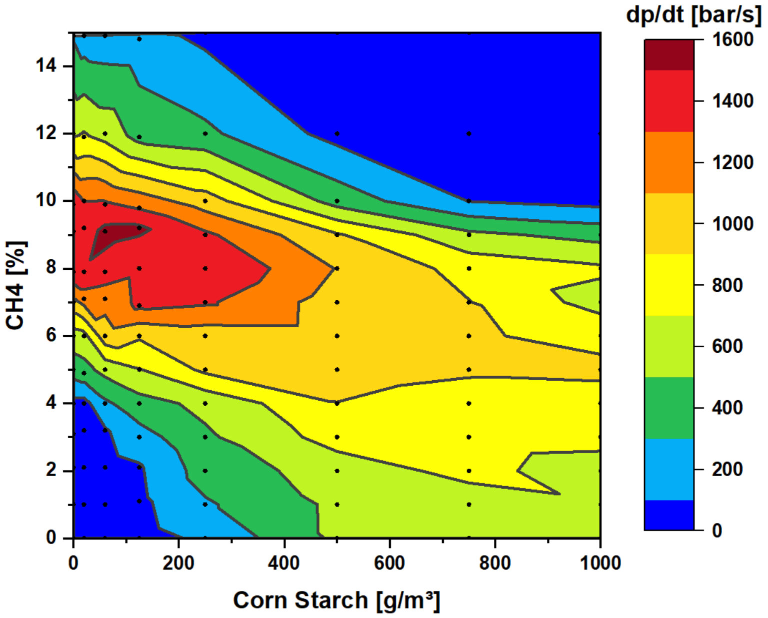

Fig. 7: *(dp/dt) for methane and corn starch, black dots indicate the measuring points or their average*

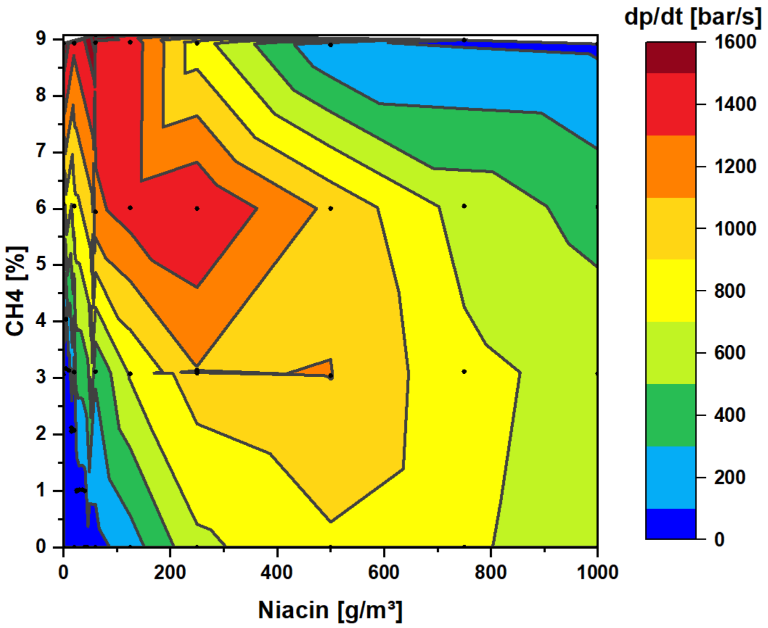

Fig. 8: *(dp/dt) for methane and niacin, black dots indicate the measuring points or their average*

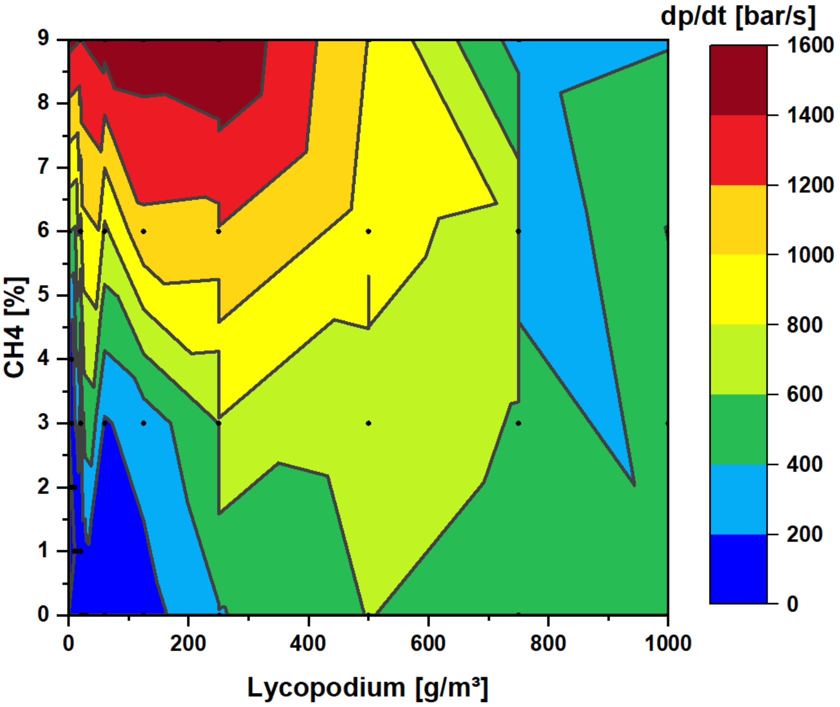

Fig. 9: *(dp/dt) for methane and lycopodium, black dots indicate the measuring points or their average*

It should be mentioned that all values were obtained having the same level of turbulence (or rather the same injection process with the same ignition delay time) and that especially the values of methane alone cannot be compared to literature values that are usually obtained under quiescent conditions. This is especially highlighted because the $(dp/dt)_{max}$ of methane under quiescent conditions is with 240 bar/s for 9 Vol-% or 277 bar/s for 10 Vol-% smaller by a factor of about six. While the literature values for the explosion overpressure of methane seem to be higher with 8.3 bar at first glance, this mainly is caused by the fact that the explosion pressures for gases are stated as absolute pressures and not as relative pressures as for dusts. So, the literature value is actually lower with 7.3 bar g compared to the value obtained in this work with 7.9 bar g (CHEMSAFE (2022)).

The maximum rate of pressure rise (dp/dt) occurs near the stoichioimetric concentration of methane (~9 Vol.-%). The addition of dust increases the rate of pressure rise slightly with low dust concentrations. This effect is apparent for all of the dusts, even the inert quartz sand (Fig. 10). This proves that it is not necessarily the combustion behaviour of the dust that enhances the combustion rate. It can be clearly seen that the highest value of (dp/dt) is as well at the stoichiometric concentration of the gas and the smallest tested concentration of dust.

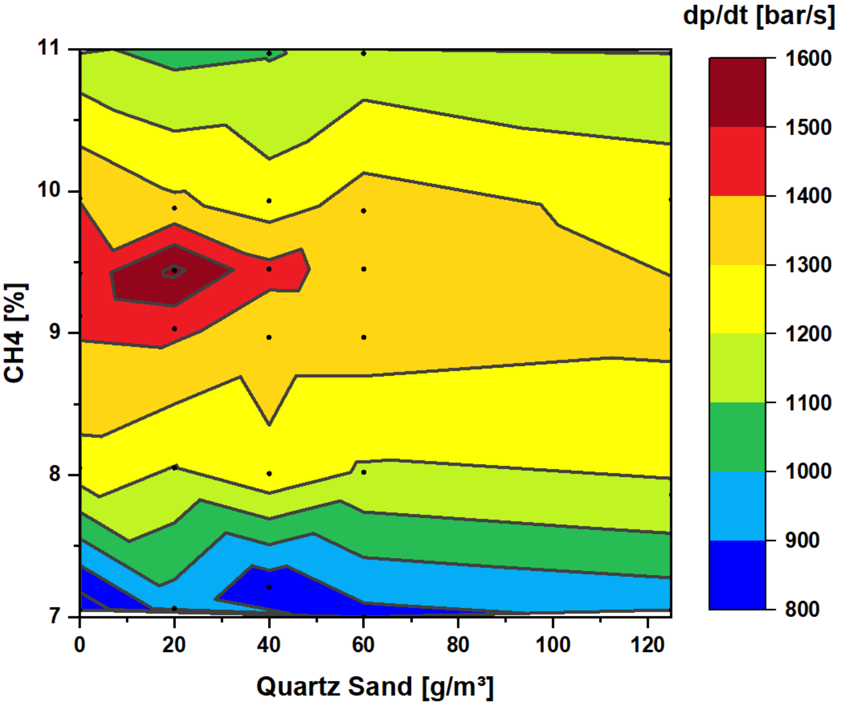

Fig. 10: *(dp/dt) for methane with quartz sand as inert dust, black dots indicate the measuring points or their average*

The observation, that even inert dust leads to a higher rate of explosion pressure rise at very little amounts was also mentioned in Banhegyi and Egyedi (1983) who concluded this is caused by the higher turbulence. Though, it cannot be seen in their research paper, that the value actually increased but that the concentration, where the maximum value occurs, widens (Fig. 11).

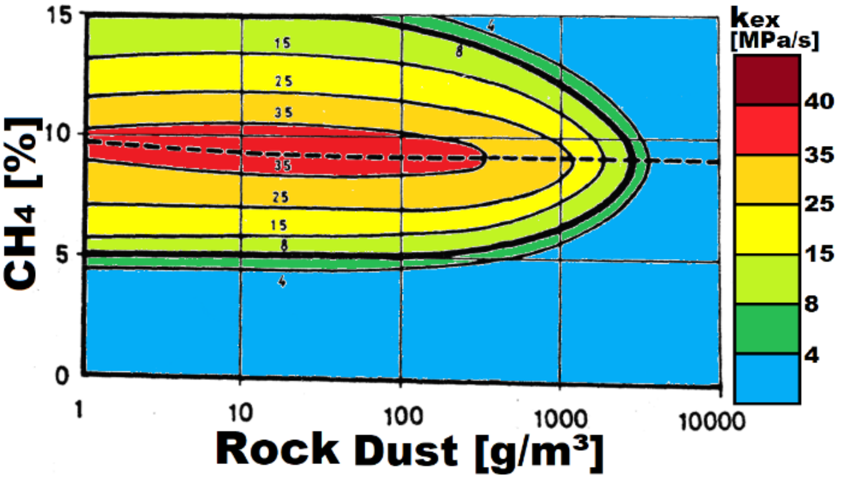

Fig. 11: *Explosion intensity of methane with inert rock dust, taken from Banhegyi and Egyedi (1983), p. 11, colors and legend added by the author*

Other than turbulence, another reason, why small amounts of any dust enhance the flame propagation and thereby the (dp/dt) is given by Ivanov et. al. (2015) who simulated the ignition of gas mixtures ahead of the flame front and identified a radiative preheating of suspended inert particles as a cause for this behavior: Because the gas is transparent, the infrared radiation does not heat up the atmosphere around the ignition point. The solid particles are nontransparent so they heat up and act as distant distributed ignition sources**.**

Another reason could be, that the dispersed particles are spiking through the flame front and by further mixing and wrinkling of the flame front cause a faster combustion.

Since the optimum point of (dp/dt) for hybrid vapour dust mixtures seems to not be around the stoichiometric vapour concentration but between the stoichiometric vapour concentration and the dust concentration with the highest (dp/dt) (Fig. 12 and Fig. 13), the influence of inert dust on the (dp/dt) of vapour explosion shall be investigated in the future to understand the mechanism of these hybrid mixtures.

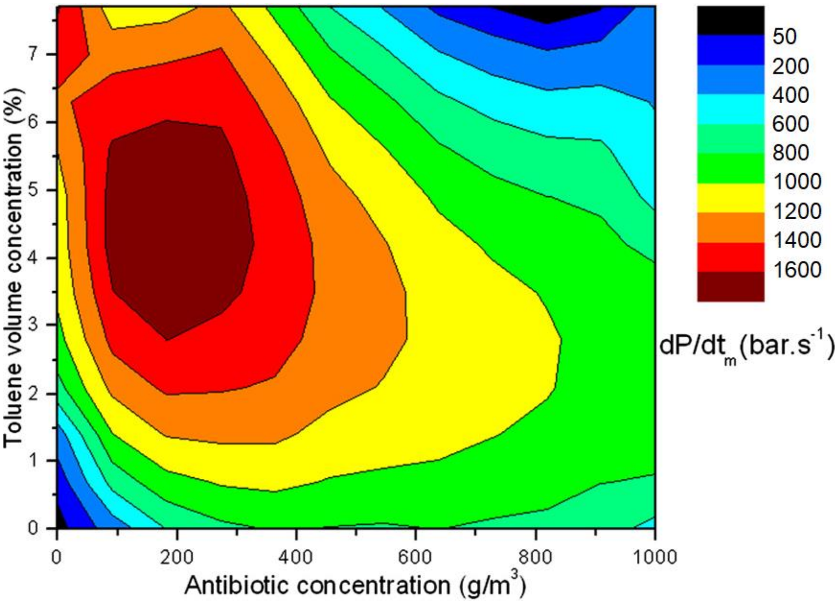

Fig. 12: *2D projection graph of the maximum rate of pressure rise of antibiotic/toluene mixtures, taken from Dufaud et. al. (2009)*

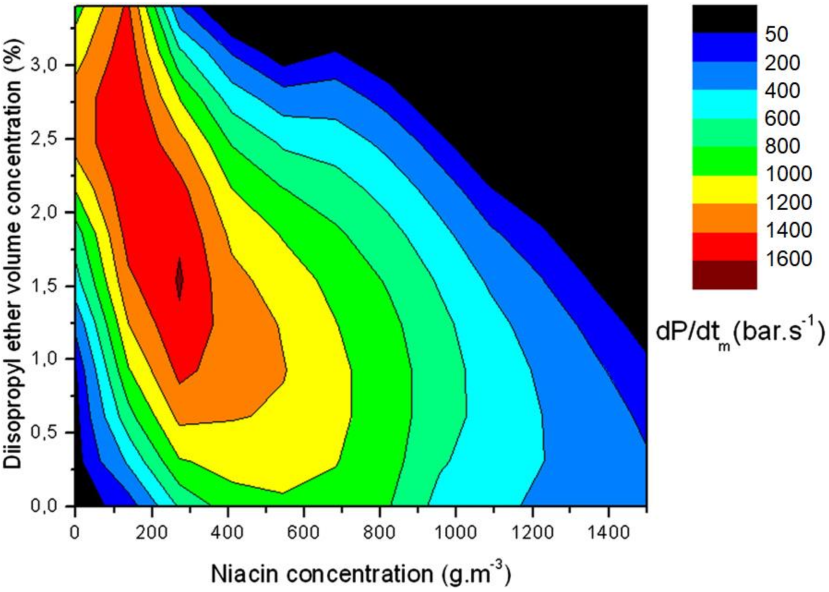

Fig. 13: *2D projection graph of maximum rate of pressure rise of niacin/diisopropyl ether mixtures, taken from Dufaud et. al. (2009)*

However, the value of the increase of $(dp/dt)_{max}$ for hybrid dust vapour mixtures is about the same magnitude than the increase of the value of hybrid dust gas mixtures.

4. Conclusions

It was shown that the maximum rate of pressure rise $(dp/dt)_{max}$ of hybrid mixtures is up to 12 % on average (in other research even 23 %) higher than that of the gas component alone under turbulent conditions and it occurs around the stoichiometric gas concentration with small amounts of dust.

This effect is often hidden by the scattering of the values, that is of the same magnitude and thus it takes several tests and averaging to clearly see this effect.

Lower values of (dp/dt) for the hybrid mixture than those of the gas component alone under turbulence in research were obtained presumably because this maximum point is usually located at very low dust concentrations and the usual step-sizes are too coarse.

Higher values in research were obtained presumably because the hybrid mixture was compared to the non-turbulent gas mixture, different ignition sources were used or other experimental parameters were changed.

Hybrid mixtures of a dust with a $(dp/dt)_{max}$ higher than of the gas component will be checked in the near future to investigate, where the highest value occurs.

The development of a standard for the determination of hybrid mixtures explosion severity will help in comparing the results obtained by the various researchers.

Furthermore, it was shown that it is probably not the combustion of the dust leading to higher values by conducting tests with flammable gas and inert dust, which showed the same effect. The higher (dp/dt)-value might be a product of the increased turbulence caused by the dust, the spiking through the flame front causing a wrinkling of it and thereby a further mixing or because the dust particles serve as additional ignition sources by heating up from the radiating heat igniting the gas outside the initial combustion zone. For the implementation of safety measures, it does not matter which of the three theories is right.

Acknowledgements

The authors would like to thank Alexander Benke, Sara Salih, Dr. Volkmar Schröder, Dr. Martin Schmidt, Prof. Dr. Ernesto Salzano, Dr. Ashok Dastidar, Dr. Lorenz Boeck and Prof. Dr. Trygve Skjold for fruitful discussions about this complex topic.

References

ASTM 1226-12a - Standard Test Method for Explosibility of Dust Clouds, ASTM International, West Conshohocken

ASTM E 1515-14 - Standard Test Method for Minimum Explosible Concentration of Combustible Dusts, ASTM International, West Conshohocken

Banhegyi, M., Egyedi, J. (1983). *Method for determining the explosive limits of a mixture of coal dust, methane and inert matter*, Paper presented at the International Conference of Safety in Mines Research Institutes, Sheffield

Bartknecht, W. (1985). *Untersuchung des Explosions- und Zündverhaltens brennbarer Stäube und hybrider Gemische*. VDI Verlag Düsseldorf

Kris Chatrathi (1994). Dust and hybrid explosibility in a 1 m³ spherical chamber, *Process Safety Progress*, Vol.13, No.4

chemsafe.ptb.de (2022) – slightly differing values for p_{max} of methane because of different sources, checked on 22nd of February 2022

EN 14034-1:2006 - Determination of explosion characteristics of dust clouds - Part 1: Determination of the maximum explosion pressure p_{max} of dust clouds, Beuth-Verlag, Berlin

EN 14034-2:2006 - Determination of explosion characteristics of dust clouds – Part 2: Determination of the maximum rate of explosion pressure rise $(dp/dt)_{max}$ of dust clouds, Beuth-Verlag, Berlin

EN 14034-3:2006 - Determination of explosion characteristics of dust clouds – Part 3: Determination of the lower explosion limit LEL of dust clouds; Beuth-Verlag, Berlin

DIN EN 15967:2011 - Determination of maximum explosion pressure and the maximum rate of pressure rise of gases and vapours, Beuth-Verlag, Berlin

Faraday, M., Lyell, C. (1844). *On the subject of the explosion at the Haswell Collieries and on the means of preventing similar accidents,* Philosophical Magazine and Journal of Science, Vol. XXI, 16-35

Dufaud, O., Perrin, L., Traoré, M. (2008). *Dust/vapour explosions: Hybrid behaviours?* Journal of Loss Prevention in the Process Industries, 21: 481–484

Dufaud, O., Perrin, L., Traore, M., Chazelet, S., Thomas, D. (2009). *Explosions of vapour dust hybrid mixtures A particular class,* Powder Technology, 90 (1-2): pp. 269-273

ISO 6184-3:1985 - Explosion protection systems – Part 3: Determination of explosion indices of fuel/air mixtures other than dust/air and gas/air mixtures - *officially under review since 2005*

Ivanov, M.F., Kiverin, A.D., Liberman, M.A. (2015). *Ignition of Deflagration and Detonation Ahead of the Flame due to Radiative Preheating of Suspended Micro Particles*, Combustion and Flame, Volume 162, Issue 10, 3612-3621

Wentao Ji, Xiang-yang Gan, Lu Li, Zhong Li, Xiao-ping Wen, Yan Wang (2022). *Prediction of the explosion severity of hybrid mixtures.* Powder Technology, 400: 117273

Khalil, Y.F. (2013). *Experimental investigation of the complex deflagration phenomena of hybrid mixtures of activated carbon dust/hydrogen/air*. Journal of Loss Prevention in the Process Industries, 26: 1027-1038

Kosinski, P., Nyheim, R., Asokan, V., Skjold, T. (2013). *Explosions of carbon black and propane hybrid mixtures*, Journal of Loss Prevention in the Process Industries, 26: 45-51

Sanchirico, R., Di Benedetto, A., Garcia-Agreda, A., Russo, P. (2011). *Study of the severity of hybrid mixture explosions and comparison to pure dust–air and vapour–air explosions,* Journal of Loss Prevention in the Process Industries, 24: 648-655

Spitzer, S., Askar, E., Benke, A., Janovsky, B., Krause, U., Krietsch, A. (2022a). *Influence of pre-ignition pressure rise on safety characteristics of dusts and hybrid mixtures,* FUEL, 311: 122495

Spitzer, S. et. al. (2022b). *1st International round robin test on safety characteristics of hybrid mixtures*, 14th International Symposium on Hazards, Prevention, and Mitigation of Industrial Explosions (ISHPMIE)

Wang, Y., Qi, Y., Gan, X., Pei, B., Wen, X., Ji, W. (2020). *Influences of coal dust components on the explosibility of hybrid mixtures of methane and coal dust*. Journal of Loss Prevention in the Process Industries, 67:104222

DOI: 10.7795/810.20221124

1st International Round Robin Test on Safety Characteristics of Hybrid Mixtures

Enis Askar [b], Alexander Benke[b], Chris Cloney[d], Sebastian D’Hyon[l], Olivier Dufaud[m], René Dworschak[f], Dieter Gabel[j], Paul Geoerg[j], Vanessa Heilmann[k], Vojtech Jankuj[n], Wang Jian[i], Jan Kleinert[f], Ulrich Krause[j], Arne Krietsch[b], Jörg Meistes[f], Miroslav Mynarz[n], Frederik Norman[a], Ernesto Salzano[e], Jan Skrinsky[n], Stefan H. Spitzer*[bk], Jerome Taveau[ch], Alexis Vignes[g], Joachim Wandt[f], Sabine Zakel[k] & Shengjun Zhong[i]

[a]Adinex NV, Noorderwijk, Belgium; [b]Bundesanstalt fuer Materialforschung und -pruefung, Berlin, Germany
[c]Delft University of Technology, Delft, The Netherlands; [d]DustEx Research Ltd., Ontario, Canada
[e]DISAT – Department of Applied Science and Technology, Torino, Italy
[f]Inburex Consulting, Hamm, Germany; [g]Ineris, Verneuil-en-Halatte, Picardie, France
[h]Jensen Hughes, Halifax, Canada; [i]Northeastern University, Shenjang, Peoples Republic China
[j]Otto-von-Guericke University, Magdeburg, Germany
[k]Physikalisch Technische Bundesanstalt, Braunschweig, Germany
[l]Simtars Sponcom, Redbank, Queensland, Australia; [m]Université de Lorraine, Nancy, France
[n]VŠB-Technical University of Ostrava, Ostrava, Czech Republic

Companies and names in alphabetical order

E-mail: stefan.spitzer@ptb.de, stefan.spitzer@bam.de

Abstract

There is no applicable existing standard for the determination of safety characteristics for hybrid mixtures. While developing a new standard in a joint research project in Germany first results from parameter studies led to a standard procedure that can be adopted by laboratories that are already testing dusts in the so called 20L-sphere with as little additional effort as necessary. In fact, one of the main objectives of this research project was to keep modifications and adjustments from the generally accepted dust testing procedures as easy and minimal as possible so as to limit potential deviations from one laboratory to another.

In this first round robin test on hybrid mixtures ever, with methane as gas component and a specific corn starch as dust sample, the practicality of the whole procedure, the scattering of the results and the deviation between the testing apparatuses is investigated. This paper summarizes the experimental procedure adopted and objectives of the first round-robin phase involving three of the four original German companies, plus volunteering laboratories from Australia, Belgium, Czech Republic, France and P.R. China. The results will have an impact on the new standard and may lead to robust data for later simulation purposes.

Keywords: *Hybrid mixtures, 20L-sphere, Round Robin Test, Turbulent Combustion*

1. Introduction

Safety characteristics are used to plan processes in a way, that they run under safe conditions. To obtain the safe handling of a plant it is either possible to avoid explosible mixtures or ignition or to mitigate the consequences of possible explosions. So far it was just possible to determine safety characteristics for single phase substances or mixtures (gaseous, liquid or solid) but not if, for example, a process is run with a combustible dust and a flammable gas component. The different standards were referring to the safety characteristics differently (lower explosion limit for gases, minimum explosible concentration for dusts) or they are characterized in different ways but called the same. The maximum explosion pressure p_{max} for dusts is the average value of three tests at the concentration with the highest obtained explosion pressures. The same characteristic for gases is the highest value of five tests at the concentration with the highest obtained explosion pressures. The same is true for the maximum rate of pressure rise $(dp/dt)_{max}$: It is called the same for dusts and gases but it is stated once as an average, the other as the maximum of several tests.

So, the confusion starts before even determining the safety characteristics. Other differences complicate both, a comparison between the different safety characteristics and a connection between the different ones, even further:

- The step-sizes are defined in different ways
- Gases are tested under quiescent conditions, dusts under turbulence
- The values for p_{max} for gases and vapours are stated in absolute pressures, the ones for dusts in relative pressure
- The values for p_{max} for dusts are further corrected when determined in the 20L-sphere but not for gases
- Different ignition sources are used
- The ignition energies differ with 2 J to 5 J for gases and liquids and 2 kJ or 10 kJ for dusts
- An “upper explosible concentration” is not determined for dusts

For all these reasons, safety characteristics of hybrid mixtures were so far just qualitative characteristics and a comparison between values from different sources was somewhere between difficult and impossible.

In the extensive literature survey about hybrid mixtures only in four of them the gas amount was verified but none of them stated how big the deviation and scattering was (Singer (1964), Ishihama et. al. (1979), Pellmont (1979), Schuber (1987)). Furthermore, none of them used the 20L-sphere or the 1m³ so the impact of the fast compression and the dynamic tests on the partial pressure method was not investigated so far aswell.

On a national basis a new approach to a standard for hybrid mixtures was developed in Germany. Four institutions, Bundesanstalt für Materialforschung und -prüfung (BAM), Physikalisch Technische Bundesanstalt (PTB), Otto-von-Guericke University (OVGU) and Inburex Consulting, were investigating several important parameters that can be varied according to the different standards, aimed for precision while keeping the complexity at a feasible level and started an international round robin test to see, how applicable their new approach was.

Fig. 1: *Map with the facilities involved in the round robin test (CC BY-SA 3.0, image cut and marked by the corresponding author)*

The following test facilities submitted their data so far:

- Bundesanstalt für Materialforschung und -prüfung, Berlin, Germany
- Physikalisch-Technische Bundesanstalt, Braunschweig, Germany
- Otto-von-Guericke University, Magdeburg, Germany
- The technical University of Ostrava, Ostrava, Czech Republic
- Adinex NV, Noorderwijk, Belgium
- The University of Lorraine, Nancy, France
- Ineris, Verneuil-en-Halatte, France
- Simtars Sponcom, Redbank, Australia
- The University of Shenyang, Shenyang, P. R. China
- Suzhou EnvSafe Test Co. Ltd, Suzhou, P. R. China

2. Experiments

An operating procedure for both, the 20L-sphere and the 1m³ can be found on the BAM-website (Hybrid2). Before the experiments started an additional absolute pressure sensor had to be installed to the test vessel. This pressure sensor is used while filling the flammable gas into the sphere and the values are used to calculate the concentration of gas (partial pressure method). To verify, whether the calculated concentration of gas matches the real amount of gas added, a gas analyzer with a pump was also installed (see Fig. 2).

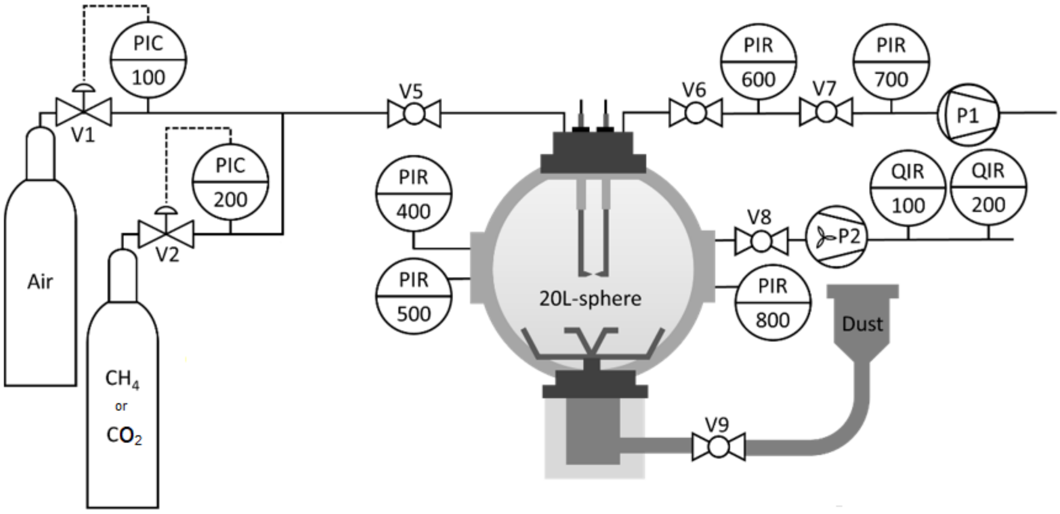

Fig. 2: *20L-sphere setup at BAM for hybrid dust gas mixtures with additional absolute pressure sensor (PIR 600 with one bar absolute or PIR 800 with 10 bar absolute resolution), gas analyzer(QIR 100 and QIR 200) and pump (P2)*

Two pre-test series are necessary before starting the hybrid explosion tests: First, a leakage test is conducted to see, how airtight the test vessel is. This step is crucial, if hybrid mixtures are tested because the accuracy of the fuel gas fraction depends on the accuracy of the absolute pressure sensor, the constant pre-ignition pressure rise just before the ignition is triggered and the tightness of the vessel avoiding additional introduction of atmospheric air into the test vessel during the filling procedure. A leakage-rate of lower than 1 mbar/minute was allowed in this test series.

Afterwards a test-series to evaluate the accuracy and scattering of the fuel gas fraction was conducted. For these tests, no ignition source or dust was placed in the test vessel respectively the dust container. It was allowed to replace the flammable gas by another gas for safer handling. The tests were otherwise conducted as normal dust tests with the pressurizing of the dust container and the injection from the dust container to the test vessel. All the pressures during this process were recorded and after the injection the pressure was measured for another three minutes before the valve leading to the gas analyzer and the pump was opened. This is necessary because there is a pressure-drop after injecting the air due to the increased temperature because of the fast compression (post-injection pressure drop, PIPD, see Fig. 3). Normally the ignition takes place at the peak pressure. The pressure drop leads to wrongly calculated gas concentrations if it is not taken into account. Due to the explosion this pressure drop after equilibration cannot be recorded in the regular explosion tests. So the values obtained in the pre-tests were averaged. The average values were used to calculate the fuel gas fractions in the regular explosion tests.

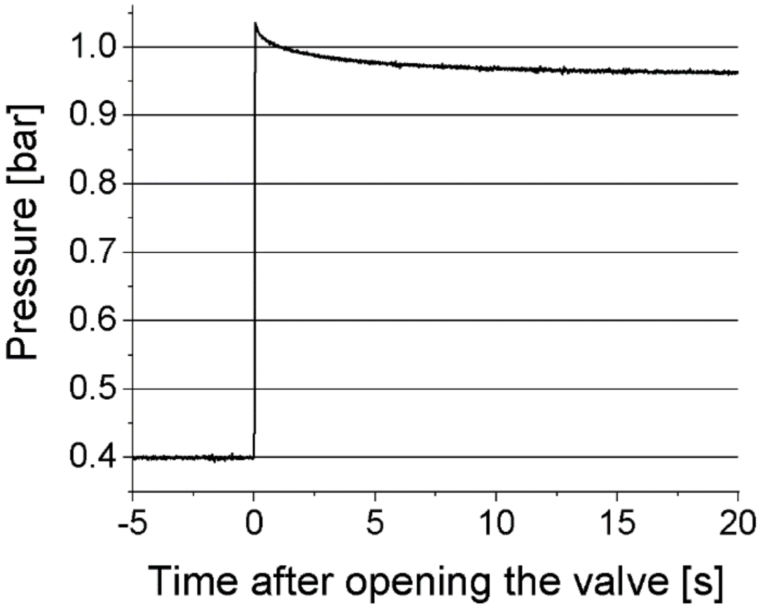

Fig. 3: *Recorded pressure against time after opening the fast-acting valve without igniter and without dust (taken from Spitzer et. al. (2022a))*

If the measured amount of gas was more than 0.2 Vol-% lower than the calculated amount of gas the partial pressure of the gas was increased and vice versa.

When both, the vacuum test and the validation of the gas mixture, were successful a dust sample was sent to the facilities. The dust samples were checked on moisture content before dispatch. The particle size distribution was also checked occasionally.

The experimental procedure for the hybrid explosion tests was derived from the European standard for the determination of safety characteristics of dusts (DIN EN 14034 – series). The amount of gas was filled to the sphere and the molar fraction was calculated according to the following formula (1)

$$x_{gas}=p_{gas}/(PV+PIPR-PIPD) \quad (1)$$

with x_{gas} as the fraction of the gas in mol-%, p_{gas} the partial pressure of the gas filled to the sphere, PV (partial vacuum) as the pressure in the sphere before the injection of the dust, PIPR (pre-ignition pressure rise) and the averaged post-injection pressure drop PIPD (Spitzer et. al. (2022a)) from the pre-tests.

If the measured amount of gas in the pre-tests was differing from the calculated one systematically, the equation (1) was adjusted to equation (2)

$$x_{gas}=p_{gas}/(PV+PIPR-PIPD)-Deviation \quad (2)$$

The following additional modifications and changes were made:

- For all experiments two 1 kJ pyrotechnical ignitors were taken
- The pressure in the sphere before the dust injection starts was kept at 400 mbar abs ± 2 mbar
- The Pre-Ignition pressure rise was kept constant at 0,64 bar ± 0,02 bar

The dust was tested in the concentrations of 0 g/m³, 20 g/m³, 60 g/m³, 125 g/m³, 250 g/m³, 500 g/m³, 750 g/m³ and 1 000 g/m³ with an additional 0 mol-%, 3 mol-% and 9 mol-% of methane. At the points were the highest explosion pressures and pressure rises occurred the tests were repeated twice.

The following requirements for hybrid gas dust explosion tests were explicitly not defined:

- Gas analyzing system
  - The facilities used different kinds like Infrared, catalytic or gas chromatography with a coupled mass spectrometry, the resolution was demanded to be at least 0.1 mol-%
- Amount of pressure sensors
  - Though in the dust standard two pressure sensors for measuring the explosion pressure are demanded, one research laboratory had just one sensor
- Type of pressure sensor
  - Though in the standard test equipment piezo-electric sensors are used, one research laboratory used piezo-resistive pressure transmitters
- Measuring frequency
  - The measuring frequency should be defined in a later standard, most facilities had 20 kHz except for one with 5 kHz
- Pressurized air
  - Some laboratories had synthetic air, some fully dried compressed and some normal compressed, this should be specified in the later standard because this might have an impact
- Distribution system
  - Most facilities use a rebound nozzle today, but some use a mushroom shaped nozzle or a perforated dispersion ring

Shortly before the dispatch of the dust samples the moisture content was measured. Afterwards the dust was filled in bottles and sealed. The receiving facilities were asked to open the dust samples shortly before conducting the hybrid explosion tests and to check for the moisture content again. This way we could attest each other, that the samples were not damaged on the way. The moisture content we tested over the whole time was between 7 % and 9 %. The particle size distributions were tested every three months optically (MALVERN Mastersizer 2000). The 10th percentile (d(0.1)), the median value (d(0.5) and the 90th percentile (d(0.9)) were (9 ± 1) µm, (13± 1) µm and (21 ± 2) µm.

The results from all the test facilities were averaged, if several results were sent for one point according to the dust standard. The presented values for the explosion pressure were corrected with the following equations (1, 2) derived from the standard for dusts, EN 14034-1 and ASTM 1226a:

If the measured overpressure was below 5.5 bar g:

$$p_{max} = 5.5 * (p_{max,20L} - 0.32) / (5.18) \quad [\text{bar g}] \qquad (1)$$

If the measured overpressure was above 5.5 bar g:

$$p_{max} = 0.775 * p_{max,20L}^{\ 1.15} \quad [\text{bar g}] \qquad (2)$$

3. Results and discussion

The results for p_{max} for 3 % of methane from the different facilities are shown in Fig. 4. The scattering between the different facilities is small for the highest values but for the determination of the LEL respectively the MEC this procedure seems to have too many degrees of freedom. For 3 % of methane and 20 g/m³ corn starch half of the institutions detected an explosion, one with an explosion pressure of 5 bar g, while the other half could not measure one (p_{ex} being under 0.3 bar g). One facility even detected a very slight explosion with a p_{ex} value of 0.5 bar g with no dust at all. For the aimed characteristic p_{max} this method showed comparable results with a scattering of less than 10 %.

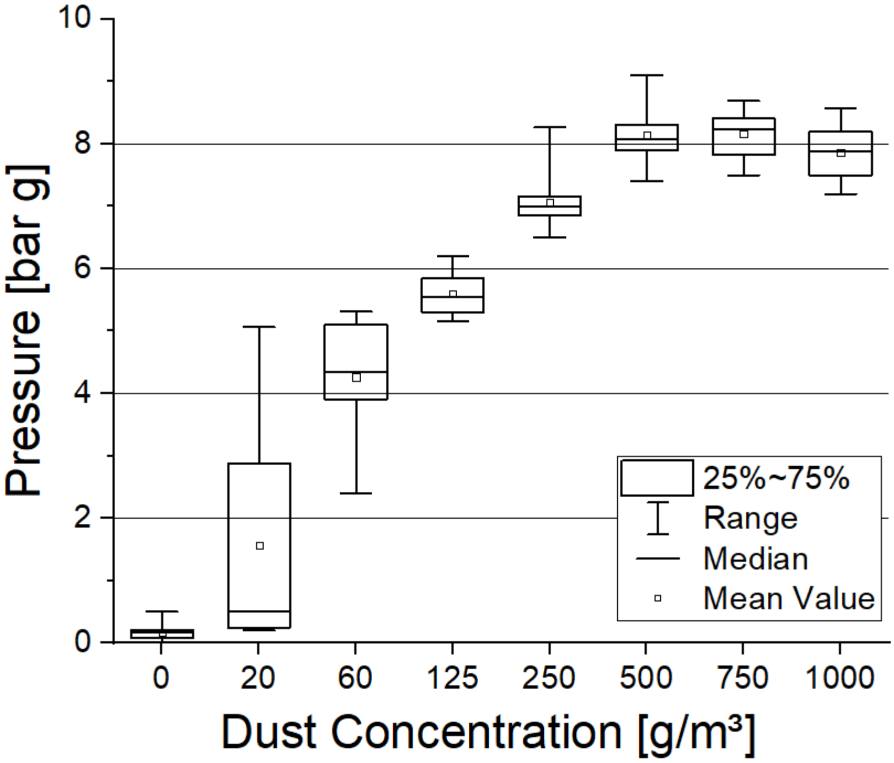

Fig. 4: *Highest explosion pressures of corn starch with 3 % methane*

The results for $(dp/dt)_{max}$ for 3 % of methane from the different facilities are shown in Fig. 5. The scattering between the different facilities is less than 20 % for the highest values. The highest values were also obtained by all facilities at the same concentration of 750 g/m³ or one step up or down. This could be an effect of different distribution systems, that were not specified in the operating procedure.

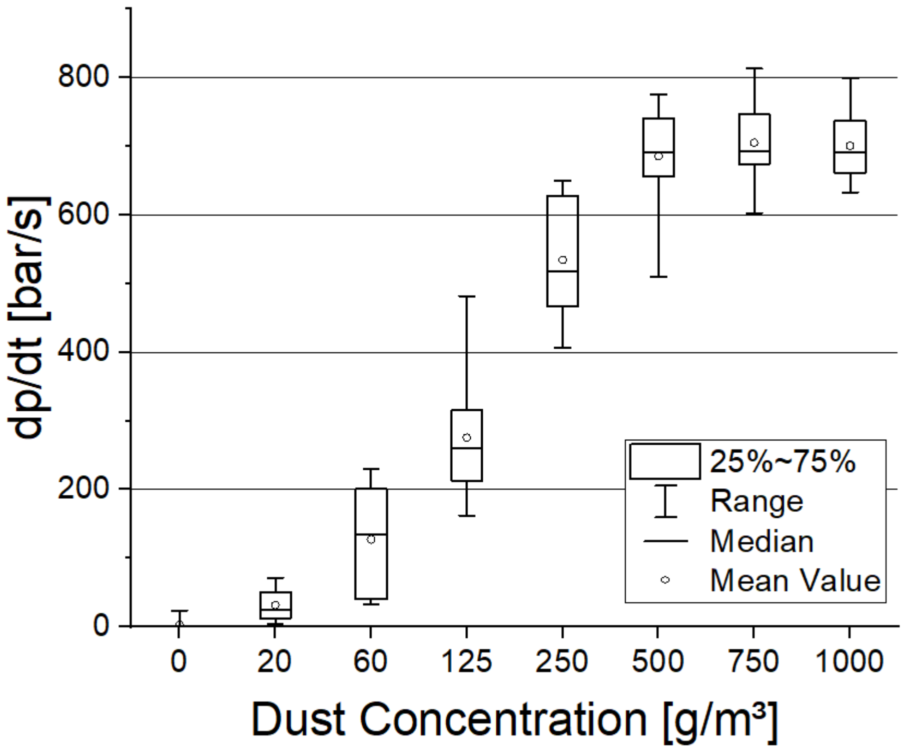

Fig. 5:*Highest rate of pressure rise of corn starch with 3 % methane*

The results for p_{max} for 9 % of methane from the different facilities are shown in Fig. 6. The scattering for all tested concentrations was 11 % and thus lower than the ones for p_{max} tested at 3 % with an increasing tendency with increasing dust concentration (below 5 % scattering with no dust, 9 % at the highest point with 60 g/m³ and 11 % at the end with 1000 g/m³). It should also be mentioned, that all the values are below the values of the dust tested alone. This may be caused by the fact, that with 9 % of methane the oxygen amount is already decreased to 19 % instead 0f 20.9 %.

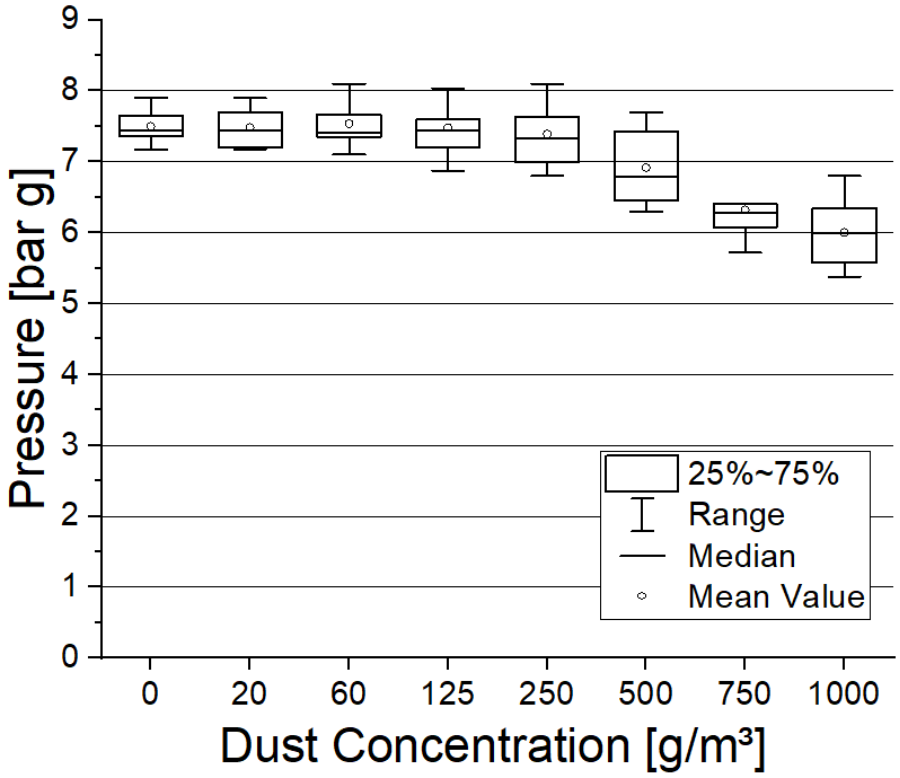

Fig. 6: *Highest explosion pressures of corn starch with 9 % methane*

DOI: 10.7795/810.20221124

The results for $(dp/dt)_{max}$ for 9 % of methane from the different facilities are shown in Fig. 7. Except for three facilities all others measured the highest value of (dp/dt) with small amounts of dust added. This exception occurred at facilities with a self-written testing program and could be caused by one or more of the following reasons:

- The distribution system was not specified
- This facility took synthetic air
- The effect is with 10 % about the same magnitude as the scattering and thereby hard to spot anyways
- The ignition delay time is defined on an event-basis[1] in the different standards and could have an impact, if it is implemented otherwise

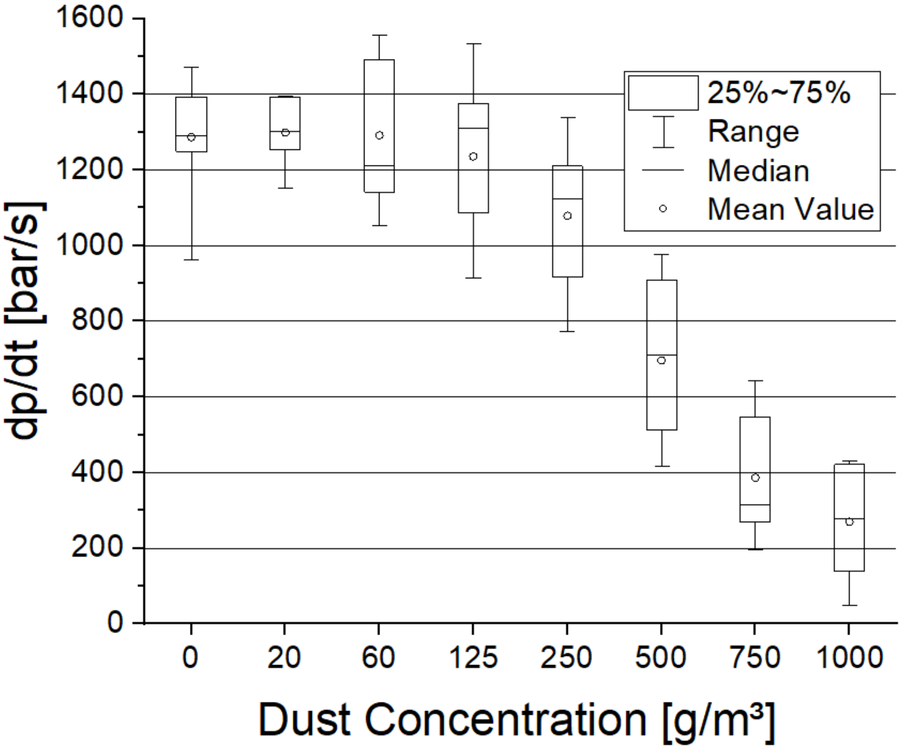

***Fig. 7:** Highest rate of pressure rise of corn starch with 9 % methane*

However, the highest values of p_{max} found by the different laboratories were still within two steps apart from each other at the very fine scale (it shall be pointed out, that the x-Axis in all plots is not linear).

The overall results are displayed in Table 1. The scattering for $(dp/dt)_{max}$ was 21 %, for p_{max} it was 8 %. This can be seen as reasonable considering, that it is higher than for gas testing alone where the scattering for methane is stated with 3.6 % for p_{max} and 3.1 % for $(dp/dt)_{max}$ (EN 15967) but of the same magnitude as for dusts alone with 10 % for p_{max} (ASTM 1226, EN 14034-1) and 20 % for $(dp/dt)_{max}$ (ASTM 1226) even though more parameters must be considered for hybrid mixtures compared to dusts alone. In the European standard for the determination of $(dp/dt)_{max}$ for dusts the allowed scattering is depending on the value. Above 200 bar/s a scattering of 10 % is allowed which is lower than the one of this procedure, but still of a comparable magnitude (EN 14034-2). The decreasing value for p_{max} with increasing fuel gas fraction may be an effect of the decreasing amount of oxygen in the vessel.

---

[1] The ignition delay time is defined as the time between the first measurable pressure rise inside the sphere until activation of the ignition source (ASTM 1226, EN 14034-series). This event-based definition is often misunderstood as the time between activation of the fast-acting valve and activation of the ignition source (descriptive definition). Since the ignition source takes 0-10 ms to ignite and the fast-acting valve takes 20-50 ms to open this is the main source of error if equipment is self-built.

Table 1: *Overall results for the different concentrations of methane and corn starch*

	$(dp/dt)_{max}$		p_{max}	
	bar/s		**bar g**	
0 % Methane	540 ± 120	± 22 %	8.5 ± 0.7	± 8 %
3 % Methane	705 ± 108	± 15 %	8.2 ± 0.7	± 8 %
9 % Methane	1291 ± 265	± 21 %	7.5 ± 0.6	± 7 %

Some of the parameters that were not specified yet might be narrowed in the upcoming standard. However, taking into account that all the parameters for the determination of the safety characteristics of hybrid mixtures of gases and dusts have an impact the variation observed in the tests is reasonable. It is of the same magnitude than the variation that is defined in the standard for dusts.

4. Conclusions

A test method for the reliable, reproducible and simplified determination for the safety characteristics p_{max} and $(dp/dt)_{max}$ of hybrid dust gas mixtures was developed. Ten facilities in six countries were able to adjust their dust testing equipment and conduct hybrid explosion tests. The results showed, that the procedure works, leads to comparable results for p_{max} and $(dp/dt)_{max}$ respectively the K_H-value. The variation between the different facilities for these safety characteristics was higher than for the safety characteristics of gases according to the standards, but of the same magnitude given in the standards for safety characteristics of dusts.

Especially the leakage-check of the test vessel before starting any test procedures and verification of the gas amount without ignitors and dust before conducting the actual explosion tests are crucial to obtain comparable results. Both was not conducted (or at least not stated) in the literature about hybrid mixture testing in the 20L-sphere. These two pre-tests will be inserted in the future standard and should be mandatory for everyone conducting hybrid tests.

Acknowledgements

The authors gratefully acknowledge the corporation of our dust testing lab, Mike Wappler and Dr. Martin Schmidt, for their help and Sara Salih for conducting the tests in BAM.

References

ASTM E 1515-14 - Standard Test Method for Minimum Explosible Concentration of Combustible Dusts, ASTM International, West Conshohocken

EN 14034-1:2006 - Determination of explosion characteristics of dust clouds - Part 1: Determination of the maximum explosion pressure p_{max} of dust clouds, Beuth-Verlag, Berlin

EN 14034-2:2006 - Determination of explosion characteristics of dust clouds – Part 2: Determination of the maximum rate of explosion pressure rise $(dp/dt)_{max}$ of dust clouds, Beuth-Verlag, Berlin

EN 15967:2011, Determination of maximum explosion pressure and the maximum rate of pressure rise of gases and vapours, Beuth-Verlag, Berlin

Hybrid2 (2022). https://rrr.bam.de/RRR/Navigation/EN/Proficiency-Testing/HYBRID/hybrid-mixtures.html

Wataru Ishihama, Hideo Takagi, and Heiji Enomoto (1979). Explosion characteristics of coal dust-methane-air mixture. International conference on scientific research in the field of safety at work in mining industry

ISO 6184-3:1985 - Explosion protection systems – Part 3: Determination of explosion indices of fuel/air mixtures other than dust/air and gas/air mixtures - *officially under review since 2005*

Günther Pellmont (1979). Explosions- und Zündverhalten von hybriden Gemischen aus brennbaren Stäuben und Brenngasen. PhD thesis, Eidgenössische Technische Hochschule Zürich

Georg Michael Schuber (1987). Zünddurchschlagverhalten von Staub/Luft- und hybriden Gemischen durch enge Spalte. PhD thesis, ETH Zürich

Joseph M. Singer (1964). Ignition of coal dust-methane-air mixtures by hot-turbulent-gas jets, Technical report, Bureau of Mines

Spitzer, S., Benke, A., Askar, E., Janovsky, B., Krause, U., Krietsch, A. (2022a). Influence of pre-ignition pressure rise on safety characteristics of dusts and hybrid mixtures; *FUEL*, Vol. 311: 122495, doi.org/10.1016/j.fuel.2021.122495

Spitzer, S., Askar, E., Gabel, D., Geoerg, P., Krietsch, A. (2022b). Influence of the mixing procedure on safety characteristics of hybrid mixtures, https://papers.ssrn.com/sol3/papers.cfm?abstract_id=4045443

DOI: 10.7795/810.20221124

Making hybrid mixtures explosion a common case

Matteo Pietraccini [a], Pierre-Alexandre Glaude [a], Anthony Dufour [a] & Olivier Dufaud [a]

[a] Université de Lorraine, CNRS, LRGP, F-54000 Nancy, France

E-mail: olivier.dufaud@univ-lorraine.fr

Abstract

Explosions of gas/dust hybrid mixtures have long been considered as particular cases encountered in specific industrial contexts. However, it should be reminded that during the explosion of an organic powder, the presence of a hybrid mixture composed of the dust itself and its pyrolysis gases is compulsory. Based on this fact and on previous studies showing that pyrolysis was often the rate-limiting stage, an experimental study was undertaken to determine the pyrolysis gases of cellulose using a modified Godbert-Greenwald furnace. The explosion severity of hybrid mixtures of these powders combined to their pyrolysis gases, obtained at two different temperatures, was studied using a 20L sphere. Several experimental strategies were chosen to demonstrate the impact of pyrolysis reaction on the explosion of organic powders: i) the fuel equivalence ratio of the reactive mixture (case 1), or ii) the mass of reactants (case 2) were respectively kept constant, iii) the effects of water vapor and char were tested. Figure 1 shows that strategies 1 and 2 lead to significantly different results: only case 2 keeps the explosion overpressure P_m almost constant, but the rate of pressure rise and deflagration index $K_{g/St}$ greatly decrease when the pyrolysis gases concentration decreases, which highlights the importance of the pyrolysis reaction on the explosion kinetics. It should also be stressed that the maximum explosion severity is not obtained for the pure gases but when a small content of dust is added. The same evolution is observed when a small amount of char is introduced to pyrolysis gases, which underlines the influence of the radiative transfers.

Keywords: *dust explosion, pyrolysis, hybrid mixture, cellulose*

1. Introduction

Gas and dust explosions are nowadays well studied and the determination of their characteristic parameters (P_{max}, K_{St} or K_g) is commonly carried out. Although some standards may be in need to be perfected, the global approach of the testing procedures allow to respond to the industrial needs. However, gas and dust explosions tests may be used as an important tool to better understand the phenomenon itself and what its fundamental steps are (Cloney et al., 2017). Particularly promising is the study of hybrid mixtures explosion, which could potentially represent and simulate complex phenomena involving two combustible phases (Abbas et al., 2022; Dufaud et al., 2009; Guo et al., 2020; Sanchirico et al., 2015). In this work, hybrid mixtures were exploited to assess the role of pyrolysis during the rapid combustion of an organic powder. In general, when such powders are heated, they undergo a pyrolysis step, which generate a vapour-gaseous phase along with a solid residue called char. Then they react with the oxidiser triggering the oxidation reactions. These phenomena occur simultaneously and the global rate of the global one strictly depends on the slowest step, the rate-limiting one. Each explosion of organic powder is thus in reality a hybrid explosion.

2. Experiments

2.1 Powder characterisation

Since both its chemical structure and thermal behaviour have been well characterized, the choice of the powder fell on micro-crystalline cellulose (Avicel ph 101). Moreover, the reaction mechanisms of cellulose pyrolysis have been the subject of several detailed studies (Ranzi et al., 2017; Wang at al., 2020; Paulsen et al., 2013), which were used to support the results obtained in this work. The char sample used in the experiments was collected in a biomass gasification plant. It was chosen to represent the solid residue generated during the pyrolysis of cellulose.

A Malvern Mastersizer 3000 equipped with an aero-dispersion unit was employed to determine the Particle Size Distribution (PSD) of both samples. Images of the samples were taken with a 5 Mp Dino-lite Pro HR digital microscope and a JEOL JSM-649-LV Scanning Electronic Microscope (SEM). The combination of these two imaging tools was exploited to characterize the appearance, the shape and the surface morphology of the particles.

A proximate analysis was performed on the two powder samples. The moisture content (MC) was determined with the aid of a Mettler Toledo HE53 Moisture Analyzer. The volatile matter (VM) and the fixed carbon (FC) were determined with a STARe System thermogravimetric balance. Finally, the ash content (ASH) was determined by the means of a Nabertherm B150 oven. Table 1 reports the characteristic diameters of the two powder samples, as well as their proximate analysis.

Cellulose presents a narrower Particle Size Distribution (PSD) than char, which however is slightly finer than cellulose. Since an organic particle tends to shrink when undergoes a pyrolysis, this last characteristic allowed the char to better represent such a phenomenon. Concerning the proximate analysis, it can be noticed that the higher value of FC in the char sample is due to the organic matter that did not entirely volatilize, but converted in a porous structure rich in carbon and hydrogen. This fraction is also characterized by a much higher ash content than cellulose.

Table 1: *Characteristic diameters and proximate analysis of the powder samples*

Sample	D10, µm	D50, µm	D90, µm	MC, %wt	VM, %wt	FC, %wt	Ash, %wt
Cellulose	22	68	146	5.3	87.4	7.2	0.10
Char	8	25	120	2.9	28.8	48.6	19.6

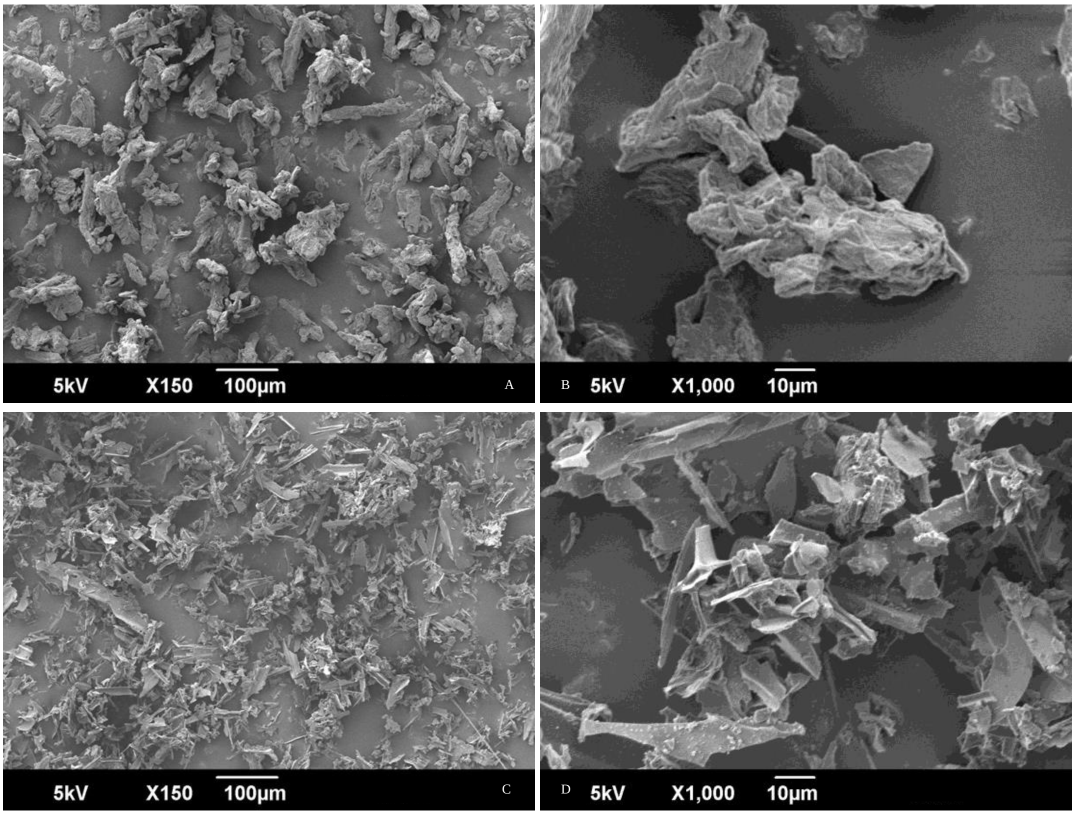

Fig. 1. *SEM photos of the cellulose (A and B) and the char sample (C and D)*

Figure 1 shows the SEM images of the two samples. No important difference in particle shape is noticeable between the two powders, but their difference in size, perceptible in the SEM images, seems coherent with the information about the characteristic diameters.

2.2 Pyrolysis simulation method

The experimental method developed to simulate the pyrolysis step consists in three parts: i) determination of the composition of two gaseous mixtures, representing the cellulose pyrolysis gaseous products; ii) hybrid mixture explosion experiments with cellulose and the gaseous mixes thus obtained; iii) hybrid mixture explosion experiments with cellulose, the two gaseous mixes and char.

2.2.1 Determination of the composition of the pyrolysis gaseous mixes

The first stage of the study was carried out in a modified Godbert-Greenwald furnace, as in Pietraccini (2021). This apparatus was chosen as it allows to reproduce the conditions of a dust explosion, with a short residence time and a very high heating gradient. The influence of the heated chamber temperature was studied and three series of experiments were performed at 700, 800 and 900 °C, for each of which the gaseous products and tar composition was measured. Cellulose was dispersed with an argon gas pulse and each test was performed thrice. In order to study the influence of the reactor temperature on the pyrolysis reaction, the two compositions chosen for the hybrid mixture explosion tests were the ones obtained at 700 and 900 °C. The main measurable components were H_2, CO, CO_2 and CH_4 and two gas bottles were prepared according to the experimental results. For a clarity purpose, from this point on, the gaseous mixture obtained at 700 °C will be called mix A, while the gaseous mixture obtained at 900 °C will be called mix B. The main compound of tar was levoglucosan, but its concentration decreases at high temperature as tar is cracked into permanent gases. It should be remembered that water vapor is also generated during the pyrolysis step. Since it was difficult to experimentally determine the water concentration, it was extracted from Piskorz (2000), whose work has been carried out in a similar experimental setup for cellulose pyrolysis. It should be underlined that the effect of the temperature does not influence only the composition of the pyrolysis gaseous products, but their yield as well. An increase of the temperature usually translates in an increase of the amount of gaseous products generated during the pyrolysis. In this work, this aspect was not considered and it will be the subject of a future work.

2.2.2 Dust explosion experiments

In Figure 2, the scheme globally resumes the approach followed during the hybrid mixtures explosibility tests. Series 1 was carried out considering only the volatilization process occurring in cellulose pyrolysis and without considering the water as a product; in series 2 the water was accounted among the pyrolysis products; finally, in series 3 both the volatilization and charring processes were considered. To include the char in the tests means to consider a more complete pyrolysis process, as well as to enlighten the role of the radiative heat transfer in the dust cloud (Torrado, 2017). In fact, char is characterized by a higher emissivity than cellulose and, thus, the addition of a small amount in the cellulose powder might result in a more important radiative heat flux from the flame front to the pre-heating zone. The choice of the amount of char added to the cellulose powder in the explosion experiments was made considering the yield values commonly encountered in a cellulose flash pyrolysis phenomenon. According to Commandré (2011) and Zanzi (1996), whose works were carried out in similar free-fall reactors for flash pyrolysis of biomass, the char yield lays between 7 and 10 wt%. For the cellulose-char-pyrolysis gas hybrid mixture explosion tests, the amount of char chosen was 10 wt% of the cellulose injected in the 20L sphere.

The explosion experiments were carried out in a standard 20L spherical vessel equipped with a rebound nozzle and two 100 J chemical igniters, as ignition sources. This energy was chosen as it is both sufficiently high to ignite the pure dust and sufficiently low to limit overdriving effect (e.g. much lower than 10 kJ) (Taveau et al., 2017). As no standard procedure exists to determine the explosion severity of hybrid mixtures (Spitzer et al., 2020), the procedure used for powders (EN 14034) has been adapted to such mixtures (Dufaud et al., 2009). The sphere was partially vacuumed to pressures as low as 30 mbar. The corresponding amount of gas is introduced in the vessel by recording the partial pressure. Air is introduced to set the absolute pressure at 0.4 bar. Finally, the test is performed ‘classically’ and the powder, stored in the dust container at 20 bar, is injected through the rebound nozzle located at the bottom of the vessel. The temperature is kept constant at 25 °C using the water jacket. The explosion overpressure P_m and the rate of pressure rise, $(dP/dt)_m$, were determined for each test. K_{St} (or K_g) were then calculated applying the cube-root law.

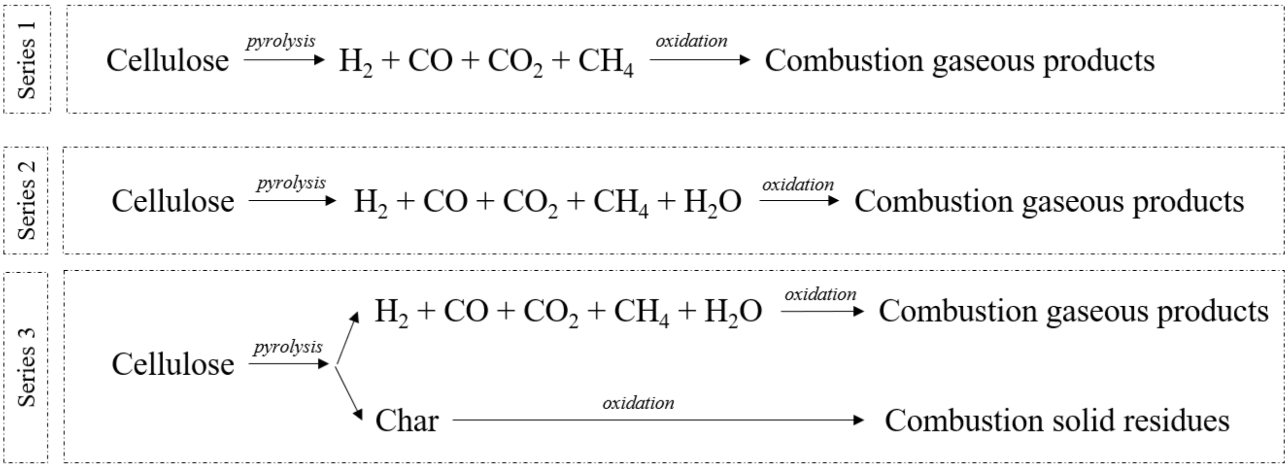

Fig. 2. *The procedure adopted for the cellulose pyrolysis experimental simulation*

Nevertheless, the procedure developed to simulate and study the role of pyrolysis in an organic dust explosion has two important limits. The experimental protocol followed to characterize the gaseous products in the G-G furnace provided for a pyrolysis performed in an inert atmosphere, while the pyrolysis step of a dust explosion occurs in an oxidative atmosphere. Kinetics and thermicity of the two processes may thus present some significant differences. Moreover, during the hybrid mixture tests in the 20L sphere, the pyrolysis mixture is already present in the gaseous phase, whilst in a “classic” dust explosion test they are generated and only then they mix with the air. This may lead to a different flame dynamic: a premixed flame in the first case and a diffusion flame in the second case.

3. Results and discussion

3.1 Pyrolysis gaseous mixes

The composition of mix A and B is reported in Table 2. Amongst the hundreds of products of fast cellulose pyrolysis, the most abundant species in the gaseous phase are CO, CO_2, H_2, CH_4, H_2O, light hydrocarbons such as C_2H_4 and C_2H_6, acetic acid and other light organics (Piskorz et al., 2000). Considering only the so-called ‘permanent gases’ (CO, CO_2, CH_4 and H_2) and neglecting the other molecules, whose concentrations were negligible, one of the main effects of the temperature is the increment of the gaseous products yield. The two gaseous mixes globally present a composition similar to that presented in Graham (1984), Funazukuri (1986) and Paulsen (2013), whose works were focused on cellulose flash pyrolysis, performed with in similar experimental setups, temperatures and residence times. CO and CO_2 are always the most abundant ones among the permanent gases. As in Funazukuri (1986), hydrogen molar fraction increases with the temperature (from mix A to mix B), while methane concentration is similar to that presented in Graham (1984). However, CO molar fraction decreases from 700 to 900°C, whereas it shows the opposite behaviour in Funazukuri (1986) and Paulsen (2013). CO_2 concentration does not seem to be importantly affected by the temperature in Funazukuri (1986) and Graham (1984), but in this work it is reduced by almost half. These differences may be due to the significant increase of the hydrogen fraction, which modifies the proportions between the chemical species, as well as to the difference of the phenomena.

Table 2: *Composition of the pyrolysis gaseous mixes used in the hybrid mixture explosion experiments*

Species	**Composition, %mol**	
	Mix A (obtained at 700°C)	**Mix B (obtained at 900°C)**
H_2	3	24
CO	61	51
CO_2	33	18
CH_4	3	7

3.2 Dust explosion experiments

3.2.1 Cellulose and gaseous mixture explosion severity

The explosion severity of cellulose and the two gaseous mixes were studied (separately), determining P_{max}, K_{St} and K_g. Figure 3 shows the classical evolution of the explosion severity of cellulose as a function of the dust concentration. The powder sample is associated to an approximate minimum explosible concentration of 60 g/m^3, a P_{max} of 7.1 bar and a K_{St} of 77 bar.m/s, which is consistent with the values of the literature, especially those of the Gestis-Dust database (IFA). Nevertheless, it should be noted that, whereas the deflagration index is in the range of values identified in the database (from 30 to 130 bar.m/s for particles of similar sizes), the maximum explosion overpressure is slightly lower than expected (from 7.5 to 9.5 bar).

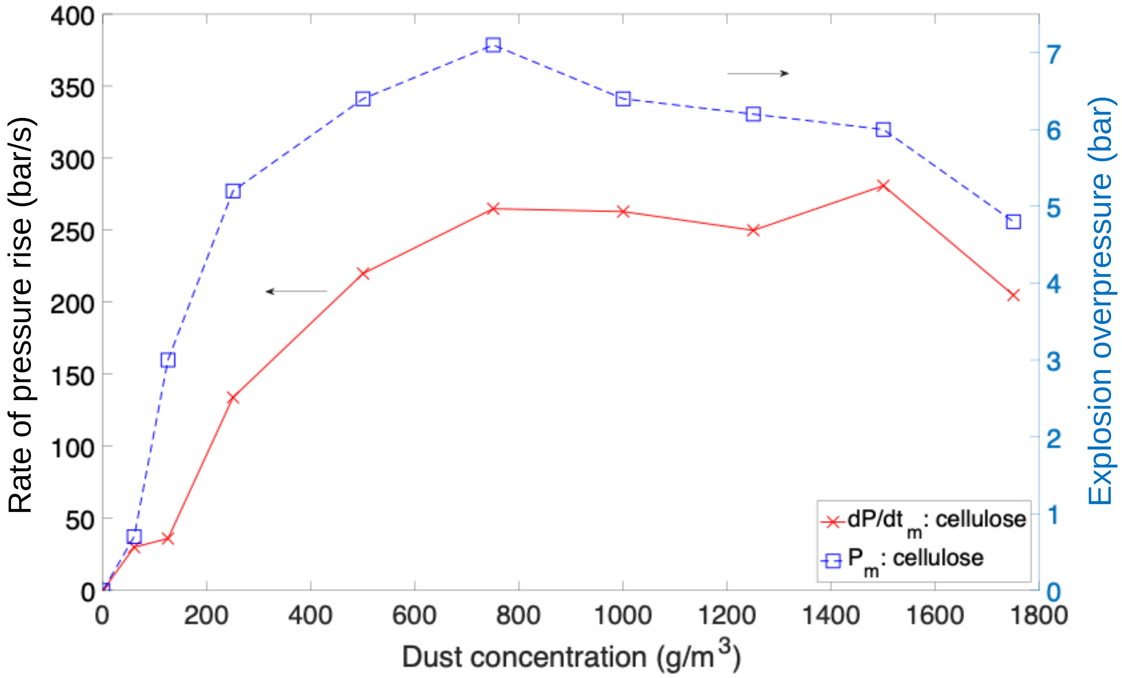

Fig. 3. *Explosion severity of pure cellulose (d_{50}: 68 µm)*

The maximum explosion overpressure obtained with the pyrolysis gases are of the same order of magnitude as for cellulose, i.e. 6.2 and 6.5 bar for mix A (700 °C) and mix B (900 °C), respectively. However, they differ consistently in terms of K_g with 242 and 587 bar.m/s for mix A and mix B, respectively. The small difference of the P_{max} values is related to the small difference of composition between the two mixtures. In fact, their energetic content (in terms of enthalpy of combustion) is

208 kJ/mol for mix A and 278 kJ/mol for mix B. It should also be stressed that the maximum explosion overpressure of pyrolysis gases and dust are close.

If the influence of the pyrolysis temperature on the gas composition seems to be negligible when considering the mass concentrations, Table 1 shows that the molar composition is greatly affected especially with regard to the hydrogen content. Therefore, the higher fraction of hydrogen in the pyrolysis gases obtained at 900 °C leads to a higher combustion reaction rate and, by consequence, to a higher K_g. Moreover, the presence of a larger amount of hydrogen lowers significantly the Lower Explosible Limit (LEL) of the gases, from 10.8 vol% (mix A) to 7.1 vol% (mix B) using Le Chatelier's law, which is also enlightened in Figure 4. Due to the presence of carbon dioxide in the mixture, the experimental LEL are higher than the theoretical values. It also immediately appears that both the sensitivity to ignition and the severity of the explosion depend on the temperature at which the pyrolysis of the organic powder takes place. This parameter will of course depend on the physical properties of the dust, but also on the heating rate to which it is subjected.

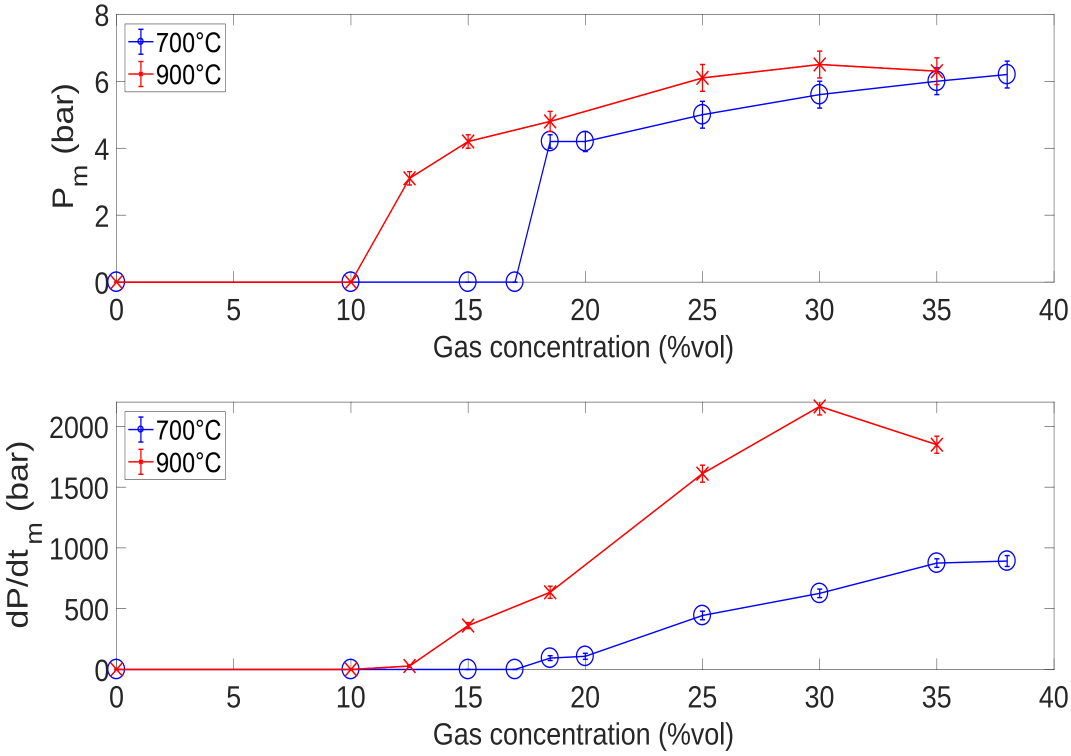

Fig. 4. *Explosion overpressure (top) and rate of pressure rise (bottom) of pyrolysis gases generated at 700 and 900 °C*

3.2.2 Constant Equivalent Ratio experiments

In order to highlight the effect of the pyrolysis step on cellulose explosion, tests were performed on cellulose/pyrolysis gases mixtures in the 20L sphere using the procedure described in section 2. The evolution of the rate of pressure rise and explosion overpressure are shown in Figures 5 and 6.

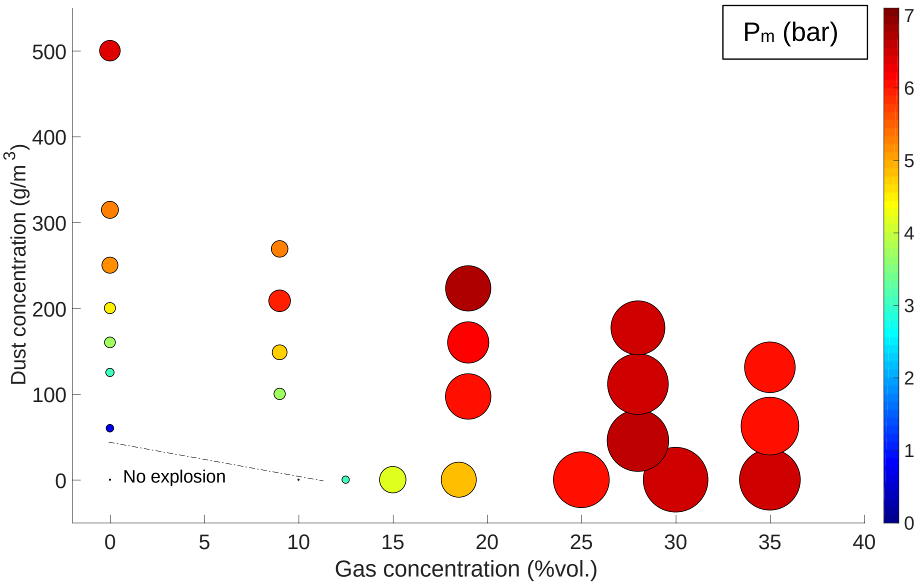

Fig. 5. *Explosion overpressure of cellulose/pyrolysis gases (900°C). The presence of water vapor is considered for hybrid mixtures; no char. Both size and color of the circle are related to P_m*

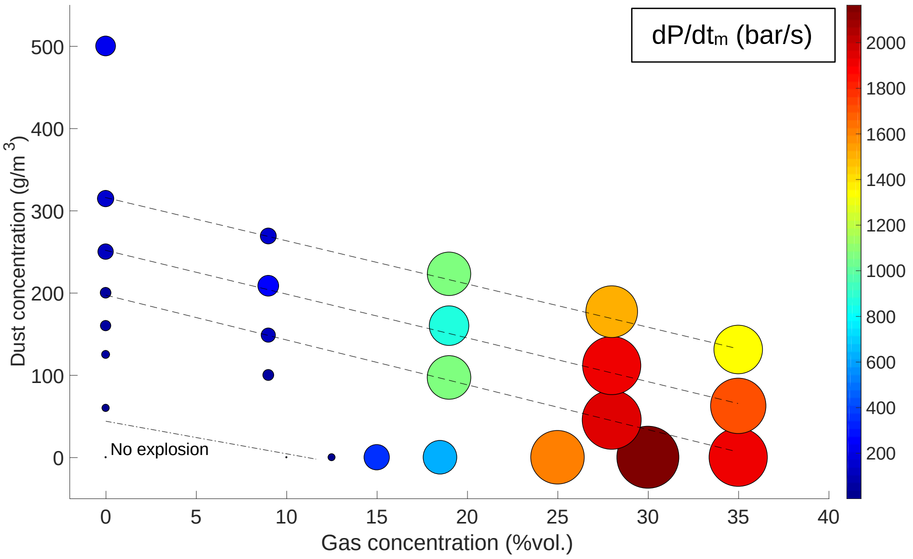

Fig. 6. *Rate of pressure rise of cellulose/pyrolysis gases (900°C). The presence of water vapor is considered for hybrid mixtures; no char. Both size and color of the circle are related to dP/dt_m*

At least three sets of experiments were performed by keeping the fuel equivalence ratio constant, as represented by the dotted lines in Figure 6. The water content generated during the pyrolysis step was considered constant at 8 wt% of the total gases. The explosion test procedure was adjusted by vacuuming the 20L sphere and vaporizing a certain water volume before the gas injection. It appears clearly that the explosion overpressure varies slightly at constant FER (Figure 5). Over the concentration range displayed in Figure 5, the highest explosion pressures were obtained for gas concentrations comprised between 19 and 35 vol% and dust concentrations lower than 300 g/m^3.

The impact of the pyrolysis step on the explosion kinetics is obvious in Figure 6. At a constant fuel equivalence ratio (FER), the rate of pressure rise rate can vary by a factor of 30 depending on the composition of the hybrid mixture. At low FER, the highest rates of pressure rise are obtained for hybrid mixtures and not for pure gas, e.g. 1955 bar/s for a mixture of 28 vol% gas and 0.91 g cellulose compared to 1910 bar/s for 35 vol% pure gas. Although the increase described here is small and remains questionable due to experimental errors, similar trends were obtained for mixtures made from gases generated at 700°C (from 900 bar/s to 1315 bar/s by adding 1 g of cellulose to 38 vol% gases – Figure 7). On the other hand, increasing slightly the gas content from a pure dust-air cloud (left-hand side of Figure 6) does not change significantly its explosion severity. In this specific case, the effect of pyrolysis gas addition on the explosion kinetics is clearly visible for gas concentrations greater than the lower explosible limit. As soon as the local concentration of pyrolysis gases is higher than the LEL, the rate-limiting step of the explosion is no longer the particle pyrolysis but becomes related to the oxidation of the pyrolysis products in homogeneous phase. However, as previously mentioned, this does not mean that the solid particles present in the mixture do not play a specific role in the explosion. This will be particularly highlighted when studying the influence of char.

3.2.3 Constant reactant mass experiments

Tests were also carried out on hybrid mixtures by keeping the reactant mass constant at 10 g, i.e. by testing 10 g of pyrolysis gases, 10 g of cellulose or any combination of x grams of cellulose and y grams of gases (with x + y = 10 g). Results are shown in figure 7 for both gas mixtures. At first, it appears that, whatever the gas mixture, the explosion overpressure remains nearly constant and unaffected by the hybrid mixture composition.

These results also confirm that the maximum value of dP/dt_m is not necessarily obtained for pure gases and that the addition of a slight amount of dust can significantly increase the rate of pressure rise. Moreover, it is confirmed that for high dust concentrations, a gas concentration increases up to 8 vol% does not modify significantly the explosion severity. This assertion is especially true when dealing with the gas generated at 700 °C. For the mix B (900 °C), the high content of hydrogen leads to an increase of the maximum rate of pressure rise, from approximately 1000 bar/s for a mixture of 2 g cellulose and 8 g of mix A to 2080 bar/s with mix B. Again, the impact of both the pyrolysis step and the gas composition on explosion kinetics is then clearly stressed. It should be noted that the influence of particle heating has been neglected due to the small PSD.

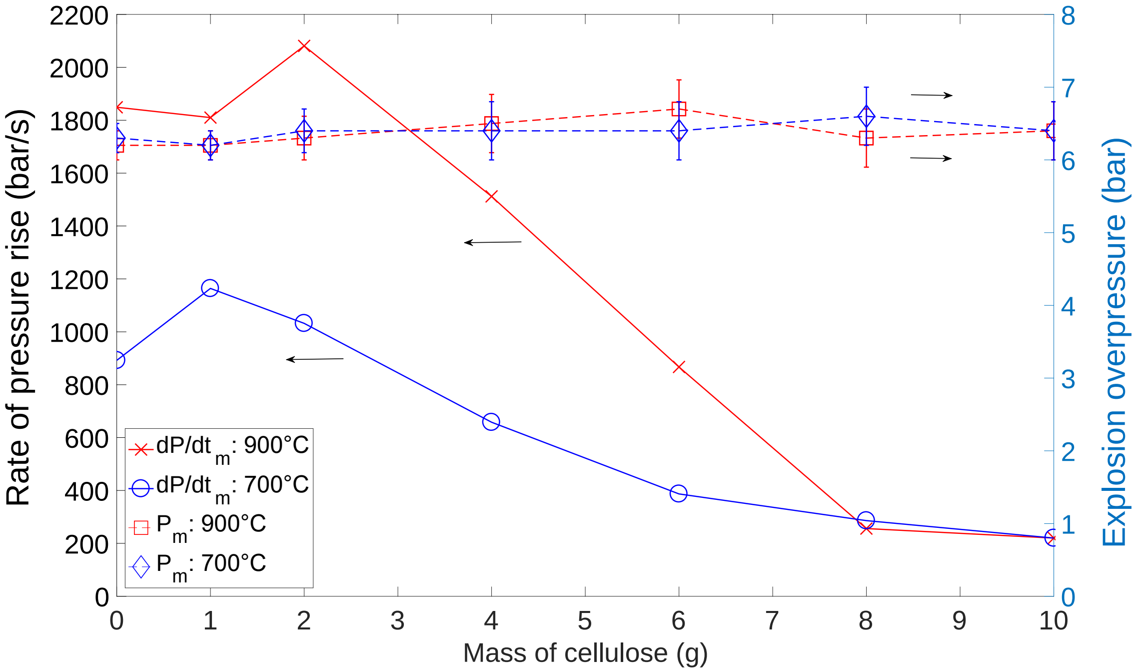

Fig. 7. Explosion severity of cellulose/pyrolysis gases (generated at 900 and 700°C) for a constant reactant mass of 10 g and considering water vapor; no char

3.2.4 Influence of water vapor

The previous experiments were performed by adding water vapor up to 8 wt% of the gas composition, in order to take the water generated by pyrolysis into account. Figure 8 shows a set of tests realized at constant fuel equivalence ratio (FER = 0.7) with or without adding water vapor. A slight pressure decrease is observed when water vapor is added to the reactive mixture; however, this effect should be examined with caution due to experimental uncertainties and can even be considered negligible.

The influence of water vapor on the combustion kinetics appears to be more pronounced, while remaining moderate. Tests performed with hybrid mixtures of mix A (700 °C) and cellulose confirmed that the deflagration index slightly decreases (less than 7 %) when water vapor is added to the reactive mixture. Such effect is especially well known and used in hydrocarbons combustion to reduce the flame temperature and, therefore, decrease the NOx emission.

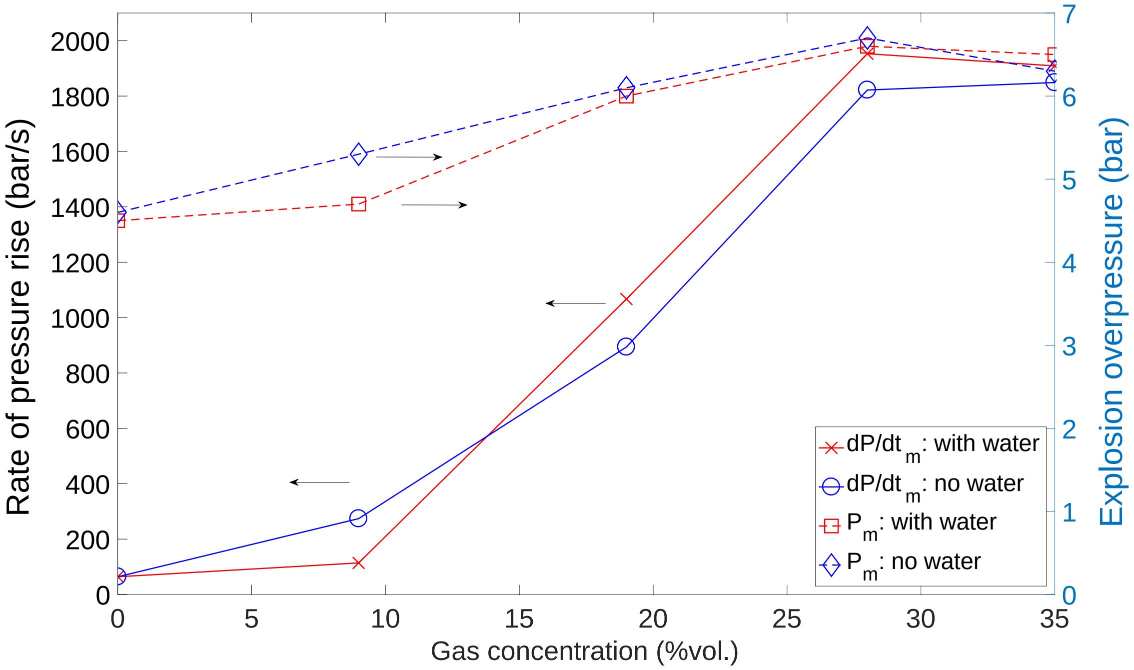

Fig. 8. *Influence of water vapor generated during pyrolysis on the explosion severity of cellulose/pyrolysis gases (generated at 900 °C) for a theoretical fuel equivalence ratio of 0.7; no char*

3.2.5 Influence of char

As described in Figure 2, the products generated by the pyrolysis of an organic particle are mainly permanent gases, water vapor, tars, which can be gasified at high temperatures, and also char. Even if the char quantity is usually low, especially during a flash pyrolysis (between 5 and 10 wt%), it is legitimate to ask if its impact is negligible or not on the dust explosion kinetics. ‘Kinetics’, as from a thermodynamic point of view, the char contribution can be regarded as negligible, which seems to be confirmed by the evolution of the explosion overpressure in Figure 9.

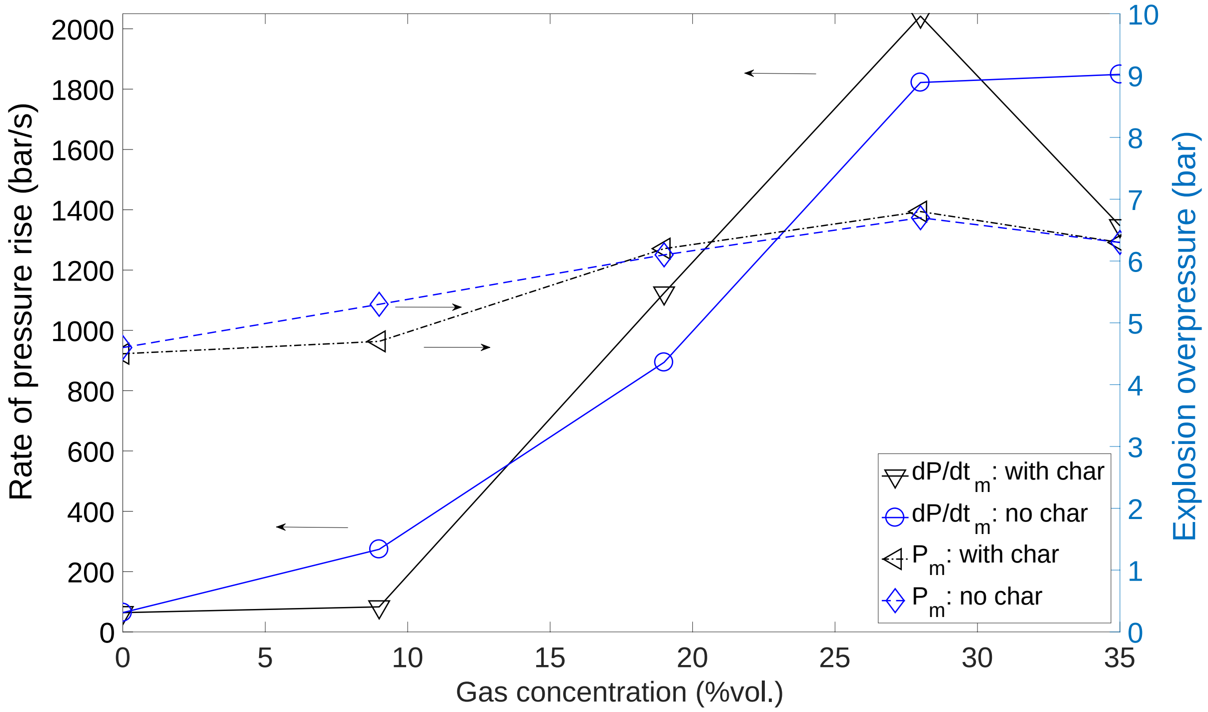

Fig. 9. *Effect of char generated during pyrolysis on the explosion severity of cellulose/pyrolysis gases (generated at 900 °C) for a theoretical fuel equivalence ratio of 0.7; no water vapor*

On the contrary, the rate of pressure rise appears to be influenced by the presence of char, even for very low quantities added (here, only 50 mg). At 28 vol% gas concentration and 0.91 g of cellulose, the addition of char leads to the augmentation of the dP/dt_m from 1955 to 2045 bar/s. Similar tests were performed on mix A and demonstrated a significant increase of the maximum rate of pressure rise from less than 900 bar/s to 1315 bar/s when 100 mg of char was added to pure gases.

Such evolution confirms the positive effect already noticed when a small amount of cellulose is combined to pure gases. The origins of the explosion severity enhancement of these hybrid mixtures can notably be found in the essential role of the powders on the radiative transfer (Torrado, 2017). Nevertheless, their effect on the flame stretching but also the fact that they can act as solid kernels for soot nucleation should also be considered.

4. Conclusions

The role of pyrolysis in an organic dust explosion phenomenon was studied. The influence of the gaseous products, the char and the water was also analysed. Moreover, by the means of the modified configuration of the Godbert-Greenwald furnace was possible to underline the role of the temperature of the pyrolysis step in a dust explosion. The main conclusions are:

i) Keeping both the fuel equivalence ratio or the reactive mass content constant is not sufficient to obtain the same rate of pressure rise for hybrid mixtures of cellulose and pyrolysis gases. Pyrolysis reaction is then the rate-limiting step during an organic dust explosion, as long as the particle heating is very fast.

ii) The presence of a sufficient amount of pyrolysis gases around the particles enhances the explosion kinetics, but replacing all or part of an organic powder by its pyrolysis gases modifies very little the energetic content of the hybrid mixture and thus the explosion thermodynamics.

iii) The hydrogen fraction in the gaseous mixtures, and therefore, the temperature at which the pyrolysis takes place, had a strong influence on the explosion sensitivity as well as on the combustion kinetics. During the development of an organic dust explosion, the flame temperature evolves as well as the pyrolysis gases composition, which impacts the flame propagation dynamics.

iv) The amount of solid particle, char or unburnt cellulose, present ahead of the flame front plays an important role on the flame propagation, as it increases significantly the radiative heat transfer towards the pre-heating zone.

v) The water vapor produced during the pyrolysis does not affect greatly the thermodynamic of the combustion reaction, but it seems to slightly influence the kinetics by modifying the flame temperature.

In conclusion, studying hybrid mixtures reveals several aspects of organic dust explosion and appears to be essential to better understand and model this phenomenon (Pico et al., 2020). More than a particular case, this makes hybrid mixtures explosion ‘a common case’.

References

Abbas, Z., Gabel, D., Krietsch, A., Krause, U. (2022). Quasi-static dispersion of dusts for the determination of lower explosion limits of hybrid mixtures *Journal of Loss Prevention in the Process Industries*, 74, art. no. 104640.

Cloney, C.T., Ripley, R.C., Pegg, M.J., Amyotte, P.R. (2017). Evaluating regime diagrams for closed volume hybrid explosions, *Journal of Loss Prevention in the Process Industries*, 49: 912-918.

Commandré, J.-M., Mahmidi, H., Salvador, S. & Dupassieux, N. (2011). Pyrolysis of wood at high temperature: The influence of experimental parameters on gaseous products. *Fuel Processing Technology*, 92: 837-844.

Dufaud, O., Perrin, L., Traore, M., Chazelet, S. & Thomas, D. (2009). Explosions of vapour/dust hybrid mixtures: A particular class. *Powder Technology*, 190: 269-273.

Funazukuri, T., Hudgins, R. R. & Silveston, P. L. (1986). Product distribution in pyrolysis of cellulose in a Microfluidized bed. *Journal of Analytical and Applied Pyrolysis*, 9: 139-158.

Graham, R. G., Mok, L. K., Bergougnou, M. A., De Lasa, H. I. & Freel, B. A. (1984). Fast pyrolysis (ultrapyrolysis) of cellulose, *Journal of Analytical and Applied Pyrolysis*, 6: 363-374.

Guo, C., Shao, H., Jiang, S., Wang, Y., Wang, K., Wu, Z. (2020). Effect of low-concentration coal dust on gas explosion propagation law, *Powder Technology*, 367: 243-252.

Paulsen, A. D., Mettler, M. S., & Dauenhauer, P. J. (2013). The role of sample dimension and temperature in cellulose pyrolysis, *Energy & Fuels*, 27(4): 2126-2134.

Pico, P., Ratkovich, N., Muñoz, F., Dufaud, O. (2020). Analysis of the explosion behaviour of wheat starch/pyrolysis gases hybrid mixtures through experimentation and CFD-DPM simulations *Powder Technology*, 374: 330-347.

Pietraccini, M., Delon, E., Santandrea, A., Pacault, S., Glaude, P.-A., Dufour, A. & Dufaud, O. (2021). Determination of heterogeneous reaction mechanisms: A key milestone in dust explosion modelling. *Journal of Loss Prevention in the Process Industries*, 73: 104589.

Piskorz, J., Majerski, P., Radlein, D., Vladars-Usas, A. & Scott, D. S. (2000). Flash pyrolysis of cellulose for production of anhydro-oligomers. *Journal of Analytical and Applied Pyrolysis*, 56: 145-166.

Ranzi, E., Amaral Debiagi, P. E. & Frassoldati, A. (2017). Mathematical modeling of fast biomass pyrolysis and bio-oil formation. Note I: Kinetic mechanism of biomass Pyrolysis. *ACS Sustainable Chemistry & Engineering*, 5: 2867-2881.

Sanchirico, R., Russo, P., Saliva, A., Doussot, A., Di Sarli, V., Di Benedetto, A. (2015). Explosion of lycopodium-nicotinic acid–methane complex hybrid mixtures, *Journal of Loss Prevention in the Process Industries*, 36: 505-508.

Spitzer, S., Schröder, V., Askar, E., Krietsch, A. (2020). Developments on determination procedures for safety parameters of explosion protection for hybrid mixtures [Entwicklungen zu bestimmungsverfahren für sicherheitstechnische kenngrößen des explosionsschutzes für hybride gemische] *VDI Berichte*, 2376: 3-15.

Taveau, J.R., Going, J.E., Hochgreb, S., Lemkowitz, S.M., Roekaerts, D.J.E.M. (2017). Igniter-induced hybrids in the 20-l sphere, *Journal of Loss Prevention in the Process Industries*, 49: 348-356.

Torrado, D., Effect of carbon black nanoparticles on the explosion severity of gas mixtures (2017). PhD thesis from University of Lorraine, Nancy, France (in English).

Wang, Q., Song, H., Pan, S., Dong, N., Wang, X. & Sun, S. (2020). Wang (2020) Initial pyrolysis mechanism and product formation of cellulose: An experimental and Density Functional Theory (DFT) study. *Nature Scientific Reports*, 10: 3626.

Zanzi, R., Sjöström, K. & Björnbom, E. (1996). Rapid high-temperature pyrolysis of biomass in a free-fall reactor. *Fuel*, 75(5): 545-550.

DOI: 10.7795/810.20221124

Experimental study on inert products, moisture, and particle size effect on the minimum ignition energy of combustible dusts

Isabel Amez [a,b], Blanca Castells [a,b], *David León* [a,b], Javier García-Torrent [a,b] & Ljiljiana Medic [a,b]

[a] Universidad Politécnica de Madrid (UPM), Madrid, Spain
[b] Laboratorio Oficial J.M. Madariaga (LOM), Madrid, Spain

E-mail: isabel.amez@upm.es

Abstract

Handling combustible dusts not only continues to pose a risk to industry but can also affect the safety of society. Explosion risk could be avoided or mitigated trying to guaranty an inherent safety throughout the product life chain. One way to reduce the risks when dealing with combustible dusts is to increase the Minimum Ignition Energy (MIE) in order to decrease combustible dust ignition sensitivity. To achieve this decrease, the inertization technique, also known as moderation, will be used. It consists of adding inert powders or humidity to the combustible dusts. As sometimes end-users also must deal with the handling of flammable dusts, this study aims to find the most optimal inert for toner waste from printers and Holi powder (organic coloured dust from Indian parties), taking Lycopodium as a reference. Calcium carbonate, sodium bicarbonate and gypsum are proposed as inert materials. In addition, with the aim of giving a second use to biomass boiler waste or boiler slagging, this waste will be analysed as inert, as well as how humidity affects the combustible dusts. Then, sodium bicarbonate will be tested at different granulometries to evaluate the effect of particle size on moderation process. The tests were carried out in the modified Hartmann apparatus or MIKE 3.0. Mechanisms such as decomposition of inert dust have been analysed by thermogravimetric analysis (TGA)). The results show that gypsum and moisture are the best performing inert followed by calcium carbonate. Boiler slagging and solid bicarbonate contribute to a decrease in the MIE in some of the tests. The reasons for this deviation are discussed in the presented article. When sodium bicarbonate is analysed at different particle sizes, it is found that the optimum particle size does not match the particle size of the combustible dust. According to the tests, there is an optimum point for which the inert powder provides better results.

Keywords: *hazards, mitigation, moderation, dust explosions, industrial explosions*

1. Introduction

Dust explosions continue to be a challenge for industry, which unfortunately has had to cope with numerous human losses (Eckhoff 2020; Yuan et al. 2015). Despite continuous research and implementation of prevention measures, technological developments present new risks that need to be investigated (Fernandez-Anez et al. 2020). Improving the efficiency of some processes involves changes in the physical properties of the powder. If these changes result in a decrease in particle size or moisture content of the dust, the risk of explosion may be increased. One example is biomass torrefaction, which increases the risk of ignition, or the particle size decrease in some pharmaceutical processes (Castells, Amez, Medic, and García-Torrent 2021). Likewise, toner production for printers has improved considerably in recent years. As a result, toner powder has been reduced from 14-16 µm to 8-10 µm to improve image resolution (Nifuku et al. 2005). Moreover, it is expected that its size could be lower in the coming years (Addai, Gabel, and Krause 2016).

But the risk of handling flammable dust does not only affect industry. Some powders are manufactured for recreational purposes. Hence, there is a risk not only in the production processes but also in their end-use. This is the case of Holi dust, which originates from an Indian festival ((FOPH) 2017). Its use has spread in recent years, especially for outdoor parties. Their organic origin implies a risk of explosion, which was confirmed in 2015 in Taiwan when more than 500 people were injured after a cloud of Holi dust ignited inside a club (Hutcherson, Botelho, and Wang 2015).

Risk assessments characterize critical flammability parameters, Minimum Ignition Energy (MIE) being one of them. MIE helps to quantify the ignition sensitivity of dust and is defined as the lowest energy required to ignite a dust cloud. This parameter has been extensively studied in recent years due to the study of combustible dust dispersion (Bagaria, Hall, et al. 2019; Eckhoff 2004, 2019). The method and equipment required to obtain this parameter are defined in the EN ISO-IEC 80079 standard (European committee for standardization CEN-CENELEC 2017). The interest of researchers in this parameter lies in the ignition source it studies. Electrostatic discharges, electric sparks and hot surfaces are some of the most common ignition sources. Studies generally focus on specific substances, so fewer data are found on dust mixtures. (Chaudhari et al. 2019).

Adding non-combustible or inert dust to flammable dust is an effective way to reduce explosion risk and ignition sensitivity (Bu et al. 2020). This principle of inerting could be considered as inherent safety (moderation) (Amyotte et al. 2007). This technique is currently applied in industry but has two major issues to solve. One is the tendency to facilitate ignition of the dust cloud by adding small amounts of inerts. Recent research suggests that low inert concentration ranges result in inefficient inertisation that can reduce MIE and Minimum Ignition Energy (MIT) (Cai et al. 2019). The main contributor to this effect is the improvement of dust dispersibility in the presence of inerts, which results in a more dispersed dust cloud (Bu et al. 2020; Han et al. 2020). This phenomenon can lead to an increase in the maximum explosion pressure and is named Suppressant Enhanced Explosion Parameter (SEEP). This effect is greatest in gas-generating inerts, such as sodium bicarbonate (Jiang et al. 2019).

The segregation phenomenon occurring during dust dispersion also requires further clarifications. This phenomenon occurs when the differences between particle size on inerts and flammable dust are large, also resulting in low inerting efficacy (Janès et al. 2014). According to bibliographic results, particle size distribution is a key parameter in inerting efficiency (Huang et al. 2019). Larger particles generally have a faster volatilisation rate. If the larger particles are the inhibiting particles, the thermal effect predominates over the chemical effect of the inert reducing the quality of the inertisation (Bu et al. 2020; Castells, et al. 2021). Therefore, it is generally stated that as the particle size of the inert material decreases, the efficiency of the inertisation phenomenon increases (Jiang et al. 2018). This trend is the opposite of that observed for flammable dusts where it is understood that the larger the particle size, the lower the risk of explosion (M. C. Wei et al. 2020). Inert effectiveness is based on the amount of inert needed to prevent propagation. Inerts substances are added for two main purposes. The first is to prevent the explosion of the explosive atmosphere, and the second is to prevent combustible dust from becoming suspended.

The inert choice will depend mainly on the physicochemical properties of the combustible dust. Currently, the substances used in the moderation technique can be divided into inert substances and active chemical explosion suppressants (X. Wei et al. 2021). The inert substances block heat transfer by absorption and the suppressants act through the endothermic decomposition reaction that takes place and can interrupt the chain reaction. For industry, the choice of inert material is a key factor in ensuring the economic viability of products. Thus, the amount of inert material required should be as low as possible and should not affect the final quality of the product.

Calcium carbonate and sodium bicarbonate, are some of the most common inert due to their low cost and availability (Addai, Gabel, and Krause 2016; Chaudhari et al. 2019; Yang et al. 2019). However, it is of great relevance to find new inert to maximize the value chain of the processes. This refers to the valorisation of waste by using it as inert material in other process steps (Nifuku et al. 2005). Thus, the circular economy is promoted by using waste to reduce explosion risk. This study will explore this idea using boiler slagging as an inert. Boiler slagging is the biomass ashes residue collected after combustion in power plants. In addition, calcium carbonate, sodium bicarbonate, gypsum, and moisture will be analysed as inert materials.

In this present paper, three combustible dusts (lycopodium, toner waste, and Holi dust) were mixed with four inert dusts (calcium carbonate, sodium bicarbonate, and gypsum) to determine their MIE at different concentrations. To avoid low inert concentrations, inert mixtures between 30% and 70% have been used. Moreover, the effect of moisture on the MIE will be analysed for the three combustible dusts. To analyse the thermal mechanisms of the inerts, a thermogravimetric analysis (TGA) will be carried out. Finally, the particle size of sodium bicarbonate will be varied to study the effect of particle size on the MIE. The results will be analysed by means of flammability maps comparing the particle size of combustible and inert dusts with the MIE.

2. Materials and methods

2.1 Materials

Industrially relevant dusts such as toner waste were chosen because of their low MIE values in air. Due to its complexity of production, the composition of toner varies significantly from company to company. It is generally composed of carbon, iron, chromium, copper, inorganic cyanides, styrene acrylate copolymer, polyester resin, and thermoplastic particles (Addai, Gabel, and Krause 2016). Electrically conductive and magnetic metals are of particular importance (Castellanos et al. 2014). The printers transfer the pigment powder to the paper by means of a series of electrical discharges, which generate heat and the ink is impregnated into the paper. Most of the components of toner waste can be recycled, but there are two basic problems with waste management. Firstly, it is highly polluting and secondly, there is an associated explosion risk to handling toners. The sample used for this research was provided by a Spanish company that manages waste toner.

Holi powders were selected because of their handling risk and the lack of existing studies analyzing their flammability. These are mainly composed of corn starch (99% by weight) and food dye. The main purpose of this dust is to generate large clouds of color which produce explosive atmospheres when dispersed in enclosed spaces. Flammability results of Holi dust and toner waste will be compared with Lycopodium as a reference substance. Lycopodium clavatum is a medicinal plant spore commonly used in flammability investigations because of its flowability, dispersibility, monodispersity, and combustibility. Their shapeless particle size distribution results in low-variable explosion characteristics (Bagaria, Li, et al. 2019; Janovsky et al. 2019). The sample used for this research is 100% natural Lycopodium.

The inert substances used in this study are calcium carbonate, sodium bicarbonate, boiler slugging, gypsum, and moisture. Calcium carbonate is the most widely used material for inerting combustible dust due to the ease of modifying its granulometry and its low cost. It is also suitable for human consumption, so it is of great utility for organic dust. The same applies to sodium bicarbonate. Besides these common inerts, gypsum will be used in this study. Gypsum is a mineral compound that is easily compacted when wetted. Its contact with some sensitive parts of the human body can irritate, so it is not commonly used as an inert.

The use of inert materials implies an extra cost for production and transport processes, so using waste as inert material can be an advantage for industries. Hence, the residue from the combustion of biomass power plants will also be used in this study. Boiler slagging results in a fine ash dust, of varying composition, which could be used as inert.

2.1.1 Dust characterization

Moisture content is a relevant property as it directly affects the flammability characteristics. Moisture content was obtained using a Mettler Toledo HB43 halogen analyzer. The temperature range was set at 105 ºC ±1ºC. Particle size distribution was determined by laser diffraction with a Mastersizer 2000, that allows particle distribution curve together with d10, d50 and d90 parameters. All the samples were tested as received. Moisture content and particle size distribution for all the sampled are collected in table 1 and table 2 and figure 1.

Table 1: *Particle size distribution and moisture content of combustible dust explosions*

Sample	Abbreviation	Molecular formula	d10 [µm]	d50 [µm]	d90 [µm]	Moisture [%]
Lycopodium	LY	$C_{5.77}H_{9.59}O_{1.23}S_{0.001}N_{0.08}$	23.91	32.31	43.30	2.46
Toner waste	TO	$C_{7.17}H_{7.75}O_{0.33}$	4.29	6.64	10.19	0.72
Holi dust	HO	$C_6H_{10}O_5$ + additives	9.24	13.83	20.25	10.04

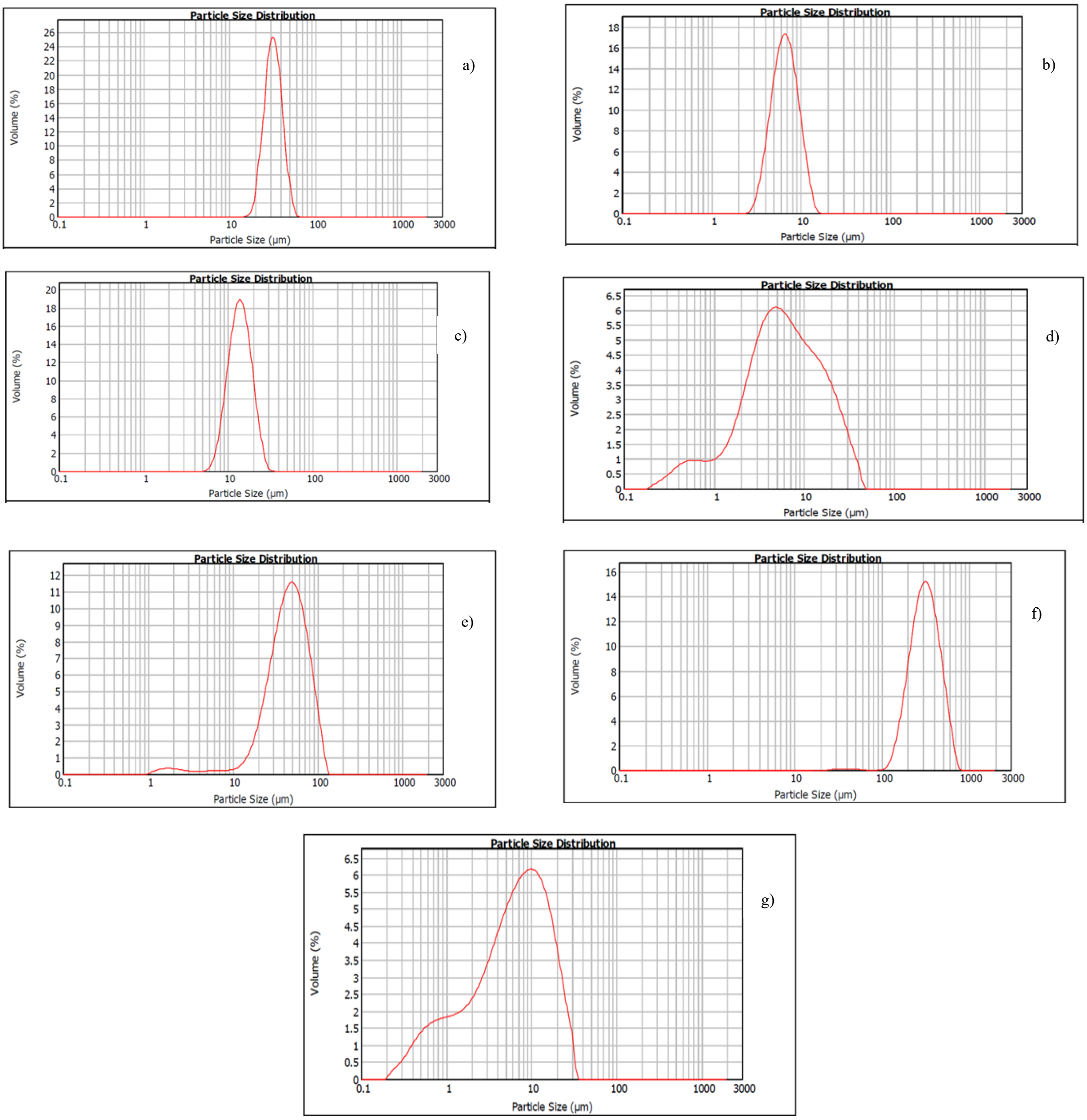

Fig. 1.*Particle distribution curves a) Lycopodium b) Toner c) Holi dust d) Calcium carbonate e) Sodium bicarbonate f) Sodium bicarbonate g) Gypsum.*

***Table 2:** Particle size distribution and moisture content of inerts*

Sample	Abbreviation	Molecular formula	d10 [µm]	d50 [µm]	d90 [µm]	Moisture [%]
Calcium carbonate	CC	$CaCO_3$	1.41	5.74	20.36	0.13
Sodium bicarbonate	SB-1	$NaHCO_3$	188.22	311.79	504.79	35.68
Gypsum	GY	$CaSO_4\ 2\cdot H_2O$	0.88	6.29	18.19	14.42
Boiler slagging	SL	-	21.04	45.72	83.58	0.51

2.1.2 Minimum ignition energy

The inerting study was conducted in a modified MIKE3 MIE apparatus which is commonly used in investigations for testing ignition sensitivity. The explosion occurs inside the Hartman tube, which is a 1.2 L modified glass tube with a mushroom-shaped powder dispersion system at its base. The dust dispersion is triggered by a 7 bar compressed air blast. This blast is responsible for the dust cloud and the corresponding turbulence. The spark is created by two electrodes about one-third of the distance from the base, which is about 6 mm apart. The device allows adjusting the energy of the spark at 1, 3, 10, 30, 100, 300, and 1000 mJ. The ignition time delay can be also adjusted at 90, 120, 150, and 180 ms. Tests have been carried out in accordance with the ISO IEC 80079-20 (European committee for standardization CEN-CENELEC 2017)standard. The test conditions shall be at a temperature between 20°C and 25°C and a pressure between 0.8 bar and 1.1 bar.

2.3. Thermogravimetric analysis

Thermogravimetric Analysis was performed using a Mettler Toledo TGA/DSC 3+, placing 60±1 mg of sample inside a 70 µL crucible and applying air atmosphere inside the furnace. The test conditions were the following:

- Initial temperature: 30 ºC
- Final temperature: 800 ºC
- Heating rate (β): 10 K/min

Furthermore, when 800 ºC are achieved, the temperature remains constant for 5 minutes to stabilize the final mass.

From TGA, differential thermogravimetry curve (DTG) is defined as TG curve first derivative. Both curves provide important data such induction temperature, which is the temperature at which the combustion reaction accelerates, maximum weight loss temperature, which is the temperature at which the maximum rate of mass loss is produced, and final mass percentage, which provides information regarding the completion of the reaction.

3. Results and discussion

3.1 Minimum ignition energy of combustible dust

Inert material addition can affect the homogeneity of the dust cloud, leading to increased initial turbulence, which can significantly affect the ignition energy (Addai, Gabel, and Krause 2016). Before mixing, MIE of combustible dust and inert substances was obtained experimentally. Table 3 shows the results obtained. It was confirmed that boiler slagging does not show ignition sensitivity.

***Table 3:** MIE results of combustible dust*

Parameter	Lycopodium	Toner waste	Holi dust
MIE (mJ)	14.0	2.1	79.0
Optimum concentration (mg)	1200	750	3000

Optimum delay time (ms)	120	120	60

In general, there is an increasing trend in the MIE which results in a decrease in the ignition sensitivity of combustible dust as the inert proportion increases. The permissible range of the inert mixture to minimize ignition risk has been found to be between 60% and 80%. Although lycopodium has a higher MIE than toner waste, the inerts used in this study were less effective for lycopodium. On the other hand, Holi powders obtained the best inertisation results for the inerts studied, in other words, Holi dust was found to be more susceptible to the inert materials. Finally, the toner waste could reduce its ignition sensitivity significantly with 60% gypsum.

If inert materials are compared, it is noticed that sodium bicarbonate tends to be less effective compared to the other inerts. The mixture is fully inertised only for Holi powders, which require more than 70% sodium bicarbonate. In addition, figures 2, 3, and 4 show a decrease in MIE that is related to the SEEP effect of sodium bicarbonate. This effect of sodium bicarbonate has been observed in previous research and occurs mainly due to the emission of gases. (Jiang et al. 2018). Compound impurities play a key role in this process.

Boiler slagging is effective in inertising Holi powders, requiring 50% to reach 1000mJ (figure 4). When toner is inertised with boiler slagging (figure 3), MIE decreases for concentrations below 60%. From this point on, an increasing trend in the MIE is observed. This trend is also observed in figure 2 for lycopodium dust. The chemical composition of boiler slagging is complex and can vary significantly depending on combustion process conditions. The presence of unburned fuels can affect ignition sensitivity in several respects. These particles may have particle sizes larger than those of ash, which may have an effect on dust cloud dispersion. On the other hand, the chemical nature of the unburned particles is very relevant for this study. If these are non-reactive substances, the effect on the MIE may be similar to that of ash. However, if they are reactionary in nature, such as biomass, the presence of small particles of this type may affect the ignition of the cloud. The presence of these particles, as well as gases such as CO_2, might affect processes such as the cooling effect or the absorption of radiation. If inert particles face the propagating flame, the flame cools down, and its velocity changes. However, if these particles are reactive, this propagation speed can increase.

Besides the addition of an inert, the moisture content was also analyzed as a moderation technique. This technique proves to be effective for Holi powders and lycopodium, but not for toner residue.

Optimization of inerts is essential to ensure the effectiveness of the prevention measure. But it is also essential to ensure that the inert dust meets the required standards for the final product. Thus, although figure 4 highlights moisture as the most effective measure for increasing the EMI of Holi powder, the compaction involved makes it unsuitable for end-use. However, it is possible to apply it to treat the residues of this dust. As for toner waste, given that it is a product not intended for use, all the measures studied could be applied. The cost of adding inerts must also be taken into account. The smaller the amount of inert dust added for inertisation, the lower the cost of implementing the measure.

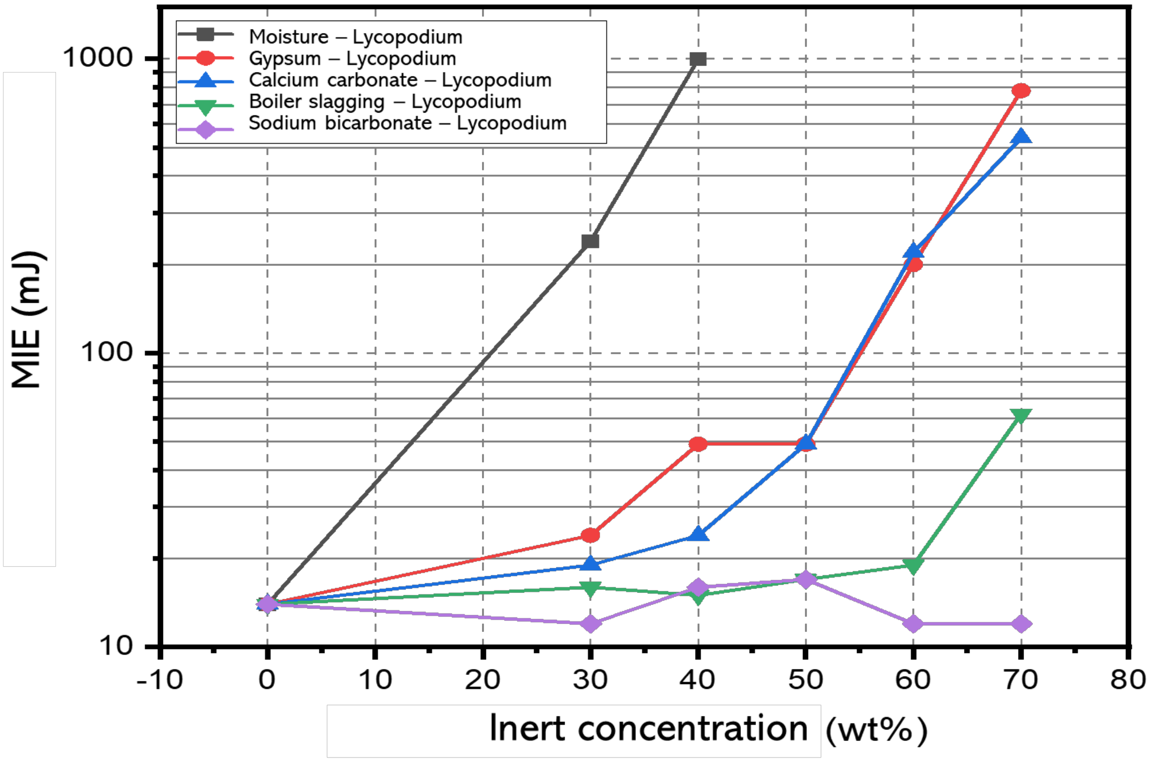

Fig. 2. Effect of the concentration of four inert powders and moisture on the MIE of Lycopodium.

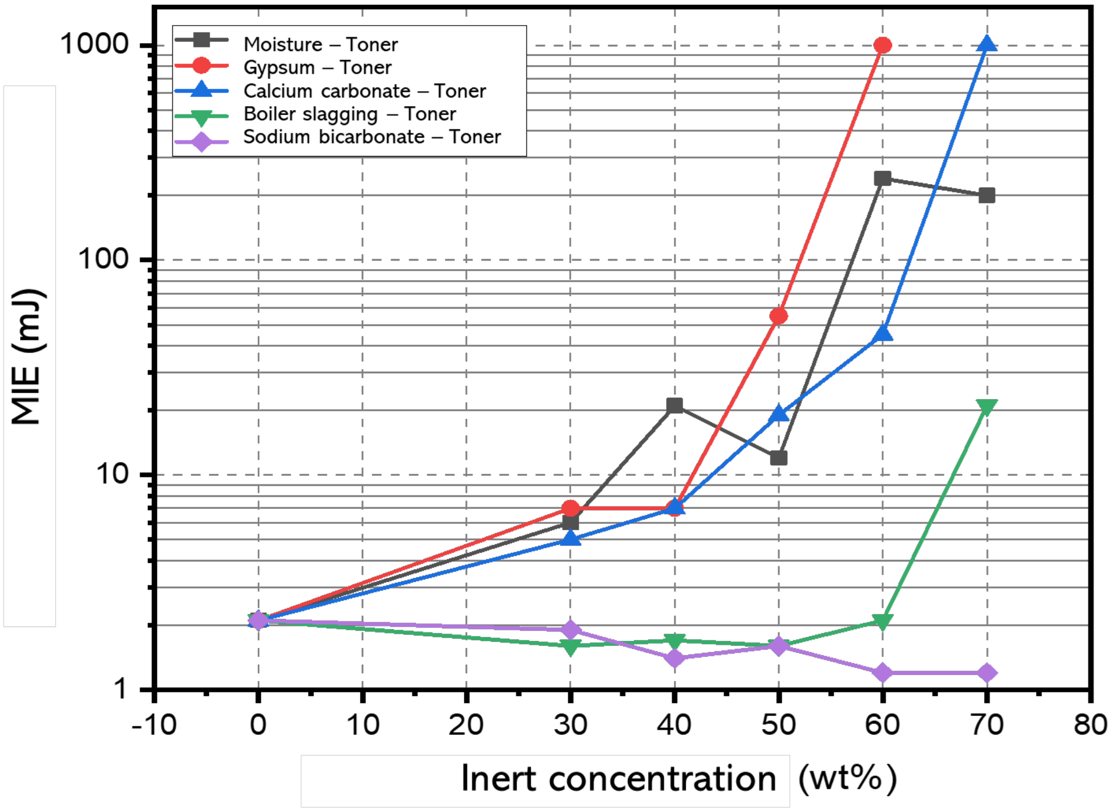

Fig. 3. Effect of the concentration of four inert powders and moisture on the MIE of Toner waste.

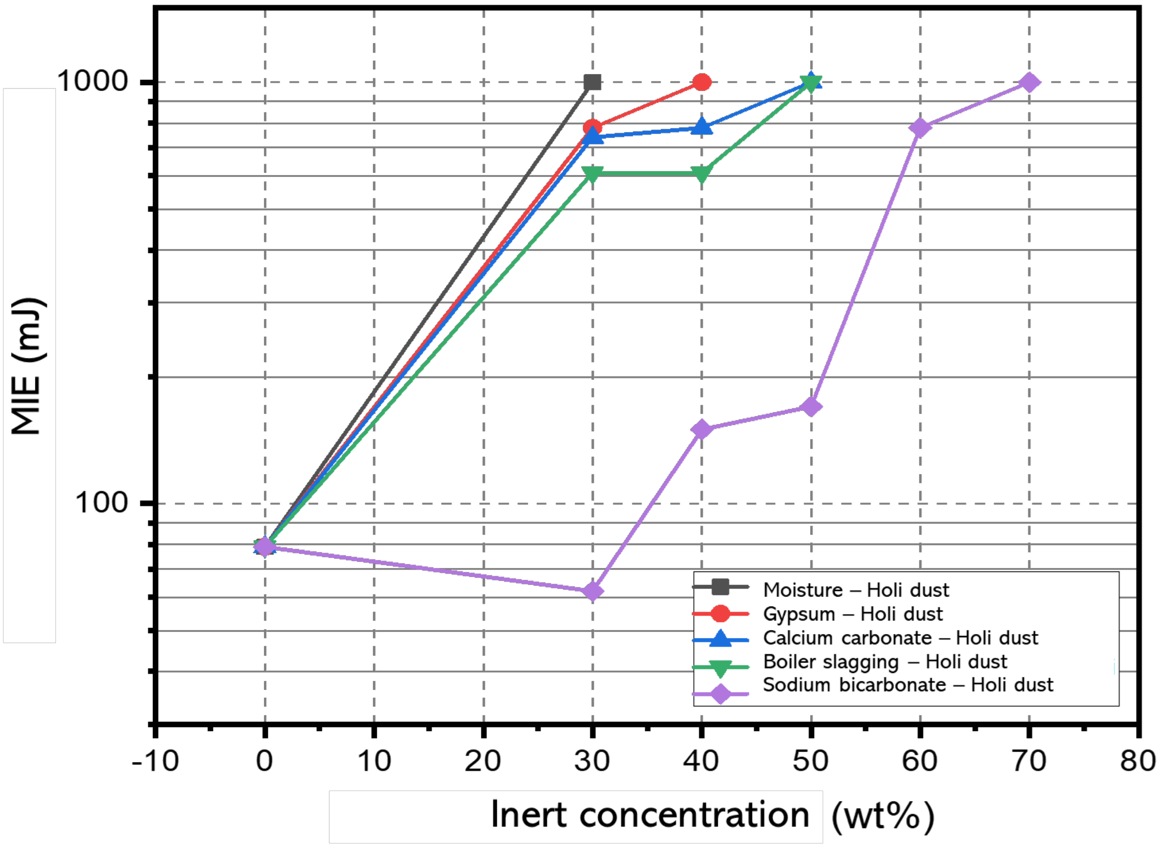

***Fig. 4.** Effect of the concentration of four inert powders and moisture on the MIE of Holi dust.*

3.2 Granulometry effect on minimum ignition energy

Particle size plays a key role when approaching combustible dust inertization. To analyze particle size influence on the inertization processes using the modified Hartman tube, three different particle sizes for sodium bicarbonate were used. Identification and particle size parameters are shown in table 4. The first particle size coincides with the one analyzed in figures 2, 3, and 4 (SB-1). The second particle size is obtained by grinding the initial sample. It is then passed through a 300 µm sieve (SB-2). The third sample is purchased from a manufacturer who assures an average particle size of 75 (SB-2). However, when the particle size is determined, this is not the case.

***Table 4:** Particle size distribution of sodium carbonate at different granulometries*

Sample	Abbreviation	d 10 [µm]	d 50 [µm]	d 90 [µm]
Sodium bicarbonate	SB-1	188.22	311.79	504.79
Sodium bicarbonate	SB-2	8.910	161.143	283.549
Sodium bicarbonate	SB-3	5.466	119.998	254.026

Figure 5 show a different inertization trend for sodium bicarbonate than the one analyzed above in figures 2, 3, and 4. Ground sodium bicarbonate (SB-2) does not facilitate ignition for low amounts of inert as opposed to the initial sample (SB-1). In fact, although SB-3 sodium bicarbonate has a lower particle size than SB-2, the results are better for the SB-3.

In accordance with the criteria set out in ISO/IEC 80079-20, the Holi powder would be inertised with 30% sodium bicarbonate SB-2. If SB-3 bicarbonate is used, the amount of inert required to inert the sample would be higher than 70%. This difference is also observed for lycopodium and toner residue. According to the results shown in figures 5 and 5, 60% and 40% SB-2 are respectively needed to reach 1000 mJ without ignition, while SB-3 does not inert the sample.

SB-3 records MIE lower than the initial MIE of the toner (2.1 mJ) in the same way as SB-1. The main difference between SB-2 and SB-1 and SB-3 may be the particle shape. When grinding the sample, the particles size decrease but particle breakage can also take place. This may have implications for particle dispersion which, in this case, have improved inerting capacity. On the other hand, in view of the results, it could be concluded that there is an optimum particle size for inerting combustible dust, which does not need to be the minimum particle size.

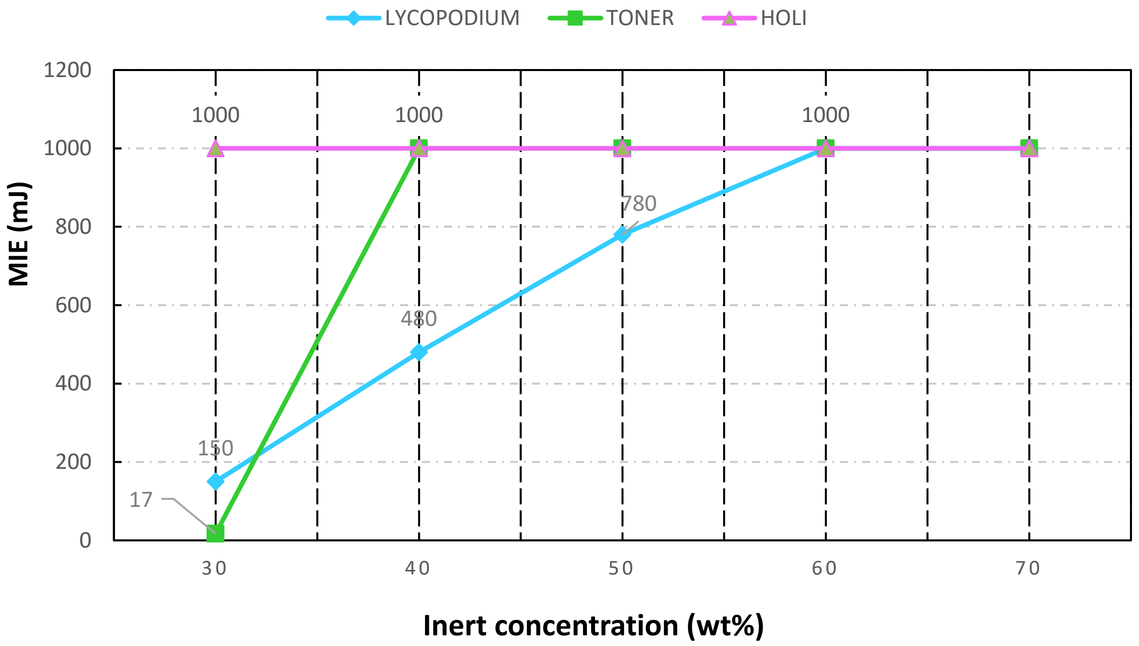

Fig. 5. Effect of the concentration of SB-2 on the MIE of the three combustible dust

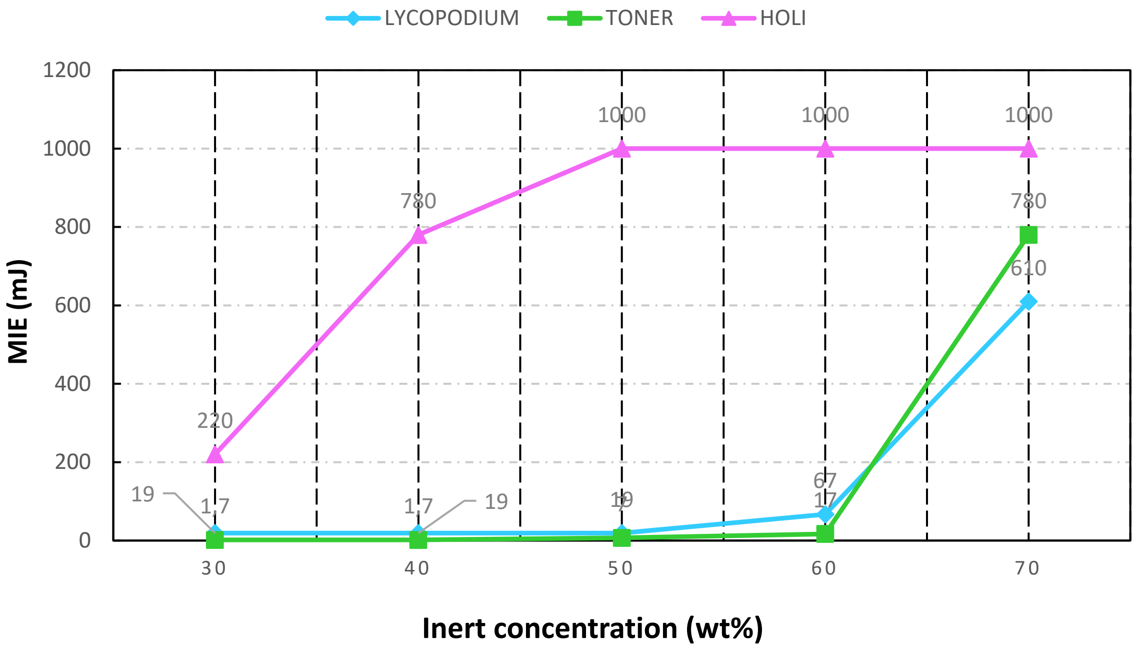

Fig. 6. Effect of the concentration of SB-3 on the MIE of the three combustible dust

3.3 Thermal degradation mechanism analysis

Inerting efficiency depends on thermodynamic mechanisms that can promote cloud cooling and modify physicochemical ignition conditions. The heat balance will therefore be a relevant parameter of the efficiency (Abbasi and Abbasi 2007). Heat balance is a broad concept, but according to recent research, thermal decomposition will be a predominant mechanism. Figure 7 shows the results obtained after applying thermogravimetric analysis (TGA) under an air atmosphere conditions to BS-1 and BS-2 sodium bicarbonate, calcium carbonate, and gypsum. The results of the boiler slagging are discarded as its inert content has prevented the obtaining of analyzable results.

Calcium carbonate, sodium bicarbonate, and gypsum only have a single mass loss stage in the thermal ramp studied. The induction temperature (IT) is reached at 114.25 ºC for gypsum, at 120.75 ºC for sodium bicarbonate SB-1, and at 141.84 ºC for SB-2. The thermal degradation mechanisms of SB-1 and SB-2 are very similar, although the decomposition processes of SB-2 begin approximately 20K later than those of SB-1. Although the difference is slight, there is an impact on the thermal degradation mechanisms due to the decrease in particle size and the change in particle shape. Calcium carbonate starts its thermal degradation processes at 710 ºC, which implies that it is a compound that is not very reactive to temperature increase, proving to be the most stable of the inerts analyzed.

In all cases, the IT is recorded after 100 °C. Generally, the first phase of mass loss is directly related to moisture loss, which ends at around 105 °C. However, the decomposition processes of the three substances studied start after this threshold. These results differ from what was expected especially for sodium bicarbonate, which has a moisture content of 35%. Devolatilization of the compound is the next predominant process, which in all cases occurs rapidly. The final mass percentage exceeds 60% in all samples, which represents ash content. The high values of final mass indicate that the analyzed compounds contain a low percentage of volatile matter. This implies that they are more stable compounds and therefore less reactive than combustible dust. The samples have a higher ash content which is not affected by high temperatures. The minimum peak recorded on the DTG curve indicate the maximum weight loss temperature (MWLT) of each substance, which represents the temperature at which greatest volatilization rate is produced. Thermal decomposition processes occur in small temperature ranges for all substances. While the MWLT of gypsum and sodium bicarbonate for both particle sizes are between 130 and 170 ºC, that of calcium carbonate is at 800.48 ºC.

Rapid weight loss implies low emission of volatiles. However, the CO_2 and H_2O emission during the degradation processes could contribute to the cooling mechanisms. CO_2 is a molecule with high power to absorb radiation and therefore heat. It is also important to note that the presence of these gases, i.e., diluent gases, can contribute to the displacement of oxygen from the surrounding atmosphere, thus reducing the risk of explosion.

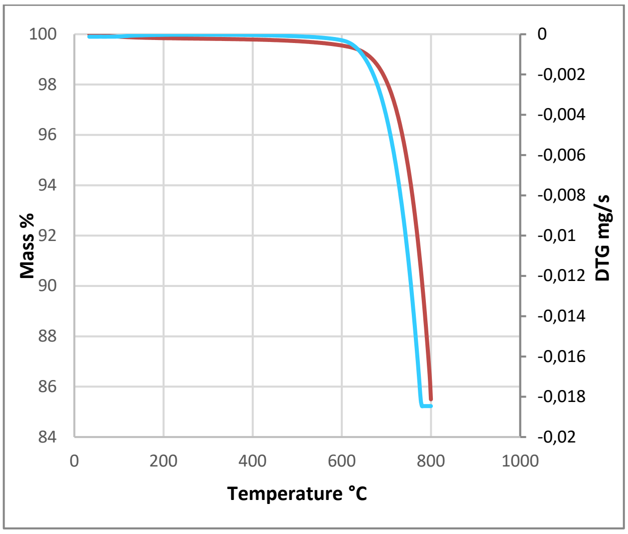

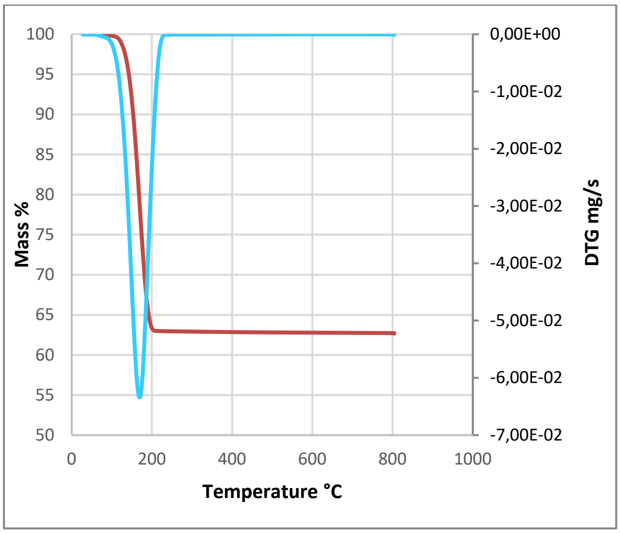

a) Calcium carbonate b) Sodium bicarbonate SB-1

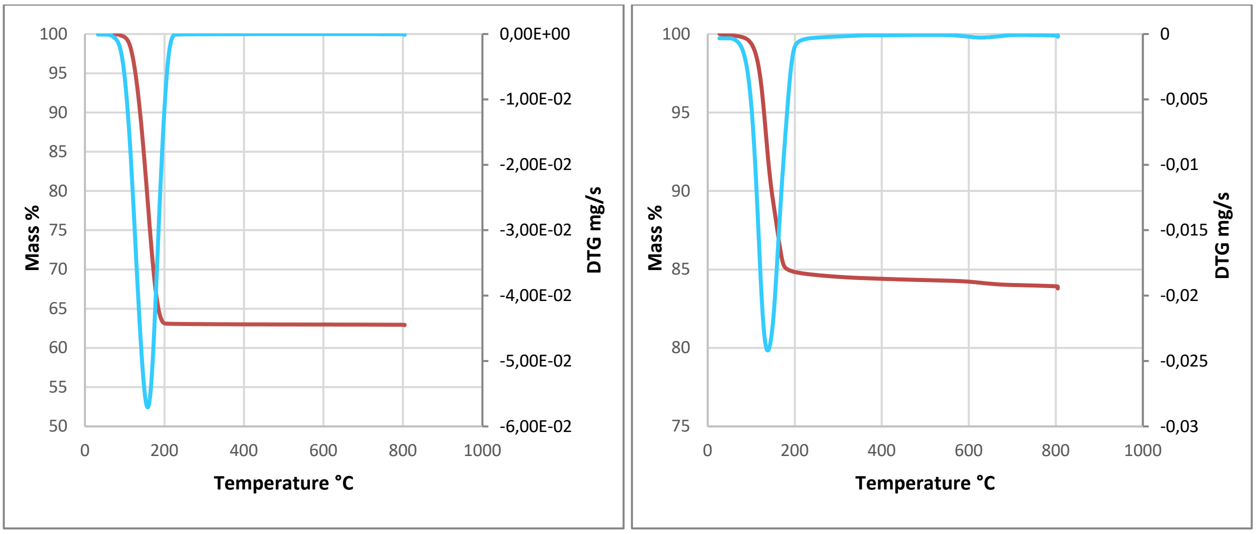

c) Sodium bicarbonate SB-2 b) Gypsum

***Fig.** 7. analysis of the mechanism of thermal degradation of calcium carbonate.*

3.4 *Inert and fuel particle size ratio*

In this section all the parameters investigated are analyzed together. The ratio between the particle size of combustible dust and inert dust has a direct impact on inertization efficiency. To analyze this effect, a graphical map has been designed to place the different mixtures in three groups. Each group is divided according to MIE. The most flammable mixtures are placed in the red group (MIE $<$ 100 mJ), the intermediate ones in the orange one (100 mJ $\leq$ MIE $>$ 500 mJ), and those with the lowest ignition sensitivity in the green one (500 mJ $\leq$ MIE $>$ 1000 mJ). As established in ISO 80079-20 (European committee for standardization CEN-CENELEC 2016) substances whose MIE $\geq$ 1000 mJ can be considered as low risk materials. After defining these three regions, the inert mass percentage contained in each mixture is placed on the left axis. Each mixture is represented in the section corresponding to its MIE and the percentage of inert added. Then, the ratio between the particle diameter of the combustible and inert dust is studied through an ellipse. The major axis of the ellipse corresponds to the combustible dust d50 ratio and the minor axis corresponds to the inert dust d50 ratio. Inertization effectiveness is greater if the particle size of combustible and inert dust is similar. Inertization will be most effective when the elliptical shape is close to that of a sphere. Thus, the more spherical the ellipse, the better the ratio between the particle diameter of the inert and the fuel. Furthermore, the moisture (HR) is represented by a rhombus. A map is obtained for lycopodium (figure 8), toner residue (figure 9), and Holi powders (figure 10). To obtain the d50 ratio for each sample, the d50 value of SB-1 is taken as a reference. The results are shown in table 5.

***Table 5:** Ratio d50 for each sample in reference to d50 of SB-1*

Sample	d50 ratio
LY	1.0
TO	0.2
HO	0.4

CC	0.2
SB-1	10.0
SB-2	5.2
SB-3	3.8
GY	0.2
SL	1.5

Maps depicted in figures 11, 12, and 13 reveal similar behaviors for calcium carbonate (CC) and gypsum (GY). When they are mixed with lycopodium both inerts change the MIE group for the same percentage of inert. In the case of the toner residue, the trend is the same, although gypsum achieves a better inertising effect at 60% concentration. Again, this trend is observed for Holi powder, with gypsum being more effective in this case, reaching 1000 mJ for 40% concentration. According to the moisture results obtained in this study, while gypsum contains 14.42 % water, calcium carbonate contains only 0.13 % water. Furthermore, thermal decomposition mechanisms observed for the two compounds differ considerably. Therefore, the only apparent relationship is the ratio between the d50 of the inert dust and the combustible dust. As can be seen in figures 8, 9, and 10 both gypsum and calcium carbonate maintain the most spherical ratios in all cases. In other words, the particle size of combustible and inert dust is similar and are therefore more effective than the other inert dust. Moreover, calcium carbonate and gypsum are the only inerts in this study where the particle size of the inert dust is smaller than that of the combustible dust.

However, ground sodium bicarbonate of soda ash (BS-2) proves to be the most effective in inerting lycopodium, toner residue, and Holi dust. As can be seen from the flammability maps, although its d50 is considerably higher than that of the combustible dust, in all cases it achieves EIMs above 1000 mJ for inert percentages below 60%. This can be partially explained by the fact that grinding is a physical process that modifies not only size but shape of particles. Segregation occurs when the difference between particle size on inerts and flammable dust is large. If the larger particles are non-reactive, the thermal effect predominates over the chemical effect. Generally, this process implies a reduction in the quality of the inertization, but in the case of SB-2, it has led to a considerable improvement. This may be because the dispersion of the ground particles behaves similarly to that of combustible dust, generating a very homogeneous cloud. Although boiler slagging has a nearly spherical ratio in its mixtures with lycopodium, it is not effective in reducing the ignition sensitivity of lycopodium.

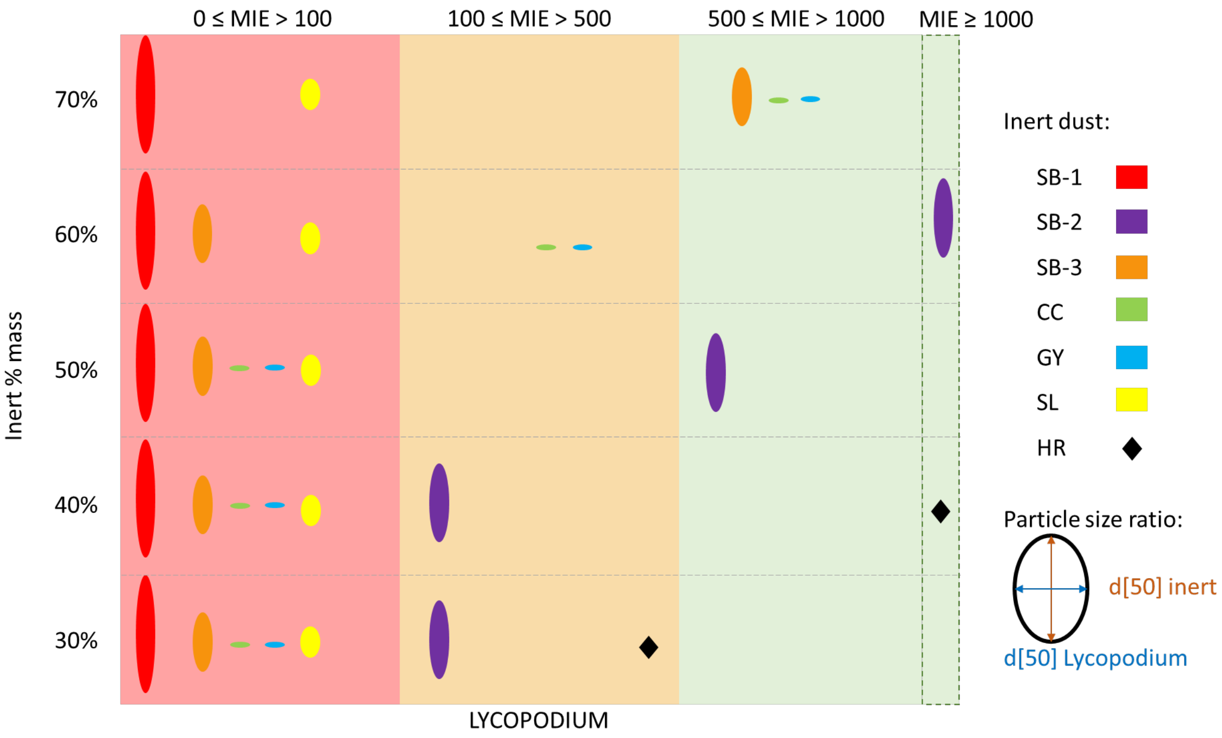

Fig. 8. *Flammability map of lycopodium vs. d50 ratio of combustible dust to inert dust*

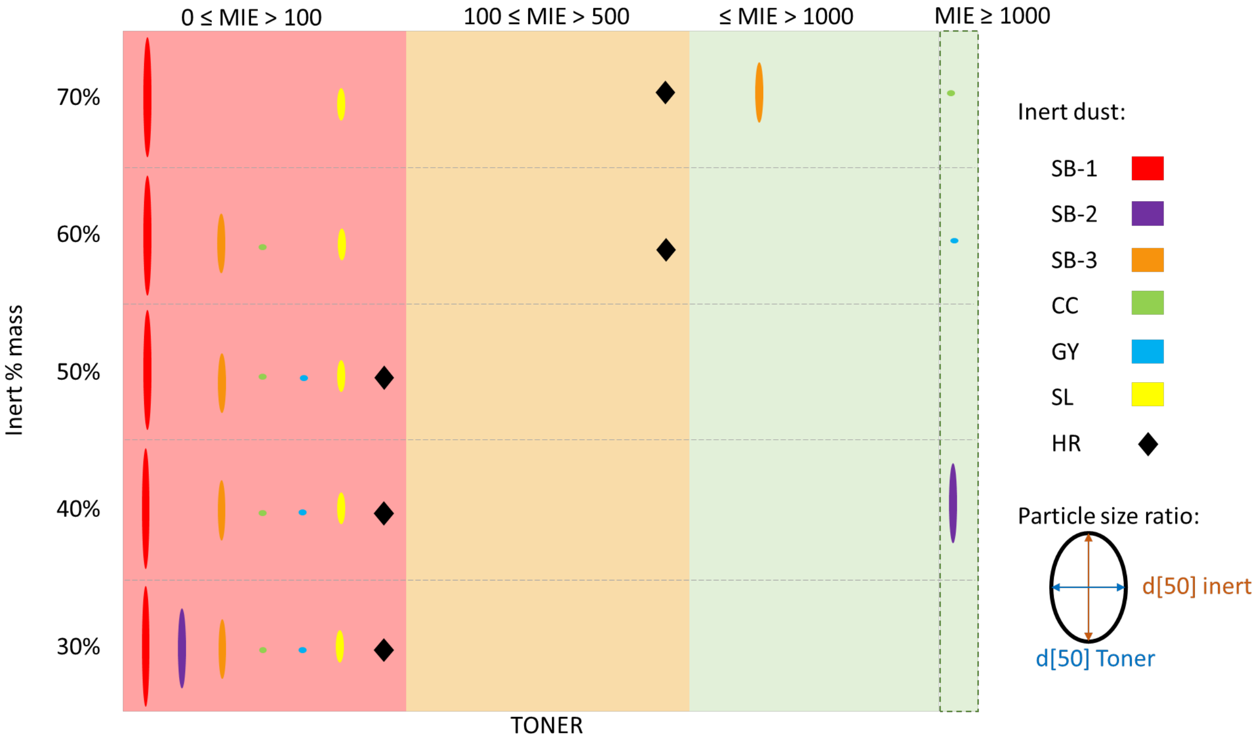

Fig. 9. *Flammability map of toner waste vs. d50 ratio of combustible dust to inert dust*

DOI: 10.7795/810.20221124

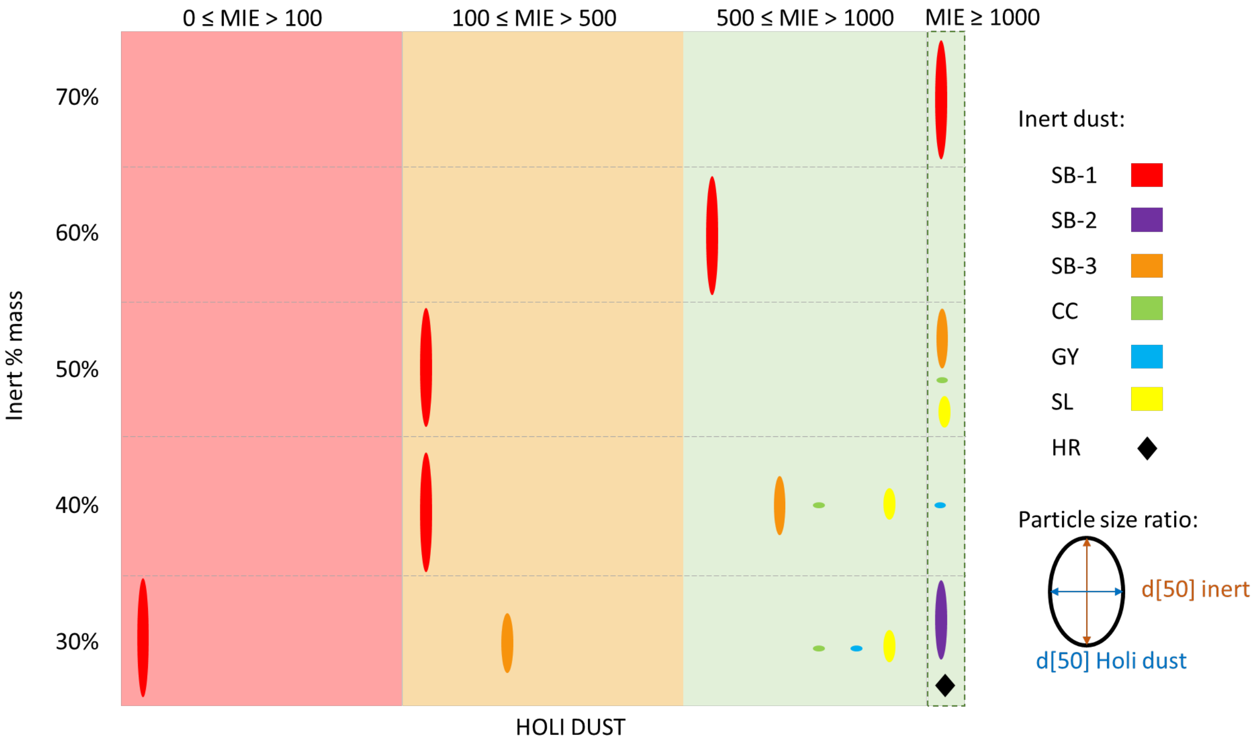

Fig. 10. *Flammability map of toner waste vs. d50 ratio of combustible dust to inert dust*

4. Conclusions

The inerting effect of calcium carbonate, sodium bicarbonate, gypsum, and moisture on MIE of toner waste, Holi dust, and lycopodium was investigated in a modified 1.2-L Hart-mann.. The main findings are as follows.

(1) The inerts investigated are not very effective in reducing the ignition sensitivity of lycopodium. Gypsum is the most effective inert, requiring 70% to increase the MIE to 780 mJ. Moisture is effective, reaching 1000 mJ for 40%.
(2) Although toner has a lower MIE than lycopodium (2.1 mJ versus 14 mJ) the inertisation results are considerably improved. Again, gypsum is the most effective inert as 1000 mJ is achieved for 60% inert, whereas calcium carbonate requires 70%.
(3) Holi dust has the highest MIE of the combustible dust studied (49 mJ). In this case, the inerts are highly effective. The mescal is inertised with 40% gypsum and 50% calcium carbonate or boiler slagging.
(4) Sodium bicarbonate and boiler slagging generate the SEEP effect for low inert concentrations. This effect diminishes for smaller particle sizes and is eliminated when the inert is ground.
(5) When analyzing the inerting effect of sodium bicarbonate for different particle sizes, it is observed that the best results are not those that are closest to the particle size of the combustible dust. This could indicate that there is an optimal particle size for each inert.
(6) Flammability maps designed do not reflect a clear trend in the relationship between the particle size of inert dust and combustible dust. However, gypsum and calcium carbonate turn to be the most effective ones. These are the only ones with a particle size smaller than that of the inert.

References

(FOPH), Swiss Federal Office of Public Health. 2017. "Holi Powders: Factsheet for Importers and Distributors." (August).

Abbasi, Tasneem, and S. A. Abbasi. 2007. "Dust Explosions-Cases, Causes, Consequences, and Control." *Journal of Hazardous Materials* 140(1–2): 7–44.

Addai, Emmanuel Kwasi, Dieter Gabel, and Ulrich Krause. 2016. "Experimental Investigations of the Minimum Ignition Energy and the Minimum Ignition Temperature of Inert and Combustible Dust Cloud Mixtures." *Journal of Hazardous Materials* 307: 302–11. http://dx.doi.org/10.1016/j.jhazmat.2016.01.018.

Amyotte, Paul R. et al. 2007. "Moderation of Dust Explosions." *Journal of Loss Prevention in the Process Industries* 20(4–6): 675–87.

Bagaria, Pranav, Ben Hall, Ashok Dastidar, and Chad Mashuga. 2019. "Effect of Particle Size Reduction Due to Dust Dispersion on Minimum Ignition Energy (MIE)." *Powder Technology* 356: 304–9. https://doi.org/10.1016/j.powtec.2019.08.030.

Bagaria, Pranav, Qiang Li, Ashok Dastidar, and Chad Mashuga. 2019. "Classification of Particle Breakage Due to Dust Dispersion." *Powder Technology* 342: 204–13.

Bu, Yajie et al. 2020. "Moderation of Al Dust Explosions by Micro- and Nano-Sized Al2O3powder." *Journal of Hazardous Materials* 381(July 2019): 120968. https://doi.org/10.1016/j.jhazmat.2019.120968.

Cai, Jingzhi et al. 2019. "Effect of Admixture of Solid Inertant on Fire Hazard of Dust Layers Oriented at Varying Degrees of Inclination." *Journal of Loss Prevention in the Process Industries* 57: 41–46.

Castellanos, Diana et al. 2014. "The Effect of Particle Size Polydispersity on the Explosibility Characteristics of Aluminum Dust." *Powder Technology*.

Castells, Blanca, Isabel Amez, Ljiljana Medic, Nieves Fernandez-Anez, et al. 2021. "Study of Lignocellulosic Biomass Ignition Properties Estimation from Thermogravimetric Analysis." *Journal of Loss Prevention in the Process Industries* 71(October 2020): 104425. https://doi.org/10.1016/j.jlp.2021.104425.

Castells, Blanca, Isabel Amez, Ljiljana Medic, and Javier García-Torrent. 2021. "Torrefaction Influence on Combustion Kinetics of Malaysian Oil Palm Wastes." *Fuel Processing Technology* 218(April): 106843. https://doi.org/10.1016/j.fuproc.2021.106843.

Chaudhari, Purvali, Bharatvaaj Ravi, Pranav Bagaria, and Chad Mashuga. 2019. "Improved Partial Inerting MIE Test Method for Combustible Dusts and Its CFD Validation." *Process Safety and Environmental Protection* 122: 192–99. https://doi.org/10.1016/j.psep.2018.12.009.

Eckhoff, Rolf K. 2004. "Partial Inerting-an Additional Degree of Freedom in Dust Explosion Protection." *Journal of Loss Prevention in the Process Industries* 17(3): 187–93.

Eckhoff, Rolf K.. 2019. "Measurement of Minimum Ignition Energies (MIEs) of Dust Clouds – History, Present, Future." *Journal of Loss Prevention in the Process Industries* 61: 147–59.

Eckhoff, Rolf K. 2020. "Fighting Dust Explosion Hazards in the Process Industries." *Journal of Loss Prevention in the Process Industries* 67: 104225. https://doi.org/10.1016/j.jlp.2020.104225.

European committee for standardization CEN-CENELEC. 2016. *ISO/IEC 80079-20-2:2016 Explosive Atmospheres - Part 20-2: Material Characteristics - Combustible Dusts Test Methods*.

European committee for standardization CEN-CENELEC. 2017. *UNE-EN ISO/IEC 80079-20-2:2016/AC:2017 Explosive Atmospheres - Part 20-2: Material Characteristics - Combustible Dusts Test Methods*.

Fernandez-Anez, Nieves, Blanca Castells Somoza, Isabel Amez Arenillas, and Javier Garcia-Torrent. 2020. *Explosion Risk of Solid Biofuels*.

Han, Bo, Gang Li, Chunmiao Yuan, and Qingsheng Wang. 2020. "Flame Propagation of Corn Starch in a Modified Hartmann Tube with Branch Structure.” *Powder Technology* 360: 10–20.

Huang, Chuyuan et al. 2019. “Suppression of Wood Dust Explosion by Ultrafine Magnesium Hydroxide.” *Journal of Hazardous Materials* 378(January): 120723. https://doi.org/10.1016/j.jhazmat.2019.05.116.

Hutcherson, Kimberly, Greg Botelho, and Kevin Wang. 2015. “More than 500 Injured in Explosion at Taiwan Water Park.” *CNN*: 1. http://www.cnn.com/2015/06/27/asia/taiwan-water-park-explosion/.

Janès, Agnès, Alexis Vignes, Olivier Dufaud, and Douglas Carson. 2014. “Experimental Investigation of the Influence of Inert Solids on Ignition Sensitivity of Organic Powders.” *Process Safety and Environmental Protection* 92(4): 311–23. http://dx.doi.org/10.1016/j.psep.2014.04.008.

Janovsky, B., J. Skrinsky, J. Cupak, and J. Veres. 2019. “Coal Dust, Lycopodium and Niacin Used in Hybrid Mixtures with Methane and Hydrogen in 1 m3 and 20 l Chambers.” *Journal of Loss Prevention in the Process Industries* 62(February): 103945. https://doi.org/10.1016/j.jlp.2019.103945.

Jiang, Haipeng et al. 2018. “Inhibition of Aluminum Dust Explosion by NaHCO3 with Different Particle Size Distributions.” *Journal of Hazardous Materials* 344: 902–12. http://dx.doi.org/10.1016/j.jhazmat.2017.11.054.

Jiang, Haipeng, Bi, Mingshu, Li, Bei, Zhang, Dawei, Gao, Wei. 2019. “Inhibition Evaluation of ABC Powder in Aluminum Dust Explosion.” *Journal of Hazardous Materials* 361(July 2018): 273–82. https://doi.org/10.1016/j.jhazmat.2018.07.045.

Nifuku, Masaharu et al. 2005. “A Study on the Ignition Characteristics for Dust Explosion of Industrial Wastes.” *Journal of Electrostatics* 63(6–10): 455–62.

Wei, Min Chi et al. 2020. “Applications of Dust Explosion Hazard and Disaster Prevention Technology.” *Journal of Loss Prevention in the Process Industries* 68(October): 104304. https://doi.org/10.1016/j.jlp.2020.104304.

Wei, Xiangrui et al. 2021. “Study on Explosion Suppression of Coal Dust with Different Particle Size by Shell Powder and NaHCO3.” *Fuel* 306(April): 121709. https://doi.org/10.1016/j.fuel.2021.121709.

Yang, Jie et al. 2019. “Inerting Effects of Ammonium Polyphosphate on Explosion Characteristics of Polypropylene Dust.” *Process Safety and Environmental Protection* 130: 221–30. https://doi.org/10.1016/j.psep.2019.08.015.

Yuan, Zhi, Nima Khakzad, Faisal Khan, and Paul Amyotte. 2015. “Dust Explosions: A Threat to the Process Industries.” *Process Safety and Environmental Protection* 98: 57–71. http://dx.doi.org/10.1016/j.psep.2015.06.008.

DOI: 10.7795/810.20221124

Thermal Ignition: Effects of Fuel, Ambient Pressure and Nitrogen Dilution

Conor D. Martin & Joseph E. Shepherd

Graduate Aerospace Laboratories, California Institute of Technology, Pasadena, CA, U.S.A
E-mail: *cdmartin@caltech.edu*

Abstract

We report new results for the pressure and nitrogen dilution dependence of thermal ignition thresholds of laminar external natural convection flows on a hot vertical cylinder. Experiments were conducted using an electrically-heated vertical cylinder (25.4 cm long, 2.54 cm diameter) in a 40 L vessel. Mixtures investigated included stoichiometric n-hexane, hydrogen and ethylene in oxygen/nitrogen atmospheres. A range of initial pressures (1, 0.7, 0.466, 0.238 atm) and nitrogen dilution levels ($N_2/O_2 = \beta = 3.76$, 5.64, and 7.52, equivalent to $X_{O_2} = 20.6$, 14.8, 11.6%) were explored for n-hexane. Two-color pyrometry was used to measure and control the cylinder surface temperature. Surface chemistry effects during hydrogen ignition testing provided further insight into the effectiveness of the two-color pyrometry measurement technique. Measurements of ignition threshold temperatures also have an intrinsic variability and were analyzed using a logistic regression methodology with the temperature corresponding to an ignition probability of 50% ($\mathcal{P}_{ign}$=0.5) is reported as the ignition temperature (T_{ign}). The ignition threshold for atmospheric hydrogen and ethylene were 982±30 K and 996±30 K respectively. These results are consistent with previous studies which have shown a positive correlation in ignition threshold and fuel molecular weight. A modest increase of ignition temperature threshold was observed for both decreasing pressure and increasing nitrogen concentration at fixed stoichiometry for hexane-air mixtures. A semi-empirical correlation based on the work of Ono et al. (1976) was found to be a reasonable representation of the pressure dependence for each β.

Keywords: *Thermal Ignition, Hydrogen, Hydrocarbon Fuel, Sub-atmospheric Pressure, Nitrogen Dilution*

1 Introduction

Accidental thermal ignition events are a significant potential hazard in many industrial applications including chemical processing, transportation and aviation. A thorough understanding of the conditions underlying these ignition processes is necessary to evaluate and mitigate potential hazards. Laboratory investigations of surface geometries and orientation have led to conflicting results, particularly for larger size surfaces that are encountered in industrial settings. For hot surface ignition, it is important to consider the fluid motion induced by buoyancy and a crucial distinction must be made between external and internal natural convection flows (Jones and Shepherd, 2021, Martin and Shepherd, 2021).

We have performed extensive testing in our laboratory with various fuels (See the discussion in Martin and Shepherd, 2021, Jones, 2020); in the present study we have focused on n-hexane, using this as a surrogate for aviation kerosene. Many other fuels are of interest in evaluating potential industrial hazards. For this study, we have also performed a limited number of ignition experiments with hydrogen and ethylene to enable comparisons with data from experiments with smaller heated surface area (Boeck et al., 2017) as well as the typical autoignition temperature

(AIT) criteria (ASTM, 2005).

Sub-atmospheric mixtures and mixtures with reduced oxygen concentration are of particular importance for aircraft fuel tank flammability reduction (FAA, 2017). Aircraft fuel tanks are vented to the atmosphere and pressures can be as low as 17 kPa (0.17 atm) at cruise altitudes of up to 13 km (43 kft). In order to minimize fuel tank flammability, nitrogen-enriching systems have been developed (Moravec et al., 2006), tested (Cavage and Summer, 2008) and are now extensively used in commercial aircraft. These systems are designed to reduce the oxygen concentration below the limiting value (approximately 12% by volume at ground level) for flammability . It is therefore of interest to understand how thermal ignition events are affected by variations in pressure and oxygen concentration. Summer (2004) used high-energy spark ignition and hot ($\approx$ 1000 K) surfaces to establish limiting oxygen concentrations at sub-atmospheric pressures. However, the hot surface tests used a fixed geometry and surface temperature and did not quantify the thermal ignition threshold dependence on pressure and oxygen concentration.

The effect of pressure on thermal ignition thresholds has primarily been studied only at elevated pressures, for example Hirsch and Brandes (2005). Zabetakis (1965) report that flammability limits of alkane-air mixtures have a negligible dependence on pressure down to about 200 torr. Brandes et al. (2017a,b) studied ignition with elevated oxygen concentration (21-100%) and alternative oxidizers (N_2O) at atmospheric pressure. Those experiments involved internal natural convection (heated vessels) rather than external convection (heated surfaces). Ignition by external natural convection at reduced pressure was studied by Ono et al. (1976) who examined thermal ignition by small vertical hot plates (1.5-9 cm^2) at initial pressures between 0.13 and 1.0 atm. Ono et al. (1976) developed a semi empirical correlation between ignition temperature, surface height and pressure for laminar natural convection. With the exception of Summer (2004), two factor combinations of lowered pressure and oxygen content have not been systematically examined in previous studies.

The present study is an external natural convection experiment where the ignition source is a vertical cylinder. These experiments build upon the work performed by Jones and Shepherd (2021) who investigated thermal ignition by vertical cylinders and the effects of both length and surface area on ignition. Jones' study explored ignition source surface areas ranging from 25 to 200 cm^2 for stoichiometric n-hexane/air mixtures as well as Jet A samples and surrogates. Jones and Shepherd (2021) demonstrated that contrary to previous attempts at correlating thermal ignition thresholds with area, in external natural convection there is only a very modest decrease in the ignition threshold with increased surface area. Therefore, the present study used only the largest cylinder from Jones and Shepherd (2021), labelled 200A (length = 25.4 cm, diameter = 2.54 cm, surface area = 200 cm^2) using hydrogen/air, ethylene/air mixtures, and n-hexane-oxygen-nitrogen mixtures at reduced pressures.

2 Experimental Methodology

The experimental setup is identical to that described by Jones and Shepherd (2021) and in more detail by Jones (2020). The surface is a vertical cylinder constructed from stainless steel tubing and heated resistively using a Magna Power XR5-600 computer controlled power supply. The experiments are conducted inside a 40 L cylindrical combustion vessel with a 30.4 cm inner diameter and a height of 66.0 cm. The cylinder is held in place in the center of the combustion vessel with a copper support structure as shown in Figure 1. The support structure both mechanically stabilizes the heated surface and provides a path for electrical current to flow from. The cylinder temperature is monitored using a custom built two-color pyrometer as well as a K-type thermocouple welded to the center of the cylinder. The thermocouple is not present for all tests as prolonged exposure

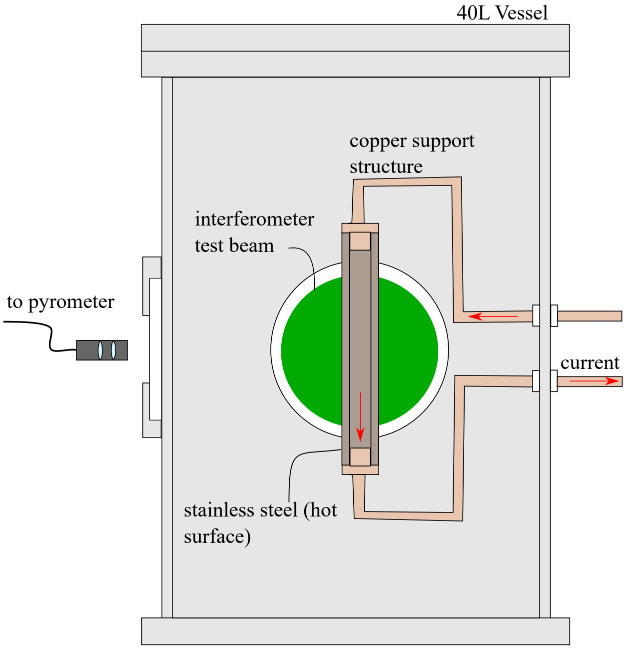

***Fig. 1**: Schematic of heated cylinder setup. (Adapted from Jones, 2020).*

to high temperatures tended to weaken the spot weld and led the thermocouple to become disconnected from the surface periodically. For this reason, the pyrometer is found to be more reliable and is used in a feedback control loop with the power supply to maintain a set surface temperature. This system is controlled remotely via LabVIEW and the control loop is only initiated after an initial ramping period where the current supplied is fixed. The ends of the cylinder are water cooled using a NESLAB system III heat exchanger whose flow rate is adjusted using a ball valve and volumetric flow controller. This extracts the heat that otherwise would be conducted into the support structure during testing. A modified Mach-Zehnder interferometer in conjunction with a Phantom V7100 high speed camera is used to visualize ignition and make quantitative measurements of the gas surrounding the hot cylinder for nonreactive mixtures.

The method of partial pressures is used to control the gas conditions for each shot. The vessel is evacuated to less than 0.1 torr before the start of the filling process. The fuel is then added using either a syringe in the case of liquid fuels or a gas supply system for gaseous fuels. Nitrogen and oxygen are then added independently in appropriate amounts to make the desired fuel-air mixture. A capacitive pressure gauge (MKS model 121A-01000B) with an accuracy of 0.1 torr is used to monitor the pressure during filling. After the vessel is filled, a fan mixer is turned on for three minutes to promote mixing of the gases and then turned off for three minutes to allow the gases to settle and produce a quiescent mixture at the start of each test. The test time is limited to 300 s in order to prevent recirculation of the gas through the heated boundary layer. At the end of the test time if there has been no ignition, then the test is ended and is reported as a non-ignition result. In the cases where ignition occurred, the data acquisition system was triggered by a thermally-protected, piezoresistive pressure transducer (Endevco 8530B-200) which was used to record pressure rise during the test. The magnitude of the pressure rise and the appearance of a flame in the interferometer imaging were used to determine if ignition took place.

Ignition data were analyzed statistically by the logistic method, assigning to each shot a binary outcome variable of 0 or 1, representing a non-ignition and ignition result respectively. Details of the logistic approach can be found in Bane et al. (2011), Jones (2020). Outcome data paired with the surface temperature (T_S) of each test demonstrate that there are both ignition and non-ignition cases at a given temperature near the ignition threshold. This overlap can be attributed to intrinsic uncertainty related to the ignition process as well as typical small experimental parameter (composition, temperature, heating ramp etc.) variability for tests nominally at the same initial conditions. The temperature corresponding to an ignition probability of 50% ($\mathcal{P}_{ign}$=0.5) is reported as the ignition temperature (T_{ign}).

2.1 Surface Temperature Measurements

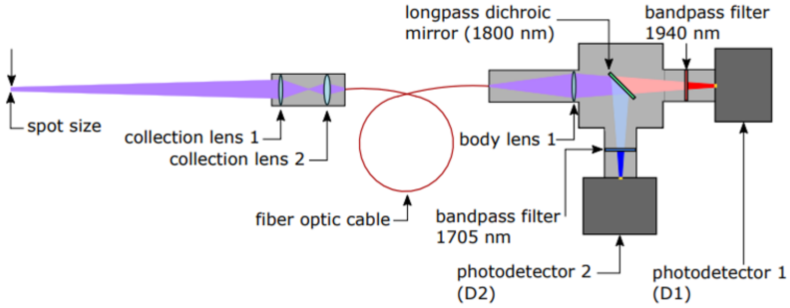

***Fig. 2**: Schematic of pyrometer construction with detectors, filters and collection optics shown (Adapted from Jones, 2020).*

Non-contact measurements of surface temperature are made using a two-color pyrometer (Michalski and Michalski, 2001). The design is described in Jones (2020) and shown in Figure 2. The outputs of the detectors are analyzed using Planck's law of blackbody radiation assuming gray-body (e.g. wavelength-independent) emissivity of the hot surface. The pyrometer was calibrated using a blackbody thermal radiation source (Process Sensors BBS1200) over a range of 700 – 1050°C in 25°C increments. Previous extensive testing (documented in Jones, 2020) using comparisons with thermocouple data indicates that this assumption is valid for oxidized, high temperature stainless steel surfaces. However, the surface conditions are a function of time and properties can significantly vary in some cases as discussed subsequently for hydrogen/air tests.

Pyrometery is an attractive technique for temperature measurement as this eliminates any flow disturbances introduced by spot welding a thermocouple wire to an otherwise uniformly smooth cylinder surface. A weld bead could potentially cause early onset of ignition by either forming a localized hot spot or by "tripping" the flow into the turbulent regime. We found that this was not a significant issue and to obtain reliable temperature measurements, we used both the thermocouple and the pyrometer during most ignition tests.

3 Results and discussion

A summary of all conditions studied are given in Table 1. Ignition thresholds for hydrogen and ethylene were obtained at only one condition, 1 atm and normal air composition and stoichiometric ratios of fuel to oxygen. Ignition thresholds for n-hexane were obtained for a range of initial pressures and nitrogen dilution levels.The initial pressures were chosen based on various altitudes in the standard atmosphere (e.g., P_0 = 1, 0.7, 0.466, and 0.238 atm correspond to altitudes of 0, 10 kft, 20 kft, and 35 kft respectively). The hexane mixture compositions were defined by $\phi C_6H_{14} + 9.5(O_2 + \beta N_2)$. Previous work on thermal ignition by Boeck et al. (2017) has shown minimal dependence of ignition threshold on equivalence ratio (ϕ) for n-hexane up to the flammability limits. This was confirmed in the present study by some preliminary testing on n-hexane mixtures (ϕ = 0.88, 1, 1.6, β = 3.76, P_0 = 1 atm) with ignition temperature thresholds of 1020 K which are consistent with previous work by Jones (2020) and is well within the experimental uncertainty bounds of the pyrometer and logistic regression analysis. For all hexane tests, the composition used was stoichiometric.

Table 1: *Summary of all experimental conditions and reported ignition temperatures (T_{ign}) with 95% confidence limits (95% CL) from logistic regression. Note that the uncertainty bounds on the pyrometer are much larger in all cases (± 30 K). All conditions are stoichiometric (ϕ=1.0).*

		β	3.76	5.64	7.52	
		(X_{O_2}(%)	20.6	14.8	11.6)	
Fuel	P_0 (atm)					
n-hexane	1.0		1020	1045	1066	T_{ign} (K)
			±4	±6	±3	95% CL (K)
	0.7		1060	1078	1098	T_{ign} (K)
			±5	±5	±3	95% CL (K)
	0.466		1091	1119	1128	T_{ign} (K)
			±5	±3	±4	95% CL (K)
	0.238		1143	1153	1171	T_{ign} (K)
			±4	±5	±1	95% CL (K)
hydrogen	1.0		982	-	-	T_{ign} (K)
			±13	-	-	95% CL (K)
ethylene	1.0		996	-	-	T_{ign} (K)
			±6	-	-	95% CL (K)

3.1 Hydrogen/Air

Hydrogen/air mixtures introduced some unexpected challenges that were not present in previous experiments working with n-hexane, Jet A or surrogate fuels. After several tests with hydrogen mixtures, we observed a large discrepancy in the temperatures recorded by the thermocouple and the pyrometer which had been in good agreement (±10 K) in the hexane and ethylene tests. The reason became apparent upon visual inspection of the heated surface, see Figure 3. A reddish-orange oxide layer had formed on top of the gray-black oxide that normally persists on the surface. This layer is likely composed of Fe_3O_4 (gray) and Fe_2O_3 (red) or one of many possible hydrated iron oxides which will subsequently be referred to as "rust". No chemical analysis was conducted to confirm which oxides were present.

The "rust" build up could be sanded off along with the gray oxide layer, revealing the underlying polished steel surface. Before further testing using the pyrometer, the oxide layer then had to be rebuilt by holding the cylinder at an elevated temperature (1000 K) for 5-10 minutes in an air atmosphere. Once this was done the pyrometer readings again fell into agreement with the welded thermocouple (within ±10 K). We therefore speculate that the differences in the wavelength de-

Fig. 3*: Comparison of the surface conditions observed in these experiments. (left) Polished stainless steel (middle) Typical oxide layer built up on surface after being held for 5-10 mins above 1000 K in an air atmosphere and (right) Surface after approximately 5 hydrogen ignition tests.*

pendence of the emissive properties of the rusty surface and the oxidized steel are the cause of this discrepancy. The rusted surface apparently is not a sufficiently gray body and there is substantial variation in the emissivity for the two wavelengths measured by the pyrometer.

The sensitivity of the surface temperature measurement to emissivity dependence on wavelength is substantial. For example a 3% difference in emissivity between the two wavelengths of interest will results in an approximately 40 K temperature difference. This is on the order of the discrepancy observed between the pyrometer and thermocouple measurements on the rusty surface. We found that the surface disruption and "rust" was found to develop for non-ignition cases as well as cases with ignition. This indicated that there was some significant reaction with hydrogen taking place near the surface in addition to the obvious potential of high temperature oxidation by water vapor in the post-combustion environment. This was also observable through a gradual decline in vessel pressure over the testing period. Similar declines were also evident in ignition cases in the lead up to ignition. This observation was in opposition to the pressure rise observed in tests with other fuels. A pressure rise is expected and was observed due to the bulk heating of the gas over the testing period of 300 s and slight decomposition of hydrocarbon species in the thermal boundary layer. However, decomposition of H_2 should lead to a decrease in total number of moles in the gas phase which would result in a declining pressure. The pressure data and surface change both indicate that there is significant low temperature decomposition in the case of hydrogen.

The procedure employed in performing the hydrogen tests therefore had to be modified to account for the heater surface changes. After each shot, the hot ignition products were immediately evacuated to minimize time exposed to the hot post-combustion products. Additionally, the surface was "cleaned" with sandpaper after every 5 shots and the gray oxidation layer was built back up before doing additional testing. Ignition kernels formed near the middle of the cylinder which was unique in that previously studied hydrocarbon fuels formed ignition kernels very close to the top of the heated surface (Jones, 2020). The results of the ignition testing were fit using a logistic regression and the results are shown in Figure 4. The ignition temperature was 982 ± 30 K. This corresponds to an ignition probability of 50% with the uncertainty determined by the pyrometer measurements.

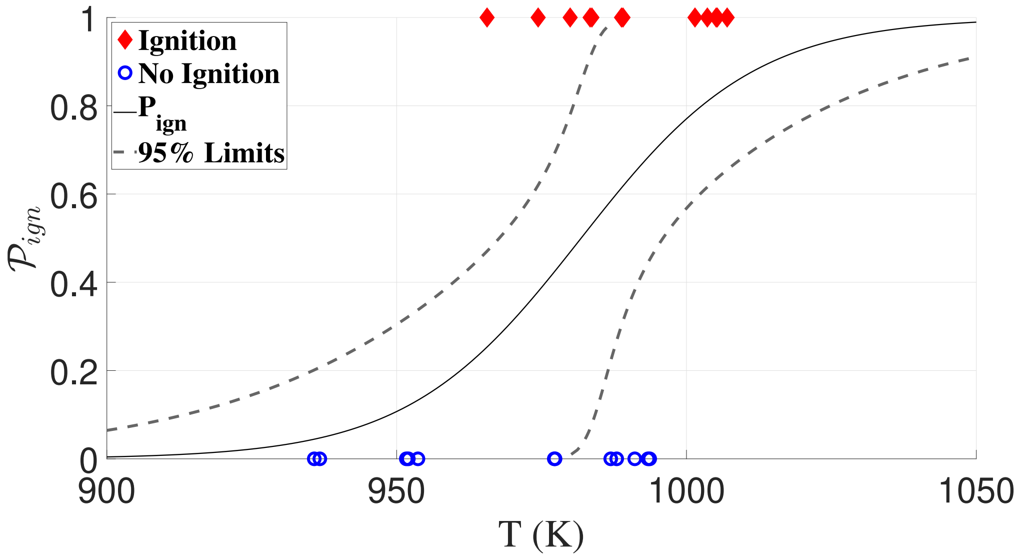

Fig. 4: *Probability of ignition ($\mathcal{P}_{ign}$) vs surface temperature (T_s). The probability curve and 95% confidence limits for the fit are found using logistic regression of stoichiometric hydrogen/air ignition data.*

3.2 Ethylene-Air

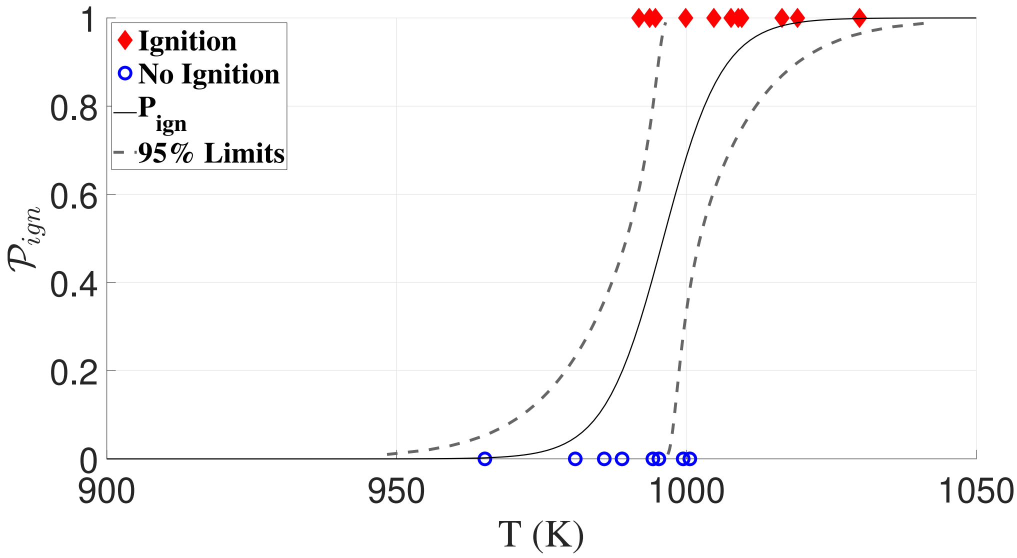

Fig. 5: *Logistic regression of stoichiometric ethylene/air ignition data.*

With the experience gained from the hydrogen tests, the ethylene/air shots were monitored closely for anomalous system behavior but none was observed. Ignition kernels formed near the top of the cylinder as was the case with other hydrocarbon fuels. Near the ignition threshold, ignition events appeared to be instigated by fluid ejections from the boundary layer. These ejections of hot fluid travel upward to the top of the cylinder where they are able to mix with hotter fluid at the top of

DOI: 10.7795/810.20221124

the heated surface length where the thermal layer is thickest. It is unclear what role these ejections play in the early stages of ignition but they may contain some partially reacted mixture that would aid in instigating ignition and may promote mixing of fluid in the thermal layer. These ejections were also observed for n-hexane mixtures and nonreactive mixtures (pure nitrogen) so it seems they may be purely fluid mechanical in origin. The ignition data is presented in Fig. 5 and again fit with a logistic regression. The ignition temperature is 996 ± 30K as determined by the 50% probability of ignition.

3.3 Sub-atmospheric n-hexane/oxygen/nitrogen mixtures

A two factor factorial experimental approach was taken to study 12 total test conditions consisting of mixtures of stoichiometric n-hexane/oxygen/nitrogen. The two factors under investigation were initial pressure and nitrogen dilution (equivalently, oxygen concentration). Each test condition was repeated at least 12 times to produce a statistically significant data set which could be reliably analyzed using the logistic regression approach. Full results are shown in Fig. 6 for all tests. These results demonstrate that decreasing pressure at fixed nitrogen dilution (constant β) results in increasing ignition temperatures. Similarly, increasing nitrogen dilution (β) at fixed initial pressure results in increasing ignition temperatures.

Figure 8 plots the ignition temperatures at fixed pressures against β. The ignition temperatures shown in this plot are those corresponding to 50% ignition probability as determined by the logistic curves shown in Fig. 6. The error bars correspond to the error in the pyrometer readings which are estimated based on the 95% confidence intervals of the linear fit to the calibration data. This error is ± 30 K in this case which is much larger than the uncertainty resulting from the logistic regression to noisy ignition data which is only on the order of ± 3-7 K in the cases shown in Fig. 6. Ignition temperatures for all pressures show a similar trend with β and vice versa. There does not appear to be any significant interaction between pressure and β effects on ignition thresholds in these experiments. Ignition was achieved for all pressures at 11.6% O_2. This is in contrast to the results of Summer (2004) where limiting oxygen concentrations (LOC) of at least 14% were found for tests with a heated surface ($\sim$ 350 cm^2) at temperatures up to about 1050 K using Jet fuels. The pressure for these tests was not stated. Summer's study primarily used a low-power arc of relatively short duration (1 s) and in those tests a LOC of around 12% was reported for sea level and increasing up to 14.5% for pressures corresponding to 40 kft altitude. Coward and Jones (1965) report a minimum LOC of 11.9% for n-hexane with nitrogen as the inerting agent. However this minimum was for slightly rich mixtures whereas for stoichiometric mixtures the LOC was 13.4%. The approach to determining flammability was the Explosion Tube Method and did not involve ignition by a hot surface but used an open flame. We did not dilute our mixtures systematically in order to determine the LOC but were able to obtain ignition at all pressures and dilution equivalent to an oxygen concentration of 11.6%.

Fig. 7 shows representative pressure traces obtained from an ignition experiment at each of the test conditions near the ignition thresholds. The plots show a reduction in peak pressure and decrease in the rate of pressure rise (dP/dt) with increasing β. The decrease in peak pressure with increasing β and decreasing initial pressure is consistent with the thermodynamics of the combustion process and the dependence of flame speed on mixture composition. These effects becomes especially evident at lower pressures. For example in the P_0=0.466 atm, β=7.52 case the flame speed is much lower than in mixtures with lower β at the same P_0. This causes an increased duration of the pressure transient as the flame propagates more slowly through the combustion chamber. This also leads to increased heat loss from the flame causing lower peak temperatures and pressures. More

DOI: 10.7795/810.20221124

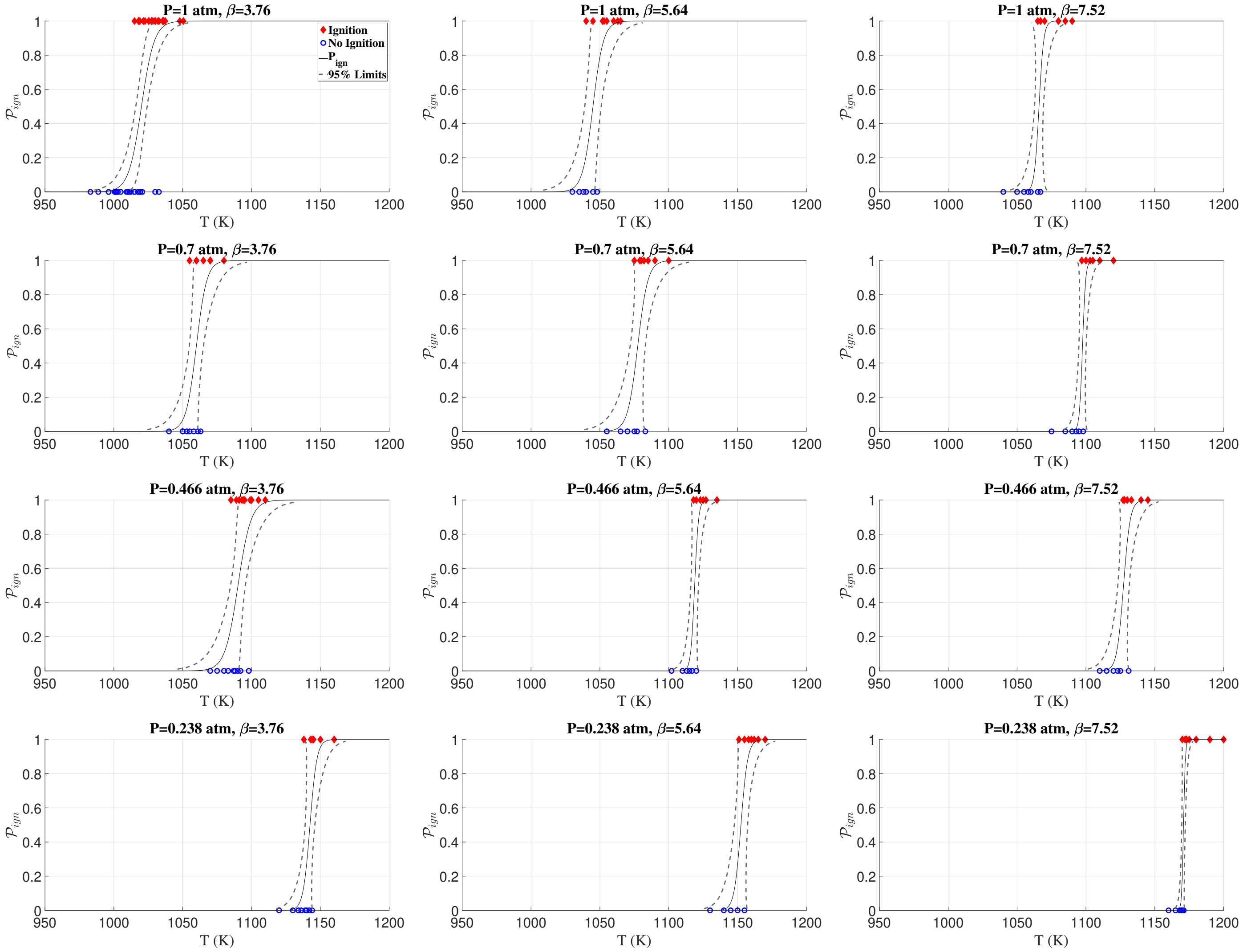

***Fig. 6**: Ignition data and logistic regression for hexane/air mixtures at combinations of P_0 = 1, 0.7, 0.466, 0.238 atm and β = 3.76, 5.64, 7.52 (X_{O_2} = 20.6, 14.8, 11.6%). Pressure decreases from top to bottom and β increases from left to right.*

dilute mixtures also have lower energy content and consequently lower flame temperatures and peak adiabatic combustion pressures.

All other factors being the same, we expect that the peak pressure should scale directly with the initial pressure so that the ratio of peak pressure to initial pressure should depend mainly on β and have only a modest dependence on initial pressure. The decrease in pressure rise rate with increasing β is consistent with the decrease in observed and computed flame speeds for diluted mixtures. The magnitudes of the pressure rises can be compared to thermodynamic estimates as well as the peak pressure data from Summer (2004). For more dilute mixtures and at lower pressure, the effects of heat transfer and buoyancy on the flame are more pronounced, resulting in significant departures of the measured peak pressures from the adiabatic, constant-volume, complete-combustion (AICC) estimates as shown in Table 2. As anticipated, the AICC pressure ratios are essentially independent of initial pressure, $P_{AICC}/P_0 \approx$ 9.5, 8.0 and 7.0 for β = 3.76, 5.64

DOI: 10.7795/810.20221124

and 7.52 respectively.

***Table 2**: Thermodynamic estimates (AICC) and measurements of peak combustion pressure (atm) observed in the hexane testing as a function of β and initial pressure P_0.*

β	3.76	5.64	7.52	
(X_{O_2}(%)	20.6	14.8	11.6)	
P_0 (atm)				
1.0	9.58	8.08	6.95	AICC
	7.48	5.44	2.28	Experiment
0.7	6.67	5.64	4.86	AICC
	5.24	3.77	1.55	Experiment
0.466	4.41	3.74	3.23	AICC
	3.56	2.32	1.02	Experiment
0.238	2.23	1.90	1.65	AICC
	1.69	1.06	0.78	Experiment

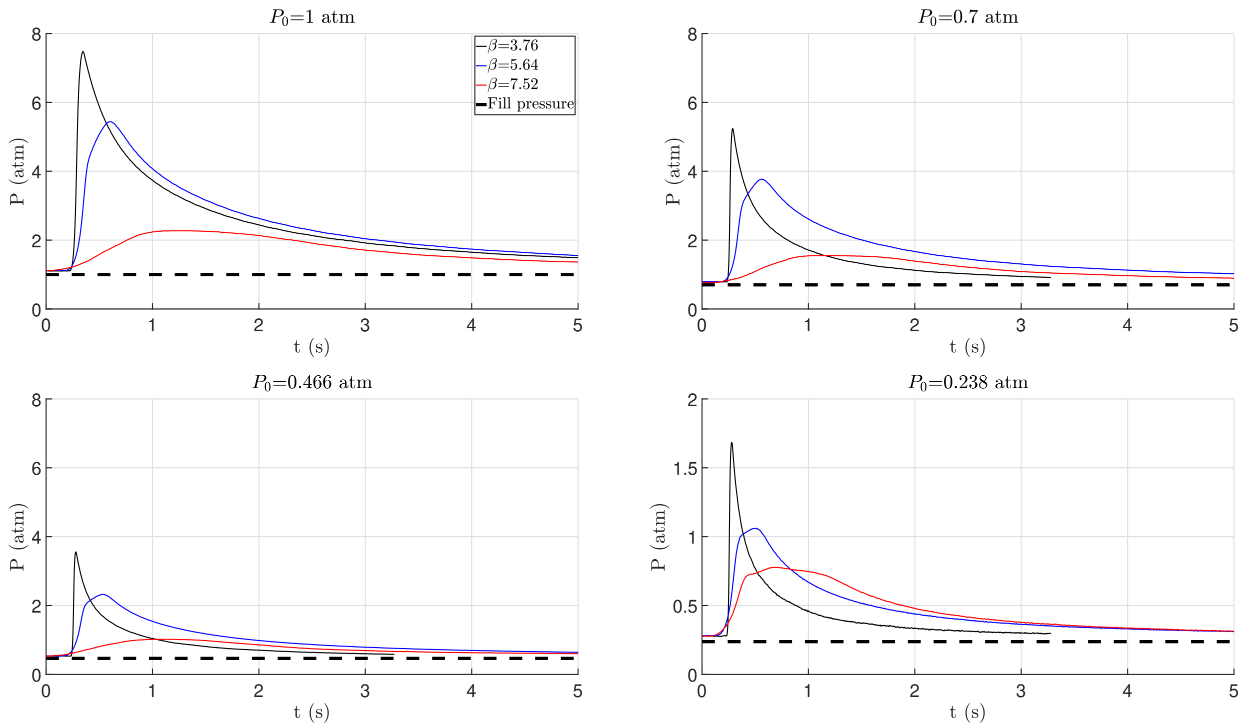

***Fig. 7**: Representative pressure traces from ignition in each of the sub-atmospheric n-hexane conditions. Note the reduced y-axis scale for the P_0 = 0.238 atm case.*

In contrast with Summer (2004) results, our measured peak pressures are substantially higher for even the lowest O_2 concentration (11.6%) condition and pressure (0.238 atm) tested. The peak pressure rises reported by Summer at oxygen concentrations 1-2% higher than his LOC values were on the order of 0.4 to 2.5 psi (.027 to 0.17 atm). One key difference in test procedure that may explain this is that in Summer's tests the combustion products are vented early in the ignition process where our vessel remains closed throughout. The peak pressure rises in the present tests for the lowest O_2 concentration ranged from 7.3 to 17.2 psi (0.50 to 1.17 atm) for initial pressures between 0.238 and 1 atm. We also observed consistent ignition at an oxygen concentration of 11.6% at an initial pressure equivalent to 35 kft whereas Summer reported a limiting O_2 concentration of 14% at this altitude.

There are multiple factors for these differences in peak pressure and flammability limits observed in the present tests and those of Summer (2004). Our test facility used a single component gaseous fuel (hexane) with precise control over the fuel concentration rather than using the vaporization of liquid jet fuel/hexane mixtures and total hydrocarbon characterization reported by Summer. We also tested at a fixed equivalence ratio and it is appears from the measurements reported by Summer that the equivalence ratio was increasing with decreasing altitude and pressure with a large variability in measured hydrocarbon concentration for tests at similar conditions. Our ignition system and mixing methods as well as the geometry of combustion vessel are significantly different than used by Summer (2004). All of these factors are known to contribute to differences in observed flammability limits.

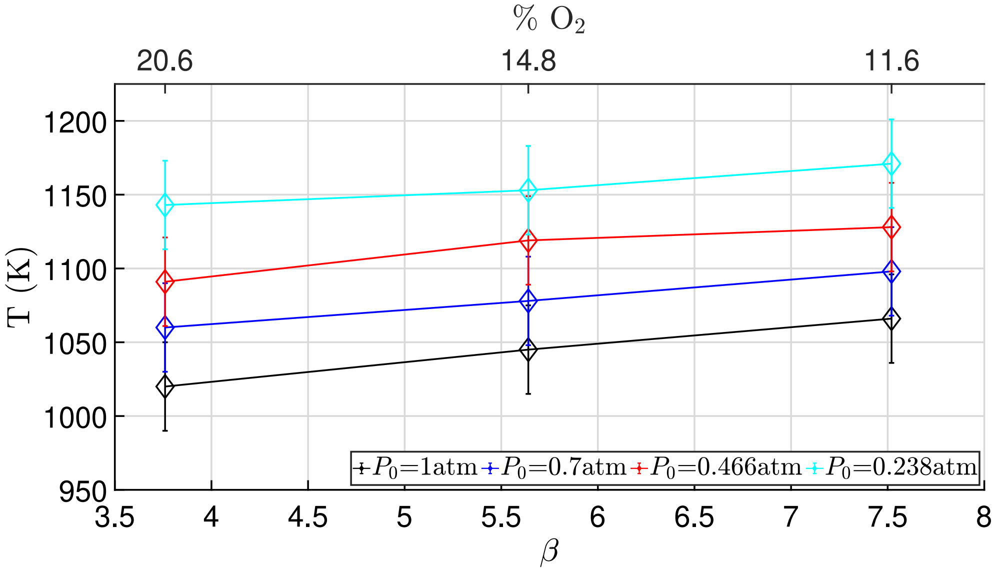

***Fig. 8**: Summary of ignition threshold temperatures vs β and O_2 concentration for each pressure condition.*

Ono et al. (1976) proposed a semi empirical correlation for their work with a small heated flat plate. This has the form shown in equation 1 where n is a fuel-dependent constant, H is the flat plate vertical length, T_{ign} is the ignition temperature, and P_0 is the initial pressure of the flammable mixture.

$$\ln(P_0^{n-1}H^{1/2}) = \frac{C_1}{T_{ign}} + C_2 \tag{1}$$

A least-squares fit is performed to determine the constants C_1 and C_2 using the ignition data for varying pressure at a fixed β. We note that n and H are both constant for our cases so these values are absorbed into the regression coefficients. The resulting relationship T_{ign} as a function of P_0 is shown in Fig. 9. The fit of the Ono et al. model to the present data gives confidence to the use of this model in extrapolating atmospheric pressure ignition data to lower pressures. Previous examination of this model by Jones and Shepherd (2021) demonstrated the validity of this correlation for extrapolating data obtained for a given height H over at least one order of magnitude for atmospheric hexane-air mixtures. Further work is needed and in progress in our laboratory to ground this correlation in fundamental properties of the flammable mixture in order to make this a more predictive tool.

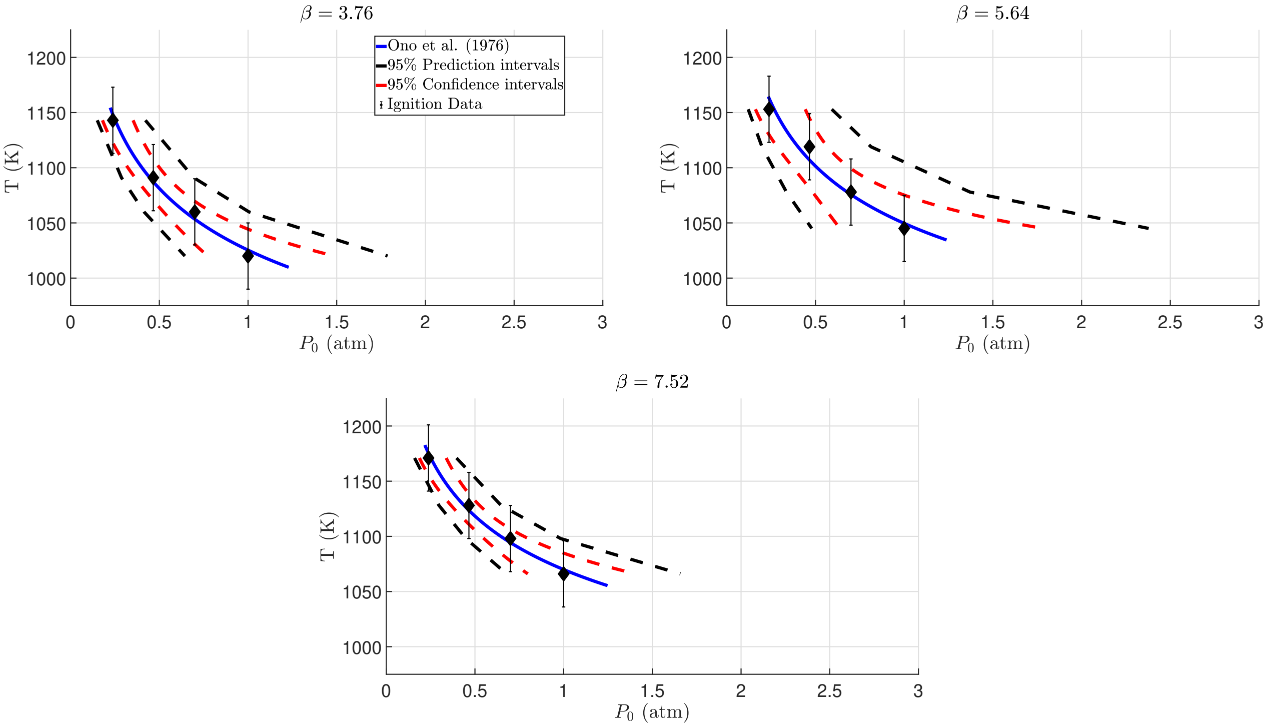

Fig. 9*: Ignition temperature vs initial pressure for* β *= 3.76, 5.64, and 7.52 (*X_{O_2} *= 20.6, 14.8, 11.6%). The blue line is the semi empirical correlation derived by Ono et al. (1976). The red and back dashed lines are the 95% confidence and prediction intervals computed from the linear regression.*

3.4 Ignition Testing Summary

The results of the logistic regression of the ignition testing for each of the fuels is summarized in Table 3. The reported ignition temperatures are also compared with those reported from previous studies using a small cylinder and the ASTM-E659 method respectively (Boeck et al. (2017), Martin and Shepherd (2021), Zabetakis (1965)). These results are also plotted in Figure 10 where the trend seems to be increasing ignition temperatures with fuel size int he case of external flow experiments. The opposite seems to be true for the internal flow AIT test however caution should be taken in giving any merit to the H_2 and C_2H_4 data since the AIT numbers for these are likely found using a different apparatus that the ASTM-E659.

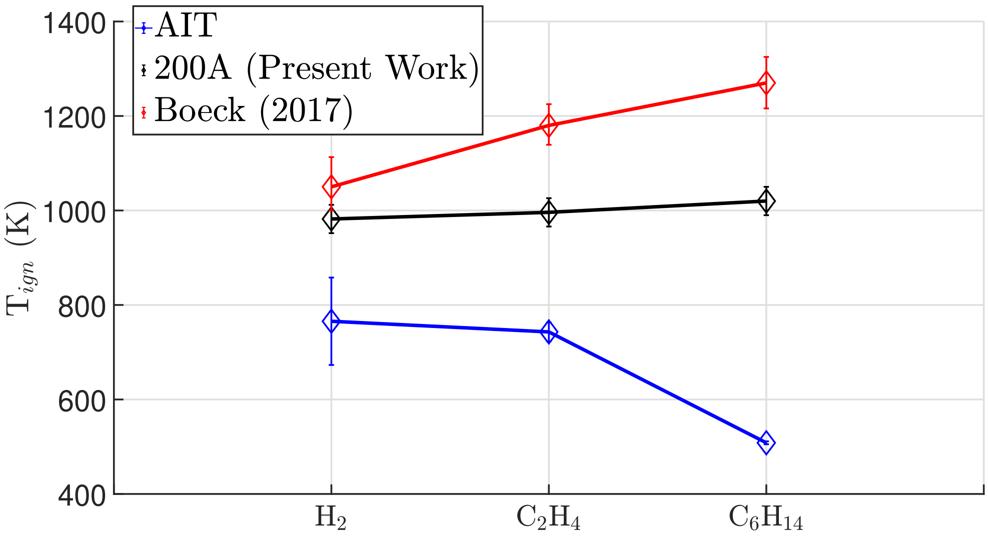

***Fig. 10**: Comparison of ignition temperatures for the three fuels studied with alternative ignition test methods. Error bars for H_2 and C_2H_4 ignition data represents range of values typically reported in literature.*

***Table 3**: Ignition temperatures for all fuels as compared with previous work. Boeck et al. (2017) used a 10 mm X 10 mm cylinder. AIT values for the gaseous fuels are of uncertain provenance and the method used in obtaining these data are not always clear. [a]Zabetakis (1965) [b]Martin and Shepherd (2021)*

Ignition test	H_2	C_2H_4	C_6H_{14}
AIT	673 K [a]	763 K [a]	508.3 ± 3.1K[b]
Boeck et al. (2017)	1050 K	1180 K	1270 K
Cylinder 200A (Present work)	982± 30K	996± 30K	1020± 30K

4 Conclusions

We conclude that both decreasing pressure and increasing nitrogen dilution lead to increasing thermal ignition thresholds in hexane-air mixtures. These studies were carried out with a single type and size of ignition source, a heated vertical cylinder which produced external laminar flow. Ignition thresholds increased over 100 K with a decrease in pressure from 1 to 0.238 atm. The effect of nitrogen dilution on ignition threshold at constant initial pressure was much smaller, within the range of uncertainty of the instrumentation.

In contrast to previous studies we were able to obtain ignition for oxygen concentrations as low as 11.6% for all initial pressures that we examined. The dependence of ignition temperature threshold on initial pressure is consistent with the correlation suggested by Ono et al. (1976). Tests with hydrogen and ethylene were consistent with the trends of ignition temperature threshold dependence on fuel and the decrease in ignition temperature with increasing vertical height of the hot surface. This was consistent with the observations of Jones and Shepherd (2021) for hexane and Ono et al. (1976) for a range of fuels.

Tests with hydrogen demonstrated that surface reactions - not observed in tests with hydrocarbon

DOI: 10.7795/810.20221124

fuels - had a significant effect on the wavelength dependence of thermal emission. The accumulation of a reddish-orange oxide layer was observed indicating some hydrated iron oxides were being formed at the surface. We had to monitor the surface condition and use a cleaning regimen in order to obtain reliable surface temperature measurements using optical pyrometry.

Acknowledgements

This work was carried out in the Explosion Dynamics Laboratory of the California Institute of Technology and supported by The Boeing Company Strategic Research and Development Relationship Agreement CT-BA-GTA-1. Conor Martin was also supported by the Department of Defense (DoD) through the National Defense Science & Engineering Graduate Fellowship (NDSEG) Program.

References

ASTM (2005). *ASTM-E659: Standard test method for autoignition temperature of liquid chemicals*.

Bane, S. P. M., Shepherd, J. E., Kwon, E., Day, A. C. (2011). *Statistical analysis of electrostatic spark ignition of lean H2/O2/Ar mixtures*. International Journal of Hydrogen Energy, 36(3):2344–2350. doi:10.1016/j.ijhydene.2010.05.082.

Boeck, L. R., Meijers, M., Kink, A., Mével, R., Shepherd, J. E. (2017). *Ignition of fuel–air mixtures from a hot circular cylinder*. Combustion and Flame, 185:265–277. doi:10.1016/j.combustflame.2017.07.007.

Brandes, E., Hirsch, W., Stolz, T. (2017a). *Zündtemperaturen In anderen oxidationsmitteln als luft; Projekt – Zündtemperaturen brennbarer Flüssigkeiten bei erhöhtem Sauerstoffanteil im O2+N2-Gemisch*. Technical report, PTB Braunschweig.

Brandes, E., Hirsch, W., Stolz, T. (2017b). *Zündtemperaturen In anderen oxidationsmitteln als luft; Projekt – Zündtemperaturen brennbarer Flüssigkeiten in Luft+N2O-Gemisch*. Technical report, PTB Braunschweig.

Cavage, W. M., Summer, S. (2008). *A Study of the Flammability of Commercial Transport Airplane Wing Fuel Tanks*. Final Report DOT/FAA/AR-08/8, Federal Aviation Administration, William J. Hughes Technical Center, Atlantic City International Airport, NJ.

Coward, H. F., Jones, G. W. (1965). *Limits of Flammability of Gases and Vapors*. Technical Report BM–BULL-503, Bureau of Mines, Washington D.C. doi:10.2172/7328370.

FAA (2017). *Operator Information for Incorporating Fuel Tank Flammability Reduction Requirements into a Maintenance and/or Inspection Program*. Advisory Circular AC No. 120-98A CHG 1, Federal Aviation Administration.

Hirsch, W., Brandes, E. (2005). *Zündtemperaturen binärer gemische bei erhöhten ausgangsdrücken*. Technical report, PTB Braunschweig and Berlin.

Jones, S. (2020). *Thermal Ignition by Vertical Cylinders*. Ph.D. thesis, California Institute of Technology.

Jones, S. M., Shepherd, J. E. (2021). *Thermal Ignition by Vertical Cylinders*. Combustion and Flame, 232:111499. doi:10.1016/j.combustflame.2021.111499.

Martin, C. D., Shepherd, J. E. (2021). *Low temperature autoignition of Jet A and surrogate jet fuel*. Journal of Loss Prevention in the Process Industries, 71:104454. doi:10.1016/j.jlp.2021.104454.

Michalski, L., Michalski, L., editors (2001). *Temperature Measurement*. J. Wiley, Chichester ; New York, 2nd ed edition.

Moravec, B. L., Boggs, R. E., Graham, R. N., Grim, A., Adkins, D. A., Snow, D., Haack, A. (2006). *Commercial Aircraft On-Board Inerting System*. US Patent No. 7,152,635 B2.

Ono, S., Kawano, H., Niho, H., Fukuyama, G. (1976). *Ignition in a Free Convection from Vertical Hot Plate*. Bulletin of JSME, 19(132):676–683.

Summer, S. (2004). *Limiting Oxygen Concentration Required to Inert Jet Fuel Vapors Existing at Reduced Fuel Tank Pressures-Final Phase*. Technical Report DOT/FAA/AAR-04/08, Federal Aviation Administration, William J. Hughes Technical Center, Atlantic City International Airport, NJ.

Zabetakis, M. G. (1965). *Flammability characteristics of combustible gases and vapors*. Technical Report BM–BULL-627, 7328370, Bureau of Mines, Washington D.C. doi:10.2172/7328370.

DOI: 10.7795/810.20221124

Ignition energy and flame propagation in ethylene oxide- air mixtures

Christophe Proust [a,b], Didier Jamois[a]

[a] Institut National de l'Environnement Industriel et des Risques, Parc Technologique ALATA, BP 2, 60550 Verneuil-en-Halatte, France
[b] Sorbonne Universités, UTC-TIMR, 1 rue Dr Schweitzer, 60200 Compiègne, France

E-mail: christophe.proust@ineris.fr

Abstract

Although Ethylene oxide (EO) is a root product in the industry, its flammable properties are not very well known because they are difficult to measure partly because this product is very dangerous but also because the Minimum Ignition Energy is said to be very small.

The aim of this work is to provide accurate experimental data about the minimum ignition energies, the flammable limits and burning properties of ethylene oxide air mixtures at ambient conditions.

To do this a very specific device including a new type of spark generator was developed and calibrated against know mixtures (propane, hydrogen). The explosion chamber is a 7 litre transparent and closed explosion cylinder so that flame velocities and pressure effects could be obtained.

Systematic measurements were performed for EO-air mixtures varying the EO concentrations from 4 to 22% v/v. The minimum ignition energy is 40 µJ for 10% EO in air at ambient conditions. This is lower than found in the literature. The burning velocity could be estimated and is about 1.6 m/s. Two reaction regimes were identified. Below about 13% a standard burning is observed (blue flame) producing CO_2 and consuming O_2. Above this value, a bright flame is seen producing smoke without any oxygen consumption nor CO, CO_2, H_2 formation suggesting a polymerization.

Keywords: *ethylene oxide, minimum ignition energy, flame speed, explosion severity*

1. Introduction

Ethylene oxide (EO) is not a new product (widely used at a raw base in the chemical industry) but its flammable properties look strange (upper flammable limit up to 100% v/v….) and seem difficult to obtain because of the significant toxicity of the product (Bonnard et al., 2006) but also because of the Minimum Ignition Energy (MIE) might be very small.

The aim of this work is to provide accurate experimental data about the minimum ignition energies, flammable limits of ethylene oxide air mixtures and burning properties.

In the following, the experimental device designed and operated for this purpose is described including safety consideration in the first section. In the second section the experimental results are presented.

2. Experiments

2.1 Ethylene oxide risk profile

EO is very difficult to handle because toxic, unstable (Bonnard et al.,2006)… Three exothermal reaction regimes were identified producing a propagating front. In dense phase, ethylene oxide may self-polymerise which may occur when exposed to a fire. But in vapour phase, pure ethylene oxide may decompose into carbon, methane and hydrogen (theoretical estimation) under the form of a cool flame propagating rather slowly. It can be triggered by an intense spark (tens of mJ). Mixed with air, ethylene oxide burns as a traditional fuel. The estimated MIE would be obtained for rich mixtures (10% v/v) and the maximum laminar burning velocity would be on the order of 1.08 m/s. The upper flammability limit is obviously 100% v/v. The lower flammability limit is about 3% v/v and the stoichiometry is 7.7 % v/v (Brighton, 1990).

Using the flame propagation theory (Glasmann, 1977), a laminar burning velocity of 1 m/s will give a quenching distance, D_{quench}, of about 1 mm (Peclet number=50). Using the well know D_{quench}^2 correlation with MIE (Kuchta, 1985), the minimum ignition energy should be on the order of 50 µJ.

EO is particularly toxic (Bonnard et al., 2006): irritant, carcinomic and mutagen. IDLH[1] (30 mn exposure) is 800 ppm producing oedema, and the carcinogenic and mutagen effects are possible above a few tens of ppm for a chronic exposure. The smell is detectable at 300 ppm.

2.2 Explosion vessel and associated piping

The explosion chamber is a 7-liter transparent cylindrical chamber (Figure 1) able to support a static internal pressure amounting 100 bars. It is equipped with many measuring ports and feeding lines. The supplier provides ethylene oxide under liquid form only conditioned in small (5 l) containers. The mixture is prepared into a stainless-steel mixing tank (4 l) using the partial pressure method (Kistler piezoresistive 0-10 bar gauges) . The first step is to evacuate the mixing tank, then some liquid EO is introduced using a micrometric manual valve. Enough time is provided for the pressure to reach equilibrium and air is introduced until the desired concentration is reached. Then again some time is allowed for the mixture to equilibrate. This procedure and the homogeneity of the mixture are controlled using oxygen meters located on the purge line (Servomex paramagnetic sensor). Dry air only was used. The explosion chamber is carefully dried and evacuated before introducing the mixture inside the explosion chamber. Note that because of the serious hazards associated with EO, a specific experimental design was performed following a detailed risk analysis. One consequence is that the device has to be confined into a box which was purged continuously with the outside air.

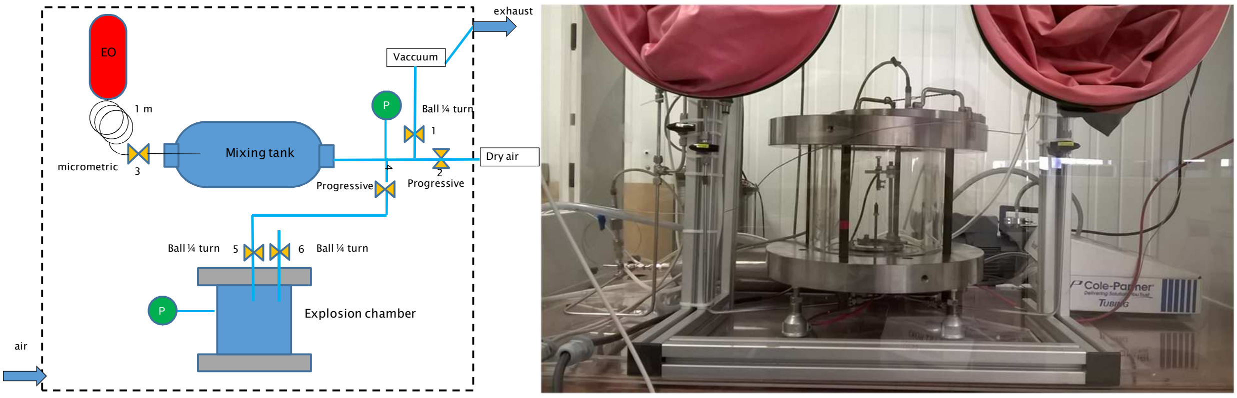

Fig. 1: *setup (left) and explosion chamber (right: 200 mm ID and 200 mm high)*

2.3 Spark gap generator

A new type of **spark generator** was devised. It is designed to reduce the overlap between ignition and no ignition zones and to better control the energy delivered inside the spark gap. Details are given elsewhere (Proust, 2020). An electrical spark is a two steps process. During the "disruption phase", a large voltage is required (typically 3000 V/mm) to ionize the atmosphere and create a "streamer". The current remains very low during that phase (micro amperes). After, the "arc" starts during which a large current flow through the spark gap. During this second phase, the voltage amounts some tens of volts with currents amounting some Amperes. In the present spark generator, it was decided to disconnect the two phases of the spark. A separate high voltage and high impedance circuit is used to produce the streamer (Figure 2). A second, low voltage and low impedance circuit, is used to produce

---

[1] Immediately Dangerous to Life or Health

the arc and dissipate the energy. The high voltage current is delivered through a set of 7 resistors (1 G Ω each) limiting the current supplied by the generator to about 1 µA. The low voltage current is delivered to the charge capacitor through a set of 11 resistors (1 MΩ each) offering the possibly to produce continuous sparking at a rate of about 10-100 Hz. A 1 mH coil is in series to limit the current through the spark (thus decreasing Joule losses). A Zener diode prevents the high voltage to be transmitted to the low voltage circuit. The contactor is on the high voltage circuit. Once the streamer is created the low voltage circuit discharges automatically. The current is measured using a standard current gauge (Wide Band Current Transformers STANGENES 2-0.1W) and the voltage with a high voltage probe (Tektronics P6015A). The electrodes are in tungsten, 0.3 mm in diameter, with rounded extremities, with a spark gap of 0.5 mm.

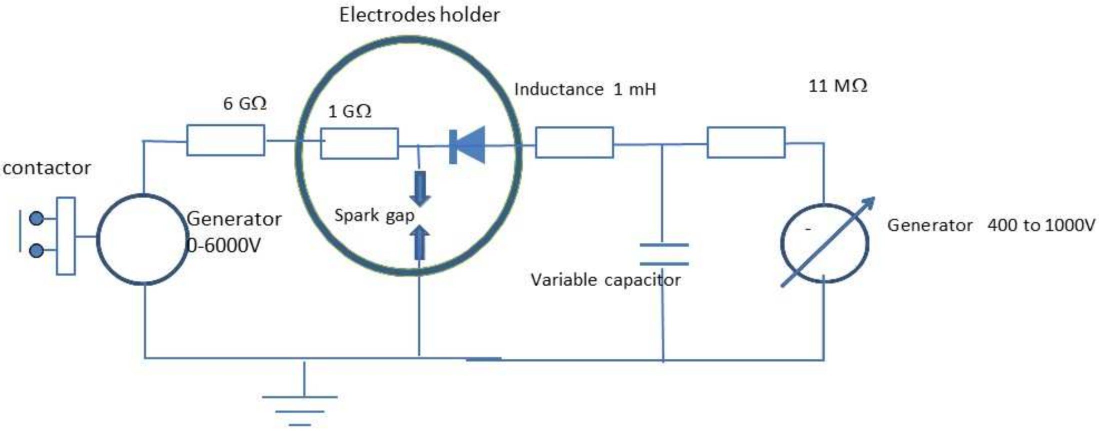

***Fig. 2:** scheme of the electrical circuit*

The spark gap and the Zener diodes being short circuited, the total capacitance of the low voltage part of the circuit is that of the charge capacitor. A residual value of 5-10 pF is constituted by the high voltage probe. If no coil is added, the inductance is 1.7 µH and the resistance is 0.1 Ω. With the coil inserted, the inductance is 1 mH and the resistance is 2 Ω. Because of the high voltage required to trigger the arc, any capacitance on the high voltage side of the circuit may store and add a significant amount of energy to the spark under the form of a tiny precursor spark. It was measured that a 1 m high voltage cable amounts about 20 pF which is much too large (energy stored = 90 µJ…). To remove this difficulty an extra resistor is added at the closest to the spark gap, on the electrode holder. Observations revealed that very tiny sparks occurred even when the low voltage circuit was not charged. This means that a residual capacitance remained. The high voltage circuit and the Zener diode are responsible for this. It was found that the residual capacitance of the high voltage circuit is only 1 pF and that of the diode is 3 pF so, 4 pF in total. It was verified that these precursor sparks are not able to ignite any mixtures (even H_2-air). The energy delivered by the precursor spark was added up to that of the low voltage capacitance. Further testing was performed to investigate the low voltage part behavior. The current and the voltage were measured at the spark gap (Figure 3). The very beginning of the current signal is an artifact probably due to the Zener diodes closing the low voltage part of the circuit. The signals resemble that of a typical RLC circuit and can be modelled rather faithfully. Such modelling can be used to estimate the yield of the spark (ratio of the electrical energy consumed in the spark gap divided by that stored in the low voltage capacitor). In the situation of Figure 8, with a reduced current, the yield is about 90%. In most situation the yield was about 70%.

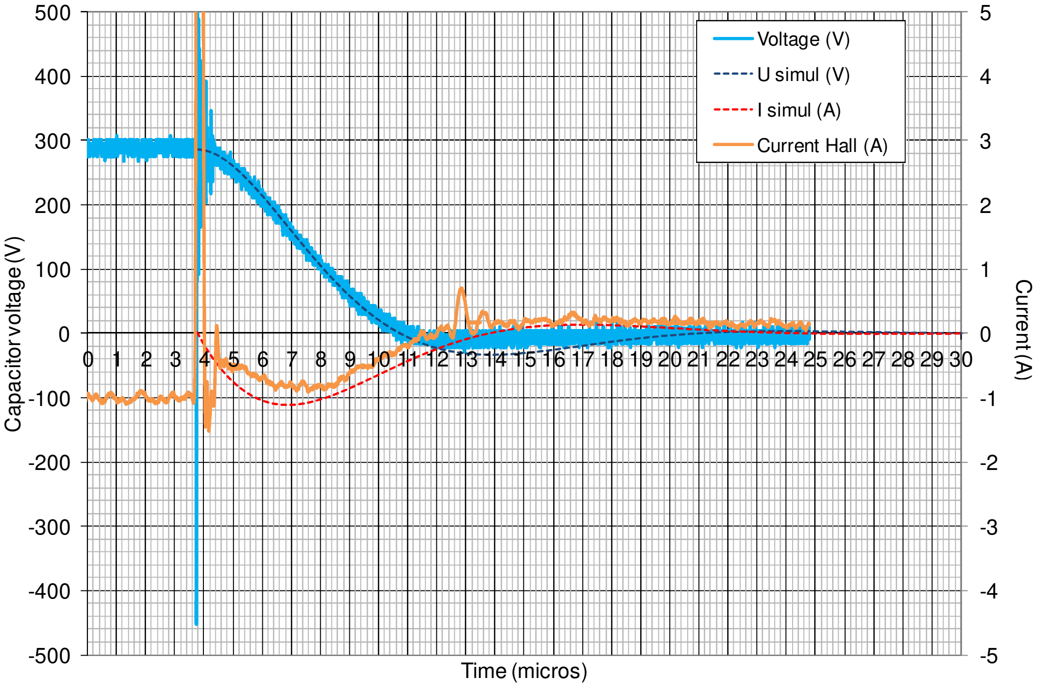

Fig. 3: *current voltage signals: streamer triggered spark, with a 1 mH additional inductance, 290 V in the 20 nF capacitor, with the diodes.*

2.4 Measurements

The maximum explosion (over)pressures is measured using a Kistler 10 b piezoresistive gauge. High speed video (up to 10000 fps: Photron camera) is used.

Normally, the ignition diagnostic is straightforward (flame propagation and pressure increase) but may be more difficult for slowly reactive mixtures (near the flammability limits for instance). In such a case, the final diagnostic rests on the behavior of the initial flame kernel. If it grows linearly with time, ignition is successful otherwise it shrinks. But even if some flame kernel growth is detected and ignition is physically achieved, in some situations, the flame ball could be convected upwards and ultimately be quenched in contact with the cold upper flange of the chamber, thus not providing any explosion. This is more likely for very small chambers and may not occur with the present experimental configuration.

The energy delivered by the spark is obtained by measuring the voltage of the arcing circuit (low voltage capacitor). The yield is depending on this and was measured while developing the spark generator. The energy delivered to the spark gap is that sored in the low voltage capacitor plus that stored by the high voltage part of the circuit times the yield.

2.5 Calibration

The **MIE measurement** method was designed and checked at ambient temperature using reference fuels propane and hydrogen since the expected MIE for EO is supposed to lie between that for those reference fuels. As experimentalists know, the ignition threshold may differ when starting from the no ignition zone and increasing gradually the spark energy until ignition than when starting from a positive ignition point and decreasing the energy. MIEs are much higher with the former procedure. The reason is unclear but perhaps the combustion “cleans up” or chemically activates the tip of the electrodes. In the following, the ignition threshold was looked for using the second procedure (starting for a positive ignition and decreasing the energy). To vary the ignition energy, the value of the capacitor was adapted (100 pF to 5000 pF) and the voltage was varied (between 400 and 1000 V). The energies on the following graphs are that stored in the low voltage capacitor and in the streamer high voltage capacitors (4 pF). To calculate the latter the breakdown voltage was measured by decreasing the high voltage until no spark occurred anymore (2700 V with the air of the bottle at ambient temperature and atmospheric pressure). Results obtained at room temperature are presented on figure 4. Note that each point represents at least 1 second of continuous sparking, so typically 50 sparks. The values are in line with the data from the literature (Randeberg and Eckhoff, 2007; Ono et al., 2007) with a minimum at 20% amounting 18 µJ for hydrogen air mixtures and about 300 µJ for stoichiometric propane air mixtures.

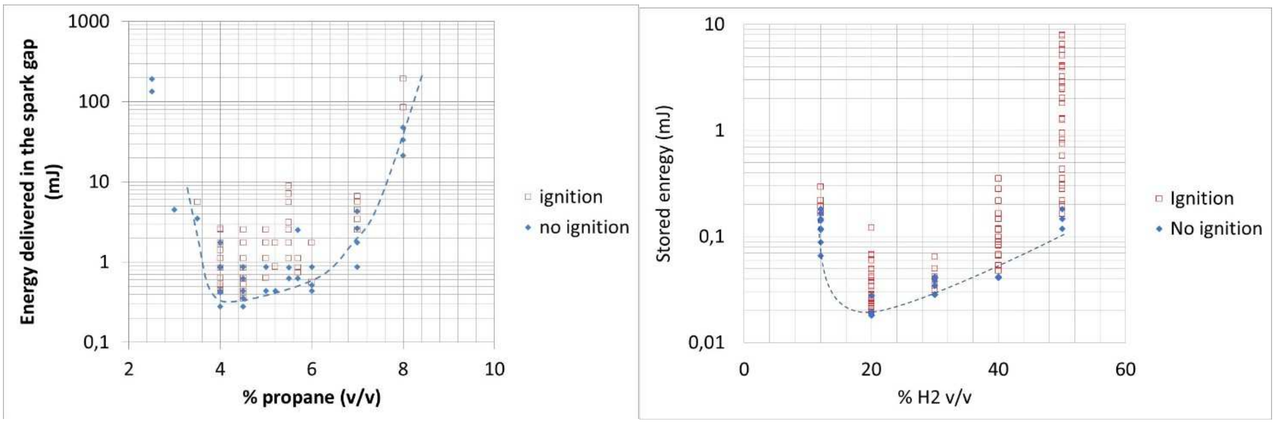

Fig. 4: *Measured MIEs for C_3H_8 air (left) and for H_2-air mixtures at ambient conditions (right)*

3. Results and discussion

3.1 Ignitability and flammability

The measurement of MIE for EO-air mixtures at ambient conditions are presented on Figure 5

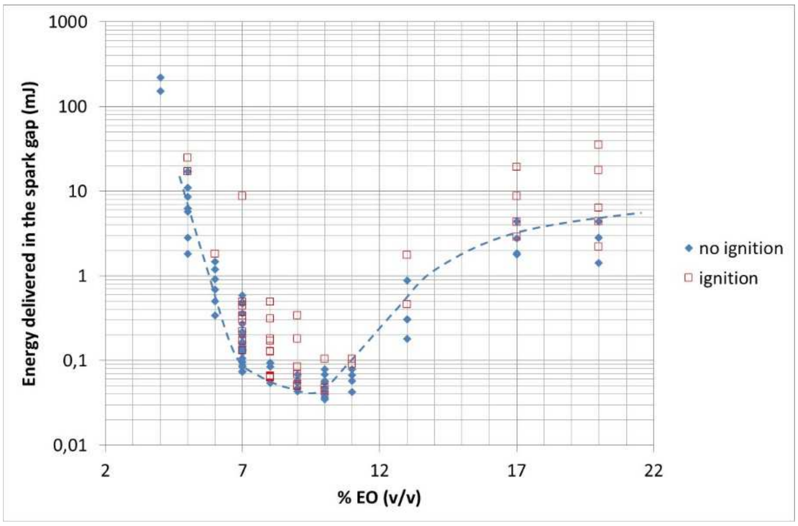

Fig. 5: *measured minimum ignition energies for ethylene oxide air mixtures at ambient conditions*

The minimum ignition energy is about 40 µJ and is obtained for 10% v/v EO in air in reasonable agreement with expectations. A change in the traditional U shape curve is noticed above 13% v/v EO in air suggesting a change in the chemical mechanism. This point is addressed later.

The lower flammability limit might be close to 4%v/v EO in air. There is not sign of upper limit but rather some plateau in the ignition energy (10 mJ) suggesting a different kind of propagation.

DOI: 10.7795/810.20221124

3.2 Explosion and flame propagation

A typical sequence of photos is shown on Figure 6 for the flame propagating a 7% v/v EO-air mixture. The pictures were postprocessed to increase the contrast and ease the calculation of the outwards flame velocity. In the present case, the outwards velocity, Vf, around the ignition point is 3 m/s (less than 10 cm from the ignition point).

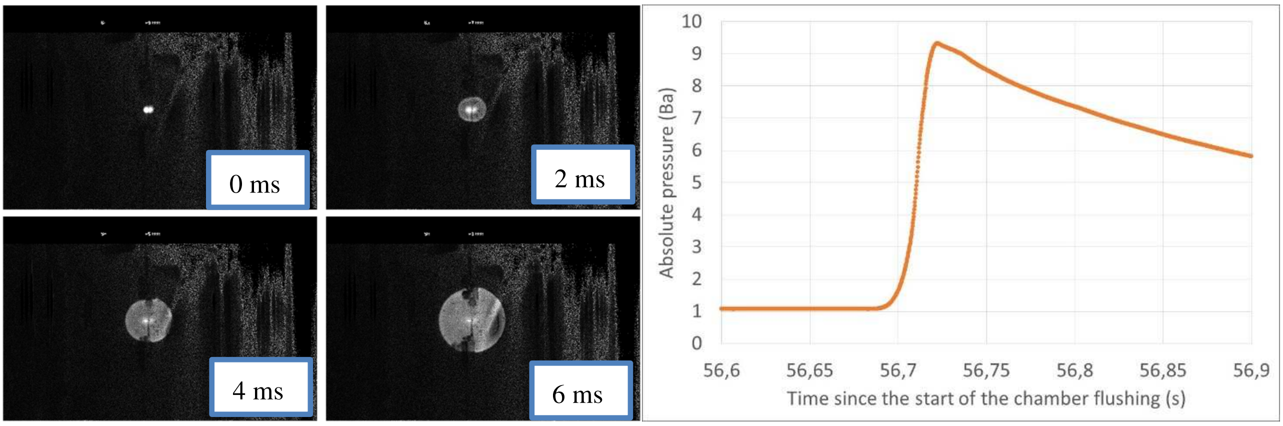

Fig. 6: *flame kernel development (7% EO, 2 ms between frames) and pressure time trace*

Explosion parameters are shown in Table 1 below. The explosion severity index K_G was derived from the maximum explosion pressure rise (dP/dt_{max}) and the vessel volume (V) using the "cubic law" recalled in expression [1] (Mittal, 2017). The expansion ratio (Exp) of the burned products was deduced from the maximum explosion pressure (P_{vmax}) using expression [2] (from Proust, 2017). The laminar burning velocity Sl is simply the ratio between the outwards flame velocity divided by the expansion ratio. Maximum explosion pressures and outward flame velocities are given in Table 1.

$$K_G = \left(\frac{dP}{dt}\right)_{max} \cdot V^{1/3} \qquad [1]$$

$$Exp \approx \frac{1}{\gamma_p} \cdot \left(\frac{P_{vmax}}{P_{init}} - 1\right) \qquad [2]$$

where P_{init} is the initial pressure and is the ratio of specific heats of the burnt product (typically 1.35).

The burning velocity at 10% is about =1.5 m/s. This is on the order of values for lean hydrogen air mixtures for which the minimum ignition energy might range between 20 and 100 µJ. Consequently, the measured minimum ignition energy for EO-air mixtures seems logical. Note the laminar burning velocity is hardly varying as function of the EO concentration which is an unusual behavior and would need clarification.

***Table 1:** explosion parameters for EO-air explosion (ambient initial conditions): accuracy of % EO ±0.1% v/v, of P_{max} ±0.01b and of Vf ±0.1m/s*

% EO v/v	P_{vmax} (ba)	$(dP/dt)_{max}$ (b/s)	Kg (b.m/s)	Vf (m/s)	Exp	Sl (m/s)
5	6,5	125	24	6,5	4,07	1,60
6	7,9	280	54	7,9	5,11	1,55
8	9,3	750	143	9,3	6,15	1,51
9	9	810	156	9	5,93	1,52
10	9,4	980	187	9,4	6,22	1,51
11	9,5	1000	191	9,5	6,30	1,51
13	9,2	650	124	9,2	6,07	1,51
17	8,6	330	63	8,6	5,63	1,53
20	8,4	200	38	8,4	5,48	1,53

3.2 Burning mechanisms ?

Perhaps the rather strange behavior of flame propagation in EO-air mixtures has to do with the flame chemistry. As said before there is a turning point in the MIE curve at 13% v/v EO in air. Pictures of the flame are presented on Figure 7. Below 11% the flame is blue, at 17% it is shallow green and bright orange above. 13% is intermediate between blue and green. The strong evolution of the luminosity suggests a significant change in the chemistry.

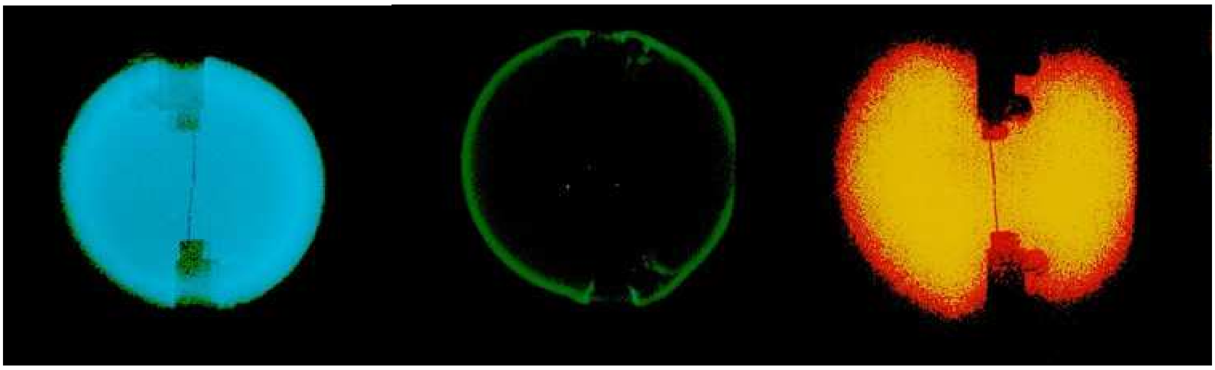

***Fig. 7:** pictures of EO-flames at 5 cm from the ignition point (left 11% v/v EO, center 17 % and right 20%)*

To start investigating this aspect the burnt gases were sampled and analyzed using gas chromatography. The results are shown in table 2. Water is condensed to perform the measurements. For the 7% EO-air mixture a classical combustion occurs producing CO_2 (and certainly water). For the rich mixture (20% EO v/v), there is no combustion (no CO, CO_2 no O_2 consumption) but a lot of smoke and dust into the vessel suggesting a polymerization of the ethylene oxide.

Table 2 : *gas chromatography of the burned gases for EO-air explosion (ambient initial conditions)*

Gas	7% EO	20% EO
H_2	< 10 ppm	< 10 ppm
O_2	11.1±0.4 %	20.0±0.7 %
N_2	81.1±7 %	76.0±6.7 %
CO_2	6.86±0.47 %	0.16±0.02 %
CO	86±14 ppm	0.51±0.04 %
CH_4	< 25 ppm	46±5 ppm

4. Conclusions

A new generation of spark generator was developed to measure very low minimum ignition energies (MIE). The performances of the device were checked by comparing the measured MIEs for propane air mixtures with various compositions and of for a H_2-air mixtures.

Systematic measurements were performed for EO-air mixtures varying the EO concentrations from 4 to 22% v/v. The minimum ignition energy is 40 µJ for 10% EO in air at ambient conditions. The burning velocity could be estimated and is about 1.5 m/s and KG amounts nearly 200 b.m/s.

Two reaction regimes were identified. Below about 13% a standard burning is observed (blue flame) producing CO_2 and consuming O_2. Above this value a bright flame is seen producing smoke without any oxygen consumption nor CO, CO_2, H_2 formation suggesting a polymerization.

Acknowledgements

The author gratefully acknowledges the support of his Institution (INERIS) and Mr. Philippe Le-grill in the achievement of this very difficult work.

References

Bonnard et al. (2006), Oxyde d'éthylène, fiche toxicologique de l'INRS, n°70, www.inrs.fr

Britton L.G. (1990), Thermal Stability and Deflagration of Ethylene Oxide, Plant/Operations Progress, 9:April, 75.

Proust C. (2020), A new technique to produce well controlled electrical sparks. Application to MIE measurements, communication to the 13th ISHPMIE held online, July 2020.

Randeberg, E. and Eckhoff, R.K, Measurement of minimum ignition energies of dust clouds in the 1 mJ region, J. Hazardous Materials, Vol. 140, 2007, 237-244.

Ono, R., Nifuku, M., Fujiwara, S., Horiguchi, S., Oda, T., Minimum ignition energy of hydrogen–air mixture: Effects of humidity and spark duration, Journal of Electrostatics, Volume 65, 2007, 87-93.

I. Glasmann , Combustion, Academic Press, London, 1977

Kuchta, J. M. (1985), Investigation of Fire and Explosion Accidents in the Chemical, Mining, and Fuel-Related Industries A Manual, U.S. Bureau of Mines Bulletin 680

Proust C. (2017), Turbulent flame propagation in large dust-air clouds, Journal of Loss Prevention in the Process Industries, volume 49, 2017, 859-869.

Mittal M. (2017), Explosion pressure measurement of methane-air mixtures in different sizes of confinement, Journal of Loss Prevention in the Process Industries, volume 46, 2017, 200-208.

DOI: 10.7795/810.20221124

Experimental study of Unconfined Lean Hydrogen-Oxygen Explosions

Keita Tanaka[a], Akihiro Ueda[a], Tomoyuki Johzaki [a], Takuma Endo [a], Yangkyun Kim[b], & Wook-yung Kim[a*]

[a]Hiroshima University, Higashihiroshima, Japan

[b]Korea Institute of Civil Engineering and Building Technology, Hwaseongsi, Republic of Korea

E-mail: kimwk@hiroshima-u.ac.jp

Abstract

Explosion hazards due to hydrogen-oxygen mixtures remain one major problem faced by the energy industries, despite hydrogen has attracted attention as alternative energy without carbon emissions. Although there are many studies on hydrogen-air explosions, the research in hydrogen-oxygen explosions remains limited. In the present study, the flame propagation behaviour in an unconfined lean hydrogen-oxygen explosion were investigated experimentally using a hemispherical soap bubble method with the hydrogen-oxygen mixture. The flame propagation behaviour was photographed using the Schlieren method. The flame in lean hydrogen-oxygen mixtures was wrinkled by the Darrieus-Landau and diffusional-thermal instabilities leading to flame acceleration. The flame acceleration of hydrogen-oxygen mixture has occurred at the early stage of flame propagation compared to that of hydrogen-air mixtures. The dimensionless flame speed increased as flame radius became larger. A linear correlation between the critical Péclet number and the Markstein number for hydrogen-oxygen mixtures is found.

Keywords: *Gas Explosion, Hydrogen, Diffusional-Thermal Instability, Soap bubble*

1. Introduction

Currently, various measures are being attempted to move toward a hydrogen society. Among these measures, hydrogen and various gases are used, some of which are hydrogen-oxygen mixtures. For example, the concept that hydrogen and oxygen from water on the lunar surface be converted into electricity using fuel cell technology for use in lunar surface activities was proposed. In addition, a plan to use hydrogen-oxygen fuel cells, which currently use hydrogen-air fuel cells, has been proposed with the aim of achieving complete zero emissions (Partheepan & Hunt, 2021). Although the use of hydrogen-oxygen mixtures continues to expand, the risk of explosions must always be considered when handling gas mixtures.

Causes of damage in a gas explosion in which a combustible gas-oxygen mixture is ignited by ignition source the includes radiation heat, scattering of objects, and blast wave. Among these, the impact of damage caused by blast wave is particularly devastating, and several models have been proposed to predict blast wave in gas explosions (Dobashi et al., 2011; Dorofeev, 2011; Strehlow et al., 1979). These models demonstrate that the intensity of the blast wave depends on the flame propagation behaviour, in particular, the flame acceleration phenomenon.

Flame acceleration is caused by intrinsic flame instabilities that increase the surface area of the flame. Among the inherent instabilities of flames classified by Williams (1985), the Darrieus-Landau instability and the diffusion-thermal instability have a significant impact on the flame acceleration.

The Darrieus-Landau instability is caused by thermal expansion of the gas by combustion. This instability manifests itself in all flames and its effect increases as the flame expands (Darrieus, 1938; Landau, 1944). In addition, the diffusional-thermal instability in the non-equidiffusive premixed flame can be evaluated by the Lewis number (Le), defined as the ratio of the thermal conductivity of the mixture to its diffusion coefficient. When $Le < 1$, mass diffusion becomes dominant and destabilizes the flame. On the other hand, for $Le > 1$, thermal diffusion dominates and stabilizes the flame. At a small flame radius, these instabilities are suppressed by strong stretching and thereby the flame becomes stable. As the flame expands, the flame is wrinkled by the reinforcement of instabilities with the reduction of the stretching effect, leading to the onset of flame acceleration.

In order to evaluate the blast wave of hydrogen-oxygen mixtures, it is necessary to understand the phenomenon of flame acceleration in hydrogen-oxygen mixtures. However, while there have been many studies on the acceleration phenomena of hydrogen-air flame (Kwon et al., 2002; Kim et al., 2015; Kim et al., 2018; Kim et al., 2019; Yaguchi et al., 2021), few experiments have been conducted on hydrogen-oxygen mixtures (Skinner et al., 2020). Skinner investigated the combustion characteristics of freely expanding hydrogen⁻oxygen explosions including flame propagation within the hydrogen-oxygen mixture and blast wave propagation in the surrounding air. Recently, Shiotani et al. (Shiotani et al., 2021) investigated that the flame propagation behaviour of hydrogen-oxygen mixture using spherical soap bubble method. Although there are many studies on the flame acceleration of hydrogen-air mixtures, the research in that of hydrogen-oxygen mixtures remains limited. This issue on the flame acceleration remains briefly addressed in the literature (Shiotani et al., 2021). In the present study, the flame acceleration in unconfined lean hydrogen-oxygen mixtures was investigated using a hemispherical soap bubbles method. In particular, the critical flame radius and the dependence of the critical Péclet number on the Markstein number of a hydrogen-oxygen flame was investigated.

2. Experiments

The experiments have been carried out with a hemispherical soap bubble method (Dennis et al., 2014; Manoubi et al., 2015) . This experimental design was employed because an unconfined space was needed to measure, the flame propagation behavior and blast wave in a lean hydrogen-oxygen mixture simultaneously. Herein, we report the flame propagation behaviors. A schematic of the apparatus used in this experiment is shown in Fig. 1. The hydrogen-oxygen mixture was prepared in a mixing chamber and a hemispherical soap bubble with the mixture created with a diameter of 200 mm. The spark plug was then activated by an ignition system. The flame propagation was visualized using the Schlieren photography with a high-speed camera (FASTCAM Nova S16) at 20000 flame per second. The laminar burning velocity (S_{u}^{0}), flame thickness (δ), the expantion ratio (σ) were calculated by the Chemkin-Pro with the San Diego Mechanism.

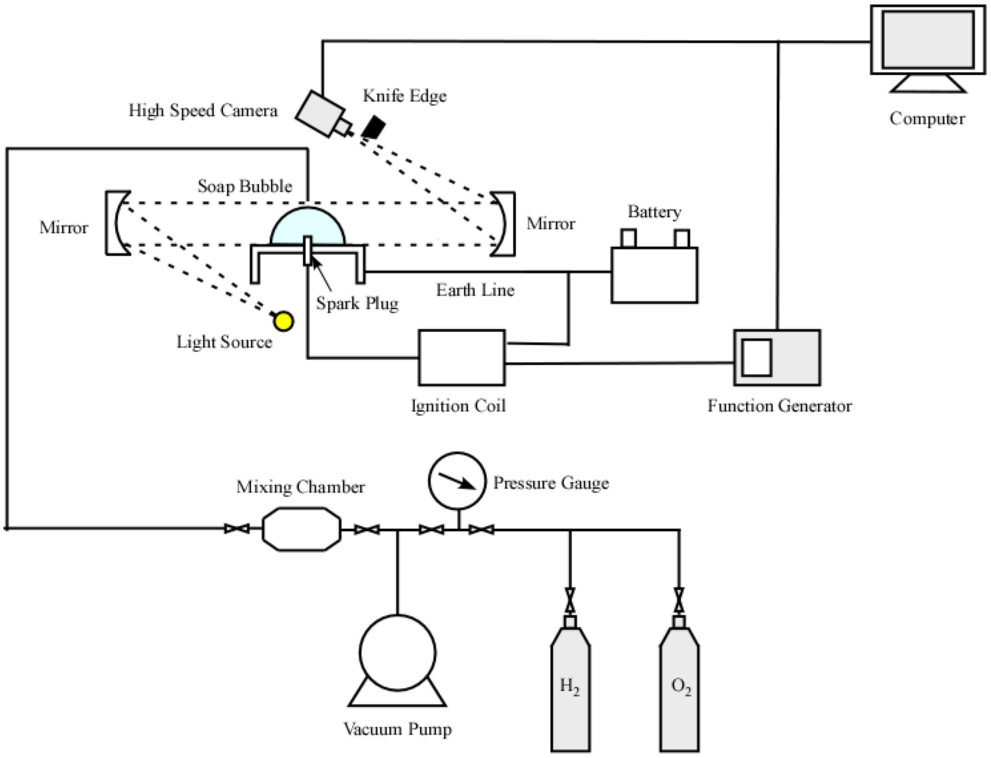

Fig. 1. *Schematic of the apparatus*

3. Results and discussion

Figure 2 shows the Schlieren images of propagating flame in the lean hydrogen-oxygen mixture. A hemispherical flame propagates in a hemispherical soap bubble as seen in Fig. 2(a). In the present study, the flame radius, r, was derived from $r = \sqrt{4A/\pi}$, where the flame area, A, was measured from the Schlieren images as shown in Fig. 2(b). The reason it was not derived from the hemispherical flame area was to consider the effect of ground surface. The flame area was evaluated by using a Sobel Filter.

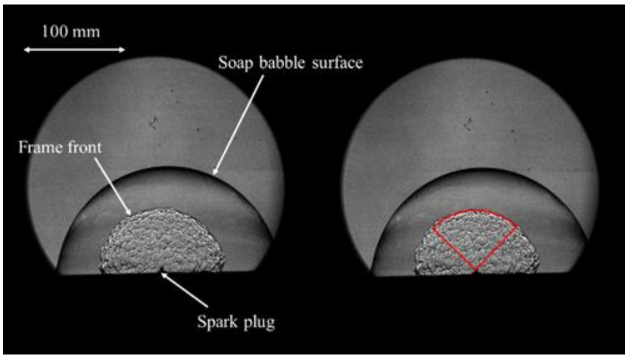

(a) *flame propagation* (b) *Measuring range*

Fig. 2. *Detail of Schlieren images*

Figure 3 shows the Schlieren images of lean hydrogen-oxygen flames at various equivalence ratios. Unstable flames were observed in all conditions notwithstanding a small flame radius. The images demonstrate that as the equivalence ratio decreases, the development of cellular flame structure appears in the early stage of flame propagation. Such a fully developed cellular flame leads to flame acceleration.

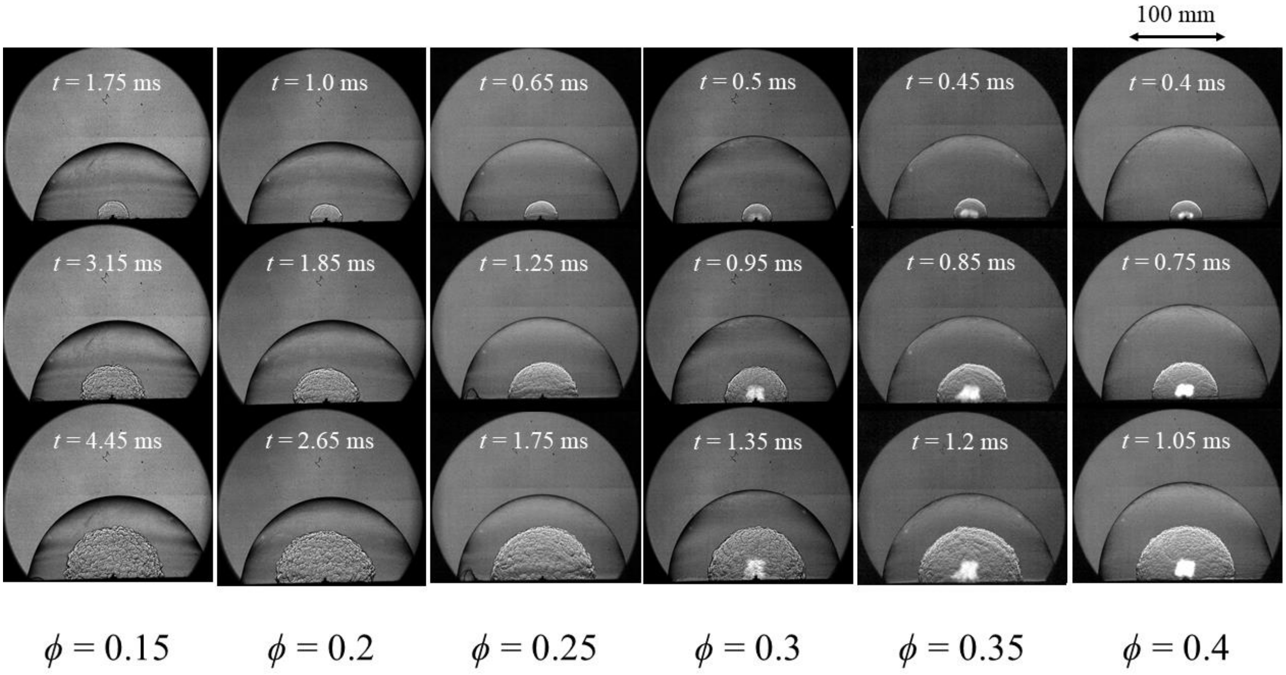

Fig. 3. *Schlieren image of lean hydrogen-oxygen flames at various equivalence ratios.*
ϕ *= equivalence ratio, t = time from ignition*

The flame radius and speed versus time from ignition at the various equivalence ratios in accordance with the above-mentioned analysis method are shown in Figs. 4 and 5. The flame speed increases with an increasing equivalence ratio. This is due to the increase in flame temperature and expansion ratio with increasing equivalence ratio. In addition, flame acceleration in the lean hydrogen-oxygen flames was observed owing to Darrieus-Landau and diffusional-thermal instabilities.

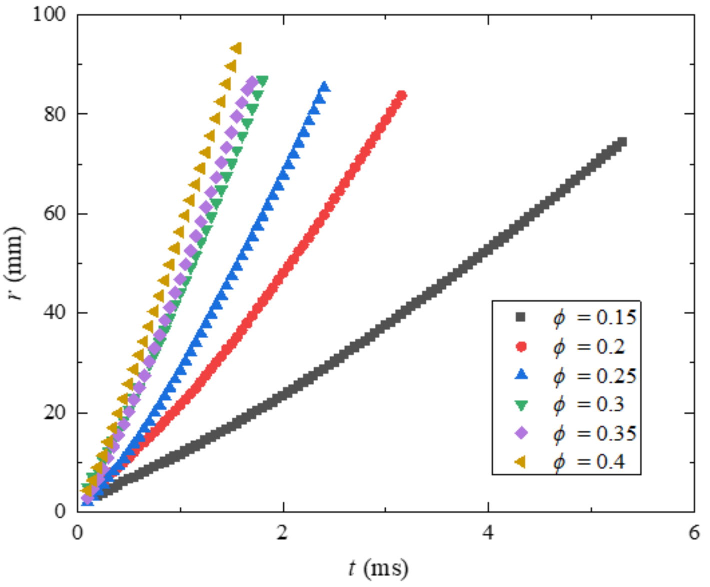

Fig. 4. *Flame radius versus time at various equivalence ratios.*

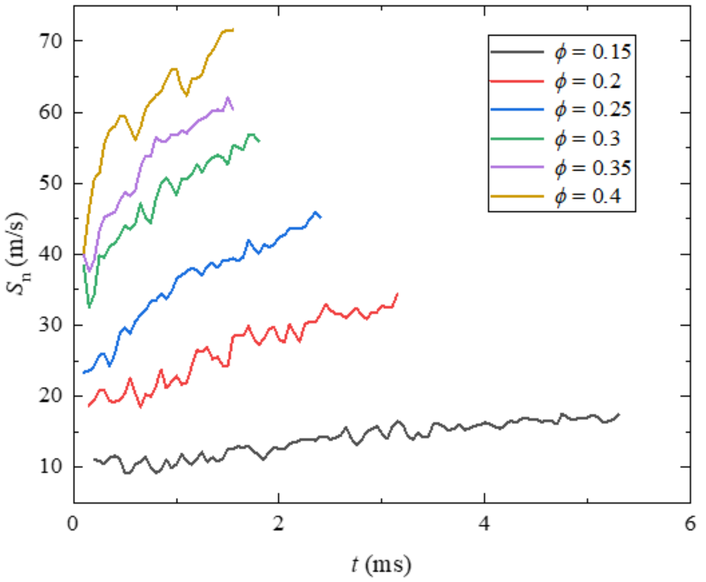

Fig. 5. *Flame speed versus time at equivalence ratio = 0.15 - 0.4.*

Figure 6 shows the measured flame speed as a function of the stretch rate at $\phi = 0.3$. Herein the flame stretch rate is defined as:

$$K = \frac{1}{A}\frac{\mathrm{d}A}{\mathrm{d}t} = \frac{2}{r}\frac{\mathrm{d}r}{\mathrm{d}t} = 2\frac{S_\mathrm{n}}{r} \tag{1}$$

The unstretched laminar flame speed S_n^0 can be obtained as follows,

$$S_{\mathrm{n}}^{0} - S_{\mathrm{n}} = L_{\mathrm{b}}K \tag{2}$$

where L_{b} is the burnged gas Markstein length (Clavin, 1985; Law & Sung, 2000). Hence, the laminar burning velocity S_{u}^{0} can be deduced using:

$$S_{\mathrm{u}}^{0} = \frac{\rho_{\mathrm{b}}}{\rho_{\mathrm{u}}} S_{\mathrm{n}}^{0} = \frac{S_{\mathrm{n}}^{0}}{\sigma} \tag{3}$$

where σ is the expantion ratio, and ρ_{u} and ρ_{b} are unburned and burned gas densities. The experimental and numerical values of S_{u}^{0} are compared in Fig. 7. The experimental values of S_{u}^{0} are in good agreement with those calculated by using Chemkin-Pro with San Diego Mechanism. The results indicate that the hydrogen-oxygen flame propagates at the concentration less than the lower limit of hydrogen-air mixture. Furthermore, the velocity for the hydrogen-oxygen mixture is much faster than that for the hydrogen-air mixture, e.g. the velocity at stoichiometric mixture is about 8 m/s faster, indicating the risk of the hydrogen-oxygen mixture. This is important because there is the hydrogen-oxygen mixture can be more dangerous than hydrogen-air mixture.

Figure 8 shows the dimensionless flame speed $S_{\mathrm{n}} \,/\, S_{\mathrm{n}}^{0}$ as a function of the Péclet number $Pe = r/\delta$ (dimensionless flame radius). Also, the laminar flame thickness δ is be defined as:

$$\delta = \frac{\lambda}{S_{\mathrm{u}}^{0} C_{\mathrm{p}} \rho_{\mathrm{u}}} \tag{4}$$

where λ is the thermal conductivity of gas mixtures, C_{p} is the specific heat at constant pressure. Contrary to flame speed, which tends to increase with increasing equivalence ratio, the value of $S_{\mathrm{n}} \,/\, S_{\mathrm{n}}^{0}$ tends to increase with decreasing equivalence ratio. Also, the Lewis number is $Le < 1$ for lean ean hydrogen-oxygen mixtures and tend to decrease with a decrease in equivalence ratio, e.g. the value estimated from the ratio of thermal conductivity and diffusion coefficient of $Le = 0.788$ at $\phi = 0.4$ decreases to that of $Le = 0.512$ at $\phi = 0.15$. Therefore, the increasing tendency of $S_{\mathrm{n}} \,/\, S_{\mathrm{n}}^{0}$ with a decrease in equivalence ratio rapidly is attributable to the diffusional-thermal instability.

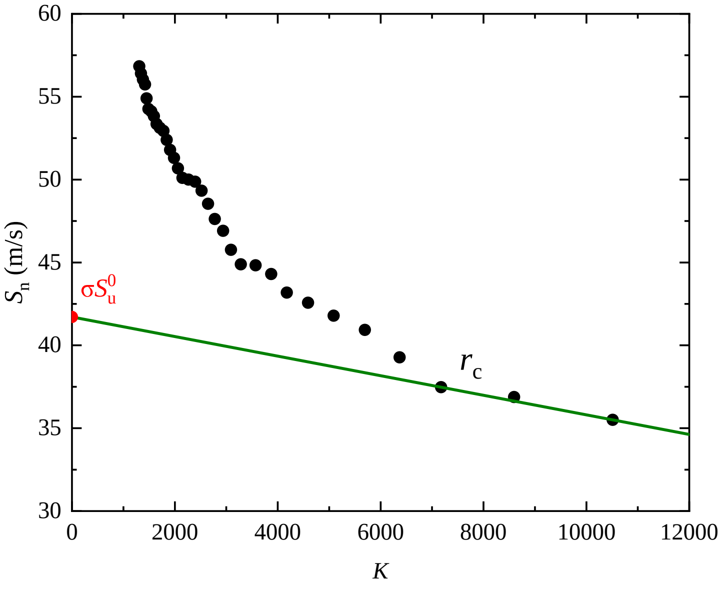

Fig. 6*. Flame speed versus flame stretch rate, ϕ = 0.3.*

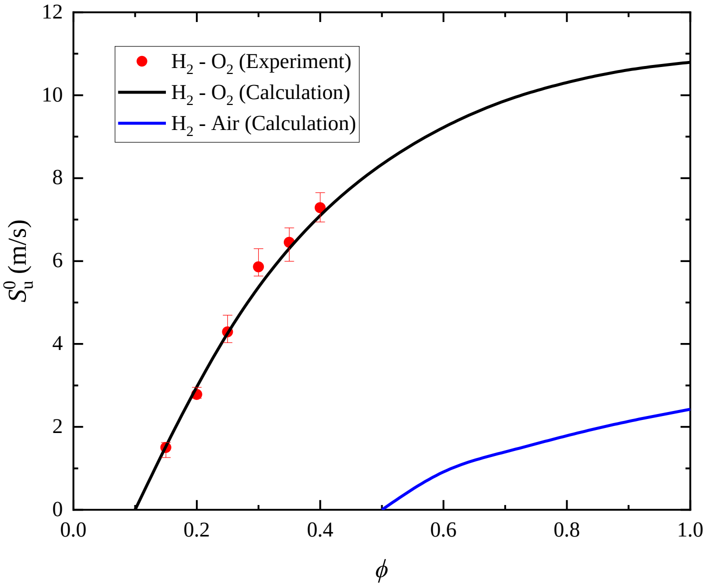

Fig. 7. *Laminar burning velocity versus equivalence ratio.*

DOI: 10.7795/810.20221124

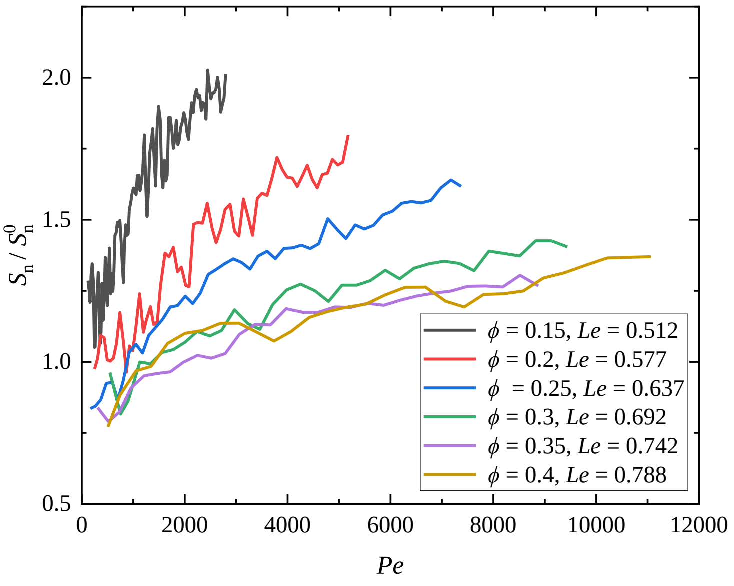

Fig. 8. *Dimensionless flame speed versus Péclet number.*

Figure 9 shows the critical flame radius as a function of the equivalence ratio. The results are in good agreement with the values was experimentally estimated by The data obtained from previous sphecial soap bubble test (Shiotani et al., 2021). In lean hydrogen-oxygen mixtures, the critical flame radius decreases as decreasing the equivalence ratio owing to the diffusional-thermal instability, causing acceleration from an earlier stage.

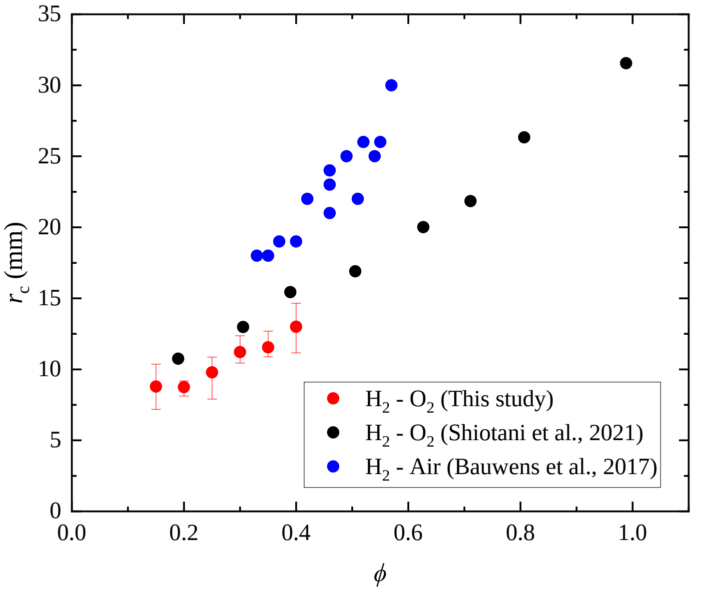

Fig. 9. *Critical flame radius versus equivalence ratio.*

Figure 10 shows the measured Markstein length as a function of equivalence ratio for hydrogen-oxygen mixtures. The results are in good agreement with the previous experiment (Shiotani et al, 2021). The theoretical Markstein length L_{b} was also calculated using:

$$\frac{L_{\mathrm{b}}}{\delta} = \sigma\gamma_1 + \frac{1}{2}(Le - 1)Ze\gamma_2 \tag{5}$$

where $\gamma_1 = 2\sigma/(1 + \lambda_{\mathrm{b}})$, $\gamma_2 = 4\{(\lambda_{\mathrm{b}} - 1) - \ln 0.5\,(\lambda_{\mathrm{b}} + 1)\}/(\sigma - 1)$, $Ze = 4(T_{\mathrm{ad}} - T_{\mathrm{u}})/(T_{\mathrm{ad}} - T^0)$ is the Zeldovich number (Müller et al., 1997), $\lambda_b = \sqrt{\sigma}$, T_{ad} is adiabatic flame temperature, T_{u} is unburned gas temperature and T^0 is the inner layer flame temperature (Jomaas et al., 2007; Bechtold & Matalon, 2001). Although there is a disagreement between the theoretical value and experimental data, the decreasing trend of L_{b} with a decrease in the equivalence ratio was consistent. The theoretical value decreased slightly, but the experimental value decreased significantly at ultra lean mixtures. An inconsistency between theoretical and experimental values is ascribed to the measurement error due to the onset of flame acceleration in the early stages.

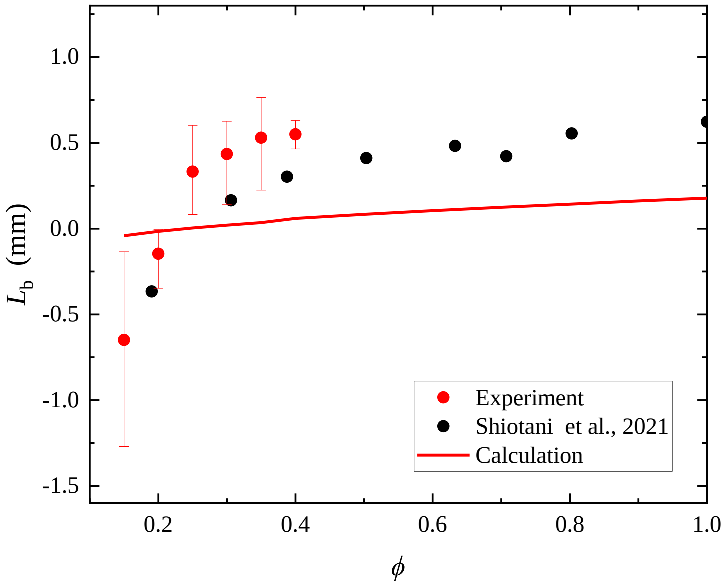

Fig. 10. *Markstein length versus equivalence ratio.*

Figure 11 shows the dependency of critical Péclet number, Pe_{c}, on the Markstein number, Ma_{b}. The Péclet number is the critical flame radius nondemensionalized by the laminar flame thickness, is defined as:

$$Pe_{\mathrm{c}} = \frac{r_{\mathrm{c}}}{\delta} \tag{6}$$

The Markstein number is the Markstein length nondimensionalized by the laminar flame thickness, is defined as:

$$Ma_{\mathrm{b}} = \frac{L_{\mathrm{b}}}{\delta} \tag{7}$$

A linear correlations is found between Pe_c and Ma_b for hydrogen-oxygen mixtures. The linear correlation between Pe_c and Ma_b for hydrogen-air mixtures is: $Pe_\mathrm{c} = 69Ma_\mathrm{b} + 1595$ (Kim et al., 2019). The depenedency of Pe_c and Ma_b comapred to preveious data for hydrogen-air mixtures (Bradley et al., 2007; Kim et al., 2019) as shown in Fig. 11. The linear correlation for hydrogen-air mixtures disagreed with the present correlation for hydrogen-oxygen mixtures. The result demonstrates that the ustable regime for hydrogen-oxygen mixtures is much wider than that of the hydrogen air mixture. The best-fit correlation between Pe_c and Ma_b for hydrogen-oxygen mixtures can be given as:

$$Pe_\mathrm{c} = 12\,Ma_\mathrm{b} + 615 \tag{8}$$

The onset of hydrogen-oxygen flame acceleration can be evaluated by this empirical expression. This is an important finding in the understanding of the onset of hydrogen-oxygen flame acceleration due to cellular flame instabilities. However, it is worth discussing these interesting facts revealed by the results of the onset of hydrogen-oxygen flame acceleration because of the lack of data for various equivalence ratios including rich mixtures.

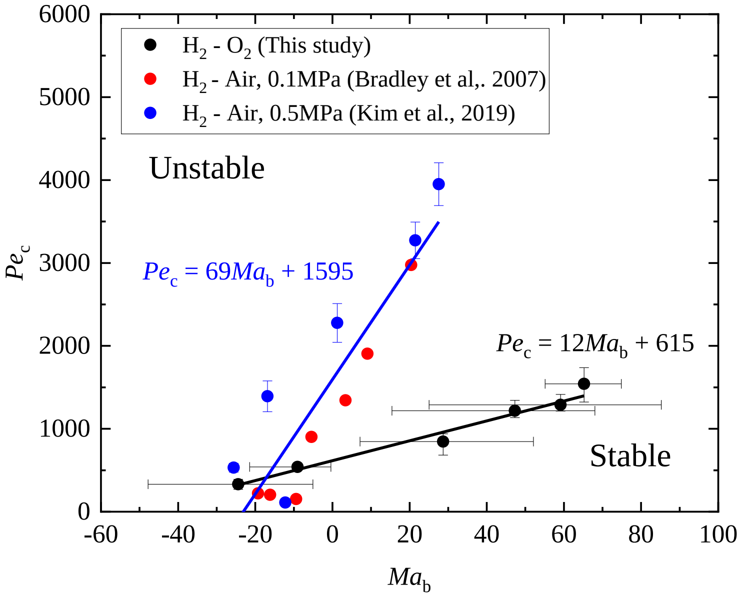

Fig.11. *Critical Péclet number versus Markstein number.*

4. Conclusions

In the present study, acceleration phenomena of a lean hydrogen-oxygen flame due to Darrieus-Landau and diffusional-thermal instabilities are experimentally investigated. While the flame speed decreased with the decrease in the equivalence ratio, the dimensionless flame speed increased rapidly. The critical flame radius associated with the onset of flame acceleration decreased as the equivalence ratio decreased. Furthermore, the values of the critical flame radius for hydrogen-oxygen mixture are smaller than those of hydrogen-air mixture. These indicate that the effect of diffusional-thermal instability due to the preferential diffusion of mass and heat is enhanced with decreasing of the equivalence ratio, thus causing the flame to accelerate earlier. In addition, the present findings confirm that the laminar burning velocity of hydrogen-oxygen mixture is much faster than that of the hydrogen-air mixture. From these results this indicates the hazardous nature of the hydrogen-oxygen mixture compared to the hydrogen-air mixture.

The dependence of the critical Péclet number on the Markstein length of a hydrogen-oxygen flame was investigated and compared to that reported in studies of hydrogen-air flame. The linear correlation between Pe_c and Ma_b for hydrogen-oxygen mixtures was obtained. In the correlation, the slope of hydrogen-oxygen mixtures is very small in comparison with that of the hydrogen-air mixtures. The result indicates that the unstable regime of hydrogen-oxygen flame is much wider than that of the hydrogen-air mixture.

Acknowledgements

The authors gratefully acknowledge the financial support from the Korea Institute of Civil Engineering and Building Technology (KICT) grant funded by the Ministry of Science and ICT.

References

Bauwens, C. R. L., Bergthorson, J. M., & Dorofeev, S. B. (2017). Experimental investigation of spherical-flame acceleration in lean hydrogen-air mixtures. *International Journal of Hydrogen Energy*, *42*(11), 7691-7697.

Bechtold, J. K., & Matalon, M. (2001). The dependence of the Markstein length on stoichiometry. *Combustion and Flame*, *127*(1), 1906-1913.

Bradley, D., Lawes, M., Liu, K., Verhelst, S., & Woolley, R. (2007). Laminar burning velocities of lean hydrogen–air mixtures at pressures up to 1.0 MPa. *Combustion and Flame*, *149*(1), 162-172.

Clavin, P. (1985). Dynamic behavior of premixed flame fronts in laminar and turbulent flows. *Progress in Energy and Combustion Science*, *11*(1), 1-59.

Darrieus, G. 1938 Propagation d’un front de flamme. La Technique Moderne 30, no. 18.

Dennis, K., Maley, L., Liang, Z., & Radulescu, M. I. (2014). Implementation of large scale shadowgraphy in hydrogen explosion phenomena. *International Journal of Hydrogen Energy*, *39*(21), 11346-11353.

Dobashi, R., Kawamura, S., Kuwana, K., & Nakayama, Y. (2011). Consequence analysis of blast wave from accidental gas explosions. *Proceedings of the Combustion Institute*, *33*(2), 2295-2301.

Dorofeev, S. B. (2011). Flame acceleration and explosion safety applications. *Proceedings of the Combustion Institute*, *33*(2), 2161-2175.

Jomaas, G., Law, C. K., & Bechtold, J. K. (2007). On transition to cellularity in expanding spherical flames. *Journal of Fluid Mechanics*, *583*, 1-26.

Kim, W., Sato, Y., Johzaki, T., & Endo, T. (2019). Experimental study on the onset of flame acceleration due to cellular instabilities. *Journal of Loss Prevention in the Process Industries*, *60*, 264-268.

Kim, W., Sato, Y., Johzaki, T., Endo, T., Shimokuri, D., & Miyoshi, A. (2018). Experimental study on self-acceleration in expanding spherical hydrogen-air flames. *International Journal of Hydrogen Energy*, *43*(27), 12556-12564.

Kim, W. K., Mogi, T., Kuwana, K., & Dobashi, R. (2015). Prediction model for self-similar propagation and blast wave generation of premixed flames. *International Journal of Hydrogen Energy*, *40*(34), 11087-11092.

Landau, L. D. (1944) On the theory of slow combustion. Acta Physicochim. URSS 19, 77–85.

Law, C. K., & Sung, C. J. (2000). Structure, aerodynamics, and geometry of premixed flamelets. *Progress in Energy and Combustion Science*, *26*, 459-505.

Müller, U. C., Bollig, M., & Peters, N. (1997). Approximations for burning velocities and markstein numbers for lean hydrocarbon and methanol flames. *Combustion and Flame*, *108*(3), 349-356.

Manoubi, M., LaFlèche, M., Liang, Z., & Radulescu, M. (2015). Experimental study of combustion characteristics of isolated pockets of hydrogen-air mixtures. *CNL Nuclear Review*, *5*(1), 133-142.

Kwon, O., Rozenchan, G., & Law, C. (2002). Cellular instabilities and self-acceleration of outwardly propagating spherical flames. *Proceedings of The Combustion Institute - PROC COMBUST INST*, *29*, 1775-1783.

Partheepan, J., Hunt, E. M. (2021). Thermodynamic Modeling of oxyhydrogen fueled combined cycle power plant. *Journal of Material Sciences & Engineering*, 10(4)

Shiotani, A (2021). An experimental study of propagating spherical flames in unconfined hydrogen-oxygen explosions. 9th International Conference on Hydrogen Safety

Skinner, T., Hargather, M., Blackwood, J., Hays, M., & Bangham, M. (2020). An apparatus for producing tunable, repeatable, hydrogen–oxygen-deflagrative blast waves. *Shock Waves*, *30*.

Strehlow, R. A., Luckritz, R. T., Adamczyk, A. A., & Shimpi, S. A. (1979). The blast wave generated by spherical flames. *Combustion and Flame*, *35*, 297-310.

Yaguchi, J., Kim, W., Mogi, T., & Dobashi, R. (2021). Flame acceleration and blast wave of H2–O2–N2–Ar mixtures in unconfined areas. *International Journal of Hydrogen Energy*,

Williams, F. A. (1985) Combustion Theory. Benjamin-Cummins.

DOI: 10.7795/810.20221124

CFD modelling of vented explosions for chambers of two different scales

Guillaume Lecocq [a], Jérôme Daubech [a] & Emmanuel Leprette [a]

Institut National de l'Environnement Industriel et des Risques, Parc Technologique ALATA, BP 2,
60550 Verneuil-en-Halatte, France

E-mail: guillaume.lecocq@ineris.fr

Abstract

Numerous practical uses of hydrogen imply a container, this latter containing process equipment and even hydrogen storage devices. Scenarios of confined explosions are often identified during risk analyses of such installations and related overpressure effects should be quantified.

CFD is theoretically attractive for vessels equipped with one or more vents as geometrical effects are intrinsically accounted for. Nevertheless, the physical sub-models of the CFD approach that are used to quantify flame speeds may vary from a modelling to another as well as the physical explanation of flame acceleration.

In this paper, CFD computations inspired of recent works (Tolias, 2018) are carried out for comparison with numerous measurements of explosions in a 4 m^3 chamber, free of obstacle, containing a homogenous H_2/air mixture (Duclos, 2019). Different mixture compositions are considered as well as several initial turbulent intensities. This step enables a first assessment of the CFD model.

Another set of computations is performed for a 37 m^3 chamber, also free of obstacle, with multiple vents in order to study the robustness of the model predictions when changing the flammable cloud length scale as well as the venting method. The limits of the modelling are finally discussed.

Keywords: *vented explosion, scale effect, hydrogen, CFD*

1. Introduction

Hydrogen is more and more used in the industrial processes in order to contribute to their decarbonization. In practice, hydrogen-based processes are often packaged in sea containers.

A representative but simplified configuration could be an electrolyser installed inside a container, surrounded with numerous pipes for conveying water and the separated gases, eventually large capacity storage vessels and a power supply network, all these elements occupying about at least 30 % of the container inner volume. Doors enable to access the technical zones of the container.

A risk analysis dedicated to this equipment could identify a scenario of a large flammable volume formation inside the container in case of hydrogen leak in the process. If an ignition occurs, a flame will be generated and propagate inside the container with a pressure rise leading to doors or vents opening, if these latter are present. At this stage, if the fresh gases are not totally burned, they can be ejected outside the container where a secondary explosion occurs due to flame propagation in the ejected flammable volume.

The pressure effects of such explosion have to be quantified for the safety study related to the equipment. Computational Fluid Dynamics (CFD) is an attractive tool for addressing an explosion in a container as numerous geometrical effects are at stake. Accounting for them could theoretically bring more accuracy in the results when compared to another approach involving approximations in the problem description. Nevertheless, performing a CFD modelling is not straightforward as it requires skills in numerical methods, knowledge of the explosion physics and of the capacities of the physical sub-models (turbulence, flame / turbulence interaction, …). Numerous CFD approaches were provided in the literature for modelling vented explosions for empty boxes, notably by Bauwens (2011), Molkov (2012) and Tolias (2018). Roughly, they are built in a similar manner but with different sub-models, which is notably explained by the different points of view of the authors concerning numerical models, explosion physics and modelling.

The current paper aims at contributing to the reflexion around the CFD modelling of vented explosion, this one being limited to free of obstacle enclosures. To meet this objective, two configurations are considered:

- A 4 m^3 enclosure with a 0.7 m x 0.7 m vent in which homogenous hydrogen/air mixtures can be ignited. The mixture can be turbulent before ignition or quiescent. Three hydrogen volume fractions are considered.
- A 37 m^3 vessel on which are mounted several vents, the total surface being conserved. The dimensions of this vessel are close to those of a 20 ft ISO container. A single equivalence ratio is studied.

CFD computations are performed for each geometry with an approach similar to the one published by Tolias in order to 1) assess if the choice of a set of sub-models can be used for modelling vented explosions with variations of the initial turbulence, hydrogen volume fraction and geometry and 2) evaluate whether the physics of the external explosion can be identified with such modelling or not.

2. Experimental set-ups

Numerous explosion tests were carried out by Duclos (2019) with an enclosure whose length, width and height are respectively 2 m, 2 m and 1 m. Homogenous flammable H_2/air mixtures were generated in the box. The parameters of interest were the initial hydrogen volume fraction and the initial turbulence intensity. The mixture is ignited at the centre of a 2 m x 1 m face and the 0.7 m x 0.7 m vent is located on the opposite face. This vent is a plastic sheet that weakly resists to pressure effects. Figure 1 shows the location of the pressure sensors.

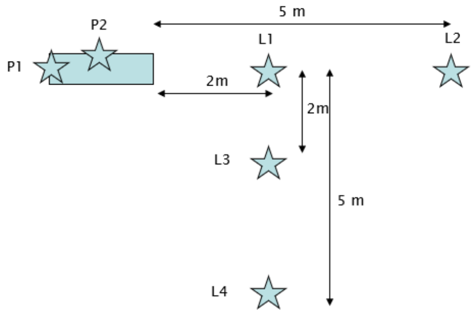

Fig. 1. Locations of the pressure sensors for the 4 m^3 enclosure. View from the top.

Tests that will be studied in the paper are listed in the Table below. Note the turbulence was experimentally characterized with a turbulent length scale and a fluctuating velocity.

Table 1: *Retained parameters values for modeling the 4m^3 vented explosions. Bold values correspond to adjustments of the original values supplied by Molkov (2012)*

Test	Hydrogen volume fraction	Regime before ignition	Damköhler number (in initial conditions)	Karlovitz number (in initial conditions)
4 and 36	16 %	Laminar	Undefined	Undefined
24 and 25	16 %	Turbulent (u' = 2,3 m/s, $L_t =$ 3,2 cm)	20	30
-	21 %	Laminar	Undefined	Undefined
23	21 %	Turbulent (u' = 5 m/s, L_t = 7 cm)	35	70
26	25 %	Laminar	Undefined	Undefined
28	25 %	Turbulent (u' = 4,5 m/s, $L_t =$ 7 cm)	70	60

Daubech et al. (2022) supply results of another experimental campaign with explosions in a larger scale enclosure. It is indeed 2.5 m wide and high and 6 m long. H_2 / air homogenous mixtures were formed in the box and the one considered in the current paper, with a hydrogen volume fraction of 15.5 %, was ignited on the small face. The mixture was quiescent before ignition. Venting was ensured by four 0.3 m x 0.4 m vents with an opening pressure of 50 mbar. Two configurations are regarded for the opening surface distribution: either they are grouped on the face opposite to the ignition location or they are split on two faces of the enclosure (Figure 2). The location of the pressure sensors can be seen in Figure 3.

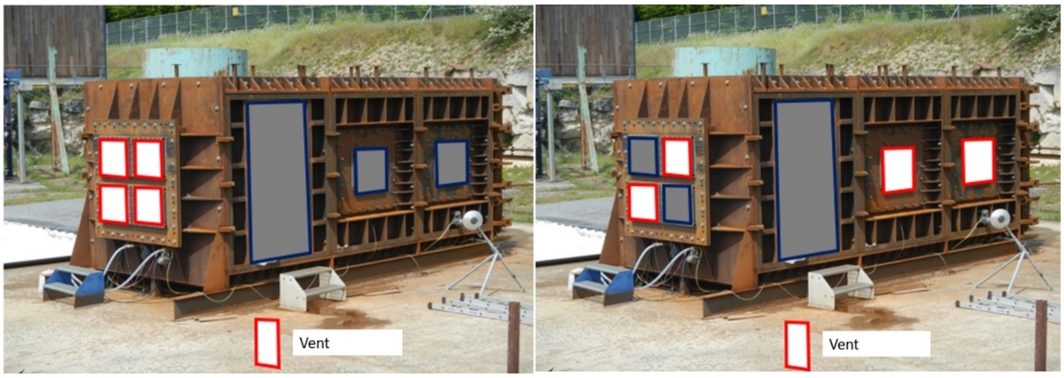

Fig. 2. *View of the 37 m^3 enclosure and of the possible locations of the vents (in red). Left: configuration 1, right: configuration 2. Panels in blue are safety vents which should not open during the explosion.*

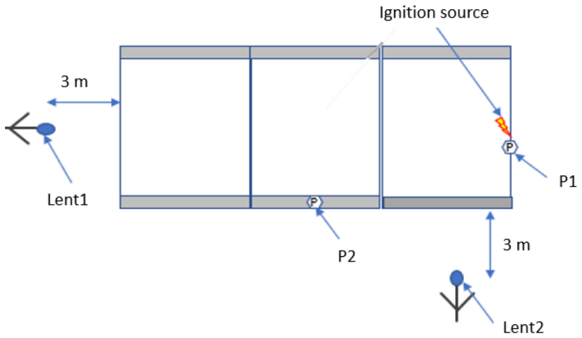

Fig. 3. Location of the ignition source and pressure sensors for the 37 m^3 confined explosions (P1, P2: inside pressure – Lent1, Lent2: outside pressure

3. Phenomenology related to vented explosions and CFD modelling

3.1 Phenomenology

If the mixture is initially quiescent, after the ignition phase the flame front is expected to self-accelerate due to Darrieus-Landau and thermo-diffusive instabilities as it was previously observed for spherical lean hydrogen flames (Bauwens, 2017). If there is an initial turbulence, the flame front acceleration is due to both intrinsic flame instabilities and flame / turbulence interaction. According to lab-scale tests, the flame front wrinkling for a given wave number can be dominantly by one phenomenon or the other depending both on the ratio of the fluctuating velocity, u', and the laminar flame speed S_L and on the Karlovitz number (Yang, 2018).

When moving, the flame pushes the fresh gases that flow out of the enclosure once a vent is open. Depending on the propagation history of the flame inside the enclosure, the outer flow of fresh gases might differ when the flame exits the enclosure. Roughly, if the flame comes out of the box shortly after fresh gases ejection, the flame will propagate in a vortex, if it exits the enclosure later, propagation will occur in a jet. According to a numerical study, in the first case, turbulence is localized to the shear layer surrounding the jet that pushes the vortex (Daubech, 2016). In the second case, it is possible to encounter on a more extended area a more intense turbulence. According to Tolias (2018), it seems that the external explosion effects can be explained mostly by a flame / turbulence interaction. Other authors like Bauwens (2011) and Keenan (2014) estimate the Rayleigh-Taylor instability, related to a sudden acceleration of the flame front when it exits the enclosure, plays a significant role in the pressure effects generation in the external explosion.

3.2 Available approaches in the literature

CFD approaches available in the literature for vented explosions mostly rely on Large Eddy Simulation (LES) for turbulence modeling. Nevertheless, applying this method is very expensive in terms of computational resources as the non-resolved kinetic energy should remain below 20 % (Pope, 2004). A RANS framework is then preferred in the current paper.

Among the available models for CFD modeling of vented explosions, the one of Tolias et al. (2018) relies on a RANS framework.

Tolias et al. approach is based on the k-ϵ model including the modification of Kato-Launder for turbulent correlation closures.

The chemical source term which pilots the propagation speed of the flame front is simply closed as the product of the gradient of the progress variable ($\tilde{c}$), the volume mass of the fresh gases (ρ^u) and a characteristic flame speed: $\bar{\rho}\,\widetilde{\dot{\omega}_c} = \rho^u S_F |\nabla\tilde{c}|$. The flame speed S_F then writes: $\Xi.S_L$ where Ξ is a wrinkling factor. As evocated previously, the lean hydrogen flames are prone to thermo-diffusive instabilities. The choice of closure for the chemical source term implicitly assumes that differential diffusion effects, responsible of these instabilities, are not accounted for by the diffusion operator in the transport equations. Furthermore, a proper modelling of instabilities might need a sufficient resolution of the flame front thickness by the mesh, which is not encountered in RANS modeling.

The wrinkling factor Ξ has to account for all physical phenomena that locally impact the flame speed. In the work of Tolias et al., the wrinkling factor is decomposed in a product of wrinkling factors representing independently the effect of a single phenomenon (turbulence, instabilities, flame-generated turbulence) on the flame front velocity: $\Xi = \Xi_{\mathrm{t}}\Xi_k\Xi_{lp}$. Most of CFD approaches that deal with under-resolved modeling of explosions rely on a similar approach (Molkov, 2012 and Bauwens, 2011). Recently, Lapenna et al. (2021) proposed a similar sub-grid scale modeling from DNS studies of small-scale premixed flames.

Ξ_{t} models the flame / turbulence interaction. It is closed with the model of Schmid et al. (1998) that can be applied in all turbulent combustion regimes. $\Xi_t = 1 + u'/S_L(1 + Da^{-2})^{-1/4}$ where Da is the Damköhler number. Ξ_k accounts for the effect of flame-generated turbulence, a phenomenon drive by hydrodynamic instability and Ξ_{lp} enables to integrate the effect of differential diffusion on the flame speed. Both models were originally proposed by Molkov (2012). They integrate a progressive increase of the corresponding wrinkling factor with the flame radius (R) towards a maximum value. Thus, $\Xi_k = 1 + (\psi\Xi_{k,max} - 1)(1 - \exp(R/R_{0k}))$ with $\Xi_{k,max} = (\tau - 1)/\sqrt{3}$, τ being the thermal expansion rate and $\Xi_{lp} = \Xi_{lp}^{max}/2(1 + \tanh((R - R_{0lp})/0.01))$. Molkov (2012) proposed values for the remaining parameters that depend on the hydrogen volume fraction of the hydrogen / air mixture. According to their formulation, the models for Ξ_k and Ξ_{lp} seem to be designed for flames with an hemispherical or spherical shape.

3.2 Approaches retained

The computations presented in the current work are based on a modelling strategy close to the one of Tolias. The transport equations are solved for momentum, pressure, a progress variable and energy with a pressure-based solver of the CFD code OpenFoam (Weller, 1998). Nevertheless, turbulence is modelled with a standard k- ϵ model and while the chemical source term closure of Tolias et al. was kept, the reference radius R_{0k} appearing in the expressions of Ξ_k was adjusted to the computed configurations in order to get a predicted pressure peak inside the enclosure at the same time as the measured one. Furthermore, for a volume fraction of 16 %, the value of Ξ_k^{max} was increased of 50 %, in order to recover the internal peak pressure. Table 2 shows the parameters values retained.

Table 2: *Retained parameters values for modeling the 4m³ vented explosions. Bold values correspond to adjustments of the original values supplied by Molkov (2012)*

Hydrogen volume fraction	S_L **(m/s)**	τ **(-)**	R_{0lp} **(m)**	Ξ_{lp}^{max} **(-)**	Ξ_k^{max} **(-)**	R_{0k} **(m)**	ψ **(-)**	**Reduction factors for turbulent cases**
16 %	0.505	4.5	0.01	2	**3**	**0.5**	1	0.5
21 %	0.9	5.75		2	$(\tau$ -1)/ $\sqrt{3}$=2,75	**0.2**	1	0.27
25 %	1.5	6.45		1,7	$(\tau$ -1)/ $\sqrt{3}$=3,15	**0.8**	**0.8**	0.37

For the explosion in the 4m³ chamber, the computational domain was 22 m long, 20 m wide and 11 m high. It was composed of 5 million hexahedra with a cell size of 4 cm on the flame path. The mesh for the largest chamber, covering a 14 m x 20 m x 12 m domain was made of 5 million hexahedra, the smallest being 4 cm wide.

4. Case of the 4 m^3 chamber

Figure 3 highlights, for an initially quiescent mixture with a hydrogen volume fraction of 16 %, the pressure signals measured inside the enclosure at two locations, P1 and P2, and outside the box on the axis of the vent. It appears that signals P1 and P2 are distinct whereas identical signals could be expected inside the enclosure for all tests carried out on this enclosure. The reason for this specificity is not known to date. All CFD computations predict same signals for P1 and P2.

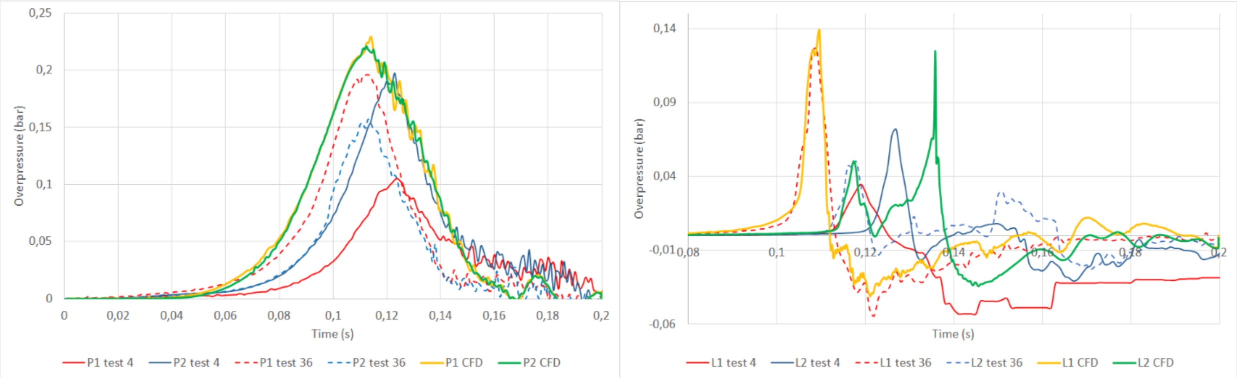

Fig. 3. Case of the initially quiescent mixture with a hydrogen volume fraction of 16 %. Comparison of the computed and measured pressure signals inside (left) ou outside (right) the 4 m^3 enclosure.

While initial conditions are similar, the signals obtained for the two tests 4 and 36 are different but both give an envelope of what should be predicted. CFD slightly overestimates the P2 peak of the test 36 but accurately recovers the L1 pressure signal. The first part of the L2 signal is predicted but unphysical secondary peak appears at 0.12 s. This secondary peak is related to a sudden flame acceleration on the jet axis due to very large values reached (about a few hundreds) by the parameter Ξ_t when the flame reaches the tip of the flammable cloud.

It can be noted here that modelling an experiment with numerous pressure probes is more challenging but brings a safer assessment basis: the L2 signal shows the qualitative agreement of the predicted explosion with the measured one is not fully representative.

Comparison of numerical prediction and measurements for a hydrogen volume fraction of 21 % (Figure 4) shows a P2 pressure peak approached and a large overestimation (about 100 %) for pressure peak L1. The time agreement for pressure peak occurrence inside the box for measurement and prediction seems to lead to a time agreement for the pressure peak occurrence outside of the enclosure.

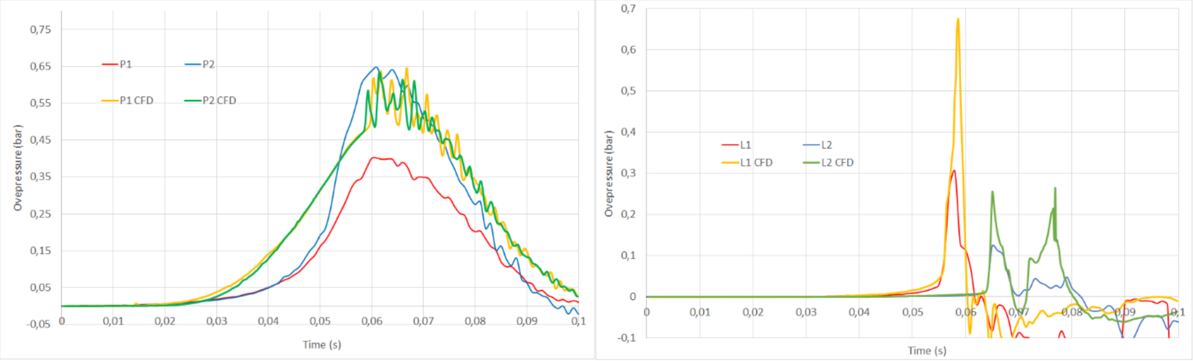

Fig. 4. Case of the initially quiescent mixture with a hydrogen volume fraction of 21 %. Comparison of the computed and measured pressure signals inside ou outside the 4 m^3 enclosure.

The observations made for the 21 % hydrogen volume fraction case can be kept for the 25 % hydrogen volume fraction case (Figure 5).

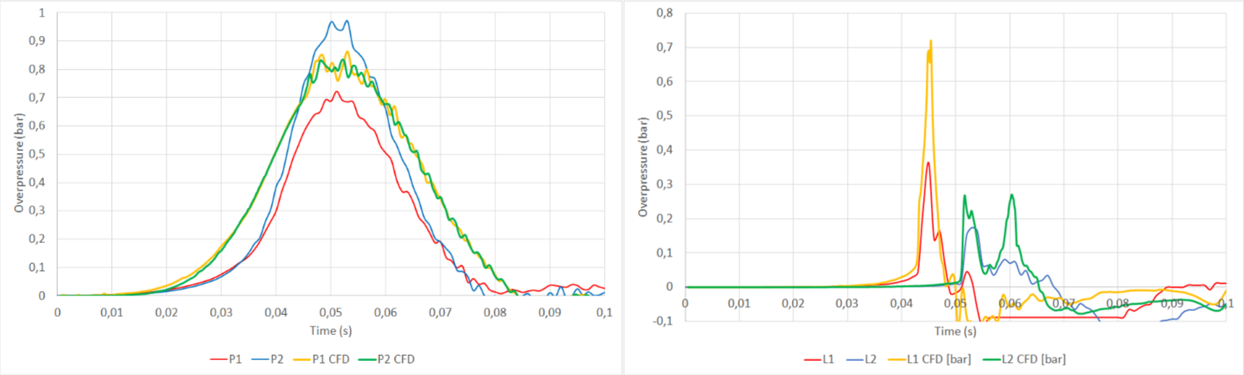

Fig. 5. Case of the initially quiescent mixture with a hydrogen volume fraction of 25 %. Comparison of the computed and measured pressure signals inside ou outside the 4 m^3 enclosure.

Finally, a case for which the velocity field inside the enclosure is turbulent before ignition is considered. For this one the hydrogen volume fraction is 21 % and turbulence is characterized by a fluctuating speed of 5 m/s and an integral length scale of 7 cm. With a Karlovitz number of 70, the combustion regime is, according to the combustion diagram (Peters, 2000), a thickened-wrinkled reaction sheet. The model that was used for the quiescent case is kept, the impact of initial turbulence being accounted for in the initialization of the scalar $\tilde{k}$ and $\tilde{\varepsilon}$. This modelling (not shown) led to significant overestimation of all pressure peaks. It was chosen to multiply the chemical source term with a damping factor in order to retrieve the pressure signal inside the enclosure. A value of 0.27 has to be taken. It can be seen as a correction for the prediction of instabilities effects when turbulence exists before ignition.

Introducing this correction factor, the pressure signal P2 is recovered (Figure 6), but the pressure peak outside of the box close to the vent, measured in L1, is overestimated (about 100 %).

For other turbulent cases with hydrogen volume fraction of 16 % or 25 %, in the same way a damping coefficient lower than 0.5 should be applied to the chemical source term to recover the pressure signal in P2 (Table 2).

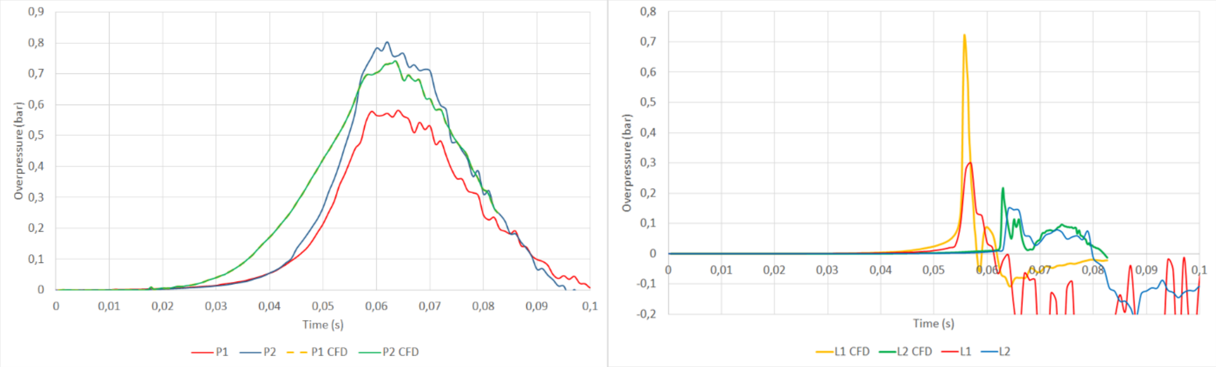

Fig. 6. Case of the initially turbulent mixture with a hydrogen volume fraction of 21 %. Comparison of the computed and measured pressure signals inside (left) and outside (right) the 4 m^3 enclosure.

It appears that the model inspired by Tolias et al. with the set of parameters given by Molkov for the sub-models accounting for the instability effects may require adaptations, at least in the case of the 4 m^3 enclosure for recovering inner pressure signal. This could be explained by the shape of the box in which the flame is elongated and not spherical.

If the mixture is initially turbulent, the chemical source term has to be damped by a coefficient which ranges from 0.3 to 0.5, depending on the hydrogen volume fraction. This shows a limit to the generic character of the model which should be applied only for initially quiescent mixtures.

The predicted pressure peak in L1 is either equal or well higher than the measured one. It is possible that the $k - \epsilon$ model produces too much turbulence outside the enclosure and/or the assumption of an equilibrium turbulent speed reached instantaneously during flame / turbulence interaction is too conservative.

A secondary peak is predicted for the L2 signal. This one is not existing in reality or is largely overestimated. It is explained by a sudden acceleration on the flame axis when approaching the tip of the flammable cloud. The causes of this can be similar the ones mentioned above for L1 signal.

5. Case of the 37 m^3 chamber

The CFD model is, in this section, applied to the case of the explosion of a quiescent and homogenous hydrogen / air mixture with a hydrogen volume fraction of 15.5 % in the 37 m^3 chamber. In the computation, the progressive opening of the vent was not modelled. Each vent was replaced with a permanent opening.

The CFD modelling proposed for a 16 % flammable volume in the 4 m^3 chamber was retained. The computation led to an overestimation of the inner pressure peak. In order to retrieve the final pressure peak, the parameter Ξ_k^{max} was divided by 2.

Figure 7 compares the measured and computed inner pressure signals for configuration 1 and 2. The effect of the vent at the beginning of the signal is not retrieved., nevertheless, in both cases the order of magnitude of the pressure peak is recovered.

DOI: 10.7795/810.20221124

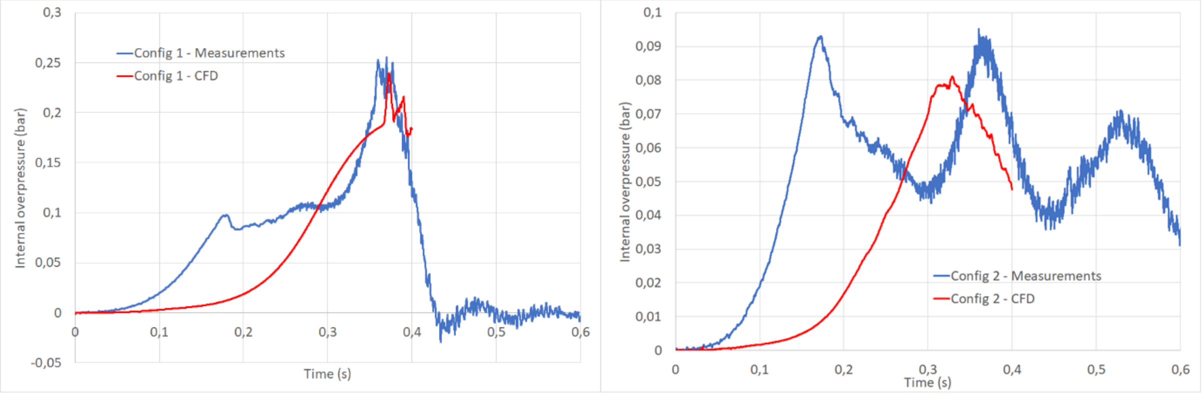

Fig. 7. Comparison of the measured and computed pressure signals inside the 37 m^3 enclosure for the two configurations.

The external pressure signals outside the chamber can be seen in Figure 8 and 9 for configurations 1 and 2. For configuration 1, the measured pressure peak at L1 is about 50 mbar while the CFD model predicts a peak of 280 mbar. For configuration 2, the measured peak is 25 mbar and the predicted one is 20 mbar.

At the pressure probe L2, the maximum measured pressure is 25 mbar for configuration 1 and 7 mbar for configuration 2 and the respective predicted values are 20 and 14 mbar. The orders of magnitude are recovered.

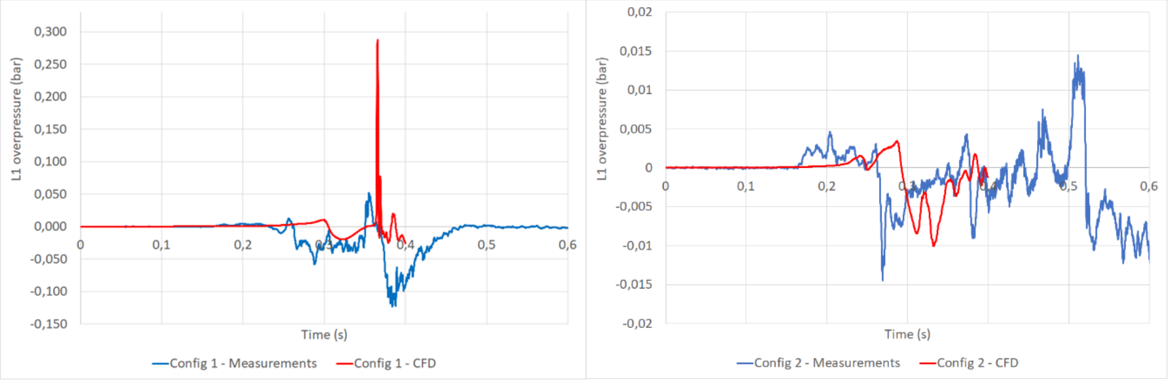

Fig. 8. Comparison of the measured and computed pressure signals at the pressure probe L1 outside the 37 m^3 enclosure for the two configurations.

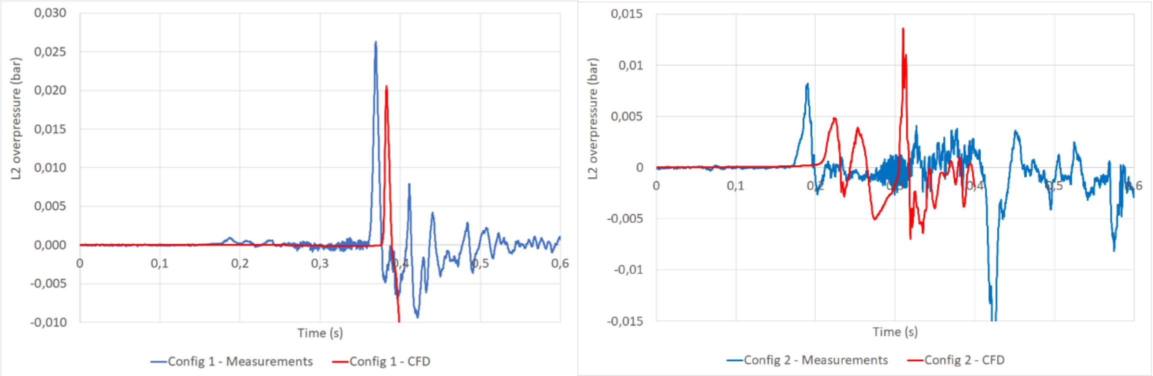

Fig. 9. Comparison of the measured (left) and computed (right) pressure signals at the pressure probe L2 outside the 37 m^3 enclosure for the two configurations.

Once more, it appears that the modeling of instabilities in the CFD model is not generic and that the model used should also depend to the geometry. The section of the combustion chamber is a square whereas it was rectangular in the smallest chamber. This may explain that Ξ_k^{max} had to be adjusted.

The global sequence of the explosion related to configuration 1 first appears similar to the explosion in the small combustion chamber. Nevertheless, the outer flammable cloud is different when the flame exits the enclosure. The outer flammable cloud appears as a jet while in the case of the 4 m^3 chamber took the shape of a large vortex. The overestimation of the prediction of the pressure peak in L1 can be explained by an exaggerated production of turbulence by the $k-\epsilon$ model, by an equilibrium assumption for the flame speed and maybe by missing a physical feature. Local extinction phenomena could be encountered.

6. Conclusions

Computations were performed for vented explosions with varying parameters (hydrogen volume fraction, initial turbulence and geometry). They aimed at verifying if a CFD model similar to these encountered in the literature could predict all these cases.

It appeared that the model for the effects of instabilities in the enclosure had to be modified for certain hydrogen volume fraction and geometries for recovering inner pressure peaks. If initial turbulence was present in the enclosure, a damping factor has to be introduced whose value is difficult to quantify a priori.

The peak pressure of most of the external explosions was overpredicted. It can be due to an overestimation of the turbulence production outside of the box, the assumption of a turbulent flame speed reaching instantaneously its equilibrium value or a part of physics which is missing, like maybe local extinction.

Going deeper in that work is needed to propose a generic way to model the effects of the instabilities on the flame inside the enclosure.

Concerning the external explosion, the pressure effects can be explained by a flame / turbulence interaction. Nevertheless, the outer fresh gases flow should be studied in detail in order to identify the reason the CFD approach of the paper overestimates the pressure effects of the external explosion.

Acknowledgements

This work was granted access to the HPC resources of TGCC under the allocation 2021-A0102B11482 made by GENCI (Grand Equipement National de Calcul Intensif)

References

I.C. Tolias et al. (2018) An improved CFD model for vented deflagration simulations – Analysis of a medium-scale hydrogen experiment. *International Journal of Hydrogen Energy* 43(52), pp. 23568-23584

A. Duclos (2019) *Développement de modèles phénoménologiques et de maitrise des risques d'explosion pour la filière émergente hydrogène-énergie*. Thesis manuscript. Compiègne Technology University

C.R. Bauwens, J. Chaffee & S.B. Dorofeev (2011). Vented explosion overpressure from combustion of hydrogen and hydrocarbon mixtures. *Int. Journal of Hydrogen Energy*, 36(3): 2329-2336.

Molkov, V. (2012). *Fundamentals of Hydrogen Safety Engineering, parts I & II.* Free download e-book, bookboon.com, ISBN: 978-87-403-0279-0.

J. Daubech, E. Leprette & C. Proust (2022) *Influence of vent distribution on the violence of a gas explosion.* Submitted to ISHMPIE.

C.R. Bauwens et al. (2017) *Experimental investigation of spherical-flame acceleration in lean hydrogen-air mixtures.* International Journal of Hydrogen Energy 42, pp. 7691-7697

S. Yang et al. (2018) *Role of Darrieus-Landau instability in propagation in expanding turbulent flames.* J. Fluid Mech 850, pp. 784-802

J. Daubech, C. Proust, G. Lecocq (2016) *Propagation of a confined explosion to an external cloud.* 11th ISHPMIE

J.J. Keenan, D.V. Makarov & V.V. Molkov (2014) *Rayleigh-Taylor instability: Modelling and effect on coherent deflagrations*. International Journal of Hydrogen Energy 39, pp. 20467-20473.

S.B. Pope (2004) *Ten questions regarding the large-eddy simulation of turbulent flows*. New journal of Physics 6.

H.-P. Schmid et al. (1998) *A model for calculating heat release in premixed turbulent flames*. Combust. Flame 113, pp. 79-91

Lapenna et al. (2021) *Subgrid modeling of intrinsic instabilities in premixed flame propagation*. Proc. Combust. Inst. 38(2), pp. 2001-2011

Weller, H.G, Tabor, G. (1998). A tensorial approach to computational continuum mechanics using object-oriented techniques. *Computational Physics*, 12: 620-631.

N. Peters (2000) Turbulent combustion. Cambridge university press.

DOI: 10.7795/810.20221124

Experimental and numerical study of the fuel effect on flame propagation in long open tubes

Guillaume Lecocq [a], Jérôme Daubech [a] & Emmanuel Leprette [a]

Institut National de l'Environnement Industriel et des Risques, Parc Technologique ALATA, BP 2, 60550 Verneuil-en-Halatte, France

E-mail: guillaume.lecocq@ineris.fr

Abstract

Previous works (Daubech, Lecocq, 2019) were dedicated to gaseous flame acceleration along long pipes with a set of cases studied both experimentally and numerically. In these cases, the flammable mixture was initially quiescent and homogenously distributed. The impact of the tube diameter and material were studied trough both approaches for rather slow flames, the fuel being methane. While main features of the real flame were recovered by the chosen CFD method, some limits remained.

A new experimental dataset is detailed and analyzed with a quicker flame, the fuel being hydrogen and the same experimental set-up as the one used for measuring slow flames. Thus, the fuel effect on the flame dynamics can be directly highlighted.

A simple CFD approach is tested for recovering two distinct flame behaviors: a deflagration flame and another undergoing deflagration-to-detonation transition. Furthermore, the modelling results are used to propose elements of interpretation for flame acceleration.

Keywords: *premixed gaseous flame propagation, hydrogen, methane, pipes, CFD*

1. Introduction

Scenarios of formation of gaseous flammable clouds in long ducts can be identified during risk analyses of industrial processes. If an ignition occurs, a flame can propagate in such flammable cloud and undergo an acceleration which is specific to this confined and elongated geometry.

If the flammable cloud formation and the ignition cannot be avoided, it is key to assess the flame acceleration process and the generated pressure effects associated to the explosion scenario. These latter should be compared to the mechanical resistance properties of the pipe in which the explosion could be triggered. To do so, the flame acceleration process has to be understood with the specificities of the explosion scenario (tube material and diameter, flammable cloud length, spatial distribution of the fuel in this cloud, …).

Previous experimental and numerical works were detailed for 24 m long pipes made of PMMA or steel, with varying diameters (150 or 250 mm), the fuel being methane (Daubech, Lecocq, 2019). The pipes were open at one end and closed at the other where ignition was triggered. The tests showed the impact of the pipe material and diameter.

In the current work, new experimental data are presented. They correspond to the case of a 150 mm wide steel tube in which a homogenous hydrogen/air cloud with a volume fraction of 20 % is ignited. They are compared to another experimental point for which the flammable cloud is made of a stochiometric methane/air cloud.

A CFD approach is proposed and tested, in order to assess its predictive capacities and study if elements could be extracted from computations for helping to interpret experiments.

2. Experimental set-up and results

The current work is dedicated to flames propagating in a straight, 24-m long steel pipe, open at one end and closed at the other. It is filled with a quiescent stoichiometric methane/air mixture. Ignition is performed on the middle of the closed end with an electrical spark whose energy is about 100 mJ.

Two flammable mixtures are studied:

- A stoichiometric methane/air mixture,
- A lean hydrogen/air mixture, with a hydrogen volume fraction in air of 20 %.

Figure 1 shows the pipe in which flame propagation is measured.

Fig. 1. *View of the experimental set-up. Steel pipe, with a 150-mm inner diameter.*

The flame position is tracked with four photovoltaic cells located at 0.5 m, 5.5 m (4.5 m for methane), 10.5 m and 15.5 m from ignition point. Pressure signals are measured with three probes close to ignition point and at 5 m and 15.5 m from ignition point.

More details about the experimental set-up are given of the paper of Daubech (2019).

Raw experimental results the flame trajectory and pressure signals are given in Figures 2-3 and Figures 6-7 for both fuels. Two different behaviors can be noticed.

For the methane/air flame, while the flame speed keeps on increasing, its maximum value remains about 140 m/s. Two main peaks can be seen for each pressure signal.

The first one can be explained with flame elongation that follows ignition, which leads to an increase of the burnt gases volume variation per time unit. When this variation becomes weaker, because a maximum in flame surface is reached, the pressure decays. The flame continues to accelerate, eventually with a change in flame shape, and the volume production of burnt gases creates the second peak which is limited by the amount of flammable mixture in the tube. A maximum overpressure about 400 mbar is reached. The time needed to burn all the flammable mixture is between 0.25 s and 0.3 s.

For the hydrogen/air flame also, a continuous flame acceleration can be noticed. A maximum flame speed higher than 2000 m/s is measured. This value can be compared to the Chapman-Jouguet velocity, about 1710 m/s. In this case, a transition from a deflagration regime to a detonation one (DDT) is observed.

At the pressure probe located 5.5 m away from ignition point, a first peak similar to the first peak identified for the methane/air flame appears. A slight pressure decay then occurs and is followed by a continuous pressure increase until a maximum overpressure of 3 bar. 15.5 m away from ignition point, a shock wave appears with a peak about 20 bar. This value is higher than the Chapman-Jouguet pressure (13 bar), which, additionally to what was said for flame velocity, indicates an overdriven detonation.

3. Phenomenology related to explosions in pipes and CFD modelling

3.1 Phenomenology

Cicarelli et al. (2008) proposed a review article dedicated to flame acceleration in pipes. With ignition, a burnt gases kernel is created, which leads to the formation of a premixed laminar flame. It is first wrinkled due to Darrieus-Landau instability, which is promoted or counteracted by thermo-diffusive effects, respectively if the Lewis number is lower or higher than 1. In the same time, the fresh gases are pushed ahead of the flame front due to thermal expansion effects. The flame front then reaches the lateral wall of the tube, leading to slight deceleration of the burnt gases production, the flame surface being reduced. It can be also promoted by heat losses, depending on the tube material. After this initial stage, the flame keeps on propagating with a shape that can sequentially change from an elongated flame to a tulip-shape flame, still pushing the fresh gases. The flame acceleration mechanism in this phase remains discussed.

With his pioneer works, Shchelkin (1940, 1965) explained flame self-acceleration in tubes with flame/turbulence interaction, turbulence being produced in the fresh gases after generation of a boundary layer on the walls. This explanation highlights the importance of the wall roughness on the flame dynamics. Experiments (Daubech, 2019) carried out for methane/air flames propagating in long open tubes with different materials (ie PMMA for a smooth tube and steel for a rough tube) indeed led to different flame dynamics provided the tube diameter was small enough. The same set of experiments also showed the wall turbulence remained limited at the walls for the widest tubes while flame acceleration was noticed.

According to Cicarelli et al. (2008), a detonation can be first initiated after a shock reflection or a shock focusing. The shock is strong enough to auto-ignite fresh gases and trigger detonation. It can also be due to more subtle mechanisms involving instabilities and mixing processes. These phenomena were first explained by Zeldovitch (1970) and Lee (1978): if an induction time gradient is formed, due to local inhomogeneities (temperature and/or concentration). The related spontaneous flame would release heat and create a shock wave. If the heat release strengthens the shock wave sufficiently, a detonation can occur. More recent works (Ivanov, 2011) called into question this mechanism. According to the authors, DDT occurs when the flame is so fast that formed shock waves sit on the flame front and a coupling mechanism leads to a sufficient increase of flame speed and pressure peak.

3.2 Modelling approaches available in the literature

CFD approaches available in the literature for flame acceleration in tubes rely either on a highly detailed description of the flow (Oran, 2007) or "under resolved" modelling that are built with numerous sub-models, each one accounting for a physical feature (Wieland, 2021).

With such models, the chemical source term which pilots the propagation speed of the flame front is simply closed as the product of the gradient of the progress variable ($\tilde{c}$), the volume mass of the fresh gases (ρ^u) and a characteristic flame speed: $\bar{\rho}\,\widetilde{\dot{\omega}_c} = \rho^u \mathrm{S_F} |\nabla \tilde{c}|$. The flame speed $\mathrm{S_F}$then writes: $\Xi.\, \mathrm{S_L}$ where Ξ is a wrinkling factor. This latter is explained as the product of characteristic wrinkling factors, each one accounting for a phenomenon accelerating the flame speed: thermo-diffusive and Darrieus-Landau instabilities, pressure effects, …

Some authors (Wieland, 2021, Bradley, 2012) describe detonation as the coupling of auto-ignition of fresh gases coupled to the propagation of a shock wave. Chemical source terms can be built from two contributions (Lecocq, 2011, Wieland, 2021): one modelling a premixed flame, the other auto-ignition, in order to account for the transition between the deflagration and the detonation.

3.3 Approach retained

The computations presented in the current work are based on a modelling strategy close to the one of Wieland (2021) for modelling deflagrations. The transport equations are solved for momentum, pressure, a progress variable and energy with a pressure-based solver of the CFD code OpenFoam v2106 (Weller, 1998). Turbulence is also modelled with a k-ω SST model (Menter, 2003).

Concerning the methane/air flame the pressure effects remain moderate. A constant laminar flame speed of 0.4 m/s was used. The pressure effects are well higher for the hydrogen/air flame and they have to be included for the estimation of the fresh gases volume mass ρ^u and the laminar flame speed $\mathrm{S_L}$. ρ^u is simply quantified under the assumption of an adiabatic compression, thanks to the pressure field. Correlations can be found in the literature for the laminar flame speed of hydrogen. Nevertheless, it is not clear according to bibliography if laminar flame speed should increase or decrease with pressure (Bougrine, 2011, Salzano, 2012). Then, for the sake of simplicity, a constant laminar flame speed value of 0.9 m/s is used for the hydrogen flame.

The wrinkling factor Ξ is closed as: $\Xi = \Xi_t . \Xi_I$ where Ξ_t represent flame wrinkling induced by flame/turbulence interaction and is closed with the turbulent flame speed correlation proposed by Gülder (1991). The wrinkling factor Ξ_I represents the effects of instabilities. The commonly made assumption of a unitary Lewis number for methane/air flames is kept and Ξ_I is set to 1.0 in this case. Concerning the hydrogen/air flame, its Lewis number, about 0.6, is smaller than 1.0 and instabilities at the flame front are expected. A value for Ξ_I remains hard to predict. An ad hoc way was to tune it in order to recover a proper flame trajectory with time. A constant value of 3.3 was identified.

The computational domain is limited to the part of the pipe filled by the flammable mixture. At walls, velocity is zero and turbulent viscosity is modelled with a wall law. At the outlet plane, the pressure is set to the atmospheric pressure and the velocity gradient is set to 0.

The walls are assumed to be adiabatic (temperature gradient set to 0). The steel roughness is assumed to be around 150 µm which corresponds to a weakly rusted steel. This characteristic is used in the wall laws.

The mesh is made of 2.5 million hexahedra. The maximum characteristic cell width is about 6 mm. The cells are refined at the walls.

4. Results

According to Figure 2, the computation enabled to recover a qualitative agreement for the evolution of the flame front position with time. The increase in flame velocity is satisfying from t=0s to t=0.05 s and from t=0.15 s to t=0.25 s but is overpredicted from t=0.05 s to t=0.15 s.

Figure 3 shows the main features of the pressure signals are predicted. At 5.5 m and 10.5 m, there is a first pressure peak, followed by a pressure decay and one or several peaks. The amplitude of the first pressure peak is about 200 mbar and the second is about 400 mbar. The overestimation of the first peak by the modelling is about 25 % while the second one ranges from 25 to 50 %.

It is interesting to go a little bit further in the computation post-processing as several quantities can explain pressure effects. Indeed, these latter are related to the volume rate at which burnt gases are produced by flame propagation, the tube acoustics and the effect of the opening.

The total flame surface captured by the mesh is quantified as: $S_{res} = \int_V |\nabla\tilde{c}|\, dV.$ A resolved wrinkling, Ξ_{res}, can be defined as the ratio of this surface to the tube section. The turbulent wrinkling averaged on the flame surface, $< \Xi_t >_s$ is also computed. The evolution of these quantities with time is plotted in Figure 4.

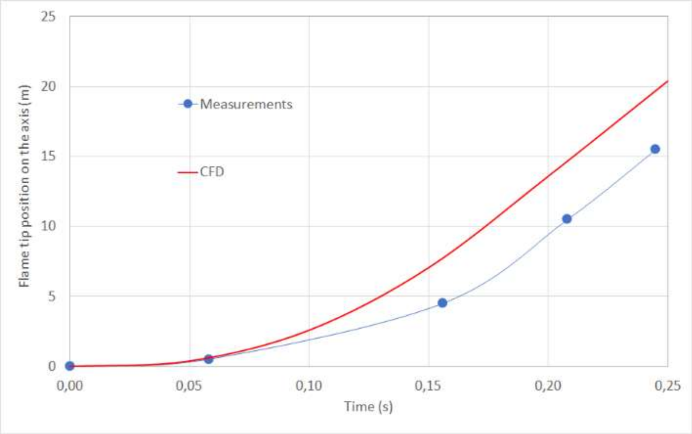

Fig. 2. Experimental and computed flame trajectory on the axis for the methane/air flame.

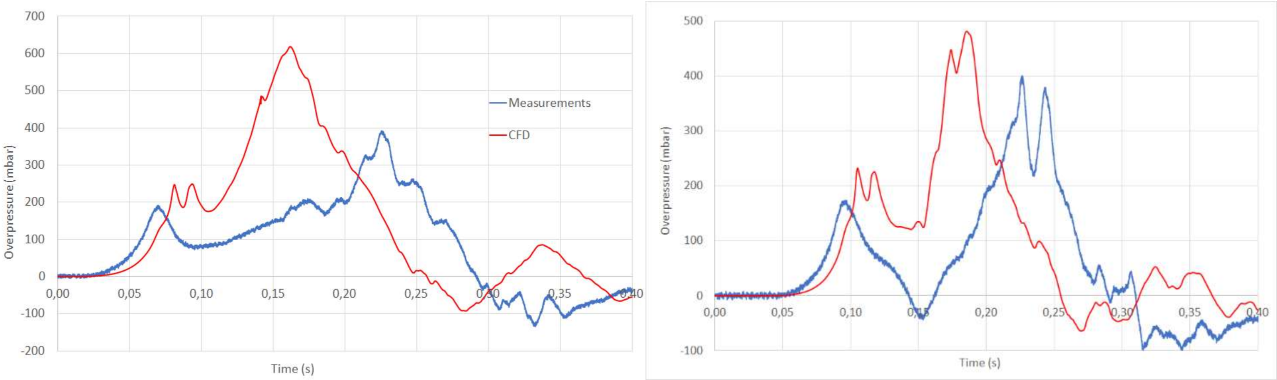

Fig. 3. Experimental and computed pressure signals at 5.5 m (left) and 15.5 m (right) from ignition point for the methane/air flame.

$< \Xi_t >_s$ mainly increases with time, starting from t=0.05 s. The final value reached is about 15. Ξ_{res} does not follow the same evolution: there are two cycles of increase/decrease and a constant value is observed for the final propagation phase. The maximum value is about 8. According to the Figure 5, the maximum values, reached for example at t=0.05 s and t=0.15 s correspond to elongated flames. The lowest values at the end of flame propagation are obtained for quasi-flat flames.

It is notably interesting to note that:

- the first pressure peak at 0.07 s seems to be mainly explained by flame elongation and very weak flame/turbulence interaction,
- the pressure decay that follows is related to the change of the flame shape (from an elongated shape to a tulip shape),
- the pressure peak at 0.15 s is obtained when the product $< \Xi_t >_s . \Xi_{res}$ is the highest.

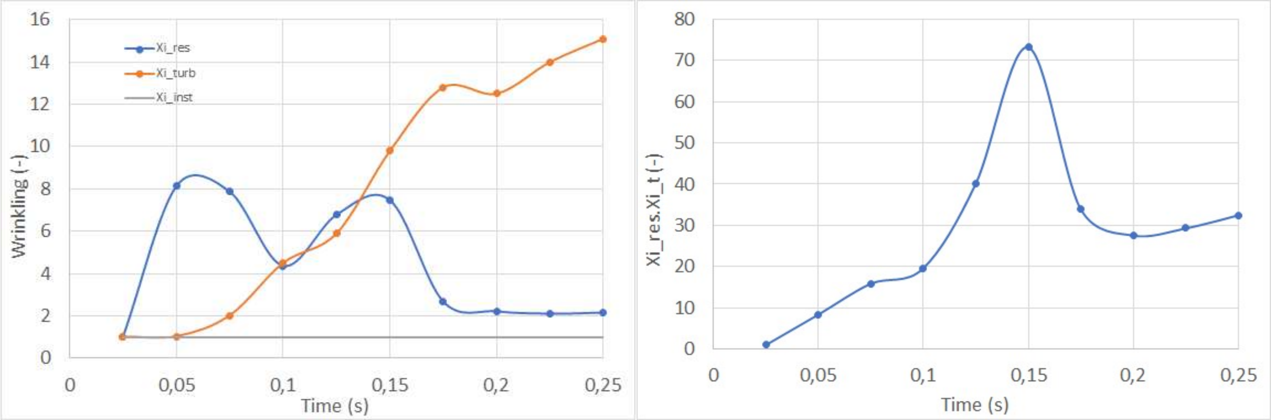

Fig. 4. Evolution of characteristic wrinkling factors for the methane/air flame with time (left) and of the products of all wrinkling factors (right)

Figure 6 shows the experimental and predicted flame trajectory. It should be recalled here that the parameter Ξ_I was adjusted to recover a satisfying flame trajectory.

Figure 7 highlights the main trends of the pressure signals were recovered. At 5.5 m, the computed pressure signal is characterized with three peaks, with an overall pressure increase. The amplitude of the pressure is closed to the measured one. 15.5 m away from ignition point, the measured shock wave is predicted, nevertheless with a peak overestimation of 75 %. This proves a pressure-based solver is able to deal with shocks. Other authors choose to change their solver when the flame velocity exceeds a critical value (Wieland, 2021).

The characteristic wrinkling factors are also plot for the hydrogen flame (Figure 8). $< \Xi_t >_s$ mainly increases, starting from 0.01 s to 0.06 s and then decreases. The peak value is very high (85 *ie* about 6 times the peak value observed for the methane/air flame). As for the methane/air flame, Ξ_{res} sequentially increases and decreases. The peak values of lower than those obtained for the methane/air flame.

The first pressure peak seems to be explained by an increased flame surface as well as flame instabilities. A pressure decay is observed, related to a rapid change of the flame shape which is not compensated by flame instabilities and flame/turbulence interaction. After this phase, while the flame shape and surface evolve (Figure 9), the flame acceleration is mainly promoted by flame/turbulence interaction, until the end of the flame propagation in the tube.

Here DDT was approached through a continuous turbulent flame acceleration until the flame front reaches the preceding shock wave. This point of view is closed to the Shchelkin one but it may be too much simple compared to realistic mechanisms. It is indeed possible that the CFD model should predict flame extinction instead of flame acceleration.

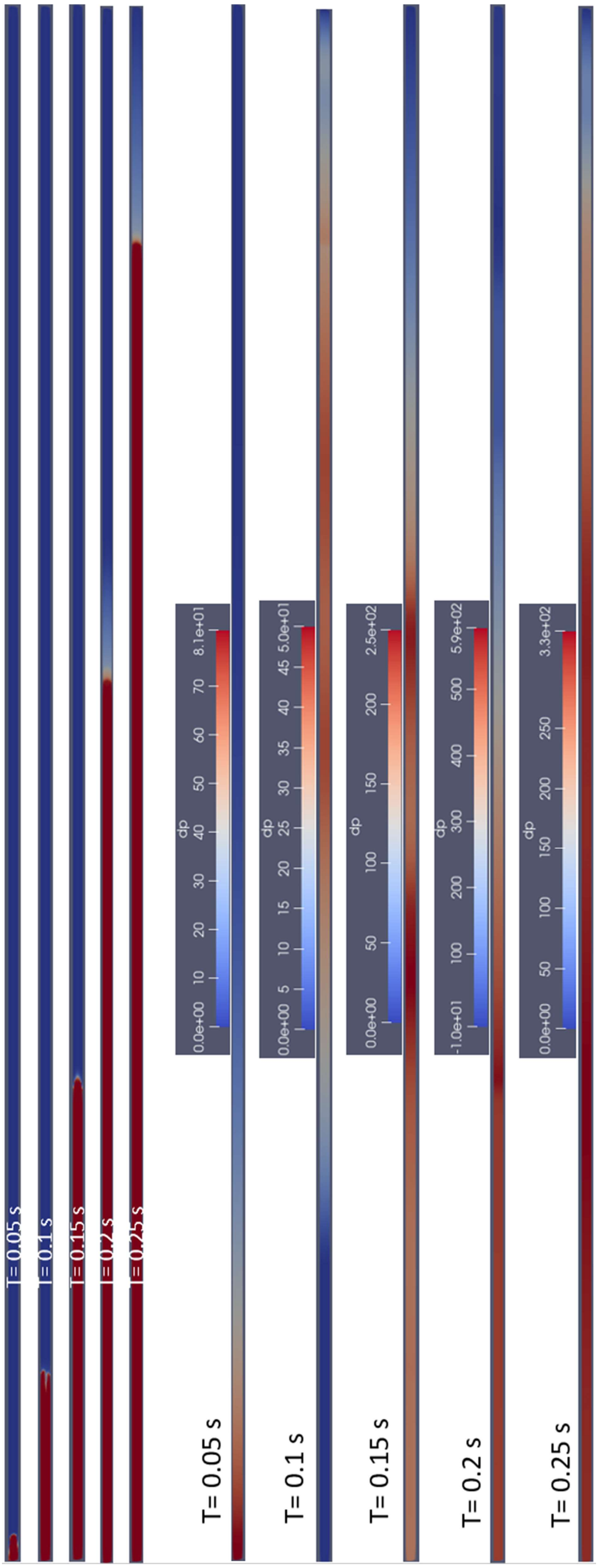

Fig. 5. Evolution with time of the flame (left) and of the pressure field (right) for the computed methane/air flame. Units for pressure are mbar.

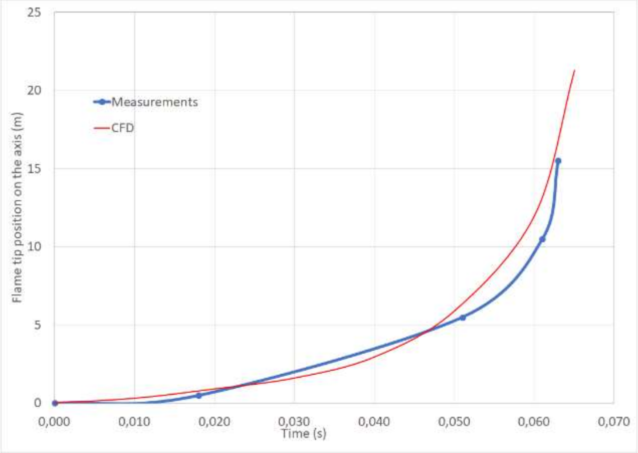

Fig. 6. Experimental and computed flame trajectory on the axis for the hydrogen/air flame

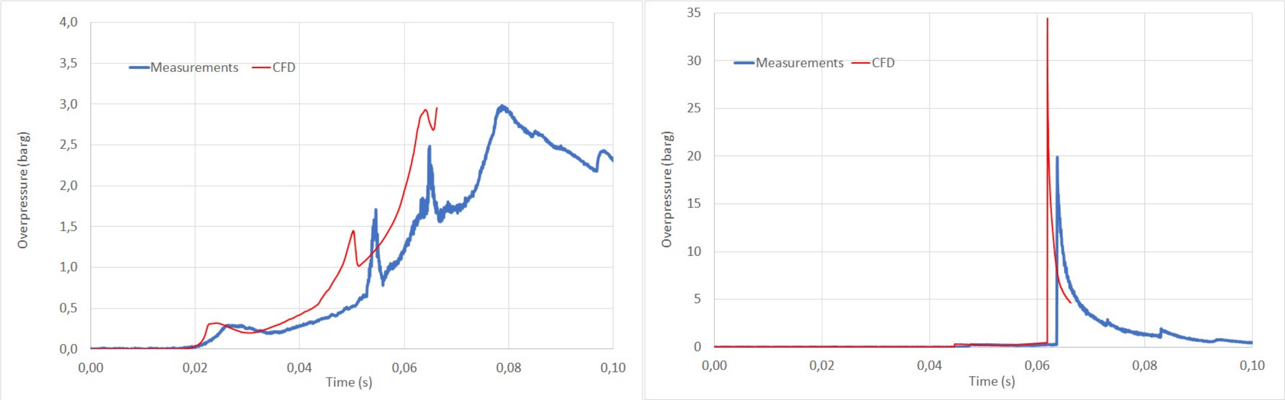

Fig. 7. Experimental and computed pressure signals at 5.5 m (left) and 15.5 m (right) from ignition point for the hydrogen/air flame.

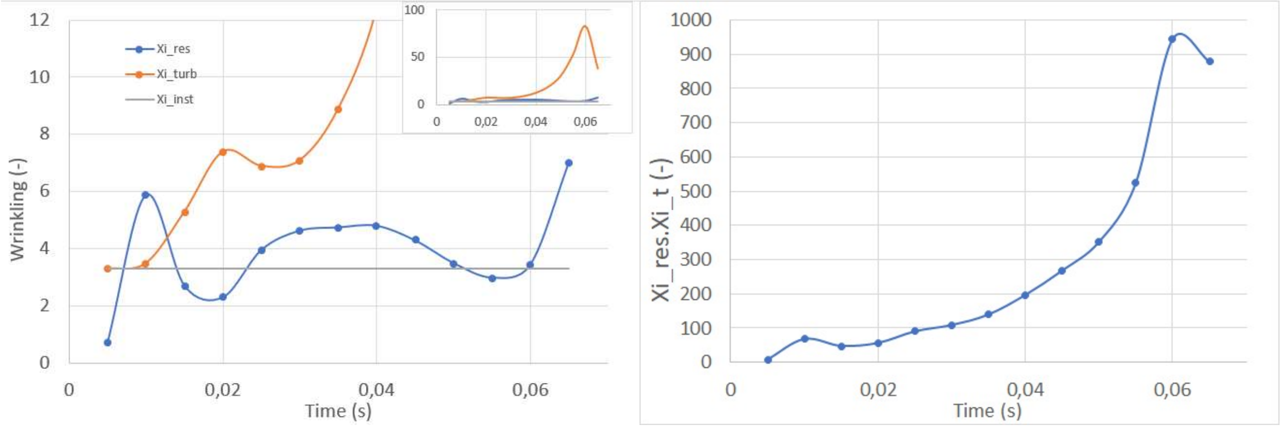

Fig. 8. Evolution of characteristic wrinkling factors for the hydrogen/air flame with time (left) and of the products of all wrinkling factors (right)

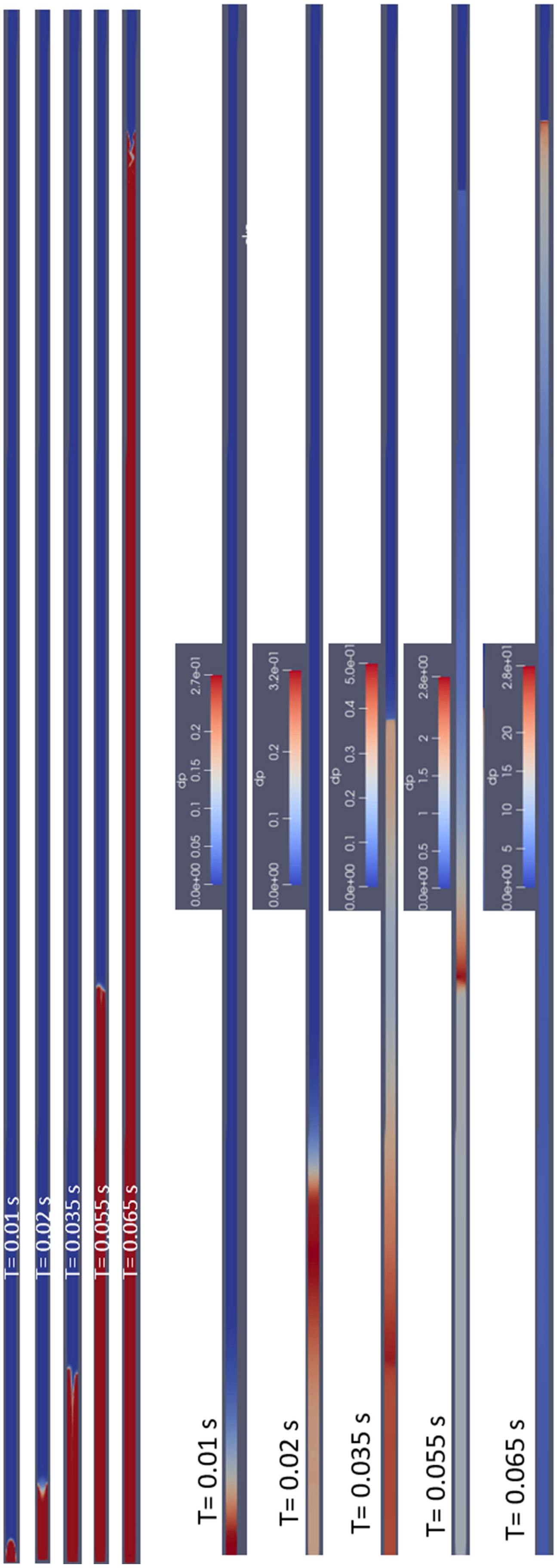

Fig. 9. Evolution with time of the flame (left) and of the pressure field (right) for the computed hydrogen/air flame. Units for pressure are bar.

5. Conclusions

Experimental results were first shown for a 24 m long steel pipe in which initially quiescent flammable mixtures were ignited, one being a stoichiometric methane/air mixture, the other a lean hydrogen/air mixture.

Two distinct flame behaviours were observed: the maximum propagation speed of the methane/air flame was about 140 m/s while DDT occurred for the hydrogen/air flame.

A simple CFD model was used to recover features of both cases. An agreement was found for flame position with time and pressure effects.

The raw CFD results were post-processed to give pieces of interpretation for what was observed. One interest of CFD here is to give access to more quantities than the measured ones. Thus, it was possible to study the effect of turbulence, instabilities and flame shape changes on the pressure effects.

Nevertheless, the current CFD model should be completed with other sub-models (extinction, autoignition sub-models, …) as it is possible that the acceleration for the hydrogen flame, numerically explained by flame/turbulence interaction is not as large as predicted.

References

Daubech, J., Proust, C., Leprette, E., Lecocq, G. (2019). Further insight into the gas flame acceleration mechanisms in pipes. Part I: experimental work. *Journal of Loss Prevention in the Process Industries* 62, 103930

Lecocq, G., Leprette, E., Daubech, J., Proust, C. (2019). Further insight into the gas flame acceleration mechanisms in pipes. Part II: numerical work. *Journal of Loss Prevention in the Process Industries* 62, 103919

Cicarelli G. and Dorofeev S. (2008*)* Flame acceleration and transition to detonation in ducts. *Progress in Energy and Combustion Science* 34, pp. 499-550

Shchelkin KI (1940*)* Influence of the wall roughness on initiation and propagation of detonation in gases. *Zh Eskp Teor Fiz* 10, pp. 823-827.

Shchelkin KI, Troshin YaK (1965*) Gas dynamics of combustion. Baltimore: Mono book corp.*

Zeldovitch YaB, Librovich VB, Makhiviladze GM. Sivanshinsky GI (1970) On the development of detonation in a non-uniformy preheated gas. *Astronautica Acta* 15, pp. 313-321

Lee JHS, Knystautas R, Yoshikawa N (1978) Photochemical initiation and gaseous detonations. *Acta Astronautic*a 5, pp. 971-972

Ivanov M.F., Kiverin A.D., Liberman M.A. (2011) Flame acceleration and DDT of hydrogen-oxygen gaseous mixtures in channels with no-slip walls. *Int. J. of Hydrogen Energy* 36, pp. 7714-7727

Lecocq G., Richard S., Michel J.-B., Vervisch L. A new LES model coupling flame surface density and tabulated kinetics approaches to investigate knock and pre-ignition in piston engines, *Proceedings of the Combustion Institute* 33(2) (2011) 3105-3114

Oran E.S., Gamezo E.N. (2007) Origins of the deflagration-to-detonation transition in gas-phase combustion. *Combust. Flame* 148, pp. 4-47

Wieland C., Scharf F., Shildberg H.-P., Hoferichter V., Eble J., Hirsch C., Sattelmayer T. (2021) Efficient simulation of flame acceleration and deflagration-to-detonation transition in smooth pipes. *Journal of Loss Prevention in the Process Industries* 71, 104504

Bradley D (2012) Autoignitions and detonations in engines and ducts, *Phil. Trans. R. Soc. A* (2012) 370, 689–714

Weller, H.G, Tabor, G. (1998). A tensorial approach to computational continuum mechanics using object-oriented techniques. *Computational Physics*, 12: 620-631.

Menter F.R., Kuntz M., and Langtry R. (2003). Ten years of industrial experience with the SST turbulence model. *Proceedings of the international symposium on turbulence, heat and mass transfer*, 4: 625–632.

Gülder O. (1991*)* Turbulent premixed flame propagation models for different combustion regimes*. Proc. Combust. Inst. 23, pp. 743-750*

Bougrine S. et al. (2011) Numerical study of laminar flame properties of diluted methane-hydrogen-air flames at high pressure and temperature using detailed chemistry. *Int. Journal of Hydrogen Energy* 36, pp 12035-12047

Salzano E. et al. (2012) Explosion behavior of hydrogen-methane/air mixtures. *J. Loss Prev. In the Process Ind.* 25, pp. 443-447

Herausgeber:

Physikalisch-Technische Bundesanstalt
ISNI: 0000 0001 2186 1887
Bundesallee 100
38116 Braunschweig, Germany

Dr. Michael Beyer
Dr. Arnas Lucassen
3.7 | Fundamentals of Explosion Protection

phone: +49 531 592-3700
e-mail: michael.beyer@ptb.de

ishpmie2022.ptb.de
ishpmie2022@ptb.de

DOI 10.7795/810.20221124

As of: 12/22